WILEY-VCH

“十三五”国家重点图书出版规划项目

Metal Oxide Varistors

From Microstructure to Macro-Characteristics

金属氧化物压敏电阻

从微观结构到宏观特性

何金良　著
Jinliang He



清华大学出版社
北　京

“十三五”国家重点图书出版规划项目

Metal Oxide Varistors
From Microstructure to Macro-Characteristics

金属氧化物压敏电阻
——从微观结构到宏观特征（英文版）

何金良（Jinliang He）著

清华大学出版社
北 京

内 容 简 介

金属氧化物压敏电阻是电力和电子系统的关键保护器件，直接决定系统运行的安全可靠性。本书系统介绍了氧化锌等压敏电阻的基础研究、制备工艺、性能调控及应用进展，包括导电及老化机理、微结构电特性、微结构测试及微结构仿真分析、高梯度低残压氧化压敏陶瓷、氧化钛及氧化锡等其他体系压敏陶瓷的研究进展等，构建了压敏电阻微结构特性与宏观特性之间的关联性。

本书可供高校和科研院所电气工程、微电子、材料等专业的师生以及电力传输、电气设备制造等行业的工程技术人员阅读和参考。

本书海外版由清华大学出版社授权 Wiley 在中国大陆以外地区出版发行：
ISBN 978-3-527-33382-0。

图书在版编目(CIP)数据

金属氧化物压敏电阻：从微观结构到宏观特性 = Metal Oxide Varistors—From Microstructure to Macro-characteristics /何金良著.—北京：清华大学出版社，2019

ISBN 978-7-302-53336-8

Ⅰ. ①金…　Ⅱ. ①何…　Ⅲ. ①压敏电阻器　Ⅳ. ①TM541

中国版本图书馆 CIP 数据核字(2019)第 159970 号

责任编辑：黎　强
封面设计：傅瑞学
责任印制：宋　林

出版发行：清华大学出版社
网　　址：http://www.tup.com.cn, http://www.wqbook.com
地　　址：北京清华大学学研大厦 A 座　　**邮　　编：**100084
社 总 机：010-62770175　　**邮　　购：**010-62786544
投稿与读者服务：010-62776969, c-service@tup.tsinghua.edu.cn
质量反馈：010-62772015, zhiliang@tup.tsinghua.edu.cn
印 刷 者：三河市铭诚印务有限公司
装 订 者：三河市启晨纸制品加工有限公司
经　　销：全国新华书店
开　　本：170mm×240mm　　**印　　张：**30
版　　次：2019 年 8 月第 1 版　　**印　　次：**2019 年 8 月第 1 次印刷
定　　价：158.00 元

产品编号：043524-01

Preface

Metal oxide varistor (MOV), or ZnO varistor, is a kind of polycrystalline semiconductor ceramics composed of multiple metal oxides and sintered by conventional ceramic technology. ZnO varistors have good nonlinear volt-ampere characteristics and excellent impulse energy-absorbing capacities. These advantages make them widely used in transient overvoltage protections for electrical/electronic systems. Now, varistors have been widely used as guardians to protect circuits over a very wide range of voltages, from a few volts in semiconductor circuits to 1000 kV AC and ± 1100 kV DC in electrical power transmission and distribution networks. Correspondingly, they can also handle an enormous range of energies from a few joules to many megajoules. Remarkably, they are also very fast, switching in nanoseconds from their high-resistance state to highly conducting state and then restores to a normal high-impedance operating conditions.

A bulk varistor is a complex multijunction device composed of large numbers of both ohmic and nonlinear elements connected in a random network. The features of bulk varistors are influenced by the geometry and the topology of the granular microstructure, as well as the properties and the distribution of electrical characteristics of grain boundaries. This book tries to bridge the Macro-Characteristics with the properties in microstructures of ZnO varistors to provide insights into some of the aspects in the microstructures of ZnO varistors, which influence the features of the bulk varistors and further the science and the understanding on microstructures of ZnO varistors and those parameters that affect the efficiency during the manufacturing process.

The book includes 12 chapters, which mainly focuses on ZnO varistors. Chapter 1 introduces and highlights the fundamental knowledge and applications of ZnO varistors. Chapter 2 introduces the conduction mechanism of the ZnO varistor, among the numerous conduction models, the one presented by G.E. Pike and further developed by G. Blatter and F. Greuter has been widely recognized and may meet most of the experimental phenomena. Various additives to improve the electrical characteristics were discovered and the synthesis conditions were optimized, which will be introduced in Chapter 3. The electrical properties of each individual grain boundary will contribute to the global electrical characteristics of ZnO varistors, Chapter 4 characterizes the microstructural electrical properties of ZnO varistors. The simulation is helpful to reveal the connection between the microstructure and the macroscopic characteristics

of varistor ceramics, the details on how to simulate varistor ceramics will be presented in Chapter 5. The breakdown of ZnO varistors is an original phenomenon during their applications, and the failure models result in different energy handling capabilities, which will be introduced in Chapter 6. ZnO varistors can be electrically, chemically, and thermally degraded during use, leading to the reduction of barrier voltage height and, consequently, to the increase of leakage current, which could be catastrophic for ZnO varistors, Chapter 7 discusses the electrical degradation of ZnO varistors. Chapter 8 introduces other ZnO varistor systems instead of bismuth, such as praseodymium, barium, and vanadium, for overcoming the shortcomings of Bi_2O_3-based ZnO varistors.

The applications in electronic systems require the miniaturized varistors and low-voltage varistors. Chemical processing, such as sol–gel, solution, precipitation, microemulsion techniques, etc., facilitates a homogeneous doping at the molecular level to obtain a miniature device with a higher breakdown voltage, which will be introduced in Chapter 9. Interestingly, the ceramic–polymer composite varistor is a composite one, incorporating varistor particles or semiconducting particles, and its field-dependent property varies with the filler concentration. The composite varistor, with a lower breakdown voltage, can be a suitable substitute for ZnO-based varistors for the purpose of protection for low-voltage systems, which will be introduced in Chapter 1.

Besides works on improving the performance of the ZnO varistor material, other new materials have also been searched in order to achieve a better stability and be used for new applications. The titanium-based capacitor–varistor dual-function varistor ceramics, such as TiO_2, $SrTiO_3$ $CaCu_3Ti_4O_{12}$ (CCTO), and $BaTiO_3$ varistor ceramics, have realized the goal to achieve component miniaturization and provide a superior high-frequency and high-amplitude transient voltage protection, which will be introduced in Chapter 10. Different from the multiphase structure of the ZnO-based varistor, the SnO_2-based varistor has a simple microstructure, good stability, and better thermal conductivity, which makes the SnO_2-based varistor one of the most promising candidates to commercially compete with the ZnO-based varistor. The SnO_2-based varistors will be introduced in Chapter 11. The WO_3-based varistor ceramic is another kind of low-voltage varistor with a low threshold electric field of 5–10 V mm^{-1} and a high dielectric constant, which enables it to act as a varistor in parallel with a capacitor, which will be introduced in Chapter 12.

This book covers main aspects of metal oxide varistors, which introduce fundamental and advanced theories and technologies related to metal oxide varistors, research achievements in the this field, and has reflected the recent research works of the authors and their students and colleagues in Tsinghua University, especially the Ph.D. dissertations of Dr. Chen Qingheng, Dr. Hu Jun, Dr. Liu Jun, Dr. Long Wangcheng, Dr. Zhao Hongfeng, Dr. Xie Jingcheng, Dr. Cheng Chenlu, and MSc thesis of Ms. Wei Qiaoyuan. The author tried to cover all the aspects of metal oxide varistors, but it is hard to avoid ten thousand may have been left out.

Professor Jinliang He
Tsinghua University
Beijing
China

Acknowledgments

My research works on metal oxide varistors in Tsinghua University were supported by the National Natural Science Foundations of China under Grants 59907001, 50425721, 50677029, and 50737001, and was supported in part by the 11th Five-Year Science and Technology Support Plan of China, and by the National Basic Research Program of China under grant 2014CB239504.

Enormous references had been cited in our book, all had been listed in every chapter, but it is hard to avoid careless omission, in this case, I beg your pardon. I am so sorry, some formulas are unable to find the original references where they came from.

I have had a long-term cooperation in the research of metal oxide varistors with Prof. Nan Cewen of Tsinghua University, who is an Academician of Chinese Academy of Sciences, and Prof. Lin Yuanhua, who is the Dean of the School of Materials Science and Technology in Tsinghua University, I have learnt a lot from them, and many cooperation results have been collected in the book. I would like to extend my sincere thanks to them.

Special thanks go to Dr. Han-Goo Cho and Dr. Se-Won Han, from Korea Electrotechnology Research Institute (KERI), for providing me the chance to do research works in the field of metal oxide varistors during 1997–1998. KERI is where I started my research in this field.

Special thanks also go to my students, including Dr. Long Wangcheng, Dr. Luo Fengchao, Dr. Xie Jingcheng, Ms. Wei Qiaoyuan, and Mr. Meng Pengfei, for their assistance on preparing the draft of the book and to my colleagues for their generous help in many ways so as to allow me to allocate time working on the book. Great gratitude is given to Prof. Hu Jun for preparing the manuscript of Chapter 5, Dr. Cheng Chenlu for preparing part manuscripts of Chapters 2 and 7, and Dr. Liu Jun for preparing the part manuscript of Chapter 7.

Gratitude is extended to Mr. Lesley Jebaraj, Project Editor at Wiley, for his editorial and technical reviews on this book. His professionalism and experience have greatly enhanced the quality and value of this book.

Lastly, but not least, my most special gratitude goes to my supporting and understanding family, my mother, Yang Ruiru, who taught me working hard and enjoying the wonderful life; my wife, Prof. Tu Youping, who had done and has been still doing a great job on supporting the family. Most of all, I am indebted to my son, Ziyu, I have not spent much time to enjoying his grow-up process, but it is gratifying that he is working hard to become a scientist in the field of statistics and machine learning.

Jinliang He

Contents

1

Introduction of Varistor Ceramics

Zinc oxide (ZnO) varistor, which is a kind of polycrystalline semiconductor ceramic composed of multiple metal oxides and sintered using conventional ceramic technology, is a voltage-dependent switching device, which exhibits highly nonohmic current–voltage characteristics above the breakdown voltage. Basic information on ZnO varistors, including the fabrication, microstructure, and typical electrical parameters, is introduced. The history and applications of ZnO varistors are also presented. The panorama of alternative varistor ceramics for Bi_2O_3-based ZnO varistors is mapped out. Especially, the ceramic–polymer composite varistors with lower breakdown voltage, incorporating varistor particles such as semiconducting particles, a combination of metal and semiconducting particles, and ZnO microvaristors, in a polymeric matrix are reported. Now, varistors are available that can protect circuits over a very wide range of voltages, from a few volts for low voltage varistors in semiconductor circuits to 1000 kV AC and ±1100 kV DC in electrical power transmission and distribution networks. Correspondingly, they also can handle an enormous range of energies from a few joules to many megajoules.

1.1 ZnO Varistors

A varistor is an electronic component with a "diode-like" nonlinear current–voltage characteristic, which is a portmanteau of variable resistor [1]. Functionally, varistors are equivalent to a back-to-back Zener diode and are typically used in parallel with circuits to protect them against excessive transient voltages in such a way that, when triggered, they will shunt the current created by the high voltage away from sensitive components.

The most common type of varistor is the metal oxide varistor (MOV), which contains a ceramic mass of ZnO grains, in a matrix of other metal oxides, such as small amounts of bismuth, cobalt, and manganese, sandwiched between two metal electrodes. The boundary between each grain and its neighbor controls the current according to the applied voltage, and allows current to flow in two directions. The mass of randomly oriented grains is electrically equivalent to a network of back-to-back diode pairs, each pair in parallel with many other pairs. A varistor's function is to conduct significantly increased current when voltage is excessive. Only nonohmic variable resistors are usually called varistors [1].

In normal use, a varistor is subject to a voltage below its characteristic breakdown voltage and passes only a tiny leakage current. When the voltage exceeds the breakdown voltage, the varistor becomes highly conducting and draws a large current through it, usually to ground. When the voltage returns to normal, the varistor returns to its high-resistance state [2]. The result of this behavior is a highly nonlinear current–voltage characteristic [3–5], in which the MOV has a high resistance at low voltages and a low resistance at high voltages; usually, the resistivity of a ZnO varistor is more than 10^{10} Ω cm below the breakdown voltage, whereas it is less than several ohm-centimeters above the breakdown voltage [6]. The switch is reversible with little or no hysteresis although it can degrade under electrical loading [2]. A varistor remains nonconductive as a shunt-mode device during normal operation when the voltage across it remains well below its "clamping voltage"; thus varistors are typically used for suppressing line voltage surges. However, a varistor may not be able to successfully limit a very large surge from an event such as a lightning strike where the energy involved is many orders of magnitude greater than it can handle. Follow-through current resulting from a strike may generate excessive current that completely destroys the varistor [1].

ZnO varistors are voltage-dependent switching devices, which exhibit highly nonohmic current–voltage (I–V) characteristics above the breakdown voltage. The nonohmic I–V characteristics are usually expressed logarithmically, as shown in Figure 1.1 [6]. The degree of nonohmic property is usually expressed by a nonlinear coefficient α defined by the following equation:

$$\alpha = \frac{V}{I}\frac{\mathrm{d}V}{\mathrm{d}I} \tag{1.1}$$

Empirically, the following simple equation is used:

$$I = \left(\frac{V}{C}\right)^{\alpha} \tag{1.2}$$

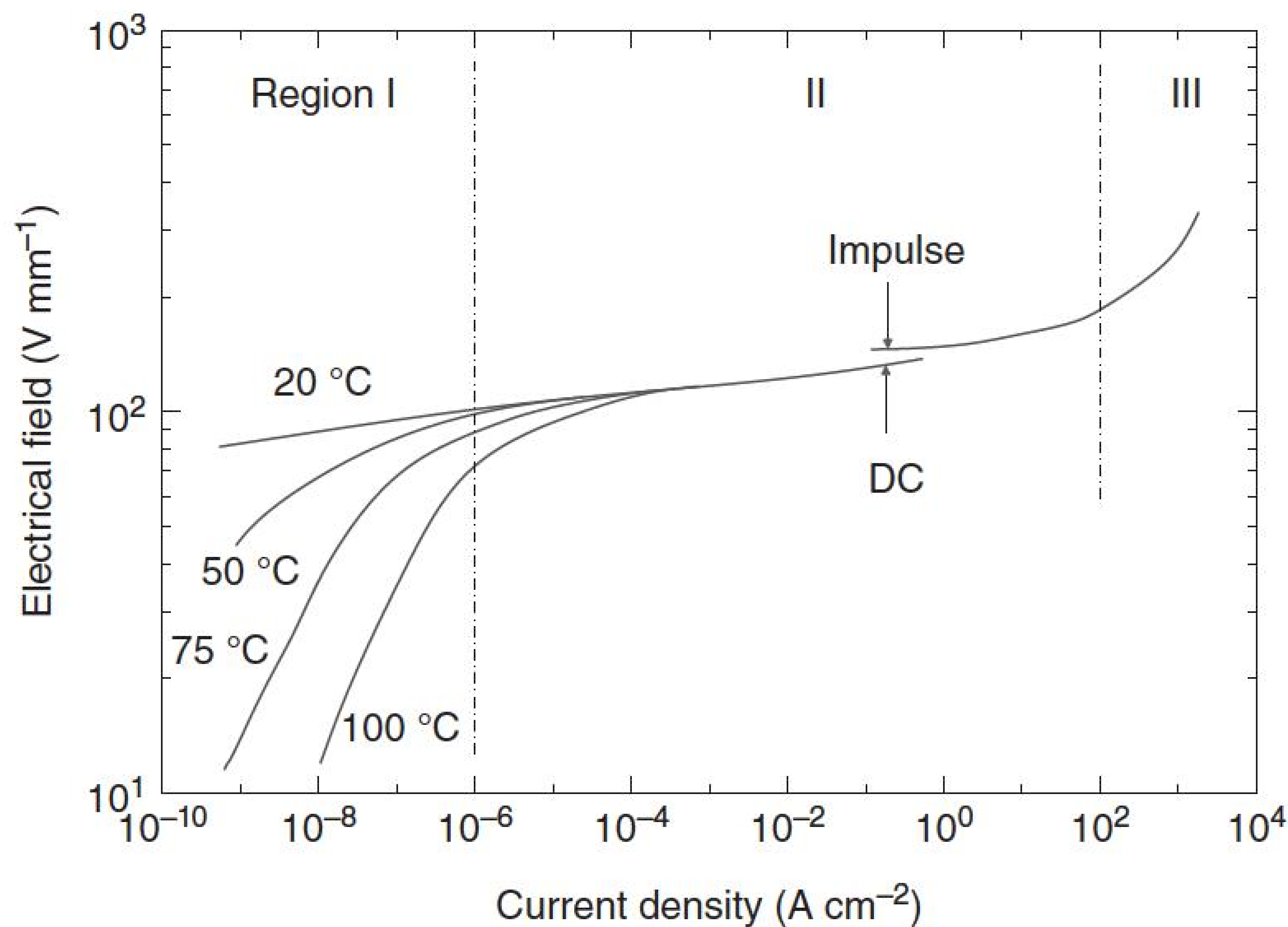


Figure 1.1 I–V characteristics of a typical ZnO varistor. Source: Adapted from Eda [6].

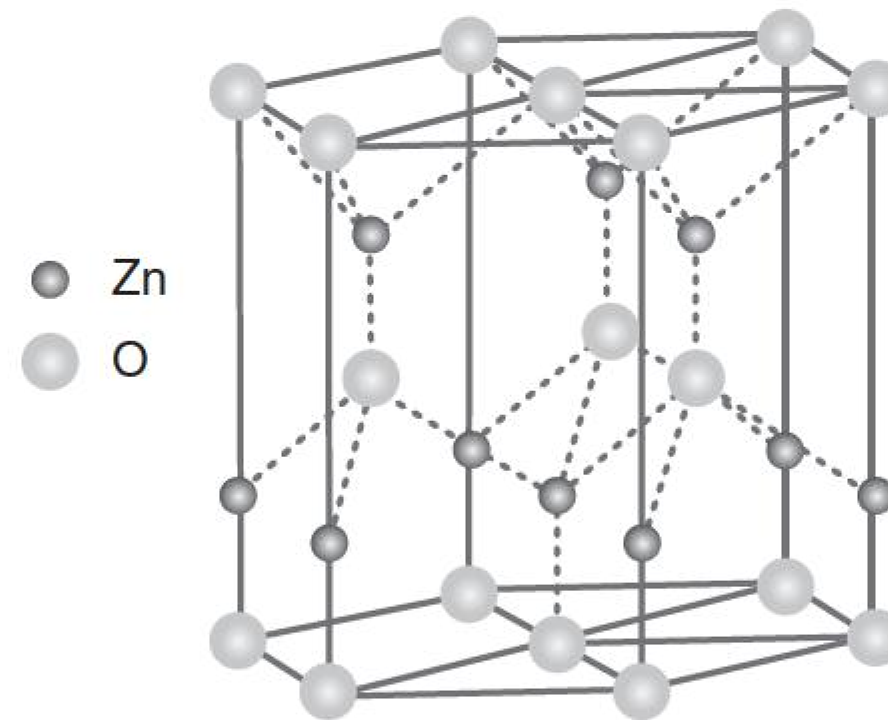


Figure 1.2 The wurtzite structure of ZnO. Source: Adapted from Addison [7].

where C is a constant. Typical α values of ZnO varistors are from 30 to 100; therefore, the current varies by orders of magnitude with only small changes in voltage. A more accurate measure of the nonlinearity is the dynamic conductance, the differential of the characteristic, at each voltage [2]. On the contrary, α values of conventional varistors such as SiC varistors do not exceed 10.

The I–V characteristics of ZnO varistors are classified into three regions, as shown in Figure 1.2 [6]. In region I (low electrical field region, or pre-breakdown region), below the breakdown voltage (typically a voltage at 1 $\mu A\,cm^{-2}$), the nonohmic property is not so prominent and can be regarded as ohmic, and the leakage current is highly temperature dependent. In region II (medium electrical field region, nonlinear region, or breakdown region), between the breakdown voltage and a voltage at a current of about 100 $A\,cm^{-2}$, the nonohmic property is very prominent and almost independent of temperature. In region III (high electrical field region or upturn region), above 100 $A\,cm^{-2}$, the nonohmic property gradually decays, and the varistor is again ohmic. These three regions in engineering applications are also called as the low current region, medium current region, and high current region, respectively.

ZnO varistors are characterized by the magnitude of the α values and the width of the range where highly nonohmic property is exhibited. In contrast to the pre-breakdown region, the nonlinear region and upturn region are little affected by temperature. The I–V characteristics below 100 $mA\,cm^{-2}$ are usually measured using a DC electric source, whereas those above 1 $A\,cm^{-2}$ are measured by an impulse current source to avoid heat generation and thermal breakdown. The waveform of the impulse current is 8/20 μs with an 8 μs rise time and 20 μs decay time up to one-half the peak value [6], which is used as a standard impulse current to test ZnO varistors. The I–V characteristics measured by the impulse currents show voltages higher than those measured using DC. The discrepancy is usually 10–20%, as shown by arrows in Figure 1.1 [6]. This discrepancy is caused by the delay in electrical response in the ZnO varistors. The response delay is speculated to be caused by electron trapping and hole creation at the grain boundaries.

1.2 Fabrication of ZnO Varistors

ZnO has a wurtzite structure in which the oxygen atoms are arranged in a hexagonal close-packed type of lattice with zinc atoms occupying half the

tetrahedral sites, as shown in Figure 1.2; Zn and O atoms are tetrahedrally coordinated to each other and are equivalent in position. The ZnO structure is thus relatively open with all the octahedral and half the tetrahedral sites empty. It is, therefore, relatively easy to incorporate external dopants into the ZnO lattice. The open structure also has a bearing on the nature of defects and the mechanism of diffusion, and the most common defect in ZnO is the metal in the open interstitial sites [8]. Pure ZnO without any impurities or dopants is a nonstoichiometric n-type semiconductor with linear or ohmic behavior, and with a wide band gap (3.437 eV at 2 K) [8, 9].

ZnO varistors are semiconducting ceramics fabricated by sintering of ZnO powders with small amounts of various metal oxide additives such as Bi_2O_3, CoO, MnO, and Sb_2O_3. The nonohmic property comes from grain boundaries between semiconducting ZnO grains. These oxides are added to control one or more of the properties such as the electrical characteristics (breakdown voltage, non-linearity, and leakage current), grain growth, or the sintering process [10–18]. Bi_2O_3 is the most essential component for forming the nonohmic behavior, and addition of CoO and MnO enhances the nonlinear properties [11, 12, 19–22]. A very low concentration of Al_2O_3 increases the ZnO grain conductivity while Sb_2O_3 controls the ZnO grain growth [23–32]. Combination of additives such as Cr_2O_3, MnO, Bi_2O_3, and CoO produces greater nonlinearity than a single dopant [10]. During high temperature sintering different phases are formed and the microstructure of a ZnO varistor comprises conductive ZnO grains surrounded by electrically insulating grain boundary regions.

Dopants play at least three major roles in forming varistors by affecting grain growth during sintering, the dewetting characteristics of the liquid phase during cooling, and the electronic defect states that control the overall varistor characteristics [2]. In order to obtain high performance ZnO varistors, the compositions, impurities, mixing methods, particle sizes, and sintering conditions, such as maximum temperature and holding time, temperature rising/lowering rates, and oxygen and Bi_2O_3 partial pressures, should be controlled precisely. This will be discussed in detail in Chapter 3.

1.2.1 Preparation of Raw Materials

ZnO varistors are commonly produced by conventional ceramic technology. The preparation process of ZnO varistors is basically the same as for general ceramics, whose primary processes include raw materials preparation, mixing, stoving and sieving, pre-sintering, smashing, prilling, molding, sintering, silvering, and testing. The preparation begins with weighing, mixing, and milling of oxide powders in ball mills. After the addition of organic binder substances, the aqueous slurry is spray-dried to produce a granulate. After sieving appropriate fractions to extract dust and large agglomerated particles, the material is transferred to hydraulic pressing machines to mold the "green" disks [33]. In the whole process, raw materials preparation and sintering are the two key steps that determine the electrical properties of ZnO varistors.

The preparation of material powders of ZnO varistors actually involves two steps: the preparation of ZnO powder and the mixing of ZnO powder with other additives. Usually, both steps are often combined as an inseparable one, so as to

achieve a one-step preparation of composite raw powders of the ZnO varistor ceramics.

The preparation of pure ZnO powder is divided into three traditional methods:

- *Direct method:* Zinc powder is added to reducing agents such as coke and coal, and heated at a high temperature to form reduced Zn steam, and then oxidized to ZnO by air.
- *Indirect method:* the zinc ingots are melted into the hot crucible to evaporate, so as to form the Zn steam, and then oxidized to ZnO by air.
- *Wet method:* The $ZnSO_4$ or Zn salt solution such as $ZnCl_2$ reacts with the Na_2CO_3 solution to crystallize the $ZnCO_3$ precipitation, and ZnO is generated by washing and filtering and heating to decompose the sediment.

In order to prepare high quality ZnO powder, some liquid- and gas-phase methods have been also used for the preparation of ZnO powders alone.

There are many ways of preparing ZnO varistor ceramic composite powders. According to the material states, the methods can be summarized as the solid phase, liquid phase, and gas phase one.

- *Solid-phase method:* it applies for the uniform mixing of ZnO solid powder and solid powder of other additives by mechanical milling. This is the conventional method used in the industry. However, it is difficult to obtain powders with uniform particle size distribution through this process.
- *Liquid-phase method:* it is developed from the wet method in the pure ZnO powder preparation. In liquid-phase synthesis, as components are fully dispersed in the liquid phase the content of each component can be precisely controlled. The solid-phase grain size produced is small with narrow size distribution, and particles of spherical or nearly spherical shape are obtained. The liquid-phase method is now becoming more and more common in the ZnO varistor ceramics industry, and it includes precipitation calcination, sol–gel, spray pyrolysis, hydrothermal method, and so on.
- *Gas phase method:* this method includes chemical vapor oxidation, laser heating, and so on. But the gas-phase method is of high cost, and it is difficult to achieve mass production using this.

Combustion synthesis technique was also used to successfully produce pure and doped pure crystalline ZnO varistor powders with good compositional control. The combustion synthesis route enables synthesis at low temperatures and the products obtained are in a finely divided state with large surface areas. Combustion synthesis offers as added advantages, the simplicity of experimental setup, the surprisingly short time between the preparation of reactants and the availability of the final product, the savings in external energy consumption, and the equally important potential of simplifying the processing prior to forming, providing a simple alternative to other more elaborate techniques [34].

1.2.2 Sintering of ZnO Varistors

ZnO varistor is fabricated by the traditional ceramic sintering technology, and the temperature control of the sintering process has a critical influence on the performances of the final products. The sintering procedure includes warm-up,

constant-temperature, and cooling periods. The pressed disks are sintered in an electric furnace at 1150–1350 °C for one to five hours in air, and the temperature is increased or decreased at 50–200 °C h^{-1}. During the warm-up and constant-temperature periods several chemical phase transformations take place, which result in a complete rearrangement of the microscopic particles and the creation of a dense polycrystalline matrix of ZnO grains and other phases, which are incorporated therein. The homogeneity of the ceramic microstructure strongly depends on the initial distribution of the reacting particles in the green body, and inhomogeneously distributed additives can result in islands of exaggerated or hampered ZnO grain growth or porosity, while such defects lead to bad electrical performance [33]. Finally, electrodes are prepared on both surfaces. The best electrodes are painted In–Ga alloys or evaporated Al films. Conventional silver electrodes painted and fired at 500–800 °C are also used [6].

The solid-state-based ceramic processing route still remains the preferred method of manufacturing because of the simplicity, cost, and availability of the metal oxide additives; this process has considerable disadvantages especially for many modern commercial applications. A major disadvantage of this route is the difficulty in obtaining additive homogeneity at a microscopic level, which is especially important for the manufacture of miniaturized electronic equipment. Processing methods and additive homogeneity are the critical parameters to produce a varistor material with favorable electrical characteristics. Inhomogeneous microstructures could cause degradation of varistors during electrical operation. Therefore, careful control of the microstructure is required to produce a varistor of desired characteristics [10].

Chemical processing, such as sol–gel, solution, precipitation, and microemulsion techniques, facilitates homogeneous doping at the molecular level. Among those various methods reported, sol–gel processing is found to be a promising one to obtain a miniature device with higher breakdown voltage, low leakage current, and reasonably good nonlinear characteristics [10]. However, controlling the grain growth at high sintering temperatures still remains a challenge for varistor ceramics, and the electrical properties could be improved if the materials could be sintered to full density with sub-micrometer or nanometer grain size. Researchers have proposed seed law method, stacking method, hot pressing method, microwave sintering method, and other technologies for the sintering of ZnO varistor ceramics [6]. Indeed, a significant enhancement in electrical properties has been achieved by novel sintering procedures such as step sintering, spark plasma sintering, or using microwave irradiation [10]. This will be introduced in Chapter 9.

1.3 Microstructure

Conventional varistors are usually prepared by mixing 0.2–1 μm sized ZnO powders with oxide additives. Although the microstructures of varistors exhibit considerable variation from one manufacturer to another, they all exhibit the characteristics of a typical ceramic prepared by liquid-phase sintering. ZnO

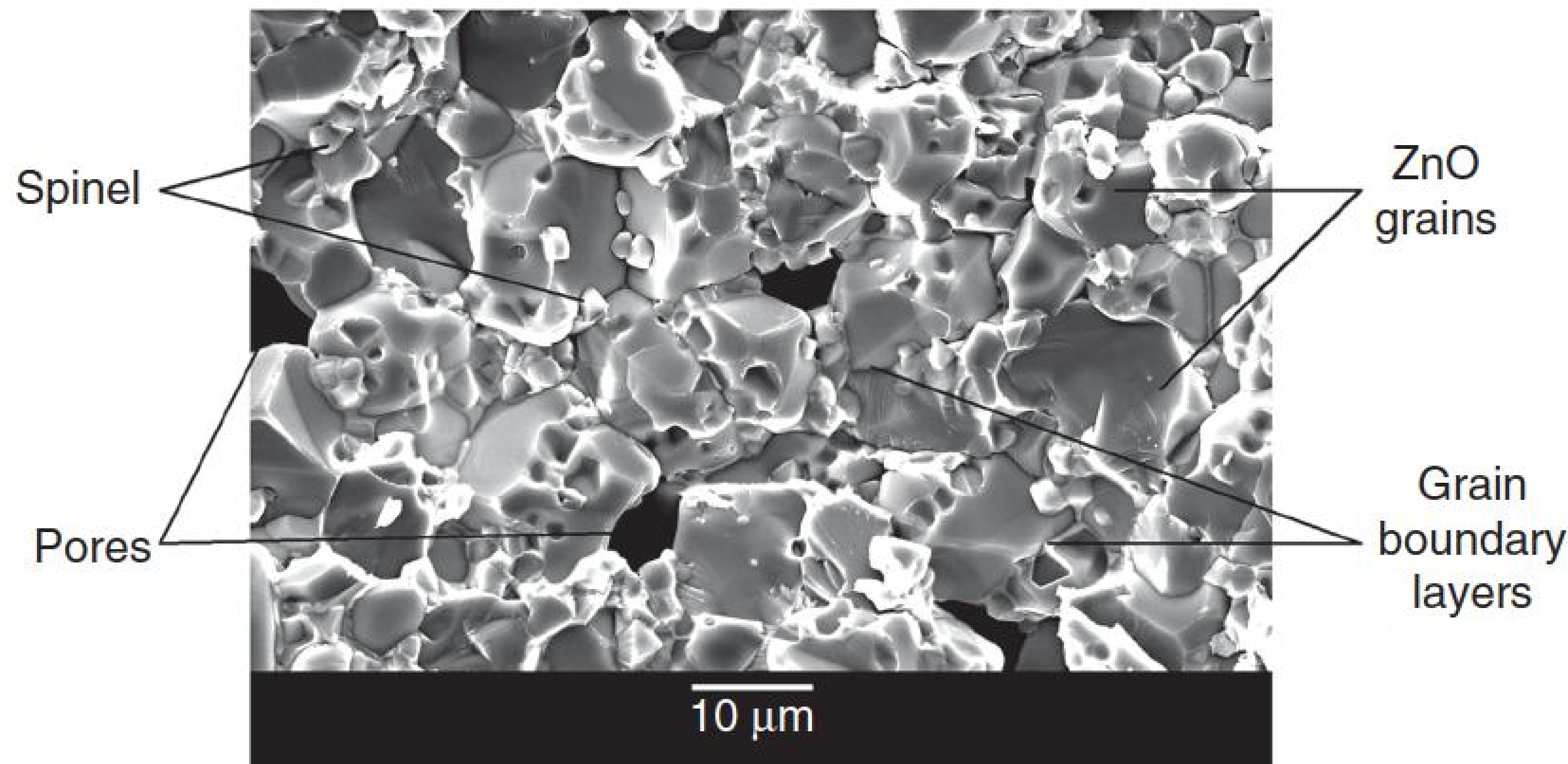


Figure 1.3 SEM photomicrograph of ZnO varistor microstructure.

varistors are polycrystalline materials composed of semiconducting ZnO grains with their attendant grain boundaries as shown in Figure 1.3. Moreover, the microstructure contains particles of one or more types of spinel, and a lot of remaining pores can be primarily found in the grain boundaries. Depending on the composition, twins within the ZnO grains and a small amount of a pyrochlore phase can also form. The ZnO–Bi_2O_3–Sb_2O_3 system forms a pyrochlore phase $Zn_2Bi_3Sb_3O_{14}$ above 650 °C. With ZnO, pyrochlore further reacts to form a spinel ($Zn_7Sb_2O_{12}$) [12, 35].

The grain boundary has a relatively thick (0.1–1 pm) Bi_2O_3-rich intergranular layer, which becomes thinner (10–1000 Å) as it approaches the contact points of the particles [6]. The sizes of ZnO grains are usually 5–20 μm and depend on the material composition, temperature, and time of sintering. The resistivity of a ZnO grain is 0.1–1 Ω cm. The grain boundaries are highly resistive and show nonohmic property, and the corresponding breakdown voltage is around 200–400 V mm^{-1} for conventional varistors, and the breakdown voltage per grain boundary is about 3 V. The breakdown voltage of the sintered body is proportional to the number of grain boundaries between the two electrodes. This indicates that the breakdown voltage is proportional to the inverse of the ZnO grain size [6].

The characteristics of ZnO varistor ceramics are closely related to their microstructure, which is characterized by the following parameters: ZnO grain size and the grain size distribution, grain boundaries, secondary phases such as the Bi_2O_3-rich phase, $Zn_7Sb_2O_{12}$ spinel-type phase, and $Bi_3Zn_2Sb_3O_{14}$ pyrochlore-type phase, the distribution of secondary phases along the grain boundaries, and the size and distribution of pores [36].

1.4 Typical Parameters of ZnO Varistors

The nonlinear voltage–current (V–I) characteristics of ZnO varistors can be approximately expressed by Eq. (1.2). In Figure 1.4 [37], the V–I nonlinear curve is shown, where the bi-logarithm coordinates are used, and the voltage and current are represented by the voltage gradient and current density, respectively.

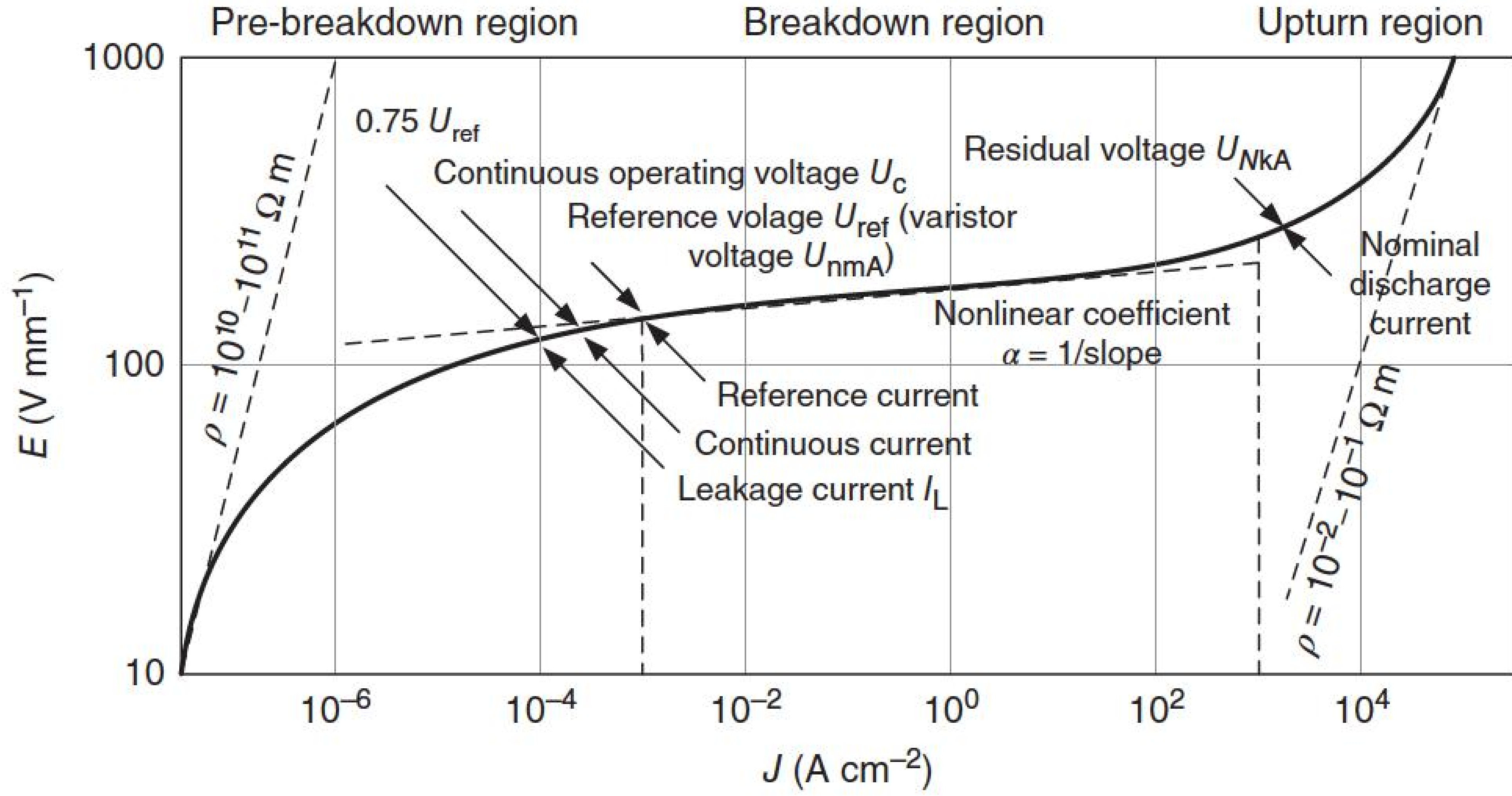


Figure 1.4 Nonlinear voltage–current (*V*–*I*) characteristics of ZnO varistors.

The nonlinear V–I characteristics of ZnO varistors is mainly indicated by the following parameters, some of which only apply to the high voltage electrical applications [37].

Nonlinear coefficient α: it represents the reciprocal of the slope of the straight part in the V–I curve, and generally refers to the corresponding value of the breakdown region. The larger the value is, the better the performance.

Varistor voltage $U_{n\text{mA}}$: it refers to the voltage of the varistor at the turning point of the curve, at a specific value of current (between 0.1 and several milliamperes, usually 1 mA), also called the reference voltage. For the convenience of performance comparison, it is usually represented by the voltage gradient $E_{n\text{mA}}$:

$$E_{n\text{mA}} = \frac{U_{n\text{mA}}}{d} \tag{1.3}$$

where d is the thickness of the varistor disk.

Chargeability (or voltage undertaking ratio) S: it is defined by the ratio of the crest value of the continuous operating voltage to the varistor voltage $U_{n\text{mA}}$; it represents the load voltage intensity at continuous operation condition.

Leakage current I_L: refers to the current flowing through the varistor at the set temperature and voltage, which is less than the varistor voltage, and usually takes 0.75 $U_{1\text{mA}}$ as the test condition.

Residual voltage $U_{N\text{kA}}$: it refers to the impulse voltage occurring at the set impulse current of N kA. In high voltage applications, it is usually represented by impulse current residual voltage, lightning current residual voltage, and steep-wave current residual voltage.

Residual voltage ratio K: it refers to the ratio of the residual voltage to the varistor voltage, namely, $U_{N\text{kA}}/U_{n\text{mA}}$.

Discharge capacity: it refers to the maximum impulse current value allowed to flow through the varistor in the set conditions, including a 2 ms square wave and a 4/10 μs impulse current.

Energy absorption capability (or energy handling capability) is the second most important property of ZnO varistors next to nonlinearity. ZnO varistors as the core elements of surge arresters in high voltage systems or surge protection devices (SPDs) in low voltage systems are required to absorb substantial amounts of energy resulting from temporary overvoltages, switching surges, or lightning impulses. Therefore, the energy absorption capabilities of ZnO varistors are crucial for the integrity of equipment and systems. However, it has been observed in experiments that differences in barrier voltages, grain sizes, and grain boundary characteristics inside the same ZnO varistor and among different ZnO varistors cause nonuniformity in the microstructurally electrical and thermophysical characteristics of ZnO varistors, and finally result in the differences in their current handling capabilities, which is also called as the energy absorption capability and has a direct relation to the failure modes. Failure modes include electrical puncture, physical cracking, and thermal runaway, which happen under different currents. The energy absorption capability can be divided into thermal energy absorption capability and impulse energy absorption capability. For the impulse energy absorption capability single impulse stress, multiple impulse stress (without sufficient cooling between the impulses), and repeated impulse stress (with sufficient cooling between the stresses) have to be considered. Thermal energy absorption capability, on the other hand, can only be considered for complete metal oxide arresters (MOAs) or SPDs, as it is mainly affected by the heat dissipation capability of the overall arrester design, besides the electrical properties of the MOVs.

Another important electrical characteristic of ZnO varistors is the dielectric property. Below the breakdown voltage, ZnO varistors are highly capacitive. The dielectric constant of ZnO is 8.5, whereas an apparent dielectric constant of a ZnO varistor is typically 1000. The dielectric properties are mainly caused by thin depletion layers (~1000 Å) at the grain boundaries [6].

1.5 History of ZnO Varistors

The ZnO varistors were first developed by Matsuoka and his research group at Matsushita Electric (Japan) in 1969 [38] and were commercialized under the trade name ZNR in the following year [6]. In 1979, they introduced many of the essential features of ZnO varistors as we know them today in detail [3], which included making ZnO semiconducting by adding substitutional ions, densification by liquid-phase sintering with a Bi_2O_3-rich liquid phase, segregation of large ions to the grain boundaries, and the main formulas with high nonlinearity by doping manganese and cobalt. Although work on the electrical properties of ZnO ceramics apparently had been underway in Russia in the early 1950s [39, 40], it was Matsuoka's work [3] that captured attention, and, shortly thereafter, a joint development effort was undertaken by GE and Matsushita [41]; one of Matsuoka's contributions was the discovery of the role of aluminum [42]. It was in the period following this that extensive literature was documented and the scientific basis for varistors as well as many of the

key technological developments was established. Concurrently, the superiority of ZnO varistors over SiC varistors for many applications was established, and expertise in utilizing ZnO varistors spread geographically. More companies began to manufacture varistors, and alternative sets of dopants were introduced, but the essential features introduced by Matsuoka remained [2]. The one exception was the use of Pr_2O_3 in the place of Bi_2O_3 [43, 44].

The performance parameters of ZnO are closely related to the raw formulas. By changing the percentage and compositions of the additives, the performance of ZnO varistors changes correspondingly. According to the additives, industrial ZnO varistors are mainly divided into two series:

- The ZnO–Bi_2O_3 series, or Bi-series, mainly includes additives such as Bi_2O_3, Sb_2O_3, Co_2O_3, MnO_2, and Cr_2O_3 [3];
- The ZnO–Pr_2O_3/Pr_6O_{11} series, or Pr-series, mainly includes additives such as Pr_2O_3/Pr_6O_{11}, Co_2O_3, and CaO [43, 44].

Many efficient additives were discovered. Eda [6] and Gupta [8] separately summarized and classified the additives into four types according to their effects:

- Additives such as Bi_2O_3, Pr_2O_3, BaO, SrO, and PbO, which make ZnO form a grain boundary structure, mainly promote liquid-phase sintering to form grain boundaries and make the materials nonlinear.
- Additives such as Co_2O_3, MnO_2, Sb_2O_3, Al_2O_3, and Ga_2O_3 improve the nonlinearity of the ZnO varistor. Part of these additives solidly solutes in ZnO grains to form impurity traps to provide carriers as donors, while the others form traps to promote the barrier height as acceptors.
- Additives such as Sb_2O_3, SiO_2, and TiO_2 affect the growth of ZnO grains by promotion or inhibition; the size of ZnO grains can be controlled, and the voltage gradient is tailored.
- Additives such as Sb_2O_3, SiO_2, NiO, and frit mainly improve the stability of ZnO varistors.

In the first decade after the Matsuoka's invention, various additives to improve the electrical characteristics were discovered and the processing conditions were optimized. This will be introduced in Chapter 3. In the next decade, the microstructures and the physical properties of the grain boundaries were gradually identified, and applications were rapidly found in protecting electrical equipment and electronic components such as transistors and integrated circuits (ICs) against voltage surges [6].

Many efforts have been made in the past several decades focusing on the conduction mechanism in the ZnO varistor; among the numerous conduction models proposed by different research groups, the one presented by Pike [45, 46] and further developed by Blatter and Greuter [47–49] has been widely recognized and may meet most of the experimental phenomena. Essentially, it is believed that the nonlinear V–I characteristic of the ZnO varistor is caused by the charge carriers transporting across the double Schottky barrier (DSB) formed at the grain boundary. The conduction mechanism of the ZnO varistor will be introduced in Chapter 2.

The electrical properties of each individual grain boundary will contribute to the global electrical characteristics of ZnO varistors. By microcontact electrical measurements on multiple-phase ZnO varistors, the grain boundaries were simply classified into good, bad, and ohmic ones according to the electrical characteristics of grain boundaries, and a high percentage of grain boundaries had bad or ohmic $I-V$ characteristics, and only a small percentage of grain boundaries had good $I-V$ characteristics. These few good grain boundaries are responsible for the good varistor effect and control the leakage current of the ZnO varistor at low values of applied voltage [50]. So, it is very important to understand the influence of the junction network on the device properties [51]. The microstructural electrical characteristics of ZnO varistors will be introduced in Chapter 4.

The influence of the geometry and topology of the granular microstructure as well as the properties and the distribution of electrical characteristics of grain boundaries on the features of bulk varistor devices is another important issue. The simulation study of such systems is helpful to reveal the connection between the microstructure and macroscopic characteristics of varistor ceramics. This was recognized early in the development of ZnO varistors, and a number of consequences were discussed based on the idea that the disorder resulted in "chains" of more conducting paths through the microstructure [2]. One of the most important simulation models is where Bartkowiak and Mahan [52] used the Voronoi network to present the actual microstructures of ZnO varistors with randomly distributed ZnO grains and grain boundaries. The details on how to simulate varistor ceramics will be introduced in Chapter 5.

The breakdown of ZnO varistors is an original phenomenon during their application, which has been reported in many publications [53–60]. It has been found that every varistor has a different destruction phenomenon under impulse current and AC or DC current. Three failure modes have been identified [61]: electrical puncture, physical cracking, and thermal runaway (or thermal breakdown); these failure models result in different energy handling capabilities. This will be introduced in Chapter 6.

ZnO varistors can be electrically, chemically, and thermally degraded during use, leading to a reduction in barrier voltage height and, consequently, an increase in leakage current, which could be catastrophic for ZnO varistors. In the past few decades, much research has been carried out to explain the observed degradation phenomena of ZnO varistors, and correspondingly various degradation mechanisms of grain boundaries have been proposed, e.g. electron trapping, dipole orientation, ion migration, and oxygen desorption [62–64]. Among these mechanisms, ion migration has found comparatively strong support on the basis of different circumstantial evidences. Electrical degradation of ZnO varistors will be introduced in Chapter 7.

Processing for increased reliability, microstructural uniformity, and resistance to degradation has continued to the present and has also become more sophisticated through the use of improvements in process control, chemical routes to homogenization of powders, and even formulation optimization through techniques such as neural network modeling [2].

Now, varistors are available that can protect circuits over a very wide range of voltages, from a few volts for low-voltage varistors in semiconductor circuits to

11 000 kV AC and ±1100 kV DC in electrical power transmission and distribution networks. Correspondingly, they can also handle an enormous range of energies from a few joules to many megajoules. Remarkably, they are also very fast, switching within nanoseconds from their high resistance state to a highly conducting state [2].

1.6 Applications of ZnO Varistors

MOV, which is also called as ZnO varistor, has good nonlinear volt–ampere characteristics and excellent impulse energy absorbing capacity; these advantages enable wide MOV usage in transient overvoltage protection for electrical/ electronic systems. In low voltage systems, MOV, shown in Figure 1.5a, is assembled as SPDs as in Figure 1.5b; in high voltage fields, MOVs, which have disk shape or ring shape as shown in Figure 1.6a, are manufactured as surge arresters as in Figure 1.6b; MOVs are also used as energy absorbing devices in electrical/electronic systems. Surge arresters are devices that help prevent

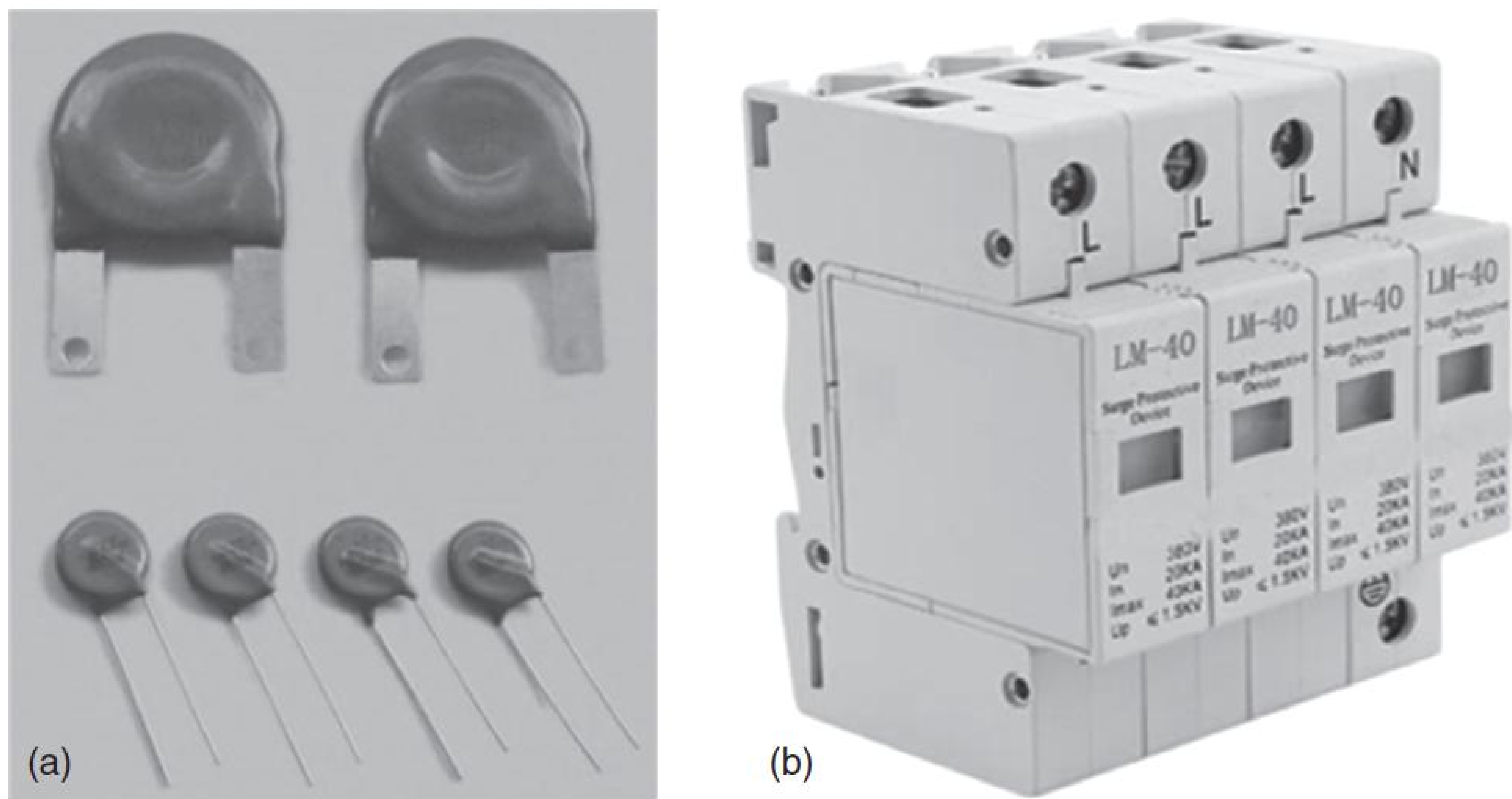


Figure 1.5 (a) Metal oxide varistors for low voltage systems and (b) surge protection devices (SPDs).

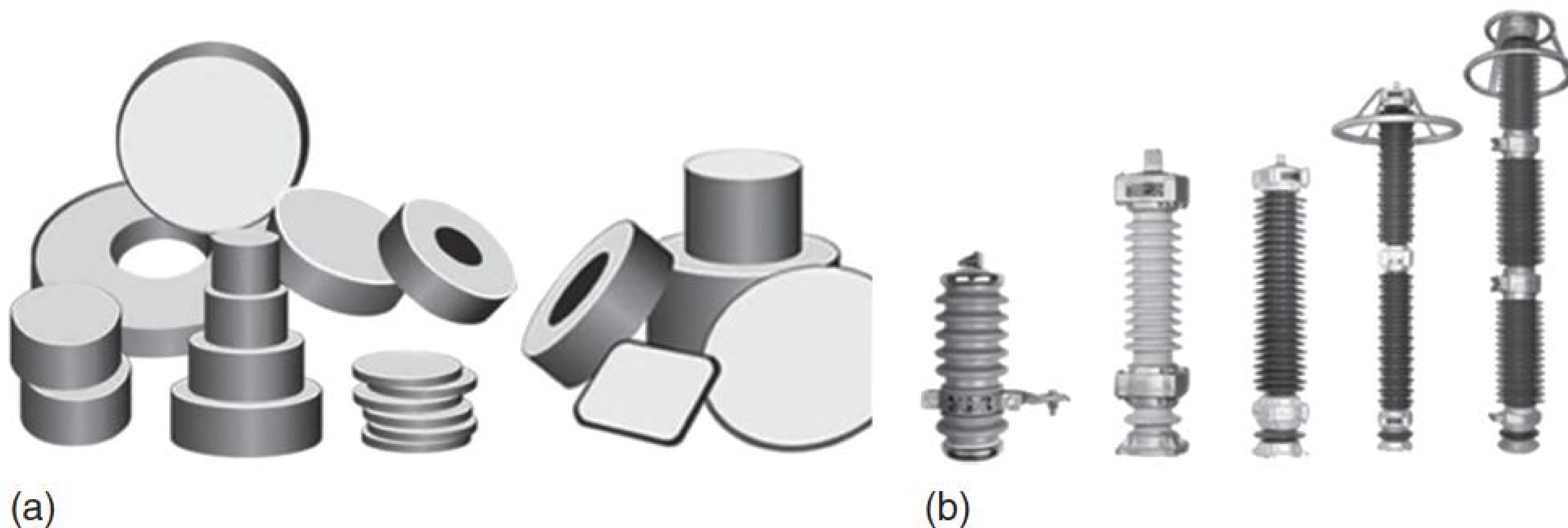


Figure 1.6 (a) Metal oxide varistors for high voltage systems and (b) surge arresters with porcelain houses.

damage to apparatus due to high voltages. The arrester provides a low-impedance path to ground for the current from a lightning strike or transient voltage and then restores to normal high-impedance operating conditions.

The surge arrester is the key overvoltage protection equipment in electrical power systems, and the insulation level of power apparatus is determined by the overvoltage protection level of surge arresters. Lightning overvoltages were causing problems on overhead lines well before Tesla and Edison argued over the merits of AC and DC. Many of the overvoltage protection methods for distribution lines follow the same philosophy as that used for telegraph and telephone lines. For example, early surge protective devices on single-phase power lines used single or multiple air gaps, as shown in Figure 1.7 [65], which followed telegraph line protection measures closely. As shown in Figure 1.8, the development of surge arresters for transient overvoltage protection in power systems has experienced gap-type arrester, expulsion-type arrester, SiC valve-type arresters with internal spark gaps and magnetic blow gaps, and ZnO surge arresters. SiC varistor ceramics were developed in the early 1930s to replace early selenium rectifiers for protecting telephone systems. The materials developed by the Bell System consisted of partially sintered compacts of SiC particles [66, 67]. Successive improvements, particularly in processing, took

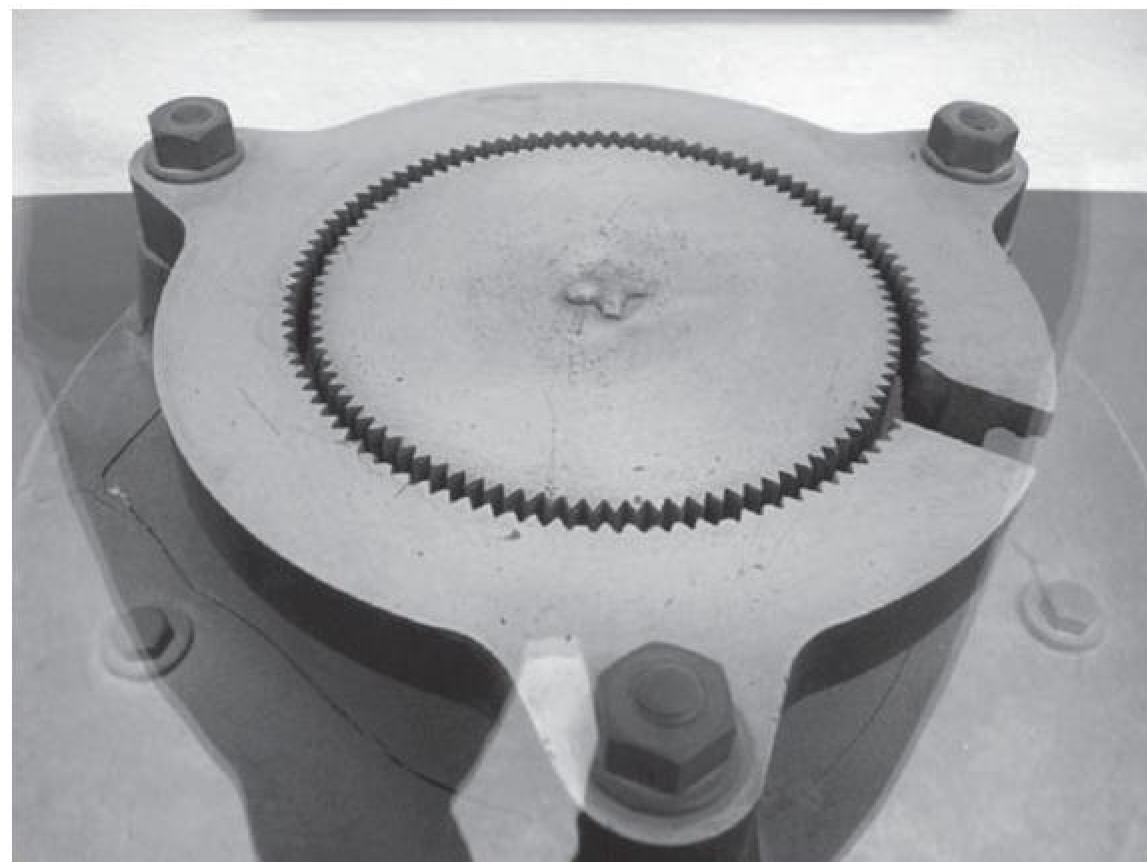


Figure 1.7 Lightning surge arrester, manufactured by Oerlikon in 1886 for Kriegstetten–Solothurn 2 kV power line. Source: Chisholm 2010 [65]. Reproduced with permission of IEEE.

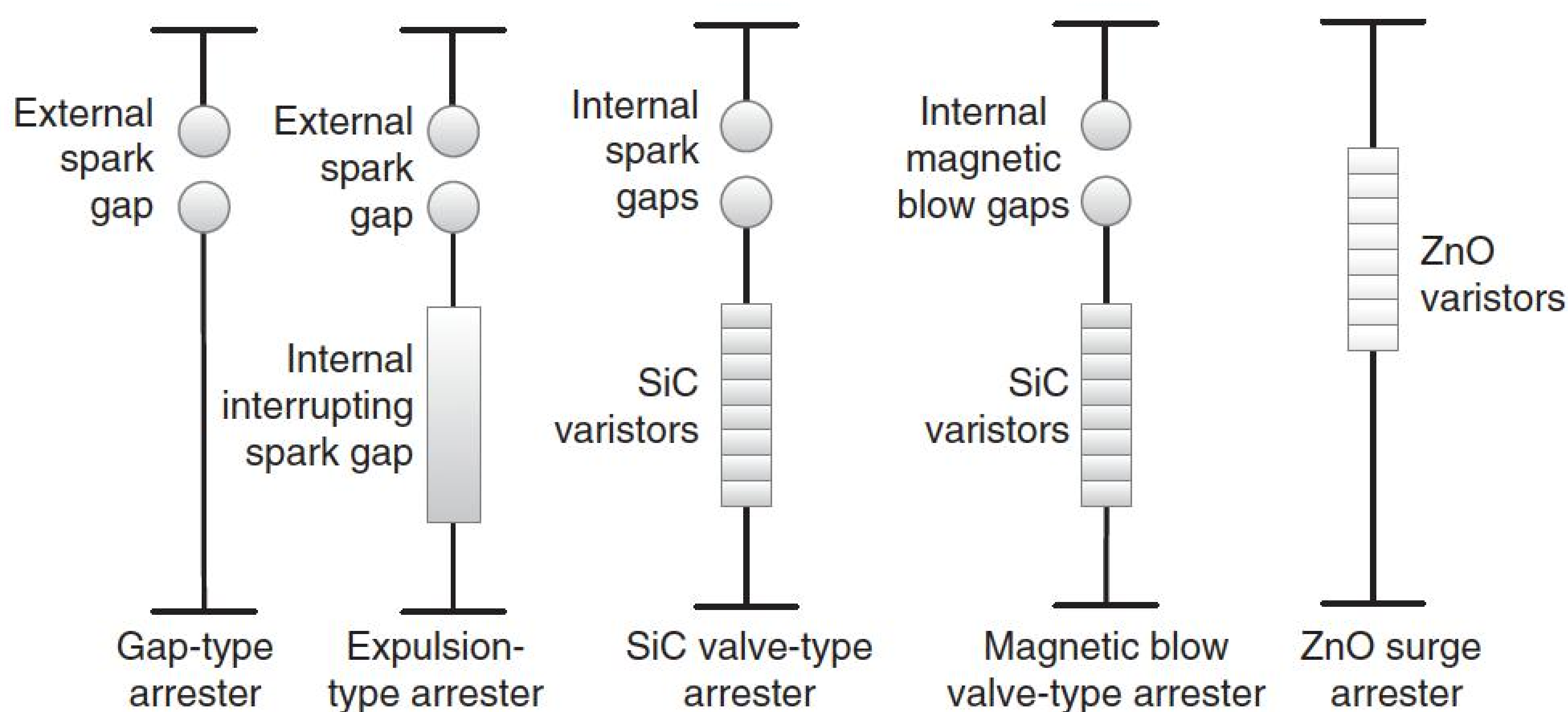


Figure 1.8 Technical development progress of surge arresters.

place both in the United States and in Japan [68]. The nonlinear coefficient of SiC varistors is less than 10, so the leakage current under operating voltage is too high and has to work with a series gap. But the ZnO varistor has high nonlinearity, and its leakage current under operating voltage is very small; usually ZnO surge arresters can work without a series gap, so ZnO surge arresters are of the gapless type. The ZnO surge arrester has good protection performance, quick response speed, and large energy handling capability; as a result, it has been widely accepted, popularized, and used in power systems. Figure 1.9 shows the application of surge arresters in 1000 kV ultrahigh voltage (UHV) AC substation.

The ZnO surge arresters used in Japan's UHV transmission systems were mainly developed by the Mitsubishi Corporation. Three kinds of ZnO varistors of different characteristics for UHV arresters, named as type A, B, and C, were manufactured. The volt–ampere characteristic of A-type varistor is similar to that of varistors used in the conventional 500 kV ZnO arresters. And B-type and C-type owned a more superior protection performance to meet the requirements of insulation of UHV systems, especially the C-type varistor. The C-type has the best performance and the lowest residual voltage, which makes it become the ultimate choice in UHV arresters in Japan [69].

The B-type arrester is used in 1000 kV systems whose rated voltage is 826 kV; when the 8/20 μs impulse current is 20 and 10 kA, the residual voltage is 1800 and 1710 kV, respectively, whereas the residual voltage of the C-type is only 1620 and 1550 kV when the current is 20 and 10 kA. Compared with the 1112 kV residual voltage with 20 kA current of the 500 kV arrester, the residual voltage



Figure 1.9 1000 kV ultrahigh voltage AC surge arresters with porcelain houses in Dongwu 1000 kV UHV AC substation. Source: Courtesy of X. Zhao.

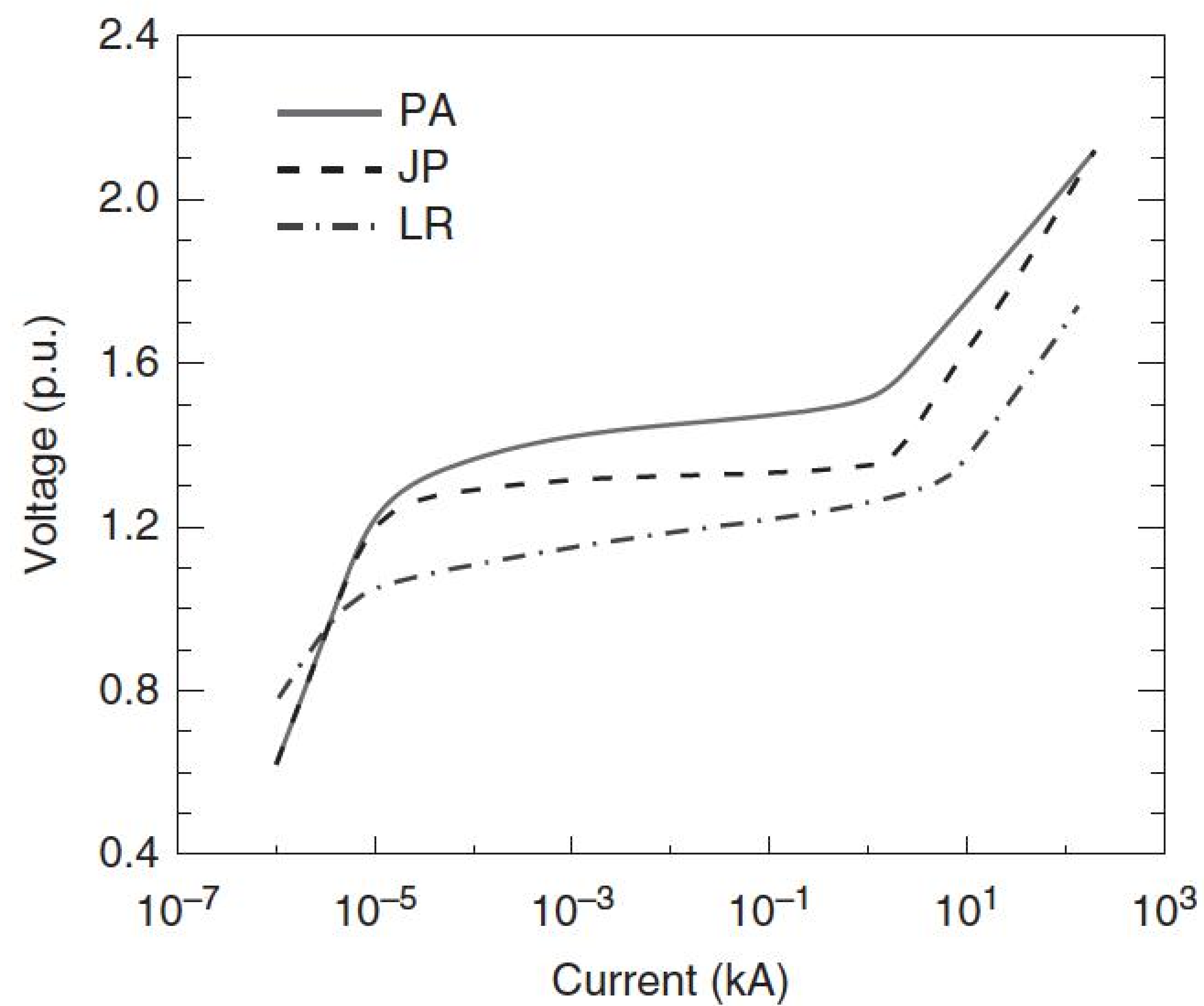


Figure 1.10 Volt–ampere characteristic curves of different UHV surge arresters: presently applied in China (PA), arrester used in Japan (JP), and low residual voltage arrester (LR), which is being developed in China. Source: He et al. 2011 [69]. Reproduced with permission of IEEE.



Figure 1.11 Ultrahigh voltage AC tank-type surge arresters in 1000 kV Jindongnan Substation in China.

of the C-type arrester increases by only 45.7% when the system voltage doubles. Figure 1.10 shows the data of volt–ampere characteristic curve of the C-type arrester used in Japanese UHV systems with a voltage base of 890 kV [69].

Except the ZnO surge arresters with porcelain houses, tank-type surge arresters in SF_6 insulation are widely used in gas-insulated substations (GISs); the 1000 kV UHV AC tank-type surge arresters, with height of 4455 mm and diameter of 2024 mm, are shown in Figure 1.11. Usually, ZnO surge arresters are assembled in porcelain houses, and applied in overvoltage protection in high voltage substations and distribution systems. Since the 1980s, ZnO surge arresters with polymeric houses have been developed, as shown in



Figure 1.12 Metal oxide surge arresters with polymeric houses.

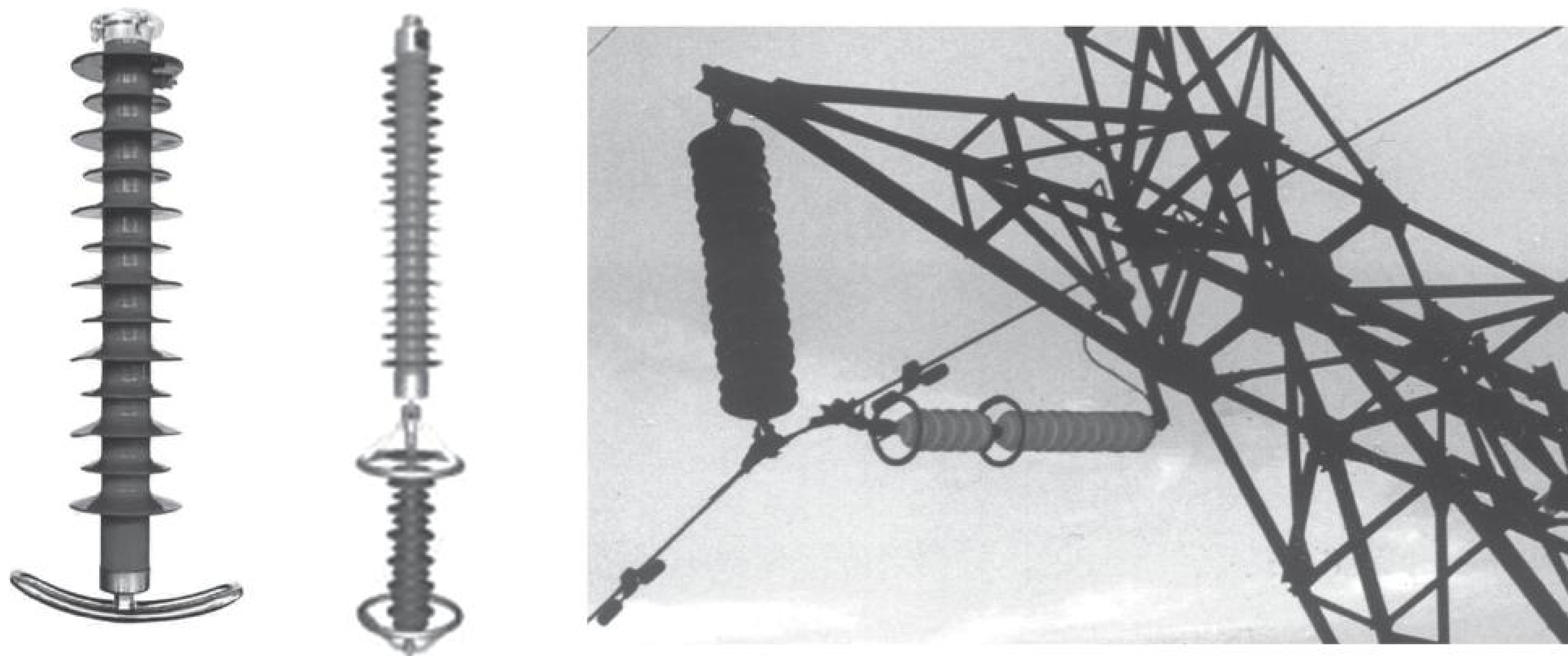


Figure 1.13 Line surge arresters and application on transmission line.

Figure 1.12. This kind of polymeric line surge arresters are very light, and have been applied in parallel with the insulators for lightning protection of high voltage transmission lines [70–77]. Typically, the polymeric line surge arrester has a whole-solid-insulation structure; all interior gaps are filled with middle temperature silicon rubber material. There is no gas gap inside the arrester [77]. We know that the main reason for porcelain house arrester failure is moisture ingress, so the failure of the whole-solid-insulation arrester caused by moisture ingress is eliminated. The polymeric housing not only makes the surge arrester smaller and lighter but also solves the problem of pressure relief due to the absence of air gap inside the polymeric arrester; the electrical, and therefore thermal, overloading of the ZnO varistors could not cause a flashover along the side surface of the ZnO varistor column. So the whole-solid-insulation polymeric surge arresters are of the safety type. Usually, the polymeric line surge arresters are assembled with series gaps as shown in Figure 1.13, and only

operate when lightning strikes the transmission line or the tower. It would not work under AC power frequency overvoltage or switching overvoltage, and keeps the state of "rest" due to the isolation of the series gap [77]. Now line surge arresters have been applied in 110–500 kV AC transmission lines, and ±500 kV to ±800 kV UHV DC transmission lines. The lightning protection performances of transmission lines have been highly improved due to the installation of these polymeric line surge arresters.

1.7 Alternative Varistor Ceramics

In order to overcome the shortcomings of Bi_2O_3-based ZnO varistors, other ZnO varistor systems have been added to ZnO varistors instead of bismuth, such as praseodymium [78, 79], barium [80], and vanadium [81]; all exhibit varistor behavior. All of them not only have a simple microstructure consisting of ZnO grain and intergranular layer, but also high nonlinearity. This will be introduced in Chapter 8.

Besides working to improve the performance of the ZnO varistor material, scientists are also searching for other new materials in order to achieve better stability and be used for new applications.

The integration of electronic circuitry into IC chips has brought large volume and weight reductions, so there is an increasing trend toward integration of passive electronic-ceramic components. In order to protect electronic circuits from damage due to surge voltages, the application of varistors within low voltage fields also rose. The titanium-based capacitor–varistor dual function varistor ceramics, such as TiO_2, $SrTiO_3$, and $CaCu_3Ti_4O_{12}$ (CCTO) varistors [82–88], have realized the goal of component miniaturization and provide superior high-frequency and high-amplitude transient voltage protection. This will be introduced in Chapter 10.

In 1995 [89], S.A. Pianaro found that SnO_2 varistor ceramics doped small amounts of additives obtained by solid-state sintering. Unlike the multiphase structure of ZnO-based varistor, SnO_2-based varistor has a simple microstructure and good stability. Dense SnO_2-based systems present values of nonlinear coefficient, breakdown voltage, and barrier voltage per grain equivalent to those of the traditional and commercial ZnO varistor [89–95], and better thermal conductivity; this makes SnO_2-based varistor one of the most promising candidates to compete commercially with ZnO-based varistor. SnO_2-based varistors will be introduced in Chapter 11.

WO_3-based varistor ceramic is another kind of low voltage varistor with a low threshold electric field of 5–10 V mm^{-1} and high dielectric constant [96–98]; this enables it to act as a varistor in parallel with a capacitor, which is attractive for applications in the elimination of electrical noise of micro-motors, protecting contact of delays, and absorbing discharges of some circuits. WO_3-based varistor ceramics will be introduced in Chapter 12.

More investigations have been carried out. The effect of CuO doping on the microstructure and electrical properties of Pr_6O_{11} varistors was investigated [99].

Minor CuO doping can improve the nonlinear electrical properties by offering more oxygen adsorption sites. Highly nonlinear current–voltage relations with voltage-limiting characteristics are observed for Mg-doped lanthanum calcium manganite polycrystalline ceramics with nonlinear coefficient of 2–9 at low electric field strengths of 2–5 V mm^{-1}, below magnetic transition temperatures [100]. The current density increases with external magnetic field, so that magnetically tunable low voltage varistors are realized.

Varistor action with a nonlinear coefficient of 3.9 and a breakdown voltage of 40 V mm^{-1} was observed in undoped terbium oxide ceramic and the sample exhibited excellent electrical stability up to 70 °C [101].

Not surprisingly, a number of polycrystalline semiconducting ferroelectrics also can be expected to exhibit varistor characteristics, albeit over a narrower range of temperature [102, 103].

1.8 Ceramic–Polymer Composite Varistors

Interestingly, the ceramic–polymer composite varistor is a composite one, incorporating varistor particles [104] or semiconducting particles, or a combination of metal and semiconducting particles, such as ZnO [105–107], SiC [108], and ZnO microvaristors in a polymeric matrix. The field-dependent property of the composites varies with filler concentration. When the filler concentration is above a critical value, which is called as percolation threshold, the composite begins to exhibit stable nonlinear properties, and current flows from one particle to the next through an interfacial region. Some studies concluded that for nonlinear composites with spherical fillers such as ZnO and SiC, high filler concentrations of typically 30–40 vol.% were required to obtain nonlinear electrical conductivity [109, 110].

The varistor particles themselves can exhibit nonlinear behavior, so the ceramic–polymer composite varistors exhibit nonlinearity in electrical conductivity [111–114] and function in a manner similar to the original incorporating varistor particles. Although the energy handling capabilities of composite varistors are generally inferior to those of solid ZnO varistors, their advantages in flexible shape and easy fabrication and formability make them attractive for many applications.

Composite varistors with lower breakdown voltage can be a suitable substitute for ZnO-based varistors for the purpose of protection of low voltage systems [114]. Low voltage varistors with good nonlinearity have been achieved using ZnO–polyaniline–polyvinyl alcohol (PVA) composites. Polymer composite thin films can be easily prepared by solution-casting technique. To increase the elasticity of final films and to prevent them from tearing PVA can be effectively employed in the varistor matrix. The devices with high nonlinearity coefficients (2.7–4.1) and low breakdown voltages (120–350 V) are useful in protecting sensitive electrical circuits [111–113]. The composite varistor with GaAs–polyaniline–polyethylene compositions can be easily prepared as thin disks using hot pressing method [111–113]. The samples with higher percentages

of GaAs (>50%) display varistor properties. They can be used to protect circuits from ~60 V up to over 90 V.

Silicon has some unique properties that make it important in the varistor industry [115]. The breakdown voltages of Si–polymer composite varistors were low in comparison with similar ZnO–polymer composite varistors [115, 116]. On the Si content exceeding 65% of the whole Si–polymer mixture, samples exhibited varistor behavior with a nonlinear coefficient of about 10. But at temperatures between 100 °C and 130 °C, the nonlinear conductivity of the varistor gradually turned to ohmic conductivity.

Polymer/perovskite manganese oxide (epoxy resin/$La_{0.8}Sr_{0.2}MnO_3$) composites were prepared using the bonded method [105]. There was no reaction between $La_{0.8}Sr_{0.2}MnO_3$ and the polymer. The nonlinear current–voltage property is significantly affected by the content of the polymer, and the nonlinear coefficient can exceed 45. The resistivity of the composites is five to nine orders of magnitude higher than that of the sintering ceramics.

In order to improve the nonlinearity of composite varistors, the ZnO microvaristor shown in Figure 1.14 [117], which was produced by the same fabrication technique and prescription of ZnO varistors, has been used as the filler in polymers [117–120]. ZnO microvaristor composites based on silicone matrix were prepared. The silicone and vulcanizing agent were mixed in 0.8 wt% with tetrahydrofuran solvent and blended by a high torque blender for about 20 minutes. After the silicone was fully dissolved in the solvent, ZnO microvaristor powders were poured into the liquor and the blending continued for 40 minutes. Then the mixture was dried in a vacuum oven for more than 10 hours till the solvents fully volatilized. This was followed by the process of vulcanization. Each time, a 3 g mixture was pressed by the vulcanizing machine at a pressure of 15 MPa at 170 °C for 15 minutes and then naturally cooled to room temperature at the same pressure. The acquired silicone rubber composite sample is about 0.5 mm in thickness and 20 mm in diameter.

Figure 1.15 presents the scanning electron microscopy (SEM) images of the ZnO microvaristor silicone rubber composites [117]; it is evident that many fillers

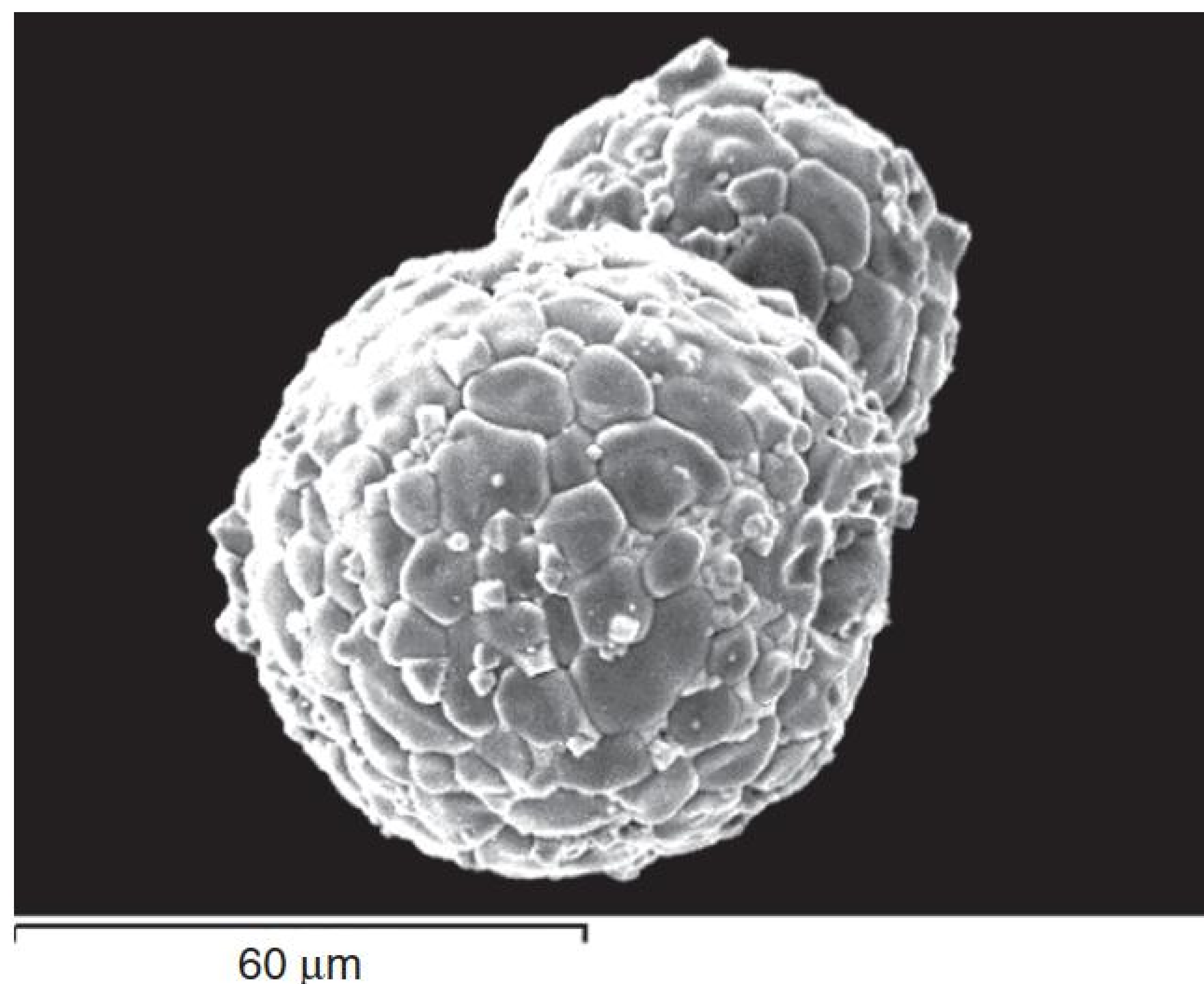


Figure 1.14 SEM image of two contacted ZnO microspherical varistors [117]. Source: https://creativecommons.org/licenses/by/4.0/.

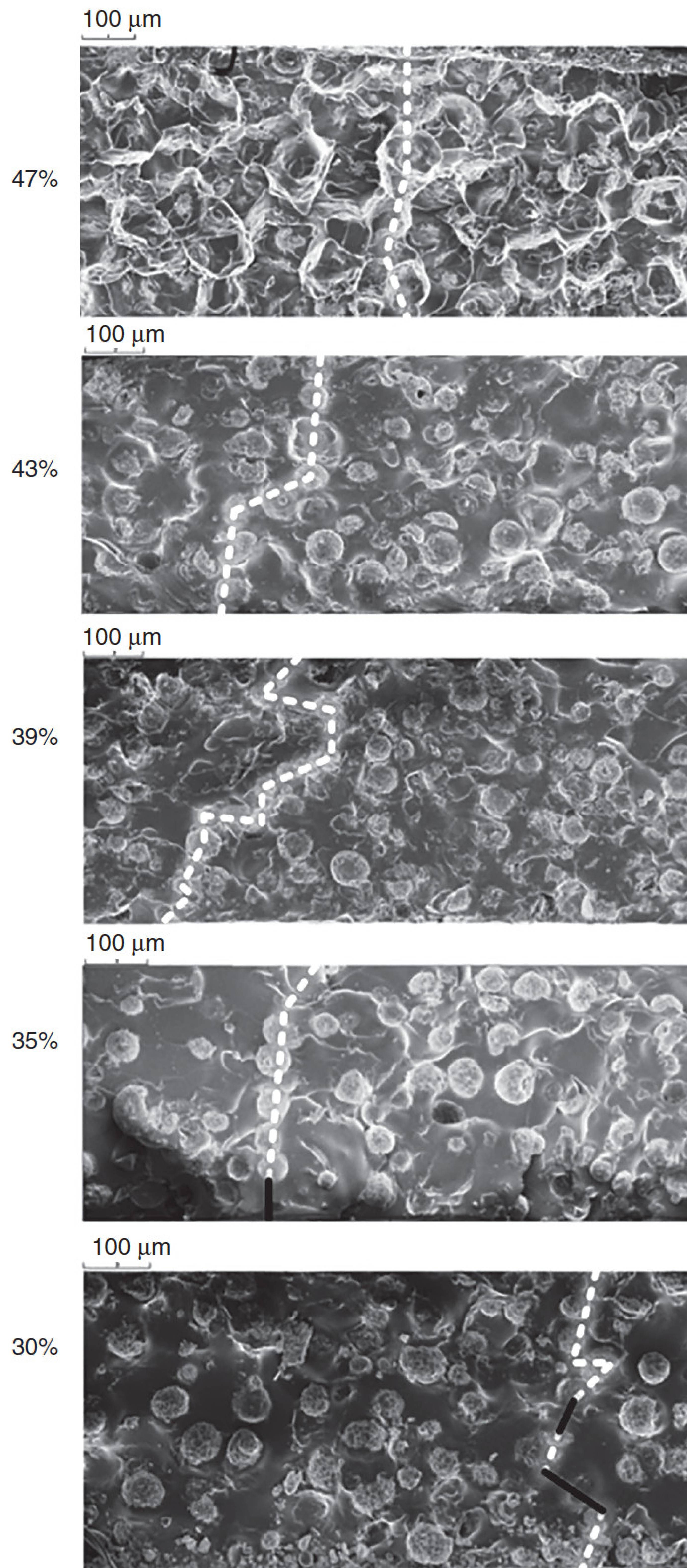


Figure 1.15 SEM images and possible conduction paths in ZnO microvaristor composites [117]. Source: https://creativecommons.org/licenses/by/4.0/.

are aligning in series. The conduction paths could be approximately determined and marked by the dotted lines. The solid lines indicate silicone rubber layers separating two adjacent fillers in a potential breakdown path. When the filler concentration is higher than the percolation threshold, which is 33%, in those samples, fillers form thoroughly connecting paths and the current selects the shortest one to flow through. It is evident that in composites with higher filler concentrations, a short conduction path is more likely to form, which means a lower switching field. The conduction paths become more and more straightforward from the 39% to 47% samples. As a result, the switching field decreases with filler concentration.

The nonlinear V–I characteristics of ZnO microvaristor/silicone rubber composites with different filler concentrations are shown in Figure 1.16 [117]. For the samples with filler volume concentrations of 39%, 43%, and 47%, the breakdown electric fields are almost the same and they decrease with increase in filler concentration. Samples with the above three filler concentrations present typical nonlinear behavior and can be attributed to the fully percolated case. For the 35% sample, the switching field is even higher and it exhibits the breakdown feature. This is a sign of approaching percolation. The switching field E_b and the nonlinear coefficient α are in the range from 330 to 826 V mm^{-1}, and from 10.2 to 17.5, respectively, with the filler's diameter ranging from 50 to 150 μm. Simulation results show good agreement with experimental ones.

ZnO microvaristor-filled related polymers, such as ZnO–epoxy [121], ZnO–LDPE (low-density polyethylene) [122], ZnO–LLDPE (linear low-density polyethylene) [118], and ZnO–polyester [107], were reported to possess different nonlinear characteristics with switching fields in the range of about

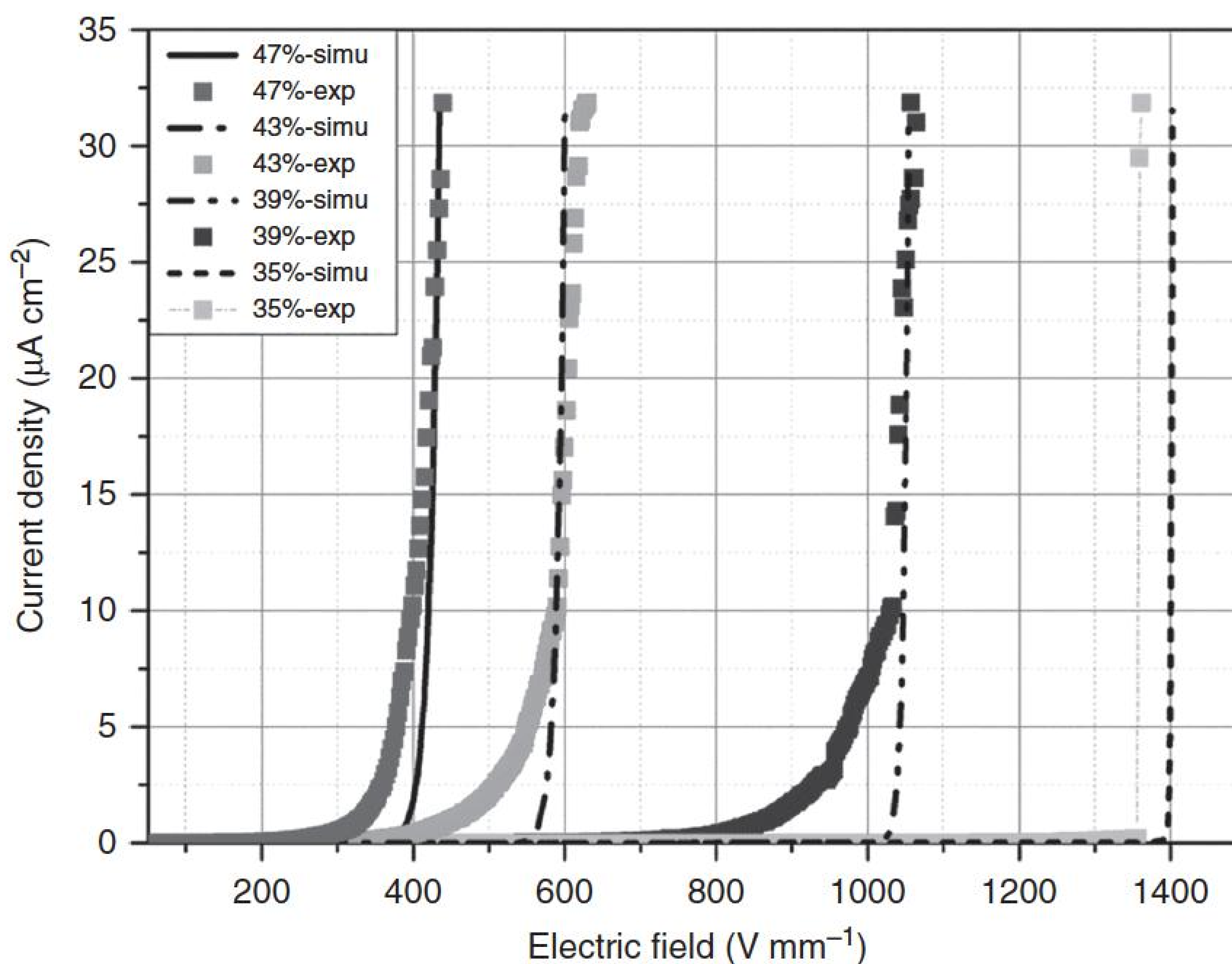


Figure 1.16 Nonlinear V–I characteristics of ZnO microvaristor composites with filler concentrations of 35%, 39%, 43%, and 47% [117]. Source: https://creativecommons.org/licenses/by/4.0/.

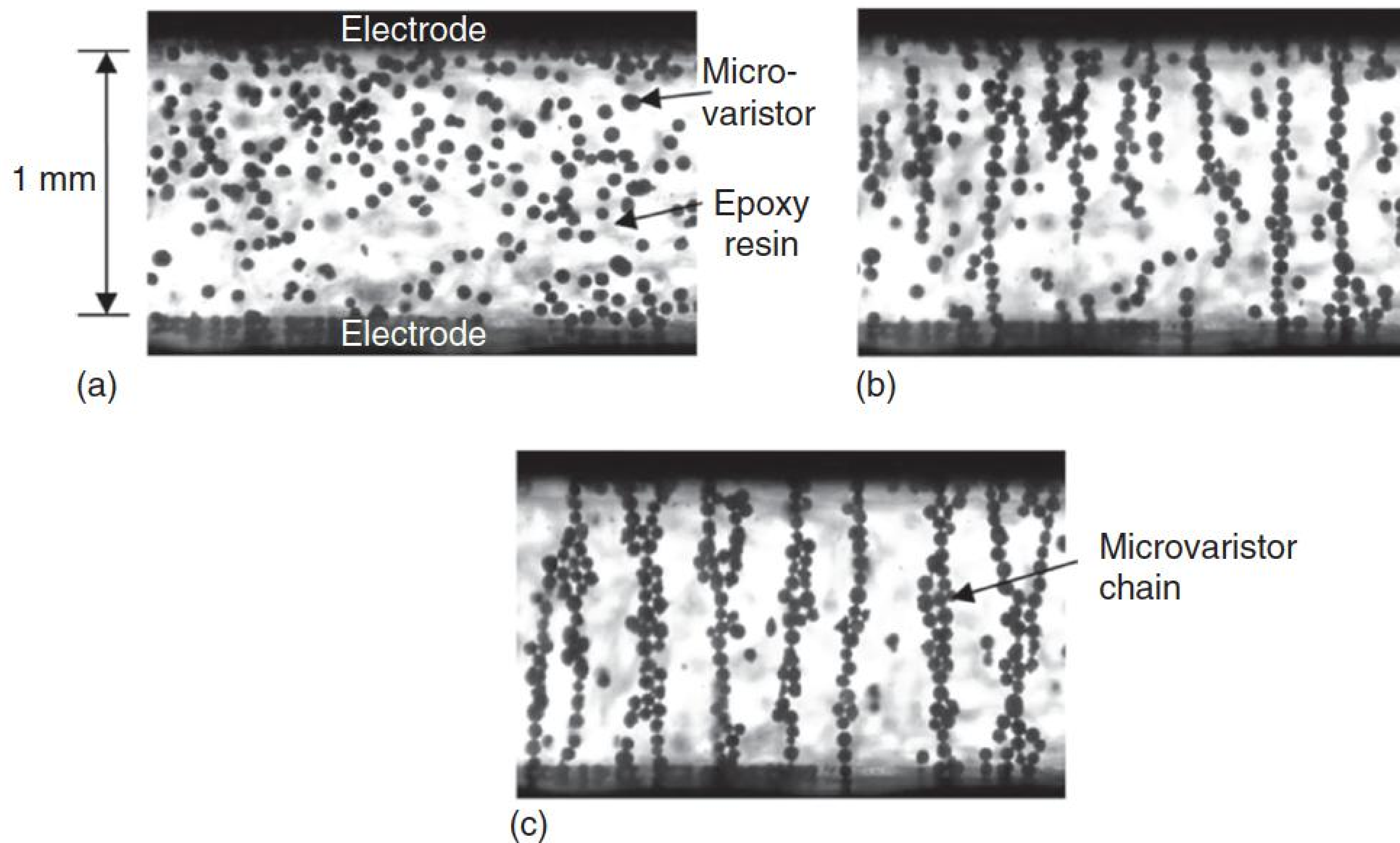


Figure 1.17 Behavior of microvaristors in an epoxy resin by field application. The microvaristor content is 20 wt%, and the applied field is 450 V_{rms} mm^{-1}. (a) Before field application; (b) 9 seconds after field application; (c) 65 seconds after field application. Source: Ishibe et al. 2014 [123]. Reproduced with permission of IEEE.

300–1000 V mm^{-1} and nonlinearity above 9. The difference is mainly due to the nature of the grain parameters such as grain size and preparing formula inside each microvaristor. Even so, all of the above ZnO composites present a similar pattern that the nonlinear conducting behavior varies with filler concentration. The switching field decreases with incremental filler concentration above the percolation threshold while the nonlinear coefficient remains stable. Under the threshold, the composites can hardly exhibit nonlinearity.

The chains of microvaristors in composite varistors were formed by applying an electric field during the curing process; these chains work as current paths, as shown in Figure 1.17 [123]. This kind of composite varistor shows superior nonlinear voltage–current characteristics despite small microvaristor content.

Besides good overvoltage protection effect, the polymer blended with microvaristor filler can function as field grading material (FGM) due to its excellent nonlinear J–E characteristics. It possesses field-dependent electrical parameters, and is thus widely used for stress control and field grading in all fields of electrical insulations [120, 121].

References

1 http://en.wikipedia.org/wiki/Varistor.
2 Clarke, D.R. (1999). Varistor ceramics. *Journal of the American Ceramic Society* 82 (3): 485–502.
3 Matsuoka, M. (1971). Nonohmic properties of zinc oxide ceramics. *Japanese Journal of Applied Physics* 10 (6): 736–746.

4 Levinson, L.M. and Philipp, H.R. (1986). Zinc oxide varistors-a review. *American Ceramic Society Bulletin* 65 (4): 639–646.

5 Einzinge, R. (1981). Grain boundary properties in ZnO varistors. *Advances in Ceramics* 1: 359–374.

6 Eda, K. (1989). Zinc oxide varistors. *IEEE Electrical Insulation Magazine* 5 (6): 28–30.

7 Addison, W.E. (1953). *Structural Principles in Inorganic Compounds*, 57. New York: Wiley.

8 Gupta, T.K. (1990). Application of zinc oxide varistors. *Journal of the American Ceramic Society* 73 (7): 1817–2177.

9 Zhou, Z., Kato, K., Komaki, T. et al. (2004). Effects of dopants and hydrogen on the electrical conductivity of ZnO. *Journal of the European Ceramic Society* 24 (1): 139–149.

10 Pillai, S.C., Kelly, J.M., Ramesh, R., and McCormack, D.E. (2013). Advances in the synthesis of ZnO nanomaterials for varistor devices. *Journal of Materials Chemistry C* 1 (20): 3268–3281.

11 Ziegler, E., Heinrich, A., Oppermann, H., and Stöver, G. (1982). Growth and electrical properties of non-stoichiometric ZnO single crystals doped with Co. *Physica Status Solidi (A)* 70 (2): 563–570.

12 Pillai, S.C., Kelly, J.M., McCormack, D.E., and Ramesh, R. (2008). High performance ZnO varistors prepared from nanocrystalline precursors for miniaturised electronic devices. *Journal of Materials Chemistry* 18 (33): 3926–3932.

13 He, J.L., Hu, J., and Lin, Y.H. (2008). ZnO varistors with high voltage gradient and low leakage current by doping rare-earth oxide. *Science in China, Series E, Technological Sciences* 51 (6): 693–701.

14 Daneu, N., Rečnik, A., and Bernik, S. (2011). Grain-growth phenomena in ZnO ceramics in the presence of inversion boundaries. *Journal of the American Ceramic Society* 94 (5): 1619–1626.

15 Leach, C., Ali, N.K., Cupertino, D., and Freer, R. (2010). Microwave-assisted sintering of ZnO varistors: local microstructure and functional property variations. *Materials Science and Engineering: B* 170 (1): 15–21.

16 Mazaheri, M., Zahedi, A.M., and Sadrnezhaad, S.K. (2008). Two-step sintering of nanocrystalline ZnO compacts: effect of temperature on densification and grain growth. *Journal of the American Ceramic Society* 91 (1): 56–63.

17 Dey, D. and Brad, R.C. (1992). Grain growth of ZnO during Bi_2O_3 liquid-phase sintering. *Journal of the American Ceramic Society* 75 (9): 2529–2534.

18 Gambino, J.P., Kingery, W.D., Pike, G.E. et al. (1987). Grain boundary electronic states in some simple ZnO varistors. *Journal of Applied Physics* 61 (7): 2571–2574.

19 Long, W.C., Hu, J., Liu, J., and He, J.L. (2010). Effects of cobalt doping on the electrical characteristics of Al-doped ZnO varistors. *Materials Letters* 64 (9): 1081–1084.

20 Fan, J. and Freer, R. (1993). Improvement of the non-linearity and degradation behaviour of ZnO varistors. *British Ceramic Transactions* 92 (6): 221–226.

21 Asokan, T. and Freer, R. (1990). Characterization of spinel particles in zinc oxide varistors. *Journal of Materials Science* 25 (5): 2447–2453.
22 Look, D.C. (2001). Recent advances in ZnO materials and devices. *Materials Science and Engineering: B* 80 (1): 383–387.
23 Bartkowiak, M., Mahan, G.D., Modine, F.A., and Alim, M.A. (1996). Influence of ohmic grain boundaries in ZnO varistors. *Journal of Applied Physics* 79 (1): 273–281.
24 Han, J.P.A., Senos, M.R., and Mantas, P.Q. (2002). Defect chemistry and electrical characteristics of undoped and Mn-doped ZnO. *Journal of the European Ceramic Society* 22 (1): 49–59.
25 Kutty, T.R.N. and Raghu, N. (1989). Varistors based on polycrystalline ZnO: Cu. *Applied Physics Letters* 54 (18): 1796–1798.
26 Carlsson, J.M., Hellsing, B., Domingos, H.S., and Bristowe, P.D. (2001). Electronic properties of a grain boundary in Sb-doped ZnO. *Journal of Physics: Condensed Matter* 13 (44): 9937–9943.
27 Fan, J. and Freer, R. (1993). The electrical properties and dc degradation characteristics of silver doped ZnO varistors. *Journal of Materials Science* 28 (5): 1391–1395.
28 Bernik, S. and Daneu, N. (2007). Characteristics of ZnO-based varistor ceramics doped with Al_2O_3. *Journal of the European Ceramic Society* 27 (10): 3161–3170.
29 Daneu, N., Rečnik, A., and Bernik, S. (2003). Grain growth control in Sb_2O_3-doped zinc oxide. *Journal of the American Ceramic Society* 86 (8): 1379–1384.
30 Han, J., Mantas, P.Q., and Senos, A.M.R. (2001). Densification and grain growth of Al-doped ZnO. *Journal of Materials Research* 16 (2): 459–468.
31 Gambino, J.P., Kingery, W.D., Pike, G.E. et al. (1987). Grain boundary electronic states in some simple ZnO varistors. *Journal of Applied Physics* 61 (7): 2571–2574.
32 Clarke, D.R. (1979). Grain-boundary segregation in a commercial ZnO-based varistor. *Journal of Applied Physics* 50 (11): 6829–6832.
33 Einzinger, R. (1987). Metal oxide varistors. *Annual Review of Materials Science* 17 (1): 299–321.
34 Sousa, V.C., Segadaes, A.M., Morelli, M.R., and Kiminami, R.H.G.A. (1999). Combustion synthesized ZnO powders for varistor ceramics. *International Journal of Inorganic Materials* 1 (3): 235–241.
35 Inada, M. (1980). Formation mechanism of nonohmic zinc oxide ceramics. *Japanese Journal of Applied Physics* 19 (3): 409–419.
36 Bemik, S. and Daneu, N. (2007). Characteristics of ZnO-based varistor ceramics doped with Al_2O_3. *Journal of the European Ceramic Society* 27 (10): 3161–3170.
37 Hu, J. (2008). Research of ZnO varistor with high voltage gradient applied in ultra-high voltage arrester. PhD thesis. Tsinghua University, Beijing, China.
38 Matsuoka, M., Masuyama, T., and Iida, Y. (1969). Voltage nonlinearity of zinc oxide ceramics doped with alkali-earth metal oxide. *Japanese Journal of Applied Physics* 8 (10): 1275–1276.

39 Valeyev, K.S., Knayazev, V.A., and Drozdov, N.O. (1964). Non-linear varistors using oxides of zinc, silicon and tin. *Elektrichestvo* 4: 72–76.

40 Kosman, M.S. and Pettsold, E.G. (1961). O wozmoznosti izgotowlenija simietriczeskich varistorov iz okisi cinka c primiestju okosi bizmuta. [On a possibility of manufacturing symmetric varistors from bismuth oxide dopped zinc oxide]. *Uczonyje Zapiski LGPT im. AI Gercena* 207: 191–196.

41 Levinson, L.M. (1989). *Ceramic Transactions, Vol. 3, Advances in Varistor Technology*. Westerville, OH: American Ceramic Society.

42 Kresge, J.S., Sakshaug, E.C., Fishman, H., and Ellis, H.F. (1989). A history of the development of metal oxide technology at GE for utility system surge arresters. *Ceramic Transactions* 3: 207–218.

43 Mukae, K., Tsuda, K., and Nagasawa, I. (1977). Non-ohmic properties of ZnO-rare earth metal oxide-Co_3O_4 ceramics. *Japanese Journal of Applied Physics* 16 (8): 1361–1368.

44 Mukae, K. (1987). Zinc oxide varistors with praseodymium oxide. *American Ceramic Society Bulletin* 66 (9): 1329–1331.

45 Pike, G. E. (1982). Electronic properties of ZnO-varistors: a new model. Materials Research Society Meeting, Boston, MA, USA.

46 Pike, G.E. and Seager, C.H. (1979). The dc voltage dependence of semiconductor grain-boundary resistance. *Journal of Applied Physics* 50 (5): 3414–3422.

47 Blatter, G. and Baeriswyl, D. (1987). High-field transport phenomenology: hot-electron generation at semiconductor interfaces. *Physical Review B* 36 (12): 6446–6464.

48 Blatter, G. and Greuter, F. (1986). Carrier transport through grain boundaries in semiconductors. *Physical Review B* 33 (6): 3952–3966.

49 Blatter, G. and Greuter, F. (1986). Electrical breakdown at semiconductor grain boundaries. *Physical Review B* 34 (12): 8555–8572.

50 Tao, M., Ai, B., Dorlanne, O., and Loubiere, A. (1987). Different single grain junctions within a ZnO varistor. *Journal of Applied Physics* 61 (4): 1562–1567.

51 Wang, H., Schulze, W.A., and Cordaro, J.F. (1995). Averaging effect on current-voltage characteristics of ZnO varistors. *Japanese Journal of Applied Physics* 34 (5A): 2352–2358.

52 Bartkowiak, M. and Mahan, G.D. (1995). Nonlinear currents in Voronoi networks. *Physical Review B* 51 (16): 10825–10828.

53 Sakshaug, E.C., Burke, J.J., and Kresge, J.S. (1989). Metal oxide arresters on distribution systems: fundamental considerations. *IEEE Transactions on Power Delivery* 4 (4): 2076–2089.

54 Kirkby, P., Erven, C.C., and Nigol, O. (1988). Long-term stability and energy discharge capacity of metal oxide valve elements. *IEEE Transactions on Power Delivery* 3 (4): 1656–1665.

55 Kan, M., Nishiwaki, S., Sato, T. et al. (1983). Surge discharge capability and thermal stability of a metal oxide surge arrester. *IEEE Transactions on Power Apparatus and System* 102 (2): 282–289.

56 Bartkowiak, M., Comber, M.G., and Mahan, G.D. (1999). Failure modes and energy absorption capability of ZnO varistors. *IEEE Transactions on Power Delivery* 14 (1): 152–162.

57 Ringler, K.G., Kirkby, P., Erven, C.C. et al. (1997). The energy absorption capability and time-to-failure of varistors used in station-class metal–oxide surge arresters. *IEEE Transactions on Power Delivery* 12 (1): 203–212.

58 Wang, S.L., Ga, S.X., Li, H.F., and Xu, Y.B. (1992). The relation between testing waveform and energy density on ZnO varistor. In: *Annual Report of Conference on Electrical Insulation and Dielectric Phenomena*, 543–548. IEEE.

59 He, J.L. and Hu, J. (2007). Analysis on nonuniformity of energy absorption capabilities of ZnO varistors. *IEEE Transactions on Power Delivery* 22 (3): 1523–1532.

60 Sweetana, A., Kunkle, N., Hingorani, N., and Tahiliani, V. (1982). Design, development and testing of 1200 kV and 550 kV gapless surge arresters. *IEEE Transactions on Power Apparatus and Systems* 101 (7): 2319–2327.

61 He, J.L., Cho, H.G., and Han, S.W. (1998). Impulse destruction mechanisms of ZnO varistors. *Journal of the Korean Physical Society* 11 (4): 460–467.

62 Eda, K., Iga, A., and Matsuoka, M. (1980). Degradation mechanism of non-ohmic zinc oxide ceramics. *Journal of Applied Physics* 51 (5): 2678–2684.

63 Gupta, T.K. and Carlson, W.G. (1985). A grain-boundary defect model for instability/stability of a ZnO varistor. *Journal of Materials Science* 20 (10): 3487–3500.

64 Liu, J. (2011). Research on the degradation characteristics and mechanisms of high voltage gradient ZnO varistor. PhD thesis. Tsinghua University, Beijing.

65 Chisholm, W.A. (2010). New challenges in lightning impulse flashover modeling of air gaps and insulators. *IEEE Electrical Insulation Magazine* 26 (2): 14–25.

66 Frosch, C.J. (1954). Improved silicon carbide varistors. *Bell Laboratory Records* 32: 336–340.

67 Dienel, H.F. (1956). Silicon carbide varistors: properties and construction. *Bell Laboratory Records* 34: 407–411.

68 Masuyama, T. and Matsuoka, M. (1968). Current dependence of voltage non-linearity in SiC varistors. *Japanese Journal of Applied Physics* 7 (10): 1294.

69 He, J.L., Li, C., Hu, J., and Zeng, R. (2011). Deep suppression of switching overvoltages in AC UHV systems using low residual arresters. *IEEE Transactions on Power Delivery* 26 (4): 2718–2725.

70 Furukawa, S., Usuda, O., Isozaki, T., and Irie, T. (1999). Development and application of lightning arresters for transmission lines. *IEEE Transactions on Power Delivery* 4 (4): 2121–2129.

71 Koch, R.E., Timoshenko, J.A., Anderson, J.G., and Shih, C.H. (1985). Design of zinc oxide transmission line arresters for application on 138 kV towers. *IEEE T Transactions Power Apparatus and System* 104 (10): 2675–2680.

72 He, J.L., Zeng, R., Chen, S.M., and Tu, Y.P. (2003). Thermal characteristics of high voltage whole-solid-insulated polymeric ZnO surge arrester. *IEEE Transactions on Power Delivery* 18 (3): 1221–1227.

73 Tarasiewicz, E.J., Rimmer, F., and Morched, A.S. (2004). Transmission line arrester energy, cost, and risk of failure analysis for partially shielded transmission lines. *IEEE Transactions on Power Delivery* 15 (3): 919–924.

74 Sadovic, S., Joulie, R., Tartier, S., and Brocard, E. (1997). Use of line surge arresters for the improvement of the lightning performance of 63 kV and 90 kV shielded and unshielded transmission lines. *IEEE Transactions on Power Delivery* 12 (3): 1232–1240.

75 Ishida, K., Dokai, K., Tsozaki, T. et al. (1992). Development of a 500 kV transmission line arrester and its characteristics. *IEEE Transactions on Power Delivery* 7 (3): 1265–1274.

76 Yamada, T., Sawada, J., Zaima, E. et al. (1993). Development of suspension-type arresters for transmission lines. *IEEE Transactions on Power Delivery* 8 (3): 1052–1060.

77 He, J.L., Chen, S.M., Zeng, R. et al. (2006). Development of polymeric surge ZnO arresters for 500-kV compact transmission line. *IEEE Transactions on Power Delivery* 21 (1): 113–120.

78 Mukae, K., Tsuda, K., and Nagasawa, I. (1977). Non-ohmic properties of ZnO-rare earth metal oxide-Co_3O_4 ceramics. *Japanese Journal of Applied Physics* 16 (8): 1361–1368.

79 Nahm, C.H. (2012). Sintering effect on ageing behavior of rare earths (Pr_6O_{11}-Er_2O_3-Y_2O_3)-doped ZnO varistor ceramics. *Journal of Rare Earths* 30 (10): 1028–1032.

80 Fan, J. and Freer, R. (1997). Varistor properties and microstructure of ZnO–BaO ceramics. *Journal of Materials Science* 32 (2): 415–419.

81 Tsai, J.K. and Wu, T.B. (1994). Non-ohmic characteristics of ZnO-V_2O_5 ceramics. *Journal of Applied Physics* 76 (8): 4817–4822.

82 Franken, P.E.C., Viegers, M.P.A., and Gehring, A.P. (1981). Microstructure of $SrTiO_3$ boundary-layer capacitor material. *Journal of the American Ceramic Society* 64 (12): 687–690.

83 Yan, M.F. and Rhodes, W.W. (1982). Preparation and properties of TiO_2 varistors. *Applied Physics Letters* 40 (6): 536–537.

84 Subramanian, M.A., Li, D., Duan, N. et al. (2000). High dielectric constant in $ACu_3Ti_4O_{12}$ and $ACu_3Ti_3FeO_{12}$ phases. *Journal of Solid State Chemistry* 151: 323–325.

85 Li, J., Subramanian, M.A., Rosenfeld, H.D. et al. (2004). Clues to the giant dielectric constant of $CaCu_3Ti_4O_{12}$ in the defect structure of "$SrCu_3Ti_4O_{12}$". *Chemistry of Materials* 16 (25): 5223–5225.

86 Ramirez, A.P., Subramanian, M.A., Gardel, M. et al. (2000). Giant dielectric constant response in a copper-titanate. *Solid State Communications* 115 (5): 217–220.

87 Chung, S.Y., Kim, I.D., and Kang, S.J. (2004). Strong nonlinear current–voltage behaviour in perovskite-derivative calcium copper titanate. *Nature Materials* 3: 774–778.

88 Chen, Y.L. and Yang, S.F. (2011). PTCR effect in donor doped barium titanate: review of compositions, microstructures, processing and properties. *Advances in Applied Ceramics* 110 (5): 257–269.

89 Pianaro, S.A., Bueno, P.R., Longo, E., and Varela, J.A. (1995). A new SnO_2-based varistor system. *Journal of Materials Science Letters* 14 (10): 692–694.

90 Leite, E.R., Nascimento, A.M., Bueno, P.R. et al. (1999). The influence of sintering process and atmosphere on the non-ohmic properties of SnO_2 based varistor. *Journal of Materials Science: Materials in Electronics* 10 (4): 321–327.

91 Pianaro, S.A., Bueno, P.R., Olivi, P. et al. (1997). Effect of Bi_2O_3 addition on the microstructure and electrical properties of the SnO_2-CoO-Nb_2O_5 varistor system. *Journal of Materials Science Letters* 16 (8): 634–638.

92 Pianaro, S.A., Bueno, P.R., Olivi, P. et al. (1998). Electrical properties of the SnO_2-based varistor. *Journal of Materials Science: Materials in Electronics* 9 (2): 159–165.

93 Pianaro, S.A., Bueno, P.R., Longo, E., and Varela, J.A. (1999). Microstructure and electric properties of a SnO_2 based varistor. *Ceramics International* 25 (1): 1–6.

94 Bueno, P.R., Cassia-Santos, M.R., Leite, E.R. et al. (2000). Nature of the Schottky-type barrier of highly dense SnO_2 systems displaying nonohmic behavior. *Journal of Applied Physics* 88 (11): 6545–6548.

95 Bueno, P.R., Leite, E.R., Oliveira, M.M. et al. (2001). Role of oxygen at the grain boundary of metal oxide varistors: a potential barrier formation mechanism. *Applied Physics Letters* 79 (1): 48–50.

96 Makarov, V. and Trontelj, M. (1994). Novel varistor material based on tungsten oxide. *Journal of Materials Science Letters* 13 (13): 937–939.

97 Filho, A.G.S., Matias, J.G.N., Dias, N.L. et al. (1999). Microstructural and electrical properties of sintered tungsten trioxide. *Journal of Materials Science* 34 (5): 1031–1035.

98 Wang, Y., Yao, K.L., and Liu, Z.L. (2001). Novel nonlinear current-voltage characteristics of sintered tungsten oxide. *Journal of Materials Science Letters* 20 (18): 1741–1743.

99 Li, T.Y., Wang, H.Q., Hua, Z.Q. et al. (2010). Densification and grain growth of CuO-doped Pr_6O_{11} varistors. *Ceramics International* 36 (5): 1511–1516.

100 Philip, J. and Kutty, T.R.N. (2001). Nonlinear current–voltage relations in polycrystalline perovskite manganites ceramics. *Applied Physics Letters* 79 (2): 209–211.

101 Li, T.Y., Zhao, H.W., Dong, L. et al. (2008). Novel varistor material based on terbium oxide. *Journal of Physics D: Applied Physics* 42 (3): 035401.

102 Rossinelli, M., Greuter, F., and Schmuckle, F. (1989). Electrically active grain boundaries in ceramics: varistors and capacitors in electroceramics. *British Ceramic Proceedings* 41: 177–188.

103 Pavlov, A.N. and Raevski, I.P. (1997). Varistor effect in semiconductor ferroelectrics. *Technical Physics* 42 (12): 1390–1394.

104 Glatz-Reichenbach, J., Meyer, B., Strümpler, R. et al. (1996). New low-voltage varistor composites. *Journal of Materials Science* 31 (22): 5941–5944.

105 Yang, X., Kim, H., Yang, L. et al. (2014). Composite varistors based on epoxy resin/$La_{0.8}Sr_{0.2}MnO_3$. *Journal of Composite Materials* 48 (6): 677–681.

106 Hashimov, A.M., Hasanli, S.M., Mehtizadeh, R.N. et al. (2006). Zinc oxide-and polymer-based composite varistors. *Physica Status Solidi (C)* 3 (8): 2871–2875.

107 Lin, C.C., Lee, W.S., Sun, C.C., and Whu, W.H. (2008). A varistor–polymer composite with nonlinear electrical-thermal switching properties. *Ceramics International* 34 (1): 131–136.

108 Modine, F.A. and Hyatt, H.M. (1988). New varistor material. *Journal of Applied Physics* 64 (8): 4229–4232.

109 Wang, Z., Nelson, J.K., Hillborg, H. et al. (2012). Graphene oxide filled nanocomposite with novel electrical and dielectric properties. *Advanced Materials* 24 (23): 3134–3137.

110 Mårtensson, E. and Gäfvert, U. (2003). Three-dimensional impedance networks for modelling frequency dependent electrical properties of composite materials. *Journal of Physics D: Applied Physics* 36 (15): 1864–1872.

111 Bidadi, H., Aref, S.M., Ghafouri, M. et al. (2013). Effect of changing gallium arsenide content on gallium arsenide–polymer composite varistors. *Journal of Physics and Chemistry of Solids* 74 (8): 1169–1173.

112 Bidadi, H., Aref, S.M., Ghafouri, M. et al. (2013). The effect of sintering temperature on varistor characteristics of gallium arsenide–polyaniline–polyethylene composite varistors. *Materials Science in Semiconductor Processing* 16 (3): 752–758.

113 Aref, S.M., Olad, A., Parhizkar, M. et al. (2013). Effect of polyaniline content on electrophysical properties of gallium arsenide–polymer composite varistors. *Solid State Sciences* 26: 128–133.

114 Anas, S., Mahesh, K.V., Jeen Maria, M., and Ananthakumar, S. (2017). Sol-gel materials for varistor devices. In: *Sol-Gel Materials for Energy, Environment and Electronic Applications*, 23–59. Springer International Publishing.

115 Ghafouri, M., Parhizkar, M., Aref, S.M. et al. (2014). Effect of temperature on the electrophysical properties of Si–polymer composite varistors. *Microelectronics Reliability* 54 (5): 965–971.

116 Ghafouri, M., Parhizkar, M., Bidadi, H. et al. (2014). Effect of Si content on electrophysical properties of Si–polymer composite varistors. *Materials Chemistry and Physics* 147 (3): 1117–1122.

117 Yang, X., Hu, J., Chen, S.M., and He, J.L. (2016). Understanding the percolation characteristics of nonlinear composite dielectrics. *Scientific Reports* 6: 30597.

118 Yang, X., He, J.L., and Hu, J. (2015, 2015). Tailoring the nonlinear conducting behavior of silicone composites by ZnO microvaristor fillers. *Journal of Applied Polymer Science* 132 (40): 42645.

119 Gao, L., Yang, X., Hu, J., and He, J.L. (2016). ZnO microvaristors doped polymer composites with electrical field dependent nonlinear conductive and dielectric characteristics. *Materials Letters* 171: 1–4.

120 Zhao, X.L., Yang, X., Li, Q. et al. (2017). Synergistic effect of ZnO microspherical varistors and carbon fibers on nonlinear conductivity and mechanical properties of the silicone rubber-based material. *Composites Science and Technology* 150: 187–193.

121 Dang, Z.M., Yuan, J.K., Zha, J.W. et al. (2012). Fundamentals, processes and applications of high-permittivity polymer–matrix composites. *Progress in Materials Science* 57 (4): 660–723.

122 Simon, P. and Gogotsi, Y. (2008). Materials for electrochemical capacitors. *Nature Materials* 7 (11): 845–854.

123 Ishibe, S., Mori, M., Kozako, M., and Hikita, M. (2014). A new concept varistor with epoxy/microvaristor composite. *IEEE Transactions on Power Delivery* 29 (2): 677–682.

2

Conduction Mechanisms of ZnO Varistors

The conduction mechanism is the fundamental to study the electrical characteristics of ZnO varistors. First, a concise introduction to the basic concepts of solid-state physics is presented to provide knowledge of the energy band structure of solids with periodic structures. The energy band structure of an individual grain boundary in the ZnO varistor as the double-Schottky barrier (DSB) is introduced, with its origin as the native donor complex defects in depletion layers providing electrons to the acceptor defects that form the interfacial state such that the energy bands bend upward near the interface. Secondly, the conduction mechanism in the ZnO varistor for the charge carriers across the DSB based on the thermionic emission process further incorporating the effect of minor carrier (hole) generation and "feedback" is introduced. Grain boundary model is introduced, which is also the basic unit for simulation when considering the multigrain effect of the varistor bulk. At last, the dielectric responses in ZnO varistor are given a glance, based on which the grain boundary parameters can be effectively estimated with the aid of appropriate frequency domain techniques. The relaxation effect of the grain boundary has a considerable effect on the response of the ZnO varistor to time-varying signals. The effect of relaxation process of the interfacial charge results in a phase shift of conduction current in advance of the applied voltage.

2.1 Introduction

After the first report on the excellent nonlinear I–V property of a ZnO-based varistor by Matsuoka in 1971 [1], researchers around the world were eager to explain where such a nonlinearity was resulted. Much effort has been made in the past several decades focusing on the conduction mechanism issue in a ZnO varistor [2–32]. Among the numerous conduction models proposed by different research groups (compiled in the list of Table 2.1) [1–19], the one presented by Pike [13, 15] and further developed by Blatter and Greuter [16–18] is widely recognized and may meet most of the experimental phenomena. Essentially, it is generally believed that the nonlinear I–V characteristic of the ZnO varistor is caused by the charge carriers transporting across the DSB formed at the grain boundary.

Table 2.1 Theories on the ZnO varistor grain boundary microstructure model and conduction mechanism.

Publication year	Author	Interface model	Barrier variation mechanism	Conduction mechanism	
				Prebreakdown region	**Breakdown region**
1971	Matsuoka	Thick insulating layer with traps		Space charge-limited currents	
1975	Levinson and Philipp	Single-barrier basing on energy band		Schottky emission	Fowler–Nordheim tunneling
1975	Levine	DSB model	Interface states filled up	Schottky emission	
1976	Morris	DSB model		Schottky emission	Field emission (electron tunnel-ing)
1976	Bernasconi	DSB model	Left barrier vanishes		Zener tunneling
1977	Emtage	DSB model	Insulating layer traps filled up	Electrons diffusion	
1978 1982	Eda	DSB model bypass effect		Schottky emission	Field emission (electron tunnel-ing)
1978	Einzinger	DSB model			
1979	Hoover and Gupta	DSB model	Right barrier vanishes		
1979	Mahan	DSB model	Surface state be filled to make holes	Two-step transport Schottky emission–low voltage electron tunneling emission–high voltage	
1979 1982	Pike	DSB model	Surface state be filled to make holes	Schottky emission	
1986	Blatter and Greuter	DSB model	Surface state be filled to make holes	Schottky emission	

Actually, the DSB also plays a critical role in various electroceramics other than the ZnO varistor, such as $BaTiO_3$, $SrTiO_3$, and so forth [19, 20], responsible for their unique properties for commercial applications. Thus, it is of significance and profound influence for a reader to understand the basic conduction mechanisms where the DSB involves. In this chapter, we will first describe the energy band diagram of a typical grain boundary where DSB is formed, present a brief introduction of the ideal Pike conduction model, the dielectric behavior of the varistor, and finally the practical bypass effect model that is useful for numerical simulations. Here, we will not bother to review the full development history of various conduction models and to compare their advantages or shortcomings, which is indeed tedious. Instead, we just give the description of the most pervasive mechanism of conduction that we expect the reader to fully interpret as it constitutes the theoretical foundation of the whole book. Besides, we spend a small amount of space discussing the microscopic origins of the electrostatic potential barrier, i.e. the DSB, for those are the underlying basis of DSB and are crucial when dealing with issues such as the degradation of DSB.

2.2 Basic Concepts in Solid-State Physics

As the potential readers of this book include engineers who may not dip into the quantum physics or more specifically the solid-state physics as those majoring in physics or material sciences do, a concise introduction to the basic concepts of solid-state physics is necessary and presented here, striving to make the energy band structure of a solid with the periodic structure appreciated. More details of mathematical derivations of various physical mechanisms are directed to common textbooks of the general college physics and the solid physics.

2.2.1 Atomic Energy Level and Energy Band of Crystal

According to the quantum physics, each electron in the atom, under the effect of the potential field of nucleus and of other electrons, locates itself in different energy levels, forming the so-called electron shells. These distinct shells are symbolized as 1s, 2s, 2p, 3s, 3p, 3d, 4s, and so forth with each one corresponding to a definite energy. When atoms approach each other to form the crystal, the inner and outer electron shells of various atoms overlap to a certain degree; the outer shells of adjacent atoms have a relatively large degree overlapping, whereas the case for the inner shells is quite limited. In crystal, electrons are no longer confined to a single atom because of the overlapping of shells while they may transfer to neighboring atoms; thus, electrons can move in the whole crystal. Such a phenomenon is termed as electron sharing. It should be further noted that the electrons can only transfer themselves between similar electron shells because the electrons in similar shells of different atoms share identical energies. Electron sharing is caused by the overlapping of similar shells among distinct atoms, e.g. the overlapping of 2p electron shells or 3s shells, as shown in Figure 2.1. Because different shells enjoy varying degrees of electron sharing, only that of outermost shell electrons is prominent.

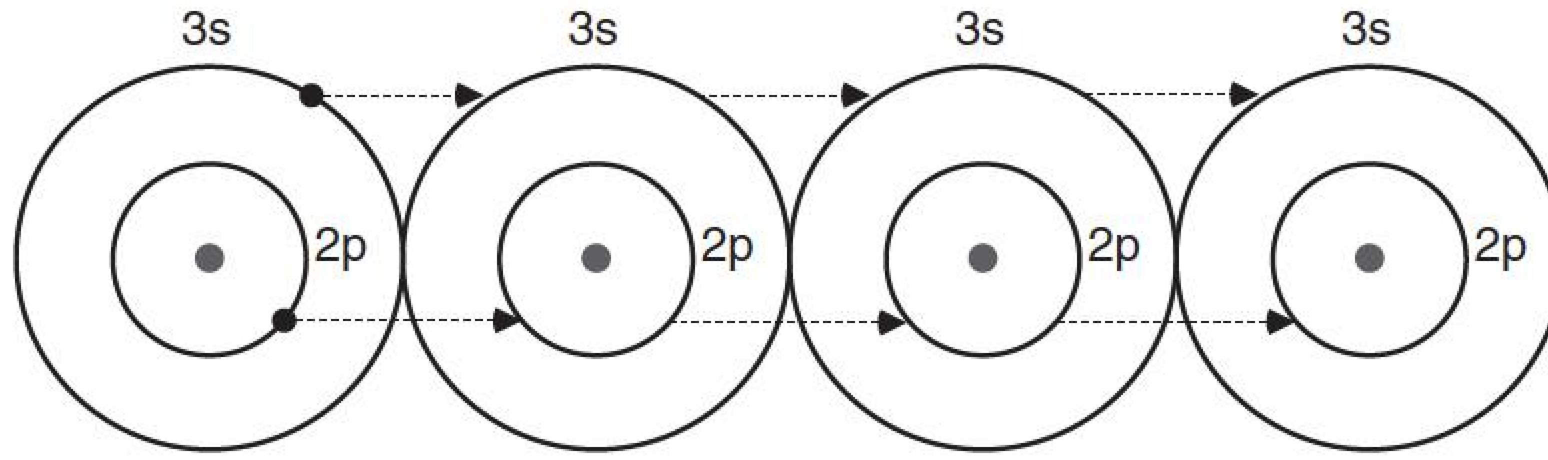


Figure 2.1 The electron sharing of atomic shells.

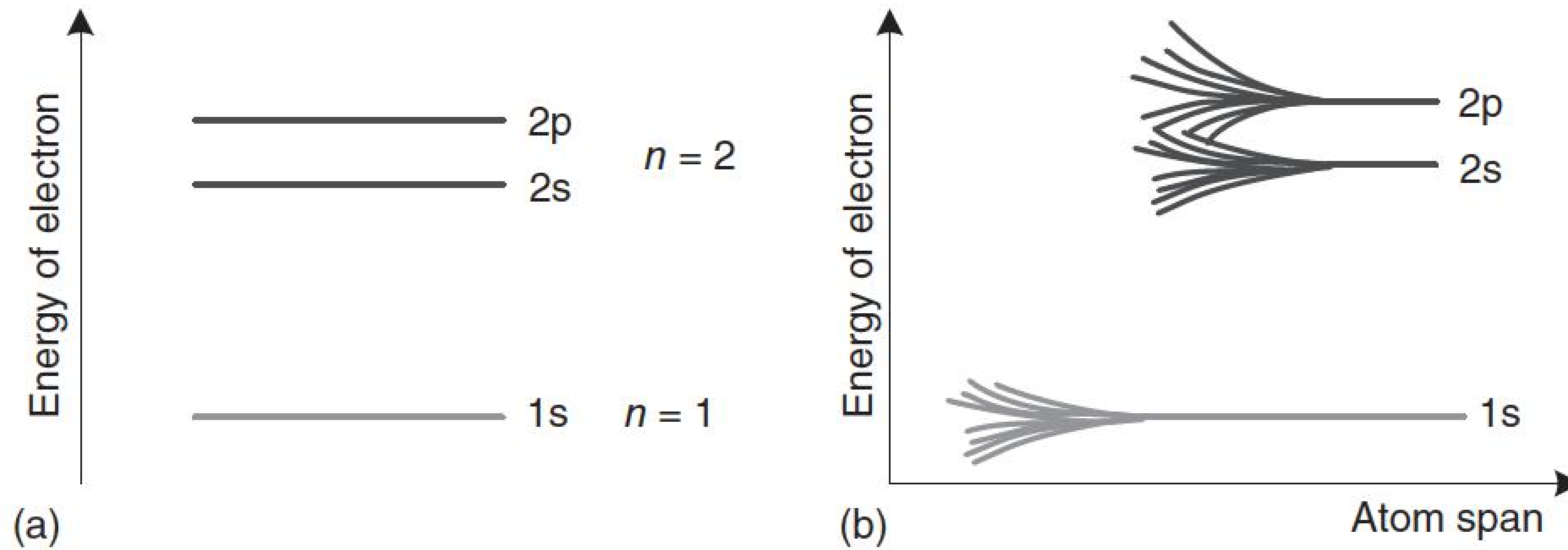


Figure 2.2 The splitting of energy level. (a) The energy levels of an isolated atom; (b) the splitting of energy levels of eight atoms.

Then, the energy of electron in a crystal when the electron-sharing effect is taken into account should be discussed. Exemplified by two atoms, when they are farther apart as two isolated atoms, the atomic energy levels can be presented as Figure 2.2a, and each energy level corresponds to two energy states and is doubly degenerated (regardless of the degeneracy of the atom itself). When two atoms approach each other, electrons are not only under the effect of the potential field of atom where they reside but also influenced by the potential field of the other atom. Then, each doubly degenerated energy level splits into two levels close together; the closer the two atoms are, the more severe is the degree of splitting. Figure 2.2b describes the case when eight atoms come closer; each energy level splits into eight levels closely located. When two atoms approach each other, the electrons in certain energy level get to locate themselves separately in the newly split two energy levels and are then shared by the two atoms instead of belonging to some single atoms. Besides, the number of split energy levels should include the degeneracy of the atom, e.g. the 2s energy level can split into two levels, whereas the 2p energy level is itself triply degenerated and can split into six energy levels.

When considering the crystal constituting of N atoms, per cubic centimeters of volume contains 10^{22}–10^{23} atoms, rendering the N an astronomical figure. Presuming that N atoms are far apart, the energy levels of each atom are exactly identical to those of the isolated atoms and are N dimensionally degenerated (temporarily disregard the degeneracy of the atom). When the N atoms come closer to form the crystal, each electron is affected by the potential fields of the surrounding atoms, resulting in the splitting of each energy level of N-dimensional degeneracy into N energy levels, which are close to each other and constitute an energy band. Then, the electrons no longer belong to single

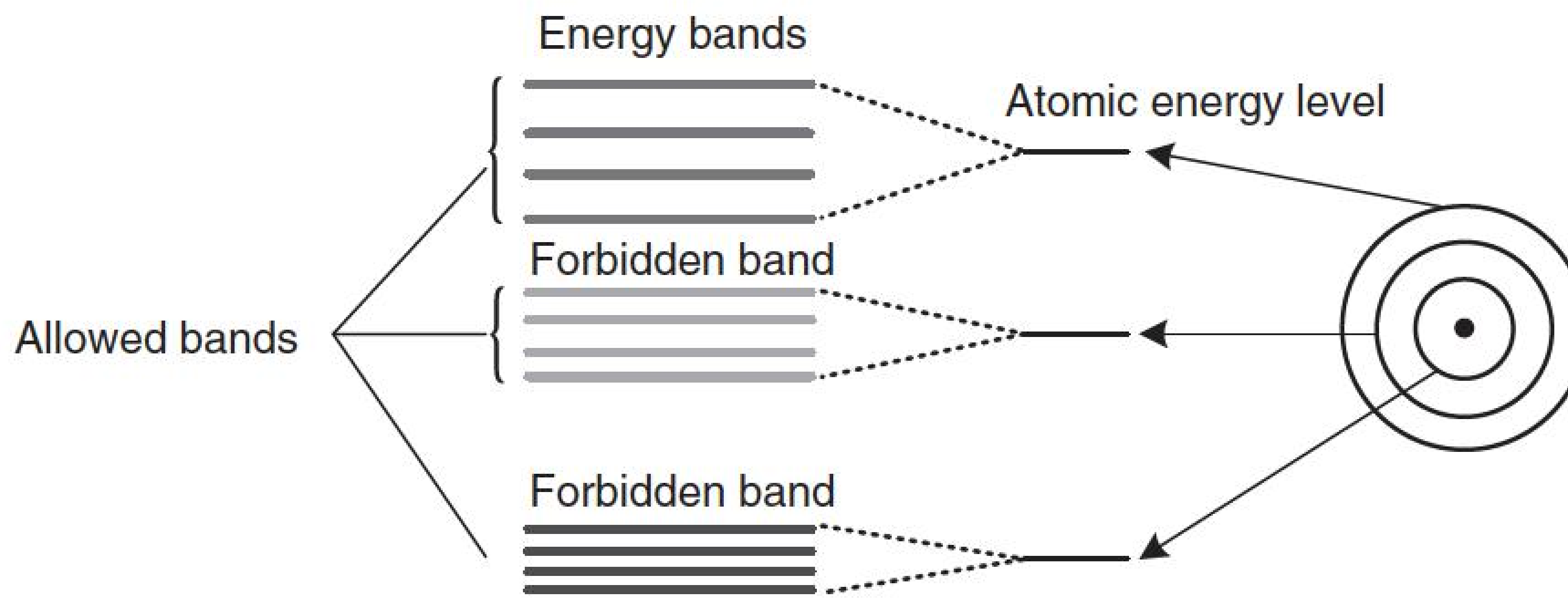


Figure 2.3 The splitting of atomic energy level and the formation of energy band.

atoms but instead are shared. Every newly split energy band is termed as allowed band, whereas the blank space between the allowed bands without the existence of energy band is called the forbidden band. Figure 2.3 presents the splitting of atomic energy level into the formation of energy band.

The electrons of inner shells are of low energy and weak electron sharing; thus, their splitting is unconspicuous, and the resulted energy band is correspondingly narrow. On the contrary, the outer shell electrons own high energy and enjoy prominent electron sharing. Especially, the valence electrons, behaving like free electrons (thus usually termed as "quasi-free electrons"), enjoy severe splitting, and the corresponding energy band is relatively broad. Figure 2.3 also demonstrates such a "narrow-broad" comparison.

The number of energy levels contained in an energy band is closely related to the degeneracy of the energy level in an isolated atom, e.g. the s energy band has no degeneracy (not accounting the spin), and thus, it may split into N energy levels closely located to form the band when N atoms come to constitute the crystal, whereas the p energy band is triply degenerated, and the resulting energy band owns $3N$ split energy levels. In an actual crystalline solid, as the N is astronomical and split energies locate themselves closely, the energy levels in each energy band can be considered as continuous (sometimes termed as "quasi-continuous"). However, it should be noted that the relationships between the energy bands in numerous actual crystalline solids and atomic energy levels are more complicated than the above simple ones, and details are directed elsewhere [21, 22].

2.2.2 Metal, Semiconductor, and Insulator

Solids can be generally classified into conductor, semiconductor, and insulator according to their conductivities, which can be interpreted on the basis of energy band structure.

The conductivity of the solid results from the directional movement of electrons inside the solid under the effect of applied electric field, as the electric field force can accelerate the electrons, altering their velocities and energies. In other words, electrons can have their energies exchanged with the exterior electric field. From the perspective of energy band theory, the variation of electron energy corresponds to the transition from one energy level to the other. For the filled

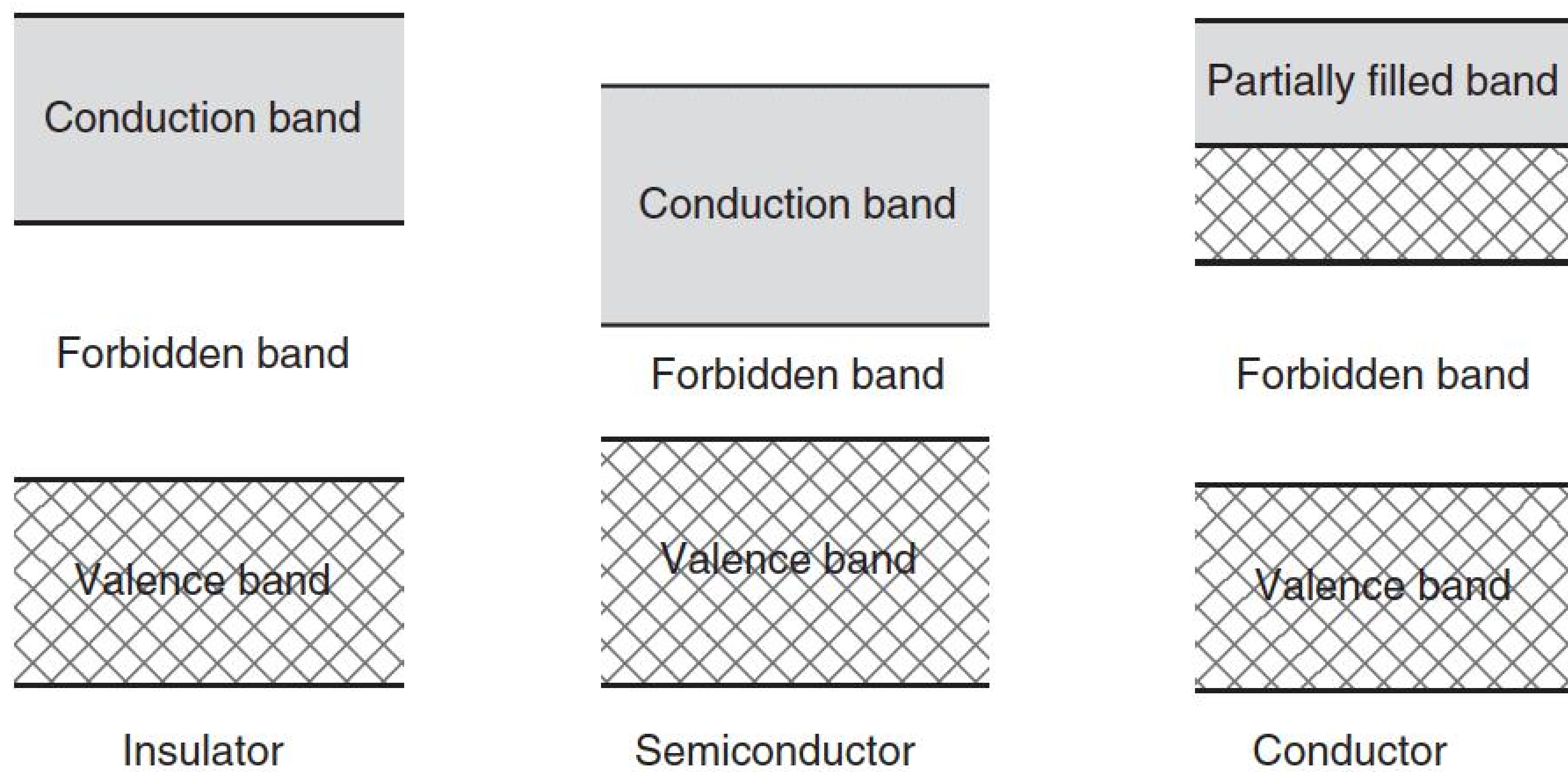


Figure 2.4 The energy band diagrams of insulator, semiconductor, and conductor.

band that is fully occupied, the electrons inside can make no contribution to the conduction under externally applied electric field. This indicates that the inner shell electrons in an atom usually fill the energy levels forming the full-filled band and thus do not participate in the conduction process. For these partially filled bands, electrons can transit to unoccupied energy levels by absorbing the energy provided by the applied electric field and thus contribute to the occurrence of current and conduction. Such bands playing roles in conduction are termed as conduction bands. In metals, the band occupied by valence electrons is partially filled, as shown in Figure 2.4, and renders the metal a perfect conductor.

Insulator and semiconductor have quite a similar energy band structure as shown in Figure 2.4, i.e. the empty conduction band above (conduction band) and the full-filled band below (termed as valence band)[1] are separated by the forbidden band (usually called band gap). With such energy band structures, they are not conductive under an applied electric field. However, this is the limiting case at 0 K (thermodynamic temperature). When the external conditions vary, e.g. with the temperature rising or light, less number of electrons can be excited to the above empty band edge to participate in the conduction. Simultaneously, because of the excitation of electrons, same amount of holes are left behind in the top of the valence band, which can also contribute to the conduction. The participations of both electron and hole are the significant difference between the semiconductor and metal. Because of the large band gap in the insulator (5–7 eV), the excitation of electrons requires enormous energy, and electrons excited to the conduction band at room temperature are rarely rendering the insulator poorly conductive. Comparatively, the band gap in the semiconductor is small (around 1 eV), and a few of electrons can be excited at room temperature, leading to the conduction ability of the semiconductor. It should be noted that even the band gap of zinc oxide is 3.34 eV, ZnO still presents the semiconductor feature, which is ascribed to the (intrinsic or extrinsic) defects inside the ZnO crystals resulting in the n-type conduction.

1 Other full-filled bands occupied by inner shell electrons below the valence band are omitted in Figure 2.4 for simplicity.

2.2.3 Characteristics of Fermi–Dirac Function

As stated above, the energy band theory is a single-electron approximation, i.e. the motion of each electron is considered as independent approximately and has a series of defined eigenstates [21]. The macrostate of such a system described by single-electron approximation can be characterized by the statistical distribution of the electron in these eigenstates. For the equilibrium state of the system, the Fermi statistics adopted is based on the Fermi–Dirac statistical distribution function:

$$F(E) = \frac{1}{e^{(E-E_F)/k_B T} + 1} \tag{2.1}$$

where E is the energy level, E_F is the Fermi energy level (or the chemical potential), k_B is the Boltzmann constant, and T is the temperature. This function directly gives the possibility of occupation of an eigenstate with energy E by electron. The Fermi–Dirac function has special properties, as shown in Figure 2.5:

$$\begin{cases} T = 0\,K & E > E_{F0} & F(E) = 0 \\ & E \leq E_{F0} & F(E) = 1 \\ T > 0\,K & E \gg E_F & F(E) \approx 0 \\ & E \ll E_F & F(E) \approx 1 \\ & E = E_F & F(E) = \frac{1}{2} \end{cases}$$

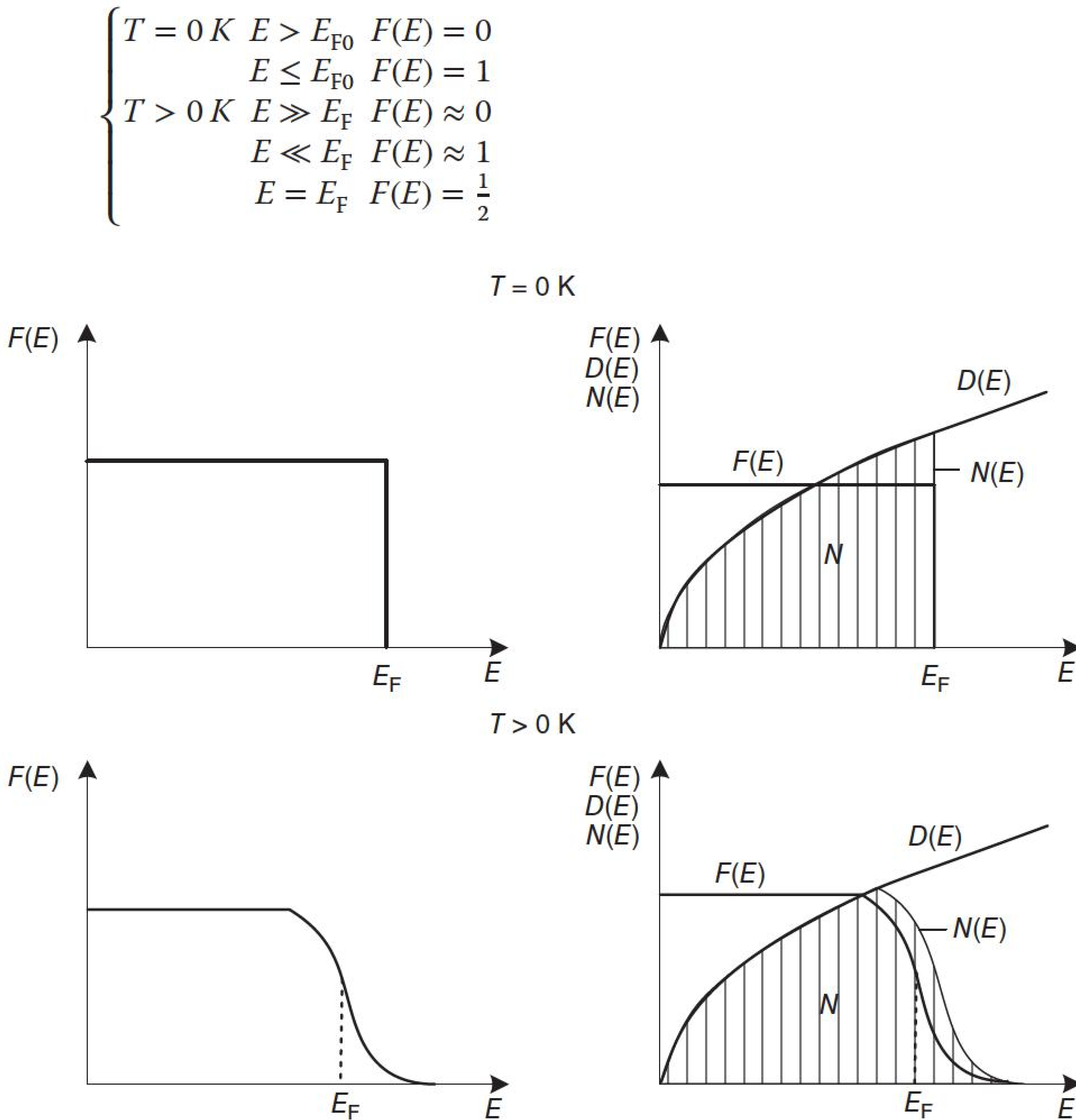


Figure 2.5 The Fermi–Dirac function $F(E)$, energy-state density $D(E)$, and the distribution of populated electron number $N(E)$. Source: Busch and Schade 2013 [21]. Redrawn with permission from Elsevier.

where E_{F0} is the Fermi energy level at 0 K. As shown in Figure 2.5, with the aid of Fermi–Dirac function, the number of electrons $N(E)$ populated between energy level E and $E + dE$ can be derived:

$$N(E)dE = 2D(E)F(E)dE \tag{2.2}$$

where $D(E)$ is the distribution of energy state density and the constant 2 comes from the Pauli exclusion principle. Moreover, in n-type semiconductor, the Fermi energy level locates itself in the band gap near the bottom of the conduction band according to Eq. (2.1), whereas in the p-type semiconductor, the Fermi level is above and close to the top of valence band.

2.2.4 Impurity and Defect Energy Level

In actual crystalline solid, the strictly periodic structure is generally not satisfied because of the following factors: firstly, the atoms are not static at the sites of crystal lattice, whereas they vibrate around their equilibrium positions; secondly, the crystal is not pure and usually contains a quantity of impurities (unintentionally or intentionally doped); thirdly, the actual crystal lattice is not intact because of the existence of numerous defects (point, line, or plane defects).

It is found that even a trace amount of impurity or defect can impose decisive effect on the chemical and physical properties of the semiconductor because they can disturb the periodic potential field generated by the periodic repeated array of atoms and introduce new energy states (levels) into the forbidden band.

Throughout this book, we mainly center the discussion on the role of atomic defects (the impurity atoms and point defects are both included in this category), although the grain boundary (plane defect) is inevitably discussed. The defects release the electrons to participate in the conduction and form positive centers when ionized and are termed as donor defects or n-type defects. The donor defects are neutral when unionized, whereas become positively charged after ionization. Conversely, the acceptor defects or p-type defects provide holes and form negative centers when ionized. In addition, they are neutral when unionized and become negatively charged after ionization. From the perspective of energy band theory, the donor or acceptor defects can introduce the corresponding energy level in the band gap near the conduction band or valence band, respectively, and offer electrons or holes to the allowed band as shown in Figure 2.6. Moreover, the atomic defects can exist in the crystal as vacancies,

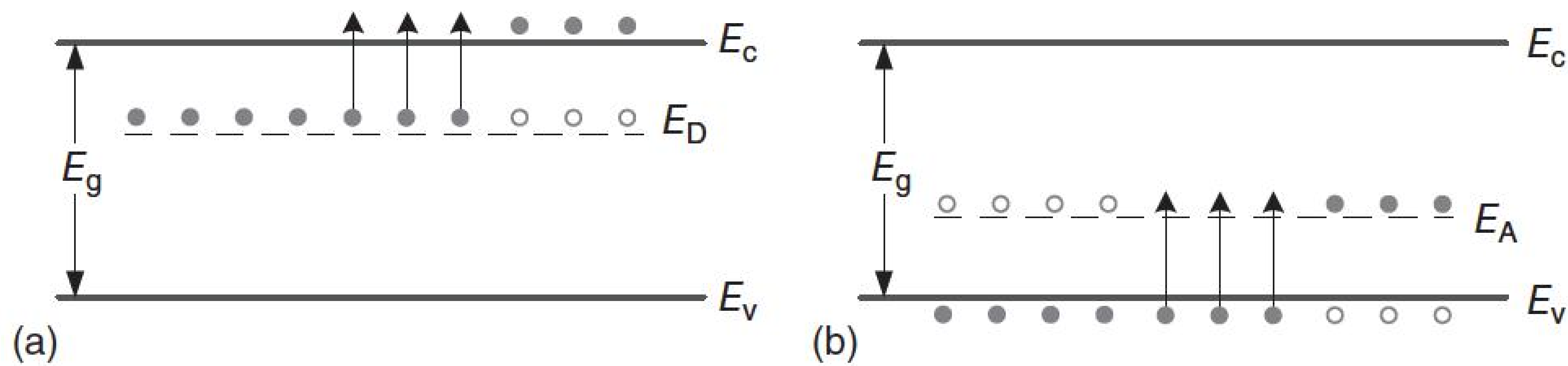


Figure 2.6 (a) The energy level and ionization of donor defects; (b) the energy level and ionization of acceptor defects, in which the conduction band minimum (E_c), valence band maximum (E_v), and band gap (E_g) are given; E_D and E_A are the energy levels of donor and acceptor defects. Source: Busch and Schade 2013 [21]. Redrawn with permission from Elsevier.

interstitials, substitutions, and antisites, which the reader will get familiar with by concrete examples presented in the following chapters.

2.3 Energy Band Structure of a ZnO Varistor

ZnO varistor as a polycrystalline electroceramic is mainly composed of grains, grain boundaries, particles, and pores, among which the electrically active grain boundaries endow the ZnO varistor with excellent nonlinear electrical properties and act as the dominant role in conduction. Based on the energy band theory discussed previously, the energy band structure of an individual grain boundary in the ZnO varistor, i.e. the DSB configuration, is presented below that constitutes the theoretical foundation for the charge carrier transportation across the boundary and the general conduction mechanism of polycrystalline electroceramics.

2.3.1 Energy Band Structure of a ZnO Grain

For wurtzite ZnO with a direct band gap of 3.37 eV at room temperature, its energy band structure is as follows: the lowest energy level of the valence band is composed of O 2s orbital, whereas the higher ones in the valence band are mainly blended by the O 2p, Zn 4s, and Zn 4p orbitals, and the lowest and highest energy levels inside the conduction band are primarily constituted by the Zn 4s and Zn 4p orbitals, respectively [23]. Besides, defects and local perturbations may introduce energy levels to the forbidden band. Figure 2.7 describes the simplified energy band diagram of ZnO (grain), regardless of those defect levels in which the conduction band minimum (E_c), valence band maximum (E_v), band gap (E_g), and the Fermi level (E_F) are given.

As stated previously, the pure zinc oxide is itself an n-type semiconductor, provided its wide band gap is much larger than that of average semiconductors (~1 eV). This originates from the effect of defects. The intrinsic defects [24] in ZnO include the interstitials (Zn_i, O_i), the vacancies (V_{Zn}, V_O), and the antisites (Zn_O, O_{Zn}), among which Zn_i, V_O, and Zn_O are donor defects, whereas O_i, V_{Zn}, and O_{Zn} are acceptor defects. Thereinto, Zn_i and V_O are long believed to be the origin of n-type conduction although this point is in dispute. Besides unintentionally doped defects, e.g., hydrogen may play a leading role in the as-grown ZnO as shallow donors.

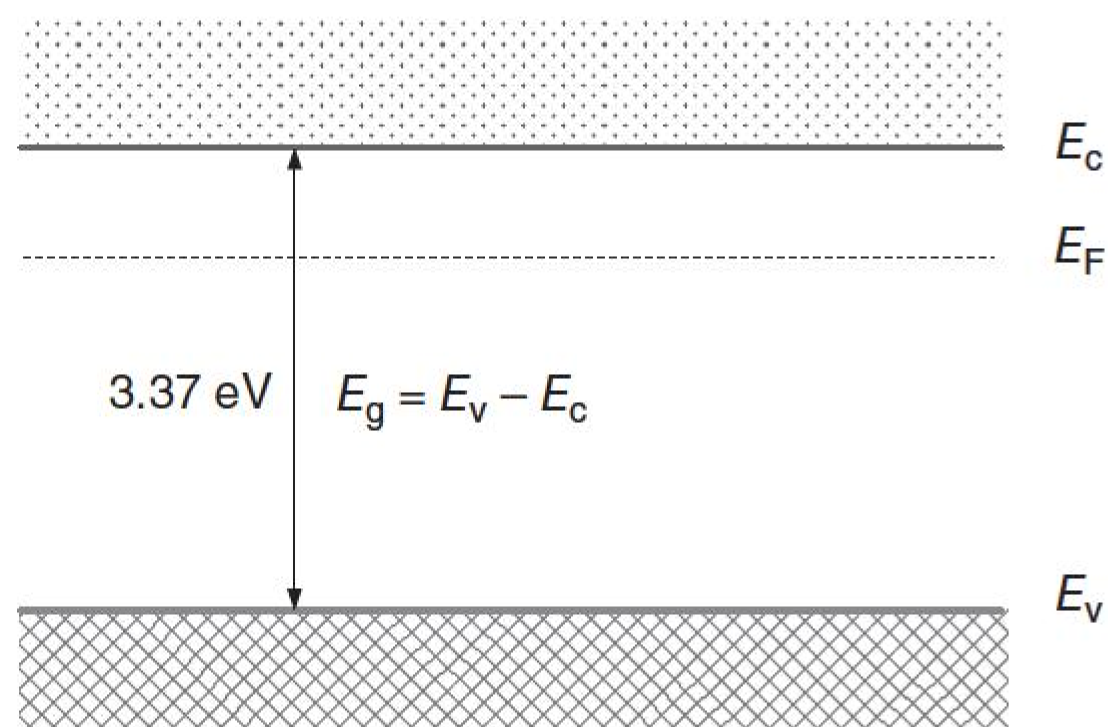


Figure 2.7 The energy band diagram of pure ZnO crystal.

2.3.2 DSB of a ZnO Varistor

The essential concept underlying varistor action is that the $I-V$ characteristics are dominated by the electrostatic barrier, i.e. the DSB, formed along the grain boundary. Therefore, the formation of the electrostatic barrier is narrated here based on the treatment proposed by Pike and Seager [15] as joining together two identical semiconducting grains with an infinitely thin layer of grain boundary materials as shown in Figure 2.8a [25]. When these three components are coming into contact to form an individual grain boundary structure, electrons flow until the Fermi level is the same everywhere in order to achieve thermodynamic equilibrium. As the Fermi level of the n-type semiconducting grain is higher than the sandwiched boundary material, electrons flow from the grain to the grain boundary, where they are trapped by the defects and dopants, to increase the local Fermi level until it is the same throughout the structure. At equilibrium, the trapped electrons act as the negative sheet charge at the boundary, leaving behind a layer of positively charged donor sites on either side of the boundary (termed as the depletion layer) that render the energy bands of grains bending upward near the boundary and thus create an electrostatic field with a barrier at the boundary, which is termed as the DSB as shown in Figure 2.8b [25].

Assuming the ZnO grain surface is a unit area, the positive charge in the two depletion layers is

$$Q_d = eN_d d \tag{2.3}$$

where e is the electron charge and N_d is the donor density. Thus, the interface charge Q_i is determined by

$$Q_i = 2Q_d = 2eN_d d \tag{2.4}$$

The interface Q_i can be expressed by interface states N_s:

$$Q_i = eN_s \tag{2.5}$$

From Eqs. (2.4) and (2.5), $N_s = 2N_d d$; thus, the depletion layer width is $d = N_s/2N_d$. The height of Schottky barrier ϕ_b could be obtained by solving

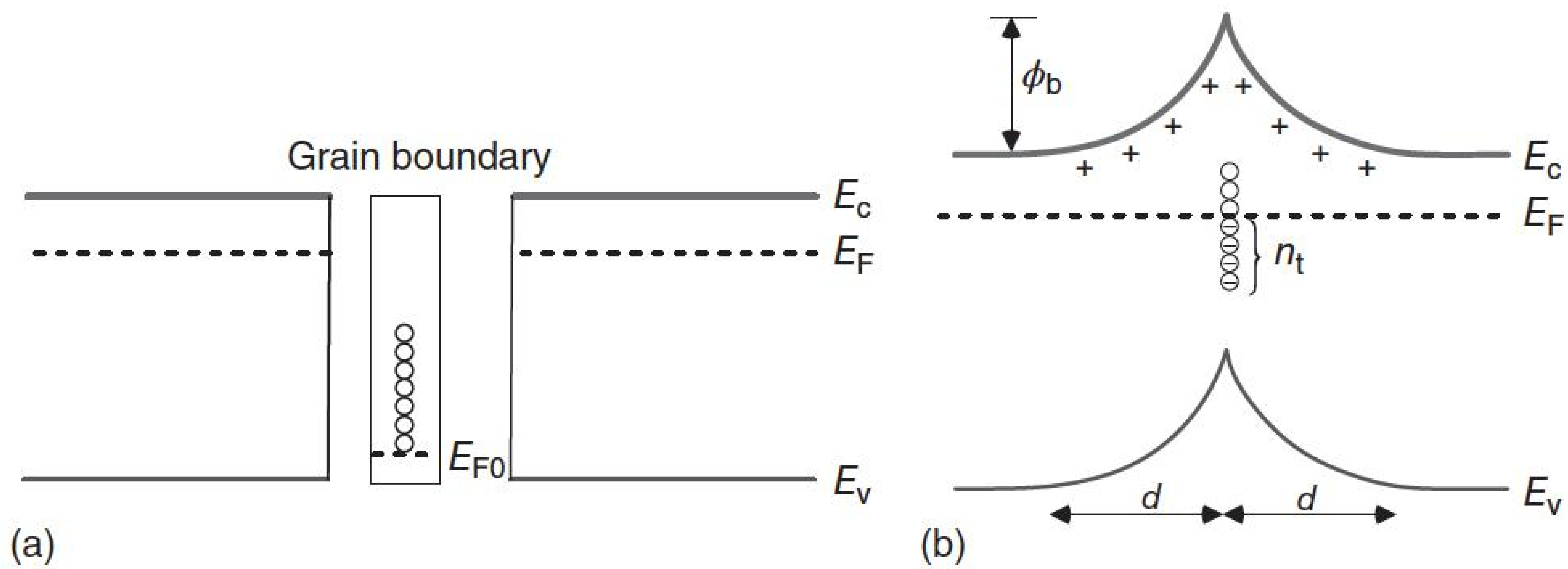


Figure 2.8 The energy band diagram of individual grain boundary in the ZnO varistor (a) before contact; (b) when joined. E_{F0} is the Fermi level of grain boundary material, and d is the depletion width of either side. Source: Clarke 1999 [25]. Redrawn with permission from John Wiley & Sons.

Poisson's equation:

$$\frac{\partial^2 \phi(x)}{\partial x^2} = \frac{e^2 N_d}{\varepsilon_0 \varepsilon_r} \tag{2.6}$$

In Eq. (2.6), we adopt the convention $e = |e|$ such that the potential energy of an electron is simply $e\phi(x)$. Solve the equation and set the boundary conditions as $\phi(x)|_{x=d} = 0$, $\left.\frac{\partial \phi(x)}{\partial x}\right|_{x=d} = 0$. For a boundary, the charge can be represented by a sheet of trapped charge of areal density, n_t. From the solution of the Poisson equation, two important parameters result: the barrier height, ϕ_b, and the width, d, of the depletion layer. And then, the Schottky barrier height when no external voltage is applied is given as follows:

$$\phi_b = \phi(x)|_{x=0} = \frac{e^2 N_d d^2}{2\varepsilon_0 \varepsilon_r} = \frac{e^2 N_s^2}{8\varepsilon_0 \varepsilon_r N_d} \tag{2.7}$$

Aside from the shallow donor that we discuss alone as in Figure 2.8, other unfully occupied deep donor can also make contributions to the formation of DSB and can participate in the conduction and dielectric response of the ZnO varistor with similar and straightforward treatment that can be found in Ref. [17]. However, throughout this chapter, we only focus on the discussing the shallow donor species.

2.3.3 Microscopic Origin of DSB

Even it is generally recognized that the electrostatic potential barrier is based on the presence of the acceptor-like grain boundary states that are trapping electrons, the microscopic origins of the DSB have not been positively identified, although various models have been proposed so far, e.g. intergranular layers [1], segregations of additives [26, 27], thin disordered layer [11], oxygen excess defects such as chemisorbed oxygen or excess amount of oxygen [28, 29], native defects such as V_{Zn} and O_i [30, 31], and complex of additives and native defects [32, 33].

Bismuth or praseodymium is the critical additive as the DSB activator that is frequently doped during the sintering of ZnO varistors, among which those doped Bi atoms could appear either as isolated atoms decorating the ZnO grain boundaries or as a thin amorphous Bi_2O_3 layer (typical thickness as 0.6–1.5 nm [17, 34]) depending on the cooling process [25, 35]. It has been debated in the literature which of these two types of Bi configurations give rise to the most pronounced nonlinearity [35]. Investigation on the Bi-decorated configuration by modeling contaminated coincidence site lattice (CSL) grain boundary has made profound achievements. It is reported that the Bi atom, because of size mismatch, usually substitutes at the Zn site (Bi_{Zn}) at the grain boundary, which actually acts as the donor defect without creating acceptor states inside band gap [32]. The presence of Bi_{Zn} at the grain boundary could significantly promote the formation of native defects, V_{Zn} and O_i in particular. Flat semioccupied states just above the valence band edge and across the Fermi level E_F are presented when either $Bi_{Zn} + V_{Zn}$ or $Bi_{Zn} + O_i$ complex defect is formed [36].

Moreover, when the complex defect $Bi_{Zn} + V_{Zn} + O_i$ is presented at the grain boundary, an unoccupied acceptor state with more dispersion could be

additionally produced [36], as shown in Figure 2.9, and such a complex defect has a comparatively very small segregation energy that there is a significant driving force for the individual Bi_{Zn}, V_{Zn}, and O_i to accumulate in grain boundary [32]. This indicates that the inclusion of complex defect $Bi_{Zn} + V_{Zn} + O_i$ could endow the grain boundary core with a prominent p-type character. When joining the grain boundary region to the surrounding bulk ZnO crystals that are naturally

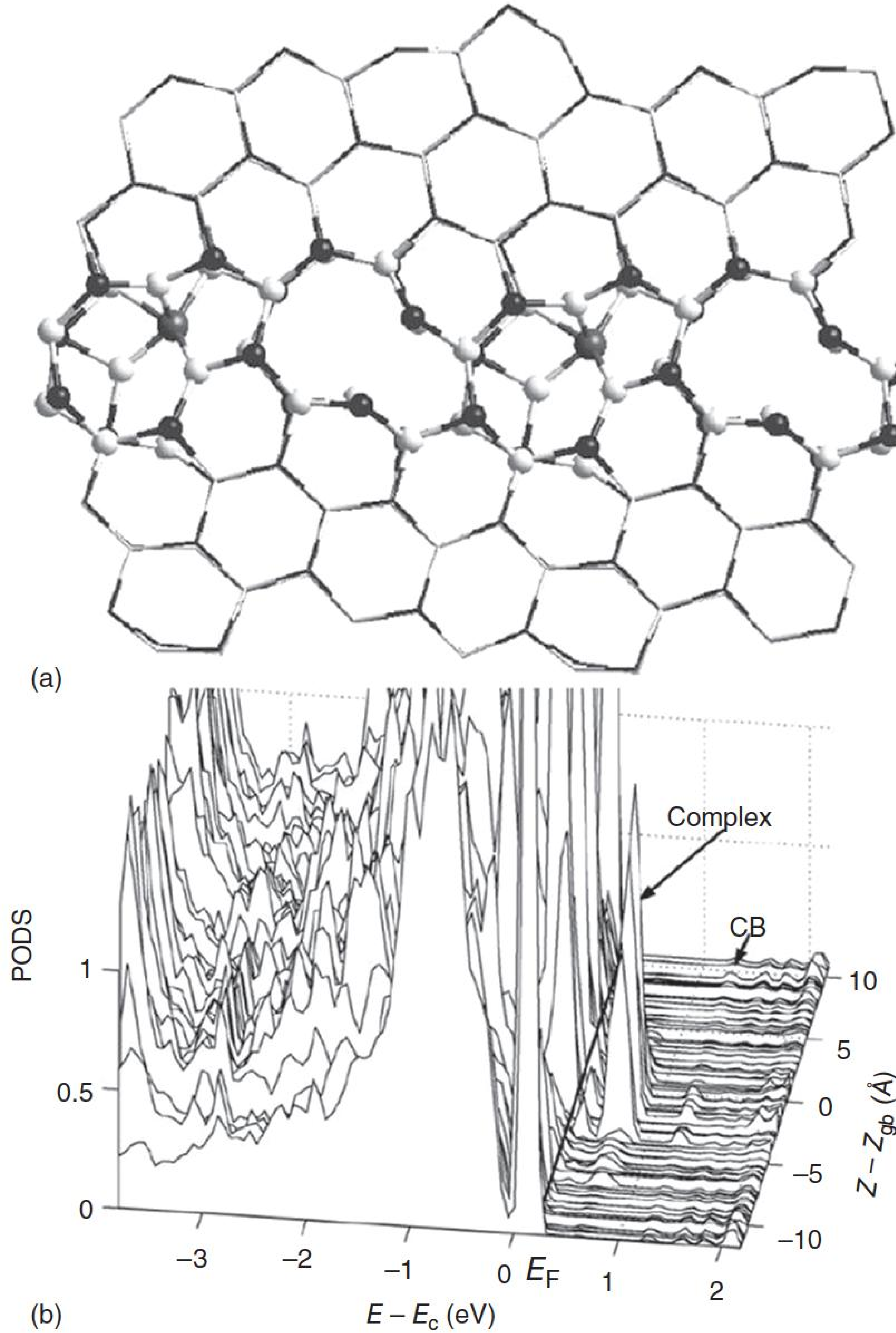


Figure 2.9 (a) Σ13 CSL tilt boundary containing the $Bi_{Zn} + V_{Zn} + O_i$ complex. The structure is viewed down the [0001] tilt axis with the atoms in the zigzag chain of 10-atom rings highlighted. (b) Projected density of states (PDOS) for individual atoms mapped as a function of distance *z* normal to the boundary. The solid line indicates the Fermi level, and CB denotes the conduction band edge. The arrow-labeled "complex" shows the position of the acceptor state in the band gap. Source: Carlsson et al. 2003 [32]. Reproduced with permission of APS.

n-type, the boundary acceptor states will capture the excess electrons provided by ZnO bulks nearby, and a grain boundary electrostatic potential barrier will be formed. Compared to the Bi-decorated grain boundary, the case where Bi_2O_3 amorphous layer involves is seldom simulated because of the difficulty in modeling. A limited number of investigations also demonstrate the critical role of native defects, i.e. the inclusion of V_{Zn} could turn the inactive metallic amorphous film into an electrical active grain boundary (promote the formation of acceptor states localized to the boundary core) [34].

In addition, discussion must be made on the excess oxygen that is vital for the occurrence and stabilization of p-type character of the grain boundary region, either for the Bi-decorated boundary or the amorphous layer case. For the former case, the oxygen-rich environment could largely reduce the formation energy of and promote the formation of $Bi_{Zn} + V_{Zn} + O_i$ complex defect [32] by tuning the value of oxygen chemical potential appearing in the defect formation (Gibbs) energy [37], reflecting the reservoirs for atoms that involved in creating the defect; although for the latter one, it can be viewed as the inclusion of V_{Zn} defect into the supercell for simulation is equivalent to relieve the oxygen deficiency of the system [34] (this is also valid for the Bi-decorated boundary case); therefore, the Bi_2O_3 intergranular layer in combination with no oxygen deficiency could eventually yield the electrical activity.

It should be further noted that for Pr-doped ZnO varistors, the situation is quite similar. Pr itself is not a direct cause of electrostatic potential barriers, whereas Pr substitutes at the Zn site of the grain boundary, acting as the donor defect, and plays an important role to promote the formation of acceptor-like native defects [20, 38], i.e. V_{Zn} and O_i, among which V_{Zn} is considered as the dominant acceptor species owing to its lower calculated formation energy.

2.3.4 Asymmetric *I–V* Characteristics of the DSB

The asymmetric I–V characteristics were observed from the measurements of individual grain boundaries between the Bi-rich phases and the ZnO grains [39–42]; with breakdowns at 3.2 V for one polarity of the applied voltage, in the reverse direction, the breakdown at 0.4, 0.6, and 0.9 V depended on the particular polymorph of the intergranular Bi_2O_3 [39, 43]. It was thought that the asymmetry was due to the intergranular difference in chemical composition, distribution of chemisorbed oxygen, and grain boundary microstructure [44]. Einzinger [41] thought that the asymmetry may be easy to understand because the Fermi energy levels in the two phases are different. However, these simple explanations are not comprehensive yet until recently the effect of ZnO polarity draws attention for the polarity dependence of the asymmetric I–V behavior found in testing quasi-bicrystal with an interfacial glass layer [45]. In these quasi-bicrystals, i.e. artificial grain boundary structures, asymmetry could be surprisingly large, e.g. electrical nonlinearity of forward direction may be 10 times larger than that of reverse direction.

Cheng et al. [46] further proposed that the polarity (spontaneous polarization) of ZnO materials may play a leading role for the occurrence of asymmetry. Owing to its polarity structure, the wurtzite-type ZnO has two kinds of (0001) surfaces,

both of which are polar face. The O-terminated surface is often denoted as $(000\bar{1})$ and the Zn-terminated surface as (0001). When the two ZnO crystals and the dopant layer are isolated as shown in Figure 2.10a, the energy bands of ZnO bend upward near the Zn-polar face and downward near the O-polar face. This results from the spontaneous polarization of n-type ZnO. When all the components are joined as shown in Figure 2.10b, the electrons flow from ZnO to the dopant layer. It is because the Fermi level of the n-type ZnO is higher than that of the dopant layer. Electrons are trapped in the dopant layer to make the Fermi levels of ZnO single crystals and dopant layer equal and to build a back-to-back DSB. However, the DSB here is a naturally asymmetrical one. The barrier of the Zn-polar face ϕ_{Zn} is higher than that of the O-polar face ϕ_O. Moreover, the bound negative sheet charge $-Q_{sp}$ and the positive one $+Q_{sp}$ arise from the spontaneous polarization of ZnO. Some kinds of metal ions, attracted by the Coulomb force of $-Q_{sp}$, may migrate and deviate to the Zn-polar face side from their original positions during the liquid-phase sintering process, which results in asymmetrical element distribution in the grain boundary region. These ions could act as acceptor-like grain boundary states or promote the formation of acceptor-like native defects

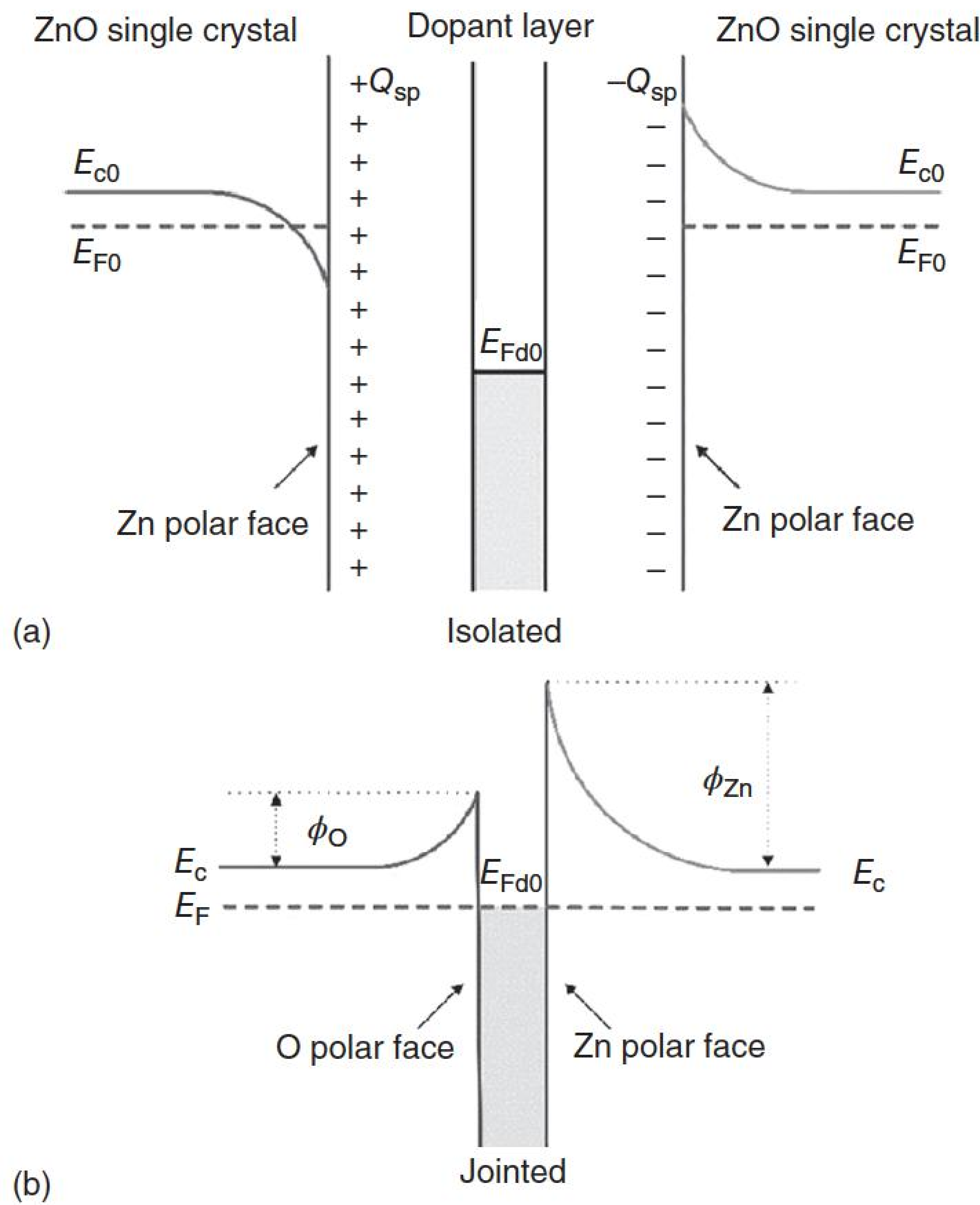


Figure 2.10 Energy band diagram of bicrystal. (a) When two ZnO single crystals and the dopant layer are isolated: E_{c0}, conduction band of ZnO single crystal; E_{F0}, Fermi level of ZnO single crystal; E_{Fd0}, Fermi level of dopant layer; Q_{sp}, bound sheet charge. (b) When all the components in (a) are joined: E_c, conduction band of ZnO single crystal; E_F, Fermi level of bicrystal. Source: Cheng et al. 2012 [46]. Reproduced with permission of AIP.

such as Zn vacancy (V_{Zn}) [38] for obtaining a higher barrier at the Zn-polar face. Conversely, the bound positive sheet charge $+Q_{sp}$ repels the dopant ions nearby. Nonmetallic ions, such as O, may also be attracted or repelled. Other boundary cases where the nonpolar face involves, i.e. no spontaneous polarization effect and has a flat energy band near the nonpolar face, are straightforward. Such an asymmetrical model can be extended to well explain various asymmetrical phenomena observed experimentally [45, 46].

Actually, such an asymmetry of individual grain boundary contributes to asymmetrical $I-V$ characteristic observations on disk varistor samples from batch to batch in laboratory, or even on the large-size surge arresters for power system. However, it should be noted that, with the increase of varistor size, such an asymmetry seems to be alleviated as the varistor is made up by an immense number of grain boundaries with varying characteristics.

2.4 Conduction Mechanism of a ZnO Varistor

As shown in Table 2.1, before 1980s, the conduction mechanisms in the prebreakdown region and the breakdown region were different. Usually, Schottky emission was used to explain the conduction mechanism in the prebreakdown region, and the field emission or the electron-tunneling effect was used for the breakdown region.

Actually, the basic conduction model of thermionic emission process across the DSB can adequately describe certain features of ZnO varistors in the prebreakdown, breakdown, and upturn regions as shown in Figure 2.11. However, this cannot account for the experimentally observed very large nonlinearities exhibited by varistor at small voltage per grain boundary, the breakdown voltage being above the band gap of ZnO [25], and so forth. Thus, the basic thermionic emission

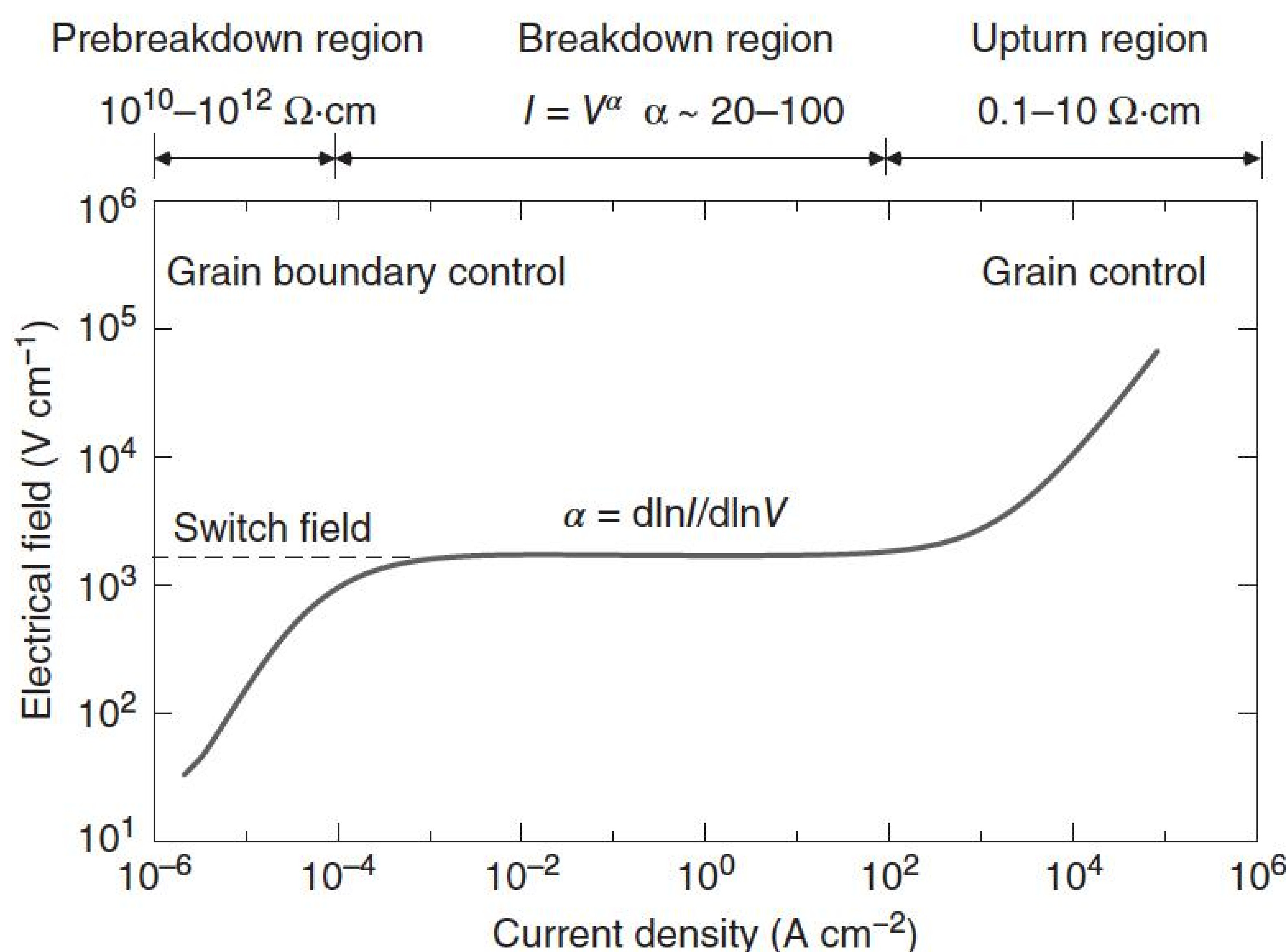


Figure 2.11 The characteristic electric field–current density response of a typical ZnO varistor. Source: Clarke 1999 [25]. Redrawn with permission from John Wiley & Sons.

model is further enhanced by Pike [13–15] for including the minority carrier generation process by "hot" electrons in the depletion layer. Here, the complete but simplified picture of the conduction model of ZnO varistor is correspondingly presented as two components, and more details of theoretical derivations can be found elsewhere [13, 17].

2.4.1 Conduction Model Based on Thermionic Emission Process

When a DC voltage V is applied across the grain boundary, the energy band structure of the individual grain boundary is deformed accordingly as shown in Figure 2.12 [25], and the current flows through the grain boundary by the thermionic emission mechanism. Simultaneously, additional electrons can be trapped at the grain boundary, and a dynamic flow of trapped charges exists between the grain and the grain boundary.

As shown in Figure 2.13, a net charge Q_i accumulates on the two-dimensional interface; one shallow donor (energy E_0, density N_0, and distribution peak value N_0^*) and several deep bulk traps (E_ν, N_ν, N_ν^*, $\nu \geq 1$) are assumed for the grains; $d_{\mathrm{l}\nu}$ and $d_{\mathrm{r}\nu}$ are the edges of boundaries, without spillover from the free bulk carriers; e_ν and e_{E_F} are the positions of the deep traps and the bulk Fermi level relative to the conduction band E_c. The theoretical derivations of thermionic emission-assisted conduction process are exhaustively narrated as follows. The detailed derivations can be found in [19].

The charge distributions in the DSB region are according to Figure 2.13 [19]:

$$\rho(x) = e\sum_{\nu=0}^{n} N_\nu[\Theta(x + d_{\mathrm{l}\nu}) - \Theta(x - d_{\mathrm{r}\nu})] - Q_\mathrm{i}\delta(x) \tag{2.8}$$

We just consider the interface-state density N_d, then Eq. (2.8) can be simplified as

$$\rho(x) = eN_\mathrm{d}[\Theta(x + d_\mathrm{l}) - \Theta(x - d_\mathrm{r})] - Q_\mathrm{i}\delta(x) \tag{2.9}$$

where $\Theta(x)$ and $\delta(x)$ are Heaviside step function and Dirac function, and d_l and d_r are the widths of the left and right depletion layers, respectively. By imposing

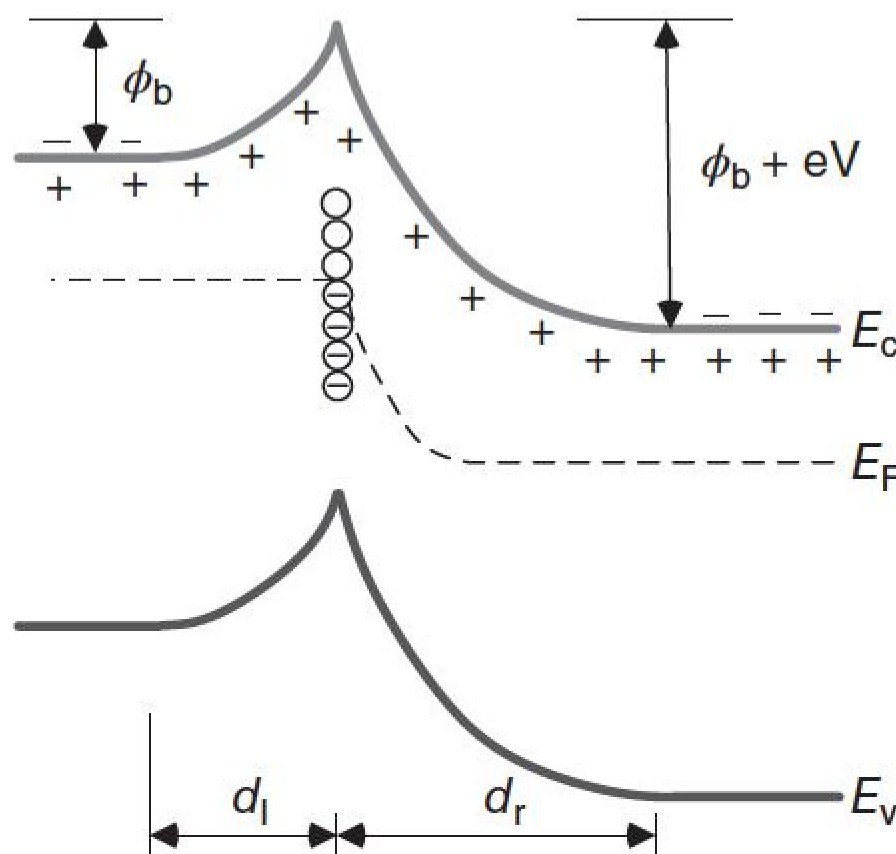


Figure 2.12 Effect of applied voltage on the band structure at a grain boundary. Source: Clarke 1999 [25]. Redrawn with permission from John Wiley & Sons.

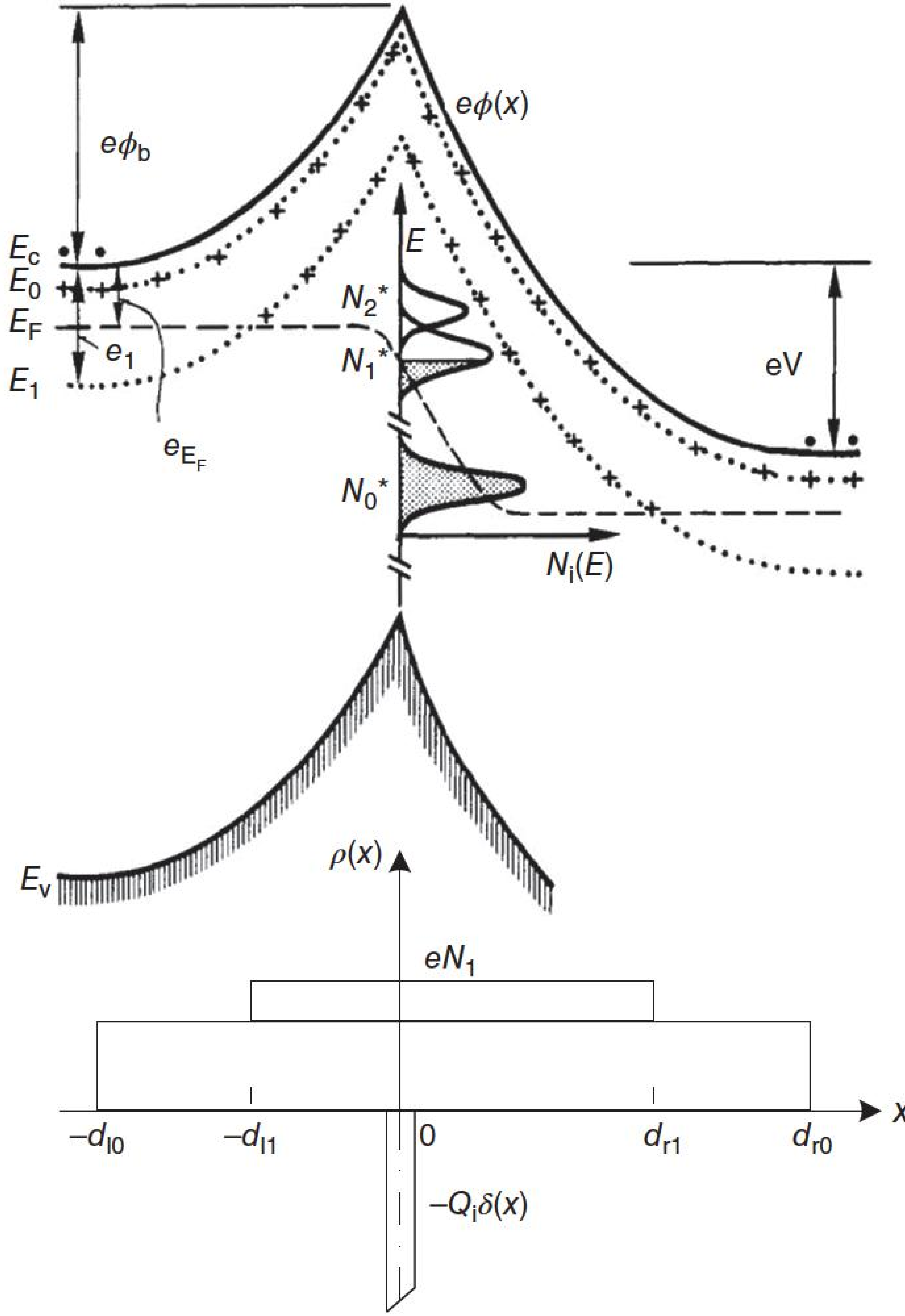


Figure 2.13 The effect of applied voltage on the energy band deformation at a grain boundary. The right side is positively biased, whereas the left side is oppositely negative. Source: Greuter and Blatter 1990 [19]. Reproduced with permission of IOP.

the boundary conditions $\phi(-\infty) = \phi(-d_\mathrm{l}) = 0$ and $\phi(+\infty) = \phi(+d_\mathrm{r}) = -V$ on Poisson's equation, the DSB configuration is obtained:

$$\begin{cases} \dfrac{eN_\mathrm{d}}{2\varepsilon_0\varepsilon}(x+d_\mathrm{l})^2 & -d_\mathrm{l} \le x \le 0 \\ \dfrac{eN_\mathrm{d}}{2\varepsilon_0\varepsilon}(x-d_\mathrm{r})^2 - V & 0 \le x \le d_\mathrm{r} \end{cases} \tag{2.10}$$

In Eq. (2.10), the width d_l and d_r can be determined by the conditions $\phi(0^-) = \phi(0^+) = \phi_\mathrm{b}$ and $\phi'(0^-) - \phi'(0^+) = Q_\mathrm{i}/\varepsilon_0\varepsilon_\mathrm{r}$ as:

$$d_\mathrm{l} = \frac{Q_\mathrm{i}}{2eN_\mathrm{d}}\left(1 - \frac{V}{V_\mathrm{c}}\right), \quad d_\mathrm{r} = \frac{Q_\mathrm{i}}{2eN_\mathrm{d}}\left(1 + \frac{V}{V_\mathrm{c}}\right) \tag{2.11}$$

And the result of barrier height turns out to be quite simple:

$$\phi_b = \frac{V_c}{4}\left(1 - \frac{V}{V_c}\right)^2, \quad V \leq V_c \tag{2.12}$$

where the parameter V_c is the critical voltage, $V_c = Q_i^2/2\varepsilon_0\varepsilon_r eN_d$. When a voltage is applied, the barrier height lowers accordingly, and the height vanishes when $V \to V_c$.

Then, the remaining free parameter in the barrier geometry is the voltage-dependent interfacial charge Q_i. This is determined by the density of state (DOS) $N(E)$ with respect to the valence band. The electron traps are filled up to the quasi-Fermi level E_{Fi} of the interface:

$$Q_i = e\int_{E_{Fi}^n}^{\infty} N(E)f_i(E)\mathrm{d}E \tag{2.13}$$

where $f_i(E)$ is the Fermi–Dirac function as $f_i(E) = \frac{1}{1+e^{(E-E_{Fi})/k_BT}}$. Various types of DOS functions [17] can be adopted in the discussion, among which the simplest but effective one is the Dirac-type distribution with single interface level as $N(E) = N_i\delta(E - E_{Fi})$. The integral in Eq. (2.13) proceeds from the Fermi level E_{Fi}^n of neutral interface [15, 17]. For zero-biased condition, the Fermi level is constant throughout the individual grain boundary structure, i.e. $E_{Fi} = E_F$, whereas for $V > 0$, the quasi-Fermi level at the interface is shifted with respect to the bulk Fermi level:

$$\Delta E_F = E_F - E_{Fi}^n = k_BT \ln\frac{2}{1 + e^{-eV/k_BT}} \tag{2.14}$$

This shift is closely related to the detailed balance condition for the interface, i.e. number of electrons trapped and emitted by the interface must be equal [17]. An example of the calculated relationships of barrier height and interface charge versus applied voltage is shown in Figure 2.14, where the DOS with single interface level is considered.

The relationship between current density and externally applied voltage can be described as [17]

$$J = A^*T^2 \exp[-(e\phi_b(V) + E_C - E_F)/k_BT][1 - \exp(-eV/k_BT)] \tag{2.15}$$

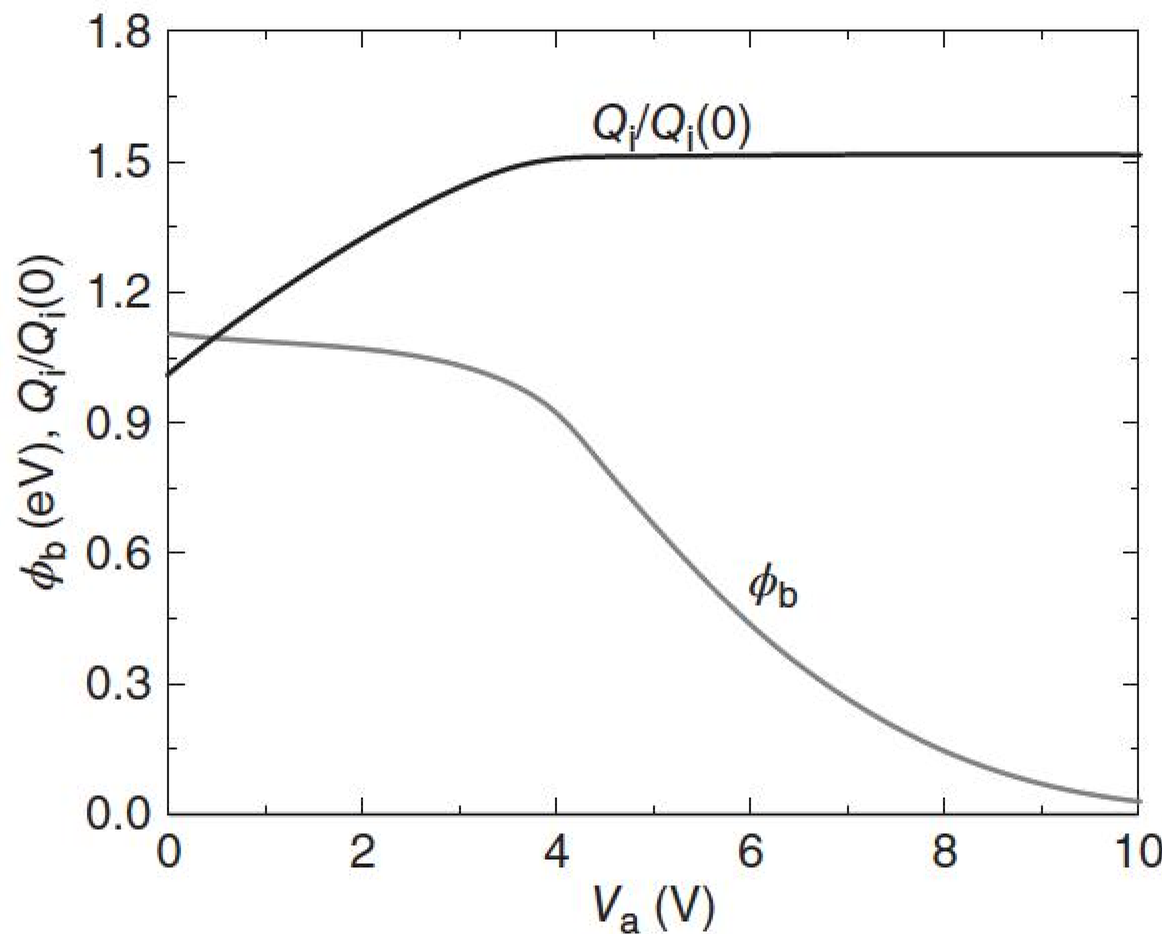


Figure 2.14 Barrier height ϕ_b and interface charge Q_i versus applied voltage V_a. Source: Adapted from Blatter and Greuter 1986 [17].

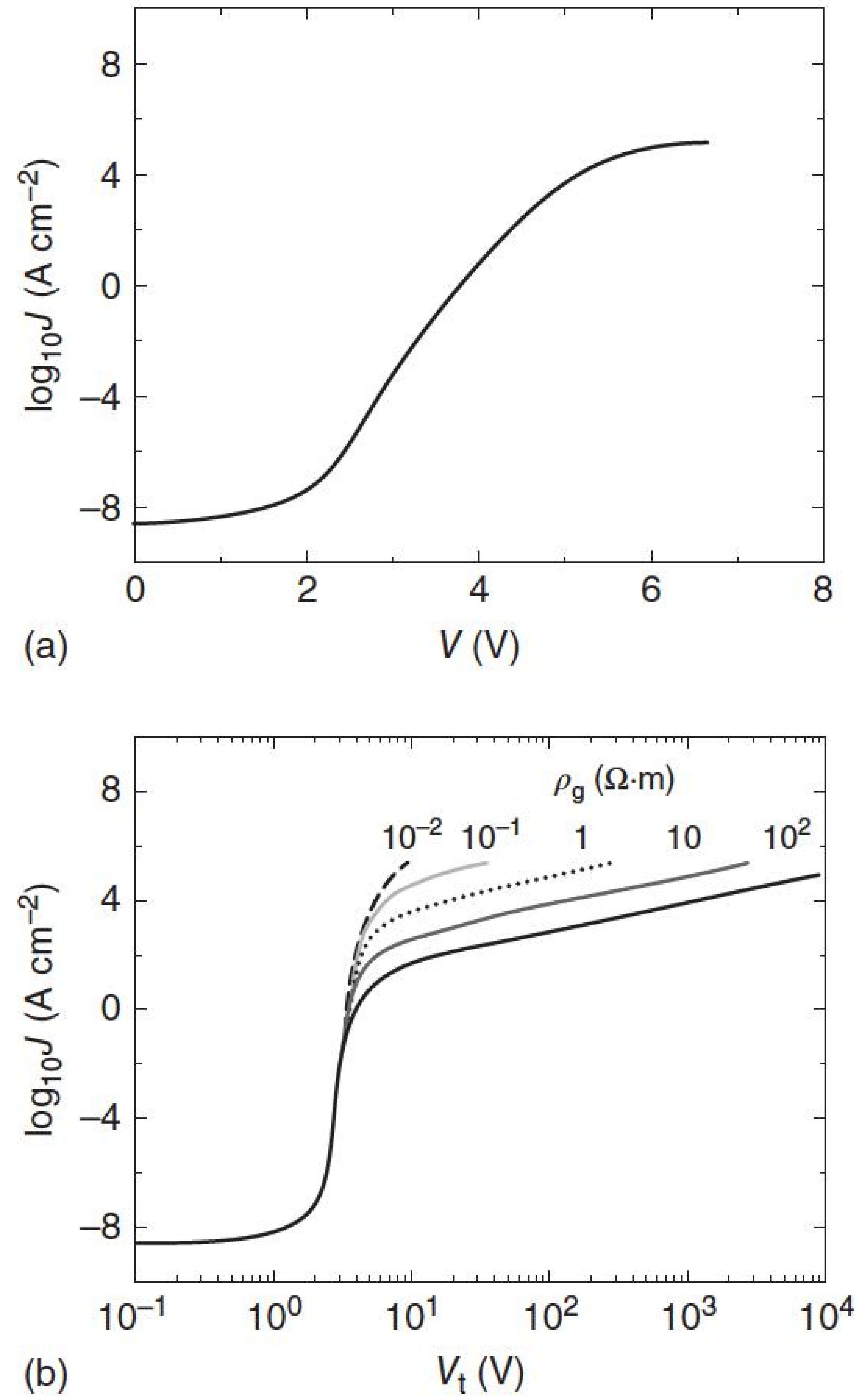


Figure 2.15 The effect of grain resistivity on the *I*–*V* characteristics. (a) Without considering grain resistivity; (b) considering the grain resistivity.

where A^* is the Richardson constant. In effect, the voltage V employed above is the one across the barrier at the grain boundary, V_{gb}, and if the resistances of the grains on both sides are further included, the current should be

$$J = (V_t - V)/\rho_g l_g \tag{2.16}$$

where V_t is the total voltage applied on the grains and grain boundary, ρ_g is the resistivity of the grain, and l_g is the geometry of the grain. The effect of grain resistivity on the I–V characteristics is demonstrated in Figure 2.15.

2.4.2 Minority Carrier Generation Process

This nonequilibrium process, i.e. the minority carrier generation by "hot" electron in the depletion region, is demonstrated in Figure 2.16 [25]. Under a very high electric field, some of the electrons crossing the barrier have gained sufficient kinetic energy that they can produce minority carriers by influencing the ionization of the valence states and acceptor states within the depletion region. The minority carriers, i.e. holes, diffuse back to the grain boundary under the influence of the electrostatic field at the boundary and compensate part of the trapped negative charge, lowering the potential barrier and thereby increasing the electron flow across the barrier. This impact ionization "feedback" process provides

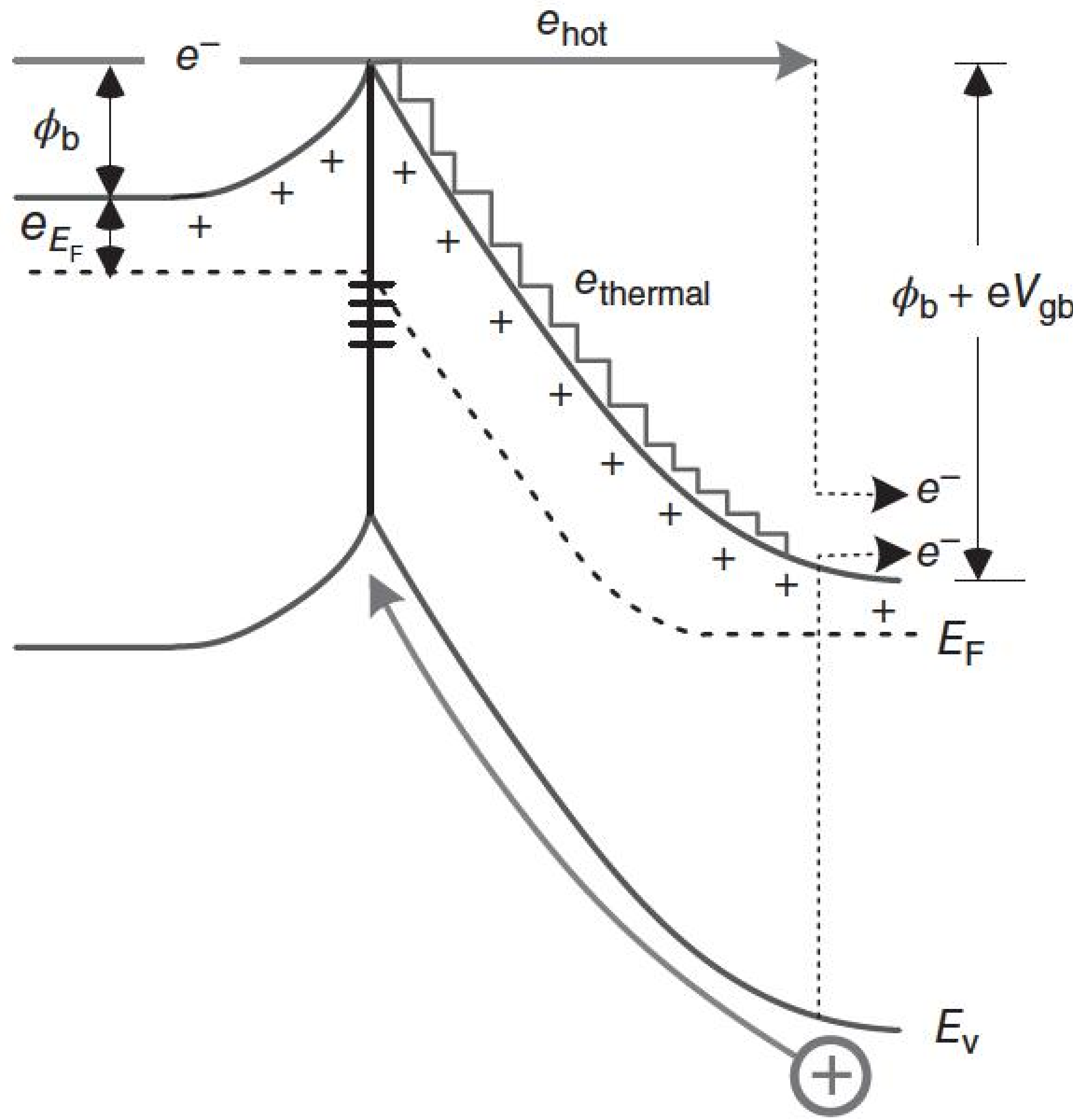


Figure 2.16 Energy band diagram for a varistor grain boundary under an applied voltage V_{gb}, illustrating the process of interband impact ionization and the generation of holes. $e_{thermal}$ refers to the thermionic emission and e_{hot} refers to hot electrons. Source: Adapted from Clarke 1999 [25].

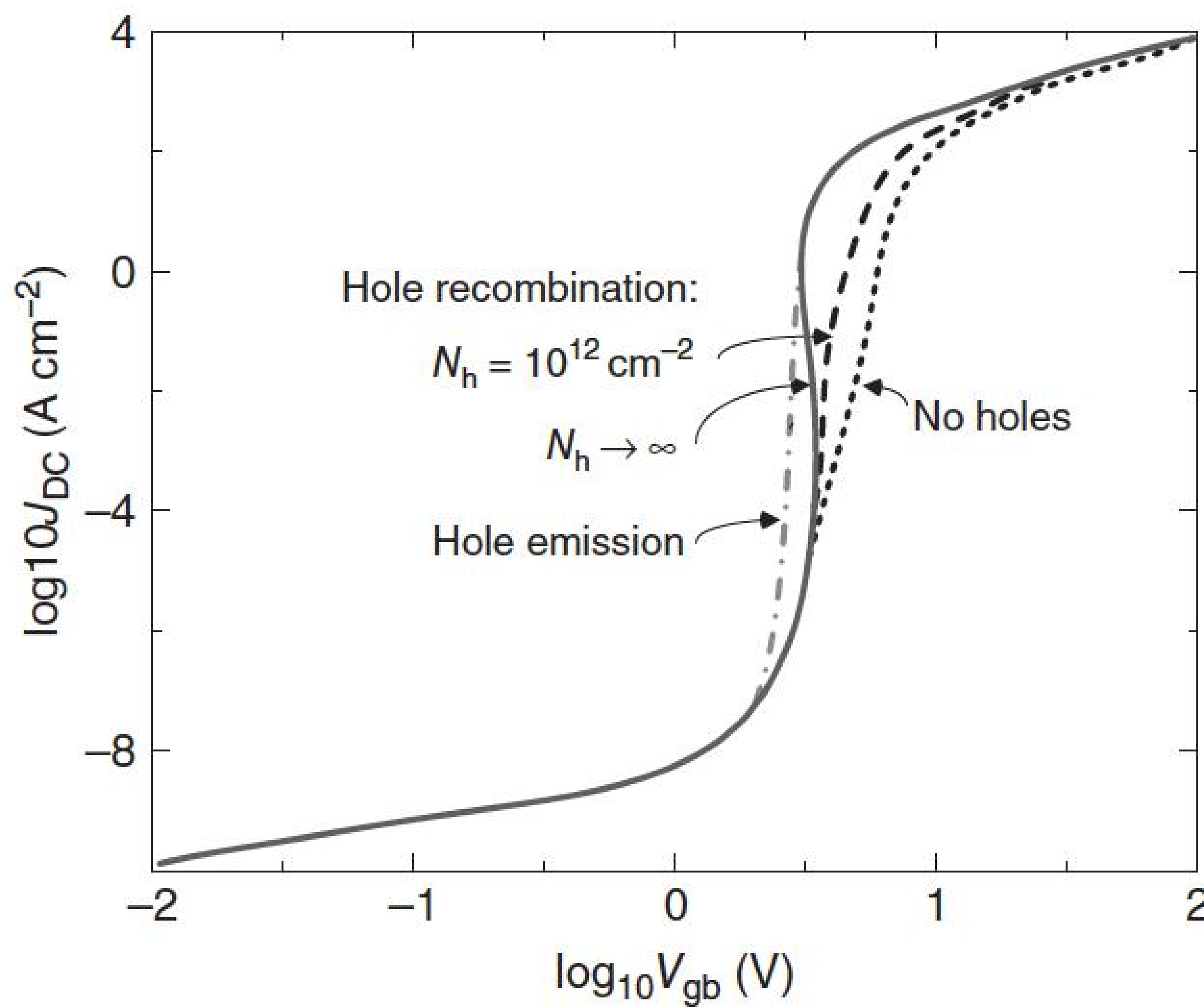


Figure 2.17 The relationship between DC current density J_{DC} versus applied voltage per grain boundary V_{gb}. Source: Adapted from Blatter and Greuter 1986 [18].

a high degree of nonlinearity in the electron transport across the grain boundary and results in very large nonlinearity coefficients as shown in Figure 2.17 [18]. A more detailed description of this process and the theory of varistor behavior incorporating minority carriers can be found in references presented by Blatter and colleagues [16, 18]. This minority carrier generation process has obtained experimental support as the observation of recombination band gap luminescence from the grain boundary regions by Pike et al. [47]; the electroluminescence phenomenon occurs when the applied voltage exceeds the breakdown field and that the luminescence intensity is proportional to the current squared.

The above thermionic emission conduction model across the DSB incorporating the effect of minority carriers has one obvious limitation that it merely attempts to account for the electron transport across an individual grain boundary. However, varistors are polycrystalline materials containing a huge

number of grains and grain boundaries, and each of the boundaries may have varying nonlinear characteristics. This necessarily leads to percolative flow of current through the varistor bulk [25]. Because varistors are also nonlinear, the voltage across an individual grain boundary is not linearly dependent on the voltage applied to the varistor as a whole. These multigrain effects and their consequences are discussed in the later chapter describing the Voronoi networks.

2.4.3 The Bypass Effect Model

Levinson and Philipp found that the current–voltage characteristics in ZnO varistors are influenced by leakage paths acting in parallel with the Schottky barrier-controlled current flow; the evidence for this hypothesis is derived from the observed low current action energy and leakage in "primitive" varistors containing only Bi as an additive [46]. Actually, in addition to the DSB at the grain boundary that acts as the main nonlinear conduction channel, there are thicker phases between grains, which always have the high-resistance characteristics to form the low current leakage channels. Thus, when considering the multigrain effect in the simulation of properties of the whole varistor bulk, the DSB further incorporating the impact of thicker phases nearby should be regarded as a basic unit. Based on this, Eda has proposed the bypass effect model [8], which forms the basis for the numerical simulation on conduction mechanism of ZnO varistors and will be further introduced in Chapter 5.

2.5 Dielectric Characteristics of a ZnO Varistor

As the ZnO varistor is widely utilized in AC power transmission system as a surge arrester or in low-voltage power source as a surge protection device (SPD), it becomes necessary to gain a basic insight into the dielectric behaviors of ZnO varistor. We start our discussion with Maxwell's equation when AC voltage with frequency f is applied on the varistor bulk:

$$I = \sigma_0 E + \partial D/\partial t \tag{2.17}$$

where σ_0 is the direct current conductivity and $\partial D/\partial t$ is the displacement current. By taking the Fourier transform of both sides of Eq. (2.17), we obtain

$$\begin{aligned} I(\omega) &= \sigma_0 E(\omega) + i\omega\varepsilon(\omega)E(\omega) \\ &= \sigma_0 E(\omega) + i\omega[\varepsilon'(\omega) - i\varepsilon''(\omega)]E(\omega) \\ &= [\sigma_0 + \omega\varepsilon''(\omega) + i\omega\varepsilon'(\omega)]E(\omega) \end{aligned} \tag{2.18}$$

where we define the frequency-dependent permittivity as $\varepsilon(\omega)$=$\varepsilon''(\omega)$-$i\varepsilon'(\omega)$ and ω is the angular frequency. It is significant to note that the real component of permittivity $\varepsilon'(\omega)$ is in quadrature with the driving field and thus does not contribute to the power loss, which is the permittivity we may ordinarily refer to. Conversely, the imaginary component is in phase with the driving force, representing the power loss together with the conductivity, and thus is referred as dielectric loss.

It is critical for readers to realize that both the real and imaginary components of permittivity show dispersion phenomena, i.e. varying with frequency, whereas the single-valued dielectric permittivity that electrical engineers frequently used is the one measured at certain frequency point, for instance, 1 kHz, for $\varepsilon'(\omega)$. In effect, this dispersion is an essential property of all dielectric materials.

With the aid of popular frequency domain techniques, for instance, the broadband dielectric spectroscopy, it is convenient to obtain the variation spectrum of the complex permittivity (susceptibility, capacitance, admittance, etc.) with frequency, applied voltage, ambient temperature, and so forth. Then, it is essential to decide the appropriate representation for fully exposing the information contained in the spectrum, for example, the basic plot of $\varepsilon'(\omega)$ or $\varepsilon''(\omega)$ versus frequency, or the cole–cole plot [48] that is frequently used to estimate the grain and grain boundary impedances. Sincerely, we recommend the log–log representation instead of semi-log or linear representations.

In this section, we prefer to pay asymmetrical emphasis to the experimental characterization of the dielectric behavior in the ZnO varistor, for instance, the introduction of two experimental methods probing the underlying mechanisms in the ZnO varistor based on dielectric responses, while to spend certain space in describing the theoretical treatment of dielectric behavior in the ZnO varistor for a better understanding.

2.5.1 Explanation to Dielectric Properties of a ZnO Varistor

Blatter and his colleagues [18, 19] have investigated and calculated the steady-state and AC (small-signal) properties for the majority of carrier transport through a grain boundary with DSB. The AC small-signal capacitance is governed by both the finite response time of the interface and the deep bulk traps. Three cases of DOS for interface were considered: single level (without deep bulk defects), Gaussian, and rectangular types [18]. The model with electron–hole recombination at the interface is used, where the barrier is dominated by the hole charge dynamics.

They have found a negative small-signal capacitance at a large bias by calculation. At a moderate bias, where the electron interface states play the dominant role, a lowering of the barrier is followed by an increased electron trapping, as empty electron traps are shifted below the Fermi level. This stabilizing charge accumulation lags behind in time, thereby giving rise to a capacitive component in the modulated over-barrier current. As the bias is increased, the interface states for the electrons are filled, and the stabilization effect dies away as the electron charge remains at its maximum value – the capacitance decreases. As the barrier is lowered further, holes are created in the depletion region and a positive interface charge is built up. A lowering of the barrier is followed by an increase in the hole production and therefore in the interface charge. The barrier is destabilized, and the capacitance goes in the opposite direction, shown in Figure 2.18a. The calculation result is confirmed with the relative experiment of the ZnO varistor.

Blatter's calculation can also describe the frequency dependence of the capacitance, as shown in Figure 2.18b. At low frequencies, the time-delayed charging

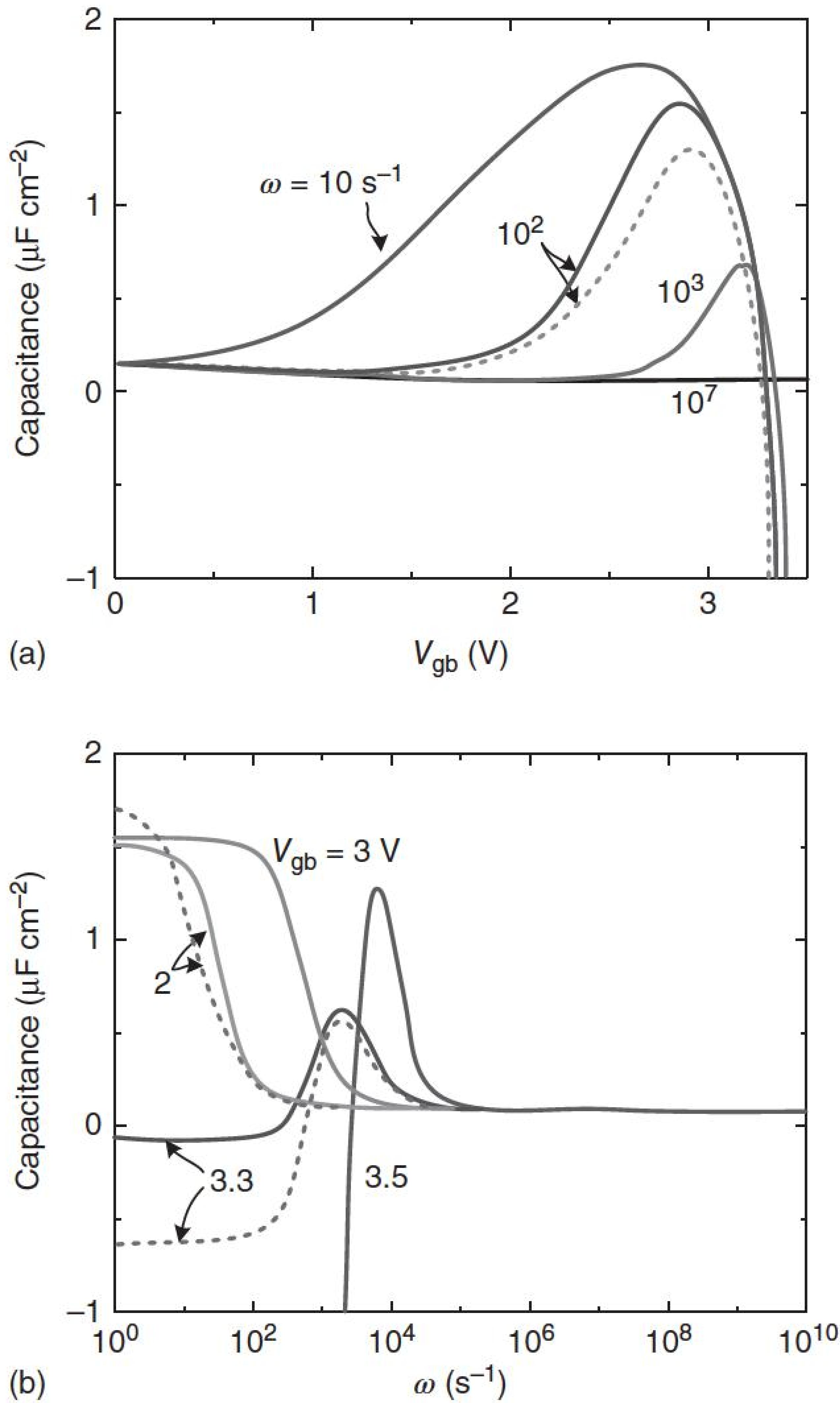


Figure 2.18 (a) Theoretical capacitance variations with bias voltage per grain boundary, V_{gb}, a continuous (Gaussian) interface density of states (DOS) was taken, and perfect relaxation among the electron traps were considered. The capacitance becomes negative at a bias V_{gb} of ~3.3 V considerably lower than the voltage of ~3.6 V, needed to suppress the barrier. For comparison, the result for the same DOS, but treating the electrons at the interface as completely localized is shown as dashed lines. (b) Theoretical capacitance dependence of the frequency; the dashed lines are the comparison to the model with localized states. This is the simplest case of a single-level interface DOS for the electronic interface traps and no deep bulk defects. Source: Adapted from Blatter and Greuter 1986 [18].

and discharging of the interface produces a large capacitance, which disappears when the interface cannot follow the signal any longer. At high bias, the hole dynamics dominates and the capacitance turns to negative values.

When deep bulk traps are further considered in the discussion, new resonance effects can be expected in the small-signal response of the grain boundary, owing to the finite response time of the deep states [17]. The presence of the deep bulk traps leads to a zero-bias dispersion in conductance and capacitance. On the

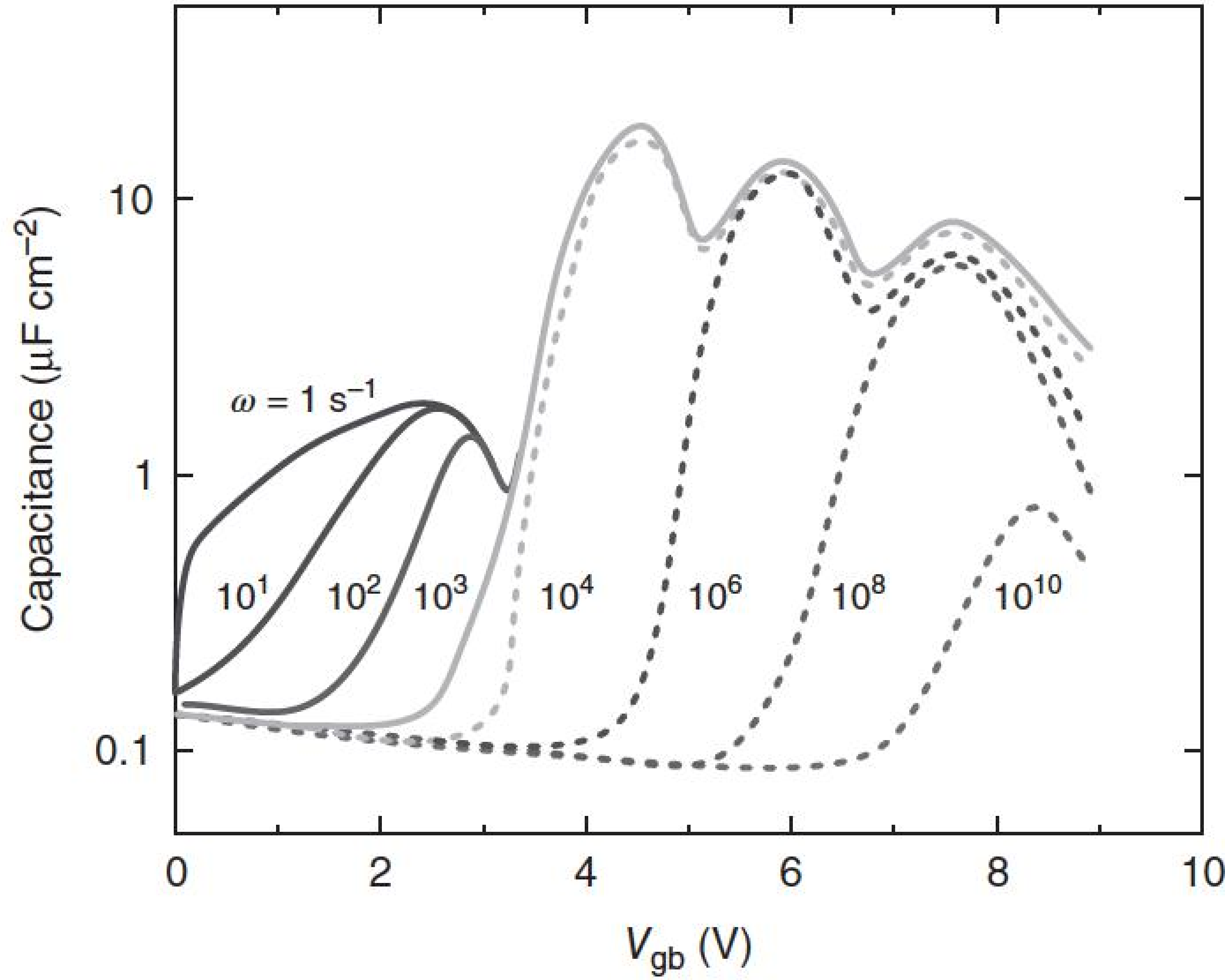


Figure 2.19 Capacitance C versus bias V_{gb} in the presence of deep bulk traps for a Gaussian DOS. Source: Blatter and Greuter 1986 [17]. Reproduced with permission of AIP.

other hand, for moderate bias, the capacitance strongly depends on the relaxation properties of the interface. Therefore, the effects due to the deep bulk traps and the interface states can be well distinguished and separately analyzed through a study of $G(\omega, V, T)$ and $C(\omega, V, T)$, respectively.

Figure 2.19 is an illustration of the admittance for a grain boundary characterized by three deep bulk traps of moderate density and a Gaussian DOS for the interface [17]. At moderate frequencies, the curves are characterized by four well-separated resonances. The first, at lower bias values, is due to the interface. The three peaks at 4.5, 6.0, and 7.6 V indicate the neutralization of the deep traps as they disappear below the Fermi level. With the Fermi level parallels to the deep trap level, a lot of charge is dynamically captured and released at these bias values, leading to large peaks in the capacitance. As all deep traps are neutralized at high bias, the capacitance returns to its high-frequency value. Moreover, the interface resonance at moderate bias shows a strong dispersion. The interface relaxation time decreases with increasing bias. Therefore, the resonance shifts to higher bias values with increasing frequency. Because of the limit of length, more discussion and illustrations can be found in Ref. [17].

2.5.2 Effect of Interfacial Charge Relaxation on Conducting Behavior of ZnO Varistors Under Time-Varying Electric Fields

The relaxation effect of the grain boundary has considerable effect on the response of ZnO varistor to time-varying signals [49, 50]. Blatter and Greuter (hereafter denoted as BG) introduced in Section 2.5.1 theoretically derived a nonlinear conducting model of ZnO grain boundaries under the DC voltage with a small AC signal, which reveals that the time delay process of interfacial charge leads to a capacitance effect [17, 18]. Recently, Yang et al. [51] proposed the conducting model of ZnO grain boundaries considering the relaxation

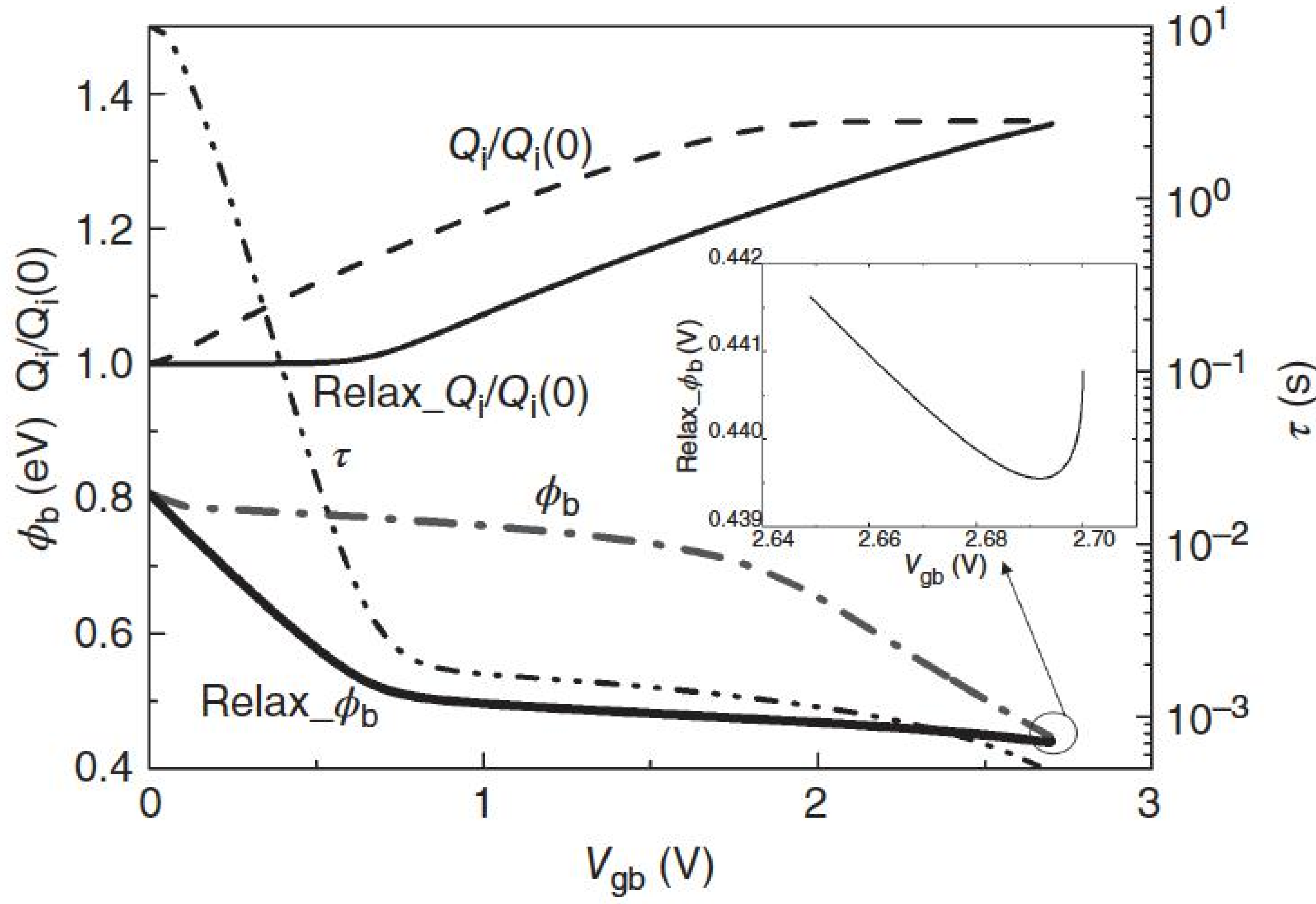


Figure 2.20 Simulated interfacial charge in steady state ($Q_i/Q_i(0)$) and in AC field (Relax_$Q_i/Q_i(0)$), and barrier height in steady state (ϕ_b) and in AC field (Relax_ϕ_b), and the time constant τ in the AC field as a function of the applied bias V_{gb}, where $Q_i(0)$ is the interfacial charge when no bias is applied. Source: Yang et al. 2017 [51]. Reproduced with permission of AIP.

process of the interfacial charge under pure AC fields; this model was validated by experimental results.

In the model, the interfacial charge under steady-state $Q_{i\text{-steady}}$ can be calculated by Eq. (2.13). Based on BG's model, the $\phi_b(V)$ and $Q_i(V)$ curves are calculated and shown in Figure 2.20 as dashed lines, the increase in Q_i partially compensates the reduction in ϕ_b and prevents it from a sharp decay. When all the interface states are filled, Q_i becomes saturated and ϕ_b decays rapidly.

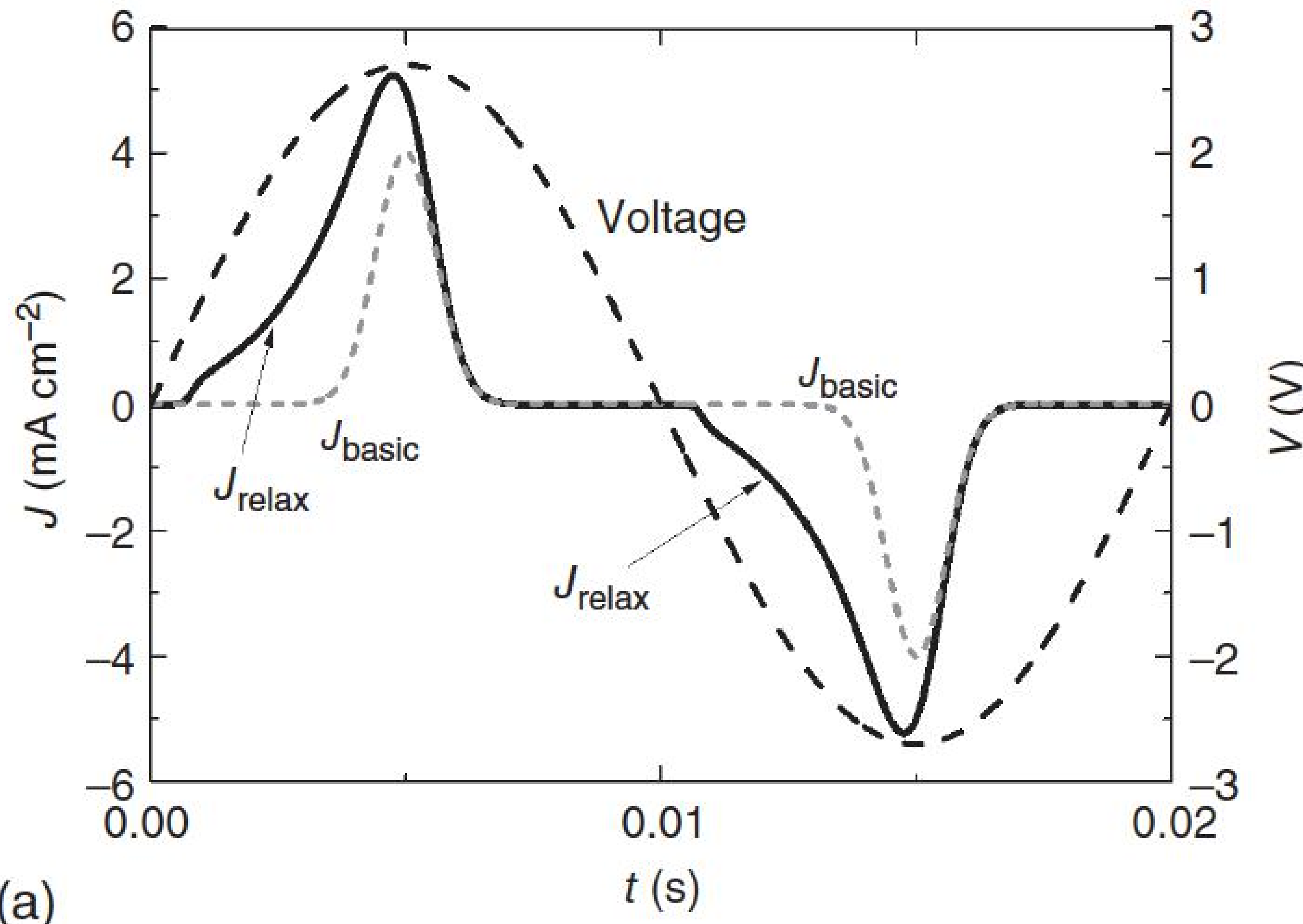
In time-dependent fields, the relationship between V_{gb} and Q_i is different as the filling-in of the interface state cannot be instantaneous, which means that a relaxation process of Q_i exists and Q_i lags behind V_{gb}. The dynamic behavior of Q_i depends on the charge emission current J_{em} and the charge trap current J_t. Their expressions may be quite different under pure AC fields as V and Q_i change considerably with time. As the variation of Q_i is a process of interfacial charging, this complex process can be simplified into a charging process by a circuit model. The charging capacitance for the interface is $C_i = \varepsilon S/d$, where ε, S, and d are the permittivity, the cross section area, and the thickness of the grain boundary layer (about 10 nm [52]), respectively. The resistance in this charging circuit is the effective resistance of the Schottky barrier $R_{eff} = V_{gb}/I = V_{gb}/(JS)$, where J is the current density that flows through the barrier. Thus, the time constant τ for this charging process is $\tau = R_{eff}C_i = \varepsilon V_{gb}/(Jd)$. Therefore, the relaxation process can be described by

$$Q_i(t) = Q_{i\text{-steady}} - [Q_{i\text{-steady}} - Q_i(t - \Delta t)]e^{-\Delta t/\tau} \tag{2.19}$$

where $Q_i(t)$ is the momentary value of the interfacial charge under time-dependent fields and $Q_{i\text{-steady}}$ is the steady-state value corresponding to the momentary voltage.

To take into account the relaxation process, the responsive conduction current density of a single ZnO grain boundary under a 2.7 V AC voltage is shown in Figure 2.21a, where J_{basic} is the current density calculated by the basic version of GB's model and J_{relax} is the conduction current density calculated by the adapted equation considering the relaxation process. Figure 2.21a shows that the relaxation process leads to two main effects:

(a) J_{relax} is considerably higher than J_{basic} as the applied voltage V increases, but J_{relax} is close to J_{basic} as V decreases. This can be explained by the $Q_i(V)$, $\phi_b(V)$ curves under AC fields, shown in Figure 2.20 as solid lines, corresponding to the period of $0 < t < 0.005$ s in Figure 2.21a. Figure 2.20 shows that the Q_i and ϕ_b lag behind the steady state because of the relaxation process. When V is low, τ is relatively large, and Q_i can hardly follow V. Thus, the discrepancy



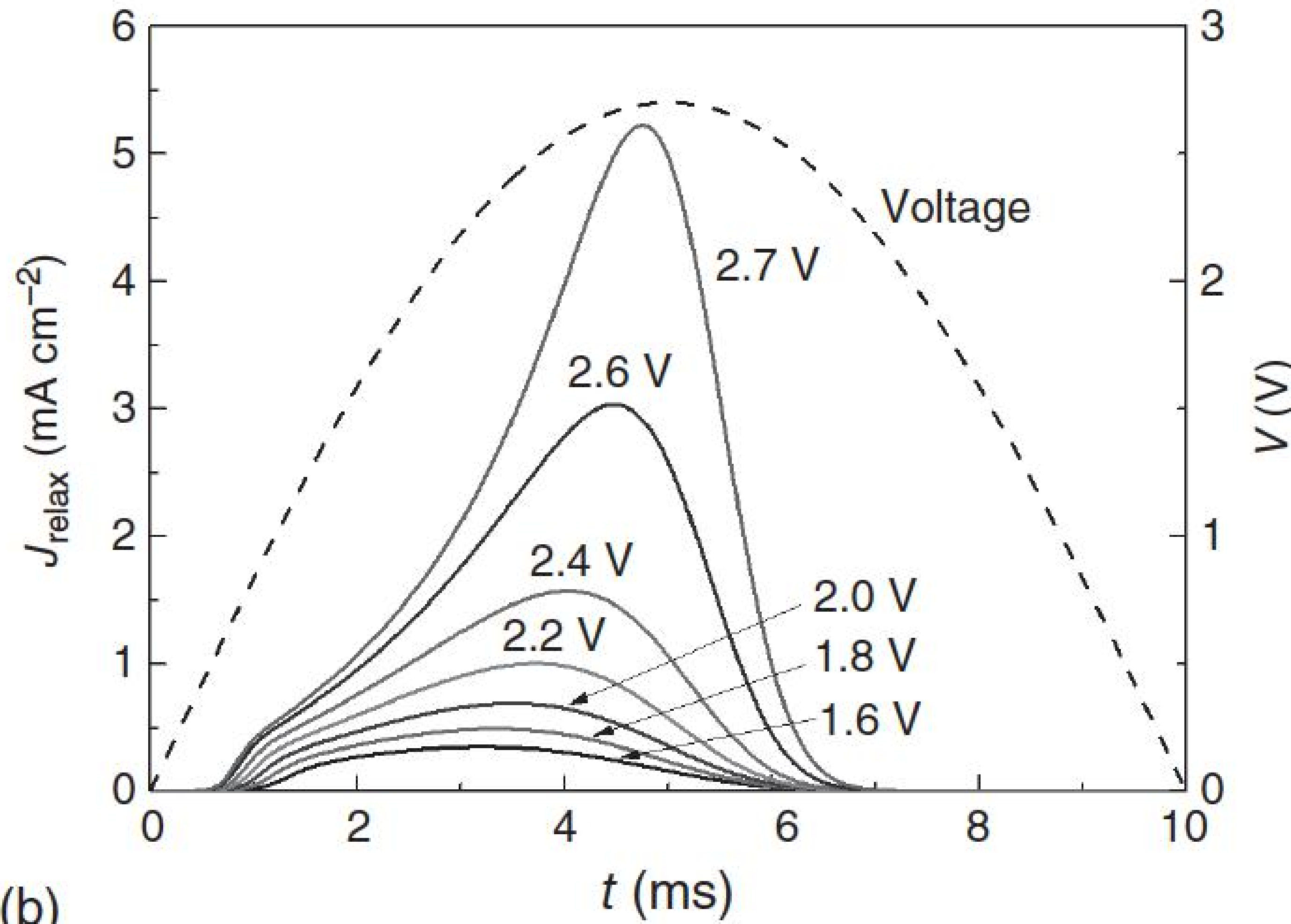


Figure 2.21 (a) Calculated current density J_{basic} in the steady-state and conduction current J_{relax} under AC field; (b) calculated conduction current density under different applied voltages. Source: Yang et al. 2017 [51]. Reproduced with permission of AIP.

between $Q_i(t)$ and $Q_{i\text{-steady}}$ is large. When V is high enough, τ becomes very small. Thus, Q_i is almost synchronous to V and gradually keeps up with the steady state. In steady state, ϕ_b decays slowly at first because of the compensation effect of Q_i. Under AC fields and when Q_i cannot keep pace with V, its compensation effect is much weaker and ϕ_b decays rapidly with the increase in V. Thus, lower ϕ_b leads to a much higher J_{relax} than J_{basic}. As V decreases from peak to zero, τ is initially very small and then gradually increases. Thus, Q_i can almost follow V at first. Then, when Q_i begins to lag behind, J_{relax} becomes very small. Therefore, despite of the relaxation process, J_{relax} seems close to J_{basic} as V decreases.

(b) Figure 2.21a shows that the peak value of J_{relax} shifts in advance of the applied voltage V because of the relaxation process. The reason is that when V nearly reaches its peak value, Q_i is not saturated and keeps increasing, as shown in Figure 2.20. At this time, the effect of Q_i overweighs the increase in V, which leads to the increase in ϕ_b. Therefore, J_{relax} reduces with the increase in ϕ_b even before V reaches its peak value and J_{relax} exhibits a peak value in advance of the applied voltage.

Both the above two effects result in a phase shift of the conduction current density in advance of the applied voltage, which gives rise to a capacitive effect. Figure 2.21b shows the calculated J_{relax} in half period under AC voltages with the amplitude from 1.6 to 2.7 V. When the amplitude is lower, J_{relax} has even greater phase shift. This is because lower voltage means larger τ; thus, Q_i lags more behind V. For instance, when the amplitude is 2.7 V, Q_i can almost follow V and reach steady state when V is large enough, as shown in Figure 2.20; however, when the amplitude is 1.6 V, the time delay of Q_i is quite large even when V reaches its peak value. As mentioned above, the relaxation process of Q_i results in a capacitive effect. The larger the time delay, the greater J shifts in advance of V. Thus, lower voltage amplitude in Figure 2.21b corresponds to larger phase shift of the conduction current.

The capacitive current I_{cap} can be easily separated from the total current, and an effective capacitance $C_{eff}(V)$ can be calculated by Eq. (2.20) with a hysteresis loop of $Q(V)$ [53]:

$$C_{eff}(t) = Q_{eff}(t)/V(t) = \left(\int_0^t I_{cap}(\tau)\mathrm{d}\tau\right) \Big/ V(t) \tag{2.20}$$

where Q_{eff} is the total effective polarization charge in the material. Figure 2.22 shows $C(V)/C_0$ curve of a ZnO varistor and the simulated result for a single grain boundary calculated by Eq. (2.20) [51]. Both the simulation and measured curves show that under pure AC fields, the capacitive effect of the conduction current makes the effective capacitance increase with the applied voltage [51]. Figure 2.22 also shows the C_{eff}–V characteristics under the ramped DC voltage with small-signal AC bias and under the ramped pure AC voltage. The C_{eff}–V characteristics under various voltage sources are different, which resulted from different effects of the relaxation process.

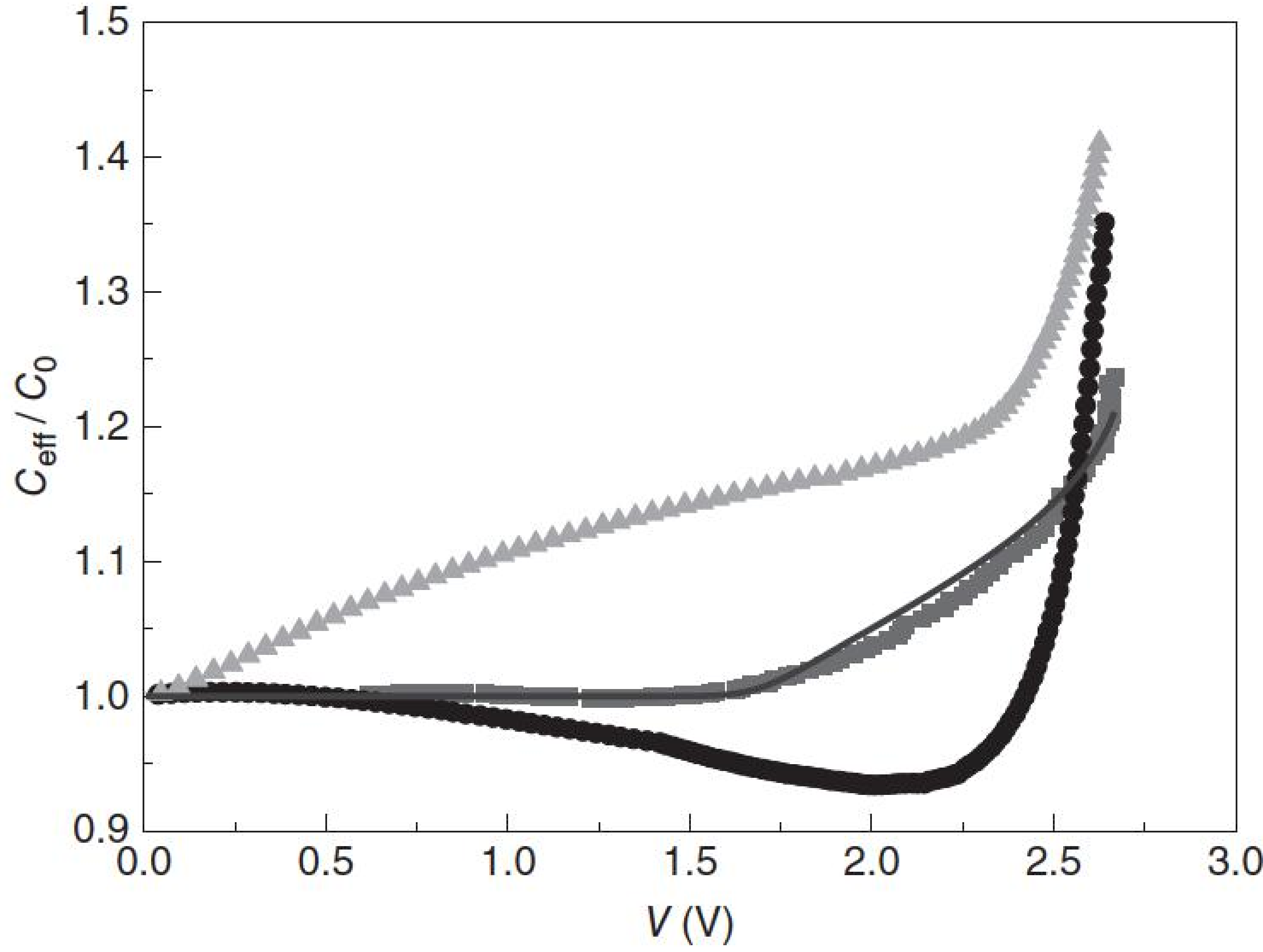


Figure 2.22 Measured effective capacitance C_{eff} of ZnO varistors as a function of the applied voltage V. • curve was measured under DC voltages with small AC bias, $V = 0.1–2.6$ V(DC) + 4.4 mV(AC); ▲ curve was measured under ramped AC voltage; ■ single AC curve was measured under pure AC voltages and acquired by Eq. (2.20); — single AC curve was the simulated curve under pure AC voltage acquired by Eq. (2.20). C_0 is the capacitance when no bias is applied, which is about 1.8 nF for the measurement result. Source: Yang et al. 2017 [51]. Reproduced with permission of AIP.

This enhancement effect of the effective capacitance provides a reasonable explanation to the so-called nonlinear permittivity of field-grading materials reported in recent literatures [53–55].

2.5.3 Determination of Barrier Height and Related Parameters

The well interpretation of the dielectric behavior in a ZnO varistor can directly contribute to the experimental determination of parameters of DSB, e.g. barrier height, donor density, density of interfacial state, and so forth, which in turn promotes the understanding in the underlying mechanism in a ZnO varistor. A classic $C–V$ method was introduced by Mukae et al. [56], which simply and effectively determines the barrier height and related parameters among numerous proposed experimental ways [57] probing the barrier configurations.

The capacitance per unit area of a grain boundary C is defined as [56]

$$\left(\frac{1}{C}-\frac{1}{2C_0}\right)^2=\frac{2}{e\varepsilon_0\varepsilon_r N_d}(\phi_b+V) \tag{2.21}$$

where $1/C_0 = 2\sqrt{2\phi_b/(e\varepsilon_0\varepsilon_r N_d)}$. By the approximation that ϕ_b is invariant (not voltage-dependent) when applied d voltage V is small (that renders the varistor in the prebreakdown regime), plotting the left term versus the voltage V according to Eq. (2.21) should yield a straight line as shown in Figure 2.23. Density of donor N_d and the barrier height ϕ_b can be estimated from the slop of the line and the

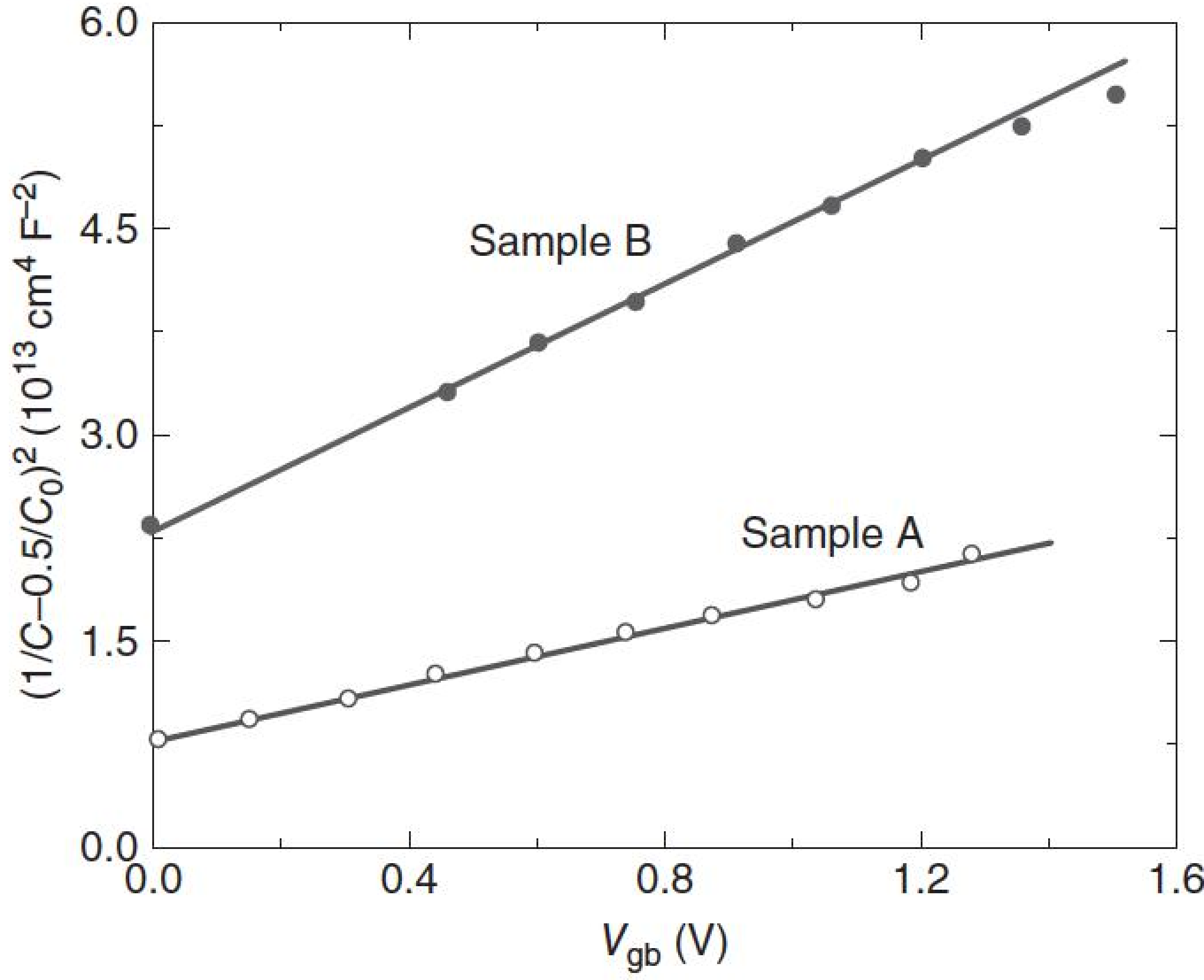


Figure 2.23 The example of $(1/C - 0.5/C_0)^2$ versus applied voltage plot. Source: Adapted from Mukae et al. 1979 [56]

intercept of the line on the voltage axis. The density of interfacial states N_s can also be derived according to Eq. (2.7).

It should be noted that for contemporarily popular dielectric spectroscopy device that can tune the frequency and be used for the implementation of this C–V method, a comparatively small AC voltage is simultaneously applied on the sample in addition to the DC voltage, and the applied AC voltage is in the frequency range from 10 to 100 kHz [57] to ensure the effectiveness of method.

2.5.4 Determination of Deep Donor Level in the ZnO Varistor

Even the underlying mechanism of the occurrence of loss peaks in the imaginary dielectric permittivity spectrum is quite limited, we can still abstract useful information and relate it to the deep donor energy levels to characterize the potential origins of loss peak with the aid of broadband dielectric spectroscopy. Among numerous methods probing the origin of loss peak, we select and present temperature spectroscopy [58].

It is known that the relaxation time τ_ν of a deep bulk donor is [19]

$$\tau_\nu = \frac{e}{2gA^* T^2 c_\nu} \exp\left(\frac{E_\nu}{k_B T}\right), \quad \nu = 1, 2, 3, \ldots \tag{2.22}$$

where A^* denotes the effective Richardson constant, which is 30 A cm^{-2} K^{-2} for ZnO; g is the spin degeneracy factor (usually equals to 0.5), and c_ν and E_ν are the capture cross section and energy level of the donor species below the conduction band edge, respectively [58]. As the relaxation time is temperature dependent, it is feasible to scan the relaxation time by varying the temperature at a fixed angular frequency of the applied field, ω. When the relaxation time is equal to the reciprocal of that angular frequency, a resonance in the conductance occurs, and a loss peak appears in the temperature spectrum accordingly [58]. Hence,

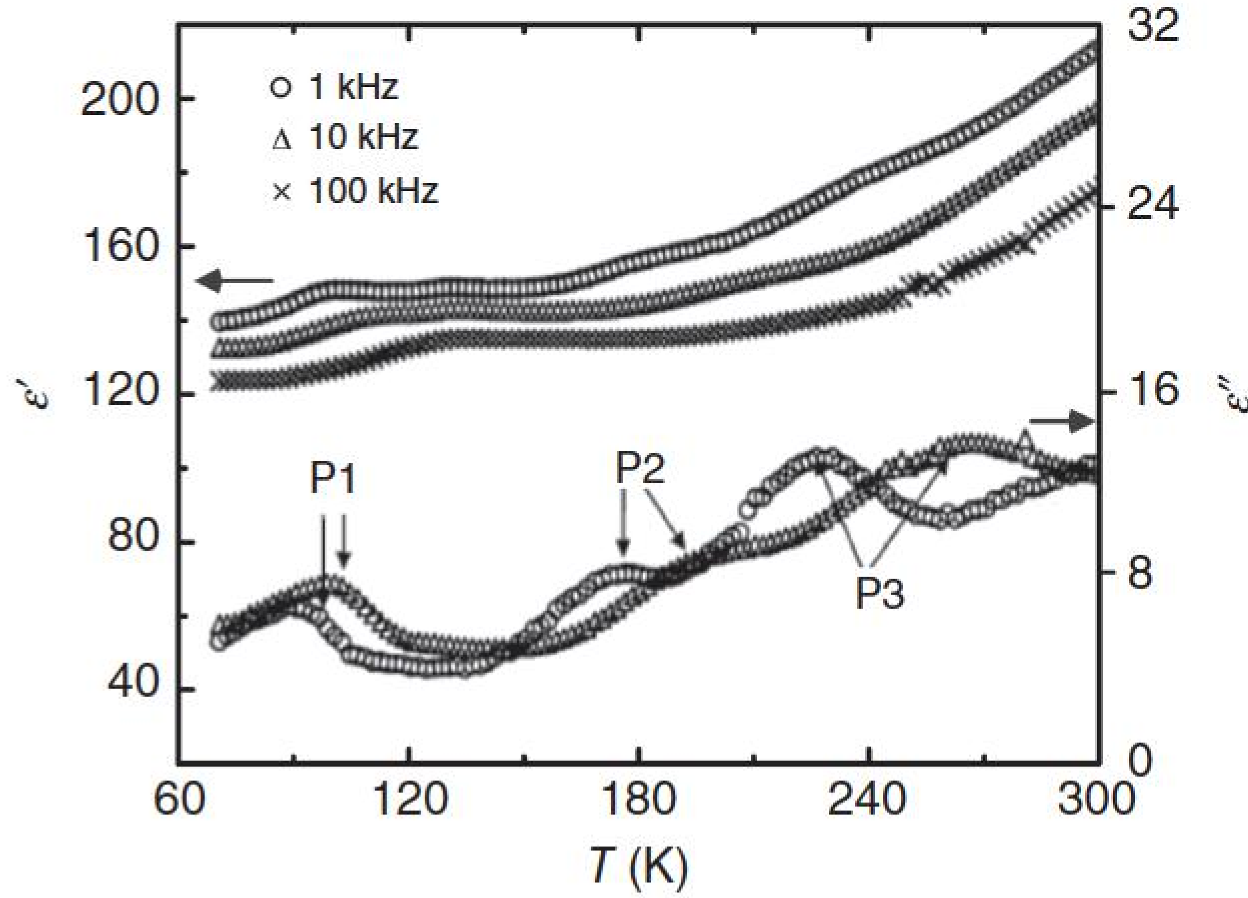


Figure 2.24 Temperature dependence of the real (ε') and imaginary (ε'') parts of the complex permittivity at several frequencies. Source: Alim et al. 2006 [58]. Reproduced with permission of John Wiley & Sons.

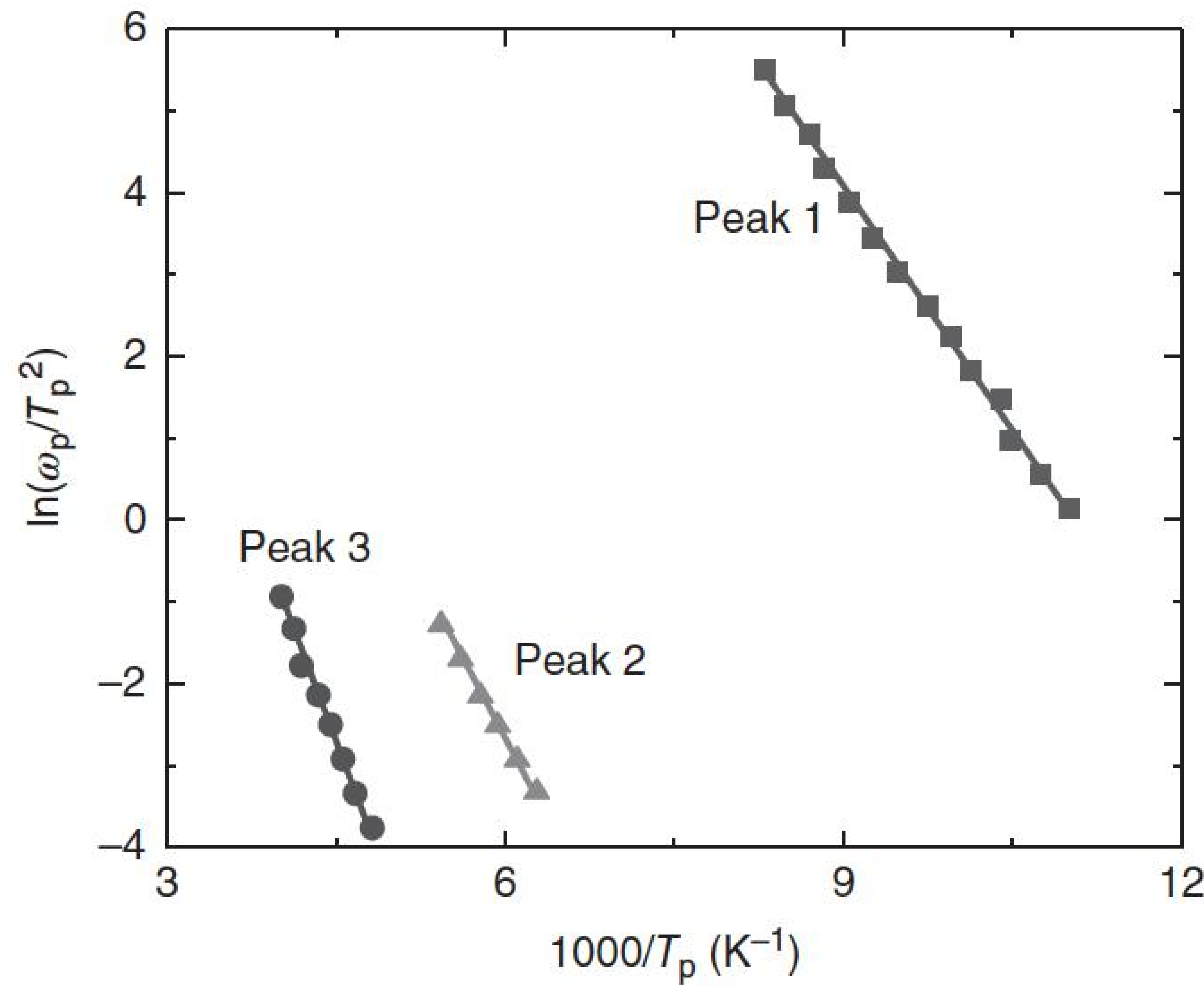


Figure 2.25 Plots of $\ln(\omega_p/T_p{}^2)$ versus $1/T_p$ for all the relaxation peaks observed in the sample. Source: Adapted from Alim et al. 2006 [58].

for each donor, a series of loss peaks will appear by measuring the admittance at various temperatures and frequencies, as demonstrated in Figure 2.24 [58].

From the spectrum, each peak temperature T_p can be obtained at the applied angular frequency ω_p. According to Eq. (2.22), a plot of $\ln(\omega_p/T_p^2)$ versus $1/T_p$ yields the slop proportional to the energy level of deep donor E_ν and the intercept proportional to the capture cross section c_ν with the example in Figure 2.25.

2.5.5 Determination of Grain and Grain Boundary Conductivity

Impedance spectroscopy can be used to study the electrical properties of grain boundaries, the intergranular electrical barriers, origin of resistance or capacitance, their dispersion with small-signal frequencies, and the role of defects within the regime of the electric field [58].

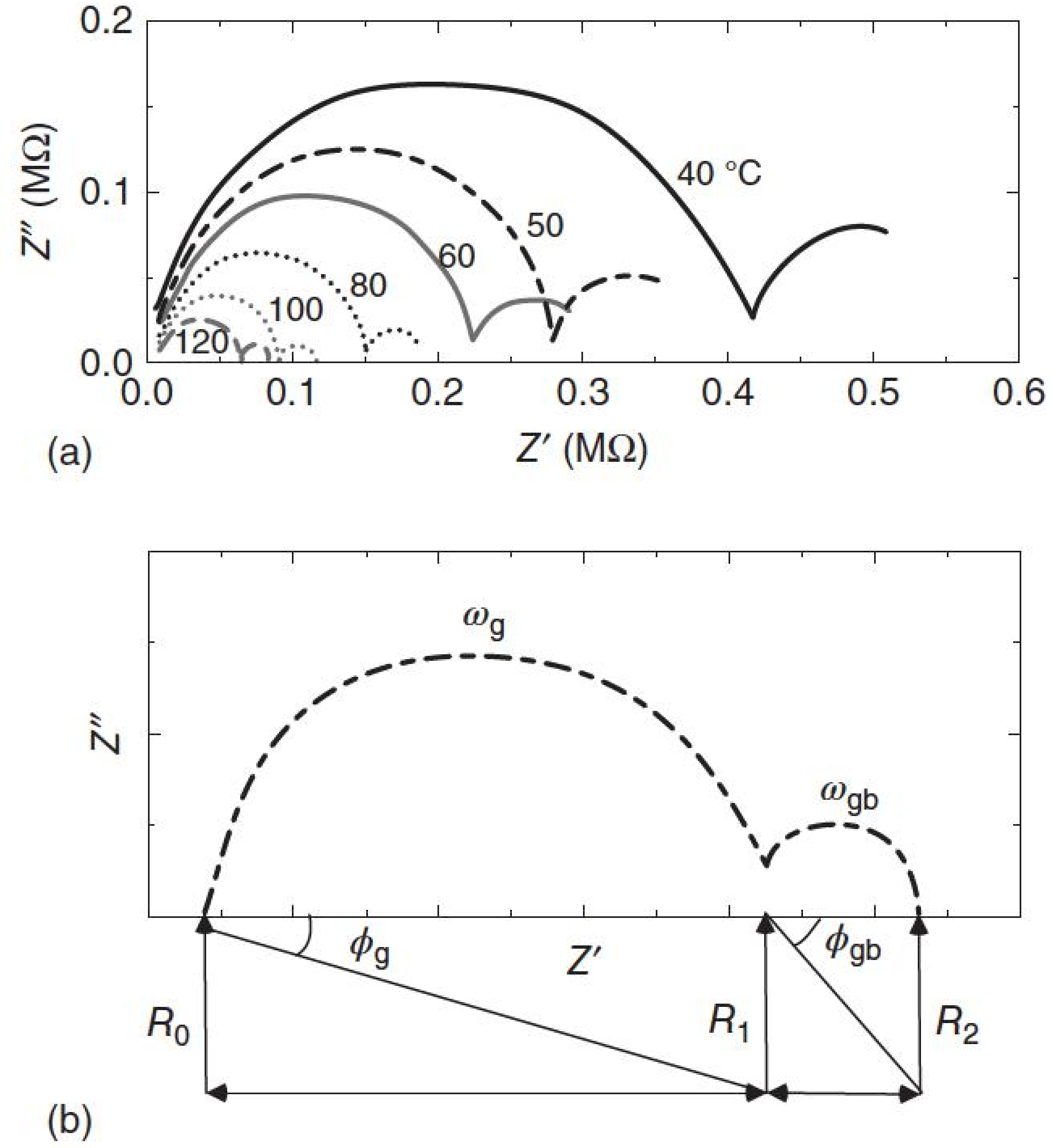


Figure 2.26 (a) Impedance spectra at various temperatures and (b) a typical impedance spectrum showing all fitted parameters. Source: Han et al. 2002 [59]. Redrawn with permission from Elsevier.

The impedance spectra of the ZnO varistor at different temperatures are shown in Figure. 2.26a [59]. The spectrum exhibits two partially overlapping semicircles; the left is respective to the results under high frequencies and the right is respective to the results under low frequencies. The low-frequency semicircle is interpreted as effects of grain boundaries and the higher frequency arc as the effects of grain interiors.

The complex impedance data can be interpreted using the Maxwell–Wagner two-layer equivalent circuit model [58]. The modified Cole–Cole expression, for the distribution of impedance on the two-layer model (grain and grain boundary), in which the resulting complex impedance $Z^*(\omega)$ consists of two overlapping semicircles, can be written as [59]

$$Z^*(\omega) = R_0 + \frac{R_1 - R_0}{1 + (i\omega\tau_g)^{1-\alpha_g}} + \frac{R_2 - R_1}{1 + (i\omega\tau_{gb})^{1-\alpha_{gb}}} \tag{2.23}$$

where R_0 and R_2 are the intercepts with the real impedance axis of the high-frequency end of the high-frequency arc and low-frequency end of the low-frequency arc, respectively. R_1 is the impedance corresponding to the intersecting point of the arcs, which is illustrated in Figure 2.26b; τ_g and τ_{gb} are the mean relaxation times for the grain and grain boundary conduction processes, respectively; α_g and α_{gb} are the parameters that measure the deviations of the shapes of the impedance plots from the ideal semicircular shapes of the Debye model for the grain and grain boundary, respectively. This deviation is due to the distribution of relaxation times [58].

The real and imaginary parts of the complex impedance are given by [59]

$$Z'(\omega) = R_0 + \frac{R_1 - R_0}{a}[1 + (\omega\tau_g)^{1-\alpha_g}\sin(\pi\alpha_g/2)] + \frac{R_2 - R_1}{b}[1 + (\omega\tau_{gb})^{1-\alpha_{gb}}\sin(\pi\alpha_{gb}/2)] \quad (2.24)$$

$$Z''(\omega) = \frac{R_1 - R_0}{a}(\omega\tau_g)^{1-\alpha_g}\cos(\pi\alpha_g/2) + \frac{R_2 - R_1}{b}(\omega\tau_{gb})^{1-\alpha_{gb}}\cos(\pi\alpha_{gb}/2) \quad (2.25)$$

where

$$a = 1 + (2\omega\tau_g)^{1-\alpha_g}\sin(\pi\alpha_g/2) + (\omega\tau_g)^{2(1-\alpha_g)}$$

$$b = 1 + (2\omega\tau_{gb})^{1-\alpha_{gb}}\sin(\pi\alpha_{gb}/2) + (\omega\tau_{gb})^{2(1-\alpha_{gb})}$$

α_g and α_{gb} are given by $\alpha_g = 2\phi_g/\pi$ and $\alpha_{gb} = 2\phi_{gb}/\pi$, where ϕ_g and ϕ_{gb} are the angles of depression of the semicircle centers due to the tilting of the semicircles. The values of ϕ_g and ϕ_{gb} lie between 0° and 90°, and the corresponding values of α_g and α_{gb} lie in the range 0 and 1. $\tau_g = 1/\omega_g = R_g C_g$ and $\tau_{gb} = 1/\omega_{gb} = R_{gb} C_{gb}$, where ω_g and ω_{gb} are the peak frequencies of the impedance arcs because of the grains and grain boundaries, respectively. The values of R_g and R_{gb}, the contributions to the total resistance of the sample by the grains and grain boundaries, respectively, are given by the diameters of the arcs. The values of C_g and C_{gb} are computed from the frequencies corresponding to the peaks of the semicircles. The conductivities of grain (σ_g) and grain boundary (σ_{gb}) can be calculated from the values of R_g and R_{gb}.

References

1 Matsuoka, M. (1975). Non-ohmic properties of zinc oxide ceramics. *Japanese Journal of Applied Physics* 10 (6): 736–746.

2 Levinson, L.M. and Philipp, H.R. (1975). Physics of metal-oxide varistors. *Journal of Applied Physics* 46 (3): 1332–1341.

3 Philipp, H.R. and Levinson, L.M. (1975). Tunneling of photoexcited carriers in metal-oxide varistor. *Journal of Applied Physics* 46 (7): 3206–3207.

4 Levine, J.D. (1975). Theory of varistor electronic properties. *Critical Reviews in Solid State and Material Sciences* 5 (4): 597–608.

5 Morris, W.G. (1976). Physical properties of the electrical barriers in varistors. *Journal of Vacuum Science and Technology* 13 (4): 926–931.

6 Bernasconi, J., Klein, H.P., Knecht, B., and Strässler, S. (1976). Investigation of various models for metal oxide varistors. *Journal of Electronic Materials* 5 (5): 473–495.

7 Emtage, P.R. (1977). The physics of zinc oxide varistors. *Journal of Applied Physics* 48 (10): 4372–4384.

8 Eda, K. (1981). Electrical properties of ZnO-Bi_2O_3 metal oxide heterojunction—A clue of a role of intergranular layers in ZnO varistors.

MRS Online Proceedings Library Archive, Materials Research Society 5: 381–392.

9 Eda, K. (1978). Conduction mechanism of non-ohmic zinc oxide ceramics. *Journal of Applied Physics* 49 (5): 2964–2972.

10 Eda, K. (1979). Transient conduction phenomena in non-ohmic zinc oxide ceramics. *Journal of Applied Physics* 50 (6): 4436–4442.

11 Hower, P.L. and Gupta, T.K. (1979). A barrier model for ZnO varistors. *Journal of Applied Physics* 50 (7): 4847–4855.

12 Mahan, G.D., Levinson, L.M., and Philipp, H.R. (1979). Theory of conduction in ZnO varistors. *Journal of Applied Physics* 50 (4): 2799–2812.

13 Pike, G.E. (1981). Electronic properties of ZnO varistors: a new model. *MRS Online Proceedings Library Archive, Materials Research Society* 5: 369–380.

14 Pike, G.E. (1984). Semiconductor grain-boundary admittance: theory. *Physical Review B* 30 (2): 795–802.

15 Pike, G.E. and Seager, C.H. (1979). The dc voltage dependence of semiconductor grain-boundary resistance. *Journal of Applied Physics* 50 (5): 3414–3422.

16 Blatter, G. and Baeriswyl, D. (1987). High-field transport phenomenology: hot-electron generation at semiconductor interfaces. *Physical Review B* 36 (12): 6446–6364.

17 Blatter, G. and Greuter, F. (1986). Carrier transport through grain boundaries in semiconductors. *Physical Review B* 33 (6): 3952–3966.

18 Blatter, G. and Greuter, F. (1986). Electrical breakdown at semiconductor grain boundaries. *Physical Review B* 34 (12): 8555–8572.

19 Greuter, F. and Blatter, G. (1990). Electrical properties of grain boundaries in polycrystalline compound semiconductors. *Semiconductor Science and Technology* 5 (2): 111–138.

20 Sato, Y., Buban, J.P., Mizoguchi, T. et al. (2006). Role of Pr segregation in acceptor-state formation at ZnO grain boundaries. *Physical Review Letters* 97 (10): 106802.

21 Busch, G. and Schade, H. (2013). *Lectures on Solid State Physics: International Series in Natural Philosophy*, vol. 79. Elsevier.

22 Han, R.Q. and Huang, K. (1998). *Solid State Physics*. Beijing: Higher Education Press.

23 Kobayashi, A., Sankey, O.F., Volz, S.M., and Dow, J.D. (1983). Semiempirical tight-binding band structures of wurtzite semiconductors: AlN, CdS, CdSe, ZnS, and ZnO. *Physical Review B* 28 (2): 935–945.

24 Janotti, A. and Van, de Walle, C.G. (2007). Native point defects in ZnO. *Physical Review B* 76 (16): 165202.

25 Clarke, D.R. (1999). Varistor ceramics. *Journal of the American Ceramic Society* 82 (3): 485–502.

26 Gambino, J.P., Kingery, W.D., Pike, G.E. et al. (1987). Grain boundary electronic states in some simple ZnO varistors. *Journal of Applied Physics* 61 (7): 2571–2574.

27 Magnusson, K.O. and Wiklund, S. (1994). Interface formation of Bi on ceramic ZnO: a simple model varistor grain boundary. *Journal of Applied Physics* 76 (11): 7405–7409.

28 Stucki, F. and Greuter, F. (1990). Key role of oxygen at zinc oxide varistor grain boundaries. *Applied Physics Letters* 57 (5): 446–448.
29 Bueno, P.R., Leite, E.R., Oliveira, M.M. et al. (2001). Role of oxygen at the grain boundary of metal oxide varistors: a potential barrier formation mechanism. *Applied Physics Letters* 79 (1): 48–50.
30 Oba, F., Adachi, H., and Tanaka, I. (2000). Energetics and electronic structure of point defects associated with oxygen excess at a tilt boundary of ZnO. *Journal of Materials Research* 15 (10): 2167–2175.
31 Gupta, T.K. and Carlson, W.G. (1985). A grain-boundary defect model for instability/stability of a ZnO varistor. *Journal of Materials Science* 20 (10): 3487–3500.
32 Carlsson, J.M., Domingos, H.S., Bristowe, P.D., and Hellsing, B. (2003). An interfacial complex in ZnO and its influence on charge transport. *Physical Review Letters* 91 (16): 165506.
33 Kim, Y.S. and Park, C.H. (2009). Rich variety of defects in ZnO via an attractive interaction between O vacancies and Zn interstitials: origin of n-type doping. *Physical Review Letters* 102 (8): 086403.
34 Domingos, H.S. (2010). A model bismuth oxide intergranular thin film in a ZnO twist grain boundary. *Journal of Physics: Condensed Matter* 22 (14): 145503.
35 Carlsson, J.M., Hellsing, B., Domingos, H.S., and Bristowe, P.D. (2003). The effects of doping a grain boundary in ZnO with various concentrations of Bi. *Surface Science* 532: 351–358.
36 Domingos, H.S., Carlsson, J.M., Bristowe, P.D., and Hellsing, B. (2004). The formation of defect complexes in a ZnO grain boundary. *Interface Science* 12 (2-3): 227–234.
37 Freysoldt, C., Grabowski, B., Hickel, T. et al. (2014). First-principles calculations for point defects in solids. *Reviews of Modern Physics* 86 (1): 253–306.
38 Sato, Y., Yamamoto, T., and Ikuhara, Y. (2007). Atomic structures and electrical properties of ZnO grain boundaries. *Journal of the American Ceramic Society* 90 (2): 337–357.
39 Olsson, E. and Dunlop, G.L. (1989). Characterization of individual interfacial barriers in a ZnO varistor material. *Journal of Applied Physics* 66 (8): 3666–3675.
40 Rodrigues, R.P., Hwang, J.H., and Dravid, V.P. (1999). 4-Probe micropatterning and electrical measurements across individual grain boundaries in electroceramics. *Journal of Electroceramics* 3 (3): 245–254.
41 Einzinger, R. (1987). Metal oxide varistors. *Annual Review of Materials Science* 17 (1): 299–321.
42 Schwing, U. and Hoffmann, B. (1985). Model experiments describing the microcontact of ZnO varistors. *Journal of Applied Physics* 57 (12): 5372–5379.
43 He, J.L., Zeng, R., Chen, Q.H. et al. (2004). Nonuniformity of electrical characteristics in microstructures of ZnO surge varistors. *IEEE Transactions on Power Delivery* 19 (1): 138–144.
44 Wang, H., Li, W., and Cordaro, J.F. (1995). Single junctions in ZnO varistors studied by current-voltage characteristics and deep level transient spectroscopy. *Japanese Journal of Applied Physics* 34 (4R): 1765–1768.

45 Ohashi, N., Kataoka, K., Ohgaki, T. et al. (2003). Synthesis of zinc oxide varistors with a breakdown voltage of three volts using an intergranular glass phase in the bismuth–boron–oxide system. *Applied Physics Letters* 83 (23): 4857–4859.
46 Cheng, C., He, J., and Hu, J. (2012). Naturally asymmetrical double-Schottky barrier model: based on observation of bicrystal. *Applied Physics Letters* 101 (17): 173508.
47 Pike, G.E., Kurtz, S.R., Gourley, P.L. et al. (1985). Electroluminescence in ZnO varistors: evidence for hole contributions to the breakdown mechanism. *Journal of Applied Physics* 57 (12): 5512–5518.
48 Levinson, L.M. and Philipp, H.R. (1976). AC properties of metal-oxide varistors. *Journal of Applied Physics* 47 (3): 1117–1122.
49 Vlasova, M.V., Kakazey, N.G., Milosevic, O. et al. (1990). Electronic paramagnetic resonance (EPR) study of the structure of ZnO varistors prepared by various chemical methods. *Journal of Materials Science* 25 (10): 4324–4330.
50 Baraki, R., Zierep, P., Erdem, E. et al. (2014). Electron paramagnetic resonance study of ZnO varistor material. *Journal of Physics: Condensed Matter* 26 (11): 115801.
51 Yang, X., Hu, J., and He, J. (2017). Effect of interfacial charge relaxation on conducting behavior of ZnO varistors under time varying electric fields. *Applied Physics Letters* 110 (18): 182104.
52 Eda, K. (1989). Zinc oxide varistors. *IEEE Electrical Insulation Magazine* 5 (6): 28–30.
53 Blatt, S. and Hinrichsen, V. (2015). Mathematical model for numerical simulation of current density in microvaristor filled insulation materials. *IEEE Transactions on Dielectrics and Electrical Insulation* 22 (2): 1161–1170.
54 Argaut, P. and Luton, M.H. (1995). Dry terminations: applicability to EHV. In: *Proceedings of Jicable*, 67–71. Montereall, France: Jicable.
55 Gao, L., Yang, X., Hu, J., and He, J. (2016). ZnO microvaristors doped polymer composites with electrical field dependent nonlinear conductive and dielectric characteristics. *Materials Letters* 171: 1–4.
56 Mukae, K., Tsuda, K., and Nagasawa, I. (1979). Capacitance-vs-voltage characteristics of ZnO varistors. *Journal of Applied Physics* 50 (6): 4475–4476.
57 Hari, N.S., Padmini, P., and KUTTY, T.N. (1997). Complex impedance analyses of n-$BaTiO_3$ ceramics showing positive temperature coefficient of resistance. *Journal of Materials Science: Materials in Electronics* 8 (1): 15–22.
58 Alim, M.A., Li, S., Liu, F., and Cheng, P. (2006). Electrical barriers in the ZnO varistor grain boundaries. *Physica Status Solidi (A)* 203 (2): 410–427.
59 Han, J., Senos, A.M.R., and Mantas, P.Q. (2002). Deep donors in polycrystalline Mn-doped ZnO. *Materials Chemistry and Physics* 75 (1-3): 117–120.

3

Tuning Electrical Characteristics of ZnO Varistors

The ZnO varistor is a very complex chemical system that contains many dopants, such as Bi_2O_3, CoO, MnO, Sb_2O_3, and Cr_2O_3. The majority of bismuth-doped ZnO varistors are usually prepared by a liquid-phase sintering ZnO powder with Bi_2O_3 and other additives, according to the desired formulation, and the secret of the varistor material lies in the liquid phase, which facilitates rapid distribution of dopants during sintering. The role of Bi_2O_3 is mainly to provide a medium for liquid-phase sintering, enhancing the growth of ZnO grains. Dopants play at least three major roles in forming varistors: they can affect grain growth during sintering, the dewetting characteristics of the liquid phase during cooling, and the electronic defect states that control the overall varistor characteristics. In order to obtain high-performance ZnO varistors, the compositions, impurities, mixing methods, particle sizes, and sintering conditions, such as maximum temperature and holding time, temperature rising/lowering rates, and oxygen and Bi_2O_3 partial pressures, should be controlled precisely. The dopant can act as a donor, an acceptor, or both, depending on the size of the guest ion, crystal structure of the host lattice, and the relative valency of the guest and host ions. However, the contribution of each additive has often been considered within the multicomponent system; the performance of a ZnO varistor is the synergistic effect of multiple additives, so it is difficult to investigate the specific role of each dopant in the multicomponent system. The main functions of different additives in ZnO varistors are summarized in this chapter. The recent works on high voltage gradient and low residual voltage ZnO varistors are also introduced.

3.1 Introduction

Pure ZnO is a nonstoichiometric n-type semiconductor with a linear I–V behavior. To make it nonlinear, various additive oxides are incorporated in ZnO [1–6]. A typical ZnO-based varistor is a very complex chemical system that contains several dopants, such as Bi_2O_3, CoO, MnO, Sb_2O_3, and Cr_2O_3 [1–4]. It has been proposed that the dopants responsible for the formation of the varistor behavior are cations of large ionic radii, with low solubility in ZnO at low temperature, like Bi [5, 6], Pr [7, 8], Ba [9, 10], or V [11–18]. These dopants are often called "varistor

formers," without which it is difficult to make a varistor. The other dopants are added for improving the nonohmic property, such as CoO and MnO, or the densification of ceramics and their reliability, such as Sb_2O_3 and Cr_2O_3 [19]. Many studies were carried out to investigate the roles of various additives on the formation of microstructures and electrical properties of ZnO varistors. Incorporation of these oxides causes atomic defects to form at the grain and the grain boundary, with donor or donor-like defects dominating the depletion layer and acceptor and acceptor-like defects dominating the grain boundary states [19].

In order to obtain high-performance ZnO varistors, the compositions, impurities, mixing methods, particle sizes, and sintering conditions, such as maximum temperature and holding time, temperature rising/lowering rates, and oxygen and Bi_2O_3 partial pressures, should be controlled precisely [20].

It is believed that the nonlinearity of ZnO varistors is controlled by grain boundary barriers that develop as a result of electronic defects in ZnO polycrystalline ceramics [21, 22]. It has been found that the nonlinearity and electrical stability depend critically on the minor additives and the processing methods [20, 23]. For these reasons, considerable efforts have been devoted to understanding the effect of additives on the electronic defects and consequently the electrical properties of ZnO varistors by combining the results from a variety of physical measurements, especially those performed in recent years. These methods have included well-established techniques for the identification of defect states at interfaces in semiconductors [3], such as deep-level transient spectroscopy (DLTS), deconvolution of the I–V curves, and admittance spectroscopy, as well as techniques suited to bulk defects, such as photoluminescence and electron paramagnetic resonance.

In this chapter, the dopant effects of different additives and the influence of sintering conditions on the microstructural and electrical behaviors of ZnO varistor ceramics are introduced.

3.2 Liquid-Phase Fabrication

Although the microstructures of ZnO varistors appear complex and vary from one formulation to another, the secret of varistors seems to be in the liquid phase. The liquid phase facilitates the rapid redistribution of dopants during sintering, so that they are uniformly incorporated into the ZnO grains. The dewetting of the liquid phase from the grain boundaries on cooling provides a means of distributing the large-ion dopants along the grain boundaries. Finally, during intermediate annealing in air or oxygen, the solidified liquid phase provides a continuous path for oxygen to enter the material [3].

3.2.1 Microstructure of ZnO Varistor

Since Matsuoka proposed the initial formulations of ZnO varistors, the majority of bismuth-doped ZnO varistors are usually prepared by the liquid-phase sintering ZnO powder with Bi_2O_3 and other additives [3], according to the desired formulation, and the secret of the varistor material lies in the liquid phase, which

facilitates rapid distribution of dopants during sintering. The role of Bi_2O_3 is mainly to provide a medium for liquid-phase sintering, enhancing the growth of ZnO grains [24].

Bismuth oxide forms a liquid phase at a relatively low temperature (860 °C) during sintering, dissolves a large amount of ZnO grains, and forms grain boundaries after sintering between 1100 and 1300 °C. During cooling, the liquid phase solidifies at the multiple-grain junction [25, 26]. Observations of this sintered material have suggested that its microstructure essentially consists of ZnO grains surrounded and separated by a thin continuous intergranular Bi_2O_3-rich phase, which sits at the triple junctions [27–30]. A simplified sketch of the microstructure is shown in Figure 3.1 [30]. The microstructure can also contain one or more types of spinels, pores embedded in the triple points or the ZnO grains, and in addition, depending on the composition, a small amount of pyrochlore phase between the ZnO grains, and inversion boundaries (IBs) (or twins) within the ZnO grains.

From scanning transmission electron micrograph (STEM) observation, there is a continuous second phase of substantially enhanced Bi concentrations at all grain boundaries, as shown in Figure 3.2 [31], which was confirmed by many researchers [32–36]. First scanning secondary ion mass spectrometry (SIMS) data reveal a homogeneous lateral distribution of Bi over the microjunctions and a constant concentration of the dopants Mn and Co in the depth profile perpendicular to the interface [35].

The solidified liquid phase, which is the white network, is shown in Figure 3.3 [35]. White regions are the bismuth-rich phase formed by the solidification of the remnant liquid phase. A wide variety of grain sizes and variations in the length of the sides of individual grains apparent in this micrograph are typical of many varistors. Etching the microstructure with perchloric acid to preferentially remove the ZnO grains reveals that the bismuth-rich phase is interconnected and continuous, along the multigrain junctions, through the microstructure. This network provides a continuous path for the transport of oxygen into the material during postsintering annealing [3], as discussed in Section 3.4.

The microstructures at the grain boundaries are quite complicated, which are roughly classified into three types [30, 31, 34, 36]. The first one (type I) is the grain boundary with a relatively thick (1000 Å–l μm) Bi_2O_3-rich intergranular layer [37]. The melting point of Bi_2O_3 is 825 °C, which decreases to 750 °C when coexisting with ZnO. Hence, a liquid phase is formed during sintering. The liquid phase is likely to gather at the holes created by the packing of the ZnO grains.

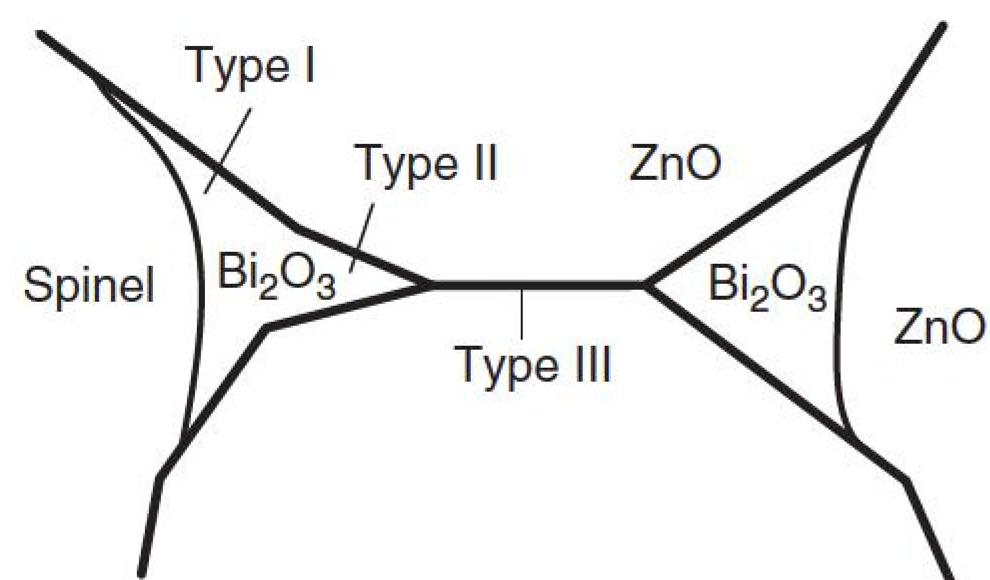


Figure 3.1 Schematic arrangement of phases in a ZnO varistor ceramic. Source: Adapted from Cerva and Russwurm 1988 [30].

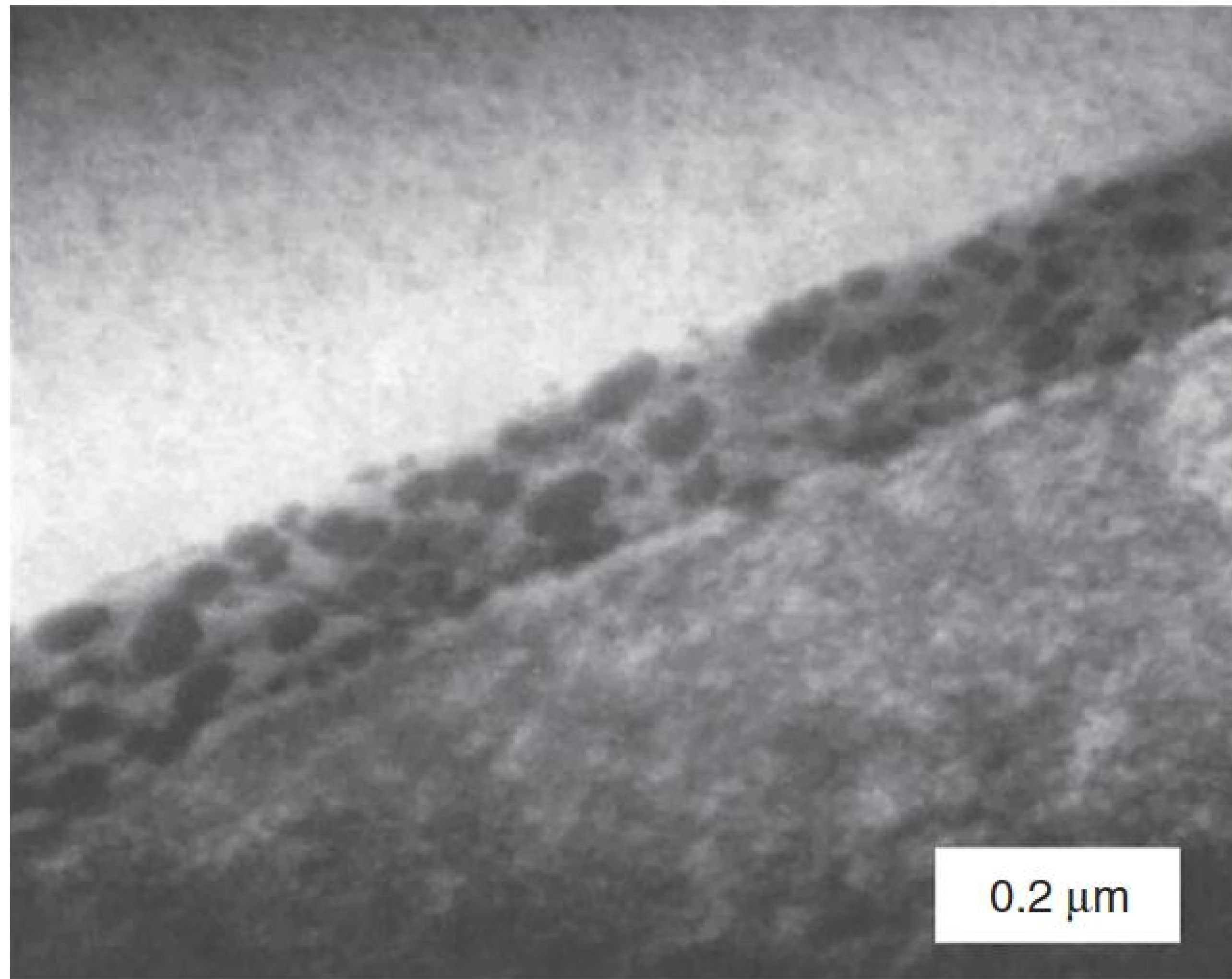


Figure 3.2 STEM image of second-phase particles on a typical grain boundary of the ZnO sample containing 0.04 wt% Bi_2O_3. Source: Kingery et al. 1979 [31]. Reproduced with permission of John Wiley & Sons.

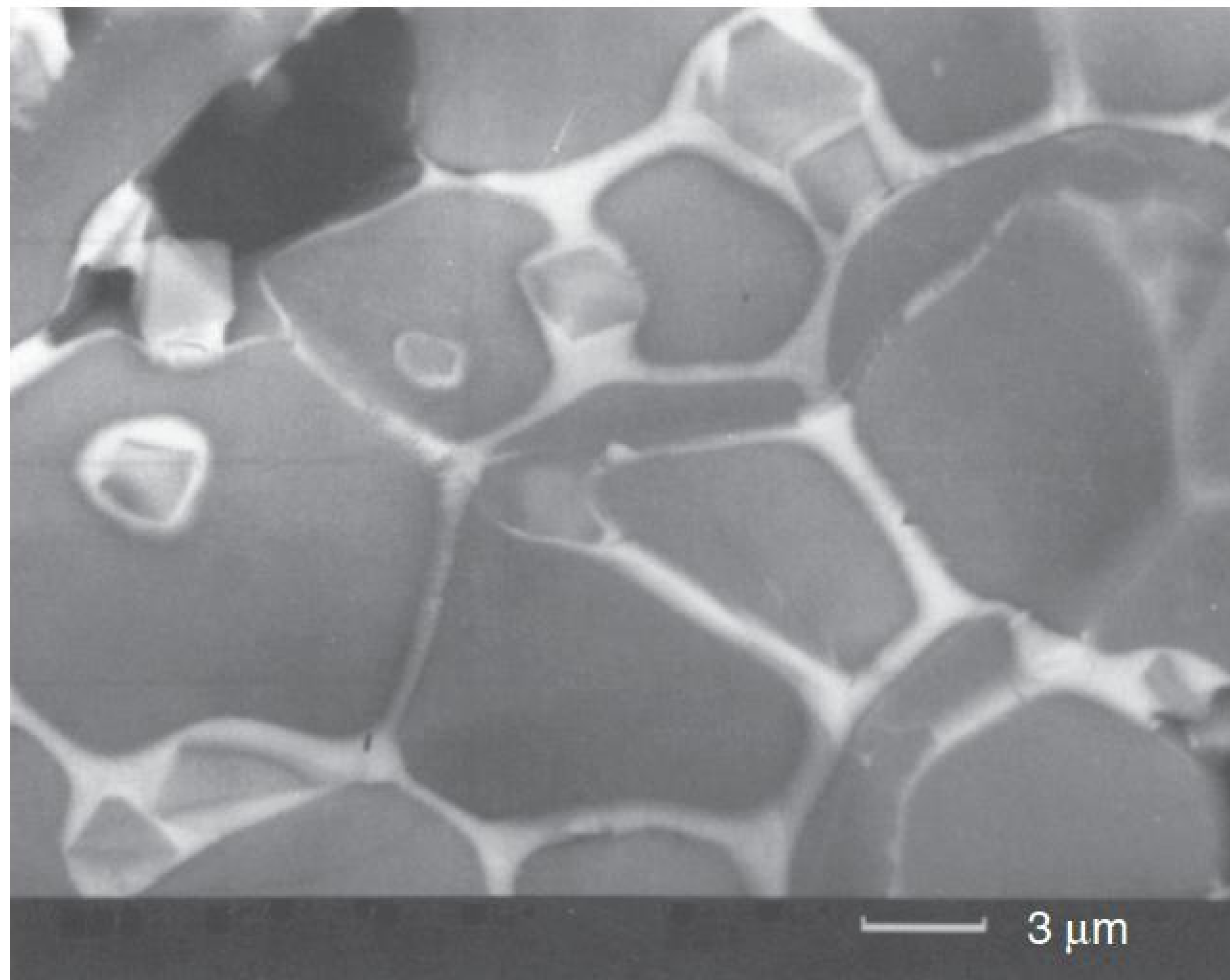


Figure 3.3 Microstructure of a multiphase ZnO varistor. Main phase: polyhedral ZnO grains, white network: Bi_2O_3, small octahedra: insulating spinel. Spinel particles, the small equiaxed grains, are located inside many of the ZnO grains and at several of the grain boundaries. Source: Greuter 1995 [35]. Reproduced with permission of Elsevier.

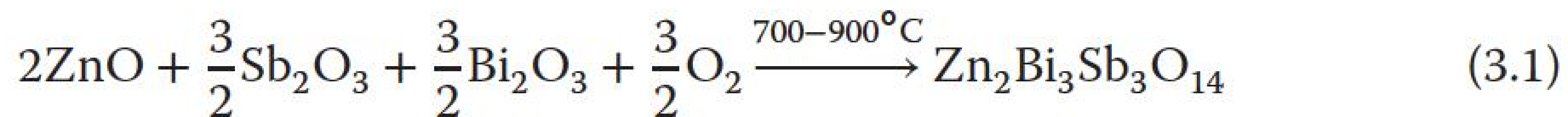
Type II structure is where the Bi_2O_3-rich intergranular layer becomes thinner (10–1000 Å) as it approaches the contact points of the grains. Type III structure is the contact region; no distinct intergranular layer can be observed by scanning electron microscopy (SEM) or transmission electron microscopy (TEM). For the type III structures, Bi, Co, and an excess amount of oxygen ions were detected in the interfacial region of the grain boundaries to a thickness of several nanometers by Auger Electron Spectroscopy (AES) or X-ray photoelectron spectroscopy (XPS) measurements. The collision of grains covered with Bi_2O_3 liquid makes the intergranular layer in the contact region very thin. On the other hand, the wettability of the Bi_2O_3 liquid phase is not so good; therefore, when the amount of Bi_2O_3 is diminished, the ZnO grains are not completely surrounded by the Bi_2O_3 liquid phase; this also makes the thin intergranular layer more thinner. However, the diffusion velocity at a grain boundary is usually higher than that in bulk by one or two orders of magnitude. As a result, the ions of Bi, Co, Mn, and Sb diffuse into the grain boundaries with ease [38].

The ZnO–ZnO grain boundary is recognized to be the Schottky barrier at the grain boundary of the ZnO microstructure and responsible for the varistor performance [39, 40], and the monoatomic layers of excess bismuths and oxygens at the grain boundaries are responsible for the electrical activity of the interfaces. Characteristic bulk and interface defect levels govern the electrical behavior [36]. This homojunction can be electrically bypassed by bismuth oxide phases, and therefore, the ideal varistor characteristics can be changed. The resulting additional leakage current enhances the power consumption of the system. Experiments by Einzinger with microvaristors clearly verified the leakage current contribution of the Bi_2O_3 phases. Moreover, it was reported [41–44], that several stabilized high-temperature phases or metastable phases of Bi_2O_3 exhibit an extremely high ionic conductivity, which supports the assumption of additional leakage currents through the Bi_2O_3 grains [30].

3.2.2 Polymorph of Bismuth Oxide

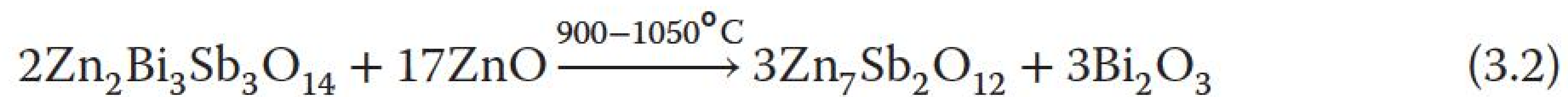
The bismuth-rich phase appears to have particular importance because the varistor characteristics are dependent on the type of the polymorph of crystalline Bi_2O_3 [25, 26]. The crystallization sequences and temperatures can be very different from one varistor formulation to another. Bi_2O_3 has at least four polymorphs: α, β, γ, and δ. The monoclinic form α is stable from room temperature up to 730 °C, where it is transformed into δ-Bi_2O_3. The δ-form is stable between 730 and till 825 °C, which is the melting point of Bi_2O_3. The β and γ forms are known as metastable polymorphs, which result from cooling from high temperature and are subsequently transferred to α-Bi_2O_3 at 500 °C. However, δ-Bi_2O_3 can be retained at room temperature by quenching [43]. Heat treatment induces transformation of the α- and β-Bi_2O_3 phases into γ-Bi_2O_3. The β-Bi_2O_3 phase was also found to transform into the nonstoichiometric crystalline $Bi_2O_{2.33}$ phase [30].

Usually, Sb_2O_3 is added to control grain growth, and inclusions of $Zn_7Sb_2O_{12}$ spinel-type crystallites are formed at the grain boundaries as shown in Figure 3.3. At temperatures in the range of 700–900 °C, Sb_2O_3 reacts with both ZnO and Bi_2O_3 and forms $Zn_7Sb_2O_{12}$ and $Zn_2Bi_3Sb_3O_{14}$ pyrochlore-type crystalline phases [45]:



$$2ZnO + \frac{3}{2}Sb_2O_3 + \frac{3}{2}Bi_2O_3 + \frac{3}{2}O_2 \xrightarrow{700-900\,°C} Zn_2Bi_3Sb_3O_{14} \quad (3.1)$$

During sintering, $Zn_2Bi_3Sb_3O_{14}$ forms a Bi_2O_3-rich liquid phase and $Zn_7Sb_2O_{12}$ by the decomposition of zinc oxide and pyrochlore at temperatures in the range of 900–1050 °C by reactions [45]



$$2Zn_2Bi_3Sb_3O_{14} + 17ZnO \xrightarrow{900-1050\,°C} 3Zn_7Sb_2O_{12} + 3Bi_2O_3 \quad (3.2)$$

By means of transmission electron microscopy and X-ray powder diffraction, the δ-Bi_2O_3, $Bi_2Sb_3Zn_2O_{14}$ (pyrochlore), and β-$Zn_7Sb_2O_{12}$ (spinel) phases were observed [46]. $Zn_7Sb_2O_{12}$ precipitates at the grain boundaries and hinders ion movement [37]. Bi_2O_3 helps in densification and wetting of ZnO grains.

$Bi_2Sb_3Zn_2O_{14}$ (pyrochlore) and β-$Zn_7Sb_2O_{12}$ (spinel) phases are useful for restricting the growth of ZnO grains. Generally, $Zn_7Sb_2O_{12}$ spinels are present in triple junctions as well as inside the ZnO grains in the form of inverse grain boundary [47].

More than one crystalline phase based on Bi_2O_3 can also coexist [24]. Some multiple-grain junctions contain both α- and β-Bi_2O_3 grains [30]. However, it has been speculated that the presence of δ-Bi_2O_3, one of the fastest oxygen ion conductors, plays a vital role in the varistor stability especially while annealing in air. Also, high-resolution X-ray microanalyses indicated that the transformation to δ-Bi_2O_3 is accompanied by the rejection of dissolved elements, such as antimony, cobalt, and nickel, into the surrounding intergranular phase. The valence state of these transition elements is not known but may be dependent on the temperature at which the transformation occurs [3]. One of the works even recommends that the electrical nonlinearity can be enhanced by using a highly oxygenated Bi_2O_3 as the starting material [27]. The oxygen and bismuth concentrations at the grain boundaries are reported to be affected differently on treatment according to Stucki and Greuter [28].

3.2.3 Influence of Bi_2O_3 Concentration

The amount of added Bi_2O_3 to the starting composition, which defines the amount of liquid phase at the sintering temperature, is important as the grain growth is slowed down by the increased thickness of the liquid layer at the grain boundaries of ZnO. In low-voltage varistor ceramics, the increase in the ZnO grain size is considerable, and so, also, is the decrease in the specific surface of the grains, and this can significantly influence the thickness of the Bi_2O_3 liquid layer at the grain boundaries during sintering [48].

In the ZnO–Bi_2O_3 system, Senda and Bradt [49] reported that at low Bi_2O_3 level below 0.5 mol%, the grain growth controlling mechanism is a solution–precipitation-phase boundary reaction of the solid ZnO grains and the Bi_2O_3-rich liquid phase. In this case, grain growth is enhanced by a thin layer of Bi_2O_3 liquid phase at the grain boundaries. However, for a large amount of Bi_2O_3 above 1.0 mol%, Dey and Bradt [50] reported that the controlling mechanism of grain growth rate is the diffusion through the liquid phase, and the grain growth is hindered by the thick Bi_2O_3 liquid layer.

As shown in Figure 3.1, the ZnO varistors have three types of microstructure. The occupation ratio among them is quite different and dependent on both composition, especially Bi_2O_3 content, and sintering condition. The ZnO varistors with the addition of 0.5 mol% Bi_2O_3 into the starting material and sintered at 1250 °C for two hours mainly have the type II and type III structures, whereas the varistors sintered at 1400 °C for several hours mainly have the type III structure. The varistors with more than 5 mol% Bi_2O_3 added to the starting material mainly have the type I structure. Even in this case, highly nonohmic properties were still observed [37].

3.2.4 Volatilization of Bismuth Oxide

Bi_2O_3-doped ZnO ceramic varistors are usually sintered at temperatures near 1200 °C in the presence of a Bi-rich liquid phase, which is partially vaporized

during the sintering process. Bismuth oxide easily vaporizes above 1400 °C, and the nonohmic property will disappear if Bi_2O_3 vaporizes extensively [37]. Volatilization of bismuth oxide depends on the total surface area in direct contact with the reaction atmosphere, and this, in turn, is related to the area/volume ratio of the ceramic disc [51]. The loss of Bi_2O_3 has a significant role in the development of the varistor microstructure and more specifically in ZnO grain growth, which is strongly enhanced by the presence of the liquid phase and should be particularly affected.

Several efforts were carried out to describe the influence of different Bi_2O_3 contents on the microstructure and electrical properties of the varistor devices. Chiang et al. [52] reported a loss of 19 wt% bismuth oxide when sintering at 1150 °C for 90 minutes by emission spectroscopy. They also found cobalt oxide vaporization when using this technique. Metz et al. [43] reported the results that show Bi_2O_3 losses up to 95 wt% depending on the temperature and soaking time. Peiteado et al. [51] performed X-ray fluorescence analysis to describe the Bi_2O_3 vaporization profile as a function of distance to the outer surface. In this way, the area/volume ratio of the green ceramic plays a determining role in varistor manufacturing because it limits the total amount of liquid Bi-rich phase that will be lost by vaporization. The microstructural development and more specifically the kinetics of ZnO grain growth are strongly affected by this vaporization in such a way that the grain size of ZnO tends to decrease as the bismuth oxide vaporization increases.

Figure 3.4 shows the content of residual Bi_2O_3 in the sintered body after sintering for two hours at each of the temperature point [37], and the amount of Bi_2O_3 gradually decreases from the sintered mass.

The importance of bismuth segregation was demonstrated in a series of experiments performed by Morris and Cahn [53, 54]. They studied the *I*–*V* characteristics of sintered ZnO with different concentrations of Bi_2O_3 and examined the grain boundaries by AES and ISS. The key finding was that the *I*–*V* characteristics were essentially independent on the amount of added Bi_2O_3, and the grain boundaries had an adsorbed layer of constant bismuth content with the excess

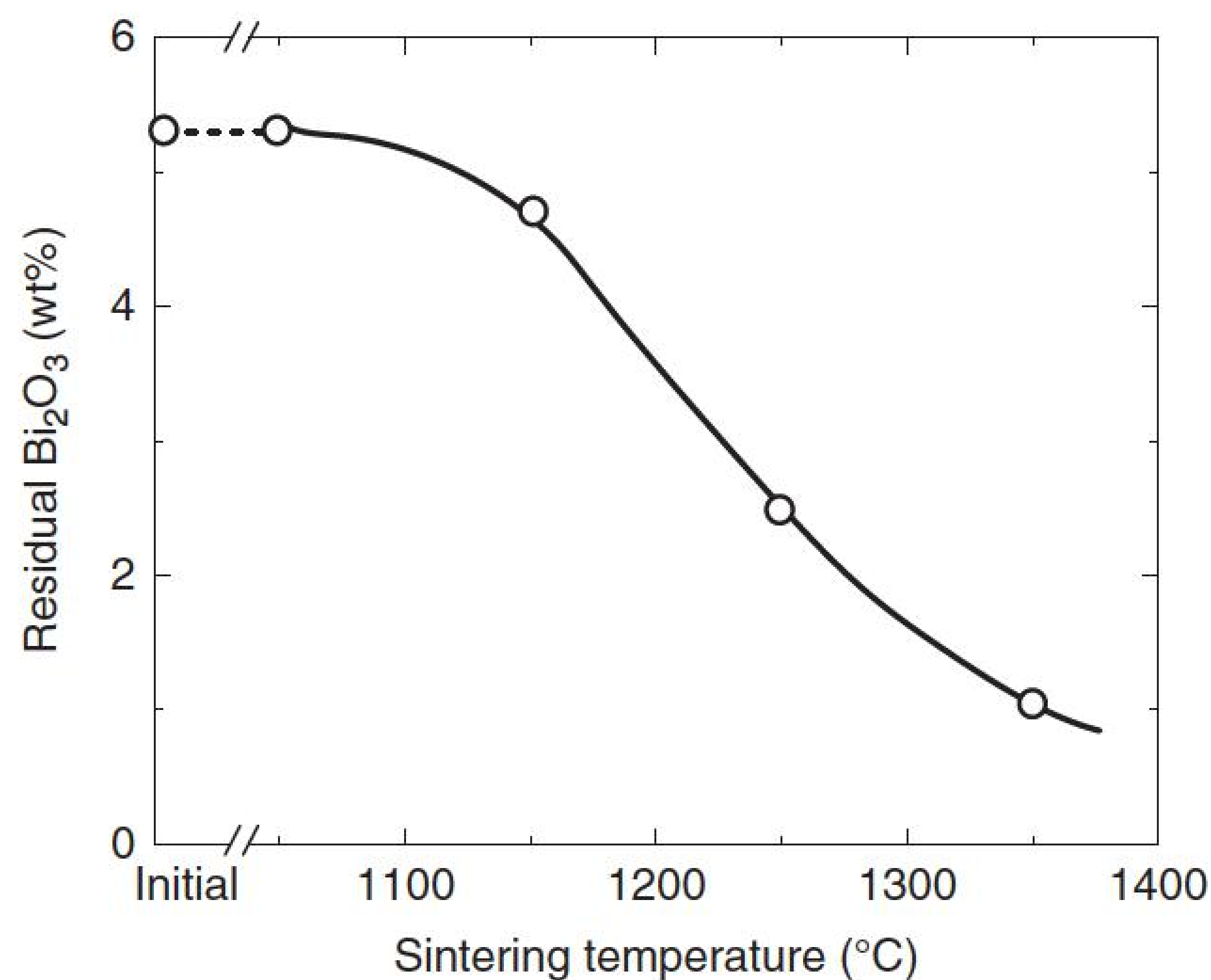


Figure 3.4 Residual Bi_2O_3 in the ZnO varistors with a diameter of 14 mm and a thickness of 2 mm after sintering for two hours at each temperature. The starting material contained 1 mol% each of Bi_2O_3, CoO, and $_2O_3$; 0.5 mol% MnO; and 96.5 mol% ZnO. Source: Adapted from Eda 1989 [37].

Bi_2O_3 located at the triple junctions. The total amount of Bi_2O_3 was only sufficient to create about a monolayer of bismuth on all the grain boundaries. The resulting material exhibited obvious varistor behavior, although, as might be expected for the binary material with no annealing treatment or additional dopants, the degree of nonlinearity was not large (~3) [3].

3.3 Preparing and Sintering Techniques

3.3.1 Fabrication

ZnO varistor is fabricated by the conventional ceramics sintering technique. A standard composition contains 0.5 mol% each of Bi_2O_3 and MnO, 1.0 mol% each of CoO and Sb_2O_3, and 97.0 mol% ZnO. Reagent-grade chemicals are usually used. The powders are mixed by a conventional method using a mortar in the dry form or a ball mill in the wet form, usually mixed and homogenized in alcohol using a planetary mill. After drying at 90 °C, the mixture is pressed into arbitrary forms by a conventional molding method, for example, pressed with 350 MPa into discs of 30 mm diameter and 2.0 mm thickness. The pressed discs are sintered in an electric furnace at 1150–1350 °C for one to five hours in air using a heating rate of 6 °C min^{-1} and a cooling rate of 2 °C min^{-1}. Finally, electrodes are prepared on both surfaces. The best ohmic electrodes are painted In–Ga alloys or evaporated Al films. Conventional silver electrodes painted and fired at 500–800 °C are also used [37].

The morphology depends on how the varistor material is processed [3]. If the material is quenched from above the eutectic temperature, the bismuth-rich phase wraps the ZnO grains, and no varistor behavior results. If, instead, the material is slowly cooled down in air, as is the commercial practice, the liquid phase retracts from the two-grain junctions and is localized along the triple-grain junctions. The fact that devices that are annealed at 800 °C show nonlinear characteristics, whereas devices annealed at temperatures higher than 900 °C show a linear behavior, gives rise to the possibility of surface evaporation of some critical elements required for nonlinearity [55]. The results of energy-dispersive X-ray analysis (EDXA) showed all the elements present on the surface of the devices annealed at 800 °C. However, for devices annealed 1200 °C, it was found that Bi, Pb, and Sb were absent, although the concentration of these elements was highest in the starting oxide. This result is in agreement with the observation of Matsuoka [5] and is expected from the high vapor pressure data of these elements.

Wong reported the relation between the grain size and the sintering condition [7]; the grain size of ZnO–Bi_2O_3 ceramics increases by sintering at much higher temperatures or for much longer times. However, even if sintered at 1400 °C, the average ZnO grain size was below 50 μm. Furthermore, such high-temperature sintering resulted in the vaporization of Bi_2O_3 from the sintered body, so that the nonlinear property was damaged [56]. To suppress the evaporation of these elements at a high temperature ($T > 900$ °C), annealing was carried out in an evacuated closed-tube system in the presence of a source mixture of the oxides

[55]. Nevertheless, nonlinearity was not observed. Moreover, devices annealed at conditions that previously gave linear I–V characteristics, i.e. 800 °C, showed a linear I–V dependence when annealed under these conditions in an evacuated sealed tube. This result indicates that annealing in air is an essential requirement even in the presence of the elements Bi, Pb, and Sb. This agreed with the investigations of Einzinger in which it was found that an oxidizing ambient is essential to achieve nonlinearity in the ZnO varistor [57].

DLTS measurements were performed to study the annealing-induced changes in trap centers in ZnO varistors and to shed more light on varistor stability mechanism [58]. Two electron traps, $E_c - 0.26$ eV and $E_c - (0.2–0.3)$ eV, were observed in the unannealed samples in large quantities ($7–9 \times 10^{14}$ cm^{-3}). The density of the E_c–0.26 eV trap gradually decreases to 4.7×10^{13} cm^{-3} at the annealing temperature of 600 °C. Beyond the 600 °C annealing, the $E_c - 0.26$ eV trap begins to grow along with the appearance of another electron trap at $E_c - 0.17$ eV. The minima in the $E_c - 0.26$ eV trap density, coupled with the observation that unannealed devices are unstable, whereas devices annealed at 600 °C are most stable, suggest that the ZnO varistor instability is related to the $E_c - 0.26$ eV trap. Rohatgi et al. [58] supported the ion migration model for device instability where the $E_c - 0.26$ eV defect may be the Zn interstitial or the migrating ion.

3.3.2 Fabrication Stages

Four distinct stages can be distinguished associated with the fabrication of a varistor ceramic [3]. In the first stage, a liquid phase forms from low melting eutectics in the ZnO, Bi_2O_3, and/or Sb_2O_3 system. Depending on time, temperature, and formulation, secondary phases, such as pyrochlore and spinel, can also form at this stage, but the principal process is the dissolution of the dopants into the liquid phase. In the second stage, dopants diffuse into the ZnO grains, and their uniform distribution leads to liquid-phase densification. Concurrently, grain growth occurs. The sintering temperature and time are chosen so as to optimize compositional uniformity, densification, and grain size. In the third stage, during cooling to intermediate temperatures, crystallization of secondary phases from bismuth-rich liquid phase and retraction of liquid phase into the triple junctions occur. Potential barriers are formed at the grain boundaries during this stage. In the fourth stage, processes occurring during the annealing stage (slow cooling) are unresolved but found to be critical in deciding the varistor properties. The major development of the electrical properties occurs on slow cooling through an intermediate temperature (450–700 °C) or on subsequent annealing in this temperature range. This heat treatment is a key feature of the manufacture of varistors, especially for high-voltage applications.

The rationale for the annealing stage is that it is necessary for both the attainments of high nonlinearity and stability against degradation. Several intriguing explanations were proposed, but the detailed processes that occur during the annealing stage remain essentially unresolved, although it is highly likely that several processes, including the phase transformation from δ- to α-Bi_2O_3, occur concurrently. The most pronounced microstructural, as distinct from electrical,

changes occur during the third stage, cooling from the sintering temperature. Among these is the wetting behavior of the bismuth-rich phase [3].

3.3.3 Effect of Pores

A lot of remaining pores can be primarily found in the grain boundaries [59, 60]. Pore is an intrinsic property of the ZnO varistor, which is an inherent part of liquid-phase sintering. Pores are present in the powder compact as interparticle voids. Also, pores can be resulted from uneven liquid distribution, unbalanced diffusion events, and reactions with the vapor [61]. Pores are related to the densification of ZnO varistors. There are two different shapes of pores in the ZnO varistor samples: sphere and irregular polyhedron.

There are two different pore formation mechanisms. The first is related to wrapped air particles in an initial varistor compact. Before sintering, different ingredients are milled, mixed, and pressed into the initial ZnO varistor compact. Air particles are wrapped inside the varistor compact during the mixing course. During the sintering course, the wrapped air particles expand and form pores in the ZnO varistors. The expansion force of air in the pore leads to the formation of a spherical shape. Another mechanism is related to pore coarsening induced by particle arrangement [61]. During the liquid sintering course, the ZnO grains grow and move, and several ZnO grains surround a space to form a pore. One part of this kind of pores is filled by liquid grain boundary materials, and the other part is not filled, and then pores are formed in the ZnO varistors. Ordinarily, these kinds of pores have an irregular polyhedron shape and sometimes form the shape of a sphere, which is related to the sintering course.

During sintering, liquid Bi_2O_3 wraps the ZnO grains and air particles. The air particles move arbitrarily with the mobility of Bi_2O_3, and a part of air particles are expelled outside the ZnO varistor. If the air particles are wrapped by growing the ZnO grains, then they form pores inside the ZnO grains; the air particles left in the liquid Bi_2O_3 phase form pores in the grain boundaries, and some air particles emerge into large particles with the mobility of liquid Bi_2O_3. Pores with a larger diameter locate in the grain boundaries and triple junctions of the grains. When Al_2O_3 is added, $ZnAl_2O_4$ spinel is formed to inhibit the mobility of a part of pores; the inhibited pores merge into a large-sized pore in the grain boundaries. These pores certainly inhibit the mobility of the liquid grain boundary, ZnO grain, and spinels and hinder the grain growth of ZnO grains during the sintering course [62]. The grain growth inhibiting effect is partly related to the pore dragging mechanism as supposed by Gupta [63].

It is also worth noting that there is a change in the shape of the pore as Bi_2O_3 is added into ZnO [64]. The shape of the pores is governed by the magnitude of the dihedral angle θ, which is controlled by the balance between the surface energy γ_s and grain boundary energy γ_{gb} [65], as demonstrated in Figure 3.5 [64]:

$$\gamma_{gb} = 2\gamma_s \cos\frac{\theta}{2} \tag{3.3}$$

The addition of Bi_2O_3 reduces γ_{gb}, which consequently increases the value of dihedral angle as shown in Figure 3.5b. Then, the pores in the Bi_2O_3-doped ZnO

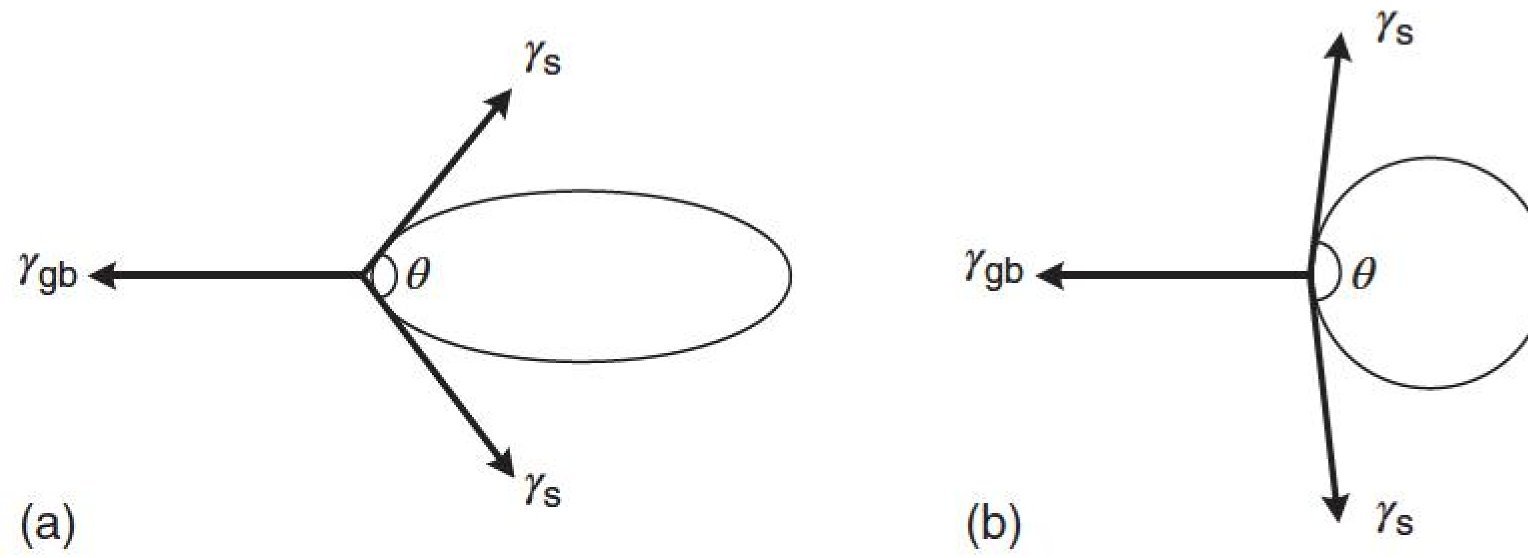
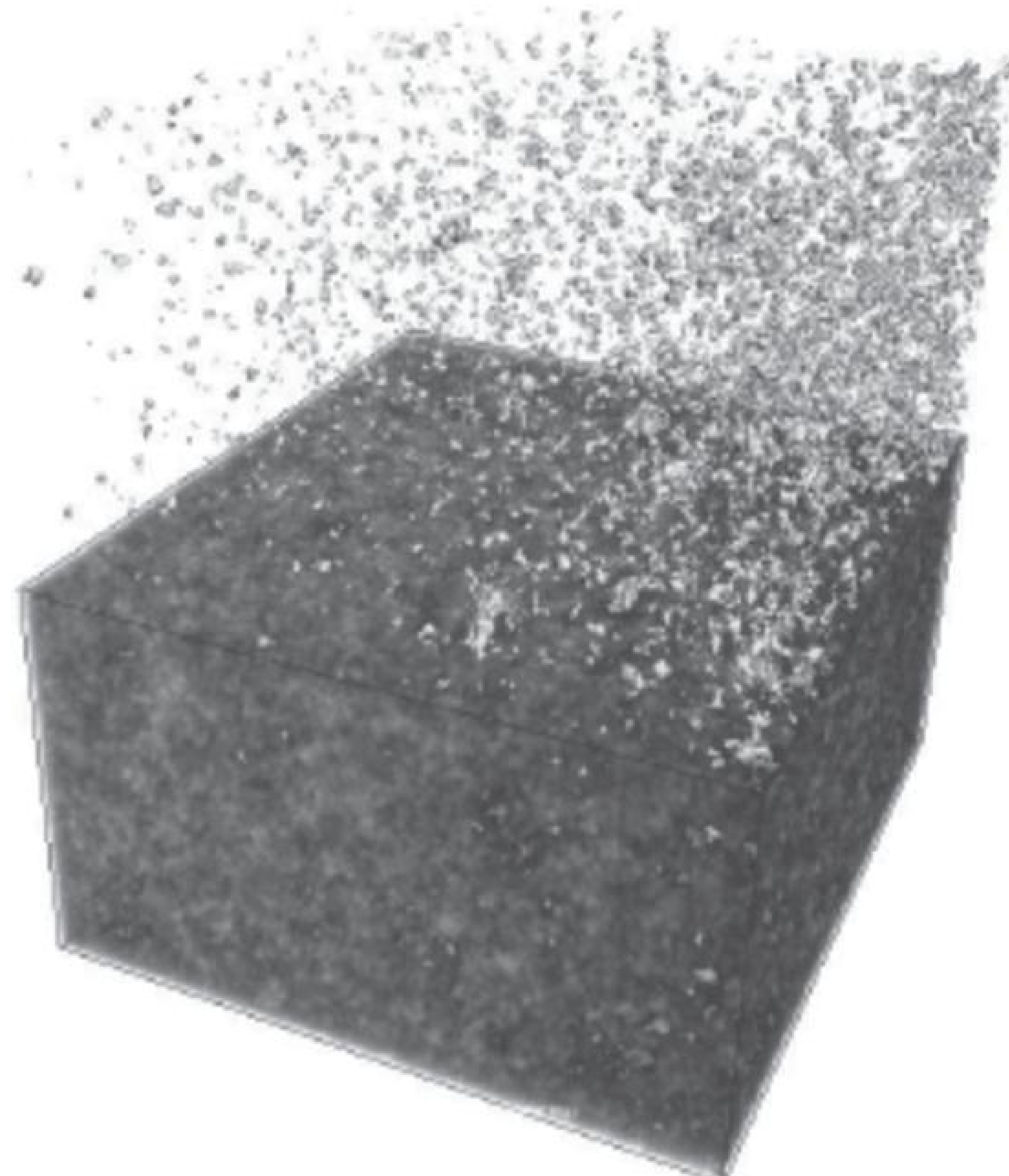


Figure 3.5 Schematics of the pore in the sintered (a) ZnO and (b) ZnO–Bi_2O_3 specimen. Source: Adapted from Lao et al. 2007 [64].

specimens are more round in shape, and the ability of the pore to pin the grain boundary is reduced [65]. Therefore, many pores are trapped within the ZnO grains, indicating that the grain boundaries sweep easily through the ZnO grains and left behind many pores. Because the pores are no longer able to attach to the grain boundaries and prohibit the grain growth, the size of the ZnO grains in the ZnO–Bi_2O_3 varistors is larger than that in the ZnO specimens. However, the size variation of the ZnO grains is also increased because of the change in the dihedral angle [66–69].

Recently, the pore distribution inside a ZnO varistor was measured by 3D X-ray computed tomography (XCT) (ZEISS Xradia 510 Versa), which revealed a three-dimensional (3-D) pore distribution inside the ZnO varistors, which achieves a 0.7 μm true spatial resolution with a minimum achievable voxel size below 70 nm. A typical laboratory micro-CT system is mainly based on the measurement of transmission of X-rays through the object over a range of angles. The test sample size was Φ2 × 2 mm. As shown in Figure 3.6 [70], the total pore volume in the sample is 1.43%. More pores are observed in the

Figure 3.6 The pore distribution inside a ZnO varistor sample. The test specimen was taken from the side of a varistor, and the right is the side face; the pore distribution is shown above the test specimen.



side face region of the varistor disc, which may be the reason that puncturings often occur in the varistor side region.

3.4 Role of Oxygen at the Grain Boundary

Han et al. [19] prepared undoped and Mn-doped ZnO samples sintered at 1200 °C in air; a set of samples was slowly cooled from the sintering temperature, and another set was quenched from that temperature. The slowly cooled Mn-doped samples showed a varistor behavior, whereas the quenched and the undoped ones showed an ohmic behavior. It could be concluded that the migration of defects to the grain boundaries during the cooling period is negligible. This, together with the experimental fact that Mn homogeneously distributed in ZnO, pointed to the possibility that the varistor behavior arose from an "intrinsic" mechanism. The quenched samples were then annealed at 800 °C in air, a process allowing the oxidation of the grain boundaries by ambient oxygen, without changes in the bulk defect chemistry conditions. They confirmed that the varistor behavior is not directly related to the presence of the dopant. The oxidation of the grain boundaries, proceeded by the elimination of the zinc interstitial species (the intrinsic donors in ZnO), and the analysis of the defect chemistry of undoped and Mn-doped ZnO samples allowed to conclude that the oxidation process takes place only when the majority of these species are double ionized. The amount of these species in the varistor samples is several orders of magnitude lower than that of the MnO added, a similar situation observed in the case of Bi-doped ZnO varistor systems [19]. In Mn-doped samples, the varistor behavior arises mainly by the oxidation of the double-ionized zinc interstitials near the grain boundaries, and probably, the same is true for any other dopants used to decrease the concentration of shallow donors below the deeper ones.

When the ZnO varistor was annealed in a reducing atmosphere (N_2, Ar, or vacuum), the leakage current increased [28, 71], and, in some cases, destroyed its nonlinear electrical behavior. Moreover, samples annealed at conditions that previously gave linear I–V characteristics, i.e. 800 °C, showed a linear I–V dependence when annealed under these conditions in an evacuated sealed tube. These effects can be reversed by annealing in air or oxygen [71]. This result indicates that annealing in air or oxygen is an essential requirement even in the presence of the elements Bi, Pb, and Sb [55]. This is in agreement with the investigations of Einzinger in which it was found that an oxidizing ambient is essential to achieve nonlinearity in the ZnO varistor [57].

It has been suggested that the varistor characteristics are related to the particular crystalline form that the Bi_2O_3 takes on [28, 71] with oxygen at the grain boundary interface [26]. The role of Bi as the "grain boundary activator" may, in the simplest scenario, be limited to supplying excess oxygen to the grain boundaries [28, 71]. As introduced before, the bismuth-rich phase is interconnected and continuous along the multigrain junctions throughout the microstructure. This topology is considered to be crucial for the transport of oxygen into the material during postsintering annealing. It is also stated that nonohmic properties can be enhanced using "highly oxygenated" Bi_2O_3 as the starting material [27].

The role of oxygen is to form a potential barrier at the grain boundary of metal oxide varistors [72]. Transitional elements, such as Co and Mn, are added to increase the varistor nonlinearity. The oxides formed by Co and Mn are acceptors, and their valence states may change in the grain boundary region, particularly with local changes in the oxygen potential. These transitional metal oxides generally have several oxidation states, which increase the amount of oxygen at the grain boundary. Therefore, the transition metal precipitated at the grain boundary becomes more oxidized when treated in an O_2-rich atmosphere, causing the electron-trapping interfacial region to become richer in the oxygen species. It is proposed that the grain boundary region has a "p-type semiconductor nature" because of the Co_3O_4- and Mn_3O_4-like phases precipitated at the grain boundary, whereas the bulk of ZnO-based varistor has an "n-type semiconductor nature" [72]. This structure enables electrons to become localized on the surfaces, giving rise to a negative surface (negative interfacial states). In order to maintain the local electrical neutrality, the charges are compensated by ionized shallow donors and bulk electron traps. As a result, electron depletion layers are formed and act as potential barriers. The potential barriers have a Schottky-like nature because of the negative interfacial states, and the selfsame nature is often found in all metal oxide varistors at higher temperature. Considering such a grain boundary configuration, annealing under a reducing atmosphere will eliminate excessive oxygen, allowing the metal atoms to remain and, thereby, decreasing the nonlinear electrical properties of the varistor. Therefore, the physical origin of the interfacial states is not an intrinsic one because of the lattice mismatch at the boundary, but an extrinsic one resulting from the metal atoms precipitated at the grain boundaries [72].

3.5 Dopant Effects

3.5.1 Effects of Additives

The basic structure of ZnO varistors is formed by adding Bi_2O_3 to ZnO. Bi_2O_3 makes potential barriers at the grain boundaries by behaving as a layer of intergranular material and by supplying ions to the ZnO grain boundaries [37]. In order to form the nonlinear property, at least 0.1 mol% Bi_2O_3 should be added to ZnO, but the potential barriers are not good enough with the nonlinear coefficient never higher than 10. By adding transition metal oxides such as CoO and MnO, the nonlinear property is dramatically improved by involving in the formation of interfacial states and deep bulk traps, and the nonlinear coefficients are as high as 40. By adding Sb_2O_3 to ZnO–Bi_2O_3–CoO–MnO varistor system, the grain size becomes smaller, and the nonlinear performance is further improved. Furthermore, the I–V characteristics become stable against electrical stresses, as shown by the higher breakdown voltages. The potential barriers of high nonlinear property are created and determined by using those four additives. Other monovalent or trivalent additives, such as Li and Al, also affect the shape of the potential barriers and the I–V characteristics by acting as donors or acceptors.

Prototype bismuth oxide doped ZnO varistors were devised in the early 1970s by Matsuoka [5]. It is composed of 97.0 mol% ZnO, 1.0 mol% Sb_2O_3, and 0.5 mol% each of Bi_2O_3, CoO, MnO, and Cr_2O_3. The electrical resistivity and dielectric constant of segregation layers are estimated to be 10^{13} Ω cm and 170, respectively. The nonlinear coefficient reached 50, and the average grain size was 10 μm. Commercially manufactured ZnO varistors usually contain four basic additives (Bi_2O_3, CoO, MnO, and Sb_2O_3) along with some additives to control the grain size, resistivity of ZnO, and stability.

Dopants play at least three major roles in forming varistors. They can affect grain growth during sintering, the dewetting characteristics of the liquid phase during cooling, and the electronic defect states that control the overall varistor characteristics [3]. Each of the dopants plays a distinctive role in the subtle tuning of the final nonlinear characteristics of the varistor ceramics and cannot be omitted. The dopant can act as a donor, an acceptor, or both, depending on the size of the guest ion, crystal structure of the host lattice, and the relative valency of the guest and host ions [73]. Usually, Bi is added as a nonlinearity inducer; Co, Mn, Sb, and Cr as nonlinearity enhancers; Sb and Si as grain growth inhibitors; and Cr as a stability enhancer. On the contrary, TiO_2 promotes grain growth. Also, the proper ratios among the dopants have to be set in order to obtain the required electrical performance of the varistor ceramics through the process of microstructure development [74]. However, the contribution of each additive has often been considered within the multicomponent system, and the performance of a ZnO varistor is the synergistic effect of multiple additives, so it is difficult to investigate the specific role of each dopant in the multicomponent system [19]. The main functions of different additives in ZnO varistors are summarized in Table 3.1.

Although the overall electrical characteristics of varistor ceramics result from the collective effect of all the microstructural features caused by dopants, two factors play key roles [74]. The first is the grain boundaries that exhibit nonlinear current–voltage characteristics and define the characteristics of the varistor in the prebreakdown region. The second is the ZnO grains that, with their size, define the number of grain boundaries between the electrodes and hence the breakdown voltage of the varistor and, with their conductivity, define the performance of the varistor at high currents in the upturn region of the current–voltage characteristic. Therefore, the "prebreakdown" current–voltage (I–V) characteristics are "grain boundary" controlled and the "upturn" I–V characteristics are "grain controlled." Some dopants have a significant effect on the prebreakdown and the upturn current–voltage characteristics of varistors even when much lower amounts of additives than standard are added to the varistor [74]. As illustrated in Figure 3.7 [73], the effect of donor doping on the grain and grain boundary will shift the entire I–V curve to the right and that of acceptor doping to the left. However, many additives have dual functions both as donors and acceptors to influence the grains and the grain boundaries.

How to isolate and study the effects of donor and acceptor dopings on the grain and grain boundary properties was called as "microstructural engineering" [73], which can be formalized into three hierarchical levels. The first level consists of identifying the dopants that are grain specific, grain boundary specific, or both.

Table 3.1 Roles of additives on the properties of varistors.

Additives	Roles
Bi_2O_3, Pr_6O_{11}, V_2O_5, BaO	Acts as varistor makers [1, 2, 5, 6, 9, 37, 75–80]
Sb_2O_3	Inhibits ZnO grain growth, enhances the nonlinearity and breakdown voltage, decreases the leakage current of varistor, triggers the formation of IBs in ZnO grains [5, 81–85]
MnO_2	Promotes ZnO grain growth, increases the grain boundary resistance [86], reduces the electrical conductivity of ZnO [87], helps to build up the potential barrier in the grain boundary, prevents the Bi_2O_3 evaporation, enhances the nonlinearity [2, 3, 88–91]
CoO	Reduces grain boundary resistivity [4, 92, 93], leads to the formation of the potential barrier in the grain boundary, and enhances the nonlinearity [2, 3, 88–91], and prevents Bi_2O_3 evaporation, improves stability [37]
Cr_2O_3	Enhances the nonlinearity and the energy absorption capability of ZnO varistor [2, 3, 88–91]
SnO_2	Forms spinel phase and controls the grain size by triggering the formation of inversion boundaries (IBs) in ZnO grains [48, 94]
CuO	Decreases both the grain and grain boundary electrical conductivities [95–98]
NiO	Controls the grain size, decreases the leakage current, increases the nonlinear coefficient and breakdown voltage [99]
TiO_2	Enhances grain growth, decreases breakdown field and improves DC degradation behavior, triggers the formation of IBs in ZnO grains [37, 100]
CeO_2	Inhibits grain growth, enhances the ohmic resistance and breakdown voltage, and reduces the leakage current [101]
Fe	Improves the nonlinear property and electrical barrier and reduces electrical conductivity of ZnO as a deep donor [102]
Al_2O_3, Ga_2O_3, or In_2O_3	Reduces the grain resistance [47, 103, 104] to increase the leakage current in the prebreakdown region and decreases the resistivity in upturn region [76, 105–108]
K^+, Li^+, Na^+	Controls the grain size, lowers the grain and grain boundary electrical conductivities [109, 110], decreases the leakage currents, and improves the stability of the varistor [73]
Ag_2O	Reduces the grain resistance of ZnO, promotes the densification and grain growth of ZnO, increases both the grain and grain boundary resistances in low doping level [111], and improves the stability of the varistor [73]
Rare earth oxides (REO): Pr_6O_{11}, Y_2O_3, La_2O_3, Nd_2O_3, Er_2O_3, Ce_2O_3, Dy_2O_3, and Ho_2O_3	Promotes the pyrochlore-phase formation, controlling different electrical parameters, inhibits grain growth, significantly increases the breakdown field and energy absorption capability [112–121], but degradation is accentuated with REO addition
Ta_2O_5	A small concentration results in high grain conductivity, but excessive Ta_2O_5 decreases both bulk conductivity and grain size [120]
WO_3, Nb_2O_5	Increases the conductivity of ZnO [122–124]
CeO_2	Inhibits grain growth [101]
SiO_2	Inhibits grain growth [37] and increases nonlinearity

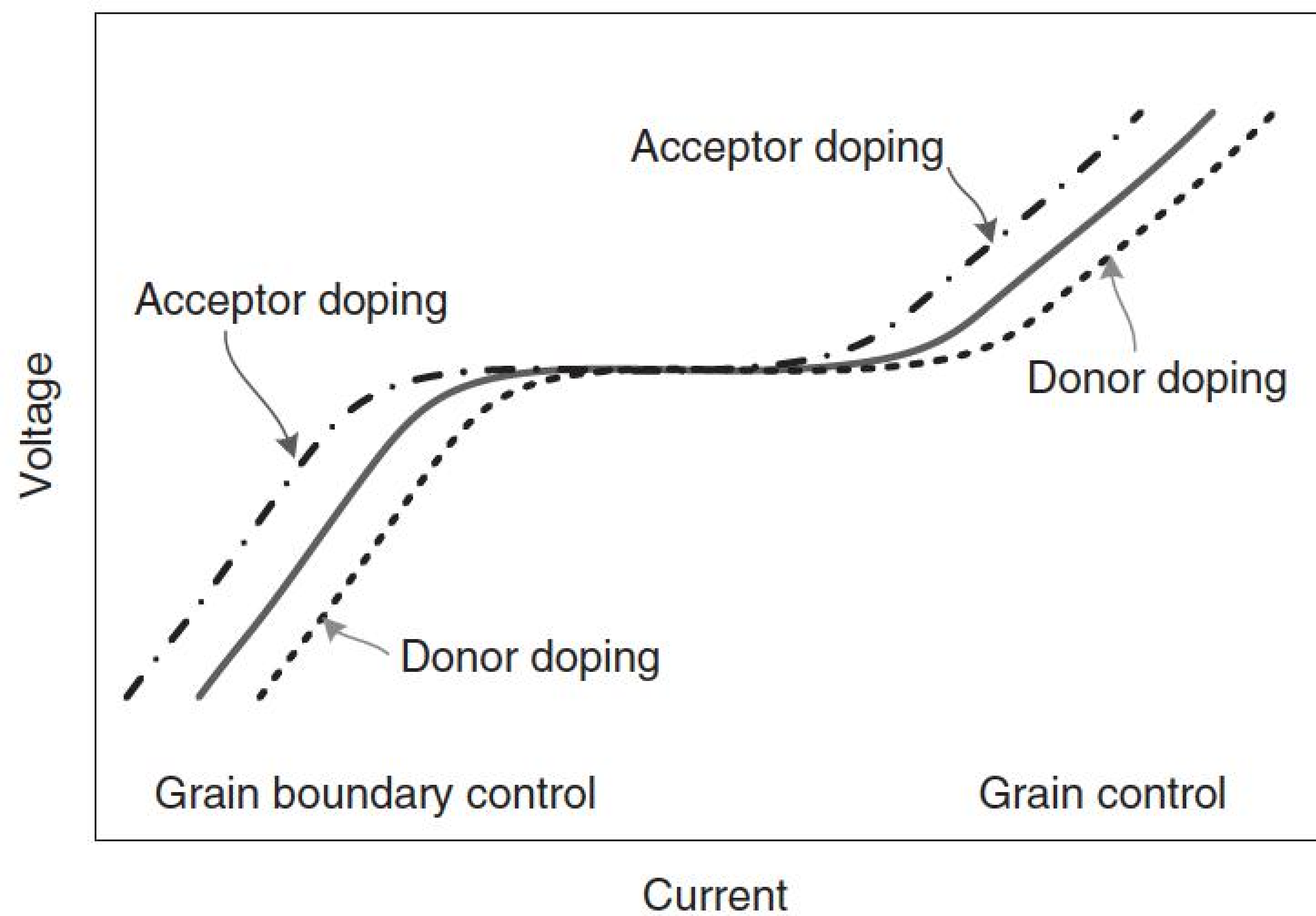


Figure 3.7 Effect of donor and acceptor doping on the current–voltage characteristics of the ZnO varistor. Source: Adapted from Gupta 1992 [73].

The second level is to determine whether the dopant is acting as a donor, an acceptor, or both. In the third level, the interactions between the dopants and the crystal lattice sites are of importance.

3.5.2 Donor Dopants

Donor dopants, as performance enhancers, generally increase the surface-state density and barrier height to improve the nonlinearity of ceramics at lower current density region and enhance the energy absorption capability of ZnO varistor systems, through the formation of interstitial states and deep bulk traps [20, 125]. There have been many investigations in an attempt to improve the voltage–current nonlinearity; these kinds of metal oxides have been so far incorporated into common commercial varistors for reducing leakage current [126].

Most transition metals have more than one oxidation state, with their valence electrons being present in more than one shell. These metals have unusual and useful electronic and magnetic properties, many of which strongly depend on material defects such as grain boundaries, vacancies, dislocations, and stacking faults. These defects affect local oxygen bonding. Usually, transition metal oxides, such as MnO_2, Co_2O_3, and Cr_2O_3, are added as donors [87]. These ions, in their divalent state, are known to go into solution in ZnO, but the energies of these donor states are not known, and their valence state may change in the vicinity of a grain boundary, especially with local changes in the oxygen potential [3, 127]. Most of the researchers thought that 3d transition metal impurities could enhance the excess oxygen concentration in the grain boundary region because of their decompositions from trivalence to divalence [4, 92, 93], and a potential barrier is formed there preferentially.

The nonlinear property is dramatically improved by involving in the formation of interfacial states and deep bulk traps when transition metal oxides such as CoO and MnO were added [37].

Mn is regarded behaving as a deep donor in ZnO with an ionization energy of around ~2.0 eV at room temperature and significantly depresses the concentration of intrinsic donors, interstitial zinc, during sintering [128]. When the samples are cooled to room temperature quickly, the condition at the sintering temperature could be frozen and the concentration of the intrinsic donors would also be low at room temperature [19, 128–131].

Consequently, Mn makes ZnO a more resistive material at room temperature, although the doping content is very low [87]. It plays no direct role in the conductivity of ZnO at room temperature because it is a deep donor, but it controls the carrier density through the interference on the concentration of the intrinsic donor defect. A similar conclusion was drawn by Einzinger [132], who stated that deep donors shift the concentrations of the intrinsic defects at the grain boundaries, decreasing the donor concentration and increasing the acceptor one, in such an amount that electrical barriers can be built up in those regions. Further study showed that samples quenched from the sintering temperature showed an ohmic behavior, up to 0.6 mol% MnO; any nonlinear behavior was not observed on the I–V curves of these quenched samples at room temperature [128], whereas a pronounced varistor behavior was found in the Mn-doped ZnO obtained by slow cooling from the sintering temperature or by annealing at a lower temperature [132]. From the defect equilibrium analysis, it was suggested that the varistor behavior in these samples was due to the oxidation of the double-ionized zinc interstitial defects present at the grain boundaries by ambient oxygen during cooling or annealing, and the presence of Mn in the ZnO grains induces this process [19].

Mn doping also promotes ZnO grain growth during sintering, and this promoting effect is enhanced with an increasing Mn doping level. From complex impedance measurements, it was observed that Mn doping mainly increases the grain boundary resistance with keeping the grain resistance almost unchanged. This fact suggests that excess Mn probably exists in the grain boundary region, either as a very thin second phase or as an amorphous film, which could benefit the grain boundary transport for grain growth [86].

The electrical resistivity of the intergranular region at lower ohmic current region is drastically increased by doping with Co [8]. Therefore, the origin of varistor action should be attributed not to this layer but to the interfacial region between the intergranular layer and the Co-doped ZnO grain where electronic depletion layers are formed.

Kim et al. [126] reported the onset of voltage upturn descended to lower current density because of the decrease of ZnO grain conductivity, as the Co_2O_3 concentration increases. Carlson and Gupta [76] reported that the grain conductivity is not always increased with the additions of such donor ions, but it seems to be because of a change in the carrier mobility in the ZnO grains. The change of grain conductivity by additions of Co_2O_3 is due to the variation of the carrier concentration N_d or the mobility [133]. By means of capacitance–voltage measurements, it is found that the N_d decreases as the dopant concentration increases. Co_2O_3 decomposes at about 900 °C [134] during sintering, and cobalt ions substituted for Zn^{2+} ions in the lattice sites of ZnO exist as Co^{2+} ions regardless of their initial valency state before sintering. Therefore, the substitutional

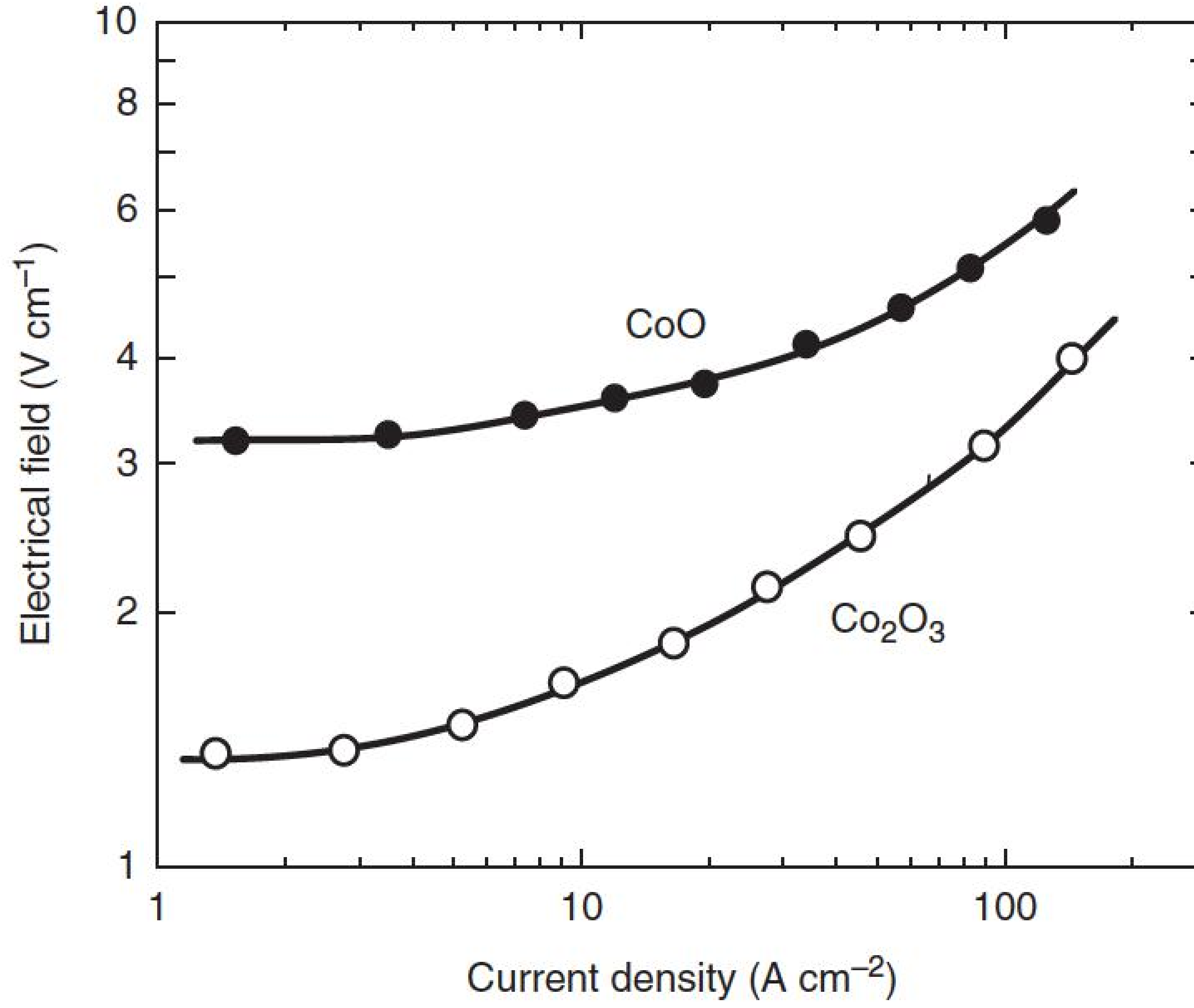
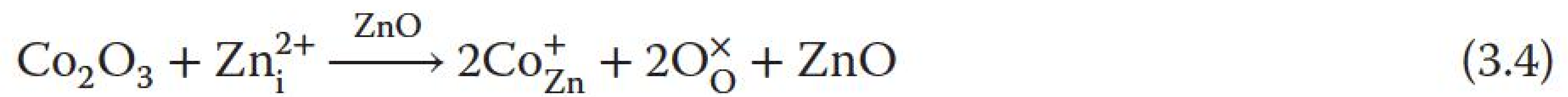


Figure 3.8 *E–J* characteristic at high current densities for the sample doped with Co_2O_3 and CoO. Co content in both systems is 1.0 at.%. Source: Adapted from Kim et al. 1985 [126].

reaction of Co_2O_3 may be the same as an addition of CoO to ZnO when that reaction occurs in an atmosphere of ambient oxygen. As shown in Figure 3.8, it can be seen that the upturn in the sample doped with CoO occurs at lower current density than in the case of Co_2O_3 doping, which reveals that the grain conductivity of the CoO-doped ceramic is higher than that of the Co_2O_3-doped ceramic. It is a well-known fact that the electrical conductivity of a ZnO crystal is limited by the oxygen partial pressure. Thus, the lowered grain conductivity of the samples doped with Co_2O_3 can be explained in terms of the increased oxygen partial pressure due to the decomposition of the Co_2O_3 during the sintering process. The substitutional reactions of Co_2O_3 to ZnO have been presented by ref. [126]:



$$Co_2O_3 + Zn_i^{2+} \xrightarrow{ZnO} 2Co_{Zn}^{+} + 2O_O^{\times} + ZnO \tag{3.4}$$

and



$$Co_2O_3 + V_O^{2+} \xrightarrow{ZnO} 2Co_{Zn}^{+} + 3O_O^{\times} \tag{3.5}$$

Co_{Zn}^{+} itself does not affect the donor density because it forms a deep trap below the Fermi level of the ZnO grain with a neutral state.

The carrier mobility is increased by the addition of Co_2O_3 at a lower dopant concentration and reaches to a maximum value about 0.5 mol% Co_2O_3 but decreases with an increased addition of Co_2O_3 beyond 0.5 mol%. The mobility variation is considered to arise from the change in the concentration of defect such as Co_{Zn}^{+}, Zn_i^{2+}, V_O^{2+}, and other impurities, according to Eqs. (3.4) and (3.5). The higher carrier mobility of the samples with the Co_2O_3 content smaller than 0.5 mol% is attributed to the remarkable decrease in donor concentration and concentration of Zn_i^{2+} or V_O^{2+} in the ZnO grains, whereas a relative reduced mobility in the samples with Co_2O_3 concentration higher than 0.5 mol% is due

to the higher concentration of Co_{Zn}. In the case of highly doped ZnO varistors containing more than 0.5 mol% Co_2O_3, the lowered carrier mobility improves the decrease in grain conductivity [126].

Long et al. [135] further studied the effect of Co_2O_3 in a larger concentration range and provided a more microstructural explanation for the doping effect of Co_2O_3. With an increased amount of doped Co_2O_3, the sample's nonlinear coefficient α has an inverted U-shape, and the respective leakage current exhibits a U-shape. In addition, the breakdown electric field E_{1mA} increases slightly, and both the donor density N_d and the barrier height ϕ_b of the varistor samples decrease with an increase in the doped Co_2O_3 content. The X-ray diffraction (XRD) patterns show that the microstructure mainly comprises the ZnO phase, spinel phase, Bi_2O_3 phase, BiO_{2-x} phase, and willemite phase. The spinel phase, which comprises $Zn_{2.33}Sb_{0.67}O_4$ and $Co_{2.33}Sb_{0.67}O_4$, almost does not change with the increase in the doped cobalt content. The spinel phase plays an important role as the grain growth inhibitor during the sintering process. The δ-Bi_2O_3 phase is observed. The BiO_{2-x} phase is also identified, whose intensity peak keeps on rising with the increase in the doped cobalt content. The BiO_{2-x} phase can reduce the leakage current and improve the nonlinear coefficient of the ZnO varistor sample. It is known that more BiO_{2-x} phase will be formed under oxygen-rich atmosphere during the sintering process [126]. On the other hand, Co_2O_3 will decompose to CoO at 895 °C and provide extra oxygen ions. Thus, the extra oxygen ions will not only decrease the donor density but also forms the BiO_{2-x} phase. As a result, the interface-state density increases and the electrical characteristics of the ZnO varistor samples are improved with the increase in the doped Co_2O_3 content. In addition, more Co^{2+} or Co^{3+} ions dissolved into the Bi-rich phase will also increase the interface-state density and improve the electrical characteristics of the varistor samples, including the increment of the breakdown electric field E_{1mA} in a small extent. The willemite phase disappears when the doped Co_2O_3 content is more than 3 mol%. It is supposed that excessive Co^{3+} ions enter into the ZnO grains, spinels, and grain boundaries with the Bi-rich phase, which destroy the original microstructure and component partly, and result in the degradation of the electrical characteristics of the varistor samples.

Ni_2O_3 is another additive to improve the grain boundary performance, including decreasing the average grain size and the leakage current and increasing the nonlinear coefficient and the breakdown voltage [99, 136]. However, the leakage current then increases with the increase in the doped Ni_2O_3 content, as Co_2O_3 does. Conversely, the nonlinear coefficient α increases firstly and then decreases. The N_d and ϕ_b decrease with the increase in the doped Ni_2O_3 content. Except the BiO_{2-x} phase, the δ-Bi_2O_3 phase is also observed. The intensity of the δ-Bi_2O_3 phase keeps on decreasing with the increase in the doped Ni_2O_3 content. A new phase, the chrombismite $Bi_{16}CrO_{27}$ phase, is observed when the content of doped Ni_2O_3 is more than 2 mol%. With an increasing doped Ni_2O_3 content, each peak of the spinel phase moves to the right obviously; this distinct movement of the spinel's diffraction peak represents the huge alteration of the lattice constant of the spinel phase. These might be caused by solidly solving the Ni ions into the spinel phase or the formation of chrombismite.

3.5.3 Acceptor Dopants

Acceptor dopants, as grain growth inhibitors, generally increase the threshold voltage by controlling the grain size to decrease the leakage currents and displace the $I-V$ curve to lower current densities, which decrease the carrier concentration. The number of grains between the electrodes decides the breakdown voltage and the energy absorption capability of ZnO varistors. Therefore, controlling the grain size is very important in the fabrication of ZnO varistors, which can be practiced by changing both the defect structure and the particle pinning of the grain boundaries. Ideally, the dopants used to control the grain growth would be different from those used to control the grain boundary potential barriers, but, at this stage, none of the dopants reported in the literatures appears to be inert and affect only grain growth [3]. Sintering in combination with some spinel-forming dopants, such as Sb_2O_3, TiO_2, and SnO_2, allows the microstructure development and grain growth to be controlled [137, 138].

Sb_2O_3 is a powerful grain growth inhibitor for ZnO [25, 66, 139] and enhances the solubility of ions, such as Zn in the Bi_2O_3-rich liquid phase; this is very important for the defect distribution formed at the grain boundaries during cooling [37], so its effect on the sintering behavior, grain boundary chemistry, and electrical performance of ZnO attracted much attention [139, 140]. Sb_2O_3 is a standard spinel-forming dopant to produce fine-grained, high-voltage varistor ceramics. It enhances the nonlinearity and breakdown voltage, decreases the leakage current of the varistor ceramics, and reduces the evaporation of Bi_2O_3 during sintering [83, 84]. However, the major role of Sb_2O_3 is to control the growth of the ZnO grains [48].

Two roles are proposed for Sb_2O_3. One is to suppress grain growth by forming the $Zn_7Sb_2O_{12}$ spinel. Above 700 °C, Sb_2O_3 reacts with both ZnO and Bi_2O_3 and forms $Zn_7Sb_2O_{12}$ and $Zn_2Bi_3Sb_3O_{14}$ pyrochlore-type crystalline phases [45]. During sintering, the $Zn_2Bi_3Sb_3O_{14}$ decomposes a Bi_2O_3-rich liquid phase and $Zn_7Sb_2O_{12}$ spinel-type crystallites. The Bi_2O_3-rich liquid phase changes to β- or α-phase Bi_2O_3-rich intergranular layers during cooling. $Zn_7Sb_2O_{12}$ precipitates at the grain boundaries. The inhibition of ZnO grain growth in the Sb_2O_3-doped samples is generally explained by a reduction in the mobility of grain boundaries by a pinning effect, caused either by the spinel particles of $Zn_7Sb_2O_{12}$ or a fine Sb-rich film on the surface of the ZnO grains [66, 83, 141, 142] – with larger additions of Sb_2O_3, more spinel grains are produced and the ZnO grains become smaller. The other is the addition of Sb_2O_3, which also triggers the formation of IBs in practically every ZnO grain of the varistor ceramics [85]. The structure and chemistry of IBs in the Sb-doped ZnO were determined by Rečnik et al. [143]. Daneu et al. [137] revealed their influence on grain growth, and the possibility to tailor the ZnO grain size with an IB-induced grain growth mechanism was confirmed in the ZnO ceramics doped with small amounts of Sb_2O_3 [48]; the number of very large grains is smaller in the ZnO–Bi_2O_3–Sb_2O_3 system [64]. The addition of Sb_2O_3 increases the breakdown voltage of the grain boundary significantly [64]. More details related to the role of IBs will be introduced in Section 3.6.

TiO_2 is commonly used as the grain-growth-enhancing additive to obtain a coarse-grained microstructure [144–147]. The TiO_2/Bi_2O_3 ratio defines the

phase equilibrium and hence the temperature at which the liquid phase occurs in the system, so the selection of a proper TiO_2/Bi_2O_3 ratio and the heating rate matter when it comes to obtaining the required low-voltage varistor ceramics. In TiO_2-doped, ZnO-based varistor ceramics, the grain growth controlled by an IB-induced grain growth mechanism results in a coarse-grained microstructure [48]. In low-voltage varistor ceramics, the grain growth is affected only by the primary Zn_2TiO_4 spinels in compositions with a TiO_2/Bi_2O_3 ratio higher than 1.5, whereas in compositions with a lower ratio, the spinels that form together with the Bi_2O_3 liquid phase in the decomposition reaction of the $Bi_4Ti_3O_{12}$ phase have no effect on the grain growth [48].

It is found that the TiO_2 and Sb_2O_3 dopants have a synergistic effect on the ZnO varistor, and the Ti/Sb ratio greatly influences the microstructure and electrical properties of the ZnO varistor. The grain size does not decrease monotonically with the decrease of Ti/Sb ratio. The specimen with a Ti/Sb ratio of 5 has the lowest breakdown field (20 V mm^{-1}) and improved DC degradation behavior. When the Ti/Sb ratio is decreased to 2, IBs appear to form in the ZnO grains, which result in the broad grain size distribution and reduce the average breakdown field of the sample [100].

Like Sb_2O_3 and TiO_2, the addition of SnO_2 to the ZnO-based ceramics also results in the formation of the Zn_2SnO_4 spinel phase and triggers the formation of IBs in the ZnO grains [48]. The substitution of Sb_2O_3 with SnO_2 results in an identical microstructure and a comparable breakdown voltage of ZnO-based varistor ceramics [94].

CeO_2 is another addition to physically significantly inhibit the grain growth of $ZnO–Bi_2O_3$-based varistor [101]. The average grain size decreases as the CeO concentration increases, resulting in a substantial increase in the breakdown field. The density of all the well-formed varistor samples was above 95% of the theoretical value. The influence of the CeO_2 addition on the nonlinear coefficient α is very weak, but the leakage current was improved via enhancing the ohmic resistance and breakdown voltage. Thus, incorporation of CeO_2 is likely to be one of the ways to achieve high electric field ZnO-based varistor materials for potential cost-effective applications.

SiO_2 was also used to suppress the growth of ZnO grains [37], a part of which solutes in the Bi_2O_3-rich liquid phase to increase the viscosity of the liquid phase and weaken the growth of ZnO varistors, and the other part of additive SiO_2 acts with the ZnO grain to grow the spinel of Zn_2SiO_4 and to obstacle the growth of ZnO grains.

3.5.4 Amphoteric Dopants

Many monovalent dopants (such as Ag, Li, and Cu) and trivalent dopants (such as Al, Ga, and In) have significant influences on the microstructural and electrical characteristics of varistors, obviously act as amphoteric dopants [105–108, 148–150], and occupy both the lattice and interstitial sites. Depending on the concentration and the site of its incorporation into the ZnO lattice – regular Zn sites or interstitial sites – amphoteric dopant can act both as a donor and an acceptor, which defines its influence on the conductivity of the ZnO grains and also

the characteristics of the grain boundaries. Being both grain and grain boundary specific, the entire $I-V$ curve is moved to the right when it acts as a donor and to the left when it acts as an acceptor.

3.5.4.1 Monovalent Dopants

Ag addition influences the microstructural evolution and electrical properties of ZnO varistors by occupying both the lattice and the interstitial sites [21, 111], which not only decrease the nonlinearity but also increase the resistance to degradation [3]. The addition of a very small amount of the Ag dopant increases both the grain and the grain boundary resistances. The Ag solutes tend to segregate at the grain boundaries, and this segregation of Ag^+ ions significantly raises the grain boundary resistance, which even increases one order of magnitude. The presence of Ag^+ segregating at the grain boundaries establishes a space charge zone near the grain boundary [151] and an electrostatic barrier against electron transportation. The barrier is approximately 2 V for a single grain boundary [111].

Ag^+ would preferentially choose to sit in the vicinity of grain boundaries because of its large ionic radius [111]. The radius of Ag^+ is much larger than that of Zn^{2+}; the segregation of Ag ions may hence induce considerable disorder or distortion near the grain boundaries [152], which may provide routes or spaces for fast mass transportation. The ZnO grains thus grow faster because of the presence of Ag solutes near the grain boundaries [111]. Because of the charge difference between Ag^+ and Zn^{2+}, the substitution of Zn by Ag at the lattice sites would result in the formation of Ag acceptors, as suggested by [21]



$$2\text{Ag} \xrightarrow{\text{ZnO}} 2\text{Ag}_{\text{Zn}}^{-} + \text{V}_{\text{O}}^{2+} \tag{3.6}$$

Because of the formation of Ag acceptors, the grain resistance increases [21].

Further increasing the Ag doping level lowers the grain boundary resistance. A large number of Ag inclusions are left at the grain boundaries and grain triple junctions after co-firing. Because the solubility of Ag in ZnO is low, a relatively large amount of Ag inclusions reduces not only the mean grain size but also the grain size scattering [111].

Doping Li has a similar effect as Ag. Both the electrical conductivities of grains and grain boundaries are lowered in the Li-doped ZnO. The Li doping causes the formation of acceptor levels in ZnO [99, 100]; this leads to lowered DC electrical conductivity of the Li-doped ZnO.

Doping Cu can significantly decrease the electrical conductivities of both grain and grain boundaries [87]. The Cu-doped ZnO varistor is the most resistive, and the electrical conductivity is five orders of magnitude lower than that of the undoped ZnO. When the Cu-doped ZnO is experienced high temperature over 1000 °C, Cu could exist in ZnO as Cu^+, which is probably more stable at high temperatures. Fons et al. [95] proved that the valence of Cu is +1 in the Cu-doped ZnO. The Cu^+ ions are substituted for Zn^{2+} ions in the ZnO lattice and exhibit as an acceptor-type impurity [96–98]. Because the extrinsic donor is absent in the Cu-doped ZnO varistor, Cu^+ has to be compensated by either the intrinsic donor or the hole to maintain the electroneutrality, and the electrical conductivity in the n-type ZnO semiconductor decreases greatly by Cu doping.

The acceptors will be compensated by electrons in the grain because there are some intrinsic donors there.

However, because the concentration of the intrinsic donors is much lower in the grain boundary, the acceptors have to be compensated by the holes in this region. Moreover, Cu doping also has a great effect on the grain boundary because of the same interaction with ambient oxygen as the other 3d transition metal impurities [87]. Because of the above two reasons, the grain boundary of the Cu-doped ZnO varistors is more resistive. The grain boundary is over two orders of magnitude more resistive than the grain, and the total resistance of the Cu-doped ZnO specimens is almost completely caused by the grain boundary. Kutty and Raghu [97] reported that the measurement range was about 1–1000 $V\,cm^{-1}$. Cu can be an effective doping element to build up the potential barrier in the grain boundary of ZnO.

3.5.4.2 Trivalent Dopants

Carlson and Gupta [76] found that small additions of Al or Ga caused a delay in the onset of the upturn region. However, at higher levels of Al or Ga, the upturn region occurs at lower current density, and only small amounts of Ga or Al are required to generate high nonlinear coefficients α. In the low current density range, larger amounts of the dopants are required to achieve the same α values as in the high current density range. Overall, small additions of Al or Ga improve the high-current upturn characteristics and the nonlinearity.

Al doping is more complex that it is accommodated both at the grain and grain boundaries; it acts as a donor in lower concentrations and as an acceptor in higher concentrations [73]. As a shallow donor, it increases the electrical conductivity of ZnO grains and improves the varistor behavior at high currents [21, 76, 98, 129, 153–156], but it also results in an increased leakage current of the varistor in the prebreakdown region. As an acceptor, it reduces the leakage current of the varistor, but it also reduces the conductivity of ZnO grains, which has a negative effect on the varistor response to high currents and hence its energy characteristics [74].

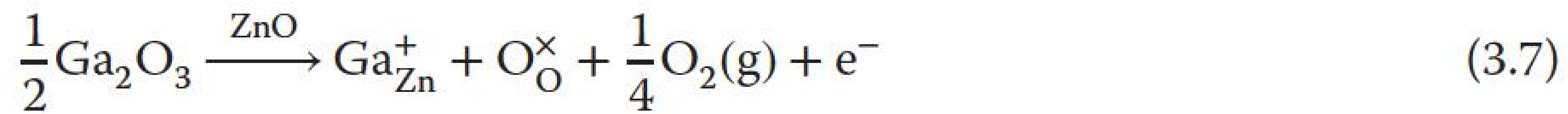
At lower concentrations of Al, up to a few thousand ppm, it is mainly the donor effect that is observed, whereas at higher concentrations, above 10 000 ppm, the acceptor effect prevails [73, 76]. Doping with Al_2O_3 influences the grain growth of ZnO even for amounts as small as several tens of parts per million added to the varistor composition [73, 76, 157]. The results indicate that the small amounts of Al_2O_3 present in the Bi_2O_3-rich liquid phase at the sintering temperature hinder the ZnO grain growth [74]. Although at higher levels of doping, i.e. several thousands of parts per million, the inhibition is attributed to the decreased mobility of the grain boundaries because of the $ZnAl_2O_4$ spinel phase [59, 158]. It showed that additions of Al_2O_3 in the range up to a few hundreds of parts per million are optimal and that they significantly and specifically influence the threshold voltage, the nonlinear coefficient, and the leakage current of the varistor [74].

By using energy-dispersive X-ray spectroscopy (EDXS) and WDXS analysis, most of the Al was distributed between the $Zn_7Sb_2O_{12}$-type spinel phase and the ZnO phase, whereas only a smaller share either remained dissolved in the Bi_2O_3-rich phase or possibly segregated at the grain boundaries of ZnO,

but which strongly influenced the current–voltage characteristics of the grain boundaries and also the grain growth [74].

There is a transition from donor-type behavior to acceptor-type behavior. Miyoshi et al. [105] observed the transition doping level for Al from 2000 to 20 000 ppm. Gupta [106] predicted that the transition for Ga would be at a lower level than that of Al because of the larger ionic radius of Ga (0.62 Å for Ga and 0.53 Å for Al). It is concluded that the transition between the donor- and acceptor-like behavior occurs for the additions of Ga between 1500 and 2000 ppm.

The breakdown fields of gallium-containing varistors are higher than those of the gallium-free varistors, as a result of the change in the grain size. As the gallium content is increased from 1000 to 1500 ppm, the leakage current density increases significantly. This is consistent with the donor-type behavior caused by the substitution of gallium on zinc lattice sites, as described by [148]



$$\frac{1}{2}\mathrm{Ga_2O_3} \xrightarrow{\mathrm{ZnO}} \mathrm{Ga}_{\mathrm{Zn}}^{+} + \mathrm{O}_{\mathrm{O}}^{\times} + \frac{1}{4}\mathrm{O_2(g)} + \mathrm{e}^{-} \tag{3.7}$$

Substitution of Ga^{3+} ions into zinc lattice sites results in an increase in carrier concentration. This increases the leakage current by decreasing the resistivity of the grain boundary.

The donor effect on the high current resistivity in the upturn region has been widely investigated [76, 105], and it has been shown that the donor ions such as Al^{3+}, Ga^{3+}, and In^{3+} can indeed delay the onset of voltage upturn to higher current density. The effectiveness of donor doping becomes clear by examining the dynamic "apparent resistivity" of the varistor, which is shown in Figure 3.9 as a series of isoresistivity lines superimposed on the I–V curve, with the magnitude of resistivity (decreasing from the left to the right) from that of the grain boundary to the grain. From this simple representation of the I–V curve combined with the knowledge of expected resistivity at each point of the I–V curve and the fact that the upturn region is grain resistivity controlled, note that a simple decrease in grain resistivity is all that is needed to increase the high current nonlinearity of

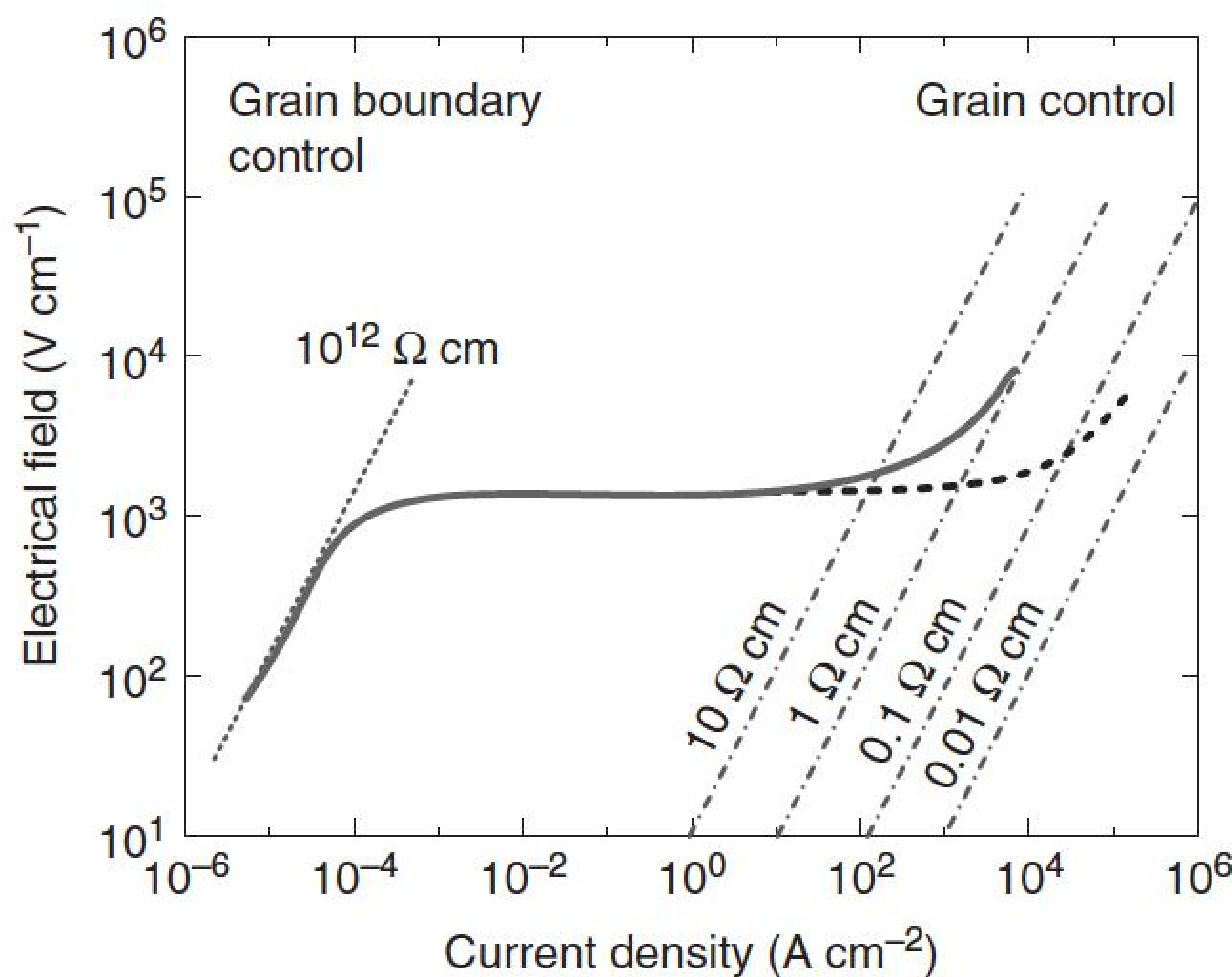


Figure 3.9 *I–V* characteristic of a ZnO varistor in relation to microstructure of the device: grain-boundary-controlled region at low current densities and grain-controlled region at high current densities and the isoresistivity lines representing the slope of the *I–V* curve. Source: Adapted from Carlson and Gupta 1982 [76].

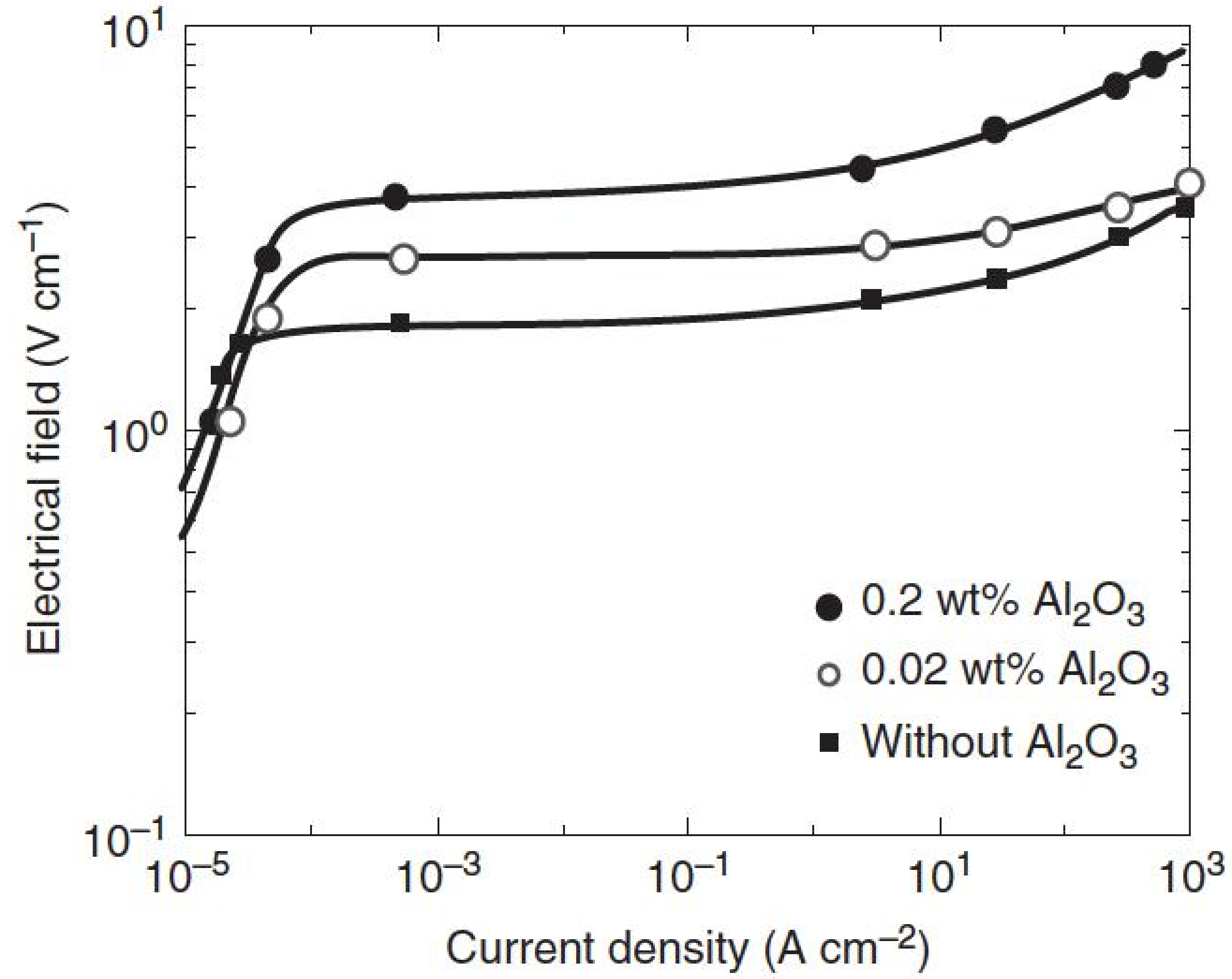


Figure 3.10 Effect of Al_2O_3 addition on the flatness (nonlinearity) of the *I–V* curves in the high current region. Source :Adapted from Carlson and Gupta 1982 [76].

the varistor. Both Al^{3+} and Ga^{3+} have been shown to decrease the grain resistivity and increase the high current nonlinearity of the varistor [3]. Figure 3.10 shows the dramatic effect of Al^{3+} doping on the high current nonlinearity of the varistor [76], and the beneficial effect of 0.02 wt% $A1_2O_3$ on the onset of voltage upturn is clearly indicated by the extended flatness of the $I–V$ curve to higher current density. This translates to a higher nonlinear coefficient from 16 with no addition of Al_2O_3 to 31 with 0.02 wt% $A1_2O_3$ in the current range of 0.5–750 A cm^{-2}. The grain resistivity decreases correspondingly from 0.76 to 0.18 Ω cm^{-1}.

The subsequent increase of gallium doping to 2000 ppm and higher caused the leakage current density to decrease and remain low. The net increase in the grain boundary resistivity, accompanying the transition to the acceptor-type behavior for Ga, may occur as Ga ions begin to occupy sites normally occupied by zinc interstitial ions [148], i.e.



$$\frac{1}{2}Ga_2O_3 \rightarrow Ga_i^- + h + \frac{3}{4}O_2(g) \tag{3.8}$$

where Ga_i^- is the gallium ion in the zinc atom interstitial site and h is the hole with a positive charge.

Fe_2O_3 is a fatal additive for the ZnO–Bi_2O_3 system [159]. The replacement of Zn^{2+} by Fe^{3+} does not influence the Wurtzite structure of undoped ZnO samples, and other impurity phases are not formed. However, Sedky et al. [102] claimed that further addition of Fe doping improved the nonlinear properties of the ZnO varistor, and the electrical barriers could be formed. Moreover, doping by Fe is found to reduce the electrical conductivity of pure ZnO samples. It seems that Fe doping affects the bulk conductivity of ZnO probably by affecting the defect chemistry of the bulk ZnO, and it behaves as a deep donor and depresses the concentrations of the intrinsic donors at the sintering temperature. However, Fe doping does not give a direct contribution to the conductivity of ZnO because the Fe deep donors cannot be ionized at room temperature because of their high ionization energy (~2 eV). It is supposed that the Fe^{3+} ion, as well as the Al^{3+} one, can enter into the structure and have preference for interstitial sites by substituting

Zn on its regular site at first and then moving to the interstitial position. At an interstitial position, the Fe ion follows the following reaction and absorbs an electron [87, 160]:



$$\frac{1}{2}Fe_2O_3 \rightarrow Fe_i^- + h + \frac{3}{4}O_2(g) \tag{3.9}$$

where, Fe_i^- is the ionized Fe atom in an interstitial site and h is the hole with a positive charge. In this case, Fe behaves as an acceptor, dominates the donor effect, and decreases the conductivity in the region ($0.00 < x \leq 0.1$). With an increasing Fe content ($0.10 \leq x \leq 0.5$), the solubility limit of Fe through the interstitial position is approached, and Fe behaves as an acceptor. The acceptors have to be compensated by the holes in this region and keep the conductivity unchanged [102].

3.5.5 Effects of Rare Earth Oxides

Many studies [112–119, 161–176] have been made in order to understand the influence of different rare earth oxides (REO) (such as Pr_6O_{11}, Y_2O_3, La_2O_3, Nd_2O_3, Er_2O_3, Ce_2O_3, Dy_2O_3, and Ho_2O_3) on the microstructure and electrical properties of the ZnO varistor ceramics. These investigations indicate that the REO play an important role in controlling different operation parameters of the ZnO varistor devices. The REO apparently promotes the pyrochlore-phase formation, significantly increases the breakdown field without deterioration in the performance of the varistor, and allows reaching a large energy absorption capability value for the high threshold voltage ZnO-based varistors. Varistors present more active grains and hence a larger conduction section, which accounts for large absorption capability [112].

The influence of REO on the microstructure of samples is very significant, which decreases the sizes of both ZnO grains and spinel phases. Compared to the case without REO, the main REO effect is to return the microstructure of more homogeneous varistor because of the spinel phases and the finer pyrochlore (with Pr and with Nd) formation, which distribute everywhere in the ZnO grain junction length. The results might be explained from the microstructure formation, and REO apparently promote the pyrochlore-phase formation. Furthermore, there is less liquid for material transfer and for spinel growth. In other words, the "pinning action" of the spinel grains directly depends on the pyrochlore formation and decomposition [112]. The morphology of ceramics is strongly modified by the presence of a small quantity of REO. Insulating spinel clusters are transformed into individual spinel grains that are distributed alternatively with pyrochlore phases Pr or Nd to the place of the triple joints of ZnO grains. There remain only ZnO grains and grain boundaries in the conduction chain between the electrodes. It results in increasing energy absorption capability [112].

It is well known that rare earth elements can improve the electric field of ZnO-based varistor ceramics and show similar effects to Bi_2O_3, which makes potential barriers at the grain boundaries by becoming itself a layer of intergranular material and by supplying ions to the ZnO grain boundaries [170].

The microstructure and electrical properties of Ho_2O_3-doped Bi_2O_3-based ZnO varistor ceramics were investigated [112]. The microstructure shows a decrease in the grain size of the ZnO phase with the Ho_2O_3 doping content. The EDAX and XRD analysis show the presence of ZnO, Bi-rich, spinel $Zn_7Sb_2O_{12}$, and Ho_2O_3-based phases. The nonlinear coefficient obtained from electric field–current density plots has a maximum value of 78 for the ceramics with 0.50 mol% Ho_2O_3 content, and the leakage current has a respective minimum value of 1.30 μA. The breakdown field was found to increase with the Ho_2O_3 content.

The ZnO–Bi_2O_3-based varistor ceramics doped with 0.3 mol% Sc_2O_3 prepared by high-energy ball milling and sintered at 1000 °C exhibited not only high nonlinearity with a nonlinear coefficient of 62.1 but also a high breakdown field with a value of 821 V mm^{-1} of the threshold voltage [172]. The results also confirmed that doping with Sc_2O_3 is a very promising route for the generation of electronic properties of the ZnO–Bi_2O_3-based varistor ceramics.

The La_2O_3-doped ZnO-based varistor ceramics with the addition of 0.08 mol% La_2O_3 exhibit comparatively ideal comprehensive electrical properties [173], the threshold voltage is 320 V mm^{-1}, the nonlinear coefficient is 36.8, and the leakage current is 0.29 μA. The doping of La_2O_3 affects the formation and decomposition of pyrochlore. Although another study [174] showed that the varistors with 0.5 mol% La_2O_3 exhibited excellent nonlinear properties, the nonlinear coefficient equals to 81.6 and the leakage current is 0.2 μA.

However, degradation is accentuated with REO addition. Nahm et al. [177] and Wang et al. [178] reported that the addition of Nd_2O_3 to the ZnO-based varistors can greatly enhance the nonlinearity of the varistor's behavior, but the varistors exhibit very poor behavior in breakdown field. The breakdown field decreases with the increase of Nd_2O_3 content when the content of Nd_2O_3 is 0.04 mol% [179]. Bernik et al. [117, 180] also found that the fine-grained Y_2O_3-containing phase present at the grain boundaries strongly inhibits ZnO grain growth, whereas the leakage current increases with increasing amounts of Y_2O_3.

3.5.6 Dopants for Improving the Stability

ZnO varistors are usually subject to a continuous electrical stress; the continuous leakage current and the resultant Joule heat may degrade the electrical properties of the device. Therefore, in addition to nonlinearity, the electrical stability is a technologically important characteristic of the ZnO varistors.

Na, K, Li, and Ag, are grain-boundary-specific dopants and act as donors in small concentrations and as acceptors in large concentrations. By being exclusively grain boundary specific, Na and K also improve the stability of the varistor, which is controlled by the grain boundary leakage [73]. Usually, AgO is added to improve the stability of ZnO varistors [21, 108, 111, 181].

The DLTS has been successfully applied to the ZnO varistors [181–186]. DLTS measurements can be used (i) to identify the traps in barrier depletion regions and the associated defects that may be responsible for the changes in the electrical properties, (ii) to probe the energy levels of the traps, and (iii) to provide information about the density of the traps. Such data can aid our understanding

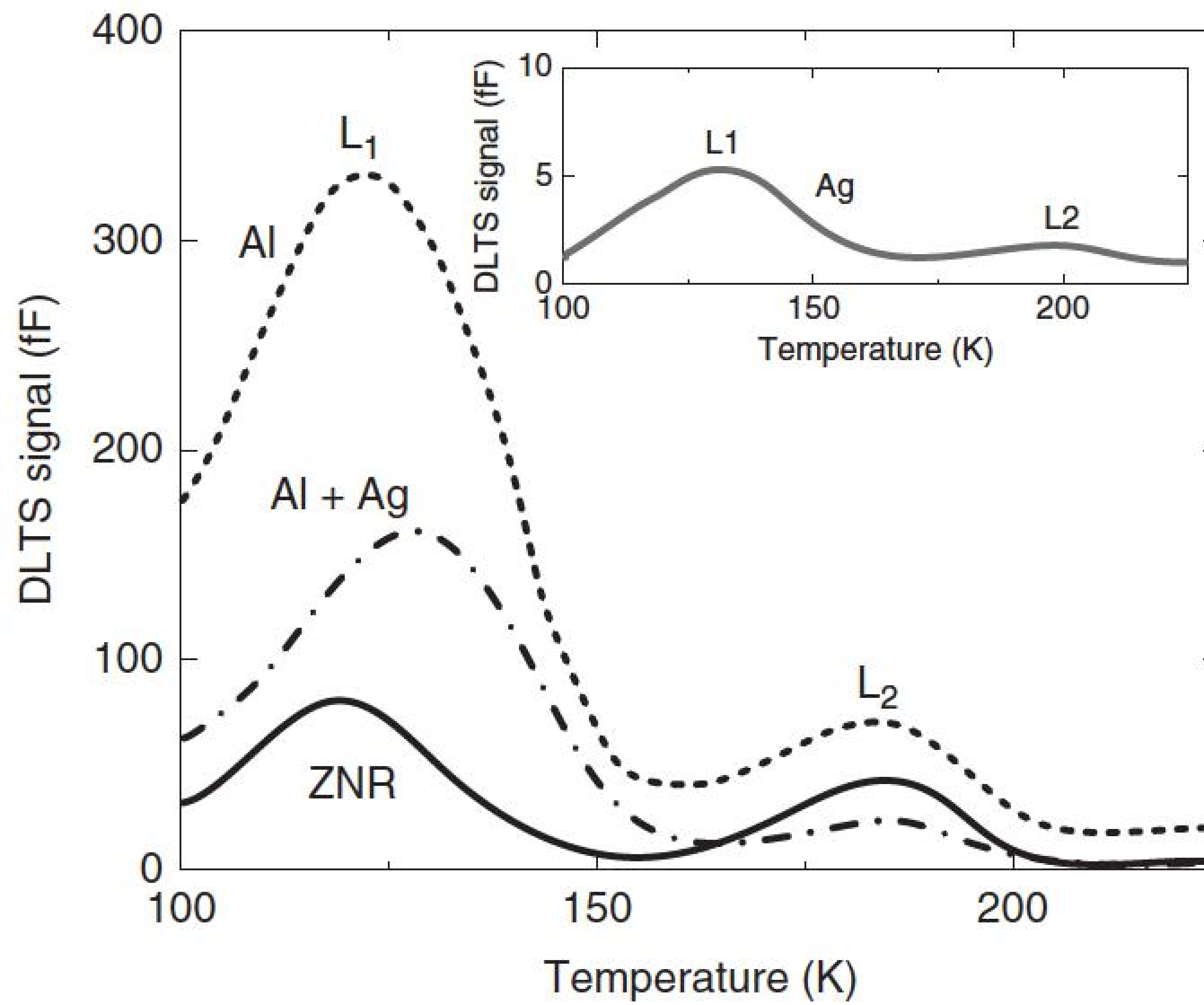


Figure 3.11 DLTS spectra for ZnO varistor samples doped with different additives (the rate window time constant, $\tau = 5$ ms). Source: Adapted from Fan and Freer 1994 [181].

of the effect of additives on the electrical properties of ZnO varistors. Figure 3.11 shows the DLTS spectrums of ZnO varistors of a typical commercial composition (ZNR) and the specimens doped with Al and Ag [181]. The traps L_1 and L_2 are located at 0.15 ± 0.01 and 0.25 ± 0.01 eV below the conduction band, respectively [187]. Therefore, the L_1 trap level can be associated with the nonlinearity of ZnO varistors; the higher the L_1 trap density, the higher the nonlinearity exponent, which may be caused by extrinsic donor defects, including monovalent and trivalent dopants.

Gupta and Carlson [187] suggested that the migration of interstitial zinc ions (Zn_i) was responsible for the lowering of the height of Schottky barriers, and this in turn caused the degradation of electrical properties. Based on this model, coupled with the observations of Kawaguchi et al. [188], from which photosensitivity in ZnO may be due to zinc interstitials, and after annealing most zinc interstitials diffused out and the photosensitivity of ZnO almost disappeared, and the experimentally determined ionization energy of zinc interstitials [189–192] (~0.2 eV for Zn_i^{2+}), Rohatgi et al. [58] suggested that the deep-level L_2 in the DLTS spectra may very well be zinc interstitials. The L_2 trap level appears to be closely associated with the stability of ZnO varistors: the higher the L_2 density, the lower the stability of the samples. The trap density may reflect the concentration of zinc interstitials.

Under the conditions of electrical stress, the movable positively charged zinc interstitials in the depletion region migrate toward the interface of the Schottky barrier [187], where they are converted into neutral zinc interstitials (Zn_i) by the reaction with negatively charged zinc vacancies, the latter are converted into neutral vacancies. This loss of charge causes a reduction in the grain boundary barrier height. Thus, the higher the concentration of zinc interstitials, the greater the reduction in the barrier height and the lower the stability of the varistor. In contrast, when the varistors are doped with monovalent Ag, the large silver ions

(ionic radius 1.25 Å) behave in a way similar to monovalent Na^+ (~1.33 Å) and K^+ (~0.97 Å) [149], which could occupy the interstitial sites. Thus, the presence of Ag ions on sites normally available for zinc interstitials would (i) effectively block the formation of zinc interstitials on such sites and (ii) restrict the routes available for the migration of zinc interstitials. Hence, Ag doping decreases the concentration of zinc interstitials, which is reflected in the lower L_2 trap density in the DLTS spectra, giving the Ag-doped varistors better degradation characteristics than the Al-doped specimens [181].

It is known that Al_2O_3 can improve the nonlinearity of ZnO varistors, but it also tends to lead to a degradation of device stability [11]. In contrast, Ag_2O additions may decrease the nonlinearity but improve the stability [12]. The optimum combination of A1 and Ag doping can improve both the nonlinearity and the stability of ZnO varistors [11]. From Figure 3.11, trivalent A1 doping increases the densities of both the L_1 and L_2 traps, and presumably, the concentration of zinc interstitials, such sample (Al), has the best nonlinearity characteristics but is less stable. In contrast, doping with monovalent Ag decreases the densities of the two traps sharply, and the Ag-doped sample (Ag) has inferior nonlinearity, but better stability. An optimum combination of A1 and Ag doping gives a high L_1 trap density and a low L_2 trap density; such samples (Al + Ag) exhibit good performance in terms of both nonlinearity and stability.

3.5.7 Evidence for Hydrogen as a Shallow Donor

Hydrogen was also investigated as a doping element in ZnO, and hydrogen was introduced into ZnO by the ion implantation method. Based on a first-principles investigation, Van de Walle [193] presented theoretical evidence that hydrogen acts as a source of conductivity: it can incorporate in high concentrations and behave as a shallow donor. It is in contrast to the traditional idea that native defects cause the n-type conductivity [194]. The recent first-principles calculation revealed that none of the native defects exhibits characteristics consistent with a high-concentration shallow donor [195]. Hydrogen is an excellent candidate for the impurity that is unintentionally incorporated into ZnO [193]. The H^+ ions in ZnO can move readily from the interstitial site to the neighboring oxygen site and forms OH ions in the form of $(O_oH_i)^\bullet$. Here, O_o, H_i, and $^\bullet$ represent the O atom on the oxygen lattice site, H atom in the interstitial site, and the singly ionized donor, respectively. According to the calculation results, the $(O_oH_i)^\bullet$ unit can be regarded as a new type of donor delivering an electron into the conduction band, which can turn the oxygen into a sort of doping element, in agreement with the present experimental results. It also gives rise to unusually large lattice relaxations. Therefore, controlling the conductivity of ZnO thus requires careful control of hydrogen exposure during and after growth [193].

3.6 Role of Inversion Boundaries

IB, which is often also called twin boundaries [74], plays an important role in both the grain growth and the electrical performance formation of ZnO varistor ceramics [83, 196]. In the noncentrosymmetric structure of ZnO, IBs are the most

common type of planar faults that can be triggered by the addition of specific spinel-forming dopants (Sb_2O_3, SnO_2, TiO_2, Fe_2O_3, and In_2O_3) [66, 197–199]. Interestingly, Rečnik et al. [143] determined the structure and chemistry of IBs in Sb-doped ZnO using quantitative transmission electron microscopy techniques. IBs are growth faults and crystallize in a head-to-head interfacial configuration with the polar *c*-axes of the two ZnO domains pointing toward the IB plane. This type of inversion alters the surface ionic configuration of ZnO grains in such a way (oxygen-terminating planes) that this might affect the ZnO–ZnO grain-boundary resistance and, consequently, improve the nonlinear characteristics of the varistor device.

In ZnO-based varistor ceramics doped with Sb_2O_3, both $Zn_7Sb_2O_{12}$ spinels [66, 83, 200] and Sb-rich IBs [83, 197], were observed, and IB almost formed in every ZnO grains [64]. The pinning effect of spinel particles and the presence of IBs inhibit ZnO grain growth, which effectively reduces the average grain size and the distribution of grain size [69, 83, 143, 146, 201, 202]. Small amounts of Sb_2O_3 can trigger the formation of IBs in practically every ZnO grain because of the high partial pressure of Sb_2O_3 at low temperatures and its effective distribution along the grain boundaries [48]. In Sb_2O_3-doped varistor ceramics with a Sb_2O_3/Bi_2O_3 ratio below 1, the major growth-controlling mechanism is an IB-induced grain growth mechanism, whereas the spinel phase that forms together with the Sb_2O_3-rich liquid phase in the decomposition reaction of the $Bi_3Zn_2Sb_3O_{14}$ pyrochlore phase has a minor influence, although the primary spinel phase formed via the reaction of Sb_2O_3 with ZnO in compositions with a Sb_2O_3/Bi_2O_3 ratio larger than 1 can have an influence on the grain growth [48].

A typical microstructure of the ZnO-based varistor ceramics is shown in Figure 3.12a [203]; the so-called particle pinning mechanism, based on Zener's drag phenomenon, should act as an inhibiting force working against the ZnO grain growth [85]. This explanation was supported by the fact that adding higher concentrations of grain growth controlling additives resulted in the formation of more spinel grains [49, 50]. As with the increasing concentration of spinel grains also the ZnO grain size becomes smaller, the spinels are consequently held responsible for inhibited ZnO grain growth. SnO_2 [204], which is occasionally used in complex varistor compositions [205–207], also triggers the formation of IBs in ZnO. Daneu et al. [137] showed that the IBs in SnO_2-doped ZnO varistor caused anisotropic grain growth in the early stages of sintering. ZnO grains that include IBs grow exaggeratedly, at the expense of normal grains, until they dominate the microstructure, as shown in Figure 3.13a [203]. In the samples with lower SnO_2 content, grains will be fewer and larger [137], and, on the contrary, higher additions of SnO_2 lead to an increase in the number of grains with IBs and to a more fine-grained microstructure. The increasing amount of secondary phases is also related to a higher level of SnO_2 addition, as shown in Figure 3.13b [203]. However, the influence of these phases on ZnO grain growth is subordinate to the role of IBs. The increase in the number of grains including IBs is accompanied by an increase in the number of spinel grains. If the starting microstructure contains only a few *nuclei*, large ZnO grains will be obtained, including intragranular spinel particles, whereas a larger number of *nuclei* will lead to a fine-grained microstructure with predominantly

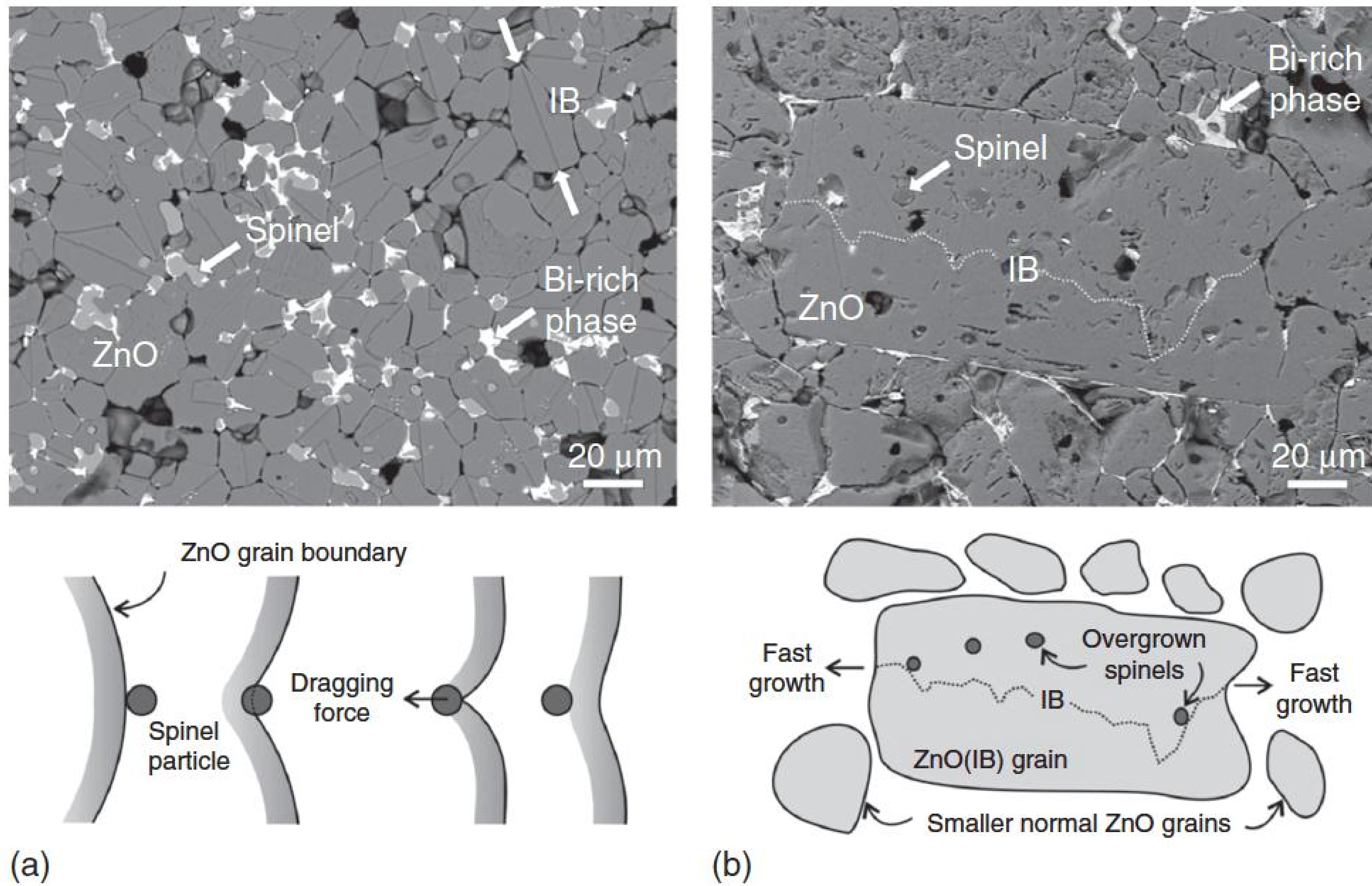


Figure 3.12 Typical microstructures of ZnO-based varistor ceramics: (a) high-voltage varistor ceramics with fine-grained microstructure – grain growth is inhibited because of (spinel) particle-pinning mechanism (dopants: Sb_2O_3 and SnO_2). (b) Low-voltage varistor ceramics with a coarse-grained microstructure – exaggerated grain growth is caused by the presence of IBs in some ZnO grains (TiO_2 doping). Spinel particles are overgrown. Source: Daneu et al. 2011 [203]. Reproduced with permission of IOP.

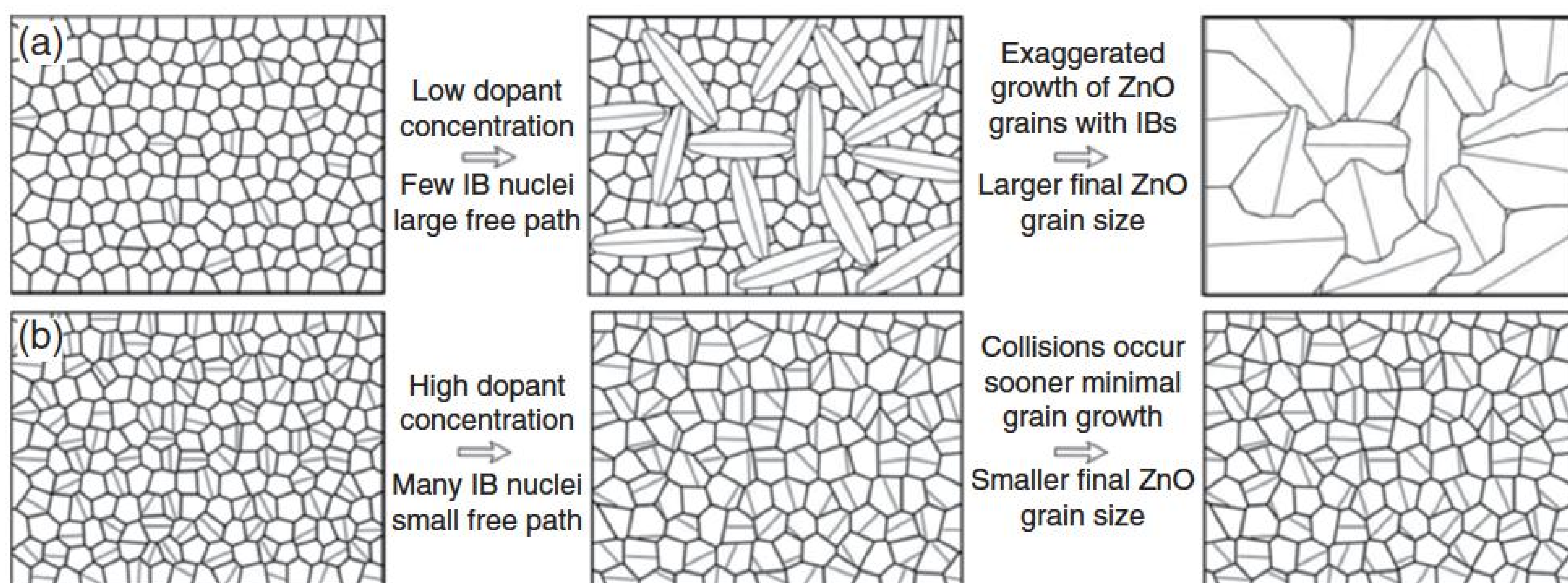


Figure 3.13 A schematic presentation of IB-induced grain growth mechanism: (a) low concentration of IB nuclei leads to the formation of larger grains as the mean free path for grain growth is larger; (b) high concentration of IB nuclei leads to the fine-grained microstructure. Source: Daneu et al. 2011 [203]. Reproduced with permission of IOP.

intergranular spinel particles [137]. The reason for this is that ZnO grains with low additions of dopants grow more extensively, and particles of secondary phases caught on a growth front are overgrown. With higher SnO_2 addition, grains with IBs grow by only a small amount before they collide, and hence, they cannot overgrow intergranular particles of secondary phases. In this view, secondary phases produced by the additions of SnO_2 in amounts typical for varistor compositions do not significantly influence the growth of ZnO grains.

However, at high additions of SnO_2, the concentration of secondary phases may additionally hinder grain growth by a particle-pinning mechanism [137].

IBs and spinel particles are also present in ZnO-based varistors doped with TiO_2 [146, 147], which, in contrast to Sb_2O_3, are known to promote the growth of ZnO grains. ZnO grains with IBs grow exaggeratedly along the fault plane as shown in Figure 3.12b [203], whereas the Zn_2TiO_4 spinel particles easily overgrow and have no obvious influence on grain growth and microstructure development [146].

Daneu et al. [137] reported that the grain growth in the early stages of sintering was strongly influenced by the presence of IBs in the ZnO grains. At the beginning of grain growth, the IB-forming dopant is homogeneously distributed throughout the sample. The distribution of the dopant is controlled by diffusion in the solid state or is liquid-phase assisted in the presence of Bi_2O_3. Below the temperature of the spinel-phase formation, IBs form in some of the ZnO grains. These grains are *nuclei* for subsequent anisotropic grain growth. In the samples with larger SnO_2 additions, more nuclei are formed. As the growth proceeds, these grains grow more rapidly than do the normal grains. The growth of the whole crystallite is controlled by the growth of an inherent planar fault. In the initial stage of the *IB-induced growth*, grains with IBs grow preferentially in the direction parallel to the IB plane and may reach unusually high aspect ratios. The resulting grains become highly elongated (tabular), as illustrated in Figure 3.12b [203]. When the longer axes of the elongated grains reach the length equal to the mean distance between the grains that contain IBs, they start to collide. If there are more nuclei, collisions occur sooner, and the resulting grains are smaller. When two such grains impinge on each other, the growth in the direction parallel to the IB is stopped. At this stage, another growth mechanism prevails, causing the elongated grains to thicken. This stage is to be compared with *seed growth*, where larger grains grow exaggeratedly in a matrix of surrounding small grains. These grains have an extremely large radius of curvature normal to the longer axis. The requirement to reduce the total particle surface area causes the small ZnO grains to dissolve and deposit onto the longer planar surfaces of larger grains containing IBs, as illustrated in Figure 3.13a [203]. The final microstructure comprises only the grains with IBs.

3.7 High Voltage Gradient ZnO Varistor

ZnO varistors with high voltage gradient will reduce the size of protection devices and surge arresters, especially for the 1000-kV ultrahigh voltage system. The metal oxide surge arresters for gas-insulated substation (GIS) are of tank type, and all ZnO varistors and related components are assembled in a steel tank fill with the SF_6 gas. If the voltage gradient can reach 400 V mm^{-1}, then the length of the 1000 kV GIS surge arrester would be shortened to about 5000 mm; this would lead to potential distribution along the varistor column uniform, and the complicated structure of the grading capacitors can be canceled. According to the analysis for 1000 kV surge arresters [208], the theoretical limit value of square-wave energy absorption density is 517 J cm^{-3}, the limit value of voltage

gradient is 686 V mm^{-1}, and the ideal voltage gradient for tank-type GIS surge arrester is 426 V mm^{-1}, while 430 V mm^{-1} was suggested [209].

The voltage gradient of the ZnO varistor is decided by an average grain size. Generally, it is suggested to develop high voltage gradient ZnO varistors by inhibiting the grain growth [210–212]. As discussed before, decreasing the sintering temperature and shortening the temperature-keeping time are available to reduce the grain size but may lead to V–I characteristics, energy absorption capability, and a decrease in the aging performance of ZnO varistors. Suitable additives, such as Sb_2O_3, CeO_2, or SiO_2, can also inhibit the growth of ZnO grains by the spinel pinning effect and the IB effect. On the other hand, the rare-earth oxides in the ZnO–Bi_2O_3-based varistor ceramics are also used to increase the voltage gradient of ZnO varistors [117, 118, 180], but the nonlinearity of the ZnO varistor becomes bad, and the leakage current is high.

In order to investigate the effects of Y_2O_3 on the electrical characteristics of the ZnO varistor, the prescription were prepared from a mixture of (95.8−x) mol% ZnO, 0.7 mol% Bi_2O_3, 0.5 mol% MnO_2, 0.5 mol% Cr_2O_3, 0.007 mol% $Al(NO)_3$, 1 mol% Sb_2O_3, 1.25 mol%SiO_2, 0.5 mol% Co_2O_3, and x mol% Y_2O_3, where x ranges from 0 to 2 mol%, and the samples were sintered at 1125 °C for four hours [118]. The electrical characteristics of the samples are shown in Table 3.2 [118]. When the ratio of rare earth oxide dopants increases from 0 to 2.0 mol%, the average size of ZnO grains, d, decreases from 10 to 5.6 μm, and the respective voltage gradient E_{1mA} increases from 263 to 584 V mm^{-1}. At the same time, the nonlinear coefficient α decreases from 53 to 14, the leakage current increases from 2 to 45 μA, and the average voltage per grain boundary, v_{gb}, is increased from 2.64 to 3.28 V [118]. The voltage gradient and the leakage current density increase as the amount of doped Y_2O_3 increases, but the nonlinear coefficient α and the average grain size monotonously decrease as the content of the doped Y_2O_3 increases. To ensure the mass density of samples reaching the maximum, the sintering temperature ought to be ranged from 1130 to 1190 °C. The high mass density might improve the aging characteristic and energy handling capability.

The ionic radius (0.90 Å) of Y^{3+} is much greater than the one of Zn^{2+} (0.60 Å). If Y^{3+} ions solidly solve into the ZnO lattices to substitute the Zn^{2+} ions, those might induce the distortion of the ZnO lattices, the large internal stress at lattices,

Table 3.2 Microstructure and electrical parameters of the varistor samples with various Y_2O_3 contents.

Y_2O_3 content (mol%)	E_{1mA} (V mm^{-1})	J_L (μA cm^{-2})	α	d (μm)	N_d (10^{23} m^{-3})	ϕ_b (eV)
0	263	2	53	10.0	2.01	0.88
0.5	355	4	30	8.4	2.29	1.01
1	401	24	20	7.7	2.92	1.24
2	584	45	14	5.6	1.58	0.96

Source: He et al. 2008 [118]. Reproduced with permission from Springer.

and high energy state. Therefore, the solid solution is difficult to appear under normal circumstances. Therefore, the Y^{3+} ions are usually observed in the grain boundaries and spinal phases by the energy-dispersive spectrometer (EDS) analysis, but not found inside the ZnO grains.

The XRD patterns indicate that the ZnO phase, $Zn_7Sb_2O_{12}$-type spinel phase, and γ-Bi_2O_3 phase are observed in the samples without Y_2O_3, whereas in the samples doped with Y_2O_3, an additional Y_2O_3-containing phase is detected, and the exact composition of this new phase is difficult to determine. Bernik et al. [117] considered it to be a Bi–Zn–Sb–Y–O phase with traces of oxides of Cr, Mn, Co, and Ni by EDS analysis. As the Y_2O_3 content increases, the relative intensity of $Zn_7Sb_2O_{12}$-type spinel phase decreases, whereas that of the Y_2O_3-containing phase increases at the same time. The Y_2O_3-containing phase forms only in the presence of Sb_2O_3; otherwise, the Y_2O_3 incorporates into the Bi_2O_3-rich phase, and the average ZnO grain size of the sample without Sb_2O_3 is more than doubled in comparison to the Sb_2O_3- and Y_2O_3-codoped samples [180].

It is widely recognized that the nonlinear I–V characteristics of ZnO varistors come from the double Schottky barriers in the grain boundaries, the experimental results that the leakage current increases as the content of the rare earth oxide increases, and cannot be well understood if only the double Schottky barriers are considered. Levinson and Philipp [1] proposed a model of parallel path conduction between grains, as shown in Figure 3.14 [166]. Path 1 is in the region of the double Schottky barrier, and Path 2 passes through the bulk intergranular materials at grain triple junction, which is almost temperature insensitive. This model gives a clue to the explanation of the above experiments.

As a conclusion, the intergranular materials at the grain corners have an important influence on the characteristics of ZnO varistors. The increased leakage currents of ZnO varistors with Y_2O_3 dopants are mainly due to the bypass paths through the intergranular materials at the grain corners. As the sintered ZnO grain sizes become smaller owing to the inhibition effect of the Y_2O_3 dopant, the ZnO grain number increases, as well as the total surface area of all grains. The amount of grain boundary additives in the raw materials almost keeps unchanged, so that the average thickness of each grain boundary reduces, including the intergranular materials at grain corners. Thus, the varistor samples with Y_2O_3 doped have large currents through the intergranular materials at grain triple junctions.

Bernik et al. [117] showed that Y_2O_3 doping results in an increase in the density of interface states and an even greater rise in the donor density. Generally, the barrier height increases with an increase in the density of interface states; however,

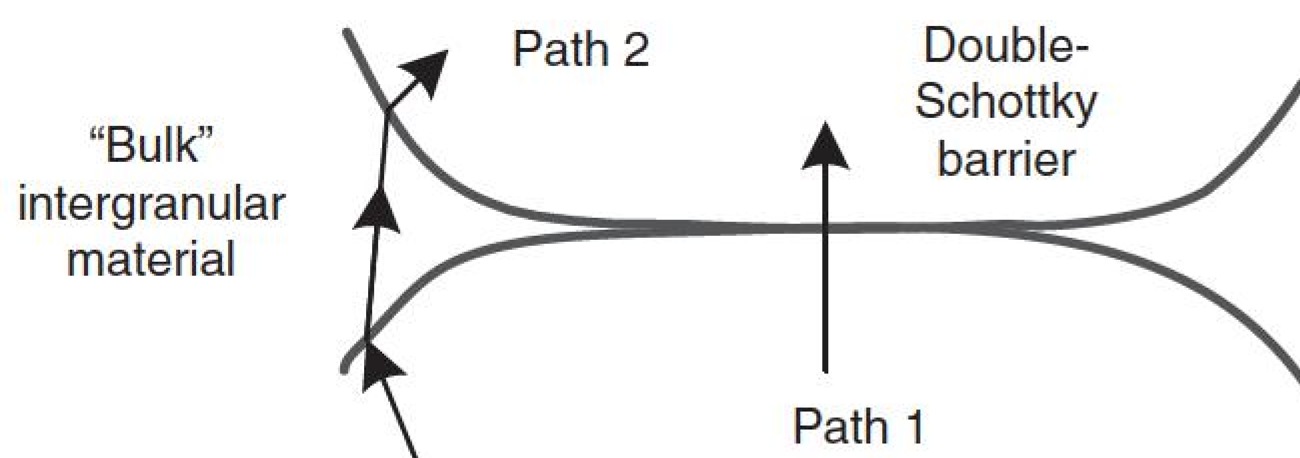


Figure 3.14 The parallel path conduction between the ZnO grains. Source: Hu et al. 2010 [166]. Reproduced with permission of John Wiley & Sons.

Table 3.3 Microstructure and electrical parameters of the varistor samples under different prescriptions [211].

No. of prescription (mol%)	E_{1mA} (V mm^{-1})	J_L (μA cm^{-2})	α	d (μm)	N_d (10^{23} m^{-3})	ϕ_b (eV)
$0.5Mn_2O_3 + 1Co_2O_3 + 0.5Ni_2O_3$	477	15	48	6.6	3.49	1.07
$0.5Mn_2O_3 + 1.5Co_2O_3 + 0.5Ni_2O_3$	455	6	53	7.6	2.27	1.14
$0.75Mn_2O_3 + 1Co_2O$	365	2	51	8.6	2.25	1.16
$0.75Mn_2O_3 + 1.5Co_2O_3 + 0.5Ni_2O_3$	492	1	76	7.0	2.09	1.43

a larger variation rate of donor concentration prevailed and the barrier height decreased with larger amounts of Y_2O_3. The barrier height decreases with the amounts of Y_2O_3, increasing from 1.12 eV in the Y_2O_3-free sample to 0.78 eV for the Y_2O_3-doped samples. The depletion layer width was observed to decrease as well. An increase in the donor concentration can also contribute to an increase in the leakage current, and this is particularly significant in the sample with 0.9 mol% of Y_2O_3.

A possible solution to effectively restrain the leakage currents of ZnO varistors doped with Y_2O_3 is doping more amount of grain boundary additives, such as MnO_2, Co_2O_3, and Ni_2O_3 [118]. These additives can improve the properties of double Schottky barriers and increase the resistance of the intergranular material. Therefore, some optimization prescriptions were prepared to inhibit the leakage current of ZnO varistors with 2 mol% doped Y_2O_3, as shown in Table 3.3 [211]; the prescription 4 is the best optimization one because of a low leakage current of 1 μA, high voltage gradient of 492 V mm^{-1}, and high nonlinear coefficient of 76.

Indium was also doped to reduce the low leakage current and tailor high nonlinear coefficient of a Y-doped ZnO varistor [213–217]. At a given concentration of the rare earth element yttrium, the leakage currents of sintered varistors first decrease markedly as the indium doping content increases, before increasing at higher doping levels. The nonlinear coefficient shows the opposite trend. The In^{3+} ions present at the grain boundaries as a donor increase the barrier height and further inhibit the increasing leakage current. When doping 0.025 mol% indium and 0.9 mol% yttrium, the sintered varistors show optimal electrical properties with a leakage current of 4.15 μA cm^{-2}, nonlinear coefficient of 51.84, and voltage gradient of 616 V mm^{-1} [213].

3.8 Low Residual Voltage ZnO Varistor

3.8.1 Residual Voltage Ratio

The residual voltage of ZnO varistor refers to the maximum voltage at both ends of the samples under nominal current. The residual voltage ratio K is defined as

$$K = \frac{V_n}{V_{1mA}} = \frac{E_n}{E_b} \tag{3.10}$$

where V_n is the residual voltage under nominal discharge current, V_{1mA} is the breakdown voltage under 1 mA DC current, usually it is replaced by the breakdown electrical field E_b, and E_n is the electrical field under nominal discharge current. ZnO varistors applied in surge arresters with different rated voltage or manufactured by different factories have different section areas. Therefore, the nominal discharge current has several rated values to measure the residual voltage of the arrester for different rated voltage levels, such as 1.5, 2.5, 5, 10, and 20 kA. The E_n in 1000 kV ultrahigh voltage AC power system is measured at the impulse current of 63.7 A cm^{-2}, which is decided according to the residual voltage experiment of the arresters used in 1000-kV power systems, in which the surge current of 20 kA is used upon four parallel varistor columns with the diameter of 10 cm to test the impulse residual voltage. However, E_n in a 10 kV distribution power system is about 662 A cm^{-2}, in which the surge current of 5 kA is used one varistor columns with the diameter of 3.2 cm. Therefore, E_n or E_b is in a range for different section areas and different nominal measurement currents, as shown in Figure 3.15, in which AB and CD are the range of E_b and E_n, respectively, where A and C are the residual voltage ratio K measuring the point of varistor with the largest section area and B and D are the residual voltage of the varistor with the smallest section area. From Figure 3.15, the K calculated from AC is less than that calculated from BD; therefore, the varistor can obtain a low residual voltage ratio K by enlarging its section area. Unfortunately, the section area is limited by the fabrication process, and it is hard to expand unlimitedly. According to Eq. (3.10), K is proportional to E_n and inversely proportional to E_b. Hence, in order to lower the K, the current density versus the electrical field (J–E) characteristic of the varistors ought to adjust as the arrows shown in Figure 3.15. Arrow 1 means increasing the E_{ref} and arrow 2 means decreasing the E_n, which are the principles to lower the residual voltage. Therefore, the methods to decrease the residual voltage ratio K should decrease the E_n and/or increase the E_{ref}. From Figure 3.15, we can see that E_n can be decreased by moving the curve to the right.

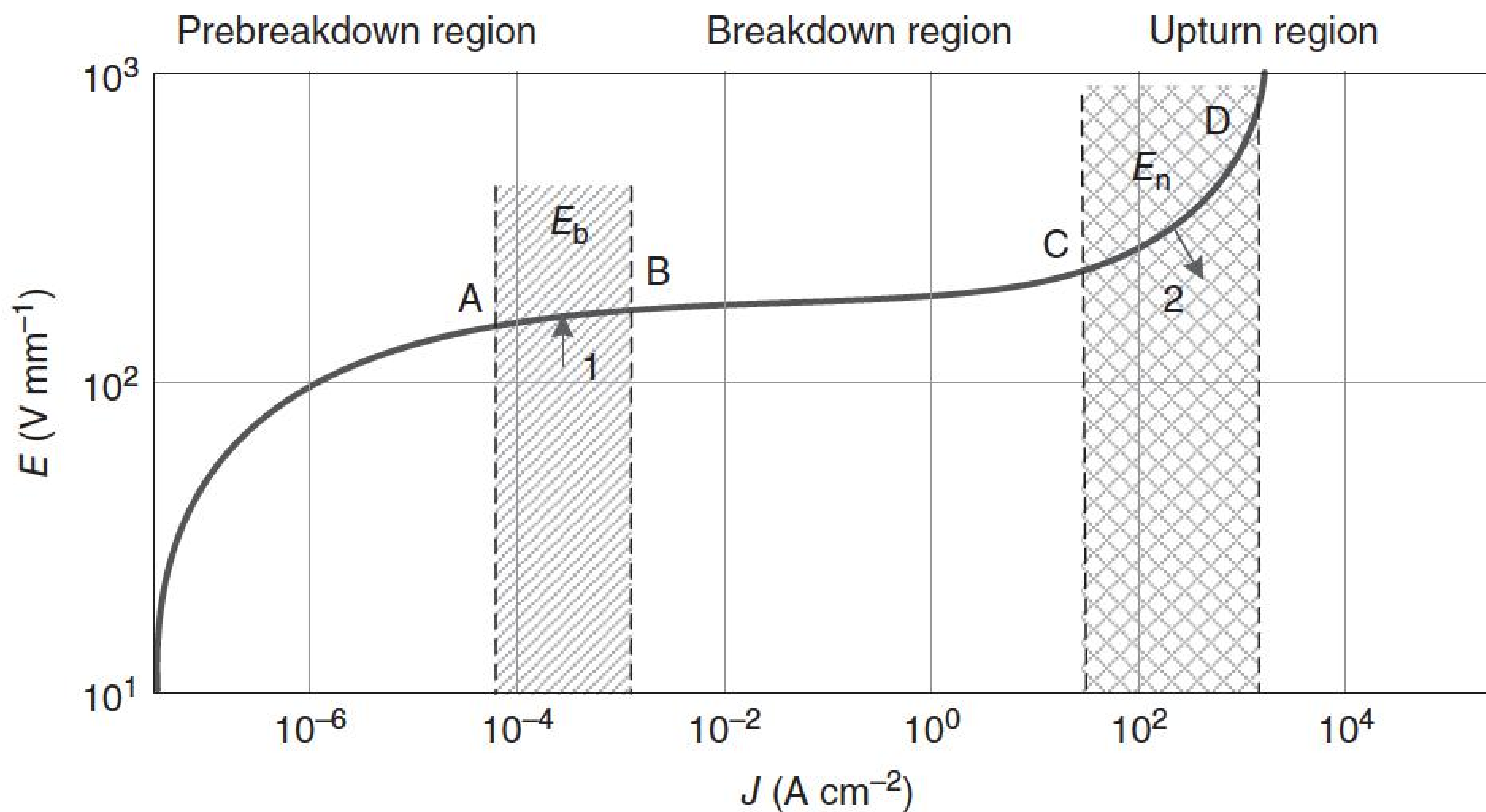


Figure 3.15 The current density vs the electrical field (J–E) characteristic of the varistors.

The upturn represents the voltage drop in the grains. If donor doping reduces the grain resistance, the voltage increase will be retarded, and the upturn will be delayed to higher current density [73]. It is known that donor ions such as Al^{3+}, Ga^{3+}, or In^{3+} can indeed delay the onset of the upturn voltage [25, 76].

The residual voltage ratio is determined by the breakdown voltage V_{1mA} and the residual voltage V_n, which present two regions in the conduction process. The conduction process inside the microstructure of the ZnO varistor was simulated [3], and the distribution of the current inside the ZnO varistor is entirely distinct under different applied voltages. In the ohmic region, the current passes uniformly through the whole varistor. However, about 75% of the current concentrates on one path when the current reaches about 1 mA. Although the current density reaches more than 60 Acm^{-2}, several current paths appear inside the ZnO varistor and the most portion of the current concentrates in those paths. The value of V_{1mA} is determined by the total series resistance of the grain boundaries in the concentrated current path. Assuming that the resistance of each grain boundary in the path is almost the same, therefore, the value of V_{1mA} is dependent on the number of grain boundaries in the path. The more the number of grain boundaries in the path, the higher the value of V_{1mA}. The number of grain boundaries in the current concentration path is the least one inside the whole varistor, which is decided by the average grain size d and the unevenness of grain sizes, σ_g, where $\sigma_g = \sigma/d$, σ is the standard deviation of grain sizes, and the value of V_{1mA} decreases when σ_g increases. In the residual voltage region, there are several current paths inside the ZnO varistor; thus, the value of V_n is influenced mainly by d and has little relation with σ_g. Therefore, the residual voltage ratio K increases as the unevenness σ_g increases, and the variation of the residual voltage ratio is in accordance with that of the unevenness of grain sizes [155].

3.8.2 Low Residual Voltage ZnO Varistors by Doping Al

The residual voltage of ZnO varistor in the upturn region is decided by the resistivity of the ZnO grain. Some literatures had reported that dopants such as Al^{3+} or Ga^{3+} ions were utilized to enhance the electrical conductivity of ZnO grains [76, 87, 129, 218–221]. Al dopants in ZnO act as donors. Al ions substitute for Zn ions in the lattice, increasing the donor density and decreasing the resistance of ZnO grains. Lower grain resistance results in improved I–V characteristics. $A1^{3+}$ is believed to easily substitute for Zn^{2+} in the lattice [76, 222], and displaced Zn ions may combine with oxygen to form ZnO, but in addition, they may occupy other available vacant interstitial sites and generate more zinc interstitials in the bulk ZnO, including the depletion region [21]. Therefore, Al doping may cause a higher zinc interstitial concentration, which, in turn, degrades the stability of ZnO varistors.

Under a suitable content of Al^{3+} addition, the DC resistance of the samples will reach a lowest value, as shown in Figure 3.16 [221]; obviously, the resistivity of samples with 0.25 mol% Al^{3+} addition is the smallest among all samples, and the lowest resistance appeared in the sample sintering at 1300 °C for four hours. However, a minimum in resistivity was observed at the maximum solid

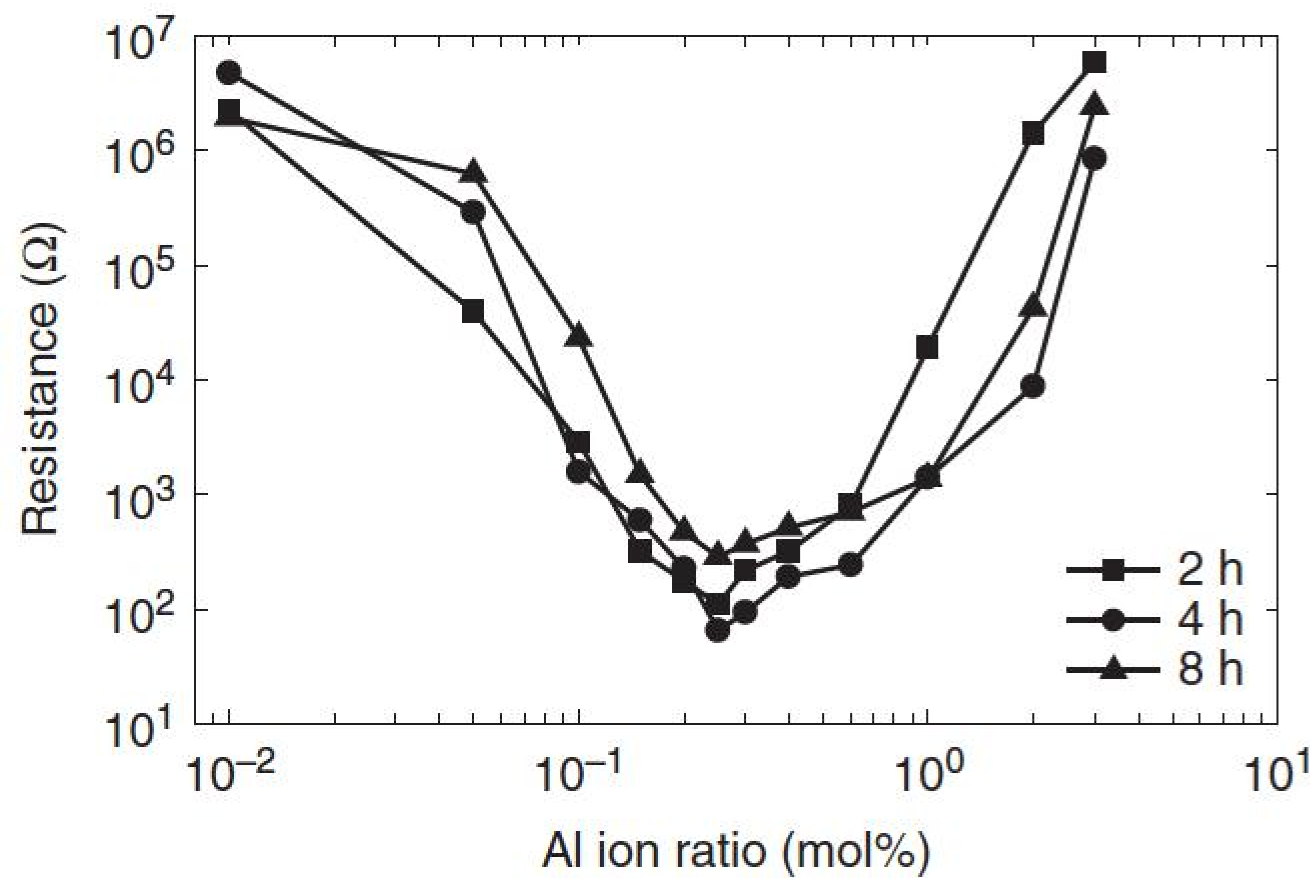


Figure 3.16 The resistance with various Al^{3+} content under different sintering times at 1300 °C [221].

solution level, under 0.25 wt% Al_2O_3 (0.42 mol% Al^{3+}) [219]. Therefore, the optimal content of Al_2O_3 dopant is related to the prescriptions and the sintering techniques.

Figure 3.17a shows the Cole–Cole plots for the impedance spectra of the samples with various contents of Al^{3+} dopants sintered for four hours [221]; every curve contains only one single arc, but the arc has a nonzero intercept with the real axis in the high-frequency region. As shown in the Cole–Cole plots, the intercept with the real axis in the low frequency moves to the left as the content of Al^{3+} dopant increases until 0.25 mol%, and the intercept moves to the right when the amount of doping Al^{3+} continues to increase, which means that the effect of decreasing ZnO resistance has a saturation point at 0.25 mol% Al^{3+} dopant. The low-frequency arc is due to the grain boundary and grain effect, and the high-frequency arc is attributable to the grain effect [117, 212]. The resistances of grains and grain boundaries under different Al^{3+} dopant ratios are shown in Figure 3.17b; the smallest grain resistance appears at 0.25 mol% doped Al^{3+}.

The I–V characteristics of the samples are illustrated in Figure 3.18a [221]; the I–V curve doped 0.25 mol% Al^{3+} is located at the right side, and the E_{1mA}

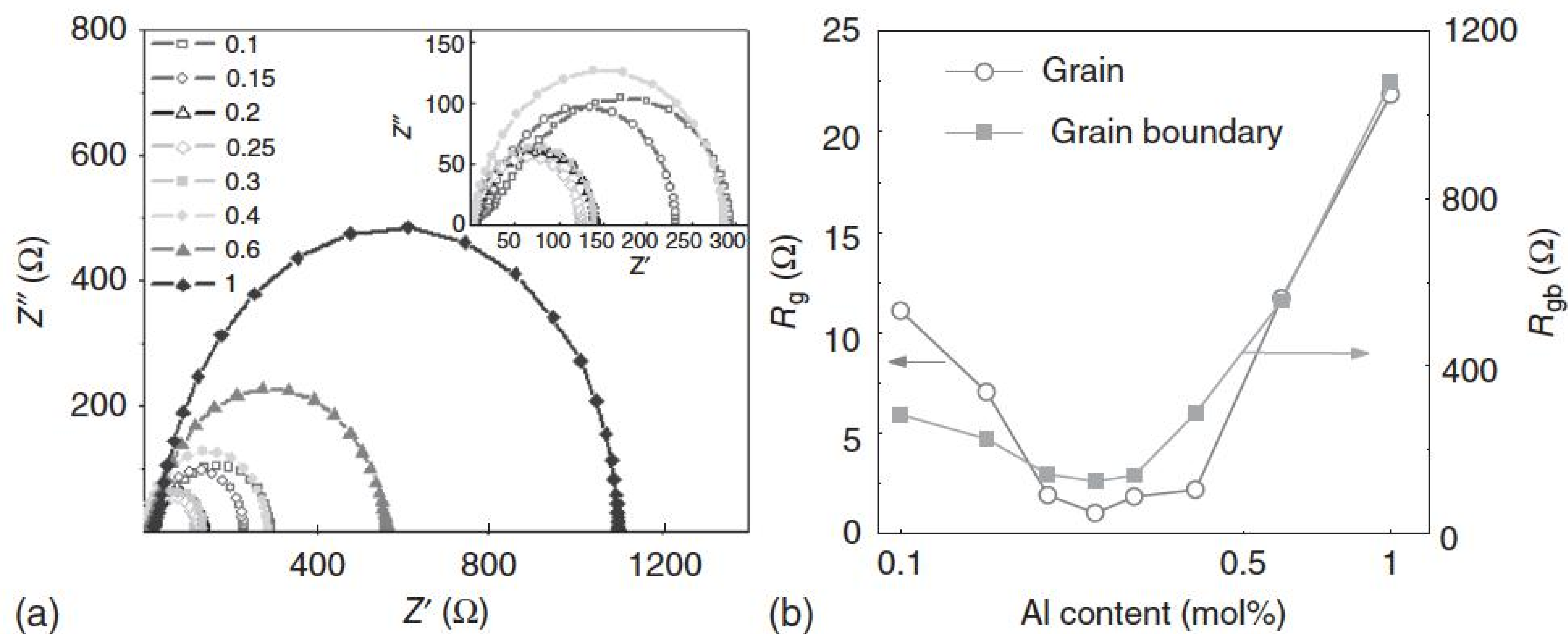


Figure 3.17 (a) The Cole–Cole plots for the impedance spectra of ZnO varistors with various Al-doped content (in mol%); (b) the resistivities of ZnO grain and grain boundaries under different Al dopant content [221].

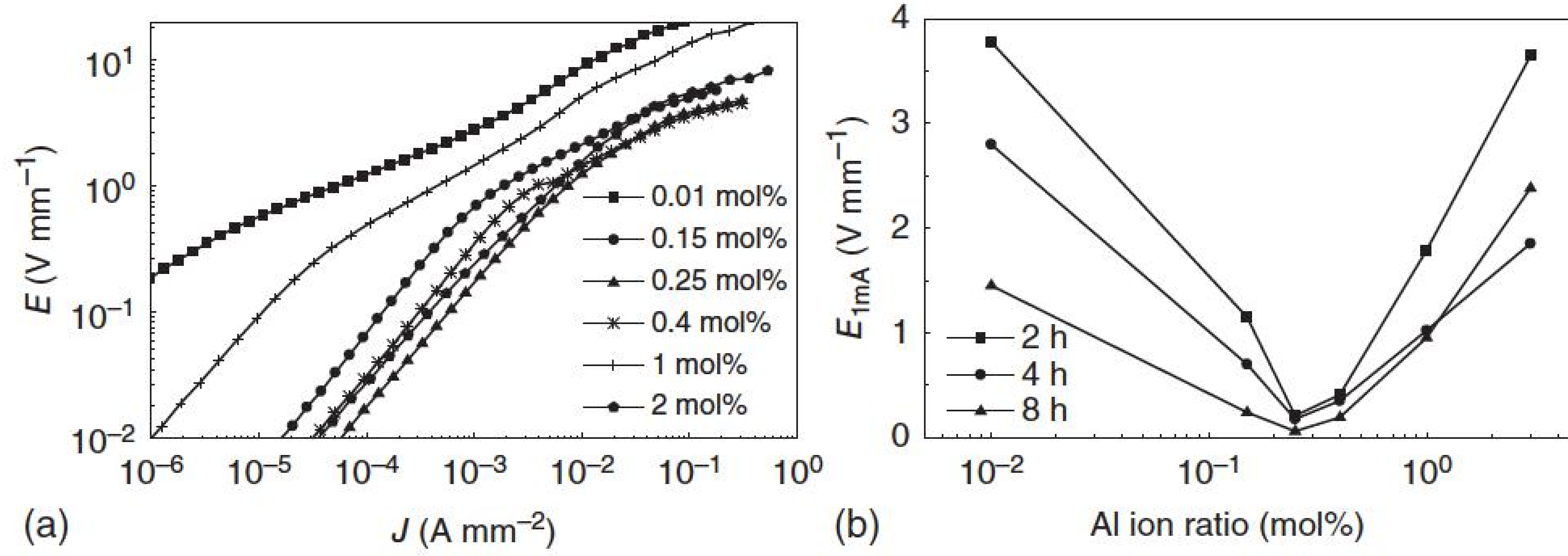
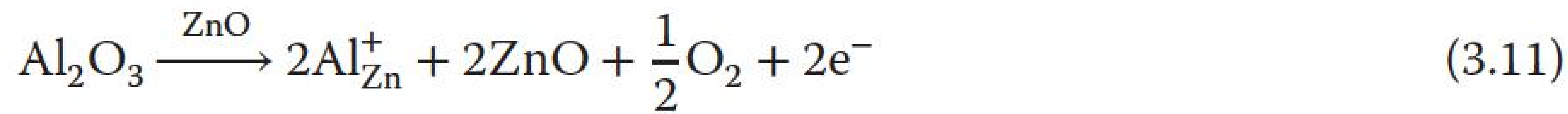


Figure 3.18 (a) The *J–E* curves of ZnO varistor samples sintering at 1300 °C for eight hours; (b) the dependence of E_{1mA} on Al doping ratio and sintering time [221].

dependence of samples on doping Al^{3+} ratio is shown in Figure 3.18b [221]; both show that the resistivity of samples with doping 0.25 mol% Al^{3+} is the lowest.

As shown in Figure 3.17b, the change of grain resistivity obviously exhibits a U-type, in the left part, the resistivity decrease is caused by the donor-type behavior of doping Al ions, and those enter into the ZnO structure and replace the Zn atoms at regular sites such as the following equation:



$$Al_2O_3 \xrightarrow{ZnO} 2Al_{Zn}^{+} + 2ZnO + \frac{1}{2}O_2 + 2e^- \tag{3.11}$$

Substituting Al_{Zn}^{+} in an Al ion occupying a zinc lattice site, the new generated free electron e^- moves to the conduction band, which results in an increase in carrier concentration. Therefore, the resistivity of ZnO ceramics decreases as the Al dopant content increases.

However, in the right part of the U-type curve, the increase in resistivity is caused by the acceptor-type behavior of Al ions. Massive Al^{3+} ions may occupy sites normally occupied by zinc interstitial ions, such as the following equation:



$$\frac{1}{2}Al_2O_3 \rightarrow Al_i^- + \frac{3}{4}O_2 + h \tag{3.12}$$

where Al_i^- is the Al ion in the zinc atom interstitial site and h is the hole with a positive charge, which results in decreasing the carrier concentration through neutralizing free electrons.

Figure 3.19 shows the normalized *J–E* characteristics of ZnO varistor samples [155], and the electrical parameters are summarized in Table 3.4 [155]. The average grain size *d* decreases as the content of Al^{3+} ionic additive increases. Compared with the donor density of the sample with no doped Al, the donor density of the sample with doped Al increases greatly, which means that the Al^{3+} ionic additive increases the conductivity of ZnO grains distinctly; correspondingly, the residual voltage ratio significantly decreases from 5 to 1.5. With the increasing content of Al^{3+} ions, the donor density increases to a maximum value of 5.71×10^{23} m^{-3} until the content of Al^{3+} additive reaches 0.25 mol%, and then decreases a little. With the content of Al^{3+} additive ranging from 0.01% to 1%, the value of E_{1mA} increases from 245.7 to 327.6 V mm^{-1}, and the leakage current J_L increases from 0.32 to 8.03μA cm^{-2} monotonously. The increase in the leakage

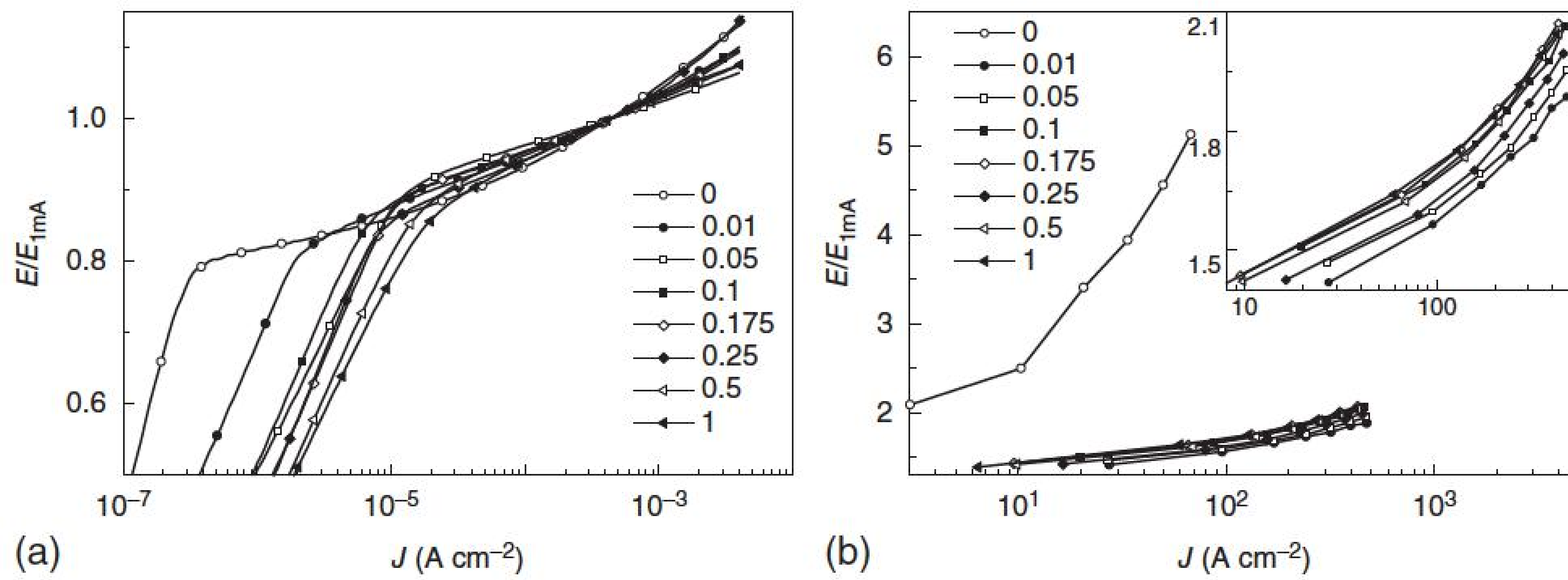


Figure 3.19 The normalized *J–E* characteristics of varistor samples with different Al ionic additive contents: (a) the small current density region; (b) the large current density region. Source: Long et al. 2010 [155]. Reproduced with permission of John Wiley & Sons.

Table 3.4 Microstructure and electrical parameters of the varistor samples with various Al contents.

Al ion additive (mol%)	E_{1mA} (V mm^{-1})	J_L (μA cm^{-2})	α	d (μm)	N_d (10^{23} m^{-3})	ϕ_b (eV)	K
0	368.98	0.32	26.2	9.38	0.49	1.02	5.00
0.01	245.70	1.40	37.81	8.58	4.4	0.98	1.50
0.05	253.23	4.23	36.70	8.42	4.98	0.89	1.58
0.1	263.88	5.76	34.33	8.30	5.32	0.80	1.59
0.175	268.47	5.85	29.63	7.79	5.45	0.76	1.64
0.25	269.30	6.19	27.38	6.89	5.71	0.72	1.55
0.5	299.62	6.74	29.72	6.82	5.21	0.63	1.59
1	327.61	8.03	26.73	5.90	5.14	0.54	1.63

Source: Long et al. 2010 [155]. Reproduced with permission of John Wiley & Sons.

currents of ZnO varistors with Al^{3+} dopants is not only caused by the decreased resistivity of grain boundaries but also by the increased donor density of ZnO grains.

From simulation, the leakage current density decreases and the nonlinear coefficient increases by increasing the interface-state density. Additives including Mn, Co, Bi, Cr, and Ni were added into Al-doped ZnO varistors; all can reduce the leakage current, and the optimal prescriptions of ZnO varistor samples contain 0.5 mol% Cr_2O_3, 0.25 mol% $Al(NO)_3$, 1 mol% Sb_2O_3, 1.25 mol% SiO_2, 0.5 mol% MnO_2, 3 mol% Co_2O_3, 2.1 mol% Bi_2O_3, and 0.5 mol% Ni_2O_3. The characteristics of samples sintered at 1150 °C in Al_2O_3 crucible are superior to those of others, and the leakage current decreases to 1.43 μA cm^{-2}; moreover, the residual voltage ratio decreases to 1.39 [221].

3.8.3 Low Residual Voltage ZnO Varistors by Doping Ga

The gallium dopant (Ga_2O_3) is also doped to make the $I-V$ curve of ZnO varistors shift right to reduce the residual voltage under a large current at the upturn region

as Al_2O_3 does; this means the nonlinearity region is extended, and the impulse current discharge capability is well improved [223]. The radius of Ga^{3+} (0.062 nm) is slightly smaller than that of Zn^{2+} (0.074 nm); Ga^{3+} ions can go into the lattice sites of Zn and decrease the resistivity of the ZnO grain [224]. In a small current region, the gallium dopant is also available to improve the surface-state density and the grain boundary barrier, which inhibits an increase in the leakage current and leads to the improvement of the stability of ZnO varistors in operation [225].

Five kinds of ZnO varistor ceramic samples were prepared by doping with various amounts of Ga_2O_3; the composition of the ZnO varistor ceramic samples contained $(94.45 - x)$ mol% ZnO, 1.05 mol% Bi_2O_3, 0.75 mol% MnO_2, 1.0 mol% Co_2O_3, 0.5 mol% Cr_2O_3, 1.0 mol% Sb_2O_3, 1.25 mol% SiO_2, and x mol% Ga_2O_3. As shown in Table 3.5 [226], the average grain size d decreases with the amount of Ga_2O_3 increased from about 8.1 to 6.1 μm. The donor density N_d increases monotonously as the gallium dopant increases, and the interface-state density N_i ascends from $1.1 \times 10^{18}\ m^{-2}$ to $1.6 \times 10^{18}\ m^{-2}$ as the amount of gallium dopants is changed in the range from 0.07 to 0.42 mol% and then descends to $1.5 \times 10^{18}\ m^{-2}$ at 0.56 mol% gallium dopant. The increment of N_i benifits to the potential barrier ϕ_b according to the formula $\phi_b = e^2N_i^2/2\varepsilon_r\varepsilon_0N_d$[227], which restrains the increase in the leakage current J_L. This characteristic improves the stability of the varistor during operation. The electrical field–current density characteristics (E–J) with various gallium contents from prebreakdown region to upturn region are shown in Figure 3.20 [226]. At prebreakdown region, the curves shift up with the increase in gallium contents until 0.42 mol% and then come down with 0.56 mol%.

When the content of Ga dopants increases from 0.07 to 0.42 mol%, the 1 mA residual voltage (E_{1mA}) changes from 398 to 432 V mm^{-1} [223]. This is attributed to the increase in the potential barrier and the number of active grain boundaries due to the decrease in the ZnO grain size with an increasing gallium content. The leakage current, which is measured at 0.75 E_{1mA}, ascends monotonously with an increase in gallium contents, which is between 0.69 and 0.91 μA cm^{-2} when the gallium dopant concentration is in the range from 0.07 to 0.42 mol%.

Benefited from the increase of 1 mA residual voltage and the upturn region shifting to the right, the nonlinear coefficient α is in the range from 56 to 80

Table 3.5 Microstructure, E–J, and C–V characteristic parameters of the samples prepared with different concentrations of Ga dopant.

Ga content (mol%)	d (μm)	N_d ($10^{27} m^{-3}$)	N_i ($10^{18} m^{-2}$)	ϕ_b (eV)	E_{1mA} (V mm^{-1})	J_L (μA cm^{-2})	α	K
0.07	8.1	0.78	1.1	1.72	398	0.69	56	2.47
0.14	7.6	0.92	1.2	1.74	407	0.72	75	2.22
0.28	7.2	1.38	1.5	1.81	417	0.75	77	2.04
0.42	6.5	1.5	1.6	1.89	432	0.91	80	1.65
0.56	6.1	2.0	1.5	1.25	431	1.04	78	1.74

Source: Zhao et al. 2016 [226]. Reproduced with permission from Elsevier.

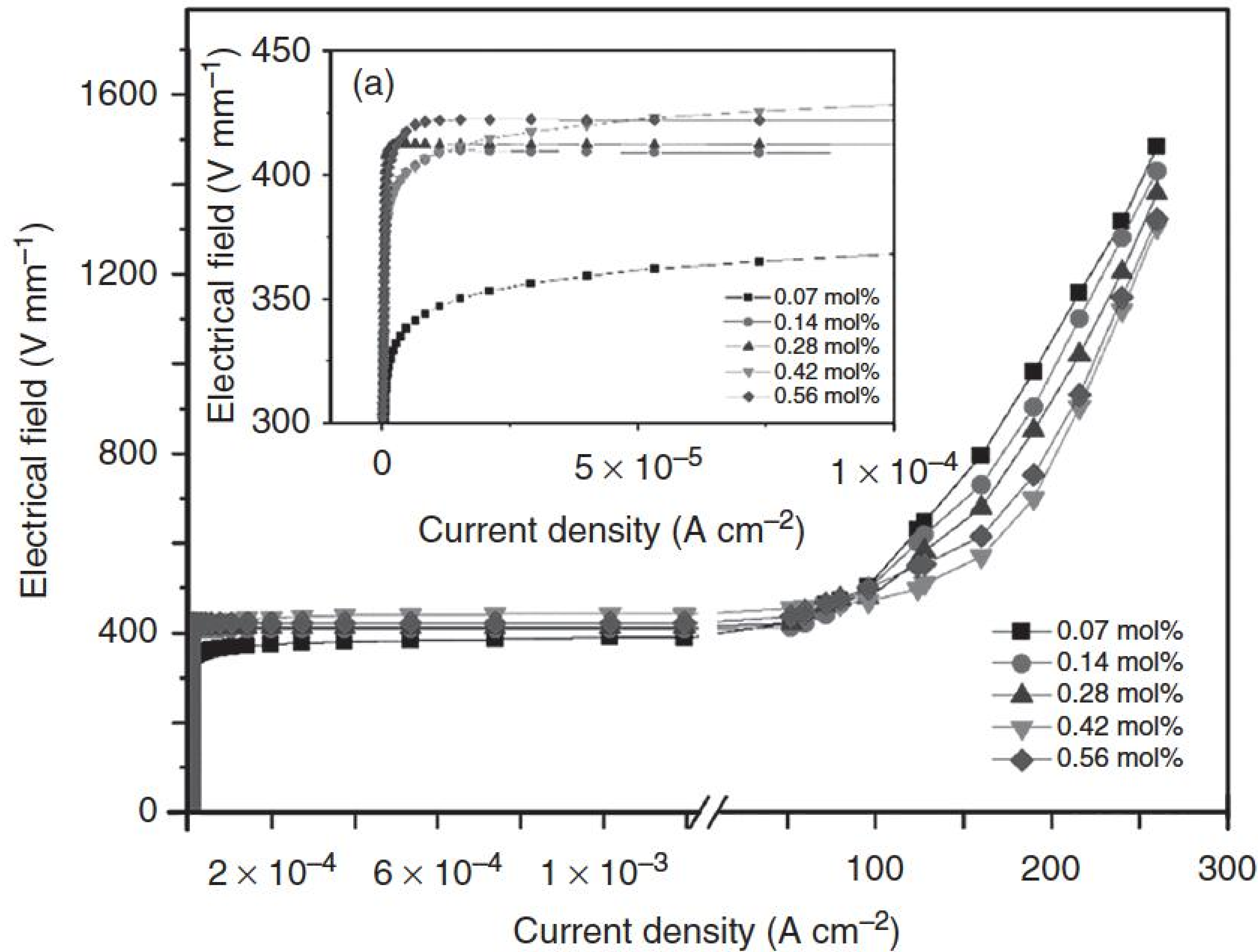


Figure 3.20 *E–J* plots of ZnO varistor samples prepared with different concentrations of Ga dopants. Source: Zhao et al. 2016 [226]. Reproduced with permission of Elsevier.

with the gallium dopant of 0.07–0.42 mol%, achieving the maximum 80 at the Ga_2O_3 content of 0.42 mol%, and the residual voltage ratio reaches the minimum 1.65, which reflects the donor behavior. However, exceeding the concentration of 0.42 mol%, the varistor exhibits the acceptor behavior [135].

Figure 3.20a is the V–I curves magnified at the prebreakdown region of ZnO varistors with both Ga^{3+} and Al^{3+} doped [228], which are displaced to the right; this phenomenon at the prebreakdown region is different from which only Ga acts as a donor at the grain boundary to shift the curves to the right. The curves in Figure 3.20a have not shifted distinctly at the origin of the coordinates, which are attributed to the increase in the potential barrier. The enhanced potential barrier inhibits the increase in leakage current and then keeps the electrical field–current density curve remain at the origin of the coordinates. The ionic radius of Ga^{3+} (0.062 nm) is comparative to that of Zn^{2+} (0.074 nm), and Ga^{3+} accumulates in the grain boundaries [148]. On the other hand, gallium and zinc were ball-milled firstly, which made gallium adhere to zinc uniformly, as benefited to increase the interface density.

3.8.4 Low Residual Voltage ZnO Varistors with High Voltage Gradient

Multiple-donor dopants (Al^{3+}, Ga^{3+}, Y^{3+}, and In^{3+}) were employed to improve the comprehensive performance of ZnO varistor ceramics and realize ZnO varistors with low residual voltage and high voltage gradient [181, 213–217, 226, 228, 229]. The leakage current of rare earth doped ZnO varistors ceramics is decreased evidently with Ga_2O_3 dopants, as shown in Table 3.6 [229]; this is benefited from the Ga^{3+} dopant that occupies the defect sites of grain boundaries to increase

Table 3.6 Microstructure, *E–J*, and *C–V* characteristic parameters of the samples prepared with different concentrations of Ga dopant.

Ga_2O_3 content (mol%)	d (μm)	N_d ($\times10^{23}$ m^{-3})	ϕ_b (eV)	N_i ($\times10^{16}$ m^{-2})	E_{1mA} (V mm^{-1})	J_L (μA cm^{-2})	α	K
0.2	7	1.9	2.38	2.0	500	0.89	82	1.61
0.4	6.9	2.1	2.76	2.3	517	0.96	87	1.60
0.6	6.6	3.1	2.37	2.6	489	1.2	81	1.62
0.8	6.4	2.8	2.14	2.4	456	1.34	76	1.63

Source: Zhao et al. 2016 [229]. Reproduced with permission from John Wiley & Sons.

the barrier. Y_2O_3 locates around the grains to restrain the ZnO grain growth and increase the voltage gradient, and Al^{3+} goes into the lattices of ZnO grains to decrease the grain resistance; thus, the residual voltage ratio is controlled at a low level under a high impulse current. From the EDXS image for a typical sample, it is obvious that both Ga and Al have high intensity within the grain and in the grain boundaries.

The potential barrier is the comprehensive result of N_i and N_d, as shown in Table 3.6 [229]; the highest potential barrier voltage is 2.76 V with 0.4 mol% Ga_2O_3. The radius of Y^{3+}(0.093 nm) is lager than that of Zn^{2+}(0.074 nm), it is difficult for plenty of Y^{3+} ions to solidly dissolve into the grains, they form small particles at the edge of the grains and pin the grains to restrict the ZnO grain growth, and benefits to enhance voltage gradient [170]. Y^{3+} affects the donor density N_d more than the interface-state density N_i, thus increasing the leakage current [117]. Ga^{3+} can reside in the grain and grain boundaries, furthermore increases the N_i much more than N_d [73], thus improve the barrier potential evidently; the increased barrier potential inhibits the increase in the leakage current. The dopant Al^{3+} decreases the grain resistance, which keeps the residual voltage at low level under high impulse current [135]. It is found that the combined action of Ga^{3+}, Al^{3+}, and Y^{3+} dopants acts as a donor until 0.4 mol% Ga_2O_3 doped, the excellent electrical property of ZnO varistors is acquired with a nonlinearity coefficient of 87, the voltage gradient is 517 V mm^{-1}, the leakage current is 0.96 μA cm^{-2}, and the residual voltage ratio is 1.60. This multiple-donor dopants will be helpful toward engineering high-quality ZnO varistors.

Doping indium in Al-doped ZnO varistors has a similar effect as doping gallium. With the increase in indium additive amounts, both the concentrations of donors and the surface states increase, which causes a high barrier potential. Besides, the high concentrations of donors further increase the conductivity of the grain and lead to a low residual voltage ratio as a result. The In^{3+} ion has a larger diameter than the Zn^{2+} ion, so it is difficult for a large amount of In^{3+} ions to dissolve into the grains. Thus, a certain amount of In^{3+} ions dissolve into the grains, which lead to the increase in the content of donors and decrease the grain resistance so as to keep the residual voltage at a low level. Besides, the residual doped In^{3+} ions form small particles at the edge of the grains and restrict the

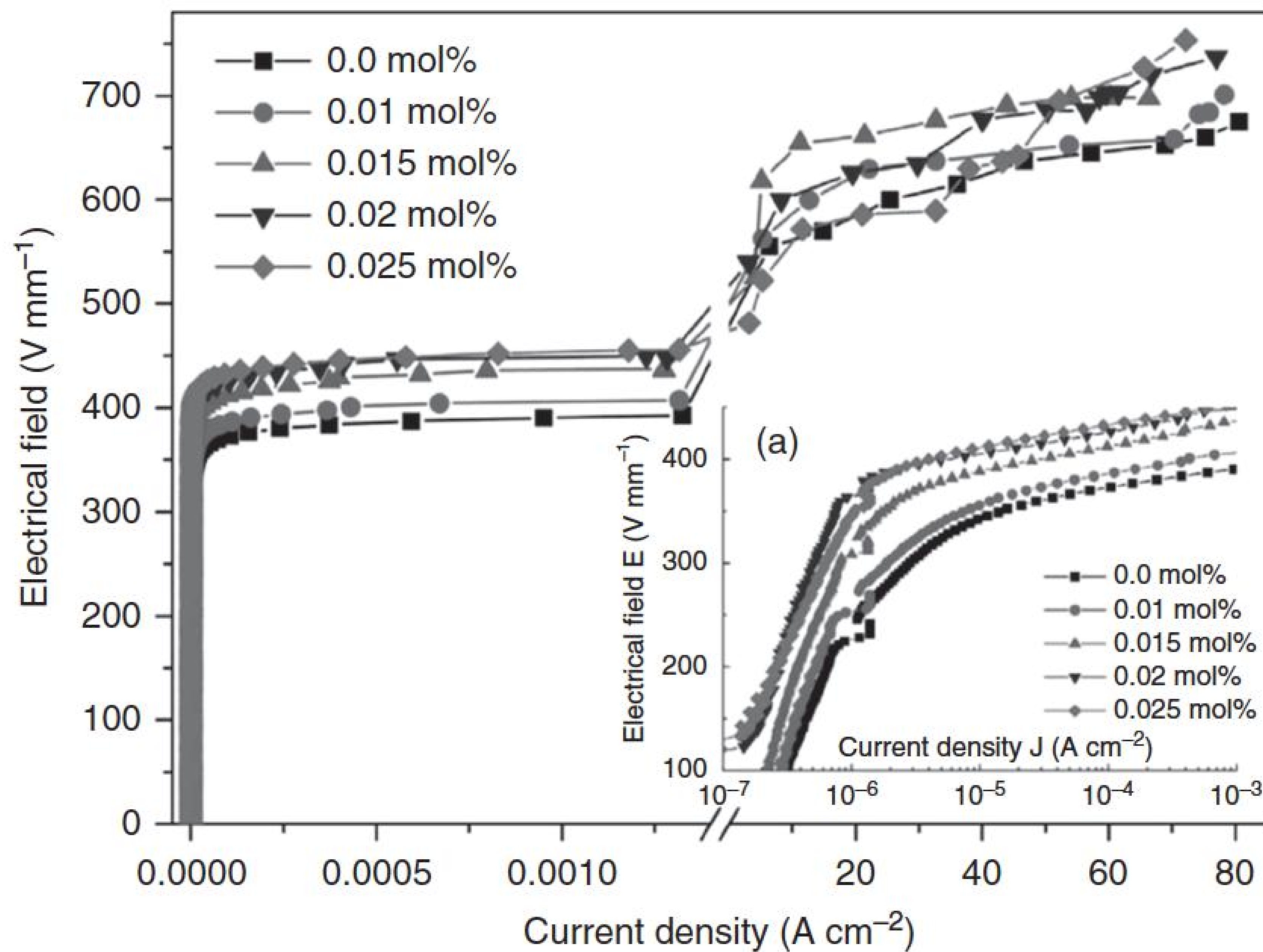


Figure 3.21 *E–J* characteristics from prebreakdown region to the upturn region and (a) *E–J* characteristics from 0 to 1 mA cm^{-2} of the ZnO varistors samples with various indium contents. Source: Meng et al. 2017 [215]. Reproduced with permission of Elsevier.

growth of ZnO grains [77], which lead to the increase of N_i as well as the breakdown voltage.

Indium was codoped with Al_2O_3 and Y_2O_3 to further improve the properties of ZnO varistors [215]. Some of the doped indium ions act as donors at the grain boundary, which lead to an increase in the barrier height from 1.56 to 2.21 eV and prevent the increase in the leakage current. Because of the decrease in the ZnO grain size and the increase in the barrier height, the breakdown voltage increases from 390 to 453 V mm^{-1} with an increased indium amount, up to 0.025 mol%. As shown in Figure 3.21 [215], the varistor ceramic with 0.02 mol% indium, 0.2 mol% aluminum, and 0.9 mol% yttrium has the optimal performance, i.e. exhibiting a 1-mA residual voltage of 448 V mm^{-1}, a leakage current of 0.69 μA cm^{-2}, a nonlinear coefficient of 76.26, and a residual voltage ratio of 1.58 with a density of 63.7 A cm^{-2} under a current waveform of 8/20 μs. The optimal properties have a great significance for the manufacture of ZnO varistor ceramics with a better protection property.

References

1 Levinson, L.M. and Philipp, H.R. (1975). The physics of metal oxide varistors. *Journal of Applied Physics* 46 (3): 1332–1341.

2 Gupta, T.K. (1990). Application of zinc oxide varistors. *Journal of the American Ceramic Society* 73 (7): 1817–1840.

3 Clarke, D.R. (1999). Varistor ceramics. *Journal of the American Ceramic Society* 82 (3): 485–502.

4 Mantas, P.Q. and Baptista, J.L. (1995). The barrier height formation in ZnO varistors. *Journal of the European Ceramic Society* 15 (7): 605–615.

5 Matsuoka, M. (1971). Nonohmic properties of zinc oxide ceramics. *Japanese Journal of Applied Physics* 10 (6): 736–746.

6 Matsuoka, M., Masuyama, T., and Iida, Y. (1969). Voltage nonlinearity of zinc oxide ceramics doped with alkali earth metal oxide. *Japanese Journal of Applied Physics* 8 (10): 1275–1276.

7 Wong, J. (1980). Sintering and varistor characteristics of ZnO-Bi_2O_3 ceramics. *Journal of Applied Physics* 51 (8): 4453–4459.

8 Mukae, K., Tsuda, K., and Nagasawa, I. (1977). Non-ohmic properties of ZnO-rare earth metal oxide-Co_3O_4 ceramics. *Japanese Journal of Applied Physics* 16 (8): 1361–1368.

9 Alles, A.B. and Burdick, V.L. (1991). The effect of liquid-phase sintering on the properties of Pr_6O_{11}-based ZnO varistors. *Journal of Applied Physics* 70 (11): 6883–6890.

10 Fan, J. and Freer, R. (1997). Varistor properties and microstructure of ZnO–BaO ceramics. *Journal of Materials Science* 32 (2): 415–419.

11 Tsai, J.K. and Wu, T.B. (1994). Non-ohmic characteristics of ZnO-V_2O_5 ceramics. *Journal of Applied Physics* 76 (8): 4817–4822.

12 Tsai, J.K. and Wu, T.B. (1995). Microstructure and nonohmic properties of ZnO-V_2O_5 ceramics. *Japanese Journal of Applied Physics* 34 (12R): 6452–6457.

13 Tsai, J.K. and Wu, T.B. (1996). Microstructure and nonohmic properties of binary ZnO-V_2O_5 ceramics sintered at 900 °C. *Materials Letters* 26 (3): 199–203.

14 Chen, C.S., Kuo, C.T., Wu, T.B., and Lin, I.N. (1997). Microstructures and electrical properties of V_2O_5-based multicomponent ZnO varistors prepared by microwave sintering process. *Japanese Journal of Applied Physics* 36 (3R): 1169–1175.

15 Kuo, C.T., Chen, C.S., and Lin, I.N. (1998). Microstructure and nonlinear properties of microwave-sintered ZnO-V_2O_5 varistors: I, effect of V_2O_5 doping. *Journal of the American Ceramic Society* 81 (11): 2942–2948.

16 Kuo, C.T., Chen, C.S., and Lin, I.N. (1998). Microstructure and nonlinear properties of microwave-sintered ZnO-V_2O_5 varistors: II, effect of Mn_3O_4 doping. *Journal of the American Ceramic Society* 81 (11): 2949–2956.

17 Hng, H.H. and Knowles, K.M. (1999). Characterisation of $Zn_3(VO_4)_2$ phases in V_2O_5-doped ZnO varistors. *Journal of the European Ceramic Society* 19 (6): 721–726.

18 Hng, H.H. and Knowles, K.M. (2000). Microstructure and current–voltage characteristics of multicomponent vanadium-dop964ed zinc oxide varistors. *Journal of the American Ceramic Society* 83 (10): 2455–2462.

19 Han, J., Senos, A.M.R., and Mantas, P.Q. (2002). Varistor behaviour of Mn-doped ZnO ceramics. *Journal of the European Ceramic Society* 22 (9): 2–1660.

20 Eda, K. (1978). Conduction mechanism of non-ohmic zinc oxide ceramics. *Journal of Applied Physics* 49 (5): 2964–2972.

21 Fan, J. and Freer, R. (1995). The roles played by Ag and Al dopants in controlling the electrical properties of ZnO varistors. *Journal of Applied Physics* 77 (9): 4795–4800.
22 Levinson, L.M. and Philipp, H.R. (1986). Zinc oxide varistors—a review. *American Ceramic Society Bulletin* 65 (4): 639–646.
23 Subasri, R., Asha, M., Hembram, K. et al. (2009). Microwave sintering of doped nanocrystalline ZnO and characterization for varistor applications. *Materials Chemistry and Physics* 115 (2): 677–684.
24 Inada, M. (1978). Microstructure of nonohmic zinc oxide ceramics. *Japanese Journal of Applied Physics* 17 (4): 673–677.
25 Takemura, T., Kobayashi, M., Takada, Y., and Sato, K. (1986). Effects of bismuth sesquioxide on the characteristics of ZnO varistors. *Journal of the American Ceramic Society* 69 (5): 430–436.
26 Olsson, E., Dunlop, G.L., and Österlund, R. (1989). Development of interfacial microstructure during cooling of a ZnO varistor material. *Journal of Applied Physics* 66 (10): 5072–5077.
27 Kutty, T.R.N. and Ezhilvalavan, S. (1994). The influence of Bi_2O_3 non-stoichiometry on the non-linear property of ZnO varistors. *Materials Chemistry and Physics* 38 (3): 267–276.
28 Stucki, F. and Greuter, F. (1990). Key role of oxygen at zinc oxide varistor grain boundaries. *Applied Physics Letters* 57 (5): 446–448.
29 Karanović, L., Poleti, D., and Vasović, D. (1994). On the possibility of pyrochlore phase formation in zinc oxide varistor ceramic. *Materials Letters* 18 (4): 191–196.
30 Cerva, H. and Russwurm, W. (1988). Microstructure and crystal structure of bismuth oxide phases in zinc oxide varistor ceramics. *Journal of the American Ceramic Society* 71 (7): 522–530.
31 Kingery, W.D., Sande, J.B., and Mitamura, T. (1979). A scanning transmission electron microscopy investigation of grain-boundary segregation in a ZnO-Bi_2O_3 varistor. *Journal of the American Ceramic Society* 62 (3-4): 221–222.
32 Clarke, D.R. (1978). The microstructural location of the intergranular metal-oxide phase in a zinc oxide varistor. *Journal of Applied Physics* 49 (4): 2407–2411.
33 Kanai, H., Imai, M., and Takahashi, T. (1985). A high-resolution transmission electron microscope study of a zinc oxide varistor. *Journal of Materials Science* 20 (11): 3957–3966.
34 Olsson, E., Falk, L.K.L., Dunlop, G.L., and Österlund, R. (1985). The microstructure of a ZnO varistor material. *Journal of Materials Science* 20 (11): 4091–4098.
35 Greuter, F. (1995). Electrically active interfaces in ZnO varistors. *Solid State Ionics* 75: 67–78.
36 Stucki, F., Brüesch, P., and Greuter, F. (1987). Electron spectroscopic studies of electrically active grain boundaries in ZnO. *Surface Science* 189: 294–299.
37 Eda, K. (1989). Zinc oxide varistors. *IEEE Electrical Insulation Magazine* 5 (6): 28–41.

38 Inada, M. (1978). Crystal phases of nonohmic zinc oxide ceramics. *Japanese Journal of Applied Physics* 17 (1): 1–10.

39 Einzinger, R. (1981). Grain boundary properties in ZnO varistors. *Advances in Ceramics* 1: 359–374.

40 Einzinger, R. (1982). Nonlinear electrical conductivity of doped ZnO ceramics (in Ger.). PhD thesis. Technical University of Miinchen, Miinchen, FRG.

41 Takahashi, T. and Iwahara, H. (1978). Oxide ion conductors based on bismuth sesquioxide. *Materials Research Bulletin* 13 (12): 1447–1453.

42 Miyayama, M. and Yanagida, H. (1986). Oxygen ion conduction in γ-Bi_2O_3 doped with Sb_2O_3. *Journal of Materials Science* 21 (4): 1233–1236.

43 Metz, R., Delalu, H., Vignalou, J.R. et al. (2000). Electrical properties of varistors in relation to their true bismuth composition after sintering. *Materials Chemistry and Physics* 63 (2): 157–162.

44 Russwurm, W. (1987). High-temperature in situ X-ray diffraction studies on ceramic ZnO varistor systems. *Phase Transitions* 8 (4): 299–300.

45 Inada, M. (1980). Formation mechanism of nonohmic zinc oxide ceramics. *Japan Journal Applied Physics* 19 (3): 409–419.

46 Hembram, K., Sivaprahasam, D., and Rao, T.N. (2011). Combustion synthesis of doped nanocrystalline ZnO powders for varistors applications. *Journal of the European Ceramic Society* 31 (10): 1905–1913.

47 Onreabroy, W., Sirikulrat, N., Brown, A.P. et al. (2006). Properties and intergranular phase analysis of a ZnO–CoO–Bi_2O_3 varistor. *Solid State Ionics* 177 (3): 411–420.

48 Bernik, S., Daneu, N., and Rečnik, A. (2004). Inversion boundary induced grain growth in TiO_2 or Sb_2O_3 doped ZnO-based varistor ceramics. *Journal of the European Ceramic Society* 24 (15): 3703–3708.

49 Senda, T. and Bradt, R.C. (1990). Grain growth in sintered ZnO and ZnO-Bi_2O_3 ceramics. *Journal of the American Ceramic Society* 73 (1): 106–114.

50 Dey, D. and Bradt, R.C. (1992). Grain growth of ZnO during Bi_2O_3 liquid-phase sintering. *Journal of the American Ceramic Society* 75 (9): 2529–2534.

51 Peiteado, M.A.D.L., De la Rubia, M.A., Velasco, M.J. et al. (2005). Bi_2O_3 vaporization from ZnO-based varistors. *Journal of the European Ceramic Society* 25 (9): 1675–1680.

52 Chiang, Y.-M., Kingery, W.D., and Levinson, L.M. (1982). Compositional changes adjacent to grain boundaries during electrical degradation of a ZnO varistor. *Journal of Applied Physics* 53 (3): 1765–1768.

53 Morris, W.G. (1976). Physical properties of the electrical barriers in varistors. *Journal of Vacuum Science and Technology* 13 (4): 926–931.

54 Morris, W.G. and Cahn, J.W. (1975). Adsorption and microphases at grain boundaries in non-ohmic zinc oxide ceramics containing bismuth oxide. In: *Grain Boundaries in Engineering Materials* (ed. J.L. Walter, J.H. Westbrook and D.A. Woodford), 223–234. Baton Rouge, LA: Claitors.

55 Selim, F.A., Gupta, T.K., Hower, P.L., and Carlson, W.G. (1980). Low voltage ZnO varistor: device process and defect model. *Journal of Applied Physics* 51 (1): 765–768.

56 Eda, K., Inada, M., and Matsuoka, M. (1983). Grain growth control in ZnO varistors using seed grains. *Journal of Applied Physics* 54 (2): 1095–1099.
57 Einzinger, R. (1978). Metal oxide varistor action-a homojunction breakdown mechanism. *Applications of Surface Science* 1 (3): 329–340.
58 Rohatgi, A., Pang, S.K., Gupta, T.K., and Straub, W.D. (1988). The deep level transient spectroscopy studies of a ZnO varistor as a function of annealing. *Journal of Applied Physics* 63 (11): 5375–5379.
59 Nunes, S.I. and Bradt, R.C. (1995). Grain growth of ZnO in ZnO-Bi_2O_3 ceramics with Al_2O_3 additions. *Journal of the American Ceramic Society* 78 (9): 2469–2475.
60 Wang, H., Li, W., and Cordaro, J.F. (1995). Single junctions in ZnO varistors studied by current-voltage characteristics and deep level transient spectroscopy. *Japanese Journal of Applied Physics* 34 (4R): 1765–1771.
61 German, R.A. (1985). *Liquid Phase Sintering*. New York: Plenum Press.
62 Tu, Y., Ding, L., He, J. et al. (2006). Dopant effects to pores in ZnO varistors. In: *Proceedings of 8th International Conference on Properties and Applications of Dielectric Materials*, 967–970. IEEE.
63 Gupta, T.K. (1971). Inhibition of grain growth in ZnO. *Journal of the American Ceramic Society* 54 (8): 413–414.
64 Lao, Y.W., Kuo, S.T., and Tuan, W.H. (2007). Effect of Bi_2O_3 and Sb_2O_3 on the grain size distribution of ZnO. *Journal of Electroceramics* 19 (2): 187–194.
65 Choi, J.H., Hwang, N.M., and Kim, D.Y. (2001). Pore–boundary separation behavior during sintering of pure and Bi_2O_3-doped ZnO ceramics. *Journal of the American Ceramic Society* 84 (6): 1398–1400.
66 Kim, J., Kimura, T., and Yamaguchi, T. (1989). Microstructure development in Sb_2O_3-doped ZnO. *Journal of Materials Science* 24 (7): 2581–2586.
67 Peiteado, M., Fernandez, J.F., and Caballero, A.C. (2005). Processing strategies to control grain growth in ZnO based varistors. *Journal of the European Ceramic Society* 25 (12): 2999–3003.
68 Lu, C.H., Chyi, N., Wong, H.W., and Hwang, W.J. (2000). Effects of additives and secondary phases on the sintering behavior of zinc oxide-based varistors. *Materials Chemistry and Physics* 62 (2): 164–168.
69 Wong, J. (1975). Microstructure and phase transformation in a highly non-ohmic metal oxide varistor ceramic. *Journal of Applied Physics* 46 (4): 1653–1659.
70 Meng, P.F., Hu, J., and He, J.L. Distribution and effect of pores inside ZnO varistors by 3D X-ray computed tomography, To be published.
71 Sonder, E., Austin, M.M., and Kinser, D.L. (1983). Effect of oxidizing and reducing atmospheres at elevated temperatures on the electrical properties of zinc oxide varistors. *Journal of Applied Physics* 54 (6): 3566–3572.
72 Bueno, P.R., Leite, E.R., Oliveira, M.M. et al. (2001). Role of oxygen at the grain boundary of metal oxide varistors: a potential barrier formation mechanism. *Applied Physics Letters* 79 (1): 48–50.
73 Gupta, T.K. (1992). Microstructural engineering through donor and acceptor doping in the grain and grain boundary of a polycrystalline semiconducting ceramic. *Journal of Materials Research* 7 (12): 3280–3295.

74 Bemik, S. and Daneu, N. (2007). Characteristics of ZnO-based varistor ceramics doped with Al_2O_3. *Journal of the European Ceramic Society* 27 (10): 3161–3170.

75 Matsuoka, M. (1981). Progress in research and development of zinc-oxide varistors. In: *Advances in Ceramics, Vol. I, Grain Boundary Phenomena in Electronic Ceramics* (ed. L.M. Levinson and D. Hill), 290–308. Columbus, OH: American Ceramic Society.

76 Carlson, W.G. and Gupta, T.K. (1982). Improved varistor nonlinearity via donor impurity doping. *Journal of Applied Physics* 53 (8): 5746–5753.

77 Nahm, C.W. (2011). Varistor properties of ZnO-Pr_6O_{11}-CoO-Cr_2O_3-Y_2O_3-In_2O_3 ceramics. *Materials Letters* 65 (9): 1299–1301.

78 Mukae, K., Tsuda, K., and Nagasawa, I. (1977). Non-ohmic properties of ZnO-rare earth metal oxide-Co_2O_3 ceramics. *Japanese Journal of Applied Physics* 16 (8): 1321–1368.

79 Mukae, K. and Nagasawa, I. (1981). Effect of praseodymium oxide and donor concentration in the grain boundary region of ZnO varistors. In: *Advances in Ceramics, Vol. I, Grain Boundary Phenomena in Electronic Ceramics* (ed. L.M. Levinson and D. Hill), 331–342. Columbus, OH: American Ceramic Society.

80 Shim, Y. and Cordaro, J.F. (1988). Admittance spectroscopy of polycrystalline ZnO-Bi_2O_3 and ZnO-BaO systems. *Journal of the American Ceramic Society* 71 (3): 184–188.

81 Takada, M. and Yoshikado, S. (2010). Effect of thermal annealing on electrical degradation characteristics of Sb–Bi–Mn–Co-added ZnO varistors. *Journal of the European Ceramic Society* 30 (2): 531–538.

82 Wu, Z.H., Fang, J.H., Xu, D. et al. (2010). Effect of SiO_2 addition on the microstructure and electrical properties of ZnO-based varistors. *International Journal of Minerals, Metallurgy, and Materials* 17 (1): 86–91.

83 Senda, T. and Bradt, R.C. (1991). Grain growth of zinc oxide during the sintering of zinc oxide—antimony oxide ceramics. *Journal of the American Ceramic Society* 74 (6): 1296–1302.

84 Ezhilvalavan, S. and Kutty, T.R.N. (1997). Effect of antimony oxide stoichiometry on the nonlinearity of zinc oxide varistor ceramics. *Materials Chemistry and Physics* 49 (3): 258–269.

85 Senda, T. and Bradt, R.C. (1991). Twinning in ZnO ceramics with Sb_2O_3 additions. *Journal of the Ceramic Society of Japan* 99 (1153): 727–731.

86 Han, J., Mantas, P.Q., and Senos, A.M.R. (2000). Grain growth in Mn-doped ZnO. *Journal of the European Ceramic Society* 20 (16): 2753–2758.

87 Zhou, Z., Kato, K., Komaki, T. et al. (2004). Effects of dopants and hydrogen on the electrical conductivity of ZnO. *Journal of the European Ceramic Society* 24 (1): 139–146.

88 Pillai, S.C., Kelly, J.M., McCormack, D.E., and Ramesh, R. (2008). High performance ZnO varistors prepared from nanocrystalline precursors for miniaturised electronic devices. *Journal of Materials Chemistry* 18 (33): 3926–3932.

89 Fan, J. and Freer, R. (1993). Improvement of the non-linearity and degradation behaviour of ZnO varistors. *British Ceramic Transactions* 92 (6): 221–226.

90 Asokan, T. and Freer, R. (1990). Characterization of spinel particles in zinc oxide varistors. *Journal of Materials Science* 25 (5): 2447–2453.

91 Look, D.C. (2001). Recent advances in ZnO materials and devices. *Materials Science and Engineering: B* 80 (1-3): 383–387.

92 Ohashi, N., Terada, Y., Ohgaki, T. et al. (1999). Synthesis of ZnO bicrystals doped with Co or Mn and their electrical properties. *Japanese Journal of Applied Physics* 38 (9R): 5028–5032.

93 Oba, F. and Tanaka, I. (1999). Effect of oxidation on chemical bonding around 3d transition-metal impurities in ZnO. *Japanese Journal of Applied Physics* 38 (6R): 3569–3575.

94 Berrnik, S. and Daneu, N. (2001). Characteristics of SnO_2-doped ZnO-based varistor ceramics. *Journal of the European Ceramic Society* 21 (10-11): 1879–1882.

95 Fons, P., Nakahara, K., Yamada, A. et al. (2002). A XANES study of Cu valency in Cu-doped epitaxial ZnO. *Physica Status Solidi* 229 (2): 849–852.

96 Bellini, J.V., Morelli, M.R., and Kiminami, R.H.G.A. (2002). Electrical properties of polycrystalline ZnO: Cu obtained from freeze-dried ZnO^+ copper(II) acetate powders. *Journal of Materials Science: Materials in Electronics* 13 (8): 485–489.

97 Kutty, T.R.N. and Raghu, N. (1989). Varistors based on polycrystalline ZnO: Cu. *Applied Physics Letters* 54 (18): 1796–1798.

98 Jun, S.T. and Choi, G.M. (1998). Composition dependence of the electrical conductivity of ZnO(n)–CuO(p) ceramic composite. *Journal of the American Ceramic Society* 81 (3): 695–699.

99 He, J., Long, W., Hu, J., and Liu, J. (2011). Nickel oxide doping effects on electrical characteristics and microstructural phases of ZnO varistors with low residual voltage ratio. *Journal of the Ceramic Society of Japan* 119 (1385): 43–47.

100 Zhang, C., Hu, Y., Lu, W. et al. (2002). Influence of TiO_2/Sb_2O_3 ratio on ZnO varistor ceramics. *Journal of the European Ceramic Society* 22 (1): 61–65.

101 Lei, M., Li, S., Li, J., and Alim, M.A. (2006). The role of CeO_2 in the high electric field ZnO varistors. *Journal of Applied Sciences* 6 (8): 1671–1678.

102 Sedky, A., Abu-Abdeen, M., and Almulhem, A.A. (2007). Nonlinear I–V characteristics in doped ZnO based-ceramic varistor. *Physica B: Condensed Matter* 388 (1-2): 266–273.

103 Puyané, R., Guy, I., and Metz, R. (1998). High performance varistor discs obtained from chemically synthesized doped zinc oxide powder. *Journal of Sol-Gel Science and Technology* 13 (1-3): 575–578.

104 Ya, K.X., Diao, W.T., Han, Y. et al. (1997). Sol-gel process doped ZnO nanopowders and their grain growth. *Materials Research Bulletin* 32 (9): 1165–1171.

105 Miyoshi, T., Yamazaki, T., Takahashi, K., and Maeda, K. (1981). Effects of dopants on the characteristics of ZnO varistors. In: *Advances in Ceramics, Vol. 1, Grain Boundary Phenomena in Electronic Ceramics* (ed. L.M. Levinson), 309–315. Columbus, OH: American Ceramics Society.

106 Gupta, T.K. (1994). Donor doping of Ga in ZnO varistor grain boundary. *Journal of Materials Research* 9 (9): 2213–2215.

107 Hu, J., Long, W.C., He, J.L. et al. (2010). Origin of leakage currents in ZnO based varistor ceramics with $Al(NO_3)_3$ dopant. *Key Engineering Materials* 2010 (434): 386–388.

108 Nahm, C.W. (2001). The electrical properties and dc degradation characteristics of Dy_2O_3 doped Pr_6O_{11}-based ZnO varistors. *Journal of the European Ceramic Society* 21 (4): 545–553.

109 Fujihara, S., Sasaki, C., and Kimura, T. (2001). Effects of Li and Mg doping on microstructure and properties of sol-gel ZnO thin films. *Journal of the European Ceramic Society* 21 (10-11): 2109–2112.

110 Inoue, M. (1979). A model for the acceptor state in II–VI compounds. *Journal of Physics and Chemistry of Solids* 40 (11): 857–862.

111 Kuo, S.T., Tuan, W.H., Shieh, J., and Wang, S.F. (2007). Effect of Ag on the microstructure and electrical properties of ZnO. *Journal of the European Ceramic Society* 27 (16): 4521–4527.

112 Houabes, M. and Metz, R. (2007). Rare earth oxides effects on both the threshold voltage and energy absorption capability of ZnO varistors. *Ceramics International* 33 (7): 1191–1197.

113 Ashraf, M.A., Bhuiyan, A.H., Hakim, M.A., and Hossain, M.T. (2010). Microstructure and electrical properties of Ho_2O_3 doped Bi_2O_3-based ZnO varistor ceramics. *Physica B: Condensed Matter* 405 (17): 3770–3774.

114 Lei, M., Li, S., Jiao, X. et al. (2004). The influence of CeO_2 on the microstructure and electrical behaviour of ZnO–Bi_2O_3 based varistors. *Journal of Physics D: Applied Physics* 37 (5): 804–812.

115 Quang, N.D. and Bernik, S. (2001). Electrical and microstructural characteristics of ZnO-Bi_2O_3-based varistors doped with rare-earth oxides. *Journal of Materials Research* 16 (10): 2817–2823.

116 Hu, J., He, J., and Chen, Q. (2006). High voltage gradient ZnO nonlinear resistor doped with rare-earth oxide. In: *Proceedings of 8th International Conference on Properties and Applications of Dielectric Materials*, 963–966. IEEE.

117 Bernik, S., Macek, S., and Ai, B. (2001). Microstructural and electrical characteristics of Y_2O_3-doped ZnO–Bi_2O_3-based varistor ceramics. *Journal of the European Ceramic Society* 21 (10-11): 1875–1878.

118 He, J., Hu, J., and Lin, Y. (2008). ZnO varistors with high voltage gradient and low leakage current by doping rare-earth oxide. *Science in China Series E: Technological Sciences* 51 (6): 693–701.

119 Nahm, C.W., Shin, B.C., and Min, B.H. (2003). Microstructure and electrical properties of Y_2O_3-doped ZnO-Pr_6O_{11}-based varistor ceramics. *Materials Chemistry and Physics* 82 (1): 157–164.

120 Silva, I.P., Simões, A.Z., Longo, E. et al. (2007). Dependence of La_2O_3 content on the nonlinear electrical behaviour of ZnO, CoO and Ta_2O_5 doped SnO_2 varistors. *Materials Letters* 61 (10): 2121–2125.

121 Nahm, C.W. (2006). Effect of sintering temperature on nonlinear electrical properties and stability against DC accelerated aging stress of (CoO, Cr_2O_3, La_2O_3)-doped ZnO-Pr_6O_{11}-based varistors. *Materials Letters* 60 (28): 3311–3314.

122 Wang, M.H., Hu, K.A., Zhao, B.Y., and Zhang, N.F. (2006). Electrical characteristics and stability of low voltage ZnO varistors doped with Al. *Materials Chemistry and Physics* 100 (1): 142–146.

123 Wang, Q., Qin, Y., Xu, G.J. et al. (2008). Low-voltage ZnO varistor fabricated by the solution-coating method. *Ceramics International* 34 (7): 1697–1701.

124 Lorenz, A., Ott, J., Harrer, M. et al. (2001). Modified citrate gel routes to ZnO-based varistors. *Journal of the European Ceramic Society* 21 (10-11): 1887–1891.

125 Kusy, A. and Kleinpenning, T.G.M. (1983). Conduction mechanism and 1/f noise in ZnO varistors. *Journal of Applied Physics* 54 (6): 2900–2906.

126 Kim, E.D., Kim, C.H., and Oh, M.H. (1985). Role and effect of Co_2O_3 additive on the upturn characteristics of ZnO varistors. *Journal of Applied Physics* 58 (8): 3231–3235.

127 Koumoto, K., Aoki, N., Kitaori, N., and Yanaoida, H. (1982). Enhancement of electrical conduction in ZnO by CoO doping. *Journal of the American Ceramic Society* 65 (6): c93–c94.

128 Han, J., Mantas, P.Q., and Senos, A.M.R. (2002). Defect chemistry and electrical characteristics of undoped and Mn-doped ZnO. *Journal of the European Ceramic Society* 22 (1): 49–59.

129 Han, J., Mantas, P.Q., and Senos, A.M.R. (2001). Effect of Al and Mn doping on the electrical conductivity of ZnO. *Journal of the European Ceramic Society* 21 (10-11): 1883–1886.

130 Han, J., Senos, A.M.R., and Mantas, P.Q. (1999). Nonisothermal sintering of Mn doped ZnO. *Journal of the European Ceramic Society* 19 (6-7): 1003–1006.

131 Han, J., Senos, A.M.R., and Mantas, P.Q. (2002). Deep donors in polycrystalline Mn-doped ZnO. *Materials Chemistry and Physics* 75 (1-3): 117–120.

132 Einzinger, R. (1982). Grain boundary phenomena in ZnO varistors. In: *Materials Research Society Symposia Proceedings: Grain Boundaries in Semiconductors*, vol. 5 (ed. H.J. Leamy, G.E. Pike and C.H. Seager), 343–355. Amsterdam: North-Holland.

133 Ziegler, E., Heinrich, A., Oppermann, H., and Stöver, G. (1982). Growth and electrical properties of non-stoichiometric ZnO single crystals doped with Co. *Physica Status Solidi (A)* 70 (2): 563–570.

134 Haynes, W.M. (ed.) (2014). *CRC Handbook of Chemistry and Physics*. New York: CRC Press.

135 Long, W., Hu, J., Liu, J., and He, J. (2010). Effects of cobalt doping on the electrical characteristics of Al-doped ZnO varistors. *Materials Letters* 64 (9): 1081–1084.

136 Zhu, J.F., Qi, G.Q., Yang, H.B., and Wang, F. (2011). Effect of composite additives on ZnO varistor ceramics. *Materials Science Forum* 687: 21–25.

137 Daneu, N., Rečnik, A., Bernik, S., and Kolar, D. (2000). Microstructural development in SnO_2-doped ZnO-Bi_2O_3 ceramics. *Journal of the American Ceramic Society* 83 (12): 3165–3171.

138 Daneu, N., Rečnik, A., and Bernik, S. (2003). Grain growth control in Sb_2O_3-doped zinc oxide. *Journal of the American Ceramic Society* 86 (8): 1379–1384.

139 Ott, J., Lorenz, A., Harrer, M. et al. (2001). The influence of Bi_2O_3 and Sb_2O_3 on the electrical properties of ZnO-based varistors. *Journal of Electroceramics* 6 (2): 135–146.

140 Clarke, D.R. (1979). Grain-boundary segregation in a commercial ZnO-based varistor. *Journal of Applied Physics* 50 (11): 6829–6832.

141 Wu, L., Shen, C.Y., Chen, Y.C. et al. (1991). The microstructure of ZnO varistor doped with antimony oxide. *Japanese Journal of Applied Physics* 30 (11R): 2850–2856.

142 Ito, M., Tanahashi, M., Uehara, M., and Iga, A. (1997). The Sb_2O_3 addition effect on sintering ZnO and ZnO+Bi_2O_3. *Japanese Journal of Applied Physics* 36 (11A): L1460–L1463.

143 Rečnik, A., Daneu, N., Walther, T., and Mader, W. (2001). Structure and chemistry of basal-plane inversion boundaries in antimony oxide-doped zinc oxide. *Journal of the American Ceramic Society* 84 (11): 2657–2668.

144 Trontelj, M., Kolar, D., and Krasevec, V. (1983). Influence of additives on varistor microstructures. In: *Additives and Interfaces in Electronic Ceramics*, vol. 7 (ed. M.F. Yan and A.H. Heuer), 107–116. Columbus, OH: The American Ceramic Society.

145 Peigney, A., Andrianjatovo, H., Legros, R., and Rousset, A. (1992). Influence of chemical composition on sintering of bismuth-titanium-doped zinc oxide. *Journal of Materials Science* 27 (9): 2397–2405.

146 Makovec, D., Kolar, D., and Trontelj, M. (1993). Sintering and microstructural development of metal oxide varistor ceramics. *Materials Research Bulletin* 28 (8): 803–811.

147 Suzuki, H. and Bradt, R.C. (1995). Grain growth of ZnO in ZnO-Bi_2O_3 ceramics with TiO_2 additions. *Journal of the American Ceramic Society* 78 (5): 1354–1360.

148 Gilbert, I. and Freer, R. (2002). Donor and acceptor doping of zinc oxide varistors. *Journal of Physics: Condensed Matter* 14 (4): 945.

149 Gupta, T.K. and Miller, A.C. (1988). Improved stability of the ZnO varistor via donor and acceptor doping at the grain boundary. *Journal of Materials Research* 3 (4): 745–754.

150 Binks, D.J. and Grimes, R.W. (1993). Incorporation of monovalent ions in ZnO and their influence on varistor degradation. *Journal of the American Ceramic Society* 76 (9): 2370–2372.

151 Chiang, Y.M. and Takagi, T. (1990). Grain-boundary chemistry of barium titanate and strontium titanate: I, high-temperature equilibrium space charge. *Journal of the American Ceramic Society* 73 (11): 3278–3285.

152 MacLaren, I., Cannon, R.M., Gülgün, M.A. et al. (2003). Abnormal grain growth in alumina: synergistic effects of yttria and silica. *Journal of the American Ceramic Society* 86 (4): 650–659.

153 Gupta, T.K. (1990). Effect of minor doping on the high current application of the ZnO varistor. *Ferroelectrics* 102 (1): 391–396.

154 Tsai, Y.L., Huang, C.L., and Wei, C.C. (1985). Improvement of nonlinearity in a ZnO varistor by Al_2O_3 doping. *Journal of Materials Science Letters* 4 (11): 1305–1307.

155 Long, W., Hu, J., Liu, J. et al. (2010). The effect of aluminum on electrical properties of ZnO varistors. *Journal of the American Ceramic Society* 93 (9): 2441–2444.

156 Long, W., Hu, J., He, J. et al. (2011). Effects of manganese dioxide additives on the electrical characteristics of Al-doped ZnO varistors. *Science China Series E: Technological Sciences* 54 (8): 2204–2208.

157 Tanahashi, M., Ito, M., Murao, M., and Iga, A. (1997). Effect of Al-doping on the grain growth of ZnO. *Japanese Journal of Applied Physics* 36 (5A): L573–L576.

158 Han, J., Mantas, P.Q., and Senos, A.M.R. (2001). Densification and grain growth of Al-doped ZnO. *Journal of Materials Research* 16 (2): 459–468.

159 Lu, Z., Cai, Y., Chen, Z., and Wu, J. (2007). Effects of Fe impurity on performances of ZnO varistors. *Rare Metal Materials and Engineering* 36 (S2): 187–190.

160 Deshpande, V.V., Patil, M.M., and Ravi, V. (2006). Low voltage varistors based on CeO_2. *Ceramics International* 32 (1): 85–87.

161 Cai, J., Lin, Y.H., Li, M. et al. (2007). Sintering temperature dependence of grain boundary resistivity in a rare-earth-doped ZnO varistor. *Journal of the American Ceramic Society* 90 (1): 291–294.

162 Ashraf, M.A., Bhuiyan, A.H., Hakim, M.A., and Hossain, M.T. (2011). Microstructure and electrical properties of Sm_2O_3 doped Bi_2O_3-based ZnO varistor ceramics. *Materials Science and Engineering: B* 176 (11): 855–860.

163 Hongyu, L., Hui, K., Dongmei, J. et al. (2007). Microstructure and electrical properties of Er_2O_3-doped ZnO-based varistor ceramics prepared by high-energy ball milling. *Journal of Rare Earths* 25 (1): 120–123.

164 Xu, D., Cheng, X., Zhao, G. et al. (2011). Microstructure and electrical properties of Sc_2O_3-doped ZnO–Bi_2O_3-based varistor ceramics. *Ceramics International* 37 (3): 701–706.

165 Liu, J., He, J.L., Hu, J. et al. (2010). Admittance spectroscopy of Y_2O_3-doped ZnO varistors sintered at different temperature. *Key Engineering Materials* 434–435: 382–385.

166 Hu, J., He, J., Long, W., and Liu, J. (2010). Temperature dependences of leakage currents of ZnO varistors doped with rare-earth oxides. *Journal of the American Ceramic Society* 93 (8): 2155–2157.

167 Liu, J., Hu, J., He, J. et al. (2009). Microstructures and characteristics of deep trap levels in ZnO varistors doped with Y_2O_3. *Science in China Series E: Technological Sciences* 52 (12): 3668–3673.

168 Meng, P., Hu, J., Zhao, H., and He, J. (2016). High voltage gradient and low residual-voltage ZnO varistor ceramics tailored by doping with In_2O_3 and Al_2O_3. *Ceramics International* 42 (16): 19437–19440.

169 He, J., Liu, J., Hu, J., and Long, W. (2011). AC ageing characteristics of Y_2O_3-doped ZnO varistors with high voltage gradient. *Materials Letters* 65 (17-18): 2595–2597.

170 Jile, L., Chen, G.H., and Yuan, C.L. (2013). Microstructure and electrical properties of rare earth doped ZnO-based varistor ceramics. *Ceramics International* 39 (3): 2231–2237.

171 Nahm, C.W. (2003). Nonlinear properties and stability against DC accelerated aging stress of praseodymium oxide-based ZnO varistors by Er_2O_3 doping. *Solid State Communications* 126 (5): 281–284.

172 Dong, X.U., Jieting, W., Lei, J. et al. (2013). Highly nonlinear property and threshold voltage of Sc_2O_3 doped ZnO-Bi_2O_3-based varistor ceramics. *Journal of Rare Earths* 31 (2): 158–163.

173 Xu, D., Cheng, X.N., Wang, M.S., and Shi, L.Y. (2009). Microstructure and electrical properties of La_2O_3-doped ZnO-Bi_2O_3 based varistor ceramics. *Advanced Materials Research* 79–82: 2007–2010.

174 Nahm, C.W. and Park, C.H. (2001). Effect of Er_2O_3 addition on the microstructure, electrical properties, and stability of Pr_6O_{11}-based ZnO ceramic varistors. *Journal of Materials Science* 36 (7): 1671–1679.

175 Abdullah, K.A.L., Termanini, M.D., and Omar, F.A. (2012). Optimization of impurities "Bi_2O_3, Nb_2O_5, MnO_2, Co_3O_4, Cr_2O_3, NiO, Ce_2O_3, and La_2O_3" to improve the ZnO based varistor nonlinearity. *Energy Procedia* 19: 128–142.

176 Nahm, C.W. (2004). Microstructure and electrical properties of Dy_2O_3-doped ZnO–Pr_6O_{11}-based varistor ceramics. *Materials Letters* 58 (17-18): 2252–2255.

177 Nahm, C.W., Park, C.H., and Yoon, H.S. (2000). Microstructure and varistor properties of ZnO-Pr_6O_{11}-CoO-Nd_2O_3 based ceramics. *Journal of Materials Science Letters* 19 (4): 271–274.

178 Wang, M.H., Tang, Q.H., and Yao, C. (2010). Electrical properties and AC degradation characteristics of low voltage ZnO varistors doped with Nd_2O_3. *Ceramics International* 36 (3): 1095–1099.

179 Yan, Q., Chen, J.Z., and Tu, M.J. (2005). Influence of Nd_2O_3 on voltage and microstructure of ZnO varistor materials. *Rare Metal Materials and Engineering* 34 (1): 154–157.

180 Bernik, S., Maček, S., and Bui, A. (2004). The characteristics of ZnO-Bi_2O_3-based varistor ceramics doped with Y_2O_3 and varying amounts of Sb_2O_3. *Journal of the European Ceramic Society* 24 (6): 1195–1198.

181 Fan, J. and Freer, R. (1994). Deep level transient spectroscopy of zinc oxide varistors doped with aluminum oxide and/or silver oxide. *Journal of the American Ceramic Society* 77 (10): 2663–2668.

182 Arakawa, T., Kurachi, H., Tsujita, M., and Shiokawa, J. (1985). Deep-level transient spectroscopy of rare-earth-zinc oxide varistors. *Journal of Materials Science Letters* 4 (12): 1442–1444.

183 Tsuda, K. and Mukae, K. (1989). Characterization of the interface states in ZnO varistors by DLTS method. *Journal of the Ceramic Society of Japan* 97 (1130): 1211–1218.

184 Shohata, N., Matsumura, T., and Ohno, T. (1980). DLTS measurement on non-ohmic zinc oxide ceramic varistor. *Japanese Journal of Applied Physics* 19 (9): 1793–1794.

185 Nitayama, A., Sakaki, H., and Ikoma, T. (1980). Properties of deep levels in ZnO varistors and their effect on current-response characteristics. *Japanese Journal of Applied Physics* 19 (12): L743–L746.

186 Shohata, N., Matsumura, T., Utsumi, K., and Ohno, T. (1981). Properties of multilayer ZnO ceramic varistors. In: *Advances in Ceramics (Grain Boundary Phenomena in Electrical Ceramics)*, vol. 1 (ed. L.M. Levinson and D. Hill), 48–59. Columbus, OH: American Ceramic Society.

187 Gupta, T.K. and Carlson, W.G. (1985). A grain-boundary defect model for instability/stability of a ZnO varistor. *Journal of Materials Science* 20 (10): 3487–3500.

188 Kawaguchi, T., Yoshida, H., and Kawai, H. (1966). Photosensitive ESR and photoconduction of Li- and Ag-doped ZnO (in Jpn.). *Electrophotography* 7 (1): 24–30.

189 Hagemark, K.I. and Chacka, L.C. (1975). Electrical transport properties of Zn doped ZnO. *Journal of Solid State Chemistry* 15 (3): 261–270.

190 Hagemark, K.I. (1976). Defect structure of Zn-doped ZnO. *Journal of Solid State Chemistry* 16 (3-4): 293–299.

191 Bylander, E.G. (1978). Surface effects on the low-energy cathodoluminescence of zinc oxide. *Journal of Applied Physics* 49 (3): 1188–1195.

192 Choi, J.S. and Yo, C.H. (1976). Study of the nonstoichiometric composition of zinc oxide. *Journal of Physics and Chemistry of Solids* 37 (12): 1149–1151.

193 Van de Walle, C.G. (2000). Hydrogen as a cause of doping in zinc oxide. *Physical Review Letters* 85 (5): 1012–1015.

194 Look, D.C., Hemsky, J.W., and Sizelove, J.R. (1999). Residual native shallow donor in ZnO. *Physical Review Letters* 82 (12): 2552–2555.

195 Kohan, A.F., Ceder, G., Morgan, D., and Van de Walle, C.G. (2000). First-principles study of native point defects in ZnO. *Physical Review B* 61 (22): 15019–15027.

196 Haskell, B.A., Souri, S.J., and Helfand, M.A. (1999). Varistor behavior at twin boundaries in ZnO. *Journal of the American Ceramic Society* 82 (8): 2106–2110.

197 McCoy, M.A., Grimes, R.W., and Lee, W.E. (1996). Inversion domain boundaries in ZnO ceramics. *Journal of Materials Research* 11 (8): 2009–2019.

198 Bruley, J., Bremer, U., and Krasevec, V. (1992). Chemistry of basal plane defects in zinc oxide–antimony oxide (0.1 mol%) ceramics. *Journal of the American Ceramic Society* 75 (11): 3127–3128.

199 Makovec, D. and Trontelj, M. (1994). Extended defects in ZnO ceramics containing $Bi_4Ti_3O_{12}$ additive. *Journal of the American Ceramic Society* 77 (5): 1202–1208.

200 Kim, J., Kimura, T., and Yamaguchi, T. (1989). Sintering of zinc oxide doped with antimony oxide and bismuth oxide. *Journal of the American Ceramic Society* 72 (8): 1390–1395.

201 Kraševec, V., Trontelj, M., and Golič, L. (1991). Transmission electron microscope study of antimony-doped zinc oxide ceramics. *Journal of the American Ceramic Society* 74 (4): 760–766.

202 Jo, W., Kim, S.J., and Kim, D.Y. (2005). Analysis of the etching behavior of ZnO ceramics. *Acta Materialia* 53 (15): 4185–4188.

203 Daneu, N., Bernik, S., and Rečnik, A. (2011). Inversion boundary induced grain growth in ZnO ceramics: from atomic-scale investigations to microstructural engineering. *Journal of Physics: Conference Series* 326 (1): 012003.

204 Daneu, N., Walther, T., Rečnik, A. et al. (2000). Structure and composition of inversion boundaries in Sn-doped ZnO. In: *Proceedings of the 12th European Congress on Electron Microscopy, Brno, Czech Republic: II*, P435–P436.

205 Glot, A.B. and Hogarth, C.A. (1985). Highly non-linear voltage-current characteristic of the contact to a ZnO-based ceramic material. *International Journal of Electronics* 58 (1): 117–121.

206 Milosevic, O. (1983). The study of the grain growth and electric properties of ZnO varistor ceramics. *Science Sintering* 15 (3): 121–130.

207 Viswanath, R.N., Ravi, P., and Ramasamy, S. (1995). Preparation and characterisation of ZnO-based materials for varistor applications. *Transactions on the Indian Institute of Metals* 48 (3): 221–224.

208 Hu, J., He, J.L., Liu, J., and Long, W.C. (2009). Analysis on voltage gradient limitation of ZnO varistor in ultra high voltage arrester (in Chinese). *High Voltage Apparatus* 45 (1): 1–4.

209 He, J.L., Hu, J., Meng, B.W. et al. (2009). Requirement of ultra-high voltage GIS arrester to voltage gradient of metal-oxide varistor. *Science in China Series E, Technological Sciences* 52 (2): 450–455.

210 Imai, T., Udagawa, T., Ando, H. et al. (1998). Development of high gradient zinc oxide nonlinear resistors and their application to surge arresters. *IEEE Transactions on Power Delivery* 13 (4): 1182–1187.

211 Chen, Q.H. (2003). Research on ZnO nonlinear resistor with large surge energy absorption capability and high voltage gradient. Doctoral thesis. Tsinghua University, Beijing, China.

212 Nan, C.W. and Clarke, D.R. (1996). Effect of variations in grain size and grain boundary barrier heights on the current-voltage characteristics of ZnO varistors. *Journal of the American Ceramic Society* 79 (12): 3185–3192.

213 Meng, P.F., Lyu, S., Hu, J., and He, J.L. (2017). Tailoring low leakage current and high nonlinear coefficient of a Y-doped ZnO varistor by indium doping. *Materials Letters* 188: 77–79.

214 Meng, P.F., Hu, J., and He, J.L. (2017). Low-residual-voltage ZnO varistor ceramics improved by multiple doping with gallium and indium. *Materials Letters* 195: 209–212.

215 Meng, P.F., Lyu, S., Hu, J., and He, J.L. (2017). Indium tailors the leakage current and voltage gradient of multiple dopant-based ZnO varistors. *Ceramics International* 43 (5): 4127–4130.

216 Meng, P.F., Gu, S.Q., Wang, J. et al. (2018). Improving electrical properties of multiple dopant ZnO varistor by doping with indium and gallium. *Ceramics International* 44 (1): 1168–1171.

217 Meng, P., Yang, X., Hu, J., and He, J. (2017). Tailoring electrical properties of multiple dopant-based ZnO varistor by doping with yttrium, gallium, and indium. *Materials Letters* 209: 413–416.

218 Houabes, M., Bernik, S., Talhi, C., and Bui, A. (2005). The effect of aluminium oxide on the residual voltage of ZnO varistors. *Ceramics International* 31 (6): 783–789.

219 Zhang, Y. and Han, J. (2006). Microstructure and temperature coefficient of resistivity for ZnO ceramics doped with Al_2O_3. *Materials Letters* 60 (20): 2522–2525.

220 West, A.R. and Andres-Verges, M. (1997). Impedance and modulus spectroscopy of ZnO varistors. *Journal of Electroceramics* 1 (2): 125–132.

221 Long, W.C. (2011). Research on the ZnO varistor with low residual voltage used in ultra-high voltage arrester. Doctoral thesis. Tsinghua University, Beijing, China.

222 Eda, K., Iga, A., and Matsuoka, M. (1980). Degradation mechanism of non-ohmic zinc oxide ceramics. *Journal of Applied Physics* 51 (5): 2678–2684.

223 Zhao, H.F., Hu, J., Chen, S.M. et al. (2016). Improving age stability and energy absorption capabilities of ZnO varistors ceramics. *Ceramics International* 42 (15): 17880–17883.

224 Bartkowiak, M., Comber, M.G., and Mahan, G.D. (2001). Influence of nonuniformity of ZnO varistors on their energy absorption capability. *IEEE Transactions on Power Delivery* 16 (4): 591–598.

225 He, J.L., Zeng, R., Tu, Y.P. et al. (2000). Aging characteristics and mechanisms of ZnO nonlinear varistors. In: *Proceedings of the 6th International Conference on Properties and Applications of Dielectric Materials*, 790–793. Xi'an, China: IEEE.

226 Zhao, H.F., Hu, J., Chen, S.M. et al. (2016). Tailoring the high impulse current discharge capability of ZnO varistor ceramics by doping Ga_2O_3. *Ceramics International* 42 (4): 5582–5586.

227 Cheng, L.H., Li, G.R., Yuan, K.Y. et al. (2012). Improvement in nonlinear properties and electrical stability of ZnO varistors with B_2O_3 additives by nano-coating method. *Journal of the American Ceramic Society* 95 (3): 1004–1010.

228 Zhao, H.F., He, J.L., Hu, J. et al. (2016). High nonlinearity and low residual-voltage ZnO varistor ceramics by synchronously doping Ga_2O_3 and Al_2O_3. *Materials Letters* 164: 80–83.

229 Zhao, H.F., Hu, J., Chen, S.M. et al. (2016). High nonlinearity and high voltage gradient ZnO varistor ceramics tailored by combining Ga_2O_3, Al_2O_3, and Y_2O_3 dopants. *Journal of the American Ceramic Society* 99 (3): 769–772.

4

Microstructural Electrical Characteristics of ZnO Varistors

A bulk varistor is a complex multijunction device composed of large numbers of grain boundaries and grains connected in a random network; the electrical properties of each individual grain boundary will contribute to the global electrical characteristics of ZnO varistors. The electrical characteristics of grain boundaries in ZnO varistors were systematically analyzed. High nonuniformity exists in barrier voltages and nonlinear coefficients in different grain boundaries. Barrier voltages have normal distributions, only a few grain boundaries are electrically active, the grain boundaries can be simply classified into good, bad, and ohmic ones according to the electrical characteristics of grain boundaries, and a high percentage of grain boundaries have bad or ohmic I–V characteristics, while only a small percentage of grain boundaries have good I–V characteristics. These few good grain boundaries are responsible for the good varistor effect and control the leakage current of the ZnO varistor at low values of applied voltage. There is a huge difference between the barrier voltages measured by direct and indirect measurement methods. Modern scanning probe microscopy-based techniques are introduced, which allow the study of electric properties of ZnO varistors on the nanometer scale, and combining all methods, a quite comprehensive assessment of the distribution of possible causes of current paths in a varistor ceramic will be presented. At last, ZnO bicrystal with controlled dopants at the interface is introduced for studying the electrical characteristics and related mechanisms, but the fabrication of Bi-doped bicrystal with excellent nonlinearity is still challenging.

4.1 Introduction

The electrical characteristics of ZnO varistors are synthetical responses of different individual grain boundaries. Many researchers [1–11] had measured the electrical characteristics of individual grain boundaries on the surfaces of ZnO varistor disks or estimated the average parameters from disk measurement by different methods. From the experimental results, differences in electrical characteristics among different individual grain boundaries, and differences between the results of individual grain boundaries and that of the global ZnO varistors can be found. That is to say, the electrical properties of different single

junctions are not identical. Many researchers had developed different kinds of techniques to study the individual grain boundary. These single-junction I–V characteristics showed that a distribution of the breakdown behavior depended on the microstructures [6, 7, 11]. When these single junctions are put together to form a bulk device, the electrical properties of each individual junction will contribute to the overall signal. It is very important to understand the influence of the junction network on the device properties [12]. So, analyzing the electrical characteristics of individual grain boundaries is useful to understand the global electrical characteristics of ZnO varistors and is helpful in simulating the microstructural characteristics of ZnO varistors. He et al. [13] presented a systematic analysis on the nonuniformity of ZnO varistors.

4.2 Methods to Determine Grain Boundary Parameters

One of the important parameters in the physical models of ZnO varistors explaining the transition phenomena from the low current region to the high current region is the value of the barrier voltage, which is the breakdown voltage per grain boundary barrier and has been typically determined by indirect and direct methods. During the initial explorations of the origins of varistor behavior, usually microcontact measurements were made to correlate electrical behavior to the principal microstructural features [4–7] as those first described by Einzinger [14], although others were made nonevasively by voltage contrast imaging.

4.2.1 The Indirect Method

The indirect method [2, 15, 16] derives this breakdown voltage from the experimental observation that the voltage at a constant current is inversely proportional to the grain size. Dividing this voltage by the average number of grains between the electrodes yields a calculated barrier voltage V_B under the assumption that all grains between two electrodes have the same grain size [17]. Generally, it is very difficult to obtain a homogeneous microstructure in a practical ceramic body, and therefore, it is not possible that all grain sizes are the same, but rather the grain sizes in the microstructure have a distribution. Moreover, numerous studies have confirmed that the results of "average" property measurements are not exact representations of the individual grain boundaries.

4.2.2 The Direct Microcontact Methods

The microcontact method [2–5] consists of contacting two adjacent grains using small and narrow electrodes and measuring the I–V characteristics of grain boundaries. The first method [2, 8, 11, 13, 18, 19] consists of obtaining the current–voltage curve of one single junction by microcontact on the two adjacent grains with the help of very sharp needles (radius of curvature $\leq 1\ \mu m$). The second one used a better electrical contact by evaporating a pair of opposing Al [1, 8] or Au [4] electrodes with a 10 μm separation on the surface of a varistor.

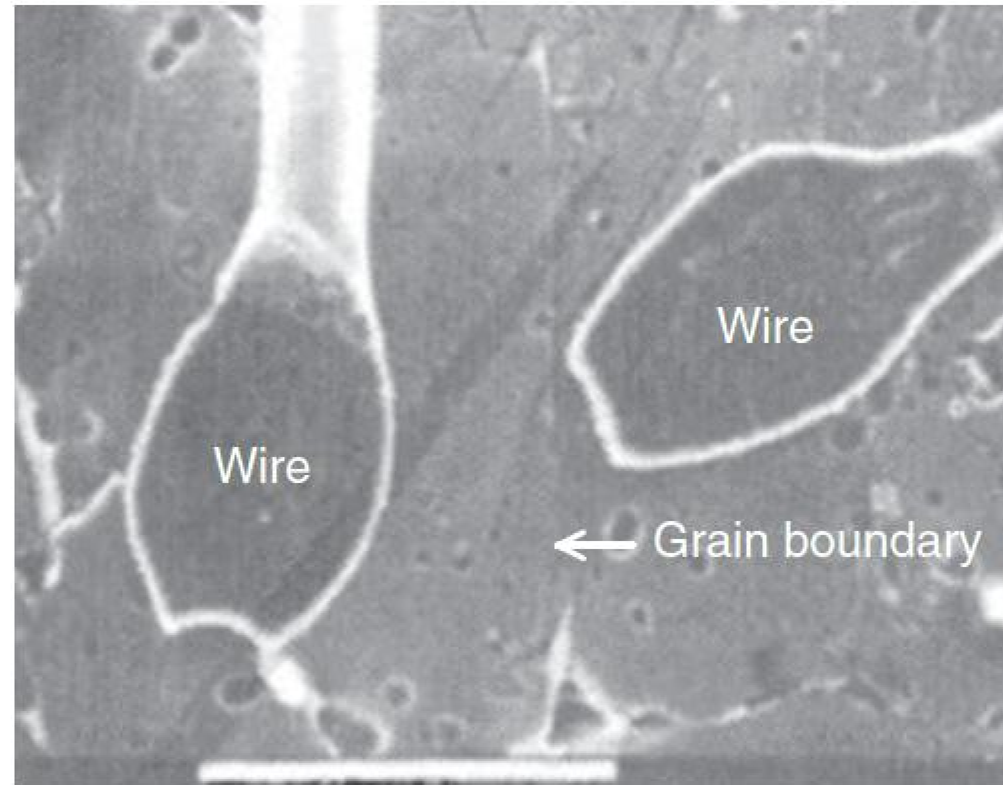


Figure 4.1 SEM photomicrograph of two wires welded with the help of an ultrasonic generator on the surface of a ZnO varistor (white line is 100-μm in length). Source: Tao et al. 1987 [6]. Reproduced with permission of AIP.

Tao et al. [6] used a microwelder technique to weld a gold wire on each surface of two adjacent ZnO grains, as shown in Figure 4.1, with the help of an ultrasonic generator under an optical microscope; the wire diameter was 25 μm.

Olsson and Dunlop [10] deposited silver electrodes on the polished surfaces using photolithography, and a special electrode configuration consisting of 35 electrode pairs distributed in a circular array, which had an outside diameter of 3 mm, was designed where the electrode tip width was 5 μm and the tip gap was 8 μm in order to often obtain single interfaces between the opposing electrode tips, which is shown in Figure 4.2. Sun et al. deposited a gold electrode array on the surface of a polished sample to measure individual grain boundary behavior [20]. Rodewald et al. [21] deposited the microelectrodes consisting of conducting $YBa_2Cu_3O_{6+x}$ (150 nm) covered with a thin Ag layer (50 nm); the silver layer reduced the contact resistance between the deposited microelectrode and the contacting tip. The electrodes were contacted by two tungsten tips (1 mm tip radius) positioned by micromanipulators.

Wang et al. [7] designed 14 special electrode "cells"; a cell contains 20 labeled electrode pairs, and the tips of the electrodes are 4 μm wide. Tanaka et al. used the photolithography technique too, to form microelectrodes on the surface of samples; the microelectrode system contained 72 pairs of aluminum electrodes,

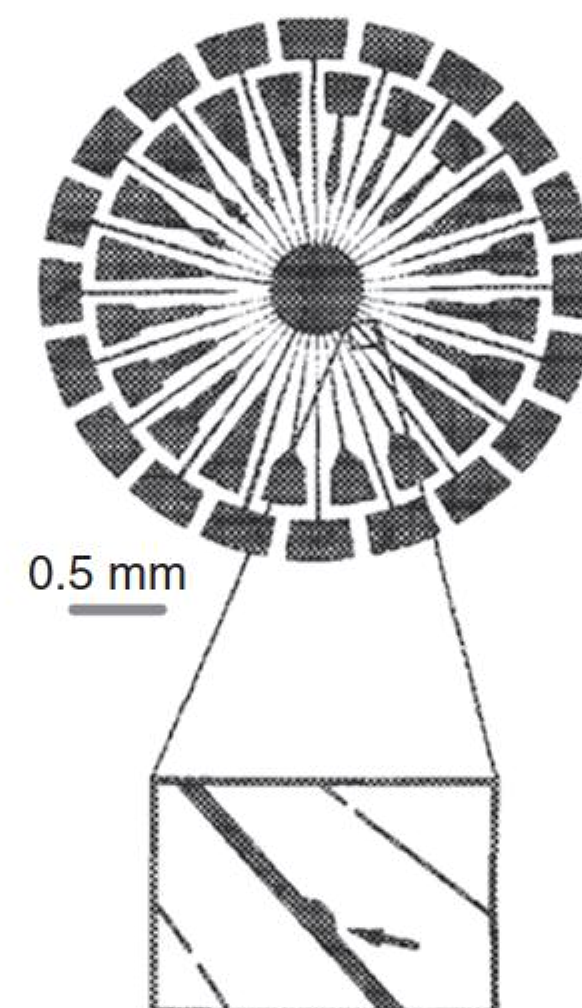


Figure 4.2 Microelectrode configuration, which is used for measurement of current–voltage characteristics across individual grain junctions. The different shapes of the contacts and the arrowed feature allow them to be identified during electron microscopy. Source: Olsson and Dunlop 1989 [10]. Reproduced with permission of AIP.

the separation between two electrode tips was 5 μm, and the distance between a pair of electrodes was 10 μm [22].

The microelectrodes designed for microcontact measurement was introduced in detail [23, 24], which was prepared by photolithograph method. The polished surfaces of the ZnO varistor sample were coated with photoresist, and then illumination through a suitable mask uncovered part of the ZnO surface. And then, a thin Ag or Au layer with 100 nm thickness was evaporated on each sample. Subsequently, the rest of excess photoresist was washed away by acetone. The schematic configuration of microcontact measurement is shown in Figure 4.3 [25]. The configuration of electrodes is shown in Figure 4.4 [23]. The electrodes are designed to be 20 μm in diameter for the convenience of microcontacts with the microprobe and observation of individual grain boundaries, and the distance between adjacent electrodes is 5 μm. Therefore, there may exist zero, one, two, or three grain boundaries between adjacent electrodes.

Microcontact measurement can be carried out on a probe station (such as Summit 11 000 M, Cascade Microtech, Inc., USA), an optical high magnification microscope (FS-70, Mitutoyo Corporation, Japan), and a couple of coaxial probes with a 0.5 μm replaceable tip (DCP-105R, Cascade Microtech, Inc., USA) secure with probe positioners (DCM-320-M, Cascade Microtech, Inc., USA). The probes are manually manipulated to form firm electrical contact with the

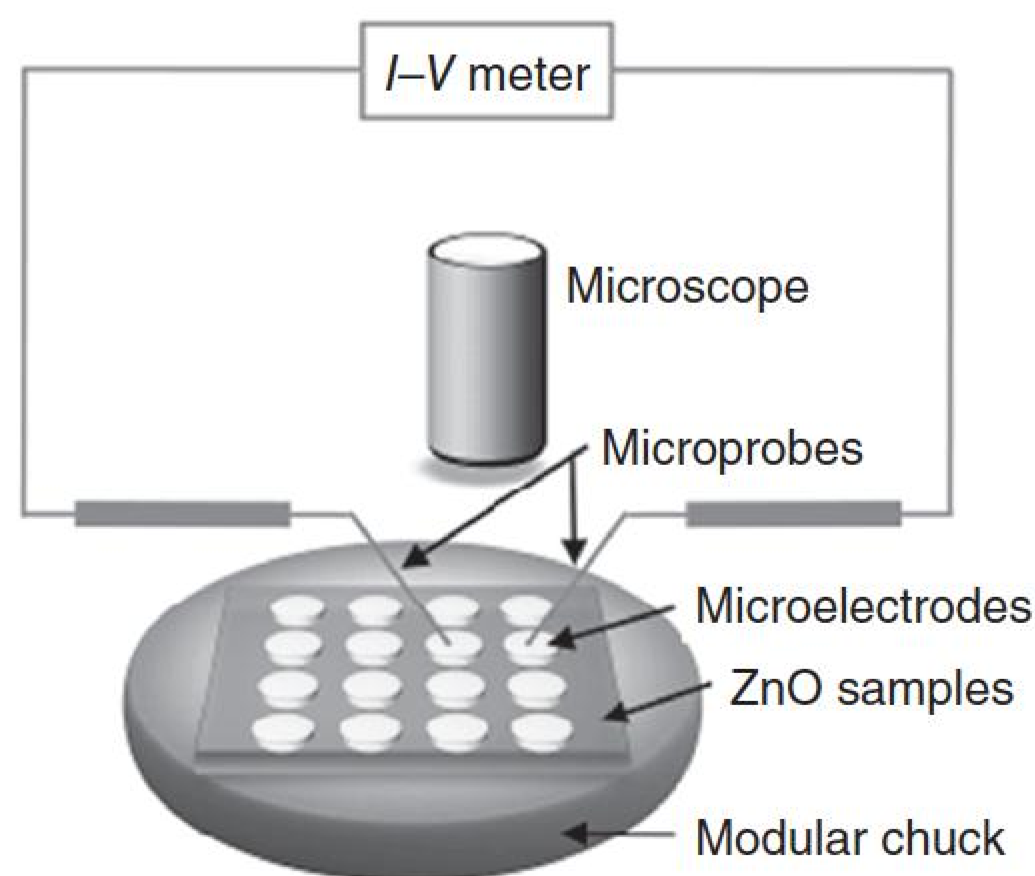


Figure 4.3 The schematic diagram of the microcontact measurement experiment performed on the individual grain boundaries in ZnO ceramics. All of the components and instruments are resized for the sake of comprehension and illustration [25].

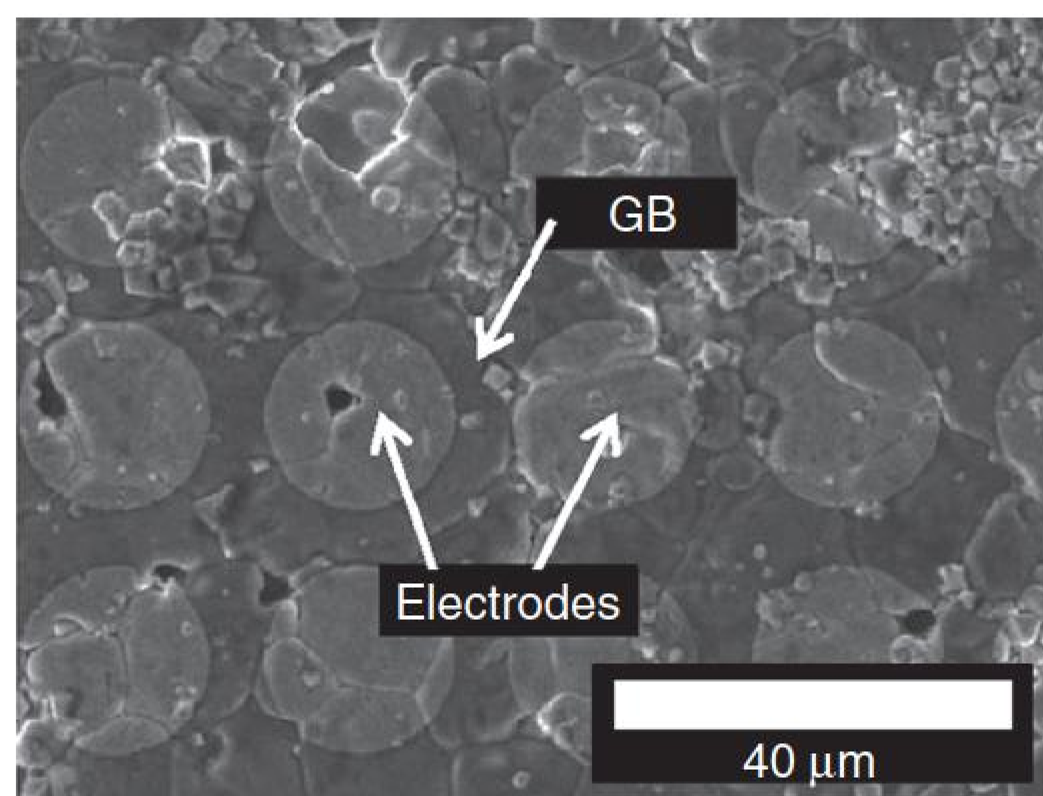


Figure 4.4 The electrodes configuration of a ZnO varistor sample for microcontact measurement. Source: He et al. 2011 [23]. Reproduced with permission of Elsevier.

surface electrodes of ZnO samples by the positioners with the aid of the optical microscope [24].

In bulk I–V measurements, varistor breakdown voltage is usually defined as the voltage at a certain current density, typically 1 μA [2–4], or 1 mA cm^{-2}. This requires an estimation of the junction area, which is difficult to be known, and may introduce error into the measurement. To eliminate the estimation of junction area, another method [6, 26] is used to determine the breakdown voltage from the relationship in Eq. (4.1); the definition of varistor breakdown voltage, V_B, is the voltage where α reaches a maximum:

$$I = kV^{\alpha} \tag{4.1}$$

where k is a constant; the nonlinear coefficient α can be calculated from the slope of $\log_{10} I$ as a function of $\log_{10} V$.

Even though the microcontact method has been widely employed, a number of important limitations remain. First, it is difficult to control the chemistry of individual boundaries; second, there is limited ability, in most case, to examine the electrical properties at elevated temperature or controlled atmosphere; third, unless all grains surrounding the individual grain boundary are removed, the current pathway is unpredictable (also known as neighboring effect), even when the specimens are thin.

4.3 Statistical Characteristics of Grain Boundary Parameters

4.3.1 Nonuniformity of Barrier Voltages

Breakdown voltages have been measured by the different direct methods described above; the measurement results are listed in Table 4.1 [13]. The reported breakdown voltages lie in a wide range from 1.8 to 6.0 V. One explanation for this relatively widespread results is the difficulty in defining the cross-sectional area, and secondly, different criteria were used to measure the breakdown voltages. But, even if the same criteria are used, e.g. at 1 μA or at the maximum of the nonlinear coefficient α, the barrier voltage is still largely different because of different prescription and different sintering courses. The grain barriers are formed during the cooling process from the sintering temperature, and it would bring a large difference if the cooling program is not the same. Nonuniformity of grain boundaries exists during their forming courses, which is the origin of nonuniformity in the electrical characteristics of ZnO varistors.

The average value of barrier voltage measurement results on individual grain boundaries [6, 7, 10, 19], which defines the voltage at the maximum values of α as the breakdown voltage, is 3.2 V, while the average of total values listed in Table 4.1 is 3.3 V per barrier [13].

The average barrier voltages measured by the indirect method, which cover a spread from 2.0 to 2.5 V, can be found in the literature [2, 6, 7, 15, 16, 18, 20, 27, 30–32] and have an average value of 2.3 V [13], which is much lower than

Table 4.1 Barrier voltages of the ZnO varistors by direct measurements on isolated grain boundaries.

Ingredients	Barrier voltage	References
	3.2–3.3 V	[27]
ZnO, 1% Sb_2O_3, 0.5% CoO, 0.5% Cr_2O_3, 0.5% Bi_2O_3	2.3–2.9 V at 1 μA 2.6–3.3 V at 1 mA	[2]
Commercial varistor	4 V at 1 μA	[3]
Commercial varistor	3.6 V at 1 μA	[4]
ZnO, 1% CoO, 0.2% Nd_2O_3, 0.25% Sn_2O_3	4 V	[5]
	2.3–3.7 V at α_{max}	[6]
ZnO, 1% Bi_2O_3, 1% MnO	6 V at 4 μA	[28]
ZnO, 1% Bi_2O_3, 1% MnO, 0.5% TiO_2	5 V at 10 μA	[28]
	2.3 V at 0.1 μA	[16]
	3.3 V	[1]
	3.5 V	[8]
Commercial varistors	3.0–3.5 V at α_{max}	[7]
90 mol% ZnO, 10 mol% additives of Bi_2O_3, Sb_2O_3, and Co_2O_3	3.2, 3.6 V at α_{max}	[10]
	3.8–4.0 V	[18]
97 mol% ZnO, 3 mol% additives of Bi_2O_3, Sb_2O_3, and Co_2O_3	1.8–6.0 V	[20]
ZnO, 0.55% Bi_2O_3, 0.5% Co_2O_3, 0.5% Mn_3O_4, 0.5% NiO, 0.5% TiO_2	3.5 V	[29]

3.3 V – the average value obtained from the direct method. Levinson and Philipp [17] reported that the calculated barrier voltage is lower than the measured barrier voltage because the current always seeks the easiest path, i.e. the path with the fewest barriers between the electrodes. Emtage [31] showed from a theoretical approach that the mean breakdown voltage per grain in the conductive ceramics is less than that of an isolated grain boundary because there are some chains of large grains through the inside of a ceramic body.

Because a nonuniformity of barrier voltages exists, when a voltage is applied to a ZnO varistor, the electrical current always passes through the lowest barrier voltage path, which is usually the least number of grain boundaries between the electrodes. Therefore, the calculated barrier voltage (by the indirect method) should be lower than the measured one. The difference between calculated and measured barrier voltages varies like the sigmoidal mode with the standard deviation of average grain size; as the standard deviation approaches zero, the difference decreases to zero, and as the standard deviation increases, the difference increases too. So, Sung et al. [28] thought that the number of grain boundary barriers for the current path should be conventionally calculated from dividing the thickness of the device by the average grain size, and they discussed

how to modify the average number of grain boundary barriers so as to calculate the most probable barrier voltage that is equivalent to the one measured by the indirect method.

4.3.2 Distribution of Barrier Voltage

Distributions in both the barrier voltage V_B and the grain size in actual ZnO varistors were measured [4, 6, 11, 12, 25]. The barrier voltages distribute symmetrically in log-normal distribution [6, 33] – an obvious normal distribution exists between barrier voltages and the number of grain boundaries. But in the past, many calculations were based on uniform barrier voltage [33–37] or simple classification of barrier voltages [38].

The normal distribution of barrier voltages can be described as

$$p(V_B) = \frac{1}{\sqrt{2\pi}\sigma} \exp\left[-\frac{(V_B - \overline{V}_B)^2}{2\sigma^2}\right] \tag{4.2}$$

where, $p(V_B)$ is a distribution function of V_B, σ is the standard deviation of the distribution function, and the average value of the barrier voltages $\overline{V}_B$. The standard deviation σ of barrier voltages of individual grain boundaries from different experimental results [4, 6, 12] are calculated, which range between 0.02 and 0.2 V under average $\overline{V}_B$ value of 3.3 V.

Microcontact measurements on 100 individual grain boundaries were carried out [24], and the nonlinear coefficient α, the breakdown voltage V_B, and the leakage current I_L of individual grain boundaries were derived from the I–V curves of individual grain boundaries. The nonlinear coefficient α was defined as the maximum of local nonlinear coefficients, which were calculated by logarithmically fitting the neighboring five data points. The voltage and current applied on the electrodes corresponding to the maximum nonlinear coefficient was defined as the barrier voltage V_B and the leakage current I_L, respectively.

The distribution of barrier voltages of individual grain boundaries is shown in Figure 4.5 [24], obviously, there are two local peaks (P1 and P2) dividing V_B data into two ranges. One is from 2 to 5 V and the other from 5 to 8 V. The center of P1 is located at 3.26 V, and the center of P2 is located at 6.59 V; the respective standard deviations are 0.59 and 0.66 V, by Gaussian distribution function fitting. The center of P2 is almost two times that of P1, which means that P2 corresponds to two grain boundaries between electrodes. The breakdown voltage corresponding to P2 can be scaled down to an average individual grain boundary by simply dividing the voltage by the number of grain boundaries. As a result, the scaled down value of V_B is 3.29 V. Therefore, the breakdown voltage of individual grain boundaries is around 3.3 V, which is the same as that tested by Olsson and Dunlop [10, 11].

Einzinger [14] showed the distribution of breakdown voltages across 200 individual grain boundaries measured using microcontact electrodes and similar results were obtained; the majority of individual grain boundaries exhibited a breakdown voltage of ∼3.5 eV.

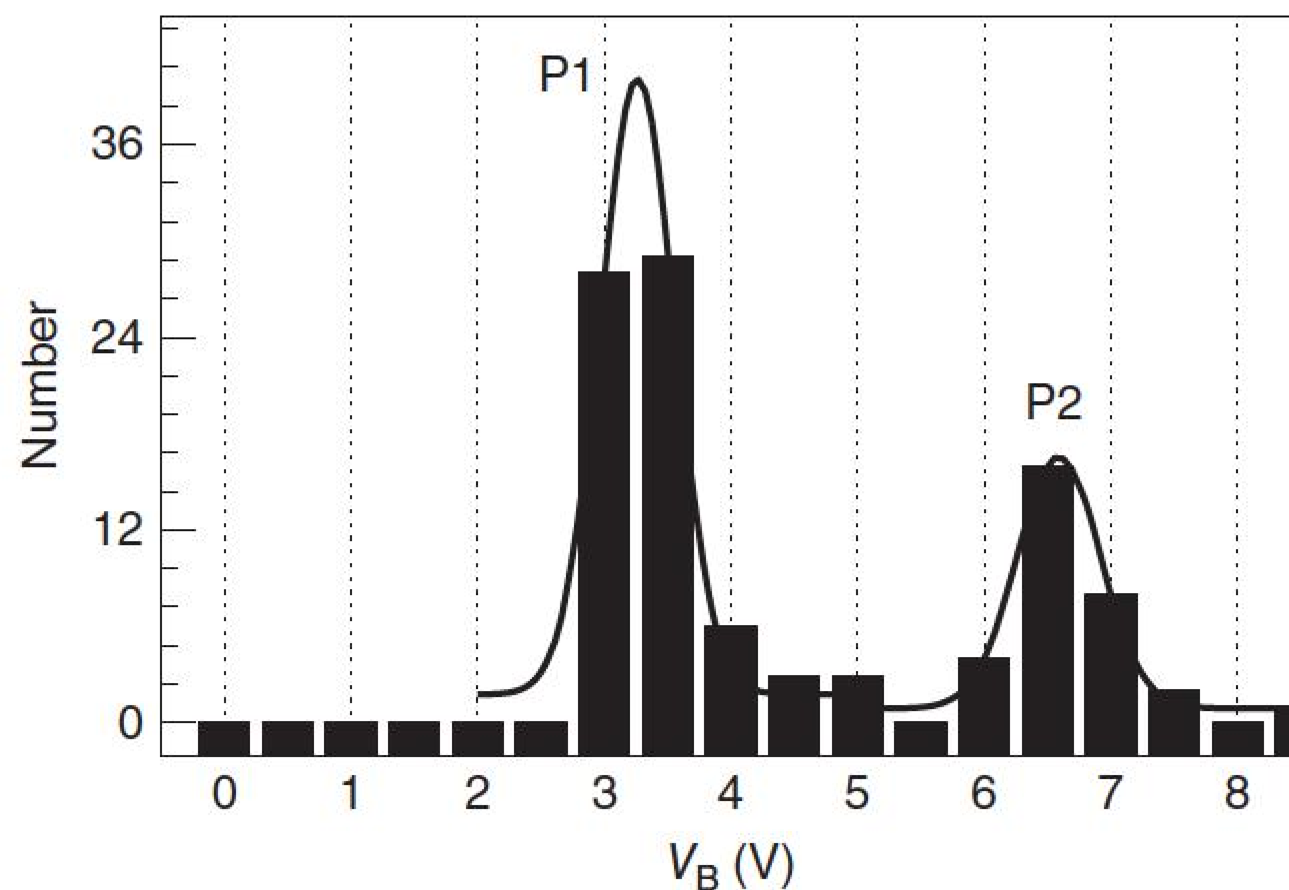


Figure 4.5 The statistics on breakdown voltages of 100 individual grain boundaries after different aging time. Source: Liu et al. 2011 [24]. Redrawn with permission from Elsevier.

4.3.3 Distribution of Nonlinear Coefficient

The distribution of nonlinear coefficient α is wide and asymmetrical [6]. A high percentage of grain boundaries have bad or ohmic I–V characteristics, and only a small percentage of grain boundaries have good I–V characteristics. But the ZnO varistors have good global I–V characteristics. Ordinarily, the nonlinear coefficient α of ZnO varistor bulk is higher than 30.

It is consequently essential for a better understanding of conduction phenomena in ZnO varistors to consider a distribution and not a mean value of α for all grain-to-grain junctions. So, it is not possible to neglect α values higher than 30, mostly because they correspond to "good" junctions responsible for a good varistor effect. Moreover, these "good" junctions have small leakage currents than other junctions. Consequently the "good" junctions control the leakage current of ZnO varistor at low values of the applied voltage [6].

From the microcontact measurement as shown in Figure 4.6 the initial nonlinear coefficients of these 100 grain boundaries mainly range from 15 to 35 [24].

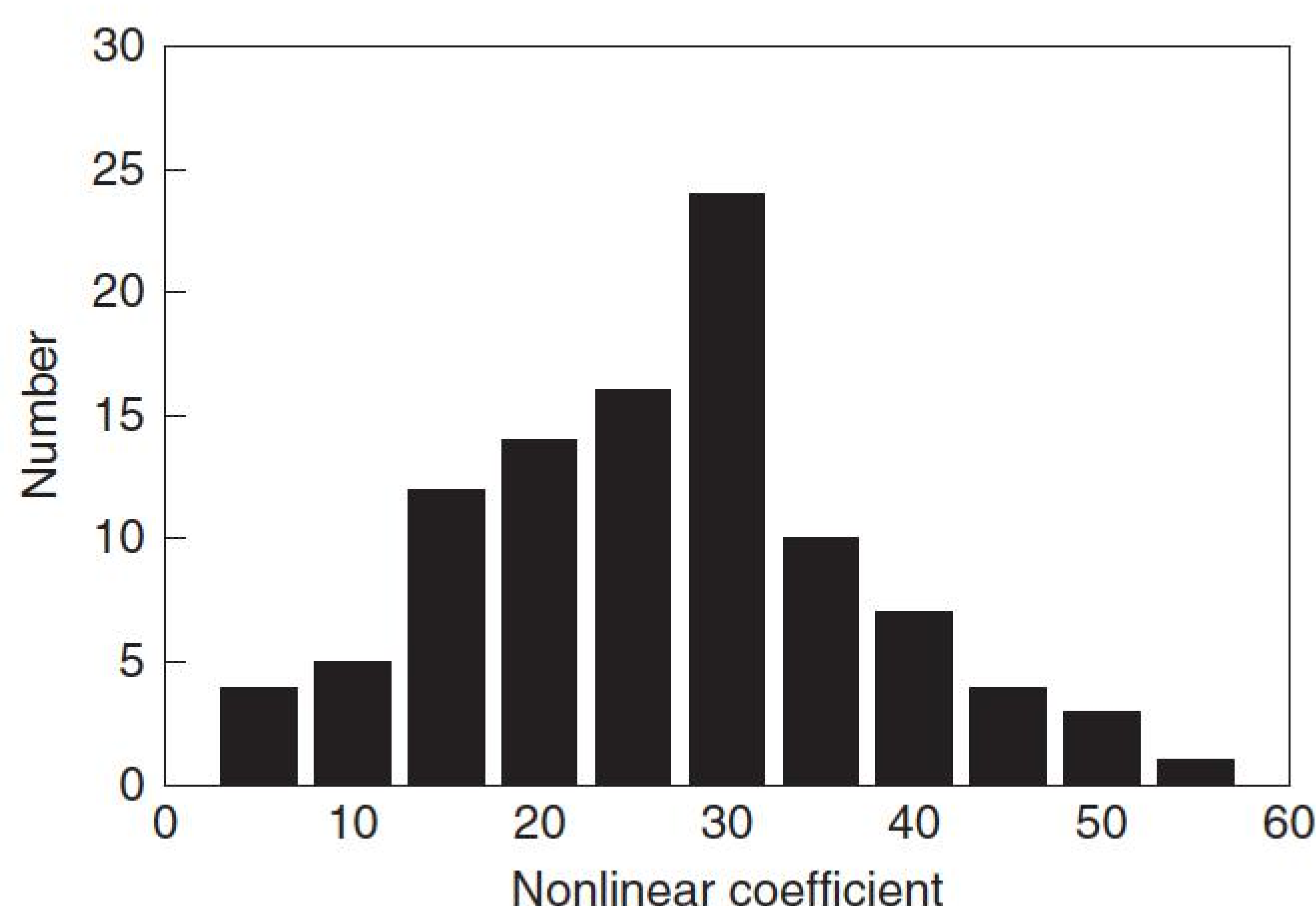


Figure 4.6 The histograms of nonlinear coefficients of 100 individual grain boundaries. Source: Liu et al. 2011 [24]. Redrawn with permission from Elsevier.

4.3.4 Distribution of Leakage Current Through Grain Boundary

The leakage currents of individual grain boundaries were tested as shown in Figure 4.7 [25]. The histogram of leakage current could be fitted by Gaussian distribution function, as well. The peak center is located at −5.75, and the standard deviation of $\log_{10}(I_L)$ is 1.52, $\log_{10}$ is simplified as log in this chapter.

4.3.5 Discussion on Microcontact Measurement

Although microcontact measurements, in which electrical contacts are made within individual ZnO grains and across grain boundaries, are fraught with uncertainty as to the actual conduction path, they clearly revealed several important findings [3].

Varistor behavior was associated with individual grain boundaries and the majority exhibited a breakdown or switching voltage of ~3.5 eV [3]. Considerable variation exists in the I–V characteristics from one boundary to another, in the barrier voltages and nonlinear coefficients among different grain boundaries. Einzinger's work remained the most comprehensive and showed that there was also considerable variation in capacitance from one boundary to another [14]. However, they quickly led to the realization that varistors are far from uniform and that they are best considered as a series and parallel network of variable resistors. So, the response of a varistor is the collection of all variable resistors. The grain boundaries can be simply classified into good, bad, and ohmic ones, and a high percentage of grain boundaries have bad or ohmic I–V characteristics, and only a small percentage of grain boundaries have good I–V characteristics. These few good grain boundaries are responsible for the good varistor effect and control the leakage current of ZnO varistors at low values of applied voltage.

Microcontact measurements continue to be reported but are generally of dubious value. Ideally, one would wish to relate the electrical measurements to the local chemistry and grain boundary structure, but there are severe difficulties in achieving this: grain boundaries in varistors are not usually planar; luminescence

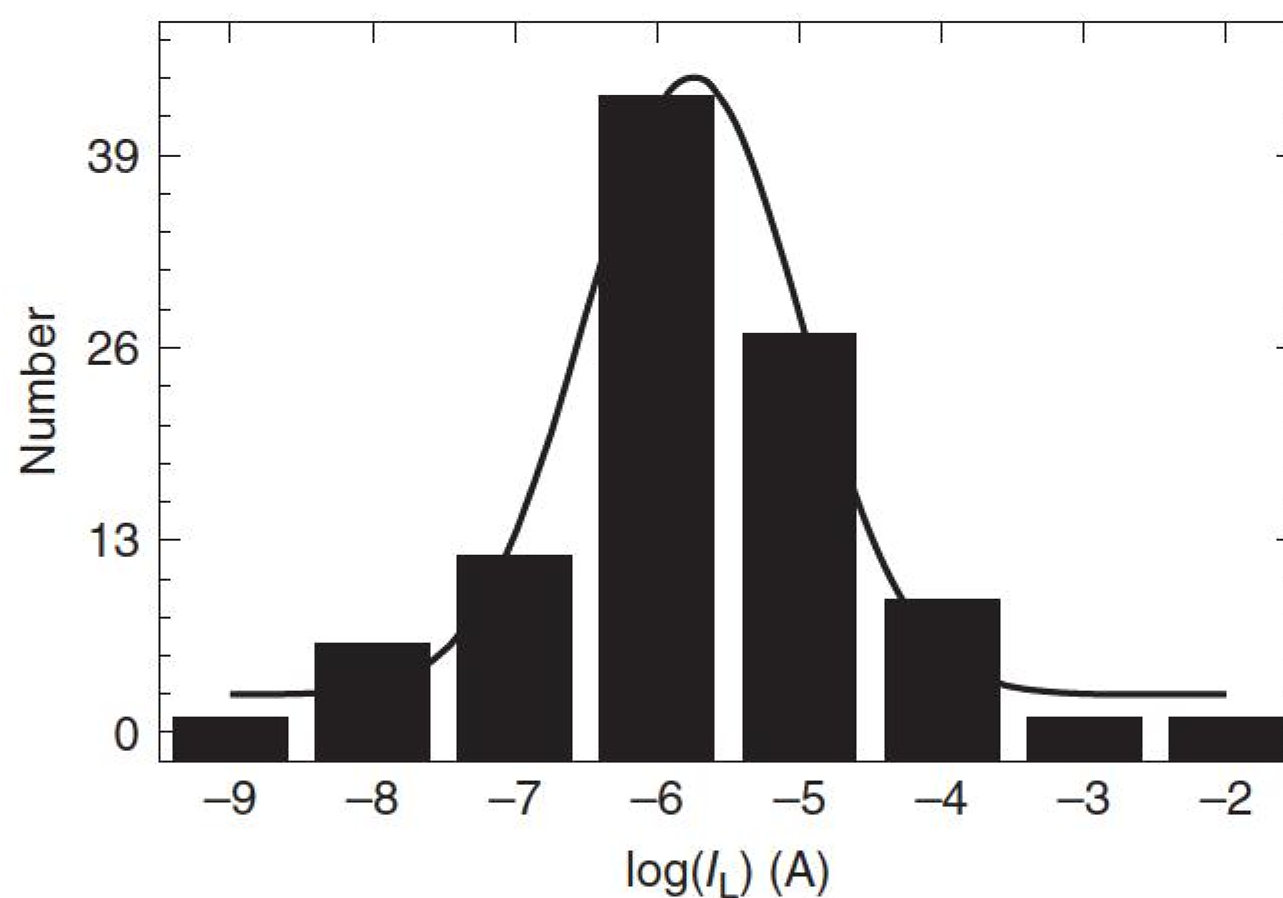


Figure 4.7 The distribution of leakage currents of 100 individual grain boundaries. Source: Liu et al. 2011 [24]. Redrawn with permission from Elsevier.

observations indicate that the electrical transport across varistor boundaries is highly inhomogeneous; the electrical conduction path depends on both the local potential and the existence of alternative current pathways [3].

4.4 Classification of Grain Boundaries

Microcontact electrical measurements on multiple-phase ZnO varistors show a wide diversity of grain boundary characteristics. Nevertheless, these measured results [4, 6, 7, 10, 26, 39] consistently indicated that the $I-V$ characteristics for the grain boundaries could be classified into three representative types: ohmic microjunctions, and “good” and “bad” nonlinear microjunctions.

Tao et al. measured $I-V$ characteristics of 54 single junctions [6]; only a few barriers were electrically active as assumed by Van Kemenade and Eijnthoven [4]. The breakdown voltage of the “good” junctions is 3.1 V with a nonlinear coefficient α higher than 30, and 24 tested junctions belong to the “bad” ones, which have about 3 V breakdown voltage with a low α, less than 10. For a voltage equal to half the breakdown voltage, the “good” junctions present a current of about 0.3 μA, but the currents are approximately 1 mA and 20 μA for different “bad” junctions. The measured breakdown voltages are in the range of 2.3–3.7 V, and the average value is 3.0 V. Wang et al. [7] measured 98 single junctions, and about 80% junctions had varistor-like $I-V$ characteristics, i.e. breakdown occurred between 3.0 and 3.5 V. The values of the maximum nonlinear coefficient α ranged over a very broad distribution from 10 to 93 with an average of approximately 40. The other 20% of the junctions did not exhibit varistor-like $I-V$ behavior, i.e. no breakdown was observed.

The “good” microjunctions have high leakage resistance and high nonlinear coefficient ($\alpha \geq 30$); estimates of the relative number of “good” junctions are between 15 and 65% [6, 10, 19, 20, 26, 40, 41]. Bad microjunctions have two to three orders of magnitude lower leakage resistance and much lower nonlinear coefficient α (about 10) [6, 7, 10]; about 30–35% of the tested microjunctions showed a bad characteristic [39], but the breakdown voltages of both good and bad microjunctions are nearly identical, at about 3 V. The ohmic microjunctions are nearly linear with a resistance two to five orders of magnitude lower than the leakage resistance of the good junction [6, 7, 12, 40]. The fraction of ohmic junctions has been estimated to be about 20% [7, 12, 25] and 5–10% [40]. Ohmic microjunctions are present in all varistors, including commercial ones, even when their quality is very good [7, 12, 39]. The ohmic grain boundary is called as ineffective grain boundary, which leads to the existence of a shortcut pathway inside ZnO varistors [20].

Olsson and Dunlop [10, 11] used microelectrodes to determine the electrical properties of individual interfaces between ZnO grains; they characterized four different types of boundary structures, as shown in Figure 4.8; each type has its own specific breakdown voltage and the nonlinearity of the current–voltage characteristics is also dependent on the fine scale structure; it was found that interfaces containing pyrochlore did not show varistor behavior. Type A is a boundary between ZnO grains containing a thin (~2 nm) intergranular

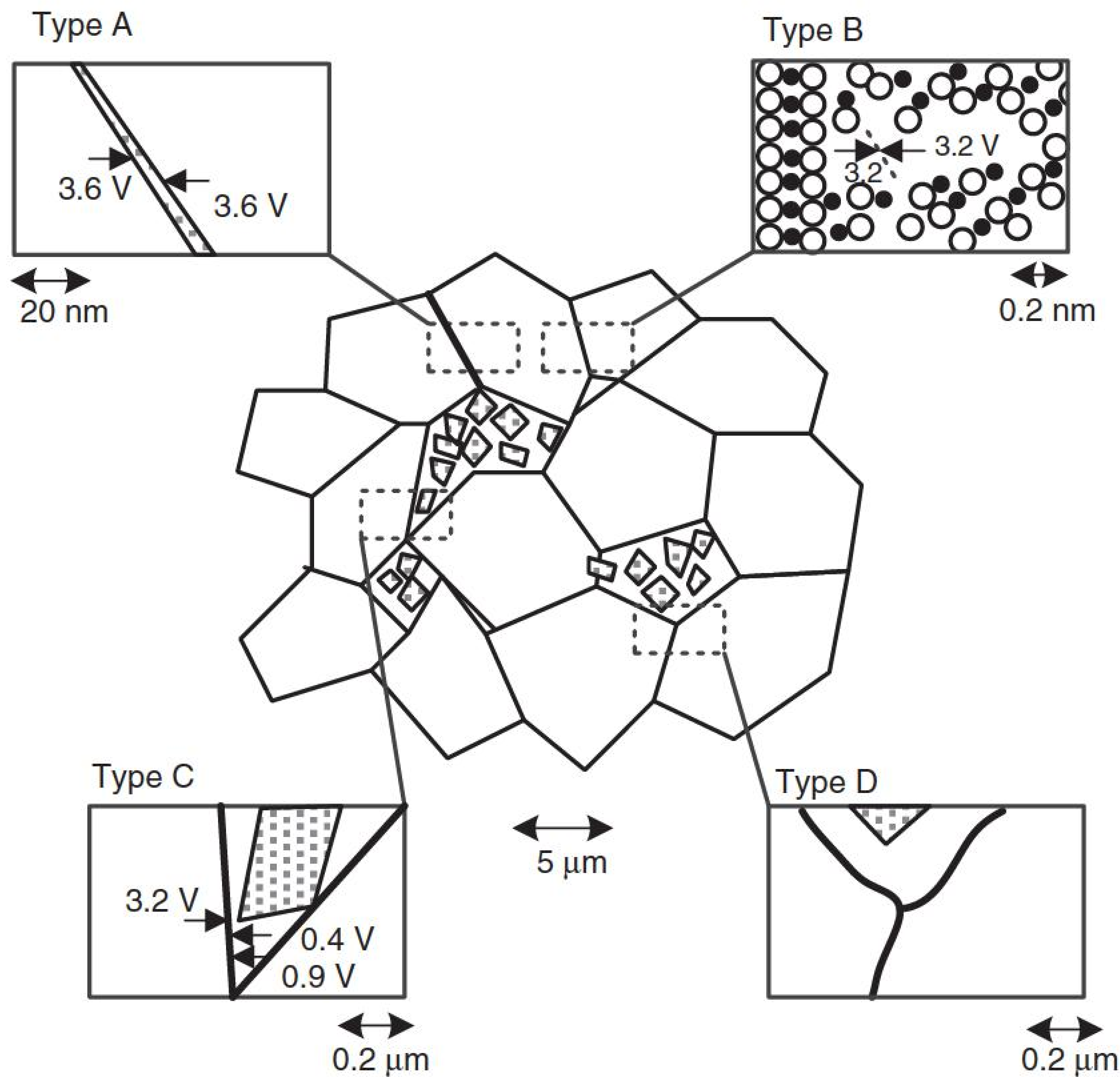


Figure 4.8 Four main types of ZnO interfaces. The arrows indicate the direction in which electrons are moving. Source: Adapted from Olsson and Dunlop [10].

amorphous Bi-rich film. It exhibited a breakdown voltage at 3.6 V, and a nonlinear coefficient α of about 66. Type B is a ZnO/ZnO interface without secondary phases but containing segregated Bi atoms. It exhibited a breakdown voltage at 3.2 V, and a nonlinear coefficient α of about 33. Type C is an interface between ZnO and an intergranular mixture of Bi_2O_3, and spinel grains. Junctions between ZnO and intergranular Bi_2O_3 exhibited asymmetric current–voltage characteristics with breakdowns at 3.2 V for one polarity of the applied voltage, in the reverse direction the breakdown was at 0.4, 0.6, and 0.9 V, which depended on the particular polymorph of the intergranular Bi_2O_3. Type D is an interface between ZnO and pyrochlore ($Zn_2Bi_3Sb_3O_{14}$) and spinel grains. This kind of interfaces did not exhibit any varistor behavior; this gives rise to a significant number of "inactive" grain boundaries in the ZnO varistors. Generally, pyrochlore occupies only a small fraction of the ZnO grain boundaries but even a small precipitate of pyrochlore along an otherwise "clean" grain boundary could make a "hole" in the barrier and seriously degrade its properties [10]. It is thus desirable to minimize the volume fraction of pyrochlore in these materials. Types A and B belong to "good" grain boundary, Type C "bad" one, and Type D ohmic one [13].

Figure 4.9 shows the voltage–current characteristics of different types of grain boundaries measured using direct microcontact measurement [25]. Actually, all grain boundaries behave different properties.

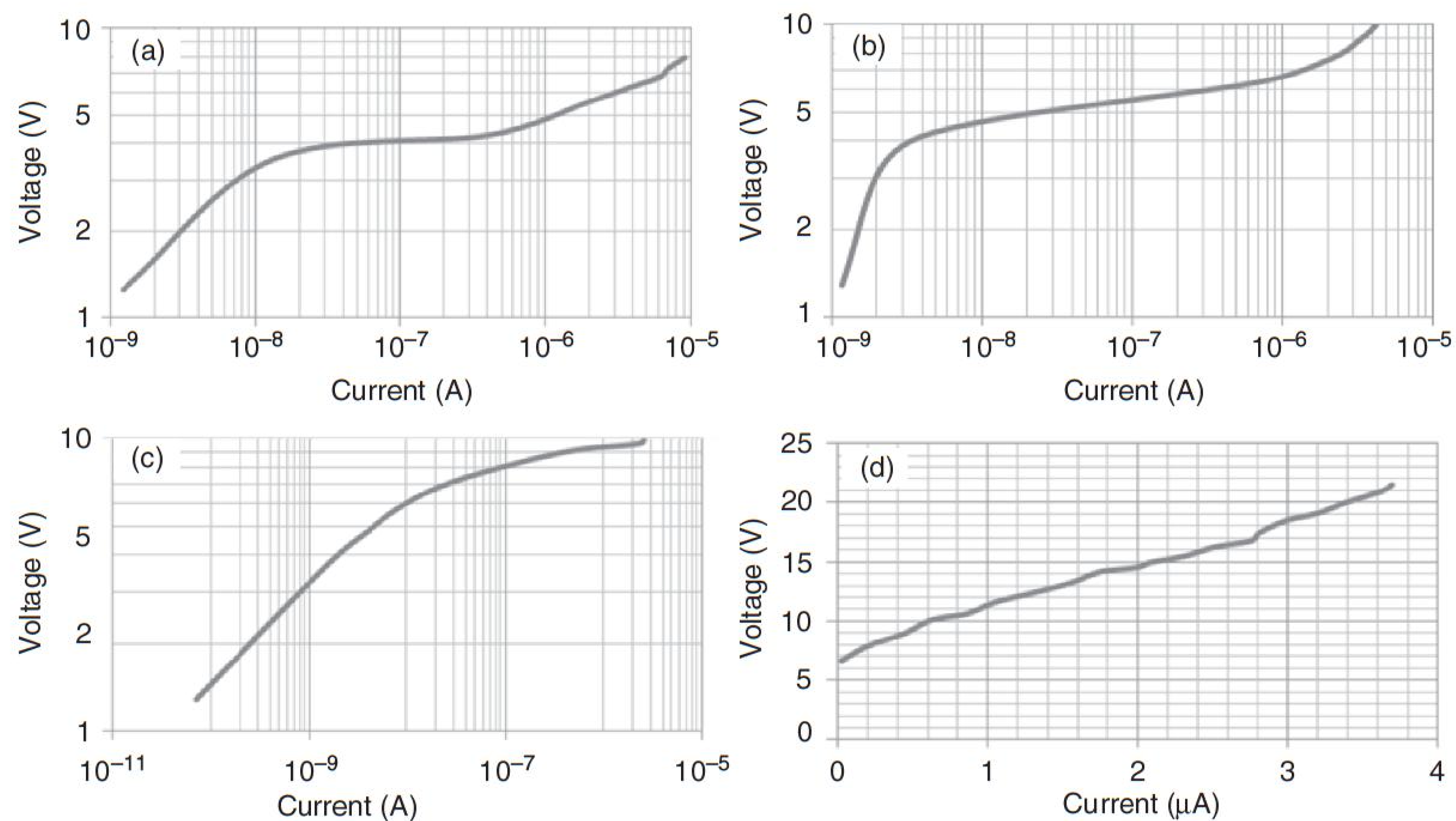


Figure 4.9 The voltage–current characteristics of different types of grain boundaries by direct microcontact measurement. (a) Very good grain boundary; (b) good grain boundary; (c) bad grain boundary; (d) ohmic grain boundary. Source: Adapted from Liu [25].

4.5 Other Techniques to Detect Microstructurally Electrical Properties of ZnO Varistors

4.5.1 Scanning Probe Microscopy-Based Techniques

Electrostatic potential barriers build up at the grain/grain interfaces due to charges being trapped in interface states and hot electrons being created at breakdown. Modern scanning probe microscopy-based techniques, such as electrostatic or piezoresponse force microscopy, allow the study of electric properties of materials on the nanometer scale. Scanning surface potential microscopy [42] and conductive atomic force microscopy (C-AFM) [43, 44] operate in contact mode to investigate the topography and current response of a given microstructure. This technique has not only been applied in the measurement of grain boundary characteristics [45] but also focused on local conductivity. The identical surface region has been inspected subsequently with electron backscattering diffraction (EBSD) to get information on individual crystal orientations [44]. C-AFM measurement was performed under ambient conditions in contact mode with a Digital Instruments Nanoscope IIIa Multimode microscope using an AS-130("J") scanner with 125 μm × 125 μm maximum lateral scan size. The voltage applied to the samples was varied from 0 to 10 V. CDT-CONTR silicon cantilevers with p-doped diamond coating on the tip were used as probes. The typical macroscopic tip radius of curvature is below 100 nm, but the grains of the polycrystalline diamond coating allow a resolution below 20 nm.

Figure 4.10 shows a typical region of a varistor sample recorded by C-AFM in topography mode (a) and current mode at constant voltage (b), and the corresponding scanning electron microscopy (SEM) image (c) after etching [44]. The results of four characteristic positions (numbered 1–4) are presented in Figure 4.11 [44]. For the spinel (No. 1), no current was detectable in the entire voltage range. At position 2 in the large (mono-domain) ZnO grain, a typical nonlinear V–I curve has been measured. Between grain No. 2 and the adjacent electrode is only one grain boundary, but the corresponding switching voltage is below the well-known "ideal" varistor voltage. Between the twin grains No. 3 and 4 and the electrode, there are two grain boundaries visible on the polished surface (see Figure 4.10c) resulting in a switching voltage in the range between 6 and 7 V. Actually, the V–I curves are slightly different in a certain voltage range [46] (around +9 V) for positions 3 and 4.

The electric force microscopy (EFM) results presented in Figure 4.12a–d of ZnO varistor sample show details of the variations in the electric field gradient across the area scanned on the sample [45]. The EFM images indicate that an increase in the applied voltage leads to an increase in the concentration of negative charges at the grain boundary, whose behavior signals the effective presence of the potential barrier. The increased conductivity resulting from doping was confirmed by the EFM images, which recorded the potential barriers present at

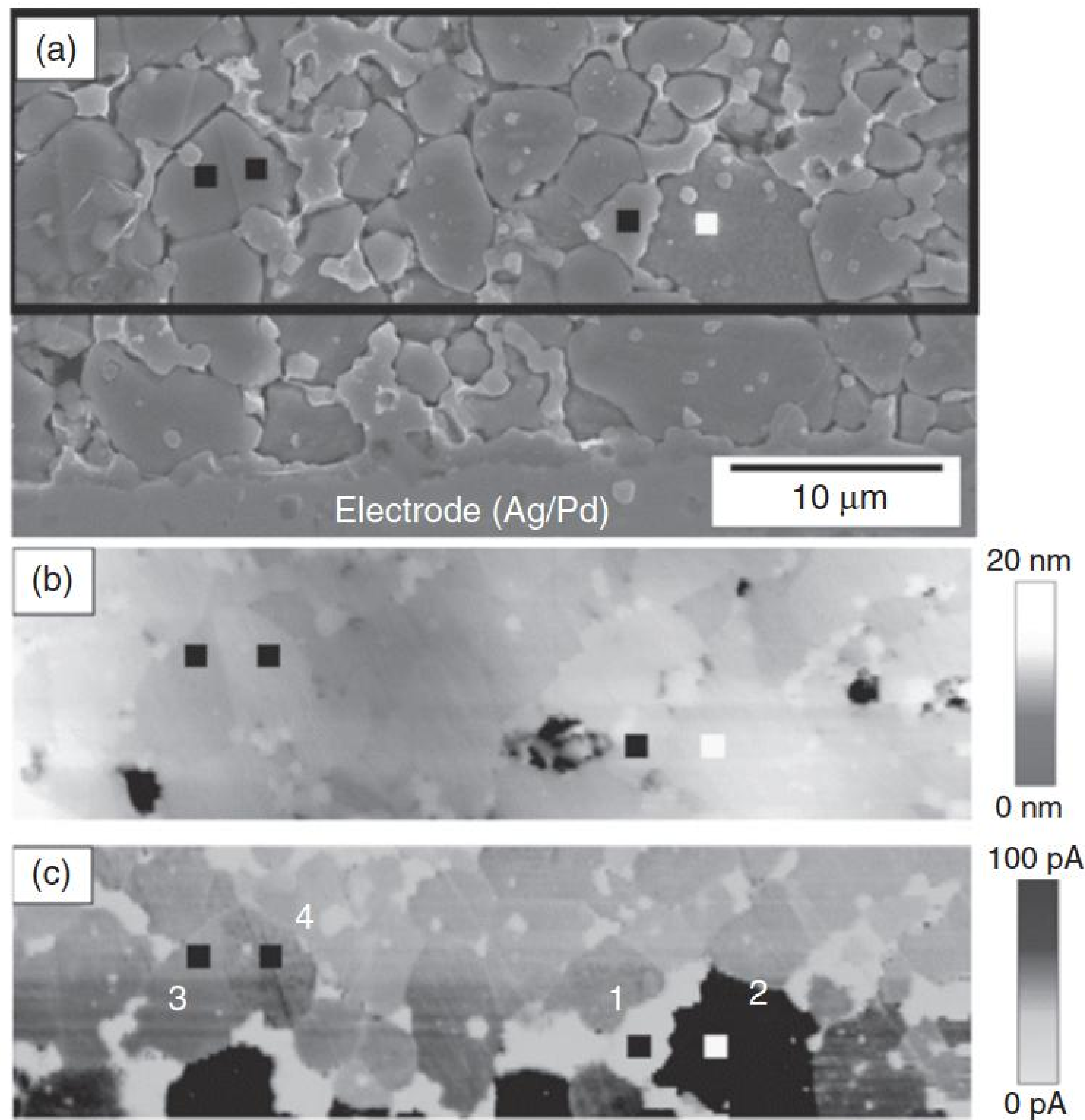


Figure 4.10 SEM and AFM images of a polished varistor with an area of 50 µm × 12.5 µm. Source: Schloffer et al. 2010 [44]. Reproduced with permission of Elsevier. (a) The SEM image of the etched surface, which shows a slightly larger area to visualize the distance to the adjacent Ag/Pd inner electrode (the framed region corresponds exactly to the scanned areas in (b) and (c)); (b) topographic AFM image and (c) simultaneously recorded 2D current image at +10 V. The spots for acquiring *V–I* curves are marked by numbered squares.

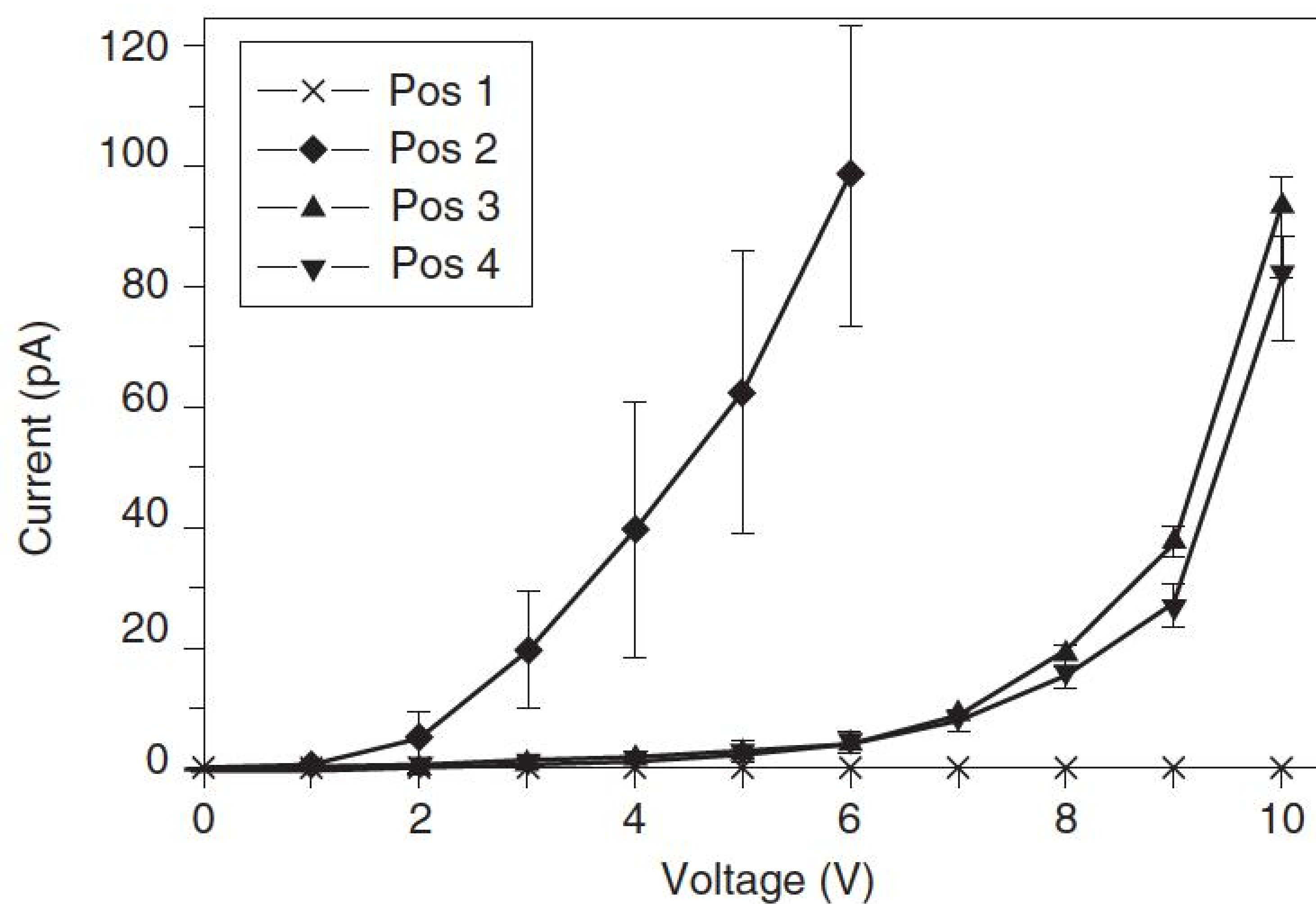


Figure 4.11 *I–V* characteristics at the spots 1–4 marked in Figure 4.10. The error bars correspond to the standard deviation of measured currents at individual pixels. Source: Schloffer et al. 2010 [44]. Reproduced with permission of Elsevier.

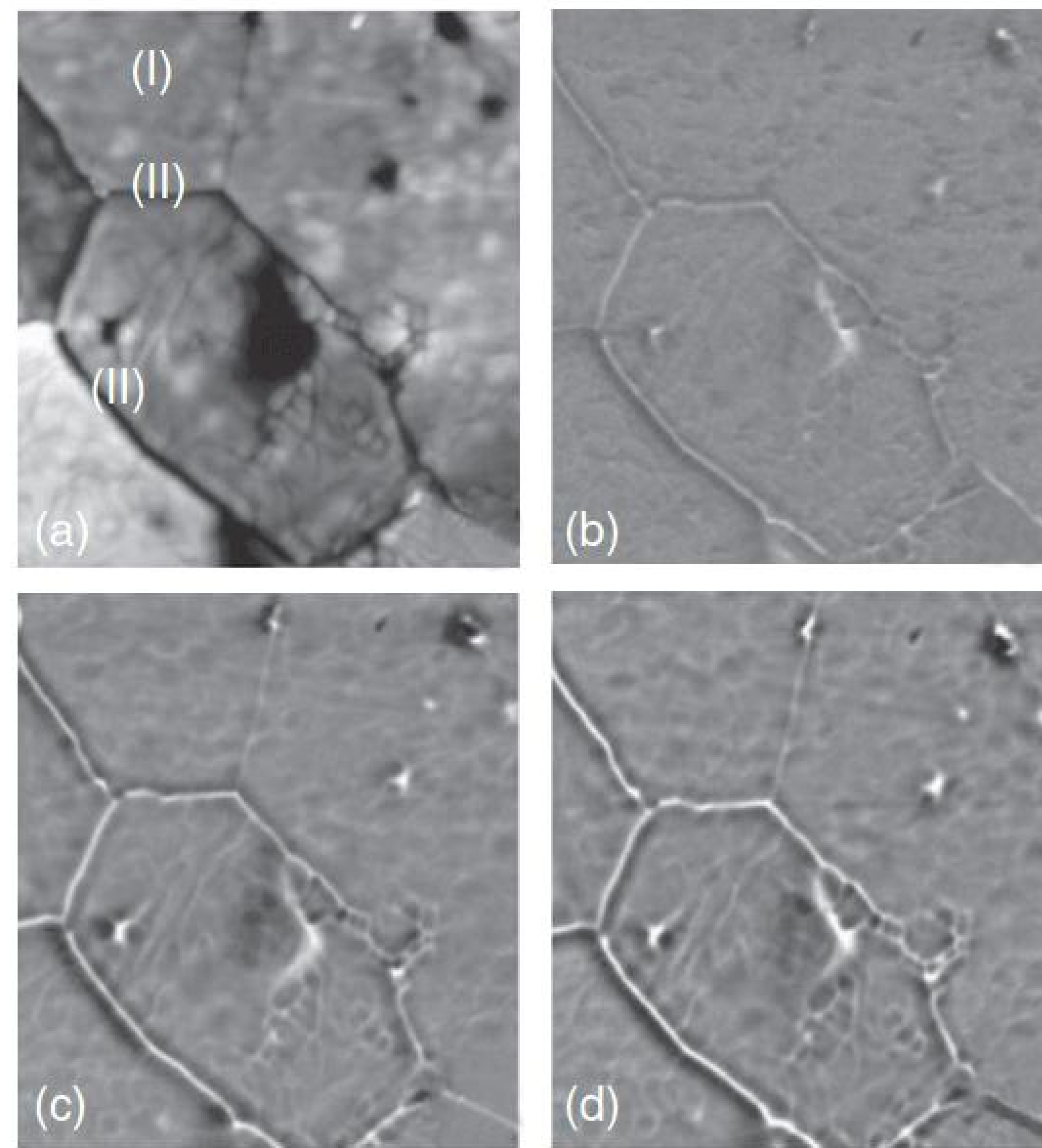


Figure 4.12 Atomic force microscopy (AFM) and electric force microscopy (EFM) profiles of a 15 μm × 15 μm area of a pure ZCF1 sample. (a) An AFM topographic scan; (b)–(d) EFM profiles of the same region as (a) are shown but at 4, 8, and 12 V DC voltage, respectively. Source: Gheno et al. 2008 [45]. Reproduced with permission of John Wiley & Sons.

the grain boundaries. When 4 V voltage is applied, grain sizes are visible (I) as well as the grain boundaries/intergranular regions (II). The bright regions, especially at the grain boundaries, could be ascribed to the electrostatic charge produced by the potential barrier. The call-out regions, which were attributed to semiconducting material, indicated that the grains were conductive. In all EFM images, the surface potential is dependent on the local electric field. Besides, the surface potential clearly identifies a grain boundary contour. The dimensions of potential barriers at the grain boundaries were determined to be 250 nm. The width of the resistive layer is a function of the material's chemistry and processing and is not expected to be very sensitive to the voltage applied [45].

4.5.2 Galvanic Determination of Conductive Areas on a Varistor Surface

Because insulating, conductive, and varistor-active grain boundaries coexist within a doped ZnO varistor, the current flows through separate paths of its microstructure. When the applied voltage is increased, the number of paths to become conducting will also increase, which is synonymous with a larger conductive cross section. This area can easily be determined at different voltages by the galvanic method. For the test, a silver paste is metallized on one side of a varistor sample, and a wire is welded to this electrode; the other side is put into contact with the surface of a salt solution, e.g. $CuSO_4$ or $AgNO_3$, as shown in Figure 4.13 [47]. A piece of metal in the solution is arranged as the anode in a DC circuit. The nonmetallized varistor surface acts as the cathode. After a current flows through the varistor for a sufficient time, all the conductive areas will become covered with metal.

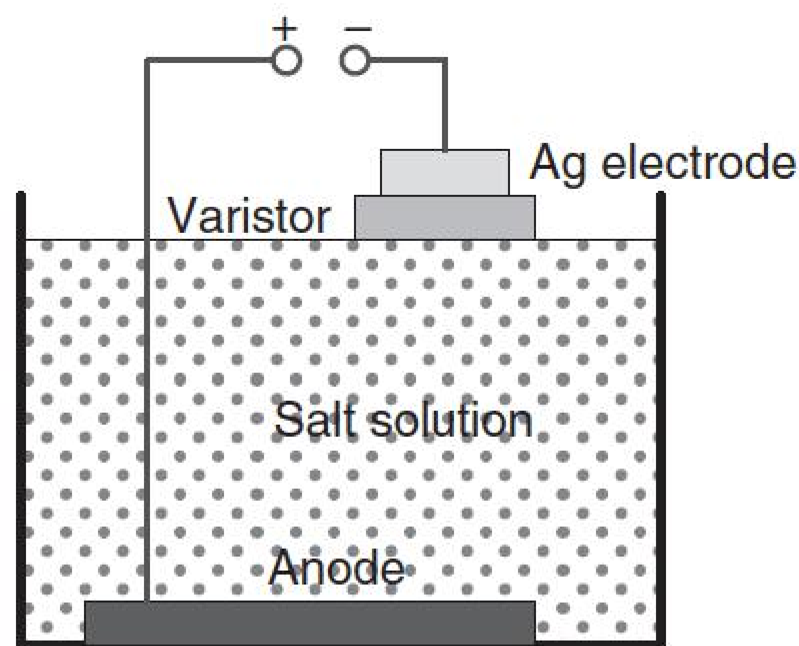


Figure 4.13 Schematic diagram of the setup for galvanic determination. Source: Adapted from Hohenberger et al. [47].

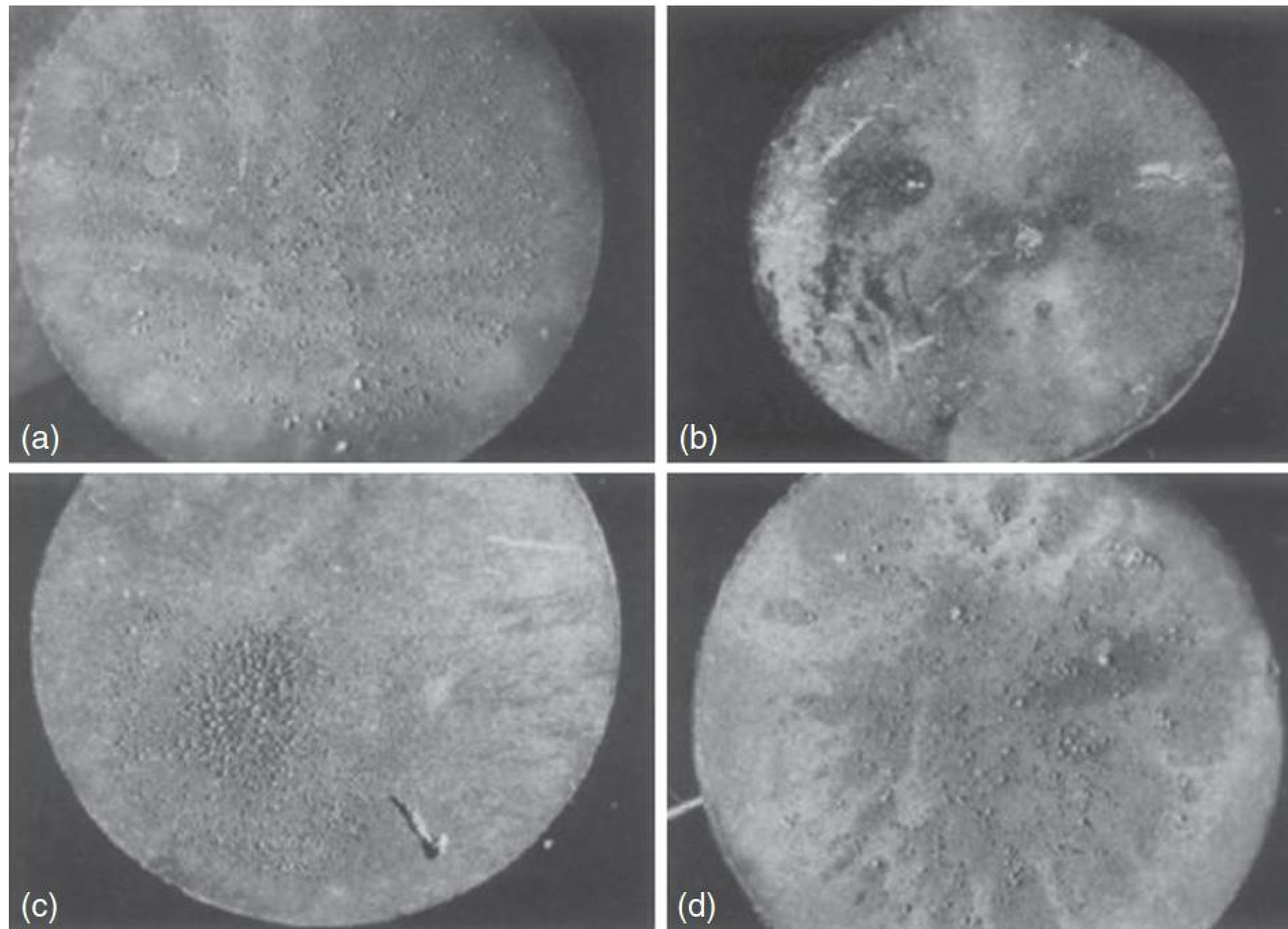


Figure 4.14 Metallic depositions on the surfaces of varistor disks with diameter of 10 mm: (a) sol–gel varistor containing an additional $A1_2O_3$ doping; (b) sol–gel varistor, normal composition; (c) mixed oxides varistor, normal composition, reduced conductive area; (d) mixed oxides varistor, normal composition. Source: Hohenberger et al. 1991 [47]. Reproduced with permission of John Wiley & Sons.

Photographs of good and bad varistor surfaces coated using the galvanic method are shown in Figure 4.14 [47]. The sample in Figure 4.14a was additionally doped with Al_2O_3, while the samples without $A1_2O_3$ dopant composition are shown in Figure 4.14b–d; significant differences can be observed in these samples. Figure 4.14a is a sol–gel sample; a very homogeneous distribution of current paths spread over the whole surface of the varistor, and this sample shows good electrical properties. Figure 4.14b is a sol–gel sample, too. Using the same dopant composition for sol–gel processing as for the mixed oxide powders results in an almost insulating material. Just a few conductive paths are formed here. These varistors do not withstand high currents. Figure 4.14c is a mixed oxide sample; this varistor shows inhomogeneous conductivity with a quarter of the available

area covered by copper spots. Figure 4.14d shows a mixed oxide sample, too. The conductive paths in this mixed varistor are homogeneously distributed over the whole surface, but less than in the sol–gel sample in Figure 4.14a.

This method is impossible to be used to differentiate the distinction between ohmic and varistor-active current paths. To be certain that a homogeneous current distribution is not a consequence of many low ohmic paths, which cause a high leakage current, the results of this investigation method have to be seen in conjunction with the current–voltage curve. No information about the differences in the breakdown voltage of the varistor-active path is given by this method [47].

4.5.3 Line Scan Determination of Differences in Breakdown Voltage Within a Varistor

The line scan method was used to determine the breakdown voltage profile within a varistor [47]. A silver electrode is painted on one surface of the varistor, and the opposite side is grounded with SiC abrasive papers followed by a 1 μm diamond polishing step. The sample is mounted on a carriage, whose movement is controlled by a stepped motor drive. The leaded silver electrode is contacted to ground. The opposite electrode is a pin with a hard metal ball tip with a diameter of 0.5 mm supported by an insulating tubular guide; it is loaded with a weight of 1 N and is slid across the polished sample surface, contacting only a few grains simultaneously. This electrode is connected to a constant current power supply, which is adjusted to 1 mA. When the ball tip is slid across the sample surface, the voltage of the power supply follows the varistor voltage of the contacted current path. This profile is recorded with the carriage displacement on an X–Y recorder. These profiles quantify voltage differences across the sample. Scanning the entire surface with parallel lines would give a two-dimensional picture of the varistor voltage distribution to estimate the steadiness of the varistor voltage with the varying current paths.

4.5.4 Current Images in SEM

The conductive paths through the microstructure on the surface of varistors can be observed by the current images in SEM. Unlike the method based on the potential contrast between two grains [4–6], the conductivity of a larger part of the microstructure can be determined. The setup for the experiment is shown in Figure 4.15 [47]. The varistor is fixed to an insulation material, e.g. glass, on the sample carrier. A silver electrode is painted on a part of the sample surface, which is connected to ground via a current-measuring instrument. The monitor brightness is proportional to the current flowing at this point.

During the normal scanning mode, the electron beam will meet the varistor surface or electrode. Hitting the electrode will cause a high current and a bright point on the monitor. On the varistor surface, the beam will cause a charged area to be formed. If the voltage is high enough, or if there is a conductive path connected to the electrode, a current will flow. This will result in a bright point on the monitor, too. Insulation grains or varistor-active paths below breakdown will

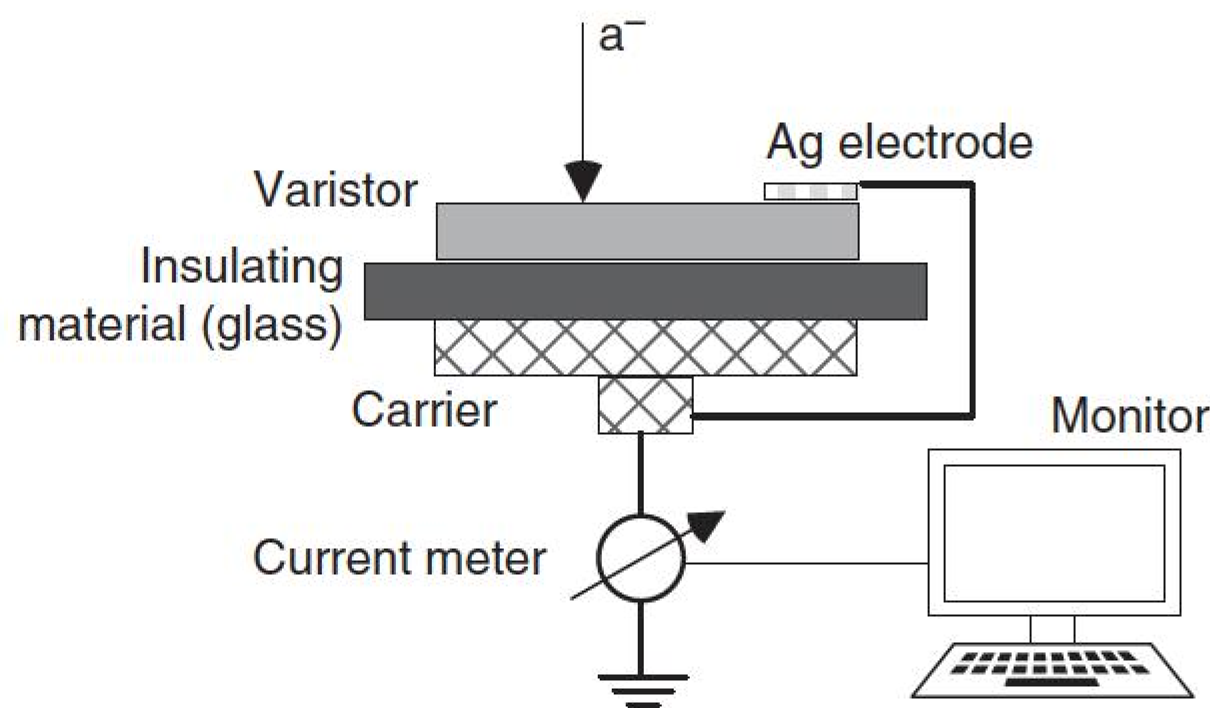


Figure 4.15 Schematic diagram of the setup for the current image. Source: Adapted from Hohenberger et al. [47].

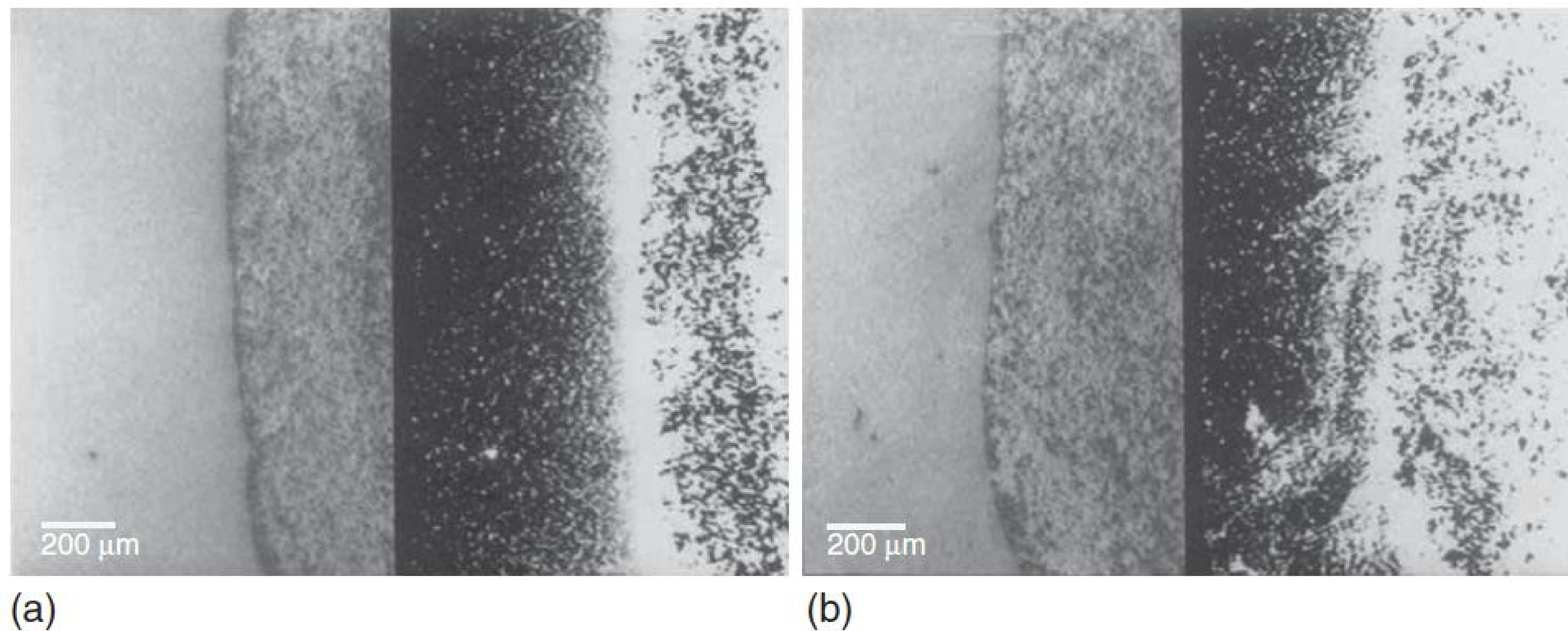


Figure 4.16 SEM images of varistor surface with SE image on the left side and current image on the right side. (a) sol–gel powder containing $A1_2O_3$; (b) sol–gel powder, normal composition. Source: Hohenberger et al. 1991 [47]. Reproduced with permission of John Wiley & Sons.

appear dark. Because of the conduction mechanism of varistors, this depends on the distance of the charge grain from the electrode. The image expected would be composed of a bright electrode seam and, if they exist, some bright conductive paths in the area appearing darker surrounding the nonconducting area.

The current image is shown in the right half of the photograph in Figure 4.16 [47]. The left half of the split screen shows the same surface as a secondary ion picture. The rough structure in the right-hand side of the image is the silver electrode. Both samples were made from sol–gel powders. Figure 4.16a shows the sample including Al_2O_3 doping and Figure 4.16b shows the sample without Al_2O_3; an inhomogeneous current distribution with a single conductive path through the microstructure can be observed.

4.6 Test on Fabricated Individual Grain Boundary

In order to study the grain boundary characteristics inside a ZnO varistor without the influence of the varistor bulk, different individual grain boundary structures were fabricated.

4.6.1 Thin Film Approach

Grain boundary structure can be simulated by forming two-layer structures in which one layer is ZnO and the other is with materials as elements typically found at the triple point between grains in the varistor.

Suzuoki et al. [48, 49] studied a ZnO–Bi_2O_3 two-layer thin film varistor prepared by RF sputtering as a model system representing a single grain boundary in the ZnO varistor. The two-layer thin film structure showed highly nonlinear, asymmetrical I–V characteristics whose nonlinear coefficient for reverse bias equals or exceeds those of actual ZnO varistors. Based on the I–V and C–V measurements, it was suggested that a negative charge and associated potential barrier at the interface provided these nonlinear I–V characteristics. Other works on the ZnO–Bi_2O_3 thin film varistor have been reported by Lou [50] and Selim et al. [51]. Furthermore, a similar study based on a ZnO–Pr/Co oxide two-layer thin film varistor has also been reported.

The advantages of the thin film approach include the ability to form single barriers and control the interfacial chemistry. However, such junctions do not accurately replicate the ZnO grain boundary; the barriers seem unstable upon biasing and dopants tend to become volatile during fabrication [52].

4.6.2 Surface In-Diffusion Approach

Nonohmic properties can also be obtained by diffusing oxides such as Bi_2OA_3 into the grain boundaries of undoped ZnO. This approach relies on the fact that the diffusion of dopant ions is more rapid along the grain boundaries. Sukkar and Tuller [53, 54] reported that single electrically active ZnO grain boundaries could be prepared by using a surface in-diffusion method. In this technique, a "sandwich" composed of undoped polycrystalline ZnO disks were assembled prior to annealing with additions to the interface between the two layers. As a result, single electrically active grain boundaries were successfully fabricated in Mn/Pr-, Co/Pr-, Mn/Co/Pr-doped ZnO samples.

4.6.3 Bicrystal Approach

Among the possible approaches to study an individual grain boundary, a ZnO bicrystal with controlled dopants at the interface would appear to be the most ideal material for study.

The fabrication of Bi-doped bicrystal with excellent nonlinearity is still challenging; the bicrystal-like structure (or called quasi-bicrystal) has been investigated. Schwing and Hoffmann [8] fabricated such structures by sandwiching an intermediate layer of common varistor additives (Bi_2O_3, MnO_2, Co_3O_4, and Cr_2O_3) between undoped ZnO single-crystal plates as seen in Figure 4.17. The microstructure of the "sandwiches" sintered at 900 °C for one hour consisted of two single crystals well separated by a 5 μm thick intergranular layer. For the structures sintered at 1100 °C, the microstructure was similar except that the ZnO single crystals were in direct contact at certain

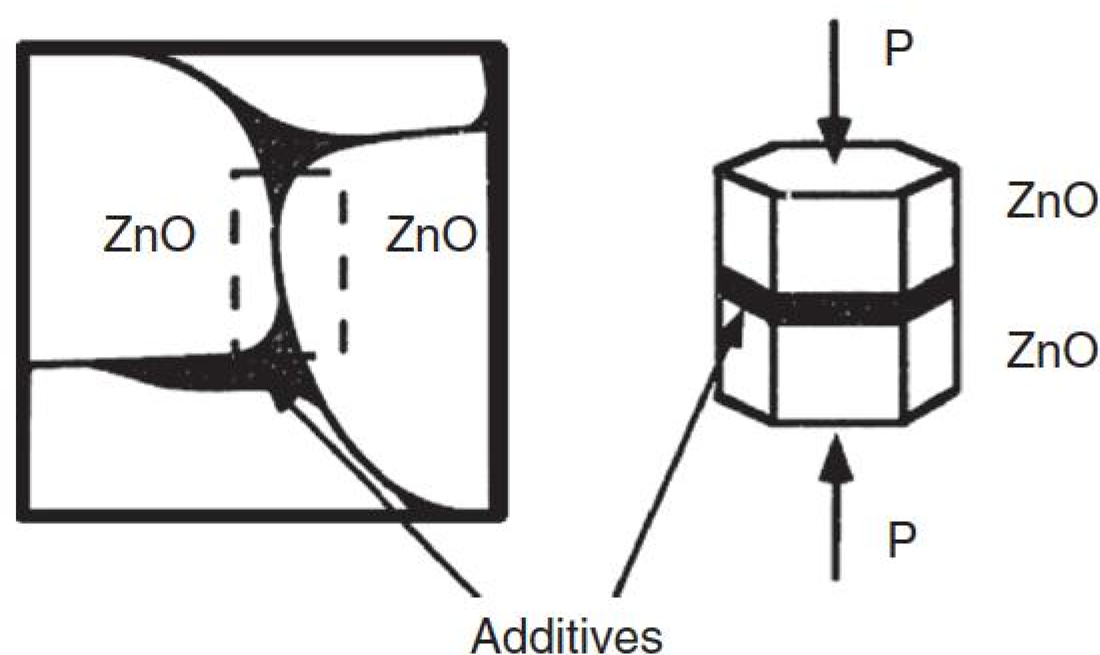


Figure 4.17 Fabrication of Bi-quasi bicrystal representing individual grain boundary. Source: Adapted from Sukkar and Tuller [54].

points along the interface. The sandwiches fired at 900 °C generally exhibited superior varistor $I-V$ characteristics, which was attributed directly to the presence of a continuous Bi_2O_3-rich layer at the interface absent in samples fired at 1100 °C. Similar works by Cheng et al. have reported Bi-doped quasi-bicrystal with excellent nonlinearity [55].

AC measurements showed that the potential barriers at the sandwich interface were due to depletion regions adjacent to the additive oxide interfacial layers rather than to the layer themselves. The interfacial layer was believed to set up depletion regions and accompanying potential barriers at the sandwich interfaces. However, the exact mechanisms of potential barrier formation during the processing were not well understood [51].

Comparatively, recent studies reported successful fabrication of high-quality Pr-doped bicrystal. Sato et al. [56, 57] sputtered an additional layer of nanometer thickness onto the contact plane of the ZnO crystal, and the sandwich structure annealed at 1100 °C for 10 hours. Such Pr-doped bicrystals of various coincidence-site-lattice (CSL) boundaries, obtained by hot-pressing joining

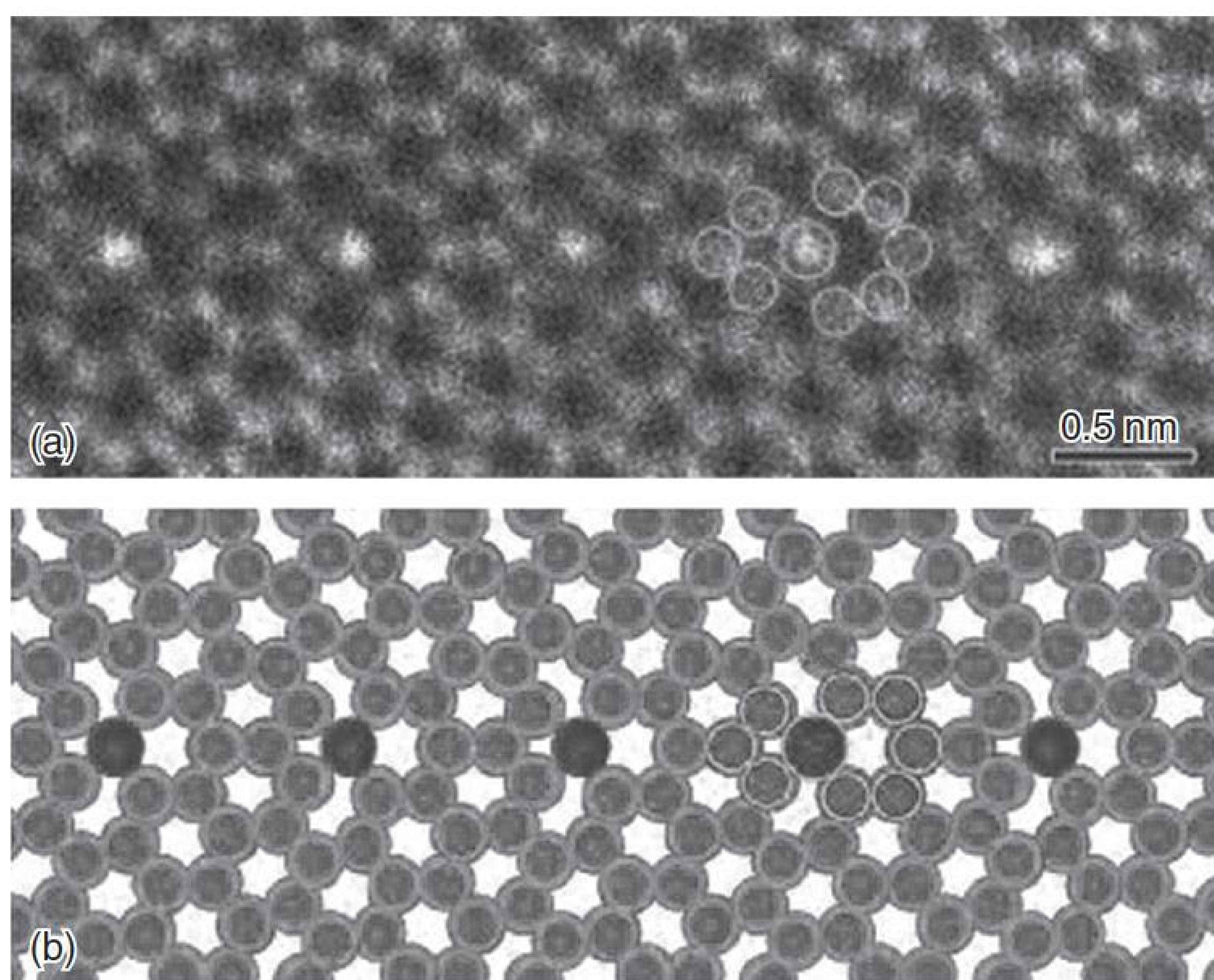


Figure 4.18 Experimentally observed and calculated Pr-doped Σ7 CSL boundary. Source: Sato et al. 2007 [56]. Reproduced with permission of John Wiley & Sons.

technique, present nonlinearity when the bicrystal interface is decorated with Pr atoms (see Figure 4.18 [56]). It is believed that the Pr dopants could promote the generation of acceptor-like states and thus endow the grain boundary with electrical nonlinearity [56, 57]. Moreover, Co-doped [58, 59], Sb-doped [60], and Mn-doped [59] bicrystals were also reported.

References

1 Mahan, G.D., Levinson, L.M., and Philipp, H.R. (1979). Theory of conduction in ZnO varistors. *Journal of Applied Physics* 50 (4): 2799–2812.

2 Bernasconi, J., Klein, H.P., Knecht, B., and Strässler, S. (1976). Investigation of various models for metal oxide varistors. *Journal of Electronic Materials* 5 (5): 473–495.

3 Einzinger, R. (1987). Metal oxide varistors. *Annual Review of Materials Science* 17 (1): 299–321.

4 Van Kemenade, J.T.C. and Eijnthoven, R.K. (1979). Direct determination of barrier voltage in ZnO varistors. *Journal of Applied Physics* 50 (2): 938–941.

5 Krivanek, O.L., Williams, P., and Lin, Y.C. (1979). Direct observation of voltage barriers in ZnO varistors. *Applied Physics Letters* 34 (11): 805–806.

6 Tao, M., Ai, B., Dorlanne, O., and Loubiere, A. (1987). Different "single grain junctions" within a ZnO varistor. *Journal of Applied Physics* 61 (4): 1562–1567.

7 Wang, H., Li, W., and Cordaro, J.F. (1995). Single junctions in ZnO varistors studied by current-voltage characteristics and deep level transient spectroscopy. *Japanese Journal of Applied Physics* 34 (4R): 1765–1768.

8 Schwing, U. and Hoffmann, B. (1985). Model experiments describing the microcontact of ZnO varistors. *Journal of Applied Physics* 57 (12): 5372–5379.

9 Olsson, E., Dunlop, G.L., and Osterlund, R. (1989). Development of functional microstructure in ZnO varistor materials. *Ceramic Transactions* 3: 57–64.

10 Olsson, E. and Dunlop, G.L. (1989). Characterization of individual interfacial barriers in a ZnO varistor material. *Journal of Applied Physics* 66 (8): 3666–3675.

11 Olsson, E. and Dunlop, G.L. (1989). Interfacial barriers to electrical conduction in ZnO varistor materials. *Ceramic Transactions* 3: 65–72.

12 Wang, H., Schulze, W.A., and Cordaro, J.F. (1995). Averaging effect on current-voltage characteristics of ZnO varistors. *Journal of Applied Physics* 34 (5R): 2352–2358.

13 He, J., Zeng, R., Chen, Q. et al. (2004). Nonuniformity of electrical characteristics in microstructures of ZnO surge varistors. *IEEE Transactions on Power Delivery* 19 (1): 138–144.

14 Einzinger, R. (1979). Grain junction properties of ZnO varistors. *Applications of Surface Science* 3 (3): 390–408.

15 Morris, W.G. (1976). Physical properties of the electrical barriers in varistors. *Journal of Vacuum Science and Technology* 13 (4): 926–931.

16 Wong, J. (1976). Barrier voltage measurement in metal oxide varistors. *Journal of Applied Physics* 47 (11): 4971–4974.

17 Levinson, L.M. and Philipp, H.R. (1986). Zinc oxide varistors-a review. *American Ceramic Society Bulletin* 65 (4): 639–646.
18 Einzinger, R. (1978). Metal oxide varistor action-a homojunction breakdown mechanism. *Applications of Surface Science* 1 (3): 329–340.
19 Tanaka, S. and Takahashi, K. (1999). Direct measurements of voltage-current characteristics of single grain boundary of ZnO varistors. *Journal of the European Ceramic Society* 19 (6–7): 727–730.
20 Sun, H.T., Zhang, L.Y., and Yao, X. (1993). Electrical nonuniformity of grain boundaries within ZnO varistors. *Journal of the American Ceramic Society* 76 (5): 1150–1155.
21 Rodewald, S., Fleig, J., and Maier, J. (2001). Microcontact impedance spectroscopy at single grain boundaries in Fe-doped $SrTiO_3$ polycrystals. *Journal of the American Ceramic Society* 84 (3): 521–530.
22 Tanaka, A. and Mukae, K. (1999). ICTS measurements of single grain boundaries in ZnO: rare-earth varistor. *Journal of Electroceramics* 4 (1): 55–59.
23 He, J., Liu, J., Hu, J. et al. (2011). Non-uniform ageing behavior of individual grain boundaries in ZnO varistor ceramics. *Journal of the European Ceramic Society* 31 (8): 1451–1456.
24 Liu, J., He, J., Hu, J. et al. (2011). Statistics on the AC ageing characteristics of single grain boundaries of ZnO varistor. *Materials Chemistry and Physics* 125 (1–2): 9–11.
25 Liu, J. (2011). Research on the degradation characteristics and mechanisms of high voltage gradient ZnO varistor. PhD thesis. Tsinghua University, Beijing, China.
26 Olsson, E. and Dunlop, G.L. (1989). The effect of Bi_2O_3 content on the microstructure and electrical properties of ZnO varistor materials. *Journal of Applied Physics* 66 (9): 4317–4324.
27 Levinson, L. and Philipp, H. (1977). ZnO varistors for transient protection. *IEEE Transactions on Parts, Hybrids, and Packaging* 13 (4): 338–343.
28 Sung, G.Y., Kim, C.H., and Oh, M.H. (1987). Effect of grain-size distribution on the barrier voltage of ZnO varistors. *Advanced Ceramic Materials* 2 (4): 841–847.
29 Brückner, W., Bäther, K.H., Moldenhauer, W. et al. (1980). Inhomogeneities and single barriers in ZnO-varistor ceramics. *Physica Status Solidi (A)* 59 (1): K1–K4.
30 Olsson, E., Falk, L.K.L., Dunlop, G.L., and Österlund, R. (1985). The microstructure of a ZnO varistor material. *Journal of Materials Science* 20 (11): 4091–4098.
31 Emtage, P.R. (1979). Statistics and grain size in zinc oxide varistors. *Journal of Applied Physics* 50 (11): 6833–6837.
32 Levinson, L.M. and Philipp, H.R. (1975). The physics of metal oxide varistors. *Journal of Applied Physics* 46 (3): 1332–1341.
33 Nan, C.W. and Clarke, D.R. (1996). Effect of variations in grain size and grain boundary barrier heights on the current-voltage characteristics of ZnO varistors. *Journal of the American Ceramic Society* 79 (12): 3185–3192.
34 Nan, C.W. (1987). A microstructure-physical model of sensitive semiconductor ceramics. *Acta Physica Sinica* 36 (10): 1298–1304.

35 Canessa, E. and Nguyen, V.L. (1992). Non-linear I–V characteristics of double Schottky barriers and polycrystalline semiconductors. *Physica B: Condensed Matter* 179 (4): 335–341.

36 Wen, Q. and Clarke, D.R. (1994). Modeling the electrical characteristics of polycrystalline varistors using individual grain boundary properties. *Ceramic Transactions* 41: 217–230.

37 Bartkowiak, M. and Mahan, G.D. (1995). Nonlinear currents in Voronoi networks. *Physical Review B* 51 (16): 10825–10832.

38 Bartkowiak, M., Mahan, G.D., Modine, F.A. et al. (1996). Voronoi network model of ZnO varistors with different types of grain boundaries. *Journal of Applied Physics* 80 (11): 6516–6522.

39 Cao, Z.C., Wu, R.J., and Song, R.S. (1994). Ineffective grain boundaries and breakdown threshold of zinc oxide varistors. *Materials Science and Engineering: B* 22 (2–3): 261–266.

40 Eda, K. (1989). Zinc oxide varistors. *IEEE Electrical Insulation Magazine* 5 (6): 28–30.

41 Chiang, Y.M., Kingery, W.D., and Levinson, L.M. (1982). Compositional changes adjacent to grain boundaries during electrical degradation of a ZnO varistor. *Journal of Applied Physics* 53 (3): 1765–1768.

42 Huey, B.D. and Bonnell, D.A. (2000). Nanoscale variation in electric potential at oxide bicrystal and polycrystal interfaces. *Solid State Ionics* 131 (1–2): 51–60.

43 Olbrich, A., Ebersberger, B., and Boit, C. (1998). Conducting atomic force microscopy for nanoscale electrical characterization of thin SiO_2. *Applied Physics Letters* 73 (21): 3114–3116.

44 Schloffer, M., Teichert, C., Supancic, P. et al. (2010). Electrical characterization of ZnO multilayer varistors on the nanometre scale with conductive atomic force microscopy. *Journal of the European Ceramic Society* 30 (7): 1761–1764.

45 Gheno, S.M., Kiminami, R.H., Morelli, M.M. et al. (2008). An AFM/EFM study of the grain boundary in ZnO-based varistor materials. *Journal of the American Ceramic Society* 91 (11): 3593–3598.

46 Haskell, B.A., Souri, S.J., and Helfand, M.A. (1999). Varistor behavior at twin boundaries in ZnO. *Journal of the American Ceramic Society* 82 (8): 2106–2110.

47 Hohenberger, G., Tomandl, G., Ebert, R., and Taube, T. (1991). Inhomogeneous conductivity in varistor ceramics: methods of investigation. *Journal of the American Ceramic Society* 74 (9): 2067–2072.

48 Suzuoki, Y., Ohki, A., Mizutani, T., and Ieda, M. (1987). Humidity dependence of electrical conduction in ZnO-Bi_2O_3 thin film composites. *Journal of Physics D: Applied Physics* 20 (4): 518–521.

49 Suzuoki, Y., Ohki, A., Mizutani, T., and Ieda, M. (1987). Electrical properties of ZnO-Bi_2O_3 thin-film varistors. *Journal of Physics D: Applied Physics* 20 (4): 511–517.

50 Lou, L.F. (1979). Current-voltage characteristics of ZnO-Bi_2O_3 heterojunction. *Journal of Applied Physics* 50 (1): 555–558.

51 Selim, F.A., Gupta, T.K., Hower, P.L., and Carlson, W.G. (1980). Low voltage ZnO varistor: device process and defect model. *Journal of Applied Physics* 51 (1): 765–768.

52 Baek, K.K. (1994). Study of electrically active ceramic interfaces: ZnO based homojunctions and heterojunctions. Doctoral dissertation. Massachusetts Institute of Technology, Cambridge, MA, USA.

53 Sukkar, M.H. (1986). Electronic transport phenomena in polycrystalline ZnO: a study in grain boundary chemistry and electronic structure. Doctoral dissertation. Massachusetts Institute of Technology, Cambridge, MA, USA.

54 Sukkar, M.H. and Tuller, H.L. (1989). ZnO interface electrical properties-role of oxygen chemisorption. In: *Non-Stoichiometric Compounds* (ed. J. Nowotny and W. Weppner), 237–263. Dordrecht: Kluwer Academic Publishers.

55 Cheng, C., He, J., and Hu, J. (2012). Naturally asymmetrical double-Schottky barrier model: based on observation of bicrystal. *Applied Physics Letters* 101 (17): 173508.

56 Sato, Y., Yamamoto, T., and Ikuhara, Y. (2007). Atomic structures and electrical properties of ZnO grain boundaries. *Journal of the American Ceramic Society* 90 (2): 337–357.

57 Sato, Y., Buban, J.P., Mizoguchi, T. et al. (2006). Role of Pr segregation in acceptor-state formation at ZnO grain boundaries. *Physical Review Letters* 97 (10): 106802.

58 Oba, F., Sato, Y., Yamamoto, T. et al. (2003). Current–voltage characteristics of cobalt-doped inversion boundaries in zinc oxide bicrystals. *Journal of the American Ceramic Society* 86 (9): 1616–1618.

59 Ohashi, N., Terada, Y., Ohgaki, T. et al. (1999). Synthesis of ZnO bicrystals doped with Co or Mn and their electrical properties. *Japanese Journal of Applied Physics* 38 (9R): 5028–5032.

60 Zou, K., Qi, X.Y., Duan, X.F. et al. (2005). Sb-induced bicrystal ZnO nanobelts. *Applied Physics Letters* 86 (1): 013103.

5

Simulation on Varistor Ceramics

A varistor can be regarded as a complex multijunction device composed of large numbers of both ZnO grains and grain boundaries. The influence of the geometry and topology of the granular microstructure as well as the properties and the distribution of electrical characteristics of grain boundaries on the features of bulk varistor devices is an important issue. The simple $I-V$ characteristic models and the full $I-V$ characteristic models from a thermionic emission description of current transport across a boundary and the actual conduction mechanism of the grain boundaries as well as the capacitances of the grain boundaries are introduced for simulating the grain boundaries. The methods to simulate the actual microstructures of ZnO varistors are presented, not only the electrical characteristics in the microstructure can be analyzed but the temperature and thermal stress distribution can also be coupled. These electrical network-based simulations will undoubtedly bring even greater insights into the behavior of varistors and other electrical ceramics. The influence of different microstructural parameters on the macroscopic characteristics of varistor bulks are presented, and the optimal measure decreasing the residual voltage ratio of ZnO varistors is also concluded from the simulations. The simulation can well direct the sintering of ZnO varistors with different purposes, such as a varistor with low residual voltage ratio.

5.1 Introduction

A bulk varistor is a complex multijunction device composed of large numbers of both ohmic and nonlinear elements connected in a random network. The microstructures of ZnO varistors are composed of numerous ZnO grains and grain boundaries. If all the grain boundaries were identical, the coordination of all the grains the same, the shape of all the grains the same, and the area of each grain face the same, then the current density–electric field (or voltage gradient) (J–E) or current–voltage (I–V) characteristics of the varistor would be the same as that of the individual grain boundary [1]. However, the microstructures of ZnO varistors are highly nonuniform, so the electrical properties of grain boundary microjunctions are not identical [2–4].

The bulk electrical characteristics of a ZnO varistor are decided by the network of ZnO grains and boundaries in series and in parallel. The influence of the

geometry and topology of the granular microstructure, as well as the properties and the distribution of electrical characteristics of grain boundaries on the features of bulk varistor devices, is an important issue. Because variations exist in each of these parameters, the overall $I-V$ characteristics are different. The question then becomes how various varistor characteristics are dependent on these variations of microscopic parameters of ZnO grains and grain boundaries [1]. Simulation analysis on the actual microstructure and electrical characteristics of ZnO varistors can effectively analyze the influences of different factors, such as grain size, barrier voltage, and nonlinear coefficient of single grain boundary, which are respective to different dopants and sintering techniques, on the global electrical characteristics, and the effect of their distributions related to the nonuniformities of ZnO varistors can be considered easily. Overall, the simulation study of such systems is helpful to reveal the connection between the microstructure and macroscopic characteristics of varistor ceramics.

The essential difficulty in addressing such questions quantitatively is that the $I-V$ characteristics of the individual boundaries are highly nonlinear. Consequently, describing current transport in polycrystalline varistors is a problem of percolation theory in a highly nonlinear medium. This was recognized early in the development of ZnO varistors, and a number of consequences were discussed based on the idea that the disorder resulted in "chains" of more conducting paths through the microstructure [1].

The simulation of the DC electrical characteristics of ZnO varistors based on their microstructures has already been reported [5–18], and 1D and 2D simple circuit simulation models were applied to analyze the $I-V$ characteristics and the thermal breakdown of ZnO varistors. In modeling the current transport in varistors, the microstructure is first described in terms of an equivalent electrical network of nonlinear resistors, and then a disorder is introduced into the network. Finally, the spatial distribution of current flow is determined in response to an applied voltage or current. A circuit model, in which the Voronoi network was applied to present the actual microstructures of ZnO varistors with randomly distributed ZnO grains and grain boundaries, was first proposed by Bartkowiak and Mahan [5].

Usually, the grain boundaries in these models were described by the approximate empirical formulas, instead of their actual conduction mechanism. This means that these $I-V$ characteristics are phenomenological rather than a detailed physical description. The detailed physical description of the grain boundaries are considered by Long et al., especially the capacitance characteristics of the grain boundaries were first considered, which makes the simulation on AC and surge performances of ZnO varistors possible [19].

A finite-difference numerical method was used to obtain current density distributions in the varistor material [20]. Defects and surrounding varistor material are represented on a fine computational mesh. The electric potentials at all mesh nodes satisfy current continuity, $\nabla \cdot \boldsymbol{J} = 0$, in each mesh cell. This results in unique, self-consistent macroscopic solutions for the electric potential and current density distributions. The local current density depends on the local electric field, and the field is obtained from the nearby mesh potentials. Material dielectric constants do not enter into these computations; the time-independent solutions are fully determined by material conductivities.

5.2 Grain Boundary Model

5.2.1 *I–V* Characteristic Model of Grain Boundary

In the past, all simulation models were based on the $I-V$ characteristic models of single grain boundaries in varistors. The $I-V$ characteristics of grain boundaries were assumed to be similar to those of varistor bulk; this model can be used in the analysis of the current flowing through the varistors at a constant applied voltage.

The $I-V$ characteristics of grain boundaries in a ZnO varistor were measured by a microcontact test and are shown in Figure 4.9, and the grain boundaries can be classified into good and bad ones as discussed in Section 4.4, where good means the grain boundary has a good nonlinear $I-V$ characteristics, and bad means the nonlinearity is bad, even presents a linear property. Therefore, two principal types of grain boundary junctions are considered in simulations. One is a purely resistive, i.e. linear, boundary having a conductance that is the same as that of the grains themselves. The second type of grain boundary is the one having a nonlinear varistor characteristic. Usually, these boundaries are treated, electrically, as shunted junctions having the following current–voltage characteristics [13]:

$$I = V\sigma_s + 0.5V\sigma_g[1 + \tanh s(V - V_B)] \tag{5.1}$$

where σ_s is the shunt conductance, describing the leakage current that flows even at voltages smaller than the barrier voltage, σ_g is the conductance of the grain, which is typically orders of magnitude larger than the shunt conductance, V_B is the barrier voltage, and s is an additional parameter that controls the numerical value of the dynamic conductance and is used to adjust the degree of nonlinearity of the $I-V$ curve.

Although both $I-V$ characteristics described by Eq. (5.1) are a phenomenological description rather than a detailed physical description, it does incorporate the essential physical features of models describing the grain boundaries of a varistor. It is also relatively straightforward to program.

In the simulation model of Bartkowiak et al. [7], the grain boundaries were divided into "good" junction with high nonlinearity, "bad" junctions with poor nonlinearity, and linear ohmic junction with low resistivity, according to the microcontact measurements upon single grain boundaries in literatures. The $I-V$ characteristics of good and bad junctions are described as switching functions composed of two pieces. A good grain boundary characteristic is described by [7]

$$J(V) = \frac{V}{R_g}\left(1 + \frac{V^{50}}{V_B{}^{50}}\right) \quad (\text{for } V \le V_{0g}) \tag{5.2}$$

$$J(V) = \frac{V}{R_g}\left(1 + \frac{V_{0g}{}^{50}}{V_B{}^{50}}\right)^{7/2}\left(1 + \frac{V_{0g}{}^{70}}{V_B{}^{50}V^{20}}\right)^{-5/2} \quad (\text{for } V > V_{0g}) \tag{5.3}$$

where $J(V)$ is the 2D current density, V is the voltage across the boundary, R_g is the leakage resistance of a unit area of grain boundary, and V_B is the barrier voltage of the junction, which is set to $V_B = 3$ [7]. V_B is the voltage for which the nonlinear coefficient $\alpha = \mathrm{d}(\log_{10} J)/\mathrm{d}(\log_{10} V)$ reaches half of its maximum

and corresponds to the position of the "knee" of the characteristic. Typically, experimental measurements give a leakage resistivity ρ_v of real varistors of order 10^{11}–10^{12} Ω cm, this corresponds to the value 10^8–10^{10} V cm^2 for the leakage resistance of a unit area of grain boundary; therefore, R_g is set to 10^9 and defines the normalization scale of the units. For $V \leq V_{0g}$, the function in Eq. (5.2) describes the prebreakdown and the breakdown regions of the characteristic. The upturn region in the I–V characteristic at high current density is modeled by the characteristic of Eq. (5.3) for $V > V_{0g}$. The parameter V_{0g}, at which the two parts join smoothly, determines the resistivity of the junction in the upturn region ρ_u, i.e. the resistivity of ZnO grains. As $\rho_u = 0.1$–$1\,\Omega$ cm, we take $V_{0g} = 3.467$, which gives $\rho_g/\rho_u = 10^{11}$ to correspond to typical experimental data. The above parameters give a behavior with a maximum nonlinear coefficient $\alpha_{mg} \approx 51$ and a sharp breakdown.

For the bad grain boundary property [7],

$$J(V) = \begin{cases} \dfrac{V}{R_b}\left(1 + \dfrac{V^{50}}{{V_B}^{50}}\right)^{1/5}, & V \leq V_{0b} \\ \dfrac{V}{R_b}\left(1 + \dfrac{{V_{0b}}^{50}}{{V_B}^{50}}\right)^{11/5}\left(1 + \dfrac{{V_{0b}}^{55}}{{V_B}^{50}V^5}\right)^{-2}, & V > V_{0b} \end{cases} \quad (5.4)$$

where the barrier voltage V_B here is the same as for the good microjunctions, i.e. $V_B = 3$. The leakage resistance of a unit area of grain boundary R_b for bad microjunctions is chosen 100 times lower than that for good grain boundaries, i.e. $R_b = 10^7$. To ensure consistency, the ratio of the prebreakdown to the upturn resistivity ρ_b/ρ_u for bad microjunctions must be 10^9. This is achieved by taking $V_{0b} = 3.622$. The electrical characteristic given by Eq. (5.4) has a maximum nonlinear coefficient $\alpha_{mb} \approx 11$.

Finally, the ohmic grain boundaries have a linear characteristic,

$$J(V) = \frac{V}{R_o} \quad (5.5)$$

where R_o is the resistance of a unit area of the boundary. It is fixed at $R_o = 2\times10^5$. This choice, as well as that for the values of the parameters in Eqs. (5.3) and (5.4), follows from the microcontact measurement data of Cao et al. [21].

Eda simulated the I–V characteristics of the ZnO varistor and its temperature dependence according to the conduction mechanism based on the theory of double-Schottky barriers [18]. The equation is available to consider the Schottky emission current, which is dominant in the small current region and has a strong temperature dependence, and the highly nonohmic current, which is dominant in the high-current region. An improved I–V characteristics of a single grain boundary was proposed by Chen et al. for two-dimensional simulation [9]:

$$J(V) = \begin{cases} \dfrac{A_1}{\rho_{gb}}\exp\left(-\dfrac{E_g - \beta V^{1/2}}{K_b T}\right) + A_2\left(\dfrac{V}{V_B}\right)^{\alpha}, & V \leq V_u \\ \dfrac{A_1}{\rho_{gb}}\exp\left(-\dfrac{E_g - \beta {V_u}^{1/2}}{K_b T}\right) + A_2\left(\dfrac{V_u}{V_B}\right)^{\alpha} + \dfrac{A_3}{d_{ij}\rho_g}(V - V_u), & V > V_u \end{cases} \quad (5.6)$$

where A_1, A_2, and A_3 are the constants for $I-V$ curve of a single grain boundary, their typical values are 2.5×10^{16} A Ω cm^{-1}, 0.01 A Ω cm^{-2}, and 1 A Ω; ρ_{gb} is the resistivity of the grain boundary, 10^{12} Ω cm is selected; ρ_g is the resistivity of the grain with a typical value of 1 Ω cm; E_g is the barrier height with a typical value of 0.8 eV; $\beta = [e^3/(4\pi t\varepsilon_0\varepsilon_r)]^{1/2}$ is a constant related to the electrical characteristic and geometrical structure of the intergranular layer of ZnO varistors (e is the electron charge, ε_0 is the permittivity of free space, $\varepsilon_0 = 8.85\times10^{-12}$ F m^{-1}, ε_r is the relative dielectric constant of the intergranular layer, which is in the range from 4 to 25 ($\varepsilon_r = 15$ is usually selected), and t is the thickness of the intergranular layer in ZnO varistors, whose actual value is about 1200 Å), we can obtain $\beta = 2.83 \times 10^{-2}$ eV$^{1/2}$; k_b is the Boltzmann constant, 1.38×10^{-23} J K^{-1}; T is the temperature in K; V is the voltage applied between the two neighboring grains; and d_{ij} is the distance between the centers of two neighboring grains i and j; V_u is the onset voltage from the breakdown region to the upturn region, $V_u = V_B(J_u/A_2)^{1/\alpha}$, under $J_u = 10^3$ A cm^{-2}. The first row in Eq. (5.6) corresponds to the $I-V$ characteristics in the prebreakdown and breakdown region within which the current behavior is determined by the thermal activated emission of electrons and the tunneling current, and the second row corresponds to the characteristics in the upturn region where the current behavior is determined by the resistivity of the ZnO grain. The $I-V$ characteristics of good and bad grain boundaries can be easily considered in Eq. (5.6) by considering the distributions of barrier voltage, nonlinear coefficient, and barrier height, etc. For linear grain boundary, the $I-V$ characteristics can be calculated by $J(V) = V/R_i$ instead of Eq. (5.5), where R_i is the resistance of a linear grain boundary, which is equal to $d_{ij}\rho_u$, and ρ_u is the resistivity of the linear grain boundary.

However, observations of the microstructure, particularly at a high spatial resolution, reveal that the microstructure can be quite complex. Second phases, such as spinel and various Bi_2O_3 polymorphs, each with a different thermal expansion coefficient and electrical conductivity, are usually present [1]. Also, a bismuth-rich intergranular film has been reported at grain boundaries by many investigators as well as bismuth-rich segregation at other grain boundaries. Additionally, experimental measurements of the current–voltage characteristics of individual grain boundaries reveal that there is a distribution in the breakdown voltage as well as variations in the nonlinear coefficient of the ZnO varistor [21–32]. Therefore, in the simulation, the grain boundary parameters, including the breakdown voltage (or the barrier voltage) and the nonlinear coefficient, should consider their wide distribution, as described in Section 4.3.

Figure 5.1 shows the J–E curve with different values of average grain size s, disorder degree d, $E(\alpha)$, and $\sigma(\alpha)$. $E(\alpha)$ and $\sigma(\alpha)$ are the mean value and the standard deviation of nonlinear coefficient α, respectively. It can be found from the simulation that in order to improve the sensitive voltage gradient, it is effective to decrease the average size of the ZnO grain and to improve the uniformity of ZnO grain size, whereas in order to decrease the residual voltage, the mean value and the uniformity of the nonlinear coefficient of ZnO grain boundaries should be increased.

When the ZnO varistor is operating in the low voltage gradient region, the $I-V$ characteristic has an obvious temperature coefficient within the low voltage gradient region as shown in Figure 5.2; this is very important to the critical

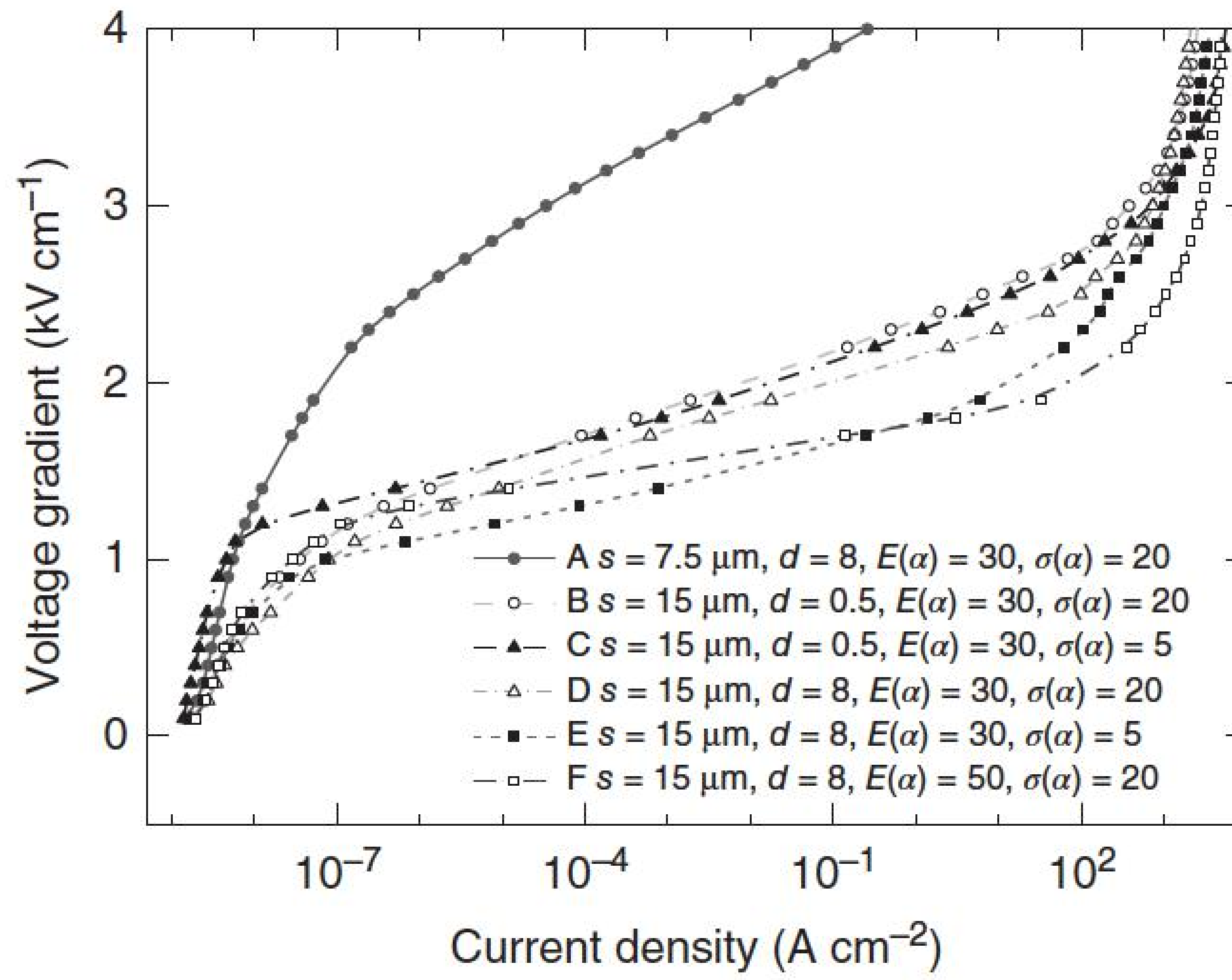


Figure 5.1 The influence of different parameters on *J*–*E* curves.

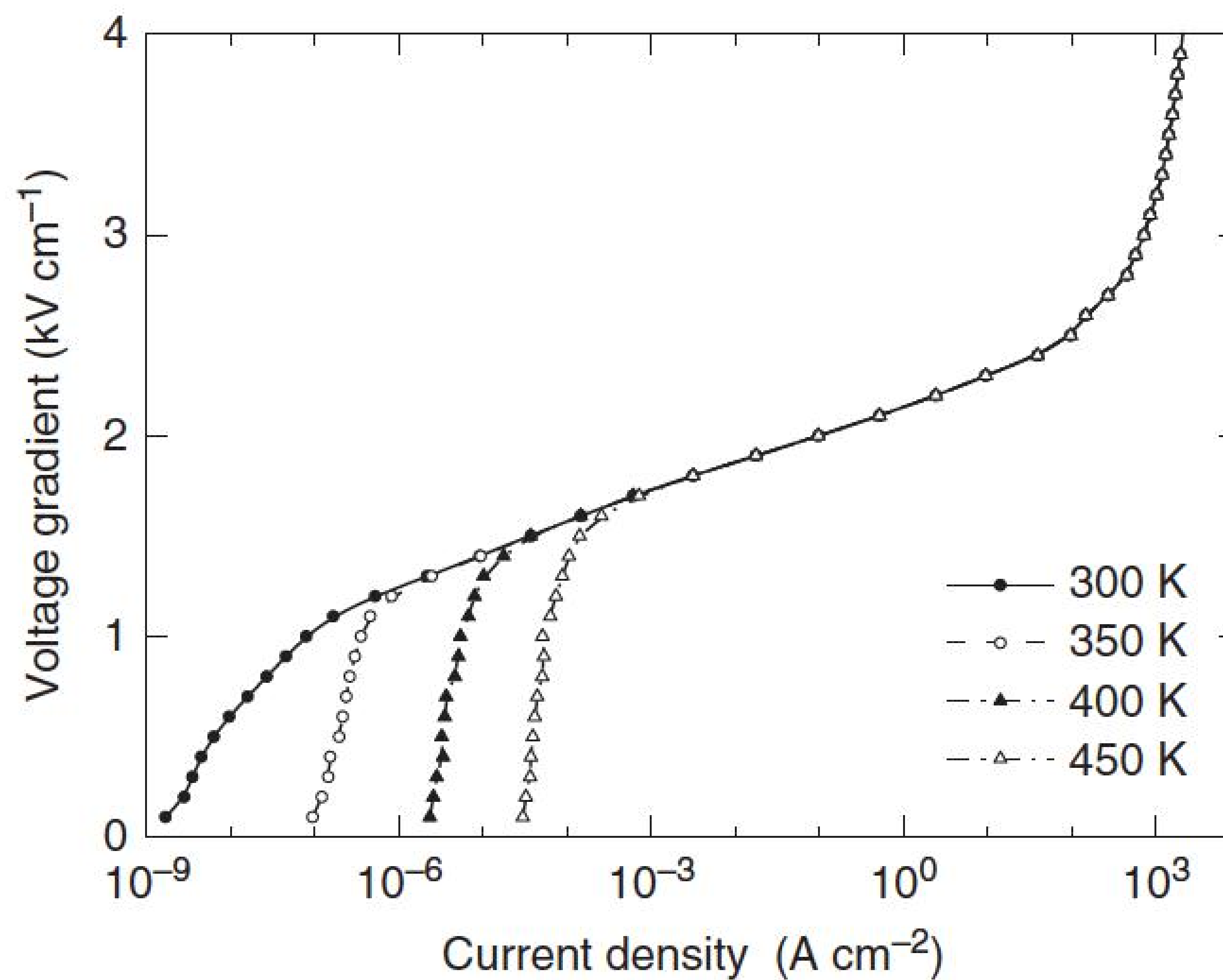


Figure 5.2 The influence of temperature on *J*–*E* curves.

temperature causing a thermal runaway. The current will increase by more than 10 times if the temperature increases to 50 K, which leads to a great increase in the temperature of ZnO varistor. The current in the low voltage gradient region can be effectively reduced by improving the electrical resistivity of the grain boundary ρ_{gb}; thus, the ZnO varistor can operate on a higher temperature, which would permit the ZnO varistor to absorb more surge energy.

Another example of the insight that can be gained through the simulations is shown in Figure 5.3 [1]. In this particular case, the effect of increasing the width of the Gaussian distribution in barrier heights on the overall *J*–*E* characteristics is shown.

5.2.2 GB Model Considering Conduction Mechanism

Ideally, the full $I-V$ characteristics from a thermionic emission description of the current transport across a boundary would be better to improve the simulation precision; the model should consider the actual conduction mechanism of the

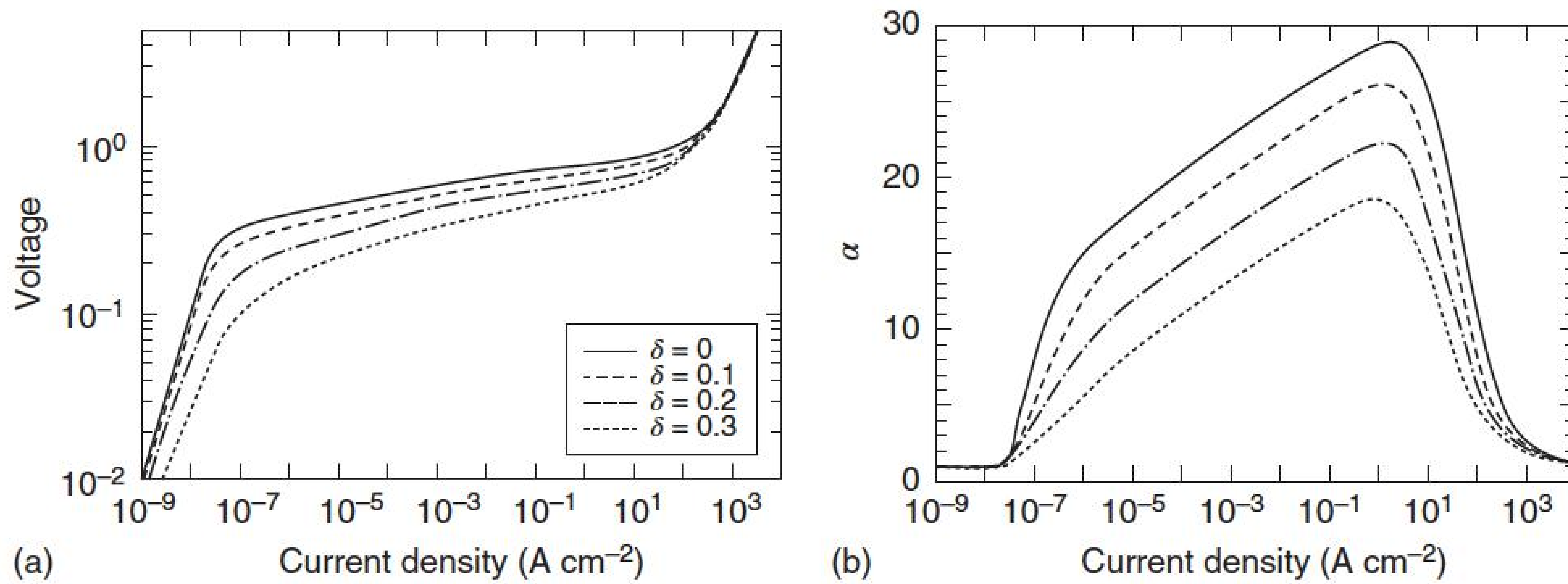


Figure 5.3 Effect of a Gaussian distribution of barrier heights on both (a) the *I–V* characteristics and (b) the nonlinear coefficient for different standard deviations. Source: Clarke 1999 [1]. Reproduced with permission of John Wiley & Sons.

grain boundaries, as well as the capacitances of the grain boundaries, although this greatly increases the computational time.

As discussed in Chapter 2, several possible theories have been reported to explain the conduction mechanism of the grain boundary of ZnO varistors [23, 26, 33–35]. The hole-induced breakdown model for the double-Schottky barrier in the ZnO grain boundary, which was proposed by Blatter and Greuter [26, 35], has become the most accepted theory at present. As this theory model was described by a large number of complex equations, simple empirical formulas were always used to present the ZnO grain boundaries in their simulation models.

The microstructures at the grain boundaries are quite complicated. Eda [36] summarized the results in literatures [37–40] and roughly classified the grain boundaries into three types:

(1) Type I – thick intergranular layer: this region exists in the corner of adjacent ZnO grains, whose thickness is thicker (about 0.1–1 μm), with rich additive segregations, for instance, Bi_2O_3. The melting point of Bi_2O_3 is 825 °C, which decreases to 750 °C when coexisting with ZnO. Hence, a liquid phase is formed during sintering. The liquid phase is likely to gather at the holes created by the packing of the ZnO grains. Therefore, one can easily find the thick Bi_2O_3-rich intergranular layers at the packing holes in the sintered body.
(2) Type II – thin intergranular layer II: the Bi_2O_3-rich intergranular layer becomes thinner (10–1000 Å) as it approaches the contact points of the particles; this region locates in the closer contact place of adjacent ZnO grains with its thickness much thinner than region I. This region is called as type II.
(3) Type III – no intergranular layer: in the closest contact region of ZnO grains, there is almost no grain boundary intergranular layer than can be observed. However, experimental results indicate that this region is rich in additive elements, e.g. Bi, Co, and plentiful O ions.

Similarly, a grain boundary is divided into three regions A, B, and C as shown in Figure 5.4, which are respective to types I, II, and III [19]. Region A is the

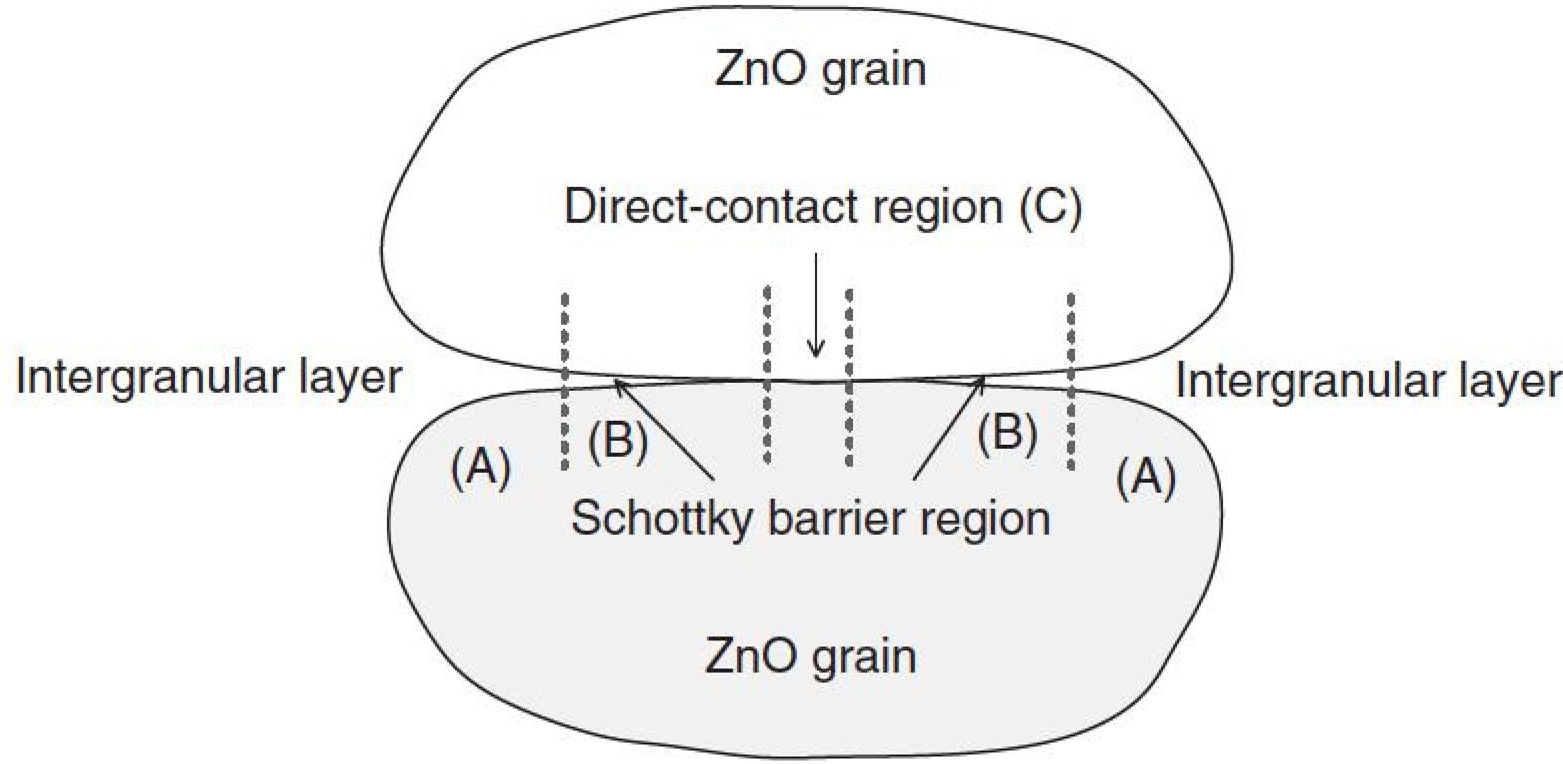


Figure 5.4 The structure of a grain boundary in the ZnO varistor.

Bi_2O_3-rich intergranular layer occupying the ZnO grain corners with large thickness and high resistivity, region B is the nonlinear double-Schottky barrier, and region C has no intergranular layer at all, where the two adjacent ZnO grains contact with each other directly.

Based on the above different regions, Eda has proposed the bypass effect model, (see Figure 5.5a [36]), where R_Z, R_S, and R_I are the resistances of the ZnO grain, Schottky barrier, and intergranular layer, respectively, C_S and C_I are the capacitances of Schottky barrier and intergranular layer, respectively, and Figure 5.5b is the respective simplified model.

The improved equivalent circuit of a ZnO grain boundary was proposed by Long et al. [19] as shown in Figure 5.5c according to its three-zone model. The model parameters can be deduced from the actual conduction mechanism proposed by Blatter and Greuter [26, 35]. For each grain boundary, Z_{DB} is composed of a nonlinear resistance R_{DB} and a nonlinear capacitance C_{DB}. Here, the nonlinear resistance R_{DB} can be calculated from the current density through the barrier and the voltage applied on the grain boundary:

$$R_{DB} = \frac{V}{JS} \tag{5.7}$$

where V is the voltage applied across the double-Schottky barrier and J is the current density through the barrier whose area is S.

The mechanism by which current flows across the boundary is generally consistent with a thermionic emission process. At the same time, additional electrons can be trapped at the boundary, and there is a dynamic flow of trapped charges between the grains and the boundary. The thermionic emission formula is used to calculate the current density through the double-Schottky barrier [1]:

$$J(V) = A^* T^2 \exp\left(-\frac{e\phi_b(V) + \varepsilon_{E_F}}{k_B T}\right) \exp\left(-\frac{eV}{k_B T}\right) \tag{5.8}$$

where ϕ_b is the barrier height, A^* is the Richardson constant, k_B is the Boltzmann constant, T is the absolute temperature, e is the electronic charge, and ε_{E_F} is the difference between the conduction band level E_C and the bulk Fermi level E_F.

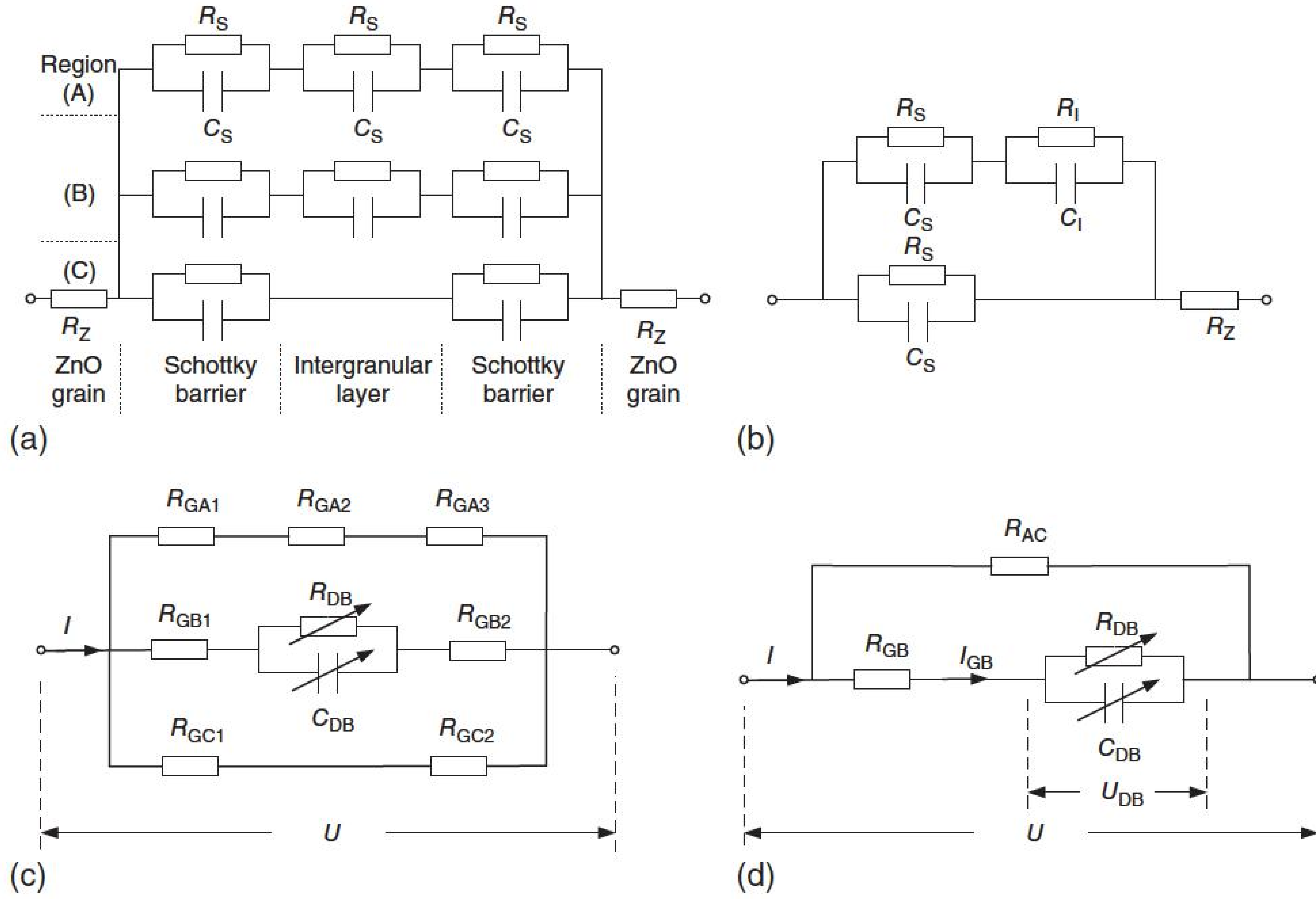


Figure 5.5 (a) The bypass effect model and (b) the simplified model proposed by Eda. Source: Redrawn after [36]. (c) The modified equivalent circuit and (d) the respective simplified equivalent circuit of a grain boundary in the ZnO varistor. Source: Modified from [19]. Z_{GA1}, Z_{GB1}, and Z_{GC1} are the partial resistance values of the ZnO grain on the left side of the grain boundary, which correspond to regions A–C, respectively in Figure 5.4. Z_{GA2}, Z_{GB2}, and Z_{GC2} are those values of the ZnO grain on the right side of the grain boundary. Z_{IL} is the resistance of the intergranular layer in region A, and Z_{DB} represents the nonlinear double-Schottky barrier in region B.

In order to obtain the current density, the Poisson equation is solved to get the barrier height:

$$\frac{\mathrm{d}^2}{\mathrm{d}x^2}\phi_\mathrm{b}(x) = \frac{Q(x)}{\varepsilon_\mathrm{r}\varepsilon_0} \tag{5.9}$$

where $Q(x)$ is the charge distribution in the grain boundary, ε_0 is the permittivity of the vacuum, and ε_r is the relative permittivity of ZnO. The barrier height ϕ_b depends on the interface charge Q_i and the applied bias voltage V [19, 35]:

$$\phi_\mathrm{b} = \frac{V_\mathrm{c}}{4}\left(1 - \frac{V}{V_\mathrm{c}}\right)^2 \tag{5.10}$$

$$V_\mathrm{c} = \frac{Q_\mathrm{i}^2}{2e\varepsilon_0\varepsilon_\mathrm{r}N_\mathrm{i}} \tag{5.11}$$

where Q_i is the charge density of the interface states in the grain boundary, which depends on the applied voltage V, V_c is an intermediate variable without practical significance, and $N_\mathrm{i}(E)$ is the energy distribution function of the interface states. The interface charge $Q_\mathrm{i}(V)$ is determined by the density of interface states $N_\mathrm{i}(E)$,

and Q_i is determined self-consistently as $N_i(E)$ is fixed with respect to the valence band at $x = 0$ [25]:

$$Q_i = e \int_{E_{Fi}^n}^{\infty} N_i(E) f_i(E)\, dE \tag{5.12}$$

where $f_i(E)$ is the Fermi distribution function, E is the energy level, and E_{Fi}^n is a fictitious Fermi level describing the neutral interface. The Fermi distribution function $f_i(E)$ can be presented as

$$f_i(E) = \frac{1}{1 + \exp((E - E_{Fi})/k_B T)} \tag{5.13}$$

where E_{Fi} is the quasi-Fermi level at the interface that shifts with respect to the bulk Fermi level E_F for $V \geq 0$:

$$E_{Fi} = E_F - k_B T \ln \frac{2}{1 + \exp(-eV/k_B T)} \tag{5.14}$$

Obviously, E_{Fi} is shifted from the bulk Fermi level due to the applied voltage V.

From Eqs. (5.9)–(5.14), the barrier height ϕ_b and the interface charge Q_i as the applied bias V can be solved, and then the current density through the barrier will be obtained. From Eq. (5.7), the dynamic resistivity of the double-Schottky barrier with an applied bias between the two neighboring grains with voltages V_k and V_{k+1} per unit area is

$$\rho_k = \frac{V_{k+1} - V_k}{J(V_{k+1}) - J(V_k)} \tag{5.15}$$

The nonlinear capacitance of the unit area C_{DB} also depends on the applied voltage V [41]:

$$C = \sqrt{\frac{e\varepsilon_0 \varepsilon N_d}{2}} \cdot \frac{1}{\sqrt{(\phi_b + V)} + \sqrt{\phi_b}} \tag{5.16}$$

where N_d is the donor density.

Figure 5.3 can be simplified as the circuit shown in Figure 5.5c, and the respective parameters of the equivalent circuit will be

$$Y_{AC} = \frac{1}{R_{GA1} + R_{IL} + R_{GA2}} + \frac{1}{R_{GC1} + R_{GC2}} \tag{5.17}$$

$$R_{GB} = R_{GB1} + R_{GB2} \tag{5.18}$$

$$Y_{DB} = \frac{1}{R_{DB}} \tag{5.19}$$

The ratios of these three-zone areas to the total area of the grain boundary are defined as P_A, P_B, and P_C, respectively. By adjusting these ratios, the different types of grain boundaries can be described. When P_A equals to 1, the grain boundary is "ohmic"; when P_A is larger than P_B, the grain boundary shows a "bad" nonlinear property; when P_B exceeds P_A, the grain boundary shows a "good" nonlinear property. Generally, the value of P_C is always set to zero except some special conditions. For example, when a ZnO varistor sample is sintered under

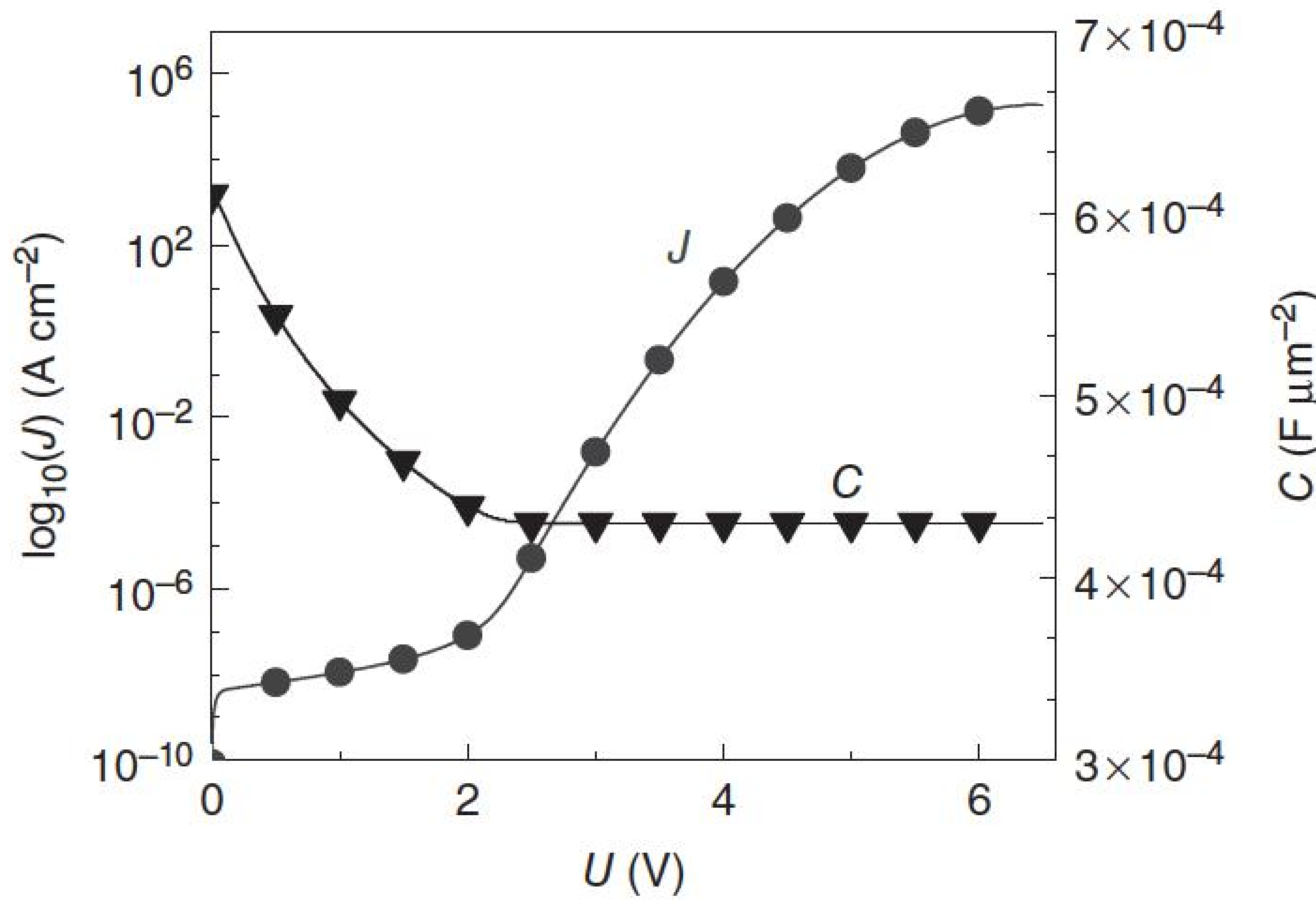


Figure 5.6 The dynamic resistivity and the capacitance per unit area of zone B. Source: Long et al. 2010 [19]. Reproduced with permission of John Wiley & Sons.

too high temperature or with too long time, the most amount of Bi_2O_3 volatilizes from the grain boundaries. As a result, the adjacent ZnO grains merge with each other closely, which can be observed obviously through the SEM photos. Then, P_C should be set to a nonzero value, and zone C would play a dominant role in the deteriorated electrical characteristic of the varistor sample [19].

The typical parameter values of ZnO varistors used in the simulation can be selected from literatures [23, 34], including the ZnO grain resistivity ρ_g of 1 Ω cm^2, the ZnO grain band gap E_g of 3.2 eV, the ZnO grain Fermi level E_F of 3.133 eV, the grain boundary surface-state energy level E_i of 2.3 eV, the ZnO grain donor density N_d of 1×10^{18} cm^{-3}, and the grain boundary interface density N_i of 1×10^{13} cm^{-2}. The time step dt is selected as 10^{-5} s, the percent of zones A, B, and C in whole grain boundaries are $P_A = N(0.2, 0.3)$, $P_C = N(0, 10^{-6})$, and $P_B = 1 - P_A - P_C$. The typical curves of dynamic resistivity and capacitance per unit area of zone B as the functions of applied voltage are shown in Figure 5.6.

5.3 Simulation Model of *I–V* Characteristics

5.3.1 Simple 2D Simulation Model

Although considering the nonlinearity of the individual resistor of the grain boundary makes the simulation of the I–V characteristics very complicated, the essential ideas involved in each step are quite straightforward [1, 11]. The first step is to represent the microstructure by an electrical network [1]. Usually, the representative microstructure used to simply model ZnO varistor is shown in Figure 5.7 [1], which consists of an array of square grains with an insulating phase at each corner and a nonlinear resistor representing the grain boundary at each of the two grain junctions. The array of nonlinear junctions, which will be used to calculate the I–V characteristics of the material, is the mathematical dual of this square array and is thus also the square array in this case. Once the

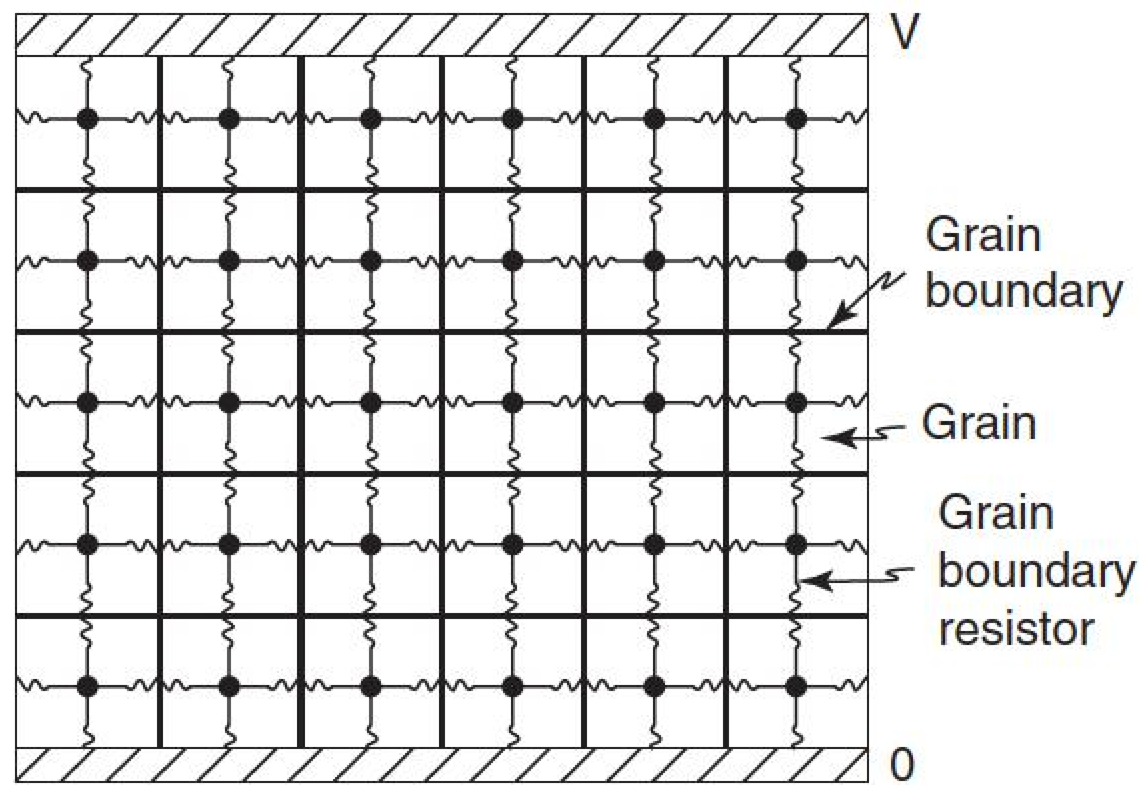


Figure 5.7 The simplified network model of a varistor with nonlinear resistors residing between the nodes. The array of grain boundary resistors is the topological dual of the microstructure of square grains. Source: Clarke 1999 [1]. Reproduced with permission of John Wiley & Sons.

network topology is defined, the I–V characteristic of each grain boundary resistor is selected, and, at this stage, the disorder is introduced.

Secondly, variations in the observed microstructures are incorporated in the model by varying the electrical characteristics of individual boundaries. For instance, the observation that different proportions of the grain boundary area are covered by the wetting phase at the multiple grain junctions can be expressed by variations in the grain boundary resistance from one boundary to the next. Similarly, the crystallographic texture of the microstructure can be included by assigning the crystallographic orientation of each grain according to an appropriate rule. In the present scheme in which piezoelectric effects are neglected, the orientation of each grain is chosen at random. In order to simplify the simulation, the second phase is also assumed to have no effect on the electrical characteristics, and the resistance of all the grains is fixed to the same value. In order to take into account the fact that the grain size of most ceramics is not uniform and that not every grain boundary has a Schottky barrier, a certain portion of the boundaries in the microstructure is assigned to be normal, linearly resistive grain boundaries. Therefore, an effective grain size is introduced to characterize the microstructure of the modeled polycrystalline system. The latter may be compared with the nonlinear exponent as a function of junction voltage calculated by Mahan et al. from a modified back-to-back Schottky barrier model [22].

In the third step, the overall electrical characteristics of the polycrystalline microstructure are calculated. First, however, each junction in the microstructure is assigned either a linear or nonlinear electrical characteristic at random with a prescribed probability. Then, the barrier voltage of each nonlinear junction is picked, again using a random number generator, from a Gaussian distribution chosen to represent the distribution of junction voltages observed in the experiment. Having assigned the junction characteristics, current flow through the network of junctions is computed. This corresponds to a bond percolation model in which the individual bonds are either linear or nonlinear resistors, as distinct from usual percolation models in which each bond is a linear resistor [42].

Once the network is selected and the disorder is introduced, the current flow through the network at a constant applied voltage is computed subject to the

constraint that the current conservation is maintained at each node as shown in Figure 5.7. This is invoked by applying Kirchhoff's law to each node [13]:

$$\sum_j I_{ij} = \sum_j (V_i - V_j)[\sigma_s + 0.5\sigma_g(1 + \tanh s[|V_i - V_j| - V_B^{ij}])] \tag{5.20}$$

where i and j denote the node and its neighbors, respectively, σ_s is the shunt conductance, describing the leakage current that flows even at voltages smaller than the barrier voltage, σ_g is the conductance of the grain, which is typically orders of magnitude larger than the shunt conductance, and s is an additional parameter that is used to adjust the degree of nonlinearity of the I–V curve.

Equivalently, Kirchhoff's law may be expressed in terms of the voltages and conductances across each boundary [11]:

$$\sum_j (V_i - V_j)\sigma_{ij} = 0 \tag{5.21}$$

where the conductance of the individual boundary is

$$\sigma_{ij} = \begin{cases} \sigma_g^{ij} & \text{for a resistive boundary} \\ \sigma_s^{ij} + 0.5\sigma_g^{ij}\left(1 + \tanh\left[s\left(1 - \dfrac{|V_i - V_j|}{V_B^{ij}}\right)\right]\right) & \text{for a nonlinear boundary} \end{cases} \tag{5.22}$$

In the computations, a voltage source is applied across the network with ohmic contacts being established at both the top and the bottom ends of the network by assigning the first and last row of boundaries as being resistive. Periodic boundary conditions are also applied to the network in the direction perpendicular to the applied voltage. For a system of N grains, there are N separate Kirchhoff's equations, from which the electrical potential at each grain is solved numerically for each applied voltage across the varistor. The total current through the network is then calculated for each applied voltage. The dynamic conductance, or the nonlinear coefficient, α, is then calculated according to the definition $\alpha = \mathrm{d}\ln I/\mathrm{d}\ln V$. Other parameters can be set as $s = 20$, $\sigma_s/\sigma_g = 10^{-6}$, the average of V_B^{ij}, $V_B = 1$ and the conductance of the grains, $\sigma_g = 1$, i.e. voltages are normalized to V_B and the currents are normalized to $\sigma_g V_B$.

5.3.2 2D Simulation Models Based on the Voronoi Network

The grain structure of a ceramic is an example of a space-filling cellular structure. One of the simplest ways to model such structures is the Voronoi construction or Voronoi tessellation [43]. The geometry and topology of Voronoi networks closely resemble those found in grain growth from random nucleation sites. In this way, Voronoi networks provide a natural model for the study of transport through disordered structures such as ceramic materials. The Voronoi construction also allows one to cross the whole range from regular lattice to completely random networks and address the question of how a disorder in the local connectivity affects the global properties across the network. The Voronoi network, a kind

of geometric diagram, has been proved as a reasonable model to simulate the microstructures of ZnO varistors [5].

The microstructures of ZnO varistors are highly nonuniform, and the electrical properties of grain boundary microjunctions are not identical. In order to consider the microstructural nonuniformity, Bartkowiak et al. [4–6] described the electrical properties of polycrystalline ZnO varistors by a two-dimensional Voronoi network model, which can consider the actual microstructure of ZnO varistors.

A Voronoi polygon structure comprises randomly generated polygons that cover a spatial region with no gaps between adjacent polygons. This structure is generated using an algorithm that the spatial region to be partitioned around a random set of geometric centers in such a way that each polygon represents the region closer to a given center than any other center. As the structure consists of flat-sided polyhedron perfectly packed together, there is an interdependence in the shape between any polygon and its neighbors [44, 45]. Voronoi networks are formed by intersecting perpendicular bisectors of lines connecting the neighboring seeds. The distribution of the geometric centers determines the granular geometry. When using different initial distributions of geometric centers, different granular geometries can be generated. The nonuniformity of Voronoi network can be regulated by changing the disorder degree. If the seed points are arranged in the same clearance $L = 1$, a disorder is introduced by displacing individual seeds within a disk of radius d around their original seed positions, where d is defined in units of the distance between the nearest neighbors in the triangular lattice and is called as disorder degree. Physically, a Voronoi network can be interpreted as a two-dimensional growth process starting simultaneously at all nucleation seeds and proceeding in the plane at a constant uniform rate until it is terminated whenever two approaching growth fronts reach each other. Therefore, the geometry and topology of Voronoi networks closely resemble those found in grain growth from random nucleation sites [5]. Therefore, it can effectively simulate the disordered structures of ZnO varistors, and the nonuniformity of ZnO varistors can be simulated by changing the disorder degree. Each cell represents a ZnO grain, and each edge corresponds to a grain boundary.

ZnO varistors simulated by Voronoi networks with different disorder degrees are generated and shown in Figure 5.8 [46]. Each polygon in the Voronoi network represents one of ZnO grains, and each sideline of the polygon represents the grain boundary between the two ZnO grains. The ZnO grain has a wurtzite structure, and the ideal two-dimensional microstructure of the ZnO varistor consists of standard hexagons, which is respective to the disorder degree $d = 0$ (Figure 5.8a). When the disorder degree increases, the microstructure changes. As discussed by Priolo et al. [47], it is observed that the lattice becomes topologically disordered when the disorder degree above $d = (\sqrt{3} - 1)/4 = 0.183$. When the disorder degree is larger than 3, the generated Voronoi network is very similar to the actual microstructure of the ZnO varistor as shown in Figure 5.8f, and the topological structure can be regarded as generated from a fully random distribution of seed points.

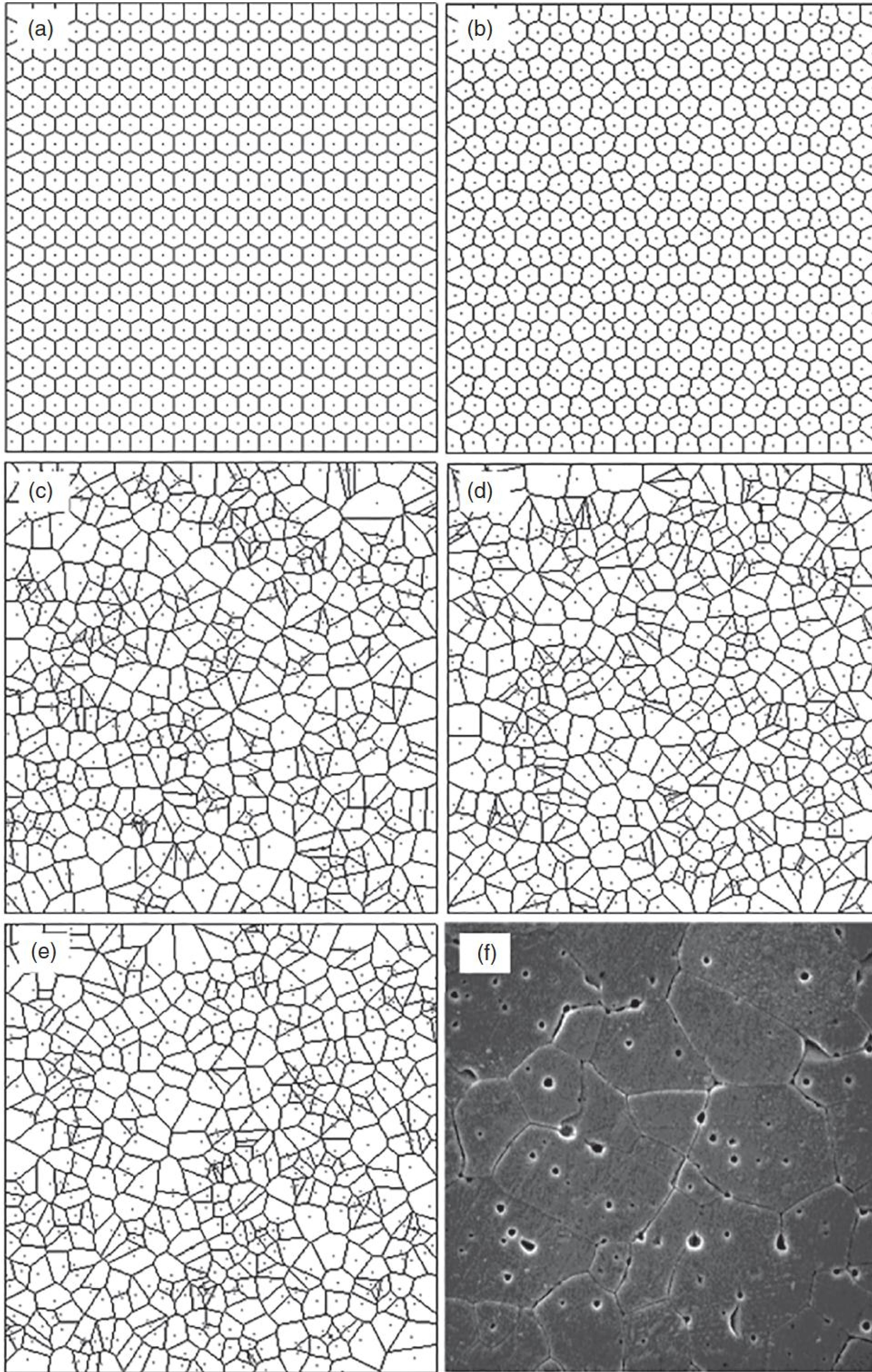


Figure 5.8 The generated Voronoi networks with a different disorder degree d: (a) $d = 0$, (b) $d = 0.18$, (c) $d = 3.0$, (d) $d = 5.0$, (e) $d = 20$; (f) SEM image of the actual ZnO varistor. Source: Adapted from Han et al. [46].

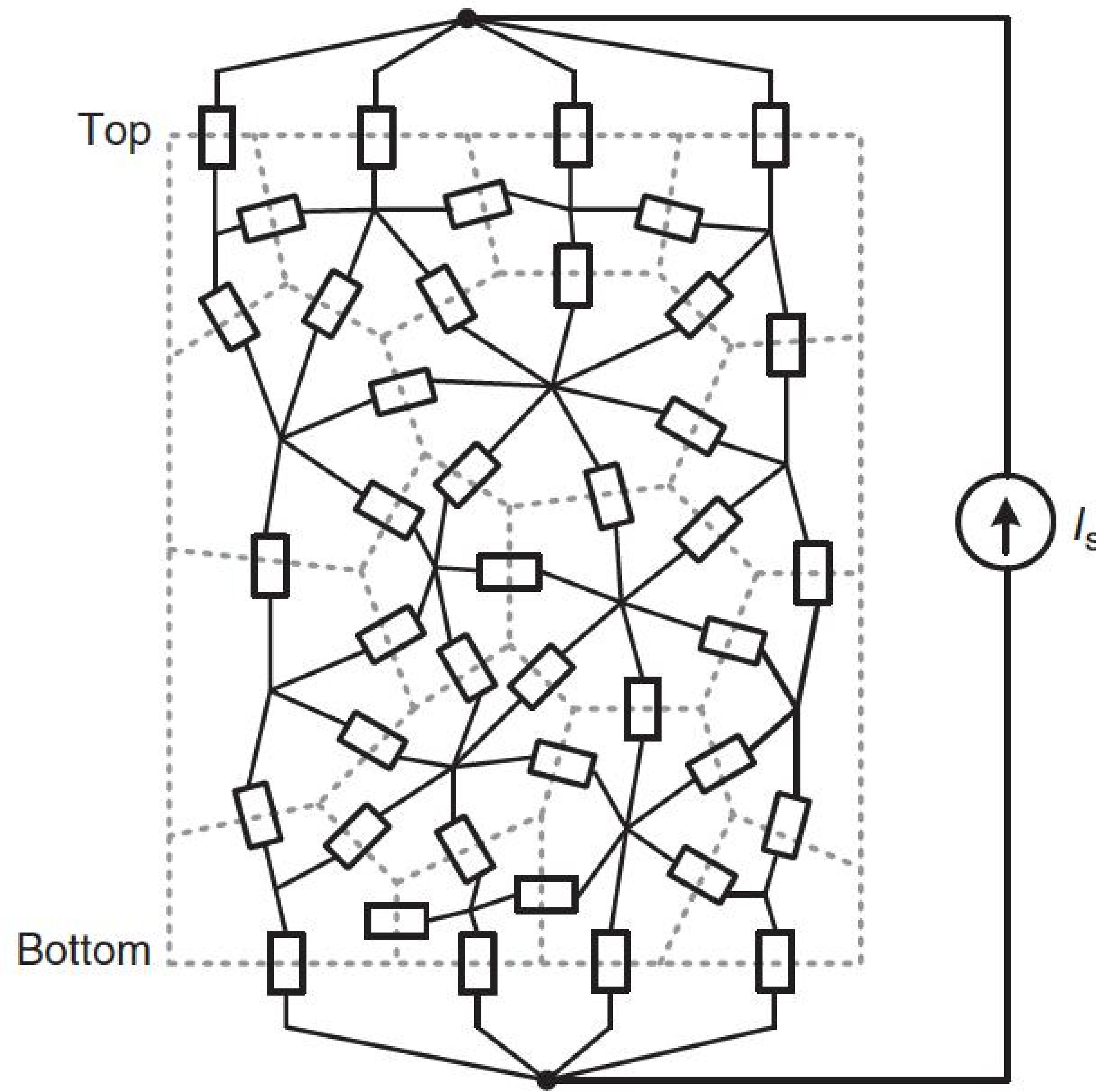


Figure 5.9 The simulation of the grains and their connections in the ZnO varistor.

The respective equivalent circuit of the two-dimensional Voronoi network is shown in Figure 5.9 to simulate the microstructure of a single film (thickness = h) of the polycrystalline ZnO varistor. Each polygon represents a ZnO grain, and each edge of the polygon shared by adjacent polygon corresponds to their grain boundary. When the thickness t varies, the corresponding microstructure represents the ZnO varistor polycrystal of different average grain size. Similarly, the varied disorder degree d can represent the polycrystalline ZnO varistor with different uniformity of grain sizes.

Then, the electrical relations among the grains can be deduced following the Voronoi network model. If there is a shared edge between the two polygons, a nonlinear resistor is used to simulate the electrical relation between them. The inner region of a polygon is considered as an ideal conductor.

As the simulations are one dimensional and two dimensional rather than three dimensional, it is likely that some of the functional dependencies measured will differ from those analyzed by one-dimensional and two-dimensional models. However, in common with other percolation problems, one can expect that the three-dimensional results will be related to those in two dimensions through an appropriate scaling. Thus, grain size variations and variations in boundary-to-boundary breakdown voltage will still cause decreases in both the dynamic conductance and the polycrystalline breakdown voltage, but the numerical values will be different [11].

5.3.3 Consideration on Pores and Spinels

Obviously, the pores and spinels produced during the sintering process of ZnO varistor have an influence on the electrical characteristics of the ZnO varistor. This can be considered by adjusting the parameter of Voronoi network's edge to simulate the pores and spinels. The edges inside the Voronoi network are selected stochastically according to the set ratios of the pores and spinels. The conductivity

of the edge is set as 0 to simulate a pore, which means that this edge is in the insulation state. For the simulation of spinel, the edge is set as the high-resistivity state [48, 49].

5.3.4 Algorithm to Solve Equivalent Circuit

Figure 5.9 can be transferred as a standard circuit as shown in Figure 5.10 [19]. If the grain boundaries are handled as a resistance decided by their I–V characteristics as shown in Section 5.2.1, R_{ij} is a resistance, so the analysis will be simple. The external voltage is applied between the top and the bottom edges of the Voronoi network, i.e. the potential of the top edge is U_s and that of the bottom edge is 0. The node voltage equations of the circuit can be deduced according to Kirchhoff's law. Therefore, we obtain

$$I_i(\boldsymbol{U}) = \sum_{\substack{j=1 \\ j \neq i}}^{N+2} l_{ij} m(\text{sign}(U_i - U_j) J_{ij}(U_i - U_j)) = 0 \tag{5.23}$$

where $\boldsymbol{U}$ is the vector $(U_1, U_2, \ldots, U_N)$ and l_{ij} is the length of the common edge between the polygon i and polygon j. If grain j is not a neighbor grain of grain i, then $l_{ij} = 0$. m is the thickness of the ZnO varistor.

The grain voltages $(U_1, U_2, \ldots, U_N)$ in Eq. (5.23) can be derived iteratively; hence, the current passing through every edge can be calculated. However, if the capacitance and the actual conduction mechanism of the grain boundaries of ZnO varistors are considered as discussed in Section 5.2.2, then R_{ij} will be a dynamic impedance, which consists of resistance and capacitance in parallel. This makes the simulation of the I–V characteristics require considerable computational resources [48, 49].

In this case, the dynamic resistivity in Eq. (5.15) and capacitance in Eq. (5.16) change with the applied voltage, and they are handled based on time discretization and the piecewise linear method. The current through the capacitance is $i = C\,\mathrm{d}u/\mathrm{d}t$, the admittance of the capacitance Y_C can be expressed as $Y_C = C/\mathrm{d}t$,

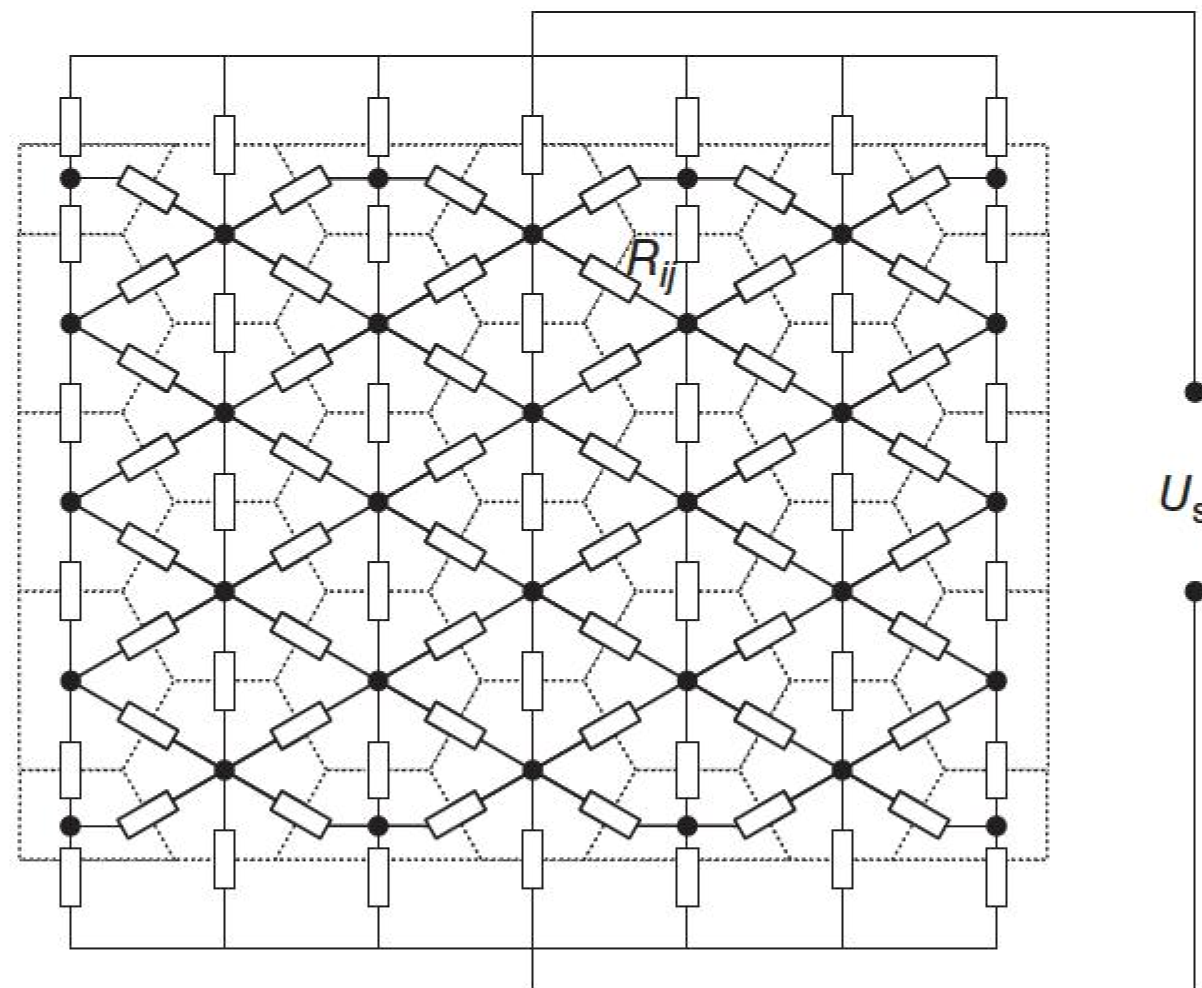


Figure 5.10 The bulk equivalent circuit of a ZnO varistor sample. Source: Long et al. 2010 [19]. Reproduced with permission of John Wiley & Sons.

whereas the time step dt should be small enough. Based on Kirchhoff's law, the electrical network of ZnO varistor can be solved in each time step, the voltage waveform is discretized by time step, and the dynamic resistivity and the capacitance in this time step are determined by the applied voltage in the last time step on the grain boundaries; the impedance is changed at each time step. According to this nonlinear impedance network of the ZnO varistor as shown in Figure 5.10, a group of nonlinear equations can be established by Kirchhoff's laws:

$$\begin{cases} \boldsymbol{AI} = 0 \\ \boldsymbol{U} = \boldsymbol{A}^{\mathrm{T}}\boldsymbol{U}_{\mathrm{N}} \\ U_{\mathrm{N}(n-1)} = U_{\mathrm{s}} \\ I_j = f(U_j)\ \ (j = 1, 2, \ldots, (b-1)) \end{cases} \tag{5.24}$$

where $\boldsymbol{I}$ and $\boldsymbol{U}$ are b dimension vectors of branch currents and voltages, whereas b is the number of circuit branches; $\boldsymbol{U}_{\mathrm{N}}$ is a $(n-1)$ dimension vector of node voltages, whereas n is the number of circuit nodes and its last element equals to external applied voltage U_{s}; $\boldsymbol{A}$ is a $(n-1)\times b$ dimension matrix describing the relation of all nodes and branches; and f are the functions of each branch current and voltage (excluding the branch of external applied voltage source). If the external applied source is a current source I_{s}, the third equation in Eq. (5.24) will be changed as $I_b = I_{\mathrm{s}}$.

In equation sets shown in Eq. (5.24), the first and second rows are the equations decided by Kirchhoff's laws, the third row is the constraint condition of voltage or current source, and the fourth row is the dynamic I–V characteristics of grain boundaries.

By solving the above group of nonlinear equations based on the nonlinear equivalent circuit, the bulk electrical characteristics of a ZnO varistor sample under a special applied surge current I_{s} can be simulated. Usually, the Newton iterative method was used to solve the DC response of ZnO varistors. However, the grain boundary model in Eq. (5.24) is much more complex than a simple empirical formula proposed by former researchers. In addition, this grain boundary model is time related because of the nonlinear capacitance C_{DB} of the double-Schottky barrier. As a result, it is impossible to solve the above nonlinear equivalent circuit of the ZnO varistor by the traditional Newton iterative method. Thus, a quick piecewise linear method is proposed, which is illustrated as Figure 5.11 [49].

The differences of currents and voltages between time steps t_k and t_{k+1} are defined as [49]

$$\begin{cases} \Delta\boldsymbol{I}^{(k+1)} = \boldsymbol{I}^{(k+1)} - \boldsymbol{I}^{(k)} \\ \Delta\boldsymbol{U}^{(k+1)} = \boldsymbol{U}^{(k+1)} - \boldsymbol{U}^{(k)} \\ \Delta\boldsymbol{U}_{\mathrm{N}}^{(k+1)} = \boldsymbol{U}_{\mathrm{N}}^{(k+1)} - \boldsymbol{U}_{\mathrm{N}}^{(k)} \\ \Delta I_{\mathrm{s}}^{(k+1)} = I_{\mathrm{s}}^{(k+1)} - I_{\mathrm{s}}^{(k)} \end{cases} \tag{5.25}$$

The functions $f(U^{(k+1)})$ can be expanded with Tailor series as below. As the differences of branch voltages between t_k and t_{k+1} are quite small, those higher

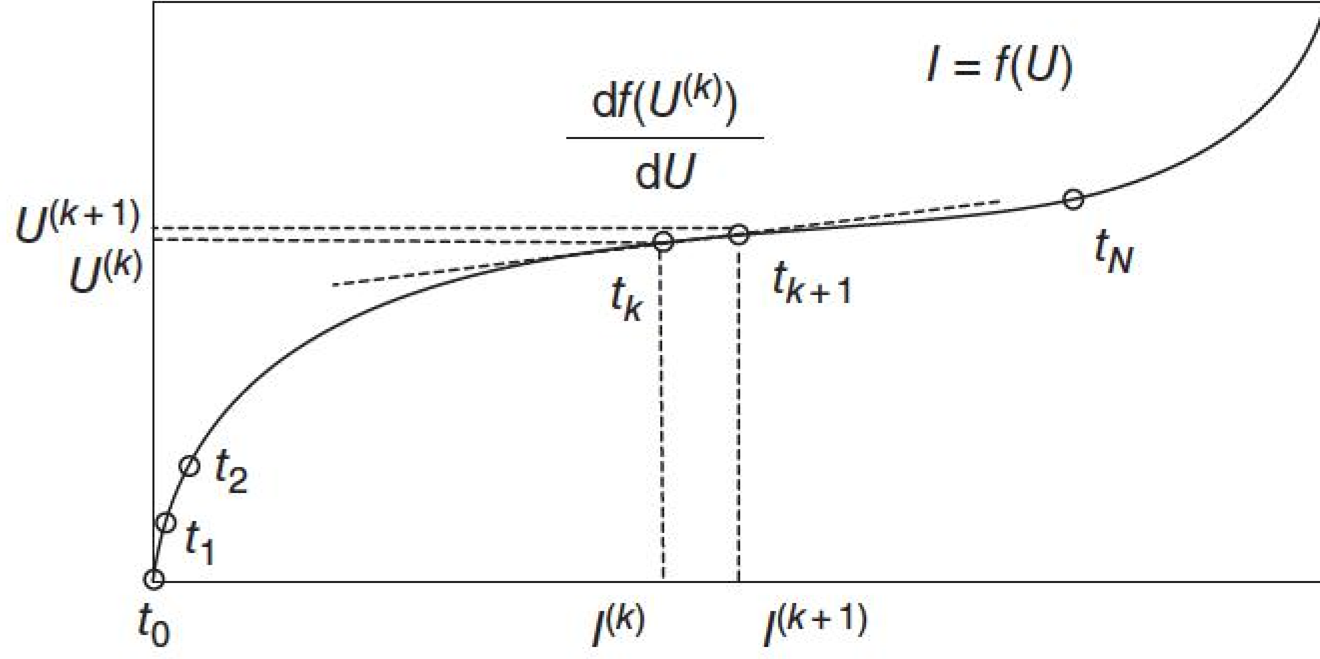


Figure 5.11 The quick piecewise linear method for solving the nonlinear equivalent circuit of the ZnO varistor [49].

power items of Tailor series are omitted [49]:

$$f(U^{(k+1)}) = f(U^{(k)} + \Delta U^{(k+1)}) \approx f(U^{(k)}) + \frac{\mathrm{d}f(U^{(k)})}{\mathrm{d}U} \cdot \Delta U^{(k+1)} \tag{5.26}$$

From Eqs. (5.24)–(5.26), a new group of linear equations can be deduced, in which the differences of currents and voltages between t_k and t_{k+1} are unknown variables. If the applied source is a voltage source, then

$$\begin{cases} A\Delta I^{(k+1)} = 0 \\ \Delta U^{(k+1)} = A^{\mathrm{T}} \Delta U_{\mathrm{N}}^{(k+1)} \\ \Delta U_{\mathrm{N}(n-1)}^{(k+1)} = \Delta U_{\mathrm{s}}^{(k+1)} \\ \Delta I_{(j)}^{(k+1)} = \dfrac{\mathrm{d}f(U_{(j)}^{(k)})}{\mathrm{d}U} \cdot \Delta U_{(j)}^{(k+1)} = \mathrm{d}Y_{(j)}^{(k+1)} \Delta U_{(j)}^{(k+1)}, \quad (j = 1, 2, \cdots, (b-1)) \end{cases} \tag{5.27}$$

If the source is a current source, then the third equation in Eq. (5.27) should be changed as $\Delta I_b^{(k+1)} = \Delta I_{\mathrm{s}}^{(k+1)}$. $\mathrm{d}f(U_{(j)}^{(k)})/\mathrm{d}U$ is the dynamic admittance of a grain boundary $\mathrm{d}Y_{(j)}^{(k+1)}$.

From Figure 5.5c, we can obtain the following equations [49]:

$$\begin{cases} U = R_{\mathrm{GB}} I_{\mathrm{GB}} + U_{\mathrm{DB}} \\ I_{\mathrm{GB}} = Y_{\mathrm{DB}} U_{\mathrm{DB}} + C\frac{\mathrm{d}U_{\mathrm{DB}}}{\mathrm{d}t} \\ I = I_{\mathrm{GB}} + Y_{\mathrm{AC}} U \end{cases} \tag{5.28}$$

When the applied voltage source changes to $k + 1$ step from k step [49]:

$$\begin{cases} \Delta U^{(k+1)} = R_{\mathrm{GB}} \Delta I_{\mathrm{GB}}^{(k+1)} + \Delta U_{\mathrm{DB}}^{(k+1)} \\ \Delta I_{\mathrm{GB}}^{(k+1)} = \mathrm{d}Y_{\mathrm{DB}}^{(k+1)} \Delta U_{\mathrm{DB}}^{(k+1)} + \left(C^{(k+1)} \dfrac{\Delta U_{\mathrm{DB}}^{(k+1)}}{\Delta t^{(k+1)}} - C^{(k)} \dfrac{\Delta U_{\mathrm{DB}}^{(k)}}{\Delta t^{(k)}} \right) \\ \Delta I^{(k+1)} = \Delta I_{\mathrm{GB}}^{(k+1)} + Y_{\mathrm{AC}} U^{(k+1)} \end{cases} \tag{5.29}$$

Here, we define [49]:

$$\begin{cases} I^{(k)} = C^{(k)} \dfrac{\Delta U_{\mathrm{DB}}^{(k)}}{\Delta t^{(k)}} \\ \mathrm{d}YC_{\mathrm{DB}}^{(k+1)} = \mathrm{d}Y_{\mathrm{DB}}^{(k+1)} + \dfrac{C^{(k+1)}}{\Delta t^{(k+1)}} \\ U_{\mathrm{C}}^{(k+1)} = \dfrac{I_{\mathrm{C}}^{(k+1)}}{\mathrm{d}YC_{\mathrm{DB}}^{(k+1)}} \\ \mathrm{d}Y_{\mathrm{BB}}^{(k+1)} = \dfrac{1}{R_{\mathrm{GB}} + \frac{1}{\mathrm{d}YC_{\mathrm{DB}}^{(k+1)}}} \\ \mathrm{d}Y_{\mathrm{ABC}}^{(k+1)} = \mathrm{d}Y_{\mathrm{BB}}^{(k+1)} + Y_{\mathrm{AC}} \\ U_{\mathrm{CC}}^{(k+1)} = \dfrac{\mathrm{d}Y_{\mathrm{BB}}^{(k+1)}}{\mathrm{d}Y_{\mathrm{ABC}}^{(k+1)}} U_{\mathrm{C}}^{(k+1)} \end{cases} \tag{5.30}$$

Submitting Eqs. (5.30) and (5.29) to eliminate variable $\Delta I_{\mathrm{GB}}^{(k+1)}$, then

$$\Delta U_{\mathrm{DB}}^{(k+1)} = \frac{\Delta U^{(k+1)} + R_{\mathrm{GB}} I_{\mathrm{C}}^{(k)}}{1 + R_{\mathrm{GB}} \mathrm{d}YC_{\mathrm{DB}}^{(k+1)}} \tag{5.31}$$

Eliminating $\Delta U_{\mathrm{DB}}^{(k+1)}$, then

$$\Delta I_{\mathrm{GB}}^{(k+1)} = \mathrm{d}Y_{\mathrm{BB}}^{(k+1)} (\Delta U^{(k+1)} - U_{\mathrm{C}}^{(k+1)}) \tag{5.32}$$

Submitting to the third equation of Eq. (5.29), then

$$\begin{aligned} \Delta I^{(k+1)} &= \mathrm{d}Y_{\mathrm{BB}}^{(k+1)} (\Delta U^{(k+1)} - U_{\mathrm{C}}^{(k+1)}) + Y_{\mathrm{AC}} \Delta U^{(k+1)} \\ &= \mathrm{d}Y_{\mathrm{ABC}}^{(k+1)} (\Delta U^{(k+1)} - U_{\mathrm{CC}}^{(k+1)}) \end{aligned} \tag{5.33}$$

If the source is an AC or an impulse voltage source, Eq. (5.27) should be changed as [49]

$$\begin{cases} AI^{(k+1)} = 0 \\ \Delta U^{(k+1)} = A^{\mathrm{T}} \Delta U_{\mathrm{N}}^{(k+1)} \\ \Delta U_{\mathrm{N}(n-1)}^{(k+1)} = \Delta U_{\mathrm{s}}^{(k+1)} \\ \Delta I_{(j)}^{(k+1)} = \mathrm{d}Y_{\mathrm{ABC}}^{(k+1)} (U^{(k+1)} - U_{\mathrm{CC}}^{(k+1)}) \quad (j = 1, 2, \ldots, (b-1)) \end{cases} \tag{5.34}$$

If the source is an AC or an impulse current source, then [49]

$$\begin{cases} A\Delta I^{(k+1)} = 0 \\ \Delta U^{(k+1)} = A^{\mathrm{T}} \Delta U_{\mathrm{N}}^{(k+1)} \\ \Delta I_{(b)}^{(k+1)} = \Delta I_{\mathrm{s}}^{(k+1)} \\ \Delta I_{(j)}^{(k+1)} = \mathrm{d}Y_{\mathrm{ABC}}^{(k+1)} (\Delta U^{(k+1)} - U_{\mathrm{CC}}^{(k+1)}) \quad (j = 1, 2, \ldots, (b-1)) \end{cases} \tag{5.35}$$

If we set the capacitance as 0, then Eqs. (5.27), (5.34), and (5.35) can be easily changed for the case of DC sources.

From the above linear equations, the response of the original nonlinear equivalent circuit of the ZnO varistor can be quickly solved. In each time point t_k, all branch currents $\boldsymbol{I}$, branch voltages $\boldsymbol{U}$, and node voltages $\boldsymbol{U}_\mathrm{N}$ under applied DC, AC, and impulse sources become available.

5.3.5 Model Verification

The DC characteristics of some actual ZnO varistor samples were simulated and compared with the experimental results [49]. The simulated and measured results are both shown in Figure 5.12, in which the simulated waveform agrees with the measured one very well.

The simulated and measured AC characteristics of ZnO varistor sample applied with different values of power source are shown in Figure 5.13 [19]. The model parameters were measured from the ZnO varistors under test. Both the simulated and the measured waveforms show similar shapes and variation when the applied voltage changes. When the applied voltage is low, the current passing through the ZnO varistor sample behaves as the standard sine wave but has a phase difference of 90° with the voltage wave, which proves that the current is mainly capacitive. When the applied source voltage increases to the breakdown voltage of ZnO varistor, a new peak appears in the current waveform, which is almost synchronous with the peak of voltage waveform. It means that the current peak is resistive. With the further increase in the applied source, the resistive current peak becomes larger than the capacitive current peak and then increases rapidly. Such phenomenon results from the nonlinear change of grain boundary resistance and capacitance under different applied voltages. When the applied voltage is low, the grain boundary resistance is much higher than the capacitance; thus, the current is mainly capacitive. When the applied voltage is higher than the breakdown voltage of grain boundaries, the resistance becomes quite small; thus, the current is mainly resistive.

The impulse characteristics of ZnO varistor samples were also measured, and the simulated results agree well with the measured ones, as shown in Figure 5.14.

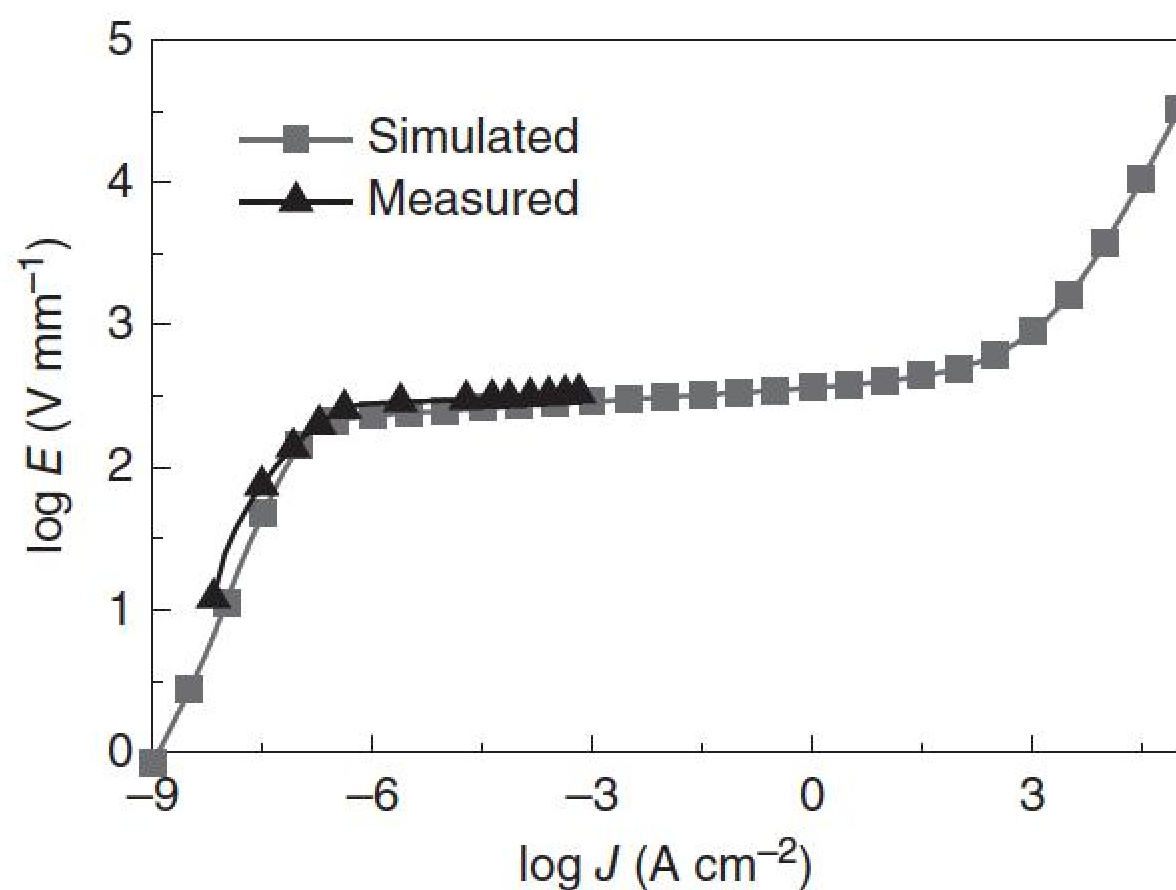


Figure 5.12 The simulated and measured DC characteristics of the ZnO varistor sample [49].

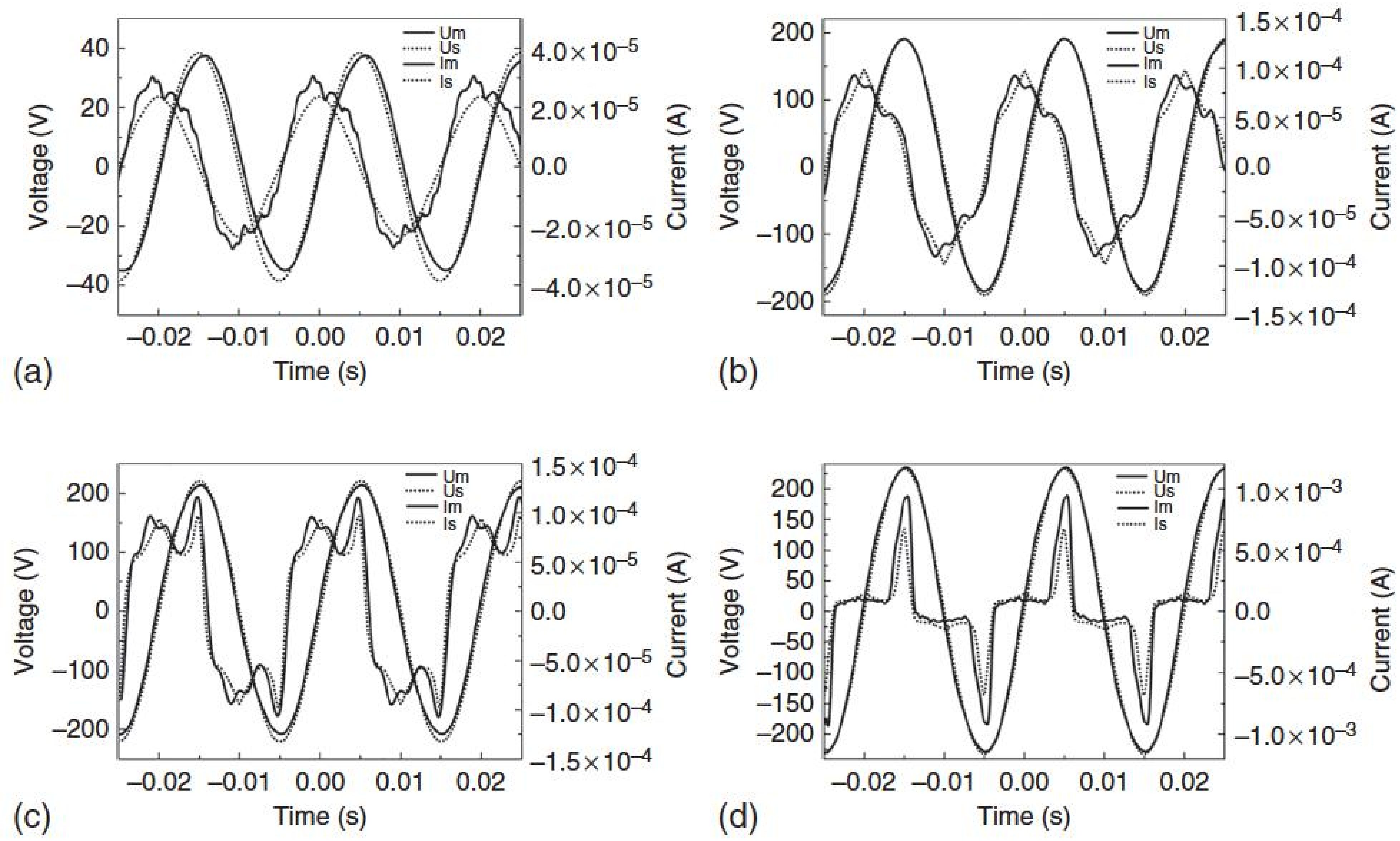


Figure 5.13 The comparison between the simulation results and the experimental results. The solid line is the experimental results; the dash line was the simulation results. The applied AC peak voltage: (a) 38.5 V; (b) 204 V; (c) 216 V; (d) 240 V. Source: Long et al. 2010 [19]. Reproduced with permission of John Wiley & Sons.

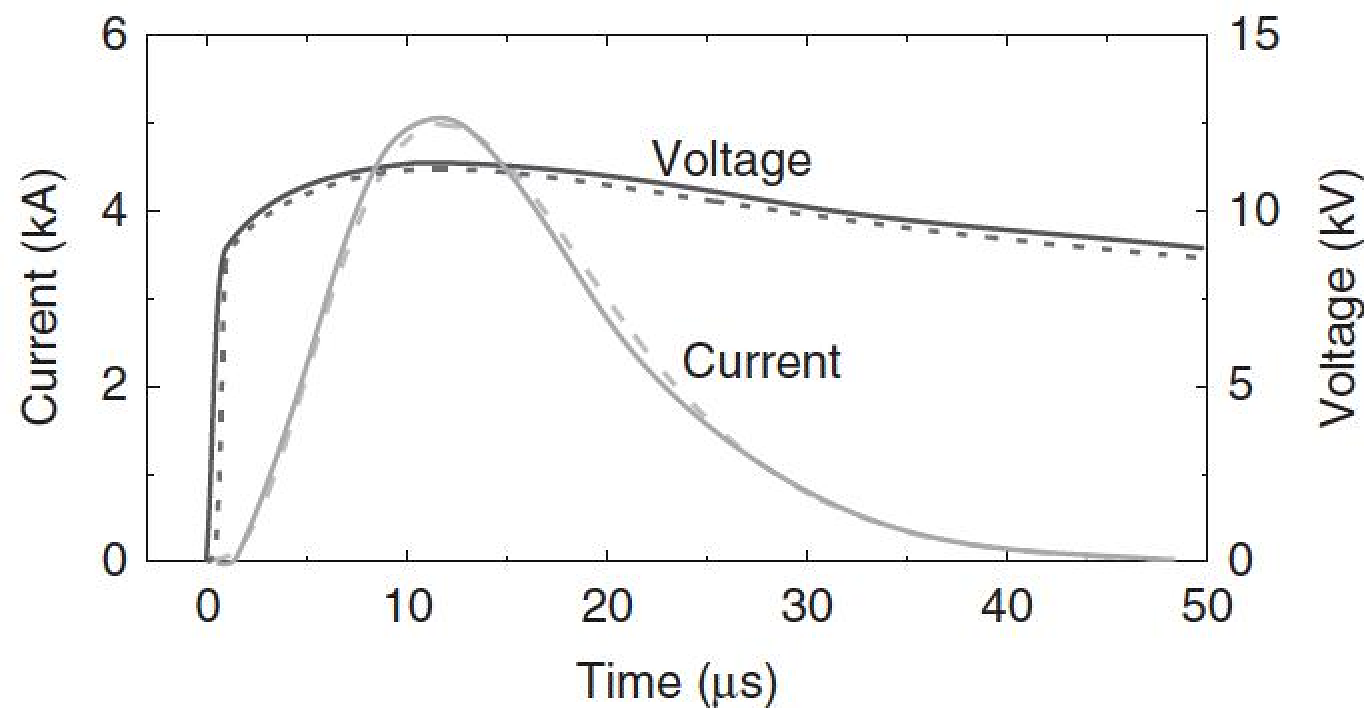


Figure 5.14 The measured and simulated impulse characteristics of ZnO varistor samples [49]. The solid lines are experimental results, and the dot lines are simulation results.

From the model verification, the numerical analysis has the ability to well simulate the DC, AC, and impulse characteristics of ZnO varistors, which makes it possible to simulate the complicated operation process of ZnO varistors to evaluate their long-term operation properties and predict their life spans.

5.4 Simulation Model for Thermal Characteristics

If the current distribution on the microstructure of ZnO varistors is obtained, then the simulations can be extended to include other dependencies, such as the temperature dependences of the leakage current and grain conductance, and for the computation of other electrical characteristics, such as capacitive currents.

It is also possible to incorporate the effects of Joule heating and so that the local current density, local temperature, and local thermal stress can be coupled [12]. With the ever-growing capabilities of computer work stations and parallel computation, the scope and sophistication of these electrical network-based simulations will undoubtedly bring even greater insights into the behavior of varistors and other electrical ceramics [1].

5.4.1 Thermal Conduction Analysis

The heat transfer inside the ZnO varistor is considered when it is injected with a surge current, typically a square wave current. The finite-difference method is used to calculate the temperature and thermal stress distributions inside ZnO varistors [18]. Eda analyzed the temperature distribution and thermally induced stress of a ZnO varistor when a current source is injected into it. The thermal transfer equation for a disk whose diameter is D in the radial direction r is expressed by [50]

$$k\frac{\partial^2 T}{\partial r^2} + \frac{k}{r}\frac{\partial T}{\partial r} + Q(r) = C_p\rho\frac{\partial T}{\partial t} \tag{5.36}$$

where T is the temperature, t is the time, and $Q(r)$ is the heat source, which is the overvoltage energy when an impulse voltage is applied to a varistor; k is the thermal conductivity; C_p is the specific heat constant; and ρ is the mass density of the ZnO varistor. The suggested values of thermal conductivity k, specific heat constant C_p, and specific gravity ρ of the ZnO varistor are 5.73 W m^{-1} °C^{-1}, 498 J kg^{-1} °C^{-1} (at 20 °C), and 5600 kg m^{-3}, respectively, and the linear thermal expansion coefficient a is selected as 4.86×10^{-6} °C^{-1} [51].

The heat conduction between the side surface Γ and the surroundings consists of natural convection and radiation thermal transfers. The heat conduction between the side surface of the ZnO varistor and the surroundings can be described as [51]

$$-k\left.\frac{\partial T}{\partial r}\right|_{\Gamma} = \xi(T_S - T_a)|_{\Gamma} \tag{5.37}$$

where T_a is the temperature of the surrounding, T_S is the side surface temperature of the varistor, and ξ is the surface thermal transfer coefficient:

$$\xi = \gamma + \eta \tag{5.38}$$

where γ is the surface natural convection thermal transfer coefficient. The radiation thermal transfer equation of the side surface is [52]

$$q = f\sigma S[(273 + T_s)^4 - (273 + T_a)^4] \tag{5.39}$$

$$q = \eta S(T_s - T_a) \tag{5.40}$$

The radiation thermal transfer coefficientη can be calculated by

$$\eta = f\sigma(546 + T_s + T_a)[(273 + T_s)^2 + (273 + T_a)^2] \tag{5.41}$$

where f is the emissivity between the side surface and the surroundings and σ is the Stefan–Boltzmann constant, $\sigma = 5.67 \times 10^{-8}$ W m^{-2} K^{-4}.

The surface natural convection thermal transfer coefficient γ can be calculated by

$$\gamma = N_u \frac{k}{h} \tag{5.42}$$

where h is the varistor height, and

$$N_u = c(G_r P_r)^n \tag{5.43}$$

$$G_r = \frac{g\beta(T_s - T_a)h^3}{\nu^2} \tag{5.44}$$

$$P_r = \frac{\nu}{\varsigma} \tag{5.45}$$

where g is the gravitational acceleration, ν is the motion viscosity, ς is the thermal diffusion coefficient, and β is the volume expansion coefficient. The medium of the surroundings is air. The following formula is used to calculate β:

$$\beta = \frac{1}{273 + T_s} \tag{5.46}$$

where c and n are constants related to the value of $G_r P_r$ [52]:

$c = 0.59$, $n = 1/4$, for $10^4 \leq G_r P_r \leq 10^5$;
$c = 0.10$, $n = 1/3$, for $10^9 \leq G_r P_r \leq 10^{13}$.

Therefore, the surface thermal transfer coefficient ξ is a function of varistor surface temperature T_s, which is not a fixed constant. Eq. (5.36) can be solved numerically by converting it to a set of difference equations [18].

For the network model shown in Figure 5.9, every polygon in Voronoi network is divided into several triangle elements, as the imaginary lines shown in Figure 5.15 [9], according to the number of the edges of each polygon. Every element is uniquely determined by a polygon edge and the center of the polygon. Therefore, for every element, there are three other triangle elements adjacent to it.

After the node voltages are solved by the iterative method introduced in Section 5.3.5, the current, which passes through the grain boundaries, can be calculated. It is supposed that the average temperature of the element i is T_i, and

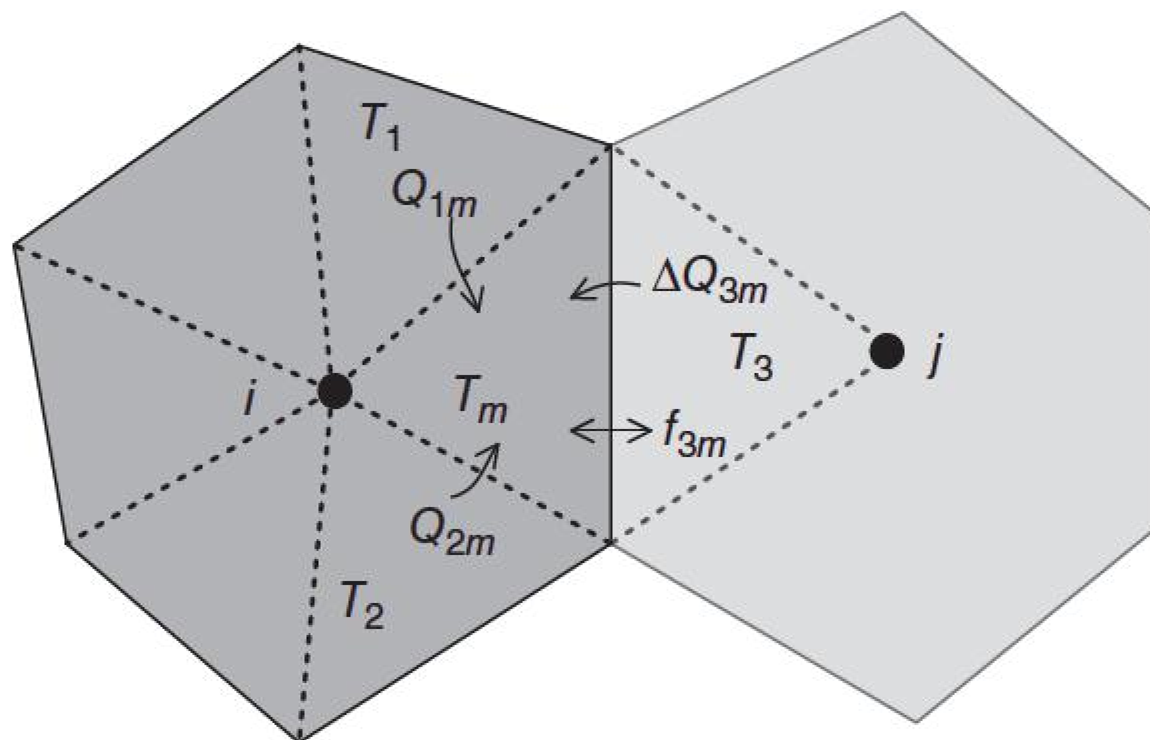


Figure 5.15 The basic structure of heat transfer model. Source: Modified from [9].

its original value is the room temperature. The heat (dQ_i) transferring into the element i during the time duration dt is determined by

$$dQ_i = \sum_k (T_k - T_i)\frac{l_{ik}h}{d_{ik}}k_T\, dt, \tag{5.47}$$

where T_k is the temperature of the adjacent element, l_{ik} is the length of the common edge of two adjacent elements, d_{ik} is the distance between the centers of the two adjacent elements, and k_T is the thermal conductivity of the ZnO varistor: $k_T = 5.7\,W\,m^{-1}{}^\circ C^{-1}$.

Out of three edges of the triangle, only one belongs to the polygon, i.e. a grain boundary. Therefore, there is Joule heat power consumption on this edge when a current passes through it, and the Joule heat P_i at the grain boundary l_{ik} can be calculated according to the current J_{ik} through this grain boundary [9]:

$$P_i = sl_{ik}U_{ik}J_{ik} \tag{5.48}$$

Then, the temperature rise (dT_i) of the element i can be calculated as [9]

$$dT_i = \frac{P_i\, dt + dQ_i}{S_i h \rho C_p} \tag{5.49}$$

where S_i is the area of the triangle element i, h is the thickness of the simulated ZnO varistor, ρ is the mass density of ZnO varistor, $\rho = 5.6\,g\,cm^{-3}$, and C_p is the thermal capacity of the ZnO varistor, $C_p = 0.498(1 + 0.000\,828(T_m - 20))$ $J\,g^{-1}\,{}^\circ C^{-1}$ [53].

Using this heat transfer model, the temperature T_i of the element i can be calculated following the finite-difference method. If the temperatures of two adjacent triangles are T_i and T_j, respectively, the thermal stress f_{ij} between them would be [54]

$$f_{ij} = \frac{Ya(T_i - T_j)}{1 - \mu} \tag{5.50}$$

where Y is Young's module of elasticity, a is the linear expansion coefficient, and μ is the Poisson ratio. The selected parameters are $a = 4.86 \times 10^{-6}\,{}^\circ C^{-1}$, $\mu = 0.30$, and $Y = 6.9 \times 10^4$ MPa [55].

5.4.2 Pulse-Induced Fracture Analysis

The pulse-induced fracture, which may occur during standardized screening testing of varistors with high-current pulses of very short duration (of some milliseconds), was simulated by Lengauer et al. [56]. This loading situation has been discussed in detail by Vojta and Clarke [57]. Using an analytical one-dimensional model, they analyzed stress waves generated by inertial forces that appear on rapid Joule heating. These stresses strongly depend on the duration of the pulse. In a 1D model, the only design parameter is the length of the varistor. It was concluded that the stress amplitude increases by increasing the length. The analysis can be extended to a full three-dimensional simulation using the finite-element method (FEM). This makes it possible to consider the reflections of stress waves not only from the bases of the cylinder but also from its shell.

5.5 Simulations on Different Phenomena

The simulation analysis on the actual microstructure and electrical characteristics of ZnO varistors can effectively analyze the influences of different factors, such as grain size, barrier voltage, and nonlinear coefficient of single grain boundary, on the global electrical characteristics. This is very helpful to design a ZnO varistor with better I–V characteristics and explain those phenomena in actual application.

5.5.1 Simulation on Microstructural Nonuniformity

The overall properties of the varistor are the collective response of all the grain boundaries and depend not only on the boundaries themselves but also on the properties of the grains and their topological arrangement in three dimensions [58]. The influence of the geometry and topology of the granular microstructure, as well as the properties and the distribution of different types of microjunctions on the features of varistor bulks, is an important and interesting problem.

The nonuniformity of the microstructure of ZnO varistors is measured by the average grain sizes and respective standard deviations. An adequate description of the behavior of varistors cannot be achieved by simply averaging the characteristics of individual grain boundaries. On the contrary, the breakdown voltage of a bulk varistor, for example, is determined by the tail of the grain size distribution [14, 20, 28].

The disorder degree is widely used to evaluate the uniformity in the microstructure. As analyzed in [46], there is a trend that the peaked number becomes lower, and the distribution range becomes wider with the increase of disorder degree, seen in Figure 5.16. When the disorder degree is larger than 3, the distributions under different disorder degrees become irregular, but vary in a range. A chaotic phenomenon exists in the grain size distribution when the disorder degree is larger than 3 according to the description to chaos by Gleick [59] and Lorenz [60].

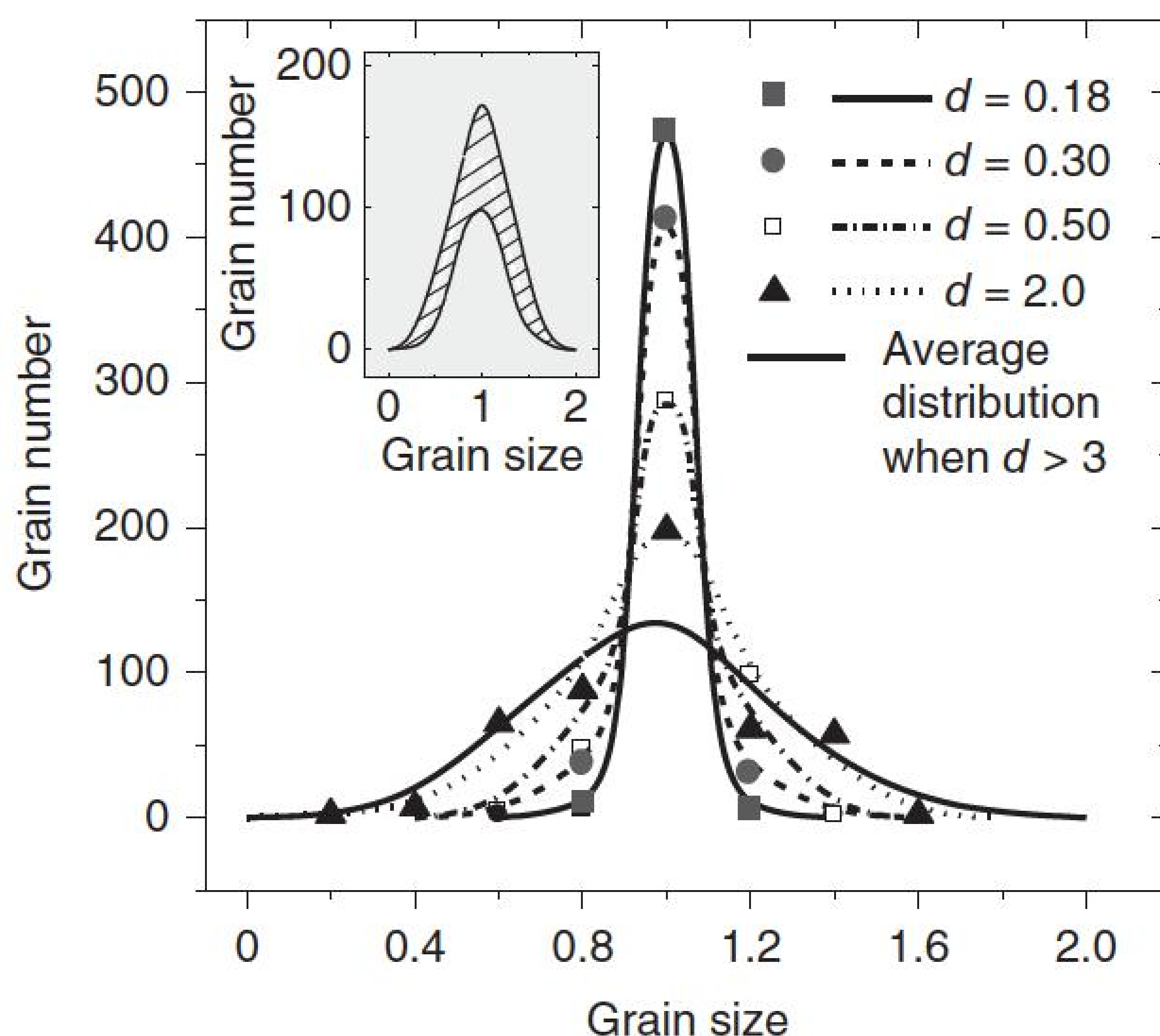


Figure 5.16 The grain size distribution of ZnO varistors simulated by Voronoi network with different disorder degrees. Source: Adapted from Han et al. [46].

The nonuniformity of electrical characteristics of ZnO varistors exits in the same varistor or different varistors. The influences of the nonuniformity of microstructure and grain boundary in the same varistor on the global electrical characteristics can be simulated by changing the disorder degree and setting different kinds of barriers [61]. If all grain boundaries are the same inside a ZnO varistor, then when a voltage is applied on the ZnO varistor, the current always look for the path with a minimum number of grain boundaries to pass through the ZnO varistor; the path with a minimum number of grain boundaries will determine the breakdown voltage and the global $I-V$ characteristics of the ZnO varistor. The minimum number of grain boundaries among all the paths between the two electrodes under different disorder degrees is shown in Figure 5.17 [46], which remains the same when the disorder degree is less than 0.18, and then decreases with the increase of the disorder degree in the region $0.18 < d < 3.0$ but becomes irregular when the disorder degree $d > 3.0$. The minimum grain boundary number has a chaotic state, which changes irregularly in the range between 14 and 18 in the case shown in Figure 5.17. The chaotic state of the minimum grain boundary number among all paths between the two electrodes leads to the nonuniformity of breakdown voltages among different ZnO varistors. The chaotic phenomenon states the nonuniformity of microstructures of ZnO varistors is an original property, which leads to the intrinsic property of nonuniformity of electrical characteristics of ZnO varistors.

5.5.2 Simulation on Current Localization Phenomenon

An early attempt to quantify the statistics of the conducting paths through the microstructure was made by Emtage [58]. Although Emtage's statistical model included several assumptions necessary to make the analysis tractable, it did predict that the switch voltage would be lower than that of the individual grain boundaries as has been indeed found experimentally [1]. A number of these simulations were done to quantify the effects of disorder on the J–E characteristics as well as on current localization as a function of applied electric field [5, 11–15]. These and other simulations reveal that the disorder in the form of distributions in the grain size, grain boundary area, or barrier height

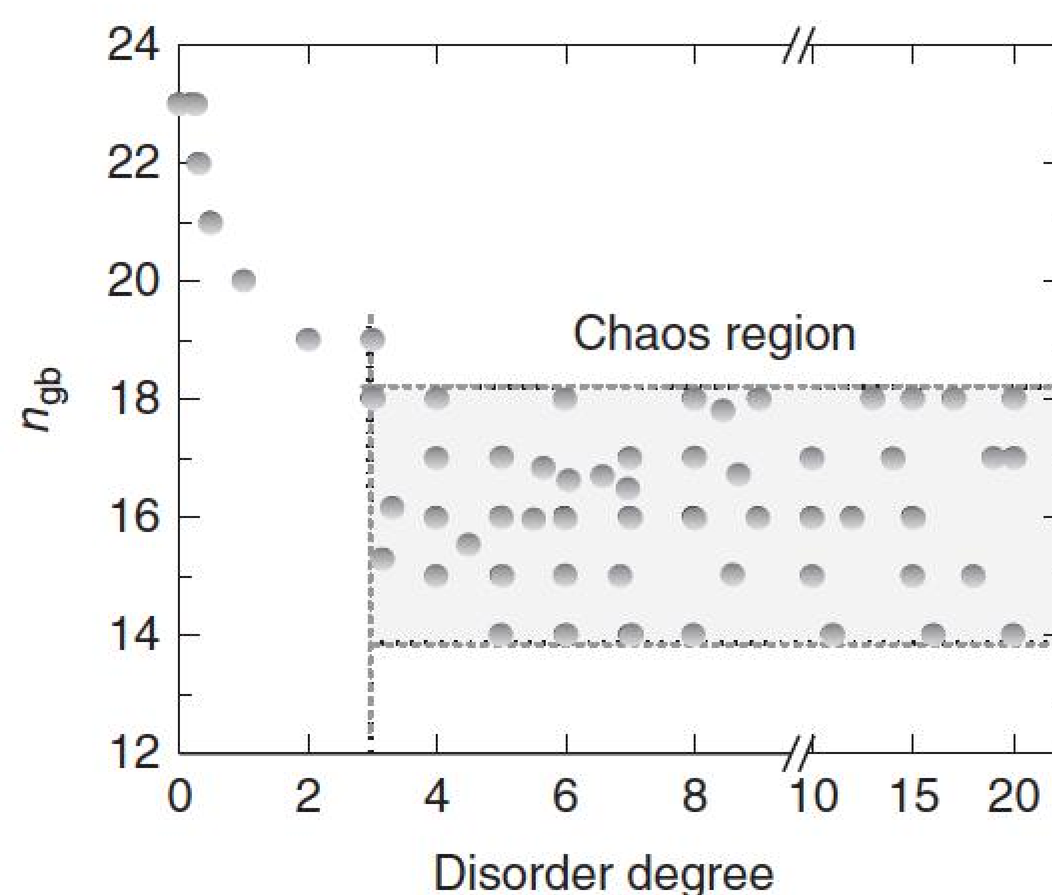


Figure 5.17 The minimum grain boundary number n_{gb} between the two electrodes of ZnO varistors simulated by Voronoi network. Source: Adapted from Han et al. [46].

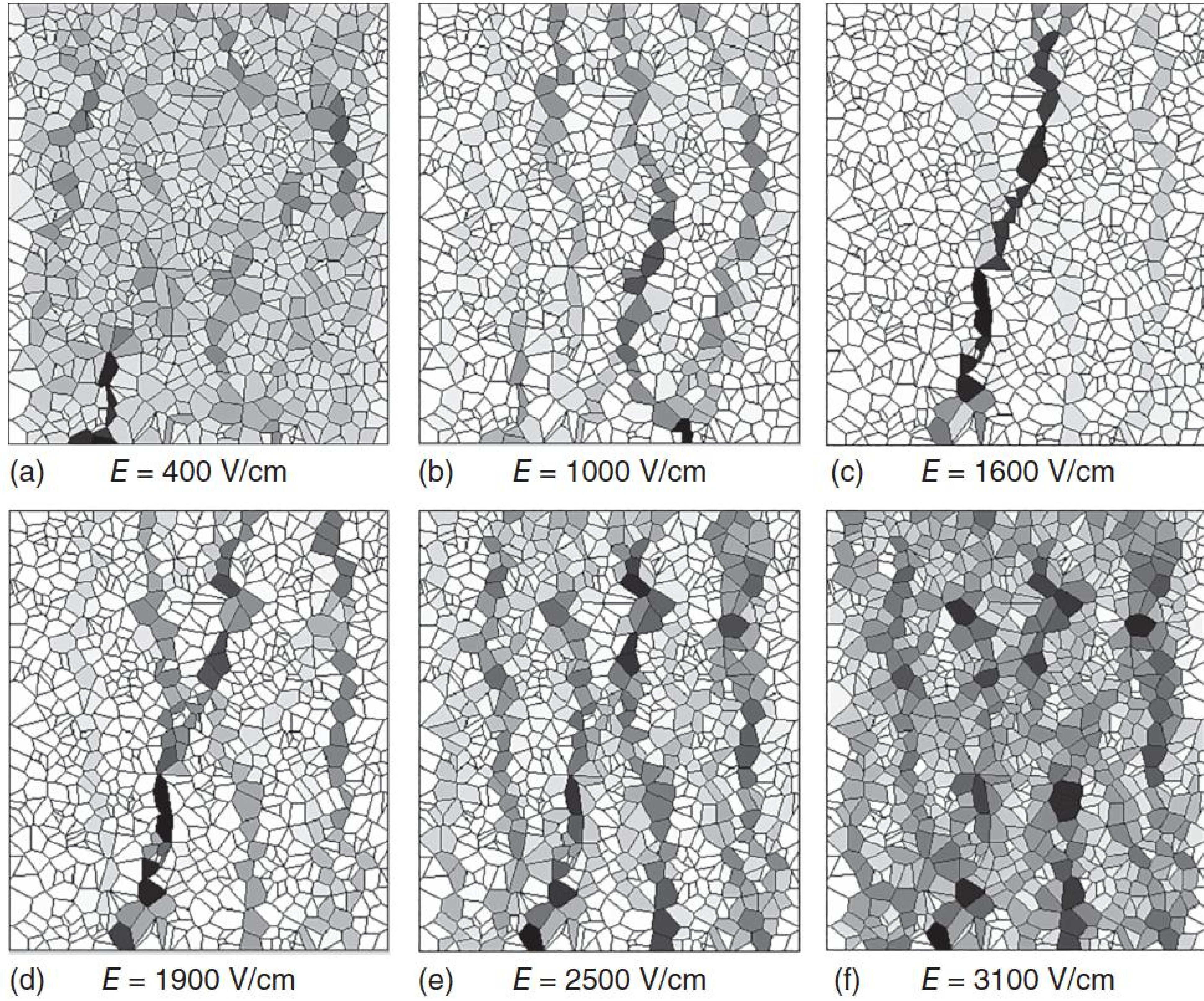


Figure 5.18 Simulated current distributions of ZnO varistors. Both the barrier voltage and the nonlinear coefficient of grain boundaries satisfy the normal distribution: $E(V_B) = 3.2$ and $\delta(V_B) = 0.2$, $E(\alpha) = 7$, and $\delta(\alpha) = 50$. (a) $E = 400\ \mathrm{V\,cm^{-1}}$, (b) $E = 1000\ \mathrm{V\,cm^{-1}}$, (c) $E = 1600\ \mathrm{V\,cm^{-1}}$, (d) $E = 1900\ \mathrm{V\,cm^{-1}}$, (e) $E = 2500\ \mathrm{V\,cm^{-1}}$, (f) $E = 3100\ \mathrm{V\,cm^{-1}}$.

decreases the attainable nonlinearity, causes a rounding of the J–E characteristic in the vicinity of the switch turn-on, and decrease the switch voltage itself [1].

As an example, the current distribution in the ZnO varistor, as shown in Figure 5.18, is simulated on a two-dimensional Voronoi network model consisting of about $900(30 \times 30)$ polygons; within each polygon cell (grain), the relative value of the current flowing through it is plotted, normalized by the maximum among them, and the gray-level spectrum from white to black to represents the values. If there is no (or nearly no) current through the cells, they are shown as white, whereas the maximum current is shown as black.

As the ZnO varistor is composed by a lot of little voltage-sensitive nonlinear resistor elements, the current distribution is closely related to the applied voltage gradient; this can be concluded from Figure 5.18 that, with the increase in voltage gradient, the current distribution becomes concentrated at first, and then uniform again. The most serious condition occurs in the breakdown region, as shown in Figure 5.18c, there is a path with black color, which carries most of the current passing through the whole varistor bulk. In Figure 5.18c, the voltage gradient E is $2.1\ \mathrm{kV\,cm^{-1}}$, and the current passing through the path with black color reaches 91.2% of the total current. As discussed in Section 5.2.1, the I–V characteristics of single grain boundaries in a varistor change with the applied

voltages; this means that the individual boundaries adjust their conductances in response to the applied voltages, which leads to the changes in the current distribution in all grain boundaries in response to the change in the applied voltage. This is particularly pronounced in the nonlinear regime [1].

Observing the current distributions in Figure 5.18, the current localization paths are typically only one or two grains wide, and the current localization can begin at one electrode and then propagate through to the other electrode. In addition, several localization paths can coexist concurrently within the microstructure. Finally, one of the interesting insights gained from the simulations is that a certain disorder degree may be beneficial [1].

The distribution of current density is also related to the uniformities of grain size and electrical characteristics of grain boundaries in the ZnO varistor. Because the more inhomogeneous these parameters are, the more likely there exist paths by which the current will pass through more easily in the ZnO varistor ceramics. In the following, the parameter of inhomogeneous degree of current J_{max}/J_{av}, which is defined as the ratio of the maximum current among all of the paths to the average current flowing through the model, is used to express the degree of current concentration. Figure 5.19 shows the relationship between the J_{max}/J_{av} and the applied voltage gradient E on the ZnO varistor bulk. Both the barrier voltage and the nonlinear coefficient of grain boundaries satisfy the normal distribution.

There are two peaks on the curves with respect to small disorder d. The first peak appearing in the prebreakdown region is mainly caused by the nonuniformity of the electrical characteristics of single grain junctions, whereas the other peak appearing in the breakdown region is mainly induced by the nonuniformity of the grain size. The current concentration phenomenon in the prebreakdown region will not reduce the energy absorption capability of the ZnO varistors because the current density is very small in this region. When $d > 3$, there is only one peak appearing in the breakdown region. In the breakdown region, the peak values of the ratios in four curves in Figure 5.19 are 9, 18, 22, and 25 when the disorder d is 0, 1, 3, and 5, respectively, which are much higher than 2 measured

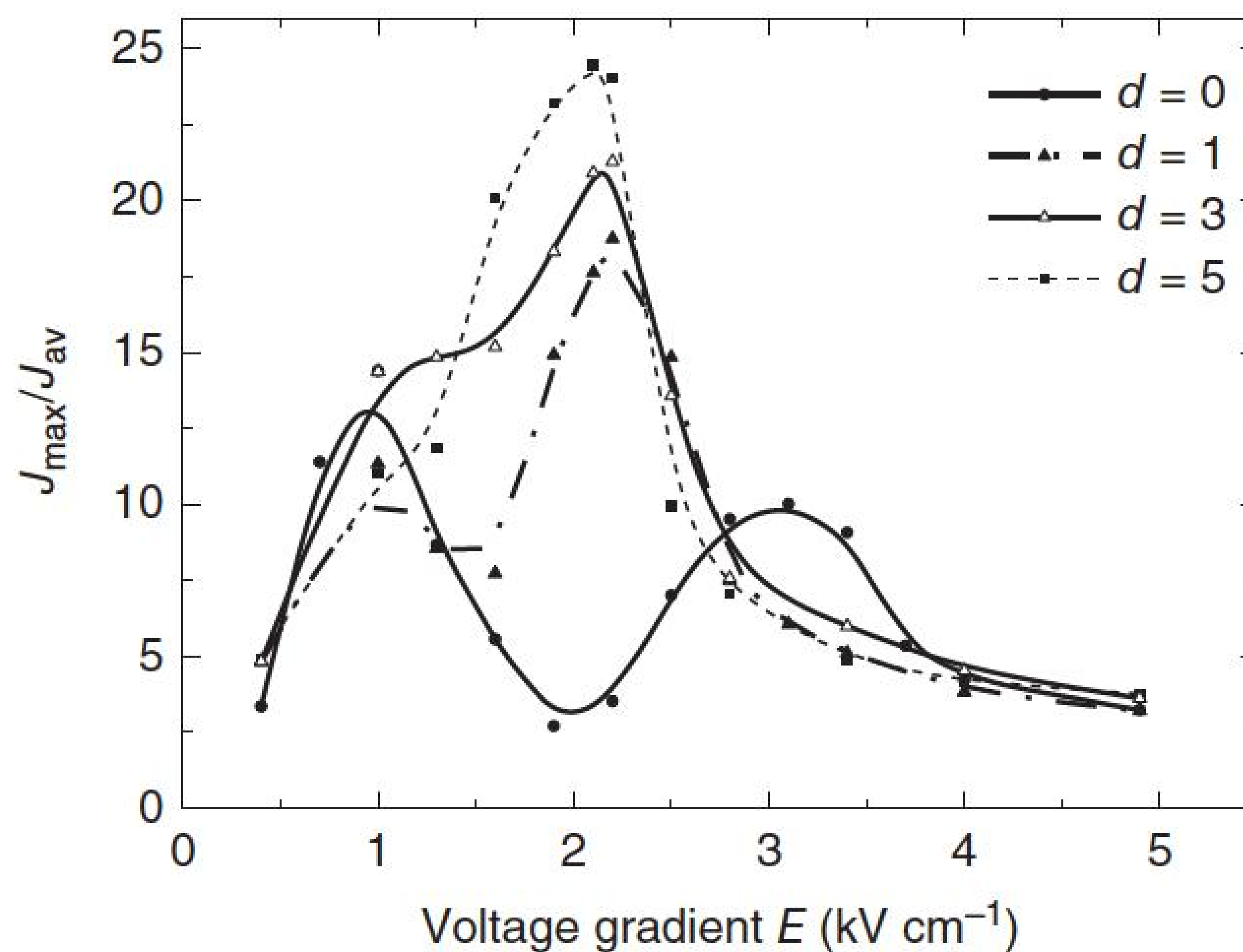


Figure 5.19 The relationship between the ratio of J_{max}/J_{av} and the applied voltage gradient E on the Voronoi networks with different disorder parameters.

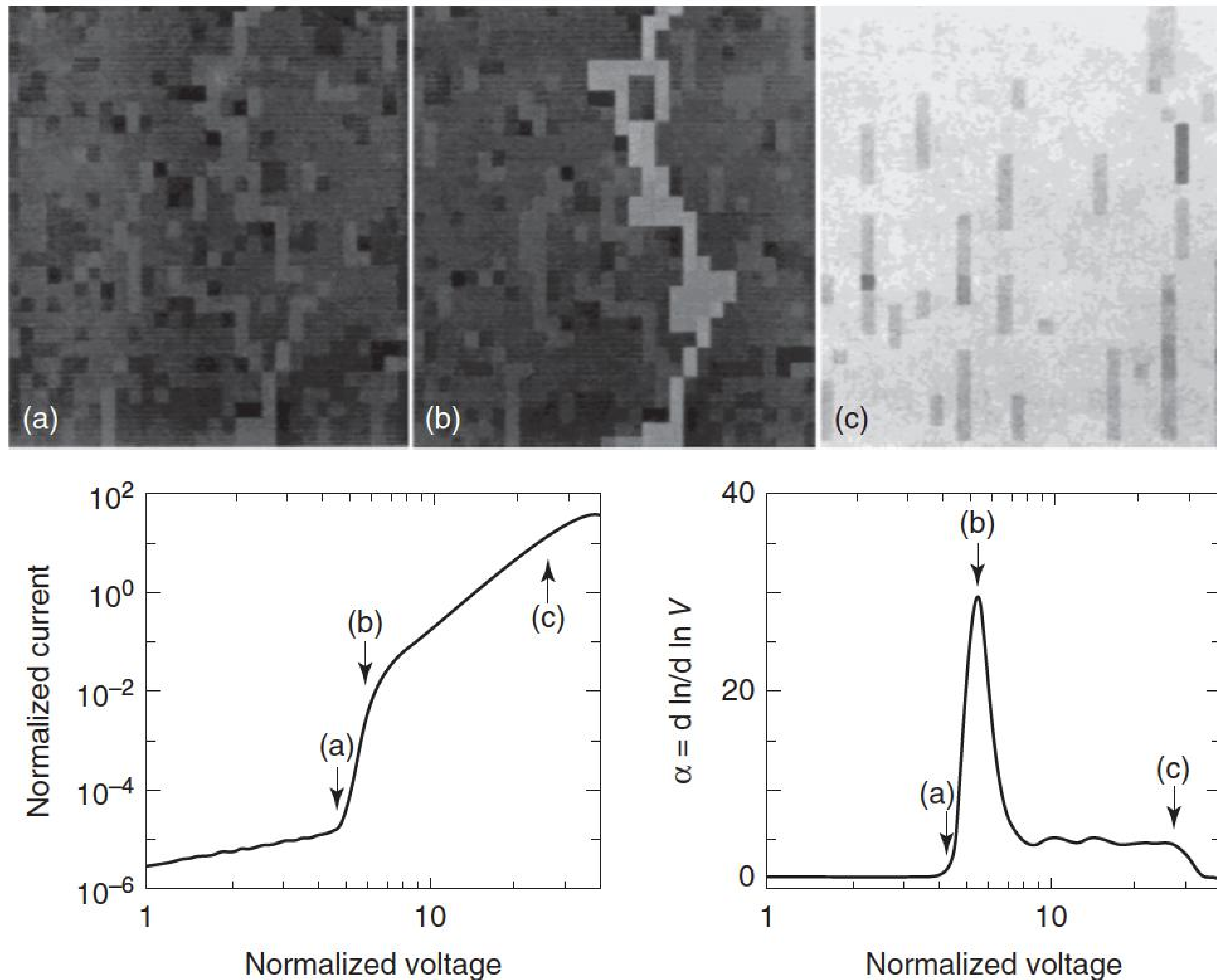


Figure 5.20 Current localization revealed in simulations at the three voltages indicated on the *I–V* characteristic curves. The gray scale is logarithmic, spanning nine orders of magnitude in current, white means high and black means low. Source: Clarke 1999 [1]. Reproduced with permission of John Wiley & Sons.

by Mizukoshi et al. [62]. Figure 5.19 shows that the worse the uniformity of grain size is, the more serious the current localization phenomenon is.

Another case shows the spatial variation in current density through a microstructure at three different values of the applied voltage, as illustrated in Figure 5.20 [1]; the overall I–V curve computed for the network and the variation in nonlinearity with an applied voltage were also shown. The three images of the current density are respective to low (just below the switch voltage), medium (corresponding to the largest nonlinearity), and high voltage (in the high-field ohmic region). Although some localization occurs within the ohmic region below the switch voltage, the localization is the severest within the nonlinear region. In the particular case shown in Figure 5.20, it reaches the maximum at the same voltage as the peak nonlinearity occurs. The current distributions in the three images in Figure 5.20, provide very similar results shown in Figure 5.18a, c, and f. Although these kinds of simple comparisons of images of the spatial distribution of currents are instructive, they are ill suited for detailed, quantitative comparison with other computed current distributions [1].

The microstructurally inhomogeneous current distribution of ZnO varistors has been certified by a wide variety of circumstantial experimental evidences. The evidence ranges from maps revealing spatial variations of the surface potential to localized hot spots on the electrode surface, and the most direct evidence

for current localization comes from thermal imaging of the surface of a varistor under electrical load. The paths of large current are visualized by the local increment in temperature caused by Joule heating [1].

Three barrier types have been confirmed by the measurements on individual grain boundaries in Chapter 4. By varying the concentrations of good, bad, and ohmic barriers, simulated $I-V$ characteristics are made to reproduce the variations in the breakdown field, nonlinearity, and shapes of switching characteristics that are found in real varistors. From these results, it is inferred that the concentrations rather than the electrical characteristics of individual barriers are changed by variations in composition and ceramic processing. The change in the current flow from one barrier type to another significantly influences the global electrical characteristic. The reduction of the nonlinear coefficient of bulk varistors, relative to that of isolated grain boundaries, can be explained only by the presence of bad barriers. Moreover, the reduction is significant only if the concentration of bad microjunctions is high. The typical rounded switching characteristic of multiphase varistors is a consequence of the presence of different kinds of grain boundary barriers. Varistors exhibiting sharp switching characteristics contain fewer phases in their microstructure and have almost all good barriers.

The statistical dispersion of the grain sizes has a little effect on the $I-V$ characteristic. This surprising result deserves a particular emphasis. It is the homogeneity of the barriers, rather than the uniformity of the grain sizes and shapes, that is important for superior varistor properties.

At this stage in the development of the varistor theory, no simple rules can be stated, but, nevertheless, the general concept may be useful in the design of varistors with improved energy absorption capability [1]. This will be further discussed in Chapter 7.

5.5.3 Influence of Microstructural Parameters on Bulk Characteristics

The influence of different microstructural parameters on the macroscopic characteristics of varistor bulks has been analyzed by Long [49], and the parameters of ZnO varistor bulks include the voltage gradient E, nonlinear coefficient α, leakage current J_L, and residual voltage ratio. The leakage current J_L is defined as the current density under $0.75E_{1\,mA}$. The residual voltage ratio, which is the ratio between the residual voltage gradient under a high current $E_{n\,kA}$ and 1 mA reference voltage gradient $E_{1\,mA}$, is related to the varistor size and the rated voltage of the power system, so the residual voltage ratio under different current densities is calculated: $K_{20\,kA}$ is the residual voltage ratio respective to the residual voltage under 20 kA standard impulse current, for ZnO varistors with a diameter of 10 cm and four columns in parallel used in 1000 kV AC UHV surge arrester; $K_{10\,kA}$ is respective to the residual voltage under 10 kA standard impulse current, for ZnO varistors with a diameter of 6 cm used in 110 kV AC surge arrester; and $K_{5\,kA}$ is respective to the residual voltage under 5 kA standard impulse current, for ZnO varistors with a diameter of 3.2 cm used in 10 kV AC distribution system.

5.5.3.1 Influence of ZnO Grain Parameters

The influence of ZnO grain resistivity ρ on the electrical characteristics of ZnO varistor is shown in Table 5.1. Figure 5.21 shows the respective I–V characteristics of the ZnO varistor. The resistivity of grains has a weak influence on the voltage gradient, leakage current, and nonlinear coefficient but has serious influence on the residual voltage ratio. As the grain resistivity increases, the residual voltage ratio obviously decreases. Observing Figure 5.21, the grain resistivity only affects the property in the high-current region, which seriously decreases the residual voltage under high current. Therefore, in order to decrease the residual voltage ratio, the grain resistivity should be decreased.

As the donor density of the ZnO grain N_d increases, the voltage gradient and the nonlinear coefficient decrease, and the leakage current increases (shown in Table 5.2 and Figure 5.22), which means the electrical characteristics of ZnO varistors become bad. The influence of the donor density of the ZnO grain on the residual voltage ratio is by means of increasing the 1 mA reference voltage. Therefore, the increase in the donor density of the ZnO grains should be controlled to decrease the residual voltage ratio.

As shown in Table 5.3 and Figure 5.23, when the grain size D increases, the voltage gradient obviously decreases, but the residual voltage ratio gradually increases. The grain size has a very weak influence on the nonlinear coefficient and leakage current of the ZnO varistors.

Table 5.1 Influence of grain resistivity on the electrical characteristics of the ZnO varistor.

ρ (Ω m)	$E_{1\,mA}$ (V mm^{-1})	α	J_L (μA cm^{-2})	$K_{20\,kA}$	$K_{10\,kA}$	$K_{5\,kA}$
10^{-2}	239.93	32.06	0.33	1.46	1.60	1.68
10^{-1}	236.84	32.15	0.33	1.55	1.80	1.99
10^{0}	238.53	32.14	0.33	1.85	2.50	3.11
10^{1}	237.96	31.88	0.33	2.99	6.27	10.56
10^{2}	239.32	30.12	0.35	10.66	40.43	81.91

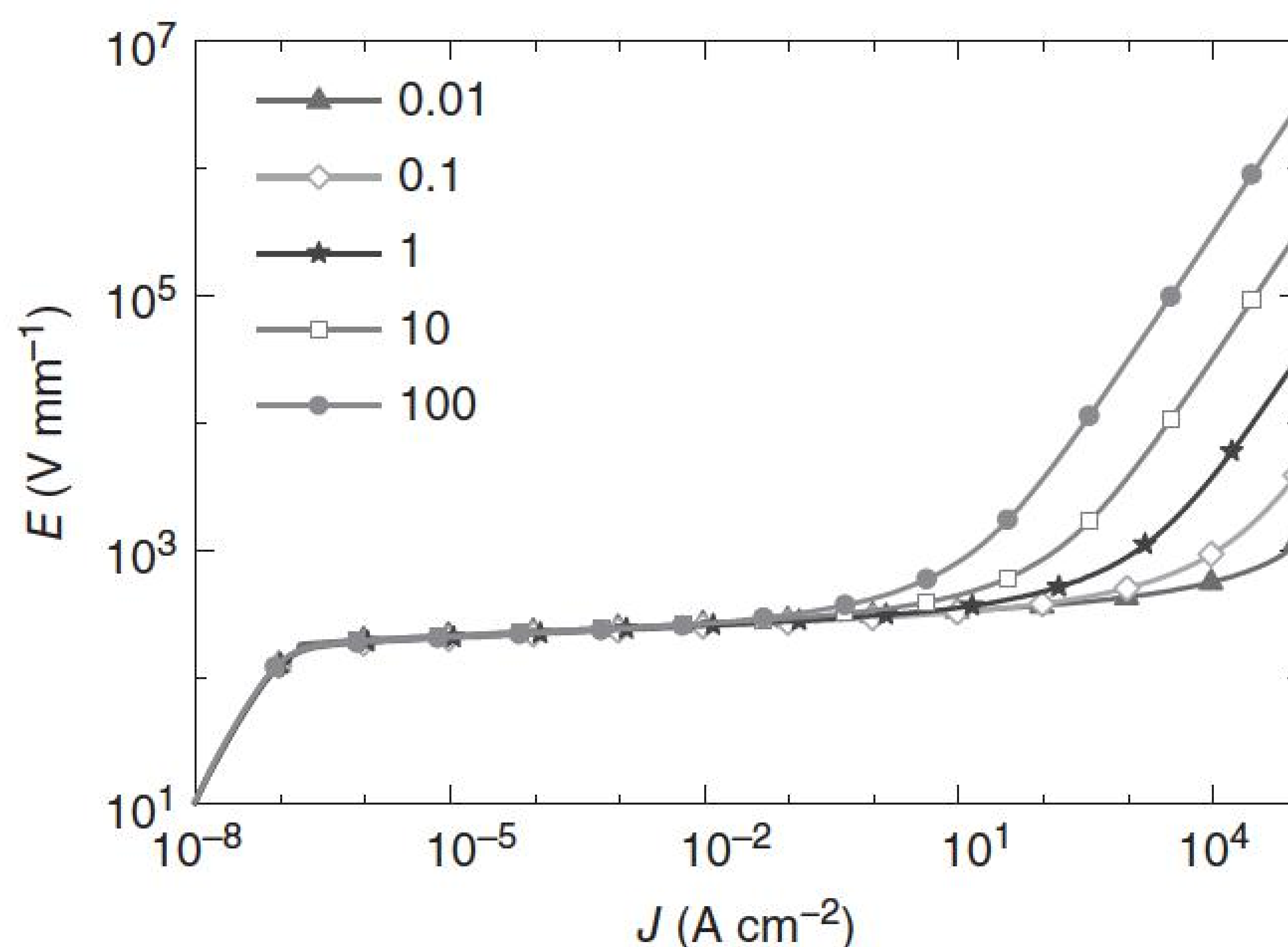


Figure 5.21 Influence of grain resistivity in Ω m on the I–V characteristics of the ZnO varistor.

Table 5.2 The influence of the donor density of the ZnO grain on the electrical parameters of ZnO varistors.

N_d (10^{23} m^{-3})	$E_{1\,mA}$ (V mm^{-1})	α	J_L (μA cm^{-2})	$K_{20\,kA}$	$K_{10\,kA}$	$K_{5\,kA}$
1.0	617.09	59.45	0.35	1.50	1.86	2.18
1.5	364.07	42.12	0.26	1.66	2.14	2.58
2.0	238.53	32.14	0.33	1.85	2.50	3.11
2.5	169.43	24.95	1.16	2.03	2.85	3.64
3.0	120.32	19.66	4.59	2.30	3.36	4.42

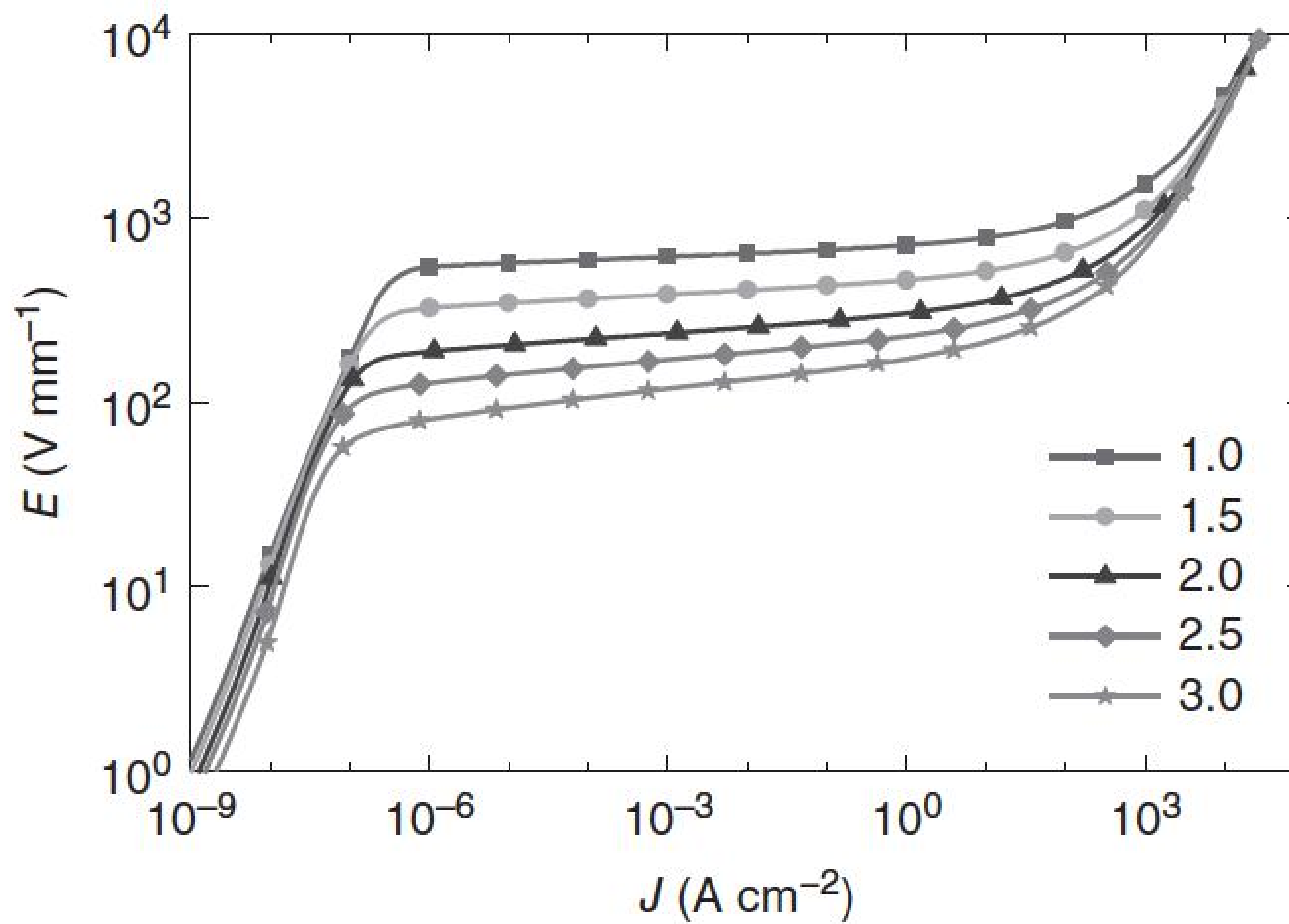


Figure 5.22 The influence of the donor density in 10^{23} m^{-3} of the ZnO grain on the *I–V* characteristics of ZnO varistors.

Table 5.3 Influence of the grain size on the electrical characteristics of ZnO varistors.

D (μm)	$E_{1\,mA}$ (V mm^{-1})	α	J_L (μA cm^{-2})	$K_{20\,kA}$	$K_{10\,kA}$	$K_{5\,kA}$
4	604.46	31.78	0.37	1.67	2.08	2.42
7	338.29	32.10	0.33	1.79	2.33	2.81
10	238.53	32.14	0.33	1.85	2.50	3.11
13	181.75	32.13	0.32	1.93	2.69	3.43
16	149.96	32.11	0.34	1.94	2.77	3.60

The influence of the nonuniformity of grains, σ_g, is shown in Table 5.4 and Figure 5.24. The nonuniformity of grains is adjusted in the Voronoi network by changing the disorder degree d of the grains. There is an identical relationship between the nonuniformity and the disorder degree; when the disorder degree exceeds 10, the nonuniformity of grains reaches about 0.54 and remains unchanged. As the nonuniformity of the grains increases, the voltage gradient

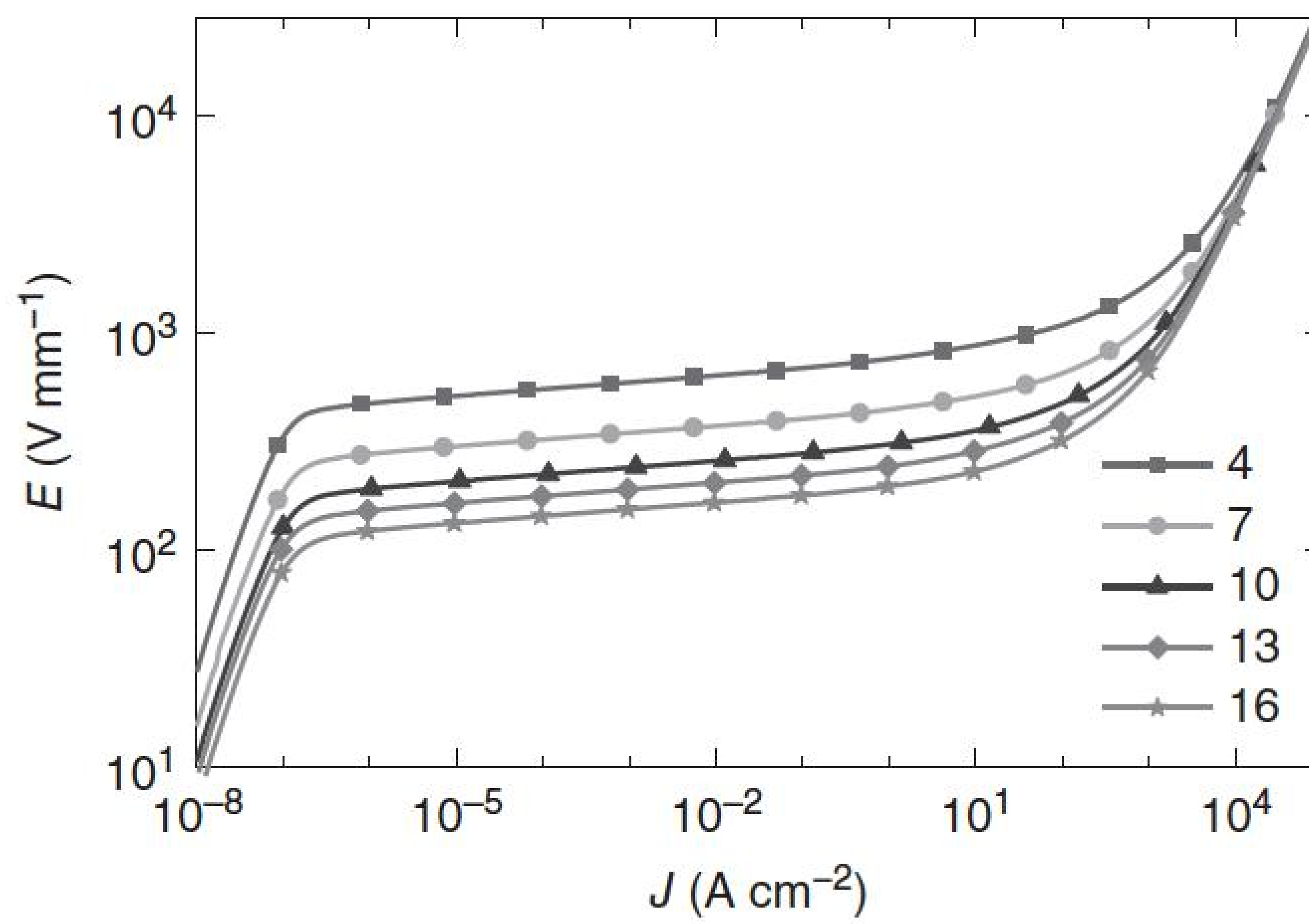


Figure 5.23 Influence of the grain size in μm on the *I–V* characteristics of ZnO varistors.

Table 5.4 Influence of the nonuniformity of grains on the electrical characteristics of ZnO varistors.

d	σ_g	$E_{1\,mA}$ (V mm^{-1})	A	J_L (μA cm^{-2})	$K_{20\,kA}$	$K_{10\,kA}$	$K_{5\,kA}$
0	0	297.41	30.33	0.47	1.55	2.00	2.49
0.5	0.2	287.75	32.05	0.40	1.63	2.11	2.59
1	0.34	258.36	32.12	0.35	1.78	2.36	2.91
3	0.47	238.53	32.14	0.33	1.85	2.50	3.11
5	0.52	233.32	32.14	0.32	1.87	2.54	3.17
7	0.53	232.83	32.14	0.32	1.87	2.53	3.19
9	0.54	222.81	32.16	0.30	1.93	2.63	3.28
15	0.54	223.09	32.15	0.30	1.95	2.65	3.31

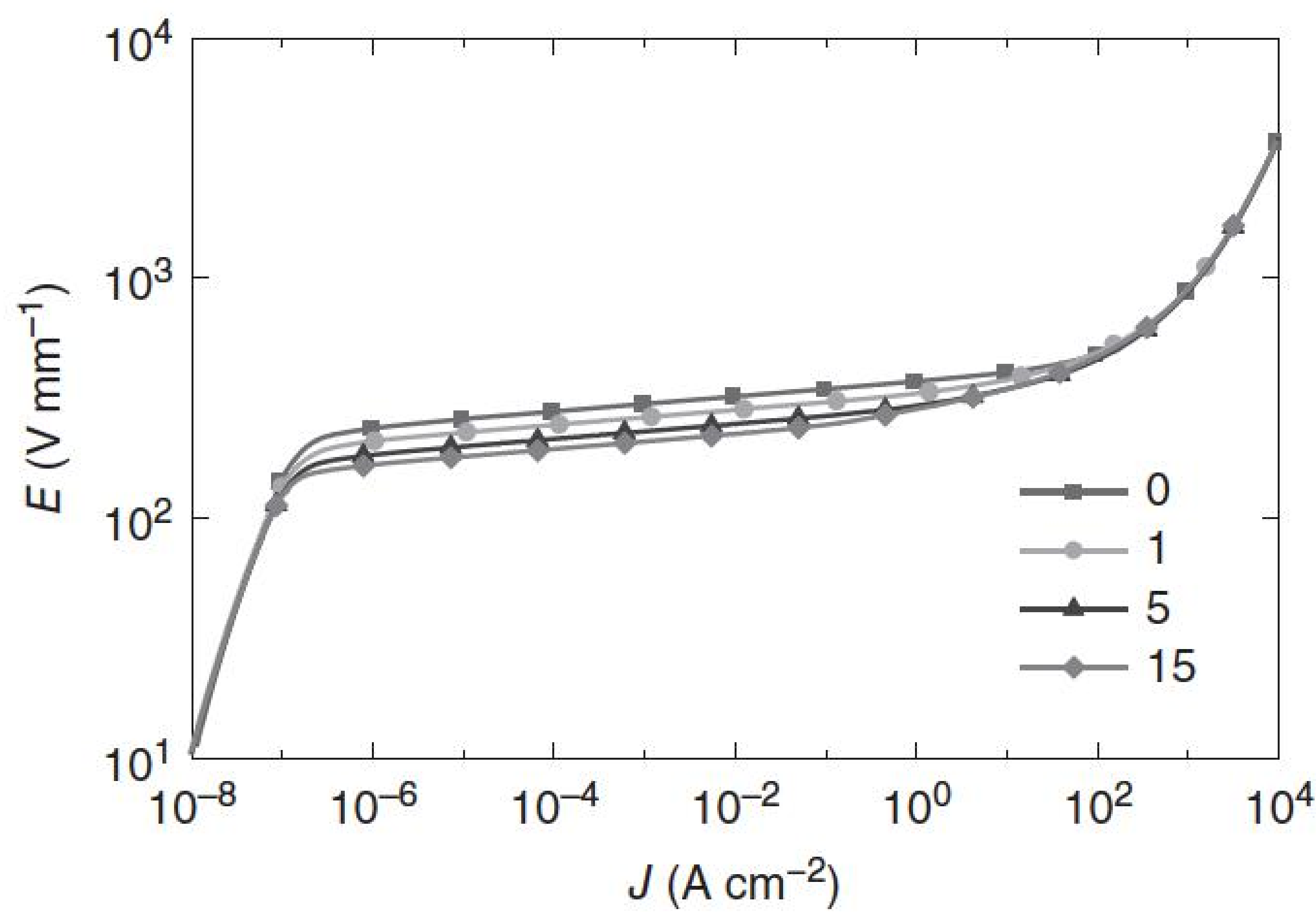


Figure 5.24 Influence of nonuniformity of grains (represented by the disorder degree *d*) on the *I–V* characteristics of ZnO varistors.

and the leakage current decrease, but the nonlinear coefficient increases weakly. On the other hand, reducing the ratio of spinels and pores inside the varistor bulk would also decrease the residual voltage ratio slightly.

5.5.3.2 Influence of Grain Boundary Parameters

The direct contact region C as shown in Figure 5.5 has no intergranular layer at all, where two adjacent ZnO grains contact with each other directly. The direct contact region ratio P_C has serious influence on the voltage gradient, leakage current, nonlinear coefficient, and residual voltage ratio (shown in Table 5.5 and Figure 5.25). As its ratio reaches 10^{-6}, the nonlinearity of ZnO varistor becomes very weak.

The influence of the intergranular layer region A, which is rich in Bi_2O_3 and occupies the ZnO grain corners with large thickness and high resistivity, on the electrical characteristics of the ZnO varistor is small (shown in Table 5.6 and Figure 5.26) but has a high influence on the residual voltage ratios $K_{10\,kA}$ and $K_{20\,kA}$. In addition, the resistivity of the intergranular layer region A has a strong influence on the electrical characteristics of the ZnO varistors (shown in Table 5.7 and Figure 5.27), as its resistivity decreases, the residual voltage ratio obviously increases, and the ZnO varistor would lose the nonlinearity.

Table 5.5 Influence of the intergranular layer region ratio on the electrical characteristics of ZnO varistors.

P_C	$E_{1\,mA}$ (V mm^{-1})	α	J_L (μA cm^{-2})	$K_{20\,kA}$	$K_{10\,kA}$	$K_{5\,kA}$
0	238.53	32.14	0.33	1.85	2.50	3.11
10^{-8}	238.13	29.20	13.05	1.85	2.50	3.11
10^{-7}	234.92	6.98	110.16	1.88	2.53	3.14
10^{-6}	174.83	1.05	679.55	2.51	3.39	4.22

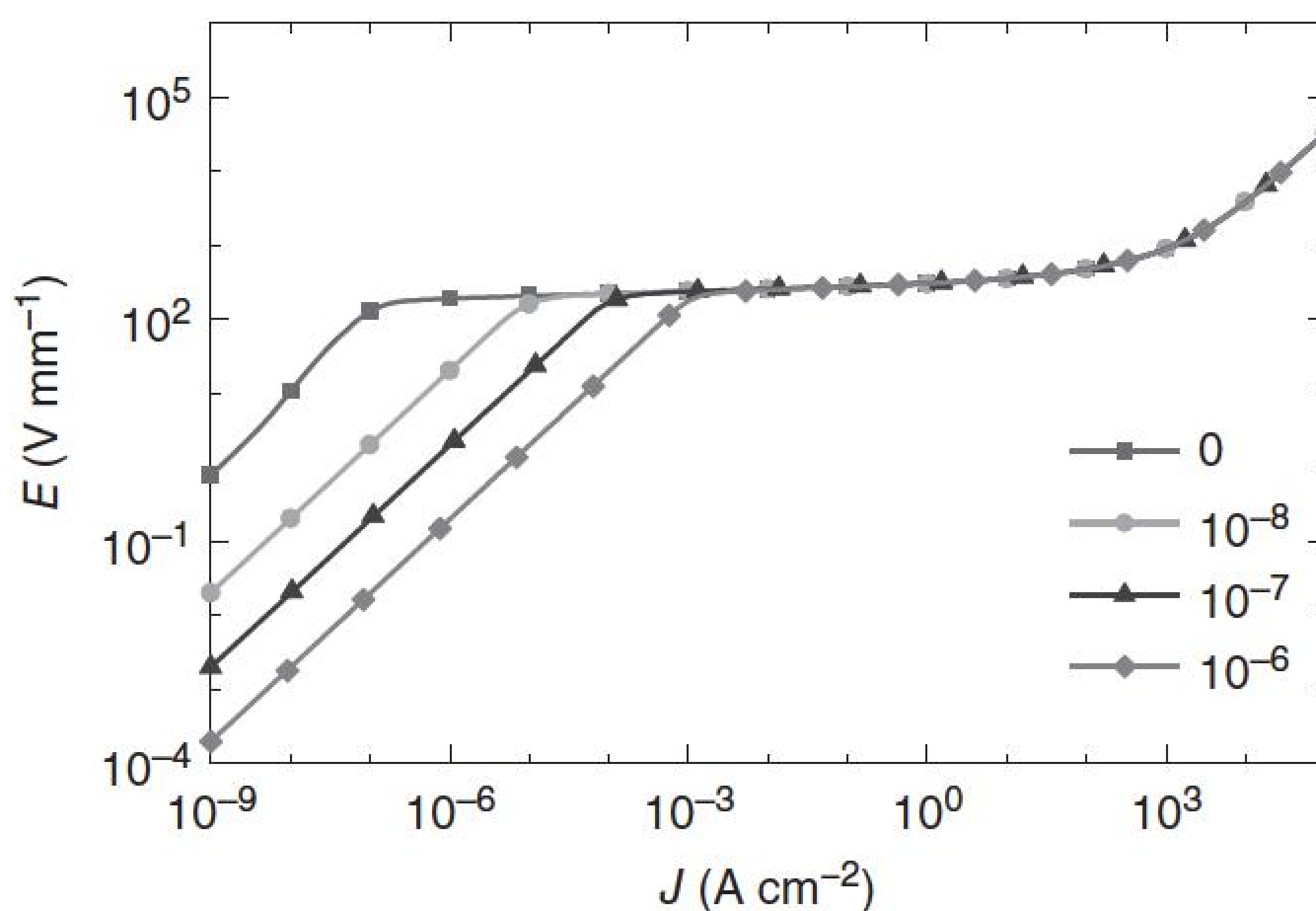


Figure 5.25 Influence of the direct contact region ratio on the I–V characteristics of ZnO varistors.

Table 5.6 Influence of the intergranular layer region ratio on the electrical characteristics of ZnO varistors.

P_A	$E_{1\,mA}$ ($V\,mm^{-1}$)	α	J_L ($\mu A\,cm^{-2}$)	$K_{20\,kA}$	$K_{10\,kA}$	$K_{5\,kA}$
0	236.44	32.11	0.27	1.82	2.42	2.98
0.2	238.53	32.14	0.33	1.85	2.50	3.11
0.4	236.83	32.13	0.35	1.93	2.65	3.37
0.6	241.82	32.05	0.43	1.98	2.85	3.73

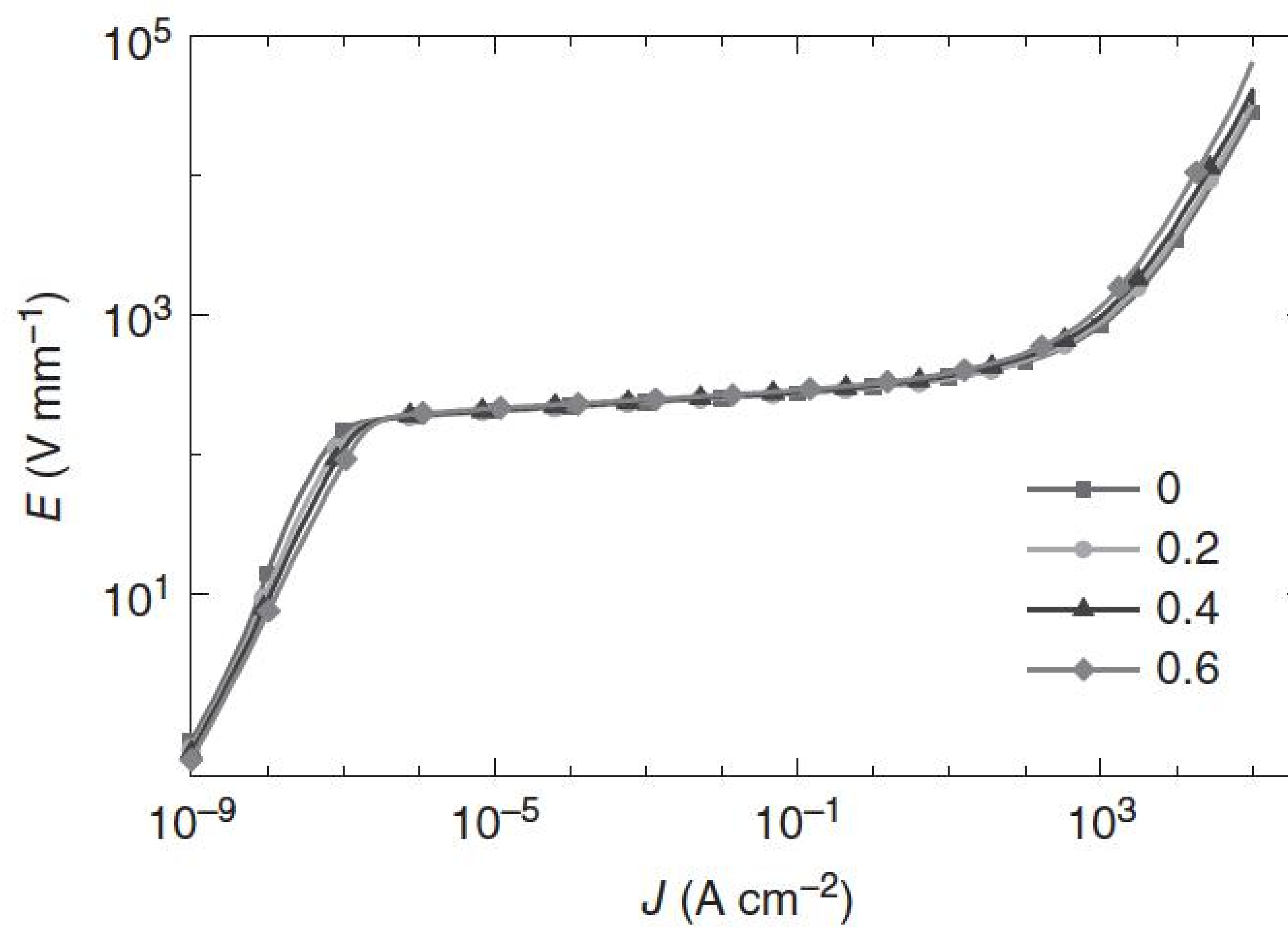


Figure 5.26 Influence of the intergranular layer region ratio on the *I–V* characteristics of ZnO varistors.

Table 5.7 Influence of the resistivity of intergranular layer on the electrical characteristics of ZnO varistors.

ρ_A (Ω m)	$E_{1\,mA}$ ($V\,mm^{-1}$)	α	J_L ($\mu A\,cm^{-2}$)	$K_{20\,kA}$	$K_{10\,kA}$	$K_{5\,kA}$
10^8	163.46	1.05	691.50	2.67	3.61	4.49
10^{10}	235.50	29.57	13.64	1.86	2.51	3.13
10^{12}	238.53	32.14	0.33	1.85	2.50	3.11
10^{14}	234.84	32.16	0.16	1.84	2.51	3.12

The influence of the surface-state density of the grain boundary N_i is shown in Table 5.8 and Figure 5.28. As the surface-state density increases, the voltage gradient and the nonlinear coefficient increase, but the leakage current and the residual voltage ratio decrease, as its influence on the residual voltage ratio is by means of increasing the 1 mA reference voltage.

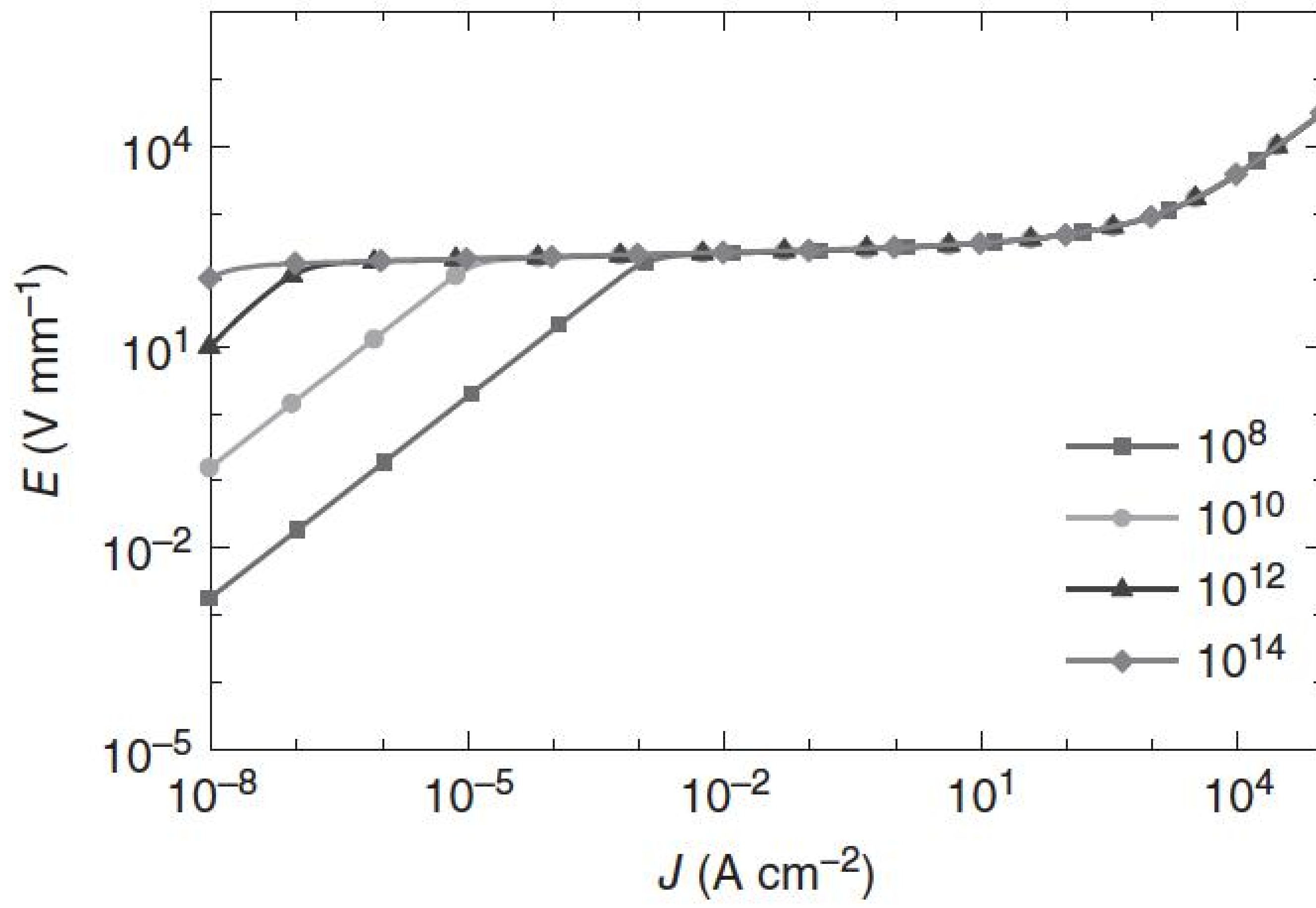


Figure 5.27 Influence of the resistivity of the intergranular layer region in Ω m on the *I–V* characteristics of ZnO varistors.

Table 5.8 Influence of the surface-state density of grain boundary on the electrical characteristics of ZnO varistors.

N_i (10^{16} m^{-3})	$E_{1\,mA}$ (V mm^{-1})	α	J_L (µA cm^{-2})	$K_{20\,kA}$	$K_{10\,kA}$	$K_{5\,kA}$
2.5	69.74	12.28	33.17	2.89	4.51	6.23
3	143.59	22.49	2.15	2.16	3.08	3.99
3.5	238.53	32.14	0.33	1.85	2.50	3.11
4	350.21	41.51	0.26	1.70	2.20	2.65
4.5	480.51	50.81	0.29	1.58	1.99	2.36

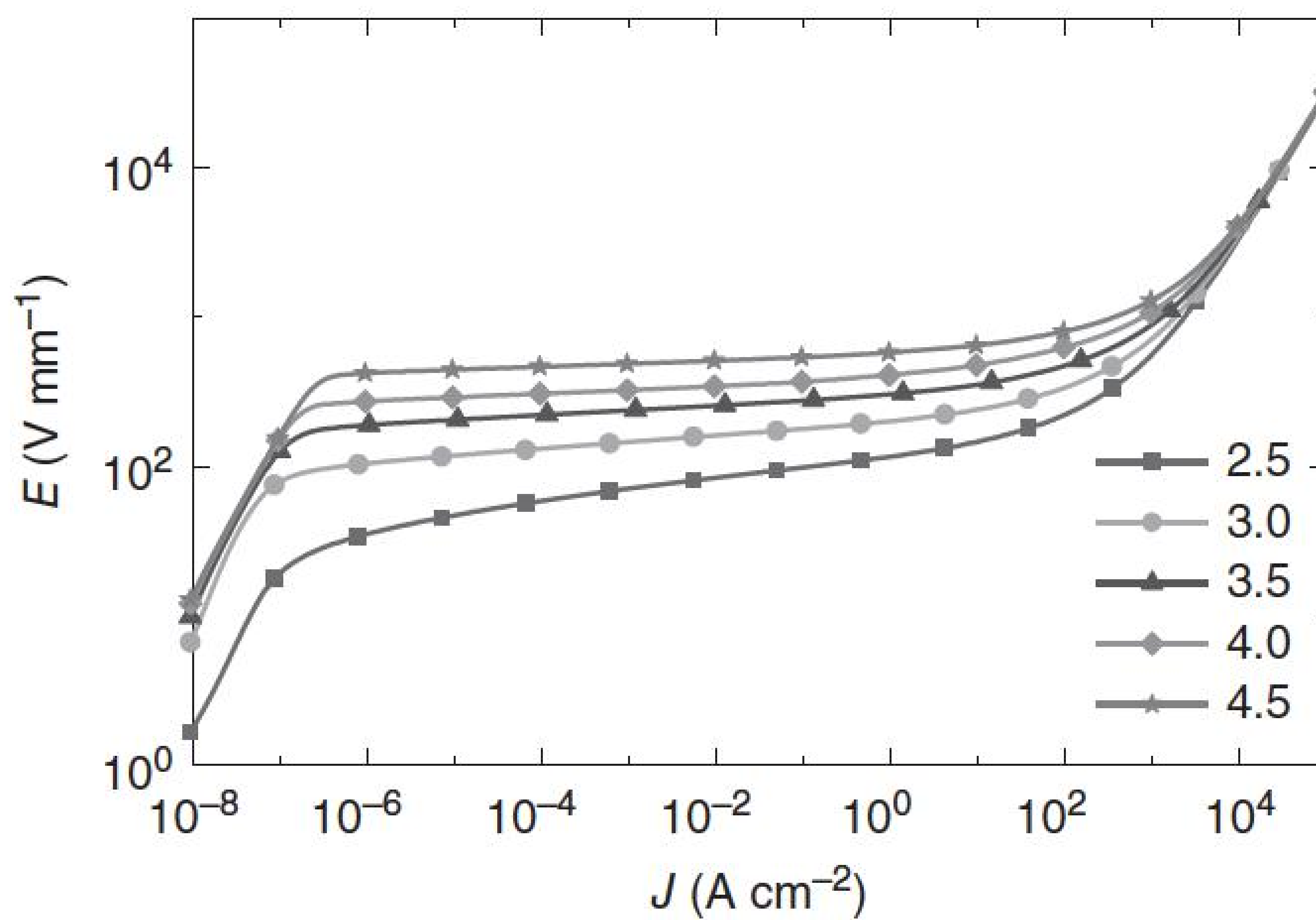


Figure 5.28 Influence of the surface-state density of the grain boundary in 10^{16} m^{-3} on the *I–V* characteristics of ZnO varistors.

Table 5.9 Influence of the barrier height and the deletion layer width on the electrical characteristics of ZnO varistors.

L (μm)	ϕ_b (eV)	$E_{1\,mA}$ (V mm^{-1})	α	J_L (μA cm^{-2})	$K_{20\,kA}$	$K_{10\,kA}$	$K_{5\,kA}$
0.198	0.83147	617.09	59.45	0.35	1.50	1.86	2.18
0.181	0.8267	480.51	50.81	0.29	1.58	1.99	2.36
0.163	0.82056	364.07	42.12	0.26	1.66	2.14	2.58
0.161	0.81992	350.21	41.51	0.26	1.70	2.20	2.65
0.142	0.81049	238.53	32.14	0.33	1.85	2.50	3.11
0.128	0.80017	169.43	24.95	1.16	2.03	2.85	3.64
0.122	0.79523	143.59	22.49	2.15	2.16	3.08	3.99
0.117	0.78853	120.32	19.66	4.59	2.30	3.36	4.42
0.105	0.75637	69.74	12.28	33.17	2.89	4.51	6.23

The barrier height and the depletion layer width under zero bias can be calculated by

$$\phi_b = \frac{e^2 N_{i0}^2}{8\varepsilon_r \varepsilon_0 N_d} \tag{5.51}$$

$$L = \sqrt{\frac{2\phi_b \varepsilon_r \varepsilon_0}{e^2 N_d}} \tag{5.52}$$

where ϕ_b is the barrier height, N_{i0} is the surface-state density under zero bias, L is the width of the depletion layer, and ε_r and ε_0 are the relative dielectric constant and dielectric constant of vacuum, respectively. The voltage gradient and the nonlinear coefficient increase as the barrier height and the depletion layer width increase (shown in Table 5.9), while the leakage current and the residual voltage ratio increase.

5.5.4 Influential Factors on Residual Voltage Ratio

Except the nonlinear coefficient, the residual voltage ratio, which is another index to present the protection effect of ZnO varistors, is a very important parameter of surge arresters with ZnO varistors as the core elements. According to the analysis above, the influence of various microstructural parameters of ZnO varistors on the macroscopic electrical characteristics is summarized in Table 5.10. The main measures to reduce the residual voltage ratio include decreasing the density of donors, grain size, and resistivity of the ZnO grains, increasing the surface-state density of grain boundary and the resistance of intergranular layer, improving the nonuniformity of the grain size, and reducing the ratio of direct contact region. Only decreasing the grain resistivity could decrease the residual voltage ratio of the ZnO varistor by means of decreasing the residual voltage gradient, whereas all other measures would decrease the residual ratio by means of increasing the reference voltage gradient.

Table 5.10 The influence of microstructural parameters of ZnO varistors on their macroscopic electrical characteristics.

Influential factors		**Macroscopic electrical parameters**				
		$E_{1\,mA}$ ↑	I_L ↓	$\alpha_{1\,mA}$ ↑	K ↓	**Affected parameter of residual voltage ratio**
Donor density, N_d	↓	√√	√√	√√	√√	$E_{1\,mA}$
Surface-state density, N_i	↑	√√	√√	√√	√√	$E_{1\,mA}$
Grain size, D	↓	√√	√	—	√√	$E_{1\,mA}$
Grain resistivity, ρ_g	↓	—	—	—	√√√	$E_{n\,kA}$
Nonuniformity of grains, σ_g	↓	√	—	—	√√	$E_{1\,mA}$
Pore ratio, P_{Pore}	↓	—	—	—	—	—
Spinel ratio, P_{Pore}	↓	—	—	—	—	—
Intergranular layer ratio, P_A	↓	–	√√√	√	–	–
Intergranular layer impedance, Z_A	↑	√√	√√	√√	√	$E_{1\,mA}$
Direct contact region ratio, P_C	↓	√√	√√√	√√	√	$E_{1\,mA}$

Note: ↑, increase; ↓, decrease; √, favorable influence; √√, obvious influence; √√√, serious influence; —, no influence; K, the residual voltage ratio; $E_{1\,mA}$, 1 mA reference voltage gradient; $E_{n\,kA}$, residual voltage gradient.

In all the measures, although decreasing the density of donors and increasing the density of surface states would obviously decrease the residual voltage ratio, but in the meantime, other electrical parameters of ZnO varistors would become bad, whereas the measures to increase the impedance of the intergranular layer and decrease the direct contact region ratio are difficultly controlled in the sintering process. Only the measure to decrease the resistivity of grains would decrease the residual voltage ratio but have no influence on other electrical characteristics of ZnO varistors, whereas in the meantime, the resistivity of the grains can be effectively controlled by doping donor-type additives. On the other hand, decreasing the grain size and the nonuniformity of grains would also have some effects to decrease the residual voltage ratio, and reducing the grain size would decrease the nonuniformity of grains. In addition, increasing the grain size would only decrease the residual voltage ratio, which would not influence other electrical characteristics of ZnO varistor bulks. Therefore, the optimal measure to decrease the residual voltage ratio is to decrease the resistivity and the size of ZnO grains.

According to the analysis, an Al ionic additive was doped to ZnO varistors; with an increase in the content of the Al ionic additive, the conductivity of ZnO grains increases significantly and the residual voltage ratio decreases correspondingly. The maximum effect of the Al additive on the grains' conductivity was observed when 0.25% Al ionic additive was added [63]. In order to further decrease the leakage currents of the Al-doped ZnO varistors, cobalt is added [64]; the leakage

currents are inhibited, and the nonlinear coefficients increase remarkably as well. The barrier heights and the donor densities of the varistor samples decrease as the cobalt content increases. This shows that the simulation has well directed the sintering of the ZnO varistor.

References

1 Clarke, D.R. (1999). Varistor ceramics. *Journal of the American Ceramic Society* 82 (3): 485–502.

2 Matsuoka, M. (1971). Nonohmic properties of zinc oxide ceramics. *Japanese Journal of Applied Physics* 10 (6): 736–746.

3 Levinson, L.M. and Philipp, H.R. (1975). The physics of metal oxide varistors. *Journal of Applied Physics* 46 (3): 1332–1341.

4 Gupta, T.K. (1990). Application of zinc oxide varistors. *Journal of the American Ceramic Society* 73 (7): 1817–1840.

5 Bartkowiak, M. and Mahan, G.D. (1995). Nonlinear currents in Voronoi networks. *Physical Review B* 51 (16): 10825.

6 Bartkowiak, M., Mahan, G.D., Modine, F.A., and Alim, M.A. (1996). Influence of ohmic grain boundaries in ZnO varistors. *Journal of Applied Physics* 79 (1): 273–281.

7 Bartkowiak, M., Mahan, G.D., Modine, F.A. et al. (1996). Voronoi network model of ZnO varistors with different types of grain boundaries. *Journal of Applied Physics* 80 (11): 6516–6522.

8 Guogang, Z., Joshi, R.P., and Hjalmarson, H.P. (2008). Electrothermal model evaluation of grain size and disorder effects on pulsed voltage response of microstructured ZnO varistors. *Journal of the American Ceramic Society* 91 (4): 1188–1193.

9 Chen, Q., He, J., Tan, K. et al. (2002). Influence of grain size on distribution of temperature and thermal stress in ZnO varistor ceramics. *Science in China Series E: Technological Science* 45 (4): 337–347.

10 Hohenberger, G., Tomandl, G., Ebert, R., and Taube, T. (1991). Inhomogeneous conductivity in varistor ceramics: methods of investigation. *Journal of the American Ceramic Society* 74 (9): 2067–2072.

11 Wen, Q. and Clarke, D.R. (1994). Modeling the electrical characteristics of polycrystalline varistors using individual grain boundary properties. *Ceramic Transactions* 40: 217–230.

12 Vojta, A., Wen, Q., and Clarke, D.R. (1996). Influence of microstructural disorder on the current transport behavior of varistor ceramics. *Computational Materials Science* 6 (1): 51–62.

13 Vojta, A. and Clarke, D.R. (1997). Microstructural origin of current localization and "puncture" failure in varistor ceramics. *Journal of Applied Physics* 81 (2): 985–993.

14 Nan, C.W. and Clarke, D.R. (1996). Effect of variations in grain size and grain boundary barrier heights on the current-voltage characteristics of ZnO varistors. *Journal of the American Ceramic Society* 79 (12): 3185–3192.

15 Nichols, C.S. and Clarke, D.R. (1991). Critical currents in inhomogeneous triangular Josephson arrays: a model for polycrystalline superconductors. *Acta Metallurgica et Materialia* 39 (5): 995–1002.
16 Wang, H., Bartkowiak, M., Modine, F.A. et al. (1998). Nonuniform heating in zinc oxide varistors studied by infrared imaging and computer simulation. *Journal of the American Ceramic Society* 81 (8): 2013–2022.
17 Nan, C.W. (1987). A microstructure-physical model of sensitive semiconductor ceramics. *Acta Physica Sinica* 36 (10): 1298–1304.
18 Eda, K. (1984). Destruction mechanism of ZnO varistors due to high currents. *Journal of Applied Physics* 56 (10): 2948–2955.
19 Long, W., Hu, J., He, J., and Liu, J. (2010). Time-domain response simulation of ZnO varistors by Voronoi network with an actual grain boundary model. *Journal of the American Ceramic Society* 93 (6): 1547–1550.
20 Anderson, R.A. and Pike, G.E. (2003). Current concentration at defects in ZnO varistor material. *Journal of Materials Research* 18 (4): 994–1002.
21 Cao, Z.C., Wu, R.J., and Song, R.S. (1994). Ineffective grain boundaries and breakdown threshold of zinc oxide varistors. *Materials Science and Engineering B* 22 (2–3): 261–266.
22 Mahan, G.D., Levinson, L.M., and Philipp, H.R. (1979). Theory of conduction in ZnO varistors. *Journal of Applied Physics* 50 (4): 2799–2812.
23 Pike, G.E., Kurtz, S.R., Gourley, P.L. et al. (1985). Electroluminescence in ZnO varistors: evidence for hole contributions to the breakdown mechanism. *Journal of Applied Physics* 57 (12): 5512–5518.
24 Miralles, A., Cornet, A., and Morante, J.R. (1986). Conduction mechanisms and temperature dependence of the electroluminescence in ZnO varistors. *Semiconductor Science and Technology* 1 (3): 230–233.
25 Blatter, G. and Greuter, F. (1986). Carrier transport through grain boundaries in semiconductors. *Physical Review B* 33 (6): 3952–3966.
26 Blatter, G. and Greuter, F. (1986). Electrical breakdown at semiconductor grain boundaries. *Physical Review B* 34 (12): 8555–8572.
27 Van Kemenade, J.T.C. and Eijnthoven, R.K. (1979). Direct determination of barrier voltage in ZnO varistors. *Journal of Applied Physics* 50 (2): 938–941.
28 Sung, G.Y., Kim, C.H., and Oh, M.H. (1987). Effect of grain-size distribution on the barrier voltage of ZnO varistors. *Advanced Ceramic Materials* 2 (4): 841–847.
29 Tao, M., Ai, B., Dorlanne, O., and Loubiere, A. (1987). Different "single grain junctions" within a ZnO varistor. *Journal of Applied Physics* 61 (4): 1562–1567.
30 Olsson, E. and Dunlop, G.L. (1989). Characterization of individual interfacial barriers in a ZnO varistor material. *Journal of Applied Physics* 66 (8): 3666–3675.
31 Wang, H., Li, W., and Cordaro, J.F. (1995). Single junctions in ZnO varistors studied by current-voltage characteristics and deep level transient spectroscopy. *Japanese Journal of Applied Physics* 34 (4R): 1765–1768.
32 Wang, H., Schulze, W.A., and Cordaro, J.F. (1995). Averaging effect on current-voltage characteristics of ZnO varistors. *Japanese Journal of Applied Physics* 34 (5R): 2352–2358.

33 Eda, K. (1978). Conduction mechanism of non-ohmic zinc oxide ceramics. *Journal of Applied Physics* 49 (5): 2964–2972.

34 Emtage, P.R. (1977). The physics of zinc oxide varistors. *Journal of Applied Physics* 48 (10): 4372–4384.

35 Greuter, F. and Blatter, G. (1990). Electrical properties of grain boundaries in polycrystalline compound semiconductors. *Semiconductor Science and Technology* 5 (2): 111–137.

36 Eda, K. (1989). Zinc oxide varistors. *IEEE Electrical Insulation Magazine* 5 (6): 28–30.

37 Olsson, E., Falk, L.K.L., Dunlop, G.L., and Österlund, R. (1985). The microstructure of a ZnO varistor material. *Journal of Materials Science* 20 (11): 4091–4098.

38 Cerva, H. and Russwurm, W. (1988). Microstructure and crystal structure of bismuth oxide phases in zinc oxide varistor ceramics. *Journal of the American Ceramic Society* 71 (7): 522–530.

39 Kingery, W.D., Sande, J.B., and Mitamura, T. (1979). A scanning transmission electron microscopy investigation of grain-boundary segregation in a ZnO-Bi_2O_3 varistor. *Journal of the American Ceramic Society* 62 (3–4): 221–222.

40 Stucki, F., Brüesch, P., and Greuter, F. (1987). Electron spectroscopic studies of electrically active grain boundaries in ZnO. *Surface Science* 189: 294–299.

41 Mukae, K., Tsuda, K., and Nagasawa, I. (1979). Capacitance-vs-voltage characteristics of ZnO varistors. *Journal of Applied Physics* 50 (6): 4475–4476.

42 Stauffer, D. and Aharony, A. (1994). *Introduction to Percolation Theory*. New York: CRC Press.

43 Weaire, D. and Rivier, N. (1984). Soap, cells and statistics—random patterns in two dimensions. *Contemporary Physics* 25 (1): 59–99.

44 Brostow, W., Dussault, J.P., and Fox, B.L. (1978). Construction of Voronoi polyhedra. *Journal of Computational Physics* 29 (1): 81–92.

45 Finney, J.L. (1979). A procedure for the construction of Voronoi polyhedra. *Journal of Computational Physics* 32 (1): 137–143.

46 Han, S.W., He, J.L., Hwang, H.D., and Kang, H.B. (1997). Microstructure characteristics of ZnO varistors simulated by Voronoi network. *The Korean Journal of Ceramics* 3 (4): 239–244.

47 Priolo, A., Jaeger, H.M., Dammers, A.J., and Radelaar, S. (1992). Conductance of two-dimensional disordered Voronoi networks. *Physical Review B* 46 (22): 14889–14892.

48 Hu, J. (2008). Research of ZnO varistor with high voltage gradient applied in ultra-high voltage arrester. Doctoral thesis. Beijing, China: Tsinghua University.

49 Long, W.C. (2011). Research on the ZnO varistor with low residual voltage used in ultra-high voltage arrester. PhD thesis. Beijing, China: Tsinghua University.

50 Ã-zisik, M.N. and Özışık, M.N. (1993). *Heat Conduction*. New York: Wiley.

51 He, J., Zeng, R., Chen, S., and Tu, Y. (2003). Thermal characteristics of high voltage whole-solid-insulated polymeric ZnO surge arrester. *IEEE Transactions on Power Delivery* 18 (4): 1221–1227.

52 Yang, S.M. (1980). *Heat Transfer*. Beijing, China: High Education Press.
53 Lat, M.V. (1983). Thermal properties of metal oxide surge arresters. *IEEE Transactions on Power Apparatus and Systems* 102 (7): 2194–2202.
54 Kingery, W.D., Bowen, H.K., and Uhlmann, D.R. (1976). *Introduction to Ceramics*. Singapore: Wiley.
55 Koch, R.E. and Songster, H.J. (1984). Development of a non-fragmenting distribution surge arrester. *IEEE Transactions on Power Apparatus and Systems* 103 (11): 3342–3352.
56 Lengauer, M., Rubeša, D., and Danzer, R. (2000). Finite element modelling of the electrical impulse induced fracture of a high voltage varistor. *Journal of the European Ceramic Society* 20 (8): 1017–1021.
57 Vojta, A. and Clarke, D.R. (1997). Electrical-impulse-induced fracture of zinc oxide varistor ceramics. *Journal of the American Ceramic Society* 80 (8): 2086–2092.
58 Emtage, P.R. (1979). Statistics and grain size in zinc oxide varistors. *Journal of Applied Physics* 50 (11): 6833–6837.
59 Gleick, J. (2011). *Chaos: Making a New Science*. New York: Open Road Media.
60 Lorenz, E.N. (1995). *The Essence of Chaos*. Seattle, WA: University of Washington Press.
61 Bartkowiak, M., Mahan, G.D., Modine, F.A., and Alim, M.A. (1996). Multiple-peaked structure in the nonlinearity coefficient of ZnO varistors. *Japanese Journal of Applied Physics* 35 (4A): L414–L417.
62 Mizukoshi, A., Ozawa, J., Shirakawa, S., and Nakano, K. (1983). Influence of uniformity on energy absorption capabilities of zinc oxide elements as applied in arresters. *IEEE Transactions on Power Apparatus and Systems* 102 (5): 1384–1390.
63 Long, W.C., Hu, J., Liu, J. et al. (2010). The effect of aluminum on electrical properties of ZnO varistors. *Journal of the American Ceramic Society* 93 (9): 2441–2444.
64 Long, W.C., Hu, J., Liu, J., and He, J.L. (2010). Effects of cobalt doping on the electrical characteristics of Al-doped ZnO varistors. *Materials Letters* 64 (9): 1081–1084.

6

Breakdown Mechanism and Energy Absorption Capability of ZnO Varistor

Energy absorption capability, which is also called as energy handling capability and is the second most important property of ZnO varistors next to nonlinearity, has a direct relation to failure modes. Failure modes include electrical puncture, physical cracking, and thermal runaway, which happen under different currents. This chapter discusses the mechanisms of different failure modes, including puncture, crack, and thermal runaway, and the energy absorption capabilities of ZnO varistors based on both experiments and simulations. How the applied current, the nonuniformity of microstructure, and the nonuniformity of microstructural electrical and thermophysical characteristics affect the energy absorption capabilities of ZnO varistors is discussed. The energy absorption capability of ZnO varistors can be notably improved by decreasing the mean value of grain size, besides improving the sintering techniques and adjusting the prescriptions.

6.1 Introduction

The primary functionality of ZnO varistors is to protect electrical devices and systems, by discharging transient surges and limiting overvoltages. The energy absorption capability is the second most important property of ZnO varistors next to nonlinearity [1]. The energy E absorbed by a ZnO varistor can be expressed as

$$E = \int_0^T vi \, \mathrm{d}t \tag{6.1}$$

where v is the voltage applied on the varistor, i is the current through it, and T is the duration that the current is applied. E is usually referred as the permitted energy absorbed per unit volume of a varistor, measured in J cm^{-3}.

ZnO varistors as the core elements of surge arresters in high-voltage systems or surge protection devices in low voltage systems are required to absorb substantial amounts of energies resulting from temporary overvoltages, switching surges, or discharges of lightning. Therefore, their energy absorption capability is crucial for the integrity of equipment and systems. However, it has been observed in

experiments that differences in barrier voltages, grain sizes, and grain boundary characteristics inside the same ZnO varistor and among different ZnO varistors cause nonuniformity in the microstructurally electrical and thermophysical characteristics of ZnO varistors, and finally result in differences in their current handling capabilities, which are also called as energy absorption capability, or energy handling capability.

Measurements of and discussions on the energy absorption capabilities of ZnO varistors have been reported in the literature [2–9]. Generally, energy absorption capability is defined as the maximum amount of energy that a varistor disk can absorb before it fails. In other words, the permitted energy indicates the point at which varistor failure happens. The energy absorption capability of a ZnO varistor is limited by its failure modes.

The breakdown of ZnO varistors is an original phenomenon during their application, which had been reported in many publications [3, 5, 10–13]. Every varistor has a different destruction phenomenon under impulse current and AC or DC current. Three failure modes have been identified [9]: electrical puncture, physical cracking, and thermal runaway (or thermal breakdown). Thermal runaway is related to current and voltage instability due to the failure of heat balance between the power loss and the thermal dispersion capability of a varistor [7, 14–16]. Thermal runaway happens when the average temperature of the disk exceeds the thermal stability temperature, which is usually selected as 180–190 °C. While physical cracking is due to huge thermal stresses, and electrical puncture is formed by the current concentration in a small region, which generates high temperatures and leads to the melting of the grain boundary to form a molten hole. Owing to thermal runaway the ZnO varistor fails with physical cracking or electrical puncture. When AC or DC voltage is applied on ZnO varistors, all these three failure modes happen, but if only impulse voltage or current is applied to a ZnO varistor, then only physical cracking or electrical puncture takes places.

In this chapter, we aim to discuss the breakdown mechanisms and the energy absorption capabilities of ZnO varistors, based on both experiments and simulations reported in the literatures.

6.2 Impulse Failure Modes of ZnO Varistors

When different impulse currents are applied to ZnO varistors, the damage phenomena of varistors can be classified into four types based on experimental results from commercial ZnO varistors [11, 12], as shown in Figure 6.1:

- *Type a*: the varistor is punctured, and a hole through the varistor can be found (Figure 6.1a).
- *Type b*: there is a punctured hole, and the varistor is cracked with an arc-shaped destruction (Figure 6.1b).
- *Type c*: there is an unpunctured hole, and the varistor is cracked with an arc shape (Figure 6.1c).
- *Type d*: the varistor is cracked with an arc shape (Figure 6.1d).

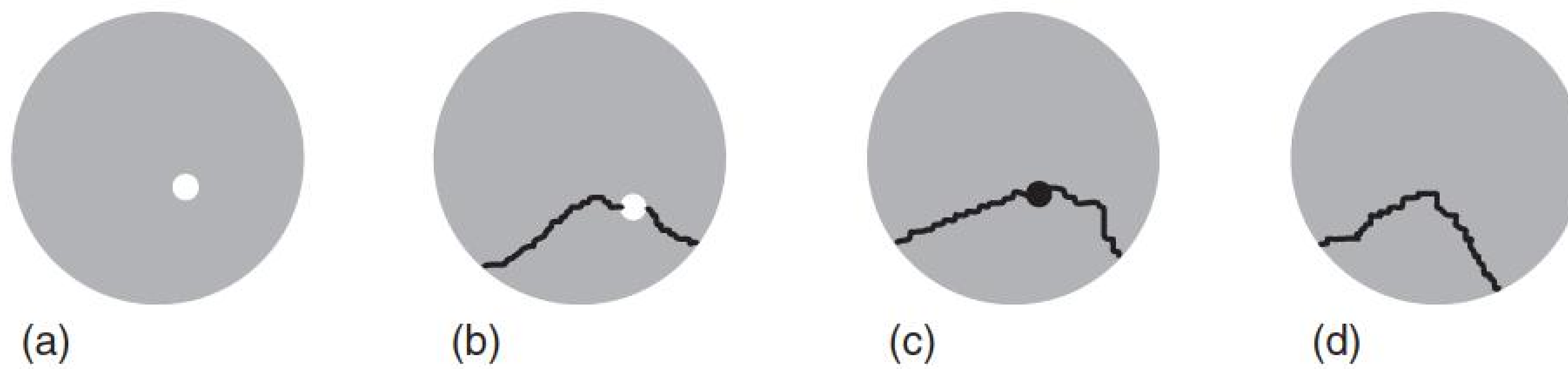


Figure 6.1 Impulse destruction phenomena of ZnO varistors: (a) puncture; (b) arc-shaped cracking destruction with a punctured hole; (c) arc-shaped cracking destruction with an unpunctured hole; (d) arc-shaped cracking destruction. Source: Adapted from He et al. [12].

Table 6.1 The test results of impulse destruction phenomena of ZnO varistors.

Duration of applied impulse square current	2 ms	8 ms
ZnO varistors (diameter 52 mm, thickness 10 mm)		
Number of tested varistors	24	20
Current density (A cm^{-2})	29.3	10.6
Ratio of cracking destruction (%)	75	40
Ratio of puncture destruction (%)	25	60
ZnO varistors (diameter 32 mm, thickness 10 mm)		
Number of tested varistors	30	32
Current density (A cm^{-2})	30.3	12.3
Ratio of cracking destruction (%)	50	10
Ratio of puncture destruction (%)	50	90

Source: Adapted from He et al. [12].

These four different destruction types can be described by two principal types of failure as done by Eda [2]; one is a "puncture" mode, in which a hole literally forms through the varistor with distinct signs of melting and vaporization. This is attributed to thermal runaway. The other is a form of failure in which the varistor fractures into two or more pieces but with no obvious thermal damage or melting. There are punctured holes in types a and b, so types a and b are classified into puncture destruction; there are no punctured holes but cracking phenomena in types c and d, so types c and d are classified into cracking destruction.

Two types of commercial disk-shaped varistors of different sizes were tested [11, 12] and listed in Table 6.1. Puncture destruction is dominant when low impulse currents are applied for long durations, while cracking destruction preponderates under high impulse currents with short duration. Pulsed currents having duration greater than 100 μs also cause destruction by the puncture mode; usually, DC and AC currents cause destruction by the puncture mode although the destruction caused by DC and AC currents can be explained by thermal runaway. On the other hand, impulse currents of duration less than 50 μs cause destruction by the cracking mode [2].

However, the experiment on commercial ZnO varistor disks of large sizes shows that cracking destruction also occurs under low impulse currents with

long duration, and puncture destruction also takes place under high impulse currents with short duration, although in both cases, the other failure mode still dominates. As shown in Table 6.1, the proportions of dominating failure modes are quite different between two types of varistors and when different currents are applied. Cracking destructions reach about 50% and 75% under a 2 ms square wave current, while puncture destructions are about 90% and 60% under an 8 ms square wave current [11].

Ringler et al. [5] also provided a significant body of data on the failure modes of varistors as a function of the applied current. Commercially available varistors of similar physical dimensions and voltage rating were procured from three different manufacturers. The varistors originated from a single batch and had a typical voltage rating of 3 kV. Varistor heights ranged from 23 to 24 mm and diameters varied from 62 to 64 mm. At the test currents with peak values of 7 and 70 A, varistor failure was typically due to a single hole through the bulk ceramic between the electrodes. Visual inspection determined that there were single holes, with diameters of up to 4 mm, located typically at a radial distance of several millimeters from the circumferential edge of the specimen. No cracking or fragmentation failures were observed in any of these tests. The most significant external damage was found for the nominal currents at a peak value of 600 A. Frequently, a thin portion of the sidewall broke off the varistor. At the peak value of 35 kA and above, many pinholes were found on the electrodes, including the annulus. Varistor failure was apparently due to overheating and attendant electrical puncture or tracking at the sidewall. Very few of the varistors cracked on failure.

In Eda's experimental results [2], most ZnO varistors of small sizes ended up with puncture destruction, when low impulse currents were applied for long durations, and almost all failures were cracking mode under high impulse currents with short duration, but both failure modes occurred above a threshold energy, as illustrated in Figure 6.2. There appears to be no distinct transition between these two modes of failure. Therefore, at intermediate pulse lengths, the failure may exhibit characteristics of both thermal effects and fracture [17]. Many works have clarified the circumstances under which two types of failure can be expected to occur [16].

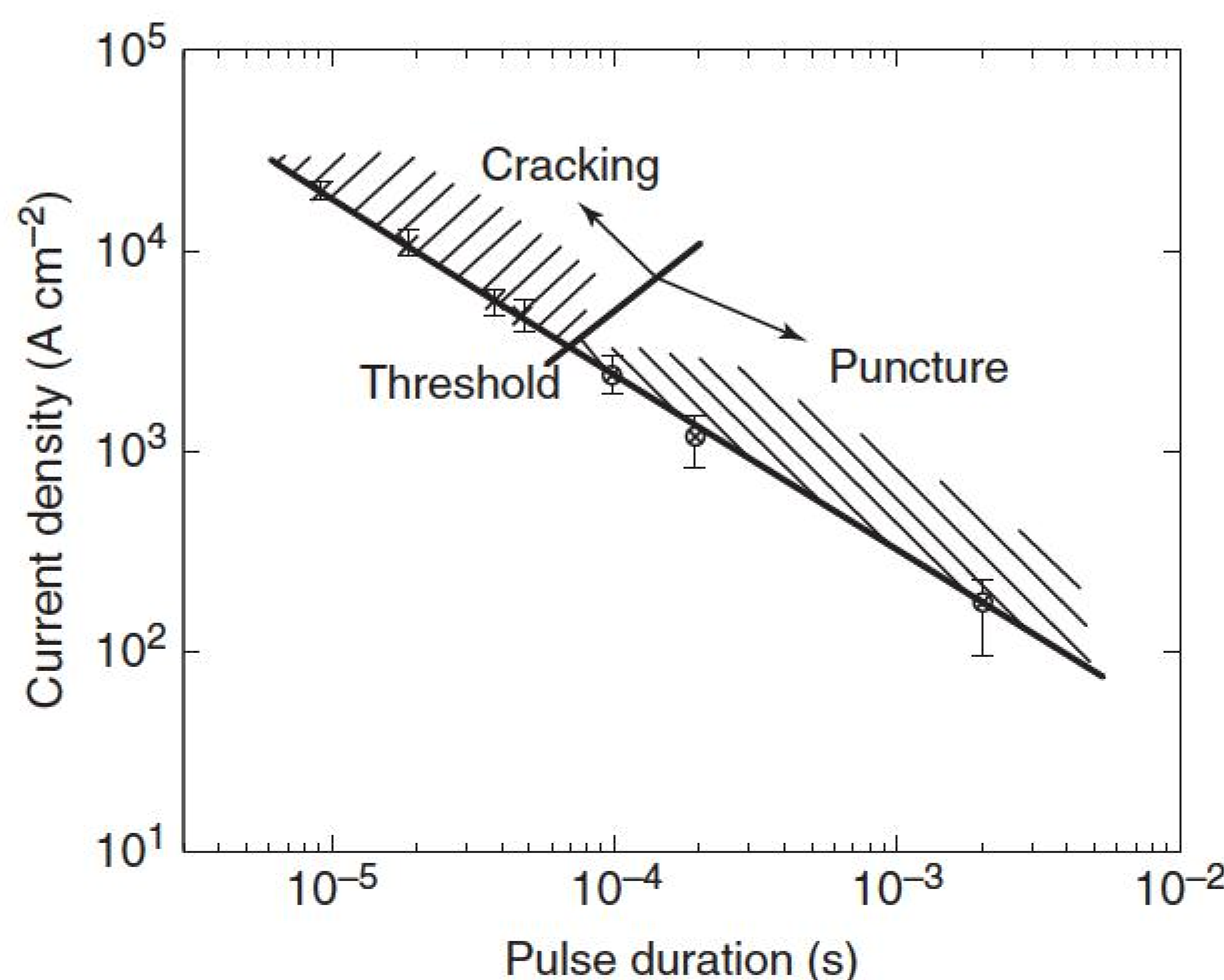


Figure 6.2 Plot of current density and pulse duration illustrating regions of failure modes and an apparent threshold for failure of ZnO varistors with 14-mm diameter and 1.3-mm thickness. Source: Eda 1984 [2]. Reproduced with permission of AIP.

Figure 6.2 demonstrates a linear dependence over approximately five orders of magnitude; this was discussed in detail by Ringler et al. [5] The finding of linear dependence between the logarithm of the mean discharge current and the logarithm of the mean time-to-failure could be useful for determining the energy absorption capability and safety margin in surge arrester applications.

The destruction of ZnO varistor blocks caused by multiple impulse currents was tested [18]. An impulse current of 8/20 μs was applied five times with a time interval of 35 ms, but an impulse current with small peak value, which is smaller than the rated current of ZnO varistor, still results in possible damage, while an impulse current with high peak value produces a high percentage of ZnO surge arrester damage. For the ZnO varistor blocks with rated impulse current of 5 kA, 600 A, 1300 A, and 2500 A, impulse current caused the damage of 28.57%, 50%, and 100% samples. Most ZnO block failures are in the form of cracking, which is caused by thermal accumulation of multiple impulses.

6.3 Mechanisms of Puncture and Fracture Failures

6.3.1 Mechanisms of Puncture Failure

The puncture and cracking failures of ZnO varistors are caused by the current concentration phenomenon, which is due to the nonuniformities of the microstructurally electrical characteristics and absorbed energies in different parts of the varistor. Injecting different currents would lead to different failure phenomenon.

When a small current is applied to a ZnO varistor for a long duration, heat conduction takes place between different portions of the varistor, and the surface of the varistor also transfers heat to the surroundings. Owing to current concentration, the temperature of the region with more current will increase quickly. Since the grain boundary is dominated by Bi_2O_3 whose melting temperature is around 820 °C, when the temperature exceeds the melting temperature of grain boundary, the grain boundaries are melted to form a punctured hole through the ZnO varistor.

The Sandia report in 2011 documented an investigation of irreversible electrical breakdown in ZnO varistors due to short pulses of high electric field and current density [19]. A few of the varistors that had electrical breakdowns were observed to have holes generated on electrode surfaces of the ZnO varistor. When the crack is forced open, an obvious track is exposed along the crack surface as seen in Figure 6.3. Both the hole and the track are typically 20 μm in diameter. The tracks are hollow, their surfaces are glassy, and occasionally they show a radial crystalline regrowth region. The hole and track structures in the varistors strongly indicate that a filament had formed with temperatures high enough to melt the ZnO locally.

The thermograph method is usually applied to observe the temperature of Zn varistors [8, 20, 21]. Figure 6.4 shows two cases of the thermographs for (a) a typical case and (b) a case with poor temperature distribution [22]; the white line is an equi-temperature line and the white area, a high-temperature part.

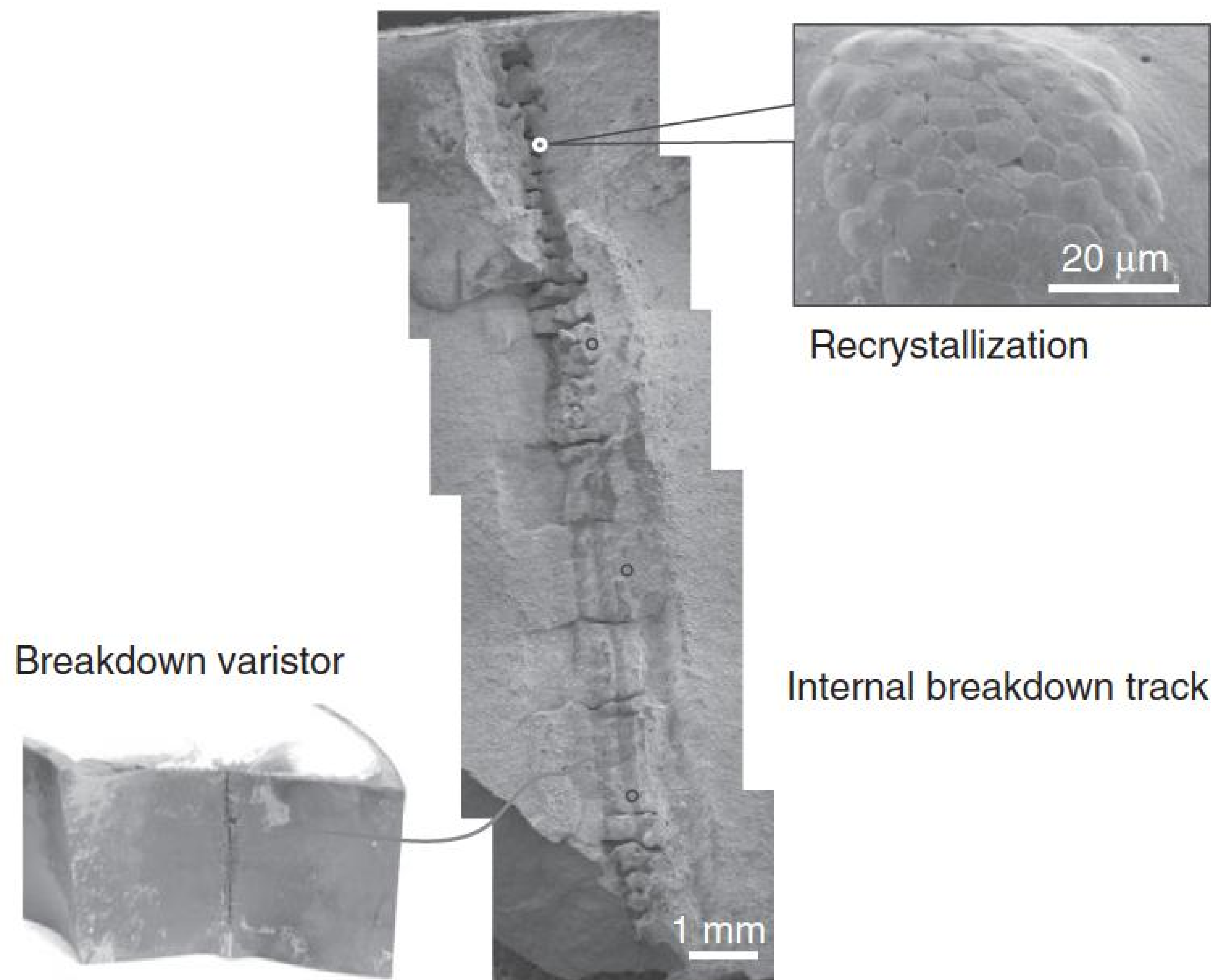


Figure 6.3 Example of an internal track caused by high voltage breakdown and recrystallization inside a breakdown track.

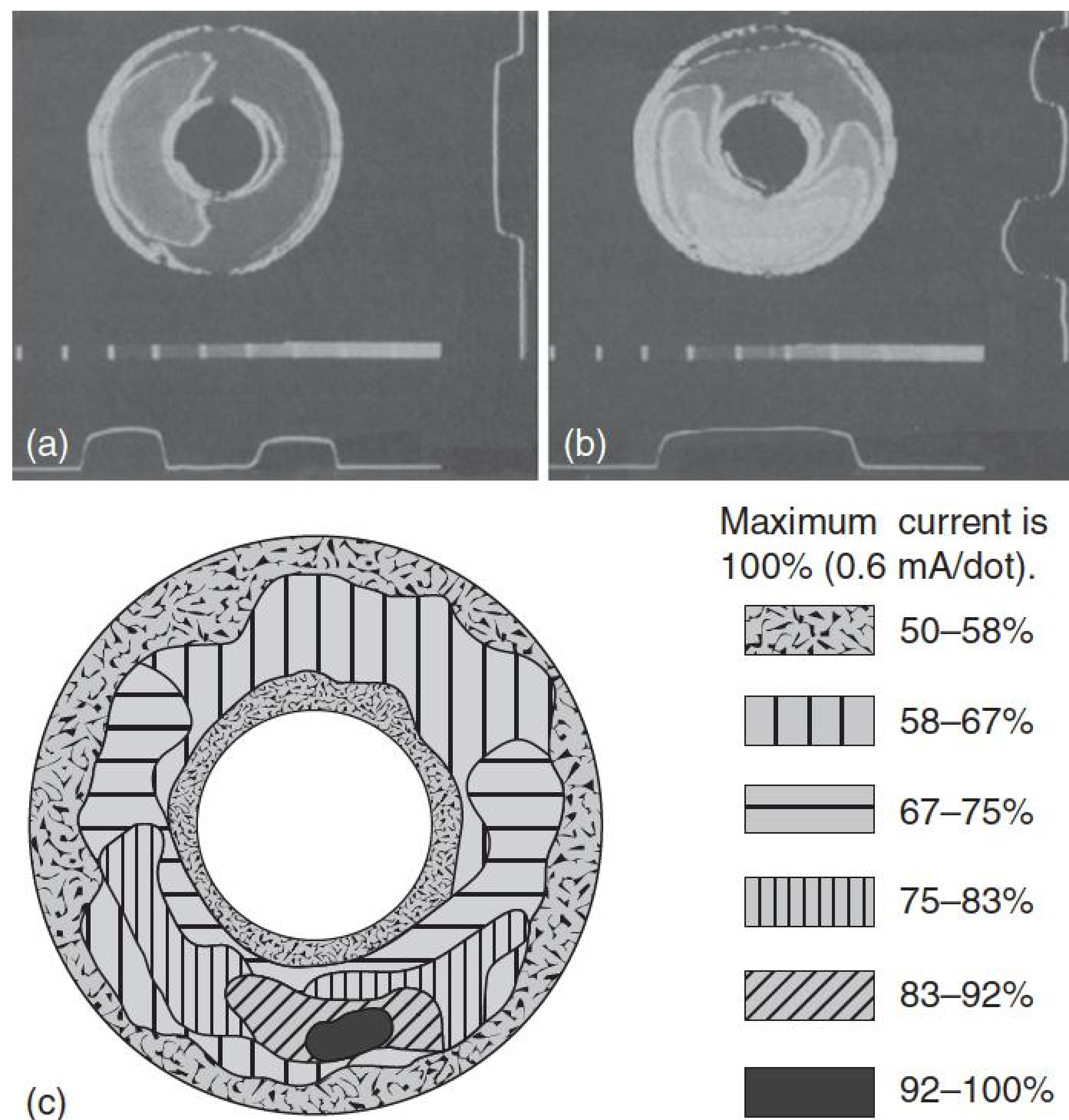


Figure 6.4 Temperature distribution and current distribution on the upper surface of the ZnO varistor [8]. (a) The typical thermograph case; (b) the thermograph case with poor temperature distribution; (c) current distribution measured by dot electrodes method. This sample is the same as for (b). Source: Mizukoshi et al. 1983 [8]. Reproduced with permission of IEEE.

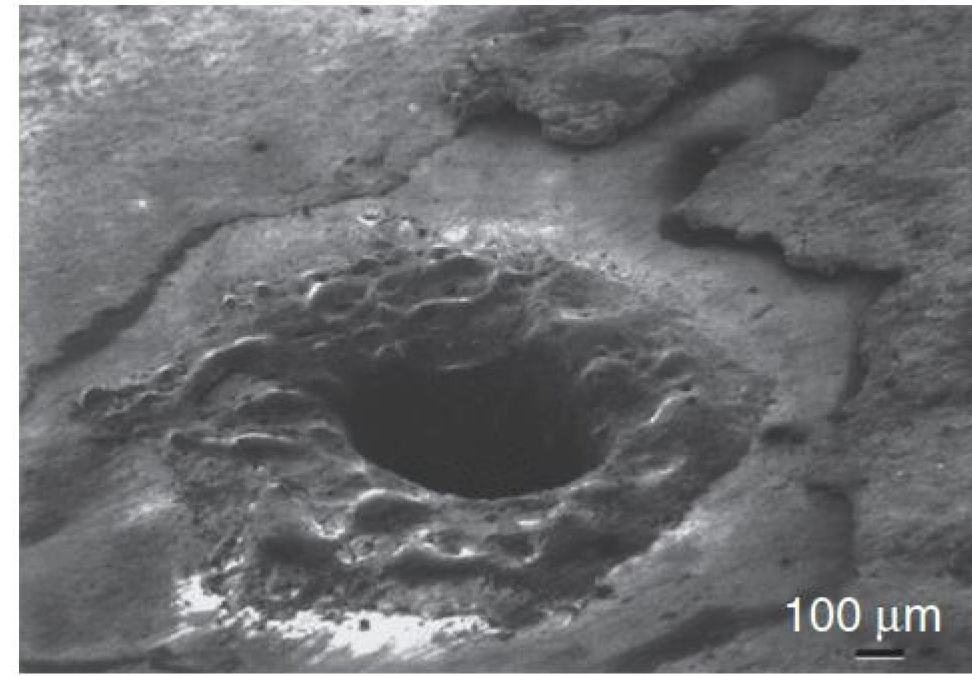


Figure 6.5 Scanning electron micrograph of the punctured hole of a ZnO varistor sample. Source: Vojta and Clarke 1997[22]. Reproduced with permission of AIP.

Local temperature could be measured by a scale in the equipment. The temperature distribution was measured by an infrared radiation thermo-camera. The thermograph was obtained at a selected time after a suitable voltage had been applied to an element, e.g. 10 seconds. The current distribution corresponds to the temperature distribution, which is seen by the comparison of Figure 6.4b,c which are for the same sample. The current distribution was measured by the method of dot electrodes with diameter of 1 .5 mm, and the two patterns agreed well [8]; a small region with serious current location was observed.

Figure 6.5 shows the scanning electron micrograph of a ZnO varistor sample failed in the puncture mode; the hole is clearly visible, which connects the electrodes on the top and bottom surface of the sample [22]; this scanning electron micrograph clearly indicates that melting occurs.

There is a wide variety of circumstantial experimental evidence for nonuniform current distribution through a varistor. The nonuniformity of current distribution was measured when currents of different waveforms were applied to varistors by arranging dot electrodes on the top surface of varistor [5] and by infrared imaging system to measure the temperature distribution on the varistor surface [23], such as shown in Figure 6.6 [24]. The paths with high currents were visualized by the local temperature rise, which was caused by joule heating of the current. From the images, several important assumptions and conclusions were drawn: the joule heating is primarily dissipated at the grain boundaries; the current localization paths are typically only one or two grains wide; usually several current localization paths coexist concurrently within the microstructure; current localization runs through the whole varistor from one electrode to the other [17].

An obvious direct relationship between the regions where puncture destructions were watched and the regions where there were spots with largest current values in the current distributions was observed. About 84% regions with the largest current distribution had punctured. The energy absorption capability was shown to be directly related to the uniformity of current distribution. When the current distribution is not uniform, then the energy absorption capability is small. It is not difficult to understand that the impulse destruction mechanism is related to the microstructural nonuniformity of ZnO varistor.

For ZnO varistors working under continuous AC or DC voltage, the puncture mode of failure is commonly associated with thermal runaway, which occurs as a consequence of current localization in the microstructure. This phenomenon can be explained as a positive feedback mechanism in which current localization

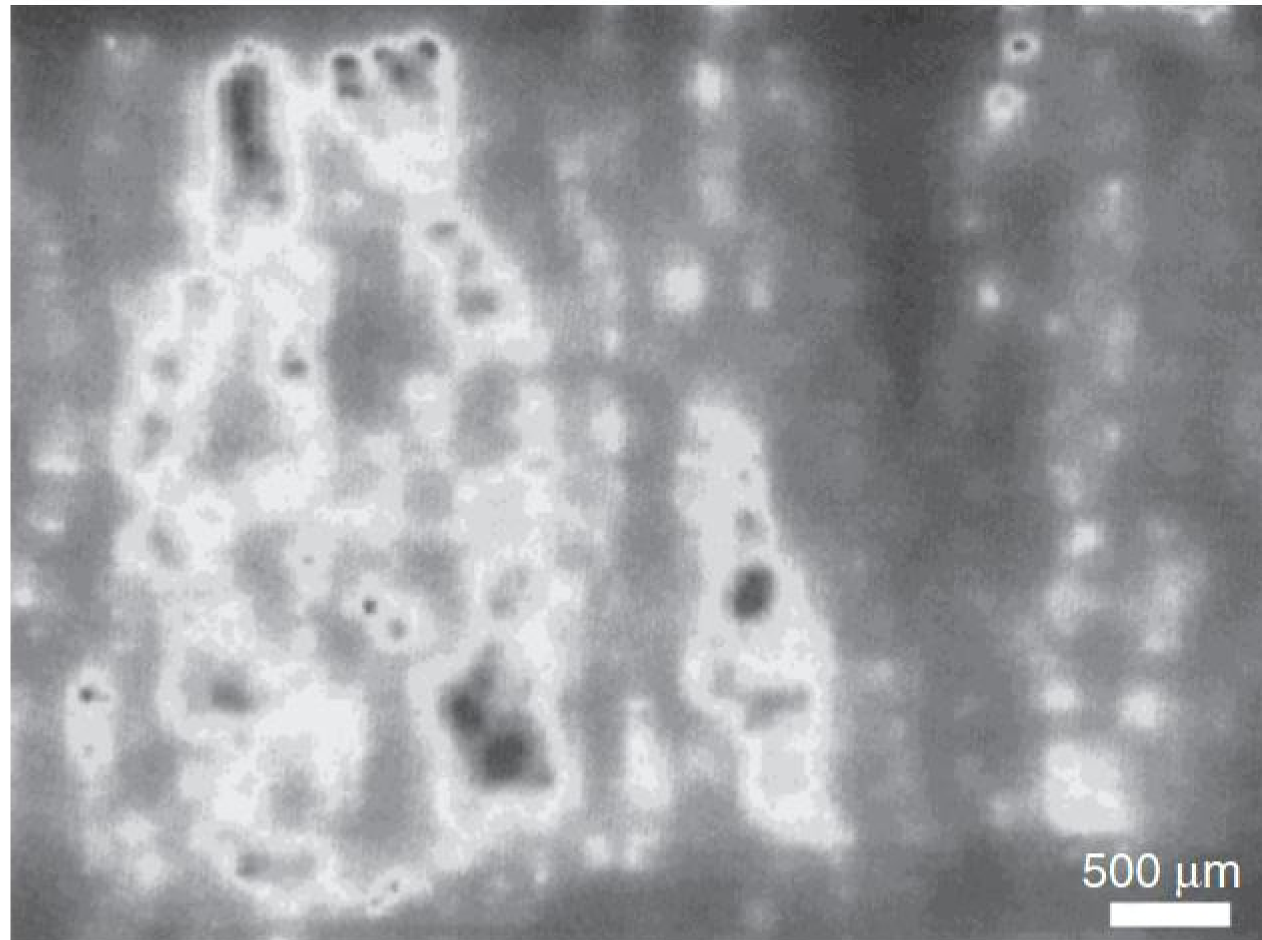


Figure 6.6 Infrared image revealing regions of current localization caused by enhanced joule heating. The voltage was applied in the vertical direction from top to bottom in this image. Source: Wang et al. 1998 [24]. Reproduced with permission of John Wiley & Sons.

occurs along some paths through the microstructure with higher current density, leading to the enhanced local joule heating. Because the resistance of ZnO as a semiconductor decreases with the increment of temperature, the lowered resistance caused by local heating along the localization path favors further drawing of more current to this path [17]. This feedback continues until melting and electrical shorting occurs. This phenomenon can be easily understood as two resistances in parallel; when one resistance decreases and the other remains unchanged, the current through the resistance, which decreases due to the local heating effect, will increase.

A more detailed explanation for this positive feedback was presented by Bartkowiak et al. [4]. As the temperature of the localization path reaches the value at which the local current and voltage correspond to the "knee region" of the I—V characteristic, electrical behavior of the hot spot becomes particularly sensitive to the temperature. Other computer simulations also reveal that almost any microstructural variation in properties leads to current localization and that the localization becomes stronger in the nonlinear regime [22, 23, 25, 26]. The rising temperature causes an increase in the local current density, and additional local heating. This, in turn, leads to a further increase of the temperature at the hot spot and a still faster increase of the local current density. Owing to this positive feedback, the temperature and the current density become highly peaked. At the time of failure, the current density at the hot spot becomes almost 100 times higher than that outside of the hot spot. Such feedback is the main mechanism of punctures for the average density of applied current lower than about $1\,\mathrm{A\,cm^{-2}}$. It also causes a dip in the energy absorption capability curves for currents in this region.

But if an impulse current or voltage is applied on a ZnO varistor, current localization is caused by the nonuniform property of the gain boundaries inside the ZnO varistor, such as the low barrier voltage of some paths; then, a large part of the impulse current will pass through these paths and generate high joule heat to increase the temperature of these paths. However, although localization is a necessary condition, puncture failure only happens if the local joule heating is not dissipated by conduction away from the localization path faster than it is

created; the continuous thermal accumulation will produce high temperature in these paths and melt them at last. Moreover, localization is a highly dynamic process, and, therefore, several different localization paths may exist through a varistor at different voltages, with only one leading to final failure and electrical breakdown [17].

Simulation suggests that microstructural defects intersecting the electrodes are particularly detrimental. Clarke thought that especially large grains in direct contact with the electrode act to draw current in from the whole electrode area rather than from just the neighboring grains; this makes the current localization more serious [17].

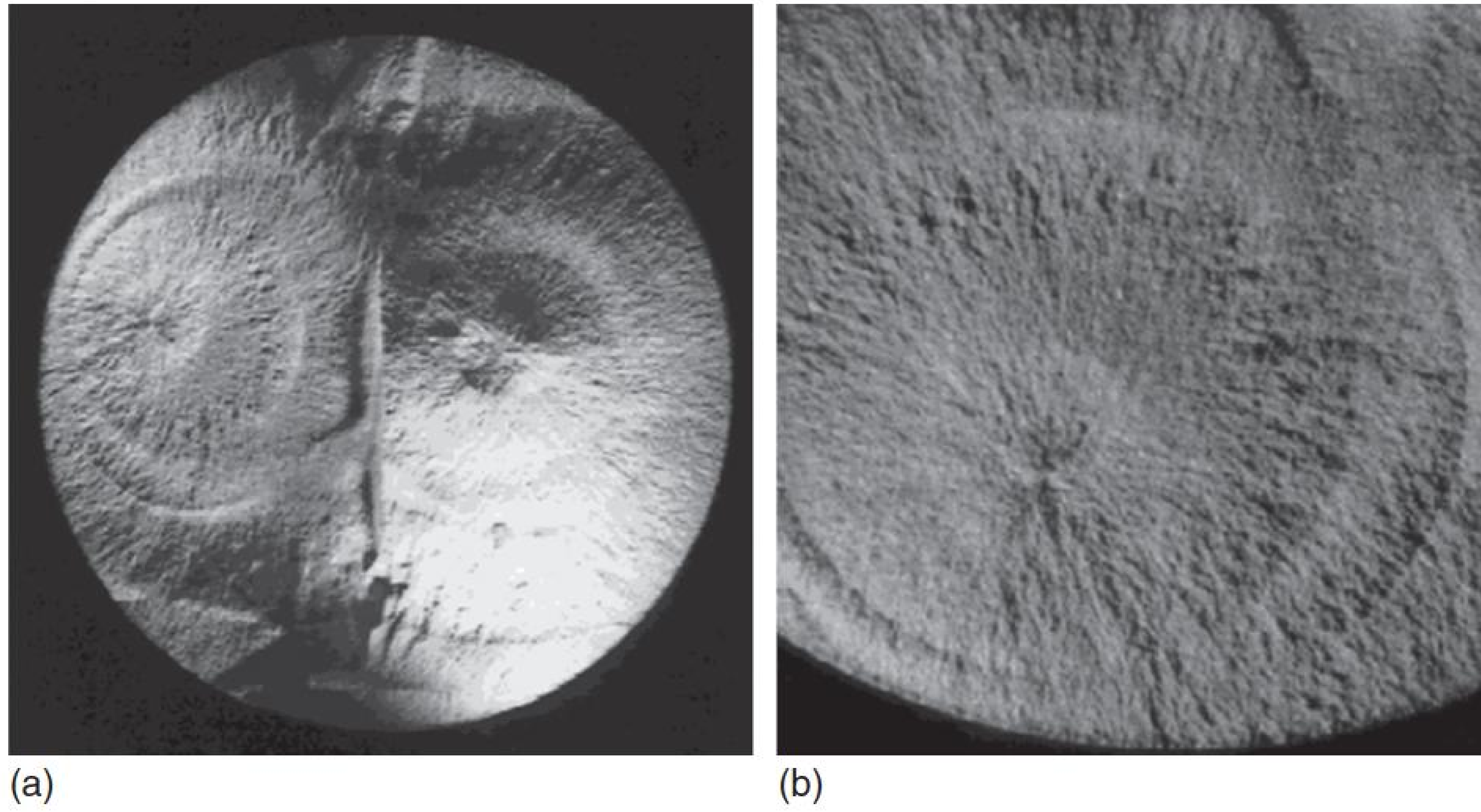
6.3.2 Mechanism of Fracture Failure

When a high current, such as an impulse current with high magnitude, is applied to a ZnO varistor for a short duration, the impulse energy could be absorbed by different small units of the varistor; the generated heat causes the temperature to rise. Because the duration of applied impulse current is very short, the heat generated in such a short time may not be transferred to other parts of the varistor, so the process could be treated as one of thermally insulated temperature rise. Temperatures of different small units increase quickly in a very short time, and the temperature gradient between two different units would generate thermal stress on the grain boundary between them. If the thermal stress between different portions inside the varistor exceeds the critic value, a cracking destruction happens.

So cracking destruction is a process of thermally mechanical destruction. There are several reasons to cause a temperature gradient between two neighboring small units, including the nonuniformities of energy absorption and thermophysical parameters, which include thermal conductivity, specific heat constant, and specific gravity [11, 12].

When varistors are subject to very short electrical pulses, they will fragment, and their fracture surfaces exhibit well-defined fracture markings. The fracture morphology and the number of fracture pieces depend on the shape and aspect ratio of the varistor as well as on the pulse power and the mechanical constraints on the varistor. However, short (compared to their diameter) varistor disks typically break with radial cracks, and tall varistor blocks tend to break across, or near, their center [27]. An example of the fracture surface of a varistor cracking across the center plane is shown in Figure 6.7, which is for a tall cylindrical varistor with a diameter of 42 mm when it was subject to a very short electrical pulse [27].

One approach to further understanding mechanical failure under such conditions is that the pulse length is so short that the varistor heats up much faster than it can expand isothermally [27]. As a result, its own inertia limits its expansion, and, therefore, an elastic compressional wave is generated within the varistor. On reflection from the ends, the elastic wave is tensile with a maximum value at the central plane of a tall cylindrical varistor [17]. The amplitude of the stress oscillation is shown to be proportional to the second derivative of temperature with respect to time which, in turn, is directly related to the rate of power increase.



(a) (b)

Figure 6.7 (a) Optical micrographs of an actual fracture surface of a varistor after failing under a high current pulse illustrating characteristic fracture markings. In this particular instance, concurrent fractures from two separate failure origins are seen. (b) An enlargement of the lower of the two fracture surfaces in (a). Source: Vojta and Clarke 1997 [27]. Reproduced with permission of John Wiley & Sons.

An upper limit for the magnitude of the peak stress is derived in terms of material parameters, varistor geometry, and the maximum electrical power.

An approximation based on the plain strain analysis [28] of the corresponding thermoelastic problem was used for the varistor disks [4]. This approach is well justified, because these disks typically have geometric aspect ratios higher than l. It is assumed that the disk can freely expand in the axial direction, i.e. that there is no traction at its end faces. In practice, varistors mounted on an arrester are under constant spring load to maintain good electrical contacts. This load, however, is very low compared to the stresses due to thermal expansion, and can be neglected. The thermal stresses caused by a nonuniform temperature distribution, $T(r)$, can be expressed as [4]

$$S_r(r) = \frac{\alpha Y}{1-\upsilon}\left(\frac{1}{R^2}\int_0^R r'T(r')\mathrm{d}r' - \frac{1}{r^2}\int_0^r r'T(r')\mathrm{d}r'\right) \tag{6.2}$$

$$S_\theta(r) = \frac{\alpha Y}{1-\upsilon}\left(\frac{1}{R^2}\int_0^R r'T(r')\mathrm{d}r' + \frac{1}{r^2}\int_0^r r'T(r')\mathrm{d}r' - T(r)\right) \tag{6.3}$$

$$S_z(r) = S_r(r) + S_\theta(r) \tag{6.4}$$

where, stresses in the radial, tangential, and axial directions are denoted by S_r, S_θ, and S_z, respectively. Experimental data for the thermal expansion coefficient α [14] in unit of K^{-1}, can be fitted by the function $\alpha = b_1 + b_2T + b_3 \ln T$, where $b_1 = -2.375 \times 10^{-5}$, $b_2 = -3.76 \times 10^{-9}$, $b_3 = 5.11 \times 10^{-6}$, and where T is in degrees Kelvin. The Young's modulus Y and the Poisson's ratio υ of the material were selected as 1.7×10^7 psi ($=1.17 \times 10^8$ kPa) and 0.25, respectively [29].

Varistor disks in station-class surge arresters typically have an aspect ratio lower than 1; then the thermal stresses in the axial direction are negligible, and

the stresses in the radial and tangential directions can be determined within the plain-stress approximation [30]; the corresponding expressions have the same form as those in Eqs. (6.2) and (6.3), but with υ set to zero. The material strength is a statistical quantity that may vary considerably for individual disks. The ultimate tensile strength of the varistor ceramic is assumed to be $S_{\text{ft}} = 20\,\text{kpsi}$, while the compressive strength of brittle materials is from three to eight times the tensile strength, and $S_{\text{fc}} = 70\,\text{kpsi}$ was suggested as a representative value of the compressive strength of varistors [4].

Usually, fracture is assumed to occur if the local tensile stress exceeds the Griffith criterion for a crack-like flaw within the varistors [17]. A direct relationship between the size a of a flaw in the varistor, the varistor diameter d, the maximum pulse power P_c, and the varistor material properties naturally results in fracture when the following criterion is satisfied [17]:

$$P_{\text{c}} \geq FK_{\text{c}} \frac{d^2}{\sqrt{a}} \sqrt{\frac{\rho C_v}{\alpha Y}} \tag{6.5}$$

where α denotes the thermal expansion coefficient, K_{c} is the varistor fracture toughness, ρ its density, C_v its specific heat, and F a geometric constant, $F = 32\sqrt{2}/\pi^{3.5}$, for a cylindrical sample with interior crack. Figure 6.8 visualizes this relationship [27]. As with other fracture problems, a statistical distribution in failures results from the flaw size as well as flaw location. Because the maximum of the tensile stress is at the center, fracture is also mostly likely to occur at the central plane, as is usually observed. Similarly, if the tensile stress is sufficiently large, all flaws above the critical size can propagate simultaneously, and, therefore, more than one failure origin can be activated [17].

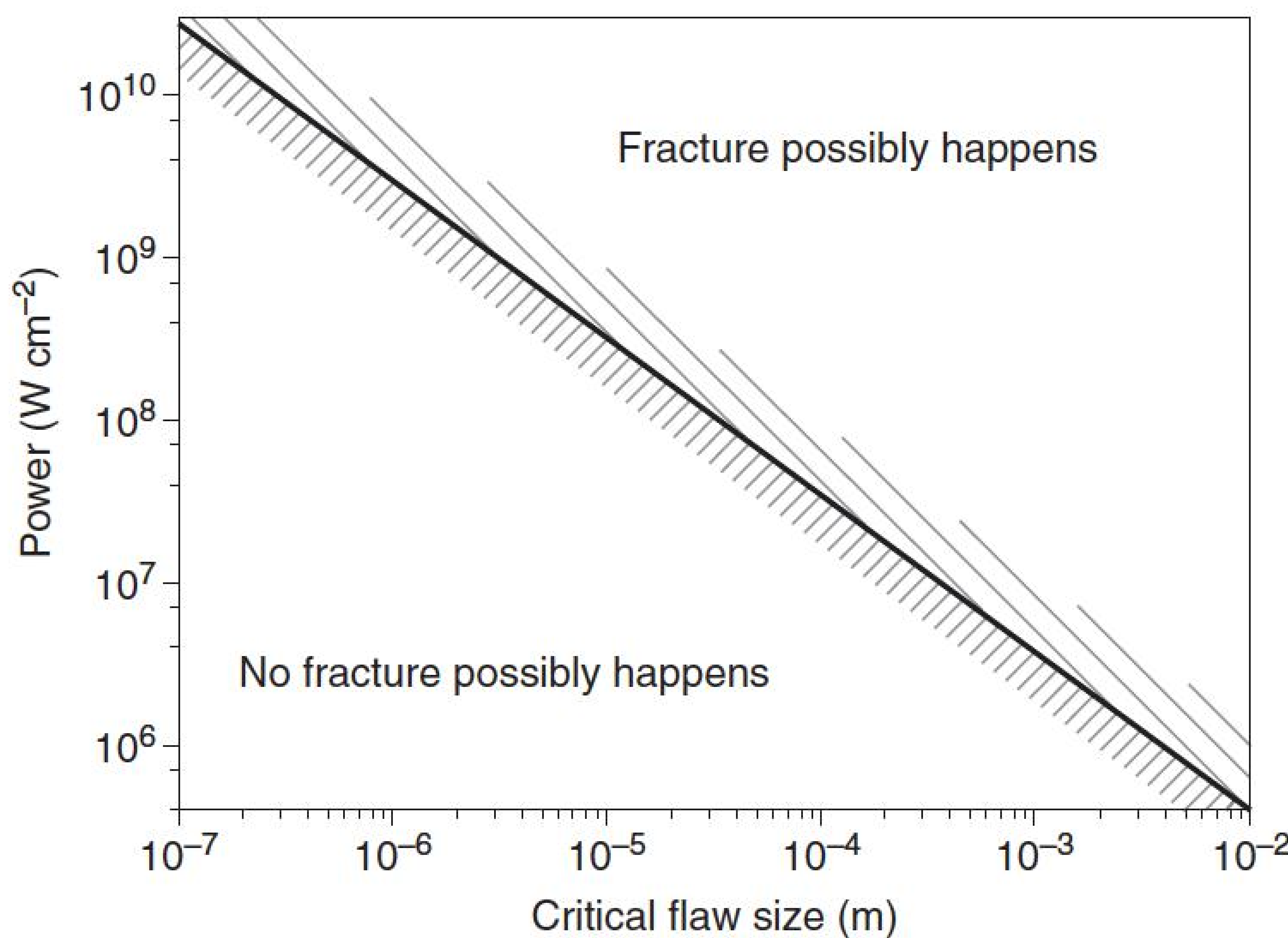


Figure 6.8 Power density vs critical flaw size. The line divides the region where the power is sufficient to activate unstable crack growth from a defect of a given size from the region in which the power is insufficient for unstable crack growth. Source: Adapted from Ahmed et al. [23].

6.4 Simulation of Puncture and Fracture Failures

As with the mechanical failure of ceramics, the failure of varistors appears to be statistical in nature with only a fraction of samples in a batch failing under the same testing conditions, suggesting that failure is related to the presence of defects in the material [17, 27]. The originally intrinsic reason for different failure modes is the nonuniformity of ZnO varistors in the microstructure, and the microstructurally electrical and thermophysical performances, except the applied current waveforms. As discussed in Chapter 5, the microstructure is highly nonuniform, and the electrical properties of grain boundary micro-junctions are not identical [31–38]. A bulk varistor is a complex multijunction device composed of large numbers of both ohmic and nonlinear elements connected in a random network. The overall property of the varistor is then the collective response of all the grain boundaries and depends not only on the boundaries themselves but also on the properties of the grains and their topological arrangement in three dimensions [36]. The influence of the geometry and topology of the granular microstructure, as well as the properties and the distribution of different types of microjunctions on the features of bulk varistor devices, is an important and interesting problem.

A chaotic phenomenon exists in the microstructural characteristics of ZnO varistors [38]. It states that the nonuniformity of microstructural characteristics of ZnO varistors is an original property. This chaotic property leads to the intrinsic behavior of nonuniformity of global electrical characteristics caused by microstructures of ZnO varistors.

Statistical analysis shows that the electrical parameters varies across different ZnO varistors [39]. Even in the same ZnO varistor, electrical parameters in different portions are not uniform. As discussed in Chapter 4, many researchers have measured the distribution of barrier voltages of single grain boundaries in ZnO varistors using different methods; then it is not difficult to understand that the nonuniformity exists in global electrical parameters, such as 1 mA DC voltages (the respective voltage when 1 mA DC current through a ZnO varistor) and the impulse residual voltages among different ZnO varistors or different portions inside a ZnO varistor.

6.4.1 Puncture Destruction Simulation

Eda performed a detailed heat transfer analysis to show that once localized, the current flow could lead to filamentary heating and subsequent localized melting [2]. Vojta and Clarke discussed the possible microstructural origins for such localization and the consequential joule heating using a network model incorporating thermal effects [22]. A similar simulation on a commercial disk-shaped ZnO varistor of 52 mm diameter and 10 mm height was completed using heat conduction analysis by He et al. [12], but the complicated thermal transfer between the sidewall and the surroundings were considered. The heat conduction inside the ZnO varistor and between the sidewall and the surroundings [40], consisting of natural convection and radiation thermal transfer, can be analyzed by the heat conduction theory introduced in Section 5.4.1.

The V—I property of a ZnO varistor could be described by [2]

$$I = A_1 \exp\left(-\frac{E_0 - mV^{1/2}}{K_B T}\right) + A_2\left(\frac{V}{V_{th}}\right)^{\alpha} \tag{6.6}$$

where V is the applied voltage on the ZnO varistor; I is the current through the ZnO varistor; E_0 is the excitation energy of ZnO varistor, $E_0 = 0.8$ eV; K_B the Boltzmann's constant, $K_B = 1.38 \times 10^{-23}$ J K^{-1}; A_1, A_2, and m are constants related to the electrical characteristics of ZnO varistor, $m = 4.5 \times 10^{-22}$ eV$^{1/2}$ [2]; V_{th} is the threshold voltage; and α is the nonlinear coefficient of the varistor. The first part of Eq. (6.6) is the Schottky emission current in the low current region of the ZnO varistor, and the second part is the nonlinear current in the high current region. For the commercial ZnO varistor with 52 mm diameter and 10 mm height, the tested parameters are $A_1 = 3410$ A cm^{-2}; $A_2 = 0.91$ mA cm^{-2}; $\alpha = 39$.

It is supposed that there is a small region with a diameter of 1% D in the center of the varistor, where the threshold voltage is 5% lower than that of other parts of the varistor; the diameter of ZnO varistors is $D = 52$ mm. When different square wave currents are applied to varistors, the small region of low threshold voltage would be punctured after different durations. The temperature distributions at different times are shown in Figure 6.9 when the current through the ZnO varistor is 3 A

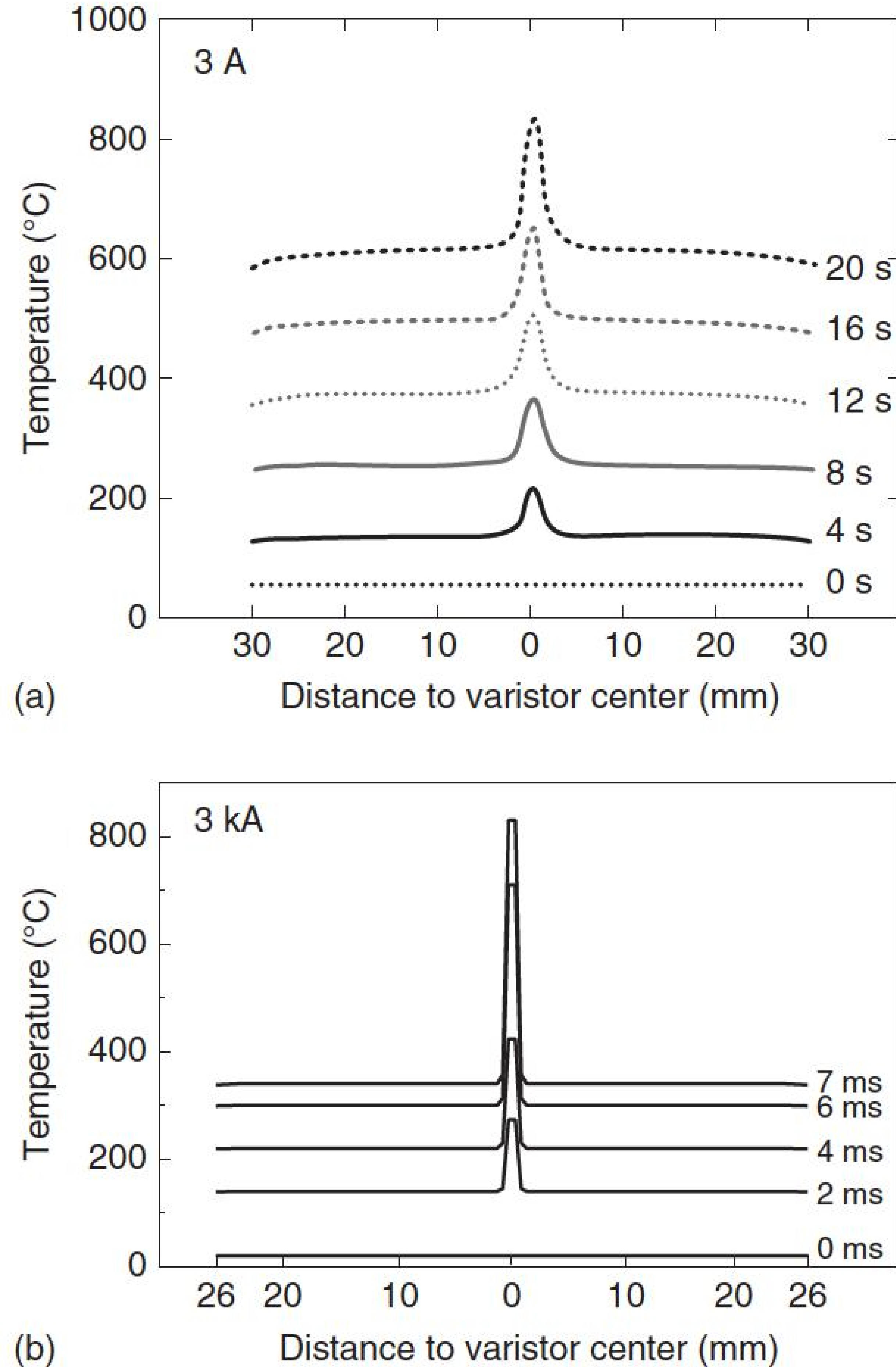


Figure 6.9 The dependence of temperature distributions on time when (a) 3 A and (b) 3 kA square wave current is injected into a ZnO varistor [41].

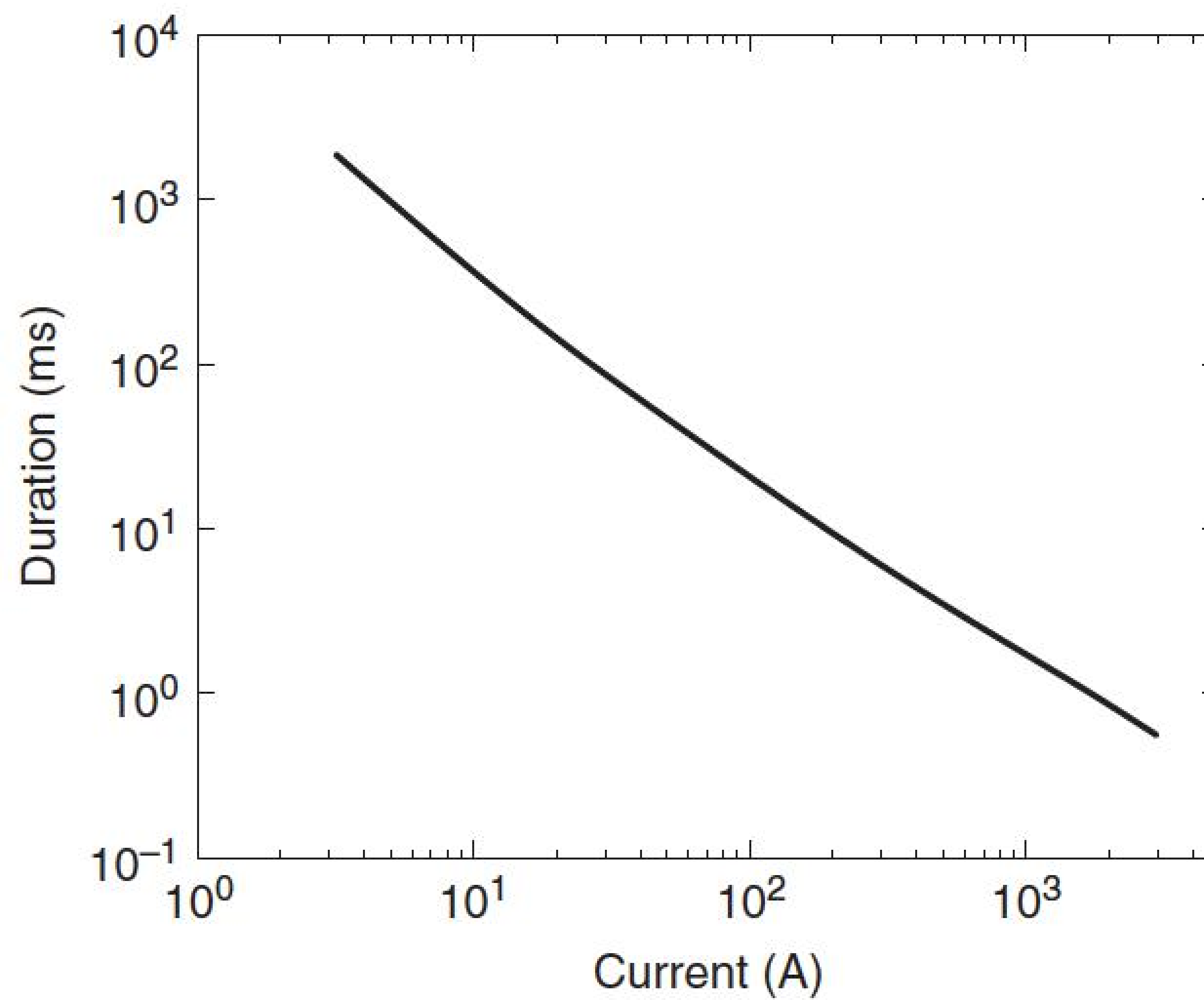


Figure 6.10 The duration t resulting in a puncture destruction [41].

and 3 kA. When 3 kA square wave current is applied, after 7 ms, the temperature of the small area of low threshold voltage exceeds 820 °C, and then it would be melted to form a punctured hole, but if 3 A square wave current is injected, a melted hole will be formed after 20 seconds [41].

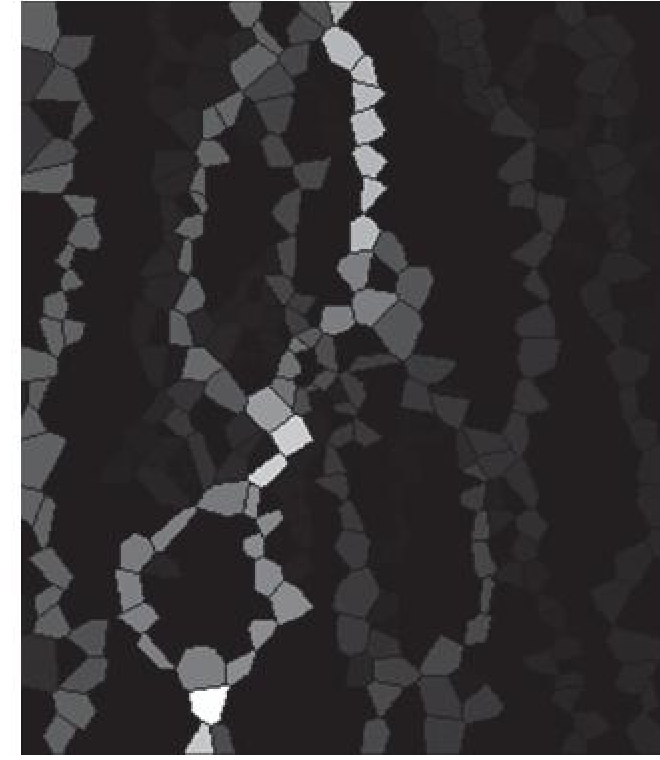
The duration for a punctured hole to be formed respectively for different applied currents is illustrated in Figure 6.10 [41], which increases linearly as the square wave current increases; this means that small currents needs more time to form a hole.

6.4.1.1 Puncture Simulation in Microstructure

Bartkowiak et al. [42] first simulated the puncture and cracking phenomena from the microstructure by Voronoi network as discussed in Chapter 5; their proposed models can be used to simulate the thermomechanical behavior of various types of metal oxide varistor disks and to estimate their energy absorption capability without performing destructive experiments. From the current distribution shown in Figure 6.11, there are only a few paths that carry most of the current within the voltage-sensitive region. For the case, the average voltage gradient applied on ZnO varistor is 2.5 kVcm^{-1} and the average current density is 98.1 A cm^{-2}; three zigzag tunnels, whose currents are much higher than that of the others out of about 30 tunnels, are formed. These three current tunnels carry 44%, 19%, and 12% of the total current, respectively [43]. So, when a high current is injected, or the duration of the applied current increases, the temperature of the current localization path will melt Bi_2O_3 of the grain boundaries to produce puncture failure.

Usually, current distribution is related to the uniformities of the grain size and the electrical character of the grain boundary. As far as nonuniform grain size is concerned, even if the electrical characters of all grain boundaries remain the same, a path with less ZnO grains and grain boundaries will be formed, and then more current flows through this path to produce a punctured hole. When nonuniform electrical characteristics of all grain boundaries are concerned, even if the

Figure 6.11 The current distribution phenomenon inside the microstructure of a ZnO varistor simulated by the Voronoi network model [43]. The light of the color within a polygon represents the current value passing through the grain; the darker the color, the less the current.



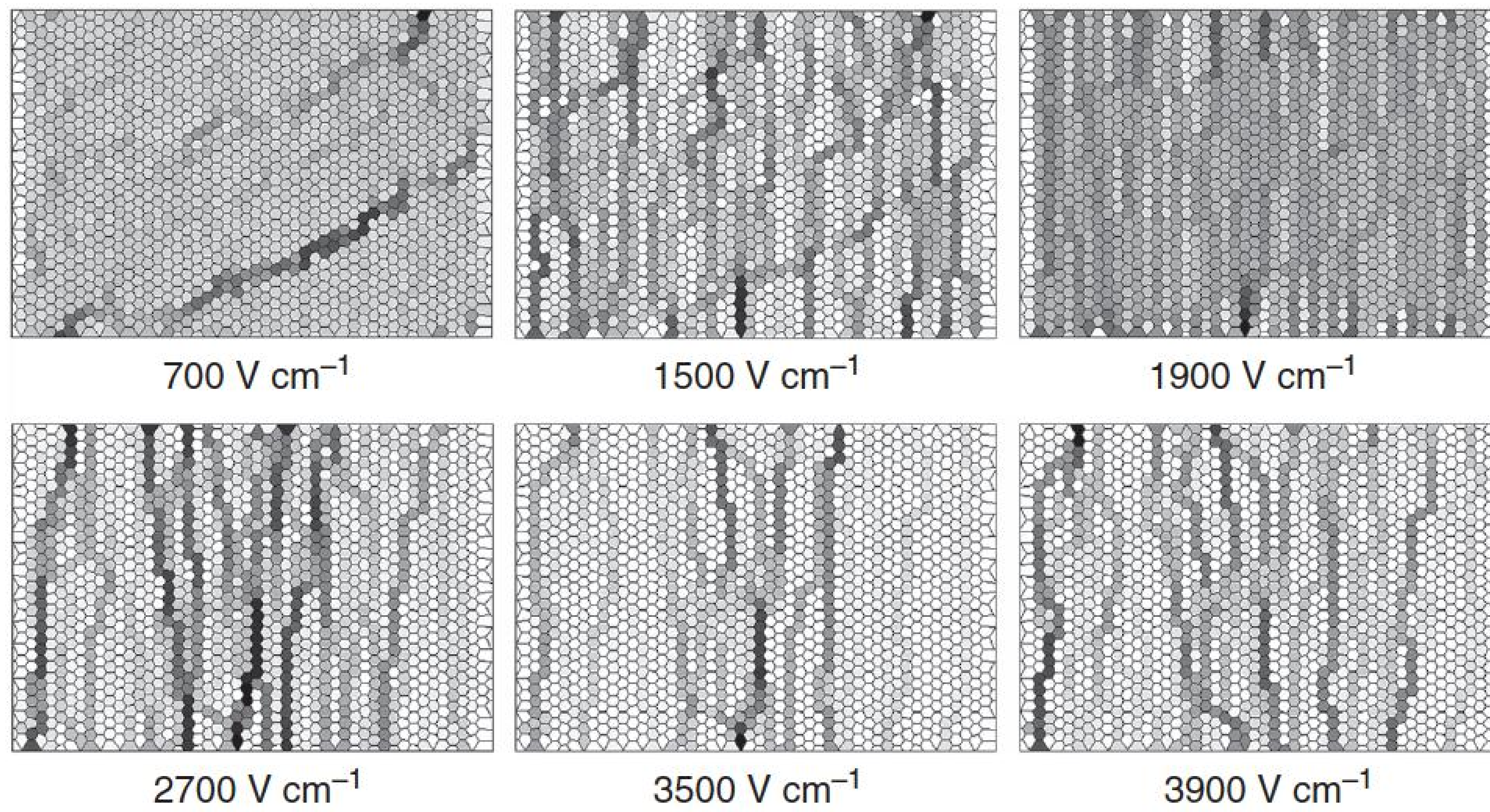


Figure 6.12 The current distribution inside the ZnO varistor under different voltages applied; all ZnO grains have the same regular hexahedron structure [43].

sizes of all ZnO grains are the same, a path with lower residual voltage exists, and more current passes through this path to form puncture failure, too.

Figure 6.12 shows the current distribution inside a ZnO varistor under different voltages applied; all ZnO grains have the same regular hexahedron structure. Only the nonlinear coefficients of all grain boundaries are in a Gaussian distribution; current centralization tunnels are still observed. The current centralization path is very different under different voltages. In the region of the threshold voltage, the current distribution is relatively uniform. In the small current region, the grain boundary with small nonlinear coefficient exhibits a small resistance, so the current centralizes in those paths where the grain boundaries have small nonlinear coefficients. But in the breakdown region, the grain boundary with large nonlinear coefficient exhibits small resistance, so the current centralizes in those paths where the grain boundaries have large nonlinear coefficients. However, in the region of the threshold voltage, the resistances of all grain boundaries are close, so the current distribution is relatively uniform.

Comparing with the current distribution of ZnO varistor with disorderly microstructure in the breakdown region, as shown in Figure 6.30, the current concentration paths in Figure 6.12 are obviously more than those in Figure 6.30, which means that the microstructure has much more influence on the current concentration than the nonlinear coefficient of grain boundary [43].

6.4.2 Cracking Failure Simulation in Microstructure

Using the heat transfer model, the temperature distribution inside ZnO varistors can be calculated following the finite difference method. If the temperatures of two adjacent ZnO grains are T_i and T_j respectively, a thermal stress f_{ij} between them is [44]

$$f_{ij} = \frac{Ya(T_i - T_j)}{1 - \upsilon} \tag{6.7}$$

where Y is the Young's modulus of elasticity, a is the linear expansion coefficient, and υ is the Poisson's ratio. The selected parameters are $a = 4.86 \times 10^{-6}$ °C, $\upsilon = 0.30$, and $Y = 6.9 \times 10^4$ MPa [45]. More detailed description of the simulation can be found in [46].

Figure 6.13 shows a temperature distribution profile of a ZnO varistor [11]. Obviously, the temperature of the region with concentrated current is always much higher than that of other regions. The average temperature rise in this case is 153 K, while the highest temperature rise reaches 376 K and the lowest temperature rise is only 22 K. The temperature profile for the disk and its time evolution allow one to calculate the distribution of thermal stresses and identify the cracking failure mode.

The thermal stress distribution with respect to the temperature distribution in Figure 6.13 is shown in Figure 6.14. The closer the region is to the current concentration path, the tenser the thermal stress is. The highest thermal stress in Figure 6.14 reaches 32 MPa. When the thermal stress exceeds the critical thermal stress f_c, the ZnO varistor ceramics would be cracked into pieces by the thermal stress. Figure 6.15 shows the results of another analysis of the thermal stress [46].

From the simulation it is found that if the microstructure is entirely uniform, a crack will propagate in a planar manner and the fracture energy will be a fixed value. However, if there are spatial variations in the microstructure, for instance,



Figure 6.13 Simulated temperature distribution inside a ZnO varistor. The color lightness of each grain represents its temperature value; the lighter the color, the higher the temperature. Source: He and Hu 2007 [11]. Reproduced with permission of IEEE.



Figure 6.14 Simulated thermal stress distribution inside a ZnO varistor with respect to Figure 6.13. The color lightness represents the value of thermal stress, the darker the color, the higher the thermal stress. Source: He and Hu 2007 [11]. Reproduced with permission of IEEE.

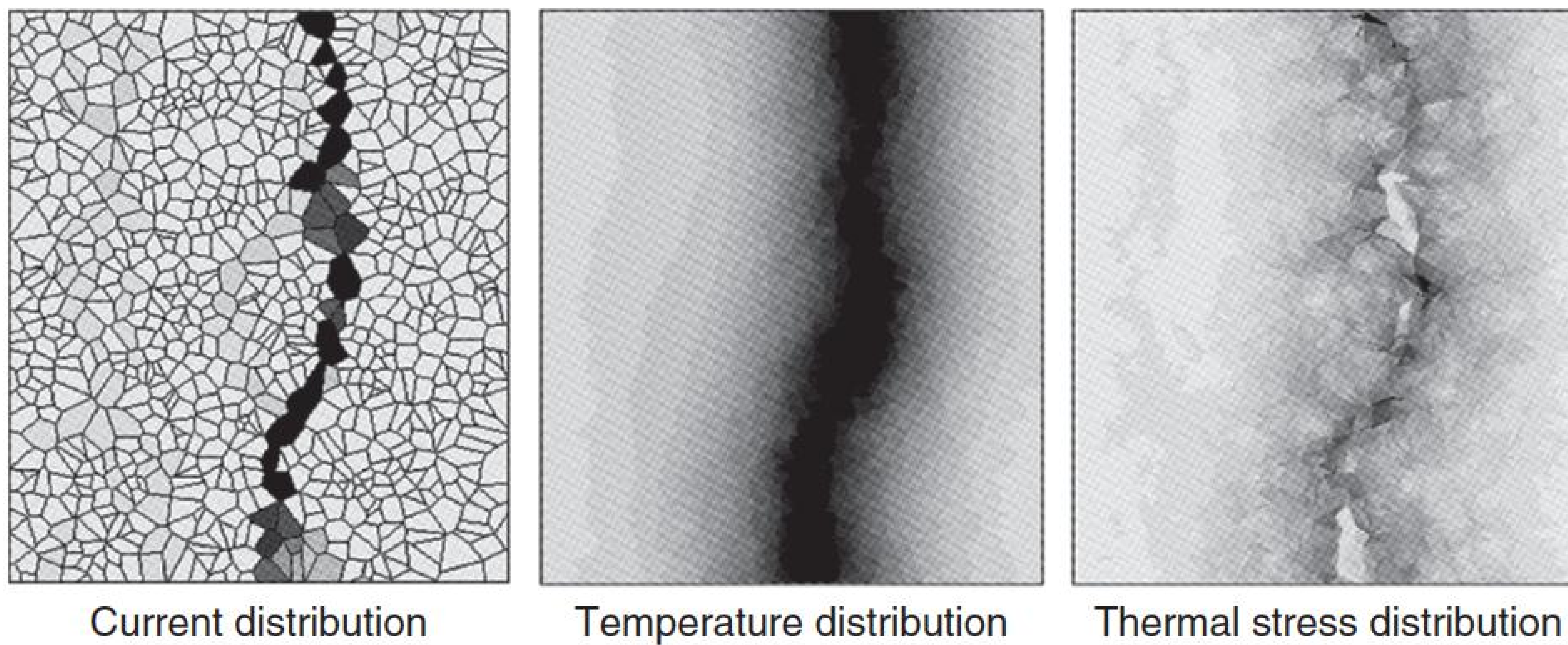


Figure 6.15 The simulated temperature and thermal stress distributions under a current distribution inside a ZnO varistor. Source: Chen et al. 2002 [46]. Reproduced with permission of Springer.

local stress-induced microcracking or randomly oriented grain boundaries with a distribution of fracture energies, the propagating crack is not planar and the fracture energy depends on the microstructure. This is the basis for the microstructure design of many structural ceramics [17].

6.5 Thermal Runaway

ZnO varistors have been widely applied in power systems, which work as surge arresters in porcelain or polymer houses. When the arrester operates in power systems, ZnO varistors must withstand the effects of AC or DC operating voltage and lightning and switching overvoltages. Whether ZnO varistors inside the arrester operate well depends on their thermal characteristics. When a surge arrester absorbs the energy of lightning or switching overvoltage, the temperature of the ZnO varistor inside the arrester increases. If the arrester cannot quickly disperse the absorbed energy into the ambient, then the temperature of ZnO varistors would exceed their limited operating temperature, and the ZnO varistors would break down; this is called thermal runaway or thermal breakdown. So the arrester should not only operate stably under the operating voltage but also

have the ability to maintain transient thermal stability; then ZnO varistors will recover to stable operating state from the temperature rise caused by overvoltage energy. The thermal properties of ZnO surge arresters were widely studied by many researchers [28, 47–50]. Lat calculated the thermal performance of an arrester by a simple equivalent thermal circuit method [49, 50] and He et al. did simulation by finite element method (FEM) [40].

6.5.1 Power Loss of ZnO Varistor

The power loss characteristics of ZnO varistors, which decide their operating reliabilities and their life spans, are fundamental to analyzing the thermal characteristics and stability of ZnO varistors and surge arresters.

The power loss characteristics of ZnO varistors, studied by He et al. [40, 51], were measured from commercial ring-shaped ZnO varistors with a diameter of 71 mm and an inner diameter of 26 mm, and thickness of 20 mm, for 110 and 220 kV surge arresters; as shown in Figure 6.16, the applied voltage ratio q is defined as the ratio of the maximum value U_{max} of applied voltage divided by 1 mA DC voltage, U_{1mA}, of the tested ZnO varistor. The power loss of ZnO varistors is a complicated function of applied voltage ratio and temperature, which can be fitted by an artificial neural network (ANN) [40]; the ANN consists of an input layer, hidden layers, and an output layer [52]. The applied voltage and temperature are the input layers and the power loss is the output layer.

6.5.2 Thermal Runaway Mechanism

Thermal runaway is caused by the failure of thermal balance between the power loss P of ZnO varistors and their heat dispersion capability Q to the ambient. The thermal stability of a ZnO varistor can be analyzed by the thermal balance diagram, as shown in Figure 6.17 [41]. When the temperature of ZnO varistors exceeds the limited operating temperature, the ZnO varistor would fail. The difference between the operating temperature and the limited one is

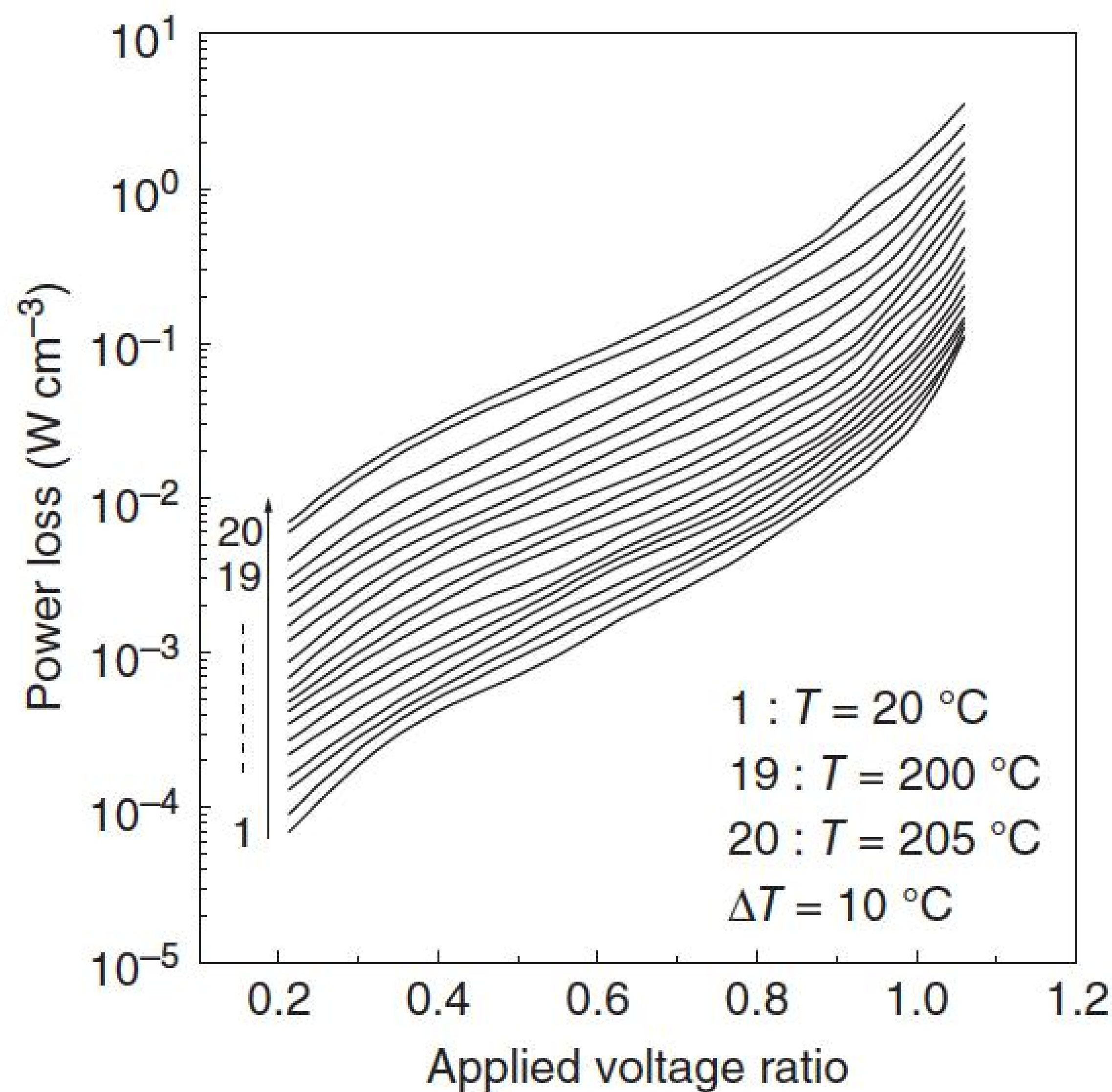


Figure 6.16 The tested relationship between the power loss and the applied voltage ratio. Source: He et al. 2003 [40]. Reproduced with permission of IEEE.

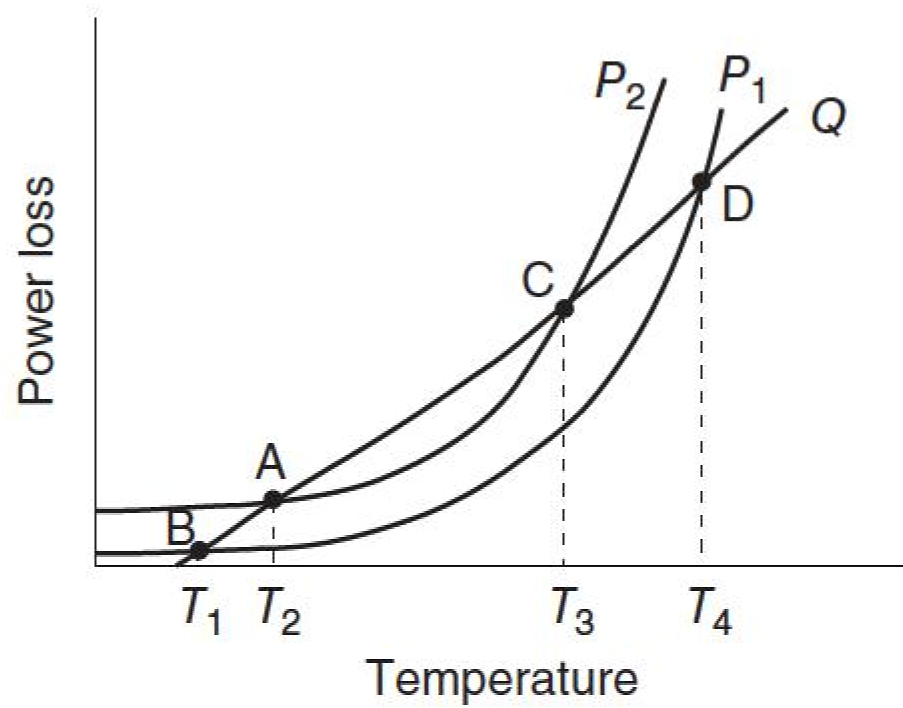


Figure 6.17 The thermal balance diagram. Q is the thermal power loss of varistors to environment at fixed ambient temperature; P_1 and P_2 are the power losses at different applied voltage ratio q_1 and q_2, respectively, and $q_2 > q_1$. Curves P and Q have two crosspoints; A and B are the stable operating points, T_1 and T_2 are the respective operating temperatures, and C and D the limited operating points, and T_3 and T_4 are the respective limited operating temperatures. Source: He et al. 2003 [40]. Reproduced with permission of IEEE.

used to measure the thermal stability of ZnO varistors or surge arresters. The temperature difference at q_2 is less than that at q_1, that is to say, the ZnO varistor operating under low voltage (small q) has a better thermal stability than that operating under high voltage (large q).

When ZnO varistors inside surge arresters absorb an energy E of lightning or switching overvoltage, their temperature increases. If ZnO varistors operate at q_2, the temperature would exceed the limited temperature T_3, and the varistors would be thermally destroyed. But if the varistors operate at q_1, then the respective temperature would not exceed the limited temperature T_4, and the temperature of varistors can go back to the operating temperature T_1. Figure 6.18 is an example of the thermal balance diagram of ZnO varistors inside a 220 kV surge arrester with polymer housing [40].

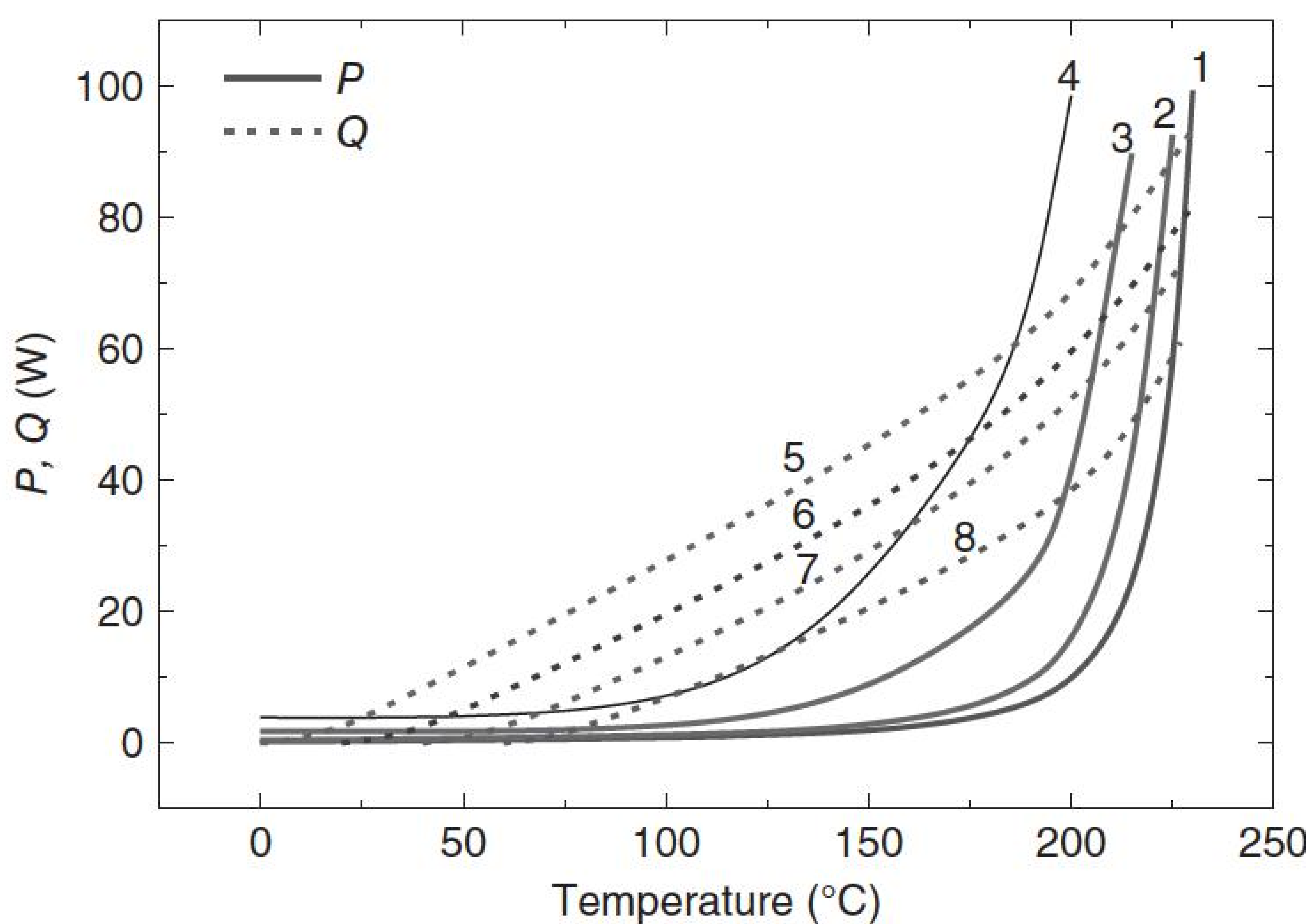


Figure 6.18 The thermal balance diagram of a ZnO surge arrester (1, $q = 0.7$; 2, $q = 0.8$; 3, $q = 0.9$; 4, $q = 1.0$; 5, $T_a = 0\,°C$; 6, $T_a = 20\,°C$; 7, $T_a = 40\,°C$; 8, $T_a = 60\,°C$). Source: He et al. 2003 [40]. Reproduced with permission of IEEE.

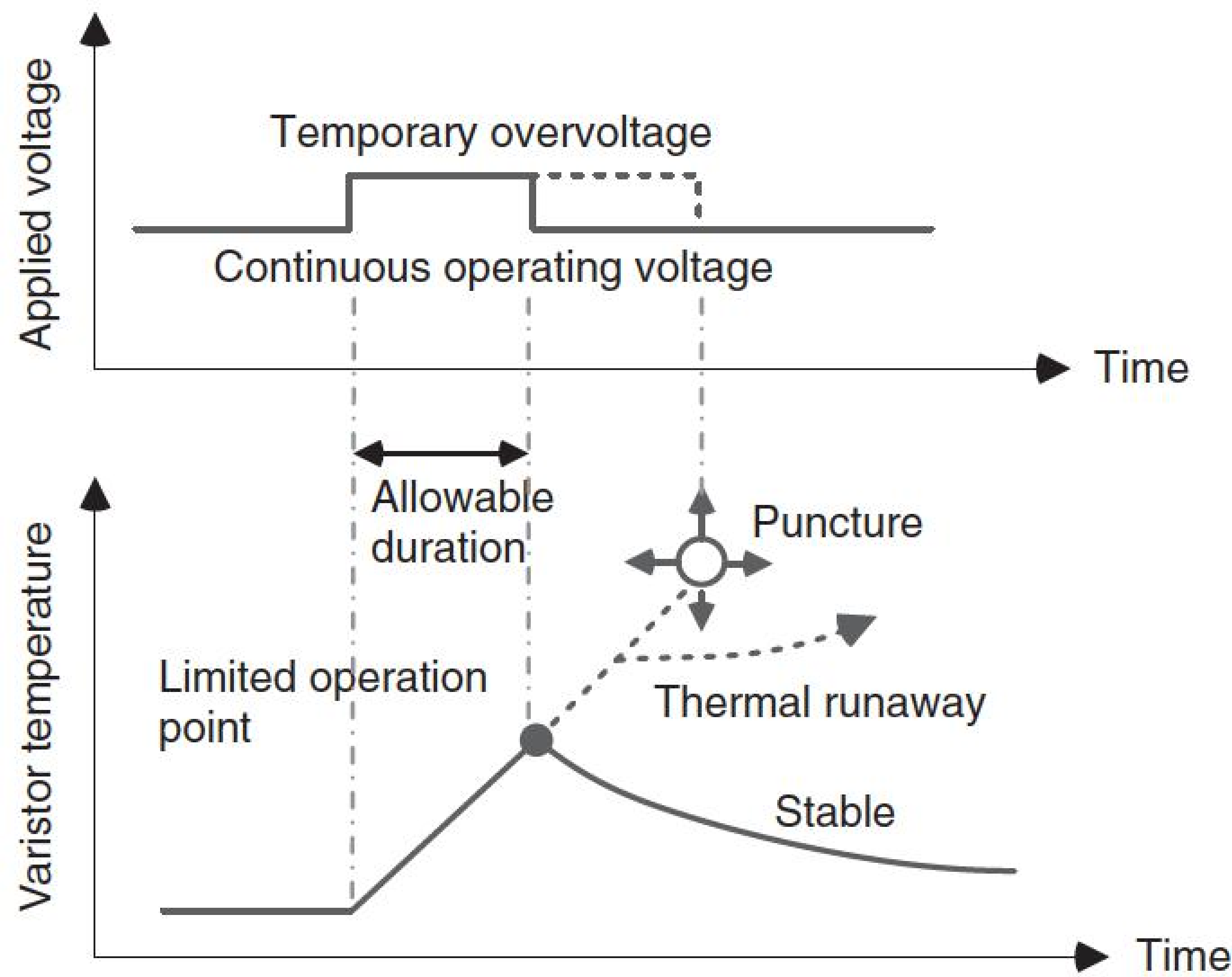


Figure 6.19 The limited operation point of ZnO varistors inside a surge arrester. Source: Mizukoshi et al. 1983 [8]. Reproduced with permission of IEEE.

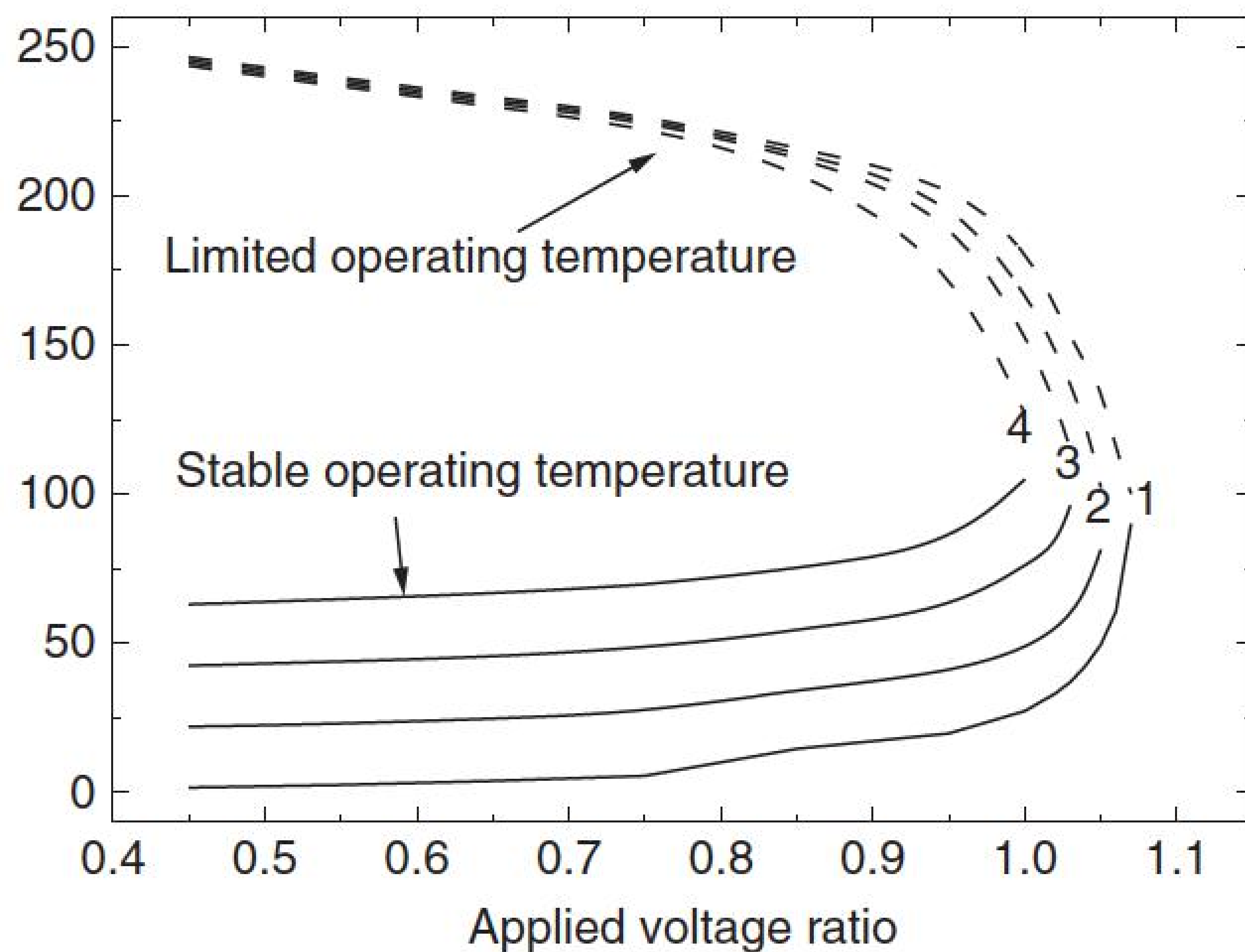


Figure 6.20 The stable and limited operating temperatures of ZnO varistors inside a 220 kV surge arrester of polymer housing (1, $T_a = 0\,°C$; 2, $T_a = 20\,°C$; 3, $T_a = 40\,°C$; 4, $T_a = 60\,°C$). Source: He et al. 2003 [40]. Reproduced with permission of IEEE.

The energy absorption capability of ZnO varistors is related to the environmental temperature and the limited operating temperature. The allowable energy absorption of the ZnO varistors should be less than the puncture energy and within the range of element temperature stability. As illustrated in Figure 6.19 [8], when the temporary overvoltage is applied, the duration should be less than the respective value of the limited operation point. If the duration exceeds this value, then the ZnO varistors will run away and further produce puncture breakdown.

The calculated stable operating temperature of ZnO varistors inside a 220 kV surge arrester of polymer housing is illustrated in Figure 6.20 [40]. The difference between the limited and stable operating temperatures under ambient temperature is defined as the rise in limited temperature, which decides the limited energy permitted to be absorbed by the ZnO varistors. If the energy absorbed by the ZnO varistors exceeds this limited one, the temperature of the ZnO varistors would

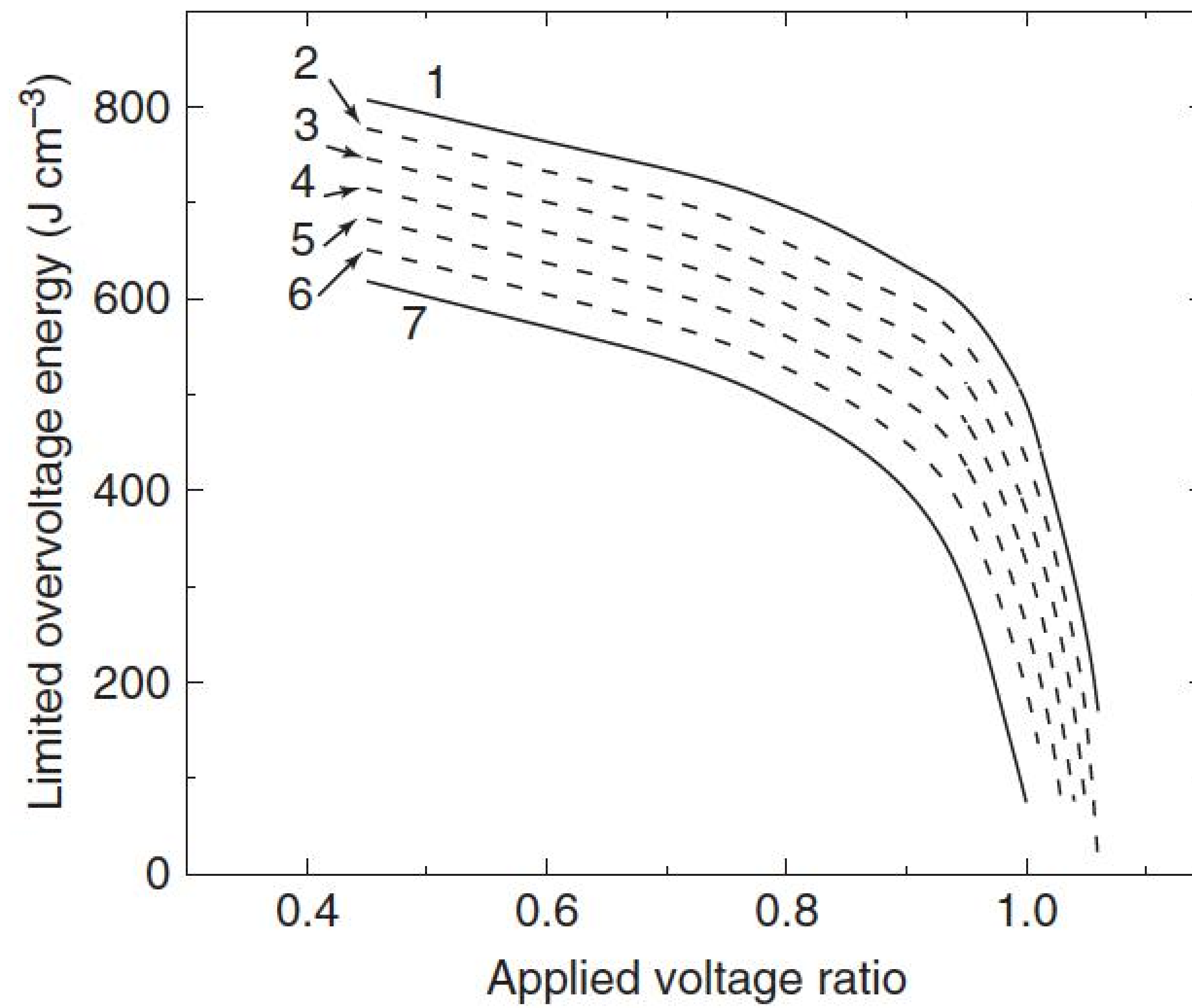


Figure 6.21 The relationship between the limited overvoltage energy permitted to be absorbed by ZnO varistors inside 220 kV polymeric surge arrester and the applied voltage ratio under different environmental temperature (1, $T_a = 0\,°C$; 2, $T_a = 10\,°C$; 3, $T_a = 20\,°C$; 4, $T_a = 30\,°C$; 5, $T_a = 40\,°C$; 6, $T_a = 50\,°C$; 7, $T_a = 60\,°C$). Source: He et al. [40]. Reproduced with permission of IEEE.

exceed the limited operating temperature, and then thermally fail. The calculated limited overvoltage energies under different applied voltage ratios and different environmental temperatures are shown in Figure 6.21 [40].

6.5.3 Tests to Ensure the Thermal Stability Characteristics

The concept that a surge arrester with ZnO varistors as the core elements has a limited operating temperature below which failure does not occur has led to the routine use of a variety of proof tests as quality control tools. One such test is to subject the varistor to a succession of electrical impulses and determine whether any increase, above a specified level, in the leakage current has occurred. Another such test is to assess the energy absorption capability by recording the time taken to failure under a constant current load [17]. The respective tests include duty cycle test and TOV (transient overvoltage) test.

6.6 Influences of Different Factors on Failures of ZnO Varistors

6.6.1 Influence of Microstructural Nonuniformity

Many works had been done on the simulation of different factors on failures of ZnO varistors [53]. The disorder degree d is used to simulate the nonuniformity of ZnO varistor microstructure; if the disorder degree is zero, the microstructure of ZnO varistor is uniform. With increment in the disorder degree, the microstructure of the ZnO varistor becomes more nonuniform. When the disorder degree is larger than 3, the generated Voronoi network is very similar to actual microstructures of ZnO varistors.

Figure 6.22 describes the current localization ratio (J_{max}/J_{av}) of ZnO varistors (the average grain size $s = 15\ \mu m$) under the same voltage [11], which is defined to represent the diversity of the current localization phenomenon, where J_{max} is

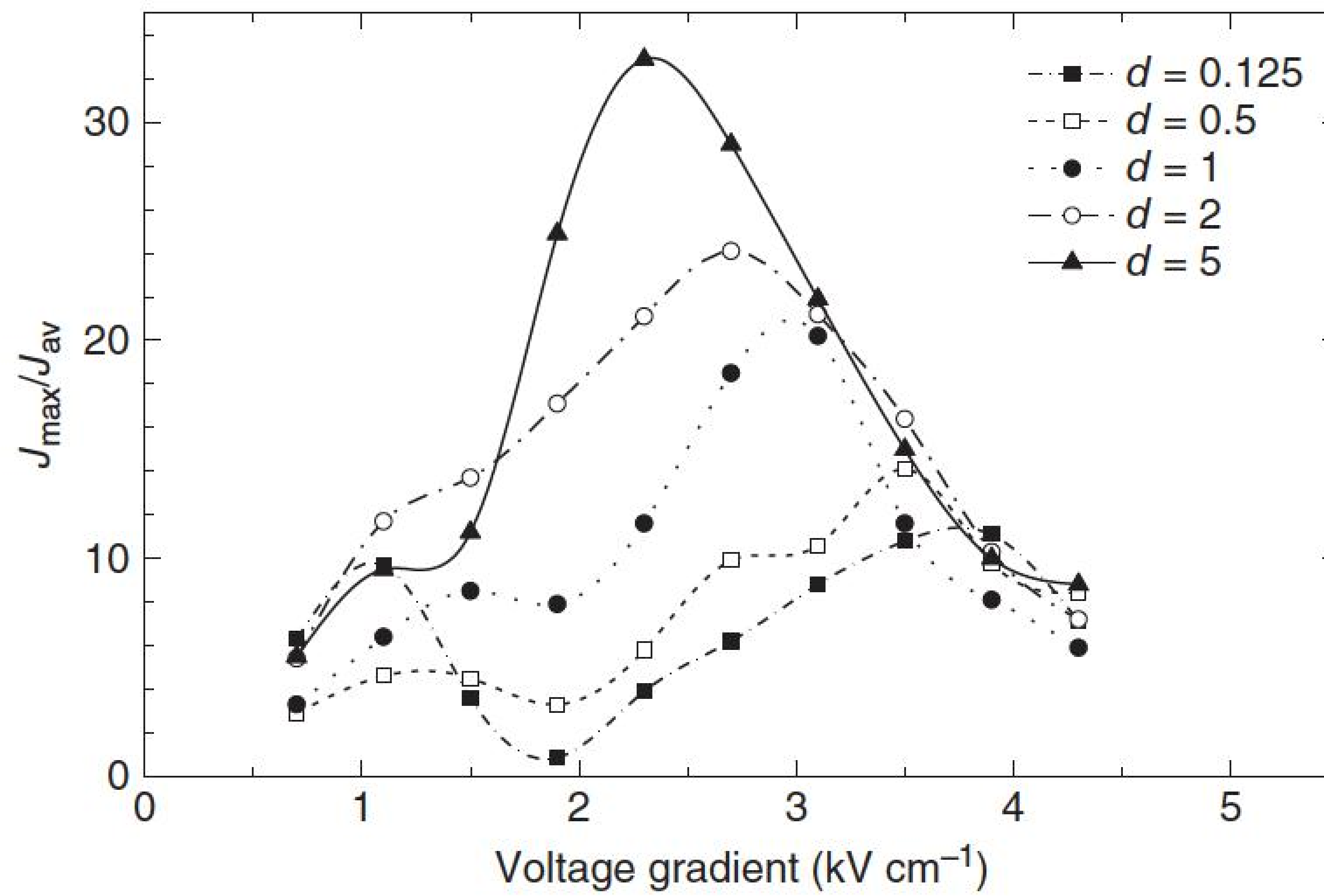


Figure 6.22 Current localization ratios of ZnO varistors of various disorder degrees. Source: He and Hu 2007 [11]. Reproduced with permission of IEEE.

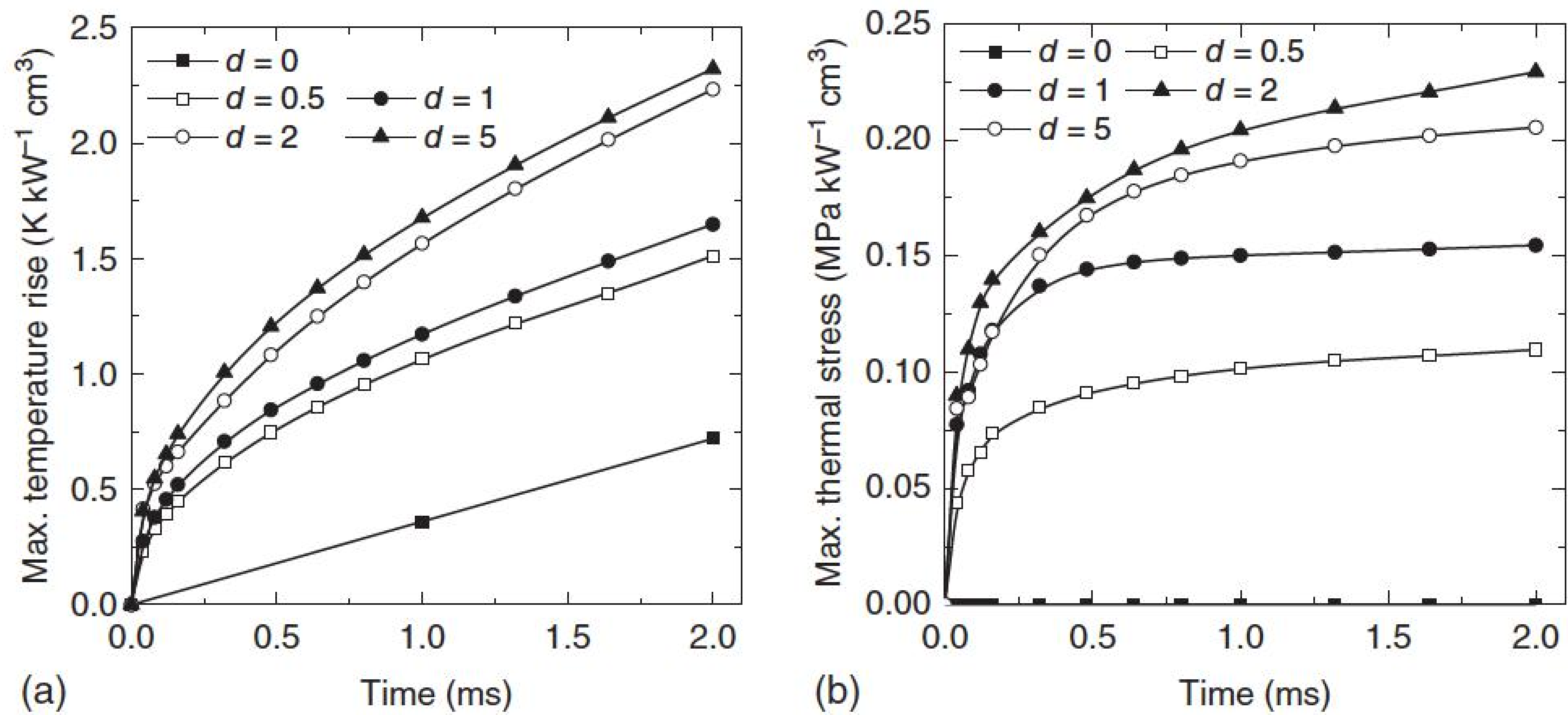


Figure 6.23 (a) The maximum temperature rise and (b) the maximum thermal stress of ZnO varistors with different disorder parameters. Source: He and Hu 2006 [54]. Reproduced with permission of IEEE.

the maximum of current density J inside the ZnO varistor and J_{av} is the average value of J.

With the increment of the disorder degree, the current concentration phenomenon becomes more serious. When the ZnO varistor is uniform (the disorder degree $d = 0.125$), the respective current localization ratio J_{max}/J_{av} is about 11, while it reaches about 33 when the disorder degree is 5. Both the maximum temperature rise and the maximum thermal stress increase with the increment of disorder degree as shown in Figure 6.23 [54].

If the current is absolutely uniform and therefore the heat source is even, there should be no temperature difference and no thermal stress within the microstructure of the ZnO varistor. It can be deduced that the temperature rise should be uniform and increase linearly with time at a speed of

0.36 K kW^{-1} cm^3 ms^{-1}. When d = 0, the concentration degree of current is relatively uniform in the microstructure of ZnO varistor ceramics, so the maximum temperature rise ΔT_{max} also increases linearly with the duration at a speed of about 0.375 K kW^{-1} cm^3 ms^{-1}, which is very close to the case with an absolute uniform distribution of current. After 2 ms, ΔT_{max} grows from 0.75 to about 2.5 K kW^{-1} cm^3 ms^{-1} (increasing about 3 times) when d increases from 0 to 5 and the maximum thermal stress F_{max} increases from 0.02 to about 0.3 MPa kW^{-1} cm^3 (increasing about 15 times). With increase in time, F_{max} tends to reach a saturation value, and the increasing speed of ΔT_{max} reaches 0.36 K kW^{-1} cm^3 ms^{-1}, which shows that the temperature difference within the ceramics reaches a steady status. The more concentrated the current, the longer the time for the temperature difference to reach a steady status.

So, the more nonuniform the microstructure of the ZnO varistor is, the more serious the current localization is, which means that puncture or cracking breakdown occurs easily in the ZnO varistors. In the meantime, the respective energy absorption capability would be smaller.

Besides current distribution, the distributions of temperature and thermal stress within the microstructures of ZnO varistor ceramics are affected by the condition of heat transfer, which is determined by the following two factors: thermal conductivity, and the cooling area and distance within the ceramic. The thermal conductivity of a fixed material is a constant for ZnO varistor ceramics. The cooling area and distance are related to the ZnO grain size beside the current distribution. The cooling area increases and the distance reduces with decrease in average grain size, thus reducing the time constant for the heat transfer and accelerating heat transfer in ZnO ceramics. The influence of ZnO grain size on the distributions of the maximum temperature rise ΔT_{max} and the maximum thermal stress F_{max} on the model with the disorder parameter d = 5 are shown in Figure 6.24 [54]. ΔT_{max} and F_{max} increase with duration; at the time of 2 ms, ΔT_{max} reaches 1 K kW^{-1} cm^3 when the average grain size s = 6 μm and F_{max} reaches 0.05 MPa kW^{-1} cm^3 ms^{-1}. When s is more than 6 μm,

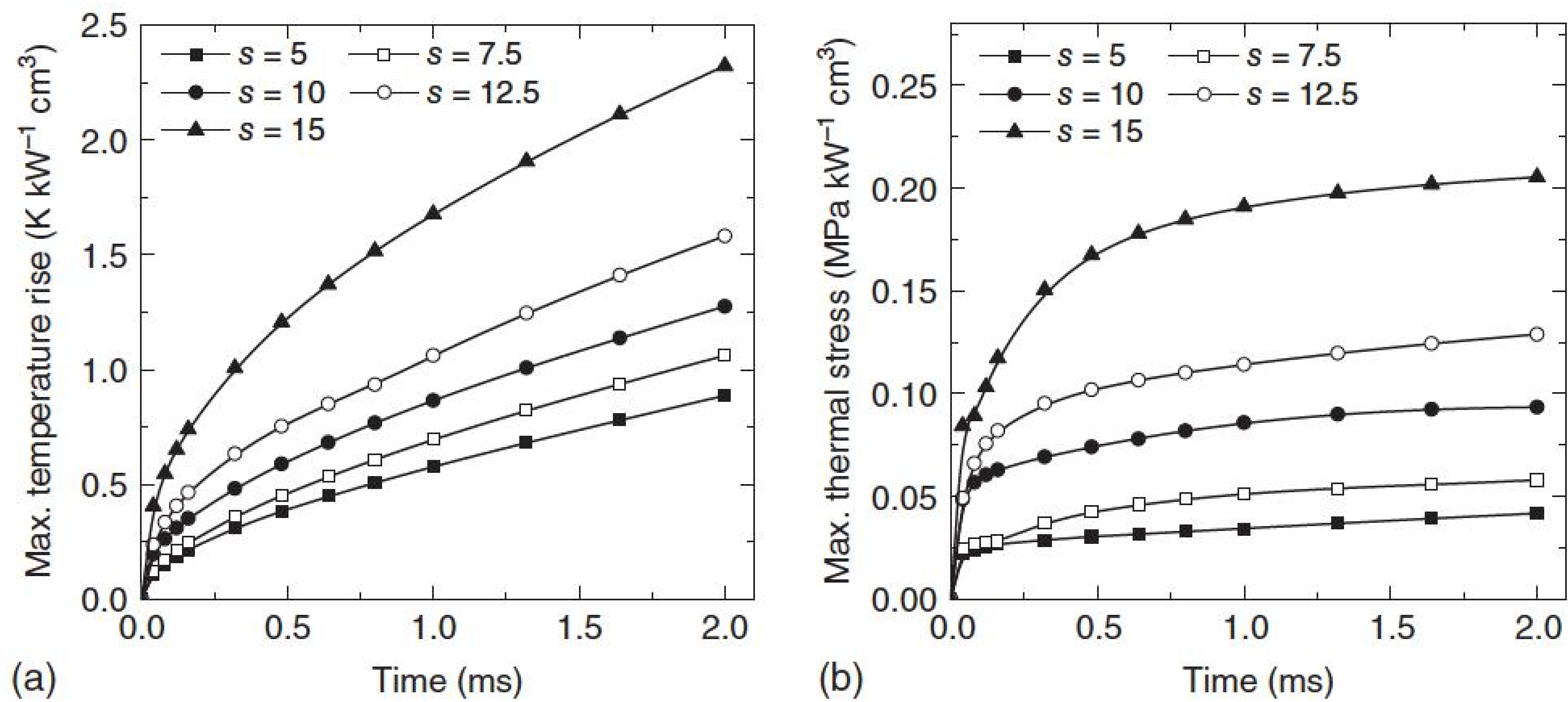


Figure 6.24 (a) The maximum temperature rise and (b) the maximum thermal stress of ZnO varistors with different grain sizes. Source: He et al. 2006 [54]. Reproduced with permission of IEEE.

ΔT_{max} increases at a speed of 0.16 K kW^{-1} cm^3 ms^{-1}, and F_{max} increases at a speed of 0.035 MPa kW^{-1} cm^3 ms^{-1}. The temperature difference and the thermal stress greatly decrease when the average size of the ZnO grain decreases, thus improving the surge energy adsorption capability of ZnO varistor ceramics.

As studied by Bartkowiak et al. [42], puncture is the dominating failure mode for only slightly nonuniform disks, but cracking becomes more likely as the degree of nonuniformity increases. Usually, it is focused on the improvement of the uniformity of the microstructure in order to increase the surge energy adsorption capability, but due to the limitation of the fabrication technology, it is very difficult to achieve good results, while decreasing the average size of ZnO grain is more feasible and effective.

6.6.2 Influence of Electrical Nonuniformity in Microstructure

Another metric that accounts for the nonuniformity of ZnO varistor in microstructure is the nonuniformity of the electrical characteristics of grain boundaries. One of the important parameters in the physical models of ZnO varistors explaining the transition phenomenon from the low current region to the high current region is the value of the barrier voltage, which refers to the breakdown voltage per grain boundary barrier. As discussed in [55], the barrier voltage has a normal distribution, and its average value by direct measures is 3.3 V. When the standard deviation of the barrier voltage is changed, Figure 6.25 shows the current localization ratios of ZnO varistors with distributed barrier voltage variances under the same applied voltage [54]. As the standard deviation of the barrier voltage, ΔV_B, increases, J_{max}/J_{av} rises. When ΔV_B is 1.6 V, J_{max}/J_{av} reaches about 30, so the current localization is very severe, and the varistor would fail easily; then the energy absorption capability would be small.

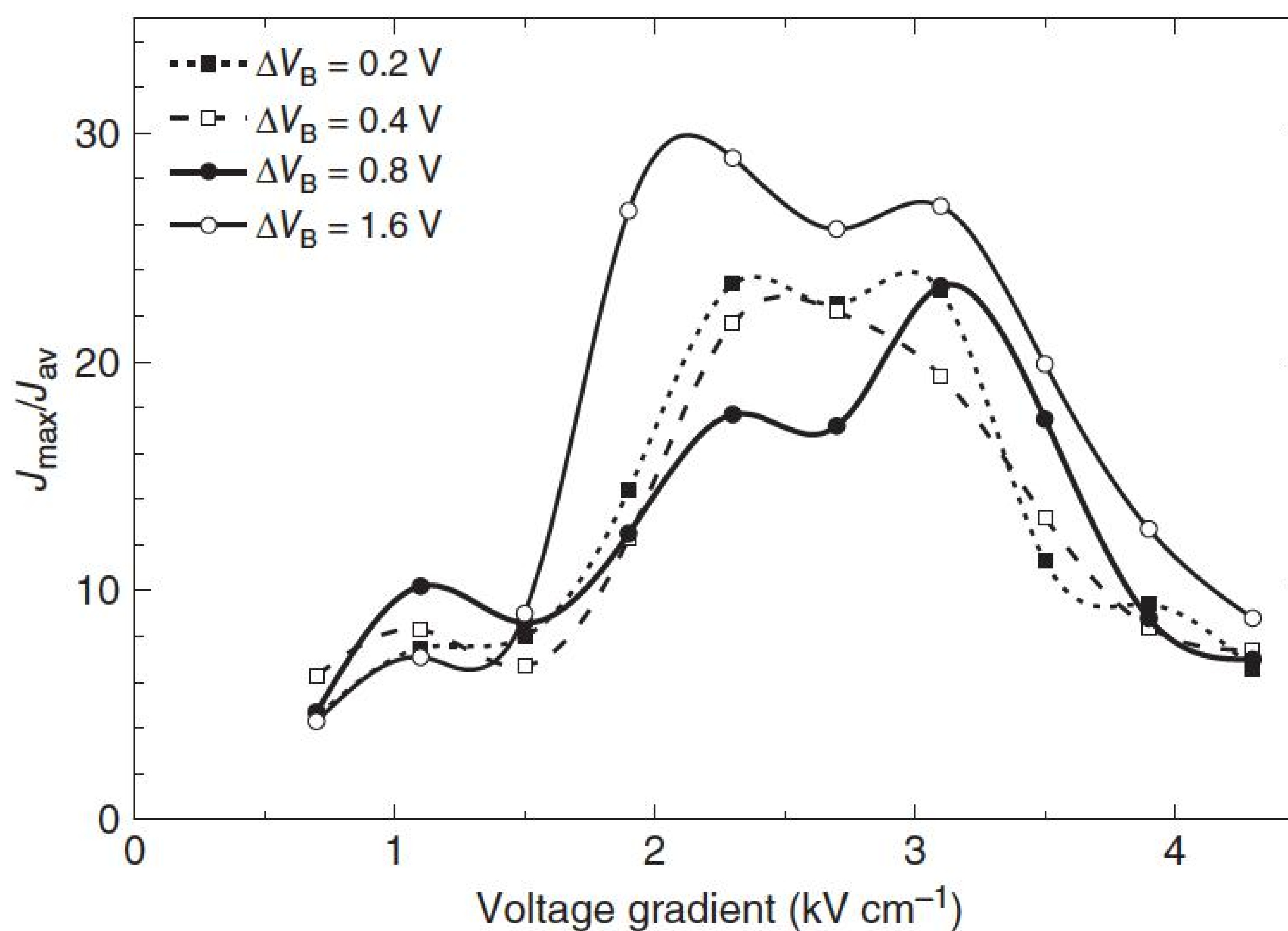


Figure 6.25 Current localization ratios of ZnO varistors with distributed barrier voltage varied. Source: He et al. 2006 [54]. Reproduced with permission of IEEE.

6.6.3 Simulation Analysis on Breakdown Modes

In order to judge what type of damage first occurs, the average temperature rise, the highest temperature rise, and the maximum thermal stress are divided by the criteria of thermal runaway, puncture, or cracking, which are selected as 180 °C, 800 °C, and 40 MPa, respectively. Figure 6.26 shows the changes of the highest temperature rise, the average temperature rise, and the maximum thermal stress of a simulated ZnO varistor as the time increases, in the case with average current density $J_{av}(t) = 98.1\ \text{A cm}^{-2}$ and average thermal stress $F_{av}(t) = 2.5\ \text{kV cm}^{-1}$. The average temperature rise has a linear relationship with time, the rising speed of the highest temperature, and the maximum thermal stress decrease with time. The maximum thermal stress has an obvious saturation phenomenon and reaches a steady state as the time increases. If a continuous operating voltage is applied on the ZnO varistor while such a surge energy is absorbed, the ZnO varistor will be damaged by cracking and thermal runaway, while puncture damage will not occur.

When the current with the same density is applied, the maximum thermal stress inside the ZnO varistor of average grain size $s = 7.5$ μm is higher than that of average grain size 15 μm. The highest temperature of the ZnO varistor whose average grain size is 7.5 μm is higher than that of the ZnO varistor whose average grain size is 15 μm only after 500 μs, but even after 2000 μs the difference is not more than 30%. The result indicates that the impulse energy absorption capability will be improved by 0.54 times when the average size of ZnO grain halves. So surge energy absorption capability can be notably improved by decreasing the mean value of grain size.

But if a continuous operating voltage is not applied on the ZnO varistor while only an impulse voltage is applied, the result will be different. Figure 6.27 shows the curves of the maximum tolerant time when a single square wave current is injected; it can be concluded that the ZnO varistor is more likely damaged by

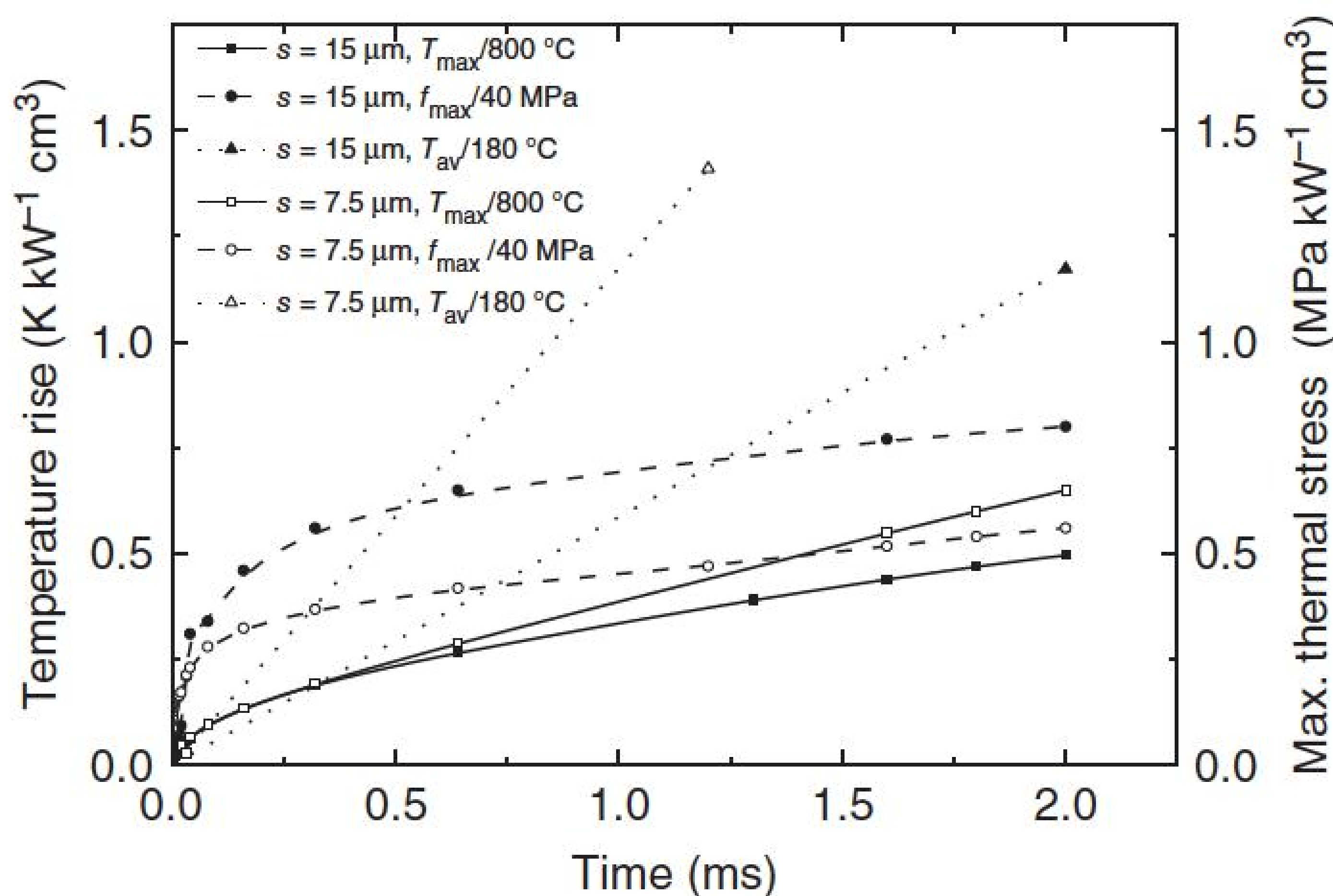


Figure 6.26 The curves of temperature rise and thermal stress of a ZnO varistor as the time increases when a continuous operating voltage is applied.

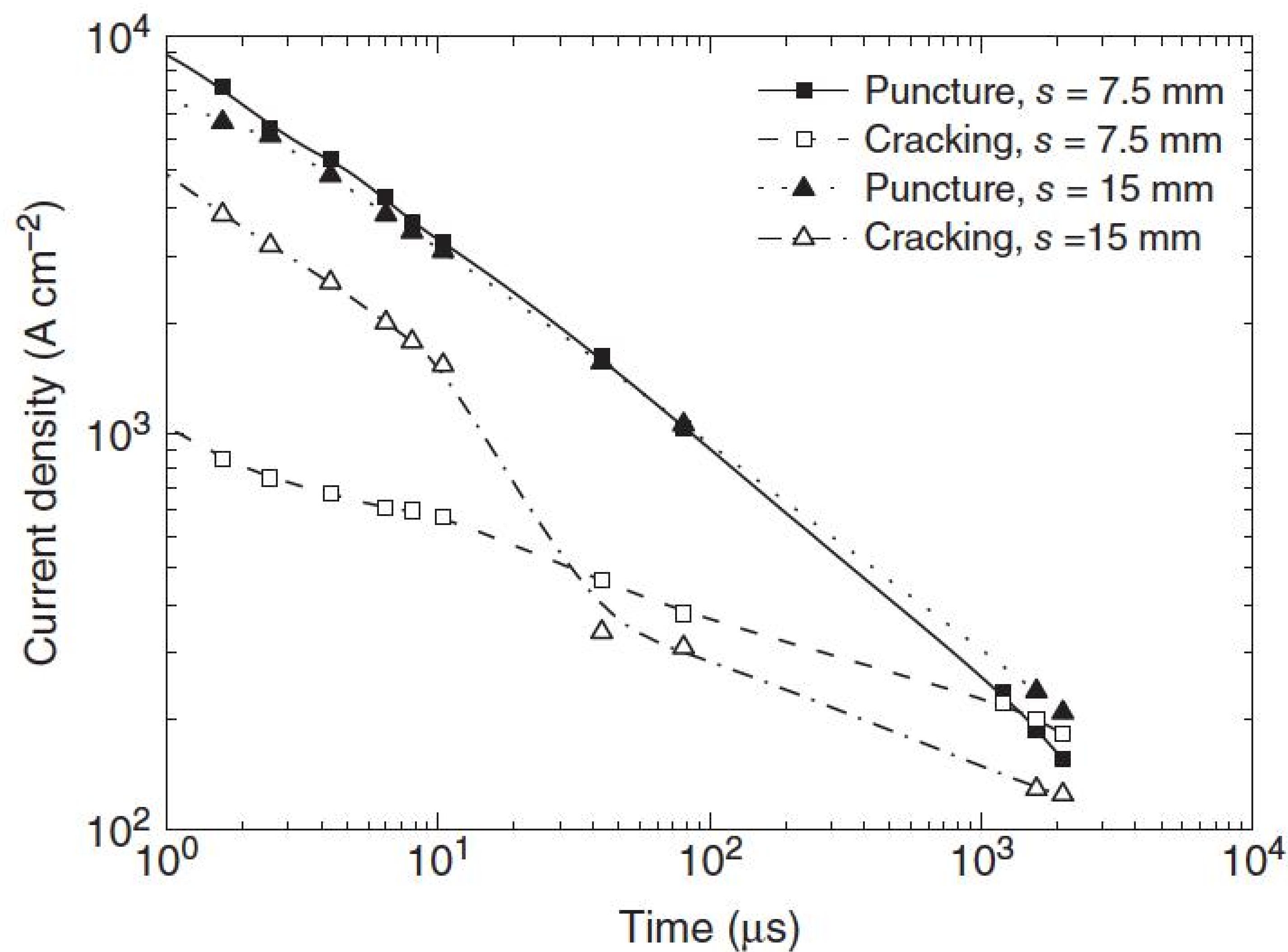


Figure 6.27 Energy absorption capability of ZnO varistors with a single square wave current applied.

cracking when suffering higher current density, but suffers melting puncture at lower current density. The smaller the grains are, the easier the ZnO varistor is damaged by melting puncture.

6.7 Influential Factors on Energy Absorption Capability

6.7.1 Influence of the Applied Current

In the experiments introduced in Section 6.2, the energy absorption capability was estimated, which is directly related to the current waveforms; the relationship between the energy absorption capability and the duration of applied current is plotted in Figure 6.28 [11], which appears as a U-shaped curve. The black line indicates the average values of experiments under the same condition, and the dotted lines indicate the respective upper and lower bounds. The energy absorption capability reaches its minimum when the pulse duration is about 1 ms. If the duration is less than this pulse duration, the energy absorption capability decreases as the duration increases, and when the duration is longer than this pulse duration, the energy absorption capability increases continuously.

The energy absorption capability of ZnO varistors has a complex dependence upon the peak and the duration of the impulse current applied. A similar result was discussed by Sakshaug et al. [3]; the energy absorption capability decreased with the increment of current, and then increased again if the current became very high and the impulse duration became very short.

Besides, the relationship between the energy absorption capability and the current density is shown in Figure 6.29 [11], which shows U-shaped behavior as well. When a small current is applied for a long time, the energy absorption capability is very high. Under such conditions, the heat produced in one portion of the varistor could be uniformly conducted to the whole varistor, so the

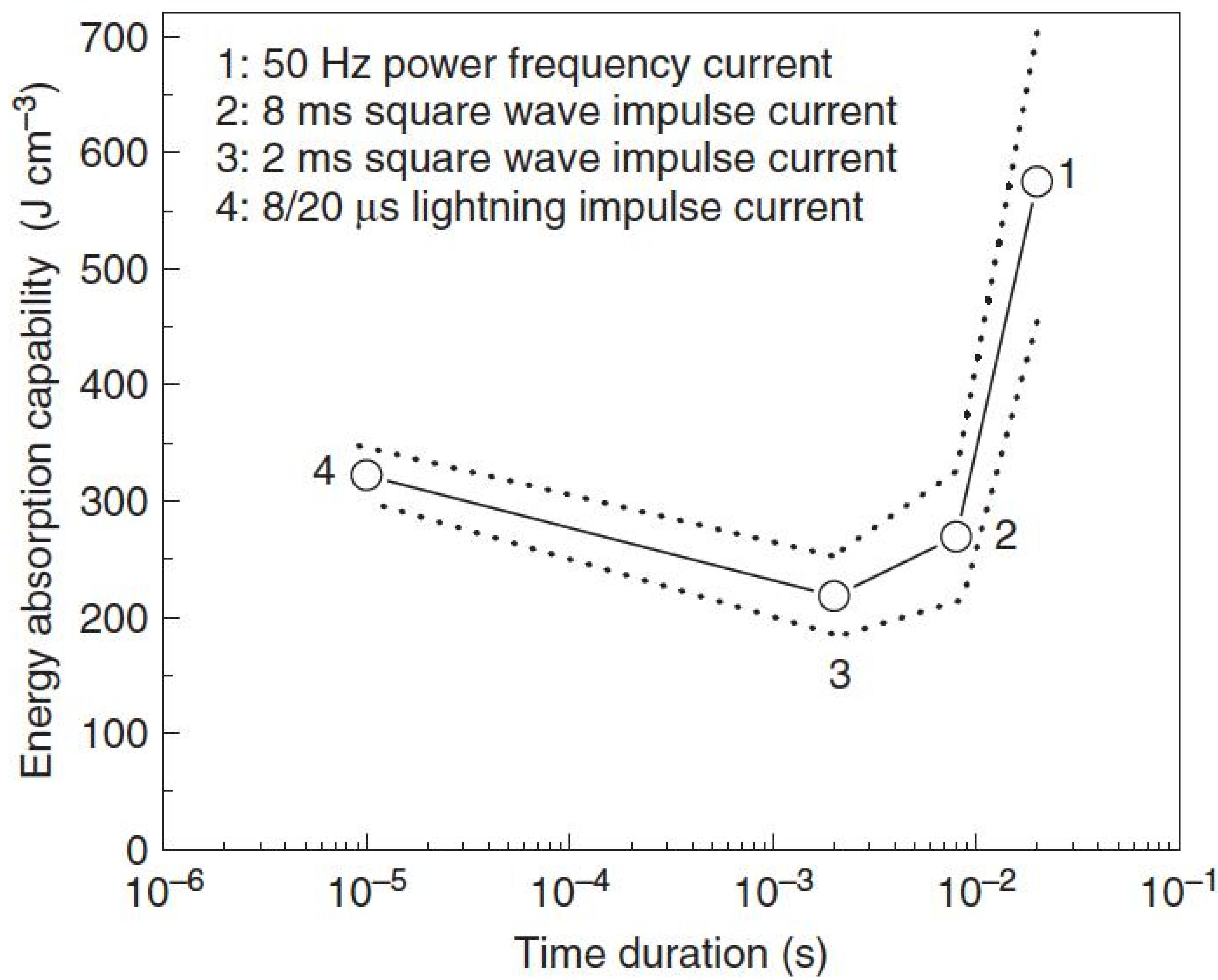


Figure 6.28 The relationship between the energy absorption capability and the duration of applied current. Source: He and Hu 2007 [11]. Reproduced with permission of IEEE.

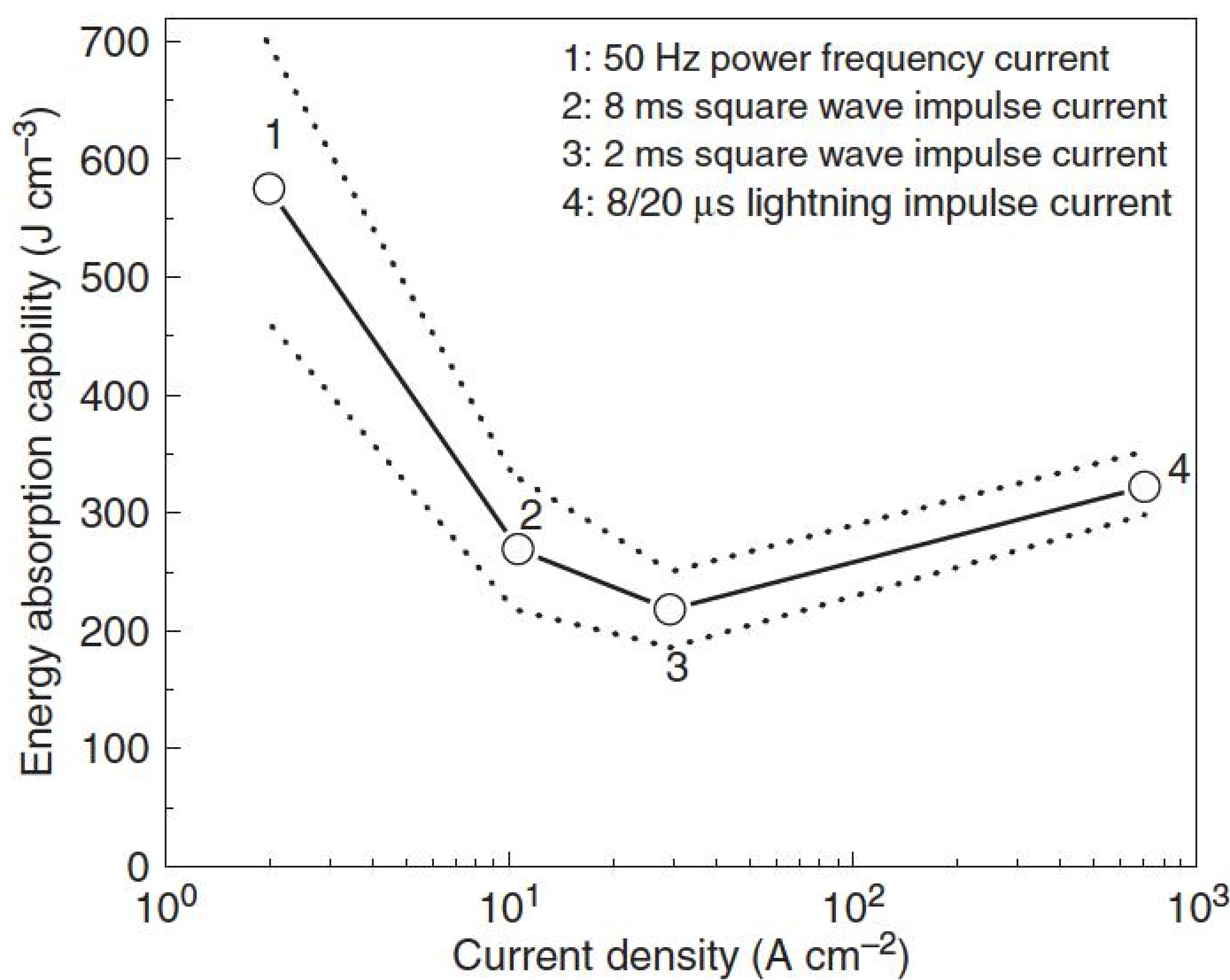


Figure 6.29 The relationship between the energy absorption capability and the current density of applied current. Source: He and Hu 2007 [11]. Reproduced with permission of IEEE.

possibility of overheat in one part is very low, and the energy required for varistor failure will be high. When a large current is applied for a very short duration, the energy absorption capability will be high, too. It is believed that ZnO varistors can hardly undergo failure in such a short duration; therefore, they present a high energy absorption capability. This behavior was interpreted as a consequence of entering the upturn region of the I–V characteristic [3], and Bartkowiak et al. [56] further proposed that the value of the upturn resistivity

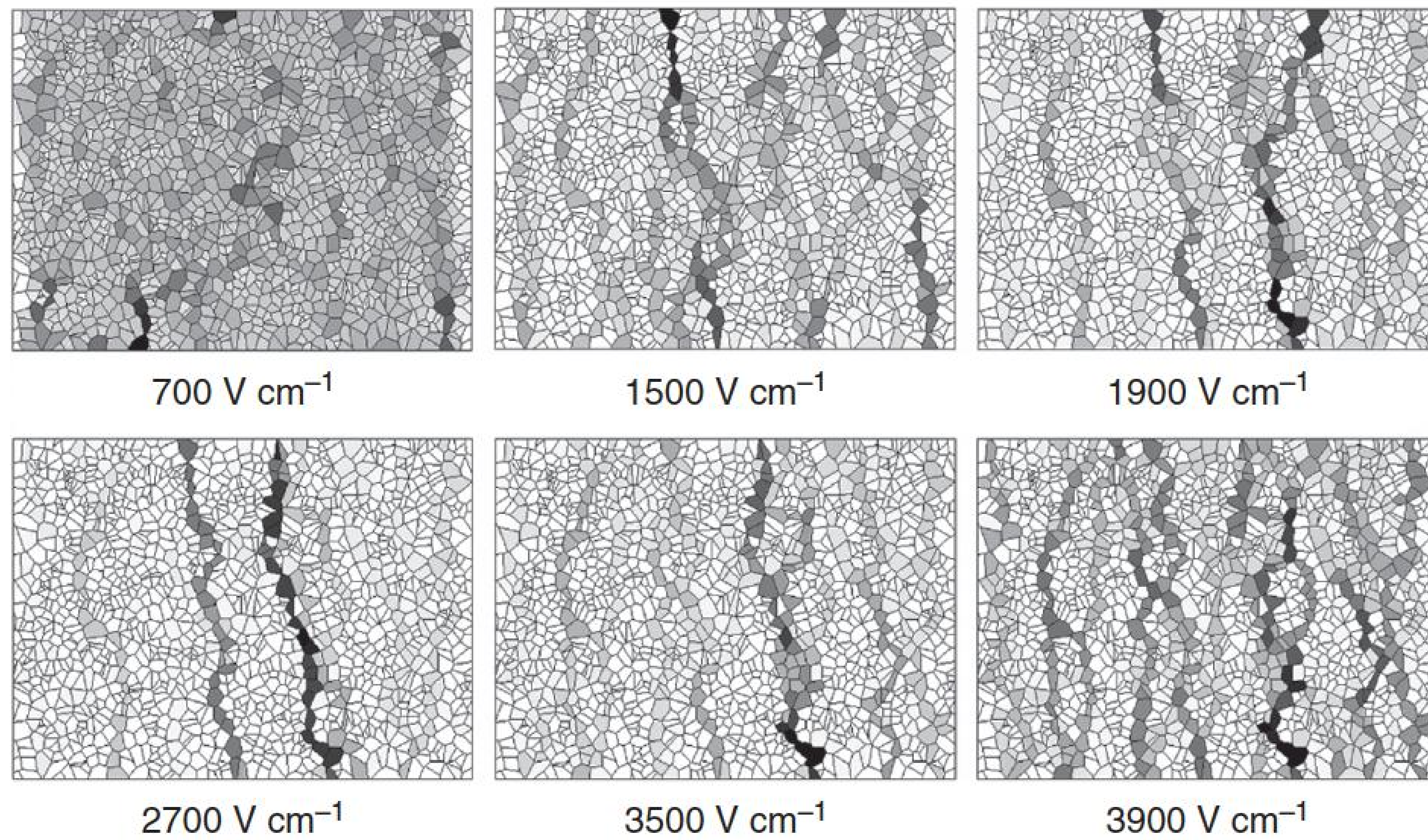


Figure 6.30 Simulated current localization phenomena (The gray-level spectrum from white to black represents the relative value of the current passing through a grain. The darker the color in a grain is, the more current passes through the grain.). Source: He and Hu 2007 [11]. Reproduced with permission of IEEE.

is important for the energy absorption capability in the high current density region. This value can be controlled by the level of aluminum doping.

From Figures 6.29 and 6.30 [11], the energy absorption capabilities disperse obviously among different varistors when a small current is applied for a long time, although it is mitigated when a large current is applied for a short time. The ratio between the maximum and minimum energy absorption capabilities is 1.56 when 50 Hz AC current is applied, which indicates that the energy absorption capability is very nonuniform. Under 8 and 2 ms square wave currents, the ratios are 1.51 and 1.40. But when an 8/20 μs impulse current is applied, this ratio is only 1.08, showing that the energy absorption capability is fairly uniform.

As analyzed above, the voltage or current applied has a dominant influence on the energy absorption capability of the ZnO varistor. The current concentration phenomenon is of crucial importance in such results, which can be easily observed from the simulation results shown in Figure 6.30. The extent of current localization is quite diverse under varied voltage. When the applied voltage is very small (the respective current is small), the current distribution inside the ZnO varistor is uniform. It is difficult to behave current concentration phenomenon, so the energy absorption capability of ZnO varistor will be high. When the applied voltage increases (the respective current increases), the current paths become less. When the applied voltage is 2700 V cm^{-1}, there are only two obvious current localization channels observed. Most of the current flows through both narrow channels, so the current concentration is very severe. Then, the energy absorption capability becomes small with the increment of the applied current. Subsequent to the increment of the voltage applied, the current concentration paths increase instead. When the applied voltage is 3900 V cm^{-1}, which is in the upturn region of the V–I characteristics of the varistor, where the current density is uniform in

the disk, we can observe many current concentration paths again; this means the energy absorption capability increases. Such varied phenomenon of the current distributions in Figure 6.30 is well fit to explain the U-shaped curve between the energy absorption capability and the applied current as shown in Figure 6.29.

6.7.2 Influence of Varistor Cross-sectional Area

The ZnO varistor can be regarded as a large number of ZnO grains and grain boundaries in parallel and in series; its surge energy absorption capability is dependent on its microstructure [2, 8]. Generally, we would think that a thicker varistor should have a higher threshold voltage, and a varistor with a larger cross-sectional area could absorb more energy proportionally. But actually, the sintered polycrystalline ceramic is not uniform in microstructure, so that the energy absorption capability does not increase linearly with its cross-sectional area. The test results state that the deviation of the destruction energy is more pronounced for the varistor with larger cross-sectional area, while the energy absorption capability per unit volume decreases accordingly.

Two types of commercial disk-shaped ZnO varistors with diameters D of 52 and 32 mm, and same thickness H of 10 mm were tested; both had the same additives and were sintered in the same technique. A square wave current with 2 ms duration was applied to the varistors, and their energy absorption capabilities were 216 and 271 J cm^{-3} on average [11]. Obviously, the energy absorption capability decreases when the cross-sectional area increases. The larger the cross-sectional area of the ZnO varistor is, the smaller its energy absorption capability is.

The uniform current distribution is particularly important to a varistor disk with large cross-sectional area, because it has higher probability of microstructural, electrical, and thermophysical nonuniformity and becomes more prone to puncture and cracking. Thus, its energy absorption capability decreases with increase in cross-sectional area.

6.7.3 Simulation Analysis on Surge Energy Absorption Capability

The energy absorption capability per cubic centimeter is defined as the energy E absorbed by the ZnO varistor before it fails [4]:

$$E = \int_0^{t_f} J_{av}(t) F_{av}(t) \mathrm{d}t \tag{6.8}$$

where t_f is the time to failure, $J_{av}(t)$ is the average current density, and $F_{av}(t)$ is the average voltage gradient. If a square wave current is applied, $J_{av}(t)$ is constant and $F_{av}(t)$ varies as the current and temperature profile change.

There is a very strict test to determine the surge energy absorption capacity of the ZnO varistor, wherein the ZnO varistor is demanded to withstand a square wave impulse current for 18 times. In the time interval between two impulse currents, the temperature of every part will become uniform and reach the average temperature, so the temperature rise will be identical during every impulse and the thermal stress is also the same. But the original temperature of every part is

higher than the last time, and the highest temperature will increase with the time. So the ZnO varistor may be more likely damaged by melting puncture in this test.

By assuming a varistor disk of 45 mm height and 32 mm diameter with a hot spot of 5 mm diameter, Bartkowiaka et al. [4] analyzed the time to failure t_f and the energy absorption capability of a distribution-class arrester disk for different failure modes, as shown in Figure 6.31. At low currents, the disk is stable. But, as the current density is increased above $J_{av} = 6 \times 10^{-5}$ A cm^{-2}, the temperature of the disk does not stabilize. After some time, it reaches the limited stable temperature $T_s = 190$ °C, and thermal runaway occurs. Although the heating of the disk is quite nonuniform, it is so slow that the heat has enough time to diffuse from the hot spot, and the temperature distribution is almost flat. The energy absorption capability for low current remains above 550 J cm^{-3}, which is in good agreement with the results in [6]. When $J_{av} = 0.14$ A cm^{-2}, the timescale becomes too short for the temperature distribution to flatten. After about two seconds of heating, the compressive stress in the axial direction S_{zz} at the hot spot becomes higher than the compressive strength S_{fc} of 70 kpsi, and the disk cracks. As the current is further increased, the energy absorption capability falls to about 330 J cm^{-3}, reaches a minimum at about 1 A cm^{-2}, and increases again. In this region of applied current densities, it is the stress at the hot spot in the axial direction that exceeds the failure stress. Therefore, the block is predicted to crack in a plane perpendicular to the cylindrical axis. When the current density becomes higher than about 50 A cm^{-2}, the failure mode is still cracking, but it is caused by the tensile stress in the tangential direction. Hence, the disks become more likely to crack along lines branching out from the hot spot, or a portion of the sidewall may break off.

The energy absorption capability imposed by cracking increases rapidly for current density $J_{av} > 300$ A cm^{-2}. The nonlinearity coefficient decreases fast at high current; consequently, the current density distribution, and the heating, become more uniform, and the thermal stresses are lower. Observations of an increase of the energy absorption capability of ZnO varistors for very high current pulses is

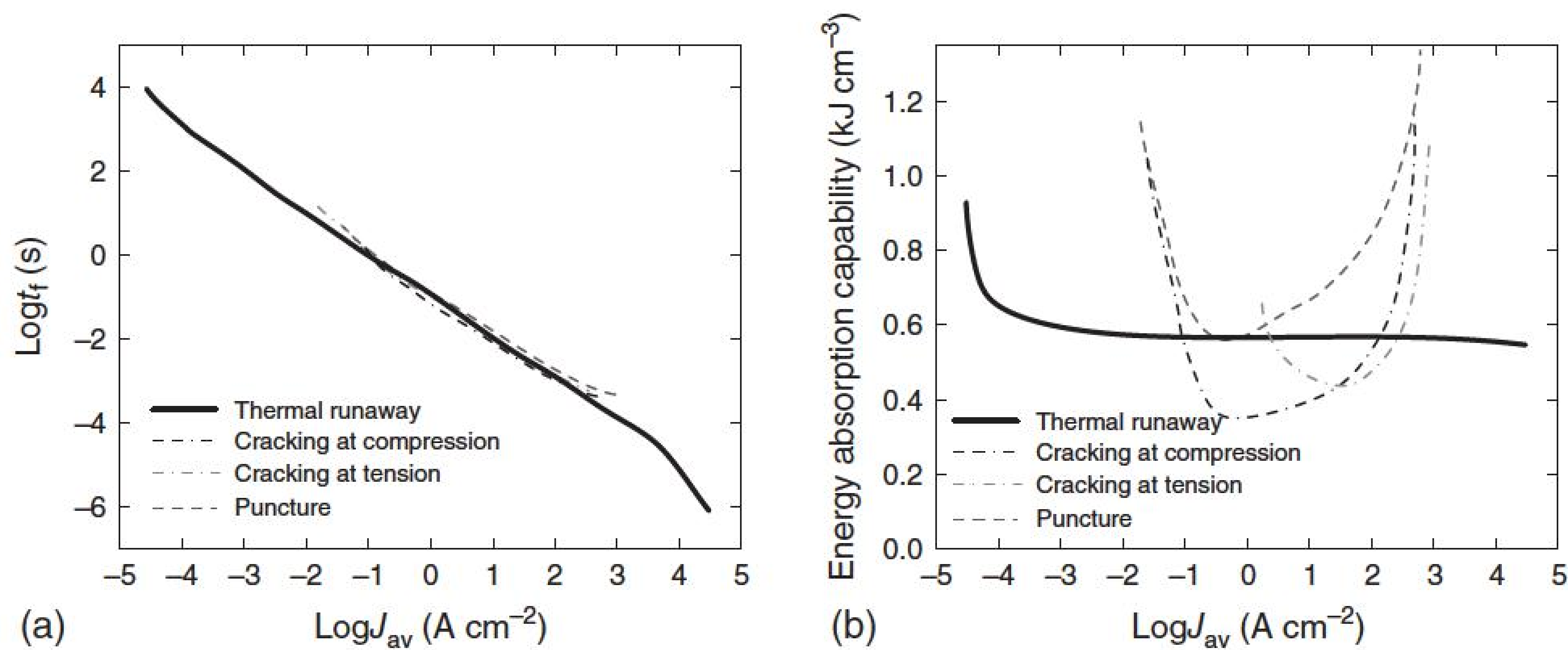


Figure 6.31 (a) The time to failure t_f and (b) the energy absorption capability of a distribution-class-arrester disk for different failure modes. Source: Bartkowiak et al. [4]. Reproduced with permission of IEEE.

thus a consequence of entering the upturn region of the I—V characteristic [3, 5], where the current localization is less.

When the average current density is above 400 A cm^{-2}, the simulations indicate that the block should thermally runaway rather than crack. The energy absorption capability for thermal runaway and the corresponding time to failure decrease more rapidly as the current density becomes higher than about 1.5 kA cm^{-2} because deep in the upturn region, the voltage gradient increases linearly with the current, causing a rapid increase in the input power. Therefore, less time is needed to heat up the disk to the stability limit temperature T_s.

As shown in Figure 6.32 [56], the energy absorption capability for puncture is always higher than those for thermal runaway and cracking. In contrast to the station-class disks discussed in the next section, puncture failures of distribution-class arresters are rare. The latter either crack under high current pulses or thermally runaway due to temporary overvoltages or switching surges [6]. The energy absorption capability curves for puncture and cracking are close to each other in the low current region. Therefore, punctures of distribution-class varistor disks can also be observed.

The energy absorption capability for the thermal runaway (measured per volume unit) does not significantly depend on the shape of the varistor disk and is not sensitive to the size and the intensity of the hot spot [56]. Therefore, also for the low aspect ratio disks, $E = 550\,\text{J cm}^{-3}$ within a wide region of applied currents. However, energy absorption characteristics for puncture and cracking failure modes are different from those for disks of high aspect ratio. These characteristics are obtained from the simulations of a disk of 23 mm height and 63 mm diameter with a hot spot of 1 cm diameter. The thermal stresses in the axial direction are negligibly small in the disks of low aspect ratio, and the radial and tangential compressive stresses calculated never reach the compressive strength of the material, $S_{fc} = 570$ kpsi. Therefore, the disk never cracks at compression, and for the current densities $10\,\text{mA cm}^{-2} \leq J_{av} \leq 3\,\text{A cm}^{-2}$, the only possible failure mode (besides a thermal runaway) is puncture. At higher current densities

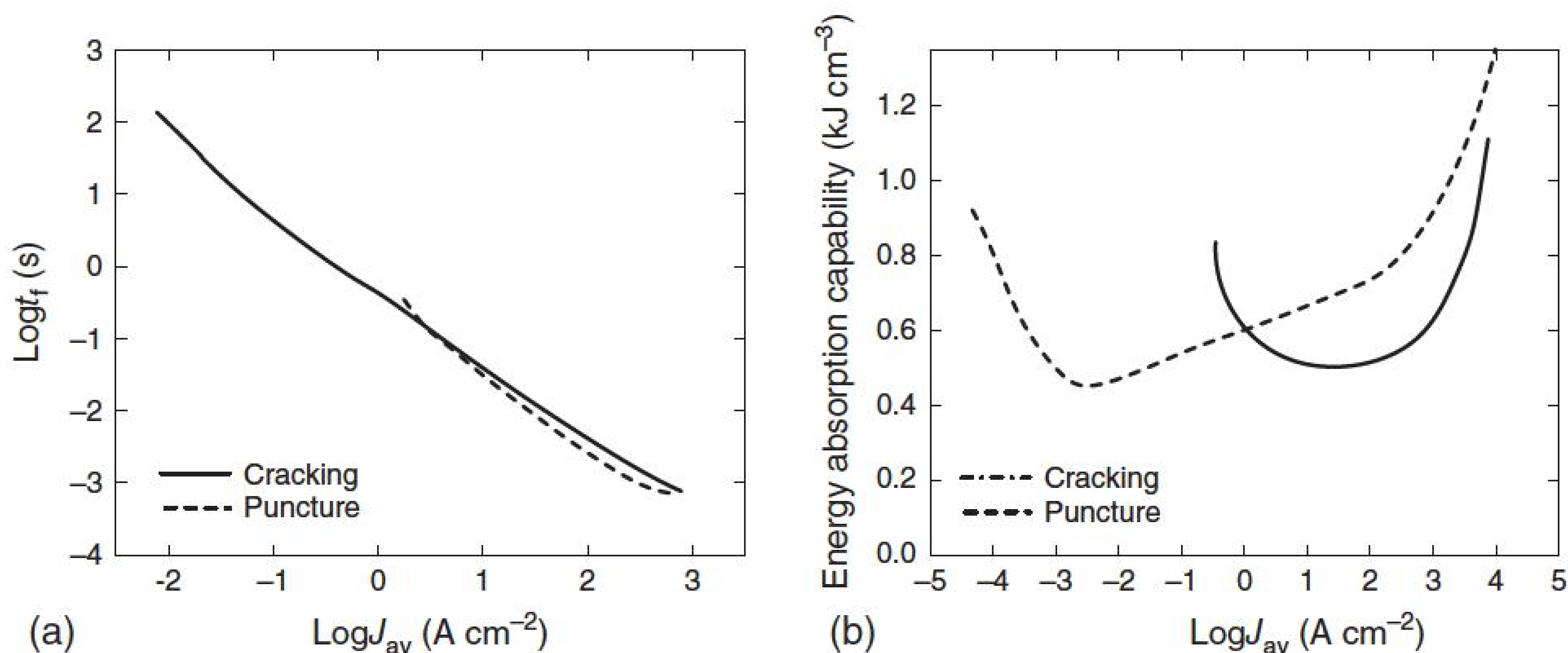


Figure 6.32 (a) The time to failure t_f and (b) the energy absorption capability of a station-class-arrester disk for cracking and puncture. Source: Adapted from Bartkowiak et al. [56].

the tensile tangential stresses around the hot spot become higher than the tensile strength of the varistor ceramic, S_{ft}, before the temperature at the hot spot reaches 800 °C. Therefore, instead of exhibiting a puncture, the disks become more likely to crack along lines branching out from the hot spot. This cracking pattern, as well as the transition described above from the puncture failure mode at low current densities to cracking at high currents, is in qualitative agreement with the experimental observations of Eda [2], who studied the relationship between the magnitude of the destruction current and the destruction modes for samples having 14 mm diameter and 1.3 mm thickness.

From analysis, the energy absorption capability crucially depends on the electrical uniformity of the disks. The influence of the size and the degree of the possible nonuniformity is evaluated for current surges of various magnitudes and durations. The uniformity of the distributions of current, temperature, and thermal stress can be notably improved by increasing the uniformity of grain size and the uniformity of the electrical character of the grain boundary. But actually, it is very difficult to improve the uniformity of grain size and electrical character of the grain boundary. Analysis indicates that the uniformity of the distribution of current, temperature, and thermal stress can be notably improved by decreasing the grain size.

As a further conclusion, the energy absorption capability of a ZnO varistor can be improved by reducing the current localization, which could be weakened by enhancing the uniformities of ZnO grain size and the barrier voltage of the ZnO varistor, while the first method is more viable and effective comparatively. As studied by Bartkowiak et al. [42], the energy absorption capability decreases rapidly with the intensity of the hot spots, where the breakdown voltage is assumed to be lower than that for the rest of the varistor blocks and more current is absorbed. The value of the minimum energy handling only weakly depends on the size of the hot spot and becomes lowest for disks with hot spots of an intermediate size. The energy absorption capability at high currents strongly depends on the position of the upturn region in the varistor V–I characteristic. It turns out that it is possible to minimize the chance of a failure of varistor disks by adjusting this resistivity to the requirements of particular applications.

One of the ANSI/IEEE standard tests for ZnO varistors is to see whether they withstand a short high current (65 or 100 kA) pulse with 4/10 μs waveform, but such high values of current density are in the upturn region of the varistor V–I characteristic, where the current density is uniform in the disk. Consequently, the temperature profile is uniform, and cracking or puncture is unlikely. The pulses are also too short to cause thermal runaway. However, varistor disks are much more prone to failures at lower currents. Therefore, the standard high current test provides very little information about the actual energy handling capability. From the analysis, the current density necessary to cause disk failure for such duration currents is likely to be in the order of 500–1000 A cm^{-1} for typical distribution arresters (corresponding to current magnitudes of 4–8 kA in 32 mm diameter disks, 6.5–13 kA in 40 mm diameter disks). A test involving discharges of duration in the range of 200–300 μs was suggested. [42] This is in a similar range obtained from the experimental result shown in Figure 6.28.

6.8 Discussions on Energy Absorption Capability

6.8.1 Energy Absorption Capability Determined by Fracture Failure

The energy absorption capabilities of ZnO varistors leading to puncture and cracking failures can be analyzed by thermodynamics. When an element inside a ZnO varistor absorbs energy P, the thermally insulated temperature rise ΔT is expressed as

$$\Delta T = \frac{P}{\Delta V \rho C_{\mathrm{p}}} \tag{6.9}$$

where ΔV is the volume of the element, ρ is the specific gravity, and C_{p} is the specific heat constant. The specific heat constant C_{p} at 20 °C is 498 J kg^{-1} °C, and the specific gravity ρ is 5600 kg m^{-3} [50]. If the temperature rises of two close elements are ΔT_1 and ΔT_2 respectively, the thermal stress f formed between them can be calculated by Eq. (6.9). The critical thermal stress f_{c}, which causes varistor cracking is in the range between 17.2 and 48.3 MPa, and 17.2 MPa was selected in the analysis [44].

Because the contact between the surface of a ZnO varistor and the electrode and the electrical characteristics among different elements in the ZnO varistor are different, the energies absorbed by different elements in the varistor vary from element to element when a current is applied to it. The energy absorption uniformity S is defined as the ratio of the minimum and the maximum energies absorbed by the inner elements. When $S = 1$, the energy absorption of a varistor is very uniform.

It is found from Eq. (6.9) that the temperature rise of an element inside the varistor caused by absorbed impulse energy is directly determined by the heat capacity ρC_{p}, but different regions inside the ZnO varistor have different heat capacities. The heat capacity uniformity B is defined as the ratio between the minimum and the maximum values of the heat capacity ρC_{p} among all elements inside a varistor, $(\rho C_{\mathrm{p}})_{\mathrm{min}}$ and $(\rho C_{\mathrm{p}})_{\mathrm{max}}$, respectively [11]:

$$B = \frac{(\rho C_{\mathrm{p}})_{\mathrm{min}}}{(\rho C_{\mathrm{p}})_{\mathrm{max}}} \tag{6.10}$$

Defining $(\rho C_{\mathrm{p}})_{\mathrm{av}}$ as the average value of $(\rho C_{\mathrm{p}})_{\mathrm{min}}$ and $(\rho C_{\mathrm{p}})_{\mathrm{max}}$, when B and S exist, the maximum temperature difference between two neighboring elements inside the varistor would be [11]

$$\Delta T_1 - \Delta T_2 = \frac{P/S}{\Delta V(\rho C_{\mathrm{p}})_{\mathrm{min}}} - \frac{P}{\Delta V(\rho C_{\mathrm{p}})_{\mathrm{max}}} = \frac{P(1+B)(1-SB)}{2\Delta VBS(\rho C_{\mathrm{p}})_{\mathrm{av}}} \tag{6.11}$$

From Eqs. (6.7) and (6.11), the surge energy absorption capability P_{B} of cracking destruction per unit volume caused by the synthetical effect of the energy absorption uniformity and heat capacity uniformity could be calculated by

$$P_{\mathrm{B}} = \frac{2f_{\mathrm{c}}(\rho C_{\mathrm{p}})_{\mathrm{av}}(1-\upsilon)SB}{Ya(1+B)(1-SB)} \tag{6.12}$$

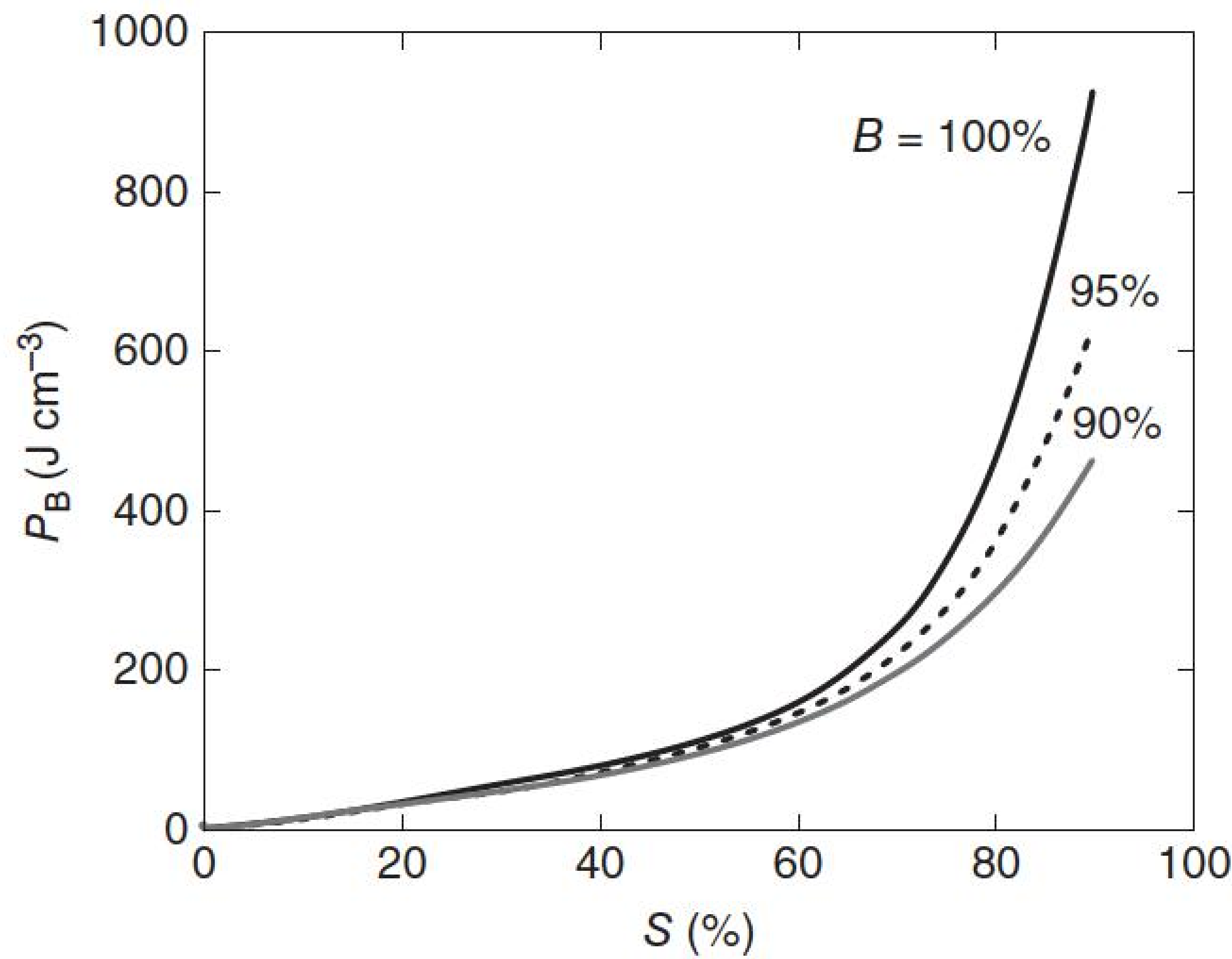


Figure 6.33 The energy absorption capability of cracking destruction P_B caused by the synthetical effect of energy absorption uniformity *S* and heat capacity uniformity *B*. Source: He and Hu 2007 [11]. Reproduced with permission of IEEE.

The energy absorption capability P_B of cracking failure caused by the synthetical effect of the energy absorption uniformity S and the heat capacity uniformity B is illustrated in Figure 6.33.

The tested actual energy absorption capabilities of the commercial ZnO varistors are in the range from 216 to 269 J cm^{-3} when switching impulse currents are applied. Thus, when $B = 100\%$, the energy absorption uniformity S of the tested varistor ranges from 63.0% to 68.9%; when $B = 90\%$, then S is between 74.0% and 79.2%. So, obvious nonuniformity exists in the energy absorption and heat capacity of ZnO varistors. The energy absorption capability is seriously affected by the uniform degree of ZnO varistors, which would increase quickly as the nonuniformity of ZnO varistors is improved.

The nonuniformity of heat capacity includes two aspects [11]. Firstly, from experimental results, the thermophysical parameters C_p and k are largely determined by temperature, while k is the thermal conductivity. Thus, different elements inside a varistor have different thermophysical parameters because the temperatures vary from unit to unit, due to different energies absorbed by different elements. Secondly, different elements inside a varistor have different thermophysical parameters ρ and C_p; this is caused during the sample preparation and sintering process.

6.8.2 Energy Absorption Capability Determined by Puncture Failure

As discussed in Section 6.4, the puncture failure of ZnO varistors is caused by current concentration, which can be produced by the electrical property nonuniformity in the microstructure. Here, the electrical property nonuniformity F is defined as the ratio of the area with the threshold voltage decreasing by 5% and the total surface area; if F is equal to 0, then the ZnO varistor would be very uniform. When 3 A and 3 kA square wave currents are applied to varistors, the limited surge energy absorption capability P_P, which results in puncture destruction, as a function of F is illustrated in Figure 6.34 [41].

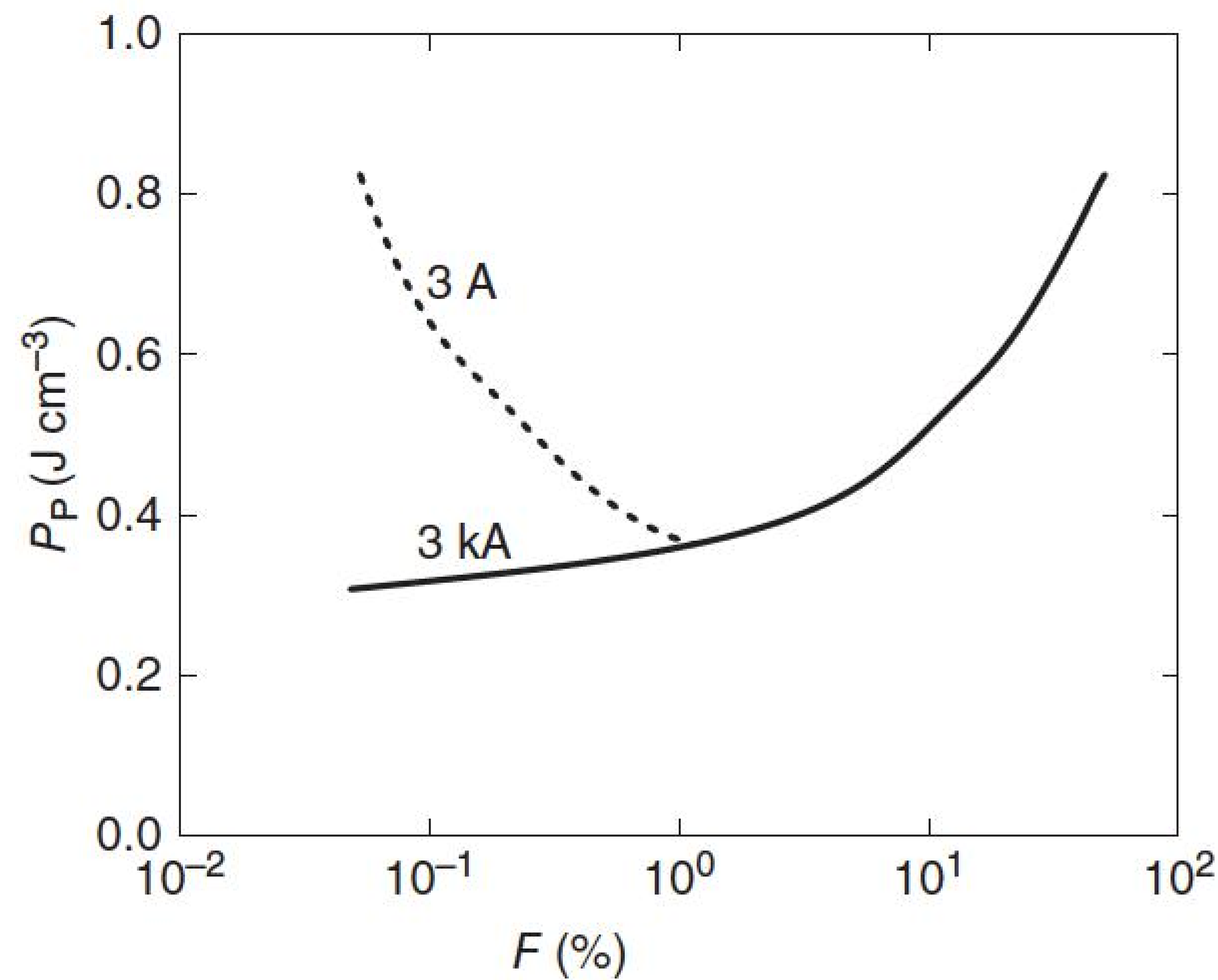


Figure 6.34 The limited surge energy absorption capability P_P resulting puncture destruction due to the effect of electrical property nonuniformity F [41].

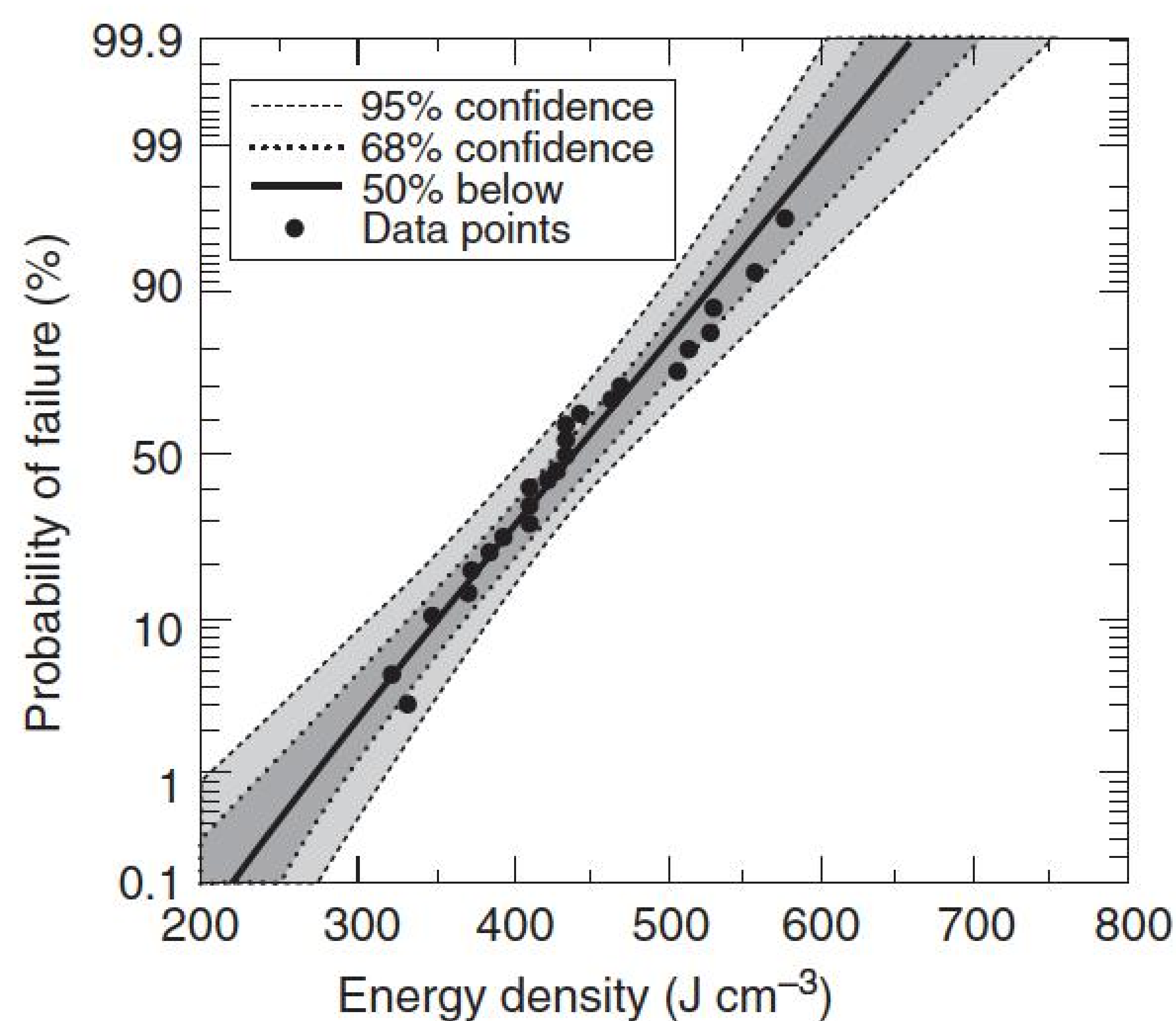


Figure 6.35 Weibull plot of varistor failures as a function of energy density. Source: Ringler et al. [5]. Reproduced with permission of IEEE.

When $F > 1\%$, the P_P values at high and low currents are the same. But, when $F < 1\%$, then P_P of 3 A current is larger than that of 3 kA current. The reason is that the time to reach the melting temperature at low current would be longer than that at high current. The less the area with low threshold voltage is, the more easily the generated heat would be absorbed by surrounding parts, so the energy to form a punctured hole at low current would be more than that at high current.

The energy absorption capability is very small when the electrical characteristic is quite nonuniform. So, improving the electrical property uniformity of a ZnO varistor will effectively improve its surge energy absorption capability.

Another test connected the puncture failure probability with the energy absorption capability of ZnO varistor [5]; an energy handling test at 60 Hz and 7 A peak current is plotted in Figure 6.35. In these tests, the failures were all by thermal runaway, leading to a distinctive puncture mode of failure. There is clearly a statistical distribution in energy absorption capability from one varistor to another.

6.8.3 Discussion on Nonuniformity of Energy Absorption Capability

Eda [2] measured the distribution of the threshold voltages in ZnO varistors by applying spot electrodes on both lapped surfaces opposite each other. For a typical sample, it had a small region with lower threshold voltage than other regions by 5%, but for a less uniform sample, the region had lower threshold voltage than the other regions by 11%. Their respective energy absorption capabilities were analyzed as 117 and 128 J cm^{-3}.

Mizukoshi et al. [8] analyzed the influence of nonuniformity on energy absorption capabilities of zinc oxide elements by monitoring the surface temperature distribution of ZnO varistors with an infrared radiation thermo-camera. Local heating was induced by current concentration in some portion of the varistor. The nonuniformity factor δ was defined as [8]

$$\delta = \frac{T_{\mathrm{max}} - T_{\mathrm{i}}}{T_{\mathrm{min}} - T_{\mathrm{i}}} \tag{6.13}$$

where T_{max} and T_{min} are the maximum and minimum temperatures inside a ZnO varistor when a voltage is applied to it and T_{i} is the initial temperature.

As shown in Figure 6.36 [8], the maximum δ reaches 1.7, and the respective energy absorption capability is only 400 J cm^{-3}. Ahmed et al. reported a test result [23] when a ZnO varistor was used to limit the repetitive pulse generated by an insulated-gate bipolar transistor (IGBT) power electronic circuit; the hottest region reached 127 °C while the lowest region reached only 30 °C. If the initial room temperature is assumed as 20 °C, then the highest δ reaches about 10.7; the energy absorption capability will thus be extremely low.

In many cases, the punctured area of a varistor agrees with the hot spot in the thermograph, proving that the varistor is melted by current concentrations. When an overvoltage is applied to a ZnO varistor, the portion with the highest nonuniformity would first reach its puncture energy, and the varistor would be cracked.

The measured energy absorption capability of commercial ZnO varistors was in the range from 218 to 269 J cm^{-3} when a switching impulse current was

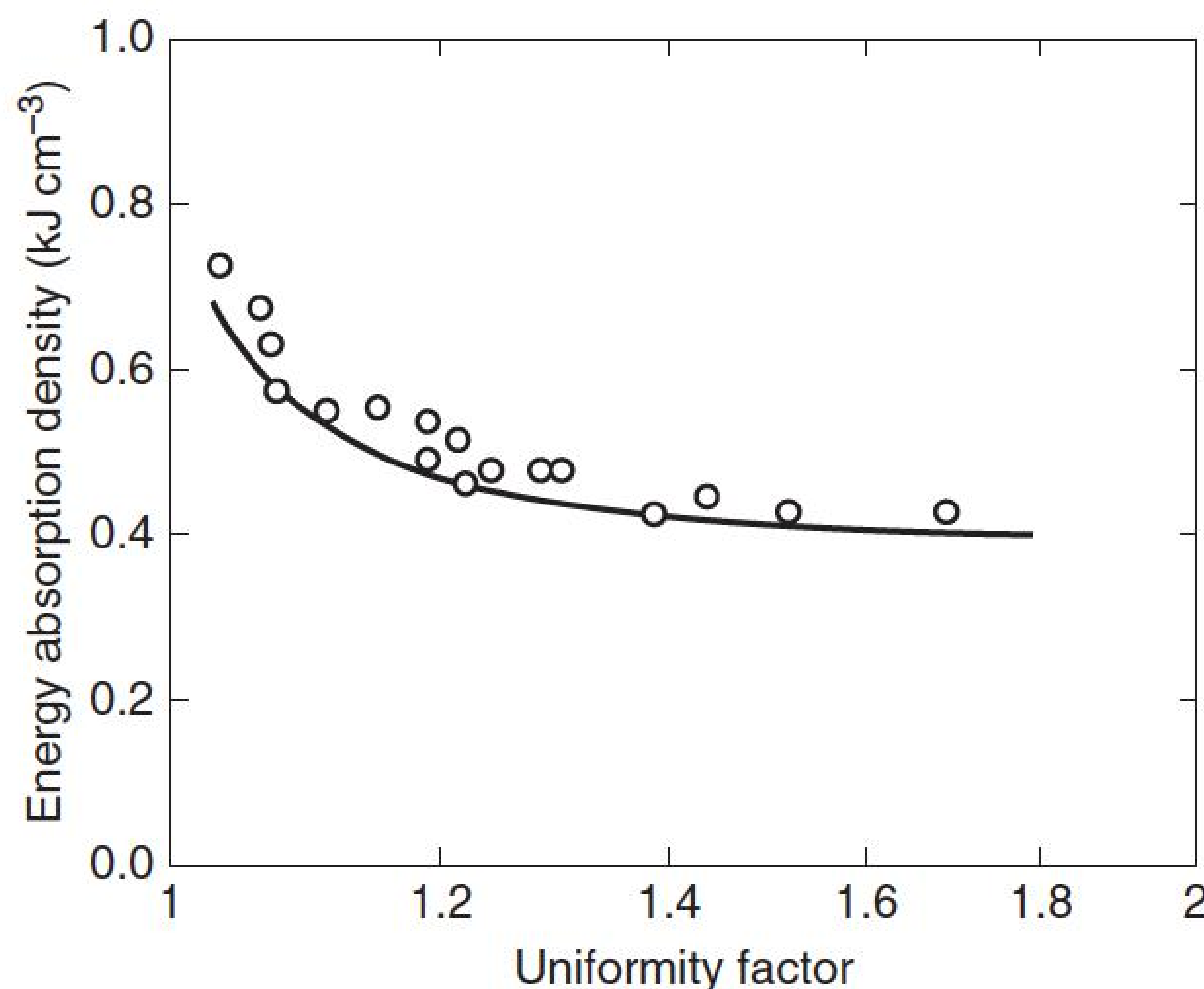


Figure 6.36 Relation between energy absorption density up to puncture and uniformity factor. Source: Mizukoshi et al. 1983[8]. Reproduced with permission of IEEE.

applied to them. It is only 31.1–38.4% of that of the uniform varistor tested by Mizukoshi et al. [8].

From Figure 6.33, if the microstructure and the electrical and thermophysical characteristics of varistors are uniform, the energy absorption capability of this ideal ZnO varistor can reach as high as 900 J cm^{-3}. Thus, the actual energy absorption capability of commercial ZnO varistors is in the range from 24.2% to 29.9% of that of the ideal varistor.

Therefore, it is reasonable that the energy absorption capability of a varistor decreases substantially if it has a high nonuniformity. So, to improve the uniformities of the microstructure, the electrical characteristics and thermophysical parameters of ZnO varistors would greatly increase their energy absorption capability, which could be improved by modifying the sintering technique and additives. In the meantime, the surface of the ZnO varistor should be very plain, and good contact conditions between ZnO varistors and high voltage electrode and between ZnO varistors when they are assembled as surge arresters should be reached.

6.8.4 Additives Effect on Energy Absorption Capability

Rare earth oxides, such as Pr_6O_{11}, Y_2O_3, La_2O_3, Ce_2O_3, and Nd_2O_3, can reduce the grain size of ZnO varistors to increase the energy absorption capability; this kind of ZnO varistor is called as a high voltage gradient one. Usually, rare earth oxides are added with contents of 0.01–0.5 wt% to ZnO standard and antimony-rich varistor compositions [23]. It is found that the rare earth oxide allows reaching large energy absorption capability values for the high voltage gradient ZnO-based varistors [57]. These results can be explained by the presence of the extra-pyrochlore phase, suggesting less bismuth oxide in the ceramics, especially at grain boundaries. Varistors present more active grains and hence a larger conduction section, which account for a large absorption capability.

The average size of the ZnO grain of common ZnO varistor ceramics is about 15 μm, while that of high voltage gradient is about 9 μm. The number of ZnO grains and grain boundaries per unit thickness increases when the average grain size reduces, and the voltage-sensitive gradient increases correspondingly. When injecting a current with the same density for a conventional ZnO varistor into the high voltage gradient varistor, the absorbed surge energy increases proportionally. However, in fact, the permitted current flowing through the high voltage gradient ZnO varistor is far larger than that of a conventional one. From the tested results for ZnO varistor with the size of 32 mm diameter and 30 mm thickness, compared with conventional varistors, the 1 mA reference voltage of high voltage gradient ZnO varistor increases from 6.3 to 8.8 kV, the tolerance value of 18 times 2 ms square wave impulse current increases from 120 to 200 A, and the respective surge energy absorption capability increases from 85 to 197 J cm^{-3}. As shown in Figure 6.37 [46], actually the uniformity difference in microstructure between these two kinds of ceramics is not significant. The main reason for the improvement in the surge energy absorption capability of the high voltage gradient ZnO varistor is that the number of current paths increases proportionally

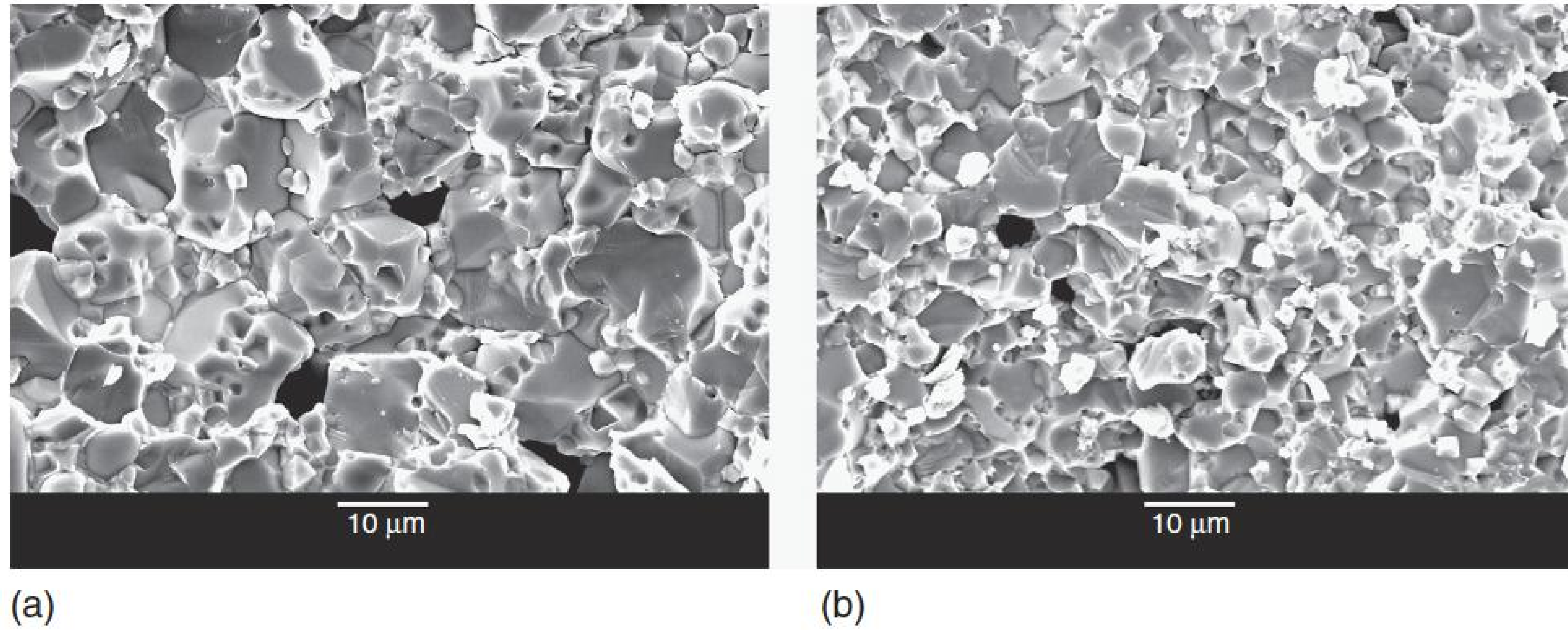


Figure 6.37 The microstructure of (a) common and (b) high voltage gradient ZnO varistor under electron microscope. Source: Chen et al. 2002 [46]. Reproduced with permission of Springer.

to the inverse of the square of the average size of ZnO grains; the cooling area increases, and the distance decreases correspondingly. All this helps the heat produced in the ceramics to transfer quickly and decrease the temperature difference and thermal stress.

6.8.5 Other Measures to Improve Energy Absorption Capability

The energy absorption capability of ZnO varistors can be increased by improving the sintering techniques and adjusting the prescriptions, and as discussed above, can be notably improved by decreasing the mean grain size.

In varistor fabrication, the passivation thickness plays an important role in varistor performance. The glass is applied on the peripheral surface of the disks to provide a collar material and acts as a barrier to heat transfer during energy testing; the coating of the glass acts as an insulator and resists the heat transfer. If the glass peripheral layer is not coated, the failure occurs mainly by side flashover and by combined side flashover and pinhole. The effect of the glass coating is more obvious in the second and third shots in the energy test. The heavier coating acts as a higher insulator and does not dissipate heat as effectively as the smaller thickness. Thus, the high temperature in the ceramics makes it more vulnerable to failure. This feature is supported by the fact that the thicker coating failed through the ceramic and most of the disks failed by electrical puncture. More than 85% of the varistors failed through the ceramic coated with thicker passivation coating compared to 27% in the case of the thin coating. Neither too low nor too high an amount of passivating material is favorable for varistor performance. Initial failure was prevented by applying glass material of thickness of 220 μm, and the survival of a larger number of disks above 500 J cm^{-3} was also increased [58].

References

1 Gupta, T.K. (1990). Application of zinc oxide varistors. *Journal of the American Ceramic Society* 73 (7): 1817–1840.

2 Eda, K. (1984). Destruction mechanism of ZnO varistors due to high currents. *Journal of Applied Physics* 56 (10): 2948–2955.
3 Sakshaug, E.C., Burke, J.J., and Kresge, J.S. (1989). Metal oxide arresters on distribution systems: fundamental considerations. *IEEE Transactions on Power Delivery* 4 (4): 2076–2089.
4 Bartkowiak, M., Comber, M.G., and Mahan, G.D. (1999). Failure modes and energy absorption capability of ZnO varistors. *IEEE Transactions on Power Delivery* 14 (1): 152–162.
5 Ringler, K.G., Kirkby, P., Erven, C.C. et al. (1997). The energy absorption capability and time-to-failure of varistors used in station-class metal-oxide surge arresters. *IEEE Transactions on Power Delivery* 12 (1): 203–212.
6 Kirkby, P., Erven, C.C., and Nigol, O. (1988). Long-term stability and energy discharge capacity of metal oxide valve elements. *IEEE Transactions on Power Delivery* 3 (4): 1656–1665.
7 Kan, M., Kojima, S., Nishiwaki, S. et al. (1983). Surge discharge capability and thermal stability of a metal oxide surge arrester. *IEEE Transactions on Power Apparatus and Systems* 102 (2): 282–289.
8 Mizukoshi, A., Ozawa, J., Shirakawa, S., and Nakano, K. (1983). Influence of uniformity on energy absorption capabilities of zinc oxide elements as applied in arresters. *IEEE Transactions on Power Apparatus and Systems* 102 (5): 1384–1390.
9 Wang, S.L., Gao, S.X., Li, H.F. et al. (1992). The relation between testing waveform and energy density on ZnO varistor. In: *Annual Report of Conference on Electrical Insulation and Dielectric Phenomena*, 543–548. IEEE.
10 Cao, Z.C., Wu, R.J., and Song, R.S. (1994). Ineffective grain boundaries and breakdown threshold of zinc oxide varistors. *Materials Science and Engineering B* 22 (2–3): 261–266.
11 He, J.L. and Hu, J. (2007). Discussions on nonuniformity of energy absorption capabilities of ZnO varistors. *IEEE Transactions on Power Delivery* 22 (3): 1523–1532.
12 He, J.L., Cho, H.G., Han, S.W., and Kang, H.B. (1998). Impulse destruction mechanisms of ZnO varistors. *The Korean Physical Society* 11 (4): 460–467.
13 Sweetana, A., Kunkle, N., Hingorani, N., and Tahiliani, V. (1982). Design, development and testing of 1200 kV and 550 kV gapless surge arresters. *IEEE Transactions on Power Apparatus and Systems* 101 (7): 2319–2327.
14 Carlson, W.G., Gupta, T.K., and Sweetana, A. (1986). A procedure for estimating the lifetime of gapless metal oxide surge arresters for AC application. *IEEE Transactions on Power Delivery* 1 (2): 67–74.
15 Mizuno, M., Hayashi, M., and Mitani, K. (1981). Thermal stability and life of the gapless surge arrester. *IEEE Transactions on Power Apparatus and Systems* 100 (5): 2664–2671.
16 Nishiwaki, S., Satoh, T., Mizoguchi, H. et al. (1984). Study of thermal runway/equivalent prorated model of a ZnO surge arrester. *IEEE Transactions on Power Apparatus and Systems* 103 (2): 413–421.
17 Clarke, D.R. (1999). Varistor ceramics. *Journal of the American Ceramic Society* 82 (3): 485–502.

18 Haryono, T., Sirait, K.T., Tumiran, T., and Berahim, H. (2011). The damage of ZnO arrester block due to multiple impulse currents. *Telecommunication Computing Electronics and Control* 9 (1): 171–182.

19 Pike, G. (2001). *Breakdown in ZnO Varistors by High Power Electrical Pulses*. Albuquerque, NM and Livermore, CA: Sandia National Laboratories. Sandia report SAND2001-2160.

20 Neto, E.W., Da Costa, E.G., Maia, M.J.A., and Ferreira, T.V. (2006). Failure analysis in ZnO arresters using thermal images. In: *IEEE/PES Transmission & Distribution Conference and Exposition: Latin America*, 1–5. IEEE.

21 Nanfa, Z., Guoyao, K., and Yaping, G. (2010). Long duration impulse withstand capability of SPD. In: *2010 Asia-Pacific Symposium on Electromagnetic Compatibility (APEMC)*, 1510–1513. IEEE.

22 Vojta, A. and Clarke, D.R. (1997). Microstructural origin of current localization and "puncture" failure in varistor ceramics. *Journal of Applied Physics* 81 (2): 985–993.

23 Ahmed, M.M.R., Putrus, G.A., Ran, L., and Penlington, R. (2001). Measuring the energy handling capability of metal oxide varistors. In: *16th International Conference and Exhibition on Electricity Distribution*, Paper No. 1.33., 33–37. IET.

24 Wang, H., Bartkowiak, M., Modine, F.A. et al. (1998). Nonuniform heating in zinc oxide varistors studied by infrared imaging and computer simulation. *Journal of the American Ceramic Society* 81 (8): 2013–2022.

25 Bartkowiak, M. and Mahan, G.D. (1995). Nonlinear currents in Voronoi networks. *Physical Review B* 51 (16): 10825–10832.

26 Vojta, A., Wen, Q., and Clarke, D.R. (1996). Influence of microstructural disorder on the current transport behavior of varistor ceramics. *Computational Materials Science* 6 (1): 51–62.

27 Vojta, A. and Clarke, D.R. (1997). Electrical-impulse-induced fracture of zinc oxide varistor ceramics. *Journal of the American Ceramic Society* 80 (8): 2086–2092.

28 Stockum, F.R. (1994). Simulation of the nonlinear thermal behavior of metal oxide surge arresters using a hybrid finite difference and empirical model. *IEEE Transactions on Power Delivery* 9 (1): 306–313.

29 Ellis, H.F., Reckard, R.M., Phillipp, H.R., and Nied, H.F. (1990). *Fundamental Research on Metal Oxide Varistor Technology*. Palo Alto, CA: Electric Power Research Institute. No. EPRI-EL-6960.

30 Boley, B.A. and Weiner, J.H. (2012). *Theory of Thermal Stresses*. North Chelmsford, MA: Courier Corporation.

31 Van Kemenade, J.T.C. and Eijnthoven, R.K. (1979). Direct determination of barrier voltage in ZnO varistors. *Journal of Applied Physics* 50 (2): 938–941.

32 Krivanek, O.L., Williams, P., and Lin, Y.C. (1979). Direct observation of voltage barriers in ZnO varistors. *Applied Physics Letters* 34 (11): 805–806.

33 Wong, J. (1976). Barrier voltage measurement in metal oxide varistors. *Journal of Applied Physics* 47 (11): 4971–4974.

34 Tao, M., Ai, B., Dorlanne, O., and Loubiere, A. (1987). Different "single grain junctions" within a ZnO varistor. *Journal of Applied Physics* 61 (4): 1562–1567.

35 Wang, H., Li, W., and Cordaro, J.F. (1995). Single junctions in ZnO varistors studied by current-voltage characteristics and deep level transient spectroscopy. *Japanese Journal of Applied Physics* 34 (4R): 1765–1771.
36 Nan, C.W. and Clarke, D.R. (1996). Effect of variations in grain size and grain boundary barrier heights on the current-voltage characteristics of ZnO varistors. *Journal of the American Ceramic Society* 79 (12): 3185–3192.
37 Emtage, P.R. (1979). Statistics and grain size in zinc oxide varistors. *Journal of Applied Physics* 50 (11): 6833–6837.
38 Han, S.W., He, J.L., Hwang, H.D., and Kang, H.B. (1997). Microstructure characteristics of ZnO varistors simulated by Voronoi network. *The Korean Journal of Ceramics* 3 (4): 239–244.
39 He, J., Chen, S., Zeng, R. et al. (2005). Statistic analysis on electrical parameters of ZnO varistors in low-voltage protection devices. *IEEE Transactions on Power Delivery* 20 (1): 131–137.
40 He, J., Zeng, R., Chen, S., and Tu, Y. (2003). Thermal characteristics of high voltage whole-solid-insulated polymeric ZnO surge arrester. *IEEE Transactions on Power Delivery* 18 (4): 1221–1227.
41 He, J.L. (1994). Study on high voltage polymeric housing ZnO surge arresters. Doctoral thesis. Beijing China: Tsinghua University.
42 Bartkowiak, M., Comber, M.G., and Mahan, G.D. (2001). Influence of nonuniformity of ZnO varistors on their energy absorption capability. *IEEE Transactions on Power Delivery* 16 (4): 591–598.
43 Chen, Q.H. (2003). Research on ZnO nonlinear resistor with large surge energy absorption capability and high voltage gradient. Doctoral thesis. Beijing China: Tsinghua University.
44 Kingery, W.D. (1976). *Introduction to Ceramics*, 2e. New York: Wiely.
45 Koch, R.E. and Songster, H.J. (1984). Development of a non-fragmenting distribution surge arrester. *IEEE Transactions on Power Apparatus and Systems* 103 (11): 3342–3352.
46 Chen, Q., He, J., Tan, K. et al. (2002). Influence of grain size on distribution of temperature and thermal stress in ZnO varistor ceramics. *Science in China Series E: Technolgical Science* 45 (4): 337–347.
47 Fritz, D.E. (1988). Polymer distribution arresters replace porcelain. *Transmission and Distribution* 104 (3): 36–40.
48 Fujiwara, Y., Shibuya, Y., Imataki, M., and Nitta, T. (1982). Evaluation of surge degradation of metal oxide surge arrester. *IEEE Transactions on Power Apparatus and Systems* 101 (4): 2–985.
49 Lat, M.V. (1983). Thermal properties of metal oxide surge arresters. *IEEE Transactions on Power Apparatus and Systems* 102 (7): 2194–2202.
50 Lat, M.V. (1985). Analytical method for performance prediction of metal oxide surge arresters. *IEEE Transactions on Power Apparatus and Systems* 104 (10): 2664–2674.
51 Han, S.W., He, J.L., and Cho, H.G. (1997). Property and ANN simulating model of power losses of ZnO Varistors. *Journal of Electrical Engineering and Information Science* 2 (6): 111–115.
52 Pao, Y. (1989). *Adaptive Pattern Recognition and Neural Networks*. Boston, MA: Addison-Wesley Publishing Co., Inc.

53 Bartkowiak, M., Mahan, G.D., Modine, F.A. et al. (1996). Voronoi network model of ZnO varistors with different types of grain boundaries. *Journal of Applied Physics* 80 (11): 6516–6522.
54 He, J., Hu, J., Tu, Y. et al. (2006). Scattered phenomenon of energy absorption capabilities of ZnO varistors. In: *8th International Conference on Properties and applications of Dielectric Materials*, 335–338. IEEE.
55 Olsson, E. and Dunlop, G.L. (1989). Characterization of individual interfacial barriers in a ZnO varistor material. *Journal of Applied Physics* 66 (8): 3666–3675.
56 Bartkowiak, M., Comber, M.G., and Mahan, G.D. (1996). Energy handling capability of ZnO varistors. *Journal of Applied Physics* 79 (11): 8629–8633.
57 Houabes, M. and Metz, R. (2007). Rare earth oxides effects on both the threshold voltage and energy absorption capability of ZnO varistors. *Ceramics International* 33 (7): 1191–1197.
58 Karim, A.N.M., Begum, S., and Hashmi, M.S.J. (2010). Performance and failure during energy testing of zinc oxide varistor processed from different powder size fraction and passivation thickness. *International Journal of Mechanical and Materials Engineering* 5 (2): 175–181.

7

Electrical Degradation of ZnO Varistors

ZnO varistors can be electrically, chemically, thermally, or mechanically degraded during use, leading to the reduction of barrier voltage height and, consequently, to the increase in leakage current, which could be catastrophic for ZnO varistors. The long-term degradation or short-term pulse degradation phenomenon of ZnO varistors, which could lead to deterioration in the electrical properties, may eventually give rise to thermal runaway or destruction of the varistors. The stabilities of ZnO varistors, including the AC/DC degradation and pulse degradation characteristics, are highly concerned with their life spans. Therefore, the degradations of ZnO varistors have attracted more attention. In this chapter, the phenomena and mechanisms of degradations of ZnO varistors are discussed thoroughly, including the variation of electrical properties of individual grain boundaries during the degradation process by microcontact measurements. The degradation phenomena under the effect of various stresses are focused, and the current achievement of investigation on the degradation mechanism is presented, aiming at the constitution of a full picture of universal electrical degradation mechanism, from the perspective of defects, portraying the ion migration process that is related to the degradation of double-Schottky barrier (DSB).

7.1 Introduction

The degradation, which is also called as aging, of ZnO varistors is defined as the variations of its properties and electrical or physical performance parameters, i.e. the gradual deviations from the original parameter values, under the effect of various applied stresses and external factors [1]. The "stress" is referred to the electrical stress or thermal stress. The electrical and thermal stresses can include both long-term operating voltage, e.g. DC or AC voltage, and the short-duration impulse current, impulse or transient voltage. In addition to the degradation caused by the electrical or thermal stress, the degradation phenomenon originating from simply mechanical stress was also discussed [2]; i.e. the degradation phenomenon can occur when a mechanical stress is applied merely (no effect of voltage involves).

The degradation of ZnO varistors, distinct from the thermal runaway discussed in Chapter 6, is a long-term and slowly growing process that ends with the sharp

increases of the resistive component of current and power loss, leading to the runaway. The degradation process and the thermal runaway share one point in common that they are both irreversible processes. After degraded by a long-term operation or a high-voltage test, the aggravated resistive current and power loss cannot be recovered to their initial values at room temperature even the applied voltage is switched off. However, it is proved by the experiments that the degraded varistor bulk can recover its properties to a certain degree if it undergoes an appropriate heat treatment.

Degradation of a ZnO varistor is related to its ingredients, sintering technique, voltages applied, and the application environment. There are a lot of discussions in the literatures [3–21] to study the degradation phenomena under AC, DC, and pulsed electric fields. The traditional techniques for characterizing the degradation process of ZnO varistors are concentrated on measuring the parameter variations of the materials [22, 23], rather than determining the inherent changes. General explanation of the degradation phenomena can be extracted and ascribed to the lowering of DSB height, to which the redistribution of charges in the grain boundary region makes great contributions [24]. In the past few decades, numerous research studies have been carried out to explain the observed degradation phenomena of ZnO varistors, and correspondingly, various degradation mechanisms of DSB have been proposed, e.g. electron trapping, dipole orientation, ion migration, and oxygen desorption [3, 19, 24], important works are listed in Table 7.1 in chronological order. Among these mechanisms, ion migration has found comparatively strong support on the basis of different circumstantial evidences, e.g. thermally stimulated current (TSC) observed in DC-biased electroceramics [3] and the stabilization of DSB by heat treatment [19].

Several works suggest that varistor degradation is a grain boundary phenomenon and is the result of ion migration in the depletion layer. Furthermore,

Table 7.1 Important works on the degradation mechanisms of ZnO varistors.

Researchers	Summarized degradation mechanism
Gupta and Carlson [19]	Migration process of zinc interstitial (the seminal grain boundary defect model)
Eda et al. [3, 18, 25]	Ion migration process
Takahashi et al. [26]	Chemical desorption of oxygen ions at the grain boundaries
Chiang et al. [27]	Asymmetrical distribution of impurity ions the in grain boundary region
Sato et al. [3, 28]	Electrons captured by traps inside the depletion layer and thus accumulated near grain boundary
Sonder et al. [29]	High mobility of oxygen ion at a high temperature and flaws like microcracks in the varistor act as conduits for oxygen
Bui et al. [30]	Partial discharges causing the formation of HNO_3 that degrades the Schottky barrier
Ramírez et al. [31]	The loss of oxygen species and β-Bi_2O_3 phase during the degradation process

the migration ions would be predominantly Zn interstitials (Zn_i). Degradation would arise as a result of field-assisted diffusion of Zn interstitials in the depletion layer followed by a chemical interaction with grain boundary defects (a process that would lead to a decrease in the barrier height and an increasing in the leakage current). The origin of Zn interstitials can be traced to the nonstoichiometric nature of ZnO, which upon heating, even in an oxidating atmosphere, can form excess Zn donors. They are accommodated at the interstitial sites in the lattice and frozen during cooling. The interstitials captured at the depletion layer are the most deleterious to varistor stability [32].

The lack of direct evidence of ion migration has made it difficult to clarify the physical processes that govern the electrical degradation of DSBs. If insights into the degradation mechanism of DSBs can be gained, e.g. the dominant mobile ion species can be positively identified, specific measurements could be adopted to effectively prolong the lifetimes of the devices. However, the elucidation of accurate mechanism of DSB is largely impeded by the fact that the ingredients doped into varistors during fabrication could profoundly influence its aging characteristics, for instance leading to abnormal degradation phenomena and determining its degradation rate [33], whereas knowledge from the atomic scale is quite limited on the role of element that is individually doped and, worse, on the codoping effect.

The degradation of varistors usually takes the form as a steady increase in the leakage current when a varistor is subject to a series of pulse or to a constant applied DC or AC voltage [34]. However, the effect of electrical pulse is complex and multiaspect. Except from electrical degradation, the transient electromagnetic force (results in fracture) and thermal effect (current localization and local joule heating) will also play critical roles. Discussion on these effects is presented in Chapter 6, and emphasis in this chapter is paid to the long-term electrical degradation mechanism of the grain boundary.

7.2 Degradation Phenomena of ZnO Varistors

Under the effect of long-term operating voltage, the degradation phenomena presented in the ZnO varistor bulks differ and depend on the distinct voltage types applied. The degradation phenomena even show differences in the samples from the same batch and the same laboratory, let alone the results reported by different manufacturers. It has been investigated that the degradation phenomena mainly occur in the prebreakdown region of the $I–V$ curve, whereas the degradation in the breakdown region of the $I–V$ curve is relatively less. Therefore, the basic characterization of degradation focusing on the prebreakdown region will be introduced as follows.

7.2.1 Degradation Phenomena of the Varistor Bulk

The deformation of DSB caused by degradation results in the variation of characteristic parameters of the varistor bulk that can be measured directly. During the degradation process, the $I–V$ (current–voltage) or $J–E$ (current density–electric

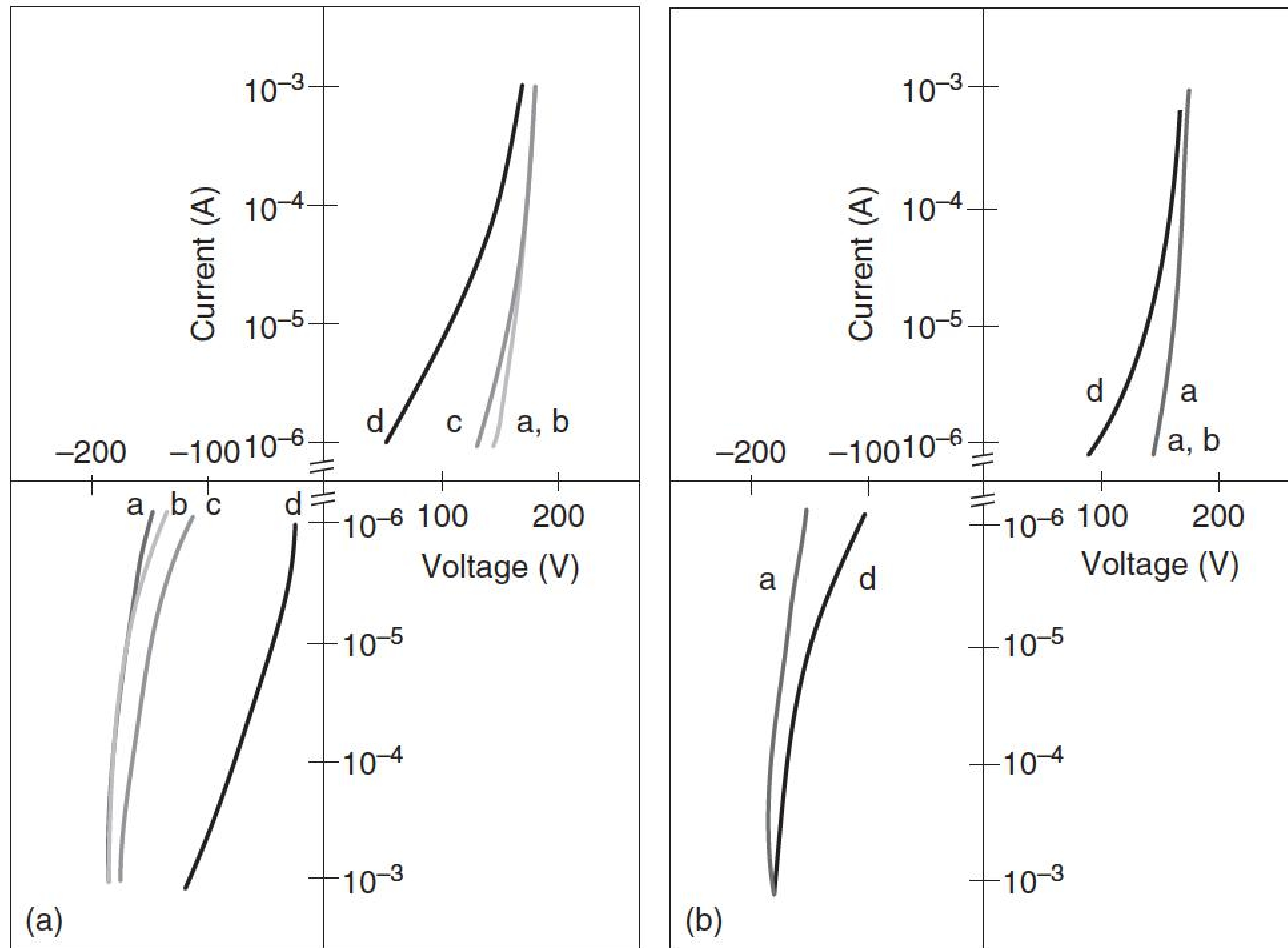


Figure 7.1 The drift phenomena of the *I–V* curve after degradation tests. (a) DC voltage; (b) AC voltage (Note: a, initial; b, voltage applied for 100 seconds; c, voltage applied for 10 hours; d, voltage applied for 500 hours). Source: Adapted from Eda et al. [3].

field) characteristics of ZnO varistors may drift nonlinearly. Typical experimental results are shown in Figure 7.1 [3] and Figure 7.2 [34]. Under the applied DC voltage, the $I-V$ curve deforms asymmetrically [3, 34], and the current flowing through the specimen increases. Conversely, when AC voltage is applied, the $I-V$ curve deforms symmetrically. Except for this asymmetrical deformation, the variational trend of AC case is quite similar to the DC case. Moreover, test results also indicate that no matter DC or AC voltage is applied, the $I-V$ characteristics in the prebreakdown region under a low electric field drift more severely after degradation test than the case involving the breakdown region under a medium electric field.

With the variation of $V-I$ characteristics of ZnO varistors, a companioning phenomenon is the increase in power loss and leakage current. After the degradation test of the ZnO varistor, as shown in Figure 7.3 [35], the power loss obviously increases, i.e. the characteristic curve of power loss versus voltage deforms and drifts leftward after the degradation test. This indicates that the degradation phenomenon with a power loss gradually increasing exists in the ZnO varistor. Usually, the accelerated aging test is used to test the aging characteristics of ZnO varistors, which is performed at 135 °C with $0.85U_{1mA}$ for continuously 100 hours according to the IEC standard (IEC-60099-4), where U_{1mA} is the applied voltage at 1 mA of the applied voltage ratio.

However, exceptions do exist in the accelerated aging test results, i.e. the curve of power loss versus voltage may drift rightward. This abnormal phenomenon was

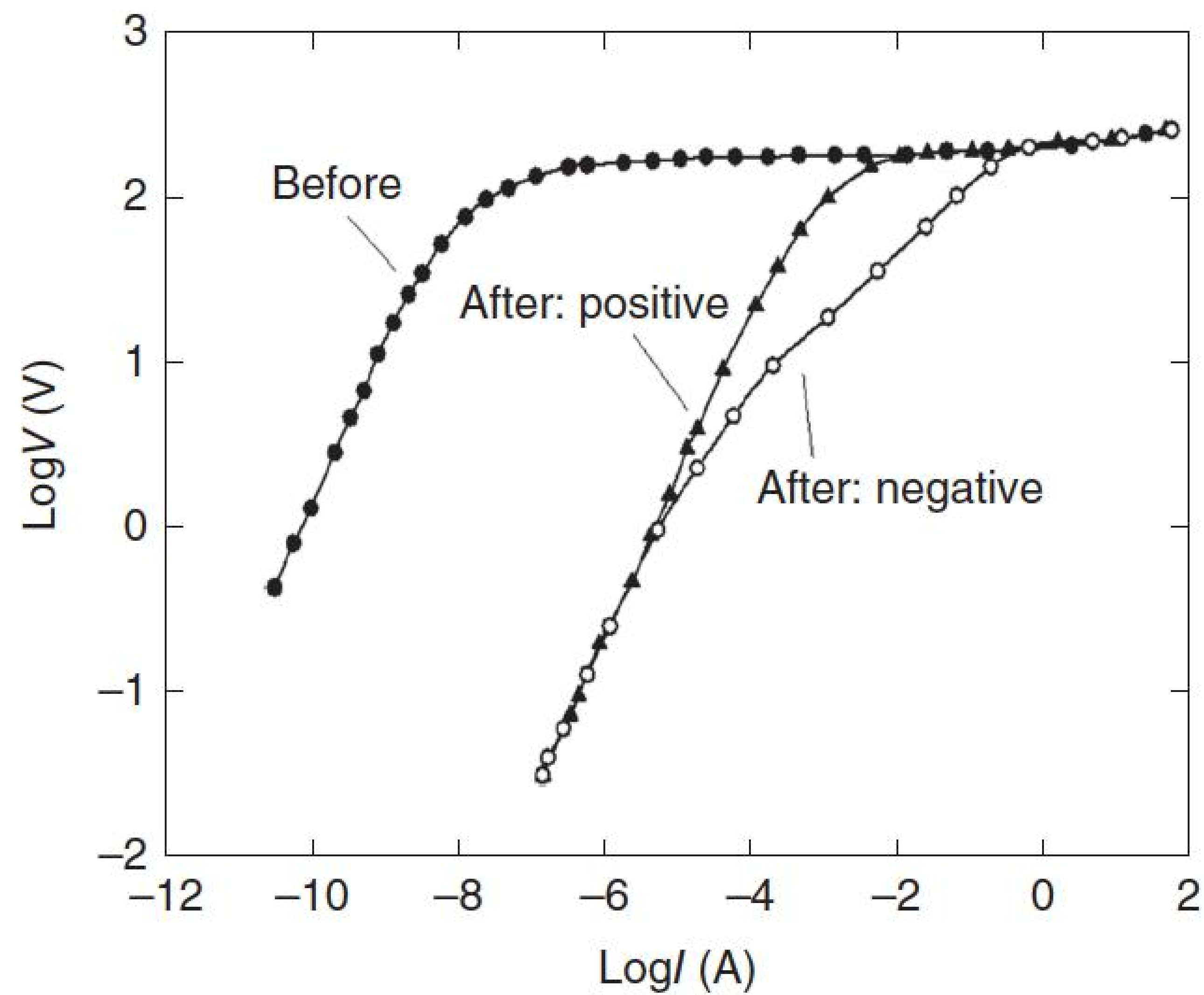


Figure 7.2 DC degradation behaviors of ZnO varistors. Source: Clarke 1999 [34]. Reproduced with permission of John Wiley & Sons.

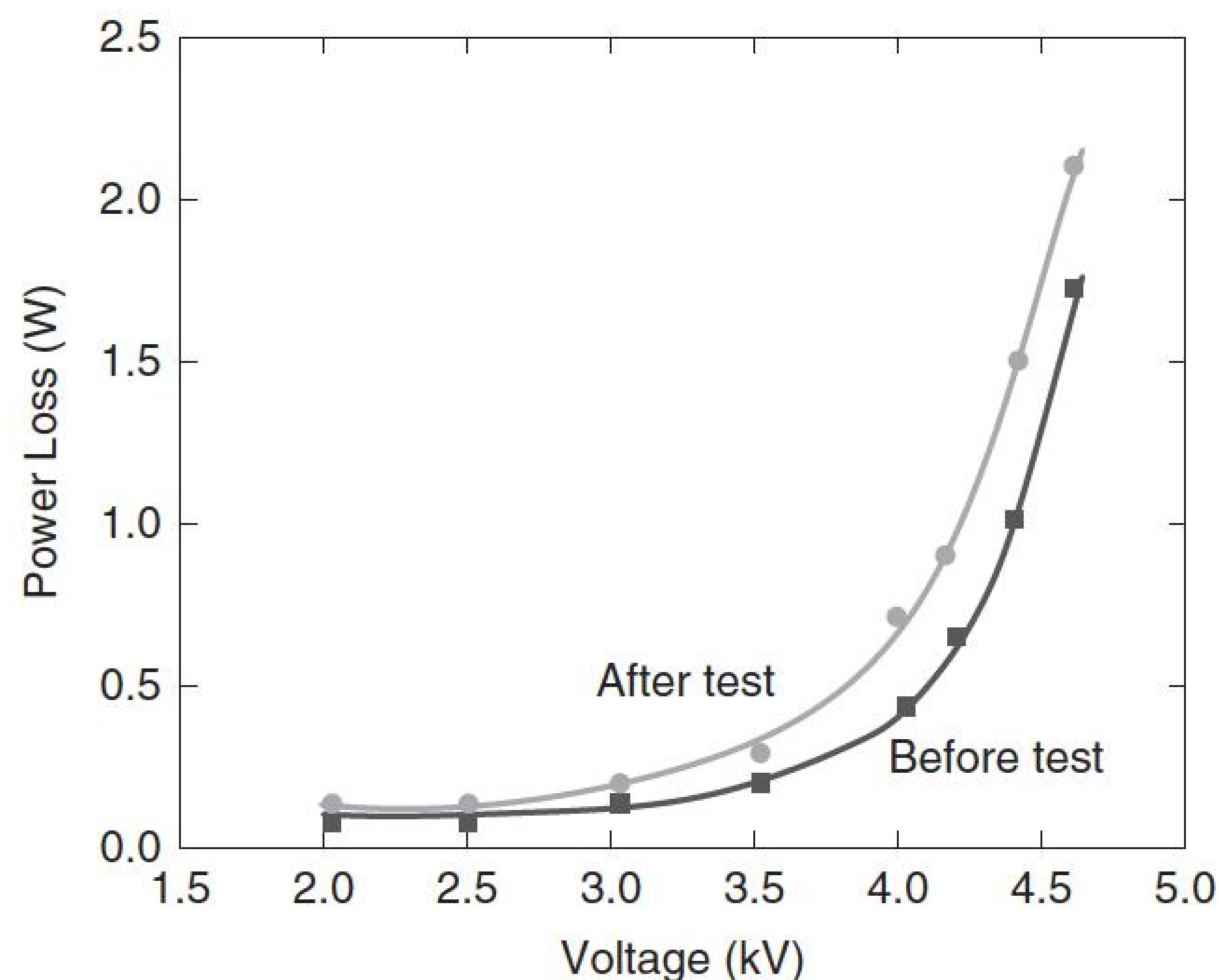


Figure 7.3 The comparison of the power loss of ZnO varistor before and after the DC-accelerated aging test. Source: Adapted from Yao [35].

reported by various literatures [36, 37], indicating the complexity of degradation in ZnO varistors under the effect of long-term operation voltage. Corresponding to the increase in the power loss after degradation test, the resistive component of current increases. When an AC voltage is applied, although the magnitude of the resistive component of leakage current through ZnO varistors, which is the main factor to degrade the ZnO varistor, is relatively small compared to the capacitive one, it may gradually increase with the power loss aggravated.

Figure 7.4 presents the typical curves of the increase in leakage current through ZnO varistors after various degradation tests (AC or DC) under different applied voltage ratios q [35], which is defined as the ratio of the maximum value U_{max} of the applied voltage divided by the 1 mA DC voltage U_{1mA} of the tested ZnO varistors. Another phenomenon is the gradual decrease in the global resistivity in the prebreakdown region of the varistor bulk, as shown in Figure 7.5 [3].

After the degradation test, the dielectric constant and dielectric loss of ZnO varistors also vary, and the change in the value of dielectric constant directly leads

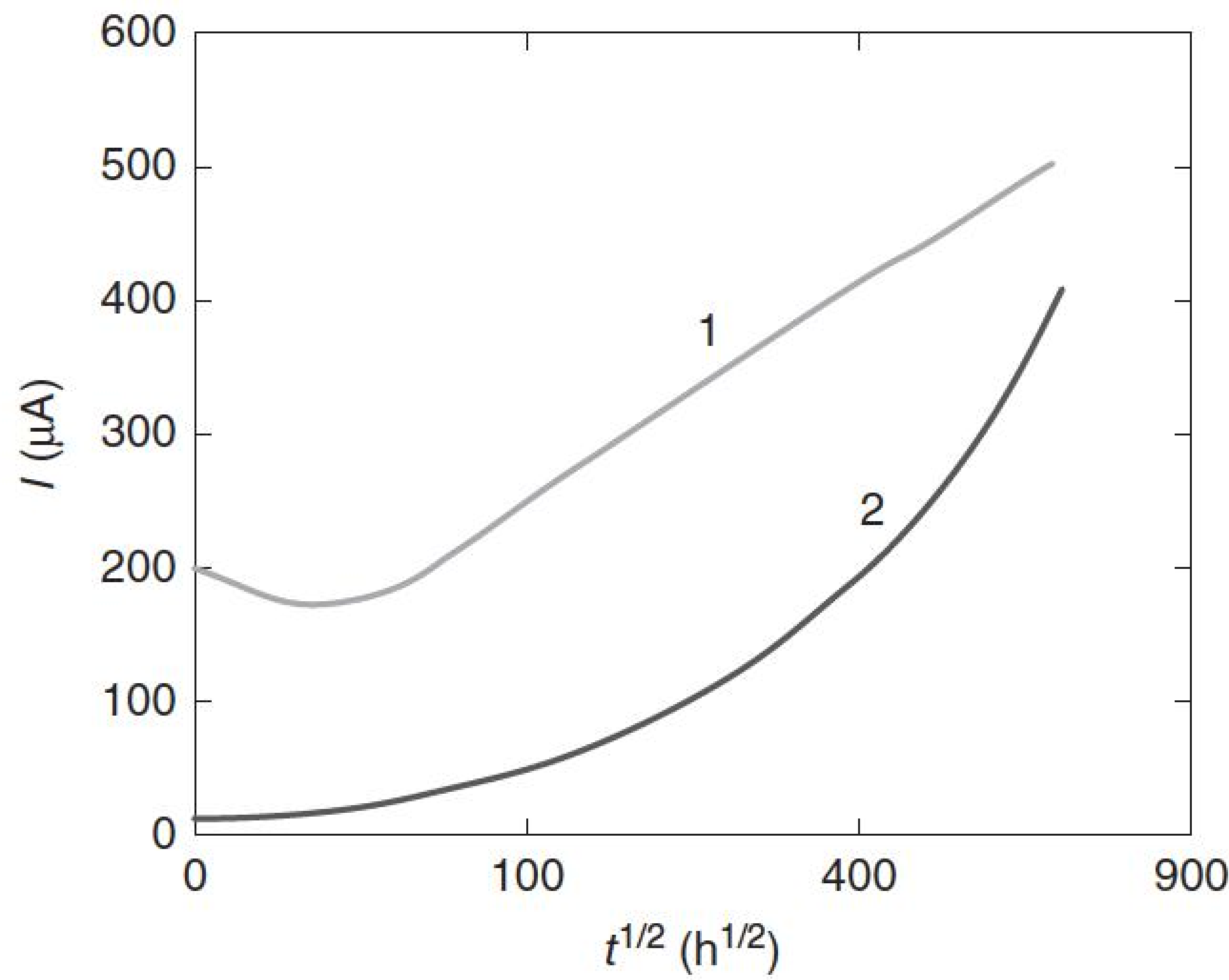


Figure 7.4 The rising of resistive component of leakage current during the ZnO varistor degradation test. 1, AC degradation: $T = 81\,°C$, $q = 0.80$; 2, DC degradation: $T = 79\,°C$, $q = 0.64$. Source: Adapted from Yao [35].

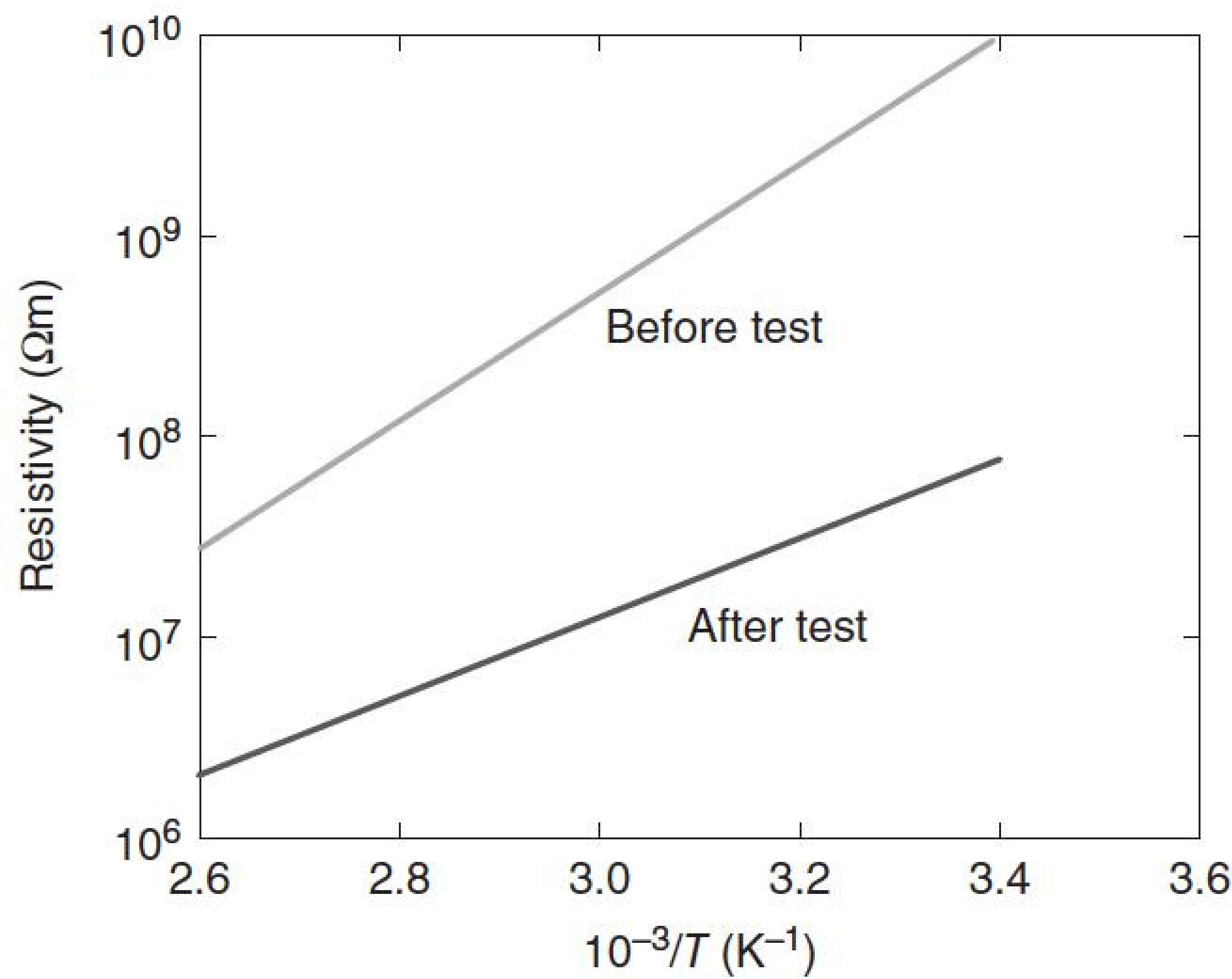


Figure 7.5 The variation of resistivity of ZnO varistor with temperature T before and after the degradation test. Source: Adapted from Wu et al. [1].

to the change of capacitance of the varistor bulk, as shown in Figure 7.6 [3], i.e. the capacitance of the varistor after degradation test decreases compared to the initial value.

Figure 7.6 also presents the variational curve of dielectric loss of ZnO varistors with frequency [3], which indicates that the dielectric loss in the range of the frequency below 1 MHz increases compared to the one before degradation.

As stated before, the leakage current increases as the degradation time increases. If the applied voltage is removed, it is found that a reverse electromotive force exists, which is in the reverse direction of the applied voltage. The trap levels can capture electrons in the band gaps of the ZnO varistor bulk. When an external electric field is applied, electrons are injected into the conduction band from negative electrode, and these electrons will be captured by traps. When the captured electrons are provided with a sufficient energy, they will be released from the traps and excited to the conduction band once again. The electrons in the conduction band will migrate along the electric field direction within the ZnO varistor and form a current through the external circuit, which is the TSC

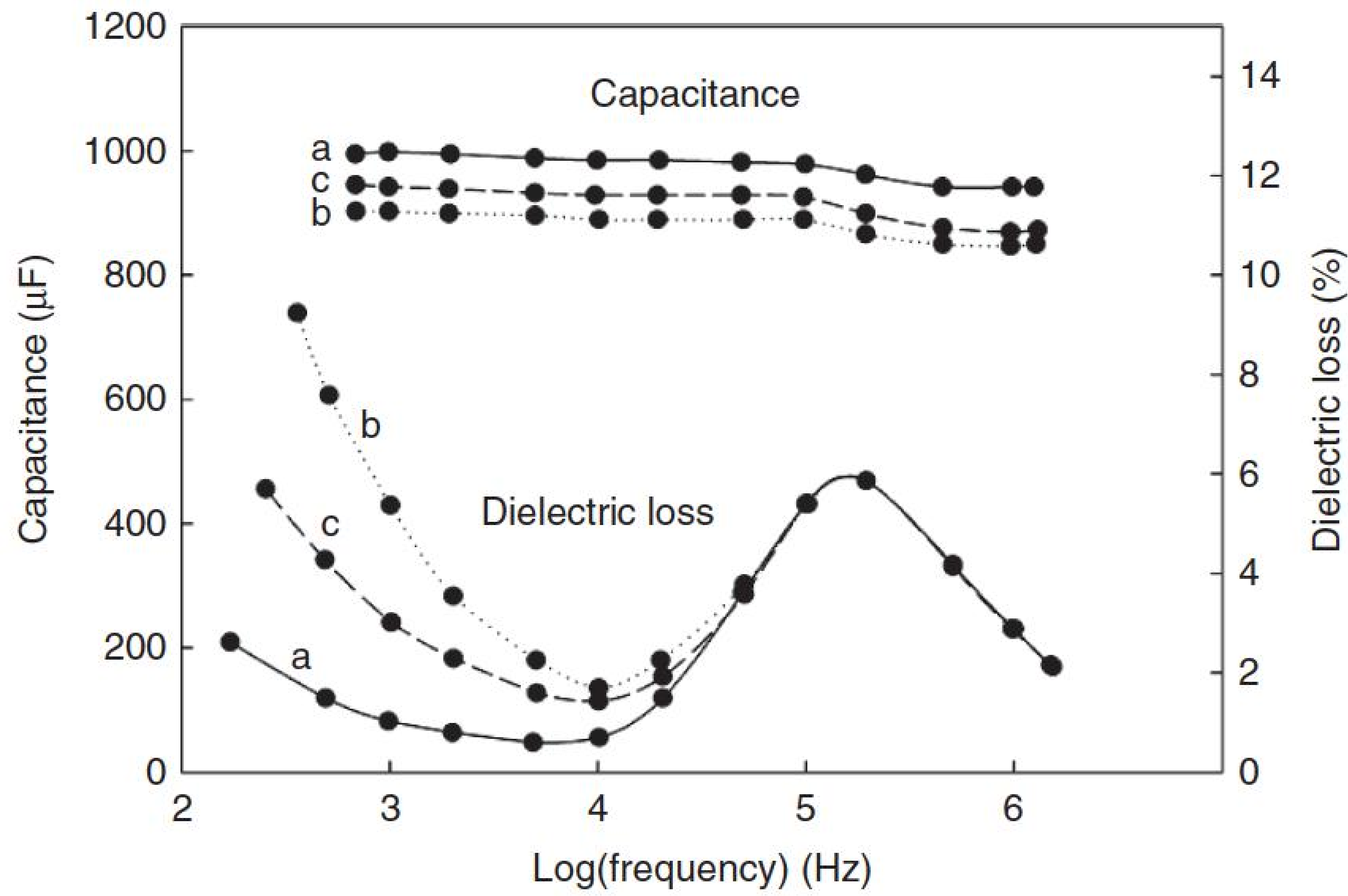
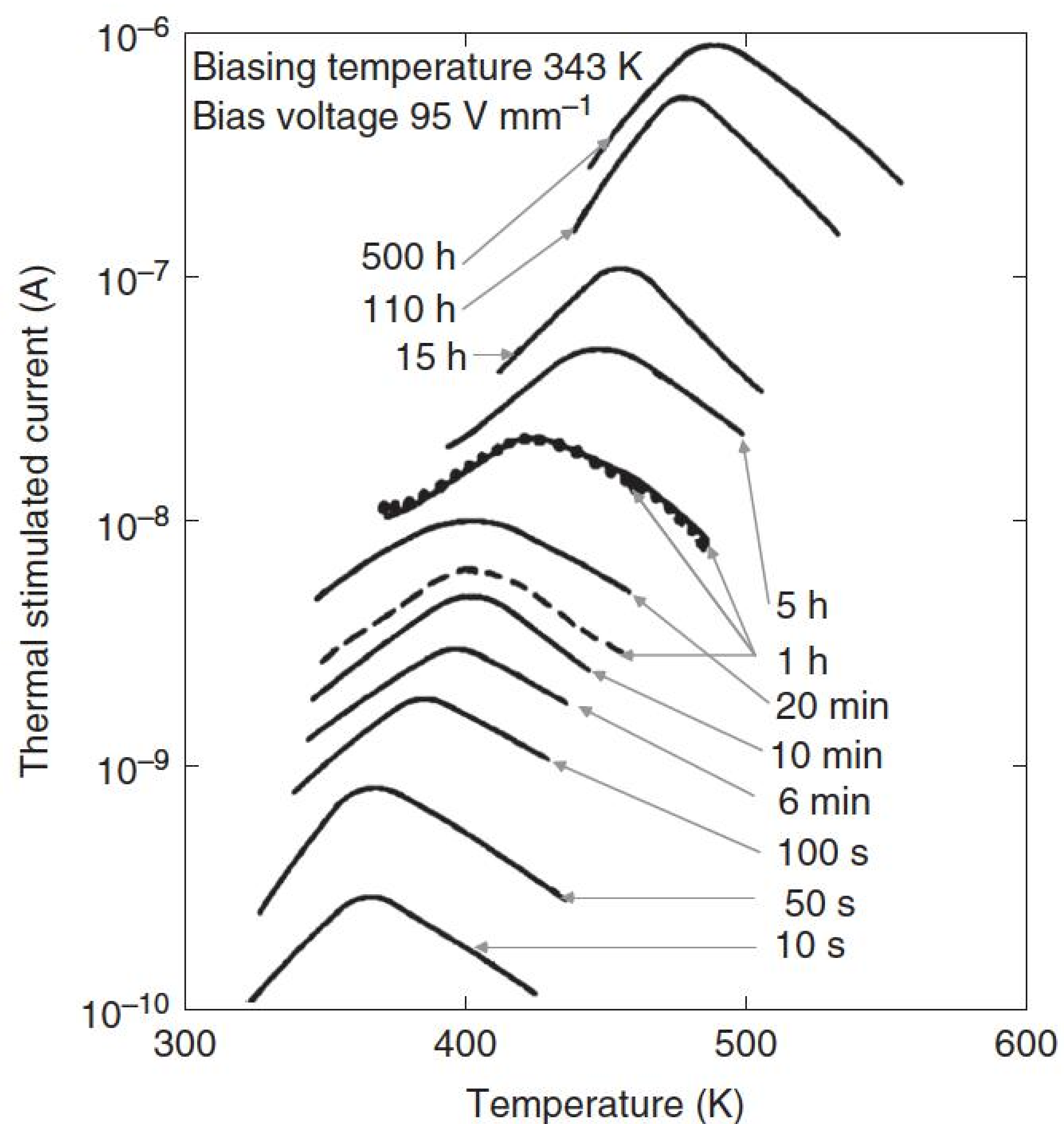


Figure 7.6 Variation of capacitance and dielectric loss of varistor before and after degradation. a, initial; b, after DC biasing; c, after AC biasing. Source: Adapted from Eda et al. [3].

Figure 7.7 The variation of the thermal stimulating current (TSC) of ZnO varistor bulk after degradation [3]. Broken line: TSC in the sample with heat treatment; dotted line: TSC in the nitrogen atmosphere. Source: Eda et al. 1980 [3]. Reproduced with permission of AIP.



caused by the trapped electrons (holes) [3, 11, 21, 38]. As shown in Figure 7.7 [3], the TSC increases after degradation, and the temperature corresponding to the current peak slightly increases.

Integrating the TSC curve to time, the respective ion charge Q_{TSC} will be obtained, which is the total charge of the migrating ions thermally stimulated during the heating process. As shown in Figure 7.8 [3], the ion charge Q_{TSC}

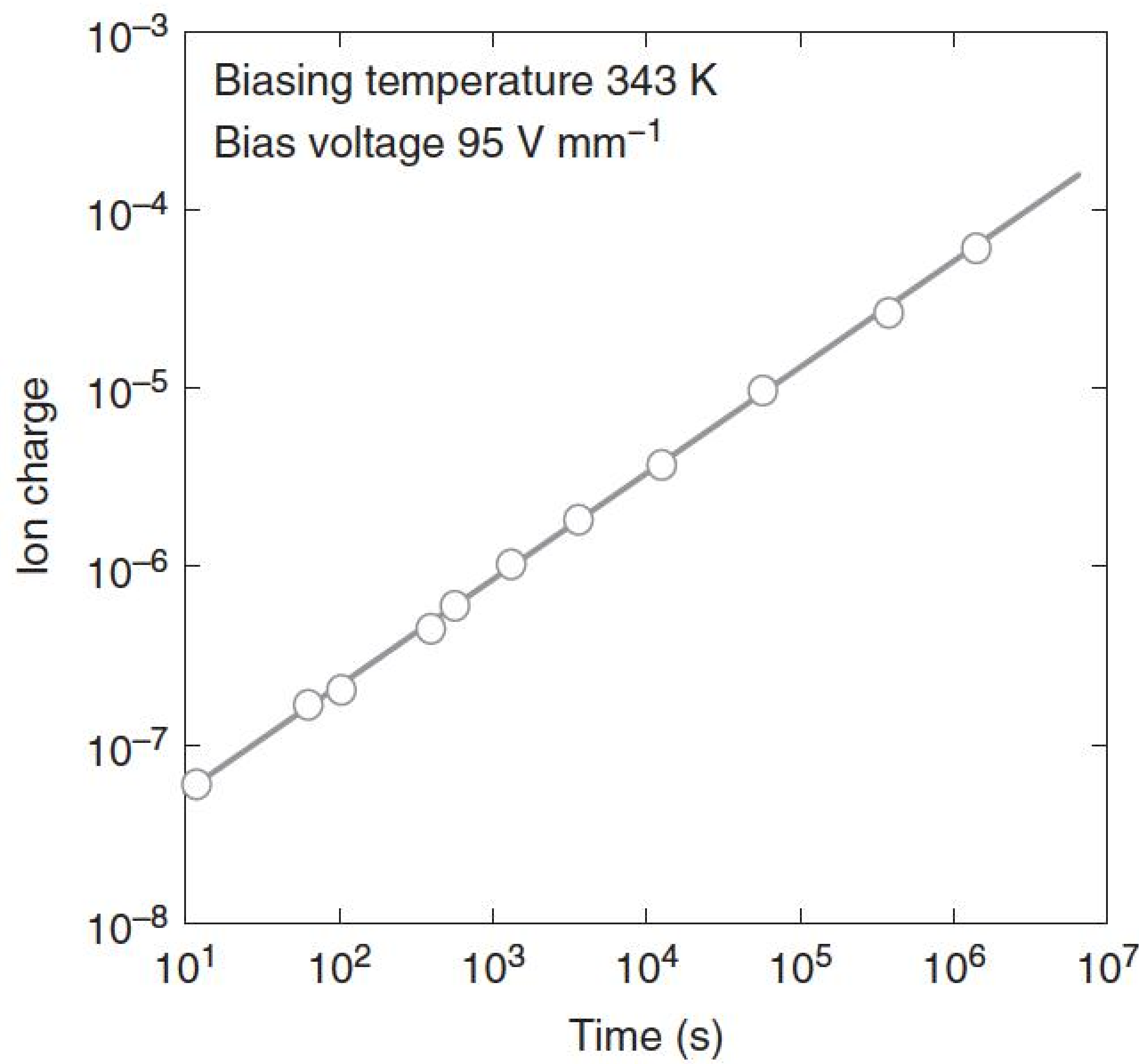


Figure 7.8 The relationship between the ion charge Q_{TSC} (relative value) and the degradation time. Source: Eda et al. 1980 [3]. Reproduced with permission of AIP.

increases with the degradation time t. which is actually in proportion to t^n, n is estimated as 0.5. The process producing TSC can be regarded as the reverse process of the degradation of the ZnO varistor by the DC voltage. TSC is caused by ion movement, so the degradation process can be regarded as ion migration.

7.2.2 Degradation of Grain Boundary

It is expected that the degradation characteristic of the ZnO varistor bulk is the synthetical effect of millions of individual grain boundaries with different degradation rates in a complicated network, so the property of ZnO varistors largely relies on the degradation characteristics of individual grain boundaries. This has been facilitated by techniques for measuring the performance of individual grain boundaries. According to the variation trend of the leakage current in the prebreakdown region, the degradation characteristics of individual grain boundaries can be distinguished and classified into two categories: monotonic and nonmonotonic. Monotonic aging process means that the leakage current of a single-grain boundary monotonously degraded at different aging stages. On the contrary, nonmonotonic aging process means that the leakage currents of multiple-grain boundaries could be recovered during the aging process [33, 37].

A typical monotonic aging process in the I–V characteristic of a single-grain boundary, measured by the microcontact technique [33], is shown in Figure 7.9a. The breakdown voltage of this grain boundary is around 3 V. The prebreakdown region and the breakdown region of the I–V characteristic curve gradually and monotonously move toward the direction where the current increases. The leakage current gradually increases, whereas the nonlinear coefficient decreases, when the aging time increases. Meanwhile, the width of the nonlinear breakdown region is significantly reduced after degradation. Such an aging

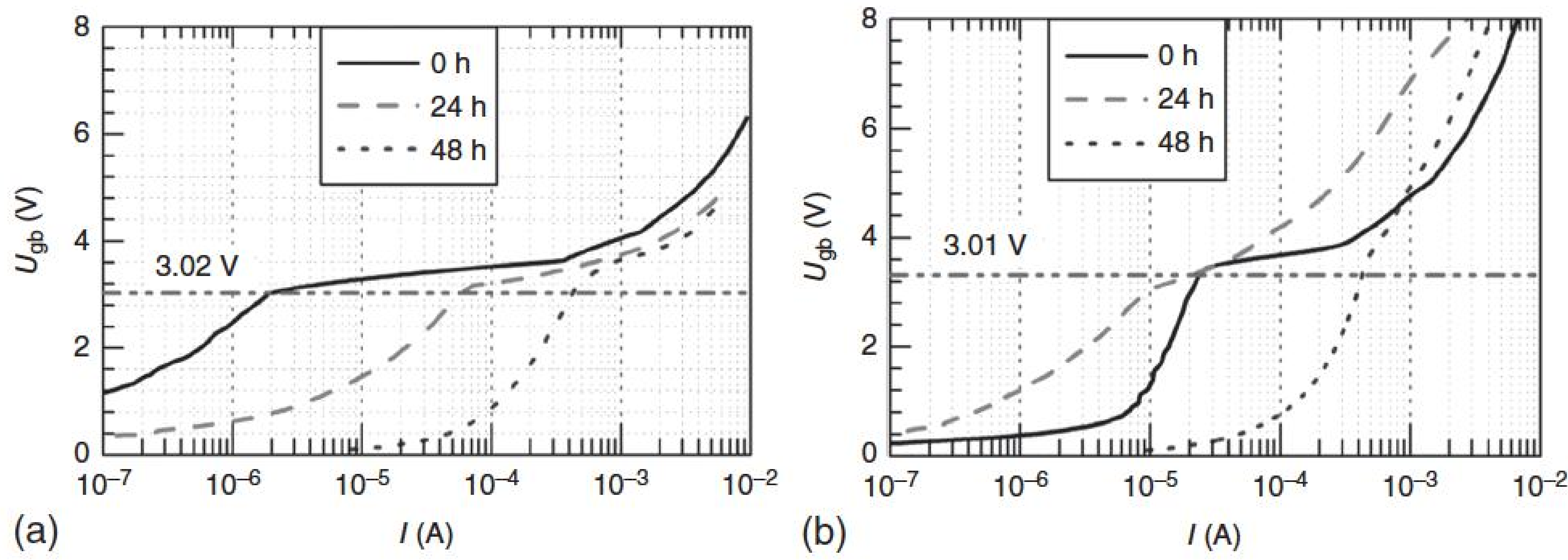


Figure 7.9 Nonuniform aging behavior of individual grain boundaries. (a) Monotonic aging process and (b) nonmonotonic aging behavior of individual boundary. Source: He et al. 2011 [33]. Reproduced with permission of Elsevier.

phenomenon of the grain boundary is common and expected. Moreover, a typical nonmonotonic aging process in the $I-V$ characteristics of individual grain boundaries is shown in Figure 7.9b [33], whose breakdown voltage is also around 3 V. As there is a recovery phenomenon in the prebreakdown region of the $I-V$ curves at an early stage of degradation, this aging process differs obviously from that shown in Figure 7.9a. However, this aging process tends to deteriorate the electrical properties of the varistor eventually. The origin of such a nonuniform aging behavior will be discussed in Section 7.3.

The electrical properties of individual grain boundaries include the breakdown voltage, nonlinear coefficient, and leakage current. As the breakdown voltage after different degradation times basically remains constant in the degradation process, the nonlinear coefficient and the leakage current are our primary parameters. The nonlinear coefficients of 25 individual grain boundaries after different degradation durations are summarized in Figure 7.10a [33]. The initial nonlinear coefficients of these grain boundaries are mainly located in the range from 25 to 40 and exhibit a nonuniform variation; after the sample is degraded for 48 hours, the nonlinear coefficient of the individual grain boundaries are mainly distributed in the range from 5 to 10. As the degradation time increases, the nonlinear coefficients of most grain boundaries gradually decrease. However, the decline in the degrees of different grain boundaries is greatly different.

As shown in Figure 7.10b [33], the leakage currents of single grain boundaries before degradation test change in the range from 0.1 to 1 μA. As the degradation test time increases, different grain boundaries show different degradation processes, and the leakage currents of several grain boundaries exceed 1 mA after subjected to the voltage stress of 48 hours, which is relatively large. Meanwhile, the corresponding nonlinear coefficient is very small, which means that the grain boundary becomes kind of "inactive" and has a higher conductivity. In other words, these grain boundaries show lower nonlinearity. Of the 25 investigated single grain boundaries, 16 exhibit the monotonic degradation behavior, whereas the rest of them are nonmonotonic. This directly reveals that the leakage currents of grain boundaries increase in the degradation process.

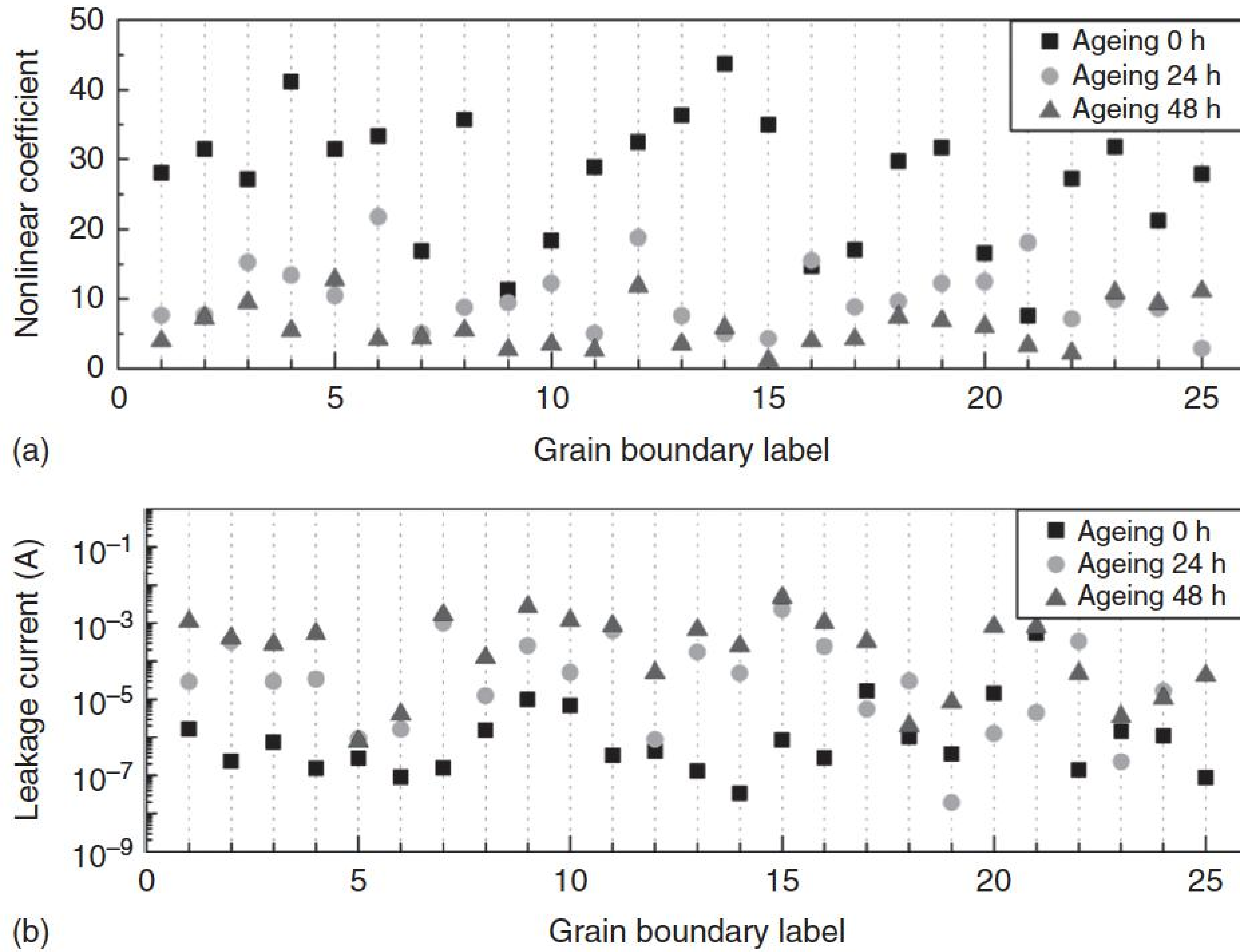


Figure 7.10 The variation of nonlinear coefficient (a) and leakage current (b) of 25 grain boundaries at different degradation times. Source: He et al. 2011 [33]. Reproduced with permission of Elsevier.

The degradation rate coefficient K_T of single grain boundaries was estimated by the empirical equation as follows [33]:

$$I_L = I_{L0} + K_T t^{1/2} \tag{7.1}$$

where I_{L0} is the initial leakage current, I_L is the leakage current after stress, and t is the degradation time. Owing to the nonuniform degradation process of individual grain boundaries, the degradation rates of different grain boundaries are consequently nonuniform and range vastly.

As the V–I characteristics of the ZnO varistor bulk is the collection of responses of all the grain boundaries, the statistical behavior of grain boundaries are meaningful in analyzing the degradation characteristics. Liu et al. analyzed the statistical AC [39] and pulse [40] degradation characteristics of hundreds of individual grain boundaries based on a microcontact measurement method. Exemplified by the AC degradation situation [39] (see Figure 7.11 [39]), during the degradation process, the nonlinear coefficients of grain boundaries become more concentrated in the lower value region, which indicates that the nonlinearity of the grain boundary is reduced. The distribution of breakdown voltage obviously presents two peaks, i.e. P1 (2–5 V) and P2 (5–8 V). The second peak of the voltage is roughly two times larger in amplitude compared to the first one, indicating that P2 is caused by the neighboring effect of the microcontact method (corresponding to two grain boundaries between the adjacent electrodes) [39]. Therefore, the breakdown voltage of most single-grain

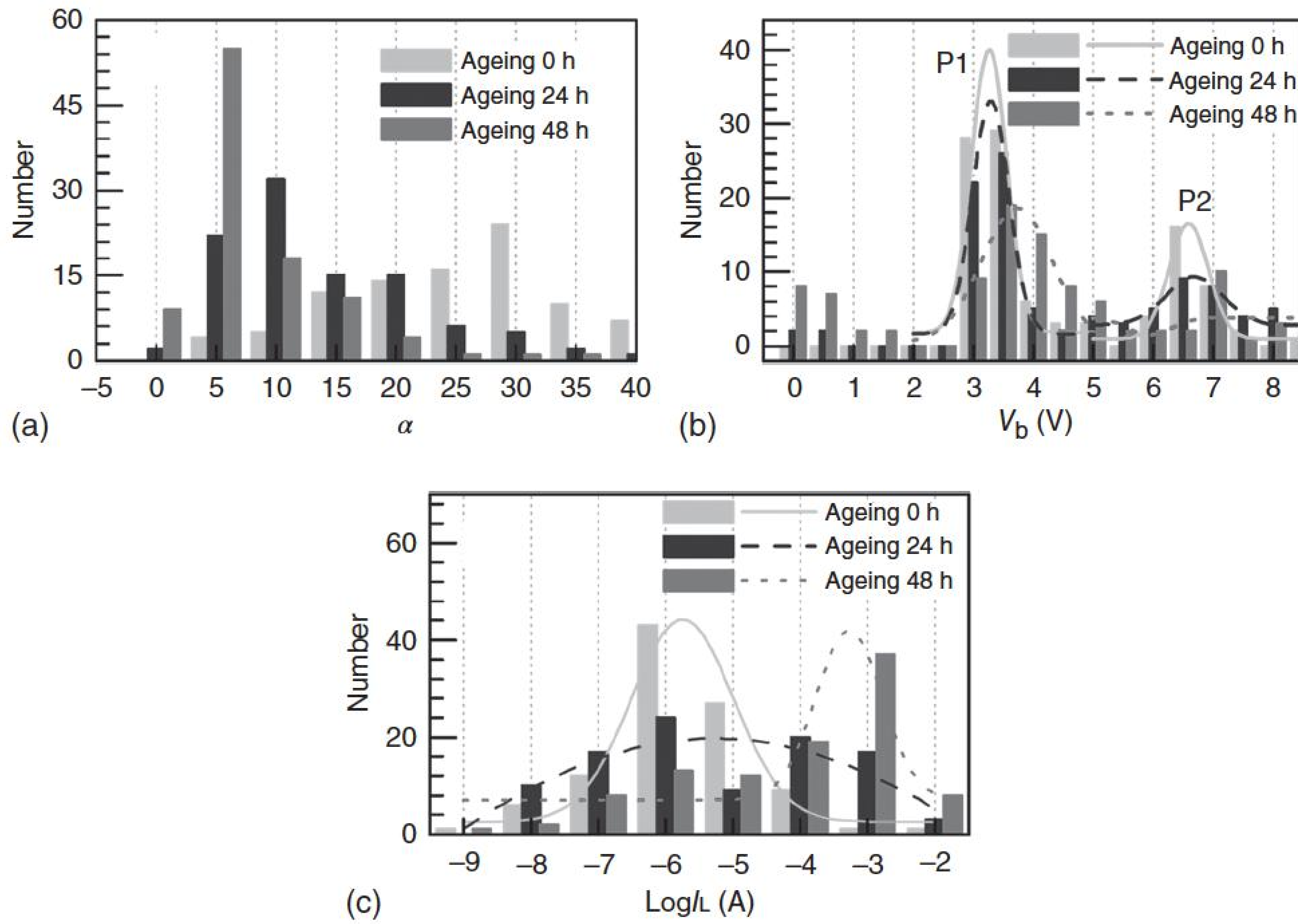


Figure 7.11 Statistics on (a) nonlinear coefficient, (b) breakdown voltage V_b, and (c) leakage current I_L of 100 individual grain boundaries during the AC degradation process. Source: Liu et al. 2011 [39]. Reproduced with permission of Elsevier.

boundaries (active boundaries) is around 3.2 V regardless of degradation. It is also found that the number of grain boundaries with a breakdown voltage less than 2 V (inactive boundary) increases as the aging time increases. Moreover, the leakage current of the grain boundaries continuously increases during the aging test.

The degradation characteristics of single-grain boundaries indicate that the histograms of nonlinear coefficients become more concentrated in the lower region and the distribution of leakage currents shifts toward larger currents during the degradation process. The breakdown voltages of single-grain boundaries, which still exhibit nonlinearity, are not obviously changed. However, there are more grain boundaries with a lower breakdown voltage less than 2 V after degradation.

7.2.3 Pulse Degradation Characteristics

Under pulse voltage, the ZnO varistor has a similar degradation phenomenon of AC or DC degradation, which will not be described again. The pulse electroacoustic (PEA) was applied to characterize the aged performances of ZnO varistors [38]; the experimental results show that the trap level and the trap charge increase as the degradation time or the impulse current increases, but the impulse current plays a more important role in the pulse degradation process of ZnO varistors. The TSC results show that ion migration happens during the pulse degradation process of ZnO varistors, which is accounts for the drift of the V–I characteristic curves. The pulse degradation of ZnO varistors is the consequence of ion

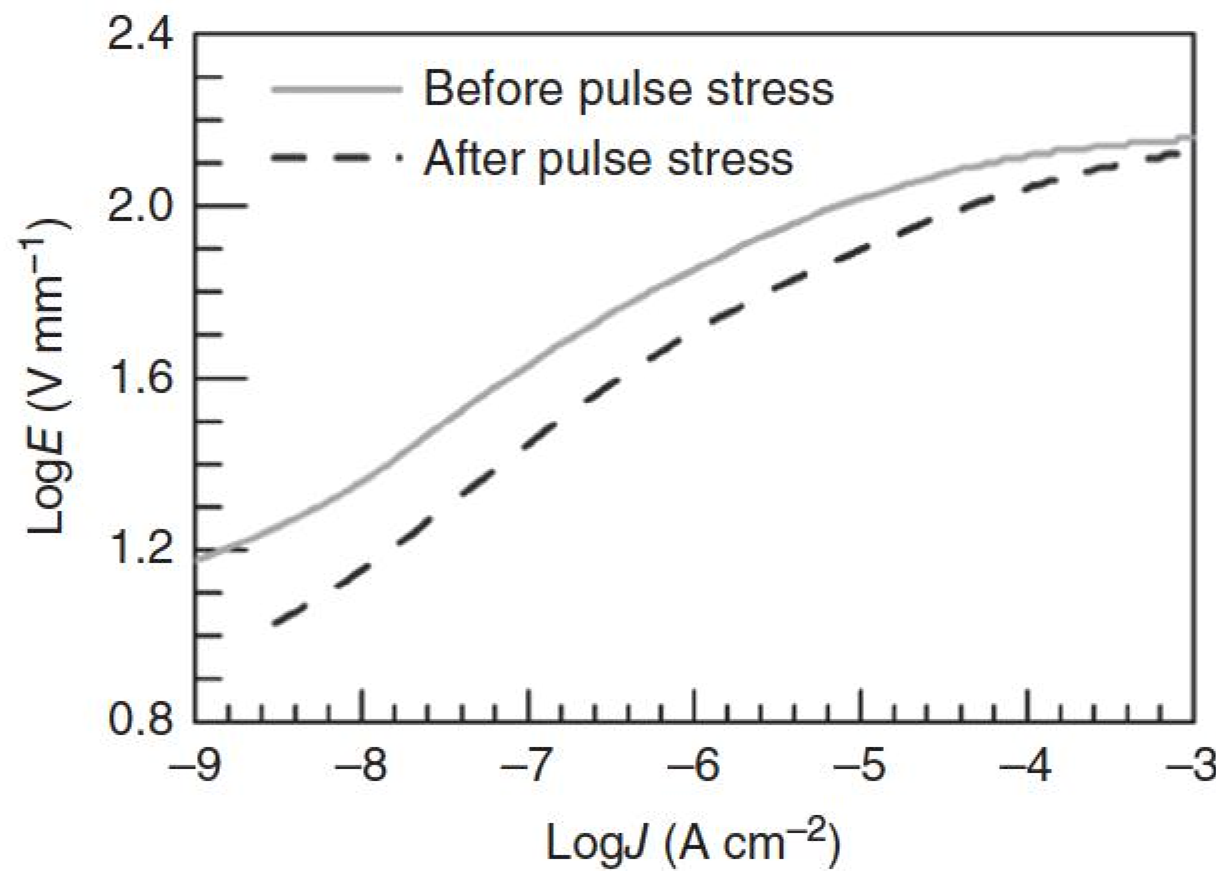


Figure 7.12 The *J–E* curves of ZnO varistor bulk before and after pulse stress. Source: Liu et al. 2010 [40]. Reproduced with permission of John Wiley & Sons.

migration and thermal aging. The space charge characteristics of ZnO varistors may provide a new view to study the pulse degradation principle of ZnO varistors.

The ZnO varistor bulk was degraded under an 8/20 μs pulse current stress whose current density is 800 A cm^{-2}, for 800 times. The J–E characteristics of this bulk sample before and after pulse stresses show an obvious degradation phenomenon as given in Figure 7.12 [40]. The electrical properties, including the nonlinear coefficient α, the breakdown voltage V_b, and the leakage current I_L, were derived from the I–V curves of individual grain boundaries of the ZnO varistors.

By randomly measuring 100 individual grain boundaries, the distributions on the electrical properties for the degraded and nondegraded samples are shown in Figure 7.13 [40]. The histograms of the electrical properties of different grain boundaries reflect the heterogeneity of the microstructure in ZnO varistors. After pulse degradation, the similar conclusions are obtained. The electrical properties of the single-grain boundary in ZnO varistors deteriorate after subjected to the pulse current stress. The number of grain boundaries with a high nonlinearity and a low leakage current decrease because of the deformation of the barriers, whereas the breakdown voltage does not exhibit an obvious change. The distribution of the nonlinear coefficient becomes more concentrated in a low nonlinear coefficient region for a pulse-degraded sample than a nondegraded sample. Several linear grain boundaries appear because of the vanishment of DSB after the pulse current stress test.

The histograms of the breakdown voltage V_B exhibit two obvious local peaks as shown in Figure 7.13b [40], both peaks correspond with single- or double-grain boundaries between the adjacent electrodes. The results reveal that the breakdown voltage of the single-grain boundary does not change a lot for the two samples. However, the number of grain boundaries with a breakdown voltage less than 2 V increases for degraded samples, which means that some grain boundaries become inactive and do not exhibit nonlinearity any more. Gaussian distribution is used to fit the distribution of the leakage current. After degradation, the distribution peak of the nondegraded sample moves right to P3, and the peak centers for the nondegraded and degraded samples are located at −6.28 and −5.66, respectively.

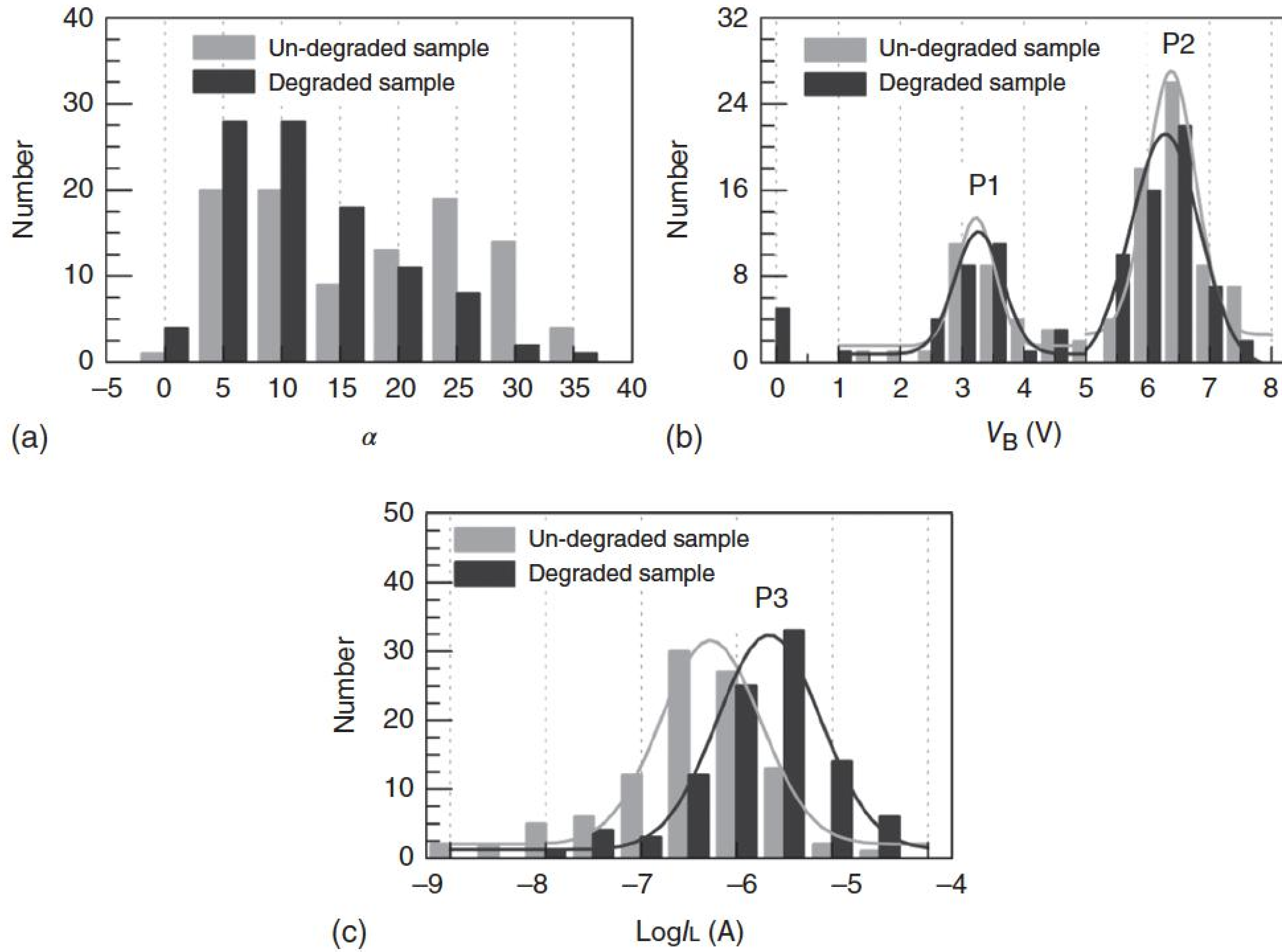


Figure 7.13 The histograms of nonlinear coefficient (a), breakdown voltage (b), and leakage current (c) of 100 grain junctions of nondegraded and degraded ZnO varistor samples. Source: Liu et al. 2010 [40]. Reproduced with permission of John Wiley & Sons.

The shift of the peak center means that the leakage currents of most grain boundaries increase after the pulse current stress. In light of the conduction mechanism of ZnO varistors, the current flow through the varistor is determined by [25]

$$I = I_0 \exp\left(-\frac{\phi_b - \beta\sqrt{E}}{kT}\right) \tag{7.2}$$

where β is the Boltzmann constant, ϕ_b is the DSB height, and T is the absolute temperature. According to Eq. (7.2), the decrease in barrier height due to pulse current leads to the increase in leakage current of an individual grain boundary.

7.2.4 Topographic Information for Degradation Analysis

The barrier voltage of ZnO-doped varistors can be electrically, chemically, and thermally degraded during use, leading to the reduction of barrier voltage height and, consequently, to the increase in leakage current, which could be catastrophic for ZnO varistors. Ramírez et al. [22] used electrostatic force microscopy (EFM) to analyze the surface charge accumulated at the grain boundary regions before and after degradation. The topographic information was stored with a selectable height offset in the EFM mode, during which the electric field data were collected simultaneously. The conductive tip (PtIr coating) was subjected to a range

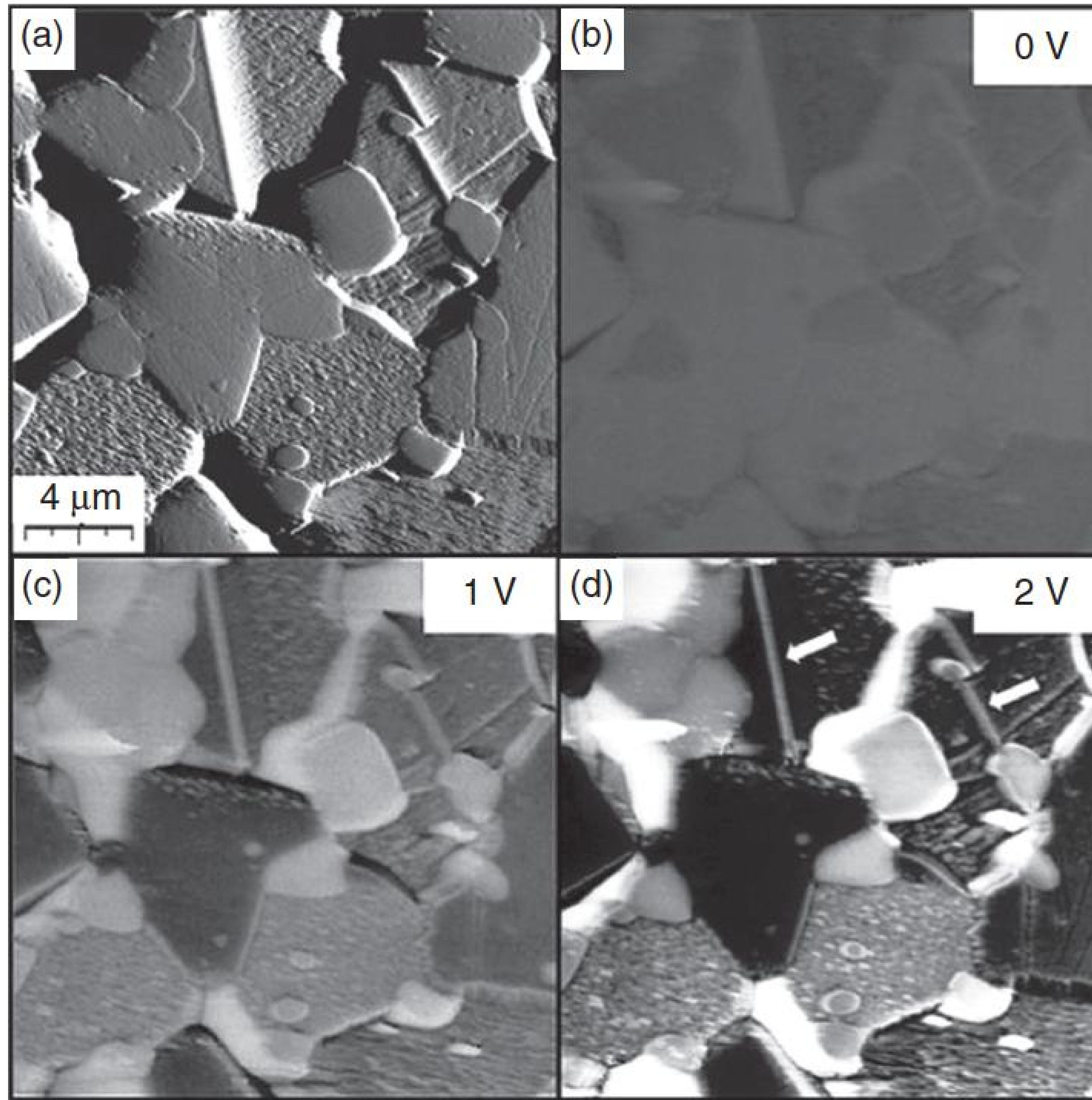


Figure 7.14 (a) AFM topographic image of the ZnO-based system before electrical degradation. Series of EFM images without applied voltage (b), with applied voltage of 1 V (c), and 2 V (d). In figure (d), arrows indicate active potential barriers. Source: Ramírez et al. 2013. [22]. Reproduced with permission of John Wiley & Sons.

of voltages from 0 to 2 V to increase the image contrast, and the EFM scan was performed at a lift height of 50 nm.

For their prepared ZnO varistor samples, Figure 7.14 shows the EFM images with voltage steps from 0 and 2 V applied to the tip [22]. The bright grain regions are more resistive compared with the dark grain regions, and the electrical responses of some grain boundaries are predominantly insulating. From Figure 7.14b–d, a clear change in the electrical behavior depending on the bias applied becomes evident, indicating that the potential barrier formed in some of the grain boundaries are of Schottky type as marked by arrows in Figure 7.14d [22]. Before the degradation process, 30% of the barriers are active, but the ratio showed changes in the electrical behavior when degraded with pulses.

As shown in Figure 7.15 [22], after electrical degradation with a DC voltage at 110 °C (thermal runaway temperature), a significant decrease in the number of effective barriers to 5% is observed. There is also a decrease in the barrier height. In addition to influencing the grain boundaries by eliminating much of the effective barriers and reducing the barrier efficiency, the degradation process also affects the electrical response of the grains as discussed before. After degradation with 8/20 μs pulsed currents, the statistical analysis determines that only 1% of the interfaces is effective. The image contrast between dark and bright grains in the EFM image is very low compared with the original sample, indicating more conductive grains with lack of the nonohmic behavior.

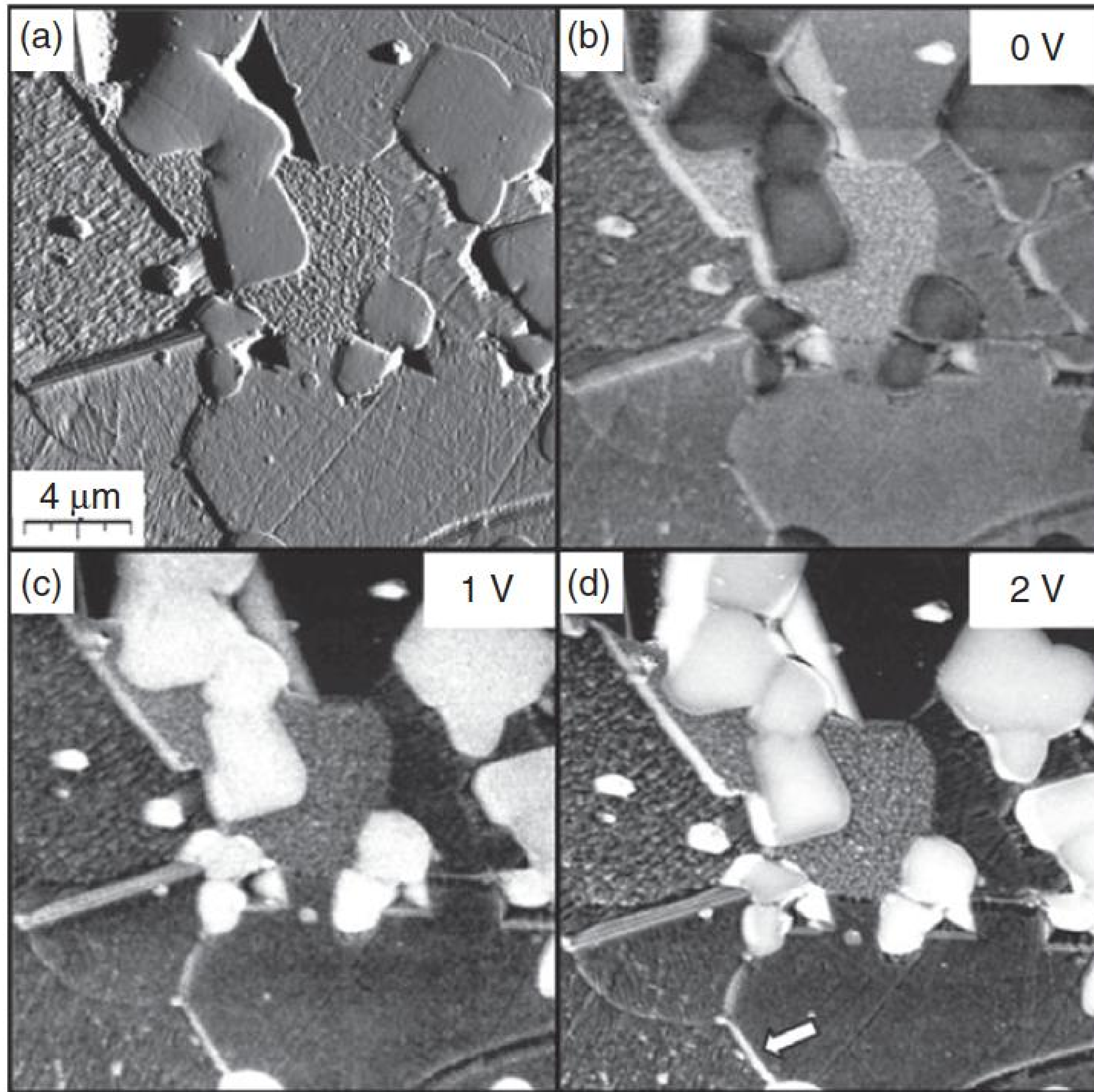


Figure 7.15 (a) AFM topographic images of the ZnO-based varistor after electrical degradation with DC voltage at 110 °C. A series of EFM images without applied voltage (b), with applied voltage of 1 V (c), and 2 V (d). In (d), arrows indicate active potential barriers. Source: Ramírez et al. 2013. [22]. Reproduced with permission of John Wiley & Sons.

7.3 Migration Ions for the Degradation of ZnO Varistors

The lowering of DSB height, i.e. the deformation of DSB, has been considered as the only reason for the increase in leakage current. Here, we focus on the degradation phenomena under the effect of various stresses and present a full picture of the universal electrical degradation mechanism of grain boundaries, from the perspective of defects, portraying the ion migration process that is related to the degradation of DSB. The main content of this section can be found in [41].

7.3.1 Grain Boundary Defect Model

It can be derived by using Poisson's equation to describe the DSB that the potential barrier height ϕ_b is proportional to N_i^2/N_d [34], where N_i is the interfacial state density and N_d is the donor concentration inside the depletion layer. This indicates that the degradation phenomenon of DSB, i.e. the lowering of barrier height, can be caused by either the decrease in interfacial states or the increase in donor density. As Blatter and Greuter's conduction model with the assumption of infinitely thin grain boundary [42] fails to explain the asymmetrical DC aging behavior of $I-V$ characteristics, Gupta and Carlson in 1985 [19] proposed their seminal grain boundary defect model, aimed at revealing the foundation of DSB and the instability of the ZnO varistor. This widely recognized

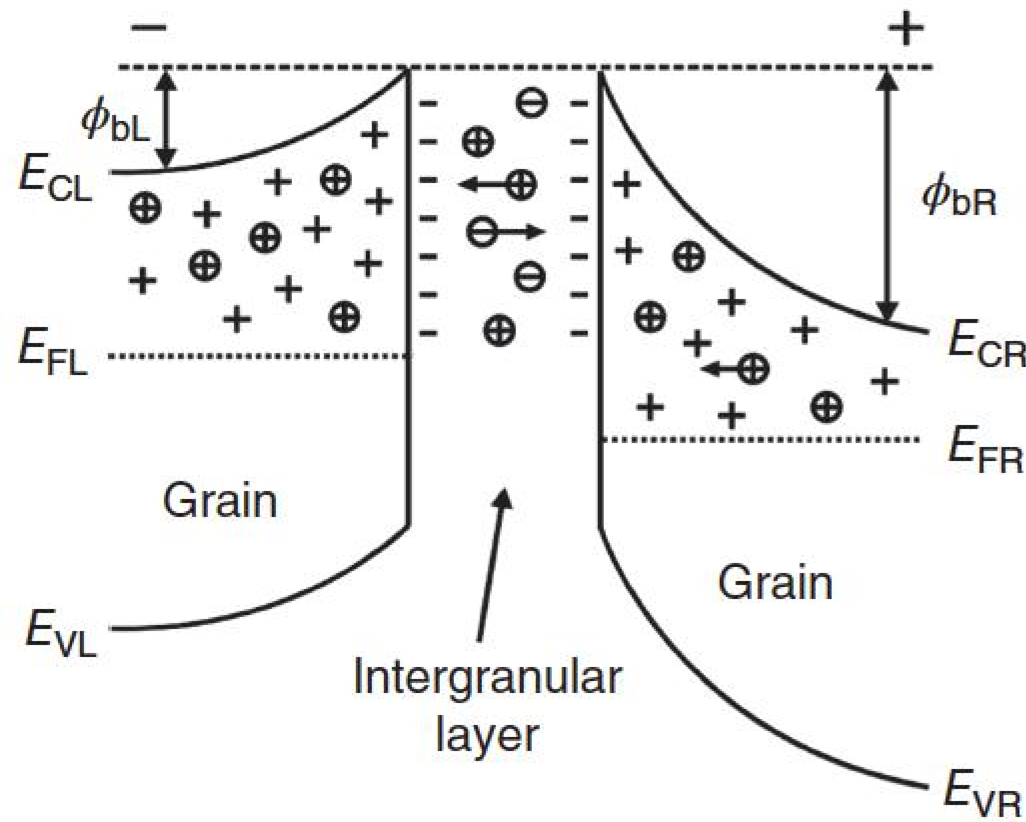


Figure 7.16 Extended Gupta and Carlson's grain boundary defect model with external DC voltage biased, where ϕ_{bX} (X: L, left side, R, right side) is the Schottky barrier height, E_{CX} represents the conduction band minimum, E_{FX} denotes the Fermi energy level, and E_{VX} stands for the valence band maximum [41]. The symbols ⊕ and ⊖ represent the positive and negative metastable defect ions, respectively, which are distributed in the grains and grain boundaries. Source: He et al. 2016 [41]. Reproduced with permission of AIP.

model (as seen in Figure 7.16 [41]), which could well explain the experimentally observed degradation phenomena, relies on the basic presumption that an intergranular layer with certain width exists, which separates the two Schottky barriers, and that the depletion layers contain two types of defect species, i.e. one is the spatially fixed positively charged ions and the other is the metastable positively charged ions, which can be perturbed by the external electrical field and become mobile. In their predictions, the zinc interstitial (Zn_i) is considered as the dominant metastable (mobile) ion that could migrate to interface and neutralize with the negatively charged interfacial states (e.g. V_{Zn}), responsible for the degradation phenomena of DSB. It should be further noted in Gupta and Carlson's original article that only the negative interfacial states that are spatially immobile (as shown in Figure 7.16) are considered. When an external DC electrical stress is applied, the reverse-biased barrier withstands most part of the voltage, and mobile ions in the reverse-biased region have a higher statistical probability of transiting and migrating to the grain boundary, compared to the ones in the forward-biased depletion layer [43], hence the prominent deformation of reverse-biased Schottky barrier. A detailed defect reaction formula portraying the degradation process of DSB and the stabilization of potential barrier by heat treatment is directed to Ref. [19], and the extension of discussion to AC electrical degradation of DSB is straightforward.

To further explain certain abnormal degradation phenomena that are occasionally observed in the experiments, e.g. a nonmonotonic degradation behavior of DSB [33, 37] such as the increment of forward-biased barrier at an early stage of degradation [37], the extended Gupta and Carlson's model [23, 44, 45] should be inevitably mentioned here, where the role of intergranular phases are taken into consideration additionally. Such an extended model centers on the charged particles (as shown in Figure 7.16) inside the intergranular layer, i.e. the charged particles can also be activated, in addition to the metastable ions in depletion

layers, and move along/against the direction of electrical field, thus participating in the degradation process. Moreover, the effect of the intergranular phases largely depends on the recipe of the additives because such abnormal degradation phenomena do not necessarily occur in every degradation experiment.

7.3.2 Experimental Proof of Ion Migration

The migration and neutralization of charged defect ions during the electrical degradation process of DSB are observed [43], offering the possibility to experimentally access the predicted defect migration behavior that causes the degradation phenomena of DSB and providing a solid foundation to validate the theoretical aging model by Gupta and Carlson [19]. This is achieved by combining the nondestructive quantitative profiling technique for charged ion distribution, i.e. the PEA method [46, 47], with artificially fabricated ZnO quasi-bicrystal [43, 48] of excellent electrical nonlinearity, which imitates an individual grain boundary inside the varistors.

The PEA method has been widely used over the past few decades to quantitatively detect the spatial distribution of charged ions inside the materials [46, 49]. This sensitive method is of high resolution [50], with its basic principles found elsewhere [46, 50, 51]. The amplitude of the measurement results is proportional to the density of charge, with its polarity straightforward denoting the polarity of charge, and the delay is related to the position of charge. Moreover, ZnO quasi-bicrystals, in which a uniformly thin dopant layer is sandwiched between two ZnO single crystals of specific orientation, are adopted. Because of that, the distribution of charged ions in the bicrystals is believed to only vary in the through-thickness direction [43], i.e. one-dimensional distribution, which is the prerequisite for performing the PEA test [46, 47, 49]. In the quasi-bicrystal samples, the intergranular layer contains Bi, Mn, and Co elements for acquiring excellent electrical nonlinearity (fabrication procedures of quasi-bicrystal are directed to Ref. [45]).

Quasi-bicrystal samples are continuously aged under a stabilized DC bias, and after each 10-minute period, the PEA measurement is carried out [45]. Typical measurements of the ion distribution in the DSB region are shown in Figure 7.17 [45]. The two positive parts of each curve (above $0\,\text{nC}\,\text{cm}^{-3}$) depict the distribution of the positively charged ions in the depletion layers. The negative part describes both the negatively charged interfacial states and the intergranular phases. Generally, the defect energy levels at the grain boundary interfaces are largely responsible for the electrical properties of ZnO varistors [52]; the intergranular phases in the grain boundary are neglected. Figure 7.17a,b shows that during the degradation process, the positive amplitude of the curve on the right side decreased continuously, whereas that on the left side only decreased slightly. This indicates the lowering of the reverse-biased Schottky barrier. Furthermore, along with the decrease in the value of interfacial state density, the geometric center of the negative part of the curve moved to the left, i.e. the magnitude of the right half of the negative curve is reduced significantly, whereas, on the contrary, that of the left side remained almost unchanged. This can be interpreted as an asymmetrical reduction in the donor concentration in

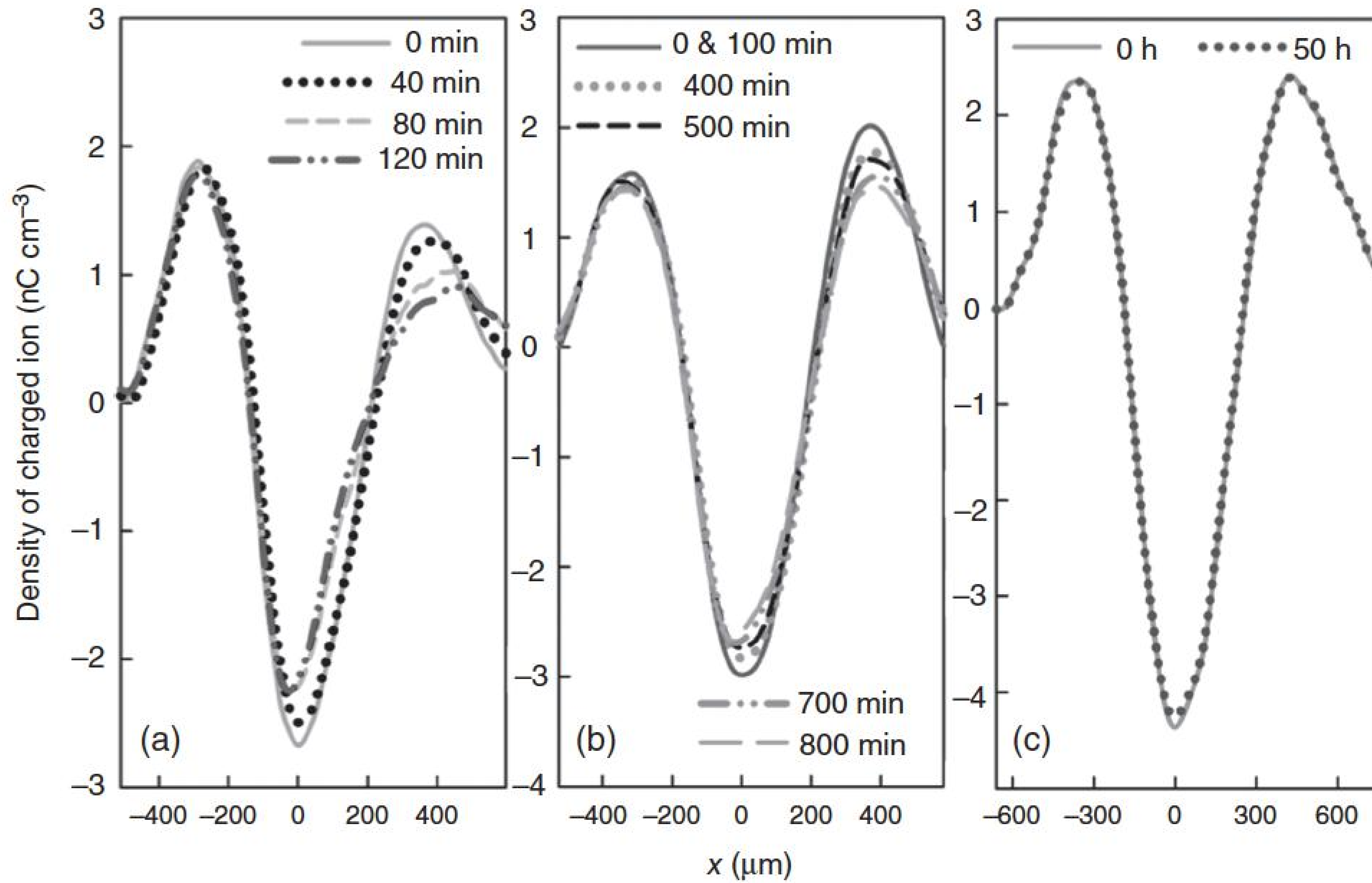


Figure 7.17 Variation with the time of the spatial distribution of charged ions in the DSB region during the degradation process. The grain boundary region in a quasi-bicrystal is located at the zero point on the horizontal axis. (a) and (b) are conventional quasi-bicrystal samples under degradation. (c) A quasi-bicrystal sample treated by aerobic oxidation for the elimination of mobile ions responsible for the degradation of DSB. For each sample, the time indicated is the respective aging time under a stabilized DC bias of +3 V at 320 K, and the positive electrode is placed at the right side of the DSB region such that mobile ions in the depletion layer of reverse-biased Schottky barrier seem likely to be activated and migrate to the grain boundary. Source: Cheng 2014 et al. [45]. Reproduced with permission of AIP.

the two depletion layers (neutralized with negative interface states). The above results indicate that the migration and neutralization of the charged ions mainly occurred in the reverse-biased Schottky barrier region in a quasi-bicrystal. This is in accordance with Gupta and Carlson's theoretical predictions [19]. By comparing Figure 7.17a,b for the reverse-biased barriers with different heights, their rates of aging are different, i.e. grain boundaries with higher reverse-biased barriers seems to be more resistive to electrical degradation.

As Zn_i^{2+} is suggested as the optimum candidate [19, 43, 53, 54] for the mobile ions responsible for the degradation of DSB in ZnO varistors, ZnO quasi-bicrystals undergo an additional brief aerobic oxidation (for six hours) at 600 °C to eliminate the zinc interstitial defects [55] (related chemical reactions are detailed elsewhere [19]), on which PEA measurements are also performed. It is found that even after a long-term degradation of 50 hours, the spatial ion distribution is almost invariant with time, as shown in Figure 7.17c, proving the thorough elimination of metastable Zn_i ions.

7.3.3 Identification of Dominant Mobile Ions

As discussed above, the defect foundation for the generation of acceptor-like interfacial states has been revealed, whereas the accurate species of dominant

donor species are still controversial and have not been positively identified yet. During the past few decades, it is believed by researchers and engineers working on ZnO varistors that Zn_i and V_O are the possible candidates for mobile donor defects responsible for the degradation phenomenon. This assumption is strongly supported by numerous experimental observations of dielectric relaxation peaks with activation energies as 0.05 and 0.20 eV that correspond to the thermal transitional levels of defects, using techniques like broadband dielectric spectroscopy and deep-level transient spectroscopy [43, 54, 56–59]. However, recent atomic-scale investigations focused on point defects in ZnO materials that use *first-principles* calculation methods have been brought to attention refreshed and distinct insights into the properties of defects. Even though various researches carried out by different groups could show certain disparities in predicting the characteristics of native defects inside the periodic structure ZnO system [60–72], owing to employing different exchange–correlation approximations, numbers of k-point sampling for Brillouin zone integration, supercell sizes, corrections for spurious defect interactions, and so forth, meaningful and significant conclusions can still be extracted for native donor defect: (i) V_O is the lowest energy donor defect, which means it can be generated in large concentrations, whereas it is surprisingly a deep donor, i.e. its (2+/0) transitional level lies ~1 eV below the conduction band minimum (CBM) and V_O at 1+ charge state is unstable; (ii) the formation energy of shallow-donor zinc interstitial Zn_i is higher compared to oxygen vacancy V_O, and its thermal dynamic (1+/0) and (2+/1+) transitional levels are predicted as 0.05 and 0.16 eV below the CBM by Vidya et al. [62], and as ~0.05 and ~0.1 eV by Oba et al. [64]; (iii) the antisite donor defect like Zn_O is much higher in energy. The occurrence and stabilization of Zn_i is quite controversial because of the calculated formation energy of a relatively high value, and its low migration energy barrier ~0.5 eV [67], which indicates that Zn_i becomes mobile even at a low temperature. It should be noted here that precise calculations for Zn_i may be impeded by its shallow-donor characteristics, i.e. the wavefunction is delocalized, and by the fact that no effective measure exists that is guaranteed to well correct the image defect interactions for shallow-donor defect if supercell size-based extrapolation procedures are not strictly included. More *first-principles* calculations have suggested that the formation energy of native defects (especially Zn_i) can be significantly reduce when undoped grain boundary exists because of the interactions between the defects and the boundary [73], and if captured by other point defect or impurity defect to form the complex defect, the formation energy of Zn_i can be further lowered [62, 74]. Hence, it is argued here that the accumulation of native donors in the depletion layers is believed to be facilitated by the Bi- or Pr-doped grain boundary and by forming certain complex donor defects, and then the remaining issue is how to identify the dominant mobile donor ions based on the long-term aging simulation method described below.

To gain an insight into the degradation process and to determine the species that is most likely to be the mobile ion, a long-term aging simulation method was performed. Such a long-term aging simulation aimed at portraying the migration process of mobile donor ions and their neutralization with interfacial acceptor states. Various kinds of defect ions were considered, and simulated aging

characteristics were compared with experimental aging data of quasi-bicrystal [75, 76] to identify the dominant mobile species.

According to the Boltzmann statistics, ΔP, the net migrating rate of defect ions along the direction of the applied electric field, is [76]

$$\Delta P = \frac{\gamma_0}{6} \exp(-U_0/kT)[\exp(+\Delta U/kT) - \exp(-\Delta U/kT)] \tag{7.3}$$

Based on Eq. (7.3), the migration velocity of ions can be obtained [76]. Basically, this value could estimate the difficulty and possibility of migration for various defect ions. Using the Blatter and Greuter's model [42, 76], the Schottky barrier $\Phi(x, t)$ and further the distribution of electric field $E(x, t)$ in the DSB region can be calculated by confining Poisson's equation with boundary conditions [76]. Then, advection equation, which is frequently used for the characterization of diffusion process, is utilized to characterize the migration process:

$$\frac{\partial \rho(x,t)}{\partial t} + \frac{\partial[\rho(x,t) \cdot v(x,t)]}{\partial x} = 0 \tag{7.4}$$

The part of ions migrating to and entering the interface would neutralize the negative interfacial states. More details of this simulation method are directed to Ref. [76] because of the length limit of this book.

In the simulation, three different kinds of native donor defects are considered as potential mobile ions: the V_O of a neutral charge state ($V_O^\times$ or V_O^0), Zn_i in a 1+ charge state (Zn_i^+), and Zn_i^{2+} from a complex defect ($V_O^0 - Zn_i^{2+}$), which are selected because they are more stable or energetically easier to be generated [62–64, 66, 67, 74] when compared to other charge states. As the Fermi level is generally accepted to lie 0.067 eV below the CBM in the grain boundary region [42] of the ZnO varistor, the individual Zn_i in the 1+ state is favored because, for instance, the (1+/0) and (2+/1+) transition levels are located at 0.05 and 0.16 eV, respectively, below the CBM in Zn-rich n-type ZnO as suggested by Vidya et al. [62], whereas the V_O is neutral simultaneously [62, 64]. Specifically, the proposal by Kim and Park [74] was adopted in favor of the novel interaction between component point defects inside the complex donor ($V_O^0 - Zn_i^{2+}$) [62, 74], i.e. the strong attractive interaction between V_O^0 and Zn_i^{2+} caused by quantum mechanical hybridization significantly lowers the formation enthalpy of the $V_O^0 - Zn_i^{2+}$ pairs, which makes it possible for Zn_i^{2+} to be generated in large quantities in the DSB region. Even though the V_O^0 owns the lowest formation energy among various individual donor defects [62–64, 66, 67], it must be excluded before simulation because of its deep-donor nature in the n-type ZnO (i.e. make no contribution to the degradation of DSB).

The comparison of simulated results with the experimental ones is presented in Figure 7.18 [76]. The Zn_i^+ defect has a low migration barrier (experimental value of 0.55 eV) [67] and the simulated curves of four different distribution functions overlap. The Schottky barrier on the foundation of Zn_i^+ collapses promptly (shown as the simulated vertical dashed line in Figure 7.18), which is consistent with its "fast diffuser" nature even at low temperatures. When it comes to the $V_O^0 - Zn_i^{2+}$ defect, Zn_i^{2+} from the complex is subject to more

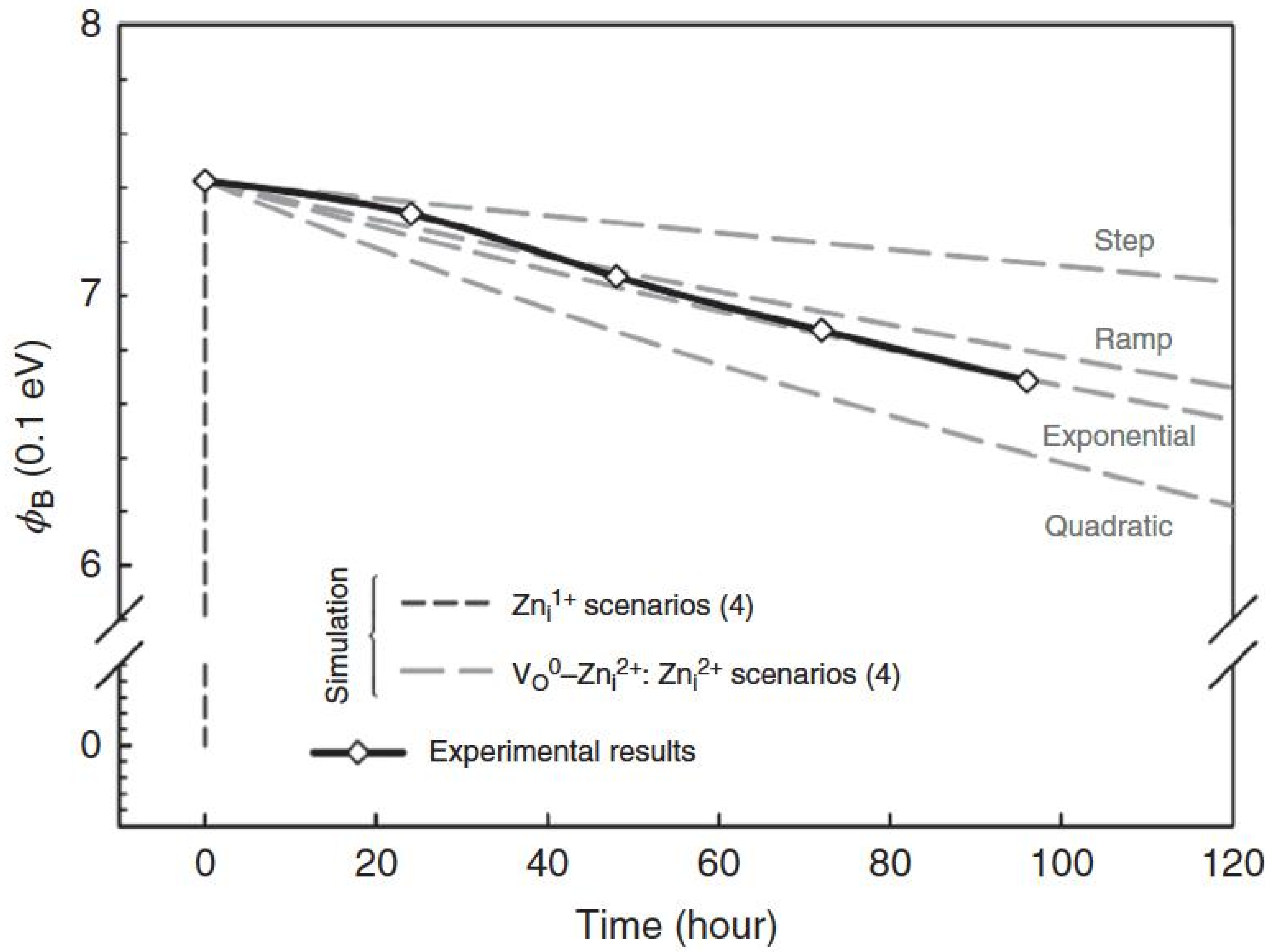


Figure 7.18 Long-term aging simulation of ZnO bicrystal suggesting $V_O^0 - Zn_i^{2+}$: Zn_i^{2+} as the dominant mobile ion resulting in the degradation of DSB. Four hypothetical kinds of charged donor distributions (step, ramp, quadratic, and exponential functions) are employed. Source: He 2015 [76]. Reproduced with permission of Elsevier.

restriction from the binding energy, which, together with the migration barrier, determines the migration behavior of Zn_i^{2+}. Among the four displayed situations of various depletion ion distributions, the experimental results lie close to the exponential ones and are enveloped by simulated curves. Given all that, it is suggested that Zn_i^{2+} from the complex defect is the optimum candidate for the mobile ions. This suggestion has been further verified by the PEA measurement on the aerobic–oxidation-treated quasi-bicrystal [43], as discussed previously.

The long-term aging simulation method has implicitly included the thermal sensitivity of degradation as portrayed by Eq. (7.2), where the vibration frequency γ_0 generally lies in the range between 10^{12} and 10^{13} vibrations per second, and the temperature T inside the exponential term has a great impact for determining the value of ΔP. In addition, the above discussion does not argue that $V_O^0 - Zn_i^{2+}$ is the only possible solution to the degradation phenomena, whereas the critical point is that the simulation method in combination with experimental aging data predicts an estimated migration barrier for potential mobile ions as ~1.0–1.2 eV. With the development of first-principles methods, e.g. the linear scaling density functional theory method [77], a larger and more sophisticated system can be considered, and possible complex defects including Zn_i $(X - Zn_i)$ may be simulated and proposed in the near future. The indispensable component as Zn_i in the complex defect is the resultant compromise of the observed thermal transitional level (~0.05 and 0.2 eV) and the low migration barrier of the individual Zn_i defect. The predicted 1.0–1.2 eV migration barrier can act as the touchstone for potential mobile ion species [76].

7.3.4 Three-Dimensional Extension

For extending the above discussion to a three-dimensional structure of varistors, it should be noticed that the degradation phenomena of quasi-bicrystal is more prominent compared to that of the polycrystalline ZnO varistors. This is because the external electric field applied is perpendicular to the grain boundary plane of the ZnO quasi-bicrystal and parallel to the average migrating path of mobile ions in the depletion layer, whereas the actual grain boundary structure in the ZnO varistors is the three-dimensional winding network such that the electric field can be screened to a certain extent.

As for Bi-doped ZnO varistors, polymorphs of Bi_2O_3 (e.g. α-Bi_2O_3 and δ-Bi_2O_3) may form at the triple junctions [78]. The occurrence and stabilization of Bi_2O_3 of certain phase is closely related to other elements codoped [79] and depends on process conditions like annealing treatment [34]. It is known that δ-Bi_2O_3 is a faster oxygen-ion conductor, and the β phase is much more oxygen conductive than the γ phase [37], which could lead to the speculation concerning its role as stabilizing/destabilizing the ZnO varistor. Recently, Takada et al. [80] have investigated the two types of Bi_2O_3 deposits (sheet-like and spot-like, as seen in Figure 7.19) on fractured surface of ZnO grains using back-scattered electron (BSE) mode in scanning electron spectroscopy. The preference for a certain type of deposit relates to the formulation, sintering temperature, and surface-free energy (surface tension); for instance, when the sample was annealed at 700 °C, a compound of Bi and excess Zn formed a uniform thin deposit or moved to triple points. The increase in the surface area of the ZnO grains by the sheet-like deposit of Bi_2O_3 contributes to the resistance to electrical degradation, as this deposit hinders the movement of oxide ions or Zn^{2+} ions across the grain boundaries under an applied voltage [80].

Actually, investigation on Bi_2O_3 of various phases is a subject with broad interest for its wide applications [81], e.g. Bi_2O_3 doped with potassium exhibits superconductivity, and hence, we cannot drop conclusion on its precise effect on DSB degradation until more atomic-scale investigations are presented, which currently lack because of the difficulties in the theoretical modeling of the corresponding systems that are also computationally demanding. Fortunately, some excellent review papers [34, 37] have provided discussions, although insufficient, on the role of Bi_2O_3, which could help for a better understanding.

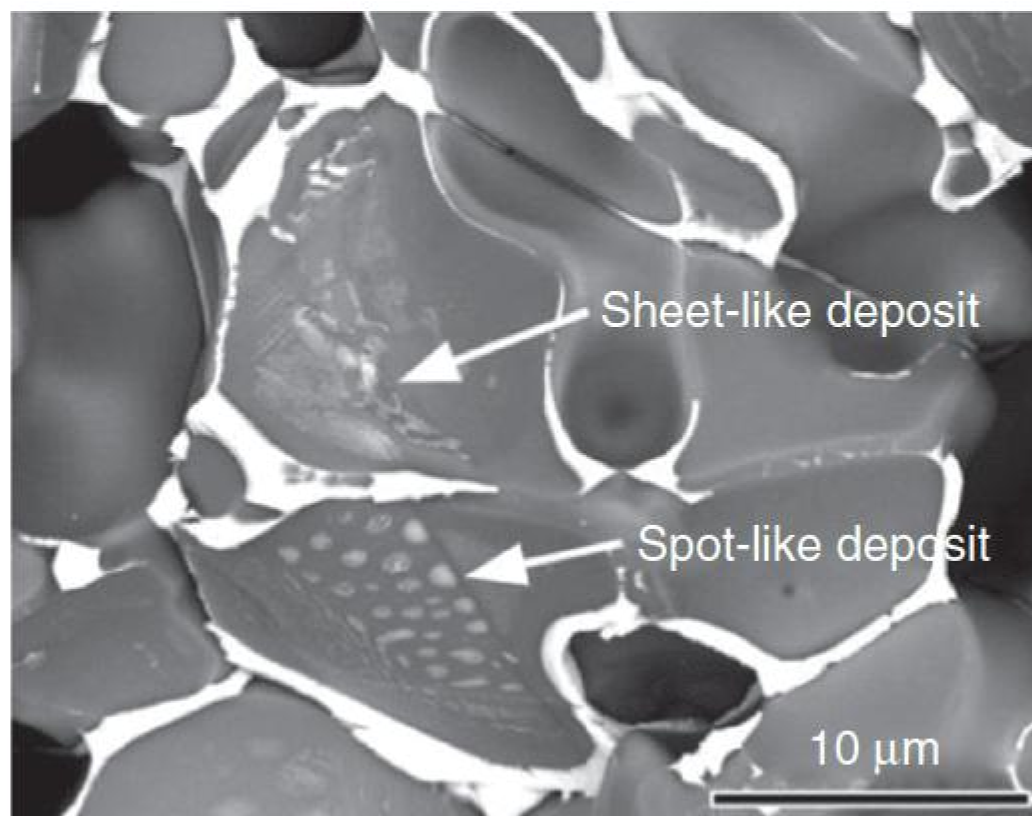


Figure 7.19 Compositional images using BSE on fractured surface of ZnO grains. Source: Takada et al. 2012 [80]. Reproduced with permission of Springer.

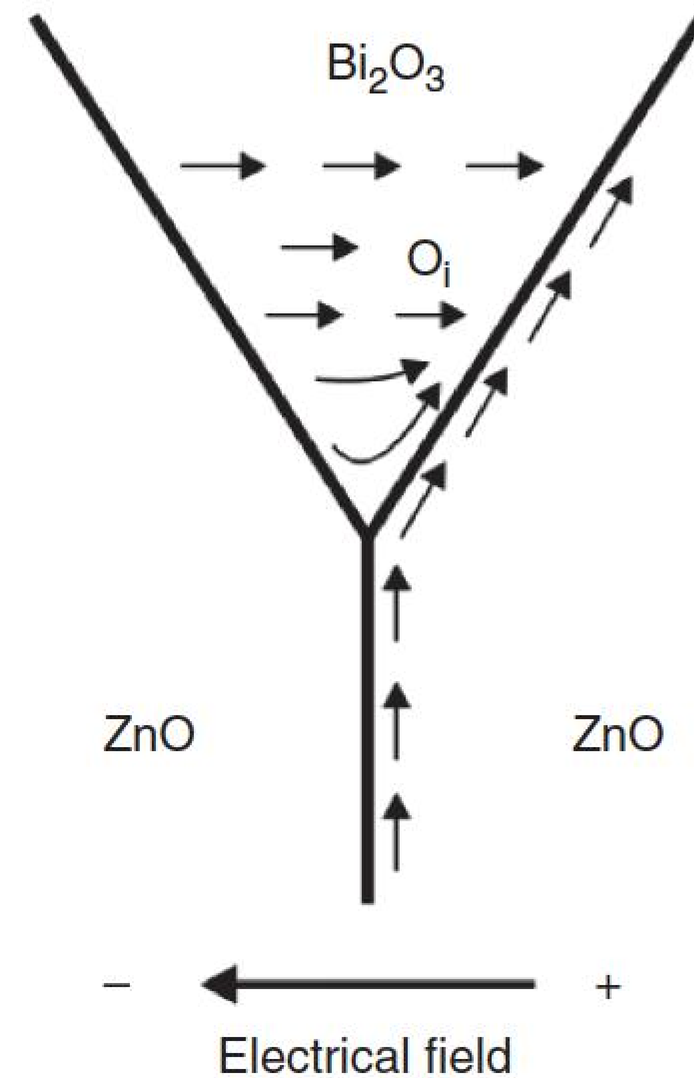


Figure 7.20 Migration of oxygen defects during the degradation process. Source: Adapted from Eda [37].

When an electrical stress is applied, the mobile ions inside the depletion layer may migrate to the grain boundary, as stated previously. Furthermore, the oxygen-related defects may also act as an important role during the degradation process of ZnO varistors. Exemplified by Bi-doped electroceramics, the O_i defect may be activated and get released from the complex defect and migrate along the grain boundary (as shown in Figure 7.20 [37]). This will, as discussed previously, inevitably decrease the density of the complex defect at the grain boundary region and thus deteriorate the acceptor-like interfacial states, thus destabilizing and lowering the Schottky barrier. Such a oxygen desorption and barrier degradation process can be mainly ascribed to two reasons, the effect of electrical stress and the gradient of oxygen defect concentration at the grain boundary region [37].

7.4 Degradation Mechanism of ZnO Varistors

The important feature of degradation is the rising of the resistive component of the leakage current through the ZnO varistors. Under a certain electrical field and an ambient temperature, the lowering of DSB height, i.e. the deformation of DSB, can be considered as the only reason for the increase in resistive current.

The capacitance of the ZnO varistor is composed of the capacitance of the grain boundary layer and the one originated from the concentrated charge of DSB under the effect of voltage. The capacitance of the grain boundary layer is determined by the geometric dimension and will not vary with the voltage biased. Thus, the variation of varistor capacitance is caused by the deformation of DSB. In addition, the deformation of DSB is closely related to the voltage biased. Therefore, the variation of varistor capacitance under a long-term electrical stress (as shown in Figure 7.6) is also caused by the deformation of DSB.

The rising of resistive component of the leakage current, the decrease in capacitance, and the increase in dielectric loss during the degradation can all be ascribed to the deformation of DSB, i.e. the deformation of DSB leads to the

degradation of the ZnO varistor. This has been verified in the experiment, the height of DSB before the degradation is 0.67 eV, whereas the one after the test becomes 0.45 eV [15].

7.4.1 DC Degradation Mechanism

Under the effect of long-term DC voltage, the I–V curve of the ZnO varistor deforms asymmetrically and the DSB also deforms asymmetrically. As the polarity of the voltage remains unchanged, the ion makes a single directional transition; this leads to the continuous lowering of Schottky barrier height. Figure 7.21a,b presents the energy band diagram of the ZnO grain boundary region before and after the DC degradation, which indicates that the reverse-biased Schottky barrier at positively biased side gradually decreases, which results that the leakage current increases with the degradation time.

The lowering of Schottky barrier height results in the increases in both leakage current and power loss. The asymmetrical variation of Schottky barrier directly leads to the asymmetrical drift of the I–V curve. In addition, the increase in leakage current with time can be expressed as [1]

$$J = A\exp(Bt^n) \tag{7.5}$$

where A, B, and n are all constants.

7.4.2 AC Degradation Mechanism

When an AC voltage is applied, the I–V curve of the ZnO varistor deforms symmetrically, and degradation characters as the increases in resistive component of current and the dielectric loss in the low-frequency range occur simultaneously. When the AC voltage is stressing, the I–V curve varies symmetrically, which is distinct from the symmetrical deformation of the DC case. Thus, the deformation of DSB under AC voltage is also different from the one under DC stressing.

When it is under the regime of positive half wave, i.e. presuming the right side is positively biased and thus the left side is forward biased and the right one is reverse biased, as seen in Figure 7.22a [3], the ion migration occurs both in the grain boundary layer and the depletion layer of reverse-biased Schottky barrier. The zinc interstitial in the depletion layer of reverse-biased Schottky barrier migrates to the grain boundary, i.e. moves leftward, and neutralizes with the negatively charged zinc vacancy at the interface of the right side to generate neutral ions, resulting in the lowering of reverse-biased Schottky barrier at the

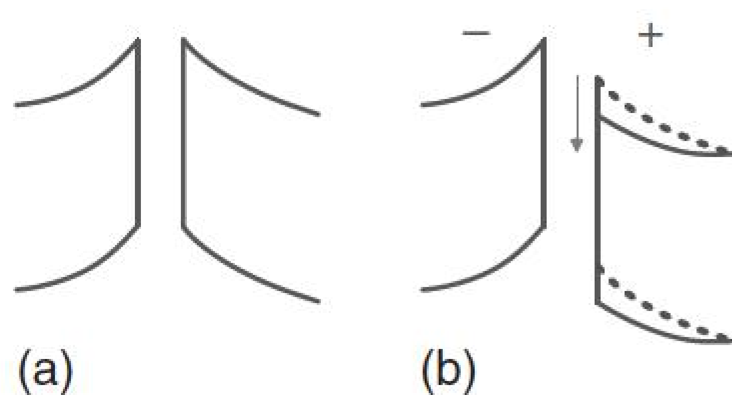


Figure 7.21 Energy band diagram of ZnO grain boundary region before and after the DC degradation. (a) Before degradation and (b) after degradation. Source: Redrawn from Wu et al. [1].

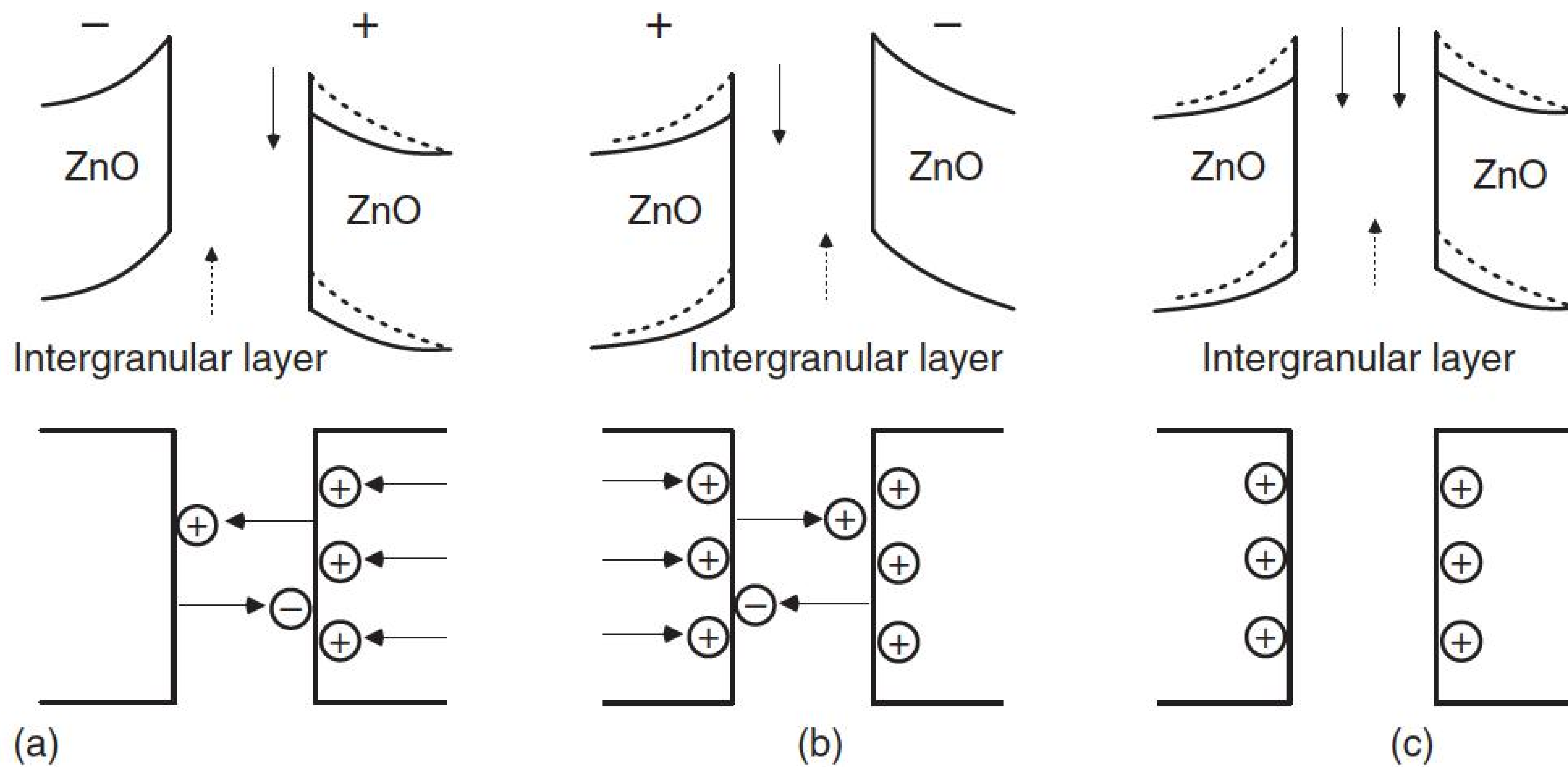


Figure 7.22 The Schottky barrier and ion migration during AC degradation. (a) Positively biased at the right side, (b) positively biased at the left side, and (c) AC biased. Source: Eda et al. 1980 [3]. Redrawn with permission from AIP.

right side. The ion migration and the deformation of Schottky barrier are in accordance with Figure 7.21.

When the polarity of voltage changes, i.e. under the regime of negative half wave, the left positively biased side becomes the reverse-biased Schottky barrier, and the right side is the forward-biased barrier. The zinc interstitial in the left depletion layer migrates to the grain boundary and neutralizes with the negative charge at the left interface to generate neutral ions, leading to the lowering of reverse-biased Schottky barrier at the left side as shown in Figure 7.22b [3].

As the AC voltage changes its polarity periodically, the ion inside the grain boundary layer also migrates leftward and rightward accordingly with identical migration distances at the left and right. Thus, the ion remains its location in the grain boundary layer on the whole, which is equivalent to no obvious migration behavior. However, the ion migration occurred in the depletion layer is not negligible. As a reverse-biased Schottky barrier withstands a high electric field, it merely tolerates the electric field of low magnitude when the voltage polarity is altered and it becomes forward biased. Thus, with the cyclic alternating of voltage polarity, the zinc interstitial migrates to the grain boundary and to the opposite direction accordingly. However, the migration distances along the two directions are distinct, and the positively charged zinc interstitial finally reaches the interface of the Schottky barrier to neutralize the zinc vacancy and generate neutral ions. This results in the asymmetrical deformation of the two Schottky barriers at the "grain–grain boundary–grain" interfaces, and both barriers decrease as shown in Figure 7.22c [3].

Similar to the case of DC, the increase in resistive current when AC voltage is applied is owing to the lowering of barrier height. By analyzing the degradation curve 1 of the resistive component of current under AC stressing in Figure 7.4, it is found that even the resistive current may decrease at the preliminary stage, it obeys the law as Eq. (7.5) and gradually increases [1].

7.4.3 Nonuniform Degradation Mechanism

The distribution of charged ions and defects in the depletion layer and boundary interface determine the DSB height. Generally, the degradation phenomenon of ZnO varistors is considered to be caused by the reduction of DSB height of the individual grain boundary. There are mainly two mechanisms used to interpret the decline of the barrier height in the degradation process: interstitial ion migration and oxygen desorption. A grain boundary defect model is widely accepted to describe the ion migration process [19, 82, 83], stable and metastable charged defect ions coexist in the depletion layer of ZnO grains, and the grain boundary interfaces, as schematically illustrated in Figure 7.16.

Stable components in the depletion layer mainly consist of trivalent substitution ions D_{Zn}^{+} (D = Bi, Sb, etc.) and native oxygen vacancies V_O^{+}, V_O^{2+}, whereas metastable components are mainly composed of positively charged native zinc interstitials Zn_i^{+} and Zn_i^{2+}. These positively charged ions are compensated by a layer of negatively charged ions at the grain boundary interface, which are composed of native zinc vacancies V_{Zn}^{-} and V_{Zn}^{2-}. The energy band diagram of these defects is summarized from previous literatures, as given in Figure 7.23 [24].

At the grain boundary interface, the acceptor levels of V_{Zn}^{-} and V_{Zn}^{2-} have been assigned around 1 and 2 eV, respectively, above the valence band edge. The oxygen interstitials, O_i^{2-} and O_i^{-}, are not considered as major defect types in ZnO. Besides that these defect ions originate from the ZnO lattice, there ought to be a lot of extrinsic defect ions V_D^{-} (D = Bi, Sb, etc.) distributed among the disorder layer close to the grain boundary interface. The formation of these extrinsic defects occurs during the cooling down stage of high-temperature sintering process. The amorphous grain boundary is formed during the sintering process; it tends toward leaving a lot of dislocated defects after cooling down. The migration features of these extrinsic defects largely depend upon the dopants and fabricating process of the ZnO varistor ceramics.

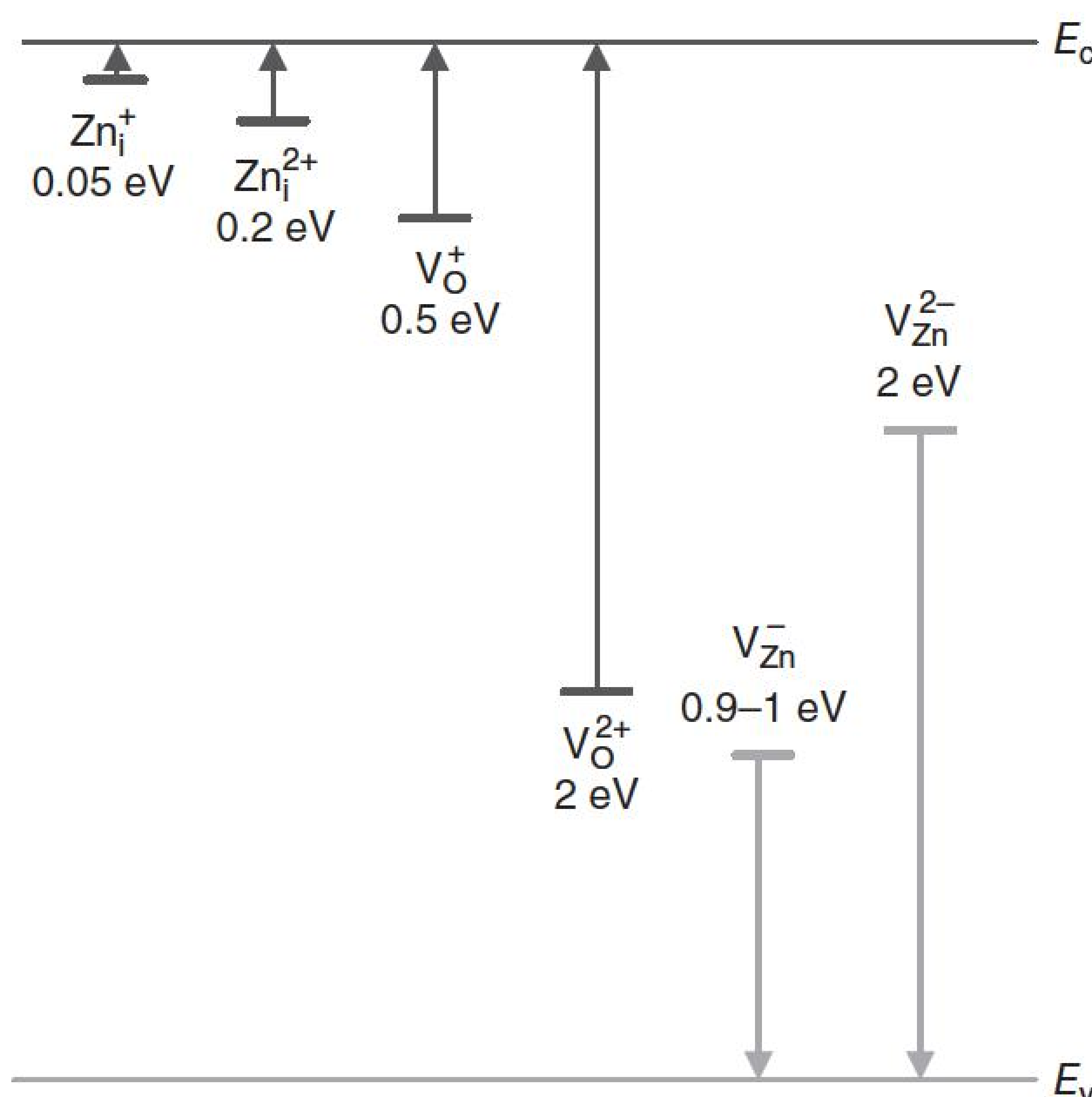


Figure 7.23 Grain boundary energy band diagram for main intrinsic defect ions located in the depletion layer and grain boundary interface. Source: Redrawn from Liu [24].

Stable components that exist both in the depletion layer and the grain boundary are relatively fixed in space, which means that the activation energies of migration for these defects are relatively high. The migrating features of the metastable defects in the depletion layer largely depend on their spatial lattice sites; therefore, it will lead to the difference in the relative mobility for different defects under long-term voltage stress and thermal stress. As all the octahedral and half the tetrahedral interstitial sites are empty in the ZnO structure, zinc interstitials can rapidly migrate within the structure via these interstitial sites. On the contrary, the migration of oxygen vacancies via vacant lattice sites are severely restricted because of low vacancy concentration and high activation energies. Normally, the positively charged interstitials migrate toward the negatively charged grain boundary interface where charged defects are converted to neutral defects because of the following chemical reaction between the defects:



$$Zn_i^+ + V_{Zn}^- \rightarrow Zn_i^\times + V_{Zn}^\times \tag{7.6}$$

As a result of these reactions at the interface, two neutral defects ($Zn_i^\times$ and $V_{Zn}^\times$) are formed at the grain boundary interface to replace the charged ions (Zn_i^+) and (V_{Zn}^-). With the continuous degradation stress on the varistor, the barrier height declined continuously because of the loss of charged ions and the accumulation of neutral defects at the grain boundary interface.

The defect model proposed by Gupta and Carlson could be easily used to explain the monotonic degradation phenomenon in the single-grain boundary degradation test. However, several grain boundaries (occupying an unignorable percentage in the randomly selected boundaries) exhibit a nonmonotonic degradation behavior. The I–V curves could be recovered after subjected to voltage stress. In Gupta and Carlson's viewpoint [19], the recovery of the electrical properties is due to the reverse reaction occurring upon the removal of electric field. The prevailing test temperature is the driving force of recovery. This statement could explain the recovery phenomenon of ZnO varistors after annealing treatment. However, in the experiments [33], the accelerated degradation voltage stress and the thermal stress were removed simultaneously. Therefore, the nonuniform degradation behavior may be caused by other reasons.

He et al. thought [41] that, except for the migration of positively charged ions from the depletion layer to the grain boundary interface, the migration of negatively charged defects from the grain boundary to the interface should also be taken into consideration. Although the major defect is distributed in the grain boundary, which is spatially fixed at the interface, the existence of an extrinsic defect may migrate toward the interface under degradation stress and partly compensate the loss of negative charges at the interface, which results in the enhancement of barrier height to some extent. The improvement of barrier height will eventually have an opposite effect on the deterioration of electrical properties. In conclusion, the migrations of zinc interstitial ions have positive effects on the degradation process. However, the migrations of zinc vacancy ions in the grain boundary exhibit opposite effects in the degradation process. The recovery of I–V characteristic is therefore easily understood. The migrating process carried out in the depletion layer and grain boundary is of great variations. Thus, the combination of these two effects leads to the variation of degradation rates.

Meanwhile, the desorption of oxygen in ZnO varistor plays an important role in the degradation process, which has been verified by Ramírez et al. [31, 84]. The tetragonal β-Bi_2O_3 phase in the ZnO varistor was regarded as the boundary activator to limit oxygen around the grain boundary, which is necessary to improve the barrier characteristics. The elimination of the β-Bi_2O_3 phase in the ZnO varistor after degradation stress would lead to the desorption of oxygen and deterioration of barrier.

According to the results for the AC degradation [26, 85], it was found the ambient gas influences the degradation of ZnO varistors and the oxygen gas suppresses the degradation, and the oxygen gas has an effect of rejuvenating the degraded samples. These suggest that the desorption of oxygen from the sintered bodies plays an important role in the degradation of ZnO varistors and imply that the migration and desorption of oxygen ions at the grain boundaries change the distribution of space charges, causing deformation of the Schottky barriers. The significant effect of ambient gases at higher temperatures reflects the rapid desorption of oxygen at the higher temperatures.

Ion migration and oxygen desorption mechanism could be easily used to explain the monotonic degradation phenomenon in the single-grain boundary degradation test. However, several grain boundaries (occupying an unignorable percentage in the randomly selected boundaries) exhibit a nonmonotonic degradation behavior. The $I-V$ curves could be recovered after subjected to voltage stress. Except for the migration of positively charged ions from the depletion layer to the grain boundary interface, the migration of negatively charged defects from the grain boundary to the interface should also be taken into consideration. Although the major defects distributed in the grain boundary are spatially fixed at the interface, the existence of an extrinsic defect may migrate toward the interface under degradation stress and partly compensate the loss of negative charges at the interface, which results in the enhancement of barrier height to some extent. In addition, there could be a reversible process as compared to the desorption of oxygen, noted as absorption, which could improve the barrier property. The desorption and absorption of oxygen around the grain boundary may coexist in the degradation process. The barrier could be recovered when the absorption of oxygen possesses a dominant ratio in the degradation process. The improvement of barrier height would eventually have an opposite effect on the deterioration of electrical properties.

7.4.4 Pulse Degradation of ZnO Varistors

Previous studies on the degradation of ZnO varistors mainly focused on the dependence of degradation states upon the number, amplitude, duration, and interval of the applied pulse current/voltage stress [86, 87]. The pulse degradation characteristics of ZnO varistors were strongly influenced by the composition and fabrication procedure, as well [36, 88–90]. The results showed that current pulses reduce both the height and the width of the barrier voltage. It was also observed that the donor density did not change, but the surface-state density decreased with degradation [91]. Meanwhile, the thermal transport properties of the varistor microstructures as well as the electronic properties

of the active intergranular phase were also taken into consideration [92, 93]. Additionally, many literatures had discussed on the degradation characteristics and mechanisms of ZnO varistors, but the electrical property variation of single-grain boundaries during the degradation process still was not clearly analyzed [94–96]. Discussions on the degradation or degradation mechanisms have revealed that the deformation of DSB plays a dominant role in the pulse degradation [97–99], which is similar to AC and DC degradation.

7.4.4.1 Degradation Mechanism Under Impulse Current

The impulse degradation can be assessed by the variation of voltage measured at 1 mA (DC) before and after the effect of impulse current. The effect of impulse current leads to the decrease in voltage at 1 mA (U_{1mA}), and simultaneously the resistive component of current has an asymmetry under different polarities, e.g. when an AC voltage is applied on the varistor treated by negative impulse current, the value of the positive peak of resistive current is slightly larger than the negative one. It was reported that for the varistor processed by 100 kA lightning impulse current [15], its power loss at U_{1mA} had a 20% increase. Figure 7.24 indicates the variation of U_{1mA} under 8/20 μs positive or negative impulse current for comparison [15], and U_{1mA} of varistor processed by negative impulse decreases more severely than that by the positive impulse. In addition, for the varistor treated by positive impulse current, the U_{1mA} firstly increases slightly and then presents the tendency to decline with the increase in impulse current. It is thus seen that the degradation degree in the negative polarity direction is larger than the one in the positive polarity direction.

The effect of impulse current can be described by four parameters, e.g. impulse current density J_i, impulse voltage gradient F_i, impulse width t_i, and impulse energy density E_i [12]. E_i can be expressed as

$$E_i = \int_0^{t_i} J_i F_i \, dt \tag{7.7}$$

The mechanism of impulse degradation lies in the emphasis on thermal degradation. Under the effect of impulse current, a huge amount of energy is injected

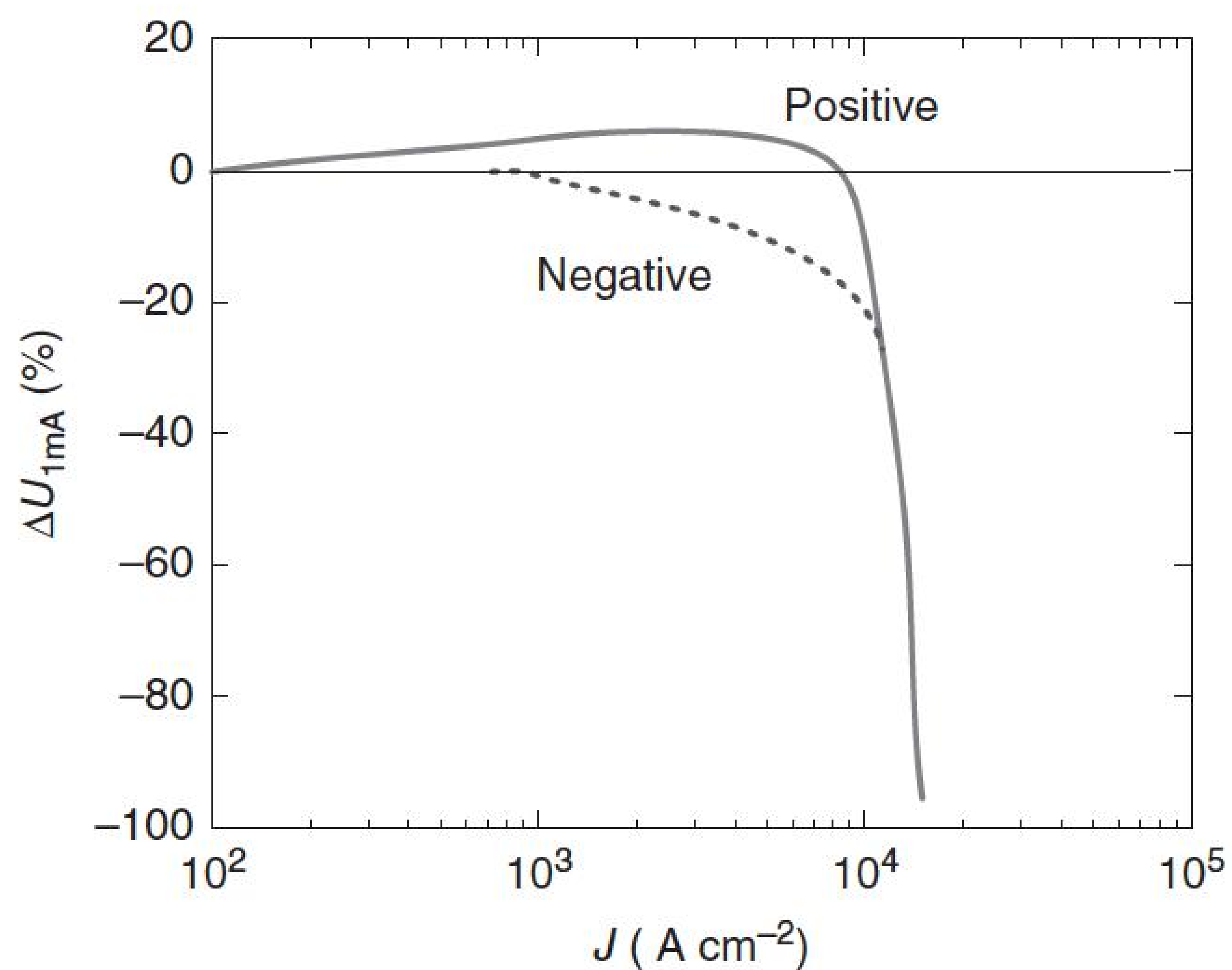


Figure 7.24 The variation of U_{1mA} of varistor under positive and negative impulse currents. Source: Adapted from Xu [15].

into the ZnO varistor in a very short time. If the heat dissipation is not included and the temperature rise process due to the absorption of impulse energy is considered as adiabatic temperature rise, the variation of temperature after absorption of impulse energy E_i is

$$\Delta T = \frac{E_i}{\rho C_p} \tag{7.8}$$

where ΔT is the temperature increment, ρ is the resistivity, and C_p is the specific heat.

With the rising of temperature owing to energy absorption, the relatively high temperature generates a large thermal activation energy inside the varistor bulk. Under the effect of single-polarity impulse voltage, cations such as Bi^{3+} inside the grain boundary layer migrate to the grain boundary of the reverse-biased Schottky barrier, and the cations in the depletion layer of the reverse-biased Schottky barrier also migrate to the grain boundary. Moreover, the migration velocity for all kinds of ions is obviously faster than the one under the low DC electric field. These two aspects contribute to the deformation of Schottky barrier and eventually lead to the severe degradation under the single-polarity impulse.

The impulse degradation is also closely related to the magnitude and waveform of impulse current, number of applied impulses, and ambient temperature. Experiment indicates that if the impulse current with a magnitude smaller than 5 kA is imposed on a varistor, it is rarely degraded, whereas if the magnitude is larger than 100 kA, severe degradation phenomenon occurs [15].

7.4.4.2 Superimposing Degradation

In practical application, the varistor withstands long-term DC or AC voltage, whereas occasionally bears impulse currents or impulse voltages, so the degradation will be caused by the superimposing effect of impulse degradation and AC or DC degradation. If a varistor is withstanding a long-term DC voltage and the impulse current of the same polarity is imposed on the varistor, the impulse current will aggravate the degradation. However, if an impulse current of opposite polarity is superimposed on the DC voltage, or if an impulse is superimposed on the AC voltage, the impulse degradation may recover to a certain degree after a period of time.

When the impulse and AC voltage coexist, the impulse may make the cations migrate to one side of the Schottky barrier, whereas when the AC voltage affects them to uniformly diffuse to the both sides of Schottky barrier to pull the ions already migrated to one side back to the another, this will relieve the impulse degradation. Thus, the degradation caused by the superposition of impulse on the AC voltage is subtractive.

Figure 7.25 shows the increase in the leakage current of the ZnO varistor under the effect of impulse superpositioned on AC voltage [12]. For the test, the applied voltage ratio is $q = 0.85$, the ambient temperature is 82 °C, and the impulse current applied is 440 $\mathrm{A\,cm^{-2}}$. The full line corresponds to the case that negative surges are applied except the final stage, and the dotted line indicates the case that the surge polarity was alternated. If the impulse current is occasionally superpositioned on the long-term operation voltage,

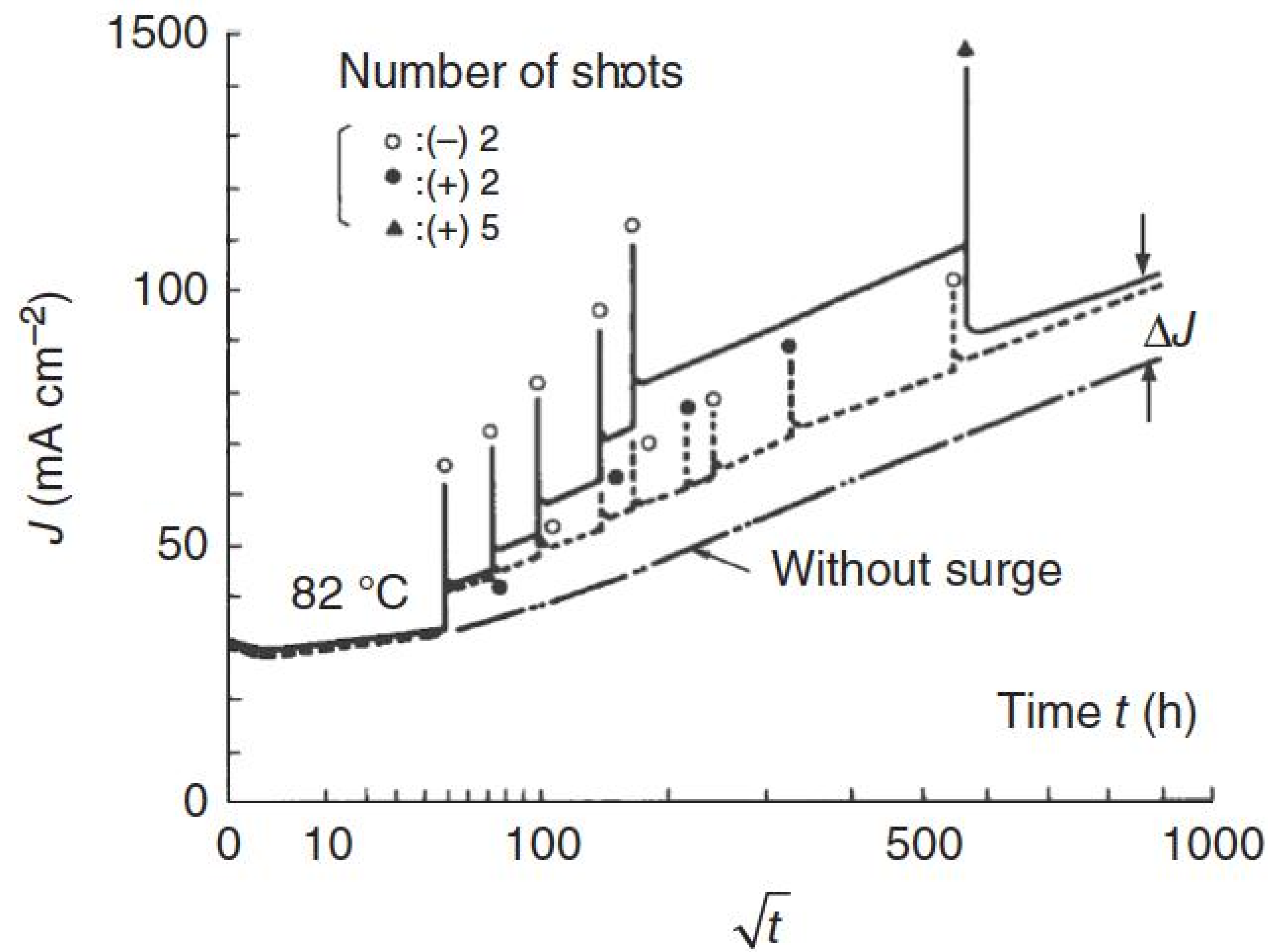


Figure 7.25 The degradation phenomena as the increase of leakage current by the superposition of impulse on AC voltage. Source: Fujiwara et al. 1982 [12]. Reproduced with permission of IEEE.

the leakage current obviously increases. The surge degradation is pronounced in the case applying unidirectional surges but can be healed to some extent by applying surges of opposite polarity. It is further noticed that the effect of surge degradation is integrated over a long period perhaps over the entire life of the element. Experimental results indicate that the rising of leakage current is mainly caused by the increase in its resistive component.

Under the effect of coexisting impulse and AC voltage, the degradation of varistor is related not only to the waveform and magnitude of impulse current but also to the number of impulses applied, the temperature of varistor, and the operation voltage, e.g. the larger the applied operation voltage is, the severer the degradation is. When the AC voltage is applied alone, the variation of resistive current density with time can be expressed as Eq. (7.5). In addition, for the superposition case, the current density is [1]

$$J = A\ \exp(Bt^n) + \Delta J \tag{7.9}$$

where A and B are constants and ΔJ is the increment of resistive current density after the impulse current is applied, which is closely related to all parameters mentioned before.

It is generally assumed that the current density ratio of the one impacted by the impulse to the one without impulse is a, and a is considered as the impulse degradation factor [12]:

$$a = \Delta J / J(0) \tag{7.10}$$

where $J(0)$ is the current density without the effect of impulse. If a varistor is sustained N impulses of identical polarity and magnitude, it can be considered that all the impulses share the identical degradation factor except the first impulse, and the total impulse degradation factor can be expressed as

$$a = b + c(N - 1) \tag{7.11}$$

where b and c represent the respective degradation factors for the first impulse and the others. From Figure 7.25 [12], it is known that the larger the number of identical polarity impulses, the severer the impulse degradation.

7.5 Role of Interior Microcracks on Degradation

The minute air microcracks of extremely microscopical size exist in the interior structure of the ZnO varistor, which are produced because of the inhomogeneous contraction during the cooling process of ZnO varistor after sintering. It was regarded that the microcrack could enhance the degradation of varistor, including the influence on degradation in a humid environment [29].

Wang and coworkers [91] thought that the electrical degradation phenomenon of the varistors is closely related to the reaction between the trap at 0.94 eV and adsorbed oxygen ions at the grain boundaries. Sonder et al. treated the varistor by reductive deoxygenation and then reoxidation at 290–780 °C and measured the interior distribution of oxygen by utilizing the secondary ion mass spectrometry (SIMS) [29]. The measuremental results indicate that the oxygen molecule can enter into depths and its distribution is quite nonuniform, and the higher the temperature for reoxidation is, the more deeply the oxygen molecule will penetrate. When the temperature reaches 300 °C, the oxygen molecule can move to a long distance along the microcracks. During the cooling process of ZnO varistor after sintering, the microcracks, as the channel for oxygen molecule diffusion, convey the oxygen molecule from the outer atmosphere to the interior of varistor. This can be regarded as the evidence of the existence of microcracks inside the ZnO varistor. The length and distribution of microcracks are of randomness, and under the assumption of Gaussian distribution length, the varistor only has a small number of microcracks with a long length, which can possibly connect the surface to the depths. The microcracks may exist in the interior of the varistor, along both the axial and radial directions, and may also be cross-linked, as shown in Figure 7.26 [1], which form the complicated pathway to the surface and/or the external environment.

The existence of oxygen molecule would affect the property of the Schottky barrier, e.g. which would react with the zinc interstitial to result in the degradation, and generate the stabilized ZnO and relieve the degradation of the varistor.

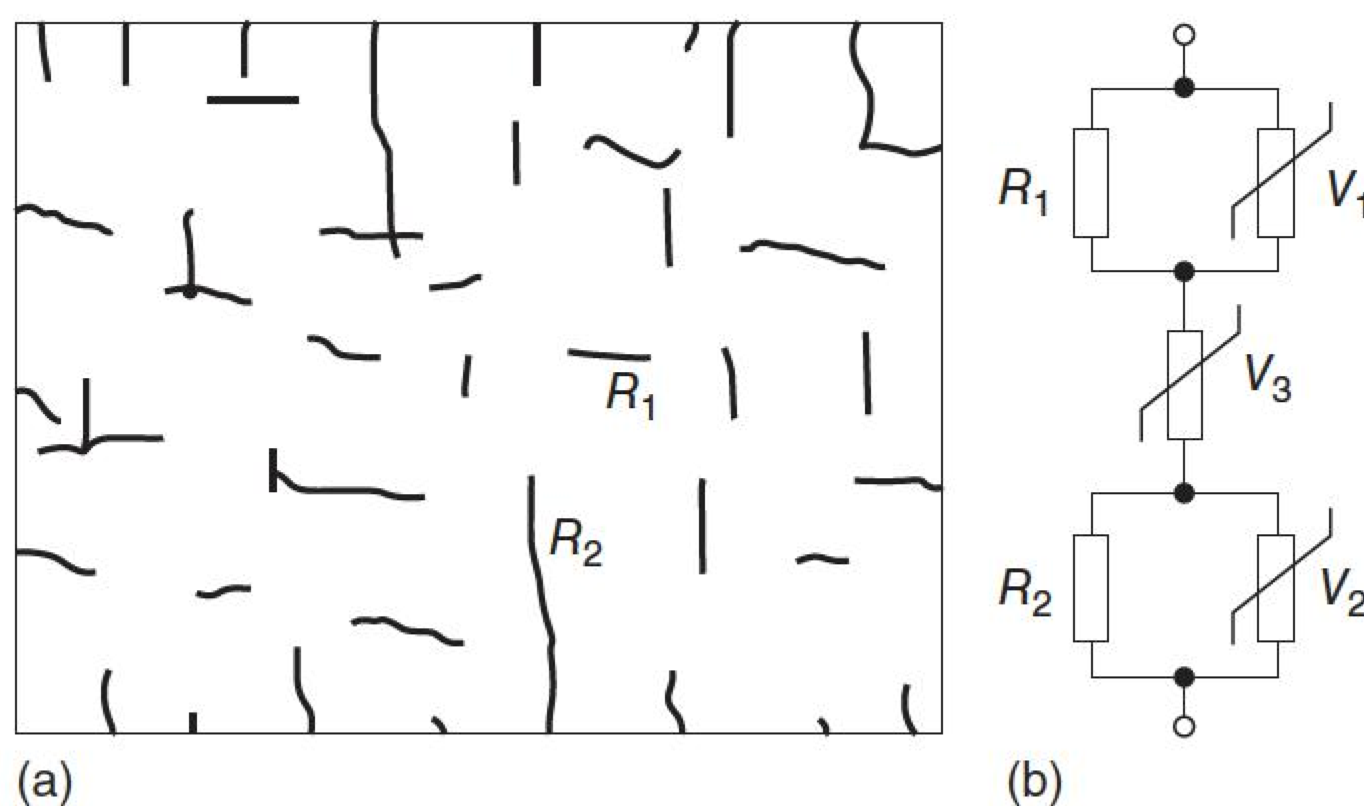


Figure 7.26 (a) The microcracks R_1 and air gaps R_2 inside the ZnO varistor offer a resistive pathway for chemical reactions and (b) the respective equivalent electric circuit. Source: Adapted from Wu et al. [1].

The microcracks have a negligible influence on the newly manufactured ZnO varistors, whereas during its long-term operation, the microcracks act as the channel linking the surface and the varistor interior to let the oxygen inside diffuse out, thus destabilizing the ZnO varistor and leading to the degradation.

The microcracks can not only act as a diffusion pathway for oxygen but also constitute the resistive channel, which may be formed after the penetration of moisture [29]. In a humid environment, the moisture may also be possible to enter into the interior of ZnO varistor through the microcracks, and the moisture may react with oxygen ions in microcracks as [29]



$$O^- + H_2O \rightarrow 2OH^- \tag{7.12}$$

i.e. by chemical reaction, the alkaline ion OH^- is generated. After such chemical reactions in microcracks, resistive pathways of good electrical conductivity form. Assuming that two long-resistive pathways R_1 and R_2 exist in the interior of varistor, as shown in Figure 7.26a. The resistive pathways R_1 and R_2 are in parallel connection with the ZnO varistor V_1 and V_2 in the radial direction and are in series connection with ZnO varistor V_3 in the axial direction, forming the equivalent electric circuit as given in Figure 7.26b [1], the respective $I-V$ characteristic can be described as

$$J = AE + BE^{\alpha} \tag{7.13}$$

Obviously, because of the existence of resistive pathway, the leakage current under low electric field may increase, leading to the occurrence of the degradation phenomena.

Besides, the moisture may also possibly react with the oxygen atom from the grain boundary layer through the microcracks as described in Eq. (7.12), leading to the decrease in the amount of oxygen atom in the grain boundary layer and accelerating the degradation of varistor. Simultaneously, the alkaline OH^- generated in the grain boundary layer may damage the grain boundary, leading to the decrease in the grain boundary resistance and increases of leakage current and power loss of the whole ZnO varistor bulk.

7.6 Antidegradation Measures

Parallel to the pursuit for accurate degradation mechanism, measures for improving the antidegradation capability of ZnO varistors are of great interest and of significant application values; hence, numerous research studies [19, 34, 37, 100, 101] have been carried out correspondingly. As discussed above, the long-term electrical degradation mechanism of ZnO varistor is due to the migration of Zn_i inside the depletion layer and the diffusion of oxygen defect along the grain boundary, corresponding measures could be taken. This suggests strategies such as the removal of mobile ions and impeding the migration of ion. To achieve this, two classes of measures, i.e. specific preparation procedures and optimization of formula, are devised.

7.6.1 Specific Preparation Procedures

As for specific handling procedure to improve the stability of varistors, a widely used technique is the heat treatment around 600 °C [19, 43]. This could improve the device stability by inducing the phase transformation of intergranular Bi_2O_3 from the initial β/δ phase to the γ phase [56], which aggravates the oxygen conduction. More importantly, such a heat annealing process could largely eliminate Zn_i as the zinc interstitial defect can react with the oxygen atmosphere, hence the decrement of the density of mobile donor defects and the improvement of antidegradation capability. Moreover, other refinement or improvement of the preparation procedures of varistors can inhibit the growth of abnormal grains and thus obtain a more uniform microstructure of varistors. This could contribute to the uniform distribution of electrical field and current and therefore also improve the stability of varistors indirectly.

By performing an appropriate thermal treatment on the ZnO varistor, the antidegradation capability of the ZnO varistor can be improved, and even the degraded varistor can recover its property after the treatment [1]. As shown in Figure 7.6, the experiment indicates that if the electrically degraded ZnO varistor is thermally treated at 800 °C for two hours in the air atmosphere, the TSC in the sample decreases when the sample is thermally treated [3], and it can almost regain its property and recover to the initial state, whereas if the treatment is done in the nitrogen atmosphere, the varistor can rarely recover. Another experiment shows the heat treatment of commercial zinc oxide based varistor ceramics at temperatures of 200–300 °C in air with 1000 ppm of NO_2 causes a strong shift of voltage–current characteristic to low voltages. Subsequent exposure to pure air leads to partial restoration of the voltage–current characteristics [100]. Moreover, if a nondegraded ZnO varistor is thermally processed at 800 °C for two hours, it becomes further stabilized and its antidegradation capability is improved, i.e. the I–V curve of treated ZnO varistor drifts slightly after degradation test. Shirley and Paulson found that the intrinsic electronic structure can be modified without changing the microstructure to greatly improve the pulse degradation performance of a varistor by annealing at low temperature (600 °C) in oxygen [92]. Thus, it can be concluded that the lack of oxygen is the reason of aging, and the oxygen is the migrating negative ion inside the intergranular layer during the heat treatment.

During the heat treatment with a high temperature, oxygen diffuses into the intergranular phase and forms oxygen atoms O. The neutral oxygen hole $V_O^\times$ in the intergranular phase reacts with the oxygen atom and forms a neutral oxygen lattice $O_O^\times$ [1]:



$$V_O^\times + O \rightarrow O_O^\times \tag{7.14}$$

The neutral oxygen lattice $O_O^\times$ reacts with a zinc hole of negative charge:



$$O_O^\times + V_{Zn}^- \rightarrow O_O^- + V_{Zn}^\times \tag{7.15}$$

The formed neutral zinc lattice $V_{Zn}^{\times}$ reacts with zinc interstitial to form a zinc lattice Zn_{Zn}^{+}:



$$V_{Zn}^{\times} + Zn_i^{+} \rightarrow Zn_{Zn}^{+} + V_i^{\times} \quad (7.16)$$

Then, the formed zinc interstitial Zn_{Zn}^{+} reacts with negative oxygen lattice O_O^{-} to form a ZnO lattice ZnO(L):



$$Zn_{Zn}^{+} + O_O^{-} \rightarrow ZnO(L) \quad (7.17)$$

Therefore, the heat treatment can reduce the unstable factor "the zinc interstitial" inside the ZnO varistor and recover the characteristics of aged ZnO varistors.

If the heat treatment is performed on the degraded ZnO varistor, the neutral defect $Zn_i^{\times}$ generated during degradation will dissolve into positively charged zinc interstitial and electron:



$$V_{Zn}^{\times} \rightarrow Zn_{Zn}^{+} + e^{-} \quad (7.18)$$

The neutral zinc vacancy reacts with electron to generate negatively charged zinc vacancyV_{Zn}^{-}:



$$V_{Zn}^{\times} + e^{-} \rightarrow V_{Zn}^{-} \quad (7.19)$$

Under the effect of electromotive force which distorts the electrical field, Zn_i^{+} migrates back to the depletion layer, whereas the generated V_{Zn}^{-} helps to recover the height of the grain boundary barrier; thus, the property of the degraded varistor is recovered by the heat treatment [1].

7.6.2 Optimization of Formula

By doping specific additives, the stability of varistors can be improved. For instance, by incorporating amphoteric dopants [102] as sodium or potassium into the ZnO lattice, the dopants could occupy both the lattice and the interstitial sites [103]. When occupying the interstitial sites, the dopants could first block the formation of zinc interstitial and secondly prevent the migration of mobile ions [56]. An atomistic simulation technique has been used to predict the spatial arrangement of the dopant species sodium, lithium, and chlorine within the zinc oxide lattice. The alkaline oxides are preferentially incorporated via a self-compensating mode, forming interstitial cations that hinder the migration of zinc interstitials and hence slow the degradation of the varistor [36]. A similar discussion applies to glass additives and silver dopants, as the former could densify the microstructure of electroceramics and restrain the migration of mobile ions, whereas the latter can act as acceptor ions and decrease the donor density [24]. It is also reported that the Sn additive can alter the ZnO crystal orientation in grain boundary region and thus affect the diffusion process of oxygen ions across the boundary [104]. These explanations for the effects of various dopants

are mainly based on speculations; therefore, atomistic investigations are needed to account for accurate roles in improving the antidegradation capability of varistors and also find new potential additives.

7.6.2.1 Dopant Effects on Improving AC Degradation Characteristics

Many works have been done on how to improve the degradation characteristics of ZnO varistors. Liu experimentally studied the effects of various dopants on improving the AC, and impulse degradation characteristics of ZnO varistors were analyzed [24]. Accelerated AC (50 Hz) aging test was carried out on the ZnO samples under continuous voltage stresses of 0.85 U_{1mA} at 135 °C for 168 hours. The electrical properties and DSB parameters before and after the degradation tests were derived from the measured electric field–current density characteristics and capacitance–voltage characteristics, respectively.

Generally, Bi_2O_3 has been considered to be one of the most important additives to provide liquid-phase ambience during sintering and is essential for the formation of the DSB of the ZnO varistor. The degradation test results indicated that the long-term AC stability of ZnO varistors became even worse when the Bi_2O_3 concentration was increased. The DSB height deteriorated in the degradation process and largely depended on the variation of interfacial state densities.

For ZnO varistors doping with Y_2O_3, the voltage gradient and the nonlinear coefficient change slightly after degradation. The decreased barrier height should be mostly attributed to the decrease in interfacial state density after degradation. Meanwhile, the variation of barrier height for ZnO samples without doping Y_2O_3 is much less than that doped with Y_2O_3 [24]. All Pr-based ZnO varistors doped with Y_2O_3 exhibit very predominant degradation characteristics, which show nearly symmetric $I–V$ characteristics after the stress, and the leakage current during the applied stress is observed to be constant in all samples, particularly in the optimal content of Y_2O_3, varistor has not only a very excellent nonlinearity but also a very stable degradation behavior [104].

Transition ions such as Cr^{3+} and Mn^{4+} are generally included to improve the nonlinearity of ZnO varistors by increasing the steady-state density, through the formation of interstitial states and deep bulk traps. Cobalt oxides are important dopants to generate/improve the nonlinearity of ZnO varistors. Nonlinear characteristics appear even in Co-doped ZnO without other key additives, such as Bi_2O_3 and Pr_6O_{11} [105]. The HRTEM observations of a cobalt-doped grain boundary show that the boundary is highly coherent and free from intergranular phases/precipitates. The presence of cobalt impurities is considered to enhance the formation of acceptor-like native defects near the boundaries to generate electrostatic potential barriers. The radius of Co^{3+} (0.054 nm) ions is less than that of Zn^{2+} (0.074 nm) ions, which means that it is easy for Co^{3+} ions to enter the ZnO grain lattice and form substitution defects. With the Co_2O_3 content increasing, the voltage gradient is elevated. Meanwhile, the nonlinearity of samples is improved. However, the degradation test results indicate that samples doped with more than 1.0 mol% Co_2O_3 behave worse AC stability [24].

The role of Ni_2O_3 played in modifying the electrical properties of ZnO varistors is similar with other transition oxide additives, such as antimony and cobalt. Ni_2O_3 is mainly segregated in the intergranular layers of the grain

boundaries. With the increasing Ni_2O_3 content, the voltage gradient increases, as well. However, the nonlinearity of these samples does not change a lot. The degradation test results indicated that the introduction of Ni_2O_3 has a negative effect on the AC stability of ZnO varistors.

Ag acts as an amphoteric dopant in ZnO causing a decrease in the donor density and a reduction in a nonlinear coefficient. Ag located in the interstitial sites is able to block the formation and migration of new Zn interstitials, thereby improving the stability.

The *first-principles* calculations and atomistic simulation techniques have been used to optimize the dopant species. An atomistic simulation technique has been used to predict the spatial arrangement of the dopant species sodium [36], lithium, and chlorine within the zinc oxide lattice. The alkaline oxides are preferentially incorporated via a self-compensating mode, forming interstitial cations that hinder the migration of zinc interstitials and hence slow the degradation of the varistor. The addition of chloride ions is shown to negate this effect by forming sodium and chloride substitutional defects rather than any species involving sodium interstitial ions.

In summary, the effects of various additives on AC degradation parameters of ZnO varistors are listed in Table 7.2 [24].

7.6.2.2 Dopant Effects on Improving Impulse Degradation Property

The effects of various dopants on improving the impulse degradation characteristics of ZnO varistors were also studied [24]. The impulse current with a waveform of 8/20 μs and a current density of 100 A cm^{-2} was applied on samples with different additives. Every sample withstood five groups of impulse degradation tests; every group of impulse degradation test includes 20 impulse currents applied with a time interval of 15 seconds. The time interval between the two groups of tests was two hours. This means every sample was applied 100 impulse currents. The effects of different additives on impulse degradation parameters of ZnO varistors are summarized in Table 7.3.

From the experiments, MnO_2 has the better effect on improving the impulse degradation characteristics of ZnO varistors, which has a similar influential regularity of AC degradation. However, Ag_2O additive, which can effectively improve the AC degradation characteristics of ZnO varistors, does not have obvious effect

Table 7.2 Summary on the effects of different additives on AC degradation parameters of ZnO varistors [24].

Additive	E_{1mA}	α	I_L	K_T
Y_2O_3	↑	↓	↑	↓
Bi_2O_3	↓	↑	↓	↓
MnO_2	—	↑	↓	↑
Co_2O_3	↑	↑	↓	↓
Ni_2O_3	↑	↑	↓	↑
Ag_2O	—	↑	↓	↓

Table 7.3 Summary on the effects of different additives on the impulse degradation parameters of ZnO varistors [24].

Additive	E_{1mA}	α	I_L	K_T
Y_2O_3	↑	↓	↑	—
Bi_2O_3	↓	↑	↓	↓
MnO_2	—	↑	↓	↑
Co_2O_3	↑	↑	↓	↓
Ni_2O_3	↑	↓	↑	↓
Ag_2O	↓	↓	↑	↓

on improving the impulse degradation characteristics of ZnO varistors and even reduces the impulse degradation performance of ZnO varistors.

Furthermore, ZnO–Pr_6O_{11}-based ceramics have been studied to enhance the varistor properties and the stability against various stresses, compared with ZnO–Bi_2O_3-based varistor ceramics. Al doping effect on electrical and dielectric aging behaviors against the impulse stress in the Zn–Pr–Co–Cr–Y–Al (ZPCCYA)-based varistors was investigated [106]. Conclusively, Al_2O_3 dopant has an optimized content, under which ZnO varistor has the best electrical and dielectric stability against the impulse current.

Recently, Ga_2O_3 was added to improve the degradation performance of ZnO varistors [107]. The AC accelerating aging of 1000 hours under $0.9U_{1mA}$ was executed. The absorbing energy is more than 327 J cm^{-3}, and the degradation rate coefficient (K_t) is 0.04. The stability of the ZnO varistors is attributed to the reduction of interstitial Zn^{2+}, which retained the height of the Schottky barrier after aging and therefore improved the aging stability. The radius of dopant ion Ga^{3+} is 0.062 nm, which is less than that of Zn^{2+} (0.074 nm). During the sintering of ZnO varistor ceramics, the dopant Ga^{3+} solidly dissolves into the lattice of ZnO and occupies the location of interstitial Zn^{2+}, as reduces the amount of interstitial Zn^{2+}.

References

1 Wu, W.H., He, J.L., and Gao, Y.M. (1998). *Properties and Applications of Nonlinear Metal Oxide Varistors*. Beijing: Tsinghua University Press.

2 Zhou, D.X., Zhang, X.L., and Li, B.Y. (1991). *Semiconductor Ceramics and Applications*. Wuhan: Huazhong University of Science and Technology Press.

3 Eda, K., Iga, A., and Matsuoka, M. (1980). Degradation mechanism of non-ohmic zinc oxide ceramics. *Journal of Applied Physics* 51 (5): 2678–2684.

4 Gupta, T.K., Carlson, W.G., and Hower, P.L. (1981). Current instability phenomena in ZnO varistors under a continuous ac stress. *Journal of Applied Physics* 52 (6): 4104–4111.

5 Eda, K., Iga, A., and Matsuoka, M. (1979). Current creep in nonohmic ZnO ceramics. *Japanese Journal of Applied Physics* 18 (5): 997–998.

6 Sato, K., Takada, Y., Maekawa, H. et al. (1980). Electrical conduction of ZnO varistors under continuous DC stress. *Japanese Journal of Applied Physics* 19 (5): 909–917.

7 Ramanachalam, M.S., Rohatgi, A., Schaffer, J.P., and Gupta, T.K. (1991). Characterization of ZnO varistor degradation using lifetime positron-annihilation spectroscopy. *Journal of Applied Physics* 69 (12): 8380–8386.

8 Tanaka, J., Hishita, S.I., and Okushi, H. (1990). Deep levels near the grain boundary in a zinc oxide varistor: energy change due to electrical degradation. *Journal of the American Ceramic Society* 73 (5): 1425–1428.

9 Vicaud, A. (1986). AC voltage ageing of zinc-oxide ceramics. *IEEE Transactions on Power Delivery* 1 (2): 49–58.

10 Nahm, C.W. (2007). The effect of sintering temperature on electrical properties and accelerated aging behavior of PCCL-doped ZnO varistors. *Materials Science and Engineering B* 136 (2–3): 134–139.

11 Hayashi, M., Haba, M., Hirano, S. et al. (1982). Degradation mechanism of zinc oxide varistors under dc bias. *Journal of Applied Physics* 53 (8): 5754–5762.

12 Fujiwara, Y., Shibuya, Y., Imataki, M., and Nitta, T. (1982). Evaluation of surge degradation of metal oxide surge arrester. *IEEE Transactions on Power Apparatus and Systems* 101 (4): 978–985.

13 Tominaga, S., Shibuya, Y., Fujiwara, Y. et al. (1980). Stability and long term degradation of metal oxide surge arresters. *IEEE Transactions on Power Apparatus and Systems* 99 (4): 1548–1556.

14 Kanai, H., Imai, M., and Takahashi, T. (1985). A high-resolution transmission electron microscope study of a zinc oxide varistor. *Journal of Materials Science* 20 (11): 3957–3966.

15 Xu, X.Y. (1984). Ageing property of ZnO varistors (in Chinese). *High Voltage Engineering* 10 (3): 71–76.

16 Iga, A., Matsuoka, M., and Masuyama, T. (1976). Effect of phase transition of intergranular Bi_2O_3 layer in nonohmic ZnO ceramics. *Japanese Journal of Applied Physics* 15 (6): 1161–1162.

17 Iga, A., Matsuoka, M., and Masuyama, T. (1976). Effect of heat-treatment on current creep phenomena in nonohmic ZnO ceramics. *Japanese Journal of Applied Physics* 15 (9): 1847–1848.

18 Eda, K. and Matsuoka, M. (1977). Thermally stimulated current in nonohmic ZnO ceramics. *Japanese Journal of Applied Physics* 16 (1): 195–196.

19 Gupta, T.K. and Carlson, W.G. (1985). A grain-boundary defect model for instability/stability of a ZnO varistor. *Journal of Materials Science* 20 (10): 3487–3500.

20 Stucki, F. and Greuter, F. (1990). Key role of oxygen at zinc oxide varistor grain boundaries. *Applied Physics Letters* 57 (5): 446–448.

21 Tu, Y.P., Wang, Q., He, J. et al. (2013). TSC characteristics of AC aged ZnO varistors. *Science China Technological Sciences* 56 (3): 677–682.

22 Ramírez, M.A., Tararam, R., Simoes, A.Z. et al. (2013). Degradation analysis of the SnO_2 and ZnO-based varistors using electrostatic force microscopy. *Journal of the American Ceramic Society* 96 (6): 1801–1809.
23 Tada, T. (2010). Degradation of ZnO varistors as estimated by aging tests. *Electrical Engineering in Japan* 170 (2): 1–18.
24 Liu, J. (2011). Research on the degradation characteristics and mechanisms of high voltage gradient ZnO varistor. Doctoral thesis. Beijing, China: Tsinghua University.
25 Eda, K. (1978). Conduction mechanism of non-ohmic zinc oxide ceramics. *Journal of Applied Physics* 49 (5): 2964–2972.
26 Takahashi, K., Miyoshi, T., Maeda, K. et al. (1981). Degradation of zinc oxide varistors. *MRS Online Proceedings Library Archive, Materials Research Society* 5: 399–404.
27 Chiang, Y.M., Kingery, W.D., and Levinson, L.M. (1982). Compositional changes adjacent to grain boundaries during electrical degradation of a ZnO varistor. *Journal of Applied Physics* 53 (3): 1765–1768.
28 Sato, K., Takada, Y., Takemura, T., and Ototake, M. (1982). A mechanism of degradation in leakage currents through ZnO varistors. *Journal of Applied Physics* 53 (12): 8819–8826.
29 Sonder, E., Levinson, L.M., and Katz, W. (1985). Role of short-circuiting pathways in reduced ZnO varistors. *Journal of Applied Physics* 58 (11): 4420–4425.
30 Bui, A., Loubiere, A., and Hassanzadeh, M. (1989). Electrical characteristic degradation of ZnO varistors subjected to partial discharges. *Journal of Applied Physics* 65 (10): 4048–4050.
31 Ramírez, M.A., Simoes, A.Z., Bueno, P.R. et al. (2006). Importance of oxygen atmosphere to recover the ZnO-based varistors properties. *Journal of Materials Science* 41 (19): 6221–6227.
32 Castro, M.S., Benavente, M.A., and Aldao, C.M. (1993). Degradation in ZnO varistors. *Journal of Physics: Condensed Matter* 5 (33A): A341–A342.
33 He, J.L., Liu, J., Hu, J. et al. (2011). Non-uniform ageing behavior of individual grain boundaries in ZnO varistor ceramics. *Journal of the European Ceramic Society* 31 (8): 1451–1456.
34 Clarke, D.R. (1999). Varistor ceramics. *Journal of the American Ceramic Society* 82 (3): 485–502.
35 Yao, J.G. (1992). Small current property of ZnO varistors for HVDC surge arresters. Master degree thesis. Beijing, China: Tsinghua University.
36 Binks, D.J. and Grimes, R.W. (1993). Incorporation of monovalent ions in ZnO and their influence on varistor degradation. *Journal of the American Ceramic Society* 76 (9): 2370–2372.
37 Eda, K. (1989). Zinc oxide varistors. *IEEE Electrical Insulation Magazine* 5 (6): 28–30.
38 Zheng, Z., Cui, H., Wang, Q., and Tu, Y. (2012). Space charge characteristics of ZnO varistors after pulse degradation. In: *2012 Asia-Pacific Power and Energy Engineering Conference (APPEEC)*, 1–4. IEEE.

39 Liu, J., He, J., Hu, J. et al. (2011). Statistics on the AC ageing characteristics of single grain boundaries of ZnO varistor. *Materials Chemistry and Physics* 125 (1–2): 9–11.
40 Liu, J., He, J., Hu, J. et al. (2010). Statistical pulse degradation characteristics of grain boundaries in a ZnO varistor based on microcontact measurement. *Journal of the American Ceramic Society* 93 (9): 2473–2475.
41 He, J.L., Cheng, C.L., and Hu, J. (2016). Electrical degradation of double-Schottky barrier in ZnO varistors. *AIP Advances* 6 (3): 030701.
42 Blatter, G. and Greuter, F. (1986). Carrier transport through grain boundaries in semiconductors. *Physical Review B* 33 (6): 3952–3966.
43 Chen, Z.X., Lin, G.C., Fu, G., and Tang, D.H. (1998). A grain boundary defect model for ZnO ceramic varistors by deep heat treatment. *Science in China Series A: Mathematics* 41 (1): 71–78.
44 Nawata, M., Kawamura, H., Kanematdu, A., and Ieda, M. (1989). Studies on degradation mechanism of zinc oxide ceramics varistor by thermally stimulated current. In: *Ceramics Transactions: Advances in Varistor Technology*, vol. 3 (ed. L.M. Levinson), 186–193. Ohio, USA: The American Ceramic Society.
45 Cheng, C.L., He, J.L., and Hu, J. (2014). Observation of the charged defect migration that causes the degradation of double-Schottky barriers using a nondestructive quantitative profiling technique. *Applied Physics Letters* 105 (13): 133508.
46 Li, Y., Yasuda, M., and Takada, T. (1994). Pulsed electroacoustic method for measurement of charge accumulation in solid dielectrics. *IEEE Transactions on Dielectrics and Electrical Insulation* 1 (2): 188–195.
47 Bernstein, J.B. (1991). Analysis of the electrically stimulated acoustic-wave method for observing space charge in semi-insulating films. *Physical Review B* 44 (19): 10804.
48 Cheng, C.L., He, J.L., and Hu, J. (2012). Naturally asymmetrical double-Schottky barrier model: based on observation of bicrystal. *Applied Physics Letters* 101 (17): 173508.
49 Morshuis, P. and Jeroense, M. (1997). Space charge measurements on impregnated paper: a review of the PEA method and a discussion of results. *IEEE Electrical Insulation Magazine* 13 (3): 26–35.
50 Bernstein, J.B. (1990). Electrical characterization of polymeric insulation by electrically stimulated acoustic wave measurements. Doctoral thesis. Cambridge, MA, USA: Massachusetts Institute of Technology.
51 Bernstein, J.B. (1992). Improvements to the electrically stimulated acoustic wave method for analyzing bulk space charge. *IEEE Transactions on Electrical Insulation* 27 (1): 152–161.
52 Zhao, X., Li, J., Li, H., and Li, S. (2012). Intrinsic and extrinsic defect relaxation behavior of ZnO ceramics. *Journal of Applied Physics* 111 (12): 124106.
53 Look, D.C., Farlow, G.C., Reunchan, P. et al. (2005). Evidence for native-defect donors in n-type ZnO. *Physical Review Letters* 95 (22): 225502.
54 Look, D.C., Hemsky, J.W., and Sizelove, J.R. (1999). Residual native shallow donor in ZnO. *Physical Review Letters* 82 (12): 2552–2555.

55 Kittilstved, K.R., Schwartz, D.A., Tuan, A.C. et al. (2006). Direct kinetic correlation of carriers and ferromagnetism in Co^{2+}: ZnO. *Physical Review Letters* 97 (3): 037203.

56 Gupta, T.K. (1990). Application of zinc oxide varistors. *Journal of the American Ceramic Society* 73 (7): 1817–1840.

57 Han, J., Senos, A.M.R., and Mantas, P.Q. (2002). Deep donors in polycrystalline Mn-doped ZnO. *Materials Chemistry and Physics* 75 (1–3): 117–120.

58 Cheng, P., Li, S., Zhang, L., and Li, J. (2008). Characterization of intrinsic donor defects in ZnO ceramics by dielectric spectroscopy. *Applied Physics Letters* 93 (1): 012902.

59 Cheng, C., Hu, J., and He, J. (2014). Characterization of dielectric behavior in ZnO electroceramic: superior grain boundary, inferior grain boundary and grain. *Materials Letters* 132: 240–242.

60 Yin, W.J., Ma, J., Wei, S.H. et al. (2012). Comparative study of defect transition energy calculation methods: the case of oxygen vacancy in In_2O_3 and ZnO. *Physical Review B* 86 (4): 045211.

61 Alkauskas, A. and Pasquarello, A. (2011). Band-edge problem in the theoretical determination of defect energy levels: the O vacancy in ZnO as a benchmark case. *Physical Review B* 84 (12): 125206.

62 Vidya, R., Ravindran, P., Fjellvåg, H. et al. (2011). Energetics of intrinsic defects and their complexes in ZnO investigated by density functional calculations. *Physical Review B* 83 (4): 045206.

63 Clark, S.J., Robertson, J., Lany, S., and Zunger, A. (2010). Intrinsic defects in ZnO calculated by screened exchange and hybrid density functionals. *Physical Review B* 81 (11): 115311.

64 Oba, F., Togo, A., Tanaka, I. et al. (2008). Defect energetics in ZnO: a hybrid Hartree-Fock density functional study. *Physical Review B* 77 (24): 245202.

65 Paudel, T.R. and Lambrecht, W.R. (2008). First-principles calculation of the O vacancy in ZnO: a self-consistent gap-corrected approach. *Physical Review B* 77 (20): 205202.

66 Lany, S. and Zunger, A. (2007). Dopability, intrinsic conductivity, and nonstoichiometry of transparent conducting oxides. *Physical Review Letters* 98 (4): 045501.

67 Janotti, A. and Van de Walle, C.G. (2007). Native point defects in ZnO. *Physical Review B* 76 (16): 165202.

68 Erhart, P., Albe, K., and Klein, A. (2006). First-principles study of intrinsic point defects in ZnO: role of band structure, volume relaxation, and finite-size effects. *Physical Review B* 73 (20): 205203.

69 Erhart, P., Klein, A., and Albe, K. (2005). First-principles study of the structure and stability of oxygen defects in zinc oxide. *Physical Review B* 72 (8): 085213.

70 Janotti, A. and Van de Walle, C.G. (2005). Oxygen vacancies in ZnO. *Applied Physics Letters* 87 (12): 122102.

71 Zhang, S.B., Wei, S.H., and Zunger, A. (2001). Intrinsic n-type versus p-type doping asymmetry and the defect physics of ZnO. *Physical Review B* 63 (7): 075205.

72 Kohan, A.F., Ceder, G., Morgan, D., and Van de Walle, C.G. (2000). First-principles study of native point defects in ZnO. *Physical Review B* 61 (22): 15019–15027.

73 Yan, Y. and Al-Jassim, M.M. (2004). Inversion domain boundaries in ZnO: first-principles total-energy calculations. *Physical Review B* 69 (8): 085204.

74 Kim, Y.S. and Park, C.H. (2009). Rich variety of defects in ZnO via an attractive interaction between O vacancies and Zn interstitials: origin of n-type doping. *Physical Review Letters* 102 (8): 086403.

75 Mukae, K., Tsuda, K., and Nagasawa, I. (1979). Capacitance-vs-voltage characteristics of ZnO varistors. *Journal of Applied Physics* 50 (6): 4475–4476.

76 He, J.L., Cheng, C.L., and Hu, J. (2015). An analytic approach to the degradation of double-Schottky barrier: Theoretical prediction of $V_O{}^0$–$Zn_i{}^{2+}$: $Zn_i{}^{2+}$ as dominant mobile ion in ZnO electroceramic. *Scripta Materialia* 104: 25–28.

77 Skylaris, C.K., Haynes, P.D., Mostofi, A.A., and Payne, M.C. (2005). Introducing ONETEP: linear-scaling density functional simulations on parallel computers. *The Journal of Chemical Physics* 122 (8): 084119.

78 Domingos, H.S., Carlsson, J.M., Bristowe, P.D., and Hellsing, B. (2002). Charge accumulation and barrier formation at grain boundaries in ZnO decorated with bismuth. *Journal of Physics: Condensed Matter* 14 (48): 12717.

79 Carlsson, J.M., Hellsing, B., Domingos, H.S., and Bristowe, P.D. (2002). Theoretical investigation of the pure and Zn-doped α and δ phases of Bi_2O_3. *Physical Review B* 65 (20): 205122.

80 Takada, M., Sato, Y., and Yoshikado, S. (2012). Relation between grain boundary structure and electrical degradation in zinc oxide varistors. *Journal of the American Ceramic Society* 95 (8): 2579–2586.

81 Walsh, A., Watson, G.W., Payne, D.J. et al. (2006). Electronic structure of the α and δ phases of Bi_2O_3: a combined ab initio and x-ray spectroscopy study. *Physical Review B* 73 (23): 235104.

82 Leite, E.R., Varela, J.A., and Longo, E. (1992). A new interpretation for the degradation phenomenon of ZnO varistors. *Journal of Materials Science* 27 (19): 5325–5329.

83 He, J.L., Hu, J., and Lin, Y.H. (2008). ZnO varistors with high voltage gradient and low leakage current by doping rare-earth oxide. *Science in China Series E: Technological Sciences* 51 (6): 693–701.

84 Marques, V.P.B., Ries, A., Simoes, A.Z. et al. (2007). Evolution of $CaCu_3Ti_4O_{12}$ varistor properties during heat treatment in vacuum. *Ceramics International* 33 (7): 1187–1190.

85 Montenegro, J.C. and Ramirez, J.L. (1995). Degradation of zinc oxide varistors. In: *Proceedings of the 1995 First IEEE International Caracas Conference on Devices, Circuits and Systems*, 352–354. IEEE.

86 Modine, F.A. and Wheeler, R.B. (1987). Fast pulse response of zinc-oxide varistors. *Journal of Applied Physics* 61 (8): 3093–3098.

87 Modine, F.A. and Wheeler, R.B. (1990). Pulse response characteristics of ZnO varistors. *Journal of Applied Physics* 67 (10): 6560–6566.

88 Ramirez, M.A., Cilense, M., Bueno, P.R. et al. (2008). Comparison of non-ohmic accelerated ageing of the ZnO-and SnO_2-based voltage dependent resistors. *Journal of Physics D: Applied Physics* 42 (1): 015503.

89 Wang, M.H., Yao, C., and Zhang, N.F. (2008). Degradation characteristics of low-voltage ZnO varistor manufactured by chemical coprecipitation processing. *Journal of Materials Processing Technology* 202 (1–3): 406–411.

90 Tonkoshkur, A.S., Lyashkov, A.Y., Gomilko, I.V., and Ivanchenko, A.V. (2000). Effect of long-term electrical degradation on the distribution of donor impurities in ZnO varistor ceramics. *Inorganic Materials* 36 (7): 745–748.

91 Wang, Y.P., Lee, W.I., and Tseng, T.Y. (1996). Degradation phenomena of multilayer ZnO–glass varistors studied by deep level transient spectroscopy. *Applied Physics Letters* 69 (12): 1807–1809.

92 Barrado, C.M., Leite, E.R., Bueno, P.R. et al. (2004). Thermal conductivity features of ZnO-based varistors using the laser-pulse method. *Materials Science and Engineering A* 371 (1–2): 377–381.

93 Shirley, C.G. and Paulson, W.M. (1979). The pulse-degradation characteristic of ZnO varistors. *Journal of Applied Physics* 50 (9): 5782–5789.

94 Chen, W.P., Wang, Y., Peng, Z., and Chan, H.L.W. (2003). Degradation mechanism of ZnO ceramic varistors studied by electrochemical hydrogen charging. *Japanese Journal of Applied Physics* 42 (1A): L48–L50.

95 Chen, W.P. and Chan, H.L.W. (2005). Electroplating-induced degradation in ZnO ceramic varistors. *Journal of Materials Science* 40 (24): 6593–6596.

96 Wang, M.H., Hu, K.A., Zhao, B.Y., and Zhang, N.F. (2007). Degradation phenomena due to humidity in low voltage ZnO varistors. *Ceramics International* 33 (2): 151–154.

97 Erhart, P. and Albe, K. (2006). Diffusion of zinc vacancies and interstitials in zinc oxide. *Applied Physics Letters* 88 (20): 201918.

98 Bueno, P.R., Leite, E.R., Oliveira, M.M. et al. (2001). Role of oxygen at the grain boundary of metal oxide varistors: a potential barrier formation mechanism. *Applied Physics Letters* 79 (1): 48–50.

99 Leite, E.R., Varela, J.A., and Longo, E. (1992). Barrier voltage deformation of ZnO varistors by current pulse. *Journal of Applied Physics* 72 (1): 147–150.

100 Takada, M. and Yoshikado, S. (2010). Effect of thermal annealing on electrical degradation characteristics of Sb–Bi–Mn–Co-added ZnO varistors. *Journal of the European Ceramic Society* 30 (2): 531–538.

101 Gupta, T.K. and Miller, A.C. (1988). Improved stability of the ZnO varistor via donor and acceptor doping at the grain boundary. *Journal of Materials Research* 3 (4): 745–754.

102 Takada, M. and Yoshikado, S. (2007). Effect of SnO_2 addition on electrical degradation of ZnO varistors. *Key Engineering Materials* 350: 213–216.

103 Gardner, T.J., Doughty, D.H., Lockwood, S.J., and Tuttle, B. (1989). Effect of low level dopants on chemically prepared varistor materials. *Ceramic Transactions* 3: 84–92.

104 Oba, F., Sato, Y., Yamamoto, T. et al. (2003). Current–voltage characteristics of cobalt-doped inversion boundaries in zinc oxide bicrystals. *Journal of the American Ceramic Society* 86 (9): 1616–1618.

105 Nahm, C.W. and Park, C.H. (2000). Microstructure, electrical properties, and degradation behavior of praseodymium oxides-based zinc oxide varistors doped with Y_2O_3. *Journal of Materials Science* 35 (12): 3037–3042.
106 Nahm, C.W. (2010). Al doping effect on electrical and dielectric aging behavior against impulse surge in ZPCCYA-based varistors. *Materials Science and Engineering B* 170 (1): 123–128.
107 Zhao, H.F., Hu, J., Chen, S.M. et al. (2016). Improving age stability and energy absorption capabilities of ZnO varistors ceramics. *Ceramics International* 42 (15): 7880–17883.

8

Praseodymium/Vanadium/Barium-Based ZnO Varistor Systems

The most commercially applied Bi-doped ZnO varistor materials have a few drawbacks because of the high volatility and reactivity of Bi_2O_3 during liquid sintering. The former changes varistor characteristics, especially the grain boundary characteristics, with the deviation of intercomposition ratio of additives, and the latter destroys the multilayer structure of chip varistors and generates an additional Bi-containing secondary insulating spinel phase at temperatures over 1000 °C, which does not play any role in the electrical conduction and deteriorate surge absorption capabilities [1]. Another drawback is that the Bi_2O_3-based varistors need many additives to obtain high nonlinearity and stable electrical properties. In order to overcome the shortcomings of Bi_2O_3-based ZnO varistors, other ZnO varistor systems have been added to ZnO varistors instead of bismuth, such as praseodymium [2, 3], barium [4, 5], and vanadium [6–14], all exhibit a varistor behavior. All not only have a simple microstructure consisting of ZnO grains and intergranular layers but also high nonlinearity. The low breakdown voltages and very large grain sizes of these three varistor systems suggest the possibility of using them to manufacture low-voltage varistors of appreciable thickness, which operate at the voltage lower than dozens of volts. At last, the ZnO–glass varistors for multilayer ceramic chip varistors are introduced, which are applied as surge protection devices in the surface-mount hybrid integrated circuit (HIC) technology.

8.1 Praseodymium System

8.1.1 Doping Effects

Pr-based ZnO varistors are reported to have only two phases, namely, ZnO grains and intergranular layers. The absence of spinel phase, which plays no electrical role at grain boundaries, increases the active grain boundary area through which the electrical current flows. Therefore, the effective cross-sectional area of the element is increased. This gives rise to compacting of systems, variety in application area, and high performance as a surge protector. Mukae et al. [2, 15, 16] reported zinc oxide varistors with praseodymium oxide in 1977. The ZnO–Pr_6O_{11}-based varistors have not only simple microstructure consisting of ZnO grains and intergranular layers, unlike the Bi_2O_3-doped varistors, but

also high nonlinearity, with a nonlinear coefficient of 25–37 only for ternary system ZnO–Pr_6O_{11}–CoO, compared with Bi_2O_3-based ZnO varistors having a nonlinear coefficient of 13–18 for only ternary system ZnO–Bi_2O_3–CoO (or MnO) [16]. However, the varistors having a high stability never exceeded 40 in the nonlinear coefficient and the varistors having a high nonlinearity exhibited very poor stability for DC stress. Further, the varistors added by Cr_2O_3 to quaternary system above behaved excellent nonlinear coefficient close to 70, and the stability for any varistor was greatly improved [17].

The electrical properties of the ZnO–Pr_6O_{11}-based varistor ceramics can be controlled by adjusting the Al_2O_3 content [18]. Doping of Al_2O_3 in the range of 0.0–0.01 mol% affected the average grain size of ZnO–Pr_6O_{11}-based varistor ceramics more strongly than it did their ceramic density. ZnO–Pr_6O_{11}-based varistor ceramics doped with Al_2O_3 of 0.005 mol% exhibited excellent nonlinearity with a nonlinear coefficient of 43.8 and a leakage current of 0.66 μA. As the Al_2O_3 content increases, the donor concentration and the density of the surface states increase, and the barrier height and depletion width decrease. Furthermore, in order to obtain the best electrical stability, Al_2O_3 at 0.001 mol% is an optimum content.

Fe_2O_3 was an important additive, acting as an inhibitor of ZnO grain growth in ZnO–Pr_6O_{11}–Co_3O_4–Cr_2O_3–Fe_2O_3-based varistor ceramic materials [1]. With a tricky and appropriate amount of Fe_2O_3 doped, the electrical property of ZnO–Pr_6O_{11}-based varistor ceramics would be significantly improved. When the doping level of Fe_2O_3 was no more than 0.005 mol%, more addition of Fe_2O_3 could improve the nonlinear coefficient and varistor voltage of the materials. The optimum nonlinear coefficient of 26 and varistor voltage of 571 V mm^{-1} were acquired when the doping level of Fe_2O_3 was 0.005 mol%. Too much more doped Fe_2O_3 would destroy the nonlinear properties of the ceramic materials.

The rare earth oxides are doped to improve the electrical properties and the stability of Pr-based ZnO varistors. Nahm et al. reported that the addition of rare earth oxides (Er_2O_3, Dy_2O_3, and Nd_2O_3) to the ternary system ZnO–Pr_6O_{11}–CoO-based varistors improved the nonlinearity and electrical stability [19–28]. Consequently, only NiO-added varistors greatly improved the stability. Cai et al. studied the effect of the doped rare earth oxide Dy_2O_3 to Pr-based ZnO varistors [29], and the analysis of the microstructure and composition indicated that the ceramic is composed of the main phase of ZnO and the second phase of rare earth oxides (e.g. Dy_2O_3, Pr_6O_{11}, and Pr_2O_3). The average grain size was markedly increased from 3 to 18 μm, with an increase in the sintering temperature from 1150 to 1350 °C; both the leakage current and the barrier voltage per grain boundary were increased. However, the varistor voltage (from 1014 to 578 V mm^{-1}) and nonlinear coefficient of samples were decreased because of the variations of the grain size and the number of grain boundary. Analysis of the resistivity of the grain and grain boundary indicates that the resistivity of the grain is almost independent of the variation of the grain size and the sintering temperature. The dielectric constant of the ZPD (ZnO–Pr_6O_{11}–Dy_2O_3) samples decreases from 105 to 45, which can be attributed to the internal boundary layer capacitance effect and the variation of the thickness of the grain boundary layer.

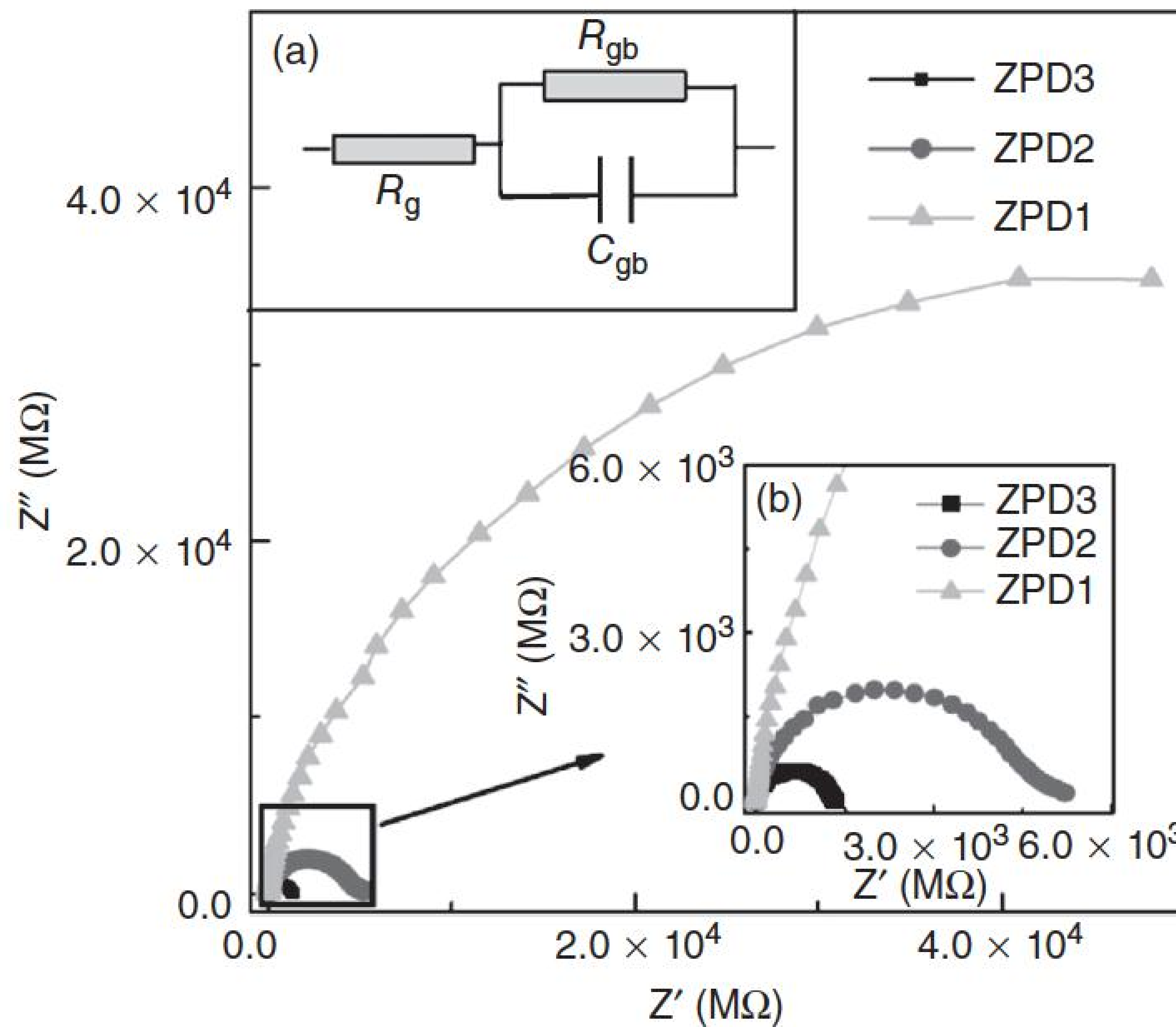


Figure 8.1 Complex impedance spectra of various ZPD samples; inset (a) shows the equivalent resistor–capacitor circuit and (b) shows the magnified part of the spectrum. Source: Nahm 2006 [29]. Reproduced with permission of Springer.

Figure 8.1 shows the complex impedance spectra of various ZPD samples [29]. The results reveal that as the ceramic sample is sintered at 1150, 1250, and 1350 °C, the corresponding resistance of grain boundary is about 8×10^4, 4.5×10^3, and 1.5×10^3 MΩ, respectively, which should be related to the amount and microstructure of grain boundaries. The microstructure and electrical properties of the ternary system $ZnO–Pr_6O_{11}–CoO$ were reported [4, 29, 30]; when Dy_2O_3 is doped in this system, the ZnO varistors have a high stability as well as a relatively good nonohmicity, and it will be sufficiently used as a basic composition in the future, but other additives are demanded to obtain further nonohmicity [22]. The degradation of ZnO varistors is associated with the lowering of the potential barrier at the grain boundaries, which is related to the annihilation of interface defect states when it is stressed continuously by an electric field [31]. The positively charged zinc interstitial (Zn_i) formed to the depletion layer migrates toward the negatively charged grain boundary interface during the stress period and it recombines with zinc vacancy (V_{Zn}) positioned in there. As a result, the recombination of these species leads to the degradation of ZnO varistors. Based on these facts, it is guessed that the reason why the varistors with Dy_2O_3 of 0.5 mol% exhibit an excellent stability is because the added Dy_2O_3 spatially restricts the migration of zinc interstitials (Zn_i) within the depletion layer or stabilizes the interface states.

The addition of Dy_2O_3 to the ternary system $ZnO–Pr_6O_{11}–CoO$ greatly improved the $V–I$ characteristics of varistor ceramics [23]. The stability of varistors sintered at 1350 °C was far higher than that at 1300 °C. The value of V_{1mA} increased in the range of 337.4–560.9 V mm^{-1} at 1300 °C and 8.85–404.3 V mm^{-1} at 1350 °C with an increasing Dy_2O_3 content. The V_{gb} is defined by $V_{gb} = (d/D)$

V_{1mA}, where d is the average grain size and D is the thickness of the sample. The value of V_{gb} was also increased in the range of 2.5–3.5 V per grain boundary at 1300 °C and 0.2–3.5 at 1350 °C as the Dy_2O_3 content is increased. The varistors with Dy_2O_3 content agreed to generally well-known 2–4 V per grain boundary. The varistors with 0.5 mol% Dy_2O_3 showed an excellent stability as well as relatively good nonlinear V–I characteristics, which were 37.8 in the nonlinear coefficient and 5.4 μA in the leakage current [23]. Their variation rate of varistor voltage was −1.7% even under very severe stress (0.80 V_{1mA}/90 °C/12 h) + (0.85V_{1mA}/115 °C/12 h) + (0.90V_{1mA}/120 °C/12 h) + (0.95V_{1mA}/125 °C/12 h). It is possible that the reason why Dy_2O_3-doped Pr_6O_{11}-based ZnO varistors exhibit predominant degradation characteristics is because the added Dy_2O_3 spatially restricts the migration of zinc interstitial within the depletion layer or stabilizes the interface states.

Doping Er_2O_3 greatly improved the nonlinear properties of ZnO–Pr_6O_{11}–CoO-based varistors, and the varistor sintered at 1300 °C exhibited a good nonlinearity, with a nonlinear coefficient of 52.8 and a leakage current of 9.8 μA. The increase in sintering temperature deteriorated the nonlinear properties, whereas it greatly improved the stability [32]. Further studies showed that doping Er_2O_3 can improve the electrical properties, and its stability against DC-accelerated aging stress of Pr_6O_{11}-based ZnO varistor ceramics, the nonlinear coefficient of varistors with an increasing Er_2O_3 content varied with V-shape, reaching a minimum at 1.0 mol% Er_2O_3. As the sintering time was increased, the nonlinear coefficient decreased, whereas its stability for the DC stress was improved. The varistor with 0.5 mol% Er_2O_3 sintered at 1340 °C for two hours exhibited the best performance for the nonlinearity and stability. This varistor exhibited not only a high nonlinearity, with the nonlinear coefficient of 43.4, but also a high stability, with the leakage current of 1.2 μA [16].

It was found that a moderate La_2O_3 content, in the vicinity of 0.5 mol%, could greatly improve the nonlinear properties of quaternary system ZnO–Pr_6O_{11}–CoO–Cr_2O_3-based varistor ceramics. The varistor ceramics with 0.5 mol% La_2O_3 exhibited excellent nonlinear properties, with the nonlinear coefficient of 81.6 and the leakage current of 0.2 μA [33]. The La_2O_3 dopant acts as a donor by increasing donor density as the La_2O_3 content is increased.

It is clear that the nonlinear coefficient and leakage current were strongly influenced by the Tb_4O_7 content. Doping Tb_4O_7 exhibited the best surge withstand capability, a moderate Tb_4O_7 content was optimized at 0.5 mol% in terms of the nonlinearity and surge withstand capability [34], and also exhibited an excellent stability for DC-accelerated aging stress of 0.85 E_{1mA}/115 °C/24 h [35]. Microstructural analysis indicated that the addition of Tb_4O_7 decreased the average grain size from 3.6 to 3.2 μm and increased the sintered density from 5.58 to 5.68 g cm^{-3}. As the mount of Tb_4O_7 increased, the breakdown field increased from 9393 to 12 437 V cm^{-1}, and the nonlinear coefficient increased from 50 to 65 [35].

The investigation has indicated that minor additions of K_2O up to 0.5 mol% are able to considerably control the grain growth of Pr_2O_3-doped ZnO and enhance the densification, probably because of the small grain size of ZnO and the large grain boundary area. This densified microstructure with a reduced grain size

results in an increased grain boundary area in the varistor and results in a higher field and a high degree of nonlinearity [36]. The doped ZnO containing 2 mol% Pr_2O_3, 0.25 mol% each of Cr_2O_3 and CoO attained grain sizes around 8.5 μm, for the sample containing 0.3 mol% K_2O, has an average grain size of 5 μm, while further addition of K_2O up to 0.5 mol% resulted in an average grain size of 3.5 μm [37].

The SnO_2 dopant played a role against the sinterability of the ZnO–Pr_6O_{11}-based varistor ceramics and the growth of ZnO grains. The average ZnO grain size decreased with the increase of SnO_2 doping contents. When the SnO_2 doping content was no more than 1.0 mol%, the varistor voltage increased with an increasing amount of SnO_2 dopant. The doped SnO_2 acted as a donor in ZnO–Pr_6O_{11}-based varistors, and minor doping of SnO_2 up to 0.5 mol% can improve the nonlinear coefficient and reduce the leakage current of the ceramic varistors [38].

8.1.2 Effect of Sintering Processes

Lee et al. [31] investigated the effect of sintering temperature on the microstructure and crystal phases of the intergranular praseodymium oxides in ZnO varistor ceramics. The ZnO grains were three-dimensionally separated from the intergranular praseodymium oxides. On the basis of microdiffraction analysis of the intergranular layer, the phase transformation from fcc-Pr_6O_{11} into hcp-Pr_2O_3 was found when the sintering temperature increased from 1300 to 1350 °C. The defect reaction equation and the decrease of donor concentration with an increasing sintering temperature can verify the certainty of phase transition during the liquid-phase sintering observed by transmission electron microscopy. Additionally, on the basis of the small variations of the breakdown voltage per grain boundary, the number of active grain boundaries is not a dominant factor for the donor concentration dependence on the sintering temperature. Figure 8.2a,b showed SEM micrographs of specimens sintered at 1300–1350 °C, respectively. The average grain size greatly increased from 29.7 to 46.7 μm. A marked change in the morphology of the intergranular material, maybe the Pr-rich phase, can also be observed for samples sintered at 1300–1350 °C. Continuous distribution of the intergranular layer materials was observed at 1350 °C. In light of variations of grain sizes and the morphology of the intergranular material, the liquid-phase formation temperature was expected to be in the range of 1300–1350 °C for the varistor system of ZnO–5 mol% Co–0.5 mol% $PrO_{1.83}$. Figure 8.3 shows the current density vs applied voltage plot of the varistor system of ZnO–5 mol% Co–0.5 mol% $PrO_{1.83}$ at different temperatures [31]. The estimated nonlinear coefficients were in the range of 25–37 in the interval of 1–10 mA cm^{-2}, and the threshold voltage, which was defined as a breakdown voltage per grain boundary at a current density of 1 mA cm^{-2}, slightly increased from 3.66 to 3.82 V with the increment of sintering temperature, the barrier height increased from 0.83 to 0.90 eV, and the donor concentration decreased from 2.50×10^{17} to 1.47×10^{17} cm^{-3} [31].

Mukae et al. [2] have suggested that oxidation of interstitial zinc donors in the grain boundary region caused by the reduction of Pr_6O_{11} to Pr_2O_3 during

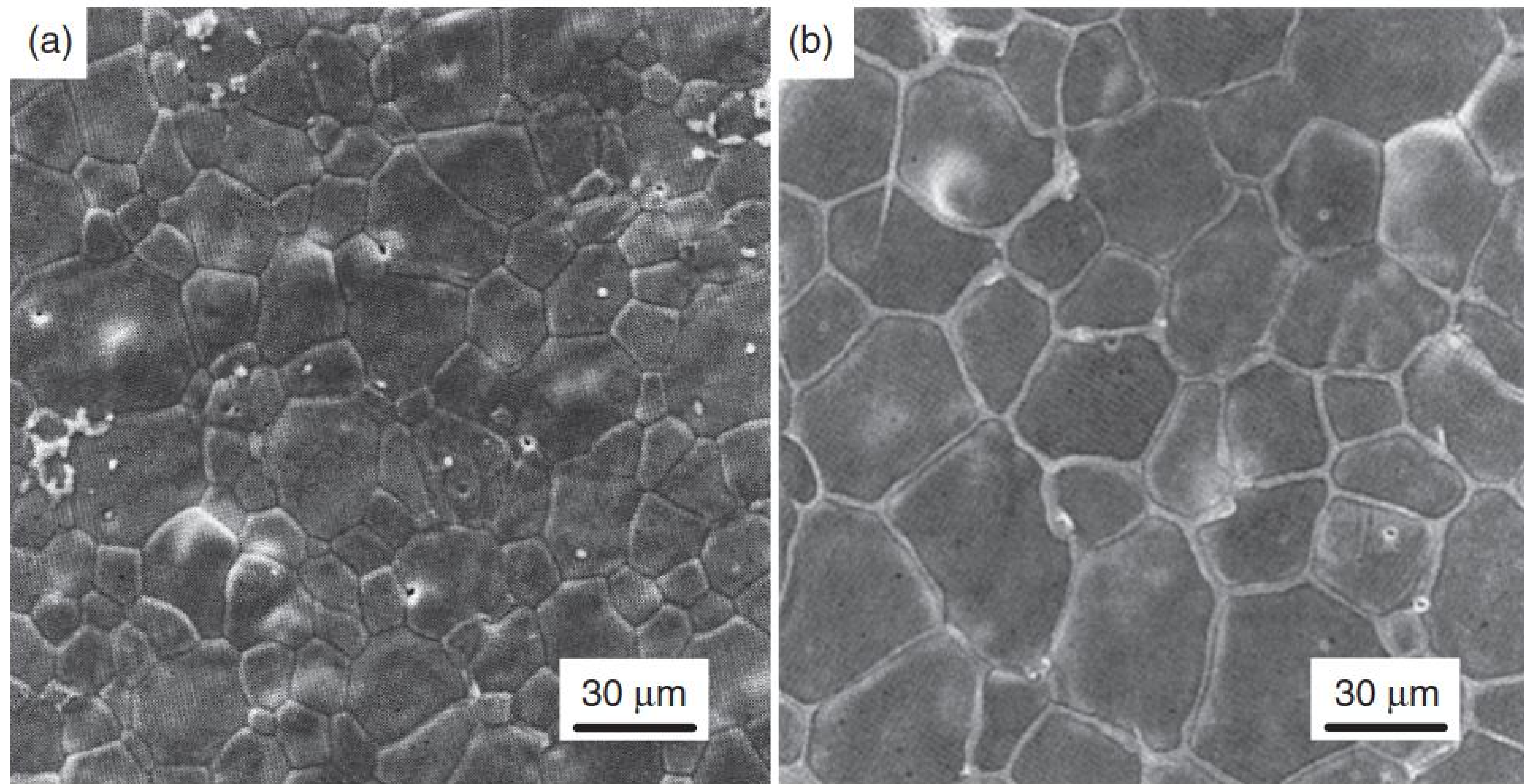


Figure 8.2 SEM micrographs of the samples containing ZnO–5 mol% Co–0.5 mol% $PrO_{1.83}$, sintered for one hour at (a) 1300 °C and (b) 1350 °C. Notice the changes in morphology of the bright intergranular phase. Source: Lee et al. 1996 [31]. Reproduced with permission of John Wiley & Sons.

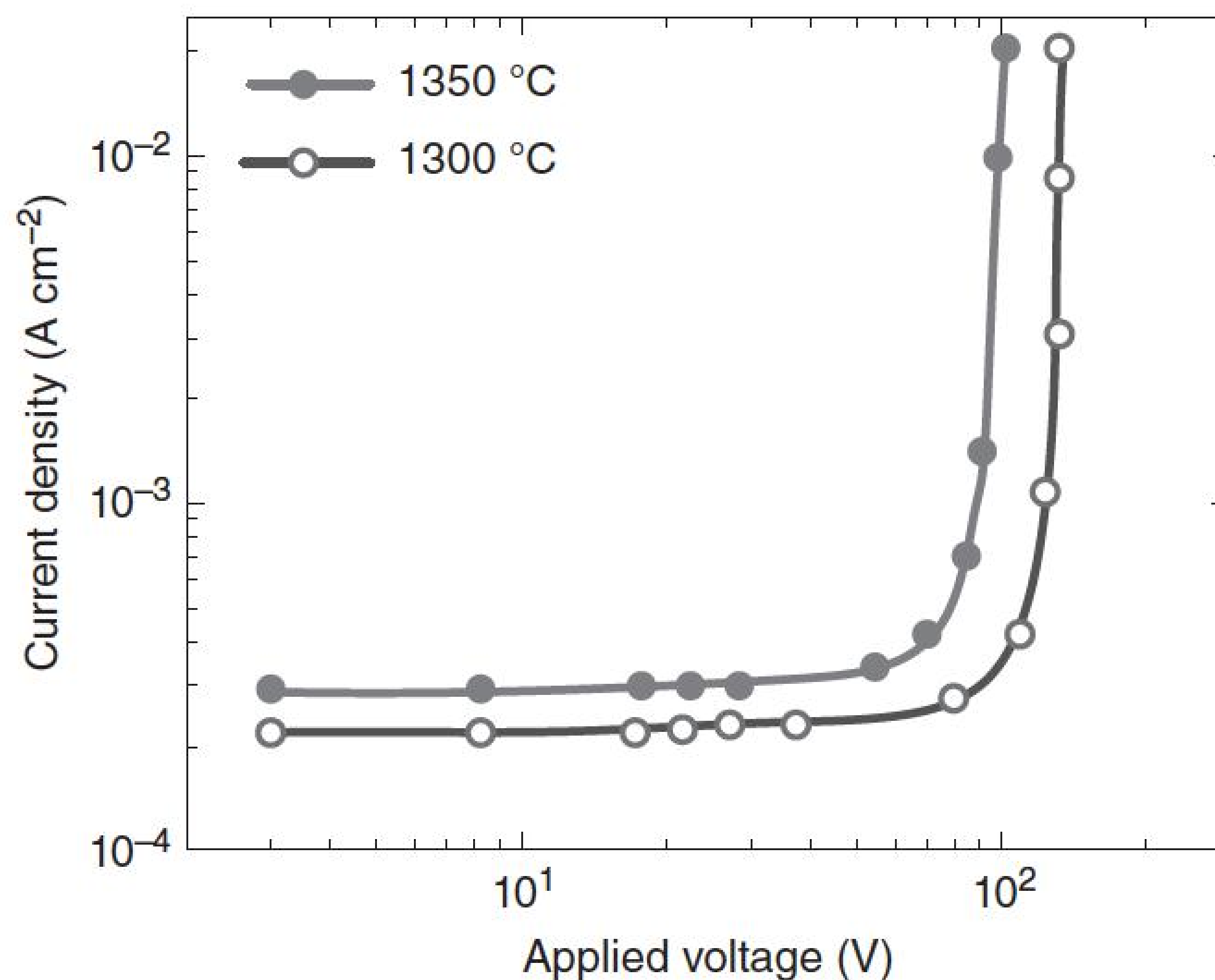


Figure 8.3 Current density vs applied voltage plot of the varistor system of ZnO–5 mol% Co–0.5 mol% $PrO_{1.83}$ at different sintering temperatures. Source: Adapted from Alles et al. [30].

liquid-phase sintering results in abrupt changes of electrical characteristics of ceramic varistors. However, Alles et al. [4, 30] studied liquid-phase sintering of the $ZnO–Co_3O_4–Pr_2O_3$ system with the content of ZnO above 90 mol% and reported that abrupt changes in donor concentration and equilibrium barrier heights result from a marked increase in the fraction of electrically active grain boundaries. Additionally, they reported that the calculated breakdown voltage per grain boundary showed an abrupt change during the liquid-phase formation and claimed that the marked increase in the breakdown voltage per grain boundary appeared to correlate with the fraction of electrically active grain boundaries.

This result was not in agreement with the observation reported by Lee et al. [31]. Sida et al. [39] provided direct evidence concerning the grain growth rate of 0.5 mol% Pr-doped ZnO that drastically changed between 1350 and 1400 °C, and an exothermic peak in differential thermal analysis (DTA) was also observed at 1380 °C in N_2, which indicated the formation of a liquid phase. As reduction of Pr_6O_{11} into Pr_2O_3 occurs above 1200 °C, praseodymium oxide will be expressed in the form of Pr_2O_3 [40]. In the ZnO–Pr_2O_3 system, only two phases composed mainly of praseodymium oxide revealed to be hexagonal Pr_2O_3 [14].

The schematic diagram of different morphologies of grain boundaries according to the sintering temperature (below and above the liquid-phase formation temperature) and atmosphere (oxygen partial pressure) can be explained by different vaporizations of components and are shown in Figure 8.4 [21]. Pr additive exists between the grain boundaries of ZnO below the liquid-phase formation temperature (1380 °C). This Pr component begins to the produce liquid phase with the reaction of ZnO above 1380 °C. In N_2, large Pr segregates are shown on the surface of fired ZnO because large vaporization of ZnO occurs at the surface. On the other hand, In O_2, a small Pr segregate is shown on the surface of fired ZnO because large vaporization of Pr occurs at the surface.

When the sintering temperature reaches 1500 °C, two kinds of mechanisms occur simultaneously [21]. One is the higher vaporization pressure during the dissociation of ZnO compared to $PrO_{1.83}$, and this is the reason of higher Pr concentrations at the surface of sample sintered in N_2. Another is the formation of a liquid that accelerates the evaporation of praseodymium oxide at 1500 °C, and this is the reason of lower Pr concentrations at the surface of the sample sintered in O_2. On the basis of the formation of varistor properties per grain boundary (e.g. threshold voltage and nonlinear coefficient), the number of active grain boundaries are believed to increase when the samples are heat treated above the liquid-phase temperature.

The cooling rate slightly affected the microstructure, the varistor voltage, and the leakage current [41]. However, the nonlinear coefficient was relatively strongly affected by the cooling rate, which decreased in the range 56.8–42.8 with increasing cooling rates. It was found that the dielectric characteristics complicatedly varied without a remarkable tendency of variation. On the other

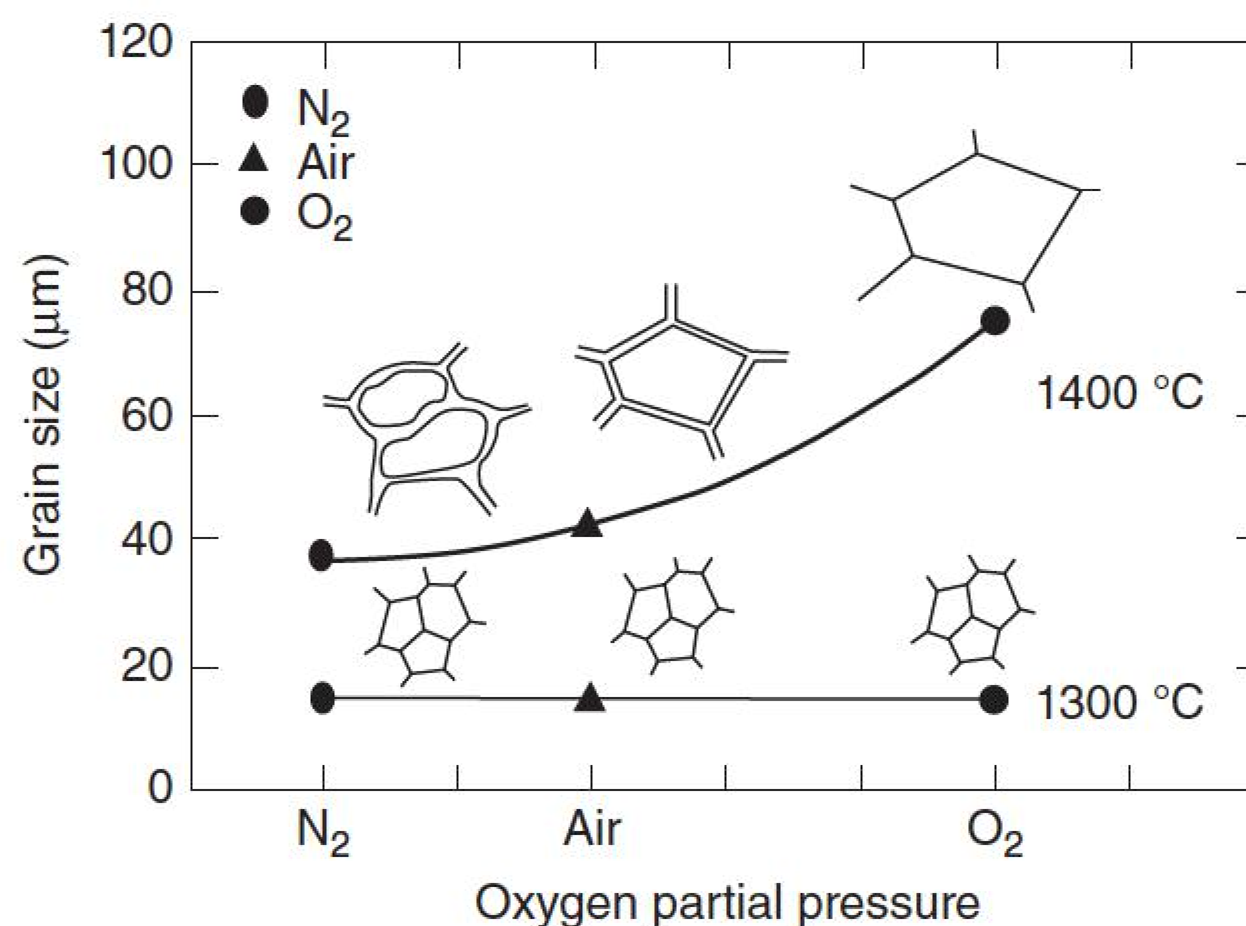


Figure 8.4 Effect of firing atmosphere (oxygen partial pressure) on the grain size and grain boundary morphology at the surface of 0.5 mol% Pr-doped ZnO samples. Source: Chun and Mizutani 2001 [21]. Reproduced with permission of Elsevier.

hand, the cooling rate also greatly affected the stability of nonlinear properties and dielectric characteristics against DC-accelerated aging stress, and the varistor ceramics cooled at 240 °C h^{-1} exhibited the highest stability. The model for analyzing the stability of varistor ceramics according to various stresses was known to be ion migration mechanism proposed by Gupta and Carlson [32]. The zinc interstitial (Zn_i) is diffused by biasing field and successively reacts with grain boundary defects. As a result, this process leads to a reduction of potential barrier and an increase in leakage current. Therefore, the way to improve the stability is to restrict the generation of Zn_i within depletion layer or the migration of Zn_i toward grain boundaries. It is proposed that the cooling rate deeply affects the migration of Zn_i within depletion layer or the stabilization of interface states.

8.1.3 High-Voltage Applications

Mukae et al. [42] developed ZnO varistor ceramics with a small amount of additive components Pr_6O_{11}, Co_3O_4, Cr_2O_3, and K_2CO_3 and other metal oxides for high-voltage applications, sintered in the furnace at higher than 1100 °C. Aluminum electrodes were sprayed on opposite sides of the sintered ceramic disks. In order to inhibit from flashover, insulating layers of glass and epoxy resins were coated around the cylindrical surface. Two types of elements, depending on the equivalent capacitance at the switching surge operating duty test, i.e. 25 and 50 μF, were developed. The diameters were 48 and 72 mm, respectively, and the thickness was 22 mm for both elements. These elements are applicable to high-voltage arresters for power systems. The gapless surge arresters have been developed using these elements for power stations up to AC 360 kV rated voltage and for railroad power stations of DC 2100 V rated voltage. The current concentration at the edge of electrodes generated the jump of the angular thermal stress, which was the major cause for the destruction by long-duration surge. Doping with boron improved the energy absorption capability by decreasing the grain size of the peripheral area of the elements and reducing the current concentration at the electrode edge.

The change in the resistive leakage current by applied AC voltage was tested. The applied voltage ratio is 85% and the ambient temperature is 105 °C. Although the leakage current initially increased to 120% level, it gradually decreased to 110% level, which was maintained subsequently until the steep rise at the thermal runaway. The results show the stable and long performance life for arresters. Arrhenius' plot of the time at which thermal runaway happens is shown in Figure 8.5 [41]. This figure shows that a life more than 100 years at 95% applied voltage ratio can be expected when the ambient temperature is 40 °C.

8.1.4 Low-Voltage Applications

However, most of the Pr_6O_{11}-based ZnO varistor systems that have been reported so far have been developed toward high-voltage applications. The work by Horio et al. [43] was one of the very few attempts to extend the use of Pr_6O_{11}-based ZnO ceramics for low-voltage applications. They have successfully

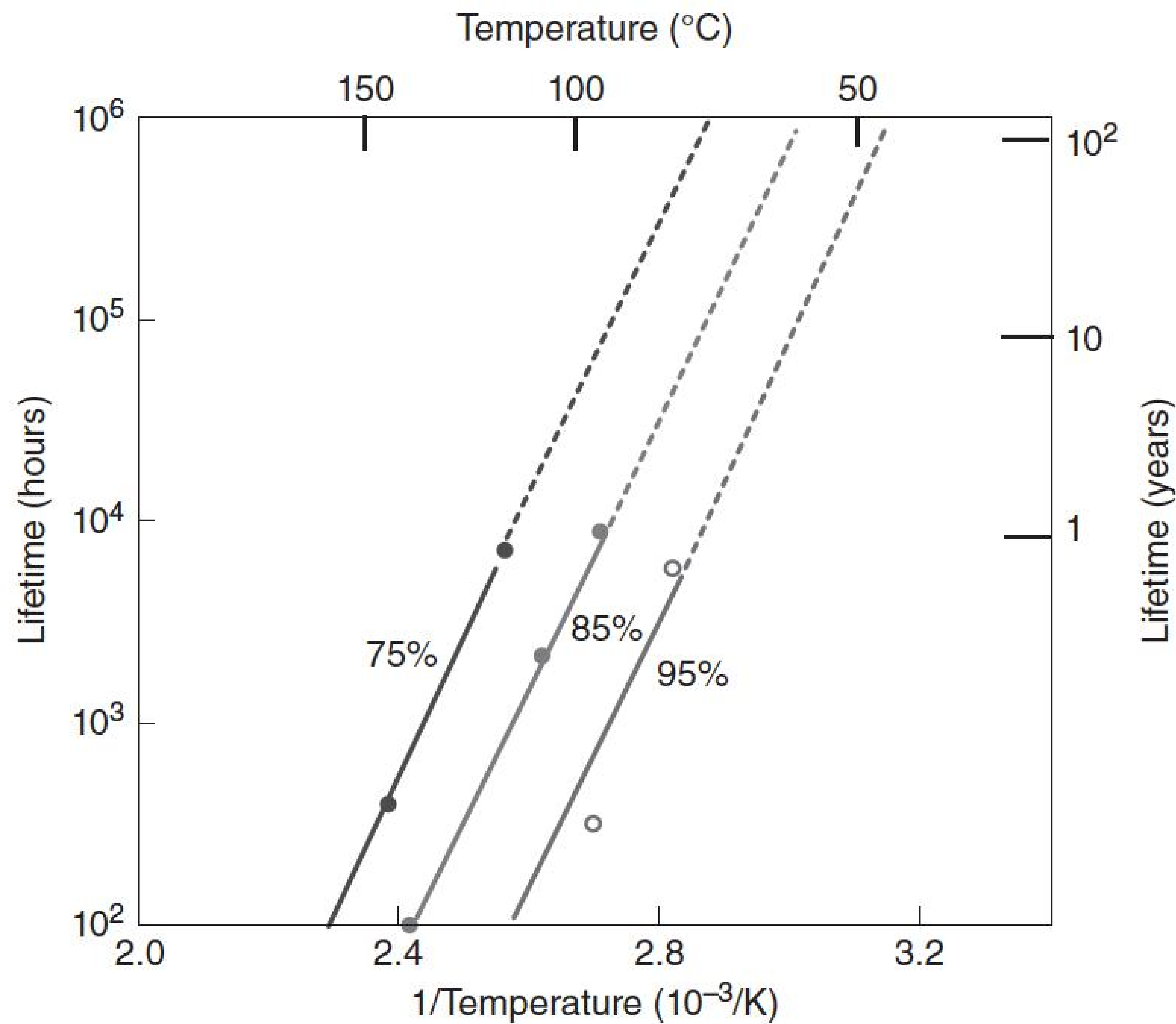


Figure 8.5 Arrhenius plot of the element life under different applied voltage ratio. The element life is defined as the time at which thermal runaway begins. Source: Adapted from Nahm [41].

fabricated ZnO/Pr_6O_{11}-multilayered thin films having a nonlinear coefficient α of 10 and E_b of 20 V by the radio frequency (RF) sputtering. Zinc oxide/metal oxide multilayered composite thin film varistors have been fabricated by the RF (13.56 MHz) sputtering method in an Ar/O_2 environment. After the Au electrode was formed on a quartz substrate by vacuum evaporation, zinc oxide (ZnO) layer was deposited by the RF sputtering with ZnO target at room temperature, Ar partial pressure of 2.5 Pa, O_2 partial pressure of 2.5 Pa, and RF power of 50 W. Pr_6O_{11} layer was formed on the ZnO layer by the RF sputtering with Pr_6O_{11} target at room temperature, Ar pressure of 5 Pa, and RF power of 80 W. The upper Au electrode was formed on the Pr_6O_{11} layer by vacuum evaporation. From the results of V–I and C–V measurements, it was found that a depletion region was formed in the ZnO layer close to the interface between ZnO and Pr_6O_{11} layers.

8.2 Vanadium System

Vanadium oxide (vanadia) is the inorganic compound with the formula V_2O_5. Commonly known as vanadium pentoxide, it is a brown/yellow solid, although when freshly precipitated from aqueous solution, its color is deep orange. Because of its high oxidation state, it is both an amphoteric oxide and an oxidizing agent, and its crystal structure is shown in Figure 8.6 [44]. V_2O_5 has an orthorhombic crystal structure with lattice constants of a = 1151 pm,

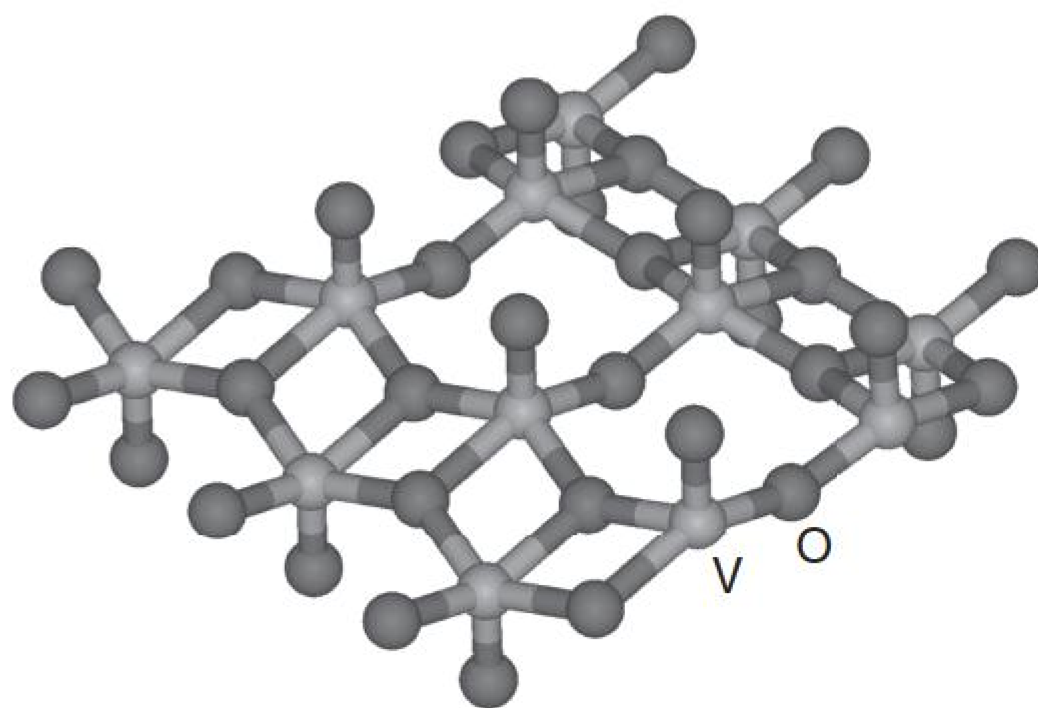


Figure 8.6 The crystal structure of vanadium oxide (V_2O_5). Source: Modified from [44].

$b = 355.9$ pm, and $c = 437.1$ pm, which is a distorted tetragonal pyramidal crystal structure, and the V ions are in an octahedral coordination of oxygen. Formally, V is 5+ and the d band is empty, although as will be shown the V-3d–O-2p covalent mixing results in a partial occupation of the d orbitals [44].

Nonohmic behavior was observed for polycrystalline zinc oxide with V_2O_5 as the only additive [6]. The electrical conduction in ZnO–V_2O_5 binary ceramics is a typical Schottky barrier-controlled current behavior, and the nonlinearity characteristics are in response to the grain boundary barrier layer. On the basis of the back-to-back Schottky barrier model and thermionic emission theory, the I–V and C–V experimental data had been satisfactorily applied to calculate the grain boundary parameters.

The advantage of vanadium-doped ZnO varistors is that ceramic can be sintered at a relatively low temperature of ~900 °C [6]. This is important for multilayer components because such ceramics can be cofired with a silver inner electrode, which has a melting point of ~960 °C [6]. V_2O_5 is also a better sintering aid compared with Bi_2O_3, which can densify ZnO varistors to the same density at a lower temperature compared with Bi_2O_3-doped ZnO varistors sintered at a high temperature [9]. It has been evidenced that V_2O_5 shows great promise in being able to replace Bi_2O_3 as the varistor-forming ingredient in ZnO varistors. The lower sintering temperature that can be used is an especially attractive feature.

8.2.1 Doping Effects

Many additives, which have been doped in Bi_2O_3-doped ZnO varistors, such as Mn_3O_4, CoO, NiO, Nb_2O_5, and sodium glass, have been added to improve the performance of V_2O_5-doped ZnO varistor ceramics [9]. MnO_2 and Co_3O_4 as "performance enhancers" are added to increase the nonlinear coefficient, whereas Sb_2O_3 is doped to control the growth of ZnO grains [45–47].

Sb_2O_3 is a commonly used grain growth inhibitor for Bi_2O_3-doped ZnO varistors [48], which is believed to enhance the solubility of ions, such as zinc in the Bi_2O_3-rich liquid phase, which is important for the defect distribution formed at the grain boundaries during cooling [46]. Addition of Sb_2O_3 to the binary system of ZnO and V_2O_5 controls the abnormal grain growth and produces a more uniform microstructure, but at the expense of a higher sintering temperature of 1200 °C in order for the pellet to be sintered [49], and the nonlinear coefficient

increases after doping Sb_2O_3, suggesting that it is possible that it also enhances the solubility of zinc in the vanadium-rich liquid phase, hence improving the defect distribution at the grain boundaries.

Additions of either MnO_2 [50–55] or Co_3O_4 do not change the general microstructure of the V_2O_5-doped ZnO varistors that consist mainly of ZnO grains with a vanadium-rich intergranular layer. The nonlinear coefficient increases as the amount of MnO_2 additive is increased. Moreover, it was found that 0.5 mol% V_2O_5 gives the optimum electrical properties, a low leakage current, and a nonlinear coefficient of 31.8 were obtained [56]. It was found that MnO_2 is the most effective in increasing the nonlinear behavior compared to Co_3O_4 and Sb_2O_3. Mn_3O_4 has a similar effect as MnO_2 does, which does not significantly modify the sintering properties of varistors but do markedly alter their nonohmic behavior [11]. The microstructure of the ternary system $ZnO–V_2O_5–Mn_3O_4$ consisted of mainly ZnO grains and secondary phase $Zn_3(VO_4)_2$ [52]. MgO was found to be effective as a densifying aid and a grain growth inhibitor in $ZnO–V_2O_5$ [57]. The average ZnO grain size reduced significantly to about 4 μm when 40 mol% MgO was doped to the binary ZnO–0.5 mol% V_2O_5 system. The electrical properties deteriorated when more than 10 mol% MgO was added.

Addition of Cr_2O_3 to the binary ZnO–0.5 mol% V_2O_5 system controls the abnormal ZnO grain growth and produced a more uniform microstructure [58]. The microstructure of the samples consists mainly of ZnO grains with $ZnCr_2O_4$ and α-$Zn_3(VO_4)_2$ as the minority secondary phases. The nonlinear coefficient α increases as the amount of Cr_2O_3 additive is increased up to 3 mol%. A further increase in the Cr_2O_3 content causes a decrease in the nonlinear coefficient.

The Co and Dy and other dopants were added to $ZnO–V_2O_5$-based ceramics to improve the varistor properties [50]. The electrical and dielectrical properties and their accelerated aging behavior of $ZnO–V_2O_5–MnO_2–Co_3O_4–Dy_2O_3$ (ZVMCD) ceramics were investigated with different dopants (Al, Nb, Bi, and La). Nb and Bi dopants enhanced the nonlinear coefficient, whereas Al and La dopants decreased it. On the other hand, Nb and Al dopants improved the stability against aging stress. The Nb-doped ZVMCD ceramics exhibited the best nonlinear property ($\alpha = 36$) and the highest stability.

Nahm [59] investigated the effect of erbium addition on microstructure, electrical properties, and aging behavior of vanadium oxide-doped zinc oxide varistor ceramics. When erbium oxide was doped, the microstructure consisted of ZnO grain as a main phase and secondary phases such as $Zn_3(VO_4)_2$, ZnV_2O_4, $ErVO_4$, V_2O_5, and Mn rich. The average grain size decreased from 5.5 to 5.2 μm up to 0.05 mol%, whereas a further addition gradually increased it to 5.7 μm at 0.25 mol%. With an increase in the amount of Er_2O_3, the sintered density increased from 5.51 to 5.61 g cm^{-3}.

8.2.2 Electrical Characteristics

A varistor composition of ZnO–0.5 mol% V_2O_5–1 mol% MnO_2, in which γ-$Zn_3(VO_4)_2$ is produced at ZnO grain boundaries, produces encouraging $I–V$ characteristics with a low leakage current and a high nonlinear coefficient [60].

The average breakdown voltage per ZnO junction (V_B) for V_2O_5-doped ZnO varistors is ~0.6 V, which is estimated from the breakdown field under 1 mA cm^{-2} DC ($E_{1mA\ cm^{-2}}$) and ZnO grain sizes (d), through the equation $V_B = d\ E_{1mA\ cm^{-2}}$. This value is much lower than that for Bi_2O_3-doped ZnO varistors, which ranges from 2 to 4 V [48]. Such a low breakdown voltage suggests the possibility of using the V_2O_5-doped ZnO varistor system to manufacture low-voltage varistors operating at the voltage lower than dozens of volts, whereas for Bi_2O_3-doped ZnO varistors, the microstructure of convenient low voltage varistors with millimeter size has to be fairly coarse grained to ensure low-breakdown voltage. A highest nonlinear coefficient of 28.9 was obtained for the sample containing 3 mol% Cr_2O_3 in 0.5 mol% V_2O_5-doped ZnO varistor [58].

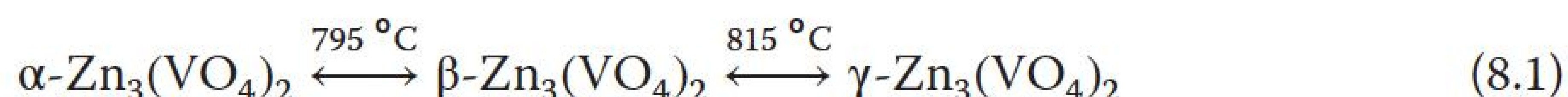
It was found that MnO_2 is the most effective in increasing the nonlinear behavior compared to Co_3O_4 and Sb_2O_3 [56]. A varistor composition of ZnO–0.5 mol% V_2O_5–1 mol% MnO_2, in which γ-$Zn_3(VO_4)_2$ was produced at ZnO grain boundaries, behaved good I–V characteristics [60]. The incorporation of Mn_3O_4 to the binary system of ZnO–V_2O_5 was found to restrict the abnormal grain growth of ZnO. The breakdown voltage increased from 17.5 to 463.5 V mm^{-1} with the increase in Mn_3O_4 content. The incorporation of Mn_3O_4 up to 0.5 mol% improved nonohmic properties by increasing the nonohmic coefficient, whereas the further additions decreased it. It was found that the highest barrier height at grain boundary was 2.66 eV for 0.5 mol% Mn_3O_4.

With an increase in the amount of Er_2O_3, the sintered density increased from 5.51 to 5.61 g cm^{-3}, the breakdown field increased from 4800 to 5444 V cm^{-1} up to 0.05 mol%, whereas a further addition decreased it to 4061 V cm^{-1} at 0.25 mol%. The varistor ceramics added with 0.05 mol% Er_2O_3 additives induced excellent nonlinear properties, with a nonlinear coefficient of 63.4 by properly adding the amount of Er_2O_3 (0.05 mol%). The study indicated that erbium acted as a donor to increase the donor concentration with an increase in the amount of Er_2O_3 [59].

Tsai and Wu [7] obtained the Schottky barrier height of 0.47 eV, and the donor concentration N_d of 7.0×10^{18} cm^{-3}. From the calculated values of N_d, a transition of defect chemistry from electron compensation to defect compensation was proposed for an increase of V_2O_5 doping in ZnO.

8.2.3 Microstructural Characteristics

Brown [60] were the first to study the ZnO–V_2O_5 system. They reported the existence of only three compounds: $Zn_3(VO_4)_2$, $Zn_2V_2O_7$, and $Zn(VO_3)_2$ in ZnO–V_2O_5 varistors. Two polymorphic transformations were proposed for $Zn_3(VO_4)_2$:



$$\alpha\text{-}Zn_3(VO_4)_2 \xleftrightarrow{795\,^\circ C} \beta\text{-}Zn_3(VO_4)_2 \xleftrightarrow{815\,^\circ C} \gamma\text{-}Zn_3(VO_4)_2 \quad (8.1)$$

The transition at 795 °C was reported to be sluggish but reversible, whereas that at 815 °C was reported to be rapid and reversible. All the three forms of zinc orthovanadate ($Zn_3(VO_4)_2$) have been detected in vanadium-doped zinc oxide varistor material samples via powder X-ray diffractometry [61]. Makarov et al. [62] worked out the phase diagram of the ZnO–V_2O_5 system.

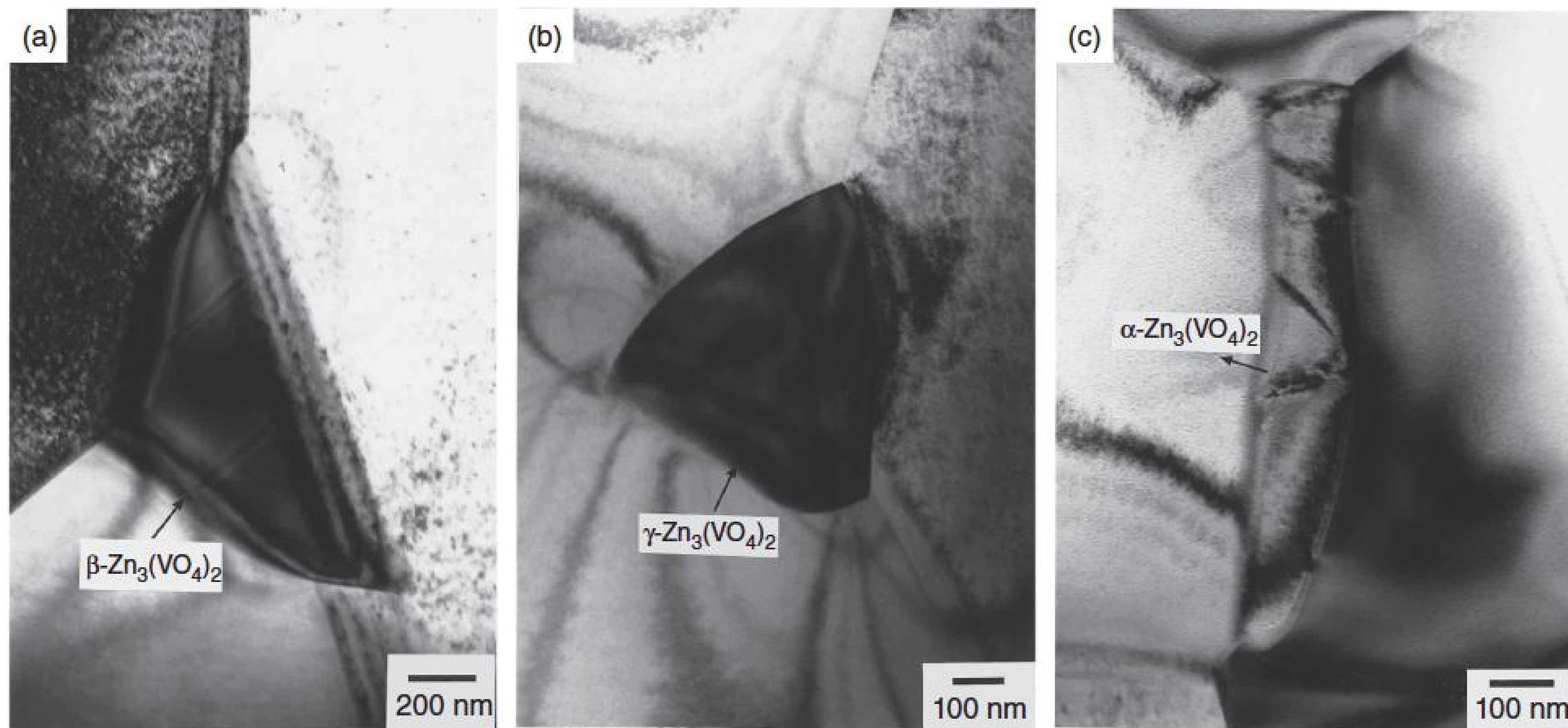


Figure 8.7 Bright-field TEM images of (a) β-$Zn_3(VO_4)_2$, (b) γ-$Zn_3(VO_4)_2$, and (c) α-$Zn_3(VO_4)_2$ grains in ZnO–V_2O_5(ZV), ZnO–V_2O_5–MnO_2 (ZVM), and ZnO–V_2O_5–Co_3O_4 (ZVC), respectively. Source: Hng and Knowles 2000 [45]. Reproduced with permission of John Wiley & Sons.

Hng and Knowles [45] provided detailed TEM microstructural studies of V_2O_5-doped ZnO varistors. The $Zn_3(VO_4)_2$ grains in ZV, ZVM, and ZVC were usually found embedded in the ZnO grains or occurring at the triple- and multiple-grain junctions, as demonstrated in the bright-field TEM images shown in Figure 8.7 [45]. The spinel grains are usually located between the ZnO grains at triple junctions or in clusters. They are mostly regular polyhedral in shape, indicating that these grains have enough time to adjust their shape to a near equilibrium form while being surrounded by a liquid phase. EDX spectra of spinel grains obtained from ZVS (ZnO–V_2O_5–Sb_2O_3) and ZVSMC (ZnO–V_2O_5–Sb_2O_3–MnO_2–Co_3O_4) show that significant amounts of vanadium and cobalt are dissolved in them. Based on the experimental results [45], it seems more desirable to have γ-$Zn_3(VO_4)_2$ as a secondary phase than to have α- or β-$Zn_3(VO_4)_2$. However, β-$Zn_3(VO_4)_2$ has a higher conductivity than γ-$Zn_3(VO_4)_2$. The lower resistivity of the β phase provides a relatively easy path for electronic conduction and contributes to a lower nonlinear coefficient. Clarke [63] pointed out that the spinel phase itself can exhibit the varistor behavior under appropriate oxidation conditions. It can provide an alternative electrical pathway with an appropriate barrier to the grain boundary regions, but the improvement in the varistor behavior is not significant [9]. The improvement in the varistor behavior could be due to the formation of interface states at the grain boundaries by the transition metals. The spinel phase in sample ZVSMC (ZnO–0.25 mol% V_2O_5–2 mol% Sb_2O_3–1 mol% MnO_2–1 mol% Co_3O_4) contains manganese and cobalt. These are likely to change the defect chemistry of the spinel phase and thus alter its electrical behavior as well [45].

A high proportion of the grain boundaries between ZnO grains contains a thin continuous second-phase film. Such an intergranular material usually originates from the α-$Zn_3(VO_4)_2$ grain situated at a triple- or multiple-grain junction. The intergranular phase usually decreases in its width and ends abruptly some distance away from the triple point, and, thereafter, ZnO grains appear to be in contact with each other, with only the grain boundary separating them. Examination

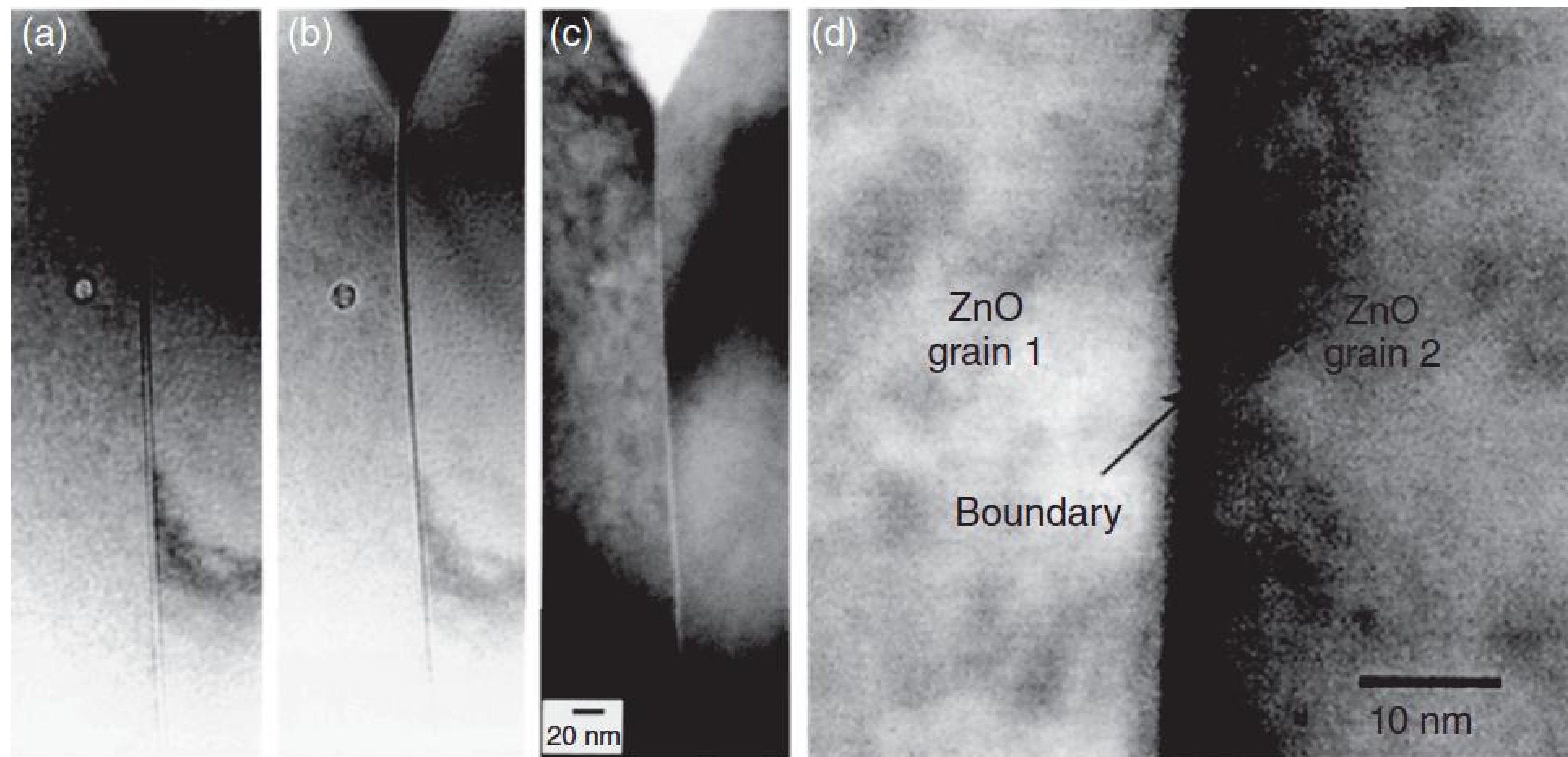


Figure 8.8 (a) Underfocus, (b) overfocus, (c) diffuse dark-field image of typical boundary in sample ZVM observed by through-focal series of Fresnel images and (d) BF image of sample ZVSMC showing vanadium and antimony segregation. Source: Hng and Knowles 2000 [45]. Reproduced with permission of John Wiley & Sons.

of these grain boundaries by diffuse dark-field imaging shows that these films are amorphous. Through-focal series of Fresnel images from such grain boundaries aligned parallel to the electron beam were also performed, which further confirmed the presence of a thin boundary layer, a typical example is shown in Figure 8.8a–c [45]. The boundaries exhibit a bright central fringe underfocus and a dark central fringe overfocus, which is a characteristic of a lower scattering potential at the boundary relative to the surrounding bulk material. The actual thickness of these boundaries obtained experimentally by HREM should range from 0.3 to 1.6 nm as shown in Figure 8.8d.

8.2.4 Effects of Vanadium Oxide on Grain Growth

The effects of V_2O_5 additions will be addressed by using an activation analysis of the kinetic parameters of ZnO grain growth, specifically the kinetic grain growth exponent and the apparent activation energy for grain growth. These parameters can be obtained from the phenomenological kinetic grain growth equation [64]:

$$G^n = K_0 t \exp(-Q/RT) \tag{8.2}$$

where G is the average grain size at time t, n value is the kinetic grain growth exponent, K_0 is the preexponential constant of the material, Q is the apparent activation energy, R is the universal gas constant, and T is the absolute temperature.

Hng and Halim [65] investigated the grain growth process in the liquid-phase-sintered ZnO–1 mol% V_2O_5 ceramics systematically. The final grain size of ZnO after sintering was substantially increased by the additions of V_2O_5. From 900 to 1200 °C, the grain growth kinetic exponent n was about 1.44, lower than for pure ZnO and ZnO–Bi_2O_3 cEramics, both are 3 and 5, respectively. The apparent activation energy for ZnO grain growth in this temperature range was substantially reduced from that of pure ZnO (224 ± 16 kJ mol^{-1}) [64] to 76 ± 7 kJ mol^{-1} [65], which is 148 ± 31 kJ mol^{-1} for ZnO–Bi_2O_3 ceramics [65].

8.3 Barium System

8.3.1 Preparation and Electrical Characteristics

For ZnO–Bi_2O_3 varistor system, multiple additives should be doped to tailor the electrical performances of ZnO varistor ceramics. The presence of multiple additives makes the system complicated and as such more difficult to understand the mechanism of nonlinearity. It is, therefore, desirable to look for a suitable single additive that could segregate out of a ZnO matrix owing to a larger cation radius and without outflowing during sintering because of its high melting point and result in a high value of nonlinearity. These criteria are best met by barium oxide, which has a melting point of 1923 °C, and its cation radius is 1.34 Å as compared with 0.74 Å for Zn^{2+}.

The addition of suitable amounts of BaO to ZnO yields nonlinear coefficient as high as that of a multicomponent ZnO–Bi_2O_3 varistor system. In 1969, Matsuoka et al. [5] observed that the nonlinearity from ZnO ceramics separately added 0.5 mol% alkali earth metal oxide (CaO, SrO, and BaO) and sintered in air at various temperatures from 950 to 1450 °C for one hour. He thought that the solubility depended on the ionic radius, added CaO, SrO, or BaO should not dissolve in the ZnO lattice but should form the segregated phase. It was believed that this segregated phase may be responsible for the observed nonlinear characteristics. Bhushan et al. [66] revealed that even a single additive in 1981, nearly 10 mol% BaO, makes ZnO highly nonlinear with a nonlinear coefficient α of 50, which is larger than that observed in binary ZnO–Bi_2O_3 ceramics. The nonlinearity is strongly dependent on the microstructure of the varistor ceramics. At BaO concentrations higher than 50 mol%, the composite exhibits a ohmic behavior because of the absence of a well-defined two-phase grain intergranular microstructure. Under suitable sintering conditions, a very large grain size can be obtained for this binary composite. This property can be utilized in making low-voltage varistors of appreciable thickness.

Fan and Freer [6] studied the change of the sintered densities of ZnO–BaO varistor ceramics as a function of the sintering temperature. At a constant sintering temperature, the sintered density of the doped samples decreases with an increase in the content of BaO, whereas at a constant doping level of BaO, the density of ZnO–BaO varistor ceramics increases as the sintering temperature is increased from 1000 to 1100 °C. As the sintering temperature is increased further, the density decreases almost linearly. This trend is different from that of the nominally "pure" ZnO ceramics, whose density increases with the sintering temperature increased up to 1300 °C, achieving the maximum value at 1300 °C. Therefore, for the range of doping levels investigated, 1100 °C appears to be the optimum sintering temperature for the densification of ZnO–BaO ceramics. The highest density of 5.45 g cm^{-3} (equivalent to 97.1% of the theoretical density of ZnO) was obtained for samples containing 0.39 mol% BaO, sintered at 1100 °C [6]. Sintering of Ba^{2+}, which has a much larger cation radius (0.134 nm) than Zn^{2+} (0.074 nm), could only have a very limited solubility in the ZnO lattice, so it mainly segregates to the grain boundary. Thus, the presence of the Ba-rich phase enhances the grain growth of ZnO during sintering and leads to a two-phase microstructure in the ZnO–BaO ceramics.

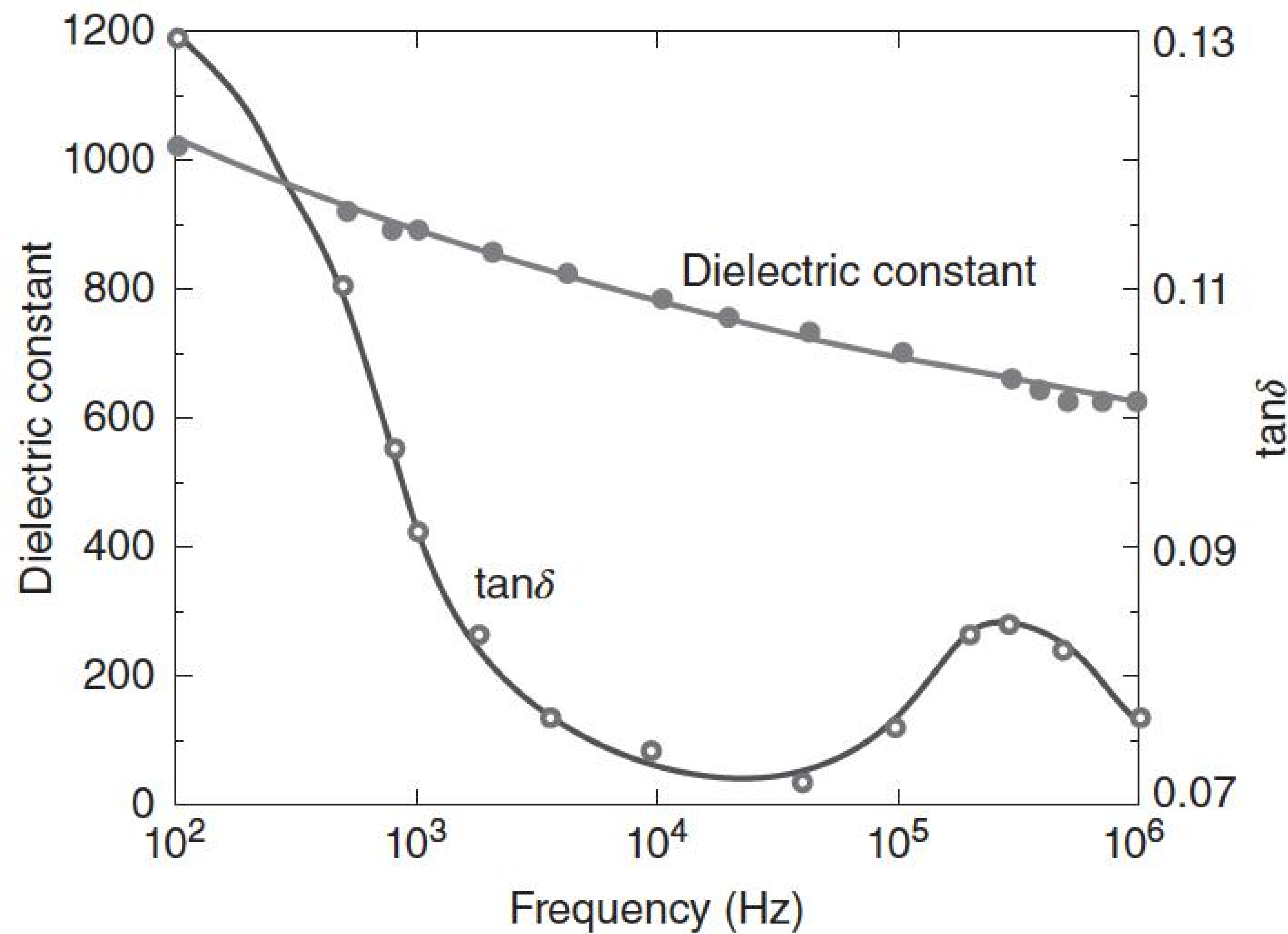


Figure 8.9 Variation of dielectric constant ε and dielectric loss tanδ with the frequency for ZnO–BaO (10 mol%) varistor systems. Source: Adapted from Bhushan et al. [66].

The dielectric constant ε and the dielectric loss tanδ of the samples were measured at room temperature in the frequency range 10^2–10^6 Hz at 1 V_{rms} with the help of an *LCR* bridge (Systronics) and a Wayne Kerr bridge [66]. The variation of both dielectric constant and dielectric loss with a frequency for ZnO–BaO (10 mol%) samples are shown in Figure 8.9. The dielectric constant for this system is nearly 10^3 at 100 Hz, which decreases with the increase in frequency. The loss factor first decreases with the frequency showing a minimum at about 2×10^4 Hz. A further increase in the frequency, however, increases its value and shows a loss peak at 3×10^5 Hz. It is noteworthy that the loss peak occurs at the same frequency for ZnO–Bi_2O_3 systems of any composition and for a multicomponent system with several additives as well [67, 68]. The observed complex behavior of the dielectric properties is similar to that reported for multicomponent systems [68]. The loss peaks at 3×10^5 Hz may be attributed to the interfacial polarization in the two-phase composite comprising a highly resistive intergranular layer sandwiched between the conducting ZnO grains.

8.3.2 Microstructural Characteristics

Figure 8.10 shows typical micrographs of the sintered surface for the samples doped with 0.39 and 2.33 mol% BaO sintered at 1300 °C [6]. The primary grains were variable in shape, but generally, they became more rounded in specimens with higher BaO contents. More interestingly, grains are surrounded by a barium-rich grain boundary phase, which is readily soluble and can be separated into individual grains by treating sintered specimens with boiling water [69]. As shown in Figure 8.11 [69], the grains have irregular but somewhat rounded shapes. Dimples are found on flat surfaces and also at corners. The origin of these dimples is believed to be pores present at the grain interface. Those on the flat surfaces and at the corners of the grains respectively correspond to those found at the grain boundaries and those at the three grain junctions in

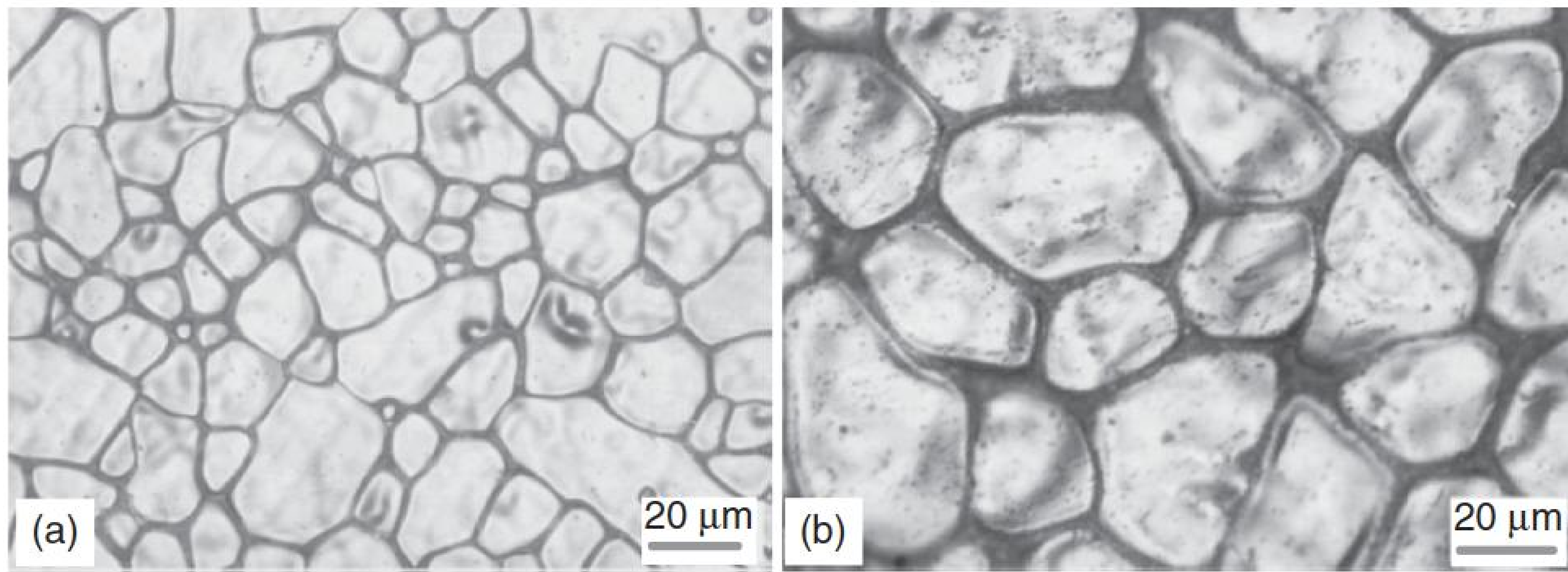


Figure 8.10 Typical micrographs of ZnO–BaO samples sintered at 1300 °C: (a) containing 0.39 mol% BaO and (b) containing 2.33 mol% BaO. Source: Fan and Freer 1997 [6]. Reproduced with permission of Springer.

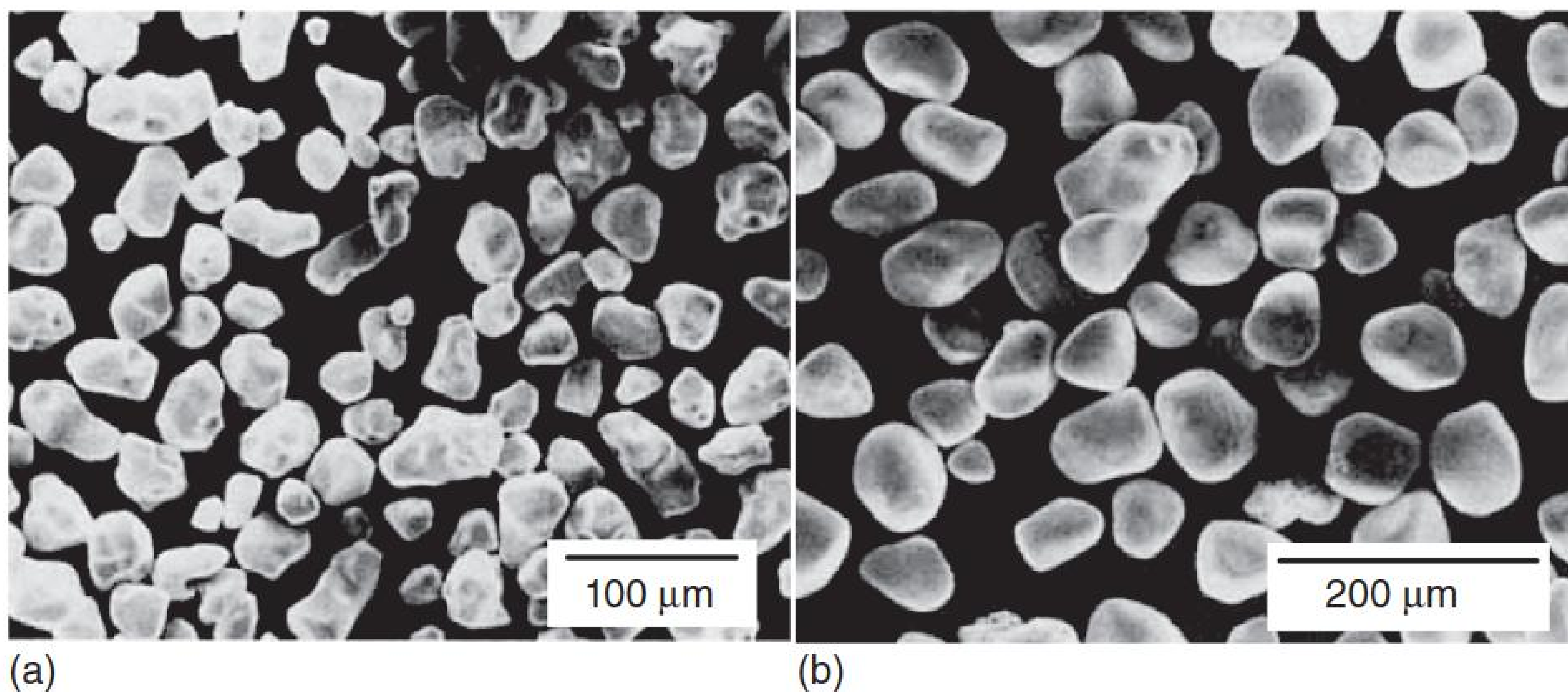


Figure 8.11 SEM micrographs of separated grains: (a) $BaCO_3$ content 4% and (b) $BaCO_3$ content 12%, all sintered at 1300 °C, for four hours. Source: Uematsu et al. 1989 [69]. Reproduced with permission of John Wiley & Sons.

polished sections commonly used for microstructural analysis. Grains in the specimens having a high BaO content had fewer dimples and more rounded smooth surfaces. The size distribution was found to be lognormal. With an increasing BaO content, the grain size increased for a given sintering condition.

The average grain sizes for doped samples are larger than those of the undoped ZnO ceramics and that the average grain sizes increased with the BaO content. It is clear that the nonlinear coefficient α is strongly influenced by the Ba content and the sintering temperature, which increases as the temperature increases, and achieves a maximum for samples sintered at 1300 °C [69]. When the sintering temperature is increased further to 1400 °C, the α value drops slightly. Therefore, to achieve the optimum nonlinearity, the sintering temperature for ZnO–BaO ceramics must be above 1200 °C. Usually, the pressed pellets were sintered for about two to three hours at 1250–1350 °C [66, 70].

Measurements of AC conductance between 30 and 350 K on the ZnO–Bi_2O_3 and ZnO–BaO systems show a common electron trap whose energy level is 0.33 eV below the conduction band [71]. The origin of this trap is likely to be

intrinsic to ZnO. Between two possible intrinsic origins, i.e. interstitial Zn atoms and oxygen vacancies, it is suggested that this trap is associated with the ionized oxygen vacancy. Heat treatment and sintering atmosphere can vary some properties such as conductivities, relative trap densities, and nonlinear coefficients. As the barrier height is dependent on both the applied bias voltage and the interface charge [71], it might be expected that the nonlinear coefficients follow the magnitude of the interface-state density. α may be proportional to the interface-state density and therefore the overall conductivity found in these materials. Thus, the air-sintered materials have a lower interface-state density than that of materials sintered using double crucibles, yielding a low nonlinear coefficient. Also, for materials sintered using double crucibles, the quenched and slow-cooled materials are expected to halve higher nonlinear coefficients than the annealed material [70].

8.3.3 Improving Stability Against Moisture

In binary ZnO–Bi_2O_3 ceramics, the BaO-rich phase located at the grain boundaries and triple points is highly soluble in water and favors the material degradation by moisture, which leads to severe damage of the electrical properties of the materials and even to structural damage if they are simply kept in air. Therefore, improving the resistance of these materials to attack by moisture is critical to consider their use for commercial varistors manufacturing.

Hoffman [72] proposed the phase diagram of the ZnO–BaO–P_2O_5 ternary system, and the incorporation of a certain amount of phosphorous can lead to the formation of $BaZn_2(PO_4)_2$ and $Ba_3(PO_4)_2$ or $Zn_3(PO_4)_2$, depending on the relative amounts of BaO and P_2O_5; the composition would lie in one of the two compatibility triangles determined by ZnO–$BaZn_2(PO_4)_2$–$Ba_3(PO_4)_2$ or ZnO–$BaZn_2(PO_4)_2$–$Zn_3(PO_4)_2$, where none of these phases exhibit significant solubility in water. The incorporation of phosphorous in ceramic $BaTiO_3$ has been reported to control the microstructure development of the varistor ceramics. Furthermore, $Ba_3(PO_4)_2$ can form at temperatures of the order of 900 °C, playing a key role on the final microstructure and changing the electrical properties of the varistor ceramics [73, 74]. Caballero et al. [73] proposed the incorporation of P_2O_5 to a ZnO–BaO material to improve its stability against moisture while maintaining its varistor characteristics. The incorporation of P_2O_5 to a ZnO–BaO ceramic avoids the presence of BaO-rich phases with high solubility in water and leads to the formation of $BaZn_2(PO_4)_2$ and $Zn_3(PO_4)_2$; none of these phases exhibit significant solubility in water.

8.4 ZnO–Glass Varistor

The chip varistor fabrication process is based on the green sheet lamination technology [75]. The multilayer ceramic chip varistors are miniaturized, highly integrated, and low power consumption devices, which are applied as surge protection devices in the surface-mount HIC technology [76]. ZnO–glass varistor is a kind of varistor ceramics for the multilayer ceramic chip varistors.

Shohata and Yoshida [77] reported the effect of glass on the electrical properties of ZnO ceramic varistors. The samples were prepared by usual ceramic fabrication techniques. The pressed bodies of ZnO with Bi_2O_3, CoO, MnO, Sb_2O_3, and glass frit ($PbO–SiO_2–B_2O_3–ZnO$) were sintered at 1200 °C for one hour. From thermally stimulated current (TSC) tests, the magnitude of the polarized charge increases rapidly with an increase in applied peak current and seems to be nearly saturated in the high-peak current region. The polarized charge of the sintered disk with a glass is almost one order of magnitude less than that of the sintered disk without the glass, in the region before saturation. This fact may suggest that the density of traps is reduced in this region. The deep trapping levels may be responsible for the degradation of $I–V$ curves, caused by electric load, in the view point of the space charge polarization of trapped charge. It was concluded that the glass addition to ZnO ceramic varistors is effective in reducing the density of traps and results in both the stabilization of nonohmic properties against the electric load and the reduction of leakage current. Later, Shohata et al. [76] reported that the multilayer-type ceramic varistors based on ZnO and lead zinc borosilicate glass instead of Bi_2O_3 exhibit a highly nonohmic behavior in their $V–I$ characteristics. The lead zinc borosilicate glass liquid-phase sinters at a low temperature, and the influence of the glass content on varistor properties is very similar to that of Bi_2O_3 and that the microstructure shows a clear grain boundary segregation phenomenon, implying a similar behavior of the glass additive during the sintering process.

Lee and Tseng [78] further studied the properties of ceramic varistors based on ZnO with lead zinc borosilicate glass instead of Bi_2O_3. Reagent-grade raw materials, in the proportions of 95 mol% ZnO, 1 mol% CoO, 1 mol% MnO, 1 mol% Cr_2O_3, and 2 mol% Sb_2O_3 and lead zinc borosilicate glass in a 10 wt% ratio to the mentioned oxide mixture were used for the preparation of ZnO–glass samples. The lead zinc borosilicate glass was composed of 58 wt% PbO, 25 wt% B_2O_3, 12 wt% SiO_2, and 5 wt% ZnO. Among the samples sintered at various temperatures and cooled at different rates, the ZnO–glass sample sintered at 1250 °C for one hour, then furnace cooled, possessed the best electrical properties characterized by the highest nonlinear coefficient of 49 and a breakdown voltage of 542 V, lowest leakage current of 26 μA, and lowest degradation phenomena.

The microstructure and crystal structure of the glass phase of ZnO–glass varistors were examined by means of scanning electron microscopy (as shown in Figure 8.12 [78]), transmission electron microscopy, and powder X-ray diffractometry. The glass phase was originally amorphous but crystallized as an intergranular layer in the sintered and furnace-cooled samples. This crystallized phase was a zinc borate phase ($5ZnO{\cdot}2B_2O_3$), which was identified by X-ray diffractometry, transmission electron microscopy, and Auger electron spectroscopy. The zinc borate phase existed in the grain boundaries of the ZnO–glass samples and enhanced the nonohmic characteristics of the ceramic varistors. The nonohmic characteristics were enhanced if the intergranular layer phase increased in resistance after it recrystallized.

Wang et al. [79] proposed another kind of ZnO–glass varistor ceramics for the chip varistor. Reagent-grade raw materials having a composition of 95 mol% ZnO,

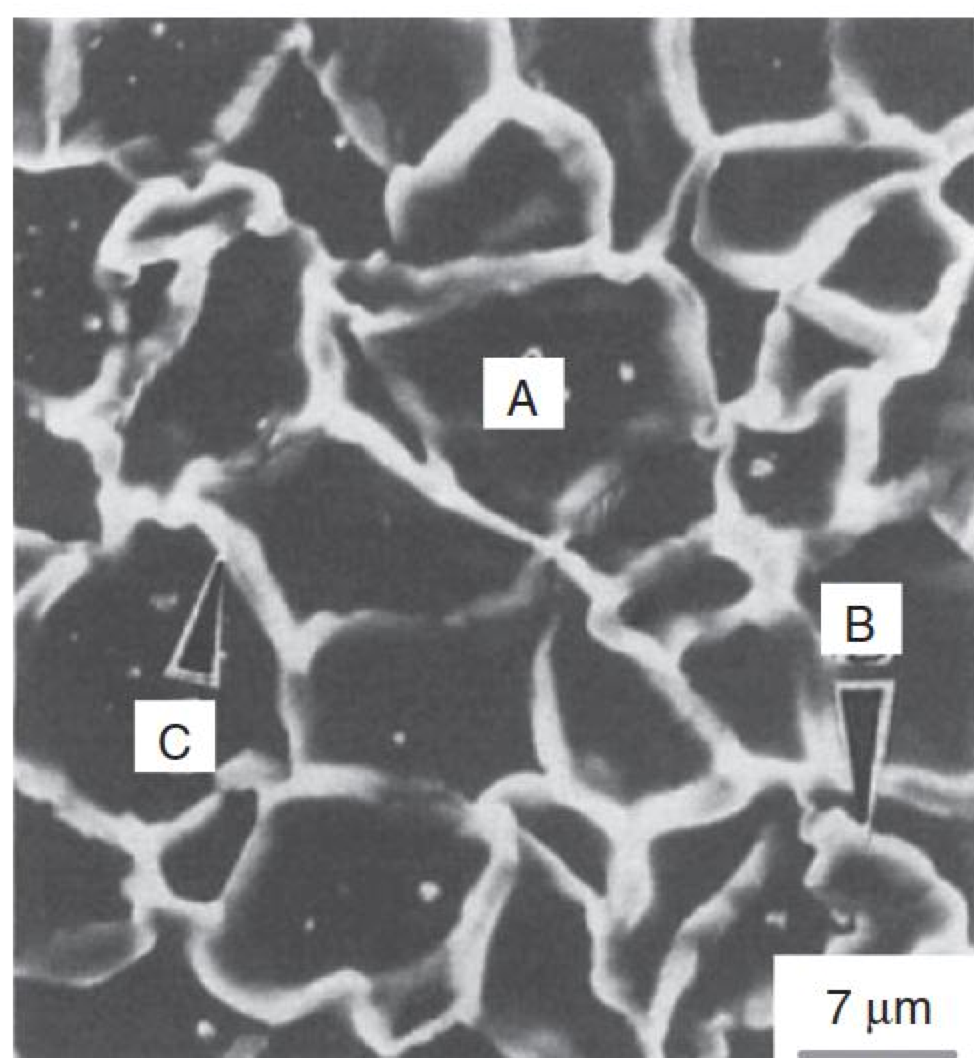


Figure 8.12 SEM micrograph of specimen: A, ZnO grain; B, $Zn_7Sb_2O_{12}$ spinel phase; and C, intergranular phase. Source: Yih-Shing Lee and Tseung-Yuen Tseng 1992 [78]. Reproduced with permission of John Wiley & Sons.

1 mol% MnO, 1 mol% CoO, 1 mol% Cr_2O_3, 2 mol% Sb_2O_3, and Pb–Zn borosilicate glass in a 10 wt% ratio to the above-mentioned oxide mixture were used for the preparation of ZnO–glass powder. The Pb–Zn borosilicate glass was composed of 64.25 wt% PbO, 10.93 wt% SiO_2, 19.25 wt% B_2O_3, and 5.29 wt% ZnO. The raw materials and glass powder were mixed by wet milling for 24 hours and calcined at 600 °C for 2 hours. A tape casting method was employed for making a green sheet on an organic film. Following exposure to air for 24 hours, the internal electrodes of the Pd paste were screen printed on each green sheet. The printed green tapes were laminated at 100 °C for one hour at a pressure of 2000 psi. The green tapes were cut to make a chip with dimensions 2.25 mm and were sintered at 1250 °C for one hour. The glass existing at the grain–boundary layer of the chip varistor sample was partially transformed into a crystalline zinc silicate phase after sintering and determined on the basis of X-ray diffraction measurement.

By means of deep-level transient spectroscopy, Wang et al. [79] found that the degradation of the ZnO–glass chip varistors because of high-intensity impulse currents was correlated with the deep trap levels. Three electron traps located at 0.11, 0.27, and 0.94 eV below the conduction band were observed before current impulse testing. These trap energy depths of the chip varistors after current impulse testing were found to be almost unchanged, but their trap densities and capture cross sections both decreased. The concentration of the trap at 0.94 eV was decreased and ascribed to oxygen vacancies existing at the grain boundaries of the varistor. The electrical degradation phenomenon of the chip varistors is closely related to the reaction between the trap at 0.94 eV and adsorbed oxygen ions at the grain boundaries.

References

1 Peng, Z., Fu, X., Zang, Y. et al. (2010). Influence of Fe_2O_3 doping on microstructural and electrical properties of ZnO–Pr_6O_{11} based varistor ceramic materials. *Journal of Alloys and Compounds* 508 (2): 494–499.

2 Mukae, K., Tsuda, K., and Nagasawa, I. (1977). Non-ohmic properties of ZnO-rare earth metal oxide-Co_3O_4 ceramics. *Japanese Journal of Applied Physics* 16 (8): 1361–1368.

3 Nahm, C.W. (2012). Sintering effect on ageing behavior of rare earths (Pr_6O_{11}-Er_2O_3-Y_2O_3)-doped ZnO varistor ceramics. *Journal of Rare Earths* 30 (10): 1028–1033.

4 Alles, A.B. and Burdick, V.L. (1991). The effect of liquid-phase sintering on the properties of Pr_6O_{11}-based ZnO varistors. *Journal of Applied Physics* 70 (11): 6883–6890.

5 Matsuoka, M., Masuyama, T., and Iida, Y. (1969). Voltage nonlinearity of zinc oxide ceramics doped with alkali earth metal oxide. *Japanese Journal of Applied Physics* 8 (10): 1275–1276.

6 Fan, J. and Freer, R. (1997). Varistor properties and microstructure of ZnO–BaO ceramics. *Journal of Materials Science* 32 (2): 415–419.

7 Tsai, J.K. and Wu, T.B. (1994). Non-ohmic characteristics of ZnO-V_2O_5 ceramics. *Journal of Applied Physics* 76 (8): 4817–4822.

8 Tsai, J.K. and Wu, T.B. (1995). Microstructure and nonohmic properties of ZnO-V_2O_5 ceramics. *Japanese Journal of Applied Physics* 34 (12R): 6452–6457.

9 Tsai, J.K. and Wu, T.B. (1996). Microstructure and nonohmic properties of binary ZnO-V_2O_5 ceramics sintered at 900° C. *Materials Letters* 26 (3): 199–203.

10 Chen, C.S., Kuo, C.T., Wu, T.B., and Lin, I.N. (1997). Microstructures and electrical properties of V_2O_5-based multicomponent ZnO varistors prepared by microwave sintering process. *Japanese Journal of Applied Physics* 36 (3R): 1169–1175.

11 Kuo, C.T., Chen, C.S., and Lin, I.N. (1998). Microstructure and nonlinear properties of microwave-sintered ZnO-V_2O_5 varistors: I, effect of V_2O_5 doping. *Journal of the American Ceramic Society* 81 (11): 2942–2948.

12 Kuo, C.T., Chen, C.S., and Lin, I.N. (1998). Microstructure and nonlinear properties of microwave-sintered ZnO-V_2O_5 varistors: II, effect of Mn_3O_4 doping. *Journal of the American Ceramic Society* 81 (11): 2949–2956.

13 Hng, H.H. and Knowles, K.M. (1998). Characterisation of vanadium-doped zinc oxide varistors. In: *Proceedings of the 4th Ceramic Congress*, 557–564. Turkish Ceramics Society.

14 Hng, H.H. and Knowles, K.M. (1999). Characterisation of Zn_3 $(VO_4)_2$ phases in V_2O_5-doped zno varistors. *Journal of the European Ceramic Society* 19 (6–7): 721–726.

15 Mukae, K. (1987). Zinc oxide varistors with praseodymium oxide. *American Ceramic Society Bulletin* 66 (9): 1329–1331.

16 Mukae, K. and Nagasawa, I. (1981). Effect of praseodymium oxide and donor concentration in the grain boundary region of ZnO varistors. In: *Advances in Ceramics*, vol. 1, 331–342. American Ceramics Society.

17 Nahm, C.W. (2003). Electrical properties and stability of praseodymium oxide-based ZnO varistor ceramics doped with Er_2O_3. *Journal of the European Ceramic Society* 23 (8): 1345–1353.

18 Nahm, C.W., Yoon, H.S., and Ryu, J.S. (2001). The nonlinear properties and dc degradation characteristics of ZPCCE-based varistors. *Journal of Materials Science Letters* 20 (5): 393–395.

19 Park, J.A. (2008). Effect of Al_2O_3 on the electrical properties of ZnO-Pr_6O_{11}-based varistor ceramics. *Physica B: Condensed Matter* 403 (4): 639–643.

20 Wakiya, N., Chun, S.Y., Lee, C.H. et al. (1999). Effect of liquid phase and vaporization on the formation of microstructure of Pr doped ZnO varistor. *Journal of Electroceramics* 4 (1): 15–23.

21 Chun, S.Y. and Mizutani, N. (2001). Mass transport via grain boundary in Pr-based ZnO varistors and related electrical effects. *Materials Science and Engineering B* 79 (1): 1–5.

22 Nahm, C.W. and Park, C.H. (2000). Microstructure, electrical properties, and degradation behavior of praseodymium oxides-based zinc oxide varistors doped with Y_2O_3. *Journal of Materials Science* 35 (12): 3037–3042.

23 Nahm, C.W., Park, C.H., and Yoon, H.S. (2000). Highly stable nonohmic characteristics of ZnO-Pr_6O_{11}-CoO-Dy_2O_3 based varistors. *Journal of Materials Science Letters* 19 (9): 725–727.

24 Nahm, C.W. (2001). The electrical properties and dc degradation characteristics of Dy_2O_3 doped Pr_6O_{11}-based ZnO varistors. *Journal of the European Ceramic Society* 21 (4): 545–553.

25 Nahm, C.W. and Park, C.H. (2001). Effect of Er_2O_3 addition on the microstructure, electrical properties, and stability of Pr_6O_{11}-based ZnO ceramic varistors. *Journal of Materials Science* 36 (7): 1671–1679.

26 Nahm, C.W. (2001). The nonlinear properties and stability of ZnO-Pr_6O_{11}-CoO-Cr_2O_3-Er_2O_3 ceramic varistors. *Materials Letters* 47 (3): 182–187.

27 Nahm, C.W. and Ryu, J.S. (2002). Influence of sintering temperature on varistor characteristics of ZPCCE-based ceramics. *Materials Letters* 53 (1–2): 110–116.

28 Nahm, C.W. (2006). Nonlinear electrical properties and stability of Zn-Pr-Co-Er-M (M=Ni, Mg, Cr) oxide-based varistors. *Journal of Materials Science* 41 (5): 1635–1638.

29 Cai, J., Lin, Y.H., Li, M. et al. (2007). Sintering temperature dependence of grain boundary resistivity in a rare-earth-doped ZnO varistor. *Journal of the American Ceramic Society* 90 (1): 291–294.

30 Alles, A.B., Puskas, R., Callahan, G., and Burdick, V.L. (1993). Compositional effects on the liquid-phase sintering of praseodymium oxide-based zinc oxide varistors. *Journal of the American Ceramic Society* 76 (8): 2098–2102.

31 Lee, Y.S., Liao, K.S., and Tseng, T.Y. (1996). Microstructure and crystal phases of praseodymium oxides in zinc oxide varistor ceramics. *Journal of the American Ceramic Society* 79 (9): 2379–2384.

32 Gupta, T.K. and Carlson, W.G. (1985). A grain-boundary defect model for instability/stability of a ZnO varistor. *Journal of Materials Science* 20 (10): 3487–3500.

33 Nahm, C.W. (2003). Nonlinear properties and stability against DC accelerated aging stress of praseodymium oxide-based ZnO varistors by Er_2O_3 doping. *Solid State Communications* 126 (5): 281–284.

34 Nahm, C.W. (2005). Effect of La_2O_3 addition on microstructure and electrical properties of ZnO-Pr_6O_{11}-based varistor ceramics. *Journal of Materials Science: Materials in Electronics* 16 (6): 345–349.
35 Jun, W., Changsheng, X., Zikui, B. et al. (2002). Preparation of ZnO-glass varistor from tetrapod ZnO nanopowders. *Materials Science and Engineering B* 95 (2): 157–161.
36 Nahm, C.W. (2013). Nonlinear behavior of Tb_4O_7-modified ZnO-Pr_6O_{11}-based ceramics with high breakdown field. *Journal of Rare Earths* 31 (3): 276–280.
37 Varma, H.K., Kumar, K.P., Warrier, K.G.K., and Damodaran, A.D. (1989). Effect of K_2O on the sintered microstructure of praseodymium-doped ZnO varistors. *Journal of Materials Science Letters* 8 (8): 974–976.
38 Feng, H., Peng, Z., Fu, X. et al. (2011). Effect of SnO_2 doping on microstructural and electrical properties of ZnO–Pr_6O_{11} based varistor ceramics. *Journal of Alloys and Compounds* 509 (25): 7175–7180.
39 Sida, M., Chun, S.Y., Wakiya, N. et al. (1996). Effect of the sintering temperature and atmosphere on the grain growth and grain boundary phase formation of Pr-doped ZnO varistor. *Journal of the Ceramic Society of Japan* 104 (1205): 44–48.
40 Chun, S.Y., Wakiya, N., Funakubo, H. et al. (1997). Phase diagram and microstructure in the ZnO–Pr_2O_3 system. *Journal of the American Ceramic Society* 80 (4): 995–998.
41 Nahm, C.W. (2009). Effect of cooling rate on electrical properties, impulse surge and dc-accelerated aging behaviors of ZPCCD-based varistors. *Journal of Materials Science: Materials in Electronics* 20 (5): 418–424.
42 Mukae, K., Tsuda, K., and Shiga, S. (1988). Zinc oxide-praseodymium oxide elements for surge arrestors. *IEEE Transactions on Power Delivery* 3 (2): 591–598.
43 Horio, N., Hiramatsu, M., Nawata, M. et al. (1998). Preparation of zinc oxide/metal oxide multilayered thin films for low-voltage varistors. *Vacuum* 51 (4): 719–722.
44 Vanadium(V) oxide https://en.wikipedia.org/wiki/Vanadium(V)_oxide (accessed 14 August 2018).
45 Hng, H.H. and Knowles, K.M. (2000). Microstructure and current–voltage characteristics of multicomponent vanadium-doped zinc oxide varistors. *Journal of the American Ceramic Society* 83 (10): 2455–2462.
46 Eda, K. (1989). Zinc oxide varistors. *IEEE Electrical Insulation Magazine* 5 (6): 28–30.
47 Bernik, S., Zupančič, P., and Kolar, D. (1999). Influence of Bi_2O_3/TiO_2, Sb_2O_3 and Cr_2O_3 doping on low-voltage varistor ceramics. *Journal of the European Ceramic Society* 19 (6-7): 709–713.
48 Gupta, T.K. (1990). Application of zinc oxide varistors. *Journal of the American Ceramic Society* 73 (7): 1817–1840.
49 Wu, J., Xie, C.S., Huang, K.J. et al. (2004). Low temperature sintering of doped ZnO–V_2O_5 varistors. *Journal of Inorganic Materials* 19 (1): 239–243.
50 Nahm, C.W. (2010). Effect of dopant (Al, Nb, Bi, La) on varistor properties of ZnO–V_2O_5–MnO_2–Co_3O_4–Dy_2O_3 ceramics. *Ceramics International* 36 (3): 1109–1115.

51 Hng, H.H. and Chan, P.L. (2004). Microstructure and current–voltage characteristics of ZnO–V_2O_5–MnO_2 varistor system. *Ceramics International* 30 (7): 1647–1653.

52 Nahm, C.W. (2007). Microstructure and electrical properties of vanadium-doped zinc oxide-based non-ohmic resistors. *Solid State Communications* 143 (10): 453–456.

53 Nahm, C.W. (2008). Improvement of electrical properties of V_2O_5 modified ZnO ceramics by Mn-doping for varistor applications. *Journal of Materials Science: Materials in Electronics* 19 (10): 1023–1029.

54 Nahm, C.W. (2008). Influence of Mn doping on microstructure and DC-accelerated aging behaviors of ZnO–V_2O_5-based varistors. *Materials Science and Engineering B* 150 (1): 32–37.

55 Nahm, C.W. (2009). Effect of MnO_2 addition on microstructure and electrical properties of ZnO–V_2O_5-based varistor ceramics. *Ceramics International* 35 (2): 541–546.

56 Hng, H.H. and Chan, P.L. (2002). Effects of MnO_2 doping in V_2O_5-doped ZnO varistor system. *Materials Chemistry and Physics* 75 (1-3): 61–66.

57 Hng, H.H. and Tse, K.Y. (2008). Effects of MgO doping in ZnO–0.5 mol% V_2O_5 varistors. *Ceramics International* 34 (5): 1153–1157.

58 Hng, H.H. and Chan, P.L. (2009). Cr_2O_3 doping in ZnO–0.5 mol% V_2O_5 varistor ceramics. *Ceramics International* 35 (1): 409–413.

59 Nahm, C.W. (2013). Effect of erbium on varistor characteristics of vanadium oxide-doped zinc oxide ceramics. *Journal of Materials Science: Materials in Electronics* 24 (1): 27–35.

60 Brown, J.J. (1965). Reactions between ZnO and selected oxides of elements of group IV and V. *Transaction of British Ceramics Society* 64 (9): 419–437.

61 Hng, H.H., Knowles, K.M., and Midgley, P.A. (2001). Zinc vanadates in vanadium oxide-doped zinc oxide varistors. *Journal of the American Ceramic Society* 84 (2): 435–441.

62 Makarov, V.A., Fotiev, A.A., and Serebryakova, L.N. (1971). Phase composition and equilibrium diagram of the V_2O_5–ZnO system. *Journal of Inorganic Chemistry* 16 (10): 1515–1517.

63 Clarke, D.R. (1999). Varistor ceramics. *Journal of the American Ceramic Society* 82 (3): 485–502.

64 Senda, T. and Bradt, R.C. (1990). Grain growth in sintered ZnO and ZnO-Bi_2O_3 ceramics. *Journal of the American Ceramic Society* 73 (1): 106–114.

65 Hng, H.H. and Halim, L. (2003). Grain growth in sintered ZnO–1 mol% V_2O_5 ceramics. *Materials Letters* 57 (8): 1411–1416.

66 Bhushan, B., Kashyap, S.C., and Chopra, K.L. (1981). Novel nonohmic binary composite. *Applied Physics Letters* 38 (3): 160–161.

67 Levinson, L.M. and Philipp, H.R. (1976). Ac properties of metal-oxide varistors. *Journal of Applied Physics* 47 (3): 1117–1122.

68 Matsuura, M. and Yamaoki, H. (1977). Dielectric dispersion and equivalent circuit in nonohmic ZnO ceramics. *Japanese Journal of Applied Physics* 16 (7): 1261–1262.

69 Uematsu, K., Terada, A., Morimoto, T. et al. (1989). Direct determination of grain growth behavior in zinc oxide with added barium oxide. *Journal of the American Ceramic Society* 72 (6): 1070–1072.

70 SHIM, Y. and Cordaro, J.F. (1988). Admittance spectroscopy of polycrystalline ZnO-Bi_2O_3 and ZnO-BaO systems. *Journal of the American Ceramic Society* 71 (3): 184–188.

71 Blatter, G. and Greuter, F. (1986). Carrier transport through grain boundaries in semiconductors. *Physical Review B* 33 (6): 3952–3966.

72 Hoffman, M.V. (1963). The systems BaO-MgO-P_2O_5 and BaO-ZnO-P_2O_5 compounds and fluorescence. *Journal of the Electrochemical Society* 110 (12): 1223–1227.

73 Caballero, A.C., Valle, F.J., Villegas, M. et al. (2000). Improved chemical stability of ZnO–BaO based varistors. *Journal of the European Ceramic Society* 20 (16): 2767–2772.

74 Caballero, A.C., Fernández, J.F., Durán, P., and Moure, C. (1995). Phosphor-doped $BaTiO_3$: microstructure development and dielectric properties. *Journal of Materials Science* 30 (15): 3799–3804.

75 Lee, Y.S. and Tseng, T.Y. (1995). Influence of processing parameters on the microstructure and electrical properties of multilayer-chip ZnO varistors. *Journal of Materials Science: Materials in Electronics* 6 (2): 90–96.

76 Shohata, N., Nakanishi, M., and Utsumi, K. (1988). Multilayer ceramic chip varistor. In: *Advances in Varistor Technology, Ceramic Transactions*, vol. 3, 329–337. Westerville, OH: The American Ceramic Society.

77 Shohata, N. and Yoshida, J. (1977). Effect of glass on non-ohmic properties of ZnO ceramic varistors. *Japanese Journal of Applied Physics* 16 (12): 2299–2300.

78 Lee, Y.-S. and Tseng, T.-Y. (1992). Phase identification and electrical properties in ZnO–glass varistors. *Journal of the American Ceramic Society* 75 (6): 1636–1640.

79 Wang, Y., Lee, W., and Tseng, T. (1996). Degradation phenomena of multilayer ZnO–glass varistors studied by deep level transient spectroscopy. *Applied Physics Letters* 69 (12): 1807–1809.

9

Fabrications of Low-Voltage ZnO Varistors

Nanoparticles, smaller than 100 nm, exhibit many properties that differ from the respective bulk material, which can be used for various functional applications in the form of granular films, nanocomposites, or nanophase materials. Except application in high-voltage power systems, the major thrust in the varistor field is the production of miniaturized lightweight varistors via a safer and much economic processing route. The only way to achieve these high-performance, low-voltage varistors is to start with fine powders such as nanopowders as the starting materials so that fine grain and homogeneous dopant distribution are retained even after sintering. Researchers have suggested various approaches for the synthesis of doped varistor-grade multicomponent powders, accompanying different sintering methods to control the grain size. The high-performance miniaturized varistors generally possess small grain size, high breakdown filed, high nonlinearity, and low leakage current. These miniaturized low-voltage ZnO varistors can be commonly used for smoothening variable voltages in modern electric and electronic devices and certainly for the purpose of suppressing high-voltage transients in high-energy fields.

9.1 Introduction

Even though the solid-state fabrication methods for ZnO varistor ceramics are commercially attractive, a major disadvantage of the conventional solid-state route is the difficulty in obtaining a compositionally homogeneous microstructure, which is particularly important for the fabrication of the miniaturized devices required for modern electronic and communication equipments [1]. Varistors prepared through the solid-state method requires high sintering temperature and extended sintering schedules and also have the limitations such as exaggerated grain growth, volatility of Bi_2O_3 liquid phase, formation of undesired reactive phases, and poor stability [2–6].

It is known that the performance of ZnO varistors can be improved by reducing the grain size, which allows the increased grain boundary per unit volume and improves the breakdown voltage [7]. The varistors normally have an average sintered grain size of 10–20 μm [8], whereas for a miniaturized varistor, this has to be controlled well below 5 μm for achieving many-fold increase in energy-handling

capability [1]. Another important factor to achieve high-performance varistors is to have the dopant distribution homogeneously throughout the grain boundary [9, 10]. The only way to achieve these high-performance varistors is to start with fine powders such as nanopowders as the starting materials so that fine grain and homogeneous dopant distribution is retained even after sintering.

In order to overcome the problems associated with solid-state varistor processing, researchers have suggested various approaches for the synthesis of doped varistor-grade multicomponent powders. Most of these precursor development methods are accompanied by a secondary sample heat treatment process like conventional, microwave, reflux, and plasma methods for the conversion of sample hydroxides to corresponding oxides [7].

High-performance miniaturized varistors generally possess high breakdown filed, high nonlinearity, and low leakage currents that can be commonly used for smoothening variable voltages in modern electric and electronic devices and certainly for the purpose of suppressing high-voltage transients in high-energy fields. In the current scenario, the major thrust in the varistor field is the production of miniaturized lightweight varistors via a safer and much economic processing route [11–14].

This chapter will introduce the synthesis methods of nanocrystalline ZnO varistor powders and the new sintering techniques for controlling the grain growth. Recently, Pillai and coworkers [12] and Anas et al. [1] comprehensively summarized the synthesis methods of ZnO nanomaterials for varistor devices. This chapter is based on their works.

9.2 Exaggerating Grain Growth by Seed Grains

For low-voltage varistor devices, such as 6 V, their thicknesses should be small (usually less than 100 μm). In order to obtain low-voltage devices having arbitrary threshold voltages, one way is to exaggerate the grain size. Usually, the grain size is increased by sintering at much higher temperatures or for much longer times [15]. However, even if sintered at 1400 °C, the average ZnO grain size is still smaller than 50 μm. Furthermore, such high-temperature sintering results in the vaporization of Bi_2O_3 from the sintered body, which is the main additive to form the nonlinearity of the varistor ceramics, so that the nonlinear property is damaged. Eda et al. [16] reported a method called "seed grain method" to obtain low-voltage ZnO varistors having a large grain size without sintering at much higher temperatures and for much longer times. The device is made by sintering a mixture of ZnO fine powder, additives, and ZnO seed grains with grain sizes of 63–105 μm, which were obtained by washing a ZnO-sintered body containing BaO in boiling water. The obtained ceramic device had a grain size around 500 μm and a low threshold voltage of 6 V mm^{-1}.

Such anomalous grain growth is caused by the difference between the radii of curvature of ZnO fine powder and ZnO seed grains [16]. The surface energy at the grain boundary depends on the radius of curvature of the grain boundary. Atoms at the concave side surface have less surface energy than those at the convex side

surface. Therefore, the jumping probability of atoms from the convex side surface to concave side surface is larger than that from the concave side surface to the convex side surface. Consequently, the concave side grows by absorbing small grains. The energy difference across a curved grain boundary is given by [17]

$$\Delta F = \gamma V \left(\frac{1}{r_1} - \frac{1}{r_2} \right) \tag{9.1}$$

where ΔF is the change in free energy ongoing across the curved interface, γ is the boundary energy, V is the molar volume, and r_1 and r_2 are the principle radii of the curvature. It is known that the growth rate is approximately proportional to ΔF [17]. Therefore, the giant grain can easily grow by absorbing the small grains.

Furthermore, much larger single crystals can be obtained by repeating the seed grain method, such as ZnO single-crystal particles having grain sizes of more than 500 μm [15].

9.3 Synthesis of Nanocrystalline ZnO Varistor Powders

Nanosized powders are helpful to solve many limitations of conventional fabrication method of ZnO varistors [9, 18]. It has been confirmed that the nanocrystalline varistor grain has a large grain boundary volume that can generate more active grain boundaries per unit varistor volume [19, 20]. Because of the high surface area, nanopowders show benefits such as low-temperature sintering, reduction in ZnO grain size, and three to four times increase in the varistors performance [20–23].

Many techniques have been developed to make nanocrystalline ZnO powders, which include sol–gel [8, 24–41], citrate gel [2, 13, 42, 43], urea decomposition [4, 42, 44], microemulsion [45], coprecipitation [46–48], intensive mechanical milling [49, 50], microemulsion [51], microwave [52, 53], thermal oxidation [54], metallorganic method [19], organometallic [9], spray pyrolysis [55], solution coating [13, 21, 56] combustion synthesis [57–59], and templated grain growth [60]. All these methods can be simply classified into gas-phase, solution-phase, or sol–gel methods [9].

9.3.1 Gas-Phase Processing Methods

Gas-phase processing methods have the following inherent advantages [61]: the gas-phase processes are generally purer than the liquid-based processes because even the most ultrapure water contains traces of minerals, detrimental for electronic-grade semiconductors, while these impurities can be avoided only in vacuum and gas-phase processing systems. Furthermore, the gas-phase processes for particle synthesis are usually continuous processes, whereas liquid-based synthesis processes or milling processes are often performed in a batch form. Batch processes can result in various product characteristics from one batch to another. Therefore, the gas-phase processing methods can guarantee the same performances for one powder.

Gas-phase processing methods have been applied to synthesize nanopowders for sintering high-quality ZnO varistor ceramics. Gas discharge and plasma techniques [62–64] have been used to produce spherical nanopowders, with a narrow size distribution, the powders are homogeneous, and there is little agglomeration.

Li et al. [62] suggested a so-called hydrothermal discharging gas method to prepare ZnO powders. First, the solution containing the ions of prepared oxide is filled in the autoclave. When the autoclave is heated to the desired temperature for a period, the discharge valve under high pressure is opened to release the gas and vapor in the autoclave. After the vessel is cooled to room temperature, the solution is washed and filtered to obtain the ZnO powders.

Lu et al. [63] proposed a gas discharge-activated reaction evaporation (GDARE) technique to produce nanopowders for sintering high-quality ZnO varistor films, in which the synthetic parameters are simply optimized and desired properties can be obtained by changing the preparation parameters. Finely ground zinc powder is vaporized in a molybdenum boat, and then a high voltage is applied between this evaporation source and the indium tin oxide (ITO) or glass substrate. Finally, the plasma thus produced activates the oxygen gas present, which then reacts with the zinc vapor, forming a ZnO film on the substrate. Atomic force microscopy (AFM) studies showed that the thin films had polycrystalline structures with grain sizes ranging from 50 to 200 nm. The nonlinear coefficient of a single-coated thin film was 33 and that of a triple-coated sample was reported as 62. It was concluded that the ZnO thin films prepared by GDARE consists of a higher number of active grain boundaries capable of absorbing oxygen that effectively generates many electronic trapping states, leading to the creation of Schottky barriers at the grain boundary region.

Lin et al. [64] employed the plasma pyrolysis technology to synthesize nanometer size precursor powders of ZnO and various additives combined with chemical coprecipitation method, in which, first, $ZnSO_4$ and $NH_4HCO_3/NH_3{\cdot}H_2O$ solutions were used as the precursors for the preparation of a nanometer $Zn_5CO_3(OH)_6$ intermediate, which was then ultrasonically dispersed in NH_4HCO_3 solution, and nitrates of Sb, Bi, Co, Y, and Mn, and antimony trichloride was added to the dispersion; secondly, the complex precipitate was further filtered, washed, and dried; finally, the dried powders were pyrolyzed by plasma technology. The powders were carried by $N_2{:}O_2$ carrier gases and passed through the reaction chamber for only a few seconds, the high-temperature plasma caused the precursor to pyrolyze very quickly, and hence, this guaranteed to obtain nanometer powders. Transmission electron microscope (TEM) and Brunauer–Emmett–Teller (BET) studies showed that the ZnO and additive composite powders were composed of spherical particles of a size ranging from 10 to 50 nm with a narrow size distribution. Varistors were fabricated by sintering the doped ZnO nanomaterial at a temperature of 1050 °C. Scanning electron microscopy (SEM) results showed that the grain size of the varistors was about 0.3–1.5 μm with the average size of 1 μm, and the prepared ZnO-based varistor ceramics had excellent electrical properties with the breakdown voltage of 500 V mm^{-1}, the nonlinear coefficient of ~54, and the leakage current only of 0.1 μA. The combination of the nanoparticle size, spherical shape, and narrow

particle size distribution was proposed to be responsible for the decrease in the sintering temperature and enhanced electrical properties.

9.3.2 Combustion Synthesis

The combustion synthesis appears to be the foremost choice when it comes to the large-scale economical production of nanopowders [65], which uses the mixture of reactants that oxidize easily (such as nitrates) and a stable organic fuel (e.g. urea and $CO(NH_2)_2$) that acts as a reducing agent [12, 59, 66]. The mixture is boiled until it ignites and a self-sustaining and rather fast combustion reaction takes place, resulting in a dry, usually crystalline and unagglomerated, fine oxide powder. Using this method, pure and doped ZnO powders can be synthesized from the mixtures of the relevant water-soluble metal nitrates and urea as the fuel. The mixtures are ignited at 500 °C resulting in the varistor precursor with particle sizes in dozens of nanometers [58].

Hembram et al. [7] synthesized nanocrystalline (15–250 nm) ZnO powders by the chemical combustion method. A breakdown voltage as high as 940 V mm^{-1} and a nonlinear coefficient as high as 134, which was calculated from the voltages at 0.1 and 1 mA cm^{-2}, were obtained from the varistor made at certain conditions (powder calcined at 550 °C for one hour with a composition of 88 wt% ZnO). This enhancement of breakdown is due to smaller ZnO grain size (~2.5 μm) compared to the commercial one (10–25 μm). Although high nonlinear coefficient may be due to better densification of the samples, it results in better ZnO matrix grain to grain contact, better homogeneous distribution of dopants, and lower grain boundary thickness. XPS results indicate that Co^{2+} and Mn^{2+} have been doped in ZnO grains, which enhance the conductivity of the varistor after breakdown. It is also known that transition metal oxides such as Co and Mn generally improve the nonlinear coefficient at lower current density region because of the increase in barrier height by trapping of electrons [67]. The leakage current density as low as ~1.29 μA cm^{-2} was obtained from the varistors made from powder calcined at 750 °C for one hour for the composition of 82 wt% ZnO. As the dopant concentrations were increased, the electrical properties including the breakdown voltage and the coefficient of nonlinearity slowly deteriorated [7].

Briefly, the combustion synthesis technique can be used to successfully produce pure and doped crystalline ZnO varistor powders, with good compositional control. The combustion synthesis route enables the synthesis at low temperature, and the products obtained are in a finely divided state with large surface areas [7]. Combustion synthesis offers as added advantages [7] the surprisingly short time between the preparation of the reactants and the availability of the final product and the savings in external energy consumption.

9.3.3 Sol–Gel Methods

Anas et al. well summarized the sol–gel materials for varistor devices [1]. The sol–gel methods have definite advantages over other chemical methods in the production of varistor powders [12, 31, 37, 68], including atomic level mixing of reactants, homogeneous distribution of low-level dopants and

additives, hydrolysis and polycondensation reactions at room/low temperatures, preparation of particles with interactions through weak forces such as van der Waals/hydrogen bonded forces, formation of stable oxide network, size-controlled particle formation through pH, and concentration controls [1]. Most of the sol–gel syntheses adopt green chemical route. Multicomponent compounds can be prepared through sol–gel methods with a strict control in the stoichiometry by merely mixing sols of different compounds.

Sol–gel techniques have been utilized for fabricating varistor ceramics [12, 33, 34, 40]. The flow diagram for sol–gel synthesis of ZnO varistors is shown in Figure 9.1 [1]. Generally, two different approaches are used: the first involves the sol–gel preparation of ZnO and the subsequent addition of solid dopant metal oxides and the second one prepares the gel from the precursor solutions of the zinc and metal additives. It has been confirmed that the sol–gel processes result in the generation of "nanoparticles" [12, 35, 40].

Many successful works on the wet chemical sol–gel synthesis of varistor powders have been reported since early 1980s. Lauf and Bond [34] did the pioneer work on the sol–gel varistors. Hohenberger and Tomandl [31] prepared ZnO varistor powders using inexpensive source materials. In their method, two solutions were prepared: hot water of 90 °C contained the acetates of Zn, Co, and Mn and H_3BO_3 as a concentrated solution, while all other dopants, including Sb-acetate and nitrates of Bi, Cr, and Al, were dissolved in an excess of ethylene glycol. The volume ratio of the water solution to ethylene glycol was smaller

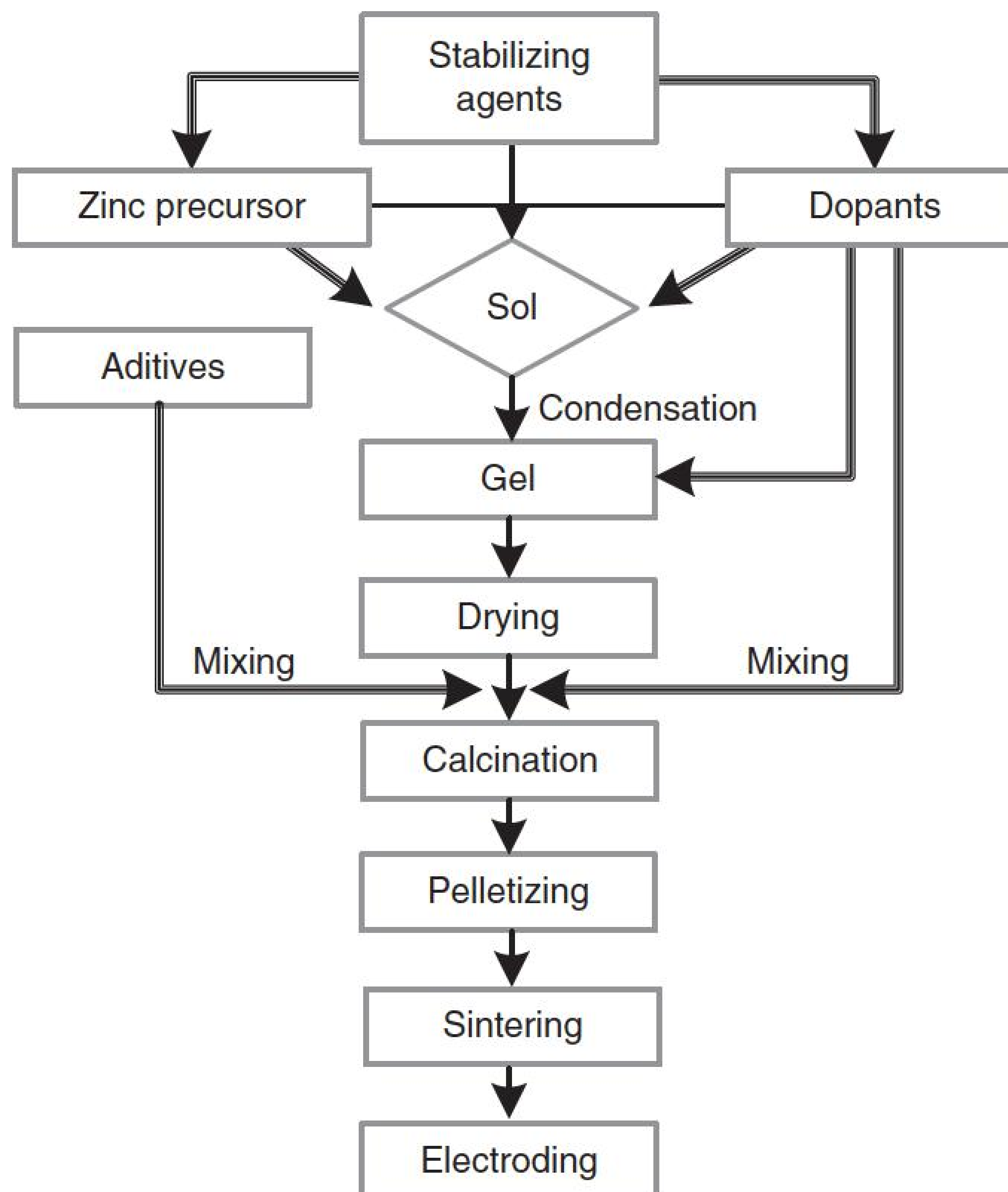


Figure 9.1 The flow diagram for sol–gel synthesis of varistors with zinc oxide as the matrix. Source: Adapted from Anas et al. [1].

than 3:1. The two solutions were mixed by shaking for a few seconds in a closed bottle to precipitate an antimony compound. On cooling, the solution became solid and formed a microcrystalline gel of Zn acetate, which crystallized upon the antimony seeds. Because of the rapid growth, the crystals contained metal ions existing in the solution or were covered with them, respectively. Solvent removal was done by freeze drying, as heating of the gel would redissolve the Zn acetate.

Pillai et al. [20] prepared nanoparticles and nanowires using novel sol–gel synthetic procedures according to the scheme shown in Figure 9.1. ZnO precursor gels were initially prepared by the reaction of an ethanolic solution of zinc acetate and ethanolic solution of oxalic acid. The gel was then dried at 80 °C and calcined at 500 °C for two hours. This produced ZnO nanoparticles with the size of 30 nm. In a further experiment, two chemical modifiers (ethylene glycol and diethanolamine) were added to the ethanolic solution of zinc acetate before the addition of the ethanolic solution of oxalic acid. Field emission scanning microscopy (FESEM) revealed that the powder had a fibrous structure containing elongated bundles with a width of 100 nm and a length of 2–4 μm, as shown in Figure 9.2a,b. Further, this material (nanoarray ZnO) was subsequently suspended in ethanol and ultrasonicated for 40 minutes to separate the individual wires from the bundle, as shown in Figure 9.2c; these wires were composed of approximately spherical nanoparticles with an average diameter of 21 nm and self-assembled to form one-dimensional arrays with a length of 2–4 μm. The wires annealed at 500 °C were further calcined to 1000 °C, and FESEM images showed that the individual particles were sintered together to form continuous wires of width 0.3–0.4 μm and length 10–20 μm, as shown in Figure 9.2d.

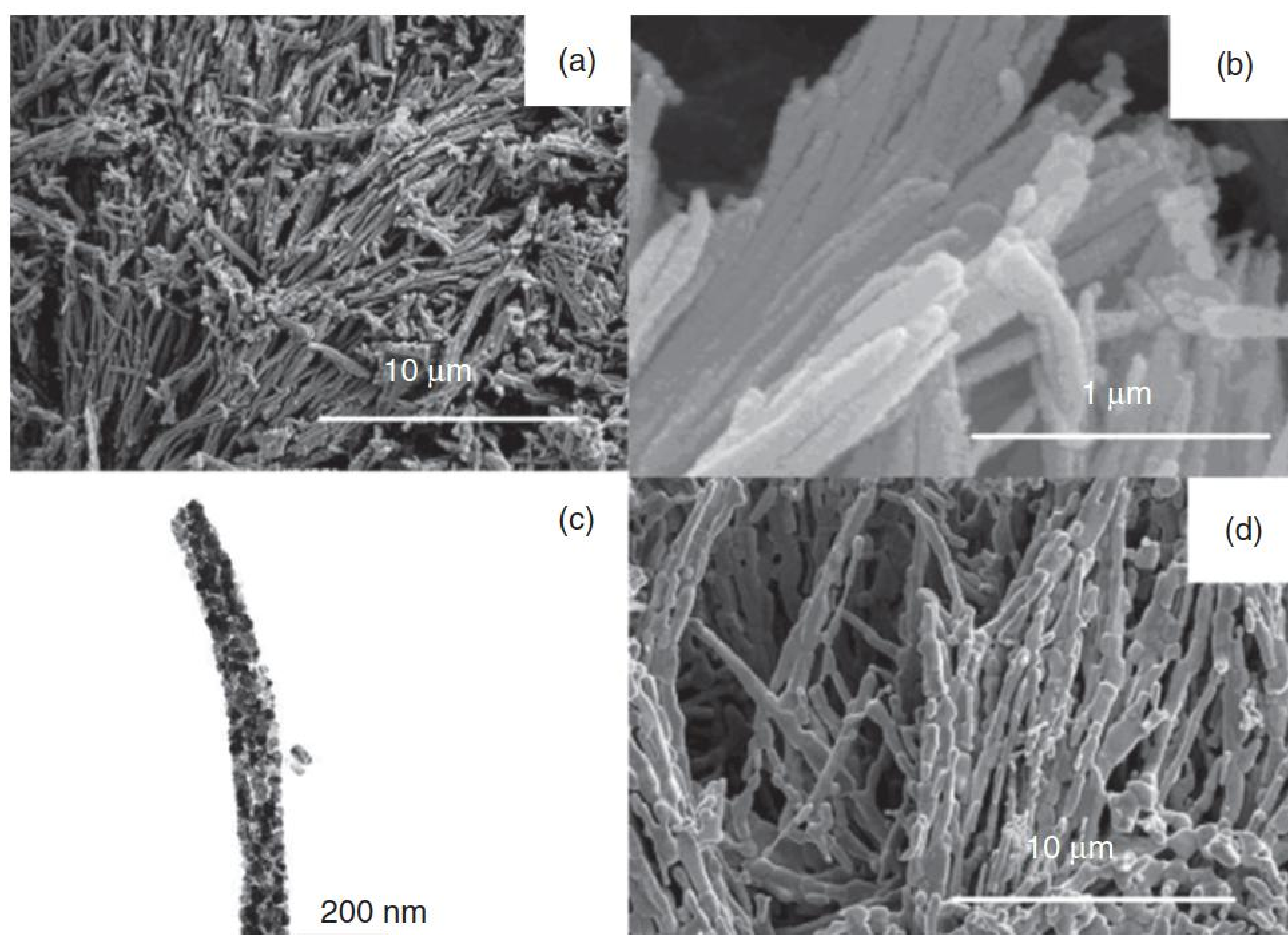


Figure 9.2 Electron microscopy images of nanoarray ZnO. (a) and (b) FESEM after calcination at 500 °C; (c) TEM of a single array of ZnO nanoparticle separated by ultrasonication in ethanol; (d) FESEM of nanoarray ZnO calcined at 1000 °C. Source: Pillai et al. 2004 [20]. Reproduced with permission of Springer.

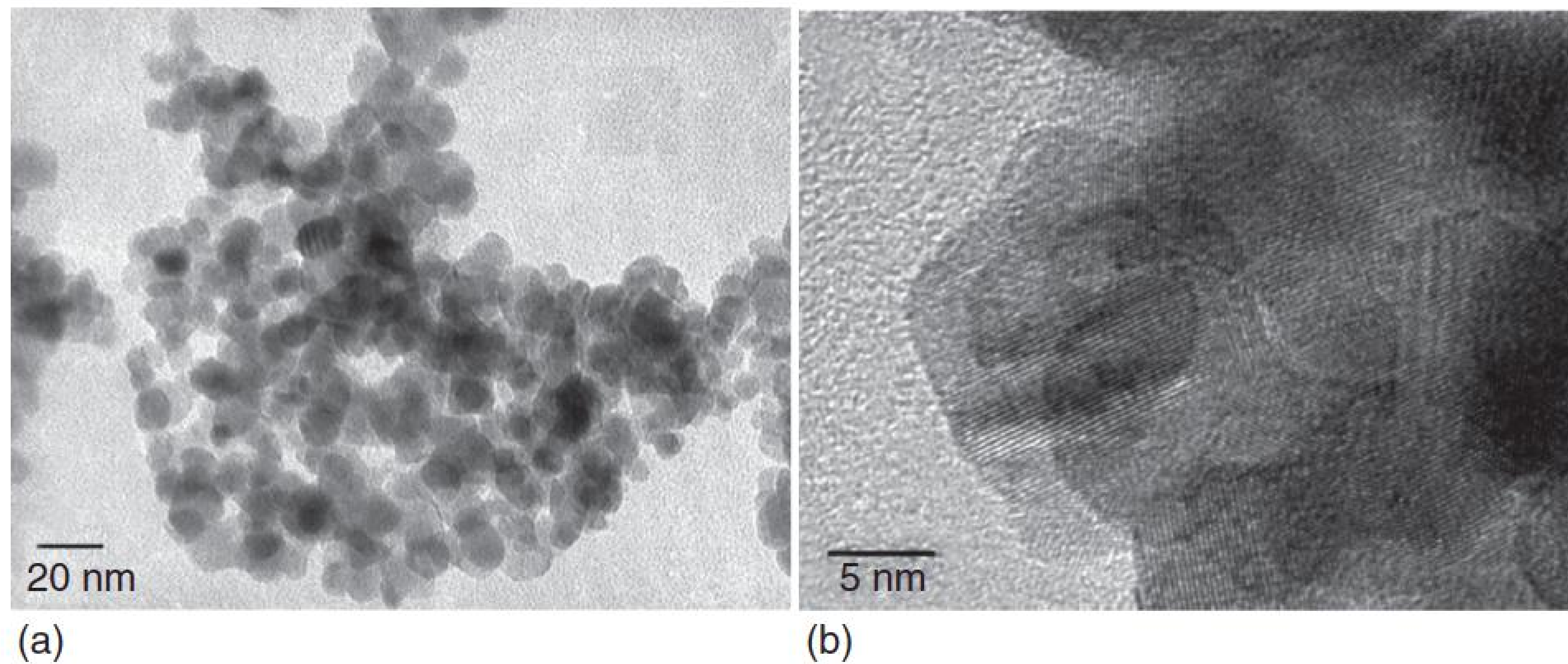


Figure 9.3 (a) TEM and (b) HRTEM images of the nanopowder synthesized by the liquid route. Source: Savary et al. 2011 [69]. Reproduced with permission of Elsevier.

Savary et al. [69] developed a liquid synthesis route for the preparation of the varistors powder. Zinc acetate was first dissolved in absolute ethanol, and the dopants were added to the solution from metal oxides powders. The resulting solution was stirred for one hour at 70 °C to achieve a good dissolution of the precursors. An oxalic acid solution was then poured, leading to the precipitation of zinc oxalate. The latter was dried under infrared lamps and calcined in air at 400 °C for one hour to get the zinc-oxide-based powder [70]. Using TEM (Figure 9.3a), the ZnO particles appeared to be nanocrystalline with a nearly spherical shape and a very narrow particle size distribution. The BET-specific surface area of the powder was 53 m^2 g^{-1}. The grain diameter was estimated as 19 nm. Moreover, on the high-resolution TEM (HRTEM) image, the characteristic contrast of a well-crystallized phase is also evident as shown in Figure 9.3b [67].

Cheng et al. [29] sintered the sol–gel-derived powers at 900 °C for two hours. Figure 9.4 shows the I–V characteristic plot of varistors sintered by sol–gel-made powders under different Al_2O_3 content. For the ZnO varistor ceramics with 0.4 wt% Al_2O_3, the breakdown voltage is 1160 V mm^{-1}, and the average grain size is 3 μm. The sol–gel-derived samples showed a smaller grain size and narrower size distribution and possessed higher breakdown voltage than the conventional. In addition, some reports revealed that the homogeneity of microstructure plays an important role in determining the electrical properties of ZnO varistors [19, 71]. Ramírez et al. [72] indicated that the number of active grain boundaries is concerned with the homogeneity of the microstructure, larger grain size, and wider grain size distribution and leads to the decrease of the number, hence the breakdown voltage occurs [4, 73]. Higher breakdown voltage could be attributed to the smaller grain size and larger number of active grain boundaries. Therefore, the increase in breakdown voltage obtained could be ascribed to the smaller grain size and the improvement of homogeneity, which leads to the formation of more active grain boundaries per unit volume. Energy-handling capability is crucial for applications in transient surge suppression, which is defined as the amount of energy that a varistor can absorb before it fails. The square wave (also called as rectangular wave) energy-handling capability was measured using 2 ms current square impulse. Results showed that the sol–gel-derived samples

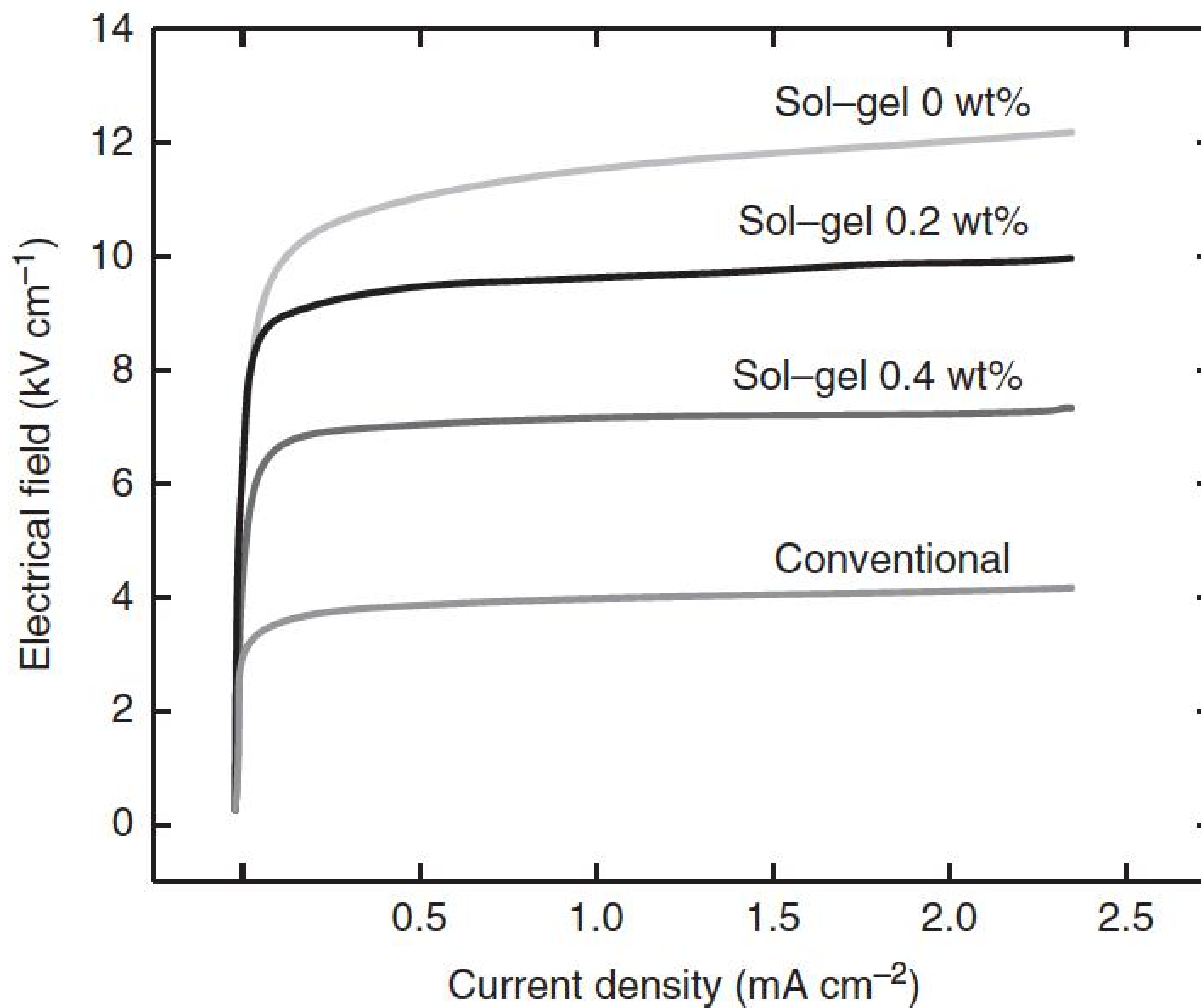


Figure 9.4 The *I–V* characteristics plot of varistors sintered by sol–gel-made powders under different Al_2O_3 contents. Source: Cheng et al. 2012 [29]. Redrawn with permission from Elsevier.

had better energy absorption capability than the conventional samples, which was improved with the donor doping of Al_2O_3. The value is 200 J cm^{-3} for conventional samples, whereas for samples obtained from the sol–gel method, the values are 323, 350, and 393 J cm^{-3} as the contents of Al_2O_3 increased, respectively. This result may be due to the improvement in the microstructure homogeneity of the sol–gel-derived Al_2O_3-doping ZnO varistor ceramics.

9.3.4 Solution-Coating Method

High-performance varistors can also be accomplished by performing wet chemical syntheses. Among the methods employed, the solution-coating method stands out as the best one for the effective distribution of dopants at the varistor grain boundaries [5, 6]. In this method, the ZnO particles are coated with additives such as Bi_2O_3, Sb_2O_3, Co_2O_3, Cr_2O_3, and other minor dopants via liquid nanocoating technique. Different solution-coating methods were reported by many researchers to coat various minor additives and dopants over ZnO surfaces.

Haile et al. [46] synthesized nanosized, well-dispersed spherical powders easily and reproducibly by aqueous precipitation, and chemical coating of these powders can also be achieved fairly uniformly by precipitation. Varistors prepared by this chemical method display electrical properties superior to those for conventionally prepared samples. A possible precipitation mechanism [46] for ZnO is that the ZnO particle precipitates out of the solution, and the surface-active ethanol amines attach to it. This produces steric stabilization, and as the ethanol amines are more soluble in ethanol than in water, a diffuse layer of ethanol-rich liquid around the particle is created. The zinc cation is, however, more soluble in water, and growth is therefore controlled by the

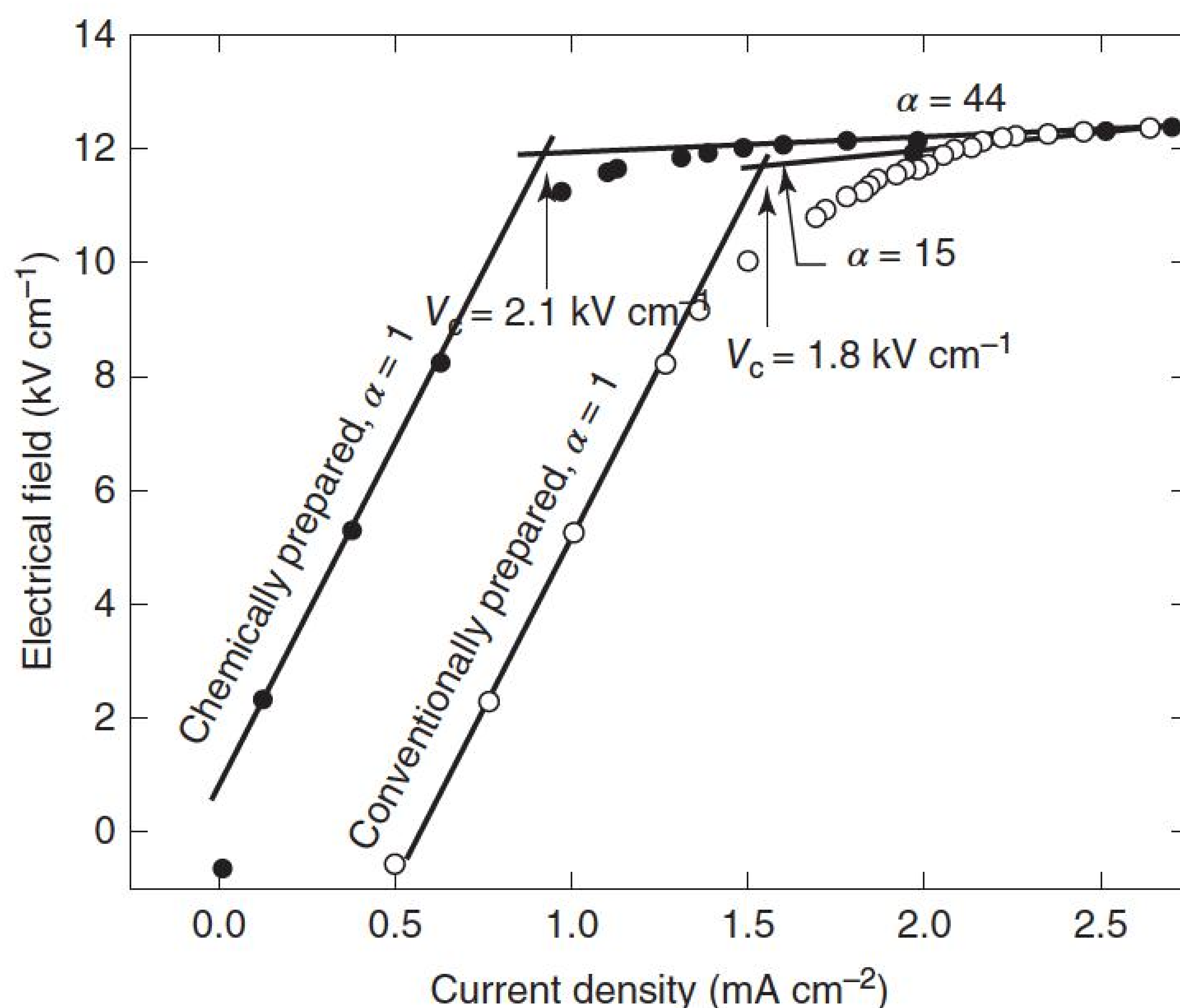


Figure 9.5 Comparison of current density vs electrical field curves of chemically prepared and conventional prepared ZnO varistor ceramics. Source: Haile et al. 1989 [46]. Reproduced with permission of John Wiley & Sons.

diffusion of Zn^{2+} ions through the ethanol-rich layer. Controlling the growth process in this manner by "evening-out" the surface energies and growth rates of different crystallographic faces with the attachment of ethanol amine leads to spherical particles. As shown in Figure 9.5, compared with the conventional ball-milled prepared samples, the chemically prepared varistor also shows a much more distinct change in behavior from ohmic to nonohmic, the maximum nonlinearity coefficient is 44, and the breakdown voltage reaches 1.8 kV cm^{-1}, whereas the respective ones are 15 and 1.8 kV cm^{-1} for the conventional prepared samples. The resistivity at low voltage of the chemically prepared varistor reaches 5×10^{12} Ω cm, which is much higher than that of the conventional one (10^{10} Ω cm). All these advantages have been argued to result from greater microstructural homogeneity.

Pillai et al. [24] prepared ZnO nanoparticles by the reaction of ethanolic solutions of zinc acetate and oxalic acid followed by drying at 80 °C and calcinating at 500 °C, and then ZnO nanoparticles were dispersed in ethanol with dissolved additive metal salts to form "core shell"-type varistor powders. First, nano-ZnO was dispersed in ethanol and ultrasonicated for 40 minutes. Then, an ethanolic solution of antimony chloride and cobalt chloride hexahydrate and an acetonic solution of bismuth chloride were added to the ethanolic suspension of zinc oxide and stirred for five minutes. Ammonium carbonate was added to the above solution and stirred for 10 minutes. An ethanolic solution of nickel acetate tetrahydrate, manganese acetate tetrahydrate, chromium nitrate nonahydrate, and aluminum nitrate nonahydrate was added to the above mixture and stirred for 20 minutes. The material thus obtained was dried in an oven at 80 °C and further calcined at 300 °C. This mixture was then plastified with one drop each

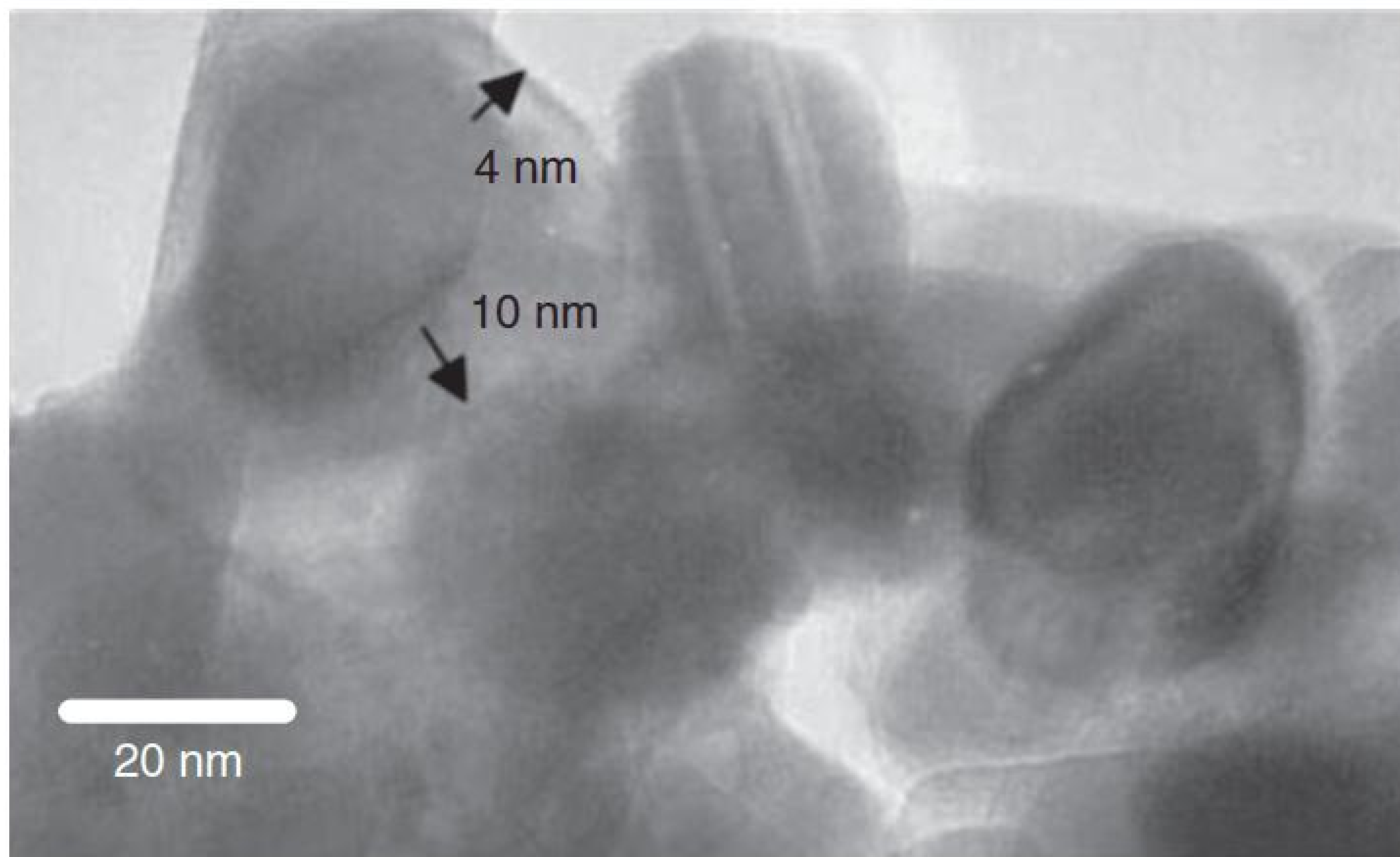


Figure 9.6 HRTEM of ZnO nanoparticles coated with oxides of Sb, Bi, and Co precursors. Source: Pillai et al. 2003 [24]. Reproduced with permission of RSC.

of 10% aqueous solution of poly(vinyl alcohol) and poly(ethylene glycol) and gum arabic. This mixture was further dried in a 100 °C oven for five minutes and pelletized. The microscopic analyses of the resultant powder showed that the ZnO composite powder was homogeneously coated and ultrafine. Figure 9.6 shows the HRTEM images of ZnO nanoparticles coated with oxides of Sb, Bi, and Co precursors, the coating thickness is about 4–10 nm [24]. Subsequently, varistor powders were fabricated at 1050 °C for two hours. The "core shell" samples achieved a high densification of 97.21%. Compared with commercial varistor samples prepared under similar conditions, "core shell"-type varistor ceramics showed considerably higher breakdown voltage of 850 V mm^{-1} as compared to a sample prepared by mixing with commercial varistor disks (507 V mm^{-1}). The high breakdown voltage obtained is attributed to the formation of more varistor-active grain boundaries per unit area. Figure 9.7 indicates a comparatively smaller average grain size (1.5 μm) for "core shell" samples

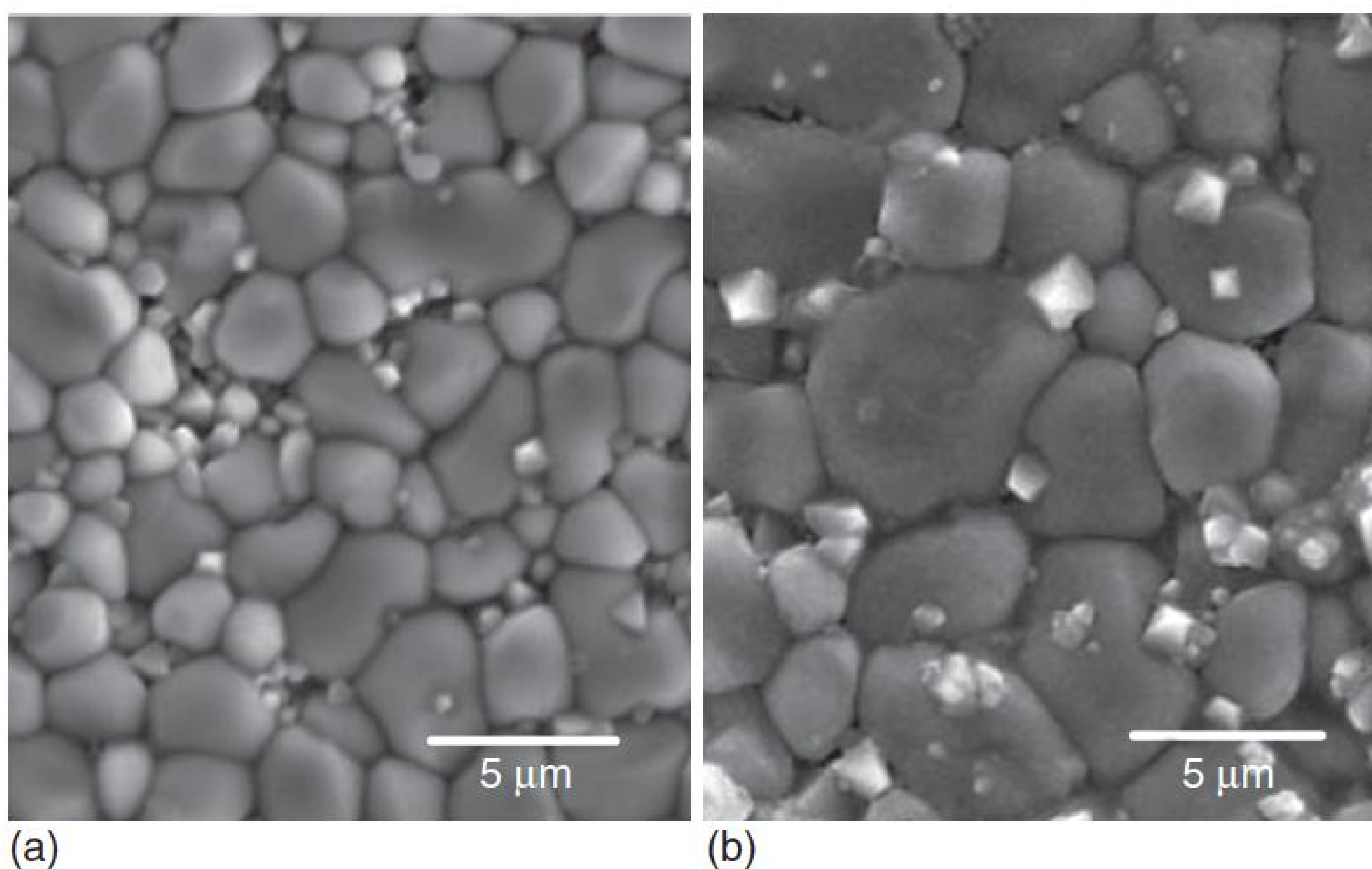


Figure 9.7 FESEM images of (a) the "core-shell" and (b) commercial varistor ceramics sintered at 1050 °C for two hours. Source: Pillai et al. 2003 [24]. Reproduced with permission of RSC.

compared to the commercial samples (3 μm), and the grains of "core shell" sample have a more uniform distribution [24].

Similar work was done by Li et al. [5], and the resultant varistors prepared through the nanocoating method showed a high threshold voltage ($540\,V\,mm^{-1}$) and a nonlinear coefficient ($\alpha = 50$). Yuan and Ryu [74] tried to deposit a homogeneous layer of Bi_2O_3 over ZnO through nanocoating, and effective distribution of dopants at the grain boundaries were achieved.

Table 9.1 summarized the grain sizes, densities, breakdown voltages, and nonlinear coefficients of ZnO varistors sintered by chemically synthesized nanopowders, TD means theoretic density. The highest breakdown voltage reaches $3300\,V\,mm^{-1}$ [33], and the highest nonlinear coefficient reaches 270 [37]. Many methods can control the average grain size smaller than 2 μm, the respective breakdown voltage about $1\,kV\,mm^{-1}$, and the nonlinear coefficient around 50.

Table 9.1 Properties of ZnO varistors sintered by chemically synthesized nanopowders.

Sintering temperature (processing method)	Grain size (μm)	Density ($g\,m^{-3}$)	Breakdownvoltage ($V\,mm^{-1}$)	Nonlinear coefficient	References
950 °C/2 h (thermogelation)	<2	5.0	557	34	[28]
1050 °C/2 h (thermogelation)	<4	5.1	493	36	[28]
1150 °C/2 h (thermogelation)	<8	5.4	323	16	[28]
1100 °C/1 h (colloidal-gel)	4–8	96%TD	1000	40	[47]
1150 °C/4 h (solution coating)	8.8		249	37	[39]
950 °C/2 h (sol–gel method)	<2	>98%TD	>1000	>45	[75]
1150 °C/1 h (citrate gel)		98%TD	515	35	[43]
1150 °C/1 h (urea)		94%TD	280	21	[43]
940 °C for 1–5 h (metal–organic polymeric method)	1–2.5	98%TD	1500	78	[19]
1100 °C/2 h (sol–gel method)	0.85	5.3		40–60	[76]
1050 °C (sol–gel condensation)		5.38, 96%TD	786	34	[20]
1050 °C/2 h (sol–gel mixed precursor route)	2	5.58, 99.6%TD	941	33	[11]
950 °C/1 h (sol–gel method)	4.4		3300		[33]

Table 9.1 (Continued)

Sintering temperature (processing method)	Grain size (μm)	Density (g m^{-3})	Breakdownvoltage (V mm^{-1})	Nonlinear coefficient	References
900 °C/2 h (sol–gel method)	3	5.4	1160		[29]
1150 °C/2 h (Xanthan gum as a polymerization agent)	4–10	5.52, 95.5%TD	310	27	[35]
1100 °C/2 h (sol–gel method)	2.4	5.42, 96.8%TD	438	16.5	[41]
1050 °C/1.5 h (solution nanocoating technique)	4.78	5.38	540	50	[5]
Spark plasma sintering 600–650 °C/15 min (organometallic approach)	0.3–1	5.9–6.1, 94–97%TD	1066–1095	5.6–5.8	[9]
Step sintering 900 °C/6 h (sol–gel method)	1.6	5.47, 97.5%TD	1192		[36]
Step sintering 825 °C/10 h (modified Pechini polymeric complex method)	~0.6	~100%TD	2000	270	[19]
1100 °C/0.5 h (Amine processing)	3.9		711	50	[77]
750 °C/2 h (precipitation)			3000	50	[52]
1050 °C/2 h (core–shell)	1.5	5.45, 97.2%TD	850	33	[24]
1200 °C/2 h (microemulsion)			450	83	[51]
1050 °C/1.5 h (plasma pyrolysis)	1		500	54	[64]
1150 °C/1 h (citrate gel)		98%TD	515	35	[42]
1050 °C/2 h (plasma pyrolysis)	~2		656		[78]

9.4 Nanofillers in ZnO Varistor Ceramics

Usually, the conventional ZnO varistors should be sintering at high temperature to reduce nano- to microscale interstitial porosities and densify the varistor ceramics. However, high sintering temperatures cause excessive grain growth in ZnO varistors. By the use of nanopowders as nanoadditives or nanofillers to the commercially available spray-dried micron-sized granules, the nanopowder enters into the pores of the micropowder and fills the varistor interstitial voids [1]. This will not only increase the particle packing but also yields high particle contact area, which favors accelerated densification at comparatively low temperatures. The resultant composite varistor powder produces sintered varistor ceramics with significant grain size reduction and possesses sintered microstructures with distributions of nano- and micrograins, called as a bimodal grain size distribution. In either case, an effective increase in the number of ZnO grains within a specific varistor volume can be achieved [1]. The microstructure modifications as expected in the nanofiller-based composite varistor approach can be depicted schematically as Figure 9.8 [14].

In addition to the grain size reduction, high densification, higher breakdown voltage, and better nonlinearity, the nanofiller addition also helps the varistor industries to have many practical advantages [14]. The blending of nanofillers with a commercial micron-sized varistor powder simply by dry or wet milling can easily be introduced as an intermediate unit operation during varistor manufacturing. Varistors made out of such nanofillers not only promises high-energy field varistors but also provide a huge potential to miniaturize varistors at low production cost. Hence, this method can be taken as a "nanofiller" for the manufacturing of varistors.

Anas et al. [14] reported that only a 5 wt% addition of the nanofiller resulted a varistor with 99% theoretical density, average sintered grain size of 1 μm,

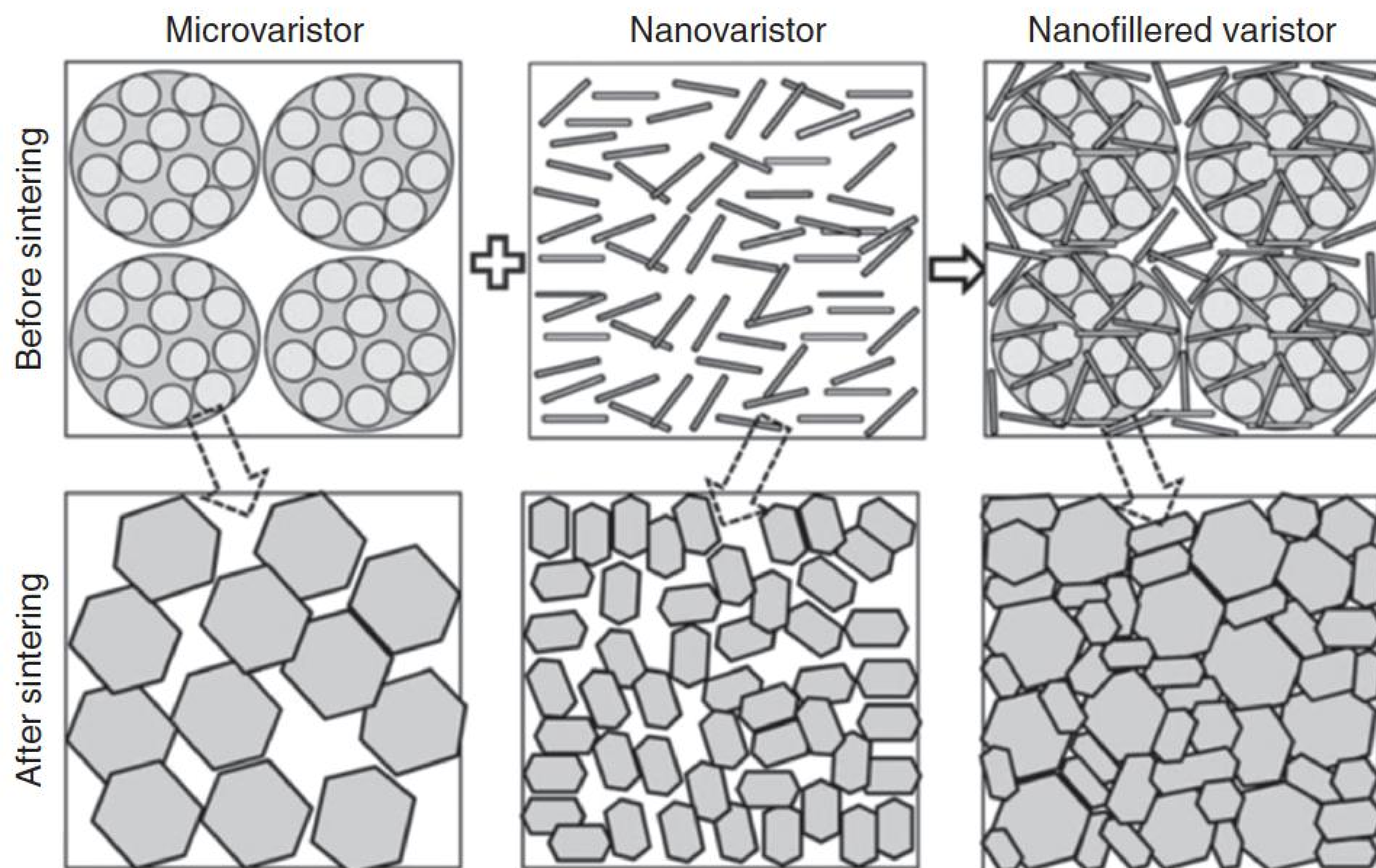


Figure 9.8 Schematic representation of the "nano/micro composite" or "nanofiller" approach for the high energy field varistors. Source: Anas et al. 2013 [14]. Reproduced with permission of John Wiley & Sons.

breakdown voltage of 875 V mm^{-1}, and nonlinear coefficient of 31, when compared to the commercial sample with an average grain size of 6 μm, breakdown voltage of 421 V mm^{-1}, and nonlinear coefficient of 17, which were processed under similar sintering conditions at ≤1100 °C.

Other than the grain size control, step-sintering reduces the formation of spinel phase for the nano and nanofillered varistors. In conventional high-temperature sintering, the spinel phase occurs predominantly as a major phase. However, it is clear from the powder X-ray analysis that the step-sintered varistors show a negligible presence of the spinel phase ($Zn_7Sb_2O_{12}$) [14]. The control in the formation of the spinel phase by the step-sintered samples was also observed earlier in the sol–gel-derived varistors when step-sintering was performed above 900 °C [20]. The TEM-EDS (energy dispersive spectrometry) images of the step-sintered varistors derived from the nanopowder samples further revealed the presence of various minor ingredients in the sample. This compositional analysis indirectly indicates the advantages of the precipitation-reflux synthesis adopted for the nanofiller preparations. As the refluxing is done only after the precipitation of all the minor ingredients (Bi, Sb, Co, and Cr) at their respective pH, the above work offers stoichiometry in varistor preparation and additive homogeneity in the prepared varistors [14]. It further proves the homogeneity of the dopant ions among ZnO grains at the atomic level. Thus, Anas et al. [14] confirmed that by adopting the step-sintering method and including the nanofillers in varistor preparations, varistors with controlled grain size and spinel phase formation can be achieved.

9.5 Sintering Techniques to Control Grain Growth

The sintering process and grain growth occurred simultaneously, and grain grows considerably at high temperature. Therefore, the grain growth at high sintering temperature still remains a significant challenge for developing miniaturized varistor devices. By carefully controlling the microstructure, through nanostructuring by chemical routes, it should be possible to produce varistors with high breakdown voltage, as this is proportional to the number of active grain boundaries in the sintered body. This property is particularly important for the production of the small-sized varistors needed for modern electronic instruments such as tablet computers and mobile phones [9]. Uncontrolled grain growth at higher temperature is highlighted as a major challenge for obtaining desirable electrical properties for nanovaristors. Various sintering techniques such as step-sintering, spark plasma, and microwave sintering methods are expected to deliver a varistor with controlled grain growth and optimum electrical characteristics. An outstanding output by these techniques is that the breakdown voltage might be increased several-fold if one could sinter the material to full density with submicron grain size [9].

9.5.1 Step-sintering Approach

The step-sintering approach [36] realizes the production of a fully sintered varistor ceramic at a lower temperature, which employs two or more steps in the heating schedule. The ceramic disk is initially heated in a furnace at a

higher temperature to achieve a reasonably good density, then cooled down, and retained at a slightly lower temperature for several hours [9]. Such a step-sintering procedure has been tried for the preparation of varistor materials [19, 36, 79].

In a typical two-step sintering schedule, the samples were heated to 1000 °C, then allowed to cool for over 30 minutes to 900 °C, and held there for six hours. Considerably, higher breakdown voltage of $1192\,V\,mm^{-1}$ was obtained for the varistors made from nanosample [9]. Another example is, a sintered density higher than 99%, submicron grain size and superior electrical properties with breakdown voltage of $2050\,V\,mm^{-1}$, and nonlinear coefficient of 96 were reported [40], the SEM micrographs of normal and two-step sintered samples are presented in Figure 9.9; for the sample in Figure 9.9b, the average grain size is only 0.75 μm. Durán et al. [19] developed ZnO varistor ceramics by two-step sintering, with the grain size of <1 μm, nonlinear coefficient of 70, and breakdown voltage (at $1\,mA\,cm^{-2}$) of $>1500\,V\,mm^{-1}$. The high electrical performance of the doped-ZnO dense ceramics is attributed to liquid-phase recession on cooling, which enhances the ZnO–ZnO direct contacts and the potential barrier effect. The longer the temperature holding time in the second step is, the smaller the size is [40].

9.5.2 Microwave Sintering Method

The microwave sintering method has received much attention in recent years [9, 41, 80, 81], which is more rapid than conventional sintering and the grain growth can be well controlled [69]. Compared with the conventional heating process, the microwave-assisted sintering provides an energy-efficient, green, and convenient method for producing ceramic materials [82–86], significantly improves electrical properties, and enhances the overall densification of ZnO varistor ceramics and the reaction kinetics between different phases;

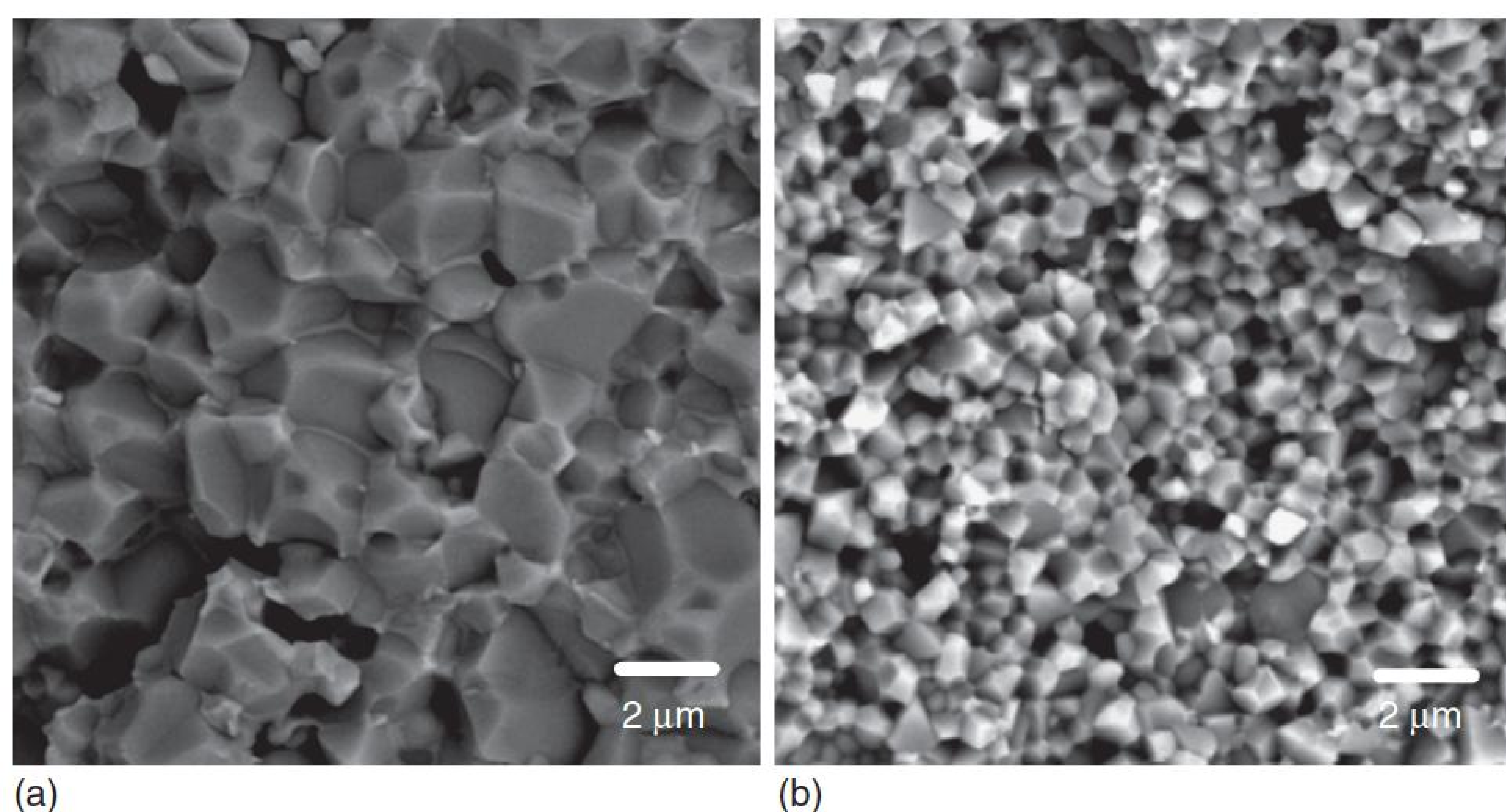


Figure 9.9 SEM images of samples (a) normally sintered at 1150 °C and (b) two-step sintered (sintered at 950 °C for five minutes and then cooled to 825 °C and held for 10 hours.). Source: Ya et al. 1997 [40]. Modified with permission from Elsevier.

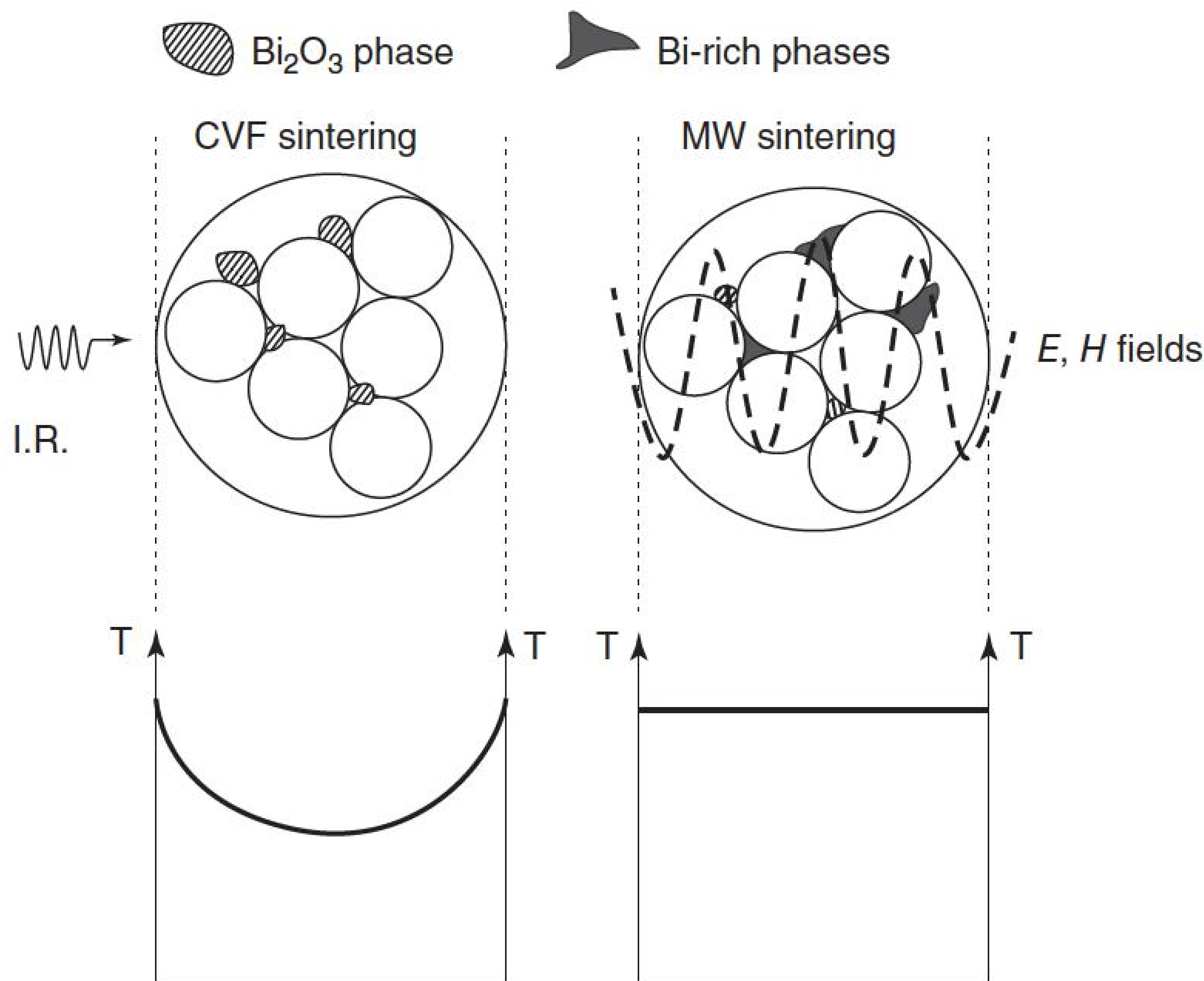


Figure 9.10 Comparison of varistor sintering in a conventional furnace (CVF) by infra-red heating (I.R.) and in a microwave (MW) furnace. Source: Savary et al. 2011 [69]. Reproduced with permission of Elsevier.

furthermore, faster dopant diffusion in microwaves is suggested from donor-state concentration measurements [69]. A better distribution of dopants and homogeneous sintering temperature inside the bulk of the ceramics are also reported as unique features of microwave sintering, as shown in Figure 9.10 [69]. The grain sizes in the case of microwave-sintered samples are smaller, and their distribution is found to be more uniform when compared to the conventionally sintered one by employing the same processing conditions [23]. These "microwave effects" may increase in the migration of atoms via peculiar phenomena such as electromigration or field-induced pressure. A preferential microwave heating of the Bi_2O_3 phase could also be a likely explanation for microwave-enhanced reactivity phenomenon.

With an ultrahigh heating rate (up to ~82 °C s^{-1}), Xu et al. [87] have reported that microwave sintering of undoped 1 μm ZnO powder provides an almost fully densified structure with a final grain size of ~4 mm. At least, 900 °C is required to attain a high density for pure ZnO materials in microwave-sintered ZnO [88]. Roy et al. [89] sintered two initial particle sizes of 30 and 100 nm at 800 °C. The results showed that 30 nm powder compacts densified to 99% theoretical density. Therefore, nanostructured ceramics can be obtained with nearly full densities.

Savary et al. [69] reported that the breakdown voltage E_b of samples by the microwave sintering reached 575 V mm^{-1}, which was more than four times the value of E_b for conventional sintering. This is obviously explained by the difference in grain size. The SEM images of the samples are given in Figure 9.11, and the average grain size is 2.5 and 4.2 μm for microwave-sintered ceramics and conventional sintered ones. In the case of conventional sintered samples, the breakdown voltages are always lower than that obtained for

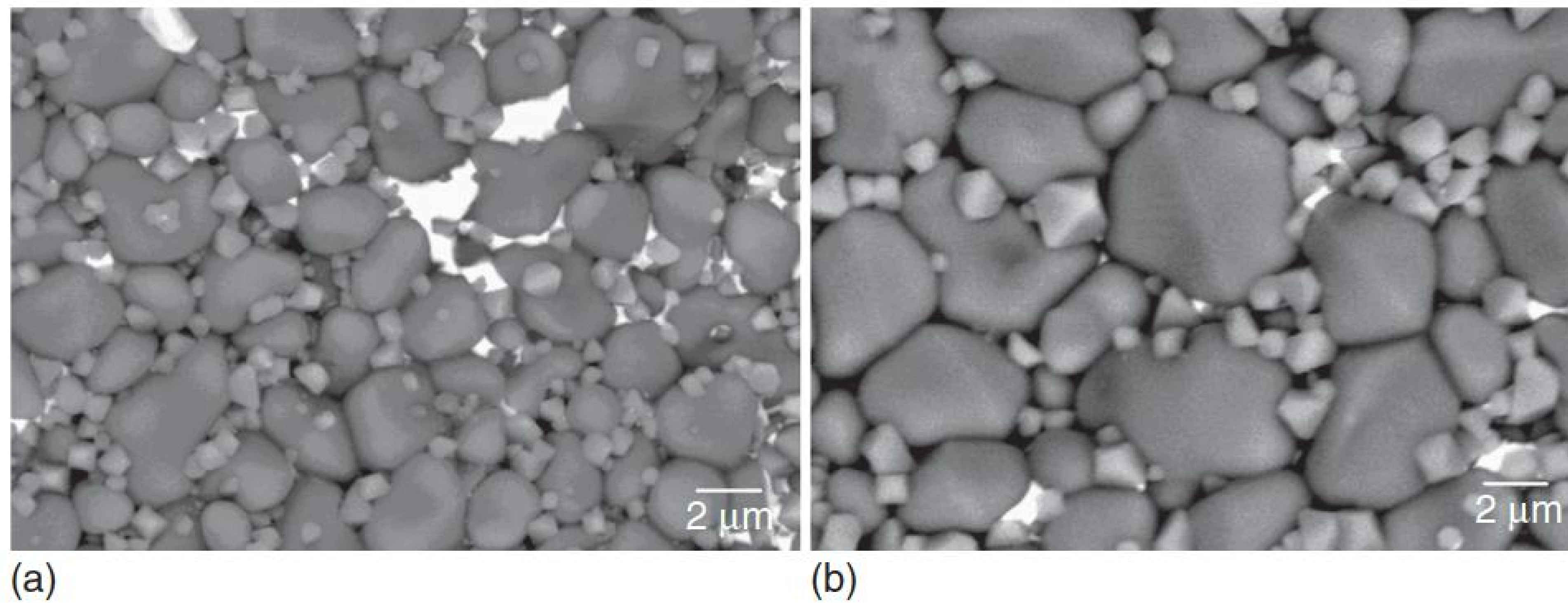


Figure 9.11 Comparison of SEM images of (a) microwave-sintered sample at 1100 °C/0.5 h and (b) conventionally sintered sample at 1100 °C/0.5 h. Source: Savary et al. 2011 [69]. Reproduced with permission of Elsevier.

the microwave-sintered samples. Subasri et al. [23] compared the electrical properties obtained using a microwave-sintering technique and those obtained on a conventionally sintered material as well as those of a commercially available product. The microwave-sintered doped nanocrystalline ZnO yielded 98% dense bodies and a breakdown voltage of 960 V mm^{-1}, a leakage current of 0.25 µA cm^{-2}, and a nonlinear coefficient of 70 when compared to 430 V mm^{-1}, 1.2 µA cm^{-2}, and 118 as measured for a conventionally sintered compact.

Investigations have been carried out on sintering of varistor materials using microwaves (2.45 GHz) and millimeter waves (24 GHz) [87, 90, 91]. Lee et al. [90] and Lin et al. [91] had sintered Bi_2O_3-based varistor materials using both 2.45 and 24 GHz radiation. They found that better properties were achieved with millimeter waves when compared to microwaves at a sintering temperature of 1100 °C with a soaking time of 10 minutes.

Overall, the microwave-sintering method has yielded such benefits as a rapid sintering rate, high densification, fine grain size, and uniformly distributed production. From a practical point of view, the enhanced reactivity by microwaves opens new ways for producing faster and cheaper high-performance functional ceramics [69].

It has been speculated that the presence of δ-Bi_2O_3, one of the fastest oxygen-ion conductors, plays a vital role in the varistor stability especially while annealing in air [92]. The microwave-sintered samples show δ-Bi_2O_3 phase composition ranging from 3% to 6% when compared to ~1.9% in a conventionally sintered sample at 1100 °C for 30 minutes, and this could lead to that microwave-sintered samples have higher breakdown voltage and low leakage current [23].

9.5.3 Spark Plasma Sintering Technique

Spark plasma sintering (SPS) or pulsed electric current sintering (PECS) technique is another powerful method [9, 39, 93–95], which is an effective process to densify difficult-to-sinter materials in a very short time at a lower temperature. This process itself is similar to conventional hot pressing; i.e. the powder precursors are located in a die made of an electrically conducting material, and

a uniaxial pressure is applied during the sintering. However, instead of heating with an external source, a pulsed DC current is applied, which passes through the pressure die as well as the sample, so that the sample is heated from outside and inside. In addition to heat and pressure, this process utilizes the self-heating action caused by spark discharges between the particles, which promote material transfer and enhance the densification. Thus, the SPS process might be advantageous in suppressing exaggerated grain growth [94]. New properties such as higher density and smaller grain size are often expected because of the special sintering mechanism.

SPS combines the application of both pressure and pulsed DC current directly on the ceramic sample [39, 93, 94], which transiently produces spark plasma at high temperatures between particles by the low-voltage DC pulse [39]. SPS method is found to be highly effective in sintering ZnO nanomaterials for varistor applications [9, 93–95]. The major interest of SPS [39], when the sintering parameters have been mastered, is linked to the extreme rapidity of the thermal treatment. Thus, the consolidation time is greatly decreased from hours, in the case of the conventional sintering, to few minutes for the SPS processing. Moreover, the sintering temperature can be diminished by a few hundred degrees compared to conventional sintering [9]. The sintering temperature can be 200–300 °C lower than that of the pressureless sintering or hot-pressed sintering, and the sintering time is only 3–10 minutes [96].

Based on this SPS technique, Macary et al. [9] reported the nanostructured varistors obtained by SPS at sintering temperatures ranging from 550 to 600 °C, the grain size of ZnO varistor ceramics sintered at 600 °C was reported as 300–500 nm (the average size of ZnO–Bi_2O_3 raw nanomaterial is in 10 nm) with a breakdown voltage of 1066 V mm^{-1}, and a reasonably high density of 97%, but the nonlinear coefficient was relatively low for being further improved by incorporating other metal oxides.

Microwave sintering is presently considered an attractive process with a rapid rate and a low temperature. However, as reported in microwave-sintered ZnO, at least, 900 °C is required to attain high density for pure ZnO materials, so that it is nearly impossible to obtain nanocrystalline ceramics by microwave sintering. However, being sintered at a much lower temperature by SPS, nanostructured densified ZnO ceramics can be obtained [94]. Gao et al. [94] observed that the nanoscale grain size remains unless the sintering temperature is above 550 °C, and the densification process is barely dependent on the sintering temperature when it is lower than 550 °C. Therefore, the driving force of the densification might be from the high pressure (50 MPa) and the special effects of the large electric current (3 kA) in the SPS process. However, above 550 °C, the grain size quickly increases, and the relative density decreases as the sintering temperature increases. This kind of rapid grain growth can result from capillary driving forces at high temperatures. Figure 9.12 shows the TEM micrograph of nanocrystalline ZnO ceramics sintered by SPS at 550 °C within 2 minutes of holding time and the high-resolution episcopic microscopy (HREM) micrograph of the grain boundaries of nanocrystalline ZnO sintered by SPS at 500 °C [94]. A typical interfacial amorphous phase was observed. The commercial varistors typically have a grain size of 10–100 μm with a doped grain boundary depletion width of 50–100 nm. Thus, if the grain size decreases to 100 nm, thin

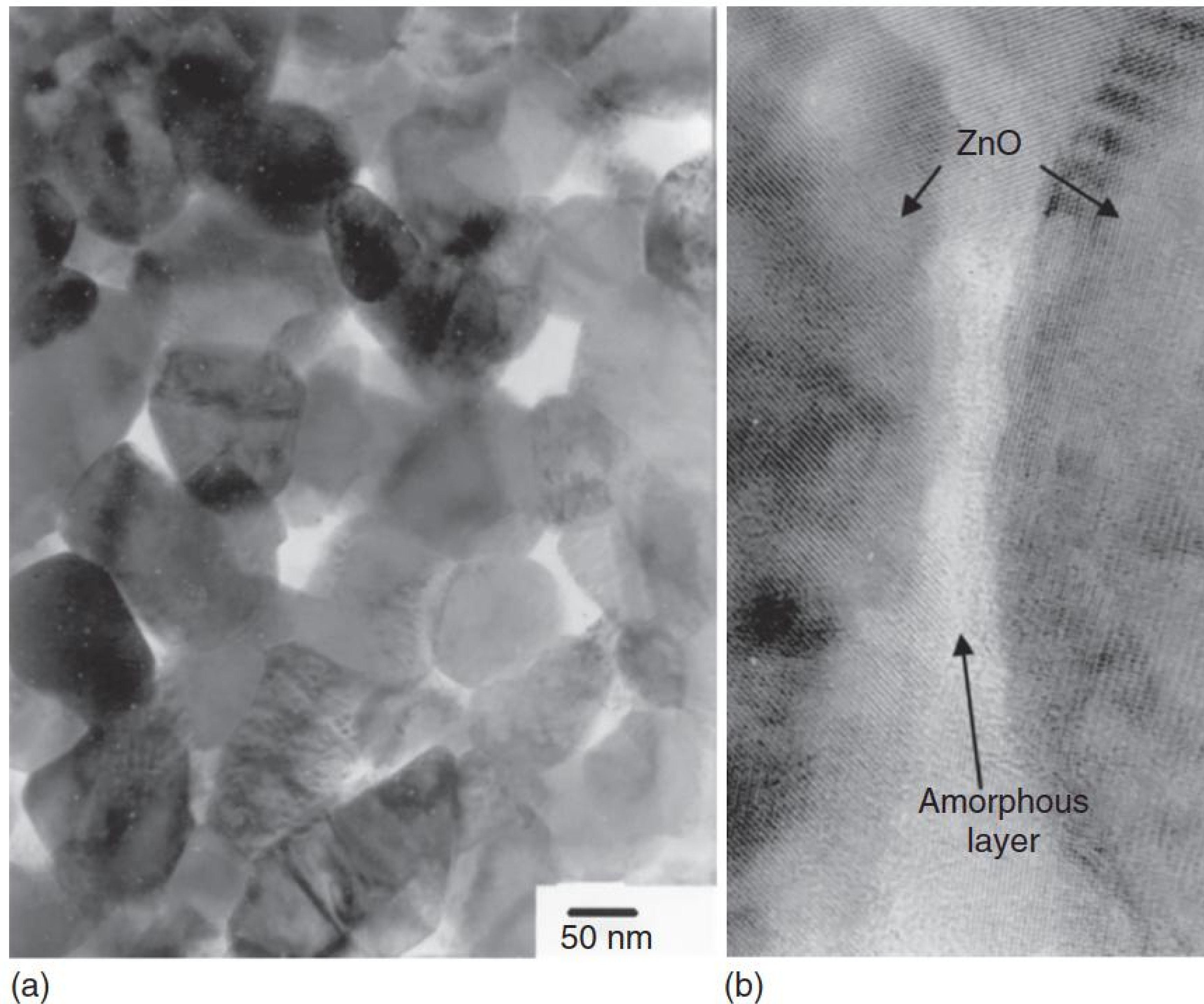


Figure 9.12 (a) TEM micrograph of nanocrystalline ZnO ceramics sintered by SPS at 550 °C within two minutes of holding time and (b) HREM micrograph of the grain boundaries of nanocrystalline ZnO sintered by SPS at 500 °C. Source: Gao et al. 2002 [94]. Reproduced with permission of John Wiley & Sons.

grain boundary depletion of 0.1–1 nm is enough to show obvious conduction nonlinearity.

Luo et al. [96] fabricated ZnO varistor ceramics by SPS. In this method, the mixed nanopowders were placed in a mold. The mold was then put into the vacuum chamber of the SPS machine. The samples were sintered for four minutes at 900 °C. A pressure of 45 MPa was applied on the samples during sintering. The grain size of the SPS samples was less than 1 μm, and the voltage gradients reached 963 V mm^{-1}. Figure 9.13 shows the SEM images of ZnO varistors

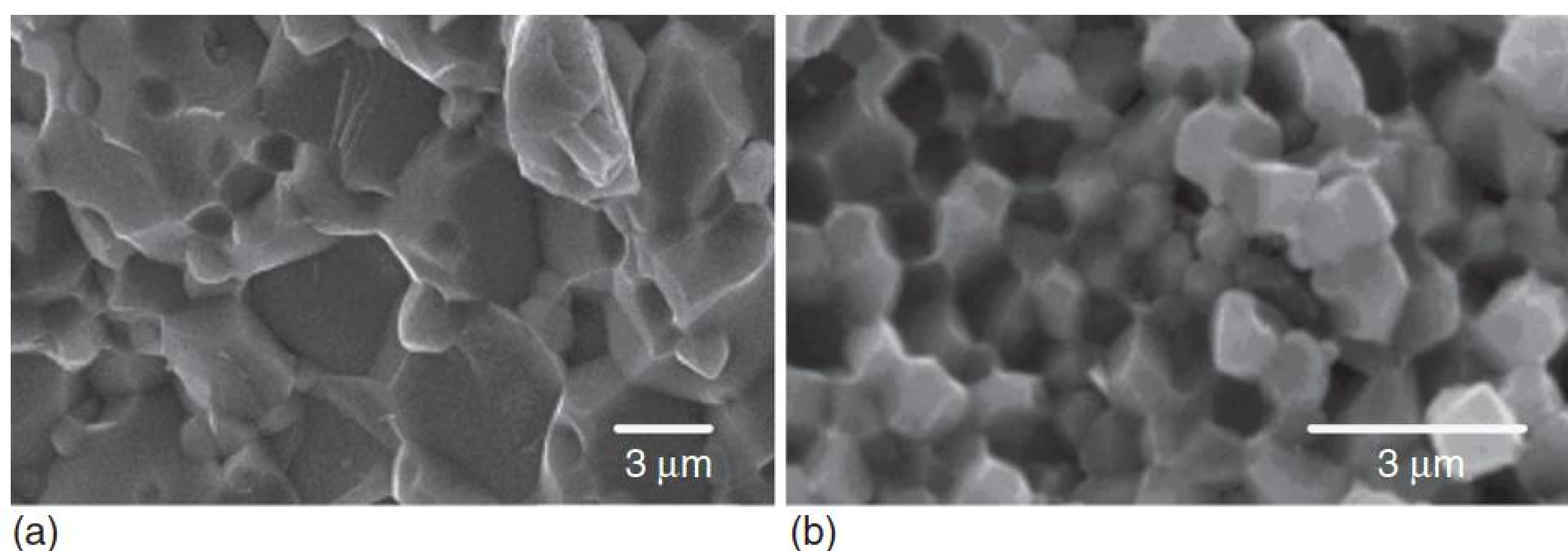


Figure 9.13 SEM images of ZnO varistors fabricated by (a) conventional sintering, 1200 °C, two hours, and (b) spark plasma sintering, 850 °C, five minutes; the length of the line in (b) is 3.46 μm.

fabricated by conventional and SPS techniques; obviously, the SPS produced very uniform grains.

Therefore, the SPS technique shows great potential as a sintering method for manufacturing ZnO materials with desirable varistor properties. It is desired to avoid extra grain growth when the SPS process is employed to densify nanocrystalline ceramics at low temperatures. The successful preparation of nanocrystalline ZnO ceramics by SPS offers a chance to study their special electric properties caused by the nanostructure.

References

1 Anas, S., Mahesh, K.V., Maria, M.J., and Ananthakumar, S. (2017). Sol-gel materials for varistor devices. In: *Sol-Gel Materials for Energy, Environment and Electronic Applications* (ed. S.C. Pillai and S. Hehir), 23–59. Cham: Springer International Publishing.

2 Fan, J. and Sale, F.R. (1994). Citrate gel route processing of ZnO varistors. *British Ceramic Proceedings* 52: 151–157.

3 Cheng, L., Li, G., Zheng, L. et al. (2010). Analysis of high-voltage ZnO varistor prepared from a novel chemically aided method. *Journal of the American Ceramic Society* 93 (9): 2522–2525.

4 Sonder, E., Quinby, T.C., and Kinser, D.L. (1986). ZnO varistors made from powders produced using a urea process. *American Ceramic Society Bulletin* 65 (4): 665–668.

5 Li, Y., Li, G., and Yin, Q. (2006). Preparation of ZnO varistors by solution nano-coating technique. *Materials Science and Engineering B* 130 (1–3): 264–268.

6 Wang, Q., Qin, Y., Xu, G.J. et al. (2008). Low-voltage ZnO varistor fabricated by the solution-coating method. *Ceramics International* 34 (7): 1697–1701.

7 Hembram, K., Sivaprahasam, D., and Rao, T.N. (2011). Combustion synthesis of doped nanocrystalline ZnO powders for varistors applications. *Journal of the European Ceramic Society* 31 (10): 1905–1913.

8 Anas, S., Mangalaraja, R.V., Poothayal, M. et al. (2007). Direct synthesis of varistor-grade doped nanocrystalline ZnO and its densification through a step-sintering technique. *Acta Materialia* 55 (17): 5792–5801.

9 Macary, L.S., Kahn, M.L., Estournès, C. et al. (2009). Size effect on properties of varistors made from zinc oxide nanoparticles through low temperature spark plasma sintering. *Advanced Functional Materials* 19 (11): 1775–1783.

10 Duran, P., Capel, F., Tartaj, J., and Moure, C. (2002). A strategic two-stage low-temperature thermal processing leading to fully dense and fine-grained doped-ZnO varistors. *Advanced Materials* 14 (2): 137–141.

11 Pillai, S.C., Kelly, J.M., McCormack, D.E., and Ramesh, R. (2008). High performance ZnO varistors prepared from nanocrystalline precursors for miniaturised electronic devices. *Journal of Materials Chemistry* 18 (33): 3926–3932.

12 Pillai, S.C., Kelly, J.M., Ramesh, R., and McCormack, D.E. (2013). Advances in the synthesis of ZnO nanomaterials for varistor devices. *Journal of Materials Chemistry C* 1 (20): 3268–3281.
13 Banerjee, A., Ramamohan, T.R., and Patni, M.J. (2001). Smart technique for fabrication of zinc oxide varistor. *Materials Research Bulletin* 36 (7–8): 1259–1267.
14 Anas, S., Mahesh, K.V., Jobin, V. et al. (2013). Nanofillers in ZnO based materials: a 'smart' technique for developing miniaturized high energy field varistors. *Journal of Materials Chemistry C* 1 (39): 6455–6462.
15 Wong, J. (1980). Sintering and varistor characteristics of ZnO-Bi_2O_3 ceramics. *Journal of Applied Physics* 51 (8): 4453–4459.
16 Eda, K., Inada, M., and Matsuoka, M. (1983). Grain growth control in ZnO varistors using seed grains. *Journal of Applied Physics* 54 (2): 1095–1099.
17 Kingery, W.D. (1960). *Introduction to Ceramics*. New York: Wiley.
18 Lee, W.H., Chen, W.T., and Lee, Y.C. (2008). Performance enhancement of ZnO-based multilayer varistor by vonstrained sintering. *Journal of the American Ceramic Society* 91 (9): 2938–2942.
19 Duran, P., Capel, F., Tartaj, J., and Moure, C. (2001). Sintering behavior and electrical properties of nanosized doped-ZnO powders produced by metallorganic polymeric processing. *Journal of the American Ceramic Society* 84 (8): 1661–1668.
20 Pillai, S.C., Kelly, J.M., McCormack, D.E., and Ramesh, R. (2004). Self-assembled arrays of ZnO nanoparticles and their application as varistor materials. *Journal of Materials Chemistry* 14 (10): 1572–1578.
21 Shi, J., Cao, Q., Wei, Y., and Huang, Y. (2003). ZnO varistor manufactured by composite nano-additives. *Materials Science and Engineering B* 99 (1): 344–347.
22 Mazaheri, M., Zahedi, A.M., and Sadrnezhaad, S.K. (2008). Two-step sintering of nanocrystalline ZnO compacts: effect of temperature on densification and grain growth. *Journal of the American Ceramic Society* 91 (1): 56–63.
23 Subasri, R., Asha, M., Hembram, K. et al. (2009). Microwave sintering of doped nanocrystalline ZnO and characterization for varistor applications. *Materials Chemistry and Physics* 115 (2): 677–684.
24 Pillai, S.C., Kelly, J.M., McCormack, D.E. et al. (2003). The effect of processing conditions on varistors prepared from nanocrystalline ZnO. *Journal of Materials Chemistry* 13 (10): 2586–2590.
25 Chandler, C.D., Roger, C., and Hampden-Smith, M.J. (1993). Chemical aspects of solution routes to perovskite-phase mixed-metal oxides from metal-organic precursors. *Chemical Reviews* 93 (3): 1205–1241.
26 Levinson, L.M. and Philipp, H.R. (1986). Zinc oxide varistors - a review. *American Ceramic Society Bulletin* 65 (4): 639–646.
27 Anas, S., Metz, R., Sanoj, M.A. et al. (2010). Sintering of surfactant modified ZnO–Bi_2O_3 based varistor nanopowders. *Ceramics International* 36 (8): 2351–2358.
28 Anas, S., Mukundan, P., Sanoj, A.M. et al. (2010). Synthesis of ZnO based nanopowders via a non-hydrolytic sol gel technique and their densification

behaviour and varistor properties. *Processing and Application of Ceramics* 4 (1): 7–14.

29 Cheng, L.H., Zheng, L.Y., Meng, L. et al. (2012). Electrical properties of Al_2O_3-doped ZnO varistors prepared by sol–gel process for device miniaturization. *Ceramics International* 38 (1): S457–S461.

30 Dong, X.U., Jiang, B., Jiao, L. et al. (2012). Sol-gel synthesis of Y_2O_3-doped ZnO thin films varistors and their electrical properties. In: *2012 Postdoctoral Symposium of China on Materials Science & Engineering – Advanced Materials for Sustainable Development*, vol. 22, s110–s114. Elsevier BV.

31 Hohenberger, G. and Tomandl, G. (1992). Sol-gel processing of varistor powders. *Journal of Materials Research* 7 (3): 546–548.

32 Huang, Y.Q., Meidong, L., Yike, Z. et al. (2001). Preparation and properties of ZnO-based ceramic films for low-voltage varistors by novel sol-gel process. *Materials Science and Engineering B* 86 (3): 232–236.

33 Zhang, J., Cao, S., Zhang, R. et al. (2005). Effect of fabrication conditions on I–V properties for ZnO varistor with high concentration additives by sol–gel technique. *Current Applied Physics* 5 (4): 381–386.

34 Lauf, R.J. and Bond, W.D. (1984). Fabrication of high-field zinc oxide varistors by sol-gel processing. *American Ceramic Society Bulletin* 63 (2): 278–281.

35 Liu, T.T., Wang, M.H., Zhang, H.P., and Zhao, Z.Y. (2015). Sol–gel synthesis of doped nanocrystalline ZnO powders using xanthan gum and varistor properties study. *Journal of Materials Science: Materials in Electronics* 26 (11): 9056–9062.

36 Pillai, S.C., Kelly, J.M., McCormack, D.E., and Ramesh, R. (2006). Effect of step sintering on breakdown voltage of varistors prepared from nanomaterials by sol gel route. *Advances in Applied Ceramics* 105 (3): 158–160.

37 Puyane, R., Toal, F., and Hampshire, S. (1996). Production of doped ZnO powders for varistor applications using sol-gel techniques. *Journal of Sol-Gel Science and Technology* 6 (3): 219–225.

38 Puyané, R., Guy, I., and Metz, R. (1998). High performance varistor discs obtained from chemically synthesized doped zinc oxide powder. *Journal of Sol-Gel Science and Technology* 13 (1–3): 575–578.

39 Westin, G., Ekstrand, Å., Nygren, M. et al. (1994). Preparation of ZnO-based varistors by the sol–gel technique. *Journal of Materials Chemistry* 4 (4): 615–621.

40 Ya, K.X., Diao, W.T., Han, Y. et al. (1997). Sol-gel process doped ZnO nanopowders and their grain growth. *Materials Research Bulletin* 32 (9): 1165–1171.

41 Wang, M.H., Zhao, Z.Y., and Liu, T.T. (2015). Synthesis of Pr-doped ZnO nanoparticles by sol–gel method and varistor properties study. *Journal of Alloys and Compounds* 621: 220–224.

42 Lorenz, A., Ott, J., Harrer, M. et al. (2001). Modified citrate gel routes to ZnO-based varistors. *Journal of the European Ceramic Society* 21 (10): 1887–1891.

43 Sinha, A. and Sharma, B.P. (1997). Novel route for preparation of high voltage varistor powder. *Materials Research Bulletin* 32 (11): 1571–1579.

44 Rahul, S.P., Mahesh, K.V., Sujith, S.S. et al. (2014). Processing of La_2O_3 based rare earth non-linear resistors via combustion synthesis. *Journal of Electroceramics* 32 (4): 292–300.

45 Hingorani, S., Shah, D.O., and Multani, M.S. (1995). Effect of process variables on the grain growth and microstructure of ZnO–Bi_2O_3 varistors and their nanosize ZnO precursors. *Journal of Materials Research* 10 (2): 461–467.

46 Haile, S.M., Johnson, D.W., Wiseman, G.H., and Bowen, H.K. (1989). Aqueous precipitation of spherical zinc oxide powders for varistor applications. *Journal of the American Ceramic Society* 72 (10): 2004–2008.

47 Nobrega, M.C.S., Zolotar, M.S., Mannheimer, W.A., and Espinola, A. (1992). ZnO varistors produced using colloidal-gel powders. *Journal of Non-Crystalline Solids* 147: 803–807.

48 Viswanath, R.N., Ramasamy, S., Ramamoorthy, R. et al. (1995). Preparation and characterization of nanocrystalline ZnO based materials for varistor applications. *Nanostructured Materials* 6 (5–8): 993–996.

49 Schulz, R., Boily, S., Joly, A. et al. (2003). Varistor based on nanocrystalline powder produced by mechanical grinding. US Patent No. 6,620,346. Washington, D.C.: U.S. Patent and Trademark Office.

50 Fah, C.P. and Wang, J. (2000). Effect of high-energy mechanical activation on the microstructure and electrical properties of ZnO-based varistors. *Solid State Ionics* 132 (1–2): 107–117.

51 Hingorani, S., Pillai, V., Kumar, P. et al. (1993). Microemulsion mediated synthesis of zinc-oxide nanoparticles for varistor studies. *Materials Research Bulletin* 28 (12): 1303–1310.

52 Varma, H.K., Ananthakumar, S., Perumal, P. et al. (1993). Microwave processing of rare earth oxide doped ZnO varistors. *Ceramic Transactions, Microwaves: Theory and Application in Materials Processing II* 36: 115–122.

53 Varma, H.K., Ananthakumar, S., Warrier, K.G.K., and Damodaran, A.D. (1996). Synthesis of zinc oxide varistors through microwave-derived precursor. *Ceramics International* 22 (1): 53–56.

54 Maria, M.J., Balanand, S., Anas, S. et al. (2016). Zn-dust derived ultrafine grained ZnO non-linear ceramic resistors via in-situ thermal oxidation of cermet reactant mixture. *Materials and Design* 92: 387–396.

55 Hembram, K., Vijay, R., Rao, Y.S., and Rao, T.N. (2009). Doped nanocrystalline ZnO powders for non-linear resistor applications by spray pyrolysis method. *Journal of Nanoscience and Nanotechnology* 9 (7): 4376–4382.

56 Shojaee, S.A., Shahraki, M.M., Sani, M.A.F. et al. (2010). Microstructural and electrical properties of varistors prepared from coated ZnO nanopowders. *Journal of Materials Science: Materials in Electronics* 21 (6): 571–577.

57 Riahi-Noori, N., Sarraf-Mamoory, R., Alizadeh, P., and Mehdikhani, A. (2008). Synthesis of ZnO nano powder by a gel combustion method. *Journal of Ceramic Processing Research* 9 (3): 246–249.

58 Sousa, V.C., Segadaes, A.M., Morelli, M.R., and Kiminami, R.H.G.A. (1999). Combustion synthesized ZnO powders for varistor ceramics. *International Journal of Inorganic Materials* 1 (3): 235–241.

59 Hwang, C.C. and Wu, T.Y. (2004). Synthesis and characterization of nanocrystalline ZnO powders by a novel combustion synthesis method. *Advanced Materials Research* 111 (2–3): 197–206.

60 Suvaci, E. and Özgür Özer, İ. (2005). Processing of textured zinc oxide varistors via templated grain growth. *Journal of the European Ceramic Society* 25 (9): 1663–1673.

61 Kruis, F.E., Fissan, H., and Peled, A. (1998). Synthesis of nanoparticles in the gas phase for electronic, optical and magnetic applications—a review. *Journal of Aerosol Science* 29 (5–6): 511–535.

62 Li, W.J., Shi, E.W., Tian, M.Y. et al. (1999). The synthesis of ZnO acicular particles by the hydrothermal discharging-gas method. *Journal of Materials Research* 14 (4): 1532–1537.

63 Lu, H., Wang, Y., and Lin, X. (2009). Structures, varistor properties, and electrical stability of ZnO thin films. *Materials Letters* 63 (27): 2321–2323.

64 Lin, Y., Zhang, Z., Tang, Z. et al. (1999). Characterisation of ZnO-based varistors prepared from nanometre precursor powders. *Advanced Functional Materials* 9 (5): 205–209.

65 Patil, K.C., Aruna, S.T., and Mimani, T. (2002). Combustion synthesis: an update. *Current Opinion in Solid State and Materials Science* 6 (6): 507–512.

66 Dhage, S.R., Navale, S.C., and Ravi, V. (2007). The influence of surfactant on ZnO varistors. *Ceramics International* 33 (2): 289–291.

67 Kim, E.D., Kim, C.H., and Oh, M.H. (1985). Role and effect of Co_2O_3 additive on the upturn characteristics of ZnO varistors. *Journal of Applied Physics* 58 (8): 3231–3235.

68 Özgür, Ü., Alivov, Y.I., Liu, C. et al. (2005). A comprehensive review of ZnO materials and devices. *Journal of Applied Physics* 98 (4): 041301.

69 Savary, E., Marinel, S., Gascoin, F. et al. (2011). Peculiar effects of microwave sintering on ZnO based varistors properties. *Journal of Alloys and Compounds* 509 (21): 6163–6169.

70 Małecka, B., Drożdż-Cieśla, E., and Małecki, A. (2004). Mechanism and kinetics of thermal decomposition of zinc oxalate. *Thermochimica Acta* 423 (1): 13–18.

71 Nahm, C.W. (2003). Nonlinear properties and stability against dc accelerated aging stress of praseodymium oxide-based ZnO varistors by Er_2O_3, doping. *Solid State Communications* 126 (5): 281–284.

72 Ramírez, M.A., Bassi, W., Parra, R. et al. (2008). Comparative electrical behavior at low and high current of SnO_2- and ZnO-based varistors. *Journal of the American Ceramic Society* 91 (7): 2402–2404.

73 Wang, C.M., Wang, J.F., Su, W.B. et al. (2006). Microstructure and nonlinear electrical characteristics of $SnO_2 \cdot CuO \cdot Nb_2O_5$ system. *Journal of Materials Science* 41 (4): 1273–1275.

74 Yuan, F. and Ryu, H. (2004). Microstructure of varistors prepared with zinc oxide nanoparticles coated with Bi_2O_3. *Journal of the American Ceramic Society* 87 (4): 736–738.

75 Ya, K.X., Yin, H., De, T.M., and Jing, T.M. (1998). Analysis of ZnO varistors prepared from nanosize ZnO precursors. *Materials Research Bulletin* 33 (11): 1703–1708.

76 Chu, S.Y., Yan, T.M., and Chen, S.L. (2000). Analysis of ZnO varistors prepared by the sol–gel method. *Ceramics International* 26 (7): 733–737.
77 Hishita, S., Yao, Y., and Shirasaki, S. (1989). Zino oxide varistors made from powders prepared by amine processing. *Journal of the American Ceramic Society* 72 (2): 338–340.
78 Pillai, S.C., Kelly, J.M., McCormack, D.E., and Ramesh, R. (2004). Microstructural analysis of varistors prepared from nanosize ZnO. *Materials Science and Technology* 20 (8): 964–968.
79 Shahraki, M.M., Shojaee, S.A., Sani, M.A.F. et al. (2011). Two-step sintering of ZnO varistors. *Solid State Ionics* 190 (1): 99–105.
80 Rustum, R., Agrawal, D., Cheng, J., and Gedevanishvili, S. (1999). Full sintering of powdered-metal bodies in a microwave field. *Nature* 399 (6737): 668–670.
81 Vaidhyanathan, B., Annapoorani, K., Binner, J., and Raghavendra, R. (2010). Microwave sintering of multilayer integrated passive devices. *Journal of the American Ceramic Society* 93 (8): 2274–2280.
82 Periyat, P., Leyland, N., McCormack, D.E. et al. (2010). Rapid microwave synthesis of mesoporous TiO_2 for electrochromic displays. *Journal of Materials Chemistry* 20 (18): 3650–3655.
83 Padmanabhan, S.C., Ledwith, D., Pillai, S.C. et al. (2009). Microwave-assisted synthesis of ZnO micro-javelins. *Journal of Materials Chemistry* 19 (48): 9250–9259.
84 Ledwith, D., Pillai, S.C., Watson, G.W., and Kelly, J.M. (2004). Microwave induced preparation of a-axis oriented double-ended needle-shaped ZnO microparticles. *Chemical Communications* 20: 2294–2295.
85 Synnott, D.W., Seery, M.K., Hinder, S.J. et al. (2013). Novel microwave assisted synthesis of ZnS nanomaterials. *Nanotechnology* 24 (4): 045704.
86 Synnott, D.W., Seery, M.K., Hinder, S.J. et al. (2013). Anti-bacterial activity of indoor-light activated photocatalysts. *Applied Catalysis B: Environmental* 130: 106–111.
87 Xu, G.F., Lloyd, I.K., Carmel, Y. et al. (2001). Microwave sintering of ZnO at ultra high heating rates. *Journal of Materials Research* 16 (10): 2850–2858.
88 Birnboim, A., Gershon, D., Calame, J. et al. (1998). Comparative study of microwave sintering of zinc oxide at 2.45, 30, and 83 GHz. *Journal of the American Ceramic Society* 81 (6): 1493–1501.
89 Roy, T.K., Bhowmick, D., Sanyal, D., and Chakrabarti, A. (2008). Sintering studies of nano-crystalline zinc oxide. *Ceramics International* 34 (1): 81–87.
90 Lee, W.C., Liu, K.S., and Lin, I. (1999). Electrical properties of microwave-sintered ZnO varistors. *Japanese Journal of Applied Physics* 38 (38): 5500–5504.
91 Lin, I.N., Lee, W.C., Liu, K.S. et al. (2001). On the microwave sintering technology for improving the properties of semiconducting electronic ceramics. *Journal of the European Ceramic Society* 21 (10): 2085–2088.
92 Kutty, T.R.N. and Ezhilvalavan, S. (1994). The influence of Bi_2O_3, non-stoichiometry on the non-linear property of ZnO varistors. *Materials Chemistry and Physics* 38 (3): 267–276.

93 Lorite, I., Rodriguez, M.A., Azough, F. et al. (2012). $ZnAl_2O_4$ and (0.79) $ZnAl_2O_4$–(0.21) Mn_2TiO_4 microwave dielectric ceramics prepared by hot pressing and spark plasma sintering. *Journal of the American Ceramic Society* 95 (3): 1023–1028.

94 Gao, L., Li, Q., Luan, W. et al. (2002). Preparation and electric properties of dense nanocrystalline zinc oxide ceramics. *Journal of the American Ceramic Society* 85 (4): 1016–1018.

95 Shen, Z. and Nygren, M. (2005). Microstructural prototyping of ceramics by kinetic engineering: applications of spark plasma sintering. *Chemical Record* 5 (3): 173–184.

96 Luo, F.C., He, J.L., Lin, Y.H., and Hu, J. (2008). Properties of ZnO varistors prepared with nano-sized powders. *Key Engineering Materials* 368–372: 514–516.

10

Titanium-Based Dual-function Varistor Ceramics

Miniaturizing electronic devices is always a desirable target. The integration of electronic circuitry into integrated circuit (IC) chips has brought large volume and weight reductions, so there is an increasing trend toward the integration of passive electronic–ceramic components. Also with the widespread use of micromotors in the electronic devices, the harmful effects of high frequency and spike surges appear; in order to protect the electronic circuits from the damage of surge voltages, the application of varistors within the low-voltage field also increased. The ZnO varistor is difficult to achieve a low breakdown voltage technology but mainly for the high-voltage varistor. The capacitor–varistor dual-function components, such as TiO_2, $SrTiO_3$, and $CaCu_3Ti_4O_{12}$ (CCTO) varistors, have realized the goal to achieve component miniaturization and provide superior high-frequency and high-amplitude transient voltage protection. Because of its outstanding dielectric properties and nonohmic characteristics and simple and straightforward preparation, CCTO is considered a very promising capacitor–varistor dual-function material. Another kind of titanium-based dual-function ceramics is donor-doped $BaTiO_3$ ceramics [1, 2], which exhibit positive temperature coefficient of resistivity (PTCR) performance and nonlinear V–I property and have been extensively used in current-limiting applications, such as overload protection devices, delay line switches, and self-regulating heaters.

10.1 $SrTiO_3$ Varistors

10.1.1 Introduction

The internal boundary layer capacitor is one of the most commercially successful of that class of electronic components in which the grain boundary plays an active role in determining the electrical properties. A thin insulating layer separating the semiconducting grains leads to a high apparent permittivity and high resistivity [3]. Strontium titanate based internal boundary layer capacitors in particular are widely applied to the electronic circuits because of the small temperature dependence of their dielectric properties and the low dissipation factor [4–6].

In the 1980s, the $SrTiO_3$ varistor was successfully developed and put into commercial application by Panasonic, Taiyo Yuden, TDK, and Murata [7]. The $SrTiO_3$

varistor has a high dielectric constant and good nonlinear characteristics, so it has both capacitor–varistor dual function. In the absence of abnormal surge (which is called as over-voltage in power systems), it plays the role of the capacitor that can filter out high-frequency interference and the role of absorbing the surge as the voltage-suppressing varistor. Particularly, the voltage temperature coefficient of $SrTiO_3$ varistors is smaller than that of ZnO varistors and can even be positive. In addition more, their temperature stability is better than that of the normal ceramic capacitors. Therefore, in the low-voltage area, the $SrTiO_3$ varistor has very broad application prospects. Depending on the application, the $SrTiO_3$ varistor ceramics are usually shaped into round or ring. The ring-shaped varistors are mainly used to eliminate the noise in the micromotors, and the round-shaped ones are usually applied in various electronic circuits, absorbing surges, protecting triacs, or being bypass capacitors.

10.1.2 Microstructure of $SrTiO_3$ Varistors

At room temperature, $SrTiO_3$ has typical perovskite-type crystal structure of cubic system, as shown in Figure 10.1. The crystal constant a is 3.905 Å. Below 106 K, $SrTiO_3$ changes into a tetragonal structure [8].

Similar to the ZnO varistor, the $SrTiO_3$ varistor also has a polycrystalline structure and is also composed of semiconductive grains and insulating grain boundaries (GB) [9]. This structure is the origin of the high permittivity and nonohmic current–voltage behavior, and it is believed that Schottky barriers exist on the grain boundaries. The Schottky barrier heights at these interfaces are strongly affected by the interface chemistry [10].

The surface states on the interfaces trap the carriers and make the layers insulating. Therefore, the ceramic is insulating under low electric field. Under high electric field, the surface states are filled, and the potential barrier is lowered. Over the threshold voltage, the ceramic becomes conductive.

10.1.3 Preparation of $SrTiO_3$ Varistors

$SrTiO_3$ varistors are usually prepared by the typical ceramic-sintering method. Generally, two steps of sintering are required in the preparation. The first step is

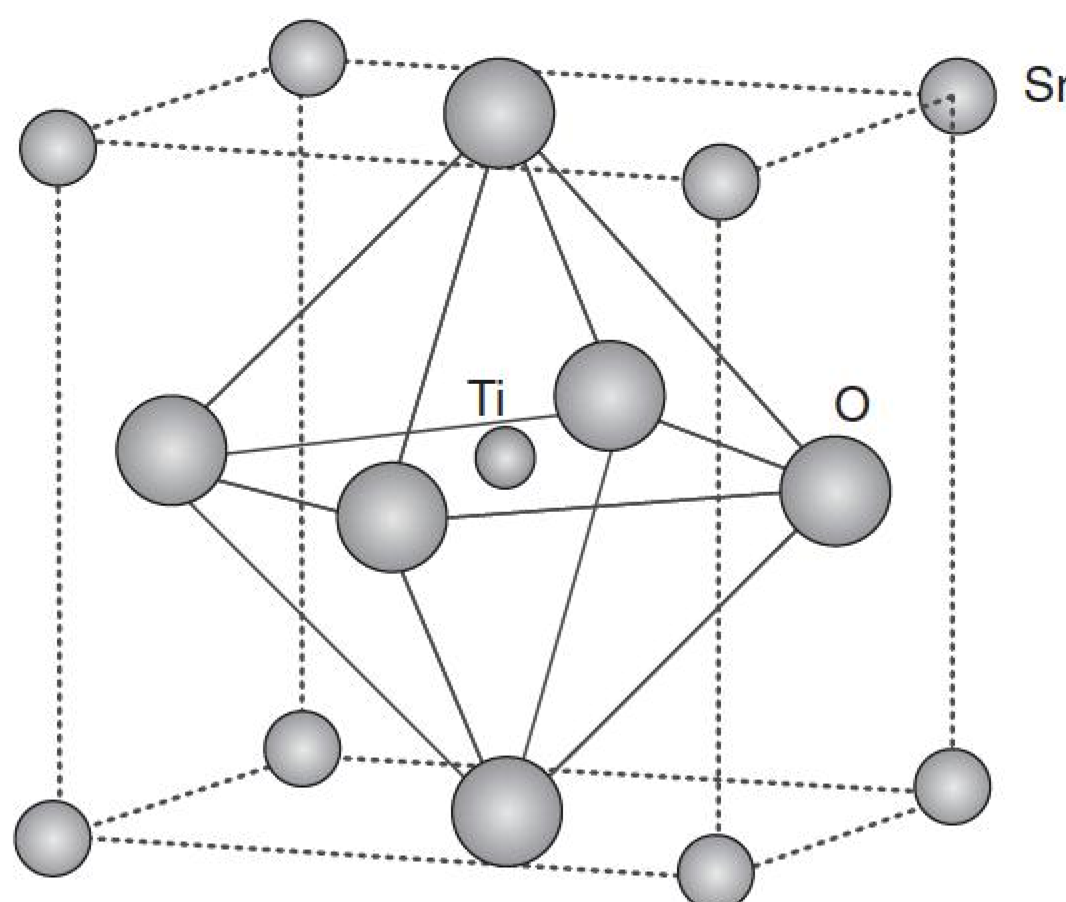


Figure 10.1 The crystal structure of $SrTiO_3$. Source: Li et al. 2003 [8]. Modified with permission from Elsevier.

to make the grains semiconductive through sintering the ceramic in a reducing atmosphere. The second step is to make the grain boundaries insulating and obtain the nonohmic property; this step is usually performed in an oxidizing atmosphere in a lower temperature.

Usually, the strontium titanate ($SrTiO_3$) powder is synthesized by calcining strontium carbonate ($SrCO_3$) and titanium dioxide (TiO_2). The powders are wet-mixed with ethanol for 24 hours. After drying, the mixture is calcined at a high temperature of over 1000 °C for three hours. During the calcination process, $SrCO_3$ dissociates as SrO and CO_2 [9]:



$$SrCO_3 \rightarrow SrO + CO_2 \uparrow \quad (10.1)$$

The solid-state reaction for the calcination step is as follows:



$$SrO + TiO_2 \rightarrow SrTiO_3 \quad (10.2)$$

The overall reaction of sintering is as follows:



$$SrCO_3 + TiO_2 \rightarrow SrTiO_3 + CO_2 \uparrow \quad (10.3)$$

The mixture is pressed into disks at a pressure of 9.8×10^7 Pa [9], and the pressed disks are then sintered at 1450 °C for three hours in air. The sintered samples are reduced at 1300 °C for five hours in a 50 mol% H_2–Ar flowing atmosphere. The obtained semiconducting samples are polished on both sides. In order to compose the n–i–n structure, the samples are partially reoxidized at 800–1300 °C for one hour in air [11].

The ratio of $SrCO_3$ and TiO_2 is essential to control the performances of the ceramic. According to the phase diagram of SrO–TiO_2, the eutectic temperature is 1860 °C when SrO_2 is excessive and 1440 °C when TiO_2 is excessive. Moderate excessive TiO_2 helps the liquid phase to be formed under a relatively lower temperature. Generally, the ratio of Sr/Ti is in the range from 0.98 to 1.02, excessive Ti is usually conducive in the liquid-phase sintering, which leads to lowered sintering temperature, and the semiconductivity improved. However, when the ratio is less than 0.98, i.e. Ti is much more than Sr, free TiO_2 enters the liquid phase and enhances its viscosity, hindering the sintering process and grain growth. When the Sr/Ti ratio is slightly more than 1.0, the sintering and grain growth are benefitted. When the ratio is bigger, the semiconducting is not well formed, and the property of the ceramic is degraded.

To make the grains semiconductive, at least one of the high-valence ions, such as Nb_2O_5, Ta_2O_5, WO_3, Pr_6O_{11}, or CeO_2, is usually doped as donors [12]; sometimes, one of the rare earth (RE) ions, such as La^{3+}, Y^{3+}, Dy^{3+}, or Sm^{3+}, is added at the same time [13–15]. As donors, the high-valence ions, such as Nb^{5+}, takes the lattice site of Ti^{4+}, and the rare earth ions takes the site of Sr^{2+}. Both reactions of replacement give out electrons as carriers and lower the resistivity of grains. The amount of donor doping is usually in the range of 0.01–5.0 mol%. As an example [16, 17], 0.5 mol% La_2O_3, 0.2 mol% SiO_2, and 0.5 mol% $MnCO_3$ were added into the $SrTiO_3$ powder for making $SrTiO_3$-based varistor materials employing conventional ceramic processing steps used in making ZnO-based varistor ceramics. After the sintering at 1350 °C for three hours, the samples were

heat treated in air at different temperatures for various durations to achieve the varistor property.

To tune the permittivity, nonohmic property, and temperature stability, additives such as Al_2O_3, Sb_2O_3, $BaCO_3$, $CaCO_3$, $MnCO_3$, Cr_2O_3,SiO_2, Bi_2O_3, Fe_2O_3, NiO, ZnO, and CuO are often doped as acceptors to effectively enhance the density of acceptors [18, 19] and raise the barrier height and the resistivity of the grain boundaries. SiO_2 forms a liquid phase in the sintering process, which can effectively promote grain growth. The addition of Al_2O_3 can improve the density of the ceramic. A mineralizer is used as the starting material in order to lower the sintering temperature and enhance the density of the ceramic. Therefore, the nonohmic performance is evidently improved. The amount of these additives are usually in the range of 0.01–3.0 mol%.

Except $SrTiO_3$ is selected as the main ingredient, sometimes, $(Ca_xSr_{1-x})TiO_3$, $(Ba_ySr_{1-y})TiO_3$, or $(Mg_zSr_{1-z})TiO_3$ is also used, where x, y, z are in the range of 0.001–0.5 mol% [20].

A few attempts were made to control the grain boundary structure and the defect chemistry in electronic ceramics by synthesizing the ceramics from surface-coated powders [21]. The $SrTiO_3$ powders were dispersed in NaOH solutions and then were dried at 120 °C for 24 hours and heat treated at 300–500 °C to transform the absorbed layer into Na_2O. The uniaxial hot-press sintering method was applied on the surface-coated powders at 1250 °C in the N_2 atmosphere for 30 minutes under a pressure of 25 MPa. This technique has the possibility of distributing additives along the grain boundaries uniformly, and the electrical characteristics of ceramics can be controlled by adjusting the chemical and electrical features of the grain boundaries as a function of the amount of the coating material on the surface of the semiconducting powders.

A $SrTiO_3$-based multilayered film with varistor characteristics has successfully been fabricated by a chemical solution deposition (CSD) method. The layered film varistor satisfies the demands for developing a varistor of miniaturized and highly integrated electronic devices [22].

10.1.4 Performance of $SrTiO_3$

$SrTiO_3$ ceramics have dual functions as a varistor and a capacitor. Presently, the commercial products of $SrTiO_3$ ceramics reach the following parameters: relative dielectric constant ~8000 at 1 kHz, the dielectric loss 0.18%, nonlinear coefficient 43, and voltage gradient 10–100 V mm^{-1} at 1 mA. Doping is an important tool to tailor the performance of the varistor ceramics. Kutty and Philip [23] reported the samples with a relative dielectric constant 10^4–10^5 at 1 kHz, the breakdown voltage from 0.2 to 1.5 V per grain boundary, the nonlinearity coefficient from 6 to 15, and the barrier height from 0.15 to 0.3 eV, depending on the conditions of the second annealing.

Many effects have been tried to improve the nonlinearity and increase the dielectric constant, but the dielectric loss increased in contrary. The Nb-doped $SrTiO_3$ varistors were prepared with the grain size of 120 μm, the relative dielectric constant ε_r of 42 000 (measured at 25 °C, 1 kHz, 1 V_{rms}), and the nonlinear coefficient α of 5 (measured at 25 °C, from 1 to 10 mA cm^{-2}), but the

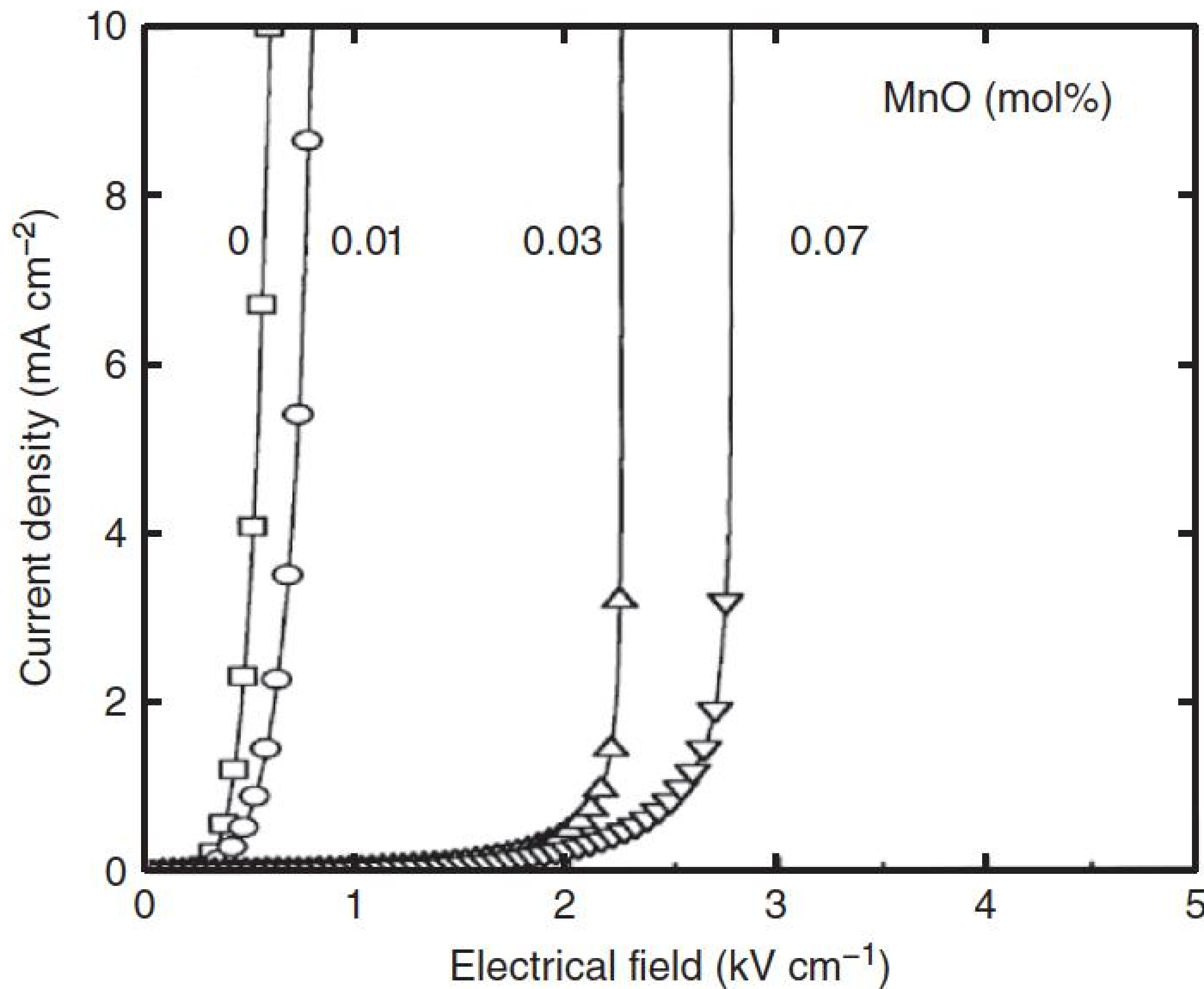


Figure 10.2 *J–E* curves of Nb-doped $SrTiO_3$ with different MnO contents. Source: Adapted from Kim and Kim [24].

dielectric loss tanδ reached 2.9%. When 0.03 mol% MnO was added, the grain size was 72 μm, the varistor nonlinear coefficient was improved to 43 (as shown in Figure 10.2), the ε_r slightly decreased to 34 000, but the dielectric loss was still as high as 4.2% [24].

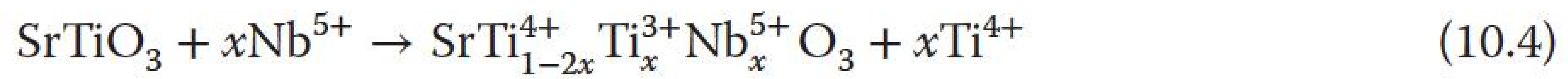
10.1.5 Conduction Mechanism of $SrTiO_3$

The stoichiometric $SrTiO_3$ under room temperature is an insulator with a band gap of 3.2 eV. In order to make a varistor out of $SrTiO_3$, donors and acceptors are added into the materials. Sintered in a reducing atmosphere, the ceramic grains are semiconductive. Sintered in an oxidizing atmosphere thereafter, the ceramic grains cover with insulating intergranular layers. Kim et al. [25] studied the influence of Na-diffusion on the electrical properties of $SrTiO_3$. When Na ions diffused at 1000 °C, the segregation of Na ions was observed by secondary ion mass spectrometry (SIMS) analysis, and the diffusion of Na significantly increased the resistance of grain boundaries. The nonlinear coefficient and the potential barrier height of the Na-diffused samples were about 15 and 0.82 eV, whereas those of air-annealed samples without the diffusion of Na were about 5 and 0.14 eV, respectively. From the complex plane analysis, it was obtained that the deep electronic levels near the grain boundaries were changed from 0.10 to 0.31 eV. From the impedance spectroscopy measurement results, it was suggested that the activation energy, 0.8 eV, measured in the grain originated from the oxygen vacancies, and the activation energy, 1.3 eV, in the grain boundary was from strontium vacancies [12].

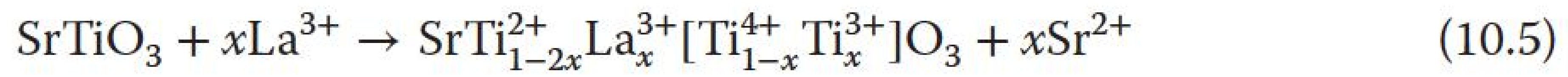
Currently, there are two theories to explain the conduction mechanism of the grains. In the first theory, the carriers are supposed to give out in the substitution reaction induced by donors and captured by Ti^{4+}. In the second theory, it is

supposed that the doped donors generate vacancies on the Sr sites and weaken the Ti—O bonds around them. The oxygen atoms are then freed in a reducing atmosphere, giving out electrons as charge carriers.

Trivalent ions that have similar size to Sr^{2+}, or pentavalent ions, such as Nb^{5+} [26], which have similar size to Ti^{4+}, are often chosen as donors to promote the semiconduction of grains. Generally, it is supposed that when a small amount of trivalent ions is doped, the ions will enter the lattice sites of Sr^{2+} and give out electrons to change Ti^{4+} into Ti^{3+} ($Ti^{4+}\cdot e^-$) and weakly bonded electrons are produced, which are in the metastable state. Under an applied electric field, these weakly bonded electrons can easily become conductive carriers to decrease the resistivity of the grains. Take $Nb^{5+}$and La^{3+} doping as examples, the substitution reactions are [20]:

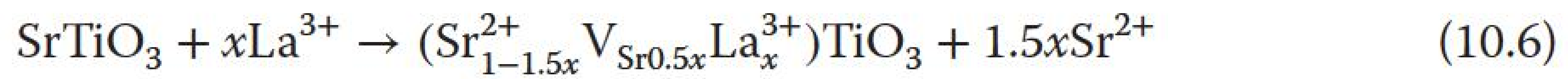


$$SrTiO_3 + xNb^{5+} \rightarrow SrTi^{4+}_{1-2x}Ti^{3+}_xNb^{5+}_xO_3 + xTi^{4+} \tag{10.4}$$



$$SrTiO_3 + xLa^{3+} \rightarrow SrTi^{2+}_{1-2x}La^{3+}_x[Ti^{4+}_{1-x}Ti^{3+}_x]O_3 + xSr^{2+} \tag{10.5}$$

When a large amount of donors is doped, the conducting mechanism is mainly the second one. Vacancies on Sr^{2+} are produced when donors enter the lattices by the following reaction:



$$SrTiO_3 + xLa^{3+} \rightarrow (Sr^{2+}_{1-1.5x}V_{Sr0.5x}La^{3+}_x)TiO_3 + 1.5xSr^{2+} \tag{10.6}$$

Affected by the vacancies on the Sr sites, V_{Sr}, the Ti—O bonds are weakened. At a high temperature and a reducing atmosphere, the oxygen tends to volatile. Electrons are given out as carriers by the reaction [12]:



$$O_O \rightarrow V^{2+}_O + 2e^- + \frac{1}{2}O_2 \uparrow \tag{10.7}$$

The insulating grain boundaries are formed in an oxidizing atmosphere [13, 27]. The high-resistive surface layer is formed by oxygen diffusion and surface chemisorption at the grain boundaries during the heat treatment in air [27]. The formation of the grain boundary layer (GBL) is closely related to the doped acceptors. The acceptors segregate at the grain boundaries and diffuse into the grains. A substitution reaction occurs and the depletion layer forms on the edge of the grain. Ag^{2+}, Ni^{2+}, and Li^+ [26] are often used as acceptors to promote the segregation at the grain boundaries to enhance their insulation by taking the site of Sr^{2+}. Divalent ions such as Cu^{2+} and Mn^{2+} are used to take the site of Ti^{4+}. Take Mn^{2+} for example, the substitution reaction is



$$MnO \rightarrow V^{2+}_O + O_O + Mn^{2-}_{Ti} \tag{10.8}$$

The segregation of acceptor ions at the grain boundaries is mainly fulfilled at the cooling stage. Also, the optimal cooling rate and oxygen atmosphere are both favorable to the decrease of tanδ and improvement of nonlinear I–V characteristics [11, 26]. In the oxidizing atmosphere, oxygen diffuses along the grain boundaries. Both the oxygen and the acceptors capture electrons and help with the formation of the grain boundary barrier. A direct comparison of the X-ray intensity ratios for each of the compositional elements present at the grain boundary in potassium-diffused $SrTiO_3$ ceramics using the high spatial resolution scanning

transmission electron micrograph (STEM) reveals not only the impurity in the grain boundary segregation but also the impurity site occupation, the presence of a potassium grain boundary segregation layer thinner than 20 nm, and potassium Sr site occupation in the samples, which could contribute to its resulting varistor characteristics [28].

Hitomi et al. [29] produced $(Sr_{0.94}Ba_{0.01}Ca_{0.05})_{0.99}TiO_3$ ceramics by sintering at an oxygen partial pressure of 10^{-8} Pa and reoxidization at 1200 °C in air, and investigated by transmission electron microscopy (TEM) and energy-dispersive X-ray spectroscopy analysis, it was found that during reoxidization, the metal atoms of Bi, Pb, and Cu come from the ceramic surface by diffusing along the grain boundaries, together with O atoms. The metal atoms migrate deeply into the ceramics, but hardly penetrate the inside of the grains so that they replace the Sr and Ti atoms in close vicinity of the boundaries. The Bi, Pb, and Cu atoms have an affinity to the O atoms and set them at the surrounding O vacancy sites. This is a reason why a thin dielectric boundary layer (poor in the O vacancies) is formed around each grain in the ceramics.

According to the Koops model [30], the effective permittivity ε_{eff} is expressed as

$$\varepsilon_{\text{eff}} = \frac{\varepsilon_{\text{gb}} t_{\text{gb}} t_{\text{g}} (\sigma_{\text{gb}} - \sigma_{\text{g}})^2}{(t_{\text{gb}}\sigma_{\text{g}} - t_{\text{g}}\sigma_{\text{gb}})^2} \tag{10.9}$$

where ε_{gb} is the permittivity of the grain boundary, t_{gb} is the average thickness of the grain boundary, t_{g} is the average diameter of the grains, σ_{gb} is the conductivity of the grain boundary, and σ_{g} is conductivity of the grains. As the conductivity of the grain boundaries is much greater than that of the grains, and the diameters of the grains are much greater than the grain boundary thickness, and assume the dielectric constants for the grain boundary are the same, the equation is simplified as

$$\varepsilon_{\text{eff}} = \varepsilon_{\text{gb}} \frac{t_{\text{g}}}{t_{\text{gb}}} \tag{10.10}$$

The effective dielectric constant ε_{eff} is inversely proportional to the ratio of thickness of the grain boundary to grain size. This expression explains why the ceramic has a relatively large permittivity.

A GBL semiconducting ceramic is integrated from many capacitor elements, which are constructed with the very thin dielectric boundary layers and the semiconducting insides (rich in the O vacancies) as electrodes and consequently has a high capacitance.

10.2 TiO_2-Based Varistors

10.2.1 Introduction

In the 1980s, the Bell Labs developed the TiO_2 varistors system in order to replace the SiC varistors [31]. Its main ingredient is TiO_2, usually doped with Nb_2O_5, SrO, $BaCO_3$, Bi_2O_3, CeO_2, Sb_2O_5, MnO_2, and other oxides. TiO_2 varistor ceramics have good nonlinear I–V characteristics and a high dielectric constant that are

good enough to replace $SrTiO_3$ varistors in performance [32]. It can be one-step sintered in atmosphere, so the production process is relatively simple and the cost is low. The surge absorption capability and the capacitance of TiO_2 varistors are higher than those of ZnO varistors. Its most prominent feature is that it is much easier to achieve low breakdown voltage technology, which makes it a better material in the low-voltage field. TiO_2-based varistors have shown a particularly good potential to meet with the requirement of modern electronic devices, in which low breakdown voltage components are essential.

Overall, the TiO_2 capacitor–varistor ceramic is a kind of composite functional element. Because of its low threshold electric field (lower than 6 V), high nonlinear coefficient (higher than 9), and large dielectric constant (order of 10^4–10^5), TiO_2 can achieve the miniaturization of components and circuits and also has the dual characteristics of a capacitor and a varistor. Therefore, TiO_2 is the dominant of composite function components in the low-voltage field.

10.2.2 Preparation of TiO_2-Based Varistors

Although different sintering processes have been proposed for producing TiO_2 varistor ceramics, the results indicated that [33] the samples prepared by one-step sintering had a low threshold electric field and a relatively higher dielectric constant.

There are three kinds of TiO_2: rutile, anatase, and brookite, of which the most stable crystal is rutile TiO_2, with a great dielectric constant and a small dielectric loss. Anatase and brookite TiO_2 can be transformed into rutile at a high temperature. An appropriate sintering temperature enables the grain growth, reduces the threshold electric field, and improves the formation of grain boundary. Extra high sintering temperature makes the grain grow too large and leads the grain boundary instable. A low sintering temperature is not conducive to the formation of the grain boundary barrier, and the varistor performance is poor. In the temperature range of 1200–1400 °C, as the temperature decreases, the threshold electric field, the nonlinear coefficient, and the grain boundary resistance all decrease, whereas the grain resistance increases [34–37].

By controlling the sintering atmosphere, grain growth can be controlled. Usually, the sintering of TiO_2 varistors can be controlled by partial pressure of oxygen, and lower oxygen pressure is favorable to form the semiconducting of grains and electrical properties of varistors.

10.2.3 Mechanism of TiO_2 Capacitor–Varistor Ceramics

The dielectric properties of high-purity rutile TiO_2 ceramics were investigated over a wide temperature (100–1073 K) and frequency (20 Hz–10 MHz) ranges [38]. The X-ray photoemission spectroscopy measurement revealed that the sample possessed mixed-valent states of Ti^{3+}/Ti^{4+}, and four thermally activated relaxations were observed. The lowest temperature relaxation featured two Arrhenius segments with the activation energy of 30 and 80 meV for the low- and high-temperature segments, respectively. This relaxation was argued to be a polaron relaxation because of the electrons hopping between Ti^{3+} and Ti^{4+} ions.

The second relaxation appeared around the room temperature showing the activation energy of 0.68 eV, which was believed to be a Maxwell–Wagner relaxation. The high-temperature relaxations with the activation energy of 0.84 and 1.26 eV were ascribed to the conduction process because of the hopping motions of singly and doubly charged oxygen vacancies.

The Schottky-type grain boundary is also applicable to TiO_2-based varistors. In the microstructure, TiO_2 varistor is similar with GBL capacitors. Thus, in addition to the significant current–voltage nonlinearity, there is also a remarkable effect of capacitance, which can effectively filter out the electric noises. The stoichiometric TiO_2 ceramic itself is an insulator. After doping, the semiconductivity of the grains can be used for capacitor electrodes; after the oxidation of the GBL forms a high resistance layer, it constitutes a grain boundary capacitor similar to a parallel plate capacitor. Because the GBL is very thin, the dielectric constant of these devices is usually very large (order of 10^4–10^5). The equivalent circuit of the GBL capacitor is a RC network consisted of grain resistance, grain boundary resistance, and capacitance. The apparent dielectric constant can be expressed by (10.10), the intrinsic dielectric constant ε_{gb} for TiO_2 is about 114. Generally, t_g is 10–20 μm and t_{gb} is 0.01–0.1 μm; thus, the apparent dielectric constant can be estimated to be 10^4–10^5.

The relative dielectric constant ε_r decreases quickly and monotonously as the frequency increases. When Ta is doped, ε_r is about or larger than 3500 in the range of 200 Hz–10 kHz. Even at the higher frequency of 2 MHz, ε_r is still larger than 1600. The value of ε_r for the sample with 2 mol% Ta dopant reaches about 37 500 at 200 Hz but reduces to 9988 at 1 kHz [39].

10.2.4 Doping of TiO_2-Based Varistors

It is discovered that the TiO_2 matrix doped with Sb_2O_3, CeO_2, and other additives can be made into capacitor–varistor dual-function ceramics. In 1982, Yan and Rhodes [31] reported that TiO_2 doped with Nb,Ba had a valid nonlinear electrical characteristics with the threshold electric field of about 30 V mm^{-1} and the nonlinear coefficient α of 3–4. After that, the TiO_2 varistor ceramics have been extensively studied. The performance of the TiO_2 varistor system is significantly influenced by the dopant type and concentration. The addition of other additives, such as BaO, MnO_2, SrO, Nb_2O_5, Cr_2O_3, and Bi_2O_3 as donor, acceptor, or sintering additives, help densifying TiO2, probably by increasing the lattice defects because of the formation of a solid solution or the formation of a liquid phase [40–49].

10.2.4.1 Acceptor-Doped TiO_2-Based Varistors

Low-valence ionic impurities with larger radius as acceptors, such as Ba, Sr, and Ca, can segregate at the TiO_2 grain boundaries during the cooling process from the high sintering temperature to help form a distinct electronic barrier in the grain boundary and characterize the material with varistor properties [32]. It was indicated that the concentration of Ba segregated at the TiO_2 grain boundaries was about 150 times higher than the Ba content in the lattice. As Ba^{2+} ions are about 1.98 times larger than the Ti^{4+} ions, the large elastic energy

(7.6 eV) associated with Ba substitution in the Ti sublattice can be relaxed by segregation at the grain boundary region. The depletion layers at the grain boundaries provide a tunneling barrier for electron transport and lead to a nonlinear conduction phenomenon.

Ji et al. [47] used Y and Cu as the acceptor dopants and SiO_2 as the sintering additives, obtaining the TiO_2 varistor ceramic with the threshold electric field of $9.4\,V\,mm^{-1}$, the nonlinear coefficient α of 4.8, the dielectric constant ε_r of 2.13×10^4, and the dielectric loss $\tan\delta$ of 0.09. Luo et al. [48] studied MnO_2 as the acceptor-doped TiO_2 varistor ceramics. In the sintering process, MnO_2 releases a highly electronegative O_2, resulting in the increase of interface-state density and grain boundary barrier height, which contributes to the improvement of the nonlinear coefficient. A similar function was found by Sousa et al. [46]; they studied the effect of Cr_2O_3 on the electrical properties of TiO_2 varistors and found that the samples showed good varistor characteristics when doped with 0.025% Cr_2O_3, having the threshold electric field of $3.4\,V\,mm^{-1}$ and nonlinear coefficient α of 8.23. It is found that dopants such as Cr_2O_3 influence the densification, the mean grain size, and the electrical properties of the TiO_2-based varistor ceramics and have an special role in the barrier formation at the grain boundary in the TiO_2 varistors, increasing the nonlinear coefficient and decreasing the breakdown electric field. The influence of Cr^-_{Ti} is to increase the O^- and O^{2-} adsorption at the grain boundary interface and to promote a decrease in the conductivity by donating electrons to O_2 adsorbed at the grain boundary [50].

Li et al. prepared the SnO_2-doped TiO_2 varistor system by a solid-phase synthesis; when the doping of SnO_2 was in the range of 0–1.5 mol% [51], the threshold electric field rose with the increase of SnO_2 dopant and the nonlinear coefficient firstly increased and then decreased; when the incorporation of SnO_2 was 0.8 mol%, the sample reached the largest nonlinear coefficient of 8.3.

Experimental evidence showed that small amounts of SrO improved the nonlinear properties of TiO_2 ceramics [52], which played a special role in the morphology of the grain boundary and nonlinear response of TiO_2 ceramics. An atomic defect model based on the Schottky-type double barrier can be adopted to explain the formation of electrical barriers in the TiO_2 grain boundaries.

10.2.4.2 Donor-Doped TiO_2-Based Varistors

Generally, high-valence ions, which have a similar radius to Ti^{4+}, were selected for donor impurities to increase the conductivity, such as Nb_2O_5, Ta_2O_5, V_2O_5, and so on. Experiments show dopants with a valence of +5, such as Nb and Ta with an ionic radius similar to that of Ti^{+4}, which has a reasonable solubility in the Ti lattice, reducing the resistivity of the TiO2 lattice by donating conductive electrons and providing extra electrons to realize semiconducting grains [32]. Navale et al. [53], by adding Ta_2O_5 into the TiO_2 varistor ceramics, obtained the threshold electric field of $40\,V\,mm^{-1}$ and nonlinear coefficient α of 25–30. The maximum nonlinear coefficient observed among all donors is 35 for the tantalum-doped sample at an optimal concentration of 0.5 at.% [54].

Su et al. studied the varistor characteristics of WO_3-doped TiO_2 [55]. As W has an ionic radius similar to that of Ti, it is dissolved easily in the TiO_2 lattice, so the O vacancies can combine with Ti vacancies. During the sintering and cooling

processes, the diffusion of molecular oxygen through the grain boundary may occur and then it can be adsorbed at the interfaces and reacts with V_{Ti}^{4-} and Ti_{Ti}^{2-}. The defects, which are produced by the presence of WO_3, form a solid solution with TiO_2 and improve the grain conductivity. At the same time, the presence of WO_3 generates abundant molecular oxygen, which is adsorbed at the interfaces and becomes O^- or O^{2-}. A depletion layer is formed by positive charges such as V_O^{2+}, V_O^+, W_{Ti}^{4+}, and Ti_i^{4+}, where Ti_i^{4+} is positively charged Ti interstitials. A negative interface is formed during the sintering process and is composed of O^-, O^{2-}, V_{Ti}^{4-}, and V_{Ti}^{2-}, which is necessary in order to compensate for the positive charged defects created at the depletion layer. When the amount of WO_3 was 0.25 mol%, the samples showed the best varistor performance with the threshold electric field of 44.5 V mm^{-1}, nonlinear coefficient α of 9.6, and ultrahigh relative dielectric constant of 74 100 measured at 1 kHz [55].

All the defects form a double-barrier voltage between the TiO_2 grains as that of the ZnO varistor. As the new phase precipitation in the grain boundary is not detected, the two barrier tops touch each other [55]. According to the boundary barrier model, the WO_3 dopant performs like a substantial donor doping, which increases the concentration of V_{Ti}^{4-} and the local oxygen partial pressure and in turn tends to increase the concentration of O^- and O^{2-}. Negatively charged defects such as O^- and O^{2-} accumulate at the grain boundary, which make the grain boundary barrier height become higher. With an increase of WO_3 dopants, the donor concentration, N_d, caused by the tungsten ion and the density of electron interface states at the boundary, N_i, caused by V_{Ti}^{4-} become larger, the large N_d and N_i are attributed to the low resistance of the grain boundary, which is the reason why the sample with 0.5 mol% WO_3 dopant has the lowest resistance. At the same time, the positive charges, especially V_O^{2+} and V_O^+, accumulate at the depletion layer with an increase of WO_3 dopant, which makes the grain boundary become wider. The relative dielectric constant of the sample is determined by the width of the grain boundary, especially in the low-frequency region. A thinner grain boundary results in a larger relative dielectric constant in the low-frequency region. However, the substitution of Ti^{4+} for a tungsten ion exists at a maximum. When the content of WO_3 exceeds this limit, superfluous tungsten ions, which cannot substitute Ti^{4+} further, will segregate toward the grain boundary interface. Thus, the potential barrier height ϕ_b, N_d, and N_i will decrease, which is attributed to the large resistance of the grain boundary. The superfluous tungsten ions also make the grain boundary become wider. Therefore, it is found that the sample with 1.0 mol% WO_3 dopant exhibits the highest resistance and the lowest relative dielectric constant [55].

Recently, it was shown that the TiO_2 varistor ceramics doped with Pr_6O_{11} had a high nonlinear coefficient, and varistor and dielectric properties were improved [56]. Good electric properties with $E_{1mA} = 5.13$ V mm^{-1}, $\alpha = 5.43$, and $\varepsilon_r = 1.34 \times 10^5$ were obtained when doped with 0.50 mol% Pr_6O_{11}.

10.2.4.3 Codoping Effects of Acceptor and Donor Dopants

The segregation of divalent cations increases the grain boundary resistivity because the pentavalent donors (Nb or Ta) are locally compensated by the divalent acceptors (Ba, Sn, Y, Sr, or Ca) [57–60]. Gaikwad et al. [57] fabricated Ba

and Ta codoping TiO_2 varistor ceramic and obtained samples with the threshold electric field of 400–700 V mm^{-1} and the nonlinear coefficient α of 20–30. Acceptor doping of Ba^{2+} accumulated in the grain boundary and changed the nature of grain boundary barrier.

CaO as an acceptor-type dopant and Ta_2O_5 as a donor-type dopant, both doped TiO_2 varistors with high nonlinearity, were obtained [58]. When 0.5 mol% Ca and 0.05–2.0 mol% Ta were doped, the nonlinear coefficients α of all samples fell in the range of 5.1–42.1, and high values of relative dielectric constants, up to 10^5, were obtained. The Ta dopant has a significant effect on improving the nonlinear electrical behavior and the dielectric properties of the Ca, Ta-doped TiO_2 varistors. In view of the nonlinearity, the optimal concentration of Ta for the 0.5 mol% Ca-doped TiO_2 varistors is 0.5 mol%, which results in the highest nonlinear coefficient, highest resistivity, and relatively lower dielectric constant with smaller dielectric loss in the whole frequency measurement range of 200 Hz to 2 MHz. The nonlinear behavior of Ca, Ta-doped TiO_2 varistors can be explained by an analogy to the grain boundary defect model as shown in Figure 10.3. The Ta^{5+} ion, which has an ionic radius very close to that of Ti^{4+} and a higher valence than Ti^{4+}, easily dissolves into the TiO_2 lattice and introduces defects. Because of the creation of electrons, Ta^{5+} decreases the resistivity of TiO_2 grains. At the same time, Ca^{2+} introduces defects and segregates preferentially at the TiO_2 grain boundary. Therefore, both the intrinsic TiO_2 defects (Ti_i^{4+}, V_{Ti}^{4-}, V_O^{2+}) and the extrinsic defects (Ta_{Ti}^{+}, Ca_{Ti}^{2-}) exist at the grain boundaries. The positive charges (Ti_i^{4+}, V_O^{2+}, Ta_{Ti}^{+}) are located on both sides of a grain boundary, and the negative charges are distributed at the grain boundary interface. A depletion layer is created at the grain boundary because of the charge compensation between the positive charges and the negative charges. As a result, a voltage barrier is formed and leads to the nonlinear electrical behavior of Ca and Ta-doped TiO_2 varistors. Based on the experimental results, there exist two kinds of effects of Ta on the nonlinear electrical behavior of Ca and Ta-doped TiO_2 varistors. On the one hand, as Ta^{5+} dissolves into the TiO_2 lattice, the Ta_{Ti}^{+} defect is introduced and is located at the grain boundary. To maintain the electrical neutrality, the positive charges (Ta_{Ti}^{+}) are compensated by negative charges. Consequently, the potential barrier height ϕ_b increases because of the increase in negative charges. Larger doping concentrations of Ta result in more positive charges (Ta_{Ti}^{+}) and more negative compensating charges. As a result, the potential barrier height ϕ_b is further increased with increasing the Ta concentration x. Therefore, the nonlinearity of the samples is improved. On the other hand, the barrier width ω increases monotonically

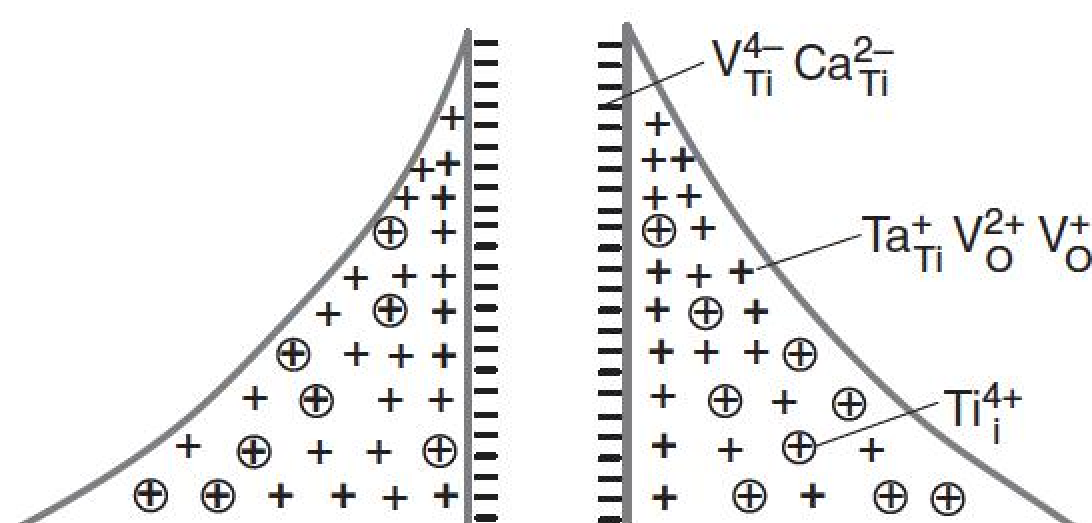


Figure 10.3 The grain boundary atomic defect model for Ca, Ta-doped TiO_2 varistors. Source: Wang et al. 2002 [58]. Redrawn with permission from Elsevier.

with the increment of x from 0.05 to 2.0 mol%. When x increases beyond a certain level, the width ω becomes so large that it will influence the tunneling process of electron transport. Consequently, the nonlinearity will become worse. Therefore, because of these two effects, there exists an optimal concentration of Ta for maximal electrical nonlinearity.

Santhosh et al. [32] found that Nb- and Sr-doped TiO_2 varistors exhibit excellent properties, with the threshold electric field of about $50\,V\,mm^{-1}$ and the nonlinear coefficient α of 7–8.

Wang et al. [60] studied the influence of Y_2O_3 doped on the Ta_2O_5–TiO_2 capacitor–varistor and found that Y_2O_3 had a significant influence on the performance of the Ta_2O_5–TiO_2 capacitor–varistor, and samples showed good comprehensive properties, with the threshold electric field of $9.7\,V\,mm^{-1}$, the nonlinear coefficient α of 4.5, and ε_r of 8.82×10^4 when the concentration of Y_2O_3 is 0.25 mol%.

10.2.4.4 Sintering Additives in TiO_2-Based Varistors

There are three main roles of the sintering additives [61]. The first is to reduce the sintering temperature and conducive to sintering; the second is to increase the density of ceramics; the last is to help with the diffusion and segregation of acceptor impurities in the grain boundary and the formation of grain boundary barrier, by making use of its low melting point characteristics to form more liquid phases enriched in the grain boundary in the sintering process.

The sintering additives for TiO_2 varistors, mainly including SiO_2 and Bi_2O_3, can promote the grain fully semiconductivity, lower the threshold electric field, and improve the uniformity of grains [61]. Xu et al. [62] found that adding SiO_2 was favorable for Nb^{5+} entering TiO_2 grains to promote the semiconductivity of grains and to change the grain boundary phases and improve the nonlinear coefficient. Meng [63] found that a moderate amount of SiO_2 can not only reduce the activation energy of Ti^{4+} to depart from the lattice, increase the content of Ta^{5+} in grains, and promote semiconducting and uniform growth of TiO_2 grains but also be conducive to sintering, leading to an increase in the ceramic capacitor and a decrease in the grain resistance and threshold electric field. The importation of Bi_2O_3 can promote grains semiconducting because its low melting point will form more liquid phases during the sintering process, making the acceptor impurity segregated at the grain boundaries, which will improve the grain boundary resistance and the effective interface-state density, and is favorable to form the grain boundary barrier and to improve the electrical properties of ceramics. When the amount of Bi_2O_3 was 0.4 mol%, the TiO_2 varistor reached the highest barrier height ($\phi_b = 0.48\,eV$), the minimum threshold electric field ($V_{1mA} = 40\,V\,mm^{-1}$), and the largest nonlinear coefficient ($\alpha = 6.2$) [64].

Ge and GeO_2 were also selected as sintering aids because of their low melting points, thereby reducing the sintering temperature [65]; both changed the microstructure of TiO_2–Nb_2O_5–$SrCO_3$ ceramics, increased α, and decreased the breakdown electric field strength E_b. When the doping contents of Nb_2O_5, $SrCO_3$, Ge, and GeO_2 were 0.1, 0.2, 0.25, and 0.75 mol%, respectively, the TiO_2–Nb_2O_5–$SrCO_3$ varistor ceramics sintered for three hours at 1260 °C exhibited high α (11.6), low E_b ($13.8\,V\,mm^{-1}$), and high barrier height (0.96 eV).

A further analysis shows that the resultant Ge^{2+} easily segregates at the grain boundary because of its larger ion radius than Ti^{4+} to increase the acceptor interface-state density and the nonlinear coefficient. GeO_2 easily dissolves in TiO_2 lattice because of the same valence state and the slightly smaller radius of Ge^{4+} in comparison with Ti^{4+}; this feature improves the semiconducting degree of grains and decrease E_b [65].

10.2.5 Development of TiO_2-Based Varistors

Lowering the dielectric loss and improving the stability are the development trends of TiO_2-based varistors. Combining doping and preparation technology to further improve the density is the key to fabricate low-loss TiO_2-based varistors. With the increases in temperature and frequency, TiO_2 varistors show significant dispersion. When the temperature is higher than 100 °C, the nonlinear coefficient decreases significantly; when the frequency is more than 10 MHz, the varistor performance begins to deteriorate [66]. To satisfy the normal use of TiO_2 varistors at a high temperature and a high frequency, improving stability has become an urgent requirement.

Developing the multilayer TiO_2 chip varistor can further improve its current capacity. The multilayer chip varistor, with a very large current capacity, very easily implements the low-voltage technology and is suitable for surface-mount technology (SMT), which will be the most potential electronic circuit protection components [67]. The key technology is how to lower the sintering temperature and production costs.

To use the submicron or nanolevel TiO_2 instead of all or part of micron TiO_2 is an important way to improve the properties of TiO_2-based varistor ceramics. As nanoparticles have the advantages of small size, large surface area, high surface energy, and activation energy, during the sintering process, the driving force that declines the surface energy is large; thus, it can reduce the sintering temperature and the samples obtained a more uniform microstructure. The samples added a small amount of nano-TiO_2 had good electrical properties [38, 68]. The Nano-TiO_2 powder addition has a significant effect on the grain boundary barrier. When 5 mol% nano-TiO_2 powders were added, the barrier height was 0.28 eV, the barrier width was 48 nm, and the Femi level was 2.62 eV. The combined action of nanopowder in grain refinement and additional barrier increases the height and width of the grain boundary barrier and the nonlinear coefficient. Therefore, making use of the special nature of ultrafine powders, combined with the thermal oxidation treatment technology, can improve the grain boundary and promote varistor performance.

10.3 $CaCu_3Ti_4O_{12}$ Ceramics

10.3.1 Introduction

$CaCu_3Ti_4O_{12}$ (CCTO) is a kind of ceramic with a nonlinear current–voltage characteristic as well as an extremely giant permittivity [69]. In 2000, Subramanian et al. found extraordinary permittivity in CCTO ceramics [70]. Studies have

shown that this perovskite can exhibit a dielectric permittivity of about 10^4–10^5 for temperatures ranging from 100 to 600 K without undergoing any phase transition [70–72]. In 2004, Chung et al. discovered its nonlinear current–voltage characteristic [73]. Later, this nonlinear current–voltage performance has been reported in ceramics [74], thin films [75, 76], and recently in nanostructures [77], which are attributed to the conductivity on the film/metal–electrode interface and/or grain boundary mechanisms [78, 79].

Compared with $SrTiO_3$, CCTO has huge superiority of simple preparation and one-step sintering in air, whereas $SrTiO_3$ needs two-step sintering, and deoxidization and oxidization environments are required. Because of its outstanding dielectric properties and nonohmic characteristics, and simple and straightforward preparation, CCTO is considered a very promising dual-function material.

Regularly, high dielectric capacitors are basically ferroelectrics or relaxor ferroelectrics. In these materials, an abnormal increase in the permittivity occurs near the Curie point. Hence, the temperature stability of the dielectric material is not very good. CCTO has a huge permittivity, which is very stable in a large temperature range and does not contain Pb and other heavy metals, which makes CCTO environment friendly. Therefore, CCTO ceramic has broad prospects in the electronics application as a dual-function device that acts as both a surge protector and a capacitor [69], and as capacitors, random access memories, microwave devices, and sensors [74–81].

10.3.2 Structure of CCTO

10.3.2.1 Crystal Structure

The CCTO of a complex perovskite structure is a kind of BCC structure and belongs to the crystallographic space group *Im3*. The crystal structure is shown in Figure 10.4 [82]; the Ca atoms occupy the body center and 8 vertices of the hexahedron, and the Cu atoms occupy the 12 edge centers and 6 face centers. In the unit cell, there are eight TiO_6 octahedrons that have an angle of 141° between each other. The lattice constant a is 7.395 Å under 25 °C [70].

Subramanian et al. [70] used neutron diffraction to measure each atomic bond length and found that from 35 to 100 K, the $CaCu_3Ti_4O_{12}$ structure does not

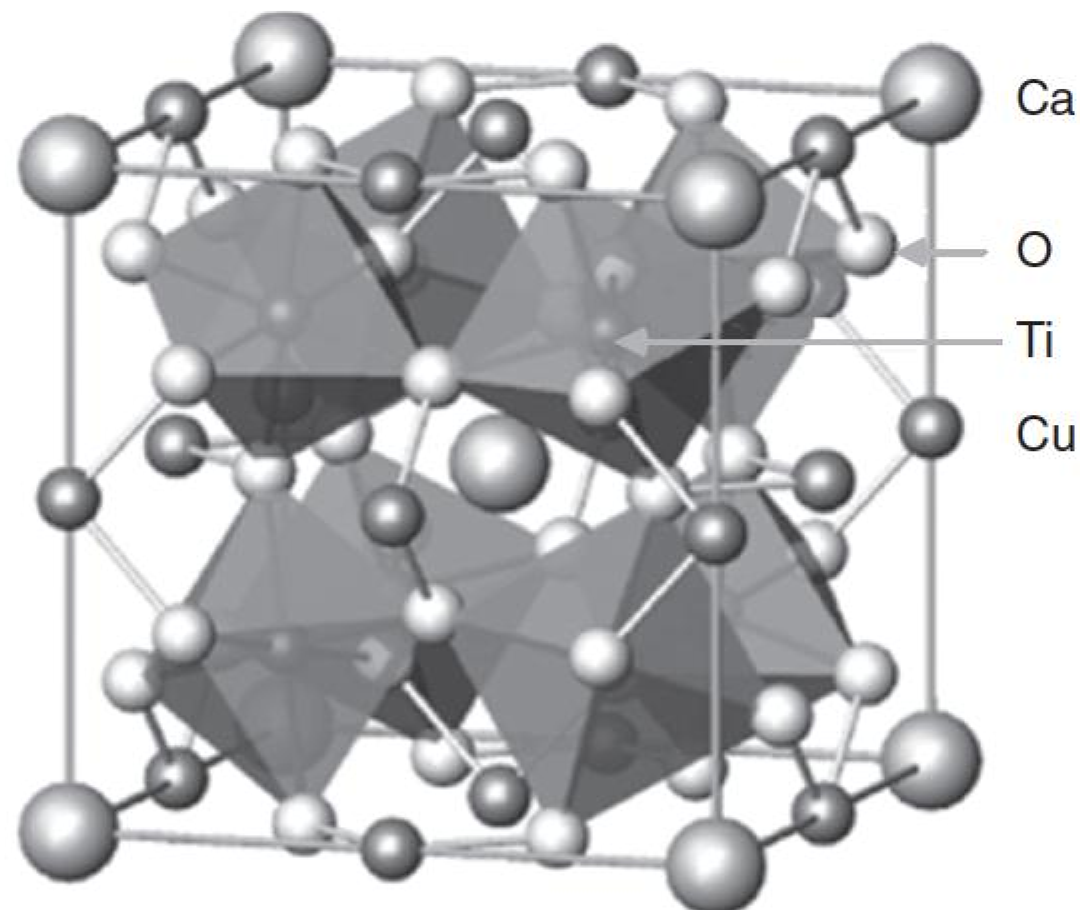


Figure 10.4 The crystal structure of $CaCu_3Ti_4O_{12}$. Source: Homes et al. 2003 [82]. Reproduced with permission of APS.

change, which means that the ferroelectric phase transition does not happen. The thermal expansion coefficient and heat capacity also show that no phase transformations occur in this temperature range. Although $CaCu_3Ti_4O_{12}$ has TiO_6 octahedral structure, like other perovskite minerals, however, the TiO_6 octahedral is subject to the square structure of Cu atoms, which makes it tilt and restricted, and difficult for ferroelectric phase transition to occur in $CaCu_3Ti_4O_{12}$.

10.3.2.2 Phase and Microstructure

The synthesis method of CCTO ceramic has played a significant role in determining the microstructural, electrical, and dielectric properties. Different from two-step sintering for $SrTiO_3$, the most common preparation method of CCTO ceramics is single-step conventional solid-state sintering method. $CaCO_3$, CuO, and TiO_2 powders and other additives are mixed together and calcined at 700–900 °C to form the CCTO powders. Then, the CCTO powder is pressed into disks and sintered in air for several to dozens of hours with the temperature ranging from 1000 to 1500 °C. The color of the as-calcined CCTO powder changes from yellow to orange, and the as-sintered CCTO bulk is black with some metallic luster on the surface.

The main phase of the as-sintered ceramic is crystalline CCTO. Electron probe microanalysis (EPMA) shows that the main phase of the composition is not the exact $CaCu_3Ti_4O_{12}$, but $Ca_{0.98(2)}Cu_{2.92(2)}Ti_{4.04(4)}O_{12}$, which is slightly off the stoichiometric. Cu atoms in the grains are inadequate [83]. Li et al. pointed out that some Ti atoms may occupy the position of Cu atoms [84]. As shown in Figure 10.5 [85], an obvious grain boundary structure can be observed between the CCTO grains, and the width of the grain boundary is about 30 nm; inset b shows that the grain boundary appears to be amorphous. However, the expanded high-resolution TEM (HRTEM) picture of the grain–grain boundary

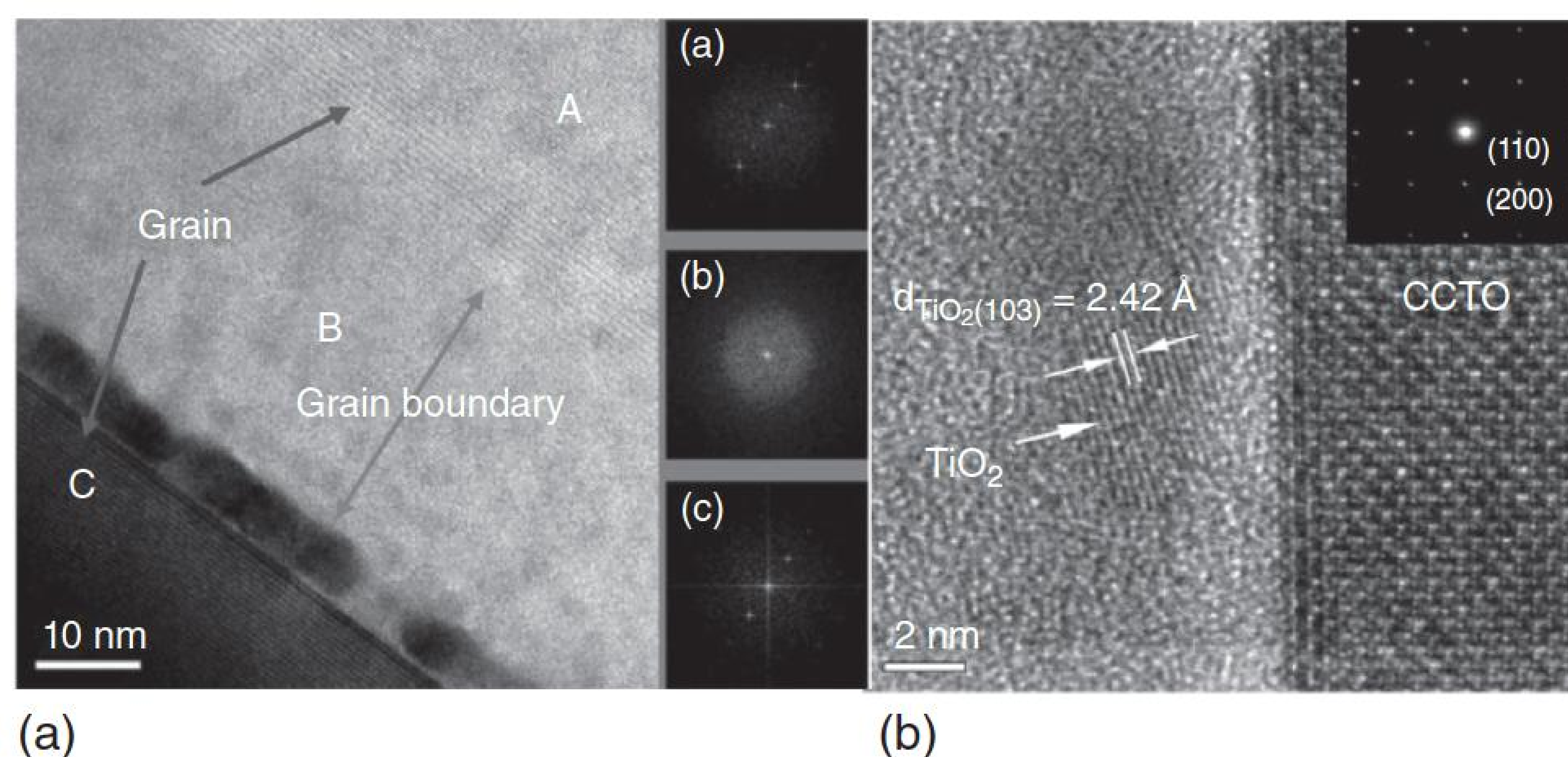


Figure 10.5 (a) A HRTEM micrograph of the grain–grain boundary grain structure for the TiO-rich $CaCu_3Ti_4O$ ceramic, in which insets a, b, and c are the Fourier analysis images of areas A, B, and C, respectively. (b) An expanded HRTEM picture of the grain–grain boundary structure for the TiO-rich $CaCu_3Ti_4O$ ceramic, the inset of which is the selected area electron diffraction (SAED) pattern of the CCTO grain. Source: Lin et al. 2008 [85]. Reproduced with permission of AIP.

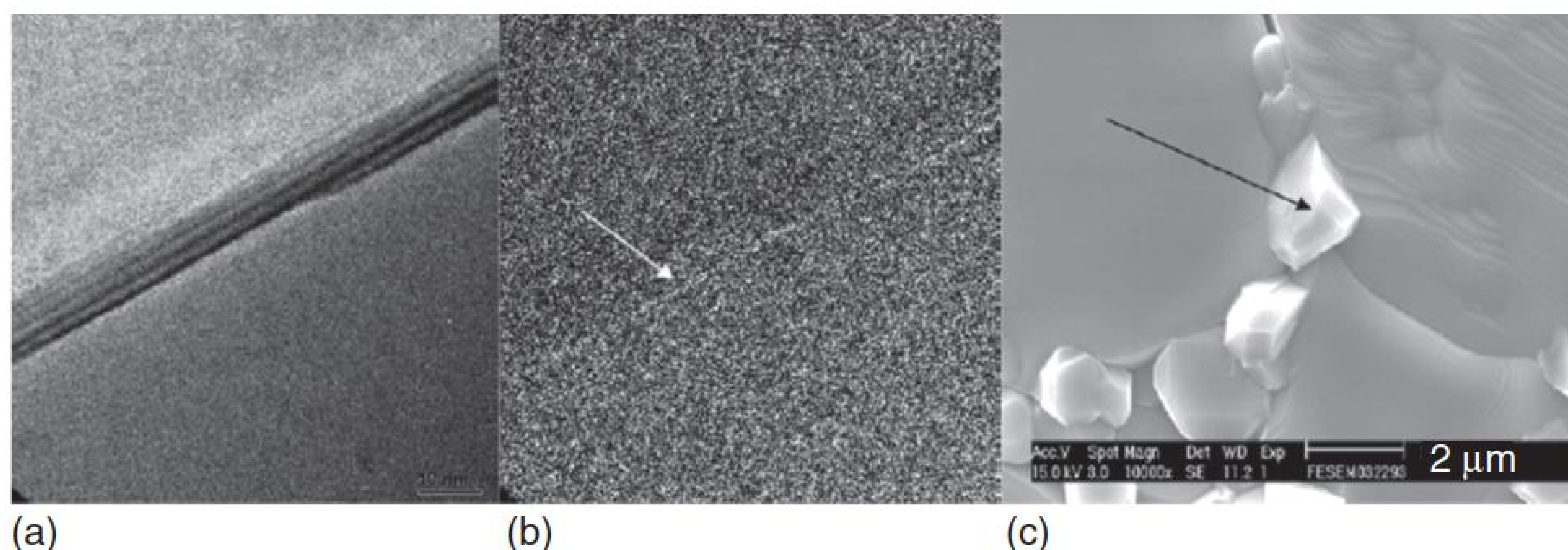


Figure 10.6 A grain boundary is shown in (a), the arrow in (b) indicating the corresponding contrast of Cu element. The arrow in (c) indicates the second-phase particles that are rich in Cu. Source: Li et al. 2007 [86]. Reproduced with permission of AIP.

region shown in Figure 10.5b, which indicates that the grain is a well-crystallined CCTO and some TiO_2 nanograins also exist.

In addition to the main phase, the X-ray diffraction (XRD) pattern indicates that there exist traces of the CuO phase. Energy spectrum analysis (EDS) and TEM analysis also proves that CuO exists as the intergranular phase (see Figure 10.6) [86]. A small amount of Cu-rich phase can be found in the amorphous grain boundary region from the line-scanned energy-dispersive spectroscopy spectra [85]. The Cu-rich phase is also observed at the grain boundary by Adams et al. [83], which may be related to the high-temperature sintering process. The special microstructure (CCTO grain-amorphous/TiO_2 nanograin–CCTO grain junction structure) should be responsible for the interesting electrical property of these Ti-rich CCTO ceramics.

Jacob et al. [87] calculated the Gibbs free energy and obtained the phase diagram of the CCTO system, and studies indicate that at 1273 K, CuO, Cu_2O, TiO_2, $CaTiO_3$, and $CaCO_3$ phases can be in the system in equilibrium with the CCTO phase coexistence. Zhang [88] found that CCTO under a N_2 atmosphere in 1000 °C partially decomposes into TiO_2, Cu_2O, and $CaTiO_3$. The scanning electron microscopy (SEM) image of as-sintered CCTO cross section is shown in Figure 10.7 [89], and the grain structure is clearly observed in the image.

When the sintering conditions or additives change, the grain size, shape, and distribution have differences, and the electrical performances change correspondingly.

Adams et al. [90] did a detailed study of the sintering time on the CCTO microstructure. At the sintering temperature of 1115 °C and the sintering time of one hour, the ceramics have fine grain structure, and the grain size is 3–5 µm. When the sintering time is extended to three to five hours, abnormal grain growth occurs, and large grains of about 100 µm are surrounded by fine grains. When the sintering time is extended to 24 hours, the samples consist of almost all coarse grains with the size of 50–300 µm, although some fine grains, pores, and second phase particles are observed between the grains. The smooth edges of the grains, together with the quick grain growth, when the sintering time is expanded from one to three hours, indicate that the sintering process is probably a liquid-phase sintering. Other studies have also confirmed the abnormal growth

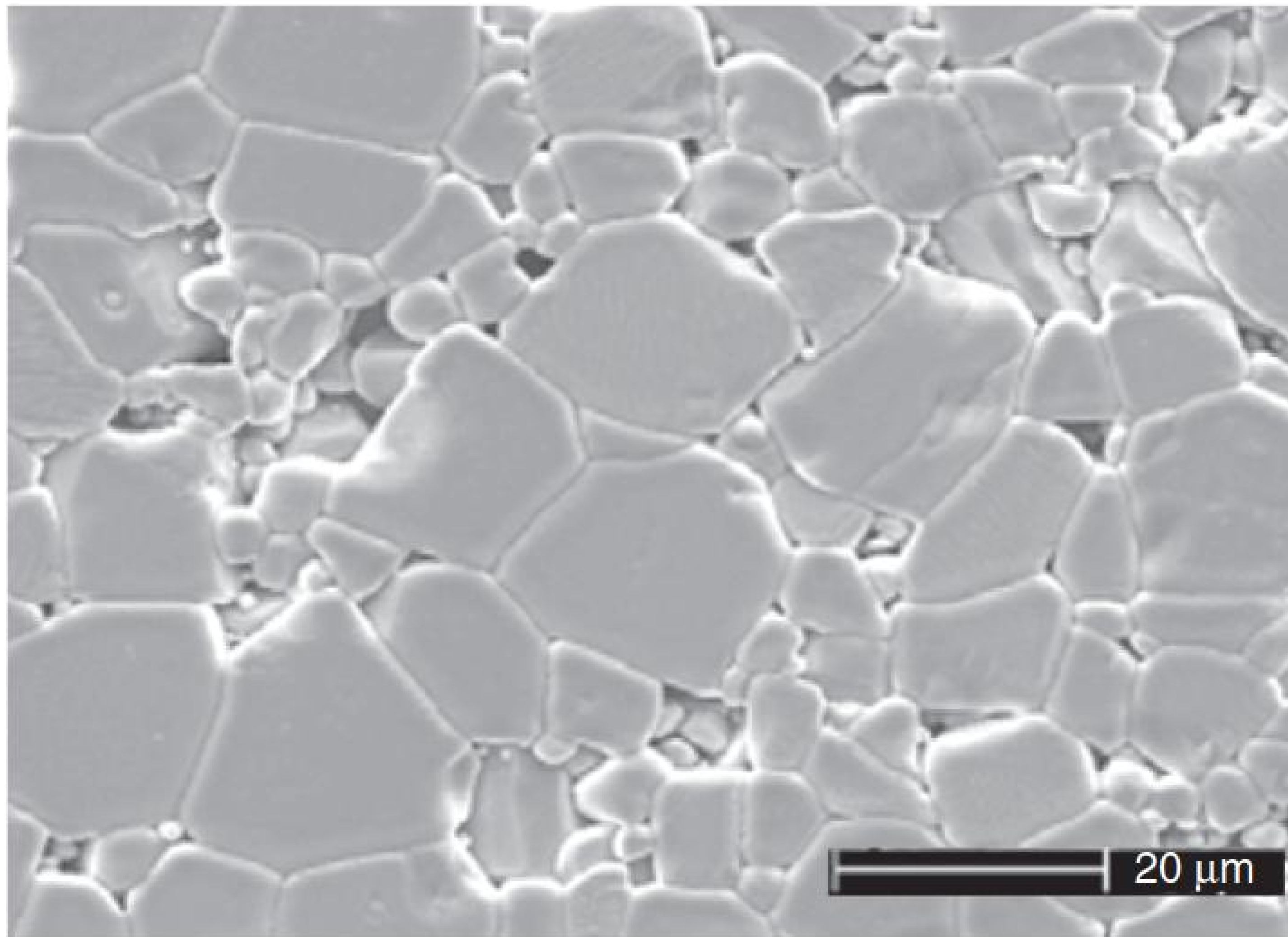


Figure 10.7 The SEM image of CCTO microstructure. Source: Fang and Shiau 2004 [89]. Reproduced with permission of John Wiley & Sons.

of CCTO grains and the change of microstructure with the sintering time, believing that the liquid phase is the driving force for sintering and the reasons for abnormal grain growth. An intergranular phase formed by the cooling liquid can be observed by SEM.

Marchin et al. [91] found that more Cu elements than stoichiometric cause significant grain enlargement in CCTO. CuO and TiO_2 form eutectic mixtures as low as 912 °C; this mixture is changed into a liquid phase in the sintering process and promotes the growth of grains. The increase in the CuO content increases the amount of the mixture and enlarges the ceramic grains. In contrast, doping of iron or niobium elements decreases the grain size evidently. The change of grain size will affect the electrical properties greatly, which is to be explained in detail below.

10.3.3 Performances of CCTO Ceramics

10.3.3.1 Nonohmic Current–Voltage Characteristic

As ZnO varistor, and $SrTiO_3$ and TiO_2 ceramics, the dielectric properties and microstructure formation of CCTO are strongly dependent on the processing conditions such as preparation routes [92–95], sintering temperatures, and dwelling time [96–99]. In 2004, Chung et al. [73] reported that CCTO ceramics sintered at 1100 °C showed evident nonlinear I–V characteristics (see Figure 10.8). They found that after sintering of three hours, the nonlinear coefficient of the CCTO sample reached as high as 912, which is significantly larger than that of the widely used nonlinear ZnO-based varistor, although the authenticity and repeatability were questioned by some researchers [100]. Ramírez et al. [101] presented a $Ca_2Cu_2Ti4O_{12}$ ceramic composed by 66.7% of $CaTiO_3$ (CTO) and 33.3% of $CaCu_3Ti_4O_{12}$ (CCTO/CTO), which reached the highest nonlinear coefficient α of 1500 that calculated in the current density range of 3–30 mA as the same in [73], but the respective nonlinear coefficient

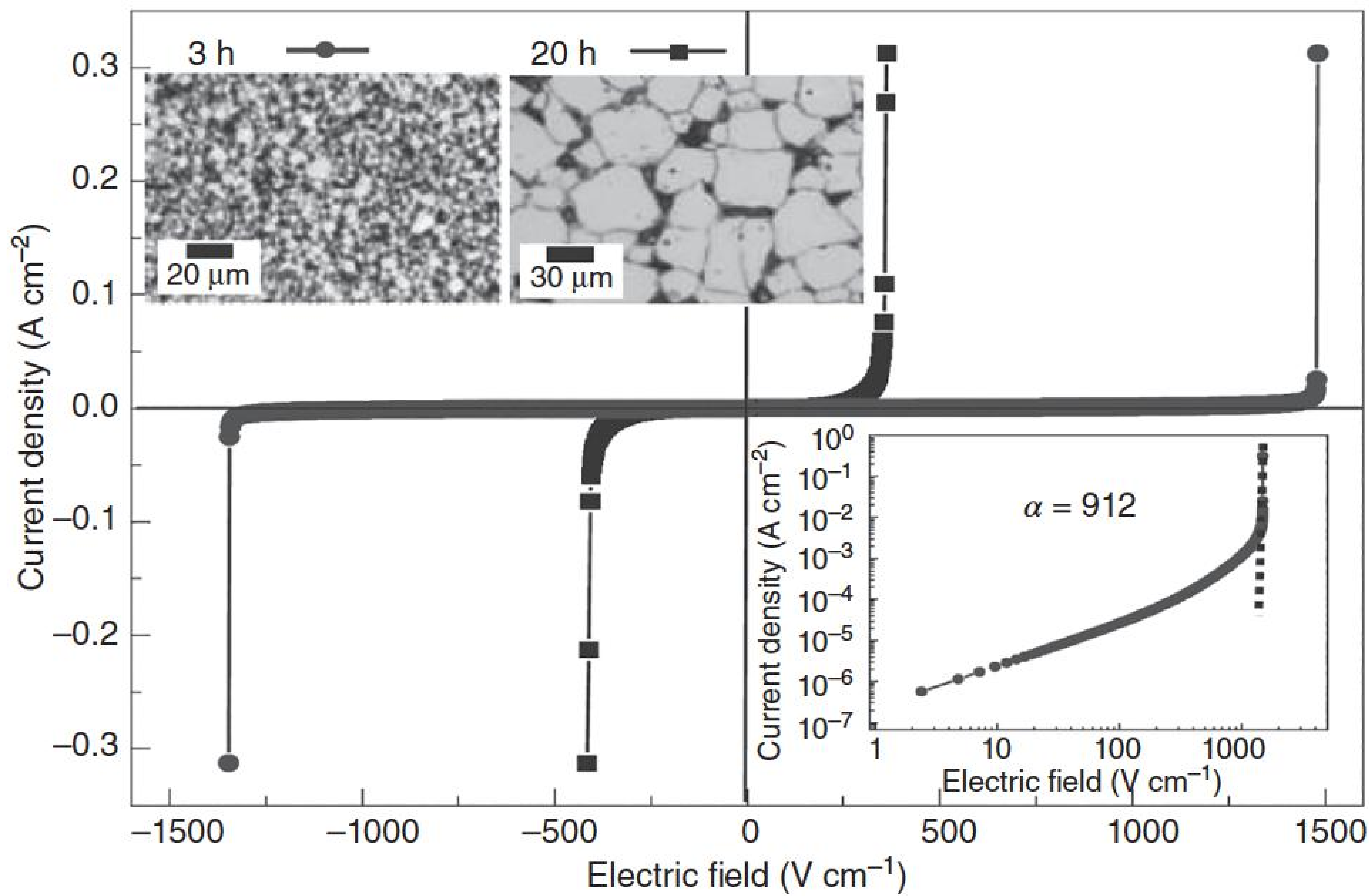


Figure 10.8 The first reported nonohmic current–voltage characteristic of CCTO by Chung et al. [73]. Source: Chung et al. 2004 [73]. Reproduced with permission of Springer Nature.

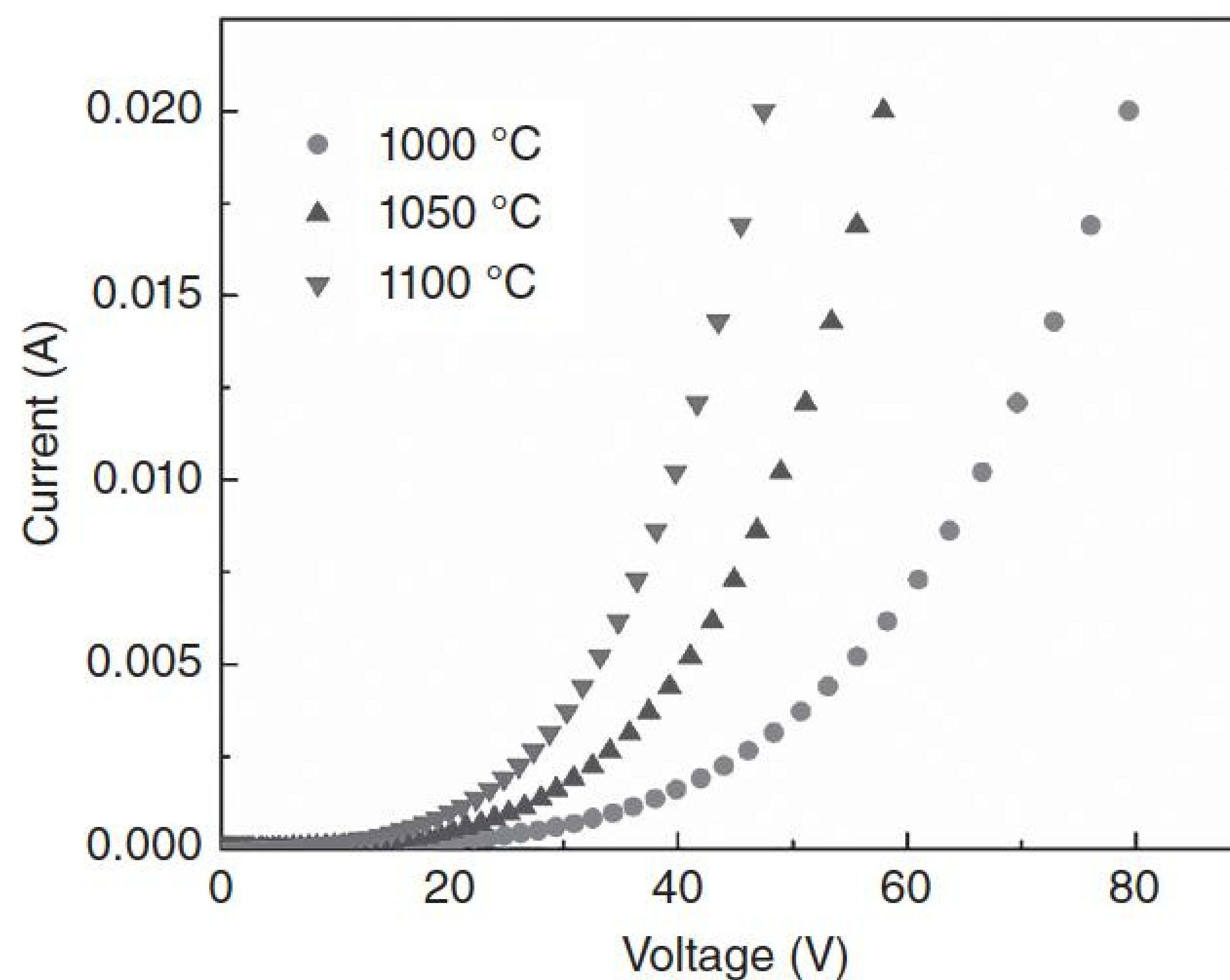


Figure 10.9 Typical current–voltage curves of CCTO ceramic. The sample is 10 mm in diameter and 1 mm in thickness, sintered at different temperature for three hours.

α was 65 for the traditional current density range of 1–10 mA cm^{-2}. Compared to the traditional $CaCu_3Ti_4O_{12}$-based composition, the imbalance between the Ca and Cu atoms, which causes the formation of a polycrystalline system, is the origin of high nonlinear electrical behavior. However, the most reported nonlinear coefficient of CCTOs is around 10 [102–104], and their varistor voltage gradients are typically no more than 100 V mm^{-1}, and a typical current–voltage curve is shown in Figure 10.9.

Both the preparation process and additives can affect the nonlinear I–V characteristics. Annealed in oxygen-rich environment, the ceramic will obtain larger nonlinear coefficients and the varistor voltage will increase. In contrast, annealed

in an environment that is lack of oxygen, the nonlinear coefficient and varistor voltage are reduced [103].

Researchers tried various additives to modify the nonlinear property of CCTO. Leret et al. [100] added Na and Ta into the system, respectively, finding that the potential barrier at the grain boundaries were lowered and the nonlinear coefficient decreased. Lin et al. added excessive Ti into the system, finding that the varistor voltage gradient can be raised to several hundred volts per millimeter, which may expand the application to high-voltage area [104]. Chung et al. doped the ceramic with Sc atoms [105] and found that the selectivity of Sc position affects the properties evidently. When Sc is on the Ti sites, samples with excellent nonohmic properties can be obtained. In contrast, the sample almost losses the nonohmic property when Sc takes the site of Cu. The selectivity of dopant atoms depends on the ratio of starting materials. Nonohmic properties of CCTO ceramics are extremely enhanced by the substitution of Tb ions [106], and the grain size of CCTO ceramics is decreased by doping with Tb ions. The nonlinear electrical properties are strongly enhanced as the doping concentration of Tb ions is increased, but the ε' (real part) value of the dielectric constant decreases greatly. The best properties with a nonlinear coefficient of ~29.67 (in the range of 1–10 mA cm^{-2}) and breakdown electric field strength E_b of ~15.2 kV cm^{-1} are obtained in the $Ca_{0.775}Tb_{0.15}Cu_3Ti_4O_{12}$ ceramic. These extremely enhanced properties are attributed to the modification of grain boundary electrical response because of the effect of Tb substitution. MgO nanopowder (with particles sizes of about 100–300 nm) dopant has the ability to improve both dielectric and electrical nonlinear properties, reduce the low-frequency loss tangent, and significantly enhance the breakdown voltage and nonlinear coefficient of $CaCu_3Ti_4O_{12}$ ceramic, which is attributed to an increase in the resistance of grain boundaries [107].

10.3.3.2 Colossal Permittivity

The extraordinary huge permittivity is a prominent property of the CCTO ceramic. Generally, the relative permittivity of CCTO ceramics can reach as high as 10^4, as shown in Figure 10.10 [108]. The permittivity of CCTO is not only extremely huge but also unchanging with temperature above 150 K [72, 109]; this nature is very necessary for the practical application. The permittivity increases as the sintering temperature rises, which reaches as high as 10^5 when sintered at 1125 °C, whereas 10^4 sintered at 1000 °C [110]. The effective permittivity ε_{eff} can be estimated by Eq. (10.10) as $\varepsilon_{eff} = \varepsilon_{gb}(t_b/t_{gb})$, where ε_{gb} is the permittivity of the insulating grain boundary phase, t_b is the average grain size, and t_{gb} is the average grain boundary thickness. The average grain size t_b keeps unchanged. It is probable that the volatilization of Cu with rising temperature decreases the grain boundary thickness t_{gb}. Therefore, the effective permittivity increases as the sintering temperature rises [109]. In the low-temperature region, the magnitude of the permittivity decreases from 10^4 to 10^2, a dielectric loss peak appears at the same time, showing a dielectric relaxation phenomenon (see Figure 10.10b).

Figure 10.10c exhibits the changes of permittivity with the frequency. When the frequency increases to a threshold value, usually above 1 MHz, the

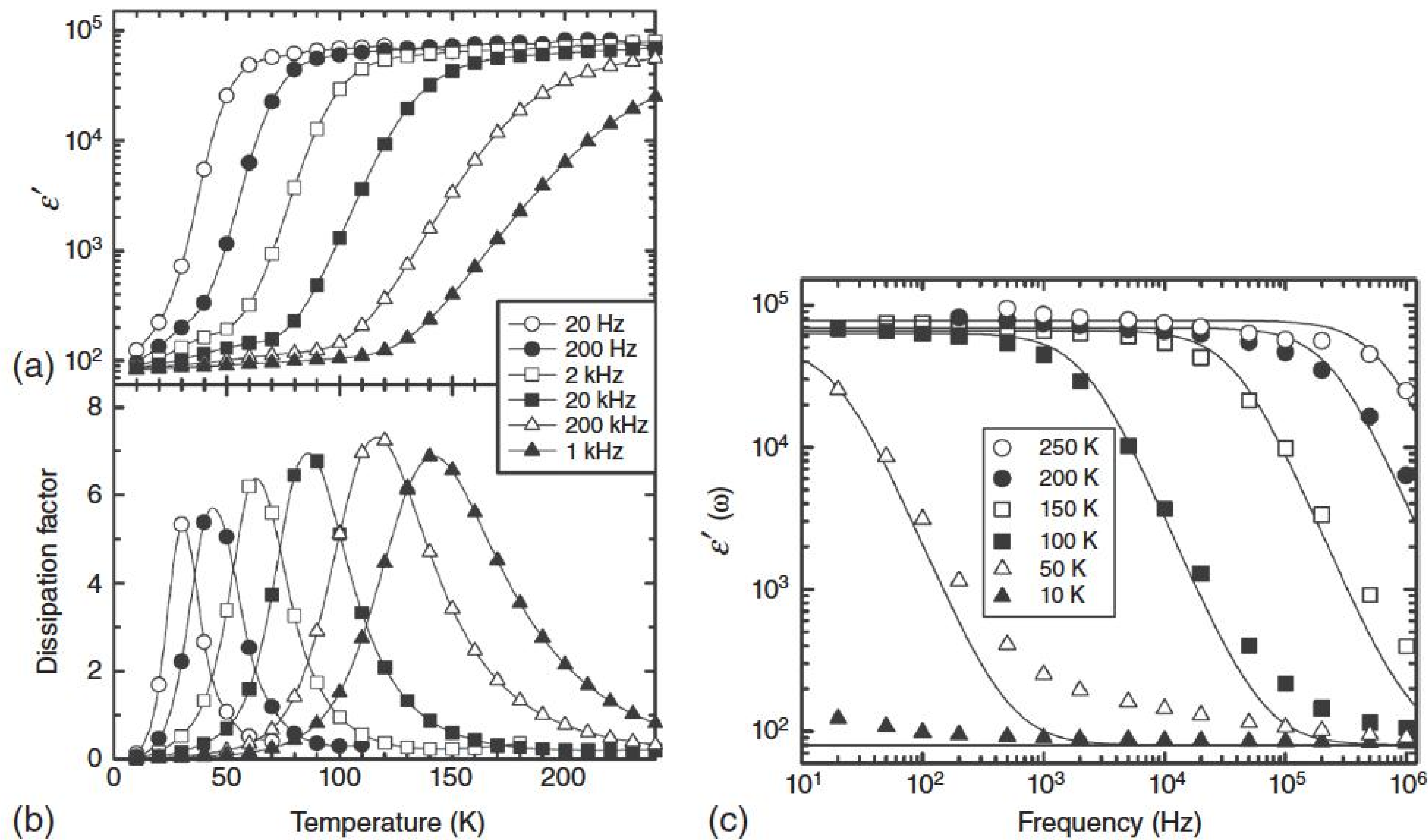


Figure 10.10 The temperature and frequency dependence of dielectric property of a $CaCu_3Ti_4O_{12}$ single crystal [108]. (a) The temperature dependence of the real part of the dielectric response ε'; (b) the temperature dependence of the dissipation factor (or loss component) of the dielectric response; (c) the frequency dependence of the real part ε' of the dielectric response. Source: Homes et al. 2001 [108]. Reproduced with permission of AAAS.

permittivity behaves strongly temperature dependent, a substantial drop to 10^2 occurs. The reasons for the drop of permittivity at low temperature and high frequency are similar. In both circumstances, the polarization cannot keep in pace with the testing frequency, resulting in the dramatic falling of permittivity. High-frequency measurements reveal CCTO having no colossal permittivity in the GHz frequencies [111].

The permittivity of CCTO highly depends on the microstructure. Generally, the effective dielectric constant increases as the grain boundary area decreases, which is a function of grain size and size distribution [112]. Therefore, the sintering conditions that affect the microstructure have a great influence on the dielectric property. CCTO behaves a very high and thermally stable dielectric constant with ε_r in the range of 10^4–10^5 when the temperature ranges from 100 to 600 K [113–115]. As the sintering temperature rises, the permittivity increases weakly. Also, the permittivity rises as the sintering time increases, as is shown in Figure 10.11 [89, 116]. Sinclair et al. prepared the sample at 1115 °C for 24 hours and obtained relative permittivity of 280 000 [109], this is the highest relative permittivity ever reported in the literature.

A detailed equivalent circuit analysis of the results and two crucial experiments, employing different types of contacts and varying the sample thickness, was performed [112]. The dependence of relative permittivity at a high frequency both on contact type and on sample thickness clearly proves that the external contacts via an interfacial polarization process lead to the detection of very high dielectric constants. The observed relaxation-like spectral features are of Maxwell–Wagner type and easily understandable within an equivalent circuit. This is easy to explain

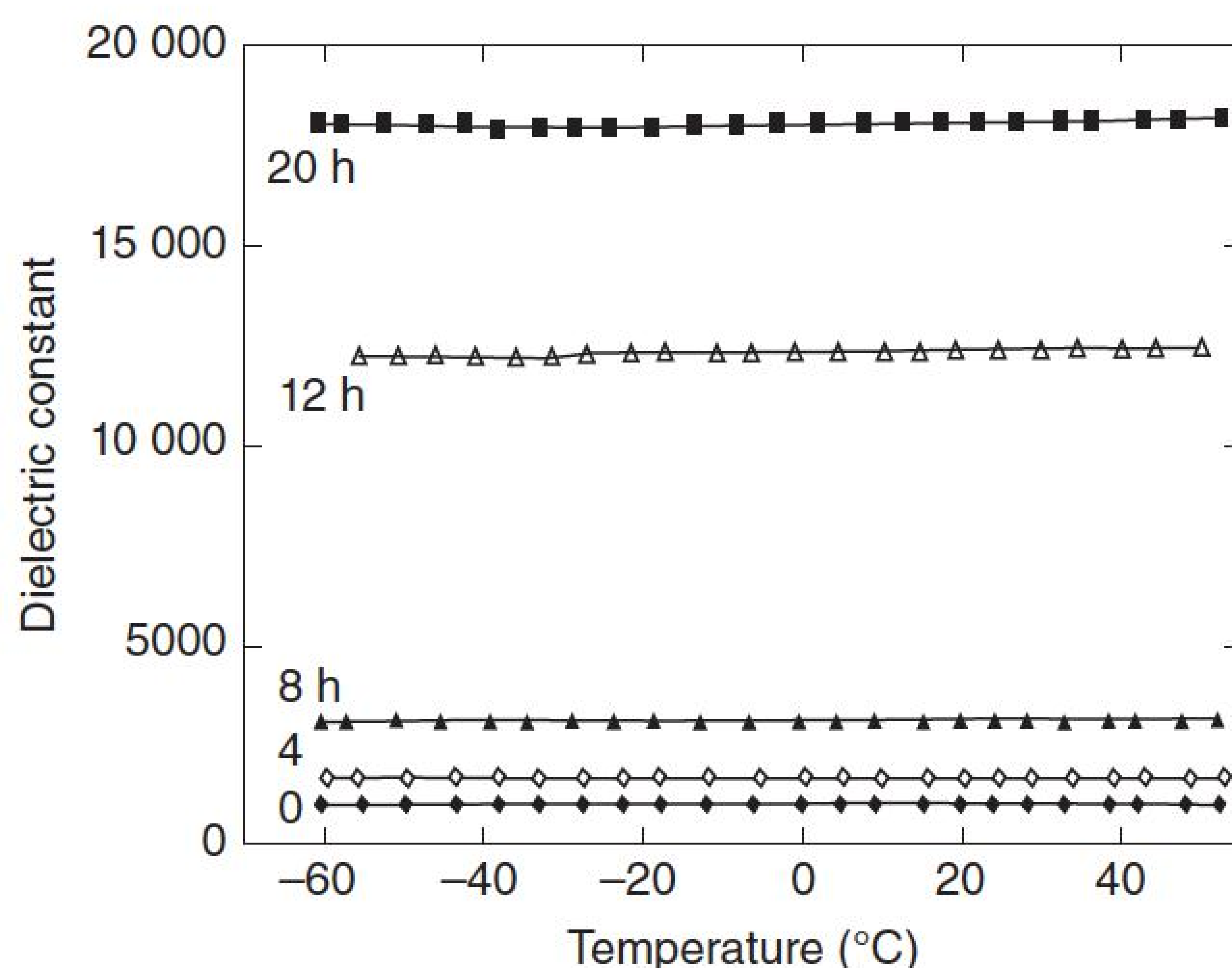


Figure 10.11 Relative permittivity of CCTO sintered at 1100 °C for different hours. Source: Fang and Shiau 2004 [89]. Reproduced with permission of John Wiley & Sons.

why the reported values of relative permittivity at high frequency vary so much: its absolute value depends on the details of contact formation, e.g. the surface roughness, type of contact, and stoichiometry at the surface.

The dielectric properties of CCTO are very sensitive to the processing conditions. CCTO ceramics were synthesized by the methods of sol–gel, traditional solid-state reaction, and thermal decomposition of organic solution, and the results exhibit that the electric characteristics are affected by the methods of synthesis [92]. Prolonging holding time leads to substantial improvement in permittivity; furthermore, the quenched sample shows a larger dielectric permittivity than the furnace-cooling one [93]. The primary factor affecting the dielectric behavior is the development of internal defects, and it appears that a higher defect concentration within the “core” of a grain, which may be achieved through milling, sintering at higher temperatures and longer times, and/or annealing in controlled atmosphere, results in higher conductivity of the core and therefore higher effective dielectric constant [112]. Sintering in oxygen atmosphere or quenching in air will help to raise the relative permittivity by several times [89, 117, 118]. The permittivity of CCTO is easily influenced by a slight difference in the preparation process. Therefore, the value given in the literature varies from each other. Lin et al. [85] explained that the permittivity may be sensitive to the surface states, which is easily affected by many factors during preparation. To date, the giant permittivity of CCTO can be best described by a model of conducting grains, insulating grain boundaries and the associated Maxwell–Wagner relaxation [94, 96]. However, this model requires that the insulating grain boundaries be thin, uniform, and robust to prevent percolation of the conducting grains [97]. This may explain why the dielectric properties of CCTO are so sensitive to processing as small changes in processing may affect the resistivity and robustness of the grain boundaries [112].

Doping of additives can evidently modify the dielectric property of CCTO. Excessive Cu atoms can effectively raise the permittivity [91], whereas less Cu than stoichiometric will decrease the permittivity. More Ti atoms than stoichiometric will decrease the relative permittivity to several thousand [98]. Additional

Co can increase the relative permittivity. At the amount of Co doping is 5 wt%, the relative permittivity can reach as high as about 150 000. The addition of Ni has a similar effect as Co. Addition of Cr can enhance the permittivity and suppress the dielectric loss tangent under 0.05 [119]. When doping with Fe or Mn, the relative permittivity will decrease sharply to less than 100. Yb-modified $CaTiO_3$ ceramics of composition $Yb_xCa_{1-x/2}Ti_{1-x/2}O_3$ was studied [120]. Ytterbium is incorporated as Yb^{3+} at both cation sites with charge self-compensation. Dense ceramics sintered for 24 hours at 1450 °C exhibit a giant apparent permittivity of about 10^4 with a remarkable temperature (30–300 K) and frequency (10^1–10^6 Hz) stability. $MgTiO_3$ is added to refine the grain size; the dielectric constant and loss of the composites are stable with the frequency and temperature; and the breakdown voltage of the composite ceramics is adjusted from 200 to 1200 V mm^{-1} by controlling the ratio of the amount of CCTO and $MgTiO_3$ composites [106]. With the increase of Zn^{2+} concentrations in CCTO, the dielectric constant increases with an increase in minimal concentration, and the dielectric loss decreases with an increase in concentration. This was explained by the impedance analysis, which shows that the conductivities of grains and grain boundaries increase as Zn^{2+} concentrations in CCTO increases [121].

Stoichiometry has also been demonstrated to play a crucial role in obtaining a giant permittivity value [122, 123], any off stoichiometry results in the decrease of the low-frequency dielectric permittivity values. In order to understand the effect of stoichiometry, some dopants have been introduced into the CCTO structure. Doping with donors such as Nb^{5+} or acceptors such as Fe^{3+} cations has been reported to decrease the value of the dielectric plateau (as shown in Figure 10.10a) because of an increase in the GBL thickness, resulting in a lower grain boundary capacitance [124]. Fe^{3+}- or Nb^{5+}-doped CCTO ceramics show a microstructure with a homogeneous grain size <60 μm that contrasts with the large grains >100 μm of the undoped samples [125]. Capsoni et al. [126] showed that the dielectric constant can be increased by up to two orders of magnitude when substituting the Ti^{4+} cations by Fe^{3+}, Co^{2+}, or Ni^{2+}. The Nb^{5+} substitution for Ti^{4+} in CCTO is achieved in a limited range without secondary-phase formation, and the dielectric constant increases up to $\sim 4.2 \times 10^5$ [127], whereas the bulk (grains) resistivity remains unchanged with Nb^{5+} substitution, the grain boundary resistivity is significantly reduced even though the grain size decreases, in contrast to the results shown in Grubbs et al. [124].

The dielectric properties can be strongly modified by annealing the ceramic at 1100 °C. The reoxidized material shows the intrinsic dielectric response of $CaTiO_3$ at low temperature and high frequency, whereas a step-like rise in the permittivity and a complex behavior is observed with an increasing temperature and decreasing frequency [120].

10.3.3.3 Dielectric Loss

Although the CCTO ceramic has an extremely huge permittivity, it has a large dielectric loss. The loss tangent of pure CCTO is usually 0.1 or larger (see Figure 10.12), which hinders its application in the industry.

Various means were tried to lower the dielectric loss. It was reported the sintering temperature has an influence on the dielectric loss of CCTO, the one sintered

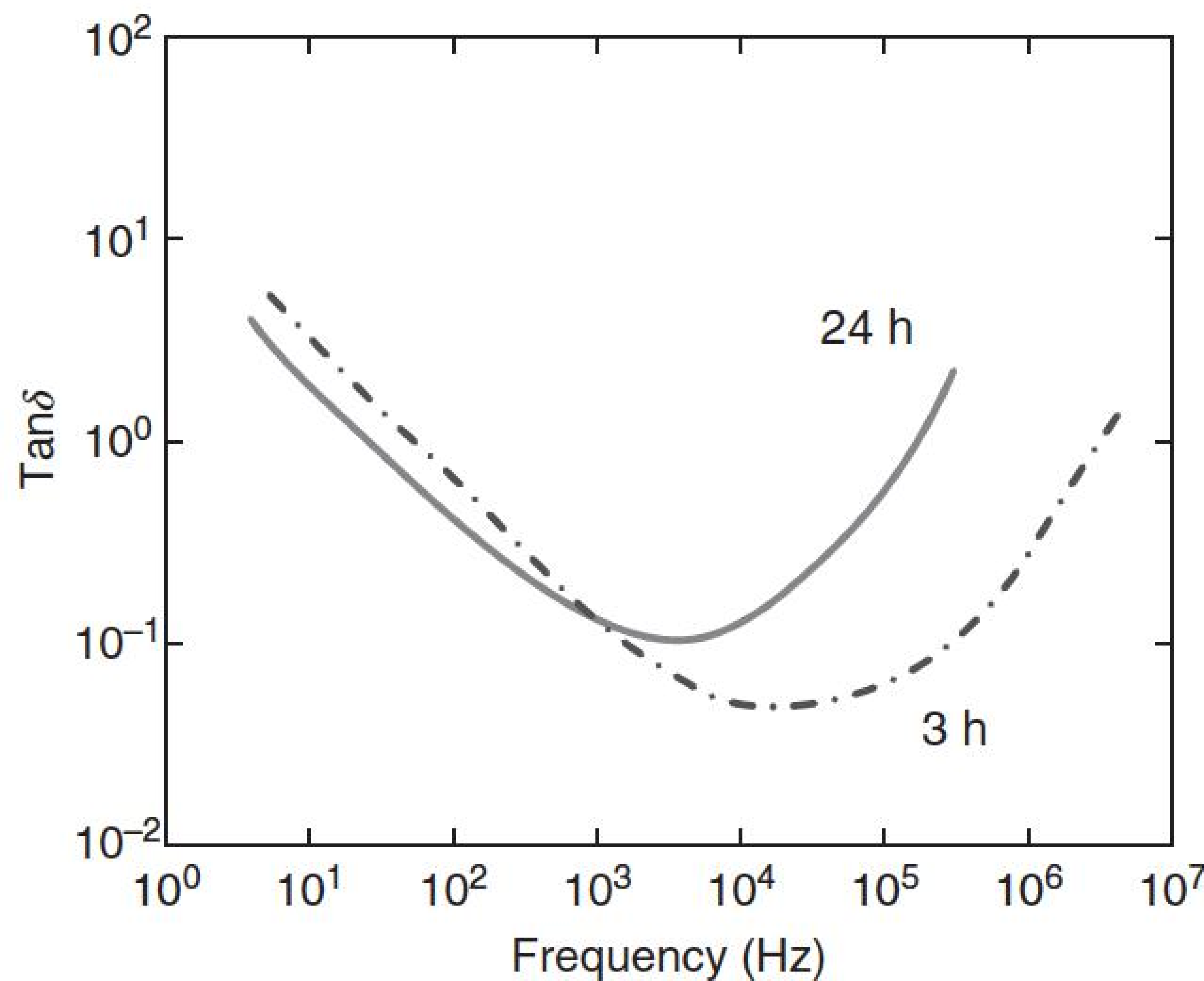


Figure 10.12 The dielectric losses of CCTO ceramics in different sintering time. Source: Kwon et al. 2008 [119]. Redrawn with permission from Elsevier.

at 1050 °C has relatively a low loss [108]. Kobayashi and Terasaki [128] added an excessive $CaTiO_3$ to fabricate $CaCu_3Ti_4O_{12}/CaTiO_3$ ceramic composite and successfully lowered the loss tangent to less than 0.02. However, the relative permittivity was also lowered to 1800. Slight doping of Fe or Mn can significantly decrease the dielectric loss. Substituting part of Ti with Al atoms could suppress the loss tangent to 0.06 and lower at the measuring frequency ranging from 100 to 1000 Hz [129]. When doping with 0.5 wt% ZrO_2, the loss tangent can be lowered to 0.05 from 50 Hz to 30 kHz [130].

Furthermore, the codoping method is effective in reducing the dielectric loss, still maintaining the high dielectric permittivity. The room temperature dielectric loss of the Cr/La codoped $CaCu_3Ti_4O_{12}$ ceramics is reduced to 43% compared to CCTO, and their dielectric permittivity is higher than the undoped, Cr-doped, and La-doped samples, and the temperature stability of the codoped sample is significantly more convenient than that of CCTO [131].

10.3.4 Mechanism

10.3.4.1 IBLC Model

The origin of the colossal permittivity is being in debate. Several mechanisms have been proposed to explain the colossal permittivity of CCTO. The first one is the polarization mechanism. Ramírez et al. [101] observed that the dielectric spectroscopy of CCTO shows a relaxation process, and the Raman spectroscopy also shows a relaxation mechanism with activation energy of 28 meV existing in the CCTO materials; they thought a polarization mode exists in CCTO. Homes et al. [108] prepared a single-crystal CCTO, the relaxation time increases to more than 10 seconds under high temperature from 500 ns under the room temperature, and thought this huge change originates from the dipole oscillation relaxation in a nanodomain. The second is the influence from an electrode. Lunkenheimer et al. [111, 132] regarded that the colossal

permittivity phenomenon of CCTO is related to the depletion layer produced by the contact between the ceramic and electrode, the relaxation peak in dielectric spectroscopy should belong to Maxwell–Wagner relaxation mode. This can explain that the dielectric constant of CCTO in different studies is hugely different. Wang and Zhang [133] found that a relaxation peak exists at 250 K under the low frequency of 100 Hz, and under this relaxation peak, the dielectric constant was strongly related to the thickness of the sample; they thought that this relaxation was caused by the Maxwell–Wagner relaxation related to the polarization of the superficial layer, but they thought that this superficial layer was caused by the concentration difference between the surface and the interior instead of the electrode contact.

Currently, the "internal barrier layer capacitance" (IBLC) model raised by Adams et al. [90] and Sinclair et al. [109] is most accepted. In this model, CCTO is considered consisting of semiconductive grains and insulating grain boundaries, such as the ZnO varistor. The schematic diagram is shown in Figure 10.13a. The impedance spectroscopy as well as the scanning probe microscopy measurements on the grains and GB supported the IBLC model [73, 109, 135]. This model states that the dielectric behavior of CCTO does not come from intrinsic or from space charge polarization mechanisms, but from heterogeneities of the ceramic structure [125, 136].

Based on an alternating current (AC) impedance spectroscopy measurement, it appears that the dielectric permittivity has a sharp drop in ε' vs f relationship curve at sufficiently high frequency and the giant extrinsic GB value ε_2 reduces

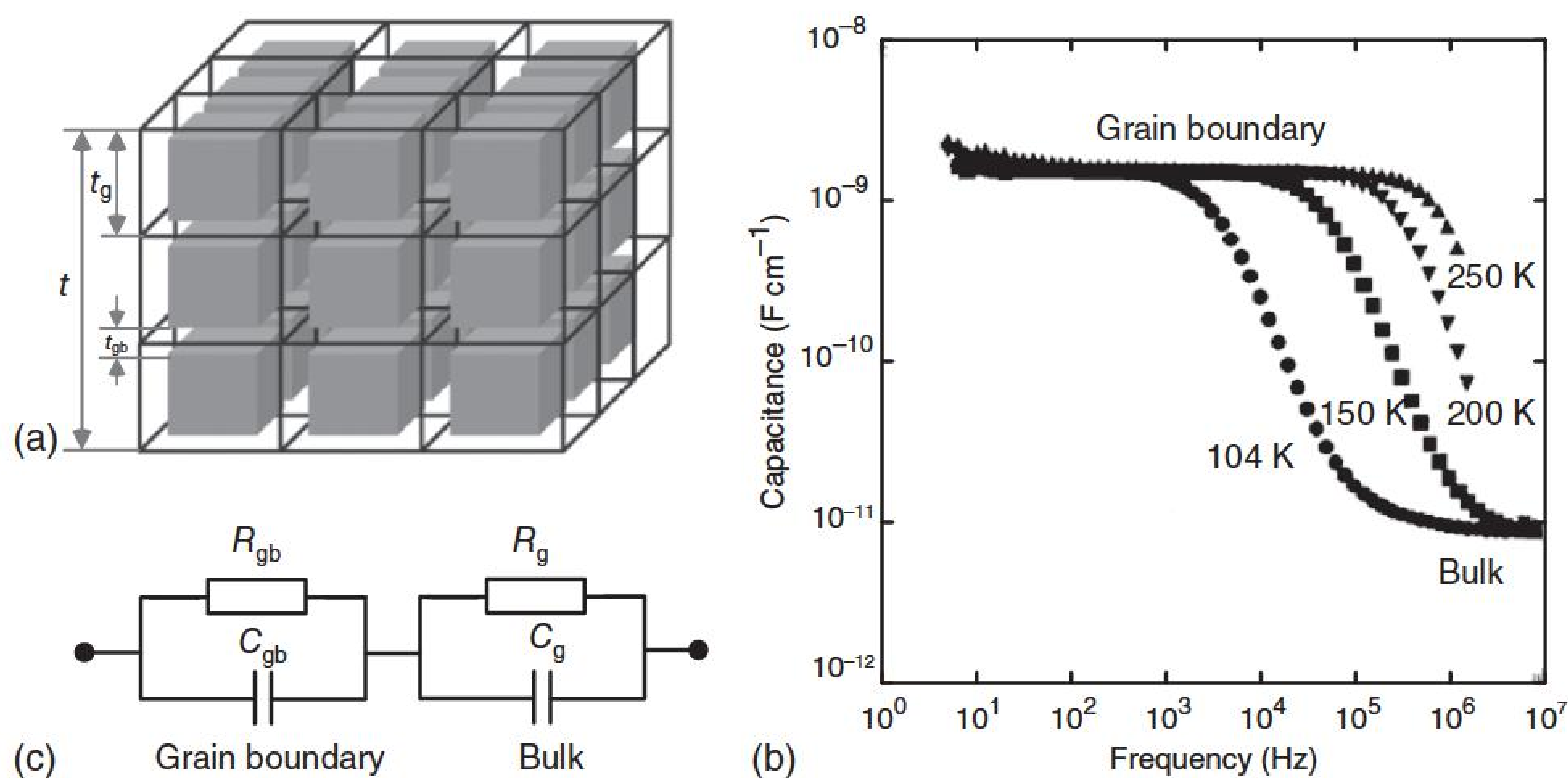


Figure 10.13 (a) The schematic figure of brick layer capacitance model, showing the semiconductive grains and insulating grain boundaries. Source: Schmidt et al. 2012 [134]. Reproduced with permission of John Wiley & Sons; (b) impedance spectroscopy (IS) data from CCTO ceramics represented in the notation of the real part of capacitance C' (effectively ε') versus frequency f. Source: Sinclair et al. 2002 [109]. Reproduced with permission of AIP.; (c) idealized equivalent circuit model to account for GB and bulk dielectric relaxation processes. Source: Adapted from Schmidt et al. [134].

to a grain's relative dielectric permittivity ε_1 of ≈100 as shown in Figures 10.10c and 10.13b. This is the typical behavior of an IBLC structure, where the sharp permittivity drop occurs when the mean electron conduction path permitted by the applied alternating voltage signal decreases below the average grain size at an increased frequency [134]. The high-frequency dielectric response is, therefore, dominated by the conducting bulk (grains) and the low-frequency response by the insulating GB contribution. Both dielectric relaxation processes of grain boundary and bulk can each be described ideally by one parallel resistance–capacitance circuit (RC element), and the macroscopic behavior can be represented by a series circuit of two RC elements as demonstrated in Figure 10.13c [134]. The resistances R_g and R_{gb} correspond to the bulk and GB resistivity (ρ_g and ρ_{gb}), respectively, and the capacitances C_g and C_{gb} represent bulk and GB permittivity (ε_g and ε_{gb}), respectively.

When a voltage is applied to the ceramic, the voltage is almost applied on the grain boundaries. The capacitance is calculated by

$$C = \frac{\varepsilon_0 \varepsilon_{rgb} S}{t_{gb}} \tag{10.11}$$

where ε_{rgb} is the relative permittivity of the grain boundary, t_{gb} is the sum of grain boundary thickness in the direction of voltage drop, and S is the area of the electrode. Then, we can get Eq. (10.10) to calculate the effective relative permittivity ε_{eff}, the average thickness of the grain boundaries, t_{gb}, generally ranges from 20 to 200 μm, and t_g is in nanometer level [135]. The relative permittivity of grain boundaries ε_{rgb} is about 200 [137]. According to this theory, the effective permittivity is proportional to the grain size.

The dielectric relaxation can be empirically described by Debye-type or Cole–Cole relaxation. The complex impedance measurement, which is usually used to analyze the properties of polycrystallines, provides evidence of this model. Sinclair et al. [109] measured the complex impedance (cole–cole plot) at the temperature around 100 K, finding that two semicircles evidently appear in each plot (see Figure 10.14). This result clearly shows the heterogeneous nature inside the ceramic.

According to Figure 10.15 [138], using the data of the peak frequency, f_p, which corresponds to the maximum of ε'', the activation energy, E_0, can be obtained from the slope of the line of $\ln(f_p/T^2)$ against $1/T$, which is 0.603 eV, close to the reported 0.60 eV. This energy can be attributed to the activation of oxygen vacancies V_O^+ to V_O^{2+} in the depletion layer. In the region of E_0 slightly lower than the Fermi level, V_O^+ are ionized when the temperature is increased up to 398 K, and the dielectric relaxation shown in Figure 10.15 is related to the activation of V_O^+ to V_O^{2+}.

As in the ZnO varistor, the nonlinear I–V characteristics are considered originating from the Schottky-type boundaries. Chung et al. [73] measured the I–V characteristic curve of individual grains and grain boundaries, finding that the grain was ohmic with relatively small resistance, whereas the grain boundaries were more insulating with nonohmic properties. This measurement gave direct evidence to this theory.

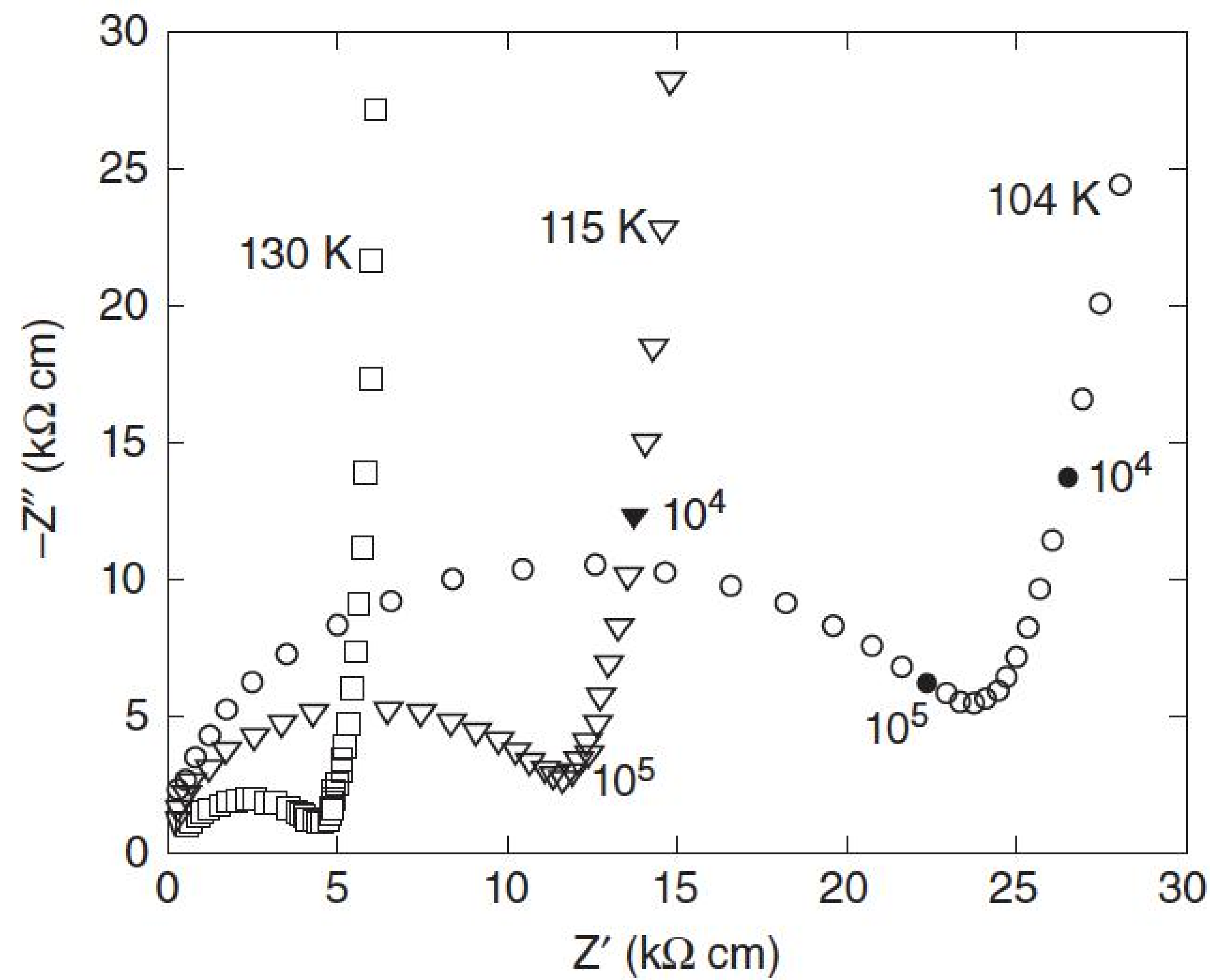


Figure 10.14 The complex impedance spectroscopy of CCTO. Source: Sinclair et al. 2002 [109]. Reproduced with permission of AIP.

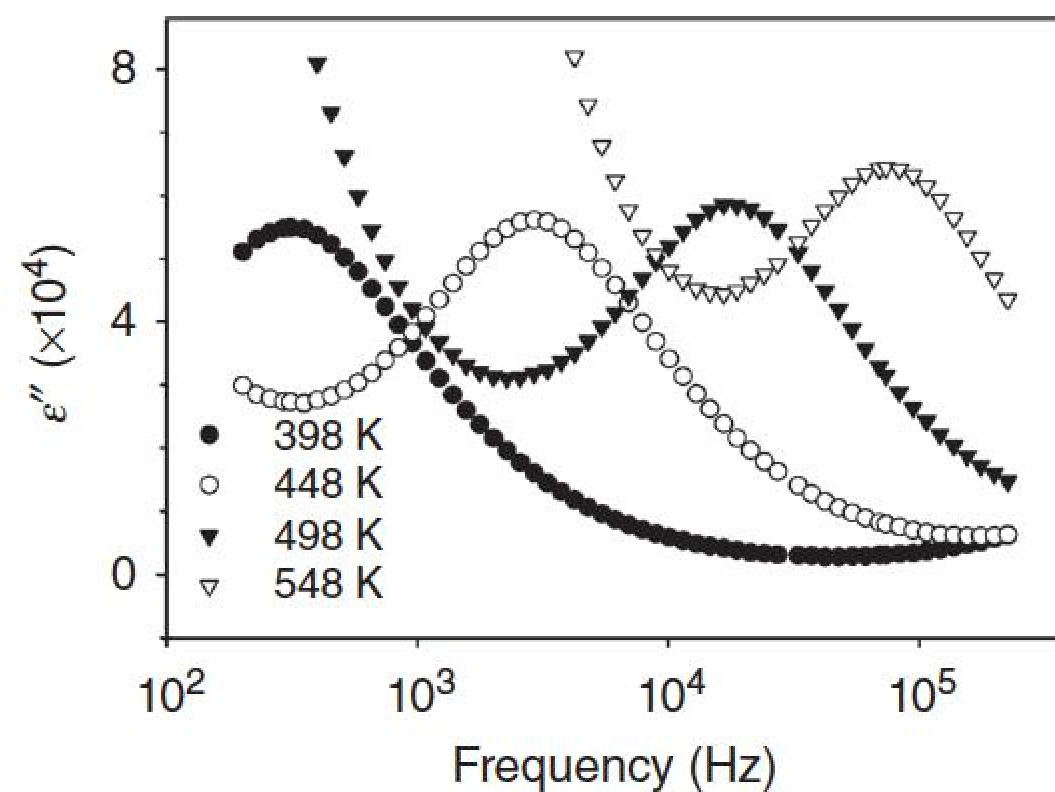


Figure 10.15 Frequency dependence of imaginary part, ε'', of dielectric permittivity of the CCTO ceramic sample. Source: Zang et al. 2005 [138]. Reproduced with permission of IOP.

De Almeida-Didry et al. [139] deduced the role of grain boundaries in the colossal permittivity ε of doped and undoped CCTO from the analysis of impedance measurements; the permittivity is primarily related to the capacitance of the grain boundaries, as well as the loss factor, which is found to be correlated with the resistance of the grain boundaries rather than that of the grains. These findings indicate the leading role of grain boundaries in the origin of the capacitance of CCTO samples.

Figure 10.16 shows the real part of conductivity σ' vs frequency f at 80 K for CCTO samples sintered at various sintering temperatures [134] and the magnitude of the high-frequency plateau associated with the bulk (grains) dielectric relaxation increases significantly with the increase of sintering temperature, which indicates an increase in bulk conductivity. In the framework of the brick-work layer RC element model as shown in Figure 10.13c, the conductivity σ' plateau at high frequency represents the intrinsic bulk conductivity. It can be seen that at 80 K, the bulk conductivity strongly increases by a factor of ~100 with the increase of sintering temperature.

The complex analysis of capacitance is useful to separate distinct relaxation processes and can sometimes be useful to separate different polarization effects that contribute to the global frequency response or to the total relaxation

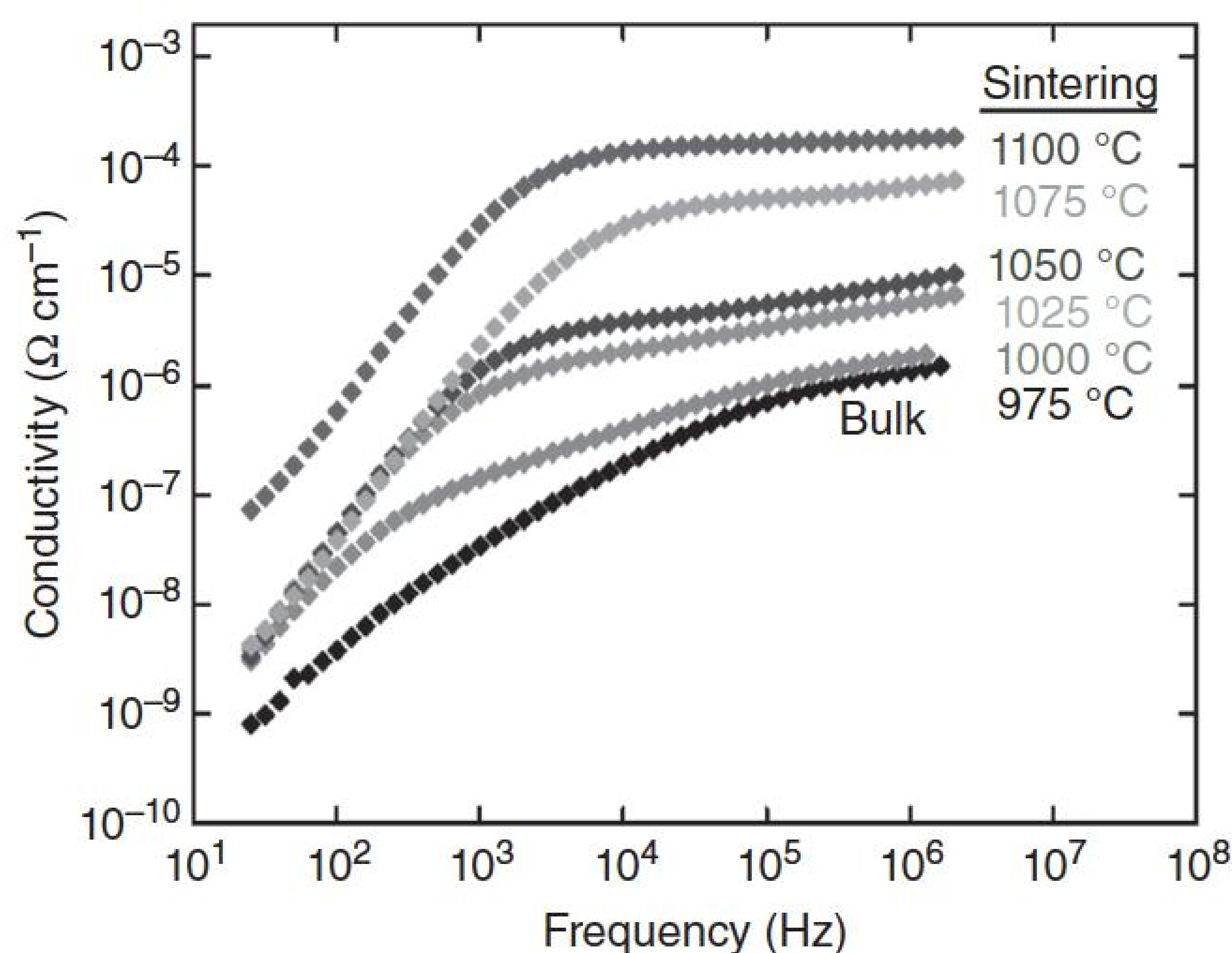


Figure 10.16 Real part of conductivity σ' versus frequency f at 80 K for CCTO samples sintered at various temperatures. Source: Schmidt et al. 2012 [134]. Reproduced with permission of John Wiley & Sons.

response [114]. Bueno et al. [114] used spectroscopic analysis to separate the bulk's dielectric dipolar relaxation contribution from the polarization contribution because of space charge in the grain boundaries of a $CaCu_3Ti_4O_{12}/CaTiO_3$ polycrystalline composite system. The *bulk dielectric dipolar relaxation* is attributed to the self-intertwined domain structures from the $CaCu_3Ti_4O_{12}$ phase coupled to *the dipole relaxation* from the $CaTiO_3$ phase, whereas *the space charge relaxation* is attributed to the Schottky-type potential barrier responsible for the nonohmic property.

$CaCu_3Ti_4O_{12}$ (CCTO) is a 1 : 3 A-site-ordered perovskite ($A'A''_3B_4O_{12}$). Much effort has been dedicated to understand the origin of the extrinsic giant-relative permittivity, but little effort has been made to study the intrinsic (bulk) relative permittivity, ε_r, which is in the range of ~100 [111]. Although this is considerably smaller than the giant extrinsic values, it is still higher than that which would be expected in a nonferroelectric material from the polarizabilities of the constituent atoms. An additional mechanism, therefore, was proposed to explain the high intrinsic ε_r of CCTO. A′–A″ antisite defects have been proposed to be responsible for such an increase in ε_r [124]. Quantitative electron diffraction (QED) and extended X-ray absorption fine structure (EXAFS) analysis were employed to demonstrate Ca and Cu disorder in CCTO on a nanometric scale, and the increased ε_r was proposed to be a result of the modified electronic structure of the defect Cu cation on the A′ site. Schmidt et al. [134] showed that lattice stretches near defect A′ site Cu, or more likely near defect A″ site Ca, in CCTO may be an alternative explanation for the large bulk dielectric permittivity ε_r.

10.3.4.2 Conducting Mechanism

The mechanism of grain boundary barrier formation is based on crystal chemistry. Ceramics often have a variety of defects, including impurity defects and component defects (ion vacancies, etc.). These grains will produce weakly bound electrons or holes, making the bulk semiconductive. The grain boundary can be in a high-impedance state because of the structure or chemical compositions

and the carriers are captured at the boundary layer, resulting in the formation of a potential barrier. The type of carriers in semiconductors can be determined by testing the sign of Seebeck coefficient. The Seebeck coefficient of CCTO was tested as $-110\ \mu V\ K^{-1}$ at 350 K by thermoelectric power measurements [84] and was found to be negative, indicating that the carriers are electrons, i.e. the bulk of CCTO is an n-type semiconductor.

Specifically, there are mainly two explanations for the formation mechanism of carrier in the bulk and barrier at the grain boundaries. In the first theory, the generation of charge carriers is considered the result of oxygen deficiency [129, 140]. In the sintering process, slight defects of oxygen deficiency will be generated in the crystal lattice, where the oxygen is supposed to lose at high temperature and electrons are given out as charge carriers, which can be presented by [109]



$$O_O \rightarrow V_O^{2+} + 2e^- + \frac{1}{2}O_2 \uparrow \tag{10.12}$$

Carriers are generated in the grains and make the bulk semiconducting. In the cooling process, the defect occurs in the reverse process of the reaction, i.e. oxygen atom enters the lattice from outside and captures two electrons, and the material loses its conductivity. However, because of a limited diffusion rate, oxygen atoms cannot enter the deep inside of the crystal lattice, and they only spread along the grain boundaries, where the defects make the diffusion much easier. In this way, the combination of semiconducting bulk and insulating grain boundary forms.

Bueno et al. [102] thought that the space charge relaxation was attributed to the Schottky-type potential barrier responsible for the highly nonohmic properties of CCTO. This theory was supported by experiments. Adams et al. [83] found that annealing in an oxygen environment reduced the grain boundary resistance of several orders of magnitude. This shows that the formation of high-resistance GBL depends on the atmosphere of oxygen. Because of the lack of oxygen in the environment, the reverse process of the reaction cannot occur, and thus, the resistance of the GBL cannot be recovered. After annealing in an oxygen atmosphere, the GBL resistance will return to its original level. This result confirms the mechanism of oxygen vacancy conductivity.

The carriers can be captured by Ti^{4+} or Cu^{2+} to form Ti^{3+} or Cu^+, and then the carriers are transferred between Ti^{4+}/Ti^{3+} and Cu^{2+}/Cu^+ to make the bulk conductive. Chakravarty et al. [141] supposed that Ti^{4+} is more stable than Cu^{2+}; thus, the carriers are more probable to transfer between Cu^{2+} and Cu^+. However, Pires et al. claimed that they found Ti^{3+} existing in CCTO by using electron spin resonance (ESR), proving that the carriers transfer among Ti atoms [117]. With X-ray photoelectron spectroscopy (XPS) analysis, it was found that the valence of Cu and Ti elements in the $CaCu_3Ti_4O_{12}$ ceramics is obviously influenced by the O_2 concentration based on the experimental comparison of $CaCu_3Ti_4O_{12}$ ceramics sintered in air and pure O_2 atmosphere, which suggests that the valence of metallic elements and defects play a key role for the origin of the giant permittivity and I–V nonlinear characteristics in the $CaCu_3Ti_4O_{12}$ ceramics [142].

Another theory to explain the conducting mechanism of CCTO is due to the valence variation of Cu ions. As Cu^{2+} is not stable at high temperature and tends to change into Cu^{+}, in the cooling process [84, 135], Cu^{+} will change back to Cu^{2+} and give out electrons:



$$2Cu^{2+} + O^{2-} \rightarrow 2Cu^{+} + \frac{1}{2}O_2 \uparrow \tag{10.13}$$



$$Cu_{Cu}^{-} \rightarrow Cu_{Cu} + e^{-} \tag{10.14}$$

The electron given out here will transfer between Ti^{4+}/Ti^{3+} ions to make the bulk conductive.

In the model suggested by Li et al. [86], the charge deficit resulting from a slight reduction in Cu^{2+} to Cu^{+} is compensated by a slight substitution of Ti^{4+} at the Cu site in CCTO at high temperatures. Upon cooling to room temperature, Cu^{+} ions are reoxidized into Cu^{2+} and partial Ti^{4+} would reduce to Ti^{3+}. Therefore, the formula can be represented as $Ca^{2+}(Cu^{2+}_{1-3x}Cu^{+}_{2x}Ti^{4+}_{x})Ti^{4+}_{4}O_{12}$ at high temperatures and $Ca^{2+}(Cu^{2+}_{1-x}Ti^{4+}_{x})(Ti^{4+}_{4-6x}Ti^{3+}_{6})O_{12}$ at low temperatures for CCTO. Because the composition is different from the starting stoichiometric CCTO composition, there should be some forms of Cu-rich secondary phases existing in the specimen. The CuO or Cu_2O phase observed using XRD in the specimen prepared in stoichiometric CCTO was reported [100, 125]. TEM observation indicates that Cu-rich secondary phases are mainly located at the grain boundaries. The XPS results reveal that Cu^{+} is the major content of the second phases. The formation of negatively charged species, V_{Cu}^{-}, $Cu_{Cu^{2+}}^{-}$, or V_{Cu}^{2-}, existing at the grain boundaries because of the oxidation of the secondary phase during cooling after sintering can act as acceptors, to form double-Schottky barriers with n-type semiconductor grains [143].

10.3.4.3 Polarization Mechanism of Grains

The capacitances of grain and grain boundary in CCTO were obtained by microcontact test, as shown in Figure 10.17 [144]. It is observed that the grain capacitance and grain boundary capacitance exhibited completely different properties. Below 1 kHz, the grain boundary capacitance is in the level of 10^{-10} F and decreases with the increase of frequency. Based on the geometric structure of the grain boundary of CCTO, the relative dielectric constant was calculated in the level of 10^4, which concurs with the result of CCTO ceramic. As the frequency of the applied voltage increases, the grain capacitance increases to 10^{-11} F from 10^{-8} F, which obviously has a low-frequency dispersion (LFD) phenomenon. This phenomenon cannot be tested from the CCTO ceramic bulk.

Jonscher explained the LFD phenomenon in different materials [145, 146], which refers to a kind of relaxation phenomenon existing in many materials with the main characteristic that the dielectric constant of the material increases rapidly with the decrease of the frequency in low-frequency region. The relationship between the dielectric constant and frequency can be represented by a log linear trend; In addition, the dielectric constant increases without the saturation trend. The LFD phenomenon can be found in materials with

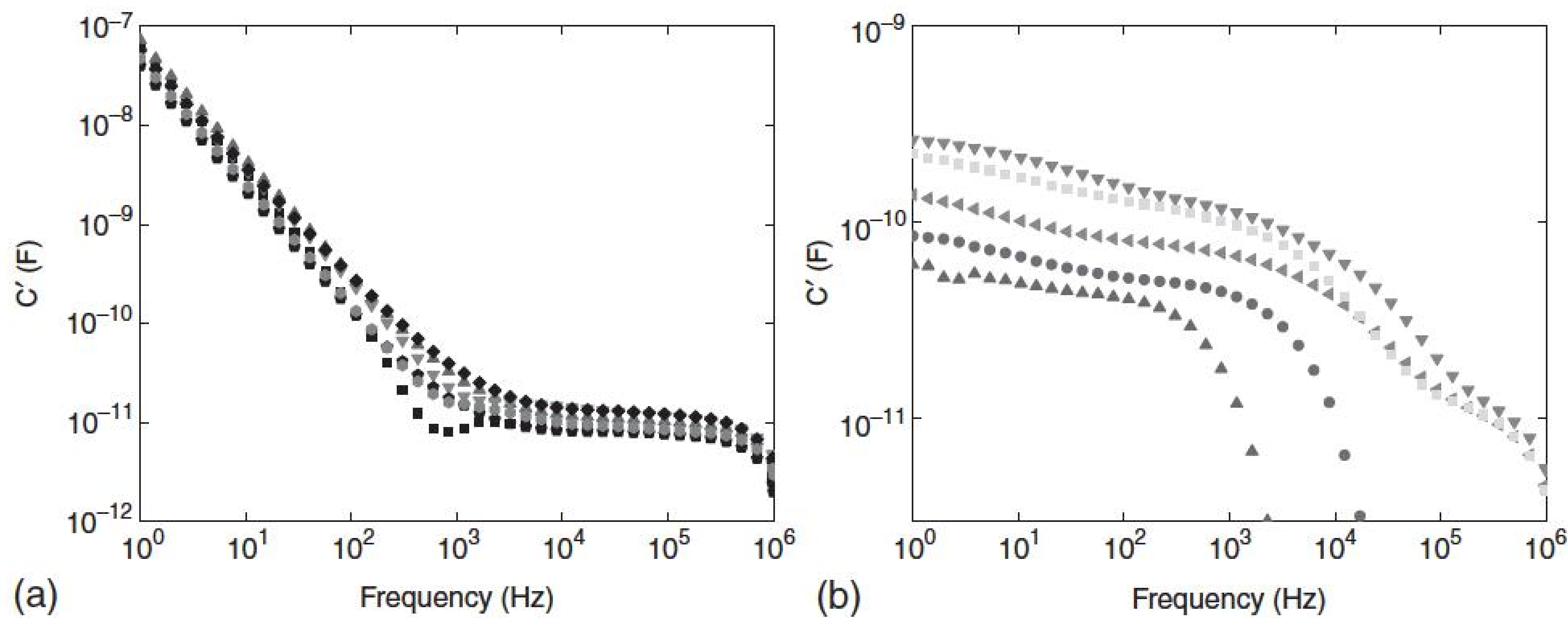


Figure 10.17 The capacitance of (a) grains and (b) grain boundaries in CCTO microstructures. Source: Luo 2011 [144].

inner "quasi-free charges" [147]. The contribution of "quasi-free charges" on the dielectric property of materials can be explained as follows. Considering a quasi-free charge A^- neighboring a fixed charge B^+, when an electric field is applied, A^- can migrate in a short range and deviate the original location, which leads to generate an electric moment. During the migration process, A^- is easy to combine with B^+ to become a neutral particle AB and then stop migration. However, this combination is weakly bonded, the neutral particle AB will be easily ionized again, and continue the migration to increase the electric moment, the migration will stop when A^- is blocked by a lattice defect. When the applied electric field is moved away, then A^- will migrate back to the original position. This polarization needs a long time to be completely established. The longer the electric field is applied, the bigger the generated electric moment is. Therefore, as the frequency of the applied electric field decreases, the dielectric constant increases rapidly.

Therefore, the LFD phenomenon in CCTO grains provides a clue to discover the conductive and dielectric mechanisms of grains. Under low frequency, the relaxation in grains caused by "the quasi-free charges" takes the dominant position. The electrons produced in grains can be classified into A^-, and Ti^{4+}/Cu^{2+} is B^+. The materials with inner fixed B^+ usually have large DC conductivity, which is consistent with the performance of CCTO [144].

10.3.4.4 A Polaronic Stacking Fault Defect Model

Bueno et al. [148], by considering stacking fault as the origin of the high dielectric constant phenomena, thought that the internal barrier layer capacitance mechanism would be enhanced by another similar, but different in nature, mechanism that operates in the nanoscale range because of the polaronic structures associated with stacking fault, a mechanism that is referred to as nanosized barrier layer capacitance (NBLC), a nanoscale effect on the capacitance, or effective dielectric constant of the system.

The NBLC mechanism reconciles the opposing views of researchers on both sides of the intrinsic versus extrinsic debates about the origin of the unusually

high values of dielectric constant measured for CCTO in its various forms. The approach is capable of explaining in a simple way how huge dielectric constant coexists with high dielectric loss, providing an explanation of the dielectric and semiconducting features in CCTO materials. This model operates simultaneously with the IBLC model so that the dielectric relaxations of the grain boundary and polaronic defect are used to explain the high permittivity values.

In a perfect CCTO crystal, Cu^{2+} ions are coordinated by 4 oxygen atoms leading to a square-planar arrangement bonded to Ca^{2+} (coordinated by 12 oxygen atoms) in such a way that an alternating Cu/Ca network extends in three different directions: [1 0 0], [0 1 0], and [0 0 1]. Furthermore, these Cu and Ca atomic layers are intercalated by Ti^{4+} ions coordinated by six oxygen atoms. The simple creation of planar defects would generate a number of imbalances that would in turn precipitate other structural changes in order to address the increase in lattice energy. The stacking fault defect chemistry is composed of Ca atoms subcoordinated, Cu^{+} and TiO_5 cluster substructures with oxygen vacancies valences. The formation of point defects (oxygen vacancies and metal valence changes) would bring about a more defective structure, albeit not necessarily an energetically stable structure [148].

10.3.5 Role of Dopants

Doping is an important tool to tailor the performance of varistors. Despite the colossal permittivity, the dielectric loss of CCTO is too high for industrial application. Various additives have been employed to diminish the dielectric loss, increase the nonlinearity, and improve the dielectric property of CCTO by controlling the chemistry and structure of the interfacial regions at the grain boundaries [104, 109, 149–167]. For example, the dielectric and nonohmic properties are enhanced with the introduction of NiO, SnO_2, and SiO_2 additives [168], or by these various cationic substitutions at Cu or Ti site [169–176]. There are two types of substitutions [95]: acceptor and donor. The acceptor cationic substitution is defined as cations replacing the ions with lower ionic charges, whereas the donor cationic substitution is defined as cations replacing ions with higher ionic charges. Only few reports were found on donor cationic substitutions of Nb^{5+}, Ta^{5+}, and Sb^{5+} at Ti site in CCTO by the conventional solid-state reaction [177–179]. The dielectric properties of CCTO are also strongly dependent on the processing conditions such as preparation routes [180, 181], sintering temperatures [182, 183], and sintering durations [184–186]. The synthesis method of CCTO ceramic has played a significant role in determining the microstructural, electrical, and dielectric properties [95].

10.3.5.1 Role of Doping CuO

Luo et al. [110] sintered the CCTO pellets, which were pressed at 150 MPa into disks with $CaCO_3$, CuO, and TiO_2 powders mixed by ball milling and calcined at 900 °C for 12 hours. The pellets were sintered at different temperatures. At 1150 and 1200 °C, there was a great loss of CCTO phase and an increase of $CaTiO_3$ and TiO_2. However, there was no corresponding increase in CuO or Cu_2O. Test results indicated that CCTO decomposed completely at 1150 and 1200 °C, and

Cu atoms volatilized, only $CaTiO_3$ and TiO_2 were kept. CCTO was discovered to partially decompose, and the segregation of Cu was supposed to have significant effects on its properties [100, 130]. Actually, CuO will be reduced to Cu_2O over 1000 °C. CuO/Cu_2O can form a liquid phase, which is supposed to help with the sintering of the ceramic [83, 130]. The gradual loss of pellets' density between 1000 and 1100 °C suggests the gradual segregation and volatilization of CuO/Cu_2O before the complete decomposition. Prakash and Varma [187] also found that sintering at more than 1100 °C in air led to Cu segregation on the sample surface.

The distribution of the elements around a triple grain boundary junction shows that Cu is richer, whereas Ca and Ti are much poorer at the grain boundaries than inside the grains. It indicates that the grain boundaries are mainly formed by CuO. Cu segregates from the CCTO lattice and forms Cu-rich intergranular layers [110]. As shown in Figure 10.14, the intergranular layer is rich in Cu.

The status of CuO is found to play an important role in the evolution of the microstructure and the electric performances. The resistance of the samples decreases as the sintering temperature increases [110]. The reduced thickness of grain boundaries is the most probable reason for the decrease of resistance, which results from the volatilization of CuO. Additionally, the ceramic acquires much higher conductivity and permittivity abruptly when the sintering temperature rises from 975 to 1000 °C, a possible explanation is that the temperature of 975 °C has not reached the critic point for the CuO to turn into Cu_2O and form a liquid phase, which is supposed to be essential for the enlargement of the grains and also the formation of the electrical properties [83, 84, 135]. In the research of Li et al. [84, 135], it is assumed that the Cu^{2+} ions are reduced to Cu^+ ions at high temperature, and the Cu^+ ions give out electrons to the 3d band of Ti^{4+} on cooling. This theory explains why the bulk phase of CCTO is so conductive. The sintering temperature of 975 °C has probably not reached the point (about 1000 °C) for Cu^{2+} ions to change into Cu^+ ions [110]. Therefore, under 975 °C, CuO will not be reduced to Cu_2O, and no electrons are provided as the charge carriers, and the bulk of the ceramic is highly resistive. Consequently, the ceramic is almost completely insulating. Sintered at 1000–1125 °C, the pellets have the CuO phase as a partial decomposition product at the grain boundaries. As the sintering temperature rises, the segregated CuO particles volatilize and leave holes at the grain boundaries. The resistance decreases and the effective permittivity increases as a result. At 1150 °C and higher temperature, the CCTO decomposes completely. The Cu atoms vaporize into atmosphere, leaving only $CaTiO_3$ and TiO_2.

When polycrystalline CCTO ceramics were prepared by a solid-state reaction at different oxygen partial pressures, X-ray powder diffraction (XRD) and SEM results indicated that the oxygen partial pressure during the sintering process is an important parameter that controls the phase stability, nonstoichiometry, and decomposition process of the CCTO phase as well as the densification and grain growth mechanisms on these polycrystalline ceramics. These results provided us further insights into the important role of copper reduction and copper/oxygen diffusion on the crystalline structure and morphological characteristics of polycrystalline CCTO ceramics [188].

10.3.5.2 Doping Mechanisms to Tune CCTO Performances

Summarizing all related works, oxide dopants can be classified into the following three tuning mechanisms to improve CCTO characteristics.

Firstly, Changing the Grain Size to Adjust the CCTO Performance Doping will influence the grain size, which is one of the important structure parameters of the polycrystalline material. According to IBLC model, the relative dielectric constant of CCTO has a positive correlation with the grain size. The decrease of grain size will reduce the relative dielectric constant. From many experimental results, except the grain size, the dielectric constant has a weak correlation with other factors, such as impedance and barrier height. We know that the decrease in grain size means the number of grain boundaries in series in unit thickness of CCTO increases, and then the impedance of CCTO will increase, if the electric performance of single-grain boundary keeps unchanged. The low-frequency dielectric loss of CCTO is usually caused by the conductive property, so the increase of impedance caused by the decrease of grain size will reduce the dielectric loss. This has been experimentally verified by doping Bi_2O_3 and PbO.

Doping both Bi_2O_3 and PbO to decrease the grain size have a similar mechanism. First, according to the migration theory of grain boundary, both the solute atoms and particles of secondary phase will reduce the migration velocity of the grain boundary to form the “pinning” effect, which will hinder the shift of the grain boundary and influence the grain growth process. Secondly, the dopants will affect the formation of the liquid phase containing Cu. CCTO has a liquid-phase sintering process, where the liquid phase containing Cu plays a very important role in the grain growth process. When the liquid-phase growth is suppressed, the grain growth velocity will be reduced, but an exception is that the liquid phase increase caused by doping Y_2O_3 will not boost the grains grow bigger [144].

Samples with the nominal composition $Pb_xCaCu_3Ti_4O_{12+x}$ (x = 0, 0.05, 0.1, 0.2) were fabricated by solid-state sintering at 1050 °C for four hours. The ceramic grain size was diminished evidently from about 100 μm to less than 4 μm, and the breakdown voltage gradient was raised from 18 V mm^{-1} to more than 600 V mm^{-1} [144]. EDS measurements (shown in Figure 10.18) revealed that the added Pb mainly accumulates between grains. For the sample of $x = 0.05$, the intergranular region is rich in Pb and Cu and lack Ti and Ca. For the $x = 0.2$ sample, the intergranular region is rich in Pb and lack Cu, Ti, and Ca. However, research showed [120] that when the doping amount x is less than 0.05, no phase related to Pb is detected; when x is higher than 0.1, the peaks of a new phase appears, which is the continuous solid solution of $PbTiO_3$ and $CaTiO_3$ with the nominal composition $Pb_{1-x}Ca_xTiO_3$. Calculated from the peak positions of XRD patterns, the lattice parameters are 0.7395 nm for $x = 0.05$ and 0.7395 nm for $x = 0.1$, respectively, which are slightly larger than the reported 0.7391 nm of undoped CCTO; some Pb^{2+} ions may take the positions of Ca^{2+} and cause the enlargement of the lattice parameter. The SEM images show that the grain size decreases evidently as the doping amount increases.

The segregation of PbO or the intergranular phase $Pb_{1-x}Ca_xTiO_3$ may hinder the grain growth and result in the reduction of ceramic grain size and changing

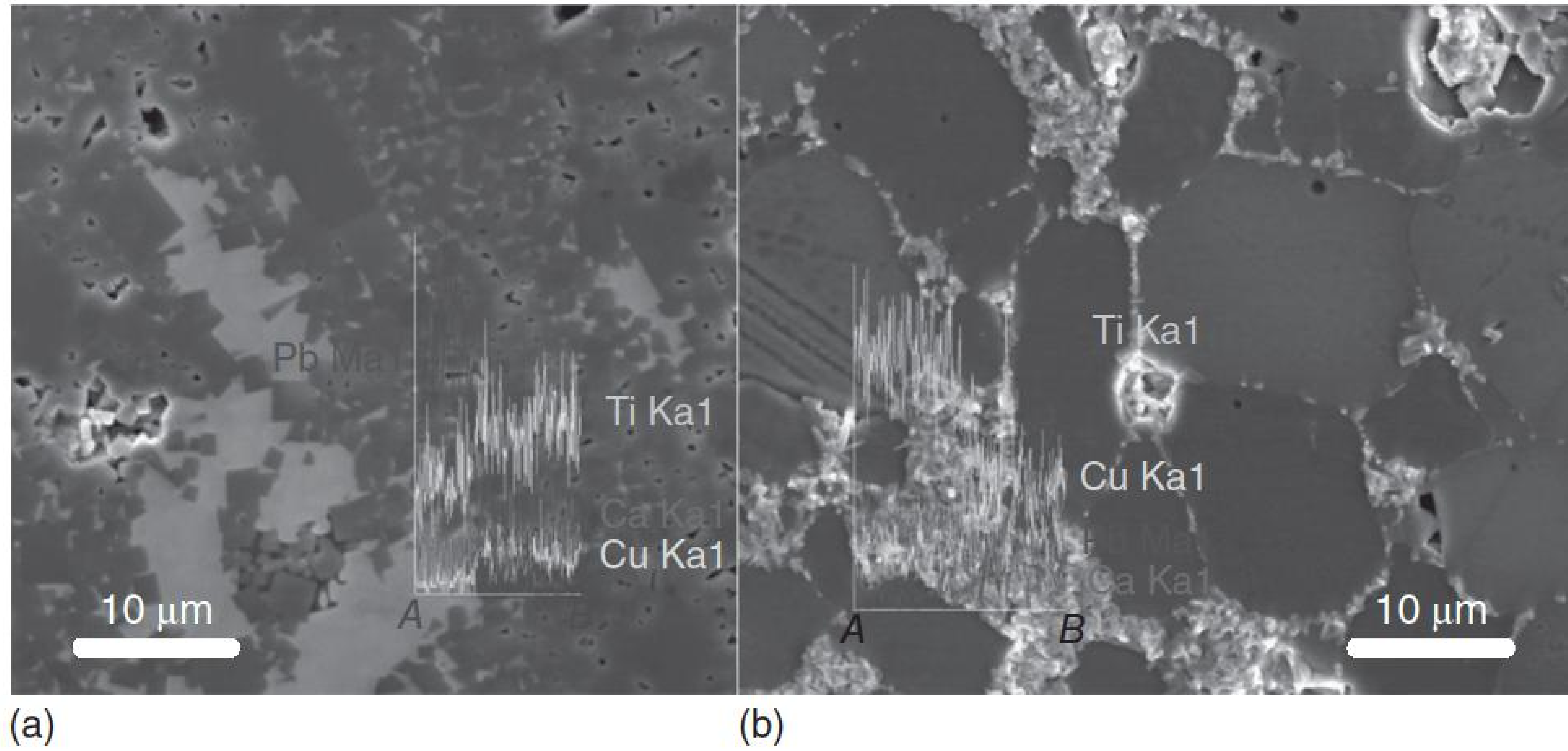


Figure 10.18 The distribution of elements in Pb doped CCTO by using EDS measurement: (a) $x = 0.05$; (b) $x = 0.2$. Source: Luo 2011 [144].

the resistivity of the grain boundaries. The doping of plumbum can evidently enhance the nonohmic property and reduces the dielectric loss and the leakage current [144].

CCTO ceramic samples with Bi doped have the nominal composition $Bi_xCaCu_3Ti_4O_{12}$ (x = 0, 0.15, 0.2, 0.3, abbreviated as CCTO, BCCTO-1, BCCTO-2, and BCCTO-3), and the average grain size decreases when bismuth content increases, which reveals that the content of bismuth can control the grain size of CCTO ceramics, the formation of the second phase $Bi_4Ti_3O_{12}$ is supposed to be the reason for the decrease of average grain size. Generally, the second-phase particles could pin the grain boundaries and stop them from moving, which helps to inhibit the grain growth and obtain fine grains.

The resistor–capacitor (RC) equivalent circuit is often used to analyze the impedance of dielectric ceramics [98]. The complex impedance is expressed as

$$Z(\omega) = \left(\frac{1}{R_{\mathrm{g}}} + j\omega C_{\mathrm{g}}\right)^{-1} + \left(\frac{1}{R_{\mathrm{gb}}} + j\omega C_{\mathrm{gb}}\right)^{-1} \tag{10.15}$$

where ω is the angular frequency. R_{g} and C_{g} are the resistance and capacitance of the grains and R_{gb} and C_{gb} are the resistance and capacitance of the grain boundaries, respectively. Based on this equation, we can see that when $\omega \to 0$, $Z(\omega) \to R_{\mathrm{g}} + R_{\mathrm{gb}}$. In CCTO ceramics, R_{gb} is much greater than R_{g}. Figure 10.19 illustrates the complex impedance plot at room temperature, and the content of bismuth has obviously affected the resistance of the grain boundaries. When the addition of bismuth increases, the resistances also increase. In the IBLC model, the ceramic consists of semiconductive grains and highly resistive grain boundaries. The refinement of the grains means that there are more grain boundaries connected in series in a certain thickness. If the resistance of each boundary remains the same, the total resistance increases. The activation energy at the grain boundary is calculated from the Arrhenius plot, the energy drops from 0.65 eV of pure CCTO to 0.47 eV of BCCTO-3 [144].

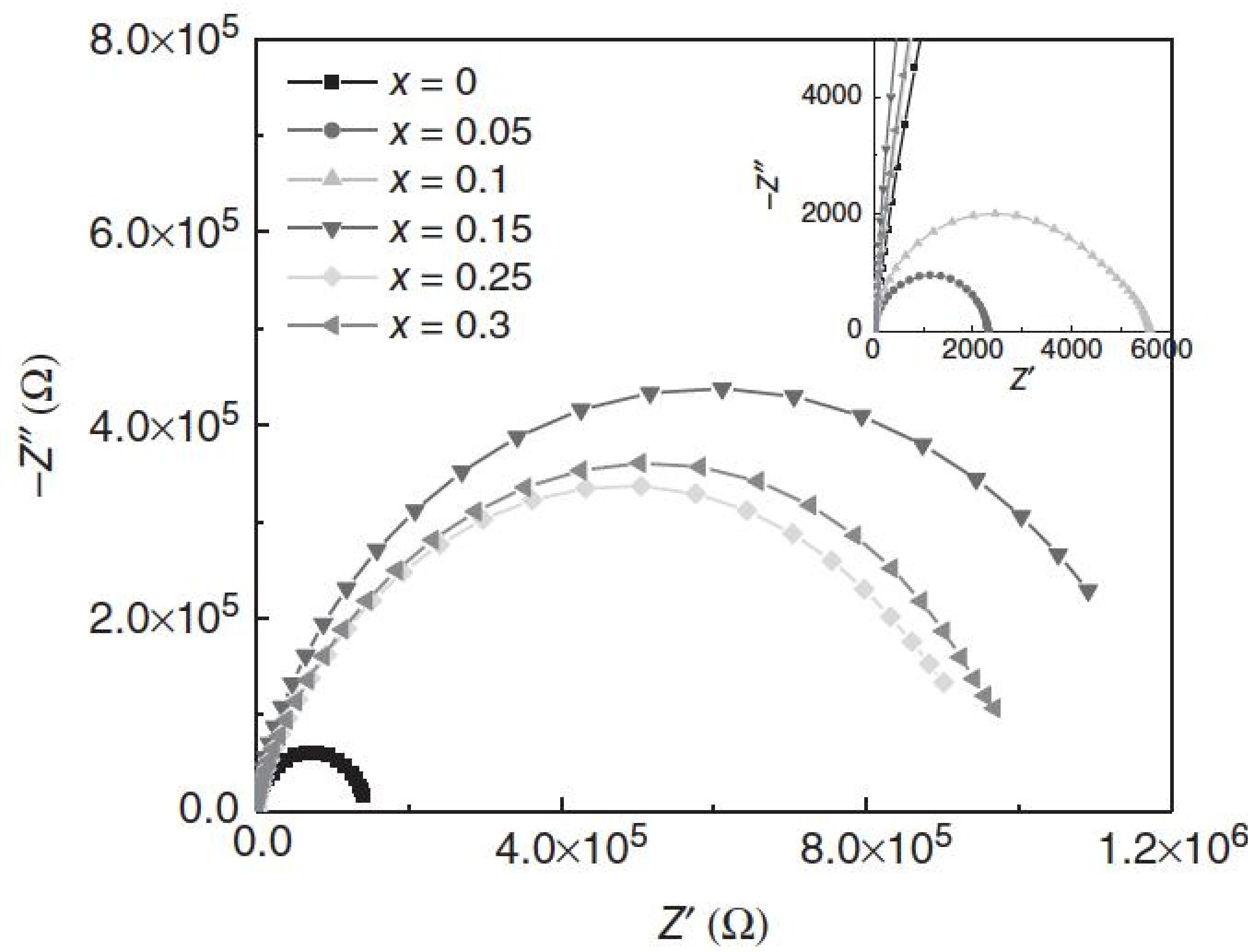


Figure 10.19 Z^* plot for the CCTO and BCCTO ceramics under the measuring DC bias of 1 V. Source: Luo 2011 [144].

The test results show that bismuth is effective in increasing the nonlinear coefficient of CCTO. The permittivity spectroscopy of the ceramics taken at room temperature is shown in Figure 10.20 [144]; according to the IBLC model, the "effective" permittivity can be estimated by Eq. (10.10) [110], and when the permittivity of the insulating grain boundary phase, ε_{gb}, keeps unchanged, the reduction of average grain size results in the decrease of permittivity. The permittivity of the samples follows this decreasing rule, respectively. It could be observed that the permittivities of the doped samples decrease by a factor of 7–10, but they still have large permittivity of 10^3–10^4. The permittivities of all samples remain almost constant in the frequency range from 10^3 to 10^6 Hz. Each of the samples has a Debye-like relaxation peak at 10^6–10^7 Hz. The relaxation for the doped ceramics is shifted to a higher frequency than that of pure CCTO. It is possible that bismuth is also available to lower the activation energy of polarization [98].

Many different dopants and sintering additives, such as P_2O_5 [189], MoO_3 [190], Te [191], $Li_2Si_2O_5$ [192], Bi [98] and lithium, barium, and magnesium carbonates [193], have been used to influence the crystalline structure, the microstructure, and the dielectric properties of sintered CCTO. Small amounts of lithium fluoride sintering aid can influence the microstructure and dielectric properties of CCTO ceramics [194]. The grain size of the CCTO phase is largely enhanced by Sn^{4+} doping [195], and the microstructural evolution can be described based on liquid-phase sintering and the pinning effect by the second-phase particles. The dielectric permittivity of Sn^{4+}-doped $CaCu_3Ti_4O_{12}/CaTiO_3$ is greatly enhanced from $\sim 2\times 10^3$ to $\sim 10^4$ at 1 kHz.

Ba^{2+} doping ions preferentially form a secondary phase and are not introduced into the $CaCu_3Ti_4O_{12}$ lattice. The grain growth rate of $CaCu_3Ti_4O_{12}$ ceramics is significantly inhibited by the Ba-related secondary phase particles. The dielectric permittivity of $CaCu_3Ti_4O_{12}$ ceramics decreases with the increase in Ba content.

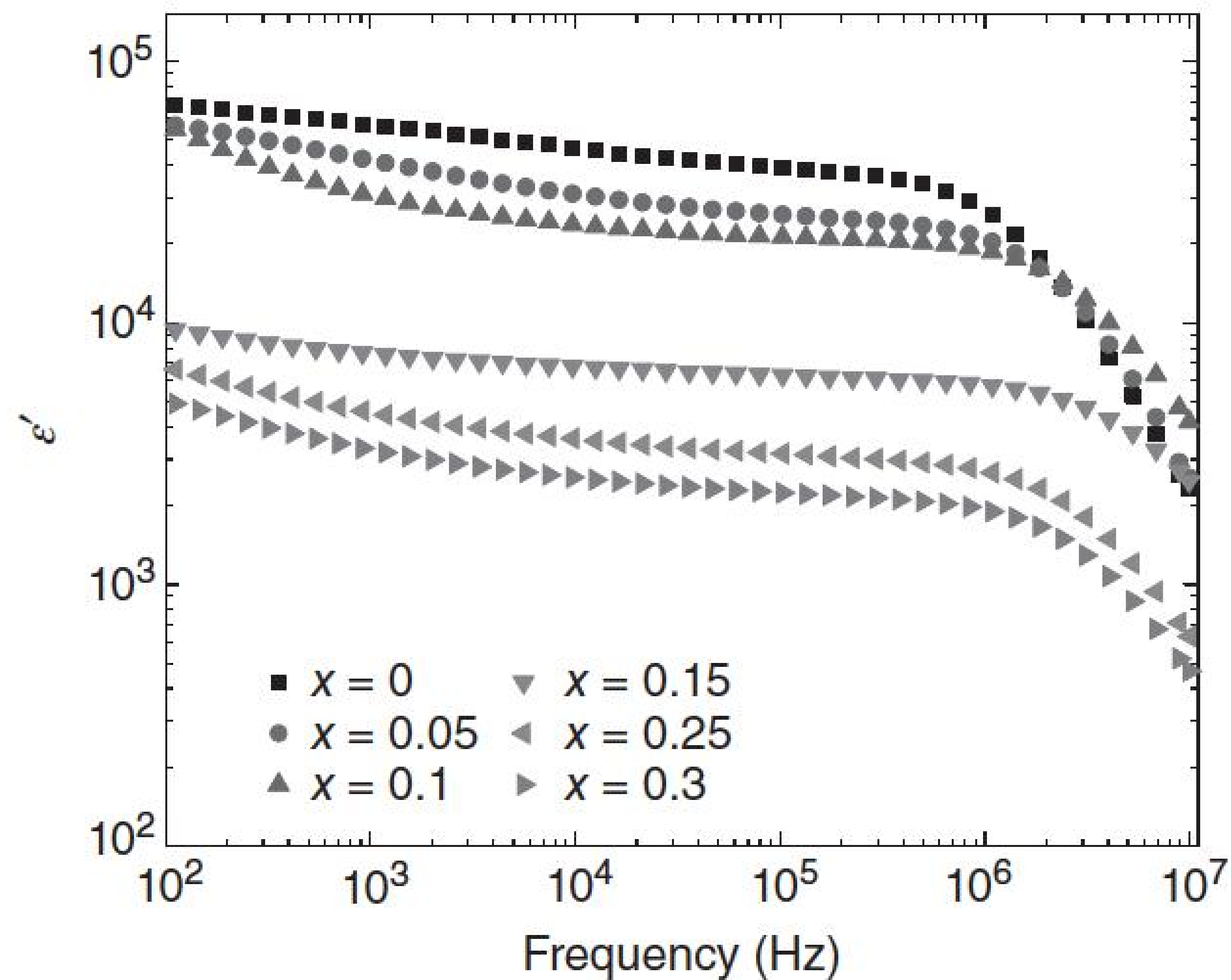


Figure 10.20 The permittivity versus the frequency plot for pure and Bi-doped CCTO samples. Source: Luo 2011 [144].

Their loss tangent decreases after the addition of $CaCu_3Ti_4O_{12}$ with 2.5 mol% Ba^{2+} and increases as the Ba content is increased to 5.0 mol%. The optimal content of Ba^{2+} is 2.5 mol%, when the nonlinear coefficient and breakdown field of the $Ca_{1-x}Ba_xCu_3Ti_4O_{12}$ ceramics are significantly enhanced [196].

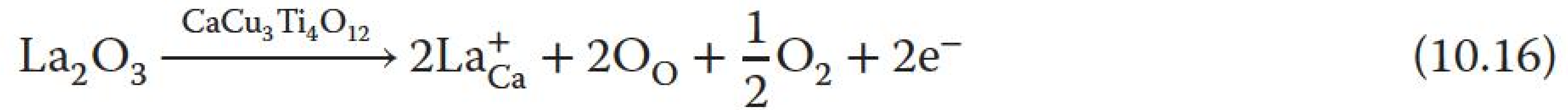
Secondly, Substituting Ions in CCTO by Doping Elements The doping elements are available to substitute partial sites of ions in CCTO. This substitution reaction may change the concentration of electron donors inside grains to change the grain conductivity and grain boundary barrier. In BCCTO with low-concentration doping, partial Bi^{3+} substitutes the site of Ca^{2+} to increase the concentration of electron donors, which leads to increase the grain conductivity and greatly decrease the grain boundary barrier height. However, in YCCTO, the substitution reaction that Y^{3+} replaces the position of Ti^{4+} will decrease the concentration of electron donors to increase the grain boundary barrier height.

Usually, it is difficult to improve the dielectric property and the nonlinear characteristic at the same time. When a suitable amount of VO_2 dopant was added [197], a secondary-phase $CaTiO_3$ (CTO) was observed, vanadium diminished the CCTO grain size, and dramatically changed the microstructure. The relative dielectric constant decreased from 13 500 to 9800 (at 2500 Hz) for undoped to V-doped-CCTO/CTO, and the breakdown voltage and the nonlinear coefficient increased from 500 to 5000 $V\,m^{-1}$ and from 3 to 25, respectively. These analyses suggested that V ions could replace Ti^{+4} and/or Cu^{+2} in the lattice. Doping did not enhance grain growth or densification, but it reduced the conductivity and increased both the nonlinear coefficient and the breakdown voltage.

A small amount of $MgTiO_3$ is good to improve both dielectric and resistivity properties of $CaCu_3Ti_4O_{12}$ ceramics [198]. The low-frequency ($<10^5$ Hz) loss tangent is greatly reduced (<0.2 for 1% mixed sample), whereas the dielectric constant is found to be higher than 3.0×10^6 at room temperature.

The impedance spectroscopy at room temperature indicates that the La doping can maintain the high dielectric permittivity of $CaCu_3Ti_4O_{12}$ ($\sim 10^4$). When La is employed as the additive, it takes the site of Ca completely and has no influence

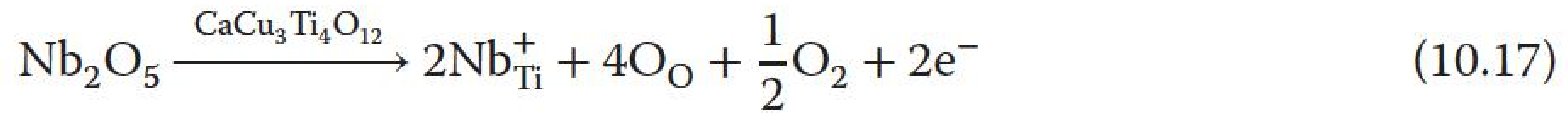
on the phase composition [157]. The reaction equation is



$$La_2O_3 \xrightarrow{CaCu_3Ti_4O_{12}} 2La^{+}_{Ca} + 2O_O + \frac{1}{2}O_2 + 2e^- \quad (10.16)$$

It is seen that doping with La can enhance the concentration of carriers. The effect of lowering the grain boundary barrier has been proved in experiments.

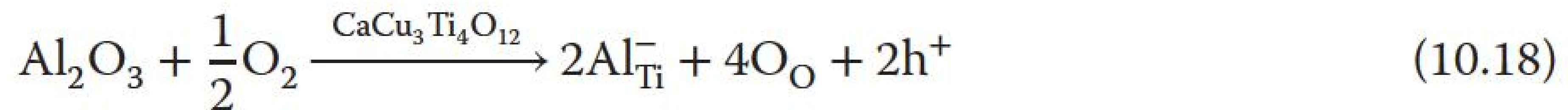
Replacement of Nb on Ti sites was also investigated [127]. The reaction equation is



$$Nb_2O_5 \xrightarrow{CaCu_3Ti_4O_{12}} 2Nb^{+}_{Ti} + 4O_O + \frac{1}{2}O_2 + 2e^- \quad (10.17)$$

It is seen that Nb has the similar effect as La. The carrier concentration is enhanced, and the barrier height and resistance at the grain boundaries are decreased.

Al doping has been shown to reduce the dielectric loss remarkably while maintaining a high dielectric constant [150]. Impedance spectra indicated that Al doping increases the resistivity of the grain boundary by an order of magnitude. The improvement of the dielectric loss in Al-doped CCTO is attributed to the enhanced grain boundary resistivity. The measurement of crystal lattice constant indicates that Al takes the site of Ti. The reaction of replacement in air atmosphere is



$$Al_2O_3 + \frac{1}{2}O_2 \xrightarrow{CaCu_3Ti_4O_{12}} 2Al^{-}_{Ti} + 4O_O + 2h^+ \quad (10.18)$$

It is seen that the doping creates holes in the ceramic, and the holes will decrease the carrier concentration and increase the barrier height and bulk resistance.

Not all doping will enhance the giant dielectric property of CCTO. Mn and Se dopings show remarkable influences on the dielectric behaviors [156, 164]. As the Mn doping increases, the dielectric constant drops from $\sim 10^4$ to $\sim 10^2$. The X-ray absorption near edge structure (XANES) spectra reveal that the valence states of Ti, Mn, and Cu in the grain and grain boundary change greatly, which lead to the difference of the activation energy of grain and grain boundary disappearing with increasing the Mn doping concentration and thus show this abnormal dielectric behavior [164]. Furthermore, Mn resites the Ti sites to produce holes in the reaction similar to Eq. (10.18), and electrons as carriers are consumed in the neutralization reaction with holes [103]. Thus, the carrier concentration is reduced, and the barrier height is increased significantly. Actually, except the permittivity drops significantly, with the doping of Mn, the bulk almost loses its conductivity, and the nonohmic property almost disappears.

Thirdly, Generating Intergrain Phases Dopants have an influence on the components in grain boundary. When the concentration of the dopant increases, the inclusion phases are segregated out in CCTO. $Bi_4Ti_3O_{12}$ in BCCTO and $Pb_{1-x}Ca_xTiO_3$ in PCCTO belong to the inclusion phases. The formation of these phases decreases the growth velocity of grains to reduce the grain sizes. On the other hand, these inclusion phases deposit on the grain boundaries to change the chemical components and influence the barrier and impedance of grain

boundary. Besides, Y doping will promote the segregation of CuO liquid phase to increase the phase containing Cu in the grain boundary. Doping excessive CuO will directly increase the thickness of the phase containing Cu in the grain boundary. In Rb-doped samples, the Cu-rich and Ti-poor GBLs are formed, and electrical properties are also changed by doping: with the increase in doping concentration, the grain resistivity and the grain boundary double-Schottky potential barrier are changed, the grain boundary resistivity is enhanced, and the low-frequency dielectric constants and loss are reduced [199]. Ba^{2+} doping ions preferentially form a secondary phase, rather than being substituted into the CCTO lattice, to inhibit the grain growth rate of Ca $Cu_3Ti_4O_{12}$ ceramics, the dielectric constant and dielectric loss are reduced, in the meantime, and the values of α and E_b of the $Ca_{1-x}Ba_xCu_3Ti_4O_{12}$ ceramics are significantly enhanced by the addition of 2.5 mol% Ba^{2+}. Impedance spectroscopy analysis reveals that the variations in dielectric and nonohmic properties are associated with electrical response of GBs, supporting the IBLC model [199].

$CaCu_3Ti_4O_{12}$ (CCTO) ceramics doped with rare earth oxides, including Y_2O_3, La_2O_3, Eu_2O_3, and Gd_2O_3, were studied [165]. The grain boundary characteristics of the CCTO–RE systems are controlled by the ionic radius of rare earth elements. Especially, the smaller RE elements such as Eu and Gd are effective dopants and nearly diffuse into the whole grain, whereas the bigger RE elements such as Y and La tend to form the core–shell structure. RE oxides significantly enhance the breakdown voltage and decrease the nonlinear coefficient of CCTO ceramics. Yttrium was employed as the additive to improve the application performance of CCTO ceramic. Samples with the nominal composition $CaCu_3Ti_{4-x}Y_xO_{12-x/2}$ (x = 0, 0.05, 0.1, abbreviated as CCTO, YCCTO-1, YCCTO-2) were fabricated by the conventional solid-state ceramic processing [154]. The SEM images of CCTO and YCCTO-2 are shown in Figure 10.21 [154]. The grain size was not changed much. It was noticeable that something precipitated on the grain boundaries and made the grain boundaries more obvious for YCCTO-2 than the pure CCTO. The precipitation was determined to be copper-rich phase, rather than yttrium-related phase (Figure 10.21c) [154]. The doping of yttrium may degrade the stability of the lattice and cause more CuO to segregate on the grain boundaries.

Microcontact measurement was employed to locally investigate the electric and dielectric properties of individual grains and grain boundaries in $CaCu_3Ti_4O_{12}$ ceramics [98]. It was evident that yttrium had dramatically enhanced the resistance values, of which individual grain boundaries in pure CCTO and YCCTO-2 were determined as 6×10^7 and $1.4 \times 10^9\,\Omega$ by using locally measured cole–cole plots (Figure 10.22). It has been detected that Cu segregation at the grain boundaries is enhanced by yttrium doping to increase the thickness of grain boundary, which may well explain the rise of resistances of individual grain boundaries. The doping of yttrium can effectively reduce the dielectric loss and enhance the nonohmic property. Further investigation on the grain boundaries proved that yttrium doping can evidently increase the resistance and the potential barrier height at the grain boundaries. These changes are attributed to the enhancement of Cu segregation induced by yttrium doping.

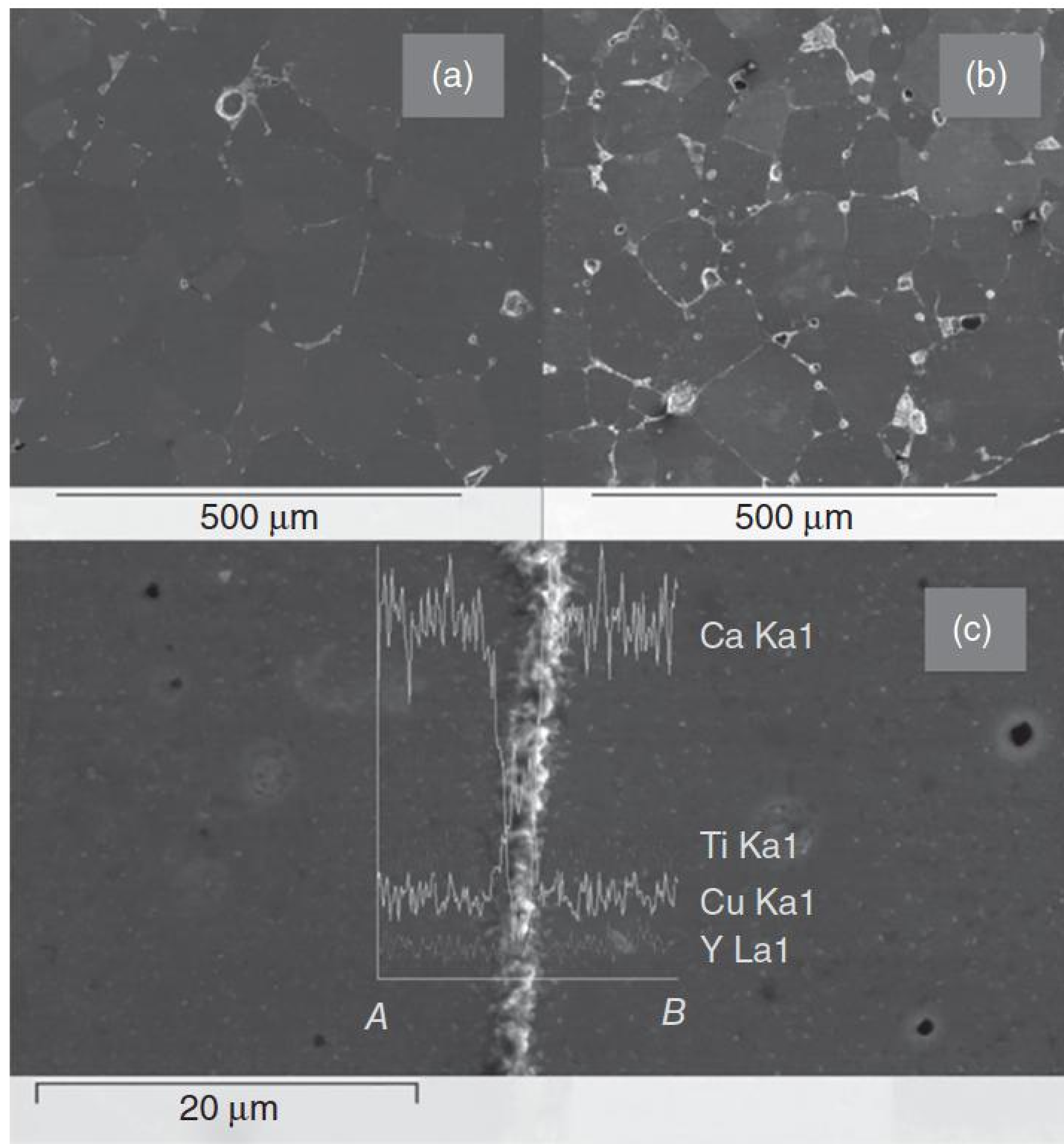


Figure 10.21 The SEM images of (a) CCTO, (b) YCCTO-2, and (c) EDS results performed on Line *AB*, which lies across a grain boundary of YCCTO-2. Source: Luo et al. 2010 [154]. Reproduced with permission of John Wiley & Sons.

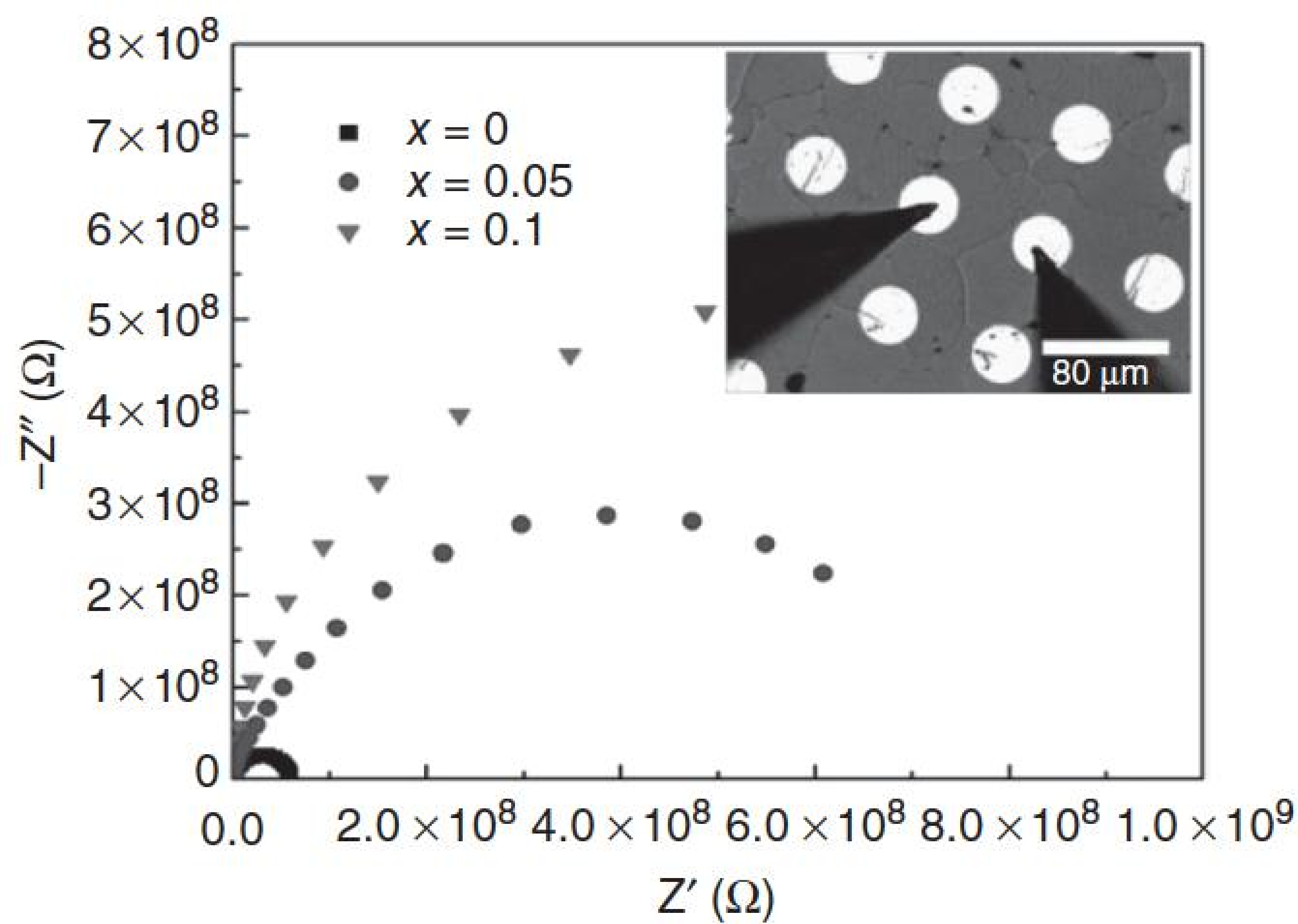


Figure 10.22 The complex impedance of the individual grain boundaries of the $CaCu_3Ti_4O_{12}$ samples doped with different content of yttrium. The inset is the surface of the sample with patterned silver electrodes and microprobes. Source: Luo et al. 2010 [154]. Reproduced with permission of John Wiley & Sons.

Table 10.1 The influence of different elements on the structure and performances [144].

Dopants or samples	Grain size	Dielectric constant	Dielectric loss	Impedance	Nonlinearity	Voltage gradient
Bi (high doping)	−−	−	−	+	+	++
Bi (low doping)	−	−	++	−−	−−	/
Y	0	0	−−	+	0	+
Pb	−−	−	−−	++	+	++
Si	0	0	0	−	0	−
Na	0	−	−	+	0	+
Pr	0	0	0	0	0	+
Excess Ti	0	0	−	+	0	+
Excess Cu	0	0	+	+	0	+
$CaTiO_3$/CCTO complex	−−	−−	−−	+	−−	+

The influence of different elements on the structure and performances has been summarized in Table 10.1 [144], where "+" and "−" mean increase and decrease, respectively, and "0" means the influence can be omitted. Suitable doping can effectively tune the performance index to reduce the dielectric loss, keep high dielectric constant, adjust voltage gradient, and increase nonlinear coefficient.

10.4 $BaTiO_3$ Varistors of PTCR Effect

PTCR materials are widely used in the electronics industry as temperature sensors, time delay circuits, and current limiters for overvoltage or overcurrent protection, overheat protection, and current stabilizers. $BaTiO_3$-based or quasi-$BaTiO_3$-based ternary perovskite compound is one of the main material groups in the PTCR family [200–321].

10.4.1 Introduction

The $BaTiO_3$ material was discovered in the United States, Russia, and Japan during the World War II, almost at the same time [210]. Polycrystalline $BaTiO_3$ ceramics is an insulator at room temperature but can easily be transformed into a semiconductor by doping a very small amount of a rare earth element such as La^{3+}, Y^{3+}, Sb^{3+}, and Nb^{5+}. Such semiconducting $BaTiO_3$, which exhibits a small resistivity at room temperature and an anomalous increase in resistivity near the ferroelectric–paraelectric Curie transition temperature (Curie point) T_c [211], as shown in Figure 10.23 [212], is widely known as a positive temperature coefficient (PTC) phenomenon. This PTCR effect in barium titanate was first developed in the early 1950s in the Philips Research Laboratories in The Netherlands [213]. The semiconductive property of $BaTiO_3$ was patented in 1954 [210]. Saburi investigated the detailed semiconductive properties of $BaTiO_3$ [214].

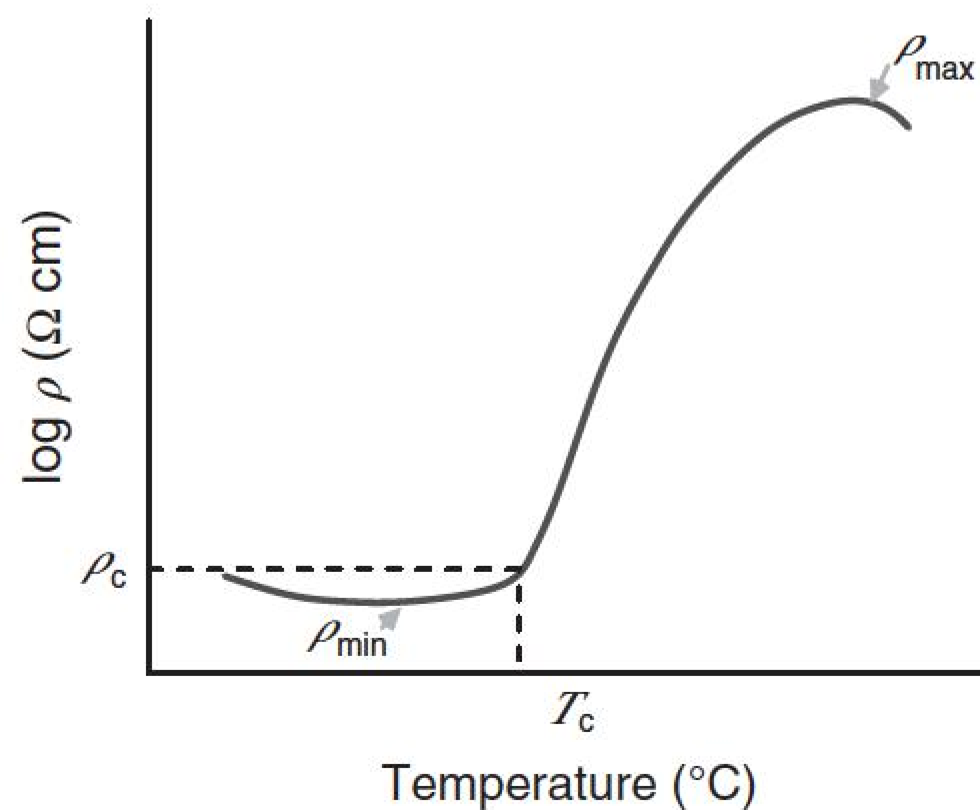


Figure 10.23 Typical resistivity–temperature characteristic of $BaTiO_3$-based PTCR material. Source: Adapted from Chen and Yang [212].

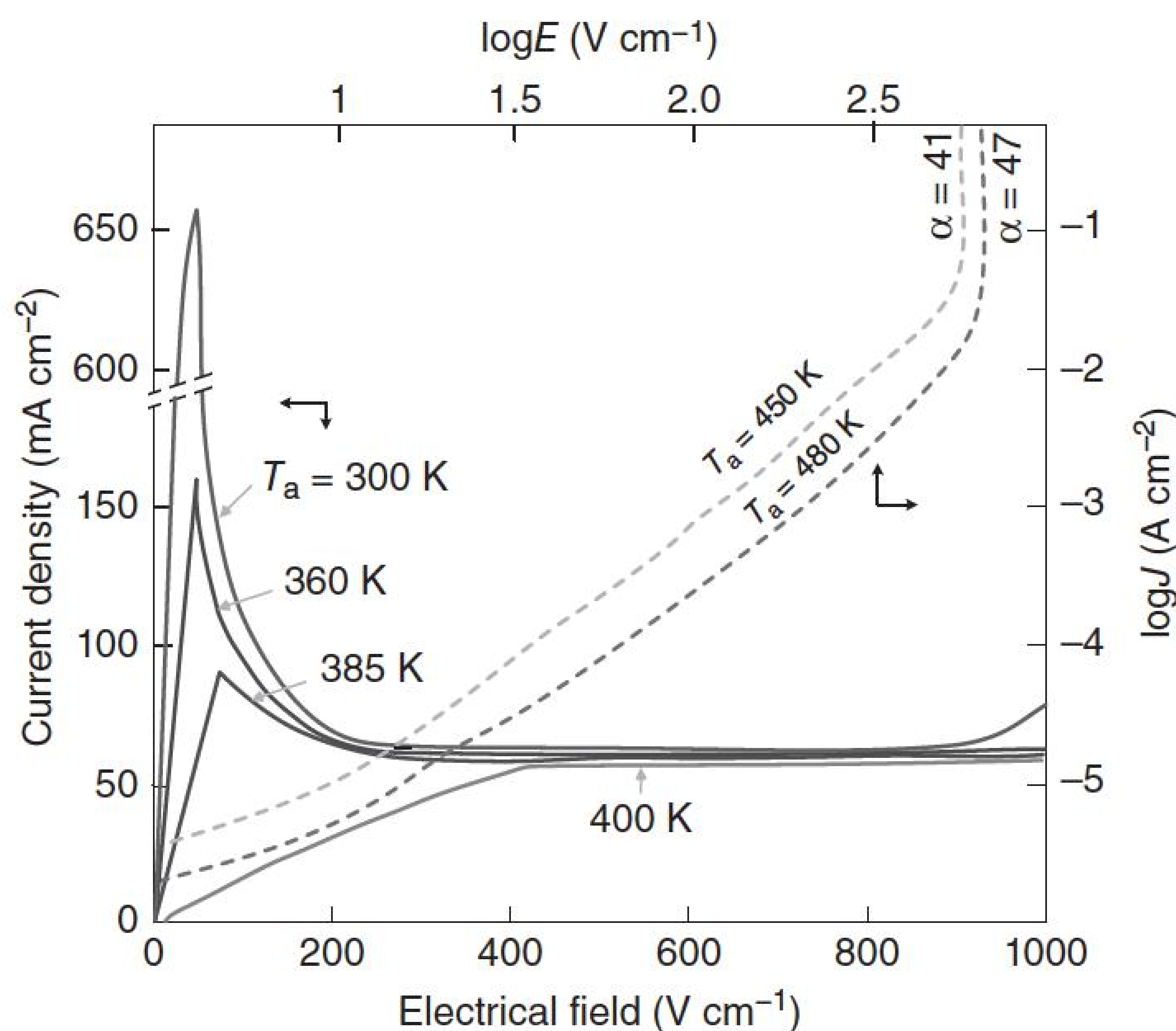


Figure 10.24 Current–voltage (*I–V*) characteristics of $BaTiO_3$: 0.3 m% La and containing 0.2% Al_2O_3, + 0.6% SiO_2 + 0.2% TiO_2, (T_c = 400 K) measured at different ambient temperatures T_a. Source: Makovec et al. 2001 [318]. Redrawn with permission from John Wiley & Sons.

Current limiting occurs when thermal equilibrium is established under an applied electric field for *n*-$BaTiO_3$ (tetragonal) that exhibits a PTC resistance. The static current–voltage (*I–V*) curves of these ceramics are distinguished by an initial current maximum (I_{max}) followed by a near-constant current, as the voltage increases [215], as shown in Figure 10.24 [1].

$BaTiO_3$ ceramics doped with different elements are widely used as grain boundary barrier layer (GBBL) capacitors or as PTC resistors. After the discovery of $BaTiO_3$, planar- and tubular-type $BaTiO_3$ ceramic capacitors were manufactured, whereas its applications and productions were broadened by the multilayer ceramic capacitors (MLCCs) using $BaTiO_3$ [216]. The first industrialization of PTC thermistor in the world, which has been applied in industrial and consumer electronics [202–204], was fulfilled by Murata in 1959 as a heater

with automatic temperature controlling. Current-limiting characteristics of donor-doped $BaTiO_3$ ceramics have been extensively used in many industrial and domestic applications such as overload protection devices, delay line switches, and self-regulating heaters [1].

The current-limiting effect is possible only when the ambient temperature T_a is less than the Curie temperature (Curie point) T_c. If $T_a > T_c$, the current-limiting effect gives way to the voltage-limiting (varistor) property as shown in Figure 10.24 when $T_a \geq 400$ K, which is well known in some of the ceramics such as SiC and ZnO. Varistor action of (Sr, Ca)TiO_3 [7, 217] and also the electrical-field-dependent nonlinear resistivity of n-$BaTiO_3$ [218] were reported. Kutty and Ravi [1] reported that the $BaTiO_3$-based ceramic exhibited both the varistor property and the current-limiting characteristics in 1991. Furthermore, by modifying the GBL compositions and the post-sintering annealing, the breakdown voltage, leakage current, and nonlinearity coefficient of $BaTiO_3$ ceramics can be varied to the desired range of utility in devices.

Over the past 60 years, diverse applications have triggered research efforts toward understanding compositional and structural issues that govern the electrical properties of $BaTiO_3$-based ceramics [212]. The screening of dopant candidates from the periodic table was well scrutinized [219–221], and several models to explain the temperature–resistivity relation have been proposed [214, 222–225].

10.4.2 Doping Effects

Pure $BaTiO_3$ sintered in air is an insulating material at room temperature and does not exhibit the PTCR effect. However, it turns to a semiconductor at room temperature by doping with various donor dopants. It can return to be an insulator when the donor content exceeds the critical concentration [212], which was set as normally less than 1 mol% by Morrison et al. [226], but actually the solubility limits of most of the dopant elements in $BaTiO_3$ perovskite lattices are far higher than this critical concentration [227]. Moreover, the resistivity versus temperature characteristic is very sensitive to the composition of dopants. For example, very small addition of Mn ranging between 0.01 and 0.04 mol% can increase the PTCR anomaly by up to a factor of 10^9 [228].

The effect of the donor dopants on the bulk electrical conductivity is strongly dependent on their substitution sites in $BaTiO_3$. The type of the incorporated dopant is determined by the difference in valence charge between the dopant and the replaced host ion. Site replacement in the crystal lattice mainly depends on the ionic radius of dopants [219]. Trivalent ions with ionic radii larger than 0.099 nm, such as rare earth elements La^{3+}, Sb^{3+}, and Y^{3+}, substitute for the Ba^{2+} site, or pentavalent ions with ionic radii smaller than 0.09 nm, such as Sb^{5+}, Nb^{5+}, and Ta^{5+}, substitute for Ti^{4+} site. While dopants, with ionic radii in the range from 0.09 to 0.099 nm, can substitute for either Ti or Ba site, which depends on dopant concentration, sintering conditions, and Ba/Ti molar ratio [212, 219, 229–233]. La-doped $BaTiO_3$ ceramics are commonly used in varistor devices because they display a strong PTCR effect for La content of about 0.5 at.% [231]. This effect is usually ascribed to the occurrence of GBLs, which are strongly affected by

the bulk cubic to tetragonal phase transition at 130 °C [218]. The heterovalent substitution La^{3+}/Ba^{2+} results in a nonmonotonic perturbation of the lattice and electronic properties by investigating the electronic excitations of the powered samples [234].

Divalent ions such as Pb^{2+}, Ca^{2+}, and Sr^{2+} are extensively used as acceptor dopants to substitute the Ba ions in the $BaTiO_3$ lattice [235–241]. The Curie point of donor-doped semiconducting $BaTiO_3$ ceramics can be shifted over a wide temperature range substantially between −100 and 480 °C by compositional modifications, where substituting Sr for Ba lowers the T_c and substituting Pb for Ba increases it [239]. The replacement by lead can increase the Curie temperature by 4.3 °C per percentage atomic replacement, whereas the replacement by strontium reduces the Curie temperature by 3.5 °C [212].

ZnO additions were doped to $BaTiO_3$ ceramics to decrease the value of the loss tangent and increase the density of the sintered body [242–245]. The Zn^{2+} cation has been considered as both an isovalent and an acceptor dopant in the $BaTiO_3$ lattice. Jaffe et al. [243] reported a solid solution limit of 0.7 wt% at 1200 °C for ZnO in $BaTiO_3$. Swilam and Gadalla [244] found that ZnO additions above this limit drove the $BaTiO_3$ ceramic to a higher density. The incorporation of Zn^{2+} cations into the $BaTiO_3$ lattice takes site in Ba^{2+} sites, i.e. as an isovalent dopant. Control of grain growth in a wide temperature range leads to ceramics with permittivity values close to 3000 and dielectric losses below 1% [246].

When Mn^{2+} ions are doped, Mn^{2+} ions occupy Ti^{4+} sites during sintering, and the excess charges are compensated by oxygen vacancies (V_O^{2+}), which form various $(Mn)_n$–V_O complexes, for example, $Mn_{Ti}^{2-} - V_O^{2+}$ [247]. During cooling, the grain boundaries oxidize, and the concentration drops. As a result, the oxidation state of the manganese ions changes from 2+ to 3+ or 4+, and they act as electron traps, increasing the electron trap density N_s. The increase in N_s is accompanied by an increase in the resistance ratio. However, at high N_s values, the resistivity ρ_{min} also rises because the grain boundary states cannot be compensated by spontaneous polarization in the ferroelectric phase. When barium titanate is codoped with donors (Y) and acceptors (Mn), the latter may not only prevent rare earth accumulation at grain boundaries but also segregate [248–250]. This process may also play an important role not only during cooling of ceramics but also during high-temperature synthesis [247, 251–253].

On the other hand, tetravalent ions, such as Zr^{4+}, Hf^{4+}, and Sn^{4+}, have been applied as substitutes for Ti ions in the $BaTiO_3$ lattices [254–256]. The substitutions of all those tetravalent dopants can significantly reduce T_c and readily make the phase transformation of tetragonal–cubic occur at room temperature [212]. Zirconium added to $BaTiO_3$ results in lowering the dielectric loss and broadening the dielectric peak near T_c [257]. Similarly, Hf and Sn exhibit strong ferroelectric relaxor behavior at high contents [258].

Desu and Payne [259, 260] found that at low donor concentrations, the charge of the donor ions is compensated by free electrons, which results in high conductivity and semiconducting properties. As the donor content increases, the donor concentration segregating at the grain boundary increases even faster until it exceeds a critical level; thereafter, the compensation mechanism shifts from the electronic compensation to the ionic compensation in the grain

boundary region [212]. The charges of the donors are compensated by negatively charged cation vacancies, which lead to a rise in the resistance of grain boundary region to the point forming a dielectric layer [221]. Hence, it creates an insulating layer at the grain boundary [212]. Furthermore, when acceptors are doped into a donor-overdoped $BaTiO_3$ insulating material, in which the concentration of donors has exceeded the critical level, the ceramic will recover some of its semiconducting property [261–264]. This phenomenon might be explained by assuming that those acceptors inhibit donor segregation at grain boundaries [249].

Very stable and highly reproducible current-limiting characteristics have been observed for polycrystalline ceramics prepared from sintering mixtures of coarse-grained, donor-doped $BaTiO_3$(tetragonal) as the major phase and ultrafine, undoped cubic perovskite such as $BaSnO_3$, $BaZrO_3$, $SrTiO_3$, or $BaTiO_3$ (cubic) as the minor phase [265].

10.4.3 Preparation of $BaTiO_3$ Ceramics

Not only the various preparation and doping techniques but also the fabrication methods for producing donor-doped $BaTiO_3$ can alter its PTCR performance [212].

The commercial approach to preparing barium titanate powder is solid-state synthesis [253]. The starting materials and fabrication procedure of $BaTiO_3$ ceramics have a strong influence on their electrical properties [266, 267]. Classic precursors are titanium dioxide and barium carbonate. The best-known alternative approach is oxalate route [268]. In the first step, $TiCl_4$, $BaCl_2$, and $H_2C_2O_4$ solutions are reacted to form barium titanyl oxalate (BTO), $BaTiO(C_2O_4)_2 \cdot 4H_2O$, as a reaction intermediate. In the second step, the BTO is calcined at temperatures above 700 °C to produce barium titanate ($BaTiO_3$) powder.

BTO can be precipitated by several techniques, which differ in mixing sequence, process temperature, and Ba/Ti and Ba/C_2O_4 molar ratios in the starting mixture [253]. The Clabaugh and Merker processes were used most widely. In the Clabaugh process [269], a mixture of $BaCl_2$ and $TiCl_4$ solutions is added to a hot oxalic acid solution. In the Merker process [270], an aqueous $TiCl_4$ solution is added to oxalic acid to give titanyl oxalic acid, $H_2TiO(C_2O_4)_2$. Next, barium chloride is added to a heated titanyl oxalic acid solution, and the resultant BTO precipitate is separated. The precipitation procedure and BTO calcination conditions significantly influence the characteristics of barium titanate powders [271].

Calcium titanate was prepared by a solid-state reaction between calcium carbonate and titanium dioxide in air at 1000 °C [253]. Ground barium titanate and calcium titanate powders were mixed with TiO_2, SiO_2, and PbO by grinding with polyamide media in deionized water. Yttrium (donor dopant) and manganese (acceptor dopant) were introduced to the starting mixture. The mixture was pressed into compacts with a green density of $3.0\,g\,cm^{-3}$. The compacts were fired in air at temperatures of up to 1320 °C with the heating rate of $350\,°C\,h^{-1}$, then cooled to 800 °C at a rate of $110–300\,°C\,h^{-1}$, depending on the required resistivity of the ceramics [253].

Chen and Yang [212] summarized the interrelationships of compositions, microstructures, processing, and PTCR properties. There is a strong correlation between the donor concentration, the surface composition of the grains, the microstructure, and the electrical properties of the ceramics. Rare earth enrichment at grain boundaries inhibits the recrystallization process [262, 272–279]. As the overall rare earth content increases, the rare earth concentration in the grain boundary increases more rapidly than the bulk concentration because of the segregation processes [278]. As a result, the rare earth elements form a zonal shell on the outer layers of the grains. This considerably reduces the mobility of the grain boundaries because of the slow diffusion of the donors [253].

The PTCR effect in donor-doped $BaTiO_3$ is very sensitive to firing conditions [233, 279, 280], which can change the PTCR characteristics by introducing intrinsic defects such as oxygen vacancies or cation vacancies. The average grain size of the ceramics decreases as the barium titanate synthesis temperature increases owing to the donor impurity enrichment at grain boundaries. The PTCR ceramics produced from the powders, which are synthesized at 900–1000 °C, has the lowest resistivity of 250–300 Ω cm, and the grain boundary barriers are less uniform at higher BTO calcination temperature. Reducing the sintering time or sintering temperature will decrease the room temperature resistance of manganese-containing $BaTiO_3$ ceramics [252]. The Schottky barrier height can be effectively controlled by varying the cooling rate, which influences the density of grain boundary acceptor states [252, 281]. Adjusting the cooling rate in the range from 1320 to 800 °C, Shut et al. [253] obtained PTC thermistors, produced from barium titanate powders of different particle sizes, with a room temperature resistance of 31 Ω. The samples, which were prepared from the barium titanate powders and synthesized at 950–1000 °C, offered the highest electric strength 350 V mm^{-1}. The average crystallite size of the parent barium titanate powder is 250–320 nm. The results demonstrate that the use of active microcrystalline materials with a small percentage of residual phases helps to optimize the dopant distribution to raise the density of grain boundary acceptor states and to improve the electrical performance of the thermistors.

Sintering atmosphere influences the preference of the incorporation site of some donor elements [282], and significant substitution of Ho to Ba sites as a donor occurs in a reducing atmosphere while Ti replacement as an acceptor is preferred when sintered in air [212]. It is generally observed that the room temperature resistivity of donor-doped $BaTiO_3$ rapidly increases beyond the critical donor concentration because donor ions are preferentially segregated at the grain boundaries [283, 284].

Oxygen from the $BaTiO_3$ lattice is gradually lost at high sintering temperature, and then the electrical conductivity of $BaTiO_3$ ceramics increases [212]. However, the oxygen-deficient material rapidly reoxidizes either on reheating at lower temperature or on cooling slowly in high oxygen partial pressure [253]. Hence, applying reducing atmosphere during sintering can facilitate the conductivity of donor-doped $BaTiO_3$ and enhance the critical donor concentration significantly [285, 286].

Generally, liquid-phase sintering can optimize the electrical properties of $BaTiO_3$ to realize a high-density and controlled microstructure. $BaTiO_3$ is usually

sintered at temperatures above 1312 °C, using the liquid eutectic $Ba_6Ti_{17}O_{40}$. This liquid phase strongly favors the polygonal crystallization of $BaTiO_3$ [287]. Many oxides such as Bi_2O_3, LiF, B_2O_3, SiO_2, and Al_2O_3 [288–292] were applied for the formation of the required liquid phase. At sintering temperatures below the eutectic point, large crystallites are found nearly in the form of lamellae [293]. The addition of B_2O_3 to barium titanate promotes sintering at low temperature by the formation of a liquid phase [294]. At a higher sintering temperature of 1250 °C, grain growth occurs because of the solution and precipitation mechanism. The addition of 0.5 mol% B_2O_3 to the Sb_2O_3 donor-doped $BaTiO_3$ ceramics retards the grain growth, whereas the addition of B_2O_3 above 0.5 mol% increases the grain size. The Ti excess samples reveal the Ti-rich platelet $Ba_2Ti_5O_{12}$ phase. This phase and the platelet-type structures are suppressed by increasing the B_2O_3 content and the sintering temperature. The XRD studies did not show any phases related to B_2O_3, which indicates to either the loss of B_2O_3 by evaporation or the presence of B_2O_3 as an amorphous phase.

The broad grain size distributions in $BaTiO_3$ because of discontinuous grain growth can be narrowed by introducing the so-called "seed grains" to the starting powder, and seed grain additives are very useful not only for producing uniform microstructures but also for control of the average grain size [287]. Seed grains are widely monocrystalline particles that are by a factor of about 10 larger than those of the original powder [295, 296]; discontinuous grain growth can be largely suppressed in this way. As seed grains increase, the average grain size of $BaTiO_3$ ceramics decreases. One of the most important advantages of seed grains is that they have the same chemical composition as the original powder and can thus not change the defect chemistry and resulting electrical properties of the materials [287].

10.4.4 PTCR Effect of $BaTiO_3$ Ceramics

Pure single-crystal $BaTiO_3$ does not have any PTCR phenomenon [297], so generally, it is thought that the sharp change in the resistance at or around the Curie point is due to the change of the grain boundary barrier. The most accepted model to explain the PTCR behavior in donor-doped $BaTiO_3$ materials is the Heywang–Jonker model proposed by Heywang [222] and extended by Jonker [224]; this model was experimentally verified [297, 298]. According to this model, the PTCR effect is due to a grain boundary double Schottky barrier formed by electron traps, as shown in Figure 10.25 [212]. Below the Curie point, the space charge of surface barrier layer is compensated by the ferroelectric polarization, so the resistance of the material at low temperature is very low, above the Curie point, because of the ferroelectric phase transition to the paraelectric phase, so the ferroelectric compensation disappears, highlighting the effect of the acceptor surface state, grain boundary surface barrier sharply increases, and the electrical resistivity of the material generates sharp mutation.

As shown in Figure 10.25 [212], there is a bidimensional layer of electron traps, i.e. acceptor states, along the grain boundaries of $BaTiO_3$; the potential barrier ϕ_b is caused by a two-dimensional electron trap along the grain boundary where acceptor states attract electrons from the bulk resulting in an electron depletion

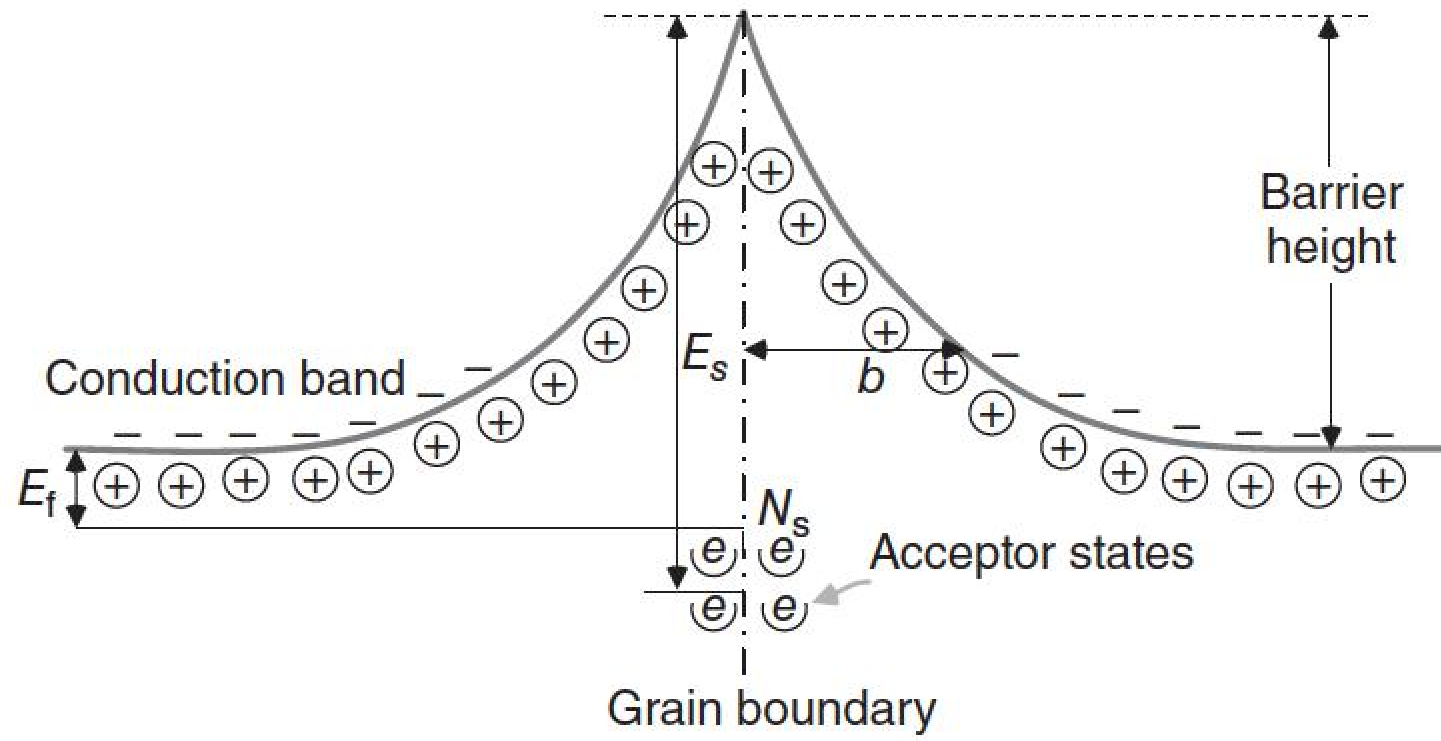


Figure 10.25 Electrical double layer at grain boundary: E_s is the electron trap energy, E_f is the Fermi level, N_s is the concentration of trapped electrons, and b is the width of electron depletion layer. Source: Adapted from Chen and Yang [212].

layer with width of b, which is related to the concentration of trapped electrons, N_s, and the charge carrier concentration, N_d. As discussed in Chapter 2, this depletion layer results in a grain boundary barrier ϕ_b, which can be calculated by Eq. (2.5). The cubic resistivity ρ of the $BaTiO_3$ ceramic is related to the height of the potential barrier by

$$\rho = A \exp\left(\frac{\phi_b}{kT}\right) \tag{10.19}$$

where A is a geometrical factor, T is the absolute temperature, and k is the Boltzmann constant. As a ferroelectric material, the dielectric constant of $BaTiO_3$, ε, obeys the Curie–Weiss law above its Curie temperature and can be calculated by

$$\varepsilon = \frac{C}{T - T_c} \tag{10.20}$$

where C is the Curie constant. Then, when the temperature is higher than the Curie point, the cubic resistivity is given by

$$\rho = A \exp\left(\frac{e^2 N_s^2}{8\varepsilon_0 N_d k C}\left(1 - \frac{T_c}{T}\right)\right) \tag{10.21}$$

where e is the electron charge, ε_0 is the permittivity of free space, and ε_{gb} is the relative permittivity of the grain boundary region.

Above the Curie point, the doped $BaTiO_3$ is in the paraelectric phase, the grain boundary permittivity, which follows the Curie–Weiss law, decreases as the temperature increases, and the corresponding potential barrier increases proportionally by following Eq. (2.5) and results in steeply increasing resistivity, which depends exponentially on the potential barrier as denoted by Eq. (10.20). The energy of the trapped electrons in the grain boundary rises with the temperature and the potential barrier. When the energy of the electron traps reaches the Fermi level, trapped electrons start to jump to the conduction band, which can depress the increase in ϕ_b and ρ and thus ultimately enhance the conductivity. This also explains the negative temperature coefficient of resistivity (NTCR) effect when passing the point ρ_{max} (Figure 10.23) in the high-temperature range [212].

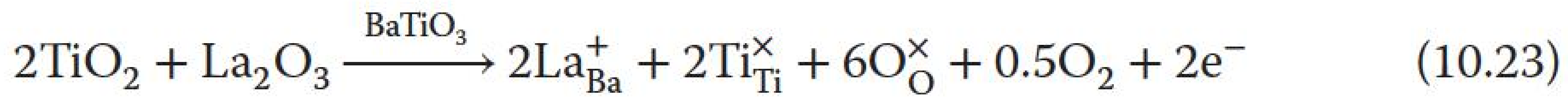
Jonker proposed a model to accurately explain the PTCR behavior below T_c [224]. Below the Curie point, $BaTiO_3$ is ferroelectric with its polarization along the tetragonal crystal axis, where the polarization direction is different from grain to grain because each adjacent grain has a different crystal orientation. Therefore, it creates a net polarization vector P_N normal to the grain boundary, producing surface charges at the grain boundaries. In the areas with negative surface charges, which are about 50% of the grain boundary area depending on the nature of the ferroelectric material, the potential barrier height diminishes or even disappears resulting in the disappearance of the grain boundary resistance. For the other half of the domains containing positive charges, the potential barrier is getting higher. However, this does not matter as the electrons always flow through the path with the lowest barrier so that the material as a whole has low resistivity, too [212]. This theory is experimentally supported by Huybrechts et al. [299].

It is believed that, for donor doped $BaTiO_3$, the initial drop in resistivity (as shown in Figure 10.23) with an increasing donor concentration is generally attributed to an electronic compensation mechanism that the substituted cation via "donor-doping" [300]. Choosing a trivalent ion (La^{3+}) as a donor dopant, free electrons in the $BaTiO_3$ lattice can be generated according to Equations [212]:



$$2O_O^{\times} \rightarrow 2V_O^{2+} + O_2 \uparrow + 4e^- \qquad (10.22)$$

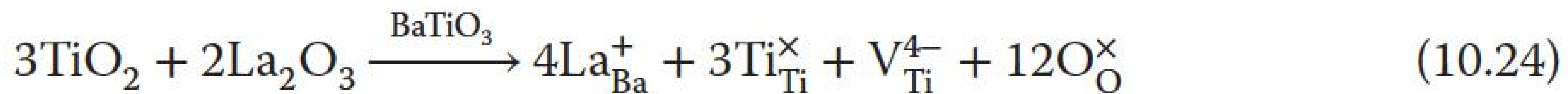
and/or [226]



$$2TiO_2 + La_2O_3 \xrightarrow{BaTiO_3} 2La_{Ba}^{+} + 2Ti_{Ti}^{\times} + 6O_O^{\times} + 0.5O_2 + 2e^- \qquad (10.23)$$

and leads to the general formula $Ba_{1-x}La_xTiO_3$. Based on Eq. (10.22), the free electrons are generated by oxygen deficiency as occurs when sintering at high temperature and/or in reducing atmospheres [301]. Based on Eq. (10.23), the electrons are associated with the replacement of barium ion by La^{3+}.

The subsequent rise in resistivity for dopant concentrations higher than 0.5 at.% is commonly attributed to a change in the doping mechanism to ionic compensation via the creation of cation vacancies [300, 302, 303]. In the case of La-doped $BaTiO_3$, the compensating defects are Ti vacancies [225]:



$$3TiO_2 + 2La_2O_3 \xrightarrow{BaTiO_3} 4La_{Ba}^{+} + 3Ti_{Ti}^{\times} + V_{Ti}^{4-} + 12O_O^{\times} \qquad (10.24)$$

giving the general formula $Ba_{1-z}La_zTi_{1-z/4}O_3$.

Actually, the grain boundary barrier has a more complex structure. It comprises a Schottky barrier and an adjacent diffusion layer with a reduced conductance because of a nonuniform distribution of defects and impurities (donors and acceptors) [304–315]. The overall origin of the electrical properties of donor-doped $BaTiO_3$ is a grain boundary effect and greatly influenced by the defect structure on the $BaTiO_3$ perovskite crystal lattice [316, 317], so the electrical properties of donor-doped $BaTiO_3$ ceramics are influenced by different dopants or processing parameters.

According to the measuring results of complex impedance spectra and microstructural analysis by TEM, Makovec et al. [318] classified the grain and grain boundary structure into three distinct regions (Figure 10.26a) and its

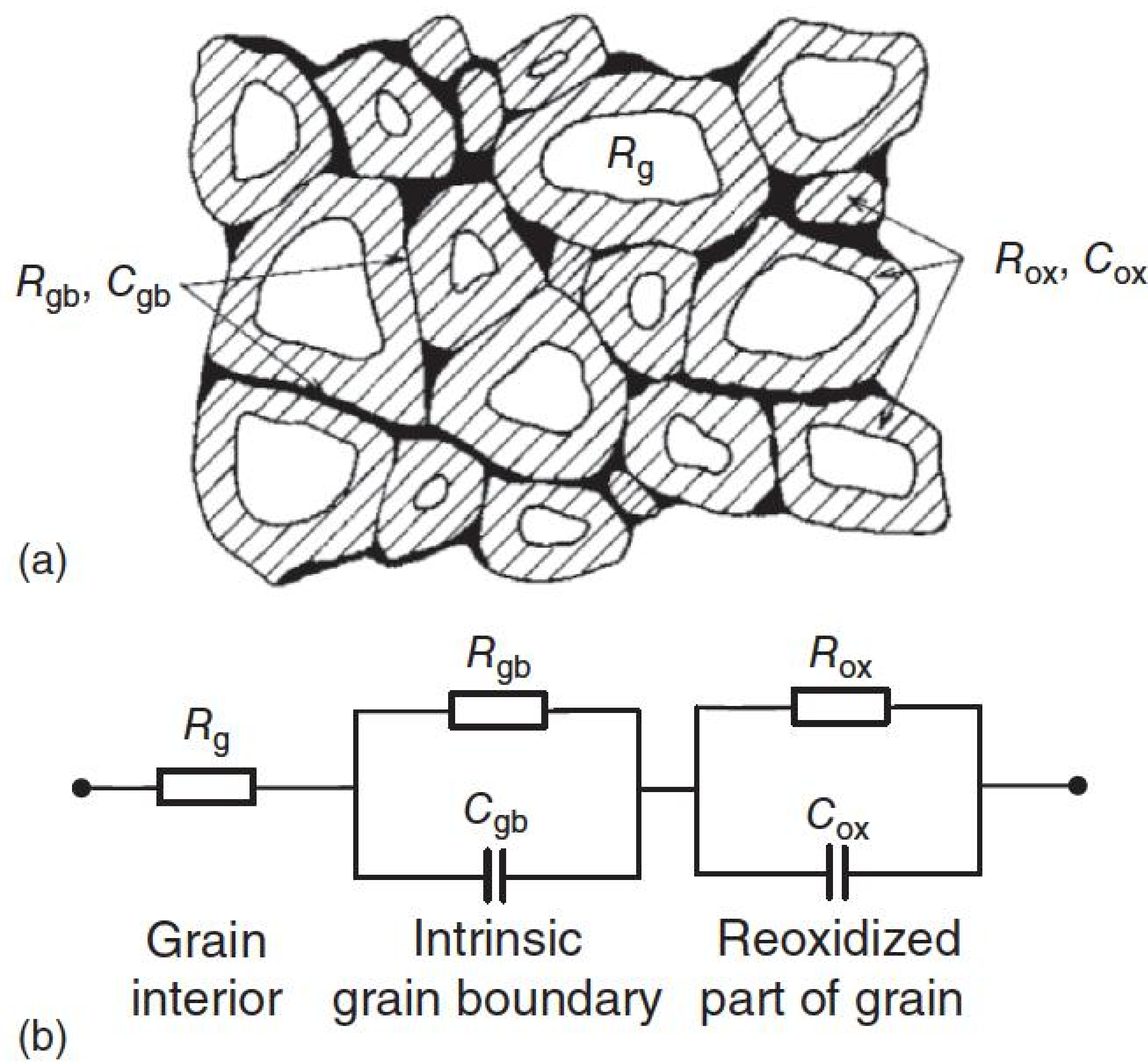


Figure 10.26 (a) Schematic model of microstructure of donor-doped BaTiO3 and (b) its equivalent electric circuit. Source: Adapted from Makovec et al. [318].

equivalent electric circuit model is shown in Figure 10.26b. The outer layer is an oxidized insulating grain boundary region; the intermediate layer is reoxidized semiconducting outer grain region and the inner layer is an oxygen-deficient semiconducting inner grain region. This heterogeneous structure in grain system is supported by both the phenomenon of heterogeneous electric structure of donor-doped $BaTiO_3$ and direct imaging from conductive atomic force microscopy technique [319, 320].

10.4.5 Varistor Characteristics of $BaTiO_3$ Ceramics

Except the PTCR effect, $BaTiO_3$ ceramic behaves varistor characteristics with voltage-limiting ability, when the ambient temperature is higher than the Curie temperature. Figure 10.24 shows the I–V curves of La-doped n-$BaTiO_3$ ceramics measured at different ambient temperatures T_a [1]. As $T_a \rightarrow T_c$, the magnitude of I_{max} decreases. When $T_a \approx T_c$ ($\approx$400 K), the linear I–V relations become current limiting without the current maximum. With $T_a > T_c$, the I–V curves follow the relation $I = kV^{\alpha}$, where k is the proportionality constant. The nonlinear coefficient α increases with the applied voltage, changing continuously from unity (ohmic) to 3.2 at low-to-intermediate current densities. The value of α measured in the range from 10 mA to 1 A rises abruptly to 30–50 at high electric fields. Depending on the processing conditions, which alter the grain size as well as the effective resistivity, the measured V_b varies from 0.2 to 2.1 V per grain boundary.

Highly stable varistor (voltage-limiting) property was observed for ceramics based on donor-doped $BaTiO_3$ ceramics ($Ba_{1-x}Sr_xTi_{1-y}Zr_yO_3$ ($x < 0.35$, $y < 0.05$), when the ambient temperature (T_a) is above the Curie point (T_c) by Kutty and Ravi [1]. As shown in Figure 10.27 [1], the I–V relation of donor-doped solid solution, $Ba_{1-x}Sr_xTi_{1-y}Zr_yO_3$ with $x = 0.3$, $y = 0.3$, at $T_a = 273$ K, is current limiting, whereas at $T_c = 300$ K, the voltage-limiting behavior is observed. By adjusting the values of x and y, the current-limiting or the voltage-limiting behavior could

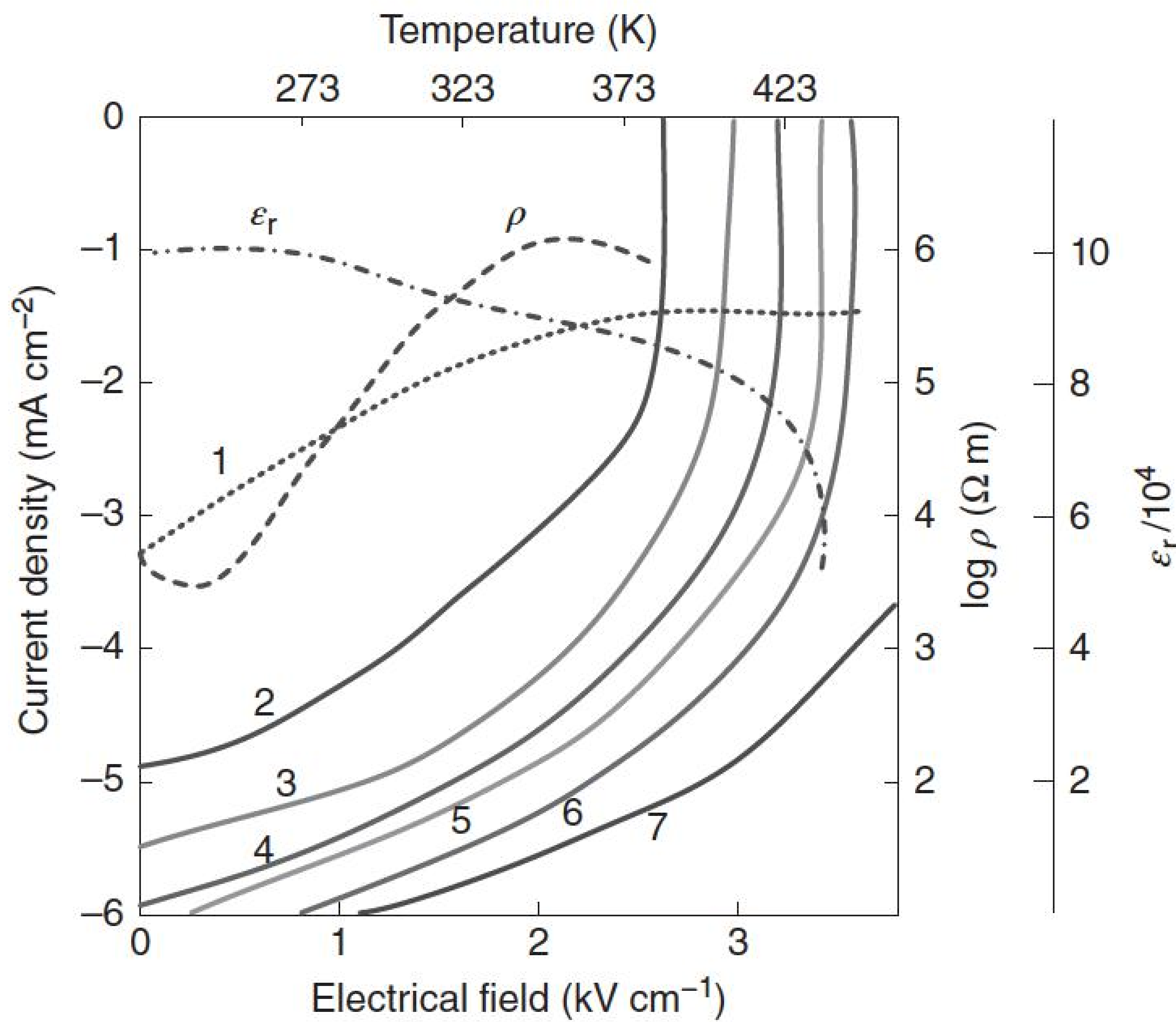


Figure 10.27 Current–voltage (*I–V*) and the variation in relative dielectric constant (ε_r) and resistivity (ρ) with temperature (T) of $Ba_{0.7}Sr_{0.3}Ti_{0.97}Zr_{0.03}O_3$ containing 0.03 mol% La, 1 at 273 K, 3 at 300 K, 2 and 6 are the same as in 3 containing 1 mol% La and 4 mol% La, respectively, of GBL modifiers ($Al_2O_3 + SiO_2 + TiO_2 + K_2O$), 4, 5, and 7 are the reannealed 1, 2, and 6 respectively, all the *I–V* curves, except 1, are measured at 300 K. Source: Adapted from Kutty and Ravi 1991 [1].

be brought to any desired temperature. This is accompanied by the shift in T_a, as shown from the break point on the ε_r–T curve. The magnitude of ε_r (usually ~10^5) as well as the PTCR characteristics indicates the dominance of GBL properties in the ceramics.

Kuwabara et al. [67] found donor, acceptor-codoped $(Ba_{0.4}Sr_{0.6})TiO_3$ ceramics with distinct varistor characteristics at room temperature, which were prepared by single-step firing in air. The materials, with the Curie point at around −90 °C, exhibited a large PTCR effect of more than seven orders of magnitude in the temperature ranging from −90 °C (the resistivity $\rho = 10^3\ \Omega$ cm) to room temperature ($\rho > 10^{10}\ \Omega$ cm). An apparent dielectric constant higher than 20 000 and tanδ smaller than 0.05 (at 100 kHz) were observed for the present materials at room temperature, and moreover, the materials exhibited nonlinear current–voltage characteristics with the nonlinear coefficient α in the range of 7–12, and the varistor field E_v in the range of 0.3–1.0 kV cm^{-1}. The value of α in the present materials increased systematically with increasing ρ in their PTCR temperature range. It has been found that there exists a close correlation between α and the grain boundary potential barrier height, ϕ_b, obtained from the ρ–T characteristic of the materials. An almost linear relationship was also found to exist between α and log E_v for the present materials [242].

Through suitable lattice substituents, the varistor property of n-$BaTiO_3$ can be brought down to room temperature. Yet the same specimen shows the current-limiting behavior at lower temperature [1].

It may be possible to conclude that simple diffusion current passing through a double-Schottky-type barrier formed at grain boundaries is not responsible for the varistor properties in the present materials. The conduction mechanism based on the Heywang model [222] can explain an α value smaller than 6, according to the calculation of Mallick and Emtage [321], but such large α values higher than 10 as observed for the $(Ba_{0.4}Sr_{0.6})TiO_3$ ceramics are difficult to be explained by the model. The conduction mechanism through surface states at the grain boundary interface layer is the most likely one for the occurrence of the varistor function in $(Ba_{0.4}Sr_{0.6})TiO_3$ ceramics [241].

References

1 Kutty, T.R.N. and Ravi, V. (1991). Varistor property of n-$BaTiO_3$ based current limiters. *Applied Physics Letters* 59 (21): 2691–2693.

2 Ihrig, H. and Puschert, W. (1977). A systematic experimental and theoretical investigation of the grain boundary resistivities of ndoped $BaTiO_3$ ceramics. *Journal of Applied Physics* 48 (7): 3081–3088.

3 Waku, S., Nishimura, A., Murakami, T. et al. (1971). Classification and dielectric characteristics of the boundary layer ceramic dielectrics (BL dielectric). *Review of the Electrical Communication Laboratory* 195 (6): 665–680.

4 Takahashi, Y., Yamaoka, N., Yamaoka, Y., and Kakubari, S. (1976). Intergranular insulation type polycrystalline ceramic semiconductive composition. US Patent No. 3,933,668. Washington, D.C.: U.S. Patent and Trademark Office.

5 Franken, P.E.C., Viegers, M.P.A., and Gehring, A.P. (1981). Microstructure of $SrTiO_3$ boundary-layer capacitor material. *Journal of the American Ceramic Society* 64 (12): 687–690.

6 Fujimoto, M. and Kingery, W.D. (2010). Microstructures of $SrTiO_3$ internal boundary layer capacitors during and after processing and resultant electrical properties. *Journal of the American Ceramic Society* 68 (4): 169–173.

7 Yamaoka, N., Masuyama, M., and Fukui, M. (1983). $SrTiO_3$-based boundary layer capacitor having varistor characteristics. *American Ceramic Society Bulletin* 62 (6): 698–700, 703.

8 Li, C.P., Wang, J.F., Su, W.B. et al. (2003). Effect of sinter temperature on the electrical properties of TiO_2-based capacitor–varistors. *Materials Letters* 57 (8): 1400–1405.

9 Fujimoto, M., Chiang, Y.M., Roshko, A., and Kingery, W.D. (2010). Microstructure and electrical properties of sodium-diffused and potassium-diffused $SrTiO_3$ barrier-layer capacitors exhibiting varistor behavior. *Journal of the American Ceramic Society* 68 (11): C-300–C-303.

10 Klein, A. (2016). Interface properties of dielectric oxides. *Journal of the American Ceramic Society* 99 (2): 369–387.

11 Nakanoand, Y. and Ichinose, N. (1990). Oxygen adsorption and VDR effect in (Sr, Ca)TiO_{3-x} based ceramics. *Journal of Materials Research* 5 (12): 2910–2922.

12 Kim, S.H., Moon, J.H., Park, J.H., and Kim, J.G.P.Y. (2001). Analysis of defect formation in Nb-doped $SrTiO_3$ by impedance spectroscopy. *Journal of Materials Research* 16 (1): 192–196.
13 Ji, H.M., Li, C.X., Meng, H. et al. (2005). Effects of rare-earth La_2O_3 addition on microstructures and electrical properties of $SrTiO_3$ varistor-capacitor dual functional ceramics. *Journal of Rare Earths* 23 (1): 55–58.
14 Li, L., Zhao, J., and Gui, Z. (2004). The thermal sensitivity and dielectric properties of $SrTiO_3$-based ceramics. *Ceramics International* 30 (7): 1073–1078.
15 Hirose, S., Nakayama, A., Niimi, H. et al. (2008). Resistance switching and retention behaviors in polycrystalline La-doped $SrTiO_3$ ceramics chip devices. *Journal of Applied Physics* 104 (5): 053712.
16 Li, J., Luo, S., and Alim, M.A. (2006). The role of TiO_2 powder on the $SrTiO_3$-based synthesized varistor materials. *Materials Letters* 60 (6): 720–724.
17 Yan, M.F. and Heuer, A.H. (1983). *Additives and Interfaces in Electronic Ceramics*, Advances in Ceramics, vol. 7. Columbus, OH: American Ceramic Society.
18 Viruthagiri, G., Praveen, P., Mugundan, S., and Gopinathan, E. (2013). Synthesis and characterization of pure and nickel doped $SrTiO_3$ nanoparticles via solid state reaction route. *Indian Journal of Advances in Chemical Science* 1 (3): 132–138.
19 Fuentes, S., Muñoz, P., Barraza, N. et al. (2015). Structural characterisation of slightly Fe-doped $SrTiO_3$, grown via a sol–gel hydrothermal synthesis. *Journal of Sol-Gel Science and Technology* 75 (3): 1–9.
20 Hong-Yun, L.I. and Xiong, X.Z. (2003). The development and manufacturing of $SrTiO_3$ ring varistors. *Electronic Components Materials* 22 (6): 20–22.
21 Park, M.B. and Cho, N.H. (2001). Grain boundaries of semiconducting $SrTiO_3$ and $BaTiO_3$ ceramics synthesized from surface-coated powders. *Journal of the American Ceramic Society* 84 (9): 1937–1944.
22 Ueno, K., Sakamoto, W., Yogo, T., and Hirano, S.I. (2003). Processing of novel strontium titanate-based thin-film varistors by chemical solution deposition. *Journal of the American Ceramic Society* 86 (1): 99–104.
23 Kutty, T.R.N. and Philip, S. (1995). Low voltage varistors based on $SrTiO_3$ ceramics. *Materials Science and Engineering B* 33 (2): 58–66.
24 Kim, S.H. and Kim, H.W.S.Y. (1998). Effect of MnO on the electrical properties of Nb-doped $SrTiO_3$ varistor. *MRS Proceedings Library Archive* 547: 121–126.
25 Kim, S.H., Byun, J.D., and Kim, Y. (1999). Effect of Na-diffusion on the electrical properties of $SrTiO_3$. *Journal of Materials Science* 34 (13): 3057–3061.
26 Zhou, L. and Yu, C. (1994). Sintering and properties of low-firing non-ohmic $SrTiO_3$, ceramics. *Journal of Materials Science* 29 (22): 6055–6059.
27 Li, J., Li, S., Liu, F. et al. (2003). The origin of varistor property of $SrTiO_3$-based ceramics. *Journal of Materials Science Materials in Electronics* 14 (8): 483–486.

28 Fujimoto, M. (1987). Potassium grain boundary segregation and site occupancy in $SrTiO_3$ ceramics. *Japanese Journal of Applied Physics* 26 (12): L2065–L2068.

29 Hitomi, A., Nomura, T., Kawasaki, M. et al. (1998). Transmission electron microscopy study of a semiconducting $SrTiO_3$ ceramic condenser. *Journal of Electron Microscopy* 47 (6): 603–610.

30 Koops, C.G. (1951). On the dispersion of resistivity and dielectric constant of some semiconductors at audiofrequencies. *Physical Review* 83 (1): 121–124.

31 Yan, M.F. and Rhodes, W.W. (1982). Preparation and properties of TiO_2 varistors. *Applied Physics Letters* 40 (6): 536–537.

32 Santhosh, P.N., Kharat, D.K., and Date, S.K. (1996). Effect of strontium substitution in (Nb, Bi) doped TiO_2 varistors. *Materials Letters* 28 (1): 37–41.

33 Meng, F.M. (2005). Influence of sintering processes on the electrical properties of TiO_2-based varistor ceramics. *Journal of Functional Materials and Devices* 11 (2): 149–152.

34 Li, J., Luo, S., Yao, W., and Zhang, Z. (2003). Role of second phase in (Nb, Ce, Si, Ca)-doped TiO_2 varistor ceramics. *Materials Letters* 57 (24–25): 3748–3754.

35 Bomio, M.R.D., Sousa, V.C., Leite, E.R. et al. (2004). Nonlinear behavior of $TiO_2 \cdot Ta_2O_5 \cdot MnO_2$ material doped with BaO and Bi_2O_3. *Materials Chemistry and Physics* 85 (1): 96–103.

36 Meng, F.M. (2005). Influence of sintering temperature on semi-conductivity and nonlinear electrical properties of TiO_2-based-varistor ceramics. *Materials Science and Engineering B* 117 (1): 77–80.

37 Pennewiss, J. and Hoffmann, B. (1990). Varistors made from TiO_2, – practicability and limits. *Materials Letters* 9 (5): 219–226.

38 Chen, H.F., Gan, G.Y., Yan, J.K., and Zhang, X.W. (2006). Influence of nano-titania additive on the property of TiO_2 varistor ceramics. *Semiconductor Technology* 31 (2): 102–104, 118.

39 Wang, W.Y., Zhang, D.F., Xu, T. et al. (2015). Nonlinear electrical and dielectric properties of (Ca, Ta)-doped TiO_2 varistors. *Physica Status Solidi A* 194 (1): 118–128.

40 Yan, M.F. and Rhodes, W.W. (1983). Low temperature sintering of TiO_2. *Materials Science and Engineering* 61 (1): 59–66.

41 Yang, S.L. and Wu, J.M. (1995). Varied atmosphere compensation—exploring the roles of barium and bismuth in (Ba,Bi,Nb)-doped TiO_2 varistors. *Journal of the American Ceramic Society* 78 (8): 2203–2208.

42 Bueno, P.R., Camargo, E., Longo, E. et al. (1996). Effect of Cr_2O_3 in the varistor behaviour of TiO_2. *Journal of Materials Science Letters* 15 (23): 2048–2050.

43 Cheng, J.J. and Wu, J.M. (1997). Effect of Mn on the electrical properties of (Ba, Bi, Nb)-added TiO_2 ceramics prepared by the sol-precipitation method. *Materials Chemistry and Physics* 48 (2): 129–135.

44 Wu, J. and Chih-Huang, L. (2010). Effect of lead oxide on niobium-doped titania varistors. *Journal of the American Ceramic Society* 74 (12): 3112–3117.

45 Bernik, S., Zupančič, P., and Kolar, D. (1999). Influence of Bi_2O_3/TiO_2, Sb_2O_3 and Cr_2O_3 doping on low-voltage varistor ceramics. *Journal of the European Ceramic Society* 19 (6–7): 709–713.

46 Sousa, V.C., Leite, E.R., Varela, J.A., and Longo, E. (2002). The effect of Ta_2O_5 and Cr_2O_3 on the electrical properties of TiO_2 varistors. *Journal of the European Ceramic Society* 22 (8): 1277–1283.

47 Ji, H.M., Sun, Q.C., and Wang, D.Y. (2002). Study on Y-based doped on TiO_2 ceramic varistors. *Bulletin of the Chinese Ceramic Society* 21 (5): 58–61.

48 Luo, J.J., Fang, X.Y., and Wu, M.T. (2000). Effect of thermal decomposition accompanying with oxidation on TiO_2 capacitor-varistor ceramics. *Journal of Inorganic Materials* 15 (1): 93–96.

49 Zhang, C., Hu, Y., Lu, W. et al. (2002). Influence of TiO_2/Sb_2O_3 ratio on ZnO varistor ceramics. *Journal of the European Ceramic Society* 22 (1): 61–65.

50 Sousa, V.C., Cassia-Santos, M.R., Barrado, C.M. et al. (2004). Effect of atmosphere on the electrical properties of TiO_2–SnO_2, varistor systems. *Journal of Materials Science: Materials in Electronics* 15 (10): 665–669.

51 Li, Z., Xu, G., Li, Y. et al. (2007). Effect of SnO_2 doping on the performance of TiO_2-based varistor. *Rare Metal Materials & Engineering* 36 (8): 177–180.

52 Delbrücke, T., Pianaro, S.A., Schmidt, I. et al. (2016). Effect of SrO on the electrical barrier formation and microstructure of TiO_2, varistors. *Materials Chemistry and Physics* 184: 91–100.

53 Navale, S.C., Murugan, A.V., and Ravi, V. (2007). Varistors based on Ta-doped TiO_2. *Ceramics International* 33 (2): 301–303.

54 Dhage, S.R. and Ravi, V. (2003). Influence of various donors on nonlinear I–V characteristics of tin dioxide ceramics. *Applied Physics Letters* 83 (22): 4539–4541.

55 Su, W.B., Wang, J.F., Chen, H.C. et al. (2002). Nonlinear electrical behavior of the $TiO_2{\cdot}WO_3$ varistor. *Journal of Applied Physics* 92 (8): 4779–4783.

56 Gong, Y., Chu, R., Xu, Z. et al. (2016). Varistor, dielectric, and luminescent properties of Pr_6O_{11}-doped TiO_2 multifunctional ceramics. *Journal of the American Ceramic Society* 99 (9): 2995–3001.

57 Gaikwad, A.B., Navale, S.C., and Ravi, V. (2005). TiO_2 ceramic varistor modified with tantalum and barium. *Materials Science and Engineering B* 123 (1): 50–52.

58 Wang, W.Y., Zhang, D.F., Xu, T. et al. (2002). Nonlinear electrical characteristics and dielectric properties of Ca,Ta-doped TiO_2, varistors. *Journal of Alloys and Compounds* 335 (1–2): 210–215.

59 Yan, J., Gan, G., Du, J., and Sun, J. (2009). Second phases of (La, Nb)-codoped TiO_2 varistor ceramic. *Journal of Physics: Conference Series* 152 (1): 012067.

60 Wang, T.G., Shao, G.Q., Li, X.B., and Zhang, W.J. (2009). Effect of Y_2O_3 doping in Ta_2O_5-TiO_2 capacitor-varistor double-functional ceramic. *Journal of Wuhan University of Technology* 31 (13): 4–6. (in Chinese).

61 Chen, H.F., Gan, G.Y., Yan, J.K., and Zhang, X.W. (2005). Influence of SiO_2 on property of TiO_2 varistor ceramics. *Foshan Ceramics* 15 (9): 4–6. (in Chinese).

62 Xu, Y.C., Li, H.F., Wang, S.L., and Wang, L.Q. (1994). Effects of SiO_2 on electrical properties of titania varistor ceramics. *Piezoelectric and Acorstooptics* 16 (5): 41–43.

63 Meng, F.M. (2006). Effect of SiO_2 on titania varistor ceramics. *Electronic Components & Materials* 25 (1): 27–29.

64 Li, L. and Qu, X.T. (2007). Effect of Bi_2O_3 additive on the properties of TiO_2 system varistor ceramics. *Electronic Components and Materials* 26 (3): 49–51.

65 Kang, K., Yan, J., Yi, J. et al. (2016). Nonlinear property of (Nb_2O_5, $SrCO_3$, Ge, GeO_2)-codoped TiO_2-based varistor ceramics. *Journal of the American Ceramic Society* 99 (1): 158–166.

66 Gupta, T.K. and Carlson, W.G. (1985). A grain-boundary defect model for instability/stability of a ZnO varistor. *Journal of Materials Science* 20 (10): 3487–3500.

67 Kuwabara, M., Matsuda, H., and Ohba, Y. (1999). Varistor characteristics in PTCR-type (Ba,Sr)TiO_3 ceramics prepared by single-step firing in air. *Journal of Materials Science* 34 (11): 2635–2639.

68 Yan, J.K., Gan, G.Y., Chen, H.F. et al. (2007). Influence of nano-particle on grain boundary barrier structure of TiO_2 varistor ceramics. *Semiconductor Technology* 32 (2): 109–112.

69 Brizé, V., Gruener, G., Wolfman, J. et al. (2006). Grain size effects on the dielectric constant of $CaCu_3Ti_4O_{12}$ ceramics. *Materials Science and Engineering B* 129 (1–3): 135–138.

70 Subramanian, M.A., Li, D., Duan, N. et al. (2000). High dielectric constant in a $ACu_3Ti_4O_{12}$ and $ACu_3Ti_3FeO_{12}$ phases. *Journal of Solid State Chemistry* 151 (2): 323–325.

71 Subramanian, M.A. and Sleight, A.W. (2002). $ACu_3Ti_4O_{12}$ and $ACu_3Ru_4O_{12}$ perovskites: high dielectric constants and valence degeneracy. *Solid State Sciences* 4 (3): 347–351.

72 Ramirez, A.P., Subramanian, M.A., Gardel, M. et al. (2000). Giant dielectric constant response in a copper-titanate. *Solid State Communications* 115 (5): 217–220.

73 Chung, S.Y., Kim, I.D., and Kang, S.J. (2004). Strong nonlinear current–voltage behaviour in perovskite-derivative calcium copper titanate. *Nature Materials* 3 (11): 774–778.

74 Luo, X.J., Yang, C.P., Chen, S.S. et al. (2010). The trap state relaxation related polarization in $CaCu_3Ti_4O_{12}$. *Journal of Applied Physics* 108 (1): 014107.

75 Shen, Y.S., Chiou, B.S., and Ho, C.C. (2008). Effects of annealing temperature on the resistance switching behavior of $CaCu_3Ti_4O_{12}$, films. *Thin Solid Films* 517 (3): 1209–1213.

76 Felix, A.A., Rupp, J.L.M., Varela, J.A., and Orlandi, M.O. (2012). Multi-functional properties of $CaCu_3Ti_4O_{12}$ thin films. *Journal of Applied Physics* 112 (5): 054512.

77 Tararam, R., Joanni, E., Savu, R. et al. (2011). Resistive-switching behavior in polycrystalline $CaCu_3Ti_4O_{12}$ nanorods. *ACS Applied Materials & Interfaces* 3 (2): 500–504.

78 Ramirez, M.A., Simões, A.Z., Felix, A.A. et al. (2011). Electric and dielectric behavior of $CaCu_3Ti_4O_{12}$-based thin films obtained by soft chemical method. *Journal of Alloys and Compounds* 509 (41): 9930–9933.

79 Shen, Y.S., Ho, C.C., and Chiou, B.S. (2009). Impedance spectroscopy of $CaCu_3Ti_4O_{12}$ films showing resistive switching. *Journal of the Electrochemical Society* 156 (6): H466–H470.

80 Kotecki, D.E. (1997). A review of high dielectric materials for dram capacitors. *Integrated Ferroelectrics* 16 (1–4): 1–19.

81 Cordeiro, M.A.L., Souza, F.L., Leite, E.R., and Lanfredi, A.J.C. (2008). Anomalous current-voltage behavior of $CaCu_3Ti_4O_{12}$ ceramics. *Applied Physics Letters* 93 (18): 182912.

82 Homes, C.C., Vogt, T., Shapiro, S.M. et al. (2003). Charge transfer in the high dielectric constant materials $CaCu_3Ti_4O_{12}$ and $CdCu_3Ti_4O_{12}$. *Physical Review B* 67 (9): 092106.

83 Adams, T.B., Sinclair, D.C., and West, A.R. (2006). Influence of processing conditions on the electrical properties of $CaCu_3Ti_4O_{12}$, ceramics. *Journal of the American Ceramic Society* 89 (10): 3129–3135.

84 Li, J., Subramanian, M.A., Rosenfeld, H.D. et al. (2015). Clues to the giant dielectric constant of $CaCu_3Ti_4O_{12}$ in the defect structure of "$SrCu_3Ti_4O_{12}$". *Stomatologiia Stomatology* 69 (2): 63–66.

85 Lin, Y.H., Cai, J., Li, M. et al. (2008). Grain boundary behavior in varistor-capacitor TiO_2-rich $CaCu_3Ti_4O_{12}$ ceramics. *Journal of Applied Physics* 103 (7): 074111.

86 Li, W., Schwartz, R.W., Chen, A., and Zhu, J. (2007). Dielectric response of Sr doped $CaCu_3Ti_4O_{12}$ ceramics. *Applied Physics Letters* 90 (11): 112901.

87 Jacob, K.T., Shekhar, C., Li, X., and Kale, G.M. (2008). Gibbs energy of formation of $CaCu_3Ti_4O_{12}$ and phase relations in the system $CaO\text{-}CuO/Cu_2O\text{-}TiO_2$. *Acta Materialia* 56 (17): 4798–4803.

88 Zhang, L. (2005). Electrode and grain-boundary effects on the conductivity of $CaCu_3Ti_4O_{12}$. *Applied Physics Letters* 87 (2): 022907.

89 Fang, T.T. and Shiau, H.K. (2004). Mechanism for developing the boundary barrier layers of $CaCu_3Ti_4O_{12}$. *Journal of the American Ceramic Society* 87 (11): 2072–2079.

90 Adams, T.B., Sinclair, D.C., and West, A.R. (2002). Giant barrier layer capacitance effects in $CaCu_3Ti_4O_{12}$ ceramics. *Advanced Materials* 14 (18): 1321–1323.

91 Marchin, L., Guillemet-Fritsch, S., Durand, B. et al. (2008). Grain growth-controlled giant permittivity in soft chemistry $CaCu_3Ti_4O_{12}$ ceramics. *Journal of the American Ceramic Society* 91 (2): 485–489.

92 Yang, Y., Wang, X., and Liu, B. (2014). $CaCu_3Ti_4O_{12}$ ceramics from different methods: microstructure and dielectric. *Journal of Materials Science: Materials in Electronics* 25 (1): 146–151.

93 Huang, Y., Shi, D., Li, Y. et al. (2013). Effect of holding time on the dielectric properties and non-ohmic behavior of $CaCu_3Ti_4O_{12}$ capacitor-varistors. *Journal of Materials Science: Materials in Electronics* 24 (6): 1994–1999.

94 Cohen, M.H., Neaton, J.B., He, L., and Vanderbilt, D. (2003). Extrinsic models for the dielectric response of $CaCu_3Ti_4O_{12}$. *Journal of Applied Physics* 94 (5): 3299–3306.

95 Singh, L., Sin, B.C., Kim, I.W. et al. (2016). A novel one-step flame synthesis method for tungsten-doped CCTO. *Journal of the American Ceramic Society* 99 (1): 27–34.

96 Raevski, I.P., Prosandeev, S.A., Bogatin, A.S. et al. (2003). High dielectric permittivity in $AFe_{1/2}B_{1/2}O_3$ nonferroelectric perovskite ceramics (A = Ba, Sr, Ca; B = Nb, Ta, Sb). *Journal of Applied Physics* 93 (7): 4130–4136.

97 He, L., Neaton, J.B., Cohen, M.H. et al. (2002). First-principles study of the structure and lattice dielectric response of $CaCu_3Ti_4O_{12}$. *Physical Review B* 65 (21): 214112.

98 Luo, F., He, J., Hu, J., and Lin, Y.H. (2009). Electric and dielectric properties of bi-doped $CaCu_3Ti_4O_{12}$ ceramics. *Journal of Applied Physics* 105 (7): 076104.

99 Löhnert, R., Schmidt, R., and Töpfer, J. (2015). Effect of sintering conditions on microstructure and dielectric properties of $CaCu_3Ti_4O_{12}$ (CCTO) ceramics. *Journal of Electroceramics* 34 (4): 241–248.

100 Leret, P., Fernandez, J.F., De Frutos, J., and Fernandez-Hevia, D. (2007). Nonlinear I–V electrical behaviour of doped $CaCu_3Ti_4O_{12}$ ceramics. *Journal of the European Ceramic Society* 27 (13–15): 3901–3905.

101 Ramírez, M.A., Bueno, P.R., Varela, J.A., and Longo, E. (2006). Non-ohmic and dielectric properties of a $CaCu_3Ti_4O_{12}$ polycrystalline system. *Applied Physics Letters* 89 (21): 212102.

102 Bueno, P.R., Ramírez, M.A., Varela, J.A., and Longo, E. (2006). Dielectric spectroscopy analysis of $CaCu_3Ti_4O_{12}$ polycrystalline systems. *Applied Physics Letters* 89 (19): 191117.

103 Marques, V.P.B., Ries, A., Simoes, A.Z. et al. (2007). Evolution of $CaCu_3Ti_4O_{12}$ varistor properties during heat treatment in vacuum. *Ceramics International* 33 (7): 1187–1190.

104 Lin, Y.H., Cai, J., Li, M. et al. (2006). High dielectric and nonlinear electrical behaviors in TiO_2-rich $CaCu_3Ti_4O_{12}$ ceramics. *Applied Physics Letters* 88 (17): 172902.

105 Chung, S.Y., Lee, S.I., Choi, J.H., and Choi, S.Y. (2006). Initial cation stoichiometry and current-voltage behavior in Sc-doped calcium copper titanate. *Applied Physics Letters* 89 (19): 191907.

106 Yuan, J., Lin, Y.H., Lu, H. et al. (2011). Dielectric and varistor behavior of $CaCu_3Ti_4O_{12}$–$MgTiO_3$ composite ceramics. *Journal of the American Ceramic Society* 94 (7): 1966–1969.

107 Thongbai, P., Yamwong, T., and Maensiri, S. (2013). Non-ohmic and dielectric properties of $CaCu_3Ti_4O_{12}$-MgO nanocomposites. *Microelectronic Engineering* 108: 177–181.

108 Homes, C.C., Vogt, T., Shapiro, S.M. et al. (2001). Optical response of high-dielectric-constant perovskite-related oxide. *Science* 293 (5530): 673–676.

109 Sinclair, D.C., Adams, T.B., Morrison, F.D., and West, A.R. (2002). $CaCu_3Ti_4O_{12}$: one-step internal barrier layer capacitor. *Applied Physics Letters* 80 (12): 2153–2155.

110 Luo, F., He, J., Hu, J., and Lin, Y. (2012). Characterization of individual grain boundaries and grains of $CaCu_3Ti_4O_{12}$ ceramic. *Science China Series E: Technological Sciences* 55 (4): 879–882.

111 Lunkenheimer, P., Fichtl, R., Ebbinghaus, S.G., and Loidl, A. (2004). Nonintrinsic origin of the colossal dielectric constants in $CaCu_3Ti_4O_{12}$. *Physical Review B* 70 (17): 172102.

112 Bender, B.A. and Pan, M.J. (2005). The effect of processing on the giant dielectric properties of $CaCu_3Ti_4O_{12}$. *Materials Science and Engineering B* 117 (3): 339–347.

113 Fang, T.T., Lin, W.J., and Lin, C.Y. (2007). Evidence of the ultrahigh dielectric constant of $CaSiO_3$-doped $CaCu_3Ti_4O_{12}$ from its dielectric response, impedance spectroscopy, and microstructure. *Physical Review B* 76 (4): 045115.

114 Bueno, P.R., Ribeiro, W.C., Ramírez, M.A. et al. (2007). Separation of dielectric and space charge polarizations in $CaCu_3Ti_4O_{12}/CaTiO_3$ composite polycrystalline systems. *Applied Physics Letters* 90 (14): 142912.

115 Feng, L., Tang, X., Yan, Y. et al. (2006). Decrease of dielectric loss in $CaCu_3Ti_4O_{12}$ ceramics by La doping. *Physica Status Solidi A* 203 (4): 22–24.

116 Fang, T.T., Mei, L.T., and Ho, H.F. (2006). Effects of Cu stoichiometry on the microstructures, barrier-layer structures, electrical conduction, dielectric responses, and stability of $CaCu_3Ti_4O_{12}$. *Acta Materialia* 54 (10): 2867–2875.

117 Pires, M.A., Israel, C., Iwamoto, W. et al. (2006). Role of oxygen vacancies in the magnetic and dielectric properties of the high-dielectric-constant system $CaCu_3Ti_4O_{12}$: an electron-spin resonance study. *Physical Review B* 73 (22): 224404.

118 Leret, P., De La Rubia, M.Á., Romero, J.J., and Fernández, J.F. (2010). Relevance of the percentage of active barriers in the dielectric response of $CaCu_3Ti_4O_{12}$ ceramics. *Journal of the American Ceramic Society* 93 (7): 1866–1868.

119 Kwon, S., Huang, C.C., Patterson, E.A. et al. (2008). The effect of Cr_2O_3, Nb_2O_5 and ZrO_2 doping on the dielectric properties of $CaCu_3Ti_4O_{12}$. *Materials Letters* 62 (4–5): 633–636.

120 Viviani, M., Bassoli, M., Buscaglia, V. et al. (2009). Giant permittivity and Maxwell-Wagner relaxation in Yb: $CaTiO_3$ ceramics. *Journal of Physics D: Applied Physics* 42 (17): 175407.

121 Singh, L., Rai, U.S., and Mandal, K.D. (2012). Influence of Zn doping on microstructures and dielectric properties in $CaCu_3Ti_4O_{12}$ ceramic synthesised by semiwet route. *Advances in Applied Ceramics* 111 (7): 374–380.

122 Fernandez, J.F., Leret, P., Romero, J.J. et al. (2009). Proofs of the coexistence of two magnetic contributions in pure and doped $CaCu_3Ti_4O_{12}$ giant dielectric constant ceramics. *Journal of the American Ceramic Society* 92 (10): 2311–2318.

123 Shao, S.F., Zhang, J.L., Zheng, P., and Wang, C.L. (2007). Effect of Cu-stoichiometry on the dielectric and electric properties in $CaCu_3Ti_4O_{12}$ ceramics. *Solid State Communications* 142 (5): 281–286.

124 Grubbs, R.K., Venturini, E.L., Clem, P.G. et al. (2005). Dielectric and magnetic properties of Fe- and Nb-doped $CaCu_3Ti_4O_{12}$. *Physical Review B* 72 (10): 104111.

125 Adams, T.B., Sinclair, D.C., and West, A.R. (2006). Decomposition reactions in $CaCu_3Ti_4O_{12}$ ceramics. *Journal of the American Ceramic Society* 89 (9): 2833–2838.

126 Capsoni, D., Bini, M., Massarotti, V. et al. (2004). Role of doping and CuO segregation in improving the giant permittivity of $CaCu_3Ti_4O_{12}$. *Journal of Solid State Chemistry* 177 (12): 4494–4500.

127 Hong, S.H., Kim, D.Y., Park, H.M., and Kim, Y.M. (2007). Electric and dielectric properties of Nb-doped $CaCu_3Ti_4O_{12}$ ceramics. *Journal of the American Ceramic Society* 90 (7): 2118–2121.

128 Kobayashi, W. and Terasaki, I. (2005). $CaCu_3Ti_4O_{12}/CaTiO_3$ composite dielectrics: Ba/Pb-free dielectric ceramics with high dielectric constants. *Applied Physics Letters* 87 (3): 032902.

129 Chiodelli, G., Massarotti, V., Capsoni, D. et al. (2004). Electric and dielectric properties of pure and doped $CaCu_3Ti_4O_{12}$ perovskite materials. *Solid State Communications* 132 (3–4): 241–246.

130 Patterson, E.A., Kwon, S., Huang, C.C., and Cann, D.P. (2005). Effects of ZrO_2 additions on the dielectric properties of $CaCu_3Ti_4O_{12}$. *Applied Physics Letters* 87 (18): 182911.

131 Ardakani, H.A., Alizadeh, M., Amini, R., and Ghazanfari, M.R. (2012). Dielectric properties of $CaCu_3Ti_4O_{12}$ improved by chromium/lanthanum co-doping. *Ceramics International* 38 (5): 4217–4220.

132 Lunkenheimer, P., Bobnar, V., Pronin, A.V. et al. (2002). Origin of apparent colossal dielectric constants. *Physical Review B* 66 (5): 052105.

133 Wang, C.C. and Zhang, L.W. (2006). Oxygen-vacancy-related dielectric anomaly in $CaCu_3Ti_4O_{12}$: post-sintering annealing studies. *Physical Review B* 74 (2): 024106.

134 Schmidt, R., Stennett, M.C., Hyatt, N.C. et al. (2012). Effects of sintering temperature on the internal barrier layer capacitor (IBLC) structure in $CaCu_3Ti_4O_{12}$ (CCTO) ceramics. *Journal of the European Ceramic Society* 32 (12): 3313–3323.

135 Li, J., Sleight, A.W., and Subramanian, M.A. (2005). Evidence for internal resistive barriers in a crystal of the giant dielectric constant material: $CaCu_3Ti_4O_{12}$. *Solid State Communications* 135 (4): 260–262.

136 Ni, L., Chen, X.M., Liu, X.Q., and Hou, R.Z. (2006). Microstructure-dependent giant dielectric response in $CaCu_3Ti_4O_{12}$ ceramics. *Solid State Communications* 139 (2): 45–50.

137 Pan, M.J. and Bender, B.A. (2005). A bimodal grain size model for predicting the dielectric constant of calcium copper titanate ceramics. *Journal of the American Ceramic Society* 88 (9): 2611–2614.

138 Zang, G., Zhang, J., Zheng, P. et al. (2005). Grain boundary effect on the dielectric properties of $CaCu_3Ti_4O_{12}$ ceramics. *Journal of Physics D: Applied Physics* 38 (11): 1824.

139 De Almeida-Didry, S., Autret, C., Lucas, A. et al. (2014). Leading role of grain boundaries in colossal permittivity of doped and undoped CCTO. *Journal of the European Ceramic Society* 34 (15): 3649–3654.

140 Calvert, C.C., Rainforth, W.M., Sinclair, D.C., and West, A.R. (2006). Characterisation of grain boundaries in $CaCu_3Ti_4O_{12}$ using HREM, EDS and EELS. *Journal of Physics: Conference Series* 26 (1): 65–68.

141 Chakravarty, D., Singh, P., Singh, S. et al. (2007). Electrical conduction behavior of high dielectric constant perovskite oxide $La_xCa_{1-3x/2}Cu_3Ti_4O_{12}$. *Journal of Alloys and Compounds* 438 (1–2): 253–257.

142 Yu, R., Xue, H., Cao, Z. et al. (2012). Effect of oxygen sintering atmosphere on the electrical behavior of CCTO ceramics. *Journal of the European Ceramic Society* 32 (6): 1245–1249.

143 Mei, L.T., Hsiang, H.I., and Fang, T.T. (2008). Effect of copper-rich secondary phase at the grain boundaries on the varistor properties of $CaCu_3Ti_4O_{12}$ ceramics. *Journal of the American Ceramic Society* 91 (11): 3735–3737.

144 Luo, F.C. (2011). Fundamental study on the dual-function ceramic of calcium copper titanate. Doctoral thesis. Beijing, China: Tsinghua University.

145 Jonscher, A.K. (2008). *Dielectric Relaxation in Solids*. Xi'an, China: Xi'an Jiaotong University Press, (in Chinese).

146 Jonscher, A.K. (1996). *Universal Relaxation Law: A Sequel to Dielectric Relaxation in Solids*. London: Chelsea Dielectrics Press.

147 Olsson, E. and Dunlop, G.L. (1989). Characterization of individual interfacial barriers in a ZnO varistor material. *Journal of Applied Physics* 66 (8): 3666–3675.

148 Bueno, P.R., Tararan, R., Parra, R. et al. (2009). A polaronic stacking fault defect model for $CaCu_3Ti_4O_{12}$ material: an approach for the origin of the huge dielectric constant and semiconducting coexistent features. *Journal of Physics D: Applied Physics* 42 (5): 055404.

149 Choi, S.W., Hong, S.H., and Kim, Y.M. (2007). Effect of Al doping on the electric and dielectric properties of $CaCu_3Ti_4O_{12}$. *Journal of the American Ceramic Society* 90 (12): 4009–4011.

150 Cai, J., Lin, Y.H., Cheng, B. et al. (2007). Dielectric and nonlinear electrical behaviors observed in Mn-doped $CaCu_3Ti_4O_{12}$ ceramic. *Applied Physics Letters* 91 (25): 252905.

151 Cheng, B., Lin, Y.H., Yang, H. et al. (2009). High dielectric permittivity behavior in Cu-doped $CaTiO_3$. *Journal of the American Ceramic Society* 92 (11): 2776–2779.

152 Cheng, B., Lin, Y.H., Yuan, J. et al. (2009). Dielectric and nonlinear electrical behaviors of La-doped $CaCu_3Ti_4O_{12}$ ceramics. *Journal of Applied Physics* 106 (3): 034111.

153 Sakamaki, R., Cheng, B., Cai, J. et al. (2010). Preparation of TiO_2-enriched $CaCu_3Mn_{0.1}Ti_{3.9}O_{12}$ ceramics and their dielectric properties. *Journal of the European Ceramic Society* 30 (1): 95–99.

154 Luo, F., He, J., Hu, J., and Lin, Y.H. (2010). Electric and dielectric behaviors of Y-doped calcium copper Titanate. *Journal of the American Ceramic Society* 93 (10): 3043–3045.
155 Yi, D., Yuan, J., Liu, H. et al. (2012). Influence of Al_2O_3 additive on the dielectric behavior and energy density of $Ba_{0.5}Sr_{0.5}TiO_3$ ceramics. *Journal of Electroceramics* 29 (2): 95–98.
156 Cheng, B., Lin, Y.H., Deng, W. et al. (2012). Dielectric and nonlinear electrical behaviors of Ce-doped $CaCu_3Ti_4O_{12}$ ceramics. *Journal of Electroceramics* 29 (4): 250–253.
157 Prakash, B.S. and Varma, K.B.R. (2006). Microstructural and dielectric properties of donor doped (La^{3+}) $CaCu_3Ti_4O_{12}$ ceramics. *Journal of Materials Science: Materials in Electronics* 17 (11): 899–907.
158 Kim, I.D., Rothschild, A., Hyodo, T., and Tuller, H.L. (2006). Microsphere templating as means of enhancing surface activity and gas sensitivity of $CaCu_3Ti_4O_{12}$ thin films. *Nano Letters* 6 (2): 193–198.
159 Wang, C.C. and Zhang, L.W. (2006). Surface-layer effect in $CaCu_3Ti_4O_{12}$. *Applied Physics Letters* 88 (4): 042906.
160 Wang, C., Zhang, H.J., He, P.M., and Cao, G.H. (2007). Ti-rich and Cu-poor grain-boundary layers of $CaCu_3Ti_4O_{12}$ detected by x-ray photoelectron spectroscopy. *Applied Physics Letters* 91 (5): 052910.
161 He, J.L., Luo, F.C., Hu, J., and Lin, Y.H. (2010). Effect of cooling rate on the properties of the grain boundary of $CaCu_3Ti_4O_{12}$ ceramic. *Key Engineering Materials* 434: 300–303.
162 Luo, F.C., He, J.L., Hu, J., and Lin, Y.H. (2010). Influence of slight bismuth additive on the properties of calcium copper titanate ceramic. *Advanced Materials Research* 105: 274–277.
163 Thongbai, P., Yamwong, T., Maensiri, S. et al. (2014). Improved dielectric and nonlinear electrical properties of fine-grained $CaCu_3Ti_4O_{12}$ ceramics prepared by a glycine-nitrate process. *Journal of the American Ceramic Society* 97 (6): 1785–1790.
164 Lin, Y.H., Deng, W., Xu, W. et al. (2012). Abnormal dielectric behaviors in Mn-doped $CaCu_3Ti_4O_{12}$ ceramics and their response mechanism. *Materials Science and Engineering B* 177 (20): 1773–1776.
165 Liu, L., Fang, L., Huang, Y. et al. (2011). Dielectric and nonlinear current–voltage characteristics of rare–earth doped $CaCu_3Ti_4O_{12}$ ceramics. *Journal of Applied Physics* 110 (9): 094101.
166 Thongbai, P., Boonlakhorn, J., Putasaeng, B. et al. (2013). Extremely enhanced nonlinear current–voltage properties of Tb-doped $CaCu_3Ti_4O_{12}$ ceramics. *Journal of the American Ceramic Society* 96 (2): 379–381.
167 Schmidt, R. and Sinclair, D.C. (2009). Anomalous increase of dielectric permittivity in Sr-doped CCTO ceramics $Ca_{1-x}Sr_xCu_3Ti_4O_{12}$ ($0 \leq x \leq 0.2$). *Chemistry of Materials* 22 (1): 6–8.
168 Liu, L., Huang, Y., Li, Y. et al. (2012). Dielectric and non-ohmic properties of $CaCu_3Ti_4O_{12}$ ceramics modified with NiO, SnO_2, SiO_2, and Al_2O_3 additives. *Journal of Materials Science* 47 (5): 2294–2299.
169 Hutagalung, S.D., Ooi, L.Y., and Ahmad, Z.A. (2009). Improvement in dielectric properties of Zn-doped $CaCu_3Ti_4O_{12}$ electroceramics prepared by

modified mechanical alloying technique. *Journal of Alloys and Compounds* 476 (1–2): 477–481.

170 Li, M., Feteira, A., Sinclair, D.C., and West, A.R. (2006). Influence of Mn doping on the semiconducting properties of $CaCu_3Ti_4O_{12}$ ceramics. *Applied Physics Letters* 88 (23): 232903.

171 Ni, L. and Chen, X.M. (2009). Enhanced giant dielectric response in Mg-substituted $CaCu_3Ti_4O_{12}$ ceramics. *Solid State Communications* 149 (9–10): 379–383.

172 Li, M., Cai, G., Zhang, D.F. et al. (2008). Enhanced dielectric responses in Mg-doped $CaCu_3Ti_4O_{12}$. *Journal of Applied Physics* 104 (7): 074107.

173 Yan, Y.Y., Jin, L., Feng, L.X., and Cao, C.H. (2006). Decrease of dielectric loss in giant dielectric constant $CaCu_3Ti_4O_{12}$ ceramics by adding $CaTiO_3$. *Materials Science and Engineering* 130: 146–150.

174 Singh, L., Rai, U.S., Mandal, K.D., and Yashpal, M. (2012). Dielectric properties of ultrafine Zn-doped $CaCu_3Ti_4O_{12}$ ceramic. *Journal of Advanced Dielectrics* 2 (01): 1250007.

175 Zheng, Q., Fan, H., and Long, C. (2012). Microstructures and electrical responses of pure and chromium-doped $CaCu_3Ti_4O_{12}$ ceramics. *Journal of Alloys and Compounds* 511 (1): 90–94.

176 De la Rubia, M.A., Leret, P., Del Campo, A. et al. (2012). Dielectric behaviour of Hf-doped $CaCu_3Ti_4O_{12}$ ceramics obtained by conventional synthesis and reactive sintering. *Journal of the European Ceramic Society* 32 (8): 1691–1699.

177 Sulaiman, M.A., Hutagalung, S.D., Ain, M.F., and Ahmad, Z.A. (2010). Dielectric properties of Nb-doped $CaCu_3Ti_4O_{12}$ electroceramics measured at high frequencies. *Journal of Alloys and Compounds* 493 (1–2): 486–492.

178 Thongbai, P., Jumpatam, J., Yamwong, T., and Maensiri, S. (2012). Effects of Ta^{5+} doping on microstructure evolution, dielectric properties and electrical response in $CaCu_3Ti_4O_{12}$ ceramics. *Journal of the European Ceramic Society* 32 (10): 2423–2430.

179 Liu, Y., Chen, Q., and Zhao, X. (2014). Dielectric response of Sb-doped $CaCu_3Ti_4O_{12}$ ceramics. *Journal of Materials Science: Materials in Electronics* 25 (3): 1547–1552.

180 Barbier, B., Combettes, C., Guillemet-Fritsch, S. et al. (2009). $CaCu_3Ti_4O_{12}$ ceramics from co-precipitation method: dielectric properties of pellets and thick films. *Journal of the European Ceramic Society* 29 (4): 731–735.

181 Jha, P., Arora, P., and Ganguli, A.K. (2003). Polymeric citrate precursor route to the synthesis of the high dielectric constant oxide $CaCu_3Ti_4O_{12}$. *Materials Letters* 57 (16–17): 2443–2446.

182 Singh, L., Rai, U.S., and Mandal, K.D. (2013). Dielectric properties of zinc doped nanocrystalline calcium copper titanate synthesized by different approach. *Materials Research Bulletin* 48 (6): 2117–2122.

183 Masingboon, C., Thongbai, P., Maensiri, S. et al. (2008). Synthesis and giant dielectric behavior of $CaCu_3Ti_4O_{12}$ ceramics prepared by polymerized complex method. *Materials Chemistry and Physics* 109 (2–3): 262–270.

184 Aoyagi, R., Iwata, M., and Maeda, M. (2007). Effect of sintering temperature on the dielectric properties of $CaCu_3Ti_4O_{12}$ ceramics. *Ferroelectrics* 356 (1): 90–94.

185 Ni, W.Q., Zheng, X.H., and Yu, J.C. (2007). Sintering effects on structure and dielectric properties of dielectrics $CaCu_3Ti_4O_{12}$. *Journal of Materials Science* 42 (3): 1037–1041.

186 Singh, L., Rai, U.S., Rai, A.K., and Mandal, K.D. (2013). Sintering effects on dielectric properties of Zn-doped $CaCu_3Ti_4O_{12}$ ceramic synthesized by modified sol-gel route. *Electronic Materials Letters* 9 (1): 107–113.

187 Prakash, B.S. and Varma, K.B.R. (2006). Effect of sintering conditions on the dielectric properties of $CaCu_3Ti_4O_{12}$ and $La_{2/3}Cu_3Ti_4O_{12}$ ceramics: a comparative study. *Physica B: Condensed Matter* 382 (1–2): 312–319.

188 Felix, A.A., Bezzon, V.D., Orlandi, M.O. et al. (2017). Role of oxygen on the phase stability and microstructure evolution of $CaCu_3Ti_4O_{12}$ ceramics. *Journal of the European Ceramic Society* 37 (1): 129–136.

189 Goswami, S. and Sen, A. (2010). Low temperature sintering of CCTO using P_2O_5 as a sintering aid. *Ceramics International* 36 (5): 1629–1631.

190 Thongbai, P., Putasaeng, B., Yamwong, T. et al. (2014). Liquid phase sintering behavior and improvement of giant dielectric properties by modifying microstructure and electrical response at grain boundaries of $CaCu_3Ti_{4-x}Mo_xO_{12}$ ceramics. *Journal of Alloys and Compounds* 582: 747–753.

191 Makcharoen, W. and Tunkasiri, T. (2013). Microstructures and dielectric relaxation behaviors of pure and tellurium doped $CaCu_3Ti_4O_{12}$ ceramics prepared via vibro-milling method. *Ceramics International* 39: S359–S364.

192 Porfirio, T.C. and Muccillo, E.N.S. (2015). Influence of lithium disilicate addition on the dielectric properties of chemically synthesized $CaCu_3Ti_4O_{12}$. *Journal of Materials Science: Materials in Electronics* 26 (6): 3970–3975.

193 Wang, J., Feng, L., Lei, A. et al. (2014). Preparation and dielectric properties of $CaCu_3Ti_4O_{12}$ ceramics with different additives. *Journal of Materials Engineering and Performance* 23 (9): 3133–3140.

194 Porfirio, T.C. and Muccillo, E.N.S. (2016). Effects of LiF addition on microstructure and dielectric properties of $CaCu_3Ti_4O_{12}$ ceramics. *Ceramics International* 42 (10): 12005–12009.

195 Jumpatam, J., Putasaeng, B., Yamwong, T. et al. (2016). Microstructural evolution and strongly enhanced dielectric response in Sn-doped $CaCu_3Ti_4O_{12}/CaTiO_3$ ceramic composites. *Materials Research Bulletin* 77: 178–184.

196 Thongbai, P., Vangchangyia, S., Swatsitang, E. et al. (2013). Non-ohmic and dielectric properties of Ba-doped $CaCu_3Ti_4O_{12}$ ceramics. *Journal of Materials Science: Materials in Electronics* 24 (3): 875–883.

197 Ramajo, L., Parra, R., Varela, J.A. et al. (2010). Influence of vanadium on electrical and microstructural properties of $CaCu_3Ti_4O_{12}/TiO_3$. *Journal of Alloys and Compounds* 497 (1–2): 349–353.

198 Nautiyal, A., Autret, C., Honstettre, C. et al. (2015). Dielectric properties of CCTO/$MgTiO_3$ composites: a new approach for capacitor application. *IJANM: International Journal of Advanced and Nanomaterials* 1 (1): 27–40.

199 Yang, Z., Zhang, Y., Lu, Z. et al. (2013). Electrical conduction and dielectric properties of the Rb-doped $CaCu_3Ti_4O_{12}$. *Journal of the American Ceramic Society* 96 (3): 806–811.

200 Moulson, A.J. and Herbert, J.M. (2003). *Electroceramics: Materials, Properties, Applications*. New York: Wiley.

201 Kuwabara, M. (1981). Effect of microstructure on the PTCR effect in semiconducting barium titanate ceramics. *Journal of the American Ceramic Society* 64 (11): 639–644.

202 Wang, Y. and Umeya, K. (1990). Electrical properties of PTCR barium titanate. *Journal of the American Ceramic Society* 73 (3): 669–677.

203 Qi, J., Gui, Z., Wang, Y. et al. (2002). The PTCR effect in $BaTiO_3$ ceramics modified by donor dopant. *Ceramics International* 28 (2): 141–143.

204 Liang, C.K. and Tsai, C.C. (2005). Evaluation of a novel PTC thermistor for telecom overcurrent protection. *Sensors and Actuators A: Physical* 121 (2): 443–449.

205 Jayanthi, S. and Kutty, T.R.N. (2006). Effect of segregative additives on the positive temperature coefficient in resistance characteristics of n-$BaTiO_3$ ceramics. *Journal of Materials Science: Materials in Electronics* 17 (11): 883–897.

206 Shimada, T., Touji, K., Katsuyama, Y. et al. (2007). Lead free PTCR ceramics and its electrical properties. *Journal of the European Ceramic Society* 27 (13–15): 3877–3882.

207 Huybrechts, B., Ishizaki, K., and Takata, M. (1995). The positive temperature coefficient of resistivity in barium titanate. *Journal of Materials Science* 30 (10): 2463–2474.

208 Nowotny, J. and Rekas, M. (1991). Positive temperature coefficient of resistivity for $BaTiO_3$-based materials. *Ceramics International* 17 (4): 227–241.

209 Brzozowski, E. and Castro, M.S. (2000). Conduction mechanism of barium titanate ceramics. *Ceramics International* 26 (3): 265–269.

210 Saburi, O. (1961). Semiconducting bodies in the family of barium titanates. *Journal of the American Ceramic Society* 44 (2): 54–63.

211 Takagi, H. (2011). Current status and future aspects of R&D activities on electro-ceramic components in Japanese industry. *Materials Science and Engineering* 18 (1): 012004.

212 Chen, Y.L. and Yang, S.F. (2011). PTCR effect in donor doped barium titanate: review of compositions, microstructures, processing and properties. *Advances in Applied Ceramics* 110 (5): 257–269.

213 Kulwicki, B.M. (1981). PTC materials technology 1955–1980. In: *Grain Boundary Phenomena in Electronic Ceramics*, Advances in Ceramics, vol. 1 (ed. L.M. Levinson), 138–154. Columbus, OH: American Ceramic Society.

214 Saburi, O. (1959). Properties of semiconductive $BaTiO_3$. *Journal of the Physical Society of Japan* 14 (9): 1159–1174.

215 Ravi, V. and Kutty, T.R.N. (1990). Current-limiting action of mixed-phase $BaTiO_3$ ceramic semiconductors. *Journal of Applied Physics* 68 (9): 4891–4893.

216 Niimi, H., Mihara, K., Sakabe, Y., and Kuwabara, M. (2007). Influence of Ba/Ti ratio on the positive temperature coefficient of resistivity characteristics of Ca-doped semiconducting $BaTiO_3$ fired in reducing atmosphere and reoxidized in air. *Journal of the American Ceramic Society* 90 (6): 1817–1821.

217 Nakano, Y., Watanabe, M., and Takahashi, T. (1991). Investigation of interface states in (Sr, Ca) TiO_{3-x}-based ceramics. *Journal of Applied Physics* 70 (3): 1539–1547.

218 Heywang, W. (1971). Semiconducting barium titanate. *Journal of Materials Science* 6 (9): 1214–1224.

219 Xue, L.A., Chen, Y., and Brook, R.J. (1988). The influence of ionic radii on the incorporation of trivalent dopants into $BaTiO_3$. *Materials Science and Engineering B* 1 (2): 193–201.

220 Jung, Y.S., Na, E.S., Paik, U. et al. (2002). A study on the phase transition and characteristics of rare earth elements doped $BaTiO_3$. *Materials Research Bulletin* 37 (9): 1633–1640.

221 Glinchuk, M.D., Bykov, I.P., Kornienko, S.M. et al. (2000). Influence of impurities on the properties of rare-earth-doped barium-titanate ceramics. *Journal of Materials Chemistry* 10 (4): 941–947.

222 Heywang, W. (1964). Resistivity anomaly in doped barium titanate. *Journal of the American Ceramic Society* 47 (10): 484–490.

223 Peria, W.T., Bratschun, W.R., and Fenity, R.D. (1961). Possible explanation of positive temperature coefficient in resistivity of semiconducting ferroelectrics. *Journal of the American Ceramic Society* 44 (5): 249–250.

224 Jonker, G.H. (1964). Some aspects of semiconducting barium titanate. *Solid State Electronics* 7 (12): 895–903.

225 Megaw, H.D. (1946). Crystal structure of barium titanium oxide and other double oxides of the perovskite type. *Transactions of the Faraday Society* 42: A224–A231.

226 Morrison, F.D., Sinclair, D.C., and West, A.R. (2001). An alternative explanation for the origin of the resistivity anomaly in La-doped $BaTiO_3$. *Journal of the American Ceramic Society* 84 (2): 474–476.

227 Makovec, D., Samardžija, Z., and Drofenik, M. (2004). Solid solubility of holmium, yttrium, and dysprosium in $BaTiO_3$. *Journal of the American Ceramic Society* 87 (7): 1324–1329.

228 Ueoka, H. (1974). The doping effects of transition elements on the PTC anomaly of semiconductive ferroelectric ceramics. *Ferroelectrics* 7 (1): 351–353.

229 Buscaglia, M.T., Buscaglia, V., Viviani, M., and Nanni, P. (2001). Atomistic simulation of dopant incorporation in barium titanate. *Journal of the American Ceramic Society* 84 (2): 376–384.

230 Murakami, T., Miyashita, T., Nakahara, M., and Sekine, E. (1973). Effect of rare-earth ions on electrical conductivity of $BaTiO_3$ ceramics. *Journal of the American Ceramic Society* 4 (35): 294–297.

231 Tennery, V.J. and Cook, R.L. (1961). Investigation of rare-earth doped barium titanate. *Journal of the American Ceramic Society* 44 (4): 187–193.

232 Tsur, Y., Dunbar, T.D., and Randall, C.A. (2001). Crystal and defect chemistry of rare earth cations in $BaTiO_3$. *Journal of Electroceramics* 7 (1): 25–34.

233 Macchesney, J.B. and Potter, J.F. (1965). Factors and mechanisms affecting the positive temperature coefficient of resistivity of barium titanate. *Journal of the American Ceramic Society* 48 (2): 81–88.

234 Kchikech, M. and Maglione, M. (1994). Electronic and lattice excitations in $BaTiO_3$:La. *Journal of Physics: Condensed Matter* 6 (46): 10159–10170.

235 Seaton, J. and Leach, C. (2003). Local property measurement in PTC thermistors. *Acta Materialia* 51 (20): 6027–6034.

236 Wang, P.J., Zeng, Z.Q., Gui, Z.L., and Li, L.T. (1997). Strontium-lead titanate ceramics with positive temperature coefficient of resistance. *Materials Letters* 30 (4): 275–277.

237 Jingchang, Z., Longtu, L., and Zhilun, G. (2002). A study of V-shaped PTC behaviour of $Sr_{0.4}Pb_{0.6}TiO_3$ ceramics. *Journal of the European Ceramic Society* 22 (7): 1171–1175.

238 Zhao, J., Li, L., and Gui, Z. (2001). Influence of lithium modification on the properties of Y-doped $Sr_{0.5}Pb_{0.5}TiO_3$ thermistors. *Sensors and Actuators A: Physical* 95 (1): 46–50.

239 Chou, C.C., Chang, H.Y., Lin, I.N. et al. (1998). Microscopic examination of the microwave sintered $(Pb_{0.6}Sr_{0.4})TiO_3$ positive-temperature-coefficient resistor materials. *Japanese Journal of Applied Physics* 37 (9): 5269–5272.

240 Völtzke, D., Abicht, H.P., Pippel, E., and Woltersdorf, J. (2000). Ca-containing additives in PTC-$BaTiO_3$ ceramics: effects on the microstructural evolution. *Journal of the European Ceramic Society* 20 (11): 1663–1669.

241 Matsuura, K., Hoshina, T., Takeda, H. et al. (2014). Effects of Ca substitution on room temperature resistivity of donor-doped barium titanate based PTCR ceramics. *Journal of the Ceramic Society of Japan* 122 (1426): 402–405.

242 Baxter, P., Hellicar, N.J., and Lewis, B. (1959). Effect of additives of limited solid solubility on ferroelectric properties of barium titanate ceramics. *Journal of the American Ceramic Society* 42 (10): 465–470.

243 Jaffe, B., Cook, W.R., and Jaffe, H. (1971). *Piezoelectric Cerumits*. Gurugram, Haryana: Academic Press.

244 Swilam, M.N. and Gadalla, A.M. (1975). Effect of additions on the sinterability of barium titanate. *Transactions and Journal of the British Ceramic Society* 74 (5): 165–169.

245 Yoon, K.H., Kim, J.W., and Jo, K.H. (1989). Dielectric properties of $BaTiO_3$ with Sb_2O_3 and ZnO. *Journal of Materials Science Letters* 8 (2): 153–156.

246 Caballero, A.C., Fernández, J.F., Moure, C., and Durán, P. (1997). ZnO-doped $BaTiO_3$: microstructure and electrical properties. *Journal of the European Ceramic Society* 17 (4): 513–523.

247 Miki, T., Fujimoto, A., and Jida, S.S. (1998). An evidence of trap activation for positive temperature coefficient of resistivity in $BaTiO_3$ ceramics with substitutional Nb and Mn as impurities. *Journal of Applied Physics* 83 (3): 1592–1603.

248 Chiang, Y.M. and Takagi, T. (1990). Grain-boundary chemistry of barium titanate and strontium titanate: I, high-temperature equilibrium space charge. *Journal of the American Ceramic Society* 73 (11): 3278–3285.

249 Yoon, S.H., Lee, K.H., and Kim, H. (2000). Effect of acceptors on the segregation of donors in niobium-doped barium titanate positive temperature coefficient resistors. *Journal of the American Ceramic Society* 83 (10): 2463–2472.

250 V'yunov, O.I., Kovalenco, L.L., and Belous, A.G. (2003). The effect of isovalent substitutions and dopants of 3d-metals on the properties of ferroelectrics-semiconductors. *Condensed Matter Physics* 6 (2): 213–220.

251 Gallego, M.M. and West, A.R. (2001). Effect of annealing treatments on positive temperature coefficient of resistance properties of barium titanate ceramics and a new model for the positive temperature coefficient of resistance effect. *Journal of Applied Physics* 90 (1): 394–403.

252 Shut, V.N. and Kostomarov, S.V. (2009). Semiconducting ceramics produced using nanocrystalline barium titanate powder. *Inorganic Materials* 45 (12): 1417–1422.

253 Shut, V.N., Kostomarov, S.V., and Trublovsky, V.L. (2012). Effect of the crystallinity of $BaTiO_3$ powders prepared using the merker method on the properties of PTCR ceramics. *Inorganic Materials* 48 (6): 648–654.

254 Anwar, S., Sagdeo, P.R., and Lalla, N.P. (2006). Ferroelectric relaxor behavior in hafnium doped barium-titanate ceramic. *Solid State Communications* 138 (7): 331–336.

255 Kumar, M., Garg, A., Kumar, R., and Bhatnagar, M.C. (2008). Structural, dielectric and ferroelectric study of $Ba_{0.9}Sr_{0.1}Zr_xTi_{1-x}O_3$ ceramics prepared by the sol–gel method. *Physica B: Condensed Matter* 403 (10–11): 1819–1823.

256 Lu, S.G., Xu, Z.K., and Chen, H. (2004). Tunability and relaxor properties of ferroelectric barium stannate titanate ceramics. *Applied Physics Letters* 85 (22): 5319–5321.

257 Yu, Z., Ang, C., Guo, R., and Bhalla, A.S. (2002). Ferroelectric-relaxor behavior of $Ba(Ti_{0.7}Zr_{0.3})O_3$ ceramics. *Journal of Applied Physics* 92 (5): 2655–2657.

258 Shvartsman, V.V., Kleemann, W., Dec, J. et al. (2006). Diffuse phase transition in $BaTi_{1-x}Sn_xO_3$ ceramics: an intermediate state between ferroelectric and relaxor behavior. *Journal of Applied Physics* 99 (12): 124111.

259 Desu, S.B. and Payne, D.A. (1990). Interfacial segregation in perovskites: IV, internal boundary layer devices. *Journal of the American Ceramic Society* 73 (11): 3416–3421.

260 Desu, S.B. and Payne, D.A. (1990). Interfacial segregation in perovskites: III, microstructure and electrical properties. *Journal of the American Ceramic Society* 73 (11): 3407–3415.

261 Langhammer, H.T., Makovec, D., Pu, Y. et al. (2006). Grain boundary reoxidation of donor-doped barium titanate ceramics. *Journal of the European Ceramic Society* 26 (14): 2899–2907.

262 Peng, C.J. and Lu, H.Y. (1988). Compensation effect in semiconducting barium titanate. *Journal of the American Ceramic Society* 71 (1): C44–C46.

263 Ting, C.J., Peng, C.J., Lu, H.Y., and Wu, S.T. (1990). Lanthanum-magnesium and lanthanum-manganese donor-acceptor-codoped semiconducting barium titanate. *Journal of the American Ceramic Society* 73 (2): 329–334.
264 Yoon, S.H., Lee, J.H., Kim, D.Y., and Hwang, N.M. (2003). Effect of the liquid-phase characteristic on the microstructures and dielectric properties of donor-(niobium) and acceptor-(magnesium) doped barium titanate. *Journal of the American Ceramic Society* 86 (1): 88–92.
265 Kutty, T.R.N. and Ravi, V. (1991). Improved current limiters based on mixed-phase $BaTiO_3$ ceramic semiconductors. *Journal of Materials Science: Materials in Electronics* 2 (2): 79–88.
266 Blamey, J.M. and Parry, T.V. (1993). The effect of processing variables on the mechanical and electrical properties of barium-titanate positive-temperature-coefficient-of-resistance ceramics. *Journal of Materials Science* 28 (16): 4311–4316.
267 Park, K., Ha, J.G., Kim, C.W., and Kim, J.G. (2008). PTCR characteristics of semiconducting barium titanate ceramics produced by high-energy ball-milling. *Journal of Materials Science: Materials in Electronics* 19 (4): 357–362.
268 Pithan, C., Hennings, D., and Waser, R. (2005). Progress in the synthesis of nanocrystalline $BaTiO_3$ powders for MLCC. *International Journal of Applied Ceramic Technology* 2 (1): 1–14.
269 Clabaugh, W.S., Swiggard, E.M., and Gilchrist, R. (1956). Preparation of barium titanyl oxalate for converstion to barium titanate of high purity. *Journal of Research of the National Bureau of Standards* 56 (5): 289–291.
270 Medvedev, E.F. (1998). Technological methods for barium titanate synthesis. *Glass and Ceramics* 55 (9–10): 311–313.
271 Shut, V.N. and Kostomarov, S.V. (2012). Properties of barium titanate powders in relation to the heat treatment of the barium titanyl oxalate precursor. *Inorganic Materials* 48 (6): 613–618.
272 Urek, S. and Drofenik, M. (1999). PTCR behaviour of highly donor doped $BaTiO_3$. *Journal of the European Ceramic Society* 19 (6–7): 913–916.
273 Buscaglia, M.T., Viviani, M., Buscaglia, V. et al. (2002). Incorporation of Er^{3+} into $BaTiO_3$. *Journal of the American Ceramic Society* 85 (6): 1569–1575.
274 Wang, S.F. and Dayton, G.O. (1999). Dielectric properties of fine-grained barium titanate based X7R materials. *Journal of the American Ceramic Society* 82 (10): 2677–2682.
275 Okino, Y., Shizuno, H., Kusumi, S., and Kishi, H. (1994). Dielectric properties of rare-earth-oxide-doped $BaTiO_3$ ceramics fired in reducing atmosphere. *Japanese Journal of Applied Physics* 33 (9S): 5393.
276 Brzozowski, E. and Castro, M.S. (2004). Influence of Nb^{5+} and Sb^{3+} dopants on the defect profile, PTCR effect and GBBL characteristics of $BaTiO_3$ ceramics. *Journal of the European Ceramic Society* 24 (8): 2499–2507.
277 Mitic, V.V., Nikolic, Z.S., Pavlovic, V.B. et al. (2010). Influence of rare-earth dopants on barium titanate ceramics microstructure and corresponding electrical properties. *Journal of the American Ceramic Society* 93 (1): 132–137.

278 Desu, S.B. and Payne, D.A. (1990). Interfacial segregation in perovskites: II, experimental evidence. *Journal of the American Ceramic Society* 73 (11): 3398–3406.

279 Sauer, H.A. and Fisher, J.R. (1960). Processing of positive temperature coefficient thermistors. *Journal of the American Ceramic Society* 43 (6): 297–301.

280 LaCourse, B.C. and Amarakoon, V.R. (1995). Characterization of the firing schedule for positive temperature coefficient of resistance $BaTiO_3$. *Journal of the American Ceramic Society* 78 (12): 3352–3356.

281 Koschek, G. and Kubalek, E. (1985). Grain-boundary characteristics and their influence on the electrical resistance of barium titanate ceramics. *Journal of the American Ceramic Society* 68 (11): 582–586.

282 Makovec, D., Samardžija, Z., and Drofenik, M. (2006). The solid solubility of holmium in $BaTiO_3$ under reducing conditions. *Journal of the American Ceramic Society* 89 (10): 3281–3284.

283 Desu, S.B. and Payne, D.A. (1990). Interfacial segregation in perovskites: I, theory. *Journal of the American Ceramic Society* 73 (11): 3391–3397.

284 Al-Allak, H.M., Brinkman, A.W., Russell, G.J. et al. (1988). The effect of donor dopant concentration on the room temperature resistivity of $BaTiO_3$ ceramics with positive temperature coefficients of resistance. *Journal of Physics D: Applied Physics* 21 (7): 1226–1233.

285 Sinclair, D.C. and West, A.R. (1994). Effect of atmosphere on the PTCR properties of $BaTiO_3$ ceramics. *Journal of Materials Science* 29 (23): 6061–6068.

286 Ozawa, M. and Suzuki, S. (1997). Influence of heat treatment with nitrogen in positive-temperature-coefficient-type $BaTiO_3$. *Journal of Materials Science Letters* 16 (7): 545–546.

287 Hennings, D. (1991). Control of microstructure with seed grains. *Ceramics International* 17 (5): 283–286.

288 Hari, N.S. and Kutty, T.R.N. (1998). Effect of secondary-phase segregation on the positive temperature coefficient in resistance characteristics of n-$BaTiO_3$ ceramics. *Journal of Materials Science* 33 (13): 3275–3284.

289 Kovalenko, L.L., V'yunov, O.I., and Belous, A.G. (1999). Semiconducting barium titanate doped with oxygen-free compounds. *Journal of the European Ceramic Society* 19 (6–7): 965–968.

290 Millet, J.M., Roth, R.S., and Parker, H.S. (1986). Phase relations between the polytitanates of barium and the barium borates, vanadates, and molybdates. *Journal of the American Ceramic Society* 69 (11): 811–814.

291 Ho, I.C. (1994). Semiconducting barium titanate ceramics prepared by boron-containing liquid-phase sintering. *Journal of the American Ceramic Society* 77 (3): 829–832.

292 Rhim, S.M., Hong, S., Bak, H., and Kim, O.K. (2000). Effects of B_2O_3 addition on the dielectric and ferroelectric properties of $Ba_{0.7}Sr_{0.3}TiO_3$ ceramics. *Journal of the American Ceramic Society* 83 (5): 1145–1148.

293 Oppolzer, H. and Schmelz, H. (1983). Investigation of twin lamellae in $BaTiO_3$ ceramics. *Journal of the American Ceramic Society* 66 (6): 444–446.

294 Erkalfa, H., Yuksel, B., and Ozkan, T.O. (2004). The effect of B_2O_3 addition on the sintering of Sb_2O_3 doped $BaTiO_3$. *Key Engineering Materials* 264: 1333–1336.

295 Hennings, D.F., Janssen, R., and Reynen, P.J. (1987). Control of liquid-phase-enhanced discontinuous grain growth in barium titanate. *Journal of the American Ceramic Society* 70 (1): 23–27.

296 Hennings, D.F., Hartung, R., and Reijnen, P.J. (1990). Grain size control in low-voltage varistors. *Journal of the American Ceramic Society* 73 (3): 645–648.

297 Viviani, M., Buscaglia, M.T., Buscaglia, V. et al. (2004). Analysis of conductivity and PTCR effect in Er-doped $BaTiO_3$ ceramics. *Journal of the European Ceramic Society* 24 (6): 1221–1225.

298 Zubair, M.A. and Leach, C. (2007). Modeling the resistance-temperature characteristic of a positive temperature coefficient thermistor, using experimentally determined permittivity data. *Applied Physics Letters* 91 (8): 082105.

299 Huybrechts, B., Ishizaki, K., and Takata, M. (1992). Experimental evaluation of the acceptor-states compensation in positive-temperature-coefficient-type barium titanate. *Journal of the American Ceramic Society* 75 (3): 722–724.

300 Daniels, J., Hardtl, K.H., Hennings, D., and Wernicke, R. (1976). Defect chemistry and electrical-conductivity of doped barium-titanate ceramics. *Philips Research Reports* 31 (6): 487–559.

301 Alles, A.B., Amarakoon, V.R., and Burdick, V.L. (1989). Positive temperature coefficient of resistivity effect in undoped, atmospherically reduced barium titanate. *Journal of the American Ceramic Society* 72 (1): 148–151.

302 Chan, N.H. and Smyth, D.M. (1984). Defect chemistry of donor-doped $BaTiO_3$. *Journal of the American Ceramic Society* 67 (4): 285–288.

303 Wu, T.B. and Lin, J.N. (1994). Transition of compensating defect mode in niobium-doped barium titanate. *Journal of the American Ceramic Society* 77 (3): 759–764.

304 Hari, N.S., Padmini, P., and Kutty, T.N. (1997). Complex impedance analyses of n-$BaTiO_3$ ceramics showing positive temperature coefficient of resistance. *Journal of Materials Science: Materials in Electronics* 8 (1): 15–22.

305 Morrison, F.D., Sinclair, D.C., and West, A.R. (2001). Characterization of lanthanum-doped barium titanate ceramics using impedance spectroscopy. *Journal of the American Ceramic Society* 84 (3): 531–538.

306 Kirstein, K., Reichmann, K., Preis, W., and Mitsche, S. (2011). Effect of commercial anatase-TiO_2 raw materials on the electrical characteristics of ceramics with positive temperature coefficient of resistivity. *Journal of the European Ceramic Society* 31 (13): 2339–2349.

307 Jonker, G.H. and Havinga, E.E. (1982). The influence of foreign ions on the crystal lattice of barium titanate. *Materials Research Bulletin* 17 (3): 345–350.

308 Chan, H.M., Harmer, M.R., and Smyth, D.M. (1986). Compensating defects in highly donor-doped $BaTiO_3$. *Journal of the American Ceramic Society* 69 (6): 507–510.

309 Smyth, D.M. (2002). The defect chemistry of donor-doped $BaTiO_3$: a rebuttal. *Journal of Electroceramics* 9 (3): 179–186.

310 Langhammer, H.T., Drofenik, M., Felgner, K.H., and Abicht, H.P. (2004). Investigation of semiconducting barium titanate ceramics by oxygen coulometry. *Journal of Electroceramics* 13 (1–3): 793–797.

311 Langhammer, H.T., Song, Q.M., Felgner, K.H., and Abicht, H.P. (2002). Investigations on the defect chemistry and the sintering of barium titanate ceramics by oxygen coulometry. *Solid State Sciences* 4 (2): 197–203.

312 Makovec, D. and Drofenik, M. (2000). Microstructural changes during the reduction/reoxidation process in donor-doped $BaTiO_3$ ceramics. *Journal of the American Ceramic Society* 83 (10): 2593–2599.

313 V'yunov, O.I., Kovalenko, L.L., Belous, A.G., and Belyakov, V.N. (2005). Oxidation of reduced Y-doped semiconducting barium titanate ceramics. *Inorganic Materials* 41 (1): 87–93.

314 Morrison, F.D., Coats, A.M., Sinclair, D.C., and West, A.R. (2001). Charge compensation mechanisms in La-doped $BaTiO_3$. *Journal of Electroceramics* 6 (3): 219–232.

315 Morrison, F.D., Sinclair, D.C., and West, A.R. (2001). Doping mechanisms and electrical properties of La-doped $BaTiO_3$ ceramics. *International Journal of Inorganic Materials* 3 (8): 1205–1210.

316 Hayes, W. and Stoneham, A.M. (2012). *Defects and Defect Processes in Nonmetallic Solids*. North Chelmsford, MA: Courier Corporation.

317 Zubair, M.A. and Leach, C. (2010). The effect of SiO_2 addition on the development of low-Σ grain boundaries in PTC thermistors. *Journal of the European Ceramic Society* 30 (1): 107–112.

318 Makovec, D., Ule, N., and Drofenik, M. (2001). Positive temperature coefficient of resistivity effect in highly donor–doped barium titanate. *Journal of the American Ceramic Society* 84 (6): 1273–1280.

319 Affleck, L., Seaton, J., and Leach, C. (2007). Characterisation of the R–T response of $BaTiO_3$ thermistors on three different length scales. *Journal of the European Ceramic Society* 27 (12): 3439–3444.

320 Fiorenza, P., Lo Nigro, R., Delugas, P. et al. (2009). Direct imaging of the core-shell effect in positive temperature coefficient of resistance-$BaTiO_3$ ceramics. *Applied Physics Letters* 95 (14): 142904.

321 Mallick, G.T. Jr. and Emtage, P.R. (1968). Current-voltage characteristics of semiconducting barium titanate ceramic. *Journal of Applied Physics* 39 (7): 3088–3094.

11

Tin Oxide Varistor Ceramics of High Thermal Conductivity

As a result of the multiphase structure of the ZnO varistor, its temperature stability and aging characteristics need further improvement. Therefore, besides working to improve the performance of the ZnO varistor material, other new materials are also searched in order to achieve better stability. In 1995 [1], S.A. Pianaro et al. found that SnO_2 varistor ceramics doped a small amount of additives exhibited good nonlinear properties. SnO_2 varistors are obtained by solid-state sintering. Different from the multiphase structure of the ZnO-based varistor, the SnO_2-based varistor has a simple microstructure and good stability. Dense SnO_2-based systems present values of nonlinear coefficient, breakdown voltage, and barrier voltage per grain equivalent to those of the traditionally commercial ZnO varistors [1–7], which means the SnO_2-based varistor has similar electrical properties of ZnO varistor, but better thermal conductivity, which is resulted from its simpler phase composition and lower dopant concentration, which makes the SnO_2-based varistor one of the most promising candidates to compete commercially with the ZnO-based varistor. In this chapter, the electrical performance and mechanisms, thermal property, degradation behavior, and role of dopants for SnO_2-based varistors will be introduced.

11.1 Preparation of SnO_2-Based Varistors

Different from ZnO-based varistors with a multiphase structure, tin dioxide (SnO_2) is a kind of n-type semiconductor with a tetragonal crystalline structure similar to the rutile structure [8], which has a simple microstructure and no phases other than the rutile SnO_2 are observed in its X-ray diffraction (XRD) pattern [9]. Rutile is the stable structure of SnO_2, as shown in Figure 11.1, which is a kind of tetragonal lattice with the shape of double cones, the lattice constants $a = b = 0.4737$ nm and $c = 0.3186$ nm, and Sn is located in the gap of oxygen octahedron.

Tin oxide does not densify when sintered without additives and has a loose structure, so the SnO_2 ceramic has been used as a gas-sensitive material. In order to obtain nonlinear electrical performance, dense SnO_2 ceramics were obtained by the introduction of densifying agents [10–13], or by the hot isostatic

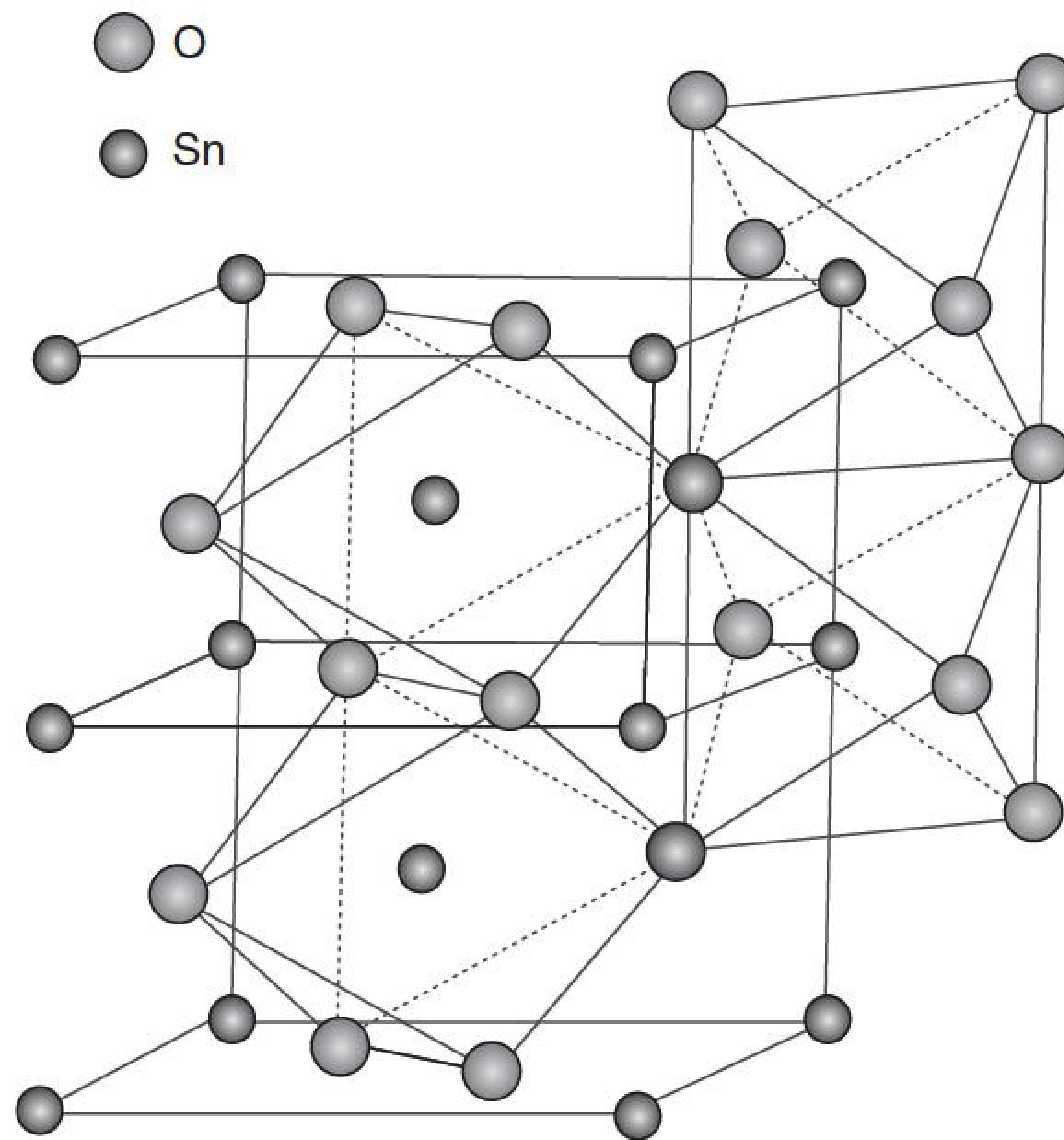


Figure 11.1 SnO_2 crystal structure diagram.

pressing [14, 15]. Tin dioxide does not densify during sintering because of the high vapor pressure of this oxide at higher temperatures, according to the following reaction:



$$SnO_2 \leftrightarrow SnO(g) + \frac{1}{2}O_2(g) \tag{11.1}$$

Thus, the evaporation–condensation mechanism controls the sintering process of this oxide [10]. The addition of CoO to SnO_2 produces high densification but still does not generate nonlinear electrical characteristics. Only when codoped with an acceptor (such as CoO and MnO_2) and a donor (such as N_2O_5 and Ta_2O_5), it can display highly nonohmic current–voltage characteristics.

By the hot isostatic pressing method, Park et al. obtained the SnO_2 ceramic, which is 97% of its theoretical density [16]. Varela and coworkers found that doping 2 mol% CuO could improve the density of SnO_2-based varistors obviously [10], and Zuca et al. reported that doping 2 mol% Sb_2O_3 and 1 mol% CuO increased the density of the SnO_2 ceramic to 94% of its theoretical one [17]. Although dense SnO_2 ceramics have been obtained through various methods very early, until 1995, Pianaro et al. firstly found a SnO_2 ceramic with a good density and nonlinear property by doping CoO and Nb_2O_5 [1]. Later, MgO_2 was also found to be an addition to make SnO_2 highly densified [18].

ZnO varistors have a complex microstructure consisting of several crystalline phases; the presence of these crystalline phases is easily verified by XRD patterns and scanning electronic microscopy (SEM). Unlike the ZnO–Bi_2O_3-based system, a secondary phase is not detectable by XRD in the $SnO_2 \cdot CoO$ ceramic. SEM analyses show that nonohmic SnO_2–CoO [1–5, 19–21] systems have a simpler homogeneous microstructure than that of ZnO varistors [22].

The preparation method of traditional electronic ceramics can be used to fabricate SnO_2-based varistors. SnO_2 powder is blended with additives and ball milled with ethanol, and the mixture is then dried out and pressed into green disks at a

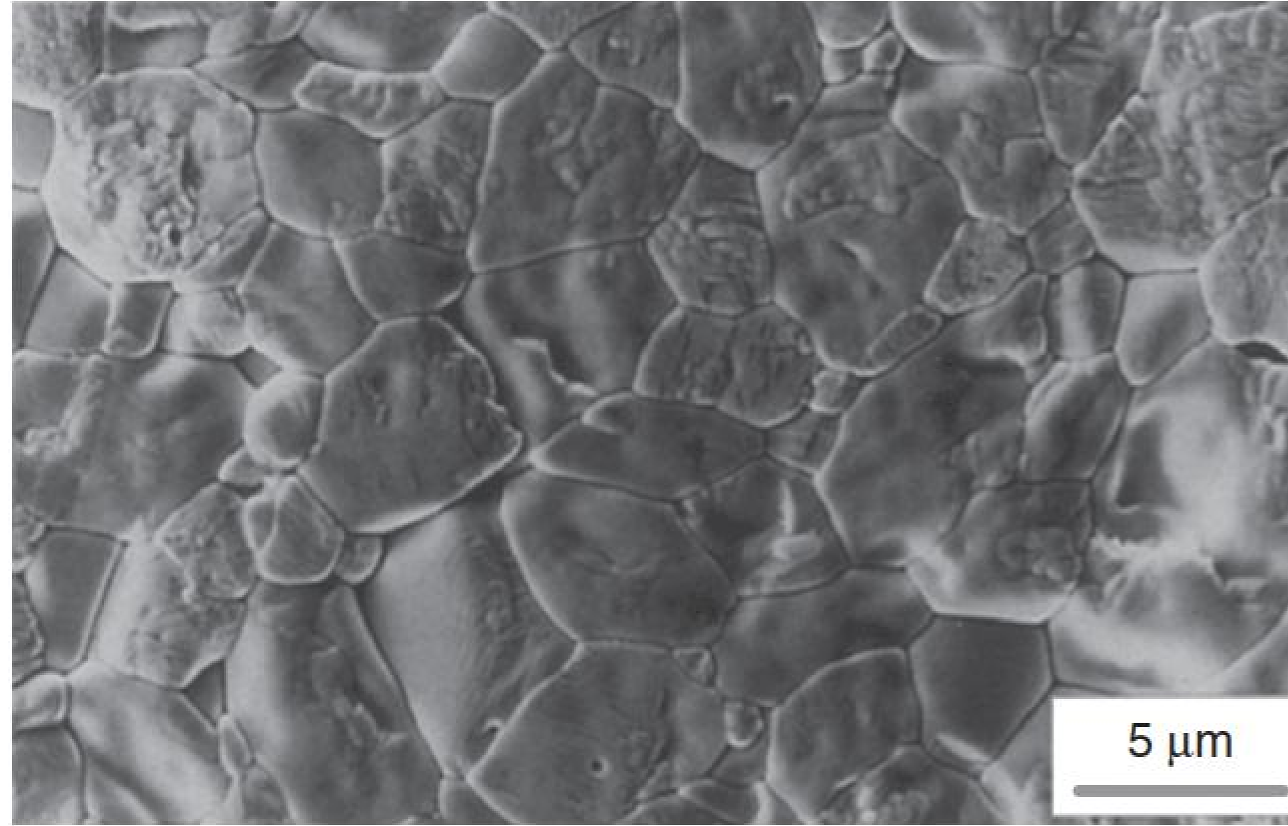


Figure 11.2 Characteristic microstructure of the system SnO_2–CoO–Nb_2O_5–Cr_2O_3. Source: Pianaro et al. 1995 [1]. Reproduced with permission of AIP.

pressure of about 160–210 MPa and subsequently sintered at 1300–1400 °C for one to two hours in air and slowly cooled down to room temperature [23]. This sintering temperature is higher than that of the ZnO-based varistor ceramics. 98.5% of theoretical density is reached for sintering at 1250 °C for one hour, and the general grain size is between 1 and 10 µm, as shown in Figure 11.2 [1].

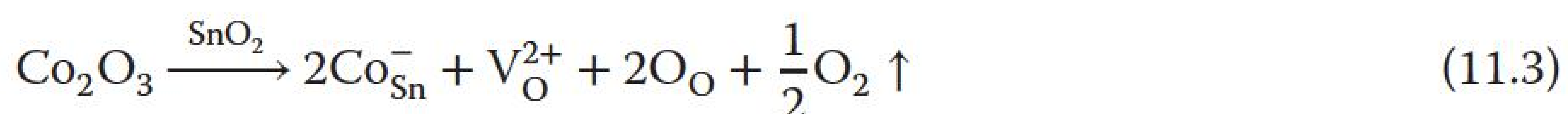
Contrary to ZnO varistors, these new ceramic materials are obtained by solid-state sintering. CoO in a SnO_2 matrix forms a solid solution by substituting Sn^{4+} ions for Co^{2+} or Co^{3+} ions [1, 18, 24, 25]. The amount of possible secondary phase precipitated at the grain boundary, if exists, is very small. Being this way, their electrical properties are closely related to dopant solid solution formation and/or solid-state precipitation of a new phase at the grain boundary. Then, the electrical barrier to electronic transport is created, which leads to a high nonlinear property [5].

Although most nonlinear electrical behaviors of SnO_2 ceramics have appeared in SnO_2–CoO-based systems [1–5, 19, 20, 22, 26], nonohmic properties have also been reported in other systems [27–29]. Wang et al. [28] demonstrated that ZnO can substitute CoO without significantly altering the nonlinear coefficient compared to the previous SnO_2–CoO-based system. Yongjun et al. [29] also obtained nonohmic properties in SnO_2–Bi_2O_3-based systems. Castro and Aldao [27] showed how dopants such as Co_3O_4, CuO, MnO_2, Bi_2O_3, and Sb_2O_3 influenced the dielectric properties, microstructure, and densification of SnO_2-based ceramics.

Doping small concentrations of Nb_2O_5 and Cr_2O_3 can highly improve the nonohmic V–I characteristics of dense SnO_2 ceramics doped with CoO [1, 4, 5, 19–21], with electrical characteristics similar to commercial metal–oxide varistors. As an example, the SnO_2 varistor samples were manufactured in the following proportions: 98.95 mol% SnO_2 (Merck), 1.00 mol% CoO (Riedel), 0.05 mol% Nb_2O_5 (Aldrich), and 0.05 mol%Cr_2O_3 (Vetec) [24]. During sintering, the CoO forms a solid solution in SnO_2:



$$\mathrm{CoO} \xrightarrow{\mathrm{SnO_2}} \mathrm{Co}_{\mathrm{Sn}}^{2-} + \mathrm{V}_{\mathrm{O}}^{2+} + \mathrm{O_O} \tag{11.2}$$



$$\mathrm{Co_2O_3} \xrightarrow{\mathrm{SnO_2}} 2\mathrm{Co}_{\mathrm{Sn}}^{-} + \mathrm{V}_{\mathrm{O}}^{2+} + 2\mathrm{O_O} + \frac{1}{2}\mathrm{O_2}\uparrow \tag{11.3}$$

The substitution of the Sn atom by Co leads to the formation of oxygen vacancies, which is responsible for the high densification of this system [10].

In contrast to the ZnO–Bi_2O_3-based varistor, SnO_2–CoO-based varistor systems present only one phase with X-ray and energy-dispersive spectrometer (EDS) stage precision, whereas a $CoSnO_4$-precipitated phase at the grain boundary is determined only when the EDS stage attached to the high-resolution transmission electron microscopy (HRTEM) and electron diffraction is used [23]. The absence of experimental evidence for an eutectic liquid suggests that the densification observed in this system is not associated with liquid-phase sintering and that the sintering of the SnO_2–CoO-based system is controlled by solid-state diffusion [18]. Other constituents of SnO_2-based varistors, such as Nb_2O_5 and Cr_2O_3, are present in small concentrations (~0.05 mol%); however, they are sufficient and necessary to render the behavior of this material highly nonlinear [1–7]. The ceramic microstructure is strongly dependent on the Cr_2O_3 concentration and the sintering temperature [5]. This oxide forms solid solution segregated at the grain boundaries and could react with CoO, also segregated at the grain boundary, precipitating as $CoCr_2O_4$ in the grain boundary and could control the sintering and grain growth rates. Thus, its excess in the chemical composition leads to the formation of a porous microstructure that is deleterious for varistor behaviors. Otherwise, small additions of this oxide create an extremely favorable microstructure for nonohmic conduction.

Because of the single-phase structure of the SnO_2-based varistor, there is no formation of deleterious phase for electrical properties, as is the case with the γ-Bi_2O_3 phase for ZnO varistors [30, 31]. Thus, the heating and cooling rates used for varistor formation are less critical during processing. This fact can be advantageous for the degradation phenomena of tin-dioxide-based varistors [24].

11.2 Electrical Performances of SnO_2-Based Varistors

The current–voltage characteristics of varistors are highly nonlinear like back-to-back avalanche diodes [6]. Pianaro et al. found that [1], by doping 0.05 mol% Nb_2O_5 into the SnO_2–CoO (1.0 mol%) system, the SnO_2-based varistor obtained the nonlinear coefficient α of 8 and the breakdown electrical field E_b of 187 V mm^{-1}. Then, adding trivalent metal oxides (e.g. 0.05 mol% Cr_2O_3) on this basis was able to further improve the nonlinear coefficient α to 41 and the breakdown electrical field to 400 V mm^{-1}, where the nonlinear coefficient α was obtained by linear regression of points in a logarithmic scale from 1 mA cm^{-2} and the breakdown electrical field was obtained at this current density. The E–J characteristics of different SnO_2 varistor systems are shown in Figure 11.3.

Brandkovic et al. reported that the SnO_2-based varistor (99.15% SnO_2 + 0.75% CoO + 0.05% Nb_2O_5 + 0.05% Cr_2O_3, all in mole) had the nonlinear coefficient α of 35 and leakage current of only 0.86 μA cm^{-2} [32]. Bueno et al. [33] studied the influence of different additives on the electrical performances of SnO_2-based varistors. The molar compositions of the system were

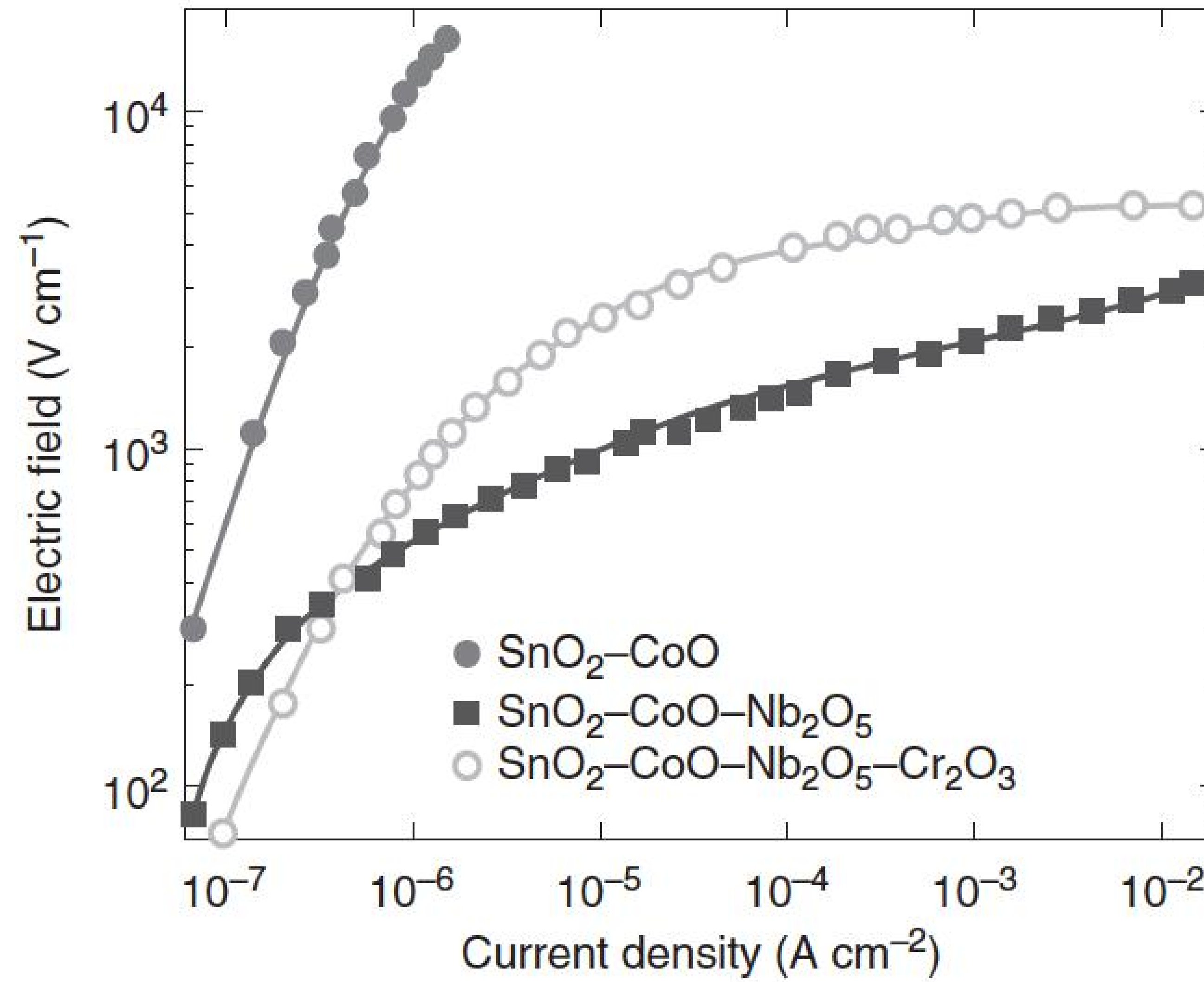


Figure 11.3 The nonlinear electrical field versus current density characteristics for different SnO_2 varistor systems. Adapted from Pianaro et al. [1]).

Table 11.1 Nonlinear coefficient α, breakdown electrical field E_b, barrier height ϕ_b, mean grain size d, and relative density ρ_r of the SCNCr–X varistor systems.

Systems	α	E_b (V mm^{-1})	ϕ_b (V/grain)	d (μm)	ρ_r (%)
SCNCr–CeO_2	55	554	2.0	3.6	94.1
SCNCr–Pr_2O_3	73	611	2.4	3.9	86.8
SCNCr–La_2O_3	142	1152	2.3	1.9	79.7

Source: Bueno et al. 2002 [33]. Reproduced with permission from AIP.

98.95% SnO_2 + 1.0% CoO + 0.035% Nb_2O_5 + 0.25% Cr_2O_3 + 0.25%x (SCNCr–X), where x is equal to 0.25% of La_2O_3, Pr_2O_3, or CeO_2. The highest α and E_b values were obtained in the SCNCr–La_2O_3 and SCNCr–Pr_2O_3 compositions, despite the higher porosity of these systems, as shown in Table 11.1 [33]. For the composition of 98.95% SnO_2 + 1.0% Co_2O_3 + 0.035% Nb_2O_5 + 0.25% Cr_2O_3 + 0.25% La_2O_3, the nonlinear coefficient α reached 142.

Ramírez et al. [34] showed that the SnO–CoO–Nb_2O_5–Cr_2O_3 system (named as SCNCr) has the higher nonlinear coefficient α in the whole range of measured current, and the breakdown electrical field (E_b) was twice as high for the SCNCr system (540 V mm^{-1}) as that for the ZnO varistor (270 V mm^{-1}) because of a smaller average grain size of the former (4.5 μm) with respect to the latter (8.5 μm). Despite the higher sintering temperature, the breakdown electrical field of SnO_2-based varistors is two to three times that of ZnO-based varistors, generally about 500 V mm^{-1} or more. As shown in Figures 11.4 and 11.5 [34], the linear ohmic region (Region I) of both systems are similar; the leakage currents measured at 0.80 E_b are similar for both systems, too. The high-breakdown electrical field of SnO_2-based varistors is associated with the combined effect of grain size and the number of electrically active interfaces in the thickness of the varistor. The SnO_2-based varistors reach the saturation current in a short time because of

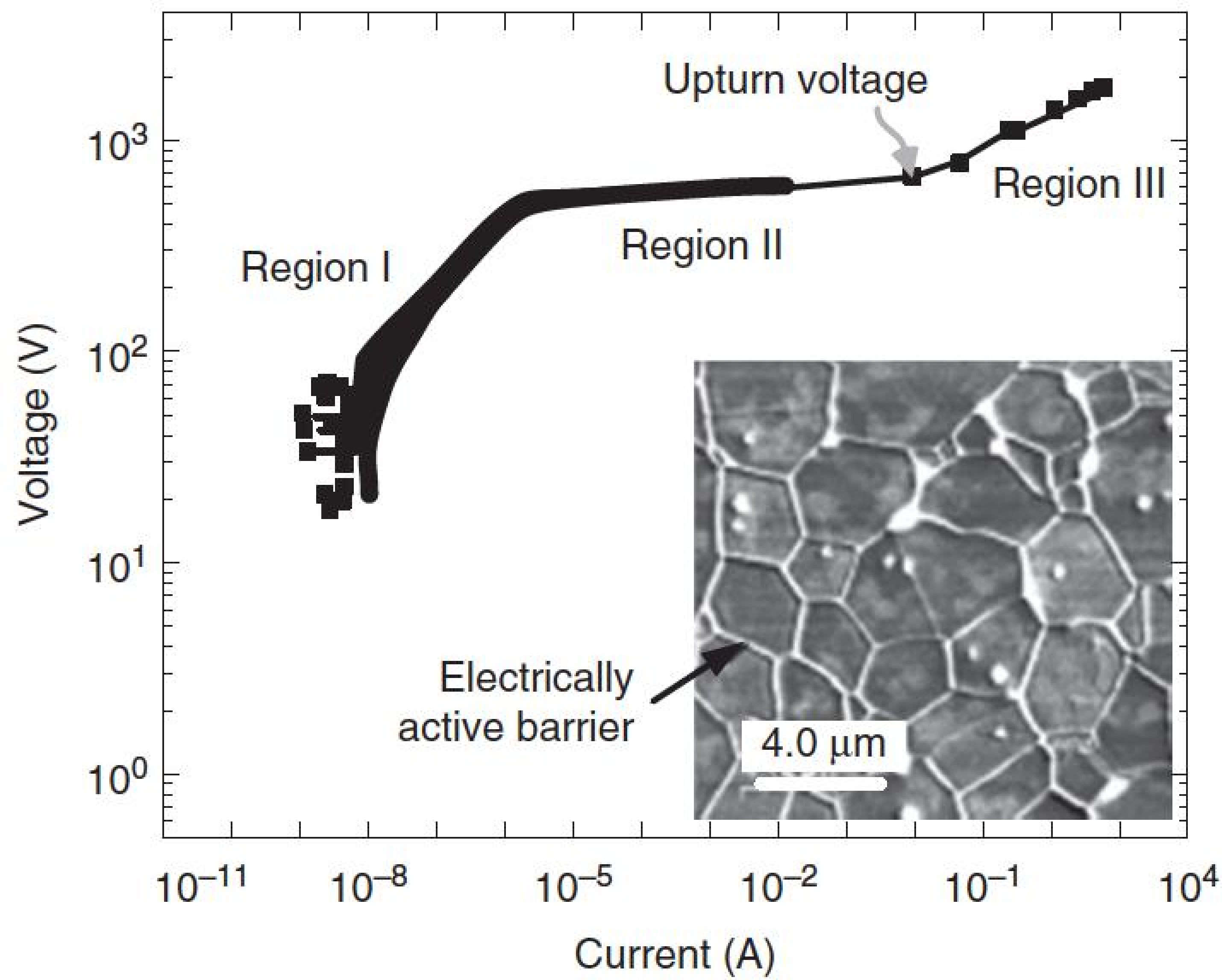


Figure 11.4 *I–V* characteristics for the SCNCr system. Electrostatic force microscopy image registered with $\Delta V = 2$ V applied between the tip and the sample (inset). Source: Ramírez et al. 2008 [34]). Redrawn with permission from John Wiley & Sons.

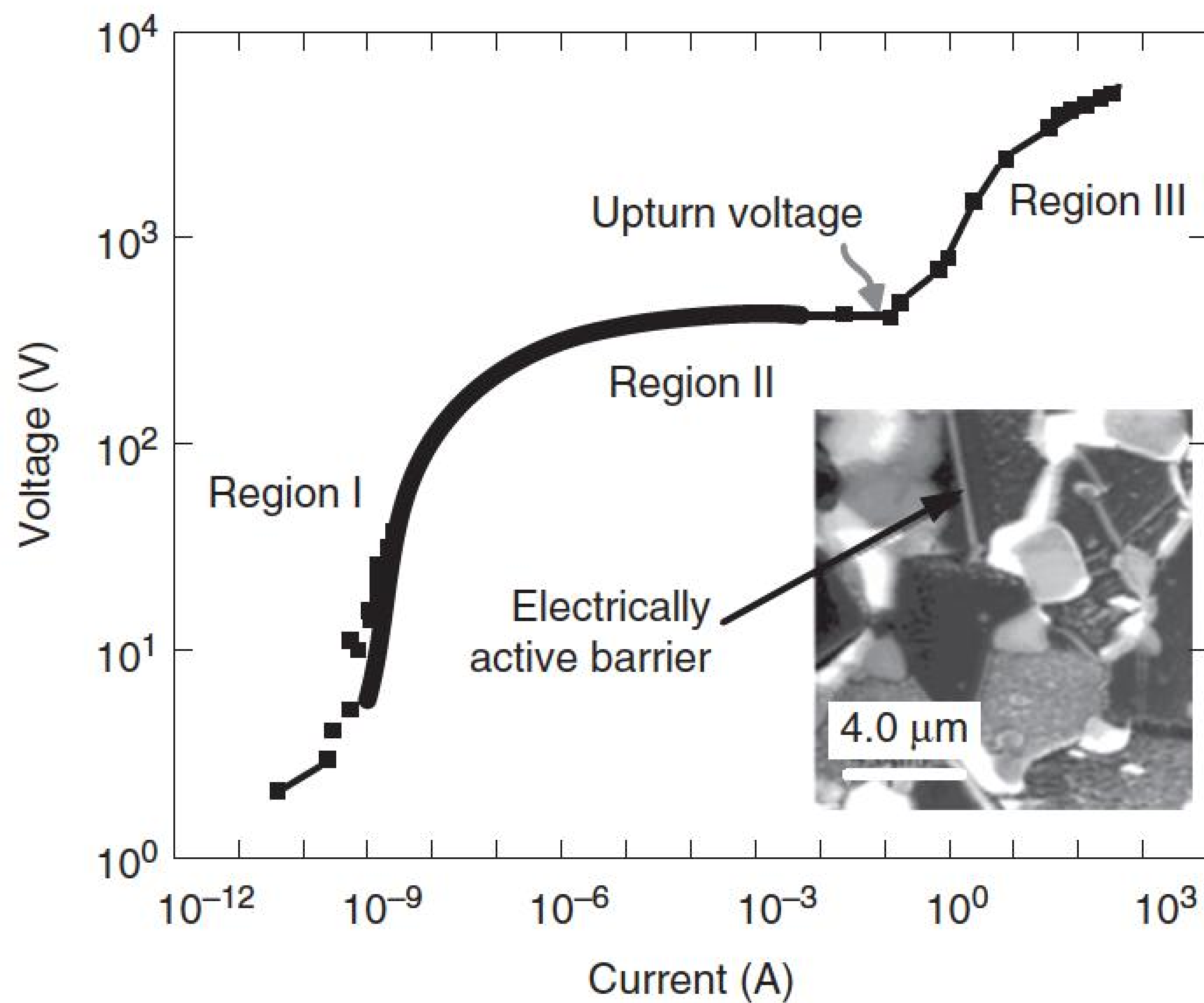


Figure 11.5 *I–V* characteristics for the ZnO system. Electrostatic force microscopy image registered with $\Delta V = 2$ V applied between the tip and the sample (inset). Source: Ramírez et al. 2008 [34]). Redrawn with permission from John Wiley & Sons.

the high resistivity of the SnO_2 grains, which is five times higher than that of the grains in ZnO-based varistors.

The electrically active interfaces were determined with the assistance of electrostatic force microscopy (EFM) [34], as shown in the insets of Figures 11.4 and 11.5 for the SCNCr and ZnO varistor systems. The accumulation of charges

Table 11.2 Comparison of parameters nonlinear coefficient α, breakdown electrical voltage E_b, barrier height ϕ_b, mean grain size d, and relative density ρ_r between commercial ZnO- and sample SnO_2-based varistor systems doped with Nb_2O_5 and Cr_2O_3.

Systems	α	E_b (V mm^{-1})	ϕ_b (V/grain)	d (μm)	ρ_r (%)
SnO_2 sample	42	676	1.62	2.4	~97
ZnO-C1	56	278	1.58	5.7	~99
ZnO-C2	48	207	1.53	7.4	~96

Source: Bueno et al. 2005 [35]. Reproduced with permission from John Wiley & Sons.

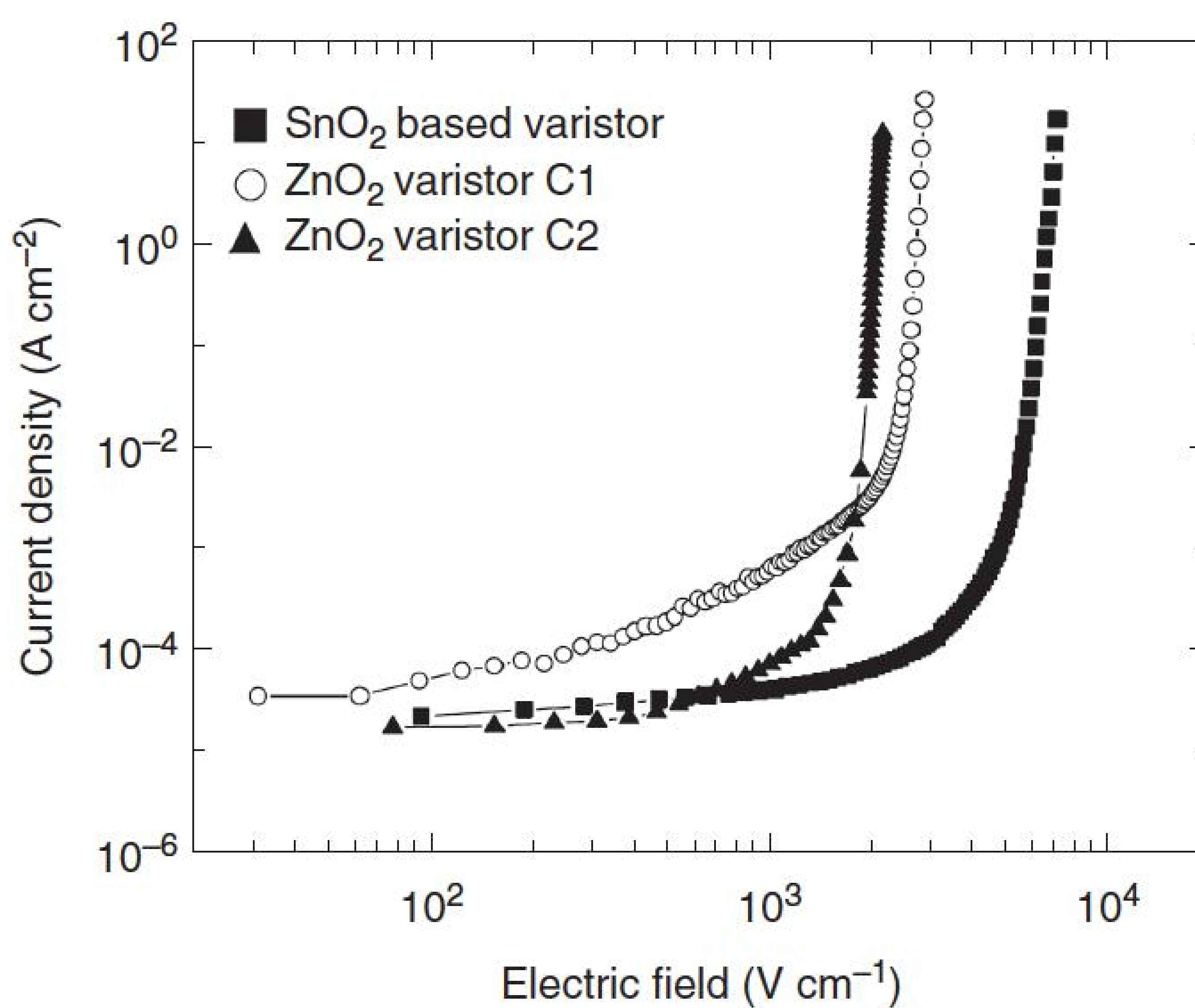


Figure 11.6 Comparison between the nonlinear electrical field versus current density characteristics of ZnO varistor systems and SO_2 varistor system (ZnO-C1 and ZnO-C2 are ZnO varistor systems). Source: Bueno et al. 2005 [35]. Reproduced with permission of John Wiley & Sons.

(bright zones) observed in certain regions of the grain boundary indicates the presence of electrically active potential barriers. It was estimated that 85% of the barriers in SCNCr were active, whereas only 35% were active in the ZnO-based system. Meanwhile, SnO_2 varistors with single microstructure have a larger flow area on a given area theoretically, compared to ZnO-based varistors, which is also one of the reasons for its higher threshold electrical field.

Bueno et al. [35] also compared the electrical properties of ZnO-based and SnO_2-based varistors. The electrical properties of the SnO_2-based varistor system are equivalent to that found in the commercial ZnO-based varistor, as shown in Table 11.2 and Figure 11.6.

Table 11.3 summarized the electrical parameters of different SnO_2-based varistors reported in the literature. The highest nonlinear coefficient reaches 142 [33], and the highest breakdown electrical field reaches 1820 V mm^{-1} [37].

Table 11.3 Comparison of electrical parameters of SnO_2-based varistors reported in the literature.

Varistor system	Nonlinear coefficient	Electrical field at current density 1 mA cm^{-2} (V mm^{-1})	References
SnO_2–Co_3O_4–Nb_2O_5–Cr_2O_3	41	399	[5]
SnO_2–Co_3O_4–Nb_2O_5–Cr_2O_3–La_2O_3	142	1152	[33]
SnO_2–Bi_2O_3–Co_3O_4–BaO–Nb_2O_5	20	350	[36]
SnO_2–CoO–Al_2O_3–Nb_2O_5	72	1820	[37]
SnO_2–Bi_2O_3–Co_3O_4–Nb_2O_5–Cr_2O_3	53	340	[38]
SnO_2–Bi_2O_3–Co_3O_4–Nb_2O_5–Cr_2O_3–B_2O_3	80	500	[39]
SnO_2–CoO–Nb_2O_5–Cr_2O_3–Y_2O_3	60	363	[40]
SnO_2–CoO–Nb_2O_5–Cr_2O_3–Ho_2O_3	55	385	[40]

11.3 Mechanism of SnO_2-Based Varistors

11.3.1 Formation of Grain Boundary Potential Barrier

The nature of nonlinearity in SnO_2-based varistor systems could be the same as that observed in ZnO-based varistors, and is related to a Schottky-type barrier at the grain boundary [6, 7, 41]. According to the barrier formation model for metal oxide varistor systems, the physical origin of interface states is not an intrinsic one caused by the lattice mismatch at the boundary, but an extrinsic one resulting from metal atoms segregated at the grain boundaries [33]. These metal atoms, being mainly transition metal oxides, generally have several oxidation states, which facilitate the chemisorption of oxygen on the grain surfaces. This mechanism enables electrons to become localized at the surface, giving rise to a negative surface (negative interface states). To maintain local electrical neutrality, the charges are compensated by the space charge formed in the depletion region adjacent to the grain boundary. As a result, electron depletion layers are formed and act as potential barriers. Therefore, because the grain boundary region of nonohmic ceramics is richer in oxygen than the bulk [7], the trap state at the interface responsible for barrier formation is related to the negative charge trapped by oxygen species, whose degree of coordination differs from that of the bulk oxygen. Hence, this oxygen in the grain boundary region can generate an interface trap state. The interface states must, therefore, be formed by electrons trapped in oxygen in the grain boundary region and by ionized shallow donors plus deep traps in the depletion layer [7]. One of the possible intrinsic ionized shallow donors is an ionized oxygen vacancy. Thus, it can be inferred that shallow and deep donor levels in the depletion layer balance the electrons trapped by oxygen in the grain boundary region. However, the distribution of electronic states in this region depends on the nature of segregated transition metals [33].

Oxygen vacancies and electronic states on SnO_2 grain surfaces play a key role in the formation of potential barriers and determine the nonlinear V–I

characteristics of SnO_2-based varistor. Charge carriers trapped at these thin interface boundaries are balanced by space charge regions in the adjacent zone of the grains. Varistors can be designed by doping an n-type polycrystalline semiconductor with an appropriate amount of p-type semiconductor, as the latter will probably segregate in the grain boundary region, acting as an acceptor, forming oxygen vacancies and electronic states, trapping electrons in this region, and thus forming the potential barrier. Two kinds of electron traps are of special importance: traps situated in the boundaries between SnO_2–SnO_2 grains (interfacial traps) and those that arise from donor-like traps within the bulk of the grain (bulk traps). The presence of a grain boundary interface establishes a potential barrier and consequently a band bending. As the depletion zone is approached, trapping levels cross the Fermi level, causing the state of occupancy of depletion layer to change. These electronic transitions may be externally modulated by applying DC voltage. Therefore, as in other semiconductor junctions, bulk traps respond to an external electrical stimulus within the depletion region of SnO_2 grains [41].

The varistor behavior of SnO_2 can be explained by the introduction of defects in the crystal lattice that are responsible for the formation of Schottky-type potential barriers at the grain boundaries. By analogy to the atomic defect model proposed by Gupta for the ZnO varistor [42], the potential barrier is formed by intrinsic defects of SnO_2 (oxygen vacancy and interstitials ionized tin atom), extrinsic defects created by solid substitution of dopants, and negative charges at the interface corresponding to vacancies of tin atom. These defects create depletion layers at the grain boundaries, leading to the formation of a potential barrier for the electronic transport. This transport occurs by tunneling and is responsible for the nonlinear property of current density versus applied electrical field [43].

11.3.2 Atomic Defect Model

An atomic defect model for the SnO_2-based varistor system was proposed by considering the grain boundary concentration of negative charge defects (O^- and O^{2-}) stabilized by positive charge defects (Nb_{Sn}^+, V_O^{2+}, V_O^+). The role of Cr_{Sn}^- is to create sites to promote the formation of O^- and O^{2-} defects, which are truly responsible for formatting the barrier at the grain boundary interface [20].

As shown in Figure 11.7 [44], the intrinsic SnO_2 defects V_{Sn}^{4-} and V_O^{2+} and extrinsic defects created by the dopants CoO and Nb_2O_5 should be responsible for the

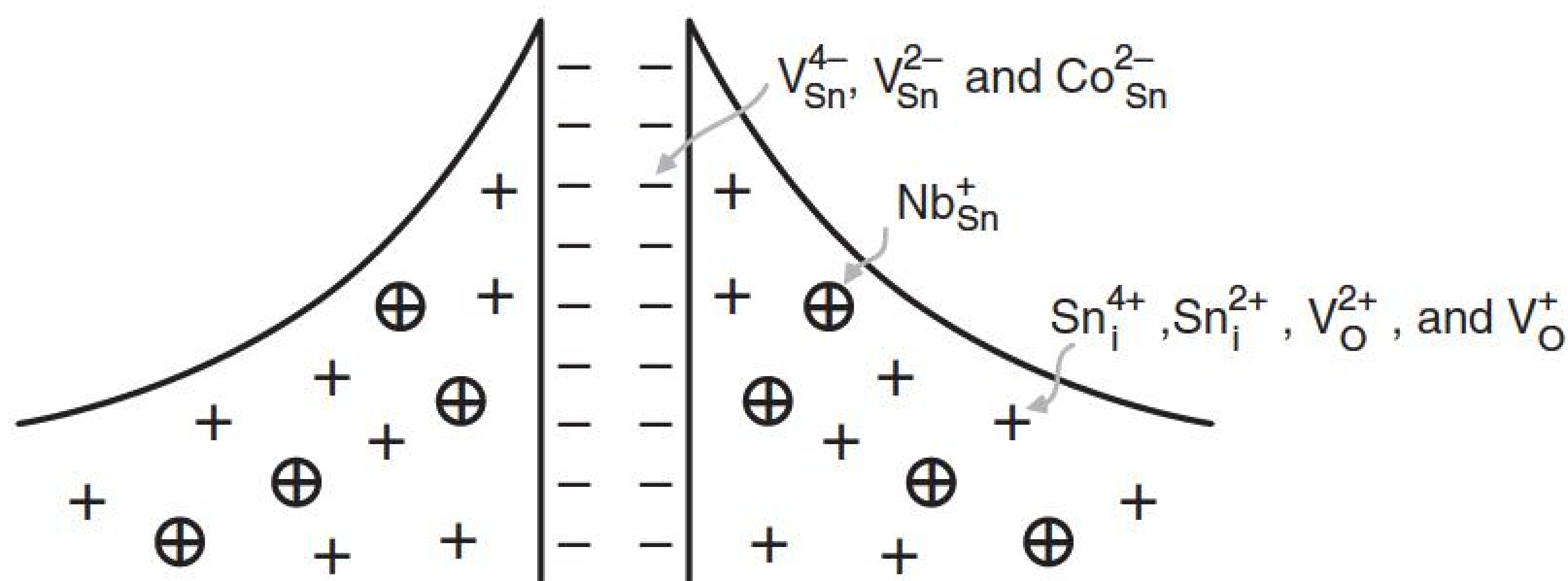


Figure 11.7 Atomic defect model to explain the barrier formation at the grain boundaries of SnO_2-based varistor systems. Source: Adapted from Antunes et al. [44].

formation of the grain boundary barrier. These dopants form a solid solution with SnO_2 at high temperatures and create defects. The positively charged donors V_O^{2+} and Nb_{Sn}^{+} extending from both sides of the grain boundary are compensated by the negative charged acceptors (V_{Sn}^{4-}, V_{Sn}^{2-}, Co_{Sn}^{2-}, Co_{Sn}^{-}) at the grain boundary interface. The oxygen can be adsorbed at the interface and react with the negative defects according to [44]:



$$O_2 \rightarrow O_{2(ad)}^{\times} \tag{11.4}$$



$$V_{Sn}^{4-} + 4O_{2(ad)}^{\times} \rightarrow 4O_{2(ad)}^{-} + V_{Sn}^{\times} \tag{11.5}$$



$$V_{Sn}^{4-} + 2O_{2(ad)}^{\times} \rightarrow 2O_{2(ad)}^{-} + V_{Sn}^{2-} \tag{11.6}$$



$$V_{Sn}^{2-} + 2O_{2(ad)}^{\times} \rightarrow 4O_{2(ad)}^{-} + V_{Sn}^{\times} \tag{11.7}$$



$$Co_{Sn}^{2-} + 2O_{2(ad)}^{\times} \rightarrow 2O_{2(ad)}^{-} + Co_{Sn}^{\times} \tag{11.8}$$

CoO is one of the components responsible for formatting the barrier in SnO_2-based varistors [7, 21, 26, 29]. The influence of cooling rates on the nonlinear electrical behavior is attributed to CoO oxidation during cooling (oxidation of Co atoms of the $SnO_2 \cdot CoO$-precipitated phase). Cobalt valence states change according to the reactions represented by [33]



$$2CoO + \frac{1}{2}O_2 \xrightarrow{600\ °C} Co_2O_3 \tag{11.9}$$



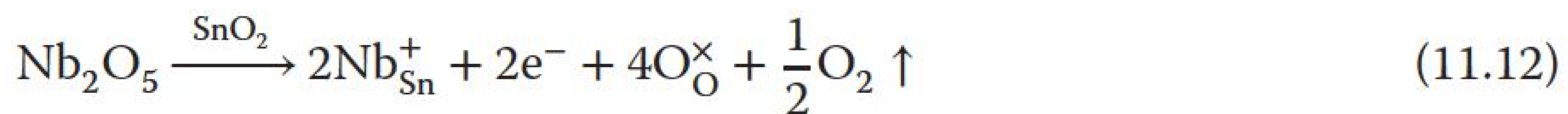
$$Co_2O_3 + CoO \xrightarrow{800\ °C} Co_3O_4 \tag{11.10}$$



$$Co_3O_4 \xrightarrow{1000\ °C} 3CoO + \frac{1}{2}O_2 \uparrow \tag{11.11}$$

Cobalt atoms can, thus, affect the trapping state at the grain boundary and modify the potential barrier, depending on the cooling rate and the atmosphere employed during the sintering process of the material [2, 7, 26, 33]. Therefore, the amounts of cobalt atoms segregated or else precipitated in the grain boundary depend on the cooling rate. This segregate or else the precipitate can become richer in oxygen through oxidation of the Co atom (e.g. CoO to Co_2O_3) below 1000 °C, thereby affecting the trapping state at the interface of the grain boundary region and, hence, the nonlinear electrical behavior of SnO_2-based varistors.

The addition of Nb_2O_5 to the SnO_2 ceramics leads to an increase in the electronic conductivity at the SnO_2 lattice because of the substitution of Sn^{+4} by Nb^{+5} as the radius of Nb^{5+} (0.070 nm) is very close to that of Sn^{4+} (0.071 nm), according to the following reactions [33]:



$$Nb_2O_5 \xrightarrow{SnO_2} 2Nb_{Sn}^{+} + 2e^{-} + 4O_O^{\times} + \frac{1}{2}O_2 \uparrow \tag{11.12}$$

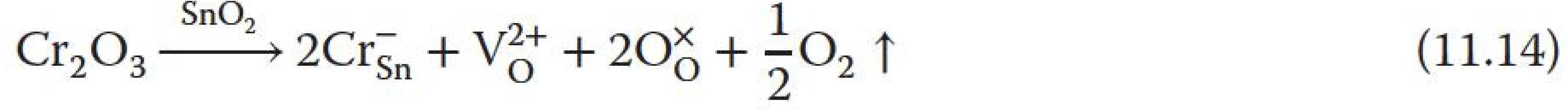


$$2Nb_2O_5 \xrightarrow{SnO_2} 4Nb_{Sn}^{+} + V_{Sn}^{4-} + 5O_2 \uparrow \tag{11.13}$$

In order to reduce the residual voltage ratio, we could extend and flatter the nonlinear zone in the I–V curve. It means that more electron carriers are

required to participate conducting. Doping Nb^{5+} produces a large number of free electrons that can greatly enhance the grain conductivity [45].

Otherwise, the introduction of Cr_2O_3 to the SnO_2 lattice leads to the substitution of Sn^{+4} by Cr^{+3}, according to the following reaction [33]:



$$Cr_2O_3 \xrightarrow{SnO_2} 2Cr_{Sn}^{-} + V_O^{2+} + 2O_O^{\times} + \frac{1}{2}O_2 \uparrow \tag{11.14}$$

Moreover, doping SnO_2 with Cr_2O_3 leads to a more homogeneous microstructure.

As shown in Table 11.2, doping La_2O_3 and Pr_2O_3 can lead to a high nonlinear coefficient and a breakdown electrical field, which may result from the fact that La_2O_3 and Pr_2O_3 can segregate in the grain boundary, inducing electronic interface states that can trap charges at the SnO_2–SnO_2 interface. These trap states mainly consist of oxygen species [7, 26]. The higher breakdown electrical field is due to the smaller mean grain size observed in this composition. The role of each dopant is summarized by the solid-state reactions [33]:



$$La_2O_3 \xrightarrow{SnO_2} 2La_{Sn}^{-} + V_O^{2+} + 3O_O^{\times} \tag{11.15}$$



$$Pr_2O_3 \xrightarrow{SnO_2} 2Pr_{Sn}^{-} + V_O^{2+} + 3O_O^{\times} \tag{11.16}$$



$$CeO \xrightarrow{SnO_2} 2Ce_{Sn}^{\times} + 2O_O^{\times} \tag{11.17}$$



$$Ce_2O_3 \xrightarrow{SnO_2} 2Ce_{Sn}^{-} + V_O^{2+} + 3O_O^{\times} \tag{11.18}$$

As a dopant, CeO_2 does not strongly influence the electrical nonlinearity of the SnO_2–CoO–Nb_2O_5–Cr_2O_3 system [1], as in the case of La_2O_3 and Pr_2O_3, nor does it alter the system's porosity, as illustrated in Table 11.2. Instead, it is believed to form a solid-state solution with SnO_2 in the grain, with insufficient segregation at the grain boundary, which is contrary to what is probably occurring in the case of La_2O_3 and Pr_2O_3.

The precipitate can be viewed through HRTEM micrographs as depicted in Figure 11.8 for the SnO_2–MnO-based varistor [7]. The precipitate observed at the grain boundaries is rich in Mn and oxygen, presenting a thickness of about 5–7 nm. The mapping of the oxygen element by the EDS stage attached to SEM in Figure 11.9 shows that the grain boundary region is richer in oxygen than the grain is [7].

11.3.3 Admittance Spectroscopy Analysis

Figure 11.10 presents the imaginary part of the complex capacitance ($C''(\omega) = G(\omega)/\omega$, where G is the conductance) measured in the SCNCr–La_2O_3 system [33]. The high-frequency region of the spectrum indicates the presence of an electrode inductance response, whereas a DC conductivity component is visible in the low-frequency region. The DC conductivity component increases as the temperature increases. Clearly well-defined loss peaks are visible at intermediate frequencies and low temperatures (from 298 to 523 K), which are

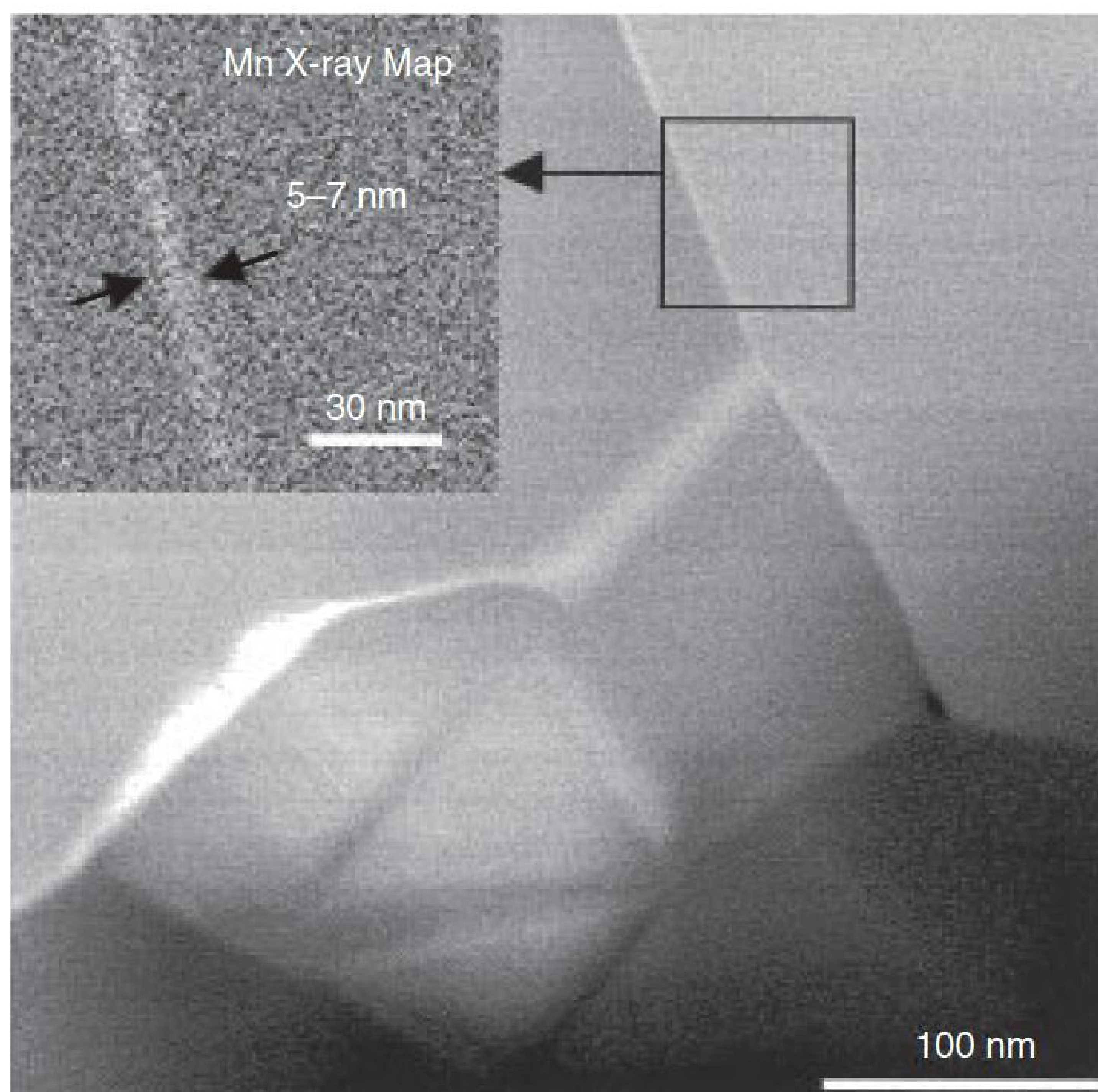


Figure 11.8 HRTEM micrographies showing the grain boundary of the SnO_2–MnO-based varistor system and a precipitate rich in Mn and O elements and about 5–7 nm of thickness. Source: Bueno et al. 2011 [7]. Reproduced with permission of AIP.

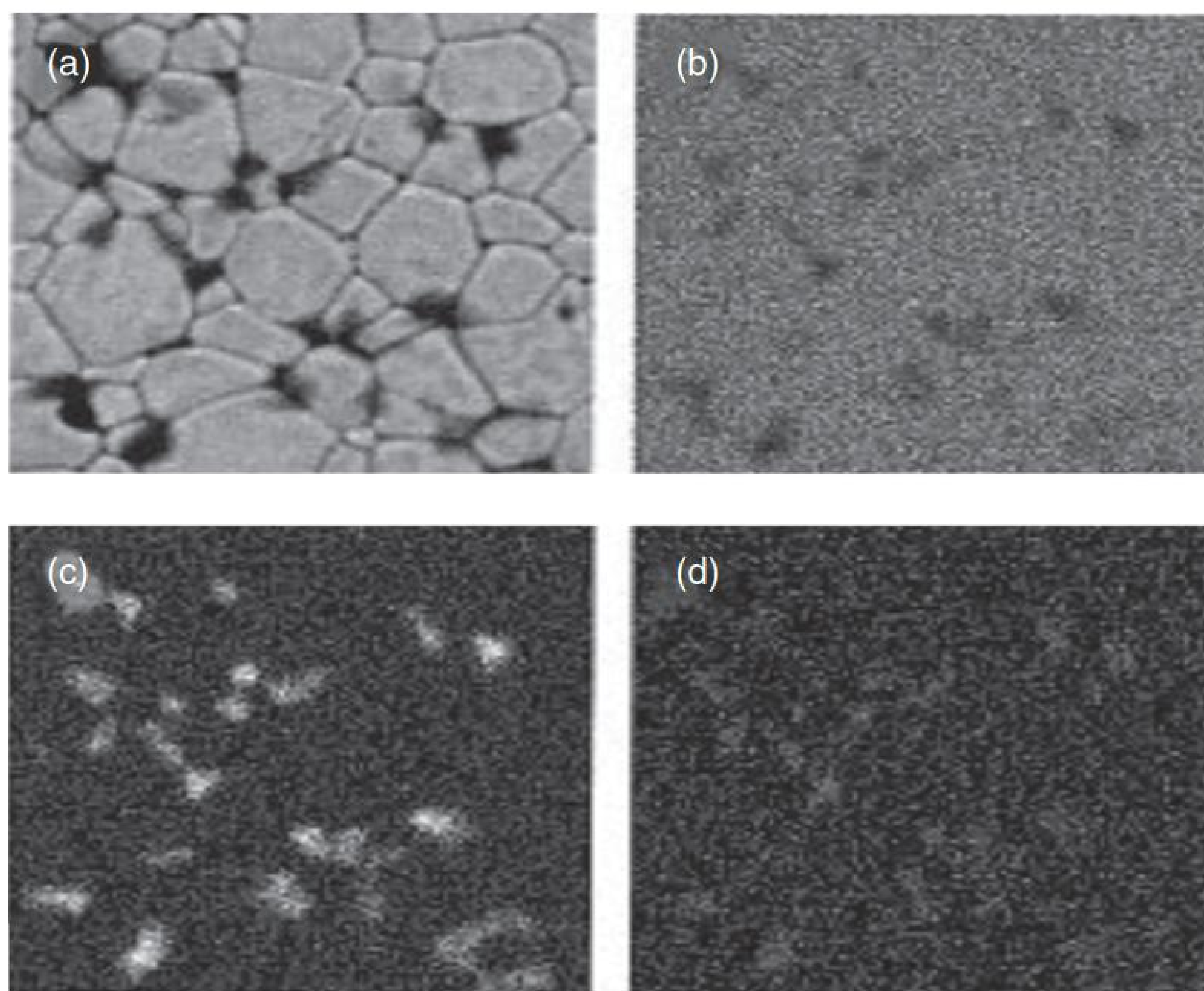


Figure 11.9 Mapping of Sn, Mn, and O elements of SnO_2–MnO-based varistor systems by the EDS stage attached to SEM. (a) A typical micrograph of the SnO_2–MnO-based varistor with partial precipitation of the Mn in the grain boundary region; (b) mapping of Sn, indicating that the precipitated region is poor in Sn but rich in (c) Mn and (d) oxygen. Source: Bueno et al. 2011 [7]. Reproduced with permission of AIP.

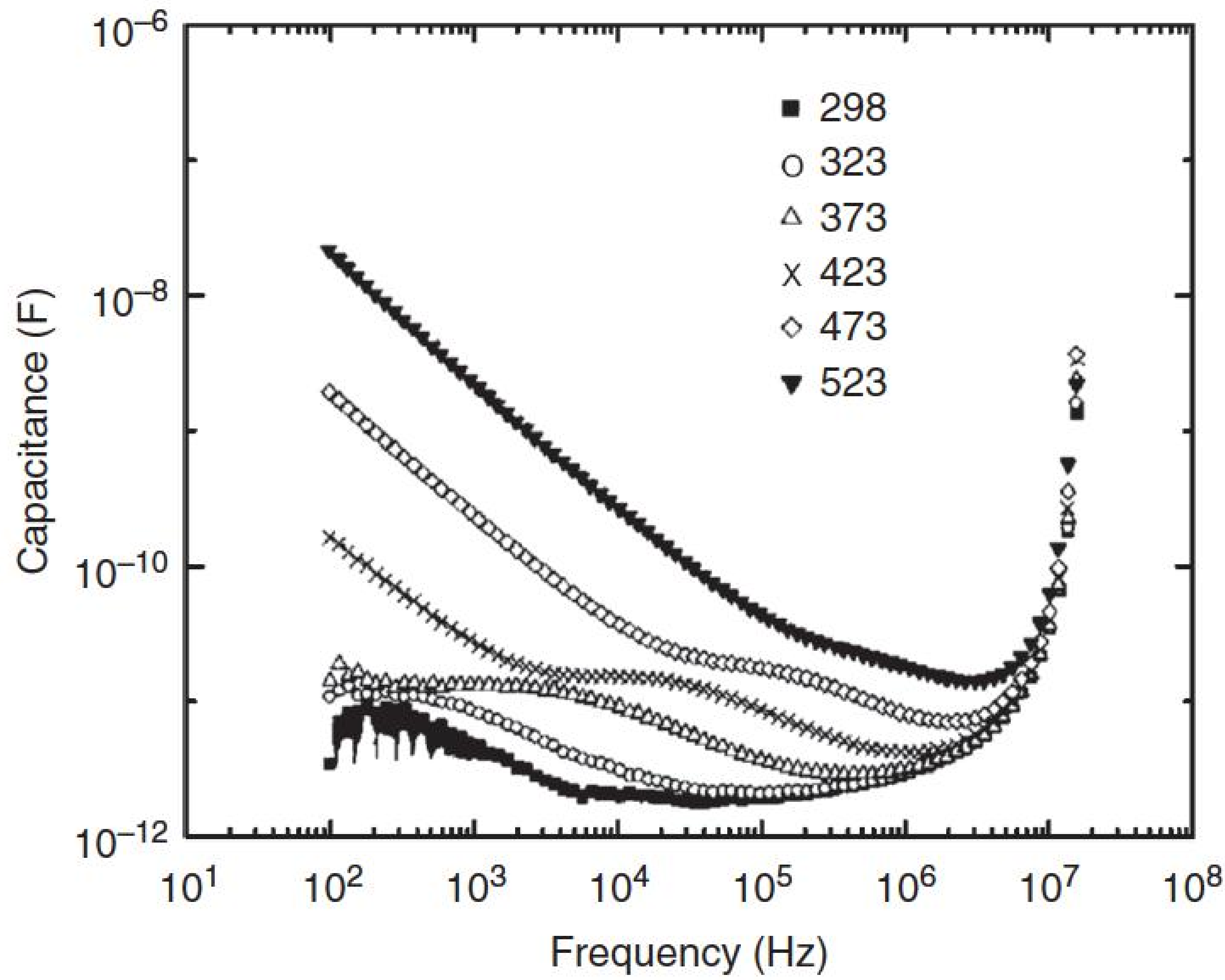


Figure 11.10 Capacitance $C''(\omega) = G(\omega)/\omega$ as a function of temperature for the SCNCr–La_2O_3 varistor system, showing a loss peak associated with the relaxation process of a deep trap state in the grain boundary region. Source: Bueno et al. 2002 [33]. Reproduced with permission of AIP.

attributed to deep levels (deep trap states) in the grain's bulk adjacent to the grain boundaries, and the loss peak of this relaxation process shifts toward higher frequencies as the temperature rises. These relaxation processes apparently follow the Cole–Cole dielectric model. The dielectric loss peak of SnO_2-based varistor appears to be even broader than that of the ZnO-based systems. The broader relaxation peak is assumed to indicate a high concentration of traps [46, 47], whose complex dynamics may be related to cooperative interactions among spatially distributed traps.

A small AC signal applied to the boundaries of the samples causes a relaxation process when the angular frequency of the AC signal becomes equal to the emission rate ω_p of the electrons in a trapping state, as shown in Figure 11.10. The general theory of semiconductor junctions, which yields Debye-like responses, ensures displacements of the loss peak ($C''(\omega)$ spectra) as the temperature increases. The e_n (which is equivalent to τ^{-1}, the time dependence of electron transition) depends on the temperature, according to the relationship [33]

$$e_n = \omega_p = \tau^{-1} = \sigma_n v_{th} N_d \exp[(E_c - E_t)/kT] \tag{11.19}$$

where ω_p is equivalent to e_n, σ_n is the capture cross section of the trap state, v_{th} is the free-electron thermal velocity, N_d represents the donor concentration as previously defined, and E_c–E_t is the energy difference between the conduction band and the trapping level. The values of E_c–E_t obtained for each sample are given in Table 11.4, which are the same for all samples and are relatively close to those obtained with the traditional ZnO-based varistor systems [33].

The fact that the energies of trap states in the bulk depletion layer remain unchanged with the composition of the samples may indicate that this trap state is formed by an intrinsic defect in the SnO_2-based varistor [33]. Natural SnO_2

Table 11.4 Values of barrier height ϕ_b, donor concentration N_d, interface-state density N_i, and barrier width δ for a Schottky-type potential barrier of SCNCr–X varistor systems.

Systems	ϕ_b (eV)	N_d ($\times 10^{23}$ m^{-3})	N_i ($\times 10^{16}$ m^{-2})	δ (nm)	$E_c - E_t$ (eV)
SCNCr–CeO_2	1.10 ± 0.05	7.79	3.64	23.4	0.43 ± 0.02
SCNCr–Pr_2O_3	1.99 ± 0.04	5.76	4.21	36.5	0.41 ± 0.03
SCNCr–La_2O_3	2.48 ± 0.06	443	41.2	4.65	0.41 ± 0.02

Source: Bueno et al. 2002 [33]. Reproduced with permission from AIP.

cassiterite or synthetic crystals are both oxygen deficient (n-type semiconductor), leading to the formation of a shallow donor level approximately 0.1 eV below the bottom of the conduction band. This shallow donor level is ascribed to the first ionization energy of ionized oxygen vacancy V_O^{2+} [48].

Therefore, it could be argued that the 0.41 eV energy observed in all the SnO_2 samples is not a shallow but a deep trap level associated with the second ionization energy of oxygen vacancies V_O^{2+} (intrinsic defect), or even to the Co_{Sn}^-, which is also common to all the compositions (an extrinsic defect). Thus, the defect that gives rise to this deep trap level can be either native to SnO_2 or involve extrinsic impurities [33].

Some impurities, such as Co, do not segregate or else precipitate to any great extent to form a large second phase in SnO_2; therefore, a great amount of Co^{3+} and Co^{2+} remains in the SnO_2 lattices probably forming only very shallow single donor-like levels. Thus, from the above-described potential barrier formation mechanism, it can be inferred that the defect generating these trap states in the bulk depletion layer is linked to the one that is present in all the compositions and is possibly related to an intrinsic defect, such as a V_O^{2+} oxygen vacancy. The first energy ionization of oxygen vacancies is shallow and is not visible at ambient temperature or above. Hence, as the second energy ionization of oxygen vacancies requires higher energy than the first one, it can only be observed in the depletion layer region [33].

In the simplest scenario, the role of transition metal segregated or else precipitated at the grain boundary is that of a "grain boundary activator," supplying excess oxygen to the grain boundary interfaces from the bulk [7], creating an interface rich in oxygen species and a deep trap level in the bulk depletion layer that is rich in oxygen vacancies. Therefore, it is believed that the traps at the interface of the grain boundary region that generate the potential barrier are formed by O^{2-} and V_O^{2+}, and trapped states in the grain bulk are also formed [33]. The thermodynamic equilibrium of solid-state defects at the grain boundary depends on the type and nature of the transition metals precipitated at the grain boundary and on how easily these metals oxidize [7].

11.3.4 Capacitance–Voltage Analysis

The Mott–Schottky plot (i.e. C_{BL}^{-2} versus DC-biased voltage V_{DC}, C_{BL} is the capacitance per unit area of a grain boundary) at room temperatures is shown

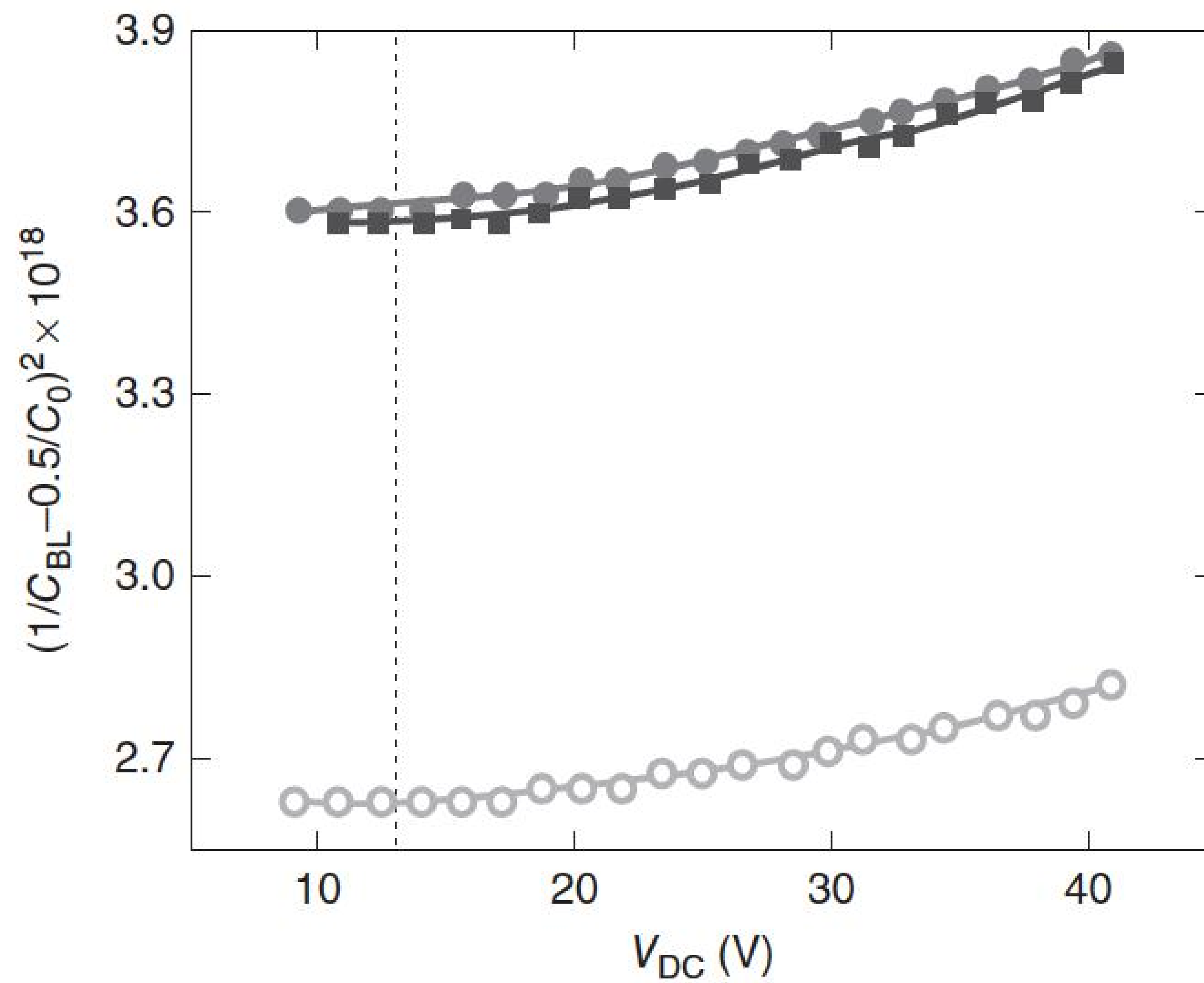


Figure 11.11 Mott–Schottky behavior without charge transport influence (true Mott–Schottky behavior) of the SCNbCr–X varistor system. (○) SCNCr–La_2O_3, (●) SCNCr–Pr_2O_3, (♦) SCNCr–CeO_2. Source: Bueno et al. 2002 [33]. Reproduced with permission of AIP.

in Figure 11.11 [33], and the value of this frequency-dependent capacitance, used in conjunction with the information on grain size, reflects the averaged Mott–Schottky response of any junction within the SnO_2-based varistor. Table 11.4 presents the ϕ_b, N_d, N_i, and barrier width δ values from this averaged Mott–Schottky response. It can be found that a composition with high ϕ_b value also has a high α value. It is found that an improved nonlinear electrical behavior in SnO_2-based varistor systems is obtained with a higher ϕ_b value, in combination with a lower δ value and higher N_d and N_i values. It should be noted that the δ value is related to the deep trap density of the grain boundary. In other words, the degree of nonlinearity in the nonlinear region of I–V curve depends significantly on the energy distribution of grain boundary states above the zero-bias Fermi level [33].

11.3.5 Effect of Thermal Treatment

Generally, the nonlinear electrical properties of varistors can be considerably improved by heat treatments in oxidizing atmospheres [2, 7, 21, 26, 33]. Experimental evidence reveals that the nonlinear coefficient α in SnO_2-based varistors is dependent on the thermal treatment under different atmospheres [26]; the values decrease when the varistors are thermally treated at 900 °C for one hour in a N_2-rich atmosphere. The same behavior is also reported in the SCNCr–La_2O_3 composition [33]. The energy of the deep trap states in the depletion layer, associated with oxygen vacancies, is not affected by the thermal treatment in different atmospheres, which indicates that the main defect of oxygen vacancies responsible for this deep trap state does not change in this region with such a thermal treatment.

In terms of the barrier formation mechanism [7], the transition metal segregated at the grain boundary becomes oxidized (Eqs. (11.9)–(11.11)) when the varistor is thermally treated in an O_2-rich atmosphere and that the interfacial region becomes rich in oxygen species that are trapped electrons (increasing the N_i). The oxygen, which produces oxidation of the segregates and maintains the electrostatic equilibrium of the interface, comes from the atmosphere and the bulk and increases donor concentration N_d when it originates from the bulk. Therefore, the density of trap states at the interface N_i should increase when the grain boundary interface of the material is oxidized, giving rise to higher ϕ_b. A thermal treatment in a N_2-rich atmosphere, on the other hand, should have the opposite effect to the one described above. This behavior appears to corroborate the proposed model for potential barrier formation illustrated in Figure 11.12 [33]. It can be concluded that the most significant electrical nonlinear features occur when the density of deep trap states in the bulk depletion layer (which is balanced by interface states) is high.

By analyzing admittance–frequency characteristics, Bueno et al. [33] proposed the presence of deep trap states at $E_c - 0.42(\pm 0.03)$ eV in SnO_2–CoO–Nb_2O_5–Cr_2O_3(SCNCr)-based varistor ceramics doped with La_2O_3, Pr_2O_3, or CeO_2. Orlandi et al. [49] subsequently used admittance and dielectric spectroscopy and obtained activation energies of about 0.49 eV for the higher frequency loss peaks and about 0.67 eV for the low-frequency dispersion in SnO_2–MnO–Nb_2O_5 (SMN)-based varistor ceramics. They noted that values obtained for the high-frequency process in SMN (~0.49 eV) are comparable with the values Bueno et al. [33] obtained for SCNCr-based ceramics (~0.42 eV) and postulated that both are associated with a deep trap in the potential barrier, namely, the second ionization energy of oxygen vacancies V_O^{2+} [33, 49].

Deep-level transient spectroscopy measurements were performed to investigate the effect of Nb_2O_5 and Cr_2O_3 on the electronic states of SnO_2-based

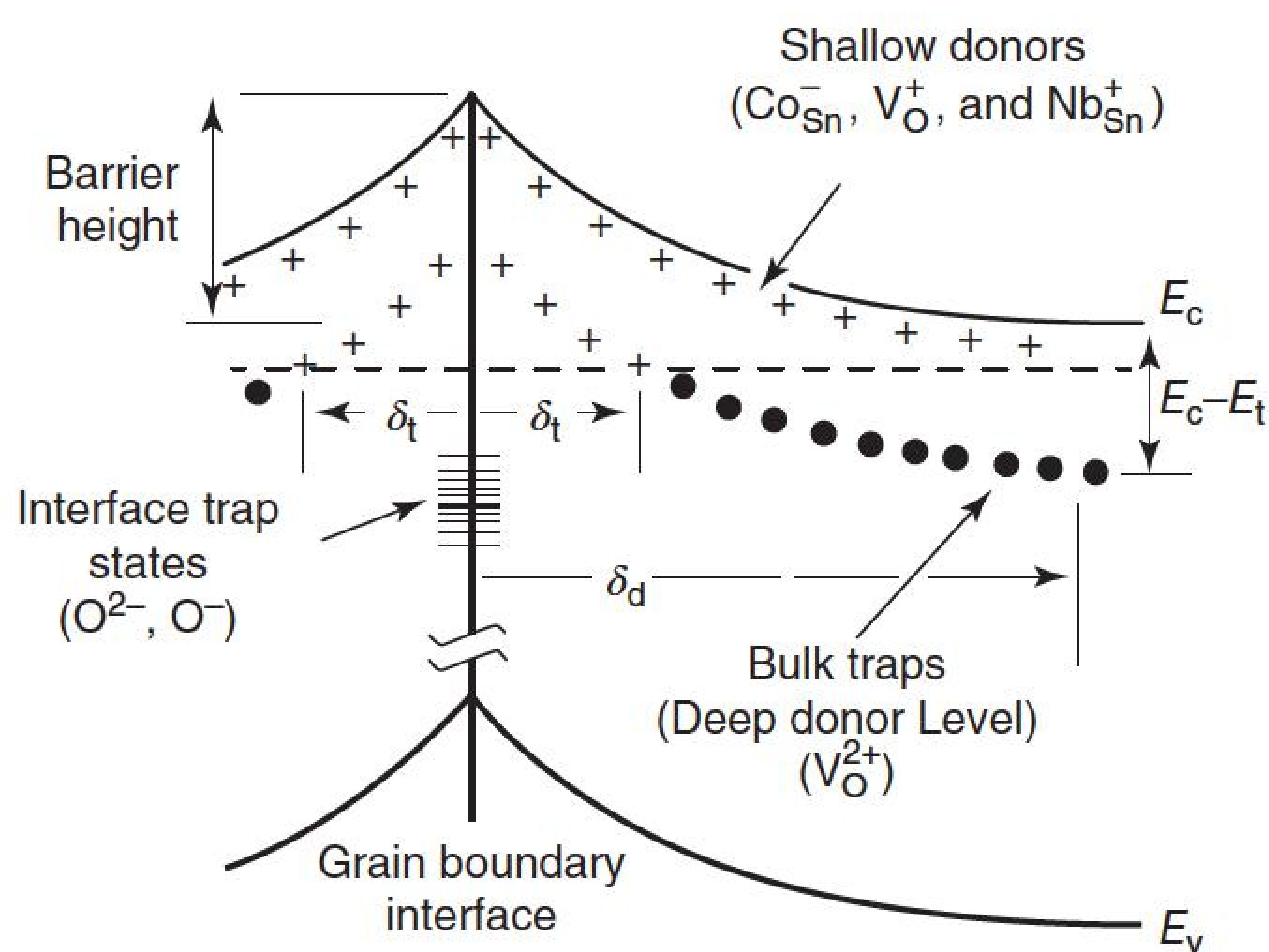


Figure 11.12 Electronic and atomic defect model proposed for the potential barrier formation in metal–oxide varistors. The SnO_2-based varistor system. Source: Bueno et al. 2002 [33]. Reproduced with permission of AIP.

varistors [33]. Two electron traps, $E_c - 0.30(\pm0.01)$ eV and $E_c - 0.69(\pm0.03)$ eV, were identified in both SnO_2–CoO–Nb_2O_5 and SnO_2–CoO–Nb_2O_5–Cr_2O_3 varistors. These two traps could be associated with the second ionization energy of oxygen vacancies V_O^{2+} or impurities on host lattice site Co_{Sn}^- or Nb_{Sn}^+. The two trap levels are not associated with chromium doping, as Cr_2O_3 doping only changes the donor concentration and trap densities.

11.4 Role of Dopants in Tuning SnO_2-Based Varistors

Commonly used dopants in the preparation of SnO_2 varistors are CoO, MnO_2, Cr_2O_3, and Nb_2O_5. CoO and MnO_2 are usually used to improve the densification of SnO_2 ceramics, and other dopants such as Cr_2O_3 and Nb_2O_5 are usually used to improve electrical properties [50–77]. Codoping Cr_2O_3, Ni_2O_3, and MnO is efficient to improve the nonlinear property and surge the current withstanding performance of the SnO_2-based varistors [54]. The role of dopants in the SnO_2-based varistors can be classified into three types: sintering-assistant dopants, acceptor-type dopants, and donor-type dopants.

11.4.1 Dopants for Densifying SnO_2-Based Varistors

The main role of CoO in the SnO_2-based varistor is to promote the sintering. At high temperature, SnO_2 will decompose and volatile easily, leading to porous internal structure and low density. The incorporation of 0.3 mol% Co_2O_3 is sufficient for getting compact SnO_2 varistors, with the relative density about 98% of the theoretical density (6.95 g cm^{-3}) [55]. Thermogravimetric analysis shows that Co_2O_3 will split into CoO and release oxygen at 950 °C:



$$Co_2O_2 \rightarrow 2CoO + \frac{1}{2}O_2 \quad (11.20)$$

As the radius of Co^{2+} (0.074 nm) is similar to that of Sn^{4+} (0.071 nm), Co^{2+} will substitute Sn^{4+} and enter the lattice. Oxygen vacancies resulted from the replacement would accelerate the diffusion and promote grain growth.



$$CoO \xrightarrow{SnO_2} Co_{Sn}^{2-} + V_O^{2+} + O_O^{\times} \quad (11.21)$$



$$Co_{Sn}^{2-} + O_2 \rightarrow Co_{Sn}^{\times} + 2O^- \quad (11.22)$$



$$2Co_{Sn}^{2-} + O_2 \rightarrow 2Co_{Sn}^{\times} + 2O^{2-} \quad (11.23)$$

The negatively charged oxygens produced in Eqs. (11.22) and (11.23) are absorbed mainly on the grain boundary and promote the formation of the barrier.

Fayat and Castro [51] concluded that cobalt, zinc, and manganese were stabilized as Co^{2+}, Zn^{2+}, and Mn^{2+} in SnO_2 varistors, increasing the oxygen vacancy concentration, which is responsible for the increase in the densification and grain growth increases as the sintering temperature increases [77]. Doping Co_3O_4 and MnO_2 increases the sintering rate of these ceramics by increasing the oxygen

vacancies and, as a consequence, the densification is larger. The addition of a higher concentration than 0.2% of Sb_2O_3 reduces the oxygen vacancy concentration and then the sintering rate decreases. The addition of 0.1% Sb_2O_3 does not affect the sintering because of the low antimony concentration, which is not enough to establish an adequate Sb^{5+}/Sb^{3+} ratio [27].

Doping SnO_2 with MnO or CoO leads to the creation of additional oxygen vacancies, which in turn increases the diffusion rate of oxygen ions and influences the sintering of SnO_2-based varistors [41]. However, the main microstructure of SnO_2–CoO-based ceramics is more homogeneous than SnO_2–MnO-based ceramics, in which the presence of precipitate phase, mainly at triple points of grain boundaries, is easily visible [41], and the formation of Mn_2SnO_4 and $MnSnO_3$ has been reported in the grain boundary region [18, 23]. When precipitates are present in higher concentrations at triple points, they can affect the nature of SnO_2–SnO_2 junctions, and hence, the number of active barriers [78]. Once these precipitates are present in triple junctions of the microstructure, they can cause adjacent SnO_2–SnO_2 junctions poor in segregated metal atoms because precipitates consume the segregated metal atoms in regions adjacent to them [41]. Such adjacent regions generate junctions with noneffective potential barriers.

CuO and Bi_2O_3 form a liquid phase during the sintering process, which increases the mass transport and then the sintering rate increases [27]. The addition of MnO_2, Co_3O_4, CuO, or $Co_3O_4 + 0.1\%$ Sb_2O_3, produces varistors with a low dissipation in the prebreakdown region. The introduction of Cu^{2+} or/and Cu^+ increases the sintering rate, which accelerates the small SnO_2 grains combining with each other to grow larger, advancing grain growth. However, because of the low melting point of this oxide, excess copper oxide will volatilize during the sintering process, which is the reason why the density does not significantly change with the increase in copper oxide [56]. It is assumed that at low CuO additions (0–0.5 mol%), the CuO-based liquid phase promotes the grain growth and facilitates the access of Co and Cr atoms to the majority of the grain boundaries. At high CuO additions (2–8 mol%), the solidified CuO-based phase with a low nonlinearity determines the electrical properties of ceramics [59].

11.4.2 Acceptor Doping

Doping materials with p-type semiconductor oxides increases the amount of oxygen species in the region of the grain boundary when compared to the bulk, which consists of a matrix with n-type features [41]. The p-type semiconductor oxides such as CoO [1, 3–5], MnO [27], Cr_2O_3 [1, 3–5], and Pr_2O_3 [21] are examples of some acceptors used to increase the amount of oxygen in the grain boundary. The mechanism of oxygen enrichment of the grain boundary is triggered by the optimization of nonohmic properties by a suitable excess of oxygen species and acceptor metal atoms precipitated or segregated at the grain boundary [6, 7, 26, 33, 41]. The presence of excess oxygen at the grain boundaries can be caused by the p-type semiconductor feature arising from the acceptor atoms of the p-type dopant semiconductor segregated metal and/or precipitated phases at the interface of the grain boundary.

Generally, the nonlinear electrical properties of varistors can be considerably improved by heat treatments in oxidizing atmospheres [2, 7, 8, 21, 26, 33]. Acceptor doping can significantly improve the nonlinear coefficient and threshold electrical field of SnO_2-based varistors, which are significant to the miniaturization of the device [9]. In addition, it has been confirmed that the grain size decreases as the doping increases, which is the reason for an improved threshold electrical field.

For example [9], when the experimental formula is $(99.15 - x)\%$ SnO_2 + 0.75% Co_2O_3 + 0.10% Nb_2O_5 + $x\%$ Gd_2O_3, the tested results show that the nonlinear coefficient is 13, 17, 23, 30, 23, and the breakdown electrical field is 325, 443, 739, 1201, 1560 $V\,mm^{-1}$, and grain size is 8.6, 7.9, 5.8, 3.2, 2.6 μm, respectively, for the content of Gd_2O_3 is 0, 0.2, 0.5, 1.5, and 2 mol%.

Obviously, doping causes grain size reduction and influences the grain boundary electrical properties. During the sintering process, Gd_2O_3 segregated on the grain boundary and reacted with SnO_2 or other doped oxides and the generated compounds $Gd_2Sn_2O_7$ hindered the grain growth, which leads to grain size decreases as the doping increases. This can be confirmed by grain boundary resistance. Typically, the grain boundary resistance of ceramic samples is expressed by the diameter of the complex impedance spectrum cole–cole circle [9]. As a high-frequency impedance analyzer cannot obtain a complete semicircle at room temperature, all the samples were measured at 300 °C. The decrease in grain size means the number of grain boundaries within the unit thickness increases, so the grain boundary resistivity will increase with the increase of doping, whereas the change in grain boundary resistance does not reflect the law. It is believed that, in addition to the number of grain boundaries in unit thickness, the segregation at the grain boundary, $Gd_2Sn_2O_7$, may also affect the grain boundary resistance. $Gd_2Sn_2O_7$ with pyrochlore structure behaves ion conduction property at high temperatures (200–600 °C). Therefore, at 300 °C, $Gd_2Sn_2O_7$ segregating on the grain boundary will promote the composite of the adsorbed negatively charged vacancies and oxygen vacancies, which greatly reduces the barrier height and increases the grain boundary conductivity. With the increase of doping, the variation of grain boundary resistance increases firstly and then decreases and is associated with a combined effect of grain size decrease and grain boundary conductivity increase caused by $Gd_2Sn_2O_7$.

With the increase of doped Gd_2O_3, the segregation of $Gd_2Sn_2O_7$ will correspondingly increase, leading to the decrease in grain size. Clearly, the grain size reduction will make the microstructure more uniform, and the more uniform the grains are, the higher the nonlinear coefficient will be. A large number of second phases segregated on the grain boundary eventually lead to the disappearance of nonlinear properties.

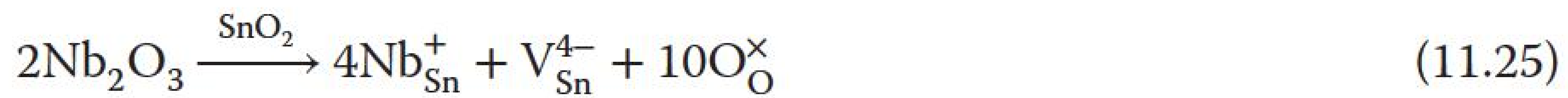
Ions distribute in different locations for their difference of the ion radius. As Co^{2+} (0.074 nm) is larger than Sn^{4+} (0.071 nm), the substitution of Sn^{4+} by Co^{2+} will lead to a significant lattice distortion. As a result, most of the Co^{2+} will stay in the grain boundary and only a spot of Co^{2+} will leak into the shallow SnO_2 lattice, substitute Sn^{4+} around the grain boundary, and form the depletion layer with donor [45]. Following the reaction (11.21), the production of oxygen vacancies would accelerate the diffusion and thus promote grain growth. A proper content

of Co_2O_3 (less than 0.8 mol%) is beneficial for the formation of a grain boundary barrier. $Co_{Sn}^{\times}$ is located at the depletion layers and is important for the formation of a grain boundary barrier [55].

In the case of Bi_2O_3-doped SnO_2 ceramics, a continuous bismuth-rich phase between the grains or precipitation of Bi_2O_3 phase at the multiple-grain junctions is not formed. The nonlinearity of the SnO_2-based ceramic increases with the addition of Bi_2O_3; this increase is very small compared with the SnO_2–CoO–Nb_2O_5 system. This increase in nonlinearity should be credited to the atomic defects created by Bi_2O_3 because of its substitution in the SnO_2 lattices [3].

The addition of Fe_2O_3 to SnO_2-based varistors decreases the mean grain size and leakage current as well as enhances the nonlinear property and increases the breakdown electrical field [44, 76]. The barrier height increases to 0.99 eV from 0.97 eV, when Fe_2O_3 is added into the SnO_2–CoO–Nb_2O_5 system. The nonlinear behavior of these ceramics can be explained by the formation of atomic defects in the depletion layer and at interface (V_{Sn}^{4-}, V_{Sn}^{2-}, Co_{Sn}^{2-}, Co_{Sn}^{-}, Fe_{Sn}^{-}) according to the following equations [44]:


$$Fe_2O_3 \xrightarrow{SnO_2} 2Fe_{Sn}^{-} + V_O^{2+} + 3O_O^{\times} \tag{11.24}$$


$$2Nb_2O_3 \xrightarrow{SnO_2} 4Nb_{Sn}^{+} + V_{Sn}^{4-} + 10O_O^{\times} \tag{11.25}$$


$$CoO_3 \xrightarrow{SnO_2} Co_{Sn}^{2-} + V_O^{2+} + O_O^{\times} \tag{11.26}$$

Moreover, the adsorbed oxygen at grain boundaries captures electrons from negatively charged defects at the grain boundary and is the major responsible for the negative charge density at the interface [44].

The effects of In_2O_3 on the properties of (Co, Nb)-doped SnO_2 varistors were investigated [57]. With the addition of In_2O_3, the average grain size decreases, the breakdown electrical field increases, and the relative electrical permittivity decreases. The reason why the permittivity decreases as In_2O_3 concentration increases is originated from the ratio of the grain size to the barrier width. The negatively charged acceptors substituting for Sn ions should not be located at the grain interfaces instead at the SnO_2 lattice sites of depletion layers.

Moreover, antimony oxide (Sb_2O_3) addition degrades the microstructure condition by inducing porosity. Subsequent addition of $CaCO_3$ promotes densification and grain growth. However, it does not lead to the increase in the nonlinear coefficient. It only lowers the electrical field, thus makes the material suitable for lower voltage applications. Observed significant increase in the relative dielectric permittivity up to a factor of about 60 and 200 in the cases of antimony or antimony and calcium addition to SnO_2–Co_3O_4 (accompanied by the appearance of varistor effect) is due to the formation of barrier depletion layers at the grain boundaries [5]. Interestingly, calcium oxide has a dual benefit because it influences both the microstructure and the electrical behavior. However, although its effect on the former is positive and strong, it only partially affects the latter. CaO has a beneficial effect on the microstructure because it reduces residual porosity and enhances grain growth. Therefore, its major effect

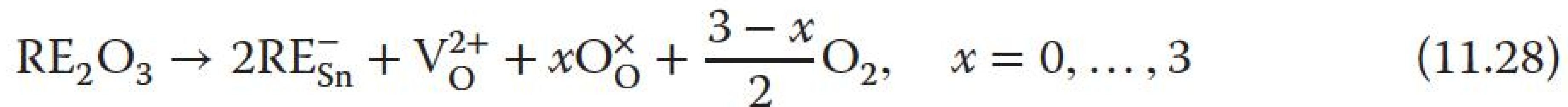
is most likely associated with the creation of vacancies according to the following defect formation equation [5]:



$$CaO \xrightarrow{SnO_2} Ca_{Sn}^{2-} + V_O^{2+} + O_O^{\times} \tag{11.27}$$

ZnO promoted an increase in the unit cell volume and in the lattice microstrain. Zn is found in the substitution position in the crystal lattice, indicating that the solid solution of the ZnO in the SnO_2 ceramic matrix occurs [75]. The SnO_2-based varistor system doped with ZnO or with Co_3O_4 presents a simple single-phase structure under X-ray resolution in which Sn^{4+} ions are substituted by Zn^{2+}, Co^{3+}, or Co^{2+} ions giving place to a solid solution [1, 51]. However, the existence of a Co-enriched second phase has been suggested by Oliveira et al. [79] on SnO_2–CoO-based varistors sintered at 1250 °C for two hours using transmission electron microscopy. Furthermore, these heterogeneities localize mainly at the grain boundaries and triple points and are not only rich in Co but also in the dopant elements eventually added to improve the nonlinear coefficient. This enrichment of grain boundaries with precipitates and segregated species is likely to control the nonohmic properties of the devices [5, 7].

The rare earth oxides can greatly improve the nonlinear properties of SnO_2 varistors and reduce the leakage current [10, 23]. The ionic radius of La^{3+}, Pr^{3+}, Er^{3+}, and Dy^{3+} is 0.106, 0.101, 0.088, and 0.098 nm, respectively, which are much larger than that of Sn^{4+} (0.071 nm). Therefore, only rare earth ions RE^{3+} can substitute Sn^{4+}, but hard to take the interstitial sites of SnO_2 lattice.



$$RE_2O_3 \rightarrow 2RE_{Sn}^{-} + V_O^{2+} + xO_O^{\times} + \frac{3-x}{2}O_2, \quad x = 0, \dots, 3 \tag{11.28}$$

As the radius of rare earth ions are larger than that of Sn^{4+}, the substitution of Sn^{4+} by RE^{3+} will lead to significant lattice distortion. Therefore, the solubility of rare earth elements in the SnO_2 crystal lattice is low, and most of the RE^{3+} will stay in the grain boundary. In other words, the incorporation of rare earth elements prevents the SnO_2 grain growth objectively. The higher the content of rare earth elements, the smaller the grain size in the samples. At the same time, the decrease in grain size of the sample means increasing the average number (N) of grain boundary within a unit thickness. The relationship between N and the breakdown electrical field E_b, single barrier voltage V_b is

$$E_b = N \cdot V_b \tag{11.29}$$

With the increase in the doping of rare earth elements, a little change in V_b occurs while the grain size of SnO_2 decreases sharply, which is the reason for the increase in threshold electrical field for the content of doped rare earth element increases.

11.4.3 Donor Doping

High-valence ions, such as Nb, Ta, Sb, and V [62], which have a similar radius to Sn^{4+}, are selected for donor impurities. The radius of Nb^{5+} (0.070 nm) is very close to that of Sn^{4+} (0.071 nm), so Nb^{5+} will replace Sn^{4+} and enter the internal location of the grain easily. Thus, it will introduce a large number of free electrons

as the reactions in Eqs. (11.12) and (11.13). Oxygen vacancies and tin vacancies may have the following reaction:



$$2V_{O}^{2+} + V_{Sn}^{4-} \rightarrow V_{Sn}^{2-} + 2V_{O}^{+} \tag{11.30}$$

Some of the oxygens released from this reaction will be attracted to the grain boundary.



$$O_2 \rightarrow 2O_{ad}^{\times} \tag{11.31}$$

This kind of oxygens captures free electrons easily and become negative ions.



$$O_{ad}^{\times} + e^{-} \rightarrow O_{ad}^{-} \tag{11.32}$$



$$O_{ad}^{-} + e^{-} \rightarrow O_{ad}^{2-} \tag{11.33}$$

A good varistor requires a high grain boundary barrier, a small grain resistivity, and a grain boundary layer of high resistance. Donor doping is crucial to the formation of barrier at the grain boundary and semiconducting grains. Ta_2O_5 contributes to an increase in the electronic conductivity in SnO_2 [26], according to the reaction:



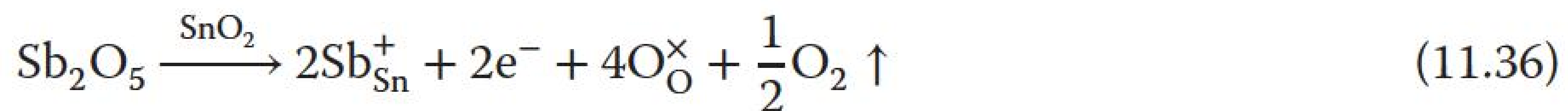
$$2Ta_2O_5 \xrightarrow{SnO_2} 4Ta_{Sn}^{+} + V_{Sn}^{4-} + 10O_{O}^{\times} \tag{11.34}$$

Ta_2O_5 dopant has a great effect on the electrical properties of SnO_2-based varistors. A high nonlinear coefficient of 52.6 for varistors doped with 1.00 mol% Ta_2O_5 was obtained [58]. Ta_2O_5 can enhance the threshold voltage of SnO_2-based varistors, which is originated from the decrease in the SnO_2 grain size.

Fayat and Castro [51] found that doping Sb_2O_3 or Nb_2O_5 can reduce the total oxygen vacancy concentration and the grain growth. In the Sb_2O_3 addition, the possible substitution equations are:



$$Sb_2O_3 \xrightarrow{SnO_2} 2Sb_{Sn}^{-} + V_{O}^{2+} + 3O_{O}^{\times} \tag{11.35}$$



$$Sb_2O_5 \xrightarrow{SnO_2} 2Sb_{Sn}^{+} + 2e^{-} + 4O_{O}^{\times} + \frac{1}{2}O_2 \uparrow \tag{11.36}$$

Sb_2O_3 addition to SnO_2–CoO-based varistor produced a diminution in the lattice volume. This diminution in the volume could not be produced by the Sb^{3+} stabilization (Sb^{3+} radius is 0.76 Å and Sn^{4+} radius is 0.71 Å). According to the volume lattice data and the ionic radii, Sb^{5+} stabilization is produced (Sb^{5+} radius is 0.62 Å). Sb_2O_5 is the stable form up to 970 °C, but Sb_2O_3 is more stable at higher temperatures. However, the Sb^{5+}/Sb^{3+} ratio depends on both the temperature and the concentration at ambient oxygen [52]. Then, it is possible that the transformation of Sb^{3+} into Sb^{5+} takes place during the cooling process. Sb_2O_3 addition favors the formation of $CoSnO_3$ particles and Nb_2O_5 favors the formation of particles with an intermediate composition between $CoSnO_3$ and Co_2SnO_4 in systems with Co_3O_4. These particles could also control the sintering and grain growth rates [51].

The addition of WO_3 inhibits the grain growth of the SnO_2–ZnO ceramic, although it does not influence the densification of the system. The segregation of WO_3 is, probably, responsible for the increase in the resistivity of the SnO_2–ZnO–WO_3 system [75].

11.5 Thermal Performances

As discussed in Chapter 6, the breakdown, energy absorption capability, and thermal runaway are all directly related to the thermal conductivity of varistors. Leakage current gradually increases the varistor temperature and eventually leads to thermal breakdown and invalidation. Bi_2O_3 in the grain boundaries of ZnO varistors will gradually melt and evaporate. Then, the leakage current increases afterward, whereas the resistivity of the semiconductors decreases as the temperature increases, and then the temperature rises continuously, leading more grain boundaries melt and evaporate. The vicious circle eventually leads to the failure of the varistor. Therefore, a good varistor device requires good thermal conductivity, which is essential to the stability and energy-handling capability.

Because of the multiphase structure, ZnO-based varistors have poor temperature stability and aging characteristics. In contrast, the SnO_2 varistor shows a higher thermal conductivity than commercial samples of the ZnO-based varistor, as shown in Figure 11.13, which is resulted from its simpler phase composition and lower dopant concentration, and much better temperature stability as a result. It is a remarkable property that enables this material to compete commercially with ZnO-based varistor devices [35]. LFA-427 equipment was used to directly determine the value of thermal diffusivity.

The thermal conductivity of the SnO_2-based varistor is remarkably different from that of commercial ZnO varistor. The value of thermal conductivity of SnO_2-based varistor is about 70% higher than that measured from commercial ZnO samples at lower temperature and almost 85% higher as the temperature increases up to 923 K [35].

The comparison of thermodynamic properties between SnO_2 and ZnO varistors is shown in Table 11.5 [80]. The thermal conductivity λ of SnO_2-based

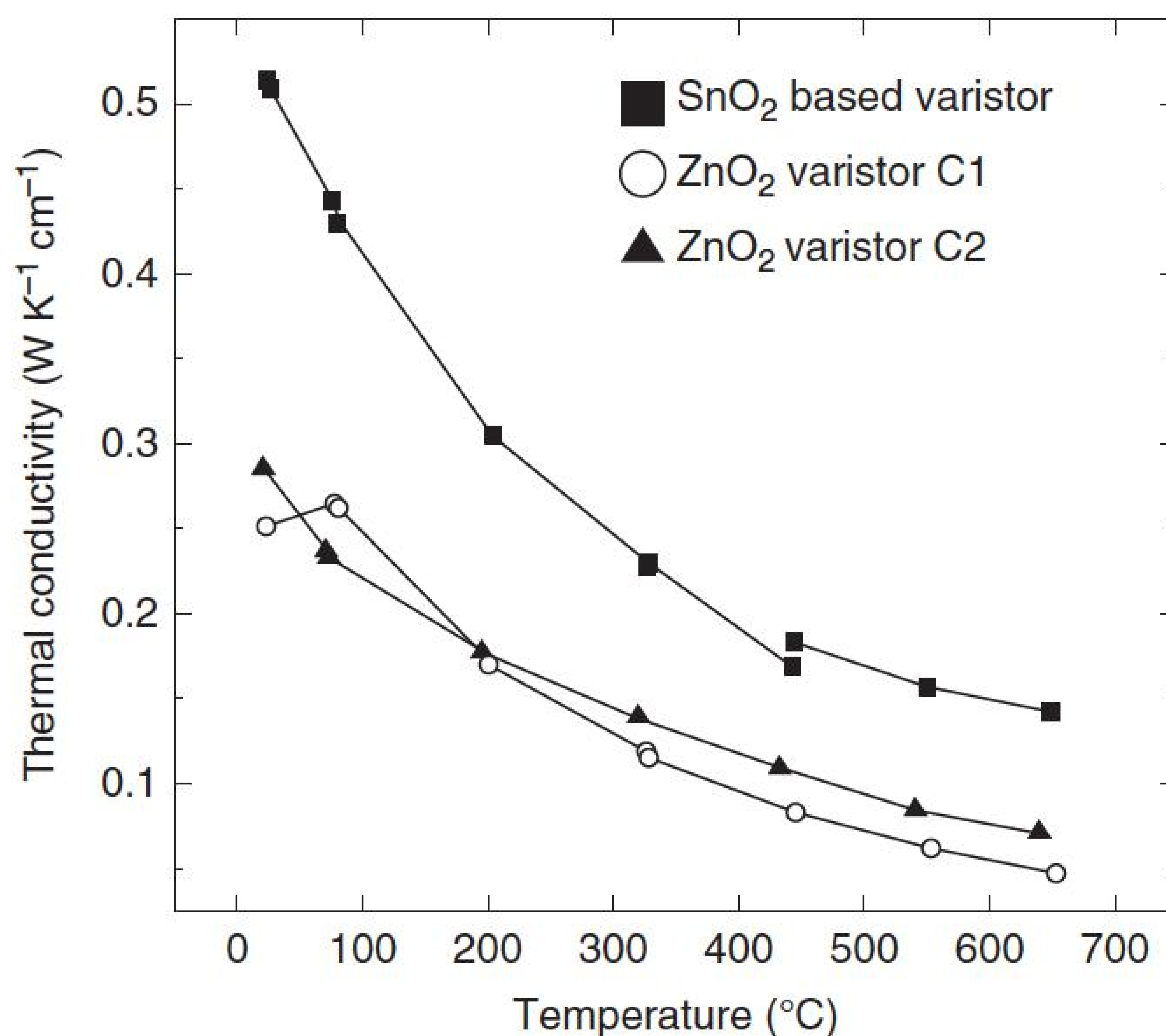


Figure 11.13 Thermal conductivities of commercial ZnO varistors and SnO_2-based varistors. Source: Bueno et al. 2005 [35]. Reproduced with permission of John Wiley & Sons.

Table 11.5 Comparison of thermodynamic properties between SnO_2 and ZnO varistors.

Parameters	ZnO varistor	SnO_2 varistor
Thermal conductivity λ ($W\,K^{-1}\,cm^{-1}$)	0.25–0.3	~0.5
Static elastic modulus E_s (GPa)	116 ± 14	212 ± 6
Dynamic elastic modulus E_d (GPa)	120 ± 2	251 ± 3
Bending strength σ_f (MPa)	106 ± 3	207 ± 5
Thermal expansion coefficient η (K^{-1})	7.10×10^{-6}	2.10×10^{-6}

Source: Ramirez et al. 2008 [80]. Reproduced with permission from John Wiley & Sons.

varistor is almost two times that of ZnO varistor [35], which is more conducive to thermal diffusion, and further improves its ability against the thermal damages. The thermal expansion coefficient η of SnO_2 varistor is much smaller than that of the ZnO varistor, and its static elastic modulus E_s, dynamic elastic modulus E_d, and bending strength σ_f are all almost twice those of the ZnO varistors [80], which makes SnO_2-based varistors have a more prominent resistance to thermal stress damage.

Thus, SnO_2-based varistor presents several advantages on the commercial ZnO-based varistor. Once the electrical properties of both are equivalent, other physical properties such as thermal conductivity favor the use of the SnO_2-based varistor. In addition, the chemical features also favor the application of the SnO_2-based varistor as a commercial device. For instance, dopants such as Nb_2O_5 and Cr_2O_3 are required in small concentrations (~0.05%), which could be good for cost and also to thermal treatments [35]. The bismuth and spinel phases in the ZnO varistor can have its composition changed by the thermal effect during operation and cause a thermal damage on the microstructure. For example, the Bi_2O_3 phases in the grain boundaries of ZnO varistor have low melting point, which is a disadvantage to thermal runway stability.

For this reason, it is expected that for the SnO_2-based varistor, these problems can be minimized because of its higher refractory features. In addition, the microstructure is simpler compared with the commercial ZnO varistor and is also a good point to control the processing of the device. The DC-accelerated aging tests on commercial ZnO varistors and SnO_2-based samples showed that SnO_2-based varistors were more stable than commercial ZnO varistors [35].

In addition, because the ZnO varistor has a complex multiphase microstructure, when it suffers a thermal stress damage, the cracks will develop along the easy paths provided by the bismuth-rich grain boundary phase and the intercrystal phase [81]. When the thermal breakdown failure or puncturing damage happens, the grain boundary formed by Bi_2O_3 of low melting point tends to melt first. The SnO_2 varistor has a simpler, more uniform single-phase structure, there is no fissile, fusible second phase, and therefore less prone to the above-mentioned various damage.

In the failure test of ZnO varistors, it is often observed that the sample is punctured or cracked [80, 82], but in the same conditions of the damage test, the SnO_2 varistor is often shown as outer insulation layer failure first and shows better resistance to damage [83].

11.6 Degradation Behaviors

Ramírez et al. [82] reported the degradation behavior of SnO_2-based varistors and commercial ZnO-based varistors under current pulses (8/20 μs impulse current), and it was found that a more severe degradation occurred in the ZnO-based varistors concerning their nonohmic behavior, whereas in the SnO_2 varistor system, a good nonohmic behavior remained after the degradation. These results indicate that the degradation in the metal oxide varistors is controlled by a defect diffusion process, whose rate depends on the mobility, the concentration of metastable defects, and the amount of electrically active interfaces [82]. During the aging process, the metastable defects, which are defects positively charged with high mobility and located in the depletion layer, $Zn_i^+, Zn_i^{2+}, V_O^+, V_O^{2+}$ in the ZnO varistors [16] and $V_O^+, V_O^{2+}, Nb_{Sn}^+$ in the SnO_2-based varistor [24] migrate to the grain boundaries where they are capable of recombining with negatively charged defects O_{ads}^-, O_{ads}^{2-} in both systems. The better performance of the SnO_2-based varistors compared with the ZnO varistors may be related to the greater number of active potential barriers. EFM was used to analyze the surface charge accumulated at the grain boundary regions before and after degradation [60], and the proportion of active grain–grain junctions was 85% for the SnO_2 varistor against 35% for the ZnO varistor [34]. The ZnO varistors has a heterogeneous microstructure with the presence of different phases and interfaces, which leads to the low number of active barriers before degradation. A degradation by current pulses will transfer more energy to the varistors than a degradation by DC voltage. This energy is sufficient to activate the diffusion of metastable defects and degrade the potential barriers. However, the SnO_2 varistor system was observed to be very stable when it was subjected to degradation under DC voltage and high temperature, and the number of active barriers was not changed [53]. Also up to this moment, the metastable interstitial defects in SnO_2 varistors had not been identified, for example, Sn_i^{4+} is capable of helping in the degradation of the potential barrier. Furthermore, the high thermal conductivity of the SnO_2 varistor system is capable of avoiding the diffusion processes related to the degradation [82].

The SnO_2 system also exhibits a minimum variation under continuous current; this result indicates the existence of metastable defects of low concentration and/or low diffusion in the SnO_2 system [53]. High energy is necessary to degrade the barriers because of defect annihilation in the SnO_2 system. The high number of active interfaces in the SnO_2 varistor system allows high voltage ratings and small thicknesses. This is helpful to further minimize the size and weight of varistors.

11.7 Development of SnO_2-Based Varistors

SnO_2 varistor ceramics are still in the developing stage. Although there are many advantages compared with ZnO-based varistors, including electrical and thermal properties, there exist some challenges for this material to be ready for lightning protection. One of the vital elements is its relatively high residual voltage ratio. The residual voltage ratio is defined as the ratio of the residual voltage under high impulse current and the voltage under the 1 mA DC current. The residual voltage ratio can intuitively reflect the overvoltage-limiting ability and the nonlinear properties of varistors at high current, normally the value is lesser than 3. The lower residual voltage ratio means the better performance in suppressing voltage. Generally, the commercial ZnO-based varistors' voltage ratio is about 1.7, whereas the value of SnO_2-based varistors is more than 2 [40].

The residual voltage ratio was lowered further by composition optimization and preparation technique to increase the capability that the SnO_2-based varistor withstands surge current [45]. The studied SnO_2-based system included the following compositions: $(94.6 - x)$ $SnO_2 + 0.5\%$ $Co_2O_3 + 0.04\%$ $Cr_2O_3 + x\%$ Nb_2O_5, all in mol%, the results are shown in Table 11.6 [45]. The sample with 0.07 mol% Nb_2O_5 has the lowest residual voltage ratio of 1.86, nonlinear coefficient α of 42.6, threshold electrical field of 364.6 V mm^{-1}, and leakage current of 1.85, all these electrical properties reach the level of the commercial ZnO varistor.

The residual voltage ratio is not only associated with the grain resistance but also with the grain size [45], which is proportional to the grain size. When the Nb_2O_5 content is less, with the increase in the Nb_2O_5 content, more Nb^{5+} ions enter into the lattices replacing Sn^{4+}, distort SnO_2 lattices, improve the diffusion of ions, promote grain growth, and make the residual voltage ratio increase. At the same time, the grain growth and reduction of the number of grain boundaries make the grain boundary resistance lowered. Secondly, the effect of grain growth due to Nb^{5+} decreased, whereas the production of a large number of free electrons in the crystal reduces the grain resistivity, provides a large number of carriers, and lead to the lower residual voltage. Excess of free electrons make the depletion layer of the grain boundary weakened or disappeared, which also reduces the grain boundary resistance [45]. Nevertheless, the substitution of Sn^{4+} by Nb^{5+} has a maximum value; over this limit, the extra Nb^{5+} ions would not enter

Table 11.6 Influence of Nb_2O_5 concentrations on parameters of SnO_2-based varistors.

Nb_2O_5 concentration (mol%)	Nonlinear coefficient α	E_b (V mm^{-1})	Leakage current (μA)	Residual voltage ratio	Mean grain size (μm)	Relative density (%)
0.05	29.4	415.4	17.6	2.29	3.04	97.5
0.06	29.5	491.2	8.5	2.71	3.11	98.6
0.07	42.6	364.6	1.85	1.86	3.00	98.2
0.08	40.0	198.1	0.19	2.22	2.90	97.0

Source: Wei et al. 2011 [45]. Reproduced with permission from Springer.

the SnO_2 lattice but accumulate in the grain boundary. These Nb^{5+} ions will in turn hinder the formation and transport of electrons and other defect ions, resulting in both the residual voltage ratio and the grain boundary resistance increase, and also to minimize the leakage current. As shown in Table 11.6 [45], the reduction of grain size also proves this.

The similar research was worked on the influence of Cr_2O_3 on the residual voltage ratio of SnO_2-based varistors, and the lowest residual voltage ratio of 1.68 was from the SnO_2-based varistor with a Cr_2O_3 concentration of 0.03 mol% [61]. The mean grain size of SnO_2-based varistor ceramics decreases from 3.63 to 2.81 μm as the Cr_2O_3 content increases from 0.02 to 0.06 mol%, and the threshold electrical field E_b is markedly improved from 364.9 to 800.9 V mm^{-1} as the Cr_2O_3 concentration increases. Figure 11.14 shows the influence of Cr_2O_3 concentrations on the residual voltage ratio of SnO_2-based varistor ceramics [61], the variation trend can be divided into three stages.

As the ionic radii are different, various ions will distribute in different locations inside the material during the sintering process. The radius of Co^{2+} ions (Co_2O_3 will decompose into CoO at 950 °C) is 0.074 nm, which is similar to that of Sn^{4+} ions (0.071 nm). It is possible for Co^{2+} ions to enter the lattice of SnO_2 to displace Sn^{4+} ions. The radius of Cr^{3+} is 0.063 nm, which is much smaller than that of Sn^{4+} ions. As a result, Cr^{3+} ions displacing Sn^{4+} ions will bring large distortion of lattices. Cr^{3+} ions will remain in the grain boundary preferentially [61]. Cr^{3+} ions accumulating in the grain boundary will hinder the growth of grains. That is why the grain size decreases as the Cr_2O_3 concentration increases and gives rise to the corresponding changes in the electrical properties of SnO_2-based varistors ceramics.

As the curve in Figure 11.14 shows [61], first, the residual voltage ratio decreases as the Cr_2O_3 concentration increases. In this stage, the decrease in

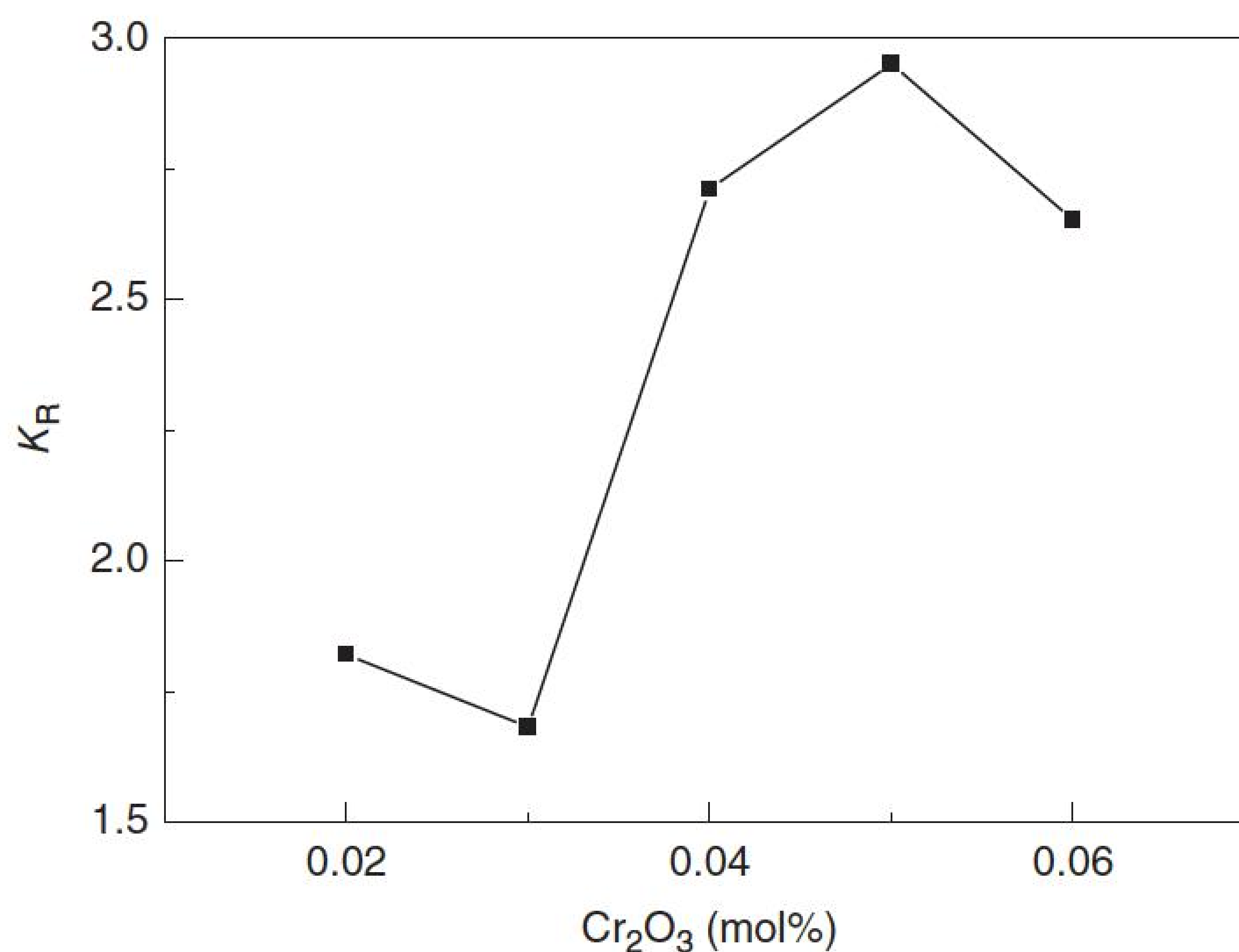


Figure 11.14 The influence of Cr_2O_3 concentrations on the residual voltage ratio of SnO_2-based varistors ceramics. Source: Wei et al. 2011 [61]. Reproduced with permission of John Wiley & Sons.

grain size is the crucial factor that influences the residual voltage ratio, which is related not only to the grain resistivity but also to the grain size. The Cr_2O_3 addition decreases the residual voltage ratio of SnO_2-based varistor ceramics by means of reducing the grain size at a low Cr_2O_3 concentration and the lowest residual voltage ratio is 1.68, when the Cr_2O_3 concentration is 0.03 mol%.

When the Cr_2O_3 concentration increases from 0.03 to 0.05 mol%, the residual voltage ratio of the samples increases [61]. With the increase in Cr_2O_3 content, abundant Cr^{3+} ions accumulate at the grain boundaries and the concentration of Cr^{3+} ions at the grain boundary becomes saturation. Meanwhile, the effectiveness due to the decrease of the grain size is weakened while a part of Cr^{3+} ions begin to enter the lattice of SnO_2 and displace Sn^{4+} ions. As mentioned above, this kind of substitution will bring large lattice distortion and a great deal of defects. When Cr^{3+} ions displace Sn^{4+} ions, Cr^{3+} ions will accept electrons and bring oxygen vacancies. The reaction process is as follows:



$$Cr_2O_3 \xrightarrow{SnO_2} 2Cr_{Sn}^{-} + V_O^{2+} + 3O_O^{\times} \tag{11.37}$$

The large number of oxygen vacancies and other defects generated in this process hinder the transport of electrons instead. Thus, the decrement of the carriers increases the residual voltage ratio. Therefore, in the stage, as the Cr_2O_3 concentration increases, the block of abundant defects makes the residual voltage ratio rise.

When the Cr_2O_3 concentration increases over 0.05 mol%, the residual voltage ratio has a slightly downtrend. This is possibly because excessive Cr_2O_3 addition forms the second phase in the grain boundary [61]. The displacement of Sn^{4+} ions by Cr^{3+} ions exists a maximum. The extra Cr_2O_3 additions beyond the saturation value in the grain boundary may create a second phase of the spinel-type structure. Varela and coworkers observed SnO_2-based varistors ceramics doped with Co and Cr by a high-resolution transmission electron microscope and found that a second phase appears in the grain boundary, like $CoCr_2O_4$ [25]. This ionic compound of spinel-type structure will deteriorate the nonlinear characteristics and depress the resistivity of the materials. Therefore, the residual voltage ratio is decreased. Thus, when Cr_2O_3 is added over the saturation value (here is 0.05 mol %), the second phase in the grain boundary caused by extra Cr_2O_3 additions decreases the residual voltage ratio slightly.

These exciting results prove that the SnO_2-based varistor is a promising varistor material as an interesting candidate to substitute the traditional multicomponent ZnO-based varistors.

References

1 Pianaro, S.A., Bueno, P.R., Longo, E., and Varela, J.A. (1995). A new SnO_2-based varistor system. *Journal of Materials Science Letters* 14 (10): 692–694.

2 Leite, E.R., Nascimento, A.M., Bueno, P.R. et al. (1999). The influence of sintering process and atmosphere on the non-ohmic properties of SnO_2 based varistor. *Journal of Materials Science: Materials in Electronics* 10 (4): 321–327.

3 Pianaro, S.A., Bueno, P.R., Olivi, P. et al. (1997). Effect of Bi_2O addition on the microstructure and electrical properties of the $SnO_2{\cdot}CoO{\cdot}Nb_2O_5$ varistor system. *Journal of Materials Science Letters* 16 (8): 634–638.

4 Pianaro, S.A., Bueno, P.R., Olivi, P. et al. (1998). Electrical properties of the SnO_2-based varistor. *Journal of Materials Science: Materials in Electronics* 9 (2): 159–165.

5 Pianaro, S.A., Bueno, P.R., Longo, E., and Varela, J.A. (1999). Microstructure and electric properties of a SnO_2 based varistor. *Ceramics International* 25 (1): 1–6.

6 Bueno, P.R., de Cassia-Santos, M.R., Leite, E.R. et al. (2000). Nature of the Schottky-type barrier of highly dense SnO_2 systems displaying nonohmic behavior. *Journal of Applied Physics* 88 (11): 6545–6548.

7 Bueno, P.R., Leite, E.R., Oliveira, M.M. et al. (2001). Role of oxygen at the grain boundary of metal oxide varistors: a potential barrier formation mechanism. *Applied Physics Letters* 79 (1): 48–50.

8 Jarzebski, Z.M. and Marton, J.P. (1976). Physical properties of SnO_2 materials II. Electrical properties. *Journal of the Electrochemical Society* 123 (9): 299C–310C.

9 Zhang, G. (2006). Study on high voltage SnO_2 varistor ceramics and exploration of new low voltage-high dielectric constant varistor materials and lead-free piezoelectric materials. Doctoral thesis. Jinan, China: Shandong University (in Chinese).

10 Varela, J.A., Whittemore, O.J., and Longo, E. (1990). Pore size evolution during sintering of ceramic oxides. *Ceramics International* 16 (3): 177–189.

11 Paria, M.K. and Maiti, H.S. (1983). Electrical conductivity of polycrystalline tin dioxide and its solid solution with ZnO. *Journal of Materials Science* 18 (7): 2101–2107.

12 Kimura, T., Inada, S., and Yamaguchi, T. (1989). Microstructure development in SnO_2 with and without additives. *Journal of Materials Science* 24 (1): 220–226.

13 Kumar, K.P. and Damodaran, A.D. (1989). Sintering of solution infiltered SnO_2 ceramics. *Journal of Materials Science Letters* 8 (12): 1425–1426.

14 Uematsu, K., Kato, Z., Uchida, N., and Saito, K. (1987). Electrical conductivity of antimony-doped tin dioxide prepared by hot isostatic pressing. *Journal of the American Ceramic Society* 70 (7): C-142–C-143.

15 Lee, J.H., Park, S.J., and Hirota, K. (1990). Temperature dependence of electrical conductivity in polycrystalline tin oxide. *Journal of the American Ceramic Society* 73 (9): 2771–2774.

16 Park, S.J., Hirota, K., and Yamamura, H. (1984). Densitication of nonadditive SnO_2 by hot isostatic pressing. *Ceramics International* 10 (3): 115–121.

17 Zuca, S., Terzi, M., Zaharescu, M., and Matiasovsky, K. (1991). Contribution to the study of SnO_2-based ceramics. *Journal of Materials Science* 26 (6): 1673–1676.

18 Cerri, J.A., Leite, E.R., Gouvêa, D. et al. (1996). Effect of cobalt(II) oxide and manganese(IV) oxide on sintering of tin(IV) oxide. *Journal of the American Ceramic Society* 79 (3): 799–804.

19 Antunes, A.C., Antunes, S.R.M., Pianaro, S.A. et al. (1998). Nonlinear electrical behaviour of the $SnO_2 \cdot CoO \cdot Ta_2O_5$ system. *Journal of Materials Science Letters* 17 (7): 577–579.

20 Bueno, P.R., Pianaro, S.A., Pereira, E.C. et al. (1998). Investigation of the electrical properties of SnO_2 varistor system using impedance spectroscopy. *Journal of Applied Physics* 84 (7): 3700–3705.

21 Oliveira, M.M., Bueno, P.R., Cassia-Santos, M.R. et al. (2001). Sensitivity of SnO_2 non-ohmic behavior to the sintering process and to the addition of La_2O_3. *Journal of the European Ceramic Society* 21 (9): 1179–1185.

22 Gupta, T.K. (1990). Application of zinc oxide varistors. *Journal of the American Ceramic Society* 73 (7): 1817–1840.

23 Wang, C.M., Wang, J.F., Chen, H.C. et al. (2004). Effects of Pr_2O_3 on the nonlinear electrical characteristics and dielectric properties of $SnO_2 \cdot Co_2O_3 \cdot Ta_2O_5$ varistor systems. *Solid State Communications* 132 (3-4): 163–167.

24 Yan, M.F. and Rhodes, W.W. (1982). Preparation and properties of TiO_2 varistors. *Applied Physics Letters* 40 (6): 536–537.

25 Varela, J.A., Cerri, J.A., Leite, E.R. et al. (1999). Microstructural evolution during sintering of CoO doped SnO_2 ceramics. *Ceramics International* 25 (3): 253–256.

26 Santos, M.R., Bueno, P.R., Longo, E., and Varela, J.A. (2001). Effect of oxidizing and reducing atmospheres on the electrical properties of dense SnO_2-based varistors. *Journal of the European Ceramic Society* 21 (2): 161–167.

27 Castro, M.S. and Aldao, C.M. (1998). Characterization of SnO_2-varistors with different additives. *Journal of the European Ceramic Society* 18 (14): 2233–2239.

28 Wang, Y.J., Wang, J.F., Li, C.P. et al. (2000). Improved varistor nonlinearity via sintering and acceptor impurity doping. *The European Physical Journal Applied Physics* 11 (3): 155–158.

29 Yongjun, W., Jinfeng, W., Hongcun, C. et al. (2000). Electrical properties of SnO_2-ZnO-Nb_2O_5 varistor system. *Journal of Physics D: Applied Physics* 33 (1): 96–99.

30 Inada, M. (1979). Effects of heat-treatment on crystal phases, microstructure and electrical properties of nonohmic zinc oxide ceramics. *Japanese Journal of Applied Physics* 18 (8): 1439–1446.

31 Iga, A., Matsuoka, M., and Masuyama, T. (1976). Effect of phase transition of intergranular Bi_2O_3 layer in nonohmic ZnO ceramics. *Japanese Journal of Applied Physics* 15 (6): 1161–1162.

32 Branković, G., Branković, Z., and Varela, J.A. (2005). Nonlinear properties and stability of SnO_2 varistors prepared by evaporation and decomposition of suspensions. *Journal of the European Ceramic Society* 25 (12): 3011–3015.

33 Bueno, P.R., Oliveira, M.M., Bacelar-Junior, W.K. et al. (2002). Analysis of the admittance-frequency and capacitance–voltage of dense $SnO_2 \cdot$CoO-based varistor ceramics. *Journal of Applied Physics* 91 (9): 6007–6014.

34 Ramírez, M.A., Bassi, W., Parra, R. et al. (2008). Comparative electrical behavior at low and high current of SnO_2- and ZnO-based varistors. *Journal of the American Ceramic Society* 91 (7): 2402–2404.

35 Bueno, P.R., Varela, J.A., Barrado, C.M. et al. (2005). A comparative study of thermal conductivity in ZnO- and SnO_2-based varistor systems. *Journal of the American Ceramic Society* 88 (9): 2629–2631.
36 Glot, A.B. and Zlobin, A.P. (1989). Nonohmic conductivity of ceramics based on tin dioxide. *Neorganicheskie Materialy* 25 (2): 322–324.
37 Santhosh, P.N., Potdar, H.S., and Date, S.K. (1997). Chemical synthesis of a new tin dioxide based (SnO_2: Co, Al, Nb) varistor. *Journal of Materials Research* 12 (2): 326–328.
38 Skuratovsky, I., Glot, A., Di Bartolomeo, E. et al. (2004). The effect of humidity on the voltage–current characteristic of SnO_2 based ceramic varistor. *Journal of the European Ceramic Society* 24 (9): 2597–2604.
39 Glot, A.B. and Skuratovsky, I.A. (2006). Non-ohmic conduction in tin dioxide based varistor ceramics. *Materials Chemistry and Physics* 99 (2-3): 487–493.
40 Lu, Z.Y., Chen, Z., and Wu, J.Q. (2009). SnO_2-based varistors capable of withstanding surge current. *Journal of the Ceramic Society of Japan* 117 (1367): 851–855.
41 Bueno, P.R., Orlandi, M.O., Simoes, L.G.P. et al. (2004). Nonohmic behavior of SnO_2-MnO polycrystalline ceramics. I. Correlations between microstructural morphology and nonohmic features. *Journal of Applied Physics* 96 (5): 2693–2700.
42 Gupta, T.K. and Carlson, W.G. (1985). A grain-boundary defect model for instability/stability of a ZnO varistor. *Journal of Materials Science* 20 (10): 3487–3500.
43 Leite, E.R., Varela, J.A., and Longo, E. (1992). A new interpretation for the degradation phenomenon of ZnO varistors. *Journal of Materials Science* 27 (19): 5325–5329.
44 Antunes, A.C., Antunes, S.R.M., Zara, A.J. et al. (2002). Effect of Fe_2O_3 doping on the electrical properties of a SnO_2 based varistor. *Journal of Materials Science* 37 (12): 2407–2411.
45 Wei, Q., He, J., and Hu, J. (2011). Dependence of residual voltage ratio behavior of SnO_2-based varistors on Nb_2O_5 addition. *Science China Technological Sciences* 54 (6): 1415–1418.
46 Jonscher, A.K. (1977). A many-body model of dieletric polarisation in solids. II. The universal model. *Physica Status Solidi B* 84 (1): 159–166.
47 Jonscher, A.K. (1990). Dynamics of deep level trapping in space charge regions. *Solid-State Electronics* 33 (1): 139–142.
48 Moulson, A.J. and Herbert, J.M. (2003). *Electroceramics: Materials, Properties, Applications*. New York: Wiley.
49 Orlandi, M.O., Bomio, M.R.D., Longo, E., and Bueno, P.R. (2004). Nonohmic behavior of SnO_2-MnO polycrystalline ceramics. II. Analysis of admittance and dielectric spectroscopy. *Journal of Applied Physics* 96 (7): 3811–3817.
50 Fan, J. and Freer, R. (2007). Deep level transient spectroscopy of SnO_2-based varistors. *Applied Physics Letters* 90 (9): 093511.
51 Fayat, J. and Castro, M.S. (2003). Defect profile and microstructural development in SnO_2-based varistors. *Journal of the European Ceramic Society* 23 (10): 1585–1591.

52 Ovenston, A., Sprinceana, D., Walls, J.R., and Caldararu, M. (1994). Effect of frequency on the electrical characteristics of tin-antimony-oxide mixtures. *Journal of Materials Science* 29 (19): 4946–4952.

53 Ramírez, M.A., Tararam, R., Simoes, A.Z. et al. (2013). Degradation analysis of the SnO_2 and ZnO-based varistors using electrostatic force microscopy. *Journal of the American Ceramic Society* 96 (6): 1801–1809.

54 Lu, Z.Y., Huang, H., and Wu, J.Q. (2009). Densification surge current performance of SnO_2–Sb_2O_3 based varistor ceramics. *Journal of Inorganic Materials* 24 (4): 841–844.

55 Zang, G.Z., Wang, J.F., Chen, H.C. et al. (2005). Effect of Co_2O_3 on the microstructure and electrical properties of Ta-doped SnO_2 varistors. *Journal of Physics D: Applied Physics* 38 (7): 1072–1075.

56 Wang, C.M., Wang, J.F., Chen, H.C. et al. (2005). Effects of CuO on the grain size and electrical properties of SnO_2-based varistors. *Materials Science and Engineering B* 116 (1): 54–58.

57 Wang, W.X., Wang, J.F., Chen, H.C. et al. (2003). Effects of In_2O_3 on the properties of (Co, Nb)-doped SnO_2 varistors. *Journal of Physics D: Applied Physics* 36 (8): 1040–1043.

58 Wang, C., Wang, J., Chen, H. et al. (2003). Effects of Ta_2O_5 on the grain size and electrical properties of SnO_2-based varistors. *Journal of Physics D: Applied Physics* 36 (23): 3069–3072.

59 Gaponov, A.V. and Glot, A.B. (2010). Electrical properties of SnO_2 based varistor ceramics with CuO addition. *Journal of Materials Science: Materials in Electronics* 21 (4): 331–337.

60 Vasconcelos, J.S., Vasconcelos, N.S.L.S., Orlandi, M.O. et al. (2006). Electrostatic force microscopy as a tool to estimate the number of active potential barriers in dense non-ohmic polycrystalline SnO_2 devices. *Applied Physics Letters* 89 (15): 152102.

61 Wei, Q., He, J., Hu, J., and Wang, Y. (2011). Influence of Cr_2O_3 on the residual voltage ratio of SnO_2-based varistor. *Journal of the American Ceramic Society* 94 (7): 1999–2002.

62 Dhage, S.R. and Ravi, V. (2003). Influence of various donors on nonlinear I–V characteristics of tin dioxide ceramics. *Applied Physics Letters* 83 (22): 4539–4541.

63 Aguilar-Martínez, J.A., Durán-Régules, A., Glot, A.B. et al. (2008). Effect of CaO on the microstructure and non-ohmic properties of (Co, Sb)-doped SnO_2 varistors. *Revista Mexicana de Física* 54 (1): 20–24.

64 Antunes, A.C., Antunes, S.R.M., Pianaro, S.A. et al. (2001). Effect of La_2O_3 doping on the microstructure and electrical properties of a SnO_2-based varistor. *Journal of Materials Science: Materials in Electronics* 12 (1): 69–74.

65 He, J., Peng, Z., Fu, Z. et al. (2012). Effect of ZnO doping on microstructural and electrical properties of SnO_2–Ta_2O_5 based varistors. *Journal of Alloys and Compounds* 528: 79–83.

66 Zang, G.Z., Wang, J.F., Chen, H.C. et al. (2005). Effects of Sc_2O_3 on the microstructure and varistor properties of (Co, Nb)-doped SnO_2. *Applied Physics* 80 (5): 1093–1096.

67 Wang, J.F., Chen, H.C., Su, W.B. et al. (2006). Effects of Sr on the microstructure and electrical properties of (Co, Ta)-doped SnO_2 varistors. *Journal of Alloys and Compounds* 413 (1): 35–39.

68 Parra, R., Varela, J.A., Aldao, C.M., and Castro, M.S. (2005). Electrical and microstructural properties of (Zn, Nb, Fe)-doped SnO_2 varistor systems. *Ceramics International* 31 (5): 737–742.

69 Wang, W.X., Wang, J.F., Chen, H.C. et al. (2003). Electrical nonlinearity of (Cu, Ni, Nb)-doped SnO_2 varistors system. *Materials Science and Engineering B* 99 (1): 457–460.

70 Bueno, P.R., Cassia-Santos, M.R., Simões, L.G. et al. (2002). Low-voltage varistor based on (Sn, Ti)O_2 ceramics. *Journal of the American Ceramic Society* 85 (1): 282–284.

71 Wang, C.M., Wang, J.F., Wang, C.L. et al. (2005). Nonlinear electrical characteristics of SnO_2·CuO ceramics with different donors. *Journal of Applied Physics* 97 (12): 126103.

72 Dhage, S.R., Ravi, V., and Date, S.K. (2004). Nonlinear $I-V$ characteristics study of doped SnO_2. *Bulletin of Materials Science* 27 (1): 43–45.

73 Li, C.P., Wang, J.F., Su, W.B. et al. (2002). Nonlinear electrical properties of $SnO_2 \cdot Li_2O \cdot Ta_2O_5$ varistors. *Ceramics International* 28 (5): 521–526.

74 Simões, A.Z., Ries, A., Perazolli, L. et al. (2006). Nonlinear electrical behaviour of the Cr_2O_3, ZnO, CoO and Ta_2O_5-doped SnO_2 varistors. *Ceramics International* 32 (3): 283–289.

75 Perazolli, L., Simoes, A.Z., Coleto, U. et al. (2005). Structural and microstructural behaviour of SnO_2 dense ceramics doped with ZnO and WO_3. *Materials Letters* 59 (14): 1859–1865.

76 Parra, R., Castro, M.S., and Varela, J.A. (2005). Analysis of secondary phases segregated and precipitated in SnO_2-based varistors. *Journal of the European Ceramic Society* 25 (4): 401–406.

77 Fan, J., Zhao, H., Xi, Y. et al. (2010). Characterisation of SnO_2–CoO–MnO–Nb_2O_5 ceramics. *Journal of the European Ceramic Society* 30 (2): 545–548.

78 Simoes, L.G.P., Bueno, P.R., Orlandi, M.O. et al. (2003). The influence of excess precipitate on the non-ohmic properties of SnO_2-based varistors. *Journal of Electroceramics* 10 (1): 63–68.

79 Oliveira, M.M., Soares, P.C. Jr., Bueno, P.R. et al. (2003). Grain-boundary segregation and precipitates in La_2O_3 and Pr_2O_3 doped SnO_2·CoO-based varistors. *Journal of the European Ceramic Society* 23 (11): 1875–1880.

80 Ramirez, M.A., Rubio-Marcos, F., Fernandez, J.F. et al. (2008). Mechanical properties and dimensional effects of ZnO- and SnO_2-based varistors. *Journal of the American Ceramic Society* 91 (9): 3105–3108.

81 Balzer, B., Hagemeister, M., Kocher, P., and Gauckler, L.J. (2004). Mechanical strength and microstructure of zinc oxide varistor ceramics. *Journal of the American Ceramic Society* 87 (10): 1932–1938.

82 Ramirez, M.A., Bassi, W., Bueno, P.R. et al. (2008). Comparative degradation of ZnO- and SnO_2-based polycrystalline non-ohmic devices by current pulse stress. *Journal of Physics D: Applied Physics* 41 (12): 122002.

83 Wei, Q.Y., He, J.L., and Hu, J. (2011). Analysis on characteristics of tin dioxide varistors. *High Voltage Engineering* 37 (3): 629–633. (in Chinese).

12

WO_3-Based Varistor Ceramics of Low Breakdown Voltage

The electronic and microelectronic systems are eager for the low breakdown voltage varistors. WO_3-based varistor ceramic is a new kind of low-voltage varistor with a low threshold electric field of 5–10 V mm^{-1}, small operating current, and high nonlinear coefficient of 5–8. The high dielectric constant of WO_3-based varistors enables them to act as a varistor in parallel with a capacitor, which is attractive for applications in the elimination of electrical noise of micromotors, protecting contact of delays and absorbing discharges of some circuits. Known experimental facts indicate the complication of electrical properties of tungsten oxide, which depends on fabricating conditions and exhibits many phase transitions in a wide temperature range. A double-Schottky barrier model is introduced to explain the nonlinear behavior of WO_3-doped ceramics. The polarization caused by phase coexistence destroys the stability of electrical properties of WO_3-based varistors. It is a great challenge to improve the stability of the physical properties of WO_3 ceramics; these instable electrical properties of WO_3 ceramics can be successfully eliminated by CeO_2 and other rare earth oxide dopings.

12.1 Introduction

It is known that the barrier voltage of ZnO varistor is 3–4 V with a grain size of about 10 μm and a breakdown voltage of 200–400 V mm^{-1}. The only two ways to decrease the breakdown voltage of varistor devices are to increase the grain size and/or to decrease the thickness of the devices. Therefore, if low breakdown field about 10 V mm^{-1} is required, the grain size must reach as large as 150–200 μm, the thickness of ordinary varistor devices can be decreased to as low as 0.5 mm, which is very difficult to obtain in practice. However, if it is possible to reduce the barrier voltage, varistors with low breakdown voltage can be made easily [1]. However, even in the new kinds of low-voltage varistors developed, such as TiO_2, SnO_2, and $SrTiO_3$, the barrier voltage is greater than 0.4 V in most cases, which is still too high to achieve good low breakdown voltage varistors.

Tungsten trioxide (WO_3) has been used in the electrochromic device [2], toxic gas sensor [3], photocatalytic degradation [4], and others. The electrical properties of WO_3, especially the nonohmic voltage–current characteristic, can

be easily changed by doping some metal oxides [5, 6]. In 1994, Makarov and Trontelj [7] first reported nonlinear current–voltage characteristics of Na_2CO_3 and MnO_2-doped WO_3 ceramics with a nonlinear coefficient about 7 in the current density range from 1 to $10\,mA\,cm^{-2}$ and relatively low breakdown voltage with the value of $6–10\,V\,mm^{-1}$. In addition, the permittivity of WO_3 is higher than that of others [8], such as $SrTiO_3$ and TiO_2.

WO_3-based varistor ceramic is a kind of low-voltage varistor with a low threshold electric field, small operating current, and high nonlinear coefficient, and its high dielectric constant enables them to act as a varistor in parallel with a capacitor, which is attractive for applications in the elimination of electrical noise of micromotors, protecting the contact of delays and absorbing discharges of some circuits. Therefore, WO_3 is a good candidate for capacitor–varistor with a low breakdown voltage and has a good application prospect in the field of microelectronics.

For practical applications, it is important for materials to exhibit stable physical properties in the course of time. Unfortunately, the electrical properties of sintered WO_3 ceramics have been found quite instable. When a constant DC voltage was applied on a WO_3 ceramic sample, the current responded very slowly and its magnitude would decay even by a factor of 10 as the time increases [9]. It is a great challenge to improve the stability of the physical properties of WO_3 ceramics.

12.2 Tungsten Oxide

The main component of WO_3-based varistor system is WO_3. The crystal structure of WO_3 is a distorted perovskite structure that has A cation vacancy in the ABO_3 perovskite structure. Oxygen atoms compose octahedral structure and a tungsten atom in the center of the octahedral [10, 11], as shown in Figure 12.1. Actually, WO_3 does not strictly meet the stoichiometric but always present a different level of oxygen deficiency within the material.

WO_3 crystals are generally formed by corner and edge sharing of WO_6 octahedra. The following phases are obtained by corner sharing: monoclinic II (ε-WO_3), triclinic (δ-WO_3), monoclinic I (γ-WO_3), orthorhombic (β-WO_3), tetragonal (α-WO_3), and cubic WO_3. However, cubic WO_3 is not commonly observed experimentally. The detail of the polyhedral representations of these six structures is shown in Figure 12.2 [11].

In the temperature range of −40 to 740 °C, WO_3 exhibits many phase transitions [12]. Like other metal oxides, WO_3 crystal-phase transitions can take place during annealing and cooling. It has been widely reported that for WO_3, in bulk form, phase transformation occurs in the following sequence [13, 14]: monoclinic II (ε-WO_3, <-43 °C) → triclinic (δ-WO_3, −43 to 17 °C) → monoclinic I (γ-WO_3, 17–330 °C) → orthorhombic (β-WO_3, 330–740 °C) → tetragonal (α-WO_3, >740 °C). The above phase transitions of WO_3 have been reported to be partially reversible. At room temperature, monoclinic I (γ-WO_3) has been reported as the most stable phase, with triclinic (δ-WO_3) also being observed [13]. When annealed at high temperature, WO_3 transforms to other crystal

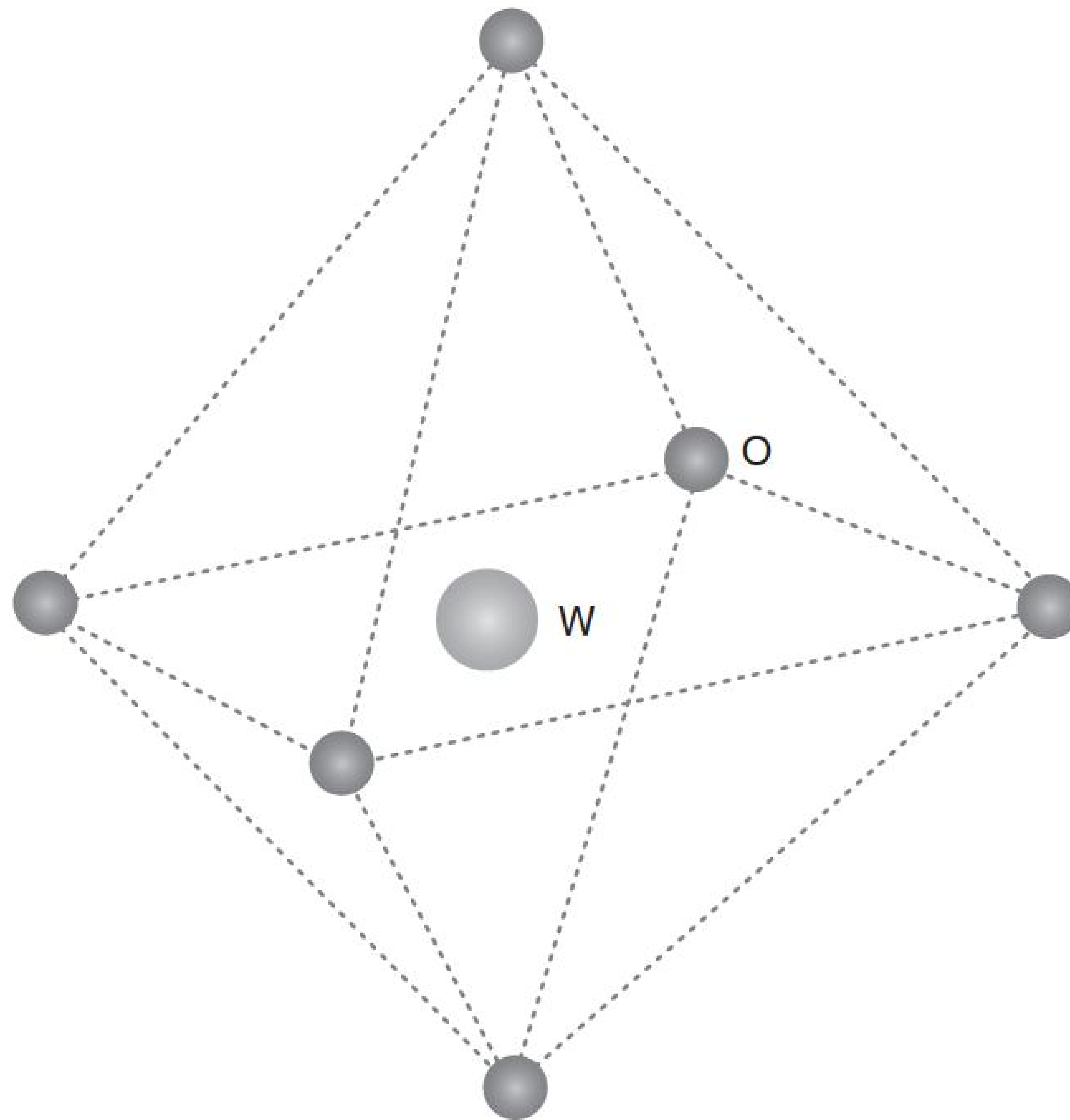


Figure 12.1 Crystal structure of WO_3.

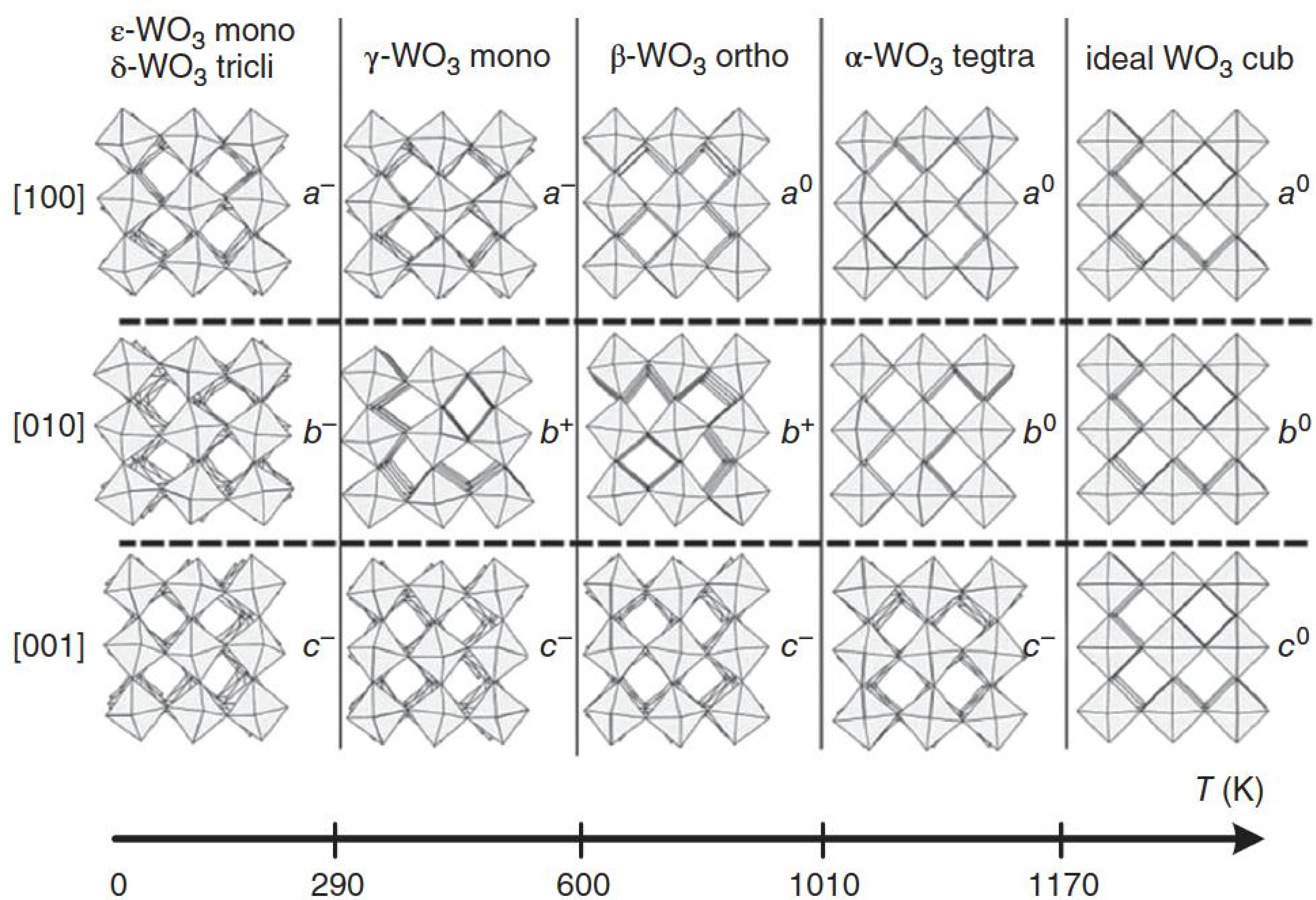


Figure 12.2 Tilt patterns and stability temperature domains of the different polymorphs of WO_3. Source: Roussel et al. 2000 [11]. Reproduced with permission of International Union of Crystallography.

phases (usually β-WO_3 and α-WO_3). However, WO_3 is generally unable to retain these alternate phases when it is returned to room temperature. The monoclinic II phase (ε-WO_3) is only stable at subzero temperature and is thus rarely encountered outside the laboratory [15]. Therefore, usually, unless specified, the term "monoclinic" refers to the monoclinic I phase.

It should be pointed out that the phase transition temperature is related to the cooling or heating history of material. On the other hand, the phase transition temperature is related to the thermal history, and there is an obvious phenomenon of thermal hysteresis. The outer electron configuration of tungsten is $5d^4 6s^2$; therefore, the compounds can present +2, +3, +4, +5, and +6 valences. Often various valences coexist in WO_3. Usually, the oxygen content in the WO_3 does not meet the strict stoichiometric ratio because of different levels of oxygen vacancies, the oxygen loss traverses many intermediary suboxides, WO_{3-x}, with some crystallographic shear planes [16]. Some W^{6+} reduced to W^{5+} ions and form a mixed-valence oxides of W^{5+} and W^{6+}. Moreover, it was found that W^{5+} and W^{6+} exist in all of the crystalline tungsten oxides; for example, $W_{18}O_{49}(=WO_{2.72})$ expressed by $W_8^{6+}W_{10}^{5+}O_{49}$ because of changing valence of tungsten ions [17]. Thus, the known experimental facts [16] indicate the complication of electrical properties of tungsten oxide, which depends on fabricating conditions.

12.3 Preparation of WO_3-Based Varistors

WO_3-based varistor is prepared by conventional ceramic techniques. The traditional preparation of electronic ceramics is also applicable for WO_3-based varistors. The samples are sintered at 1100–1300 °C in air for two hours. The nonlinear coefficient of the voltage–current characteristics of the Al_2O_3-doped WO_3 ceramics increases with sintering temperature and attains the maximum value at 1250 °C [18].

Different from other series of varistor materials, in the case of no additives, WO_3 single-crystal and polycrystalline ceramics already have certain nonlinear voltage–current (V–I) characteristics without any impurities doped because they contain monoclinic and triclinic phases. This illustrates that WO_3 ceramics may have inherent interface states [19]. Sawada and Danielson [20] first observed nonohmic V–I characteristics both in WO_3 single-crystal and polycrystalline ceramics, but the following long period of time, this phenomenon and related issues did not attract attention. Wang et al. [9] found that undoped tungsten oxide exhibits a nonlinear voltage–current characteristic with nonlinear coefficient α about 3.5 from 0.01 to 0.1 mA, and the breakdown voltage is insensitive to the thickness of WO_3 varistor disk. The voltage–current curve of WO_3 ceramics under AC and DC voltages shows different behaviors, the AC response is linear, and the DC one nonlinear. The time of current response to applied DC voltage is very long.

After doping, lower threshold electric field and more significant nonlinear voltage–current characteristic can be obtained. Until 1994, Makarov and Trontelj firstly reported the nonlinear properties of doped WO_3 ceramics [7]. Their

results showed that incorporation of MnO_2 and Na_2CO_3 significantly improved the nonlinear properties of WO_3-based varistors, but the electrical properties are very unstable. As the melting points of sodium tungstate are about 700 °C, the densification of Na, Mn-doped WO_3 ceramics occurs in the presence of a liquid phase, distributed at WO_3 grain boundaries [7]. A better proportion for WO_3–MnO_2–Na_2CO_3–$CoCO_3$ system is 95.5 : 3.0 : 0.5 : 1 (mole fraction). Dopant of Al_2O_3 can improve the electrical stability of WO_3, but in meantime reduce the nonlinear property. The additives for WO_3-based varistor system usually are Na_2CO_3, MnO_2, Co_2O_3, CuO, $SrCO_3$, CeO_2, Al_2O_3, and rare earth oxides. The conductivity of the doped WO_3 ceramics is higher than that of the undoped ones [5].

A general view of the microstructure of the WO_3–0.5Na_2O–4.0MnO_2 ceramics shows that it is composed of an intergranularly cracked matrix of grains with the diameter in the range of 10–20 μm and of a secondary phase on the edges as shown in Figure 12.3 [7]. On the backscattered electron image of the polished cross section, two types of the intergranular phase are distinguished (Figure 12.4) [7]. Energy dispersive X-ray (EDX) analysis shows that the chemical composition of the dark secondary phase corresponds to $MnWO_4$, as already shown by X-ray diffraction (XRD) analysis. The light secondary phase containing Na and W besides O is a mixture of sodium tungstate. According to EDX analysis, the matrix grains contain only W and O [7].

The sintering temperature plays an important role in the nonlinear electrical characteristics and dielectric properties of the ceramics through its influence on the microstructures of samples. The nonlinear coefficient α and the dielectric constant ε increase with the increase in the sintering temperature until it reaches the maximum value at 1150 °C. The varistor of WO_3–0.8 mol% Y_2O_3 composite sintered at 1150 °C has a maximal nonlinear coefficient of 3.5 and a high dielectric constant of 1.13×10^4. However, sintering temperature higher than 1150 °C is not favorable for the nonlinear electrical behavior of the ceramics.

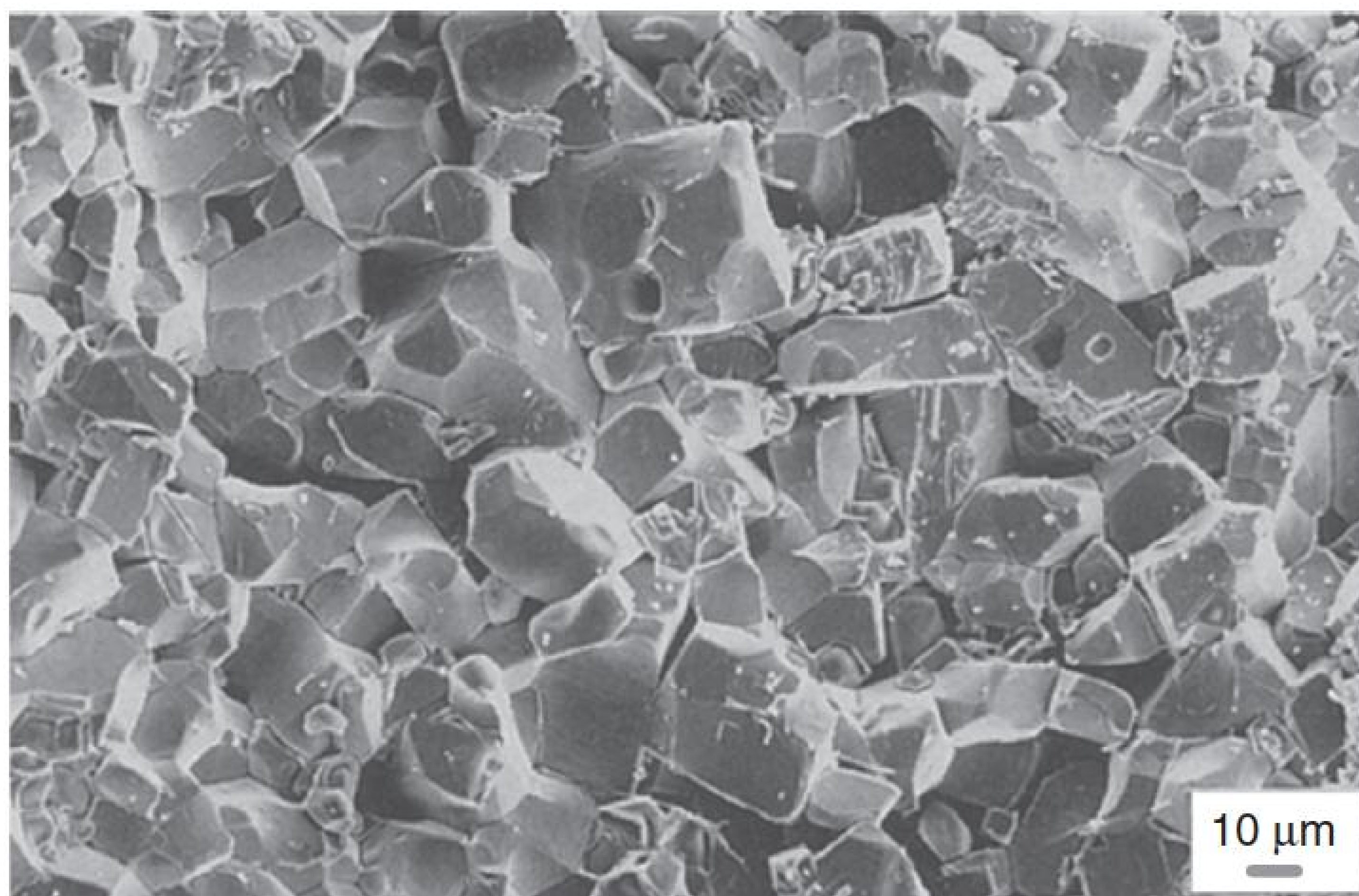


Figure 12.3 A typical SEM micrograph of WO_3–0.5Na_2O–4.0MnO_2 ceramics. Source: Makarov and Trontelj 1994 [7]. Reproduced with permission of Springer.

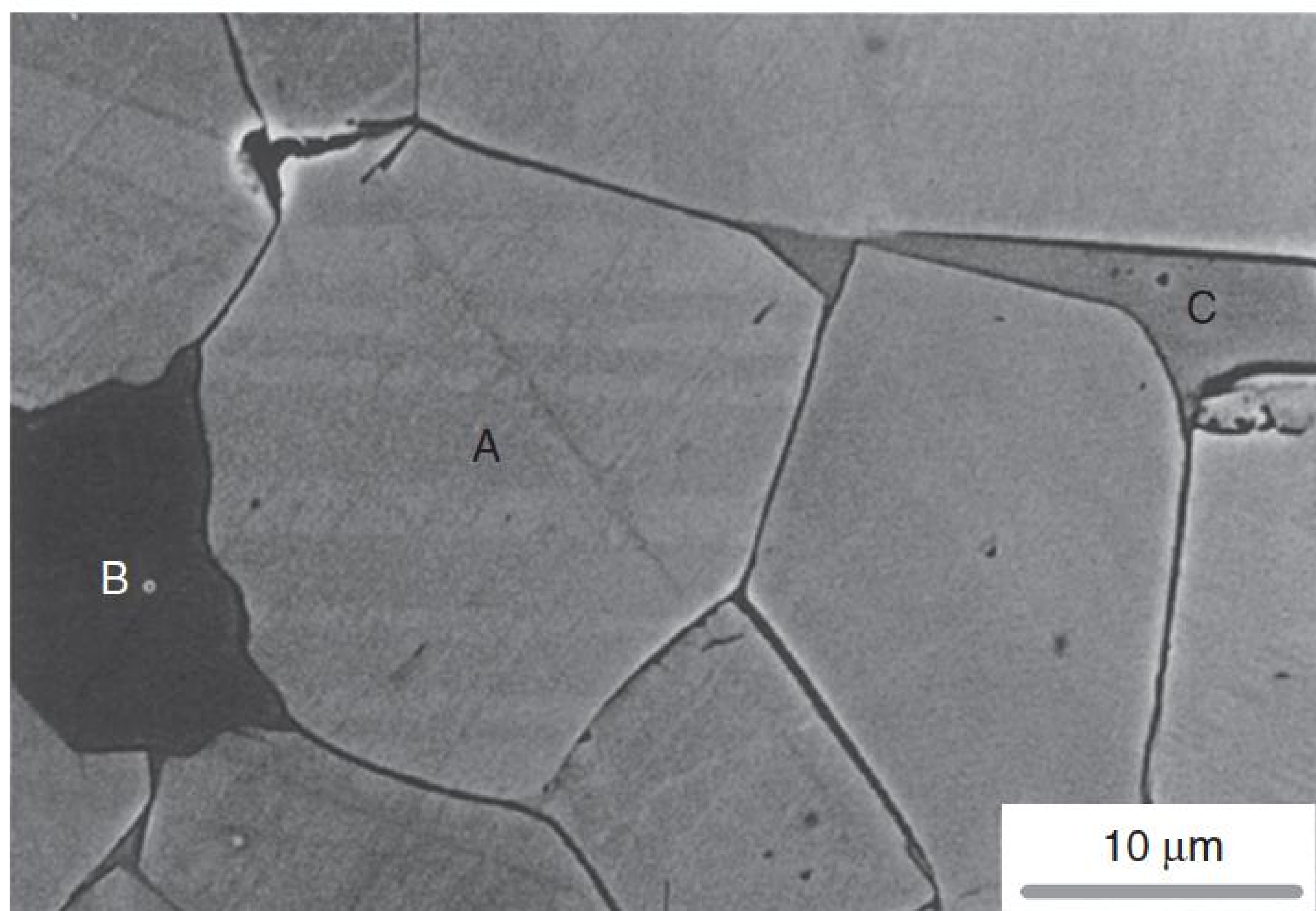


Figure 12.4 SEM micrograph of a polished cross section of a WO_3–0.5Na_2O–4.0MnO_2 ceramics. A, WO_3 grains; B, dark intergranular phase; and C, light intergranular phase. Source: Makarov and Trontelj 1994 [7]. Reproduced with permission of Springer.

The sintering temperature of 1150 °C may be a compromise which leads to the optimum nonlinear properties for the sample of Y_2O_3-doped WO_3 [21].

In addition, new preparation methods can be used to improve the properties of WO_3-based varistors. Wang et al. [22] using RF magnetron sputtering prepared WO_3 thin films on the quartz glass substrates. They found that the films had favorable nonlinear electrical behavior with a nonlinear coefficient of up to 10 or more.

Nanoinitial powder greatly affects the sintering properties of ceramics. The WO_3-based ceramic doped with nano-sized Ce did not change much the nonlinear coefficient, still with a low threshold electric field, but the dielectric constant increased significantly [10].

12.4 Electrical Performances

WO_3-based varistor ceramics developed by Wang et al. [23] were reported to have a nonlinear coefficient of 3–7, breakdown voltage of 3–10 V mm^{-1} [7], and a high dielectric constant [8]. However, compared with the TiO_2-based varistors, WO_3-based varistors have a smaller nonlinear coefficient, lower barrier voltages (~0.04 V) [1], and a higher dielectric constant [24]. WO_3 is a nonstoichiometric n-type semiconductor, and even a very small decrease in oxygen content in WO_3 gives rise to an increase in the electrical conductivity [8]. Yang et al. [25] studied the CeO_2-, Dy_2O_3-, and La_2O_3-doped WO_3 varistor ceramics, which behaved a nonlinear coefficient α of 6.8, but its breakdown electric filed E_b increased to 50.9 V mm^{-1}. The influences of different additives on the electrical performances of WO_3-doped varistors are summarized in Table 12.1. On the whole, the nonlinear coefficient of WO_3-based varistor is in the range of 5–8, and the breakdown electric field is about 5–10 V mm^{-1}.

Table 12.1 Electrical parameters of the WO3-based varistor ceramics.

Dopants	Grain size d (μm)	Breakdown electric filed E_b (V mm^{-1})	Barrier voltage v_b (V)	Nonlinear coefficient α	$\varepsilon(\times 10^4)$ (at 1 kHz)	References
WO_3–CeO_2	7.5–13.8	3.1–50.9	0.04–0.38	1.89–6.83	0.32–0.76	[1]
WO_3–(2–10)Ce_2O_3		3.65–10.4		1.4–3.3	0.3–9.7	[1]
WO_3–Na_2CO_3–(0.5–4)MnO_2	10–20	6–10		7		[7]
WO_3–(0.1–2.5)Gd_2O_3	7.2–12.1	4.9–10.3		2.41–2.56		[10]
WO_3–0.5CuO		6.2		3.7		[18]
WO_3–0.03Pr_6O_{11}		8.8		3.8	7.69	[1]
WO_3–0.5Na_2O	30	9		5.5		[26]
WO_3–0.5Na_2O–0.5Al_2O_3	6	27		5.3		[26]
WO_3–0.5Na_2O–0.5MnO_2	35	6.5		5.8		[26]
WO_3–0.5Na_2O–0.5MnO_2–0.5Al_2O_3	8	27		5.3		[26]

The WO_3-based ceramics have very high dielectric constants up to 10^4–10^5 orders, and the relative dielectric constants were found to decrease significantly with an increase in frequency from 40 Hz to about 10 kHz, whereas in the higher frequency range of 10 kHz–15 MHz, the dielectric constants of the ceramics were almost unchanged, which is very useful for application in the high-frequency region [27]. According to the theoretical analysis [28], the relative dielectric constant is expected to change rapidly near the relaxation frequency, which means the relaxation frequencies of the varistors are lower than 100 Hz. The high-temperature activation energies for conduction in WO_3-based ceramics were estimated to be 0.08–0.27 eV [29]. The high dielectric constant makes WO_3-based ceramics suitable for ceramic capacitor. These imply that WO_3 is a good candidate for capacitor–varistor ceramics with a low breakdown voltage.

12.5 Improving the Electrical Stability

The electrical stability is a problem in making WO_3 as a varistor material in practice [30]. Previous studies [9] indicated that the electrical behavior of sintered WO3 ceramics is instable and has a serious hysteresis effect; that is, the current under constant voltage decays with time, and the voltage–current characteristics depend on the electrical history of the ceramics. Compared with ZnO varistor materials, repeated V–I curves of the WO_3 are not good, and there are serious electrical relaxation phenomena in constant voltage–current decay with time [9].

The electrical instability of WO_3 originates from the coexistence of the two phases. Generally, instable properties derive from the polarization of grains caused by phase coexistence of δ-WO_3 and γ-WO_3 in the sintering process of WO_3 varistor ceramics [9]. As shown in Figure 12.2, WO_3 has at least five kinds of structural phase transitions with the increase in temperature, the crystal structure corresponds to the low-temperature monoclinic phase, triclinic phase, room temperature monoclinic, orthorhombic phase, and tetragonal phase. However, there is an obvious thermal hysteresis effect that the phase transition temperature is related to the thermal history of the material. Therefore, many works showed that in the sintering of WO_3 ceramics, the triclinic phase and monoclinic phase coexist [8, 9]. The polarization caused by phase coexistence destroys the stability of electrical properties. Therefore, how to simplify the phase structure of the WO_3-based varistors to stabilize the electrical properties has become the main problem to be solved.

It was discovered that in the WO_3–MnO_2–Na_2CO_3 system, incorporating Al_2O_3 can improve the electrical stability but suppressing the nonlinearity at the same time [19]. However, experimental results showed that [30] adding rare earth oxides to WO_3 varistors not only made a single monoclinic phase of WO_3 but also the electric performance became stable and promoted the nonlinearity. After doping with Gd_2O_3, the voltage–current characteristics of WO_3 varistors still shows a certain nonlinearity (α ~2.5), and the stability of the samples at low field is not damaged.

It was reported [1] that this instable electrical properties of WO^+ ceramics could be successfully eliminated by CeO_2 doping. In addition, its electrical

properties in low electrical field were also stable, which indicates the ion migration in the depletion layer is ignorable. From this point of view, WO_3 has its own preponderance as a kind of low-voltage varistor. This is benefited from its monophase structure characteristic when CeO_2 is doped, and then stable electrical properties are obtained. Also, WO_3 (tungsten trioxide)-based varistors doped with CeO_2 result in stable electrical properties under a high electric field, which is different from coexistence of monoclinic and triclinic phases of WO_3 in undoped WO_3 ceramics, indicating that the form of triclinic phase WO_3 is effectively depressed by doping CeO_2. Moreover, the effect of CeO_2 on phase structure of WO_3 is insensitive to the concentration of CeO_2. The nonlinear coefficient was not high, but the barrier voltage was extremely low with the value of about 0.04 V for the sample containing 2 mol% CeO_2. Small dopant ratio can inhibit the grain growth and large dopant ratio can promote the grain growth.

The EDX results revealed that the cerium element was absent in the grain regions but segregated to the grain boundaries. This result indicated that the Ce ions dissolved only slightly in the WO_3 grains during the sintering process forming an intergranular Ce-rich phase between the WO_3 grains [1].

There is only a monoclinic phase of WO_3 existing in rare earth element-doped WO_3 ceramics, indicating that the formation of triclinic phase of WO_3 is effectively inhibited by doping rare earth elements, such as Gd_2O_3 [31], V_2O_5, and Ta_2O_5 [32]. Doping Gd_2O_3 in WO_3 can improve its electrical stability, either under high electrical field or under low electrical field, which is related to its monophase structure characteristic. The electrical properties under low electrical field of Gd_2O_3-doped WO_3 ceramics are also stable, indicating that ion migration in the depletion layer can be ignorable [10].

Obviously, electrical stability is in favor of practical use of the WO_3 ceramic. It is known that the electrical degradation phenomenon is also observed in the ZnO varistor under a low electrical field. It is assumed that the degradation is a grain boundary phenomenon and is the result of ion migration in the depletion layer [33, 34].

12.6 Mechanism Model of WO_3-Based Varistors

The characteristics and mechanism of WO_3-based varistors have been widely studied [1, 7, 35–40]. To explain the nonlinear behavior of WO_3-doped ceramics, the double-Schottky barrier model was introduced by an analogy to the grain boundary defect model for ZnO varistors [1]. Compared with traditional ZnO- and SnO_2-based varistor ceramics, the property of WO_3 varistor is different, even undoped WO_3 ceramics have pronounced varistor properties. The varistor behaviors of ZnO-based and SnO_2-based varistor ceramics are caused by grain boundary doping, rather than the inherent characteristics of ceramics. Although because of the absence of grain boundary precipitates in the WO_3 ceramics, the occurrence of the grain boundary Schottky barrier may originate from the intrinsic interface states in the WO_3 ceramics [19].

The normally sintered WO_3 ceramics have significant nonlinear characteristics, whereas the samples through high-temperature quenching show no

nonlinear behavior. However, the nonlinear behavior could be restored if the quenched ceramic samples are thermally treated in oxygen-rich conditions. This indicates that the oxygen plays a key role in the formation of the nonlinear behavior of WO_3 ceramics, and in hypoxic conditions, WO_3 ceramics cannot generate nonlinear characteristics [30]. After heat treatment, WO_3 grain surface can present high levels of oxygen vacancy (V_O^+ and V_O^{2+}) very easily, which are active oxygen adsorption sites, and in the cooling process, to be able to enrich oxygen in the form of chemical adsorption on the grain surfaces [35]. The emergence of oxygen vacancies on the grain surface leads to the combination of electronic or electronic pairs around W ions; thus, the grain surface presents low reduction valent of W ions (W^{4+}, W^{5+}) [1]. Under the interaction of oxygen vacancies on the grain surface and reduction state of W ions, the grain surfaces adsorb oxygens to form interface states and then form the Schottky barriers at the grain boundaries, which is the origin of the behavior of WO_3 varistor ceramics. The following reaction illustrates the process [40]:



$$O + S \rightarrow O_{ad} \tag{12.1}$$



$$W^{4+} + O_{ad} \rightarrow W^{5+} + O^- \tag{12.2}$$



$$W^{5+} + O_{ad} \rightarrow W^{6+} + O^- \tag{12.3}$$



$$W^{5+} + O^- \rightarrow W^{6+} + O^{2-} \tag{12.4}$$

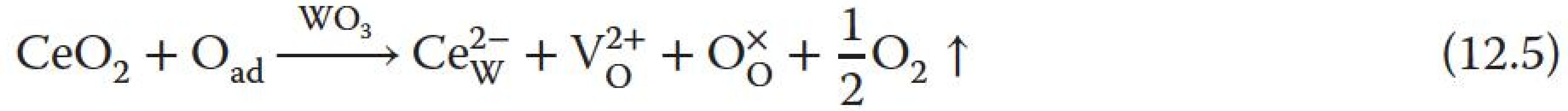
where S represents oxygen vacancies (V_O^+, V_O^{2+}) and O_{ad} is the adsorbed oxygen. The oxygen adsorbed on the grain surface combines with the electronics inside the grain and forms interface states at the grain surface. The oxygen vacancies form an electron depletion layer at the grain boundary, which forms the Schottky barrier at the grain boundary. The interface state of the barrier is mainly composed of adsorbed O^{2-} and O^-, whereas the depletion layer is composed of V_O^+ and V_O^{2+}. The effect of grain boundary barrier makes the WO_3 ceramics exhibit the nonlinear properties [40].

The AES spectra show that the surface of the ceramic grains presents excessive oxygen [40], which is the result of oxygen adsorption in the quenching process. The result of AES depth analysis of a single WO_3 grain shows that the W and O concentration ratio is 1:4 on the surface of grains and meet the stoichiometric ratio of WO_3, W, and O ion concentration ratio is 1:3, that is to say the excessive oxygen ions exist at the grain surface in adsorption state. With the increase in the sputtering depth, the oxygen content decreases gradually, and the equilibrium value reaches at 2–3 nm, which shows that there are about three to four oxygen adsorption layers on the surface of the grain [18]. These adsorbed oxygen layers interact with the electrons from the WO_3 grains to form the interface states on the grain surface and then form the Schottky barriers at the grain boundaries, which is the origin of the behavior of WO_3 varistor ceramics.

Impedance spectroscopy analysis [39], which provides further evidence, shows that the high-resistance grain boundary layer exists in the ceramics with non-linear performance but does not exist in the ceramics without nonlinear performance. A grain boundary layer with high resistance is formed in ceramic cooling process, when the production and migration of nonequilibrium defects inside

and outside the grains occur. Then, under the effect of oxygen adsorption on the grain surface, the high resistivity layer forms. Because of this huge feature difference in the resistance of grain outside and inside, an electronic barrier forms in the grain boundary.

In the WO_3 ceramics doped with CeO_2, the possible substitution equations are [1]



$$CeO_2 + O_{ad} \xrightarrow{WO_3} Ce_W^{2-} + V_O^{2+} + O_O^{\times} + \frac{1}{2}O_2 \uparrow \tag{12.5}$$



$$2WO_3 \rightarrow 2W_W^{-} + V_O^{2+} + O_O^{\times} + \frac{5}{2}O_2 \uparrow \tag{12.6}$$

Oxygen in the above equation will be partly absorbed at the WO_3 grain boundaries and reacts with Ce_W^{2-} according to the following reactions [1]:



$$\frac{1}{2}O_2 \rightarrow O_{ad}^{\times} \tag{12.7}$$



$$2O_{ad}^{\times} + Ce_W^{2-} \rightarrow 2O^{-} + Ce_W^{\times} \tag{12.8}$$



$$O_{ad}^{\times} + Ce_W^{2-} \rightarrow O^{2-} + Ce_W^{\times} \tag{12.9}$$

The positive charges (W^{5+}, V_O^{2+}) are located on both sides of the grain boundary, and the negative charges (Ce_W^{2-}, W_W^{-}, O^{-}, O^{2-}) are distributed at the grain boundary interfaces. Because of the charge compensation between the positive and the negative charges, a depletion layer is created at the grain boundary [41, 42]. As a result, the Schottky barrier is formed, leading to the nonlinear electrical behavior of CeO_2-doped WO_3 [1].

The other obvious effect is that the permittivity of doped samples is higher than that of pure WO_3 [1]. The permittivity increases as the concentration of CeO_2 increases and reaches the maximum at 0.5 mol% and decreases with a further increase in the concentration of CeO_2. Neither grain nor the grain boundary material can account for the ultrahigh value. The high permittivity of the ceramic comes from the fact that the resistivity of grains is much lower than that of the grain boundary layers, so the entire voltage is sustained across the narrow intergranular region, as pointed by Li et al. [43]. The thickness of grain boundary of the doped samples is lower than that of pure WO_3. It can be deduced that the increase in permittivity of WO_3 ceramic is attributed to the decrease in the thickness of grain boundary.

Analysts believed that [36, 37] the difference of WO_3, TiO_2 ceramics, and traditional ZnO, SnO_2 varistor ceramics on mechanisms leads to the different characteristics of their varistor properties. The nonlinear properties of ZnO- and SnO_2-based varistors originated from the Schottky barrier generated by the precipitate-doped transition metals in the grain boundary, and usually, this kind of barrier is relatively higher (about 1 eV) [1, 38]; therefore, their varistor performance is superior. The nonlinear behavior of WO_3 ceramic materials may originate from the barrier caused by the existed difference of resistivity between the grain surface and grain internal, and this kind of barrier is relatively lower (about 0.25 eV) [37]; therefore, the nonlinear coefficient and the threshold electric field are low.

12.7 Doping Effects

WO_3-based ceramics present an intrinsic varistor behavior. The addition of electron donor and acceptor dopants and heat treatments in different atmospheres also alter the nonlinear properties of these systems, as they affect the formation of the Schottky barrier [44–70].

The influences of Na_2O, MnO_2, Al_2O_3, Co_3O_4, BaO, NiO, and Fe_2O_3 additions on the electrical properties and the microstructure of WO_3-based ceramics were summarized [29]. The effect of the addition of small amounts of Li_2O, V_2O_5, Co_2O_3, and La_2O_3 on the conductivity of WO_3 ceramics were studied by Kaneki et al. [5]. All of these oxides were found to increase the conductivity of WO_3 ceramics. The electrical conductivity of tungsten oxide ceramics strongly depends on the oxide additives. It reaches a minimum value of $9 \times 10^{-7}\ \Omega^{-1}\ cm^{-1}$ for the WO_3–Na_2O system [45].

Previous results showed that Na_2CO_3 and MnO_2, no matter individually doped or codoped with other oxides together, can play a modification role [26]. However, Co cannot improve the nonlinearity when doped alone, but when codoped with others, it can improve the nonlinear performance of WO_3-based varistors. Bi can keep the nonlinearity of WO_3 ceramics if doped alone, but make the original nonlinearity lost completely for the WO_3–Na_2CO_3–MnO_2 system [6, 9]. These show that a strong synergy relationship exists among kinds of dopants, and the influence on nonlinear electrical property is not a simple superposition.

12.7.1 The Addition of Rare Earth Oxides

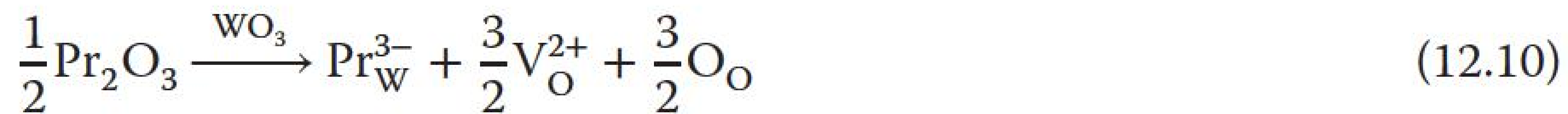
Doping rare earth oxides in WO_3 ceramics can influence the growth of the grains. As dopants, rare earth elements mainly segregate at the grain boundaries [10]. A low concentration of Gd or Ce can inhibit the grain growth and a high concentration can promote the grain growth [32]. Both Dy and La can promote the grain growth [26]. Only Yb inhibits the grain growth. The grain size of WO_3 varistors doped with rare earth oxides is in the range of 10–20 μm for most of the samples [10]. There are some porous slice-shaped materials in the Dy-doped samples and club-shaped materials in the La-doped samples. It is believed that the slice-shaped materials (Dy-rich phase) are amorphous with a weak conductivity to form the Schottky barrier [10]. However, the club-shaped materials (La-rich phase) are in the crystalline state with a good conductivity, so that the barrier is broken down, leading to the nearly linear voltage–current characteristics [10].

Doping of rare earth oxides cannot obviously increase the nonlinear coefficient of WO_3. The nonlinear coefficient is in the range of 2–5 [10]. Wang et al. [46] found that Tb_4O_7-doped WO_3 ceramics exhibit nonlinear electrical properties at ambient temperature in the range of 300–500 °C [10] under continuous DC field, and the nonlinear coefficient α is around 4 for the sample with the atom ratio of W to Tb 95/5 in the current density range of 1–0.1 mA cm^{-2}. The nonlinear coefficient of Gd_2O_3-doped varistor is about 2.5, but the barrier voltage is very low with the value of about 0.06 V [31].

Dai et al. [47] studied the effect of Y_2O_3 dopant and found that when the incorporation of Y_2O_3 is 0.8 mol%, the nonlinear coefficient reaches the maximum of

3.16. On the other hand, doping of rare earth oxides can obviously increase the dielectric constant of WO_3 ceramics, about one order of magnitude on the whole. High dielectric constant makes it more suitable as a capacitor–varistor material [10]. The doping of Gd_2O_3 in WO_3 largely increases the dielectric constant ε_r of the ceramics to about 22 700 at 1 kHz [31], a more higher value of 1.16×10^4 was reported as 1.2 mol% Y_2O_3 was doped [47].

Doping Pr_6O_{11} can reduce the breakdown voltage and barrier voltage of Pr_6O_{11}-doped WO_3 to a very low level. The WO_3–0.03 mol% Pr_6O_{11} ceramics present a nonlinear coefficient of 3.8, a low breakdown voltage of 8.8 V mm^{-1}, and a high dielectric constant of 7.69×10^4 at 1 kHz [23]. Considering that Pr^{3+} has a larger ionic radius and a smaller valence than W^{6+}, Pr_6O_{11} dopant as a substantial acceptor could be estimated when doped in a WO_3-based varistor [23]. The doping of Pr_6O_{11} leads to the increase in the donor density (N_d) and the interface states density (N_t) [23]. The barrier height increases with an increase in N_t. The depletion layer width (t) calculated from N_d and N_t decreases from 18.2 to 8.9 nm. The highest grain boundary barrier occurs in WO_3–0.03 mol% Pr_6O_{11}, which is consistent with the best nonlinear electrical properties for this composition. During sintering, Pr_6O_{11} is decomposed to Pr_2O_3. Although Pr^{3+} has much larger radius (0.099 nm) than that of W^{6+} (0.060 nm), it remains the possibility for a limited substitution, such as the following defect equation [23]:



$$\frac{1}{2}Pr_2O_3 \xrightarrow{WO_3} Pr_W^{3-} + \frac{3}{2}V_O^{2+} + \frac{3}{2}O_O \tag{12.10}$$

When a Pr^{3+} diffuses into the WO_3 lattice and occupies the W^{6+} site, three negative charges are presented. Then, oxygen vacancies (V_O^{2+}) are created for the electric charge balance. As the doping content of Pr^{3+} increases, more oxygen vacancies will be created. They increase the electron-hopping probability and increase the conductivity in grains. However, Pr^{3+} shows a limited substitution because it has a larger ionic radius and a lower valence than the W^{6+}. Most Pr^{3+} ions segregate at the WO_3 grain boundary to relieve the elastic strain energy and thus increase the grain boundary resistivity by acting as acceptors. They block the formation and transportation of electrons and defects. Owing to the above two reasons, the sample doped with 0.03 mol% Pr_6O_{11} behaves the most effective boundary barrier layer [23].

Overall, WO_3 ceramics doped with rare earth elements have low breakdown voltage and barrier voltage, indicating that WO_3 is more suitable for low voltage capacitor–varistor [10].

12.7.2 The Addition of CuO

Zhao et al. [18] studied the effects of CuO addition on the microstructure and electrical properties of the WO_3 varistors. The results indicate that the minor addition of CuO promotes the densification and grain growth of WO_3 ceramics. From the V–I measurements, the samples present a linear voltage–current characteristic and the resistivity is quite low when doping 0.2 mol% CuO. A further increase in the CuO content can recover the nonlinear electrical property because

the excessive CuO precipitates in the grain boundary and formed n–p–n-type double-Schottky barriers.

The ionic radius of Cu^{2+} is 0.72 nm and that of W^{6+} is about 0.62 nm, both approaches. In addition, Cu^{2+} as a two-valence ion combines with oxygen ions to form a symmetrical structure; therefore, with respect to W^{6+}, Cu^{2+} is more likely to bind with oxygen ions [18]. During the sintering process, Cu^{2+} ions can be easily replaced by W^{6+} ions in the WO_3 lattice:



$$CuO \xrightarrow{WO_3} Cu_W^{4-} + 2V_O^{2+} \tag{12.11}$$

As the above reaction occurs mainly at the grain boundary surface, the resulting interstitial W^{6+} can recombine with oxygen ions at the sintering temperature to form tungsten oxide on the new lattice point, so the grain size of tungsten oxide ceramics increases obviously. The defect produced by the reaction is helpful to the mass transfer inside the ceramic disk, and the relative density of the ceramic disk increases obviously, too. At the same time, a large number of defects produced by the reaction will destroy the oxygen adsorption layer on the grain boundary, thus greatly reduce the resistance of the tungsten oxide ceramics.

With the increase in the doping amount, the excessive CuO is segregated on the grain surface [18]. The segregated CuO hinders the migration of ions in the ceramics, which shows that the density of tungsten oxide ceramics decreases. WO_3 is a nonstoichiometric n-type semiconductor, and CuO is a nonstoichiometric p-type semiconductor material with the characteristics of excessive oxygen. The segregation of the p-type semiconductor at the grain boundaries leads to the formation of the nonlinear electrical behavior, which is caused by the double-Schottky barrier with n–p–n bonding formed between grain and grain boundary. In the electrical performance, the resistivity increases greatly, and the nonlinear electrical behavior is improved with the increase in the doping amount [18].

12.7.3 The Addition of Al_2O_3

Al_2O_3, either by individually doping or codoping, is generally detrimental to the nonlinear performance [6]. Codoping Al_2O_3 with Co_3O_4, MnO_2, and Na_2O promotes better densification [45, 48]. Usually, the addition of Na_2O ensures liquid-phase sintering and shifts the onset of sintering to lower temperatures, whereas the addition of Al_2O_3 shifts the onset of sintering to a higher temperature, compared with pure WO_3. The addition of Al_2O_3 inhibits the grain growth in WO_3, but all other additives enhanced the grain growth.

The influence of Al_2O_3 additive on the electrical properties and microstructure of Na- and Mn-doped WO_3 ceramics was studied [18]. Addition of Al_2O_3 shifts the voltage–current characteristics to higher field and inhibits the grain growth. The conductivity decreases as the concentration of Al_2O_3 increases, but the nonlinear coefficient decreases with the addition of Al_2O_3. The small addition of Al_2O_3 of about 0.5 mol% is an optimal.

12.7.4 The Addition of TiO_2

The addition of TiO_2 into WO_3 obviously reduces the grain size of the WO_3 ceramics, improves the density, and evidently improves the electrical conductivity of the WO_3 ceramics by about two orders of magnitude [49]. According to the work reported by Komornicki et al. [50], the solubility limit of TiO_2 in WO_3 is ~0.35 mol%. Thus, the oxygen vacancies introduced by the addition of TiO_2 improve the electronic concentration in WO_3, responsible for the enhanced electrical conductivity. Besides, the mobility of the carriers is strongly influenced by the disorder present in the materials and by impurity doping [51]. It is reported [15] that the electrical conductivity of WO_3 decreases because of an increasing volume of the grain boundaries, which contributes to more trapping and scattering of free charge carriers. With the increase of TiO_2 content in WO_3, the fraction of the small grain decreases, resulting in reducing the volume of the grain boundaries, which can explain the increment of the electrical conductivity of the doped samples with an increase in the concentration of TiO_2 [52].

Doping WO_3 with TiO_2 also enhances the absolute value of Seebeck coefficient [49], in the temperature range from 473 to 1023 K, to make the sample have better thermoelectric property because of the small grain size (as shown in Figure 12.5), which has been reported by Park et al. [52] in TiO_2-doped ZnO ceramics.

12.7.5 The Addition of Other Additives

WO_3–Na_2CO_3–CuO/CdO/Bi_2O_3/Sb_2O_3, as well as its nonlinear properties and dielectric properties, was described [27]. The samples doped with CdO and Bi_2O_3 has the largest and lowest resistivity, respectively, at a high frequency. The lowest breakdown electrical field may be related to the lowest resistivity of WO_3 grain boundaries in the sample doped with Bi_2O_3. It is found that Bi_2O_3 is not helpful to improve the nonlinearity of the WO_3–Na_2CO_3–MnO_2 varistor system, even

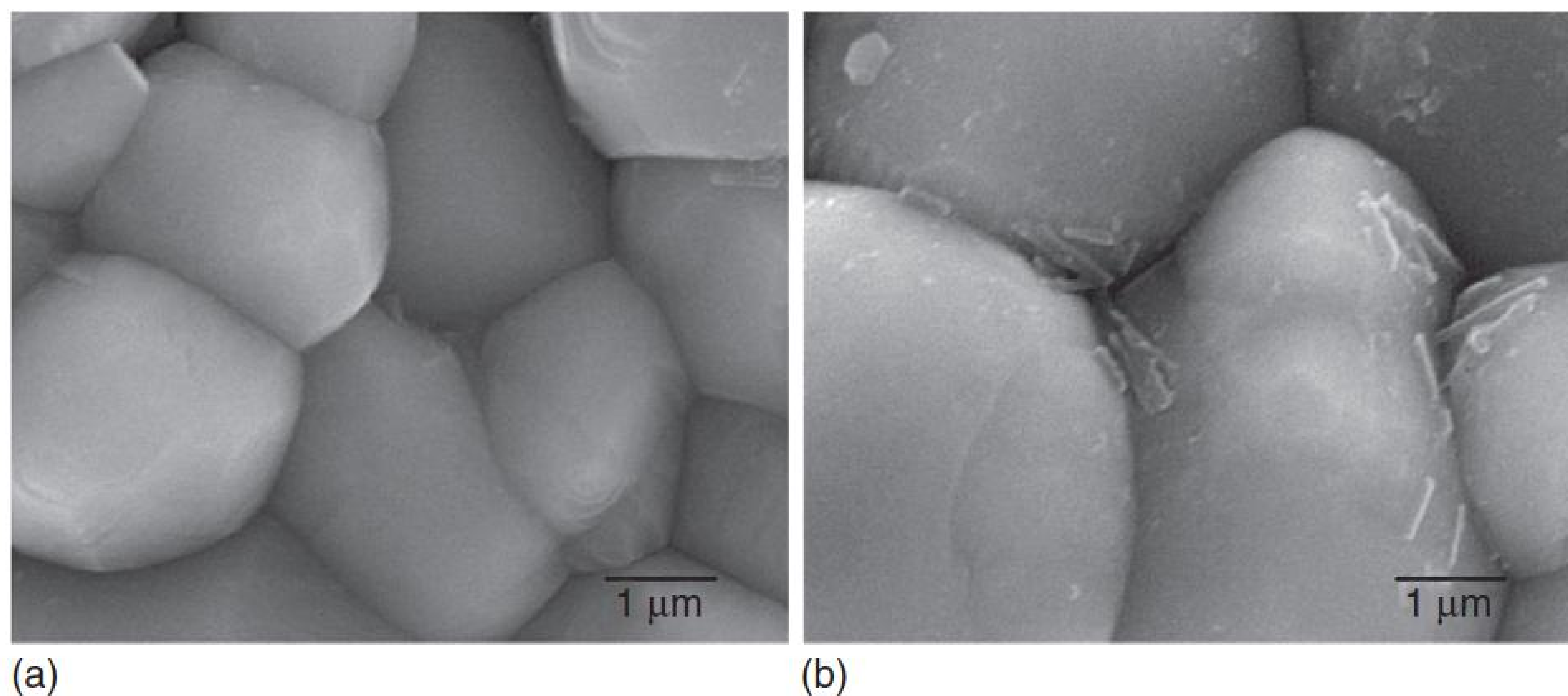


Figure 12.5 The micrographs of WO_3 varistor sample doped with (a) 0.1 and (b) 0.5 mol% TiO2. Source: Wang et al. 2012 [49]. Reproduced with permission of Springer.

harmful when the amount of Bi_2O_3 is increased to 4 mol% [6]. Doping of Co_2O_3 can improve the nonlinearity, with α about 6 and breakdown field about 5 V mm^{-1} when the amount of Co_2O_3 is 1 mol%. Doping with 0.5 mol% Al_2O_3, the nonlinearity is significantly improved at 200 °C, and it is an ohmic resistor at room temperature [6].

Yang and coworkers [46] prepared Sr-doped WO_3 varistor system and found that when mixed with 0.2 mol% Sr, the nonlinear coefficient reached 8.7, but electrical instability occurred.

References

1 Yang, X.S., Wang, Y., Dong, L. et al. (2004). Effect of CeO_2 on the microstructure and electrical properties of WO_3 capacitor–varistor ceramics. *Materials Science and Engineering B* 110 (1): 6–10.

2 Granqvist, C.G. (2000). Electrochromic tungsten oxide films: review of progress 1993–1998. *Solar Energy Materials and Solar Cells* 60 (3): 201–262.

3 Penza, M., Tagliente, M.A., Mirenghi, L. et al. (1998). Tungsten trioxide (WO_3) sputtered thin films for a NO_x gas sensor. *Sensors and Actuators B: Chemical* 50 (1): 9–18.

4 Wang, H., Xu, P., and Wang, T. (2002). The preparation and properties study of photocatalytic nanocrystalline/nanoporous WO_3 thin films. *Materials and Design* 23 (3): 331–336.

5 Kaneki, N., Hara, H., Shimada, K., and Shmzu, T. (1976). Effect of atmosphere on resistivity of WO_3 ceramics. *Journal of the American Ceramic Society* 59 (7–8): 368–369.

6 Wang, Y., Aburas, Z., Yao, K.L., and Liu, Z.L. (1999). Effects of doping and temperature on nonlinearity of WO_3 varistor. *Materials Chemistry and Physics* 58 (1): 51–54.

7 Makarov, V. and Trontelj, M. (1994). Novel varistor material based on tungsten oxide. *Journal of Materials Science Letters* 13 (13): 937–939.

8 Souza Filho, A.G., Matias, J.G.N., Dias, N.L. et al. (1999). Microstructural and electrical properties of sintered tungsten trioxide. *Journal of Materials Science* 34 (5): 1031–1035.

9 Wang, Y., Yao, K.L., and Liu, Z.L. (2001). Novel nonlinear current-voltage characteristics of sintered tungsten oxide. *Journal of Materials Science Letters* 20 (18): 1741–1743.

10 Yang, X.S. (2004). Study on the electrical properties and related problems of tungsten trioxide-based functional ceramics doped with rare earth elements. Master degree thesis. Wuhan, China: Huazhong University of Science and Technology.

11 Roussel, P., Labbe, P., and Groult, D. (2000). Symmetry and twins in the monophosphate tungsten bronze series $(PO_2)_4(WO_3)_{2m}$ $(2 \leq m \leq 14)$. *Acta Crystallographica Section B: Structural Science* 56 (3): 377–391.

12 Hirose, T. (1980). Structural phase transitions and semiconductor-metal transition in WO_3. *Journal of the Physical Society of Japan* 49 (2): 562–568.

13 Salje, E.K., Rehmann, S., Pobell, F. et al. (1997). Crystal structure and paramagnetic behaviour of ε-WO_{3-x}. *Journal of Physics: Condensed Matter* 9 (31): 6563.

14 Vogt, T., Woodward, P.M., and Hunter, B.A. (1999). The high-temperature phases of WO_3. *Journal of Solid State Chemistry* 144 (1): 209–215.

15 Zheng, H., Ou, J.Z., Strano, M.S. et al. (2011). Nanostructured tungsten oxide–properties, synthesis, and applications. *Advanced Functional Materials* 21 (12): 2175–2196.

16 Sahle, W. and Nygren, M. (1983). Electrical conductivity and high resolution electron microscopy studies of WO_{3-x} crystals with $0 \leq x \leq 0.28$. *Journal of Solid State Chemistry* 48 (2): 154–160.

17 Salje, E., Carley, A.F., and Roberts, M.W. (1979). The effect of reduction and temperature on the electronic core levels of tungsten and molybdenum in WO_3 and $W_xMo_{1-x}O_3$—a photoelectron spectroscopic study. *Journal of Solid State Chemistry* 29 (2): 237–251.

18 Zhao, H.W., Hua, Z.Q., Li, T.Y. et al. (2009). Effect of CuO doping on the microstructure and electrical properties of WO_3 varistors. *Journal of Functional Materials* 40 (12): 2004–2007.

19 Zakria, A., Yu, W., and Yao, K. (1999). Studies on fabrication conditions and doping of new low voltage WO_3-based varistor. *Journal of Functional Materials* 30 (3): 299–301.

20 Sawada, S. and Danielson, G.C. (1959). Optical indices of refraction of WO_3. *Physical Review* 113 (4): 1008–1013.

21 Tianguo, W., Gangqin, S., Xibao, L., and Wenjun, Z. (2009). Effect of sintering temperature on electrical properties of WO_3-based capacitor-varistor ceramics. *Rare Metal Materials and Engineering* 38: 329–332.

22 Wang, Y., Chen, M., Yang, X.S. et al. (2003). Nonlinear electrical property of WO_3 thin film fabricated by RF sputtering technique. *Journal of Functional Materials and Devices* 9 (1): 31–33.

23 Wang, T.G., Shao, G.Q., Zhang, W.J. et al. (2010). Electrical properties of Pr_6O_{11}-doped WO_3 capacitor–varistor ceramics. *Ceramics International* 36 (3): 1063–1067.

24 Tilley, R.J.D. (1977). Correlation between dielectric constant and defect structure of non-stoichiometric solids. *Nature* 269 (5625): 229.

25 Yang, X.S., Wang, Y., and Zhao, Y. (2006). Effect of Dy_2O_3 and La_2O_3 on the microstructure and electrical properties of WO_3 ceramics. *Materials Chemistry and Physics* 98 (2–3): 225–230.

26 Makarov, V.O. and Trontelj, M. (2000). Effect of Al_2O_3 on the microstructure and electrical properties of WO_3-based varistor ceramics. *Journal of the European Ceramic Society* 20 (6): 747–749.

27 Zang, G.Z., Wang, J.F., Chen, H.C. et al. (2004). Nonlinear electrical behaviour of the WO_3-based system. *Journal of Materials Science* 39 (13): 4373–4374.

28 Wu, J.M. and Chen, C.J. (1988). Dielectric properties of (Ba, Nb) doped TiO_2 ceramics: migration mechanism and roles of (Ba, Nb). *Journal of Materials Science* 23 (11): 4157–4164.

29 Makarov, V.O. (1997). Nonlinear electrical behaviour of WO_3-based ceramics. *Neorganicheskie Materialy* 33 (10): 1273–1275.

30 Yang, X.S., Wang, Y., and Dong, L. (2003). Low breakdown voltage WO_3-based capacitor-varistor and its stability. *Electronic Components and Materials* 22 (9): 22–23, 26.

31 Yang, X.S., Wang, Y., and Dong, L. (2004). WO_3-based capacitor–varistor doped with Gd_2O_3. *Materials Chemistry and Physics* 86 (2–3): 253–257.

32 Zhang, L.M., Wang, Y., and Dong, L. (2007). Electrical properties of WO_3 ceramics doped with V_2O_5 and Ta_2O_5. *Electrical Engineering Materials* 24 (3): 27–29.

33 Gupta, T.K. (1990). Application of zinc oxide varistors. *Journal of the American Ceramic Society* 73 (7): 1817–1840.

34 Gupta, T.K. and Carlson, W.G. (1985). A grain-boundary defect model for instability/stability of a ZnO varistor. *Journal of Materials Science* 20 (10): 3487–3500.

35 Jimenez, I., Arbiol, J., Dezanneau, G. et al. (2003). Crystalline structure, defects and gas sensor response to NO_2 and H_2S of tungsten trioxide nanopowders. *Sensors and Actuators B: Chemical* 93 (1–3): 475–485.

36 Yang, S.L. and Wu, J.M. (1995). Effects of Nb_2O_5 in (Ba, Bi, Nb)-added TiO_2 ceramic varistors. *Journal of Materials Research* 10 (2): 345–352.

37 Mantas, P.Q. and Baptista, J.L. (1995). The barrier height formation in ZnO varistors. *Journal of the European Ceramic Society* 15 (7): 605–615.

38 Bueno, P.R., Santos, M.A., Ramirez, M.A. et al. (2008). Relationship between grain-boundary capacitance and bulk shallow donors in SnO_2 polycrystalline semiconductor. *Physica Status Solidi A* 205 (7): 1694–1698.

39 Hua, Z.Q., Wang, H.Q., Zhao, H.W. et al. (2010). Study on the nonlinear I-V characteristics of tungsten trioxide ceramics. *Journal of Functional Materials* 41 (8): 1343–1346.

40 Hua, Z.Q., Wang, H.Q., Zhao, H.W. et al. (2010). Varistor behavior and mechanism of tungsten trioxide ceramics. *Journal of the Chinese Ceramic Society* 38 (8): 1415–1419.

41 Wang, W.Y., Zhang, D.F., Xu, T. et al. (2002). Nonlinear electrical behavior and dielectric properties of (Ca, Ta)-doped TiO_2 ceramics. *Journal of Alloys and Compounds* 335 (1–2): 210–215.

42 Li, C.P., Wang, J.F., Su, W.B. et al. (2003). Effect of sinter temperature on the electrical properties of TiO_2-based capacitor–varistors. *Materials Letters* 57 (8): 1400–1405.

43 Li, C., Wang, J., Wang, X. et al. (2001). Nonlinear electrical properties of TiO_2–Y_2O_3–Nb_2O_5 capacitor-varistor ceramics. *Materials Science and Engineering B* 85 (1): 6–10.

44 Oliveira, M.M., Pessoa, P.A.P., Brito, R.L. et al. (2016). WO_3-based varistors-a review. *Matéria (Rio de Janeiro)* 21 (1): 105–114.

45 Makarov, V.O. and Trontelj, M. (1996). Sintering and electrical conductivity of doped WO_3. *Journal of the European Ceramic Society* 16 (7): 791–794.

46 Wang, Y., Yang, X.S., Liu, Z.L., and Yao, K.L. (2004). Varistor effect of WO_3-based ceramics at high temperatures. *Materials Letters* 58 (6): 1017–1019.

47 Dai, J., Tang, C.Q., and Zhang, Y. (2005). Effect of Y_2O_3 on WO_3 capacitor-varistor ceramics. *Journal of Huazhong University of Science and Technology* 33 (6): 120–122.
48 Syagailo, A.L. and Makarov, V.O. (2001). Electrical properties of WO_3-based ceramics. *Inorganic Materials* 37 (3): 311–313.
49 Wang, H., Gan, Y., Dong, X. et al. (2012). Thermoelectric properties of Ti-doped WO_3 ceramics. *Journal of Materials Science: Materials in Electronics* 23 (12): 2229–2234.
50 Komornicki, S., Radecka, M., and Sobaś, P. (2004). Structural, electrical and optical properties of TiO_2–WO_3 polycrystalline ceramics. *Materials Research Bulletin* 39 (13): 2007–2017.
51 Regragui, M., Jousseaume, V., Addou, M. et al. (2001). Electrical and optical properties of WO_3 thin films. *Thin Solid Films* 397 (1–2): 238–243.
52 Park, K., Ko, K.Y., Seo, W.S. et al. (2007). High-temperature thermoelectric properties of polycrystalline $Zn_{1-x-y}Al_xTi_yO$ ceramics. *Journal of the European Ceramic Society* 27 (2–3): 813–817.
53 Hua, Z., Dong, L., Wang, H. et al. (2011). Varistor behavior study in undoped tungsten trioxide ceramic. *Physica B: Condensed Matter* 406 (14): 2807–2810.
54 Wang, H., Peng, S., Hua, Z. et al. (2011). Effect of temperature on the electrical properties of ($WO_3{\cdot}Co_2O_3$) composite. *Physica B: Condensed Matter* 406 (22): 4183–4187.
55 Wang, H., Hua, Z., Peng, S. et al. (2012). Effect of CeO_2 on the thermoelectric properties of WO_3-based ceramics. *Ceramics International* 38 (2): 1133–1137.
56 Wang, H., Dong, X., Peng, S. et al. (2012). Improvement of thermoelectric properties of WO_3 ceramics by ZnO addition. *Journal of Alloys and Compounds* 527: 204–209.
57 Patil, P.S., Mujawar, S.H., Inamdar, A.I. et al. (2005). Structural, electrical and optical properties of TiO_2 doped WO_3 thin films. *Applied Surface Science* 252 (5): 1643–1650.
58 Aguir, K., Lemire, C., and Lollman, D.B.B. (2002). Electrical properties of reactively sputtered WO_3 thin films as ozone gas sensor. *Sensors and Actuators B: Chemical* 84 (1): 1–5.
59 Pintér, Z., Sassi, Z., Kornely, S. et al. (2001). Thermal behaviour of WO_3 and WO_3/TiO_2 materials. *Thin Solid Films* 391 (2): 243–246.
60 Cora, F., Patel, A., Harrison, N.M. et al. (1996). An ab initio Hartree–Fock study of the cubic and tetragonal phases of bulk tungsten trioxide. *Journal of the American Chemical Society* 118 (48): 12174–12182.
61 Ramana, C.V., Utsunomiya, S., Ewing, R.C. et al. (2006). Structural stability and phase transitions in WO_3 thin films. *The Journal of Physical Chemistry B* 110 (21): 10430–10435.
62 Radecka, M., Sobas, P., Wierzbicka, M., and Rekas, M. (2005). Photoelectrochemical properties of undoped and Ti-doped WO_3. *Physica B: Condensed Matter* 364 (1–4): 85–92.
63 Gillet, M., Mašek, K., and Gillet, E. (2004). Structure of tungsten oxide nanoclusters. *Surface Science* 566-568: 383–389.

64 Wang, Y., Aburas, Z., and Yao, K. (1999). Anomalous temperature effect of nonlinearity of WO_3 varistor doped with Al_2O_3. *Chinese Science Bulletin* 44 (7): 671–672.
65 Wang, Y., Yang, X.S., Li, Z.Q. et al. (2004). Current–voltage characteristics and grain growth of Li_2CO_3-doped tungsten trioxide ceramics. *Materials Research Bulletin* 39 (10): 1459–1467.
66 Liu, Z.L., Yang, L.F., Wang, Y. et al. (2004). Nonlinear current–voltage characteristics of sintered tungsten–vanadium oxide. *Chinese Physics* 13 (4): 522–528.
67 Chen, M., Liu, Z., Wang, C. et al. (2004). Temperature characteristics of electrical behavior of W-Bi-Ti-O ceramics at low field. *Chinese Science Bulletin* 49 (4): 313–316.
68 Dong, L., Wang, Y., and Zhao, Y. (2007). The study on electrical behavior of Gd_2O_3–WO_3 complex ceramics at high temperature. *Materials Letters* 61 (10): 2105–2108.
69 Hongwang, Z., Zhongqiu, H., Tongye, L. et al. (2010). Origin of varistor properties of tungsten trioxide (WO_3) ceramics. *Journal of Semiconductors* 31 (2): 023001.
70 De Wijs, G.A., De Boer, P.K., De Groot, R.A., and Kresse, G. (1999). Anomalous behavior of the semiconducting gap in WO_3 from first-principles calculations. *Physical Review B* 59 (4): 2684.

Index

d

e

f

g

h

i

l

m

n

o

p